

AFRL-ML-WP-TR-2001-4159

**IMPROVED HIGH-CYCLE FATIGUE
(HCF) LIFE PREDICTION**

J.P. Gallagher, R.H. vanStone, R.E. deLaneuville, P. Gravett, R.S. Bellows, D.C. Slavik, S.J. Hudak, T.J. Dunyak, A.P. Berens, T.N. Farris, K.S. Chan, R.E. McClung, C.G. Annis, D.M. Corbly, A.F. Grandt, D.L. Anton, P. Kurath, J.W. Sheldon, C.A. Weeks, Y.N. Lenets, B.H. Lawless, and J.J. Ruschau

University of Dayton Research Institute
300 College Park
Dayton, OH 45469-0120



JANUARY 2001

Final Report for 19 December 1996 – 31 December 1999

Approved for public release; distribution is unlimited.

**MATERIALS AND MANUFACTURING DIRECTORATE
AIR FORCE RESEARCH LABORATORY
AIR FORCE MATERIEL COMMAND
WRIGHT-PATTERSON AIR FORCE BASE, OH 45433-7750**

NOTICE

WHEN GOVERNMENT DRAWINGS, SPECIFICATIONS, OR OTHER DATA ARE USED FOR ANY PURPOSE OTHER THAN IN CONNECTION WITH A DEFINITELY GOVERNMENT-RELATED PROCUREMENT, THE UNITED STATES GOVERNMENT INCURS NO RESPONSIBILITY OR ANY OBLIGATION WHATSOEVER. THE FACT THAT THE GOVERNMENT MAY HAVE FORMULATED OR IN ANY WAY SUPPLIED THE SAID DRAWINGS, SPECIFICATIONS, OR OTHER DATA, IS NOT TO BE REGARDED BY IMPLICATION OR OTHERWISE IN ANY MANNER CONSTRUED, AS LICENSING THE HOLDER OR ANY OTHER PERSON OR CORPORATION, OR AS CONVEYING ANY RIGHTS OR PERMISSION TO MANUFACTURE, USE, OR SELL ANY PATENTED INVENTION THAT MAY IN ANY WAY BE RELATED THERETO.

THIS REPORT HAS BEEN REVIEWED BY THE OFFICE OF PUBLIC AFFAIRS (ASC/PA) AND IS RELEASABLE TO THE NATIONAL TECHNICAL INFORMATION SERVICE (NTIS). AT NTIS, IT WILL BE AVAILABLE TO THE GENERAL PUBLIC, INCLUDING FOREIGN NATIONS.

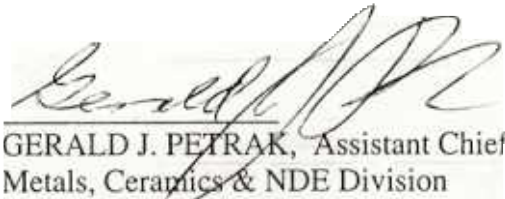
THIS TECHNICAL REPORT HAS BEEN REVIEWED AND IS APPROVED FOR PUBLICATION.



JEFFREY R. CALCATERRA, Project Engineer
Metals Branch
Metals, Ceramics & NDE Division



ROLLIE E. DUTTON, Acting Chief
Metals Branch
Metals, Ceramics & NDE Division



GERALD J. PETRAK, Assistant Chief
Metals, Ceramics & NDE Division
Materials & Manufacturing Directorate

IF YOUR ADDRESS HAS CHANGED, IF YOU WISH TO BE REMOVED FROM OUR MAILING LIST, OR IF THE ADDRESSEE IS NO LONGER EMPLOYED BY YOUR ORGANIZATION, PLEASE NOTIFY, AFRL/MLLM, WRIGHT-PATTERSON AFB OH 45433-7817 AT (937) 255-9819 TO HELP US MAINTAIN A CURRENT MAILING LIST.

COPIES OF THIS REPORT SHOULD NOT BE RETURNED UNLESS RETURN IS REQUIRED BY SECURITY CONSIDERATIONS, CONTRACTUAL OBLIGATIONS, OR NOTICE ON A SPECIFIC DOCUMENT.

REPORT DOCUMENTATION PAGE				<i>Form Approved</i> OMB No. 0704-0188	
The public reporting burden for this collection of information is estimated to average 1 hour per response, including the time for reviewing instructions, searching existing data sources, gathering and maintaining the data needed, and completing and reviewing the collection of information. Send comments regarding this burden estimate or any other aspect of this collection of information, including suggestions for reducing this burden, to Department of Defense, Washington Headquarters Services, Directorate for Information Operations and Reports (0704-0188), 1215 Jefferson Davis Highway, Suite 1204, Arlington, VA 22202-4302. Respondents should be aware that notwithstanding any other provision of law, no person shall be subject to any penalty for failing to comply with a collection of information if it does not display a currently valid OMB control number. PLEASE DO NOT RETURN YOUR FORM TO THE ABOVE ADDRESS.					
1. REPORT DATE (DD-MM-YY) January 2001		2. REPORT TYPE Final		3. DATES COVERED (From - To) 12/19/1996 – 12/31/1999	
4. TITLE AND SUBTITLE IMPROVED HIGH-CYCLE FATIGUE (HCF) LIFE PREDICTION				5a. CONTRACT NUMBER F33615-96-C-5269	
				5b. GRANT NUMBER	
				5c. PROGRAM ELEMENT NUMBER 62102F	
6. AUTHOR(S) J.P. Gallagher, R.H. vanStone, R.E. deLaneuville, P. Gravett, R.S. Bellows, D.C. Slavik, S.J. Hudak, T.J. Dunyak, A.P. Berens, T.N. Farris, K.S. Chan, R.E. McClung, C.G. Annis, D.M. Corbly, A.F. Grandt, D.L. Anton, P. Kurath, J.W. Sheldon, C.A. Weeks, Y.N. Lenets, B.H. Lawless, and J.J. Ruschau				5d. PROJECT NUMBER 4347	
				5e. TASK NUMBER 23	
				5f. WORK UNIT NUMBER 03	
7. PERFORMING ORGANIZATION NAME(S) AND ADDRESS(ES) University of Dayton Research Institute 300 College Park Dayton, OH 45469-0120				8. PERFORMING ORGANIZATION REPORT NUMBER	
9. SPONSORING/MONITORING AGENCY NAME(S) AND ADDRESS(ES) Materials and Manufacturing Directorate Air Force Research Laboratory Air Force Materiel Command Wright-Patterson AFB, OH 45433-7750				10. SPONSORING/MONITORING AGENCY ACRONYM(S) AFRL/MLLMN	
				11. SPONSORING/MONITORING AGENCY REPORT NUMBER(S) AFRL-ML-WP-TR-2001-4159	
12. DISTRIBUTION/AVAILABILITY STATEMENT Approved for public release; distribution is unlimited.					
13. SUPPLEMENTARY NOTES Report contains color.					
14. ABSTRACT An overall building block approach facilitated the development and adaptation of models for immediate application to each of the three in-service generated damage states (the foreign object damage (FOD) and fretting damage models are dependent on the low cycle fatigue / high cycle fatigue (LCF/HCF) and base-line models). The program demonstrated the overall approach for developing methods that can be adapted and integrated into engine company design practices. Approaches and models were developed to set go, no-go limits for predicting the onset of HCF- induced failures; these can be adapted and incorporated into engine company design systems and address: threshold crack nucleation and propagation behaviors, mean stresses, multiaxial stress states, load interaction (LCF/HCF) loadings, notch shapes, FOD, and contact conditions and fretting. In addition to these overall accomplishments, a great number of individual accomplishments in the baseline and LCF/HCF areas provided synergism for generating accomplishments in the FOD and fretting damage areas.					
15. SUBJECT TERMS High Cycle Fatigue, Low Cycle Fatigue, fretting damage, foreign object damage (FOD), intrinsic material capability (stress threshold), crack nucleation, and propagation behavior.					
16. SECURITY CLASSIFICATION OF:			17. LIMITATION OF ABSTRACT: SAR	18. NUMBER OF PAGES 1158	19a. NAME OF RESPONSIBLE PERSON (Monitor) Jeffrey R. Calcaterra 19b. TELEPHONE NUMBER (Include Area Code) (937) 255-1360
a. REPORT Unclassified	b. ABSTRACT Unclassified	c. THIS PAGE Unclassified			

Table of Contents

<u>Chapter</u>		<u>Page</u>
	Foreword.....	xvi
	Executive Summary.....	xviii
1	The HCF Problem and an Overview of the Approach.....	1-1
1.1	Root-Causes of HCF Problems	1-1
1.2	Limitations of Existing Analyses	1-2
1.3	Program Objective.....	1-3
1.4	Overview of Approach	1-3
1.5	Report Organization	1-6
2	Accomplishments and Recommendations	2-1
2.1	Overall Program Accomplishments	2-2
2.1.1	Design Life Methods	2-3
2.1.2	Baseline Characterization	2-3
2.1.3	LCF-Induced Damage	2-6
2.1.4	Foreign Object Impact Damage	2-6
2.1.5	Attachment Fatigue-Induced Damage	2-8
2.2	Exit Criteria	2-10
2.3	Recommendations	2-12
3	Characterizing Material Behavior - Methods and Baseline Data	3-1
3.1	Ti-6AL-4V Forged Blade Material Pedigree.....	3-3
3.2	Fatigue Crack Growth Behavior and Threshold Modeling	3-5
3.2.1	Fatigue Crack Growth Rate Behavior	3-5
3.2.1.1	Basic Material Fatigue Crack Growth Rate Behavior	3-5
3.2.1.2	Short Crack Propagation Test Results	3-8
3.2.2	Crack Growth Rate Models.....	3-11
3.2.2.1	Closure-Based Sinh Crack Growth Rate Model ...	3-11
3.2.2.2	Walker Model for Stress Ratio Effects	3-13
3.2.3	Modeling Threshold Behavior	3-15
3.2.3.1	Long Crack Modeling	3-15
3.2.3.2	Small Crack Modeling	3-16
3.3	Undamaged Material Baseline Behavior and Modeling.....	3-17
3.3.1	Smooth Specimen Material Behavior	3-17
3.3.1.1	Low Cycle Fatigue (LCF) Life Behavior.....	3-17
3.3.1.2	Baseline HCF Stress Ratio Behavior.....	3-18

Table of Contents (Continued)

<u>Chapter</u>	<u>Page</u>
3.3.1.3	Constant Life Diagrams..... 3-19
3.3.1.4	Effects of Specimen Geometry, Frequency and Surface Test Conditions..... 3-20
3.3.1.5	Smooth Specimen Multiaxial Test Data 3-23
3.3.2	Smooth Specimen Models..... 3-23
3.3.2.1	Stress Invariant Methods..... 3-25
3.3.2.2	Critical Plane Methods 3-29
3.4	Modeling Notch Fatigue Behavior 3-32
3.4.1	Notch Fatigue Behavior 3-32
3.4.2	Finite Element Modeling of Notched Specimens 3-35
3.4.3	Calculation of Critical Stresses or Strain Parameters 3-35
3.4.3.1	Stress Invariant Fatigue Analysis Methods 3-35
3.4.3.2	Critical Plane Methods 3-37
3.5	Exit Criterion for Baseline 3-40
3.5.1	Crack Growth Threshold..... 3-40
3.5.2	Smooth Specimen Threshold 3-42
3.5.3	Notched Specimen Threshold Stresses 3-44
3.6	Baseline Behavior Summary & Recommendations..... 3-47
3.6.1	Baseline Data Collection and Analysis 3-47
3.6.2	Models for Threshold Behaviors 3-48
3.6.3	Baseline for Exit Criteria 3-49
3.6.4	Recommendations..... 3-50
3.6.4.1	Material Behavior and Modeling..... 3-50
3.6.4.2	Exit Criteria..... 3-51
3.7	References..... 3-52
Chapter 3 Appendices	
3A	Summary of the Available Information on the Processing of the TI 6AL-4V HCF/LCF Program Plates 3A-0
3B	Crack Growth 3B-0
3C	Nucleation and Propagation of Small Cracks..... 3C-0
3D	Microstructural Crack Initiation and Growth During the High Cycle Fatigue Damage of a Ti-6Al-4V Alloy 3D-0
3E	Cyclic Stress Strain Behavior 3E-0
3F	Effect of Specimen Geometry and Frequency on HCF Smooth Specimen Behavior 3F-0
3G	Effect of Surface Conditions on Undamaged Material HCF Behavior 3G-0

Table of Contents (Continued)

<u>Chapter</u>		<u>Page</u>
3H	Multiaxial (Biaxial) Fatigue Behavior of Ti-6AL-4V at 20°C	3H-0
3I	Fatigue-Crack-Nucleation Modeling in Ti-6Al-4V for Smooth and Notched Specimens Under Complex Stress States	3I-0
3J	Notch Fatigue	3J-0
3K	Finite Element Modeling of Notched Specimens.....	3K-0
3L	Observations of HCF Nucleation Sites Using SEM	3L-0
3M	Analysis of Load Shed Effects on Fatigue Crack Closure During Threshold Testing.....	3M-0
3N	Short-Crack Threshold Model.....	3N-0
4	Low Cycle Fatigue Damage	4-1
4.1	Background	4-1
4.1.1	Objective and Approach	4-1
4.1.2	Engine LCF Histories.....	4-1
4.1.3	Effects of LCF Cycles on Material Response	4-2
4.1.4	Smooth LCF Fatigue Characterization	4-3
4.2	LCF/HCF Mechanical Testing	4-4
4.2.1	Specimen Test Methods and Analysis.....	4-4
4.2.2	LCF/HCF Test Results.....	4-5
4.2.2.1	LCF/HCF Crack Propagation Results.....	4-5
4.2.2.2	LCF/HCF Fatigue Test Results	4-6
4.2.2.3	Near Threshold Fatigue Crack Growth LCF/HCF Interaction Tests.....	4-10
4.3	LCF/HCF Analytical Modeling	4-10
4.3.1	Long-Crack Growth Models	4-10
4.3.2	Predictions Using Short-Crack Models	4-12
4.4	Exit Criteria for LCF/HCF Damage State.....	4-14
4.5	Summary and Recommendations	4-14
4.6	References	4-14
Chapter 4 Appendices		
4A	LCF/HCF SEM and DISMAP Observations.....	4A-1
4B	Short Crack Life Method for LCF/HCF Interaction.....	4B-1
5	Foreign Object Damage	5-1
5.1	Background	5-1
5.1.1	Objective and Approach	5-1
5.1.2	Engine FOD History	5-1
5.2	FOD Mechanical Testing	5-3

Table of Contents (Continued)

<u>Chapter</u>		<u>Page</u>
	5.2.1 FOD Characterization/Verification - Flex Tests.....	5-3
	5.2.2 FOD Characterization/Verification - Axial Tests.....	5-7
5.3	FOD Analytical Modeling	5-9
	5.3.1 FOD Event Modeling	5-9
	5.3.2 FOD Notch Stress Modeling	5-10
	5.3.3 Nucleation Models	5-11
	5.3.4 Growth Models.....	5-16
	5.3.5 Worst Case Notch (WCN) Model.....	5-19
5.4	Exit Criteria for FOD Damage State/Discussion	5-23
	5.4.1 Overview of the Requirements	5-23
	5.4.2 Stress Concentration Factor Model ($K_t = 3$).....	5-23
	5.4.3 Smith-Watson-Topper Model.....	5-23
	5.4.4 Fracture Mechanics Model	5-26
	5.4.5 Worst Case Notch Model.....	5-26
	5.4.6 Model Summary.....	5-29
5.5	Summary & Recommendations.....	5-30
5.6	References.....	5-31
Chapter 5 Appendices		
5A	Characterization of Service-Induced FOD.....	5A-1
5B	Evaluation of Simulated Foreign Object Damage in Ti-6Al-4V Fan Blades	5B-1
5C	Evaluation of Simulated Foreign Object Damage in Ti-6-4 Fan Blades and All Test Data Resulting from GEAE Portion of Program...	5C-1
5D	Simulated Foreign Object Damage Specimen Preparation Utilizing Ballistic Impact.....	5D-1
5E	FOD Analytical Modeling – FOD Event Modeling	5E-1
5F	Prediction Methodologies for FOD Tests.....	5F-1
5G	Stress and Stress Intensity Factor Analysis of Simulated FOD at an Air Foil Leading Edge	5G-1
5H	Nucleation FOD Modeling and ΔK Threshold FOD Modeling.....	5H-1
5I	Development and Application of Worst Case Notch (WCN) to FOD	5I-1
6	Fretting Damage	6-1
6.1	Background	6-1
	6.1.1 Objective and Approach	6-1
	6.1.2 Engine History	6-4
6.2	Fretting and Fretting-Fatigue Testing	6-5
	6.2.1 Evolution of Coefficient of Friction	6-5
	6.2.2 Fretting and Fretting Fatigue Experiments.....	6-7

Table of Contents (Concluded)

<u>Chapter</u>	<u>Page</u>
6.3	Analysis Methods 6-14
6.3.1	Stress Analysis Methods 6-14
6.3.2	Predicting Crack Nucleation 6-15
6.3.2.1	Equivalent Stress Methods 6-15
6.3.2.2	Life Evaluation Using Critical Plane Method..... 6-18
6.3.3	Predicting Crack Propagation Behavior 6-20
6.3.3.1	Crack Propagation in Fretting Experiments 6-20
6.3.3.2	Worst Case Fretting (WCF) Model Predictions . 6-21
6.4	Exit Criteria 6-24
6.4.1	Overview of the Requirements 6-24
6.4.2	Smith, Watson and Topper (SWT) Model 6-24
6.4.3	Worst Case Fret (WCF) Model 6-25
6.4.4	Summary 6-26
6.5	Discussion, Conclusions, and Recommendations..... 6-27
6.6	References 6-29
Chapter 6 Appendices	
6A	Evaluation of Fretting Parameters 6A-1
6B	Fretting Fatigue of Ti-6Al-4V 6B-1
6C	Characterization of Fretting Fatigue Initiated Cracks..... 6C-1
6D	Simultaneous Fretting and Fatigue of Ti-6Al-4V on Ti-6Al-4V 6D-1
6E	Development and Application of Worst Case Fret (WCF) Model to Attachment Fatigue 6E-1

List of Tables

<u>Table</u>	<u>Page</u>
1.1 Summary of Exit Criteria Statistical Parameters.....	1-5
2.1 Exit Criteria Summary.....	2-10
3.1 Chemistry of the Ti-6Al-4V Billet used in this Program.....	3-3
3.2 Constants for the Hyperbolic Sine Model.....	3-12
3.3 Ti-6Al-4V Sigmoidal Curve (Equations 3.4 and 3.5) Constants at 70°F.....	3-13
3.4 Baseline Statistical Parameters for Crack Growth Threshold Estimates	3-40
3.5 Baseline (Smooth Specimen) Statistical Parameters for Total Life Models	3-43
3.6 Equivalent Stress Model (A/P) Parameters for Uniaxial and Multiaxial Behaviors	3-44
3.7 SWT Model (A/P) Parameters for Uniaxial and Notch Behaviors	3-46
4.1 Two-Stress-Level Mission Testing Blocks Used to Evaluate the Effect of Load Interaction	4-5
4.2 Double notch LCF/HCF Results	4-8
5.1 Summary of FOD Specimens Analyzed with Stress Invariant Models	5-14
5.2 Comparison of FOD Models.....	5-29
6.1 Comparison of Fretting Models	6-26

List of Figures

<u>Figure</u>	<u>Page</u>
1.1 Illustration of In-Service Damage and Blade Locations due to (a) Foreign Object Impacts, and (b) Attachment Distress Caused by High Local Stresses and Relative Displacements in the Contact Region	1-2
1.2 For Each In-Service Damage State Establish the Limiting Stress Levels Associated with HCF Failures.....	1-4
1.3 Exit Criteria Concept for Threshold Models (see Table 1.1 for parameters)	1-5
2.1 Review of Blade HCF Critical Locations provided focus on material characterization and design methods requirements	2-1
2.2 The program demonstrated the overall approach for developing methods that can be adapted and integrated into engine company design practices	2-2
3.1 Interrelationship between Chapter 3 and the Damage State Chapters	3-1
3.2 Building block approach to modeling smooth and notch fatigue	3-2
3.3 Microstructure of the Ti-6Al-4V forgings	3-4
3.4 Fatigue crack growth rate data for R= -1, 0.1, 0.5 and 0.8	3-7
3.5 Threshold stress intensity factor range as a function of stress ratio	3-8
3.6 Fatigue crack propagation rate of naturally initiated “small” cracks as a function of: (a) crack size and (b) stress intensity factor range	3-10
3.7 Stress-ratio behavior modeled with the ΔK_{eff} (Closure) model.....	3-12
3.8 Variation of measured surface-crack growth rates in Ti-6Al-4V at room temperature as a function of (a) ΔK and (b) K_{eff}	3-14
3.9 Threshold models compared to material behavior shown in Figure 3.5	3-15
3.10 Schematic representation of Kitagawa diagram.....	3-16
3.11 Strain-life fatigue data as a function of strain ratio	3-17

List of Figures (Continued)

<u>Figure</u>	<u>Page</u>
3.12 Basic R-ratio tests results for the four stress ratios.....	3-18
3.13 Representative nucleation site from R = 0.1 test.....	3-19
3.14 A Constant Life (10^7 cycles) Haigh (Modified-Goodman) diagram showing the extrapolated non-step fatigue strengths (and 3 sigma limits) and the individual step test fatigue strengths	3-21
3.15 Schematic representation of approach used to develop, calibrate, and validate stress methods	3-24
3.16 Maximum-stress vs. maximum-strain half-life LCF data and cyclic stress-strain curve for Ti-6Al-4V	3-24
3.17 Walker equivalent stress-life curve developed for Ti-6Al-4V	3-27
3.18 Prediction of University of Illinois multiaxial tests results using the modified Manson-McKnight equivalent stress parameter (without R limit)	3-28
3.19 The Smith-Watson-Topper (SWT) model correlation for different stress ratios.....	3-31
3.20 The Findley critical plane shear stress model correlation for different stress ratio conditions.....	3-31
3.21 Basic stress-ratio tests of double notch specimens (R = -1, 0.1, 0.5 and 0.8 and T = 80°F).....	3-33
3.22 Constant life (10^7 cycles) Haigh (Modified-Goodman) diagram showing the extrapolated non-step notch ($K_t = 2.68$, T = 80°F, f = 60 Hz) fatigue strengths.....	3-33
3.23 Effects of two notch geometries on fatigue life, R = 0.1 and T = 80°F	3-34
3.24 Comparison of fatigue of peened and unpeened double notch specimens results (R = -1.0, 0.1 and T = 80°F).....	3-34
3.25 Variation of Weibull-modified alternating equivalent stress for notched specimens with lives of approximately 10^6 cycles	3-37

List of Figures (Continued)

<u>Figure</u>	<u>Page</u>
3.26 Smith-Watson-Topper (SWT) parameter using maximum principal strain amplitude at notch root compared to double edge notch fatigue behavior.....	3-38
3.27 Findley critical plane shear stress parameter at notch root ($k_2 = 0.45$) plane stress analysis.....	3-39
3.28 Normal Distributions of Room Temperature Ti-6Al-4V Crack Growth Thresholds Ratios of Measured vs. Model.....	3-41
3.29 Normal distribution of Ratio of Actual to Predicted Strength for undamaged HCF material data with lives in excess of 10^6 cycles.....	3-42
3.30 Weibull distribution of multiaxial predictions relative to the uniaxial undamaged specimen correlation shown in Figure 3.29.....	3-43
3.31 Normal Distributions of Ratios of Model SWT to Applied SWT for Notched Specimens as Compared to Smooth Specimen Ratios.....	3-45
3.32 Normal Distribution of Ratios of Applied SWT to Model SWT for Notched Specimens by Test Stress Ratio Condition.....	3-46
4.1 Fan blade with typical stress histories at HCF critical locations	4-1
4.2 Cyclic <i>versus</i> monotonic stress-strain results indicates cyclic softening	4-3
4.3 Total strain range <i>versus</i> LCF life for peened and unpeened samples at $R\epsilon = -1.0$, and 0.1	4-4
4.4 Hypothesis used to anticipate the stress intensity factor conditions associated with rapid crack growth under combined LCF/HCF loading.....	4-5
4.5 Surface crack LCF/HCF mission tests, one $R = 0.1$ plus 1000 $R = 0.8$ cycles at the 63 ksi maximum stress level mission (mission 1)	4-7
4.6 Surface crack LCF/HCF mission tests, 5,000 $R = 0.1$ plus 100,000 $R = 0.8$ cycles at the 50 ksi maximum stress level mission (mission 2).....	4-7

List of Figures (Continued)

<u>Figure</u>	<u>Page</u>
4.7 Double notch (60 Hz, R = 0.8, 80°F) HCF results indicating LCF/HCF step tests results yield lower 10^7 failure lives compared with conventional S-N results and constant stress ratio step tests.....	4-9
4.8 Double notch (60 Hz, R = 0.5, 80°F) HCF results indicating LCF/HCF step tests yield higher 10^7 failure lives compared with conventional S-N data and constant stress ratio step tests	4-9
4.9 Prediction of surface crack LCF/HCF mission 1 tests, Mission 1 has a 63 ksi maximum stress and 1001 cycles per mission (one cycle of R = 0.1 loading followed by 1000 cycles of R = 0.8)	4-11
4.10 Prediction of surface crack LCF/HCF mission 2 tests, Mission 2 has a 50 ksi maximum stress (5,000 cycles of R = 0.1 followed by 100,000 cycles of R = 0.8 cycles).....	4-11
4.11 Predictions of allowable LCF cycles before HCF threshold is exceeded, based on proposed simple LCF/HCF interaction model (stress histories expressed in terms of maximum stresses).....	4-13
4.12 Predictions of allowable LCF cycles before HCF threshold is exceeded, based on proposed simple LCF/HCF interaction model (stress histories expressed in terms of stress ranges).....	4-13
5.1 Percentage of FOD located at span locations relative to the blade tips.....	5-2
5.2 Cumulative frequency diagram of FOD depth.....	5-2
5.3 The FOD flexure specimen design.....	5-3
5.4 Comparison of blade and winged specimen stresses	5-4
5.5 Representative FOD from ballistic and solenoid gun impacts (Sharp LE Specimens, 30° Impacts, High Damage Levels)	5-5
5.6 Step test results for FOD specimens with machined notches (R=0.5).....	5-6
5.7 Comparison of S-N and Step Test Results Solenoid Gun, 30° Impacts, High Damage Levels, R=0.5).....	5-6

List of Figures (Continued)

<u>Figure</u>	<u>Page</u>
5.8 Effect of FOD notch depth and tip radius on 10^6 Step Test Durability. (Sharp LE Specimens, 30° Impact, R=0.5).....	5-7
5.9 Effect of Impact Angle. (Sharp LE, Solenoid Gun, Low Damage, 0.005 inch Indentor, R=0.5). Step Test Results.....	5-7
5.10 Effect of Stress Relief after FOD. (Sharp LE, Solenoid Gun, 0.005 inch Indentor, 30° Impact, R=0.5, No EPD). Step Test Results.....	5-7
5.11 FOD data for DCT specimens versus the baseline smooth bar data	5-9
5.12 FOD impact deformation measurements and predictions	5-10
5.13 Spanwise residual stress field (ksi) for blunt edge DCT specimen impacted by 1.33 mm steel ball at 1000 ft/sec at different angles.....	5-10
5.14 DYTRAN predictions (ksi) for blunt (0.015-inch) edge DCT specimen impacted with 1.33 mm ball at 1000 ft/sec and loaded in spanwise tension ..	5-12
5.15 Notch Dimensions for FEM Model of Winged Specimen with FOD	5-13
5.16 Stress contour plot from FEA of a low energy impact in a sharp LE	5-13
5.17 Comparison of predicted 10^6 cycle effective stress for FOD specimens to smooth bar results.....	5-13
5.18 Representative geometry and ANSYS stress predictions for unit tension and bending loads	5-14
5.19 Nucleation modeling is conservative, and shows significant bias	5-15
5.20 Nucleation modeling (w/stress area model) is conservative with bias.....	5-15
5.21 ANSYS model of a corner crack in a sharp tip FOD specimen with low damage, and comparison between predicted stress intensities from fracture code solutions and ANSYS solutions	5-16

List of Figures (Continued)

<u>Figure</u>	<u>Page</u>
5.22 Largest initial crack sizes such that $K \leq K_{th}$ for several FOD specimens containing simulated FOD and machined notches.....	5-17
5.23 Representative geometries and K vs. a from the Stress intensity prediction parametric (normalized $K = K$ for a unit load)	5-18
5.24 Stress intensity predictions (ΔK) vs. Notch depth (0.001-inch corner crack).....	5-18
5.25 Predicted $K_{residual}$ vs. notch depth.....	5-18
5.26 Modeling which accounts for $K_{residual}$ correlates well to data	5-20
5.27 WCN model predicts crack nucleation, growth and arrest, and failure	5-21
5.28 WCN model predictions versus data from FOD simulation tests	5-22
5.29 Actual/Predicted Values from $K_I=3$ Model without area correction.....	5-24
5.30 Actual/Predicted Values from SWT with Area Correction.....	5-25
5.31 Actual/Predicted Values from ΔK_{th} with $K_{residual}$ Model	5-27
5.32 Actual/Predicted Values from Worst Case Notch Model.....	5-28
6.1 Disk blade attachment and schematic diagram of the HCF critical features in the attachment	6-2
6.2 Schematic diagram of fretting design system.....	6-3
6.3 Examples of (a) fretting damage at attachments, (b) SEM micrograph of fretted surface, (c) metallographic cross-sections, and (d) laser profilometer traces of surface roughness in field hardware.....	6-4
6.4 Fretting parameter selection for fretting and fretting fatigue evaluations	6-6
6.5 SEM micrographs showing scars from fretting specimens with (a) 0.003-inch and (b) 0.0008-inch relative displacements	6-6
6.6 Evolution of Coefficient of friction.....	6-7

List of Figures (Concluded)

<u>Figure</u>	<u>Page</u>
6.7 Results of selected fretting experiments performed at UTRC	6-8
6.8 Drawing of the 0.12-inch fretting pin configuration (Dimensions in inches)	6-9
6.9 Fatigue Life results of post-fretting R = 0.5 HCF tests (SP = Shot peened) ...	6-10
6.10 Observations of (a) nonpropagating microcracks observed on pad-specimen contact surface after 10^7 cycles and (b) typical multiple crack nucleation sites observed on the fracture surface	6-12
6.11 Photograph of a specimen after 37000 cycles of bending test, following a fretting-fatigue run-out	6-13
6.12 Comparison of surface normal tractions obtained from integral equation and FEM methods	6-15
6.13 FEM analysis of 55 ksi, 0.0015-inch fretting experiment showing (a) spatial distribution of stress components and (b) corresponding fatigue cycle	6-17
6.14 Weibull-adjusted equivalent stress predictions for two fretting test conditions	6-18
6.15 Comparison of predicted nucleation lives with experimental lives	6-19
6.16 Comparisons of crack sizes observed in fretting specimens with fracture mechanics predictions	6-21
6.17 Predicted threshold stresses for crack nucleation, nonpropagation and propagation to failure compared to fretting fatigue data (UTRC and SwRI) and fretting data (GEAE)	6-23
6.18 Normal cumulative distribution of actual to predicted values of the Smith, Watson and Topper parameter for fretting fatigue crack initiation (0.004-inch deep cracks)	6-25
6.19 Normal cumulative distribution of actual to predicted values of the Smith, Watson and Topper parameter for fretting fatigue crack initiation (0.004-inch deep cracks)	6-26

Foreword

This program addressed the key issues associated with developing, verifying and implementing a material damage tolerance based design methodology capable of predicting high-cycle fatigue (HCF) limits. These limits are essential for preventing failures that could result from HCF loading applied to components which potentially contain in-service damage, such as created by HCF loading, attachment distress, and foreign object impacts. The methodology is anchored in fundamental mechanics and is developed for use in applications like the design of the Joint Strike Fighter (JSF) engine. The focus in this program was on the development of fracture mechanics and total life methods that can be applied primarily to control the potential for HCF failures in fan and compressor blades.

The Air Force Office of Scientific Research (AFOSR) sponsored this program, which was entitled "Improved High Cycle Fatigue (HCF) Life Prediction", under contract F33615-96-C-5269; Major Brian Sanders acted as the Air Force's contract monitor. Mr. Joseph G. Burns of the Air Force Research Laboratory, Materials and Manufacturing Directorate (AFRL/ML) at Wright Patterson Air Force Base, OH, acted as the technical monitor for the program. Dr. Theodore Nicholas of AFRL/ML acted as technical advisor to Mr. Burns and the contract team. The University of Dayton Research Institute (UDRI) managed this damage tolerant design technology development and verification contract for the Air Force. Organizations that supported this UDRI contract were Pratt & Whitney Aircraft (P&W), General Electric Aircraft Engines (GEAE), Honeywell Engines (previously, Allied Signal Engines), Allison Advanced Development Corporation (AADC), Southwest Research Institute (SwRI), Purdue University, United Technologies Research Center (UTRC), University of Illinois, and SRI, International.

The management structure of the program focused on addressing the type of damage that could occur in-service within a damage-state team structure. There were three damage-state teams that each addressed the effects of a specific type of in-service damage that could reduce the HCF resistance of

engine fan blade hardware. These teams were led by engine company representatives to ensure that the efforts would address engine hardware design needs. The damage-state teams and their leaders were as follows:

- LCF/HCF Damage Team, lead Robert deLaneuville (P&W), co-lead Robert vanStone (GEAE)
- FOD Damage Team, lead Philip Gravett (P&W), co-lead Thomas Dunyak (GEAE)
- Fretting Damage Team, lead Robert vanStone (GEAE), co-lead Donald Hunter (P&W)

The program managers (PM) and other key contributors involved in the program were as follows:

- For UDRI, Joseph Gallagher/Alan Berens (PM), Allan Gunderson, John Ruschau, Peggy Miedlar, Alicia Hutson, Brian Frock, Gloria Hardy, James Sebastian
- For P&W, Charles Annis (PM), Robert deLaneuville, Phillip Gravett, Jerry Sheldon, Donald Hunter, Tara McGovern, David Walls, Edward Hindle, Rajik Naik, Brad Cowles, Robert Morris
- For GEAE, Dennis Corbly (PM), Robert vanStone, Thomas Dunyak, Barney Lawless, Donald Slavik, Michael Hartle, Robert McClain, Ken Wright, Douglas Deaton, Kenneth Bain
- For Honeywell, Howard Merrick/Bernie Hoffman (PM), Richard Bellows, James Hall, Yuri Lenets, James Hartman
- For AADC, Kenneth Cornet/Charles Teague (PM), Douglas Herrmann, Craig Weeks, Phillip Bastnagel
- For SwRI, Stephen Hudak (PM), Kwai Chan, Craig McClung, David Davidson, Andy Nagy, Graham Chell, Yi-Der Lee
- For Purdue, Alten Grandt (PM), Thomas Farris, Harish Ganapathy
- For UTRC, Donald Anton
- For University of Illinois, Peter Kurath
- For SRI, Donald Shockey (PM), Takao Kobayashi.

Executive Summary

High cycle fatigue (HCF) is *not* low cycle fatigue (LCF) at a higher frequency. The recognition of this fact forms the cornerstone of efforts to mitigate the potential for HCF failures. Typically, HCF failures only occur after millions of repeated load (stress) applications. In aircraft engines, high cycle fatigue *occurs* due to both steady-state and intermittent vibratory loading of engine components; this loading occurs during engine operation (and, thus, in conjunction with low cycle fatigue loading). HCF loading is caused by aerodynamic loading, mechanical vibration, airfoil flutter, acoustic fatigue, and complex interactions among these, and can reach loading frequencies above tens of kilohertz. Methods that are so successful in controlling LCF failures have often been found ineffective in dealing with HCF failures since the ability to describe the behavior of a crack may not be useful if the propagation time to failure is measured in minutes, even if the cycle count is measured in millions. (At 20 kHz, a blade can accumulate more than a million cycles in less than a minute.) The traditional approach to mitigating HCF failures is to ensure that the applied vibratory stress levels are kept sufficiently low (below an intrinsic material capability, or stress threshold) such that cracks would not be expected to initiate for these levels.

The USAF and its allies have experienced aircraft engine cracking incidents in fan, compressor, and turbine components that have severely limited operational readiness and been the cause of high maintenance costs. High cycle fatigue damage, exacerbated by LCF, attachment distress, foreign object damage (FOD), inherent material heterogeneities, and other damage types, has been identified as a significant contributor to these events. Further, there is an impending requirement to begin design of Joint Strike Fighter (JSF) engines in the 2001-2004 timeframe. The cornerstone of the JSF Program is affordability and the design of the system is known to be the fundamental influence on operation and support costs of the propulsion subsystem.

In response to these concerns about loss of operational readiness, maintenance costs, and the adequacy of the HCF design systems used by the aircraft engine

companies, the National Turbine Engine High Cycle Fatigue Science and Technology Program was begun. The Materials Damage Tolerance Action Team of this Program has placed major emphasis on the development of a new damage tolerance life prediction and design methodology for turbine engine rotating structures subjected to high-stress-ratio, HCF loadings. This report chronicles the progress of Phase I of this methodology development, funded under USAF Contract Number F33615-96-C-5269, and aimed primarily at titanium fan and compressor airfoil components because of the historical importance of HCF in these components. The focus of this effort was to develop improved HCF methods for setting design limits for situations where the intrinsic material capability (stress threshold) has been reduced by in-service damage created by LCF loading, FOD, and attachment distress (fretting), i.e., damage which is expected to occur during normal engine operation. Both fracture mechanics and fatigue life methods were found useful in setting design thresholds that accounted for in-service damage. This development work was performed on Ti-6Al-4V with processing and microstructural features representative of turbine engine airfoils.

The work on this contract was performed by a team of engine manufacturers and research organizations that had the wherewithal to (a) define the requirements, (b) contribute to material understanding necessary to establishing HCF threshold methods, develop enhanced methods for accounting for in-service damage, and (d) verify these methods. The UDRI led team included Pratt & Whitney, General Electric Aircraft Engines, Honeywell, Allison Advanced Development Corporation, Southwest Research Institute, Purdue University, the University of Illinois, Universal Technology Research Center, and SRI, International.

This program was performed in parallel with an Air Force-sponsored Multidisciplinary University Research Initiative (MURI) program that was conducted and managed by the University of California (Berkeley). The focus of the MURI program (High-Cycle Fatigue and Time-Dependent Failure in Metallic Alloys for Propulsion Systems, grant number F49620-96-1-0478) was to establish advanced analytical and materials understanding of the crack nucleation and propagation behavior under HCF loading conditions. Joint meetings were periodically held to share findings and define future requirements.

A follow-on Air Force program (Advanced High Cycle Fatigue Life Assurance Methodologies, contract number F49620-99-C-0007) expands the evaluation of HCF methods that address threshold behaviors in other materials and for other conditions. The follow-on program also addresses the validation of methods believed ready for design system implementation. Recommendations developed from this contractual effort (F33615-96-C-5269) are being pursued in the follow-on program.

Chapter 1

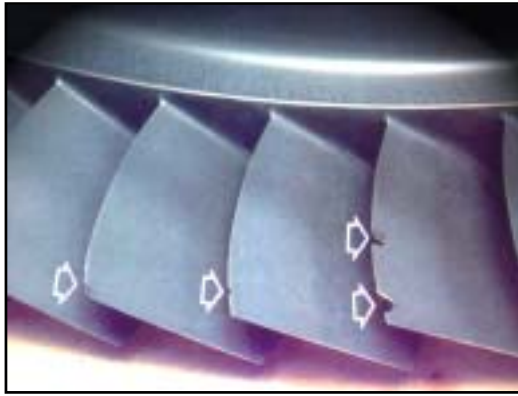
The HCF Problem and an Overview of the Approach

1.1 ROOT-CAUSES OF HCF PROBLEMS

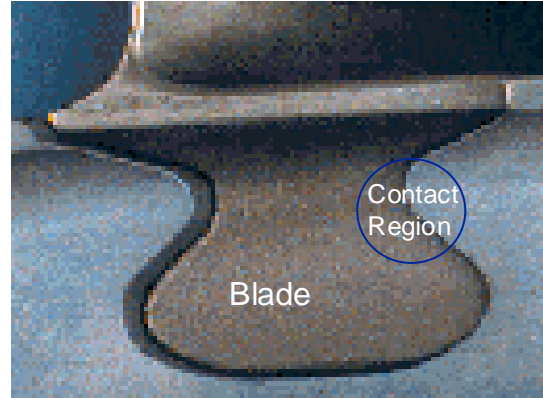
With the advent of damage tolerance methods for Low Cycle Fatigue (LCF) developed and implemented over the past two decades, High Cycle Fatigue (HCF), usually in conjunction with other damage mechanisms, has become the single largest cause of component failure in modern military gas turbine engines. HCF often exacerbates, or is exacerbated by other failure mechanisms including LCF, corrosion, overstress, manufacturing anomalies, mechanical damage and material deficiencies. Further compounding the problem are the myriad potential sources for exciting HCF, including aerodynamic loading, mechanical vibration, airfoil flutter, acoustic fatigue, and complex interactions among these.

HCF affects nearly all engine components, with rotating structures – blades and disks (and spacers) – comprising nearly half of the incidences of HCF, with stationary components – vanes and sheetmetal – adding another 25%. (Airseals, cases and housings and other miscellaneous parts round out the list.) The National HCF Initiative is organized to consider the HCF problem in its entirety, with eight action teams: 1) forced response prediction; 2) instrumentation; 3) aeromechanical characterization; 4) component analysis; 5) passive damping technology; 6) materials damage tolerance; 7) component surface treatments; and 8) engine demonstration. This report focuses on damage tolerance, which, although fundamental to solving the HCF problem, must be considered in concert with these other factors.

Because of their immediate relevancy, fan blades and disks were selected for study in this program. The material response to the HCF threat was organized into three damage state categories: LCF/HCF interaction/synergism, Foreign Object Damage (FOD), and attachment fatigue distress, which includes fretting, galling, and less obvious subsurface distress which may or may not be associated with fretting and galling. In this effort, the attachment fatigue distress is focused on fretting fatigue damage. Figure 1.1 defines typical blade locations where two types of in-service damage occur.



(a)



(b)

Figure 1.1. Illustration of In-Service Damage and Blade Locations due to (a) Foreign Object Impacts, and (b) Attachment Distress Caused by High Local Stresses and Relative Displacements in the Contact Region.

1.2 LIMITATIONS OF EXISTING ANALYSES

Before beginning this program, there was the hope that many of the tools used to understand, and thus mitigate, LCF would be directly applicable to HCF. HCF, however, is not LCF at a higher frequency. Cycle counting, fundamental to LCF analysis, has limited utility in a regime where cycle accumulation can be so devastatingly rapid. (At 20 kHz a blade can accumulate more than a million cycles in less than a minute.) This realization argues for methods based on threshold fracture mechanics and/or fatigue endurance stresses. This may have significant implications for more conventional Goodman-type methods. Historically, Goodman limits of 10^7 cycles implied cyclic runout, but this has not borne up under scrutiny: stress-life (S-N) curves for some materials (e.g., Ti-6Al-4V) appear not to have reached an asymptote (if one exists) by 10^7 cycles, and may still exhibit finite lifetimes even at 10^9 cycles. Further, Goodman methods consider only the gross mean and cyclic loadings, and ignore other potential failure modalities. In real applications, the stress state may differ significantly from that under which the Goodman allowables were estimated, influencing, among other things, the local stress ratio. In some instances, failure may be dominated by shear, which is not explicitly considered with the Goodman approach.

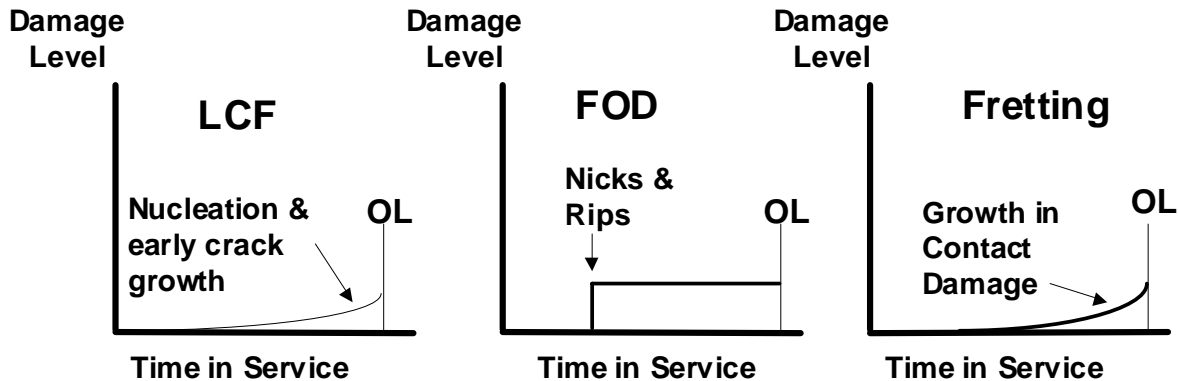
1.3 PROGRAM OBJECTIVE

The objective of this program was to develop and demonstrate damage tolerant design methodologies that could be used by industry to avoid or minimize the occurrence of HCF failures. An especially important part of the objective was to create methodologies that address the prevention of HCF failures for situations where in-service damage might be present. This program addressed the types of damage and material behaviors expected in the fan sections of aircraft turbine engines. The principal types of in-service damage expected to occur in the fan sections are a) LCF damage resulting from principal mission loading conditions, b) FOD impacts, and c) contact-induced fretting fatigue. To simplify the development and demonstration of the methodology, total life and fracture mechanics based models were only developed and demonstrated for one material (an airfoil-grade Ti-6Al-4V) and for room temperature conditions.

1.4 OVERVIEW OF APPROACH

A damage tolerant design approach ensures that a typical in-service damaged blade will not fail from expected HCF load cycles during its design life. Because the expected number of HCF load cycles can be exceedingly large but somewhat indeterminate, go/no-go threshold models provide an attractive approach for establishing the limiting HCF stress levels that prevent typical in-service damage from growing to failure under expected HCF loadings. Both total life and fracture mechanics models can be utilized to establish threshold conditions where defined levels of in-service damage would not be expected to grow to failure under expected HCF loadings. While most people associate damage tolerant design approaches with the use of fracture mechanics models, total life approaches can also be used when the level of in-service damage has been characterized. Total life approaches are based on stress or strain parameters that can be used to predict the nucleation of cracks large enough to cause a fatigue failure. This program took the broad view and considered both total life and fracture mechanics approaches for establishing limiting levels for stress and crack driving force parameters. The program also concentrated on developing the limiting stress conditions for the three in-service damage states illustrated in Figure 1.2.

Approach: “Maximum” Damage in lifetime will not grow to failure under hcf loading; Anticipate (or control) damage level, set hcf allowables



*** OL = operational life limit**

Figure 1.2. For Each In-Service Damage State Establish the Limiting Stress Levels Associated with HCF Failures.

Exit criteria were established to demonstrate improvements in the HCF design methodologies as a result of incorporating go/no-go damage tolerant models. Since the existing design methodologies did not address the effects of in-service damage states on blade resistance to HCF loading, the exit criteria were based on scaled degradations in predicting threshold behavior based on baseline behavior, i.e., without in-service damage. Figure 1.3 summarizes the exit criteria concept for predicting threshold-related behavior. The abscissa (actual/predicted) describes the ratio between the threshold behavior established by testing and the threshold model parameter predictions. Model predictions were based on either stress-based (total life) thresholds or fracture mechanics determined thresholds. Notice that the models for in-service damage estimate a parameter ratio that is about 1.0 for mean (50% occurrence) behavior, but that the scatter experienced by these models is greater than that associated with the baseline (undamaged) material behavior. Table 1.1 summarizes the expectations both for the mean model estimates and for model scatter for each of the three in-service damage states. One additional essential part of the exit criteria is

the requirement that the test data used to establish the model estimating capability does not show any appreciable bias associated with the test parameters, i.e., stress ratio, notch size, etc.

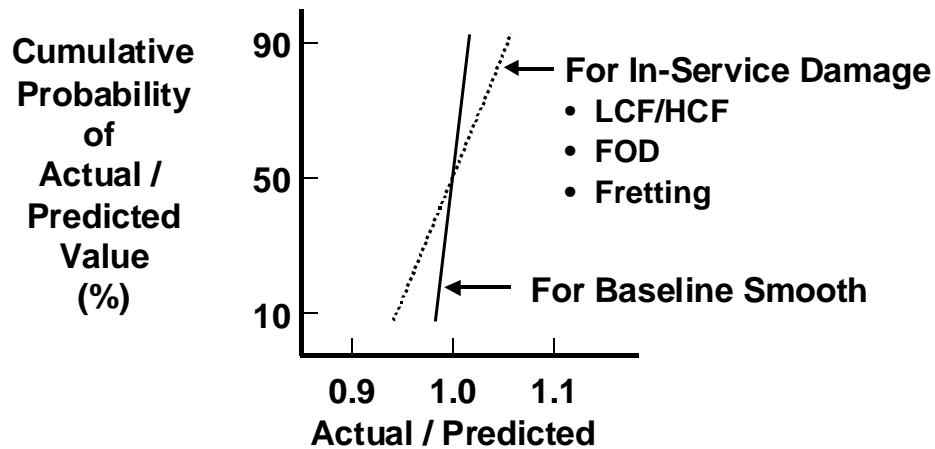


Figure 1.3. Exit Criteria Concept for Threshold Models (see Table 1.1 for parameters).

Table 1.1
Summary of Exit Criteria Statistical Parameters

In-Service Damage State	Threshold Parameters	Mean Target for Models	Model Scatter Target (multiplier applied to baseline scatter)
LCF/HCF Interaction	Net maximum stress, stress-intensity factor, local stress parameter	± 0.05 of 1.0	1.25
FOD	Local stress parameter, stress-intensity factor	± 0.15 of 1.0	2.50
Fretting Fatigue	Net maximum stress	± 0.15 of 1.0	2.50

1.5 REPORT ORGANIZATION

The chapters in this report include:

- Chapter 2 – a summary of conclusions, accomplishments, and recommendations
- Chapter 3 – a summary of basic modeling information and the baseline data used for predicting the effects of in-service damage on HCF threshold conditions
- Chapter 4 – the models that describe the interactions occurring when combined HCF and LCF loadings are applied
- Chapter 5 – the models that predict threshold conditions associated with foreign object damage impacts
- Chapter 6 – the models that predict threshold conditions associated with fretting fatigue damage occurring in attachment areas

Each of the Chapters 3 through 6 are supported by a series of appendices that provide substantially more detail on the data generation and analytical efforts conducted as part of this program.

Chapter 2

Accomplishments and Recommendations

This damage tolerant (DT) materials design methodology program significantly improved the understanding of HCF failure behavior for blades in the cold sections of aircraft turbine engines. This program demonstrated advances in fracture mechanics and total-life prediction models on airfoil grade Ti-6Al-4V material for establishing go/no-go stress limits in blades for three damage-state conditions that increase the potential for fatigue failure when high cycle fatigue (HCF) loading occurs. This program successfully developed and demonstrated mechanics models that addressed in-service generated damage caused by: 1) normal mission-related low cycle fatigue (LCF) loading, 2) foreign object damage (FOD) impacts, and 3) localized contact in attachment regions which leads to fretting. Figure 2.1 identifies the blade locations where in-service damage conditions are expected to occur and the loading conditions that these locations experience.

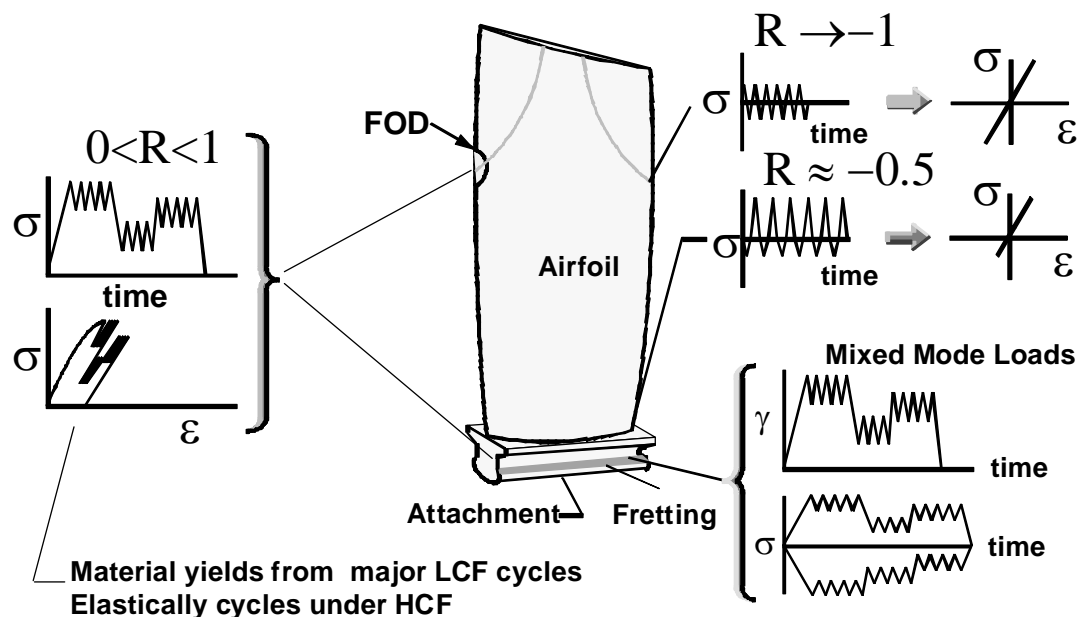


Figure 2.1. Review of Blade HCF Critical Locations provided focus on material characterization and design methods requirements.

2.1 OVERALL PROGRAM ACCOMPLISHMENTS

- ◆ An overall building block approach facilitated the development and adaptation of models for immediate application to each of the three in-service generated damage states (Figure 2.2 illustrates the dependence of FOD and fretting models on the LCF and baseline models, as well as the design requirements).

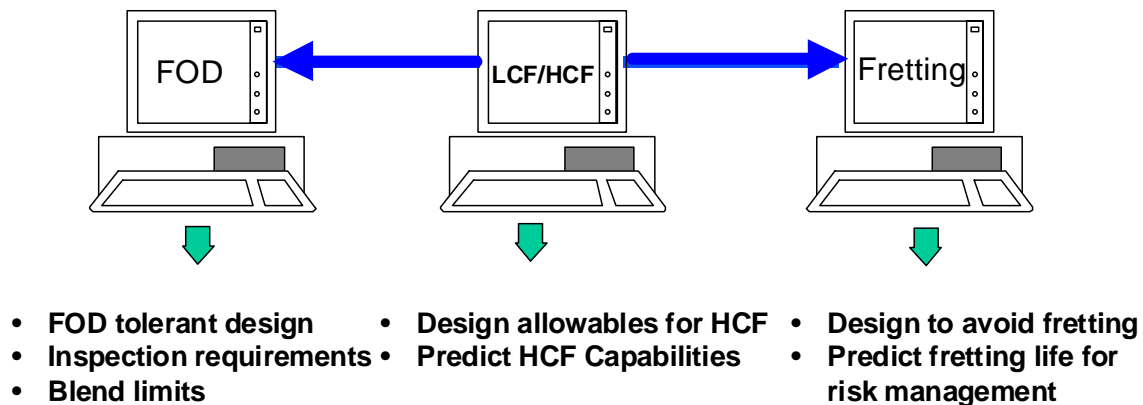


Figure 2.2. The program demonstrated the overall approach for developing methods that can be adapted and integrated into engine company design practices.

- ◆ Approaches/models now exist to set go/no-go limits for predicting the onset of HCF induced failures; these can be adapted and incorporated into engine company design systems and address as follows:
 - Threshold crack nucleation and propagation behaviors
 - Mean stresses
 - Multiaxial stress states
 - Load interaction (LCF/HCF) loadings
 - Notch shapes
 - FOD
 - Contact conditions and fretting
- ◆ In addition to these overall accomplishments, a great number of individual accomplishments in the baseline and LCF/HCF areas provided synergism for generating accomplishments in the FOD and fretting damage areas, as well as vice versa.

2.1.1 Design Life Methods

Current efforts are evaluating methodologies to predict fatigue crack nucleation and propagation capabilities under combined HCF and LCF/HCF cycles. These methods fall into two categories: total life and fracture mechanics methods.

2.1.2 Baseline Characterization

A major part of this DT material design effort focused on collecting and characterizing fatigue crack nucleation and crack growth data especially in the threshold-related regions of the stress-life and fatigue crack growth rate regimes. It was necessary to generate this information to provide input for the total-life fatigue and fatigue crack growth life prediction models, as well as to generate data, which could be used to demonstrate the accuracy of the DT models. The following summarizes the principal observations and accomplishments in each of the highlighted areas.

Undamaged Material Behavior - Response

- The undamaged fatigue test program demonstrates the sensitivity of surface effects (for different machining operations and shot peening) and showed that, in general, the fatigue strength decreased only slightly beyond 10^7 cycles to failure.
- The program generated long-life, fatigue-crack-nucleation data (10^6 – 10^9 cycles to failure) that are used to evaluate the effects of stress ratio and frequency. Except for the condition of $R = 0.1$ and frequency = 1000 Hz, the S-N data are as anticipated. However, the lives at 10^8 and 10^9 for this test condition were shown to be substantially below what was expected. *(Editor's note: In the follow on program, these low strength values were treated as invalid due to the potential lack of test control at the 1000 Hz, $R = 0.1$ condition.)*
- Data generated, for positive stress ratios, using the step test method are shown to compare well with data generated using traditional S-N approaches; step tests facilitate the generation of long life fatigue strength information. Results from $R = -1$ step test conditions show more scatter and are higher than traditional S-N approaches. (See recommendation to pursue additional effort.)
- Fractographic examinations of smooth and notch fatigue specimens characterize the crack origin sites as being primarily associated with persistent slip bands

(PSBs) initiating at grain boundaries and inclusions. Smooth specimen behavior at $R = 0.8$ is identified using fractography as having been heavily influenced by time-dependent plasticity. This is not surprising since for the smooth specimens tested at $R = 0.8$, the maximum stress was above the cyclic yield strength.

- The T-6Al-4V blade material exhibits cyclic softening response under both strain control and high stress ratio stress control loading conditions.
- The constitutive cyclic stress-strain response is generated based on half-life strain-controlled fatigue life tests. The half-life stress-strain data were collected for multiple stress ratio conditions, were modeled with a Ramberg-Osgood equation, and subsequently were used to describe notch and localized contact fatigue stress and strain states.
- Round-robin tests conducted by P&W, GEAE and Honeywell verify consistent test results for the individual test laboratories.

Undamaged Material Behavior - Total Life Models

- Haigh (modified Goodman) diagram accurately characterizes the long-life stress-ratio behavior.
- Total Life models describe mean-stress effects in uniaxial fatigue data; these models can be used to generate mean behavior Haigh (modified Goodman) diagrams for lives to 10^9 cycles.
- Total Life models provide reasonable descriptions of data generated under loading conditions that simulated blade multiaxial stress states. Loading conditions include axial and tension-torsion (in-phase and out-of-phase) types of loads.

Crack Damage Behavior Response

- Long-crack tests characterize fatigue crack growth rate (da/dN) from threshold to critical stress intensity factor levels as a function of stress ratio.
- The crack growth threshold parameter ΔK_{th} is shown to be basically independent of test geometry (CT vs $Kbar$) as well as crack size and shape.
- This threshold parameter (ΔK_{th}) is shown to be basically independent of the stress intensity factor gradient (C) for C between -2 to -20 inch^{-1} . The ASTM

Standard E647 recommends a shallow gradient of $C = -2 \text{ inch}^{-1}$ for determining fatigue crack growth rate thresholds, so this accomplishment results in improved test methods for establishing a necessary parameter for damaged materials.

Crack Damage Behavior - Fracture Mechanics Models

- Current engine company fatigue-crack-growth-rate models, i.e., MSE and Sinh models, describe da/dN from threshold to critical stress intensity factor levels. These models accurately describe the mean stress ratio effects in the threshold region established by the ΔK_{th} tests.

Integration of Total Life and Fracture Mechanics Models

- The Kitagawa diagram provides a good concept for developing limiting stress levels associated with both undamaged and damaged material behavior.

Notched Behavior Response

- The variation of notch geometry and gage volumes suggests a minimal effect on endurance limit.
- Fatigue notch factors K_f and K_q are established for $K_t = 2.5$ at $R = -1, 0.1, 0.5$ and 0.8 .
- Long life results from Step vs. extrapolated S-N tests compare well for positive stress ratios = $0.1, 0.5$ and 0.8 ; whereas the negative stress ratio ($R = -1$ condition) tests showed higher scatter and step test results are near-to, or higher than extrapolated values. These observations agree with the results for smooth (undamaged) specimens.

Notched Behavior – Modeling

- The Haigh/Goodman diagram characterizes the long-life stress-ratio behavior of the notched specimens.
- Two Total Life methods are established for modeling notch fatigue using an undamaged material behavior. One method, based on a Smith-Watson-Topper (SWT) mean-stress-life model that was tested against the notch data, was very conservative. For this method, there also appears to be significant bias that can be attributed to stress ratio. The other method, based on an area-corrected

approach to account for the stress gradient, was only compared to a limited set of data.

- Deep notch effects testing show the potential for using a limiting K_t estimate for predicting the behavior.

2.1.3 LCF-Induced Damage

Several notched tests were conducted to demonstrate the applicability of standard fracture mechanics methods for predicting the conditions for onset of rapid growth under LCF/HCF block loading conditions. One set of notch test conditions involved major-minor loading (1 LCF cycle at $R = 0.1$, followed by 1000 $R = 0.8$ cycles) and the other utilized 1000 LCF followed by 100,000 $R = 0.8$ cycles. In addition, another series of notch tests were conducted where 3,000 LCF cycles (95ksi nominal) $R = 0.1$ followed by endurance step-tests at $R = 0.5$ (two tests) and $R = 0.8$ (two tests). This limited test series seemed to show that the occurrence of rapid growth could be predicted using the $\Delta K = \Delta K_{th}$ criterion applied to the low amplitude loading conditions for LCF/HCF interaction tests. Step testing was used to estimate the threshold conditions for two low-level constant-amplitude loading conditions (stress ratios of 0.5 and 0.8 were utilized).

2.1.4 Foreign Object Impact Damage

The framework exists to reduce the potential for HCF loading to cause cracking from FOD sites that lead to blade failure. The following summarizes the observations and accomplishments in each of the highlighted areas.

Engine Experience

To develop understanding, the program sought to establish information relevant to anticipating typical engine blade FOD history. Based on the results of two separate data collection and evaluation efforts, the following two items of interest stand out:

- The majority of FOD appears to occur beyond 80% span.
- FOD depth measured ranged from 0.002-inch to 0.5-inch with an average of ~0.060-inch.

FOD Damage Behavior - Response

- Step test data appear slightly lower than the S-N data, but not significant
- The 0.025-inch radius indent is not as damaging as the 0.005-inch radius indentation.
- The effect of damage depth appears to plateau at the higher damage levels.
- Ballistic impact results are not significantly different than the solenoid gun results.
- 30° impact angle is more damaging than a 0° impact.
- Electric Potential Drop (EPD) monitoring may influence test results.

FOD Damage Behavior - Understanding

- 0° impact generates a large embedded compressive field directly behind the impact crater followed by an embedded tensile field.
- Angled impacts create a high tensile stress field on the entrance side of the damage site near the notch surface, which is not buffered by a large compressive stress field.
- Ignoring the residual stress field could lead to non-conservative stress intensity predictions under certain conditions.

FOD Damage Behavior - Modeling

- ***Total Life (Nucleation) Methods***
 - Detailed and idealized FEA analyses are conducted on FOD notch geometries, leading to estimates of the localized stress-strain behavior.
 - Nucleation methods are evaluated by FEA results and data and found to be a substantial improvement over the use of a $K_t = 3$ approach.
 - The Weibull-modified equivalent stress method appears to provide reasonable estimates for the limited data to which it was compared.
 - There appears to be significant bias between the test groups.

Fracture Mechanics Methods

- Detailed and idealized stress-intensity factor analyses are conducted on FOD notch geometries. Fracture mechanics (K_{th}) methods are evaluated with K results and data and appear promising for evaluating FOD impacts.
- It is highly recommended to evaluate fracture mechanics methods with a wider array of data and correlate with impact residual stress prediction methods.
- ***Worst Case Notch Method***
 - Worst Case Notch modeling predicts mean behavior of test results very well for various blade-leading-edge configurations containing simulated FOD.

2.1.5 Attachment Fatigue-Induced Damage

Although attachment fatigue is a complex phenomenon requiring additional research, this work has helped identify the importance of incorporating local edge-of-contact displacement into any damage model in order to account for microcrack formation. The following summarizes the observations and accomplishments in each of the highlighted areas.

Damage Behavior - Response

- The evaluation of fretting attack (i.e., localized rubbing contact, without axial loading) by GEAE included studies of the effects of (a) wear pad geometry, (b) bearing stress, (c) number of fretting cycles, (d) displacement, and (e) residual stress. These studies characterize the effect of fretting on subsequent fatigue capability, leading to conditions that can be defined as non-damaging. Crack formation conditions are characterized and fretting surface features are catalogued.
- UTRC, Purdue, and SwRI experimental evaluated the effects of (a) wear pad geometry, (b) bearing stress, (c) displacement, and (d) axial load levels on fretting-fatigue (combined axial-fatigue and fretting contact conditions) behavior. Unfortunately, these studies did not establish data that could be used to determine fretting-fatigue threshold conditions directly.

Modeling Localized Stresses

- Elastic finite-element solutions of the local edge-of-contact (EOC) region are demonstrated to converge using advanced submodeling and mesh refinement.
- Integral equation methods are developed and demonstrated for estimating the local EOC elastic stresses to a level of accuracy that duplicated finite element methods.

Total Life (Nucleation) Methods

- The SWT method is demonstrated for estimating the local stress conditions associated with fretting-fatigue failures. However, the method tends to provide very conservative estimates.
- The Weibull-modified equivalent stress method is demonstrated for a limited number of fretting fatigue and fretting test results.

Fracture Mechanics (FM) Methods

- The effectiveness of conventional FM methods is demonstrated for predicting the threshold behaviors of fretting induced damage under various conditions including the effect of shot-peening.
- The small crack FM methods are evaluated for the Worst Case Fret model. The results are less promising than those using the Worst Case Notch model for FOD damage.

2.2 EXIT CRITERIA

Table 2.1 summarizes the target exit criteria established in Chapter 1 as well as estimates of the actual-to-predicted (A/P) ratios obtained using the strength-related parameters developed and data generated in the program. Chapter 3 describes the baseline data (undamaged, smooth, axial fatigue data; fatigue crack growth data; and notch fatigue data) and the parameters used to describe these data. The baseline behavior provides the basis for the in-service damage exit criteria. Table 2.1 lists the Chapter 1 targets (exit criteria requirements) and compares these targets to the results generated to demonstrate the accuracy of the total life and fracture mechanics models used for predicting the thresholds for in-service damage.

Table 2.1
Exit Criteria Summary

Type of Behavior	Mean A/P	Standard Deviation	Models Evaluated
Baseline Behavior	1.01 1.02 0.97	~0.1 0.098 0.12	Two uniaxial fatigue models ΔK_{th} Walker – long crack Equivalent stress - multiaxial
Undamaged Notch Fatigue	1.25	0.137	SWT, approximate stress-strain, critical plane method
LCF Damage	1.0 +/-0.05	0.125	Target
Foreign Object Damage	1.0 +/-0.15 1.65 1.46 1.06 1.06	0.250 0.480 0.366 0.202 0.222	Target $K_t = 3$ SWT – based on notch model ΔK_{th} – long crack threshold Worst Case Notch
Fretting Damage	1.0 +/-0.15 1.18 1.10	0.250 0.270 0.405	Target SWT- Averaged over 0.004-inch Worst Case Fret

As can be seen in Table 2.1, no comparison for the LCF damage exists; this is because limited verification data were generated to provide a statistical comparison between the models and the verification data.

Four of the models used to describe the effect of FOD on the HCF threshold behavior were evaluated. The first FOD model listed has been referred to as the traditional model; this model does not meet either the mean or scatter targets. The second FOD model listed was based on the SWT model that was also used to estimate undamaged notch behavior (see Table 2.1), and while it performed better than the traditional FOD model, it also was far removed from the target. The third and fourth models, based on long-crack fracture mechanics thresholds and on short-crack fracture mechanics, respectively, both meet the target goals.

Two of the models used to describe the effect of fretting damage on the high cycle fatigue threshold behavior were evaluated. The first fretting model listed estimated the crack initiation life based on the SWT mean-stress parameter, the parameter value was calculated as the average of the SWT values that occurred over a depth of 0.004-inch. The second fretting model was based on short-crack fracture mechanics and is referred to as the Worst Case Fret model. Its basis is similar to that of the Worst Case Notch model used to model FOD behavior. As can be seen from Table 2.1, both models are more conservative than the target. The Worst Case Fret model also exhibits more scatter than allowed by the target.

2.3 RECOMMENDATIONS

Based on the baseline experimental data and supporting analysis generated under this project, it is recommended that additional data, evaluations or analyses be performed to take the following actions:

- Determine if the lower strength values at the lives of 10^8 and 10^9 cycles, which were generated at $R=0.1$ for a frequency of 1000 Hz, truly represent the material behavior or a test anomaly. It is recommended that additional long-life data be generated to address this question. *(Editor's note: When additional data were generated at 900 and 1000 Hz in the follow on program, it was determined that potential test control issues may have been experienced during the tests conducted at 1000 Hz, but not at 900 Hz. Furthermore, it was noted that the 900 Hz data had approximately the same strength values as those generated at lower frequencies.)*
- Modify and refine the DT design methods that showed good correlation with the data generated and analyses conducted in this program. Validate these methods with additional data where necessary: In particular:
 - Improve the methods that exist for establishing fatigue strength estimates for lives greater than 10^6 cycles. One potential method for describing the variability in the fatigue strength as function of cycles is the random fatigue limit model. In support of these analytical approaches, the application of the step-test method should be explored for determining if it can be used to establish the properties of the fatigue life distribution. The model should also be evaluated for its potential application for modeling the variability associated with the fatigue crack growth rate threshold.
 - Improve the analytical methods to accurately predict the fatigue lives of notched structures. Evaluations should consider the accuracy of the notch localized stress-strain behavior as well as the accuracy of the fatigue life prediction parameters and the methods used to establish the values of the parameters for engine structure situations. These evaluations should utilize additional sharp notch fatigue data to determine the limitations and advantages of the various competing notch methods.

- Compare Honeywell generated small-crack rate behavior with other short-crack data generated at different stress ratios and with the $\Delta K_{\text{eff}} - da/dN$ relationship (where ΔK_{eff} is based on closure concepts) to provide lower bound estimates on the small-crack rate behavior.
- Generate additional multiaxial fatigue test data on Ti-6Al-4V that better simulate the localized conditions in the attachment edge of contact region. Use these data to further evaluate the effectiveness of the total life models to describe these types of non-proportional loading conditions.
- Conduct additional evaluations of the usefulness of long-crack fracture mechanics methodology for establishing the damage sizes where HCF loading affects the behavior of LCF crack nucleation and early crack propagation.
- Investigate the effects that residual stresses have on FOD behavior and analysis. Models need to be verified on an engine component through blade tests.
- Verify the use of the DT approaches (validated for the Ti-6Al-4V blade-forging alloy) for high temperature and for other materials, especially beta-titanium alloys and nickel-base single crystal alloys typically used in advanced aircraft turbine engines.
- Develop and initiate an implementation plan to transition the models into engineering processes that can be efficiently utilized for design of advanced aircraft engines to minimize the potential for HCF induced failures when in-service damage is present as a result of (a) LCF loading, (b) FOD, or (c) fretting distress. These subsequent efforts will help transition the understanding and preliminary models developed under this program into turbine engine design practices that will eventually impact future fan and compressor blade designs.

Chapter 3

Characterizing Material Behavior – Methods and Baseline Data

The overall strategy is to develop a HCF design methodology and supporting material database for predicting 1) the onset of HCF crack growth for those locations where a high probability of crack-like defects or damage exists, and 2) the HCF (crack nucleation) endurance limit for those locations where there is a low probability of crack-like defects. This chapter describes the baseline data and materials models that provide the basic methodology for predicting threshold stress conditions below which HCF loading does not propagate damage from in-service operations. In-service blade damage addressed for verification purposes includes that due to the combined action of LCF/HCF loading, FOD, or attachment distress. Chapters 4, 5 and 6, respectively, describe how the models presented in Chapter 3 predict the limiting threshold stresses associated with each of these in-service damaging conditions. The relationship between this chapter and the damage state chapters is shown in Figure 3.1.

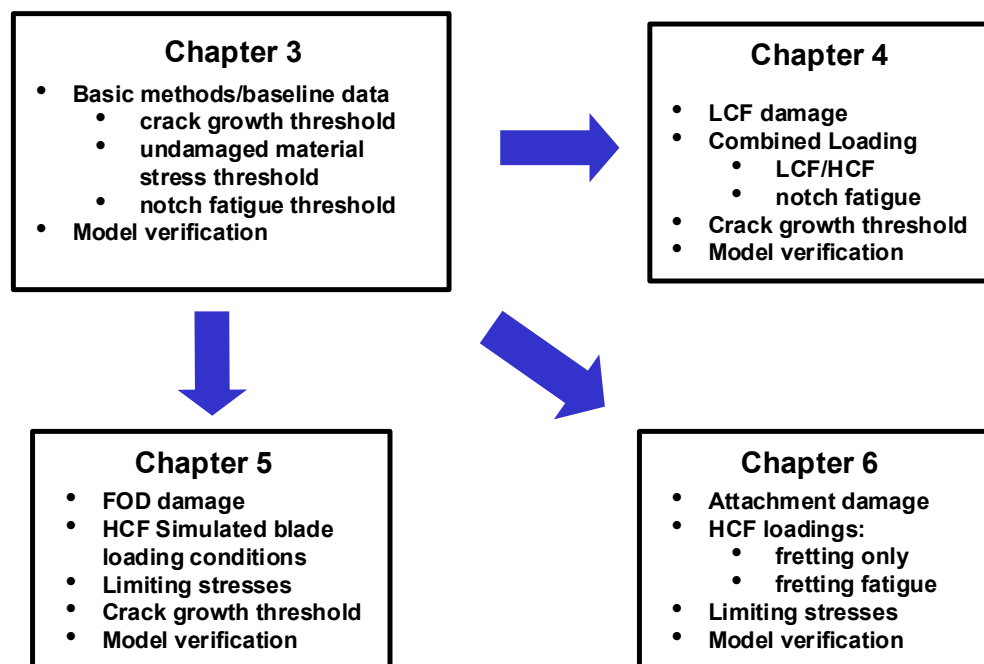


Figure 3.1. Interrelationship between Chapter 3 and the Damage State Chapters.

The modeling for the well-characterized Ti-6Al-4V material began at fundamental levels and increased in complexity following the path suggested schematically in Figure 3.2 (for the approach based on a crack nucleation philosophy). Crack growth and threshold testing for mean stress effects provided the data to model crack growth (for LCF/HCF interaction purposes) and the onset of HCF propagation. Fatigue testing for smooth (uniaxial and multiaxial) and notched specimens at a range of stress ratios provided the data to establish models to predict the HCF capabilities for more complex stress states. Limited amounts of testing for surface effects provided data to modify models to predict material conditions more closely representative of a component.

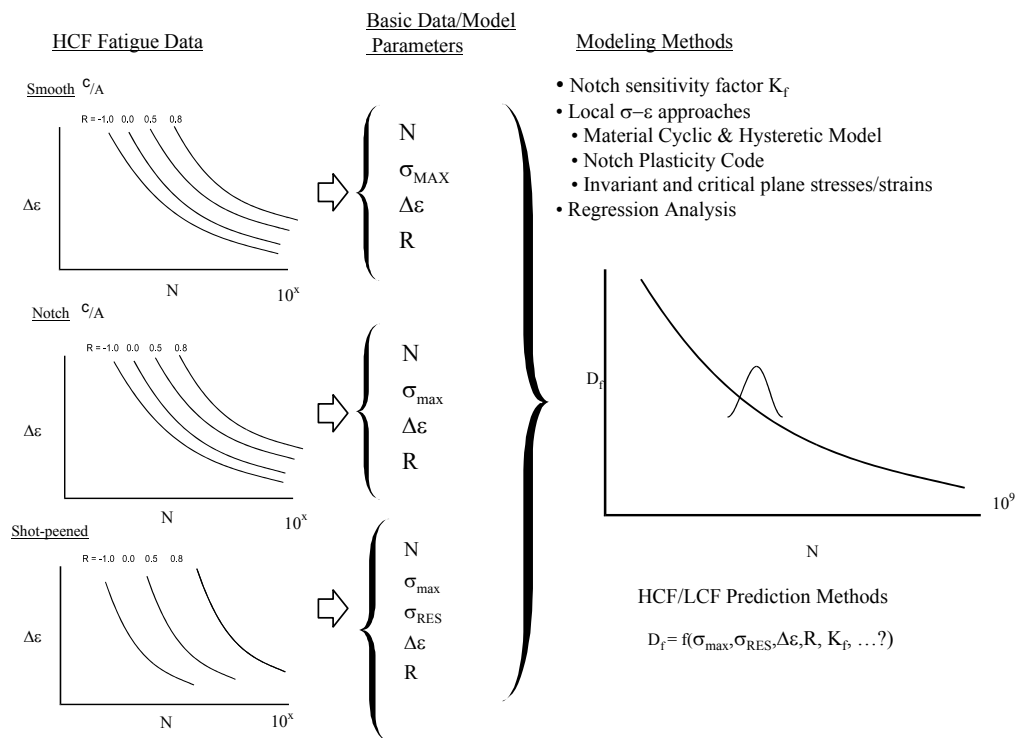


Figure 3.2. Building block approach to modeling smooth and notch fatigue.

3.1 Ti-6Al-4V FORGED BLADE MATERIAL PEDIGREE

Ti-6Al-4V was selected for this program because it is the most commonly used material for blades and disks in fan and compressor sections of military and commercial gas turbine engines. The Ti-6Al-4V material used in this study was forged into simulated fan blade forgings, measuring approximately 16 inch by 6 inch by 0.8 inch, in a single forging campaign by the Cleveland Operations of Textron Turbine Engine Components. The forging stock had been double-vacuum arc re-melted, converted to 2.5 inch (6.4 cm) diameter bar stock, and supplied by Teledyne Allvac in the mill-annealed condition in accordance with AMS4928L. More details concerning the pedigree of the blade material can be found in Appendix 3A.

The chemistry from the top and bottom of the ingot (see Table 3.1) was within the acceptable ranges of AMS4928L. The beta transus, as determined by differential thermal analysis (DTA) at the top and bottom of the ingot, ranged from 1814°F to 1837°F. This bar stock was ultrasonically inspected in accordance with AMS2631B and found acceptable. The 2.5 inch diameter bar was cut into 16 inch length multiples and preheated to 1720°F \pm 20°F for a minimum of 1 hour prior to being forged on a 7000-ton mechanical press with a variable stroke rate. The channel dies that were used were preheated to 300°F prior to the start of the forging campaign. Each forging was accomplished in one strike and with a glass lubricant. The forgings were air-cooled upon removal from the press.

Table 3.1

Chemistry of the Ti-6Al-4V Billet used in this Program

	Ti	Al	V	Fe	O	N
Ingot Top	bal.	6.27	4.19	0.2	0.18	0.012
Ingot Bottom	bal.	6.32	4.15	0.18	0.19	0.014
AMS4928	bal.	5.50-6.75	3.50-4.50	0.30 max	0.20 max	0.050 max

Although many fan blade and compressor blade forgings are given a direct mill-annealed heat treatment after forging, substantial microstructural differences can exist as a result of differences in deformation, adiabatic heating, die chill, etc. Therefore, the forgings were first solution treated at 1710°F \pm 20°F after forging to provide a uniform microstructure. This solution treatment occurred in four separate lots because of the

number of forgings in the program. After solution treatment, the forgings were fan-cooled and mill-annealed at $1300^{\circ}\text{F} \pm 25^{\circ}\text{F}$ for 2 hours. The microstructure of the forgings consisted of approximately 60% primary alpha phase with the remainder lamellar-transformed beta phase. A typical microstructure of a forging is shown in Figure 3.3. The 0.2% yield and ultimate tensile strength in the longitudinal direction were determined to be 930 MPa (134.9 ksi) and 978 MPa (141.8 ksi), respectively.

Specimens were excised from the forgings according to forging cut-up plans that are available^{3.1*}. The baseline specimen condition was: low stress grind and longitudinally-polished specimens were stress-relief annealed for 1 hour at 1300°F in vacuum to eliminate any residual stresses from machining and then chem-milled with a nitric-hydrofluoric acid solution to remove approximately 0.001 inch from the gage surface to ensure freedom from any contamination from stress relief. Post-processing hydrogen analysis indicated less than 0.006 weight percent (60 ppm) hydrogen in the gage area, confirming minimal hydrogen pick-up during chem-mill. The tests were conducted at room temperature.

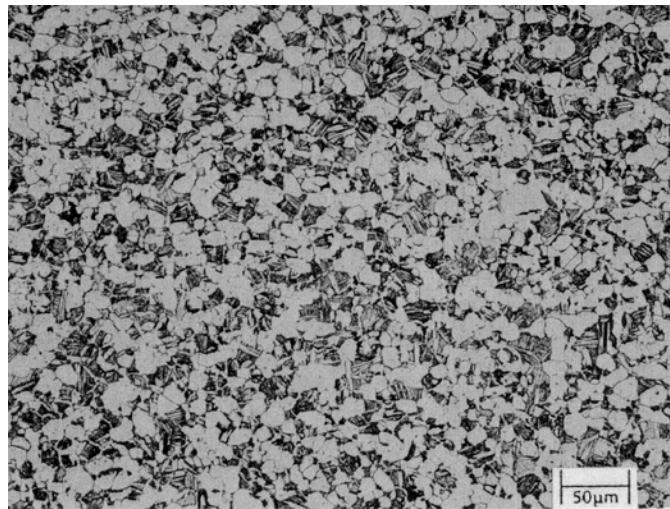


Figure 3.3. Microstructure of the Ti-6Al-4V forgings.

* See List of References at end of Chapter

3.2 FATIGUE CRACK GROWTH BEHAVIOR AND THRESHOLD MODELING

The approach was to evaluate/develop fracture mechanics methods that are capable of predicting the onset of HCF propagation. The methods use the linear elastic fracture mechanics (LEFM) stress intensity factor K , with the onset of crack propagation ($da/dN = 10^{-8}$ inch/cycle) defined as the threshold stress intensity factor range (ΔK_{th}). The primary path was to base the methods on long-crack data and model small-crack behavior (if required) as a modification thereof.

Stress intensity factor (K) solutions used in the methods development are based on the analysis algorithms used within the participating organizations and will be noted in the description of each model. Their origins range from widely-accepted (published) K -solutions, to specific company influence function solutions, to 3-D ANSYS or FRANC3D generated solutions. The general form of the stress intensity factor as presented in this report is:

$$K = \sigma F \sqrt{\pi a} \quad (3.1)$$

where: σ – represents a nominal or remotely applied stress

F – accounts for structural geometry, crack geometry, and loading configuration

a – represents a measure of crack size

The stress (σ) could be the maximum stress (σ_{max}), the minimum stress (σ_{min}), or the range in stress ($\Delta\sigma = \sigma_{max} - \sigma_{min}$); and this leads to corresponding stress intensity factor values, i.e., to K_{max} , K_{min} and ΔK , respectively. In this report, ΔK is defined as $K_{max} - K_{min}$, even for negative stress ratios ($R = K_{min}/K_{max}$).

3.2.1 Fatigue Crack Growth Rate Behavior

3.2.1.1 Basic Material Fatigue Crack Growth Rate Behavior

Fatigue crack growth rate (FCGR) testing provided data to model and predict the effects of LCF crack growth and its impact on HCF capabilities. Full-range FCGR tests were conducted at stress ratios (R) of 0.1 and 0.8, while threshold tests were conducted for $R = -1.0, 0.1, 0.5$ and 0.8.

Fatigue crack growth specimen blanks were removed from forgings to orient crack growth in the longitudinal direction with loading in the long transverse direction. The longitudinal direction was defined as coinciding with the largest forging dimension. Detailed descriptions of the two geometries used for the crack growth tests can be found in Appendix 3B. The compact tension (CT) specimen, 0.25-inch thick, conforms to the guidelines of ASTM E647. The straight-through starter notch was used. The *Kb* (surface flaw) specimen is prepared by cutting a 0.005-inch deep and 0.010-inch long EDM pre-flaw in the center of the width dimension. The *Kb* sample is then cycled to produce 0.002-inch of growth prior to testing.

FCGR data tested at $R = 0.1$, 0.5 and 0.8 were examined and modeled for R trends. The $R = 0.1$ and 0.8 data covered the full range from threshold to final fracture, while the $R = 0.5$ data were developed only in the threshold region. These long crack data are shown in Figure 3.4.

Fatigue crack growth threshold testing used the same type of specimens as described above for FCGR testing, but data collection followed a test methods development effort. A small round-robin study was conducted to determine the effects of specimen geometry, unloading gradient, and constraint. A detailed explanation of these details is contained in Appendix 3B, which documents the crack growth rate behavior. The following conclusions were drawn from the study:

- The initial characterization work focused on investigating the effect of K -gradients that ranged from normalized K -gradients of -30 inch^{-1} to -5 inch^{-1} . The ASTM Standard E647 recommended value is a more conservative $C = -2 \text{ inch}^{-1}$. The term K -gradient describes the rate at which load is reduced to determine ΔK_{th} . Results indicate that material tested to gradients from $C = -2 \text{ inch}^{-1}$ to -20 inch^{-1} were independent of the load shed rate, given that the starting value for K_{max} at the beginning of the test corresponded to a growth rate below $4 \times 10^{-6} \text{ inch/cycle}$. It is noted that for some test conditions, K -gradients as steep as -30 inch^{-1} had no effect on the threshold behavior.
- In the *Kb* (GEAE surface crack) specimen, thicknesses ranging from 0.10 to 0.25 inch did not influence the measured value of ΔK_{th} at $R = 0.1$ and 0.8 .

- For producing valid threshold results, the choice of K -gradient and starting K_{max} is not independent. As K_{max} is increased, the absolute value of the gradient must decrease to distance the crack tip stress field from the plastic wake. (See Appendix 3M for modeling justification.)

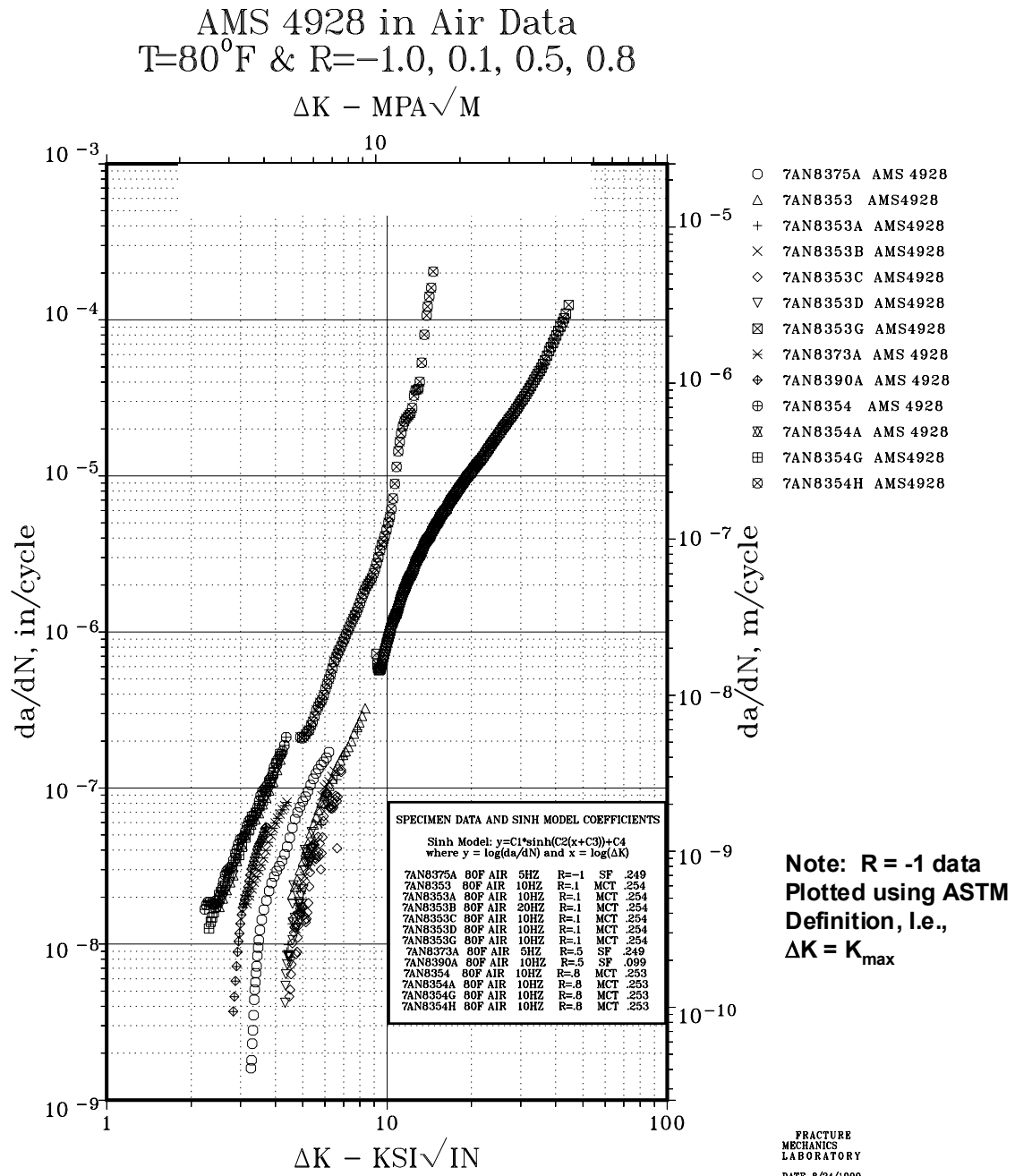


Figure 3.4. Fatigue crack growth rate data for $R = -1, 0.1, 0.5$ and 0.8 .

Threshold behavior, as determined from the load-shedding specimen tests, is summarized in Figure 3.5; this figure also includes threshold data obtained from the AFOSR MURI program^{3,2}. The valid ΔK_{th} test data are for stress-ratios ranging from -1.0 to +0.95 and represent a growth rate less than 10^{-8} inch/cycle. A full range definition of ΔK was used to present these data

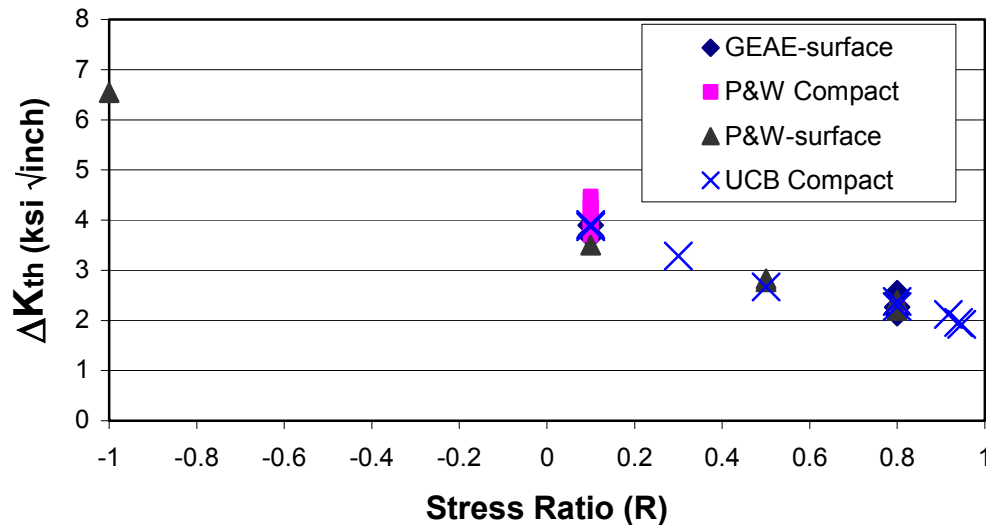


Figure 3.5. Threshold stress intensity factor range as a function of stress ratio.

3.2.1.2 Short Crack Propagation Test Results

The fatigue crack growth behavior of microstructurally-short cracks, which have been known to propagate below conventional long-crack ΔK_{th} values, were also evaluated. Naturally-initiated fatigue cracks in smooth specimens (tested at $\Delta\sigma = 80$ ksi, $R = 0.1$ and frequency 60 Hz) were documented via surface replication performed at uniform intervals of 15,000 cycles. Such information gathered in the present study for five different specimens is summarized in Figure 3.6a as crack propagation rate (da/dN) vs. crack depth (a) and in Figure 3.6b as crack propagation rate (da/dN) vs. stress intensity range (ΔK). The following assumptions were made when converting replication information into data points presented in Figure 3.6:

- Crack front shape was semi-circular (i.e., $a = c$ where a = crack depth and c = surface half-length) and crack growth was pure Mode I;

- Initial crack propagation rate (i.e., between crack nucleation and the moment when it was first replicated) was calculated as log-average of two possible extremes: da/dN_{\max} , where total crack extension documented in the first crack-containing replica occurred in one cycle, and da/dN_{\min} , where total crack extension documented in the first crack-containing replica occurred during the entire replication interval, which in the present study was equal to 15,000 cycles;
- Each da/dN value was associated with a ΔK calculated for the average crack length recorded on two consecutive replicas taken before and after corresponding crack extension.

According to the general trend observed in Figure 3.6, an initially-high crack propagation rate abruptly decreases, reaches a certain minimum value, and then gradually increases. This is accompanied by a substantial reduction in experimentally observed scatter in the crack propagation rate as the crack grows. In Figure 3.6a, the crack size corresponding to the minimum crack propagation rate is also compared to the average primary-alpha grain size. The major trend in crack propagation behavior changes from deceleration to acceleration after the crack tip passes through the first or second primary-alpha grain boundary. At the same time, in one case (specimen 2) an additional crack growth retardation event occurred when the crack size (depth or surface half-length) was five times larger than the average primary-alpha grain. Based on the data presented in Figure 3.6a, fatigue crack propagation behavior in the subject material was divided into two separate regimes with respect to microstructural sensitivity.

Similar trends in fatigue crack propagation behavior can be seen in Figure 3.6b. In this graph, the results obtained are plotted as a function of stress intensity factor range, ΔK , and are compared to the crack propagation behavior of long cracks in both compact tension and surface flaw type specimens (P&W data for $R = 0.1$). It can be seen that naturally-initiated small cracks propagate well below the long crack threshold and that naturally-initiated small cracks propagate much faster than long cracks for stress intensity range values which are slightly higher than the long crack threshold. The tendency for faster propagation persists up to $\Delta K = \sim 10 \text{ ksi}\sqrt{\text{inch}}$, at which point it appears that both sets of data merge. More details on the subject can be

found in Appendix 3C. Another “small crack” study was also conducted using bending test specimens; this study is summarized in Appendix 3D.

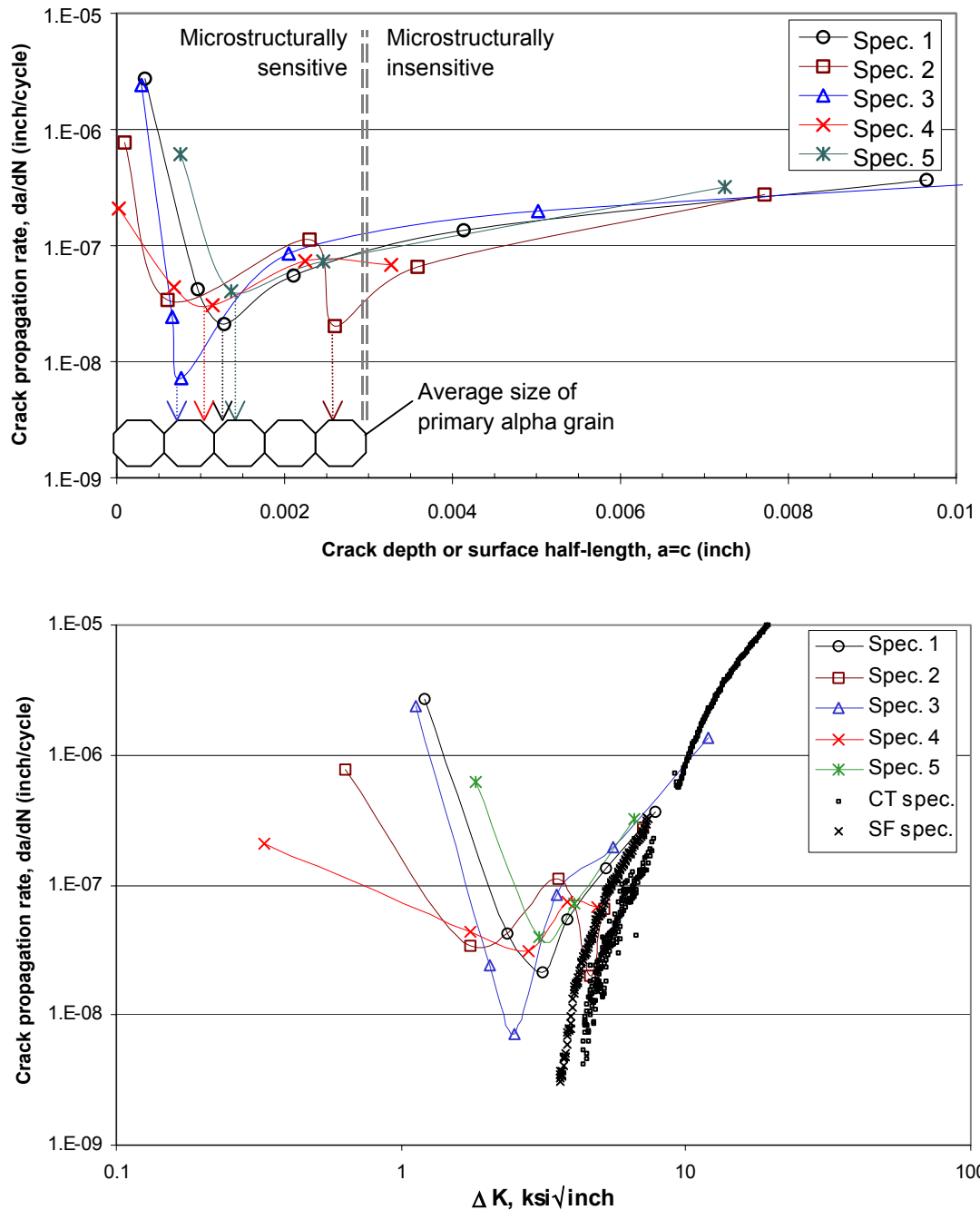


Figure 3.6. Fatigue crack propagation rate of naturally initiated “small” cracks as a function of: (a) crack size and (b) stress intensity factor range.

3.2.2 Crack Growth Rate Models

The need to model crack growth rates stems from the requirement to model and predict the influence of LCF crack propagation on the threshold for HCF. Two basic crack growth rate models were used to model R-ratio behavior over the full range of fatigue crack growth rate behavior and those two models stem from the methods currently employed at P&W and GEAE: P&W uses a crack-closure method based on Newman's equations and GEAE uses an effective stress intensity factor model based on a Walker stress-ratio method.

3.2.2.1 Closure-Based Sinh Crack Growth Rate Model

Crack-closure modeling based on J.C. Newman's equations,^{3,3} as applied by deLaneuville and Heath,^{3,4} was chosen to model the stress-ratio FCGR data shown in Figure 3.4. The mathematical function used in the modeling is the hyperbolic sine as follows:

$$\log (da/dN) = C1 \sinh (C2 (\log (\Delta K) + C3)) + C4 \quad (3.2)$$

where the coefficients C1, C2, C3 and C4 are determined from the data. The applied stress intensity range, ΔK , is reduced to an effective stress intensity range, ΔK_{eff} , as shown Figure 3.7. From this, it can be shown that:

$$\Delta K = K_{max} - K_{min} \quad (3.3a)$$

and

$$\Delta K_{eff} = K_{max} - K_{cl} \quad (3.3b)$$

where K_{cl} refers to the K level at which the crack closes. K_{cl} is related to K_{max} by the relationship:

$$K_{cl}/K_{max} = A_0 + A_1R + A_2R^2 + A_3R^3 \quad \text{for } R > 0 \quad (3.3c)$$

and

$$K_{cl}/K_{max} = A_0 + A'_1R \quad \text{for } R < 0 \quad (3.3d)$$

To develop the closure-based model shown in Figure 3.7, Newman's constraint parameter (α) was determined by a regression of the data using his equations with an effective flow stress of 1000 MPa (based on P&W experience). The regression resulted in a value of $\alpha = 1.3$ and produced the following coefficients identified in Table 3.2.

HCF Contract Ti 6-4 Data 80 F

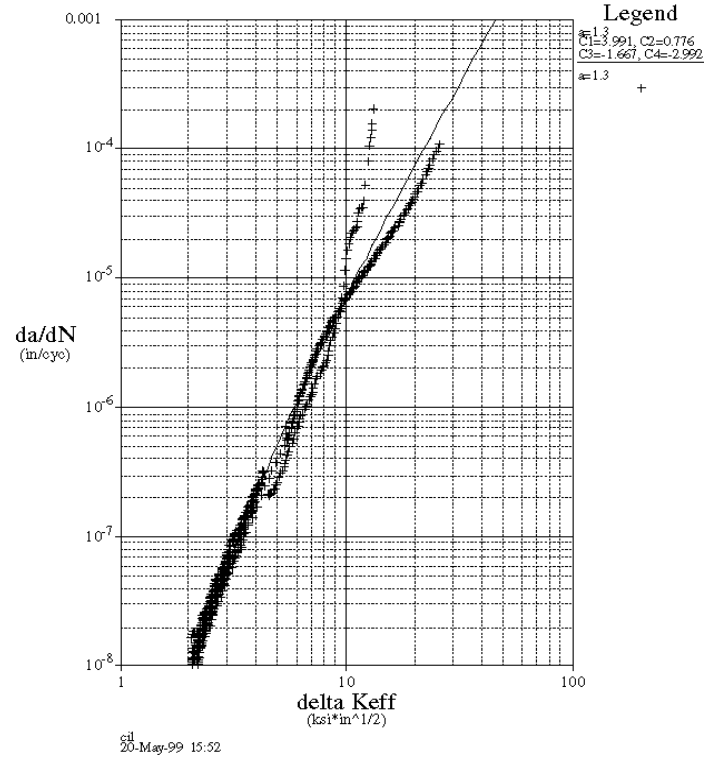


Figure 3.7. Stress-ratio behavior modeled with the ΔK_{eff} (Closure) model.

Table 3.2
 Constants for the Hyperbolic Sine Model

Constant	Value
α	1.3
C_1	3.991
C_2	0.776
C_3	-1.667
C_4	-2.992
A_0	0.4675
A_1	0.003227
A_2	0.5912
A_3	-0.0619
A'_1	0.14

3.2.2.2 Walker Model for Stress Ratio Effects

The FCGR behavior measured at the depth position in surface-crack growth tests are shown as a function of ΔK in Figure 3.8a. These data include results from shed tests at stress ratios of 0.1 and 0.8, as well as constant-load (increasing K) tests at $R = 0.1, 0.8$, and -1 . These data have been modeled using a sigmoidal crack growth equation:

$$da/dN = \exp(B) (K_{eff}/K_{th})^P [\ln(K_{eff}/K_{th})]^Q [\ln(K_c/K_{eff})]^d \quad (3.4)$$

where K_{th} , B , P , Q , D , and K_c are material constants and where:

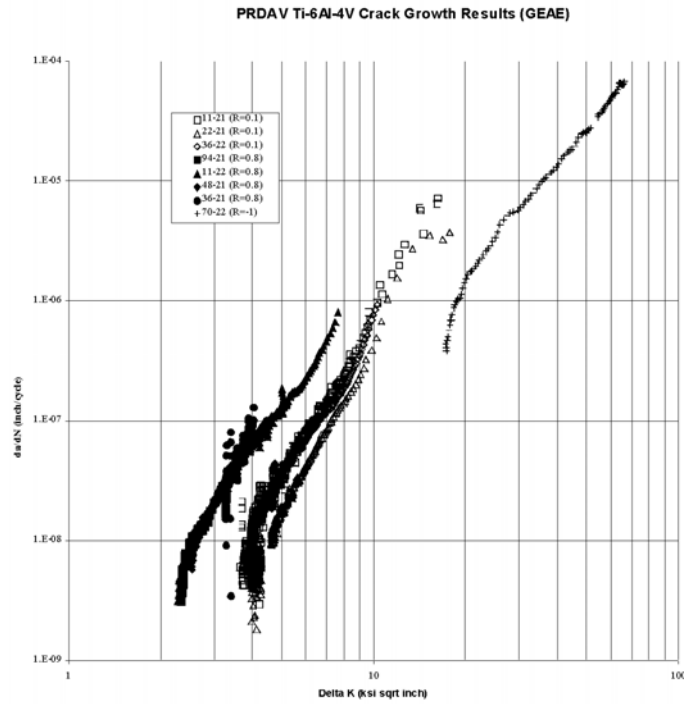
$$K_{eff} = K_{max} (1-R)^m = \Delta K (1-R)^{m-1} \quad (3.5)$$

$m = m+$ for positive R and $m = m-$ for negative R .

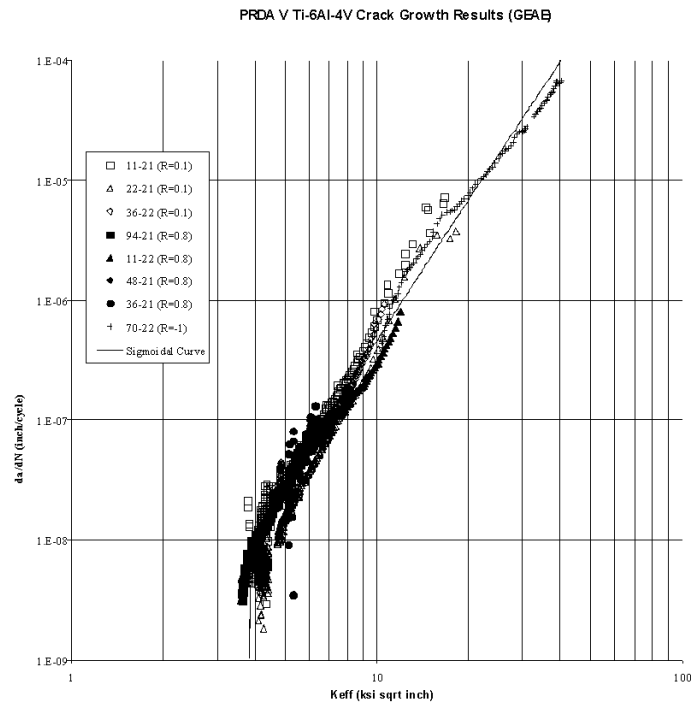
The resulting material constants are given in Table 3.3. The data in Figure 3.8a is shown as a function of K_{eff} in Figure 3.8b along with the sigmoidal curve fit. The results shown in Figure 3.8b illustrate the ability of the dual Walker exponent and the sigmoidal relationship to accurately model the influence of R on crack growth rates.

Table 3.3
Ti-6Al-4V Sigmoidal Curve (Equations 3.4 and 3.5) Constants at 70°F

Constant	Value
K_{th}	3.829
B	-18.144
P	3.7107
Q	0.2349
d	-0.0066
K_c	60
$m+$	0.72
$m-$	0.275



(a)



(b)

Figure 3.8. Variation of measured surface-crack growth rates in Ti-6Al-4V at room temperature as a function of (a) ΔK and (b) K_{eff} .

3.2.3 Modeling Threshold Behavior

3.2.3.1 Long Crack Modeling

One method for anticipating the limiting stresses associated with structural damage is based on a comparison between the applied ΔK and the material resistance to crack growth, i.e., the ΔK_{th} . This criterion for no damage propagation can be expressed as:

$$\Delta K \leq \Delta K_{th} \quad (3.6)$$

The closure-based model described by Eq. 3.2 was used to predict the ΔK at 10^{-8} in/cycle; this was compared to the ΔK_{th} threshold database as shown in Figure 3.9. The closure-based model accurately predicts threshold behavior over the complete range of stress ratio trends.

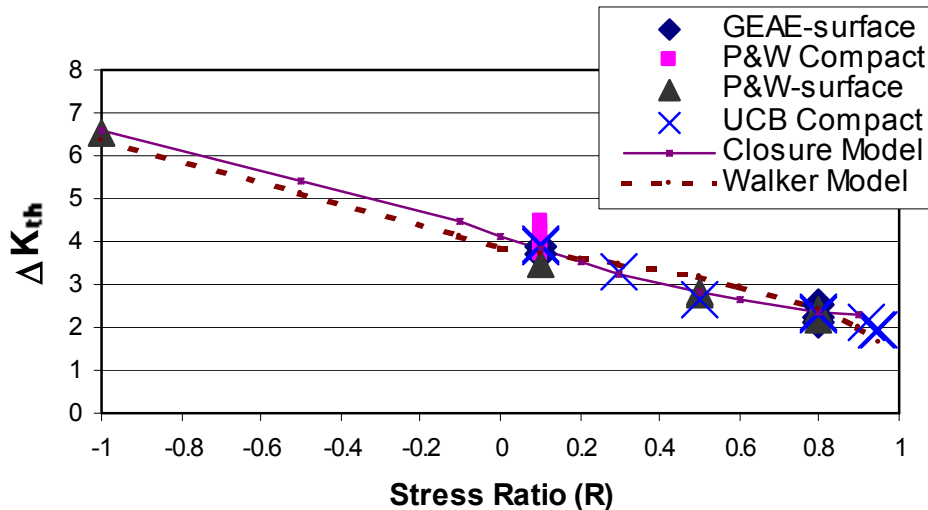


Figure 3.9. Threshold models compared to material behavior shown in Figure 3.5.

As shown in Figure 3.9, the Walker model (Eq. 3.5) was also used to predict all the threshold data measured by both PRDA and MURI participants using the material constants reported in Table 3.3. Note that, while this model was developed using only the GEAE surface crack data, it provides reasonable predictions of the compact data, including that generated at high R conditions by University of California Berkeley under the MURI program. The Walker-based model seems to provide a good engineering method of estimating threshold behavior over a wide range of R ratios, even outside the range of existing data.

3.2.3.2 Small Crack Modeling

Under some conditions, small cracks can grow at nominal ΔK values that are lower than the large crack fracture mechanics threshold, ΔK_{th} . In fact, this violation typically occurs in every smooth specimen test, since the failure crack was once so small that the nominal applied ΔK was less than ΔK_{th} . The Kitagawa^{3.5} diagram, shown schematically in Figure 3.10, integrates the large crack ΔK_{th} (the sloping line) with the smooth specimen endurance limit, $\Delta\sigma_e$, (horizontal line). The intersection of the two lines, defined as a_0 , is given by the following equation (see Appendix 3N):

$$a_0 = \frac{1}{\pi} \left(\frac{\Delta K_{th}}{F \Delta \sigma_e} \right)^2 \quad (3.7)$$

where $F = 1.12(2/\pi)$ is the geometry correction factor in the K -solution for a small semi-elliptical surface crack in the smooth bar specimen. The Kitagawa diagram indicates that cracks smaller than a_0 can grow at a nominal ΔK appreciably less than ΔK_{th} . El Haddad *et al.*^{3.6}, Tanaka *et al.*^{3.7}, and others have proposed that the fracture mechanics threshold is dependent on crack size according to the relationship:

$$\Delta K_{th}(a) = \Delta K_{th} \sqrt{\frac{a}{a + a_0}} \quad (3.8)$$

This relationship is represented in Figure 3.10 by the smooth curve that asymptotes to the endurance limit and large-crack threshold lines in the two extremes. This relationship has been confirmed experimentally in the literature for a number of materials, including titanium alloys^{3.8, 3.9}.

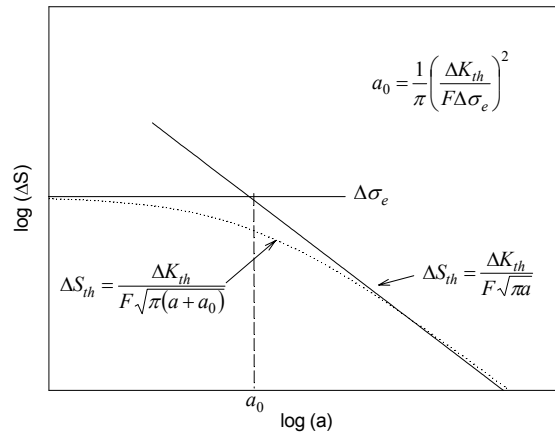


Figure 3.10. Schematic representation of Kitagawa diagram.

3.3 UNDAMAGED MATERIAL BASELINE BEHAVIOR AND MODELING

3.3.1 Smooth Specimen Material Behavior

3.3.1.1 LCF Life Behavior

Approximately 25 fatigue tests were conducted under strain-control conditions to generate fatigue-life data in the range from 5000 to 2×10^6 cycles to failure. See Appendix 3E for details. These fatigue tests were conducted at a frequency of 20 cpm and under different maximum and strain range control conditions. Figure 3.11 shows the resulting strain range *versus* life data for strain ratios ($\epsilon_{\min}/\epsilon_{\max}$) of -1.0, 0.1, 0.5 and 0.8. These data are integrated with the HCF life data generated to establish total life models with threshold estimating capability.

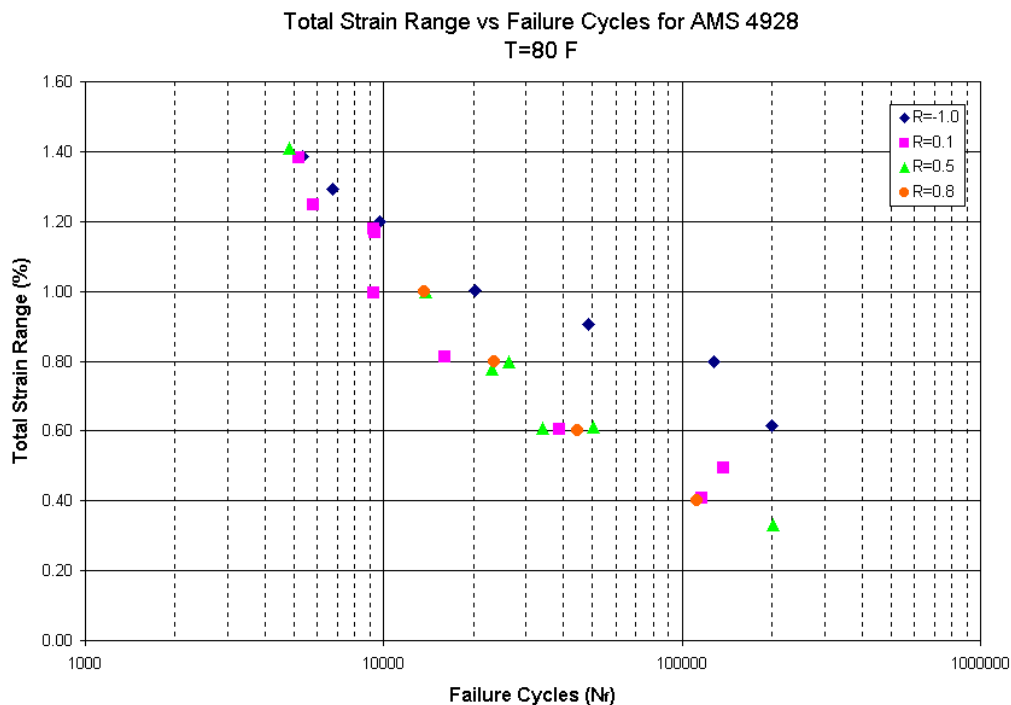


Figure 3.11. Strain-life fatigue data as a function of strain ratio.

3.3.1.2 Baseline HCF Stress Ratio Behavior

Basic testing was conducted at four stress ratios ($R = -1, 0.1, 0.5$ and 0.8) and at 60 Hz to establish a smooth-bar endurance limit baseline. ASE performed the testing and used uniform gage specimens with a nominal gage diameter of 0.200 inch that had been processed to the baseline condition. Specimens were obtained from three different forgings, but each stress ratio received an approximately equal number of specimens from each forging. Tests were considered runouts (suspended) at 10 million cycles. The test results are shown in Figure 3.12.

Fractography of representative specimens at all four stress ratios revealed a similar crack nucleation mode for $R = -1, 0.1$ and 0.5 conditions. At these values of R , failure started from a single crack nucleation site, and these sites were typically endowed with transgranular facets. The size of the facets was similar to the size of the primary alpha particles. As the crack propagated away from the nucleation site, fewer facets were observed on the fracture surface. At $R = 0.8$, however, crack nucleation sites could not be found on the surface, and the overall fracture surface appeared to be caused by ductile overload. A representative crack nucleation site from a specimen tested at $R = 0.1$ is shown in Figure 3.13.

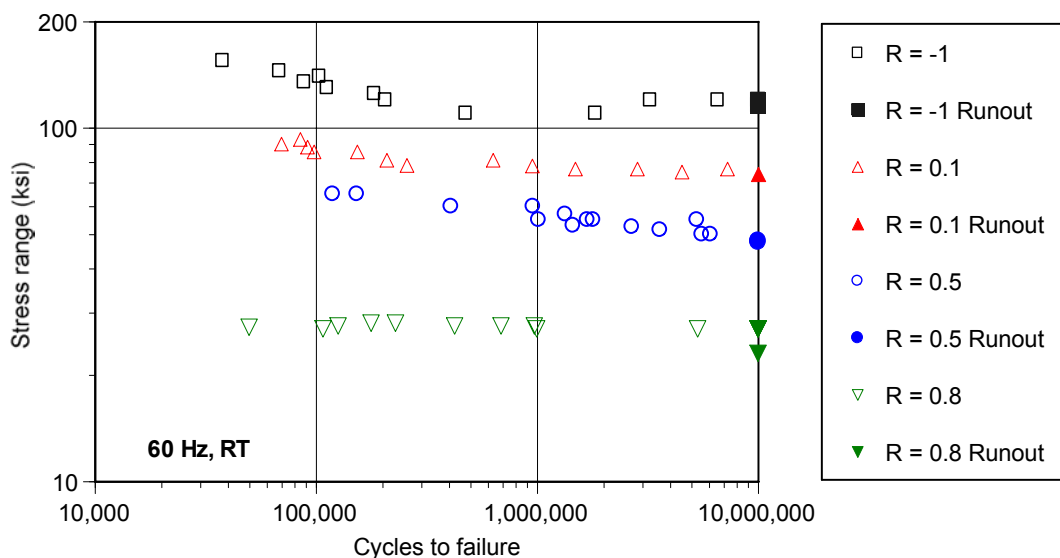


Figure 3.12. Basic R-ratio tests results for the four stress ratios.

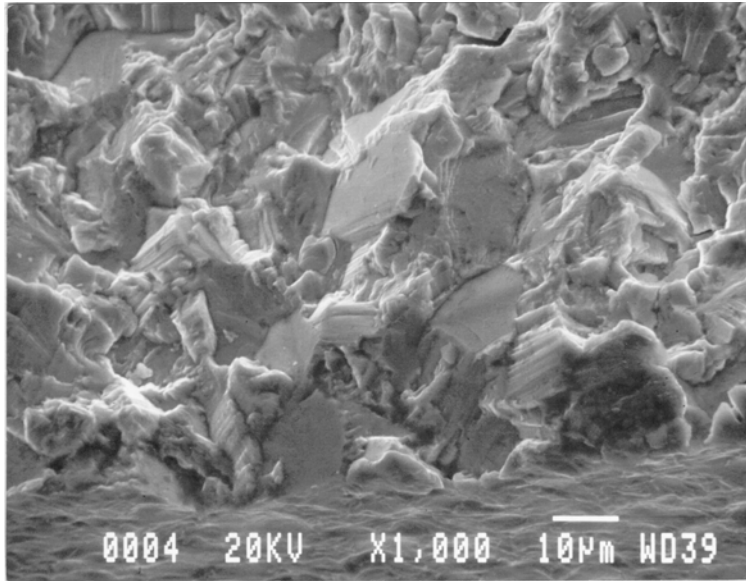


Figure 3.13. Representative nucleation site from R = 0.1 test.

3.3.1.3 Constant Life Diagrams

Constant life diagrams provide summaries of the fatigue strength behavior associated with a fixed number of cycles to failure, i.e., 10^6 , 10^7 , 10^8 or 10^9 cycles, which are considered life-limiting conditions. The type of constant life diagram utilized by the engine industry is now being referred to as the Haigh or Modified-Goodman diagram. These diagrams are typically constructed using data such as shown in Figure 3.12 (by estimating the strength at a given number of cycles to failure), but this method is both time-consuming and expensive. This program utilized an alternate approach to generate constant life data based on a single-specimen, step-test method that yielded estimates for fatigue strength for a given number of cycles to failure.

The single-specimen, step-testing method utilized in this program follows that suggested by Maxwell and Nicholas^{3,10}; they performed the initial validation tests on the material, which showed that the method had direct application to the program's Ti-6Al-4A blade material. This program further validated the use of this method in collecting fatigue strength data for Ti-6Al-4V alloys. In this method, the fatigue strength is determined by subjecting the specimen to a constant stress range for a block of cycles (typically 10^7 , 10^8 or 10^9 cycles). If failure does not occur within the block, the stress

range is increased by a small percentage (5% or less). This continues until failure is achieved. The constant life endurance stress range is calculated by:

$$\Delta\sigma_{ES} = \Delta\sigma_{PS} + (\Delta\sigma_F - \Delta\sigma_{PS})(N_f / N_{RO}) \quad (3.9)$$

where $\Delta\sigma_{ES}$ is the constant life endurance stress range (or endurance strength), $\Delta\sigma_{PS}$ is the stress range from the prior unfailed block, $\Delta\sigma_F$ is the stress range from the final block, N_f is the cycles to failure in the final block, and N_{RO} is the number of cycles considered to be a run-out (and by definition, the number of cycles of the previous unfailed block). This equation essentially interpolates linearly between $\Delta\sigma_F$ and $\Delta\sigma_{PS}$.

This method was used to generate fatigue strengths on approximately four smooth specimens at each of the -1, 0.1, 0.5 and 0.8 stress ratios. Bellows *et al.*^{3.11} then compared these results to the conventional (basic stress-ratio) fatigue strength limit results. All of the step tests at the four stress ratios fall within the 3-sigma reliability limits of the conventional (non step) tests. Therefore, the step test method was considered to be a valid method of determining fatigue strength for lives of 10^7 cycles in the Ti-6Al-4V material, but caution was suggested at negative stress ratios.

The Haigh diagram in Figure 3.14 shows both the extrapolated fatigue strength from the conventional (non step) tests and the fatigue strength for each step test specimen. The good agreement between the conventional and step tests results can be seen at the positive stress ratios. At the $R = -1$, the step tests results are near or larger than the extrapolated values, but still within the 3-sigma limits based on non step tests. The validation of the step method was important for this program because it provides a method for generating traditional Haigh diagrams for specific conditions and for generating a fatigue strength with a single specimen.

3.3.1.4. Effects of Specimen Geometry, Frequency and Surface Test Conditions

Different specimen configurations, testing frequencies and surface conditions were studied to understand their influence on undamaged, smooth bar HCF behavior.

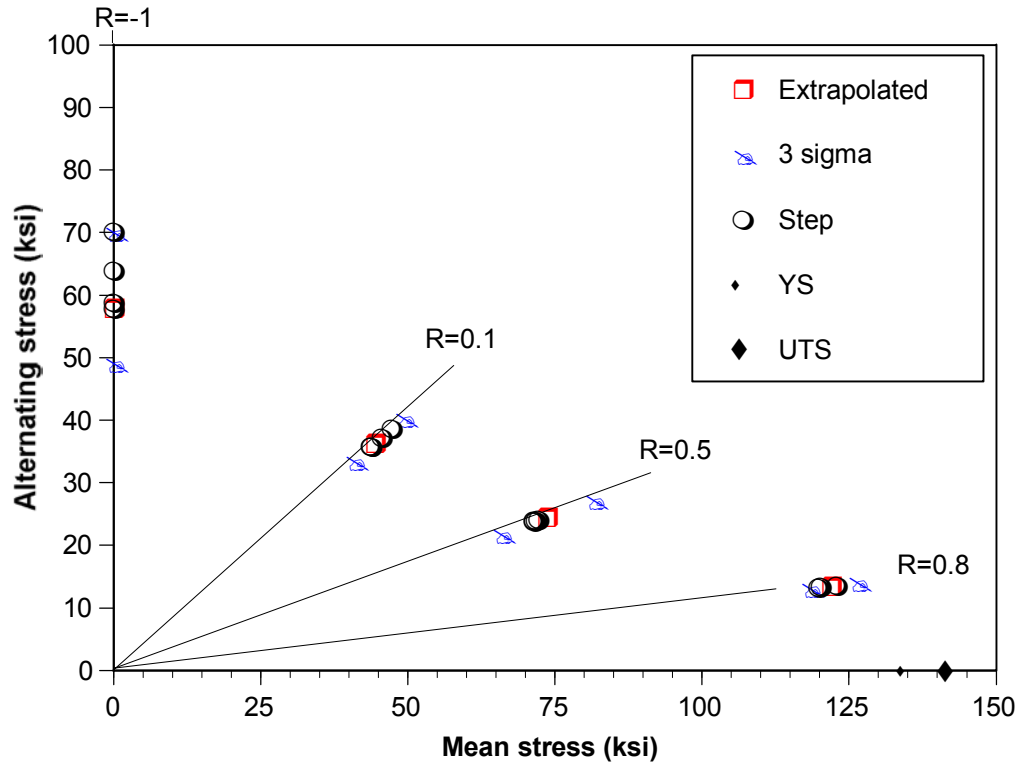


Figure 3.14. A Constant Life (10^7 cycles) Haigh (Modified-Goodman) diagram showing the extrapolated non-step fatigue strengths (and 3 sigma limits) and the individual step test fatigue strengths.

Round-robin testing was conducted at a stress ratio of 0.1 and a frequency of 60 Hz to evaluate specimen-gage geometry effects; these results are reported in Appendix 3F. Two specimens had uniform gage lengths, but different sampling volumes. A third specimen had an hourglass gage section. Because different team members were responsible for testing the different specimen geometries; it is difficult to draw conclusions from the data. However, the effect of specimen geometry appears to be minimal, perhaps as a result of the homogeneity of the material. Additional testing would be necessary to statistically verify this statement.

Smooth bars were also tested to determine the effect of frequency on total life. Frequencies of 60, 200 and 1000 Hz were evaluated at different stress ratios. Higher frequencies are more representative of actual blade HCF conditions and allow test data to be generated more rapidly. Until recently, most test frames have been limited to lower frequencies, and therefore most of the HCF data generated had been generated

at frequencies <100Hz. For the most part, the data generated under this program (See Appendix 3F) suggest that the fatigue life of Ti-6Al-4V does not depend on frequency within the range tested. One data set generated at $R = 0.1$ and 1000 Hz implies that the fatigue strength at this higher frequency condition is substantially lower than the strength at the other frequencies. Additional testing is necessary to determine if these data represent a material effect or a test anomaly. *(Editor's note: In the follow on program, it was determined that the low occasional strength levels may be attributed to potential issues with test control at the 1000 Hz frequency. Note however, that in the program being reported here, all analyses of smooth specimen results, see paragraph 3.3.2, assumed that these lower strength results represented valid fatigue test data. So all the smooth specimen models reported herein have been somewhat influenced by these $R = 0.1$, 1000 Hz test data.)*

It is well known that surface conditions can influence fatigue behavior of specimens and components. These surface conditions can result from machining operations and post machining processing. Components are often in a condition other than stress-relieved and chem-milled, so the effects of different machining and processing procedures were investigated to determine the effect of surface condition when compared to the baseline specimen condition.

Four different groups were compared to the baseline specimen condition (low stress grind and polish + stress relieve anneal + chem-mill):

- Stress Relief Anneal + Low Stress Grind + Longitudinal Polish (Group I)
- Stress Relief Anneal + Single Point Turn (Group II)
- Stress Relief Anneal + Low Stress Grind (Group III)
- Baseline Condition + Shot Peen, A7 intensity (Group IV)

Nominally four specimens from each group were tested at each of the $R = -1$, 0.1 and 0.8 conditions. The results indicated that surface conditions do affect fatigue behavior at $R = -1$ and 0.1. No effect of surface condition was seen at the $R = 0.8$ level, probably because the maximum applied stress levels were all above the cyclic yield strength. Complete results from this surface effect study – including fatigue data, residual stress data, surface roughness data, fractography and microscopy – may

be found in Appendix 3G. Only the important surface condition findings are summarized here.

The greatest influence from surface condition was seen in the Group II (Stress Relief Anneal + Single Point Turn) specimens and Group IV (Baseline Condition + Shot Peen, A7 intensity) specimens. At the $R = -1$ condition, the increase in the 10^7 cycle max-stress endurance limit was more than 22 ksi (approximately 40%) for both Group II and IV. At the $R = 0.1$ condition, the increase was about 13 ksi (approximately 15%) for Group II, but the increase for the Group IV specimen was less (about 2 ksi). This was surprising since the compressive residual stresses were greatest for the Group IV specimens.

3.3.1.5 Smooth Specimen Multiaxial Test Data

The University of Illinois performed multiaxial tests on solid-round specimens for the Ti-6Al-4V material. All these specimens were stress relieved and chem-milled. Tests for torsion, proportional tension-torsion, and non-proportional tension-torsion were evaluated for cases where cyclic plasticity was not an issue and elastic-plastic finite element results were available. These tests were primarily designed to provide a basis to identify model weaknesses and also to evaluate stress states that could exist in the attachment regions of fan or compressor components. The multiaxial fatigue data (deformation and life results) are summarized in Appendix 3H.

3.3.2 Smooth Specimen Models

The overall approach for evaluation and selection of the models is depicted schematically in Figure 3.15. Smooth HCF and LCF data is used to establish the stress-strain and life curve that includes the influence of mean stress. Once this is established, multiaxial parameters were evaluated based on multiaxial test results. Finally, a notched prediction method was established, the details of which will be presented in Section 3.4. These methods were developed in a general way so that they could also be used to predict crack nucleation in the FOD and Fretting damage states.

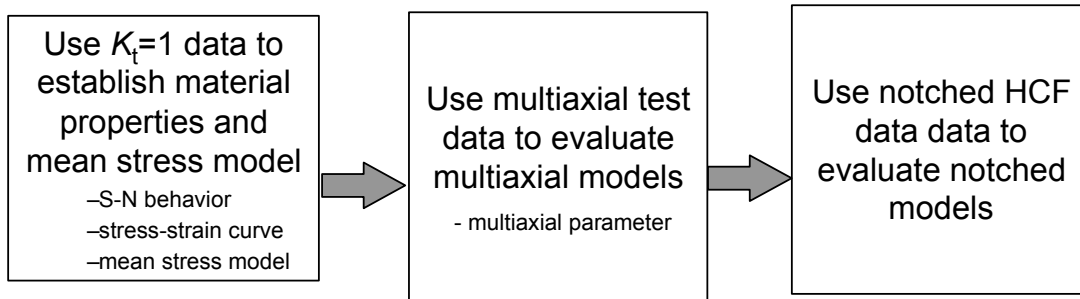


Figure 3.15. Schematic representation of approach used to develop, calibrate, and validate stress methods.

The LCF tests performed by Pratt and Whitney (see Figure 3.11) were used to determine the cyclic stress-strain curve. In Figure 3.16, the values of maximum stresses are plotted against the maximum strains recorded near the specimen half-lives from the Ti-6Al-4V strain-controlled LCF database. The figure compares the stress-strain response for these cyclic (strain-controlled) tests with that from both the monotonic and $R=0.8$ load-controlled tests. As can be noted from the behavior described in the figure, this material cyclically softens under strain-controlled fatigue loading. Figure 3.16 also compares the cyclic stress-strain response with the Ramberg-Osgood equation used to model this response.

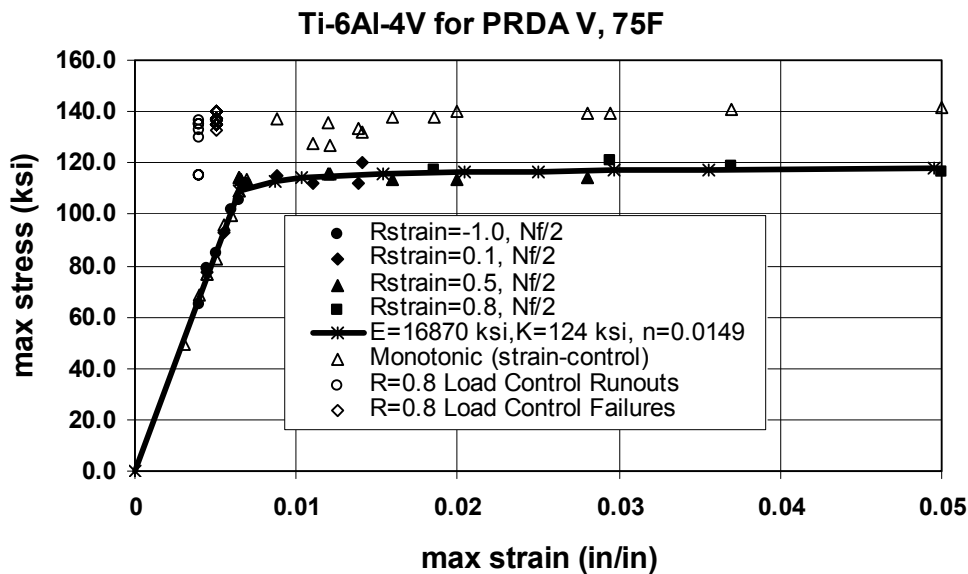


Figure 3.16. Maximum-stress vs. maximum-strain half-life LCF data and cyclic stress-strain curve for Ti-6Al-4V.

The Ramberg-Osgood stress-strain model is described by:

$$\varepsilon = (\sigma/E) + K \sigma^n \quad (3.10)$$

where:

E = elastic modulus

K = strength constant

n = strain hardening exponent

3.3.2.1 Stress Invariant Methods

This paragraph describes an improved HCF equivalent stress method that is capable of predicting mean stress effects under uniaxial and multiaxial stress states for both smooth and notched fatigue specimens. The equivalent stress method is a stress-invariant method, as described fully in Appendix 3I, that can be implemented into computationally-efficient crack nucleation codes such as NASALIFE. The overall approach for evaluation and selection of the models is depicted schematically in Figure 3.15; the Ramberg-Osgood curve shown in Figure 3.16 was used for the elastic-plastic analyses.

All of the appropriate available smooth LCF and HCF data from this program were modeled using a Walker equivalent stress relationship as given in Equation 3.11.

$$\sigma_{equiv} = 0.5 (E\Delta\varepsilon)^w (\sigma_{max})^{1-w} \quad (3.11)$$

where σ_{equiv} is the alternating Walker equivalent stress, E is the average elastic modulus for the material, $\Delta\varepsilon$ is the total strain range, and σ_{max} is the maximum stress as measured on test specimens or calculated with elastic-plastic analyses.

The equivalent stress Walker exponent (w) is a material – and temperature-dependent constant that collapses variable mean stress data into a single life curve. Given the focus of LCF/HCF life prediction for aircraft engine components is in the intermediate and long life regime, elastic cycling conditions typically dominate so that $E\Delta\varepsilon = \Delta\sigma_{psu} \approx \Delta\sigma$. This can be used to establish Equation 3.12 as:

$$\sigma_{equiv} = 0.5 (\Delta\sigma_{psu})^w (\sigma_{max})^{1-w} \quad (3.12)$$

Strain control fatigue tests have been analyzed using Equation 3.12 with the strain range and average elastic moduli. Load control fatigue tests have been analyzed using Equation 3.12 assuming $\Delta\sigma_{psu} = \Delta\sigma$ (an excellent assumption in the long-life regime where load control tests are typically performed). Figure 3.17 shows the HCF and LCF data determined in this program where the alternating Walker equivalent stress is plotted as a function of the cycles to failure. The only data excluded from this analysis is the load-controlled $R = 0.8$ data where strain ratcheting is expected to be significant given the maximum stress exceeded material yield and the tests were performed in load control. *(Editor's note: As noted previously in paragraph 3.3.1.4, in the follow on program, fatigue test results generated under conditions of $R = 0.1$ at 1000 Hz were found to be potentially test anomalies/not-valid test results. In this report, all smooth specimen analyses assumed that the $R = 0.1$ at 1000 Hz truly represented valid material behavior, and thus were used to generate model constants. In the follow on program, all smooth specimen models were updated to include the additional data generated and to exclude these points.)* The equation shown as the solid line in Figure 3.17 were generated using the data shown in the figure. The dashed line represents the minimum of this data distribution. These average and minimum values will be used in later sections of the report for notched, FOD, and fretting tests. The Walker exponent (w) for this regression is 0.433.

Since the focus of this project was to predict HCF damage, statistical analyses of the tests were performed for tests with lives $\geq 10^7$ cycles. This analysis included the alternating Walker equivalent stress calculated for each specimen based on Equation 3.12 as compared to the alternating Walker equivalent stress as calculated from the life measured on each specimen. The results of this evaluation are presented in Section 3.5.

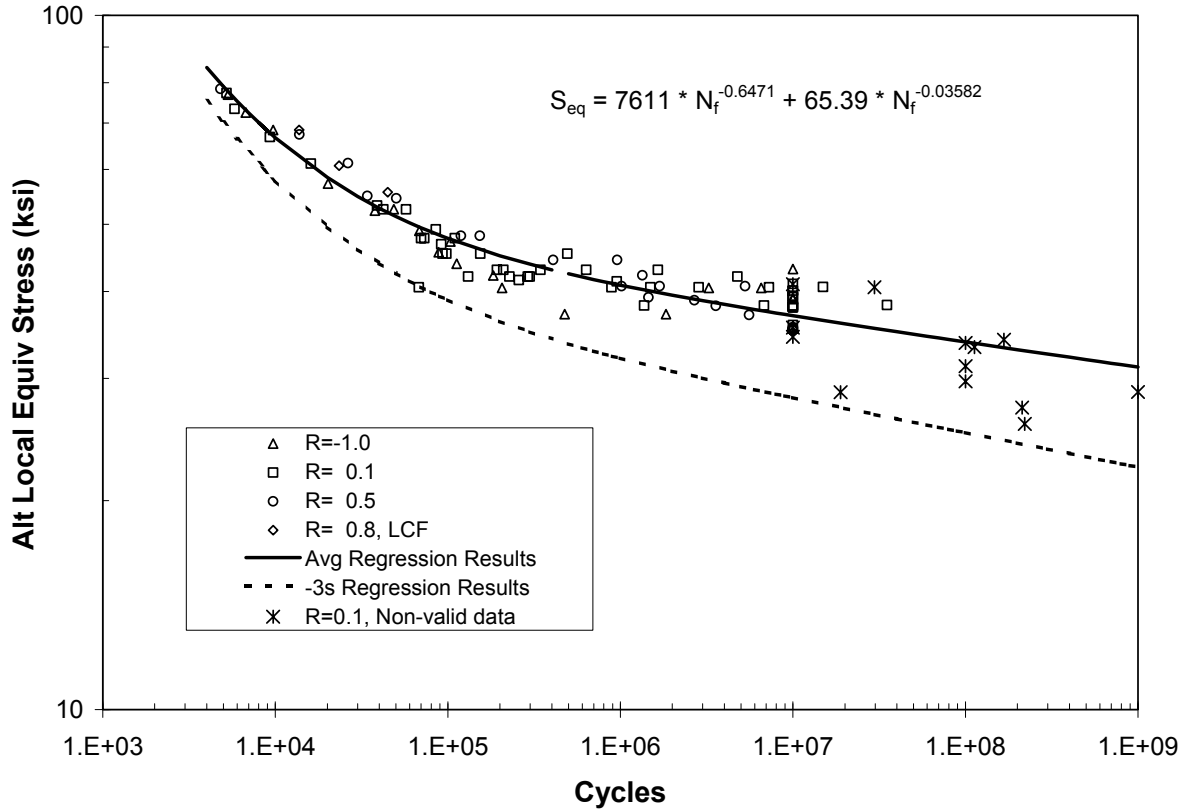


Figure 3.17. Walker equivalent stress-life curve developed for Ti-6Al-4V.

The life models were next extended to predict life for multiaxial applied stress states. A variety of stress-invariant multiaxial parameters were evaluated. The stress-invariant model that best predicted the experimental results is based on the effective stress range and a modified Manson-McKnight mean stress. The stress range term is given as:

$$\Delta\sigma_{psu} = \frac{1}{\sqrt{2}} \sqrt{(\Delta\sigma_{xx} - \Delta\sigma_{yy})^2 + (\Delta\sigma_{yy} - \Delta\sigma_{zz})^2 + (\Delta\sigma_{zz} - \Delta\sigma_{xx})^2 + 6(\Delta\sigma_{xy}^2 + \Delta\sigma_{yz}^2 + \Delta\sigma_{zx}^2)} \quad (3.13)$$

where $\Delta\sigma_{psu}$ is the alternating pseudostress range, and $\Delta\sigma_{ij}$ defines the pseudostress range for each stress component based on maximum and minimum points in the fatigue cycle. The Modified Manson-McKnight mean stress term is given as:

$$\sigma_{mean} = \frac{\beta}{2\sqrt{2}} \sqrt{(\Sigma\sigma_{xx} - \Sigma\sigma_{yy})^2 + (\Sigma\sigma_{yy} - \Sigma\sigma_{zz})^2 + (\Sigma\sigma_{zz} - \Sigma\sigma_{xx})^2 + 6(\Sigma\sigma_{xy}^2 + \Sigma\sigma_{yz}^2 + \Sigma\sigma_{zx}^2)} \quad (3.14)$$

where σ_{mean} is the mean stress, and $\Sigma\sigma_{ij}$ defines the summed stress for each stress component based on maximum and minimum points in the fatigue cycle. The coefficient β is defined as:

$$\beta = \frac{(\Sigma\sigma_1 + \Sigma\sigma_3)}{(\Sigma\sigma_1 - \Sigma\sigma_3)} \quad (3.15)$$

where $\Sigma\sigma_1$ is the sum of the first principal stresses at the maximum and minimum stress points in the fatigue cycle and $\Sigma\sigma_3$ is the sum of the third principal stress at the maximum and minimum stress points in the fatigue cycle. All stresses for the multiaxial tests are calculated assuming initial plasticity using constants given in Figure 3.16 followed by elastic unloading. This approach is consistent with the analysis of the uniaxial fatigue data as given in Equation 3.12 ($\sigma_{max} = \sigma_{mean} + 0.5\Delta\sigma_{psu}$). This situation is also directly applicable to cases of interest where initial plasticity with nearly-elastic cycling conditions dominate. The analysis of the multiaxial test results with Equations 3.11-3.15 as compared to the fatigue curve as established from uniaxial test data as shown in Figure 3.18.

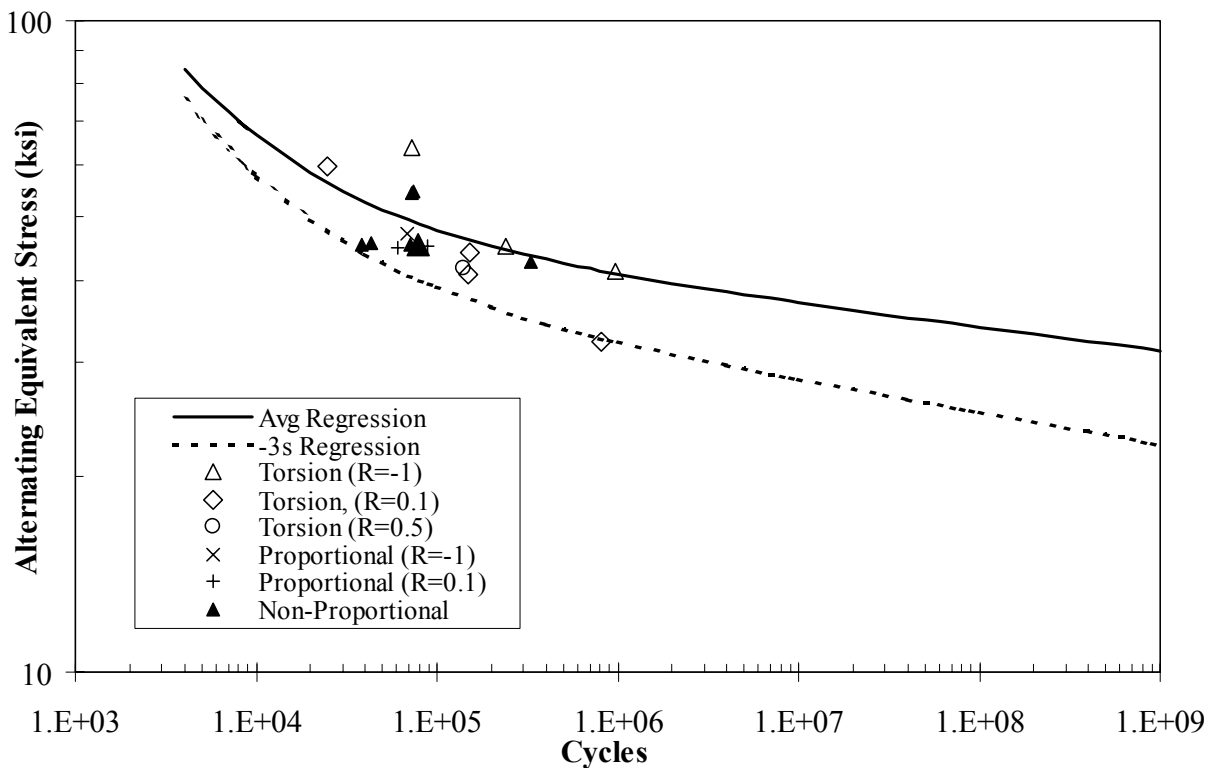


Figure 3.18. Prediction of University of Illinois multiaxial tests results using the modified Manson-McKnight equivalent stress parameter (without R limit).

3.3.2.2 Critical Plane Methods

Three different critical plane models – the Smith-Watson-Topper (SWT)^{3.12}, the Fatemi, Kurath and Socie (FKS)^{3.13, 3.14} and the Findley^{3.15} models – were evaluated. The SWT model is well-suited for tensile cracking, while the FKS and Findley models are better suited for modeling shear cracking behavior.

The SWT model can be simply expressed as:

$$\sigma_{eff} = \sqrt{\sigma_{max} \varepsilon_{a,max}} E = f(N) \quad (3.16)$$

where $\varepsilon_{a,max}$ is the maximum principal strain amplitude, σ_{max} is the maximum normal stress on the critical plane of $\varepsilon_{a,max}$, and E is the Young's modulus. Fatemi and Socie proposed the following shear strain critical plane model for shear dominated cracking behavior:

$$\gamma_{a,max} (1 + k_1 \sigma_{n,max} / \sigma_y) = f(N) \quad (3.17)$$

where $\gamma_{a,max}$ is the maximum shear strain amplitude, k_1 is a constant fitted to merge uniaxial and torsional fatigue data, $\sigma_{n,max}$ is the maximum normal stress on the critical plane of $\gamma_{a,max}$, σ_y is the yield strength, and N is the cycles to failure. For high-cycle multiaxial fatigue, Findley suggested a critical plane model based on the maximum shear stress amplitude, $\tau_{a,max}$ and the maximum normal stress, $\sigma_{n,max}$ on the critical plane of $\tau_{a,max}$:

$$\tau_{a,max} + k_2 \sigma_{n,max} = f(N) \quad (3.18)$$

All of the tension and shear critical plane models, described by Equations 3.16-3.18, were evaluated in the present study.

The SWT (Eq. 3.16) and FKS critical plane models (Eqs. 3.17 & 3.18) were applied to smooth specimen HCF data to evaluate their ability to account for mean stress effects under uniaxial loading. Both the LCF strain-control and HCF data were modeled. The SWT model was found to correlate the data with various stress ratios quite well. The FKS model (Eq. 3.17) did not correlate the data over the various stress ratios very well. The Findley stress parameter (Eq. 3.18) was found to correlate the

data reasonably well, however, further development is needed to better model the effects of mean stress in these shear-based critical plane models.

Figure 3.19 shows the SWT effective stress for different stress ratios. Both the LCF strain-control and HCF data have been modeled in this figure. The SWT effective stress is able to collapse all of the data for the different stress ratios reasonably well in the LCF regime. However, it does not seem to work well in the HCF regime.

The shear-strain and shear-stress equations (Equations. 3.17 and 3.18) were also applied to the smooth LCF and HCF data. Figure 3.20 shows the Findley effective stress model for different stress ratios. Equation 3.18 (normalized by the shear modulus, $G = 6253$ ksi) was used in Figure 3.20. A value of $k_2 = 0.45$ (Eq. 3.17) was found to fit the data well. Also shown in Figure 3.20 are some of the University of Illinois generated uniaxial-torsion data points for $R_\epsilon = -1$ and $R_\epsilon = 0.1$ which were used as a guide in choosing value for k_2 . The Findley effective stress parameter was able to collapse all of the data for the different R conditions reasonably well in both the LCF and HCF regimes. The good correlation of the HCF data using the Findley model also suggests that a shear-cracking mode might be dominant in the HCF regime in general. The FS strain parameter (Eq. 3.17) did not correlate the data as well as the Findley stress parameter. Further development is needed to better correlate data at different values of R using the critical plane methods.

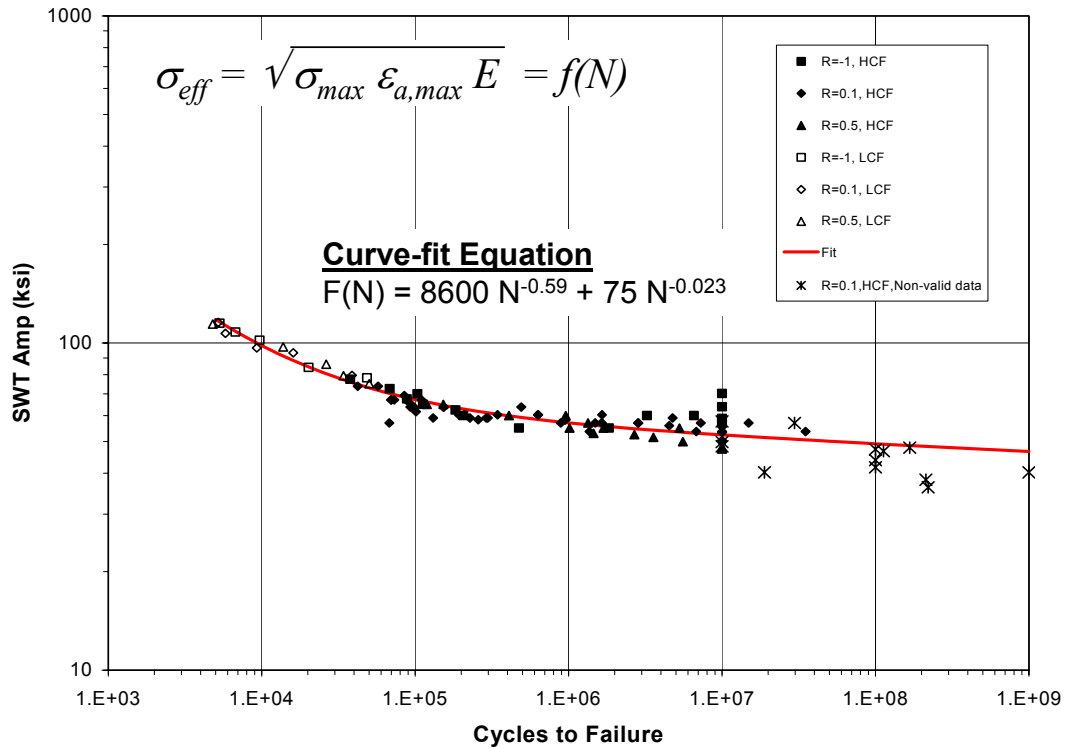


Figure 3.19. The Smith-Watson-Topper (SWT) model correlation for different stress ratios.

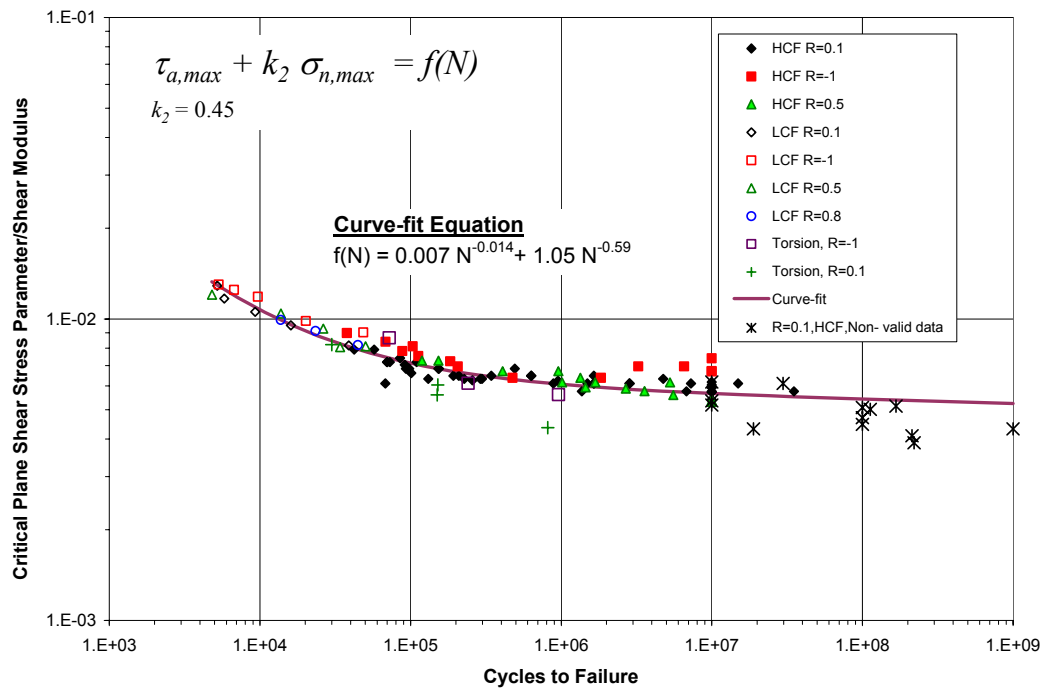


Figure 3.20. The Findley critical plane shear stress model correlation for different stress ratio conditions.

3.4 MODELING NOTCH FATIGUE BEHAVIOR

3.4.1 Notch Fatigue Behavior

Two geometries were selected for notched testing. Specimen geometry information can be found in Appendix 3J. The purpose of testing two geometries was to estimate the effect of stress gradients and notch volume on nucleation life. Each sample was designed to have a nominal K_t of 2.5. The standard V-notch specimen was used for the majority of testing.

The baseline data found in Figure 3.21 indicate significant mean stress effects for stress ratios of -1.0, 0.1, 0.5 and 0.8. Based on a finite element analysis (see Appendix 3K) of the actual specimen geometry, an elastic K_t of 2.68 was calculated for the principal stresses (compared to a handbook value of 2.52). As already shown in Figure 3.14, the Haigh (Modified-Goodman) diagram has been the standard method of modeling HCF fatigue strength (constant life of 10^7 cycles). A similar diagram for notch specimen HCF is shown in Figure 3.22. The large volume notched specimen was used only at a single condition to capture the geometry effect. A K_t of 2.52 was calculated for this specimen based on a finite element analysis (see Appendix 3K). The analysis also indicated that machining tolerances would lead to a $\pm 1.6\%$ variation in the nominal K_t value for this specimen. Results in Figure 3.23 show that both notch acuity and volume has insignificant effects on failure life for these two notch geometries.

Samples were processed according to the requirements set forth for all fatigue specimens. Testing was conducted using two methods; the first was the ASTM Standard E466-96 for load-controlled cyclic testing and the other used the step test method. Testing was performed on closed-loop servo-hydraulic test machines at 60 Hz, 80°F and lab air at stress ratios of -1, 0.1, 0.5 and 0.8.

To evaluate the effects of surface residual stresses on notch fatigue life, shot peened specimens were tested at $R = -1.0$ and 0.1. Data in Figure 3.24 indicate peening provides HCF benefits for both stress ratios, but not for LCF ($<10^5$ cycles) at $R = -1.0$.

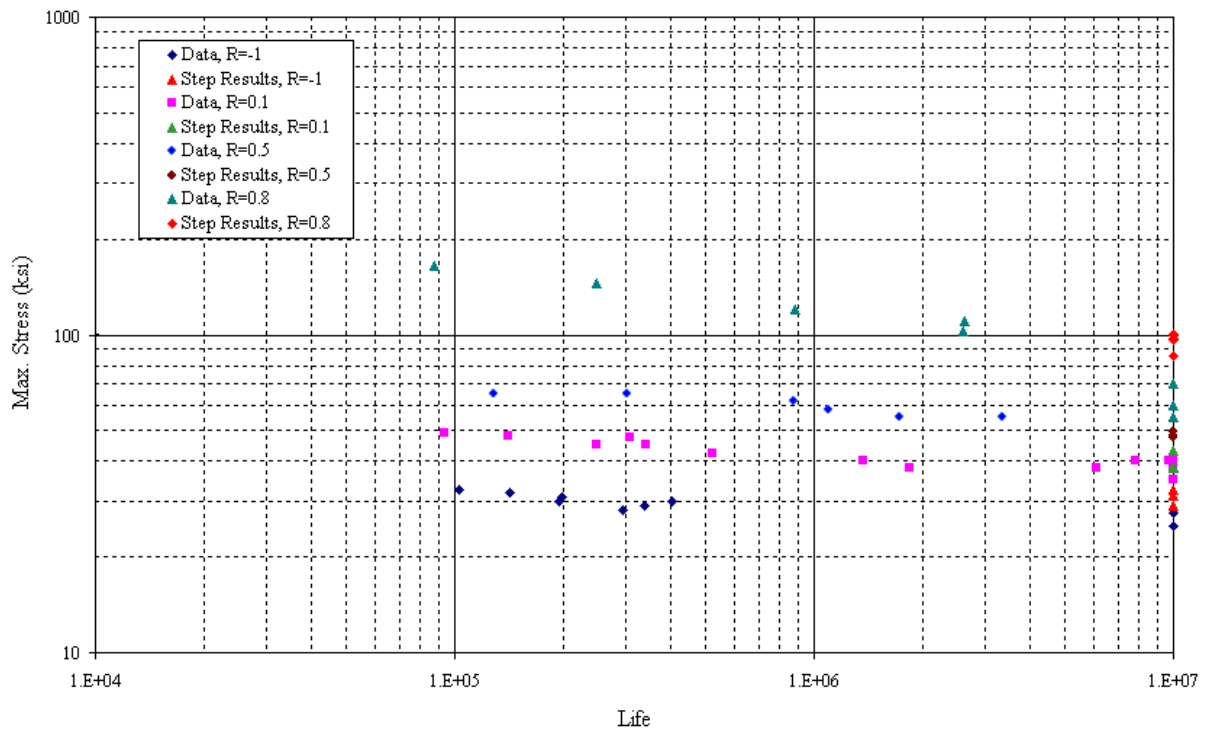


Figure 3.21. Basic stress-ratio tests of double notch specimens ($R = -1, 0.1, 0.5$ and 0.8 and $T = 80^{\circ}\text{F}$).

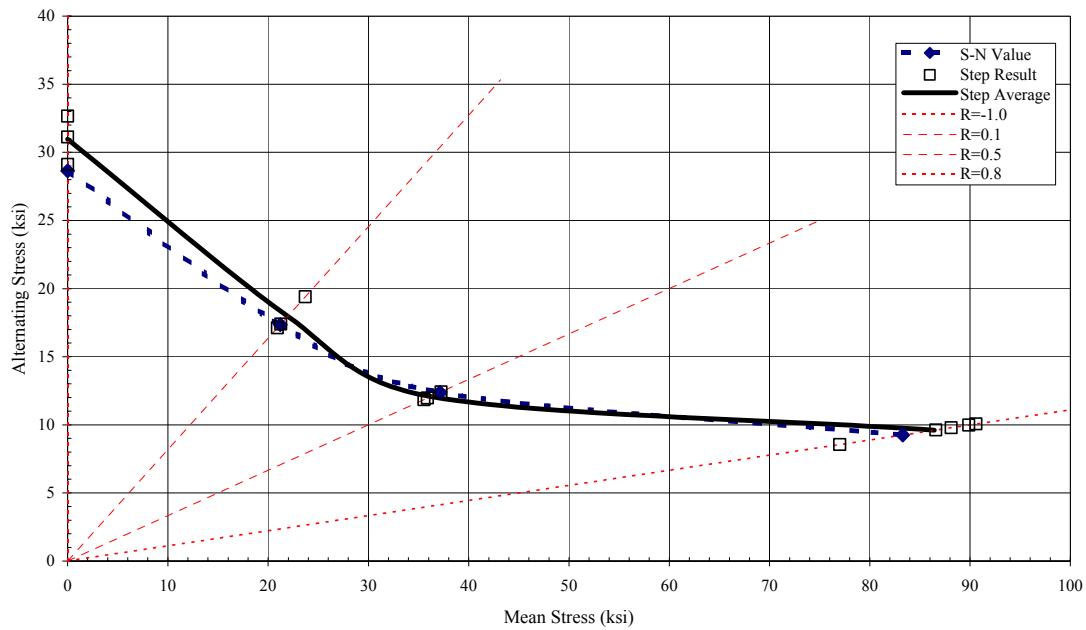


Figure 3.22. Constant Life (10^7 cycles) Haigh (Modified-Goodman) diagram showing the extrapolated non-step notch ($K_t = 2.68$, $T = 80^{\circ}\text{F}$, $f = 60$ Hz) fatigue strengths.

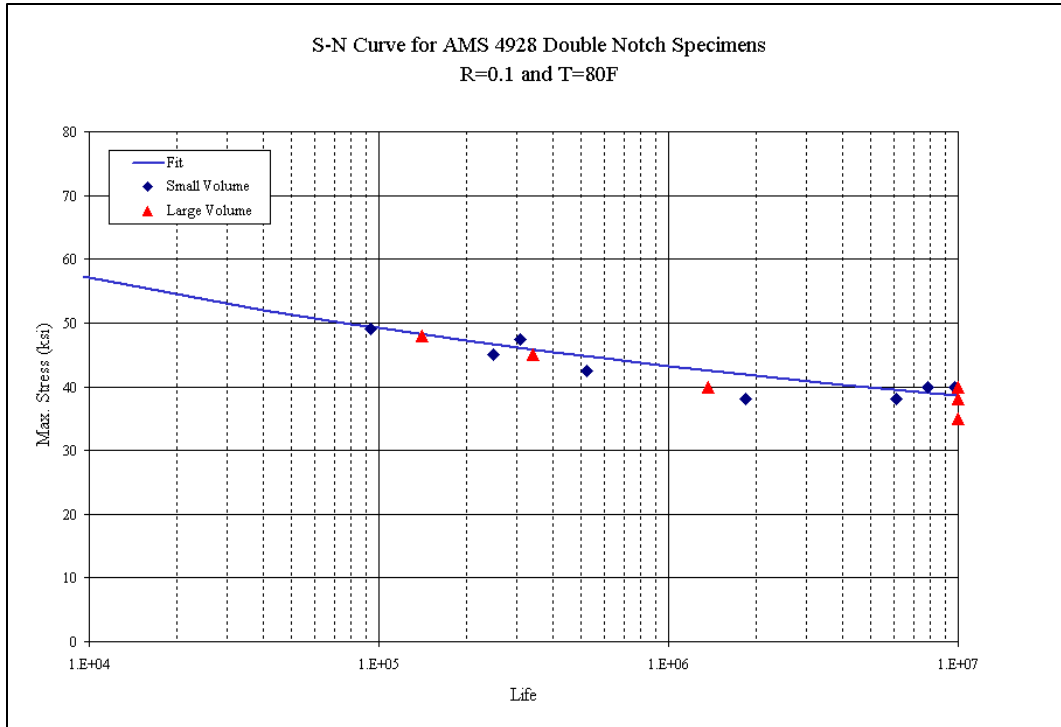


Figure 3.23. Effects of two notch geometries on fatigue life, R = 0.1 and T = 80°F.

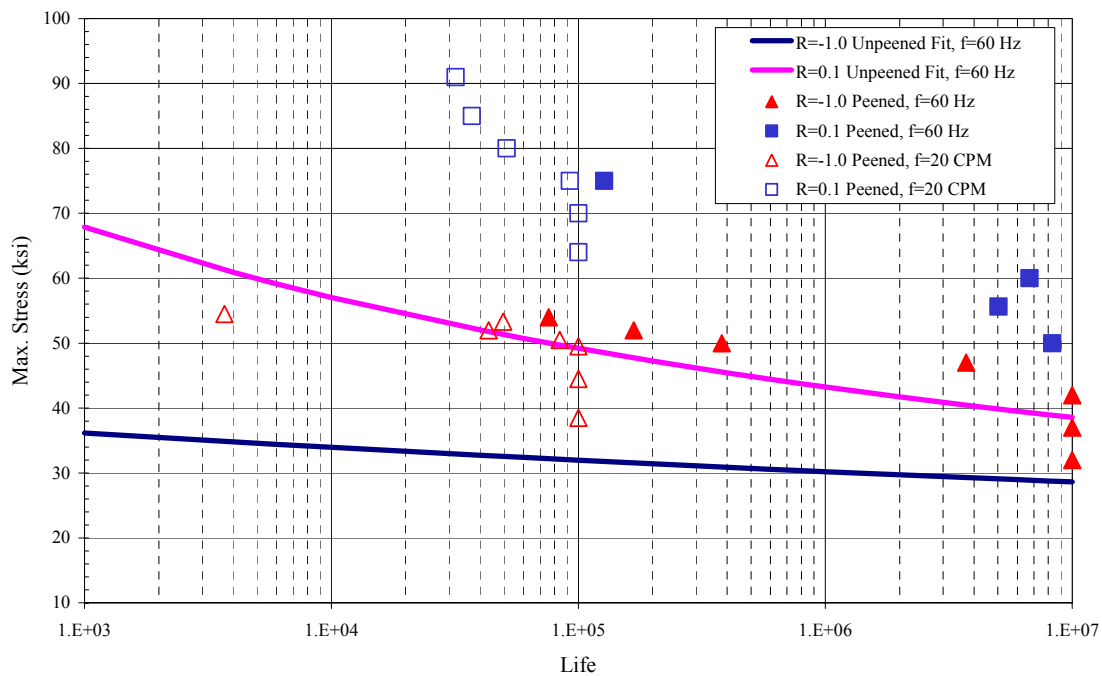


Figure 3.24. Comparison of fatigue of peened and unpeened double notch specimens results (R = -1.0, 0.1 and T = 80°F).

3.4.2 Finite Element Modeling of Notched Specimens

ANSYS was used to provide a finite element analysis of the double edge notch (DEN) specimen and the stress results are shown in Appendix 3K. Based on this FEM analysis, an elastic K_t of 2.68 was calculated for the principal stresses (compared to a handbook value of 2.52). Also included in Appendix 3K is an analysis of the large volume DEN specimen and, taking the machining tolerance into account, the calculated K_t ranged from 2.48 to 2.56.

Several representative notched specimens tested using different stress ratios were selected for scanning electron microscope (SEM) observations. An effort was made to select long and short life notched HCF specimens for these observations. The SEM observations are also summarized in Appendix 3L, which also lists the elastic principal and Von Mises stresses at the SEM observed nucleation sites. These stresses were calculated using the FEM analysis described above. The maximum deviation from the peak surface stresses was 2%. Thus, in the analysis of the notched specimens, peak stresses on the surface were used for all the specimens.

3.4.3 Calculation of Critical Stresses or Strain Parameters

The elements required to predict fatigue behavior at a notch are:

- A stress-strain curve to treat initial plasticity with finite element tools
- Fatigue life curves to correlate smooth specimen behavior
- A model to predict the influence of mean stresses on life
- A multiaxial model to predict the influence of complex stress states on life
- And in some cases, a choice of the location where the stresses at the notch is evaluated.

3.4.3.1 Stress Invariant Fatigue Analysis Methods

The GEAE method relies on a Weibull model to predict the influence of stress gradients on life using stress analysis results from finite element tools.

The final step in the development of LCF/HCF crack nucleation methods was the modeling of notched test data. The test geometries modeled included both flat notched specimens (LCF/HCF damage state) as well as the unnotched and machined notched tests of the winged FOD specimen. All of these specimens were stress

relieved and chem milled. During this evaluation, it became readily apparent that the specimens with small stressed areas had greater HCF capability (higher Walker equivalent stress prior to failure) than the smooth test data. This was especially true for the machined notch FOD test that had the smallest notch length considered of less than 0.015 inch. It was concluded that this behavior is best modeled by considering the size of the stressed surface area. This is probably related to observations that classical slip localization due to persistent slip bands and local extrusions at the surface nucleate HCF and LCF cracks in titanium alloys. One would expect that as more grains are loaded at high stress, the fatigue capability of the specimen is diminished. This was treated quantitatively with the Weibull modified equivalent stress method. The stressed area weighting term employed for a given specimen geometry and loading condition is given in Equation 3.19.

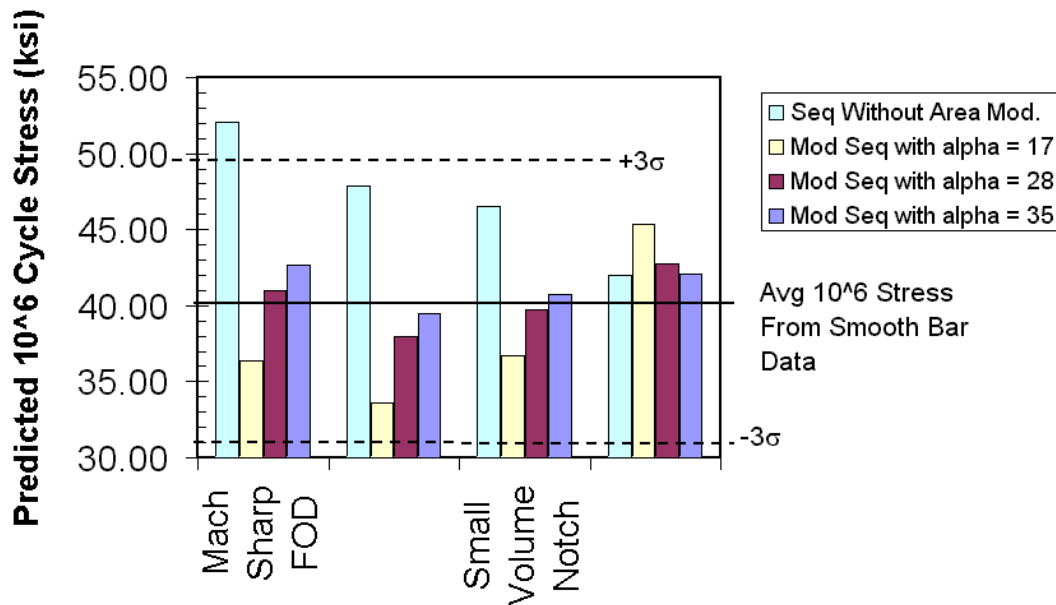
$$Fs = \sum_{i=1}^n \left[- \left(\frac{\sigma_i}{\sigma_{\max}} \right)^{\alpha} \Delta A_i \right] \quad (3.19)$$

where Fs is the stressed area weighting term, σ_{\max} is the maximum first principal stress on the surface for the maximum load case, σ_i is the first principal stress of all elemental faces on the surface, ΔA_i is the area of all elemental faces on the surface, and α is a material shape factor. Different Walkerized equivalent stresses can be normalized for each Fs , assuming an equal probability of failure as given in Equation 3.20.

$$\sigma_{equiv,2} = \sigma_{equiv,1} \left(\frac{Fs_2}{Fs_1} \right)^{1/\alpha} \quad (3.20)$$

Several notch geometries with lives of approximately 10^6 were modeled with this process with the elastic-plastic finite element results and the Weibull Fs term. The results of those evaluations are shown in Figure 3.25 for the cases evaluated. The horizontal lines represent the mean and plus and minus three standard deviations as established from smooth specimen results. Three values of the Weibull modulus are shown. The value of 17 is based on the value for the distribution of all the smooth specimen data (Figure 3.17); the value of 28 is based on smooth specimen results in the vicinity of 10^6 cycles; the value of 35 is based on the value with the best prediction for the notched tests. The two lower values are expected to be most useful in a design system where predictions over the entire life regime for multiple material heats would be

required. These results indicate that a large stressed area (unnotched FOD specimen) results in a predicted life similar to smooth specimens with a similarly highly stressed area. Yet, a relatively small notch (notched FOD specimens) can result in increased stresses prior to failure if the small area of highly stressed material is not accounted for



in the analysis.

Figure 3.25. Variation of Weibull-modified alternating equivalent stress for notched specimens with lives of approximately 10^6 cycles.

3.4.3.2 Critical Plane Methods

The SWT and the FKS/Findley critical plane models described in Section 3.3.2.2 were used to analyze the notched specimen data. A notch plasticity algorithm based on the “equivalent strain energy density” concept (Glinka, *et al.*)^{3.16} along with the cyclic stress-strain response was used to calculate the local notch stresses and strains.

Figure 3.26 shows the SWT parameter (using the maximum principal strain amplitude) for specimens tested over a range of stress ratios (-1, 0.1, 0.5, and 0.8). Also shown in this figure is the SWT fit obtained for the smooth specimens (see Figure 3.19). It appears that the SWT effective stress parameter correlates notched HCF fatigue life data for different stress ratios reasonably well. However, use of the SWT parameter along with the notch stress state (after accounting for notch cyclic plasticity) does not adequately correlate with the smooth data curve-fit.

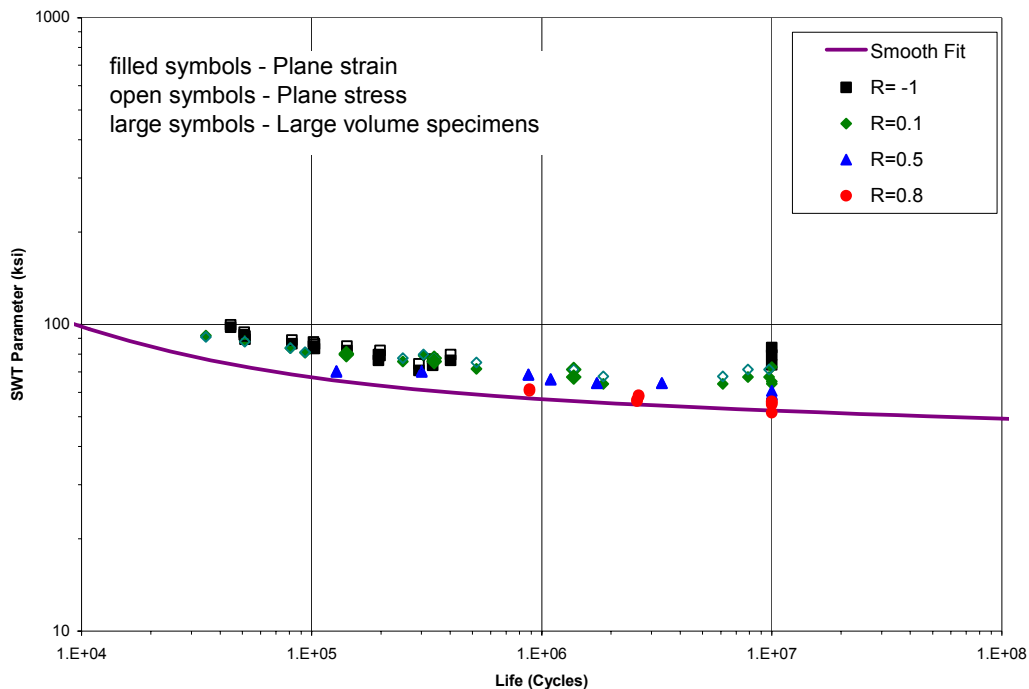


Figure 3.26. Smith-Watson-Topper (SWT) parameter using maximum principal strain amplitude at notch root compared to double edge notch fatigue behavior.

Figure 3.27 shows the correlation of smooth and notched data using the Findley critical plane stress model (Eq. 3.18, normalized by the shear modulus, $G = 6253$ ksi). The Findley stress model seems to correlate the notched data quite well, suggesting that the shear cracking mode might be dominant in the notched specimens. However, use of the Findley stress parameter along with the notch stress state (after accounting for notch-cyclic plasticity) does not adequately correlate with the smooth-data curve-fit.

Further development is needed to account for possible material volume effects in notched specimens to allow correlation of smooth and notched data.

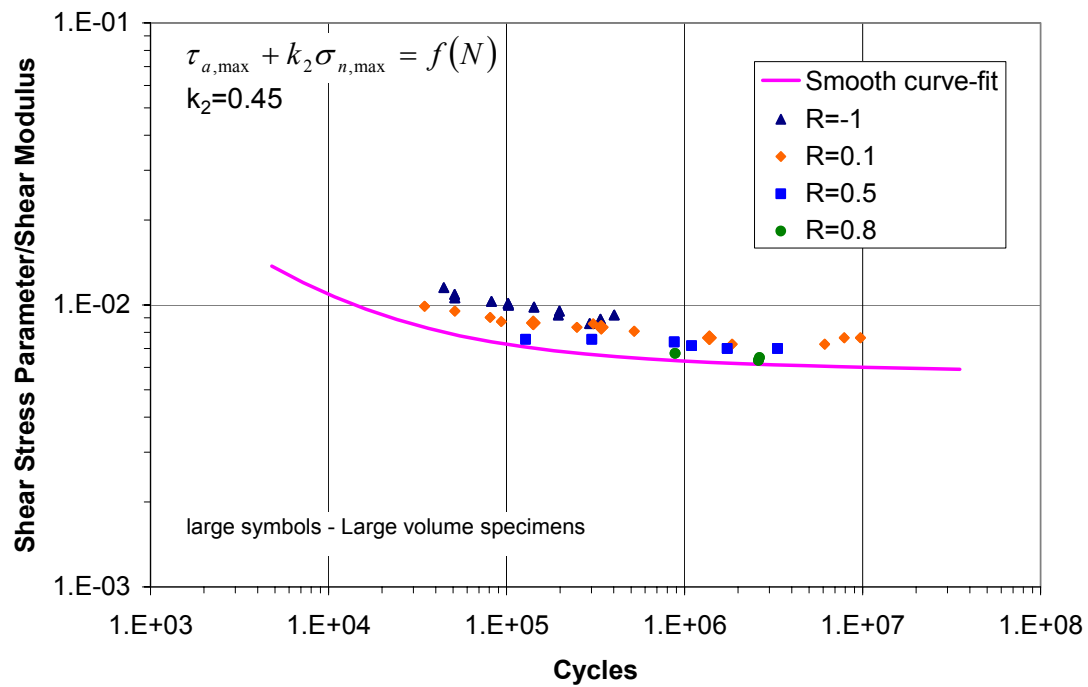


Figure 3.27. Findley critical plane shear stress parameter at notch root ($k_2 = 0.45$) plane stress analysis.

3.5 EXIT CRITERION FOR BASELINE

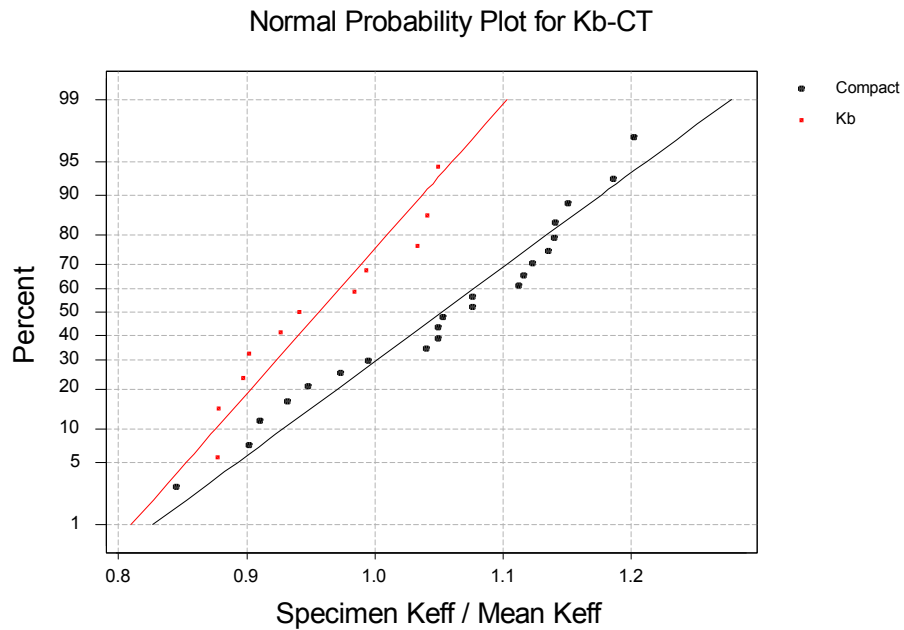
3.5.1 Crack Growth Threshold

Figure 3.28 shows a normal distribution plot of the threshold crack growth measurements normalized relative to the Walker based threshold prediction. Figure 3.28a show the individual distributions of the surface crack (*Kb* specimen) and compact specimen results, and Figure 3.28b shows the distribution of the combined populations. Figure 3.28a shows that the distribution of both types of specimens are remarkably similar. The mean value of the normalized distribution shown in Figure 3.28b is 1.021 and the mean minus 3 standard deviations is 0.721. The latter value is very similar to previous GEAE evaluations of threshold variation for other aircraft engine materials. The distribution shown in Figure 3.28 provides the basis for the baseline crack growth threshold exit criteria.

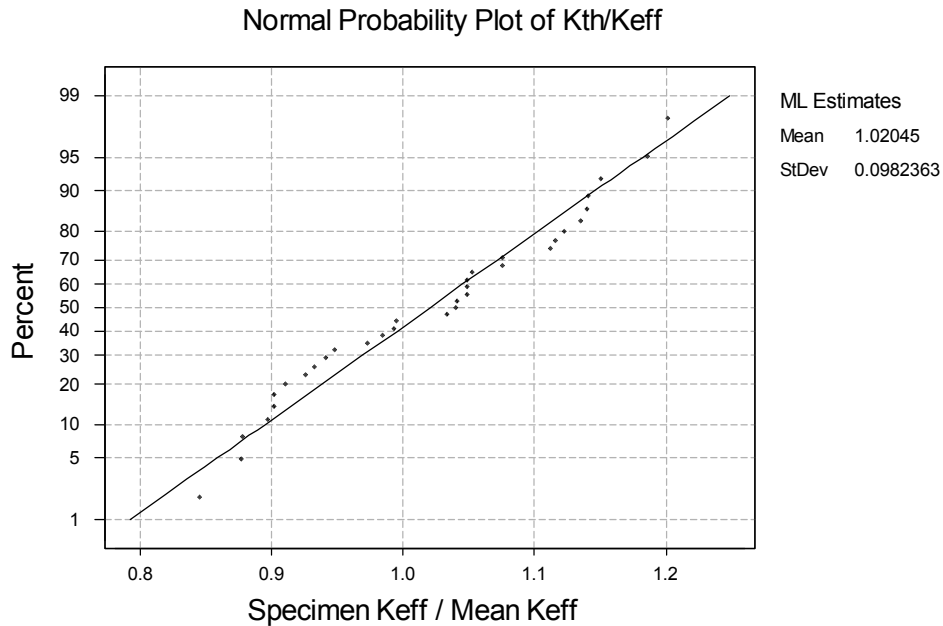
Table 3.4 summarizes the normal distribution parameters for the comparisons shown in Figure 3.28, as well as for results from a similar study conducted to evaluate the Closure model. The Walker model results give an average closer to 1.0 (less bias) than the Closure model, but it has a higher level of scatter. Table 3.4 shows that the crack-threshold baseline prediction capability is between 1.0 +/- 0.07 of the mean estimate for both models and that the coefficient of variations for each model is less than 0.10.

Table 3.4
Baseline Statistical Parameters for Crack Growth Threshold Estimates

Parameter	Walker Model (Figure 3.28b)	Closure Model (not shown)
Average (mean)	1.020	1.068
Median	1.040	1.076
Standard Deviation	0.098	0.073
Coefficient of Variation	0.096	0.068



(a) Geometries Compared for Walker Threshold Model



(b) Geometries Integrated for Walker Threshold Model

Figure 3.28. Normal Distributions of Room Temperature Ti-6Al-4V Crack Growth Thresholds Ratios of Measured vs. Model. This Figure Summarizes Experimental Results from this Program and from the University of California-managed MURI Program.

3.5.2 Smooth Specimen Threshold

Since the focus of this project was to predict HCF damage, statistical analyses of the tests were performed for tests with lives $\geq 10^6$. This analysis included the alternating Walker equivalent stress calculated for each specimen based on Equation 3.11 as compared to the alternating Walker equivalent stress as calculated from the life measured on each specimen. It also included a similar set of calculations for the SWT model (Based on Equation 3.16). A Normal distribution was used to present this behavior and is shown in Figure 3.29. The Normal distribution will be used as the basis for the exit criteria to compare different prediction techniques for subsequent strength-related test results.

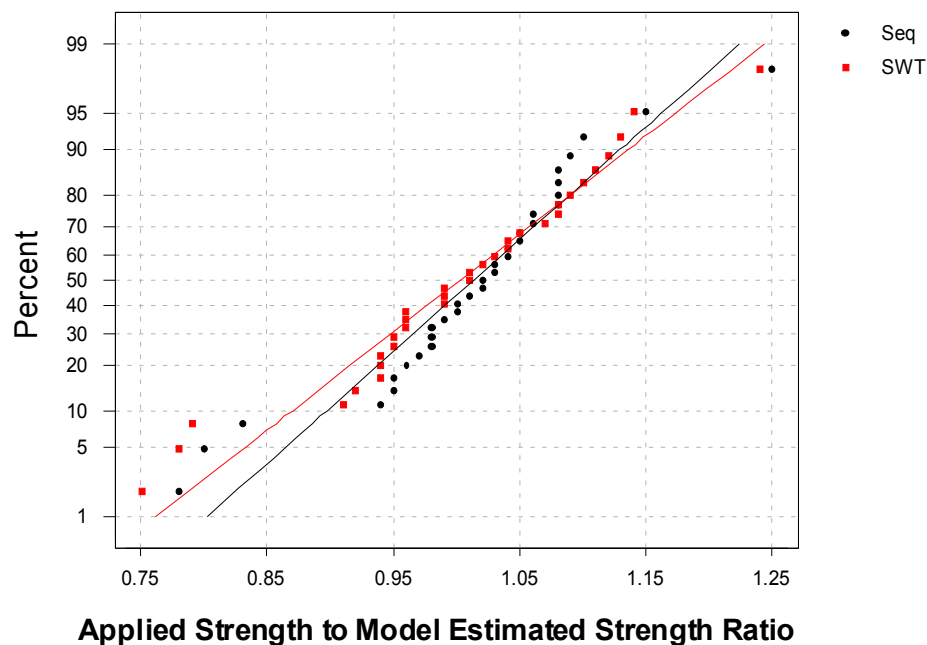


Figure 3.29. Normal distribution the Ratio of Applied to Predicted Strength for undamaged HCF material data with lives in excess of 10^6 cycles. Circles represent Equivalent Stress Model and Squares represent SWT Model.

The distribution parameters for the equivalent stress and SWT model predictions of the uniaxial smooth-specimen (undamaged-material) strength results are presented in Table 3.5. Table 3.5 shows that the undamaged-material baseline prediction capability is

between 1.0 +/- 0.015 of the mean estimate and the coefficient of variations for these two models is approximately 0.10. Exit criteria for predicting the strength of other conditions (notches, LCF/HCF interaction, FOD and attachment distress) will be referenced to this coefficient of variation level.

Table 3.5
Baseline (Smooth Specimen) Statistical Parameters for Total Life Models

Parameter	Equivalent Stress Model	SWT Model
Average (mean)	1.013	1.003
Median	1.023	1.012
Standard Deviation	0.092	0.105
Coefficient of Variation	0.091	0.105

Exit criteria information for the multiaxial results associated with the GEAE equivalent stress method are given in Figure 3.30. There is more variation in the multiaxial data predictions as compared to the smooth specimen correlation, but these results meet the program's exit criteria acceptability. Table 3.6 summarizes the parameters associated with the distributions shown in Figure 3.30

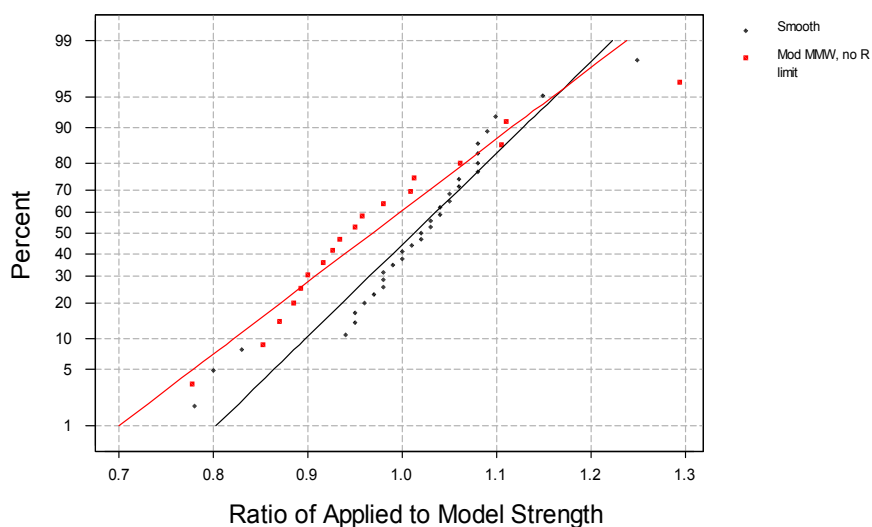


Figure 3.30. Weibull distribution of multiaxial predictions relative to the uniaxial undamaged specimen correlation shown in Figure 3.29.

Table 3.6
Equivalent Stress Model (A/P) Parameters for Uniaxial and Multiaxial Behaviors

Parameter	Uniaxial Behavior	Multiaxial Behavior
Average (mean)	1.013	0.969
Median	1.023	0.942
Standard Deviation	0.092	0.119
Coefficient of Variation	0.091	0.123

3.5.3 Notched Specimen Threshold Stresses

During the course of the program, two methods were evaluated for their ability to accurately predict the notch fatigue strength levels; these were: (1) the equivalent stress approach with a surface area correction (See Paragraph 3.4.3.1) and (2) the SWT critical plane method based on estimates of the local stress-strain behavior (See Paragraph 3.4.3.2). The results of these evaluations, relative to the exit criteria, are described in this subsection.

The equivalent stress approach with the surface area correction method was used to predict the applied failure strength behavior of four distinctly different notch conditions (See Figure 3.25). The applied to predicted (A/P) ratios ranged from 0.82 to 1.08 with an average of 0.95 (for $\alpha = 17$). These ratios are within the bounds of the exit criteria but the sample size is far too small for a general conclusion. The equivalent stress method will be used for the evaluation of crack nucleation in the FOD and fretting damage states. One of the advantages of the Weibull modified equivalent stress method is that it can be used as an element within a probabilistic HCF design system. For a given component, the Weibull modified stress can be compared to the baseline data and a probability of failure can be calculated. This has clear advantages over other purely deterministic life prediction methods.

The SWT critical plane model was applied to 49 notched specimen test results and the predicted SWT parameter was compared to the applied SWT parameter.

Figure 3.31 presents the distributions of the ratios of applied to predicted (A/P) values for the notched specimen tests and the baseline smooth bar tests. On average, there is a 25 percent bias in the model predictions (average A/P = 1.25), but care must be taken in the interpretation of this composite average. The SWT model does not sufficiently account for stress ratio (R) as can be seen in Figure 3.32 which presents the distribution of model to applied SWT ratios for each of the four test R values. The bias and scatter of the composite distribution presented in Figure 3.31 is distorted by the relative number of tests performed at the selected stress ratios.

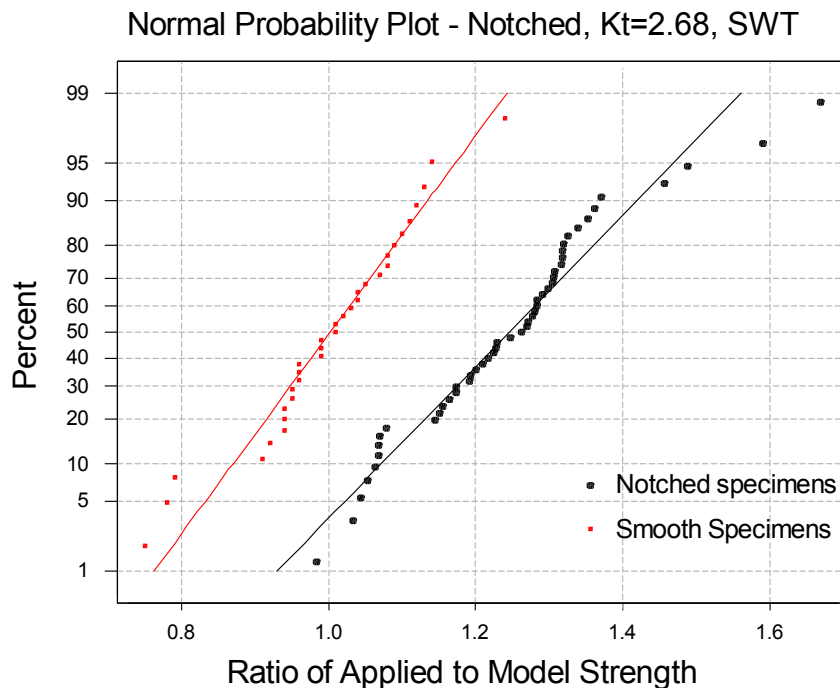


Figure 3.31 Normal Distributions of Ratios of Model SWT to Applied SWT for Notched Specimens as Compared to Smooth Specimen Ratios.

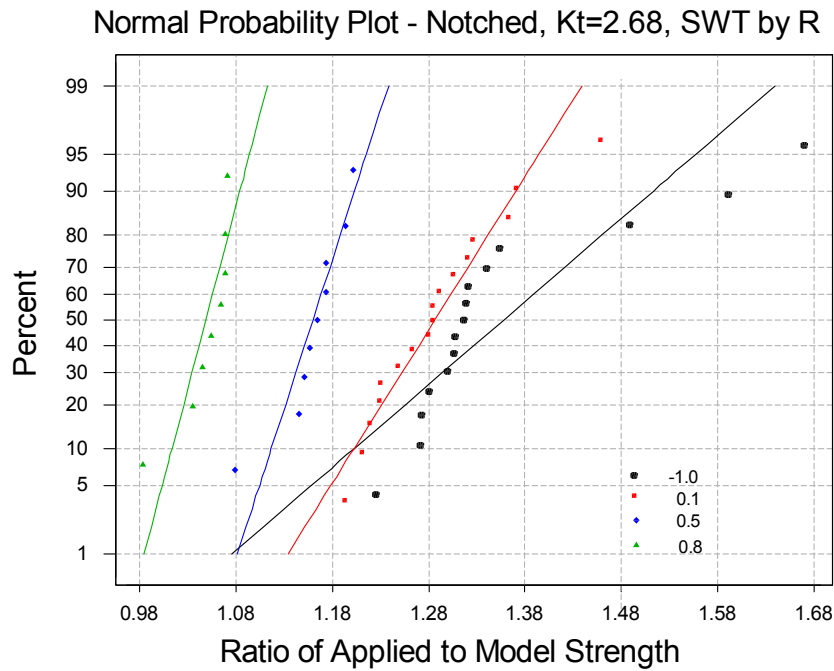


Figure 3.32 Normal Distribution of Ratios of Applied SWT to Model SWT for Notched Specimens by Test Stress Ratio Condition.

Table 3.7 compares the statistical parameters for the normal distributions associated with the uniaxial and notched specimen behaviors for the SWT model. The bias in the prediction of the notched behavior significantly exceeds that of the prediction of the smooth specimen behavior. The scatter in the notched behavior predictions exceeds that of the smooth predictions by 30 percent. Because of the large bias and the inability to account for stress ratio, further development effort will be required for the prediction of notch behavior.

Table 3.7
SWT Model (A/P) Parameters for Uniaxial and Notch Behaviors

Parameter	Uniaxial Behavior	Notched Behavior
Average (mean)	1.003	1.246
Median	1.012	1.263
Standard Deviation	0.105	0.137
Coefficient of Variation	0.105	0.110

3.6 BASELINE BEHAVIOR SUMMARY AND RECOMMENDATIONS

3.6.1 Baseline Data Collection and Analysis

A substantial part of this program focused on developing baseline data that would support the development and evaluation of structural models that could be used to predict material thresholds for crack nucleation and crack growth. As part of this baseline evaluation, new test techniques were evaluated and changes in standard ASTM test procedures were justified. The step test technique was one new test technique that proved beneficial for creating hcf fatigue strength levels.

Comparing step test results to those generated using S-N extrapolation techniques demonstrated that the step test method faithfully establishes mean fatigue strength behavior for cycle counts $> 10^6$ cycles. This test method can be used to more rapidly develop the fatigue threshold property as opposed to developing a sufficient quantity of S-N data in the long life region and developing the value by analysis.

By introducing changes in the ASTM Standard E647, the program demonstrated that the standard restrictions for shed rate could be relaxed without impacting the accuracy of ΔK_{th} levels generated by the change in the threshold crack growth rate procedures and this allowed more rapid development of this threshold property.

Using the baseline properties, both Pratt & Whitney and General Electric were able to use effective stress and effective stress intensity factor models to characterize the baseline fatigue crack nucleation and crack propagation data. These models were then used to predict, as a function of stress ratio, the long life fatigue crack nucleation threshold behavior (undamaged material behavior) or fatigue crack growth rate threshold behavior (independent of component and crack geometry). Baseline modeling of fatigue nucleation included the evaluation of equivalent stress models (modified Manson-McKnight and Smith-Watson-Topper) and several critical plane models. These performed well for characterizing the results from uniaxial loading conditions. Baseline fatigue crack growth modeling included the use of a Walkerized Sigmoidal model and a Newman-based Closure model. Both models accurately characterized the baseline fatigue crack growth rate data.

The fatigue crack nucleation models were evaluated for their capability to describe the typical multiaxial behavior experienced in regions of attachment distress and high stress concentration. There were two parts to this modeling: (1) establishing the structural fatigue parameters for specific experimental test geometries and (2) comparing the uniaxially-developed model to the fatigue data generated using tension-torsion (multiaxial) loading applied to smooth bar samples. The modified Manson-McKnight equivalent stress model provided an accurate description of the tension-torsion test results, except possibly for some non-proportional loading conditions. The Smith-Watson-Topper model showed similar results but only a limited number of test conditions were evaluated.

The fatigue crack nucleation models were also evaluated for their capability to describe notch fatigue behavior. Most of the experimental fatigue life results were generated using two different types of notches. To calculate fatigue life, it was necessary to estimate the notch localized stress-strain behavior for the test geometries. Alternate procedures were used here: cyclic finite element analysis and approximate notch analysis. Fatigue life estimates were generated based on these estimates of the localized stress-strain behavior and how they affected the fatigue life parameter (equivalent stress). In the case of one calculation, estimates of the stress-strain behaviors were generated using the critical damage plane approach. Using the modified Manson-McKnight model, General Electric was able to show (for a limited number of notch cases) that a weak-link highest-stress-area method correlated well with the behavior. The Pratt & Whitney analysis utilized an approximate notch stress-strain estimate, and a critical plane analysis to establish the Smith-Watson-Topper fatigue parameter of all the notch fatigue data; the results of the evaluation resulted in extremely conservative estimates of when a notch might nucleate a crack.

3.6.2 Models for Threshold Behaviors

Both crack growth and crack nucleation threshold behavior were evaluated to establish baseline conditions for predicting the accuracy, bias and scatter associated with fracture mechanics and total life models. The emphasis was on establishing models that could be used to predict allowable stress (or stress parameter) levels that

could be used in design to reduce the potential for high cycle fatigue failure. The emphasis in this chapter was on reporting the development and verification of these models using relatively simple loading conditions and structural geometries. The models were developed from data generated under standard test conditions and then verified by comparing the ability of the model to repredict the conditions associated with threshold or near threshold test parameter conditions. There are two exceptions to this statement: (1) uniaxial models were used to predict multiaxial material behavior and (2) integrated structural-material models were used to predict notch fatigue behavior.

In all cases, the strength (parameter) values associated with the test conditions were predicted (or repredicted) using either a fracture mechanics or total life model. These comparisons provided data for statistical distributions of the ratios of the actual (test) value of the parameter to the (model) predicted value of the parameter for each test condition, i.e., the A/P ratio. These actual to predicted ratio statistics provide the baseline condition for the damage state exit criteria, since any model should be able to accurately predict the data on which it is based. Minimum bias and low scatter are also expected with the baseline models.

Bias in a prediction can be directly judged by its deviation from unity since a mean A/P of one implies that, on average, the prediction equals the actual. The exit criteria for bias are: a) an acceptable range of the estimate of bias, and b) a demonstration that the bias is not significantly dependent on the test conditions.

The standard deviation of A/P is a normalized measure of the scatter of the predictions about the mean. The exit criteria for scatter is expressed in comparative terms with the scatter in A/P obtained from the baseline tests.

The exit criteria for the other damage states (LCF/HCF, FOD, and Fretting) are thus expressed in terms of the means and standard deviations of the ratio of actual to predicted parameters for the specific damage states.

3.6.3 Baseline for Exit Criteria

The baseline ΔK_{th} behavior as modeled by the Walker model had a statistically insignificant bias and a coefficient of variation of about 0.10. The bias from the closure

model of the ΔK_{th} behavior was statistically significant at 6 percent but the scatter was less with a coefficient of variation of 0.07.

The Walker equivalent stress and Smith-Watson-Topper (SWT) models were used to model fatigue strength of the smooth specimen tests under uniaxial loading. The bias in the baseline data (lives $\geq 10^6$) from both models was statistically insignificant with a coefficient of variation of about 0.10. Fatigue strengths obtained from smooth bar multiaxial tests were modeled using an equivalent stress model. The bias was not statistically significant and the coefficient of variation (0.012) was larger than that of the modeled uniaxial behavior.

Notch fatigue strengths in the virgin specimens were modeled by an equivalent stress approach and the SWT critical plan approach. The equivalent stress model was only implemented on three specimens and the resulting data are too sparse for conclusion. The SWT model was applied to data from 49 tests of virgin notched specimens. Because the resulting A/P ratios were significantly influenced by the stress ratio of the tests, the SWT model (or the localized stress calculations) was not adequately describing the behavior of predicted fatigue strengths. Depending on R, the biases ranged from six percent at $R = 0.8$, to 36 percent at $R = -1$. Thus, the SWT model displays a significant bias as a function of a test parameter. More effort will be required to accurately predict the notch fatigue behavior.

3.6.4 Recommendations

3.6.4.1 Material Behavior and Modeling

Based on the baseline experimental data and supporting analysis generated under this project, it is recommended that additional data, evaluations or analyses will be required to determine if:

- The lives at 10^8 and 10^9 cycles, generated at $R=0.1$ for a frequency of 1000 Hz, truly represent either the material behavior or a potential test anomaly. *(Editor's note: In the follow on program, the $R = 0.1$ data generated at 1000 Hz were treated as not valid due to potential test control issues and were discarded from subsequent analysis.)*

- Crack behavior for cracks that range in size from 0.5 mil to 0.8 mils can be described using conventional fracture mechanics models. Comparison of Honeywell generated small crack rate behavior with long crack rate data definitely shows that using an unmodified ΔK model there are differences. Other comparisons with the $\Delta K_{\text{eff}} - da/dN$ relationship (where ΔK_{eff} is based on closure concepts) provides a lower bound on the small crack rate behavior. This should be further explored.
- Improved methods exist for establishing fatigue strength estimates for lives greater than 10^6 cycles. One potential method for describing the variability in the fatigue strength as function of cycles is the random fatigue limit model^{3,17}. This model provides an analysis framework for directly characterizing the distribution of fatigue strengths and explains the extreme scatter typically observed in the long life region of the S-N curve. The model also could be generalized for different S-N relationships. Considerations should also be given for developing an analogous approach to establishing crack growth rate threshold behaviors. In support of these analytical approaches, the application of the step test method should be explored for determining if it can be used to establish the properties of the fatigue life distribution.
- Analytical methods can be improved to accurately predict the fatigue lives of notched structures. Evaluations should consider the accuracy of the notch localized stress-strain behavior as well as the accuracy of the fatigue life prediction parameters and the methods used to establish the values of the parameters for engine structure situations.

3.6.4.2 Exit Criteria

It is recommended that:

- The baseline conditions for the virgin smooth bar specimens are that A/P have a mean of unity and a standard deviation of 0.10.
- The baseline conditions for virgin notched specimens be further investigated.

3.7 REFERENCES

- 3.1 Sebastian, J.R, UDRI Forging Database, 1998
- 3.2 Private Communication between R. VanStone and Robert Ritchie, July 1999
- 3.3 Newman, J.C., Jr., "A Crack Opening Stress Equation for Fatigue Crack Growth", International Journal of Fracture, 24, 1984, R131-R135
- 3.4 R.E. deLaneuville and B.J. Heath, "Fracture Mechanics Life Prediction System Using Crack Closure methodology", AIAA-86-2094, AIAA/SAE/ASME/ASEE 23rd Joint Propulsion Conference, 1986, San Diego, CA.
- 3.5 H. Kitagawa and S. Takahashi, "Applicability of Fracture Mechanics to Very Small Cracks or the Cracks in the Early Stage," Proc. 2nd Int. Conf. Mech. Behavior of Materials, Boston, MA, 1976, pp. 627-631.
- 3.6 M.H. El Haddad, K.N. Smith, and T.H. Topper, "Fatigue Crack Propagation of Short Cracks," J. Engineering Materials Technology, Vol. 101, 1979, pp. 42-46.
- 3.7 K. Tanaka, Y. Nakai, and M. Yamashita, "Fatigue Growth Threshold of Small Cracks," Int. J. Fracture, Vol. 17, 1981, pp. 519-533.
- 3.8 K.S. Chan, "Fatigue Crack Growth Thresholds of TiAl Alloys," Proc. 2nd Int. Symp. Gamma Titanium Aluminide, TMS, 1999 (in press).
- 3.9 C. W. Brown and D. Taylor, "The Effects of Texture and Grain Size on the Short Fatigue Crack Growth Rates in Ti-6Al-4V," in Fatigue Crack Growth Threshold Concepts, TMS-AIME, 1984, pp. 433-445.
- 3.10 Maxwell, D.C. and T. Nicholas, "A Rapid Method for Generation of a Haigh Diagram for High Cycle Fatigue," ASTM STP 1321, T.L. Panontin and S.D. Sheppard, Editors, to be published in 1999.
- 3.11 R.C. Bellows, S. Muju and T. Nicholas, "Validation of the step test in generating Haigh diagrams for Ti-6Al-4V", International Journal of Fracture, Vol. 21, 1999, pp. 687-697

- 3.12 K.N. Smith, P. Watson, and T.H. Topper, “ A stress-strain function for the fatigue of metals,” J. Mater, Vol. 5, No. 4, 1970, pp.767-778.
- 3.13 Ali Fatemi and D.F. Socie, “A Critical Plane approach to Multiaxial Fatigue Damage Including Out-of-Phase Loading,” Fatigue & Fracture of Engineering Materials and Structures, Vol. 11, No. 3, 1988, pp. 149-166.
- 3.14 P. Kurath and Ali Fatemi, “Cracking Mechanisms for Mean-Stress/Strain Low Cycle Multiaxial Fatigue Loadings” Quantitative Methods in Fractography, ASTM STP 1085, B.M. Strauss and .K. Putatunda, eds., ASTM, Philadelphia, PA, pp. 123-143, 1990
- 3.15 W.N. Findley, “ A Theory of the Effect of Mean Stress on Fatigue of Metals under Combined Torsion and Tensile Load or Bending, J. of Engineering for Industry, 1959, pp. 301-306.
- 3.16 G. Glinka, W. Ott, H. Nowack, “Elastoplastic Plane Strain Analysis of Stresses and Strains at the Notch Root,” Journal of Engineering Materials and Technology, Vol. 110, July 1988, pp. 195-204.
- 3.17 “Meeker, W.Q. and Escobar, L.A., Statistical Methods for Reliability Data, John Wiley & Sons, New York, 1998.

Appendix 3A

SUMMARY OF THE AVAILABLE INFORMATION ON THE PROCESSING OF THE TI 6AL-4V HCF/LCF PROGRAM PLATES

Daniel Eylon



University of Dayton

Richard Bellows

Honeywell

Honeywell

Submitted
8 April 1999

OBJECTIVE

Summarize the available information on all the stages of processing of the program's Ti 6Al-4V plates, from alloy melting to final heat treatments.

SOURCES

- a. An internal AlliedSignal report from July 17, 1997 by James A. Hall, Rich Bellows and Bernie Hoffman entitled:

Processing of Titanium alloy forgings for Air Force Improved HCF prediction program F33615-96-C-5296.

- b. A one page memo from Jim Hall to Al Berens from April 23, 1997.
- c. A one-page report from Rick Creer of GE to Jim Hall from April 29, 1997 entitled:
Ti Heat Treatment at Textron Turbine Engine Components.
- d. Several phone discussions with Jim Hall during May 1997, summarized in my memo to Ted Nicholas from May 19, 1997 entitled:
Memo on the Characterization of Ti-6Al-4V Forgings-HCF Program.
- e. A short e-mail report from Jim Hall to me from July 18, 1997.
- f. Two meetings with Lee Semiatin of the USAF Laboratories in July 1997.
- g. HCF/LCF program review meeting in Phoenix AZ in October 27, 1997.
- h. E-mail correspondence with John Knell of Textron Turbine Engine Components in Cleveland from December 1997.

PLATE PROCESSING

Billet Material

The forging stock material was a double VAR melted Ti-6Al-4V Heat No. TE01 2.50" diameter bar stock from Teledyne Titanium, produced in accordance with AMS4928.

The bar stock was inspected by Immersion Sonic in accordance with AMS2631B and found to be acceptable.

It was supplied in random lengths of 10' to 14', in mill annealed condition: 1300F/2 Hr/AC, with no traceability of the bar segments to the location in the ingot. This is believed to be the practice in the gas turbine engine industry for blade (orbiting) and stator (static) forgings; traceability with respect to position within the ingot is, typically, required for premium quality rotating forgings (disks and hubs).

Chemistry was acceptable in accordance with AMS4928 and is reported in detail in Table 3A.1.

Table 3A.1
Chemistry of Teledyne Titanium Heat No. TE01

Element	Ti	Al	V	Fe	O	N
Top	bal.	6.27	4.19	0.20	0.18	0.012
Bottom	bal.	6.32	4.15	0.18	0.19	0.014
AMS4928	bal.	5.50-6.75	3.50-4.50	0.30 max	0.20 max	0.050 max

Hydrogen measured on bar stock delivered was 0.0041%. Specs max is 0.015%.

The ingot **beta transus** temperature, from DTA: Top: - 1814F

Bottom: - 1837F

Transus variations are consistent with the minor chemical variations from top to bottom (Table 3A.1): –higher V, Fe (beta stabilizers) and lower Al, O and N (alpha stabilizers) at the ingot top. Since there is no traceability of the bar segments to the ingot location, it is not possible to anticipate microstructural variations from plate to plate which might have resulted from the transus variations.

Table 3A.2
RT Longitudinal Tensile (5N) from 5 Positions Along the Ingot

	UTS (ksi)	TYS (ksi)	EL (pct)	RA (pct)
Average of 5	143.9	132.0	19.1	42.9
Minimum	142.8	130.9	18.4	41.8
Maximum	146.2	134.6	20.4	44.4

Forging(1720F)

The 2.5" diameter segments, with random length, were cut into 200 16" long forging preforms. Initially, 190 preform segments were anticipated from the ordered bar stock. However, 200 pieces resulted from the cutting of the supplied material. This has caused some confusion, as only 190 forgings were originally planned for.

The forging was done on a 16" long closed-end channel-die, with the *intended* plate size of 16.0" x 6.0" x 0.80". This was intended to follow with a post forging heat treatment to produce a final microstructure consisting of 60% +/- 10% primary alpha for optimum fatigue properties. It was to be followed by a vacuum anneal at 1300F/2hr to stabilize microstructure and normalize hydrogen content that might have been picked up during the descaling stage.

The 16" plate length was determined by the die's closed-end length. The width was calculated to be 6" if a 0.8" thickness was achieved by the forging. In reality, the width was slightly short of 6", and because of die friction the plates were somewhat narrower at their ends.

Forging was done on a National 8,000-ton mechanical press, using flywheel transfer of rotating motion to a linear motion in a sinusoidal manner at 34rpm and 18" stroke. Since the ram speed at top and bottom of stroke is $v = 0$, the v at 1.7" from bottom dead center (BDC) was calculated by Lee Semiatin to be = 19in/sec.

The average strain rate at impact (for plain strain case) is, therefore, 8.6/sec.

Textron forged all 200 pieces in one campaign, with dies initially heated to 300F. Glass-lubricant coated bars were preheated to 1720F +/- 20F for 30 minutes in a continuous furnace and rapidly transferred to the press. After a one stroke forging, the pieces were simply air-cooled. This is the standard practice for both GE and P&W fan blade forging. There was some initial concern about increasing the die temperature, and affecting the forged microstructure. As a result, plates 1 through 7 were assigned to ML to study the possible die heat up effect. Subsequent study did not detect any significant differences between the microstructure of the first few plates. It was also found out that the first 3 plates had non-standard thickness, as they could have been used to adjust the die location on the press to achieve the 0.8" plate thickness. The microstructure evolution was,

therefore, studied only on plates 4 and 7. The non-standard plates 1, 2 and 3 should be only used for evaluations not requiring good microstructural control.

Textron serialized after forging only #s: 1 – 7, 17, and 58 – 200. The remaining 50 plates were collected in a batch, as done in practice, and were assigned the #s: 8 – 16 and 18 to 57 *in random*. Textron used plate #17 for microstructural, transus and heat treatment evaluation.

HEAT TREATMENT

Microstructural evaluation of #17 showed about 52% primary alpha that varied with location as a possible result of temperature gradients, and different levels of work. This justified the subsequent RA treatment, which is not an industry standard practice, to provide study material with no concern about location-to-location and forging-to-forging microstructural variations. As it will be later seen, actual forged fan blades, typically, undergo only 1300-1400F/2hr mill-anneal, leading to a more elongated primary alpha structure and possibly to a different crystallographic texture.

Beta Transus Determination

In order to facilitate subsequent heat treatments to achieve the goal primary alpha content, a *transus approach curve* was established using. Textron cut #17 into several pieces and soaked each for 60 minutes at temperatures below the reported beta transus. A summary of this work is in Figure 3A.1.

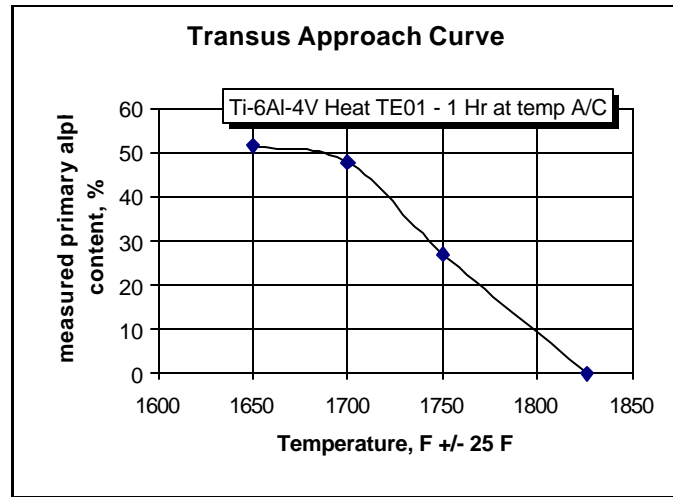


Figure 3A.1. Beta transus approach curve for heat TE01. Three sub transus temperatures were used and combined with the average reported transus to produce this curve. The heat-treated samples were rapidly cooled from the solution temperature. Point intercept method was used on metallographically prepared samples for % primary alpha determinations.

Solution Treatment (1710F/1hr)

Based on a goals of the program: to achieve first a uniform primary alpha content and secondly a level near 60%, and considering the normal uncertainties in furnace temperature associated with large heat treatment lots, a solution temperature of 1710F was selected. From Figure 3A.1 it appears as though this will yield about 45% which is expected to grow as a result of a lower cooling rate and during the subsequent 1300F vacuum anneal. Solution treatment was done in a Lindberg air furnace with 1710F +/- 25F surveyed uniformity. After set temperature was achieved, furnace was adjusted to maintain 1700F at the lowest of the 4 recording TC's to assure minimum primary alpha volume fraction (vol%) in all plates. A load-TC was embedded in a 1" diameter x 1.5" long Ti 6Al-4V bar, which was placed with the plates. The rack of forgings, heat treated on edge was rolled out of the furnace after one hour at temperature and fan air-cooled. The load time/temperature diagrams are available. I have measured from these charts a cooling rate from 1700 to 1000F of 6F/sec (3.3C/sec) [360F/min (200C/min)].

Solution treatment was accomplished in 4 lots with heat treat lot identification associated with each forging serial number. The heat treat batch-loading map for each lot is available for examination at Textron. Heat treat lots 44, 46, 48 and 50 were involved. As

this heat treatment is presumed to be most important relative to traceability, Table 3A.3 indicates the distribution of forgings for each lot.

Table 3A.3
Solution Heat Treatment Distribution by Heat Treat Lot

Lot number	44	46	48	50
Forging #s	1-16, 18-57	58-109	110-165	166-200

Cleaning

All of the solution treated forgings were cleaned of glass lubricant; oxide and alpha case using caustic and acid baths as well as grit blasting. Such processes may increase the level of hydrogen near the surface, leading to lower mechanical behavior.

Vacuum Mill-Anneal (1300F)

The cleaned forgings were vacuum annealed at 1300F for 2 hours at temperature. The vacuum annealing was done in two lots. Lots 1449 (pieces 110-200) and 1451 (pieces 1-16, and 18-109). This was done to reduce the cooling stresses from the solution treatment, to stabilize the microstructure and reduce the hydrogen level at the surface.

POST-TREATMENT PLATE CHARACTERIZATION

To detect die heating effects on the microstructure, plates #4, 7, 100, and 200 were designated for characterization by ML. A most extensive work was done on plate #7 to statistically determine the primary alpha volume fraction, possible microstructural directionality, location-to-location variations, end-of-plate morphology, longitudinal and transverse tensile, location-to-location tensile, and strain rate effects on tensile behavior.

Summary of Plate #7 characterization results was presented on October 27, 1997 in the Program Review in Phoenix, AZ and hard copies were distributed to the meeting participants.

The following is only a brief summary and some additional information.

Microstructure

Based on the extensive metallographic examination it was determined that:

- Microstructure was found to be similar-for the ST, SL and LT orientations.
- Microstructure is a duplex structure with 60vol% of equiaxed primary alpha. This precisely matches the program-planning goal.
- The microstructures of Plates #4 and 7 were very similar, indicating no die heating effects.
- Some forging related surface cracks were detected on the die-contact plate surfaces. However, these cracks were only one or two grains deep and any specimen machining practice will have them removed.
- There were no significant differences in the microstructure of the plate middle sections and the far-end zones. Therefore, there is no need to be careful about the test specimen locations in the plates. The microstructure was judged to be very uniform throughout the entire plate volume, with only minimal location-to-location variations.
- As the initial forging bar stock had a highly elongated primary alpha-structure, it is expected that the forged plate will have some crystallographic texture.

Tensile Results

The tensile results of Plate #7 are shown in Table 3A.4.

- The tensile results of the edge vs. center show almost no difference, indicating microstructural and textural uniformity.
- T results have higher modulus and strength than L, indicating a crystallographic texture.
- Higher strain rate results seem to show a higher strength and a slightly higher modulus.

Table 3A.4.
RT tensile of plate #7

Sample	Location	Orient.	Strain Rate (s ⁻¹)	UTS (MPa)	YS (MPa)	EI (%)	Modulus (GPa)
97-H86	edge	L	5X10 ⁻⁴	970	926	19.9	116
97-H98	edge	L	5X10 ⁻⁴	985	935	20.0	115
97-H90	center	L	5X10 ⁻⁴	976	929	21.2	116
97-H91	center	L	5X10 ⁻⁴	981	931	19.0	124
97-J02	center-trans	T	5X10 ⁻⁴	997	947	21.0	121
97-J03	center-trans	T	5X10 ⁻⁴	993	937	19.2	134
97-H92	center	L	5X10 ⁻²	1008	998	18.1	128
97-H93	center	L	5X10 ⁻²	1019	1007	18.4	125
97-H94	center	L	5X10 ⁰	1075	NA	15.5	NA
97-H95	center	L	highest				

Appendix 3B

CRACK GROWTH

**Robert E. deLaneuville
Jerry W. Sheldon**



Pratt & Whitney

**Submitted
28 September 1999**

CRACK GROWTH RATE RESULTS

Crack growth specimen blanks were removed from forgings to orient crack growth in the longitudinal direction with loading in the long transverse direction. The longitudinal direction is defined as coinciding with the largest forging dimension. Specimen sketches showing the three samples used are shown in Figure 3B.1. The compact tension (CT) specimen, 0.25 inch thick, conforms to the guidelines of ASTM E647 [3B.1]. The straight through starter notch was used. Prior to testing, a 0.005 inch deep and 0.010 inch long EDM pre-flaw is inserted into the center of the K_b specimen. The sample is cycled to produce 0.002 inch of growth prior to testing.

As part of the characterization effort a small round robin was conducted to determine the effects of specimen geometry, gradient, and constraint. A detailed explanation of these details is contained in the Appendix corresponding to the crack growth rate documentation. Plots of the precracking procedure for high stress ratio tests ($R = 0.8$) are shown in Figure 3B.2 and data plots in Figures 3B.3 through 3B.7. A $\pm 10\%$ criteria for variability in ΔK_{th} was used as is explained in the Appendix. Each of the plots demonstrates that the data falls within this window. The following conclusions were drawn:

1. Data tested to gradients as low as -20 inch^{-1} were independent of the load shed rate given the initial value for K_{max} corresponded to a growth rate below $4 \times 10^{-6} \text{ inch/cycle}$.
2. In the K_b specimen, thicknesses ranging from 0.10 inch to 0.25 inch did not influence the measured value of ΔK_{th} at $R = 0.1$ and 0.8 .
3. The choice of K -gradient and starting K_{max} for producing valid threshold results are not independent. As K_{max} is increased, the absolute value of the gradient must decrease to distance the crack tip stress field from the plastic wake.

ASTM E647 provides guidelines used to generate both ΔK_{th} and crack growth rate data. E647 allows latitude in choosing specimen geometry, crack size, thickness, and load shedding rate, among other variables. The load shedding parameter, C , is defined according to the following Equation 3B.1:

$$C = 1/K \cdot (dK/da) \quad (3B.1)$$

The intent is both to minimize the influence of anomalous data, and properly space data acquisition from threshold, to Region II, to toughness. Region II is defined as that range which approximates a straight line (Paris equation) when plotted in log-log space. Specific values may vary by material, but for the Ti-6Al-4V tested, 4×10^{-8} inch/cycle to 4×10^{-6} inch/cycle. Toughness (Region III) spans from above Region II to failure.

At varying points throughout the test, visual verification of the crack length using a digital traveling microscope occurs to post-test correct any error comparing the actual length to that measured with potential drop. Similarly, visual measurements are made for the change in aspect ratio. A linear change in aspect ratio is assumed over the test. The starting EDM flaw size defines the starting aspect ratio. At either threshold crack arrest, or overstress for a Region II test, a well-defined thumbnail remains for final aspect ratio. By plotting aspect ratio versus depth, intermediate ratios are defined.

The ASTM standard E647 recommends a value for the K-gradient, C , of -2 inch^{-1} , but smaller values may be used if available data substantiates this choice. This recommendation stems from the days of visually monitored, and manually adjusted load shed crack growth tests. This method is labor intensive, time consuming, costly, and does not lend itself to the efficiencies of today's technology. Much of today's testing is performed using automated methodologies such as electric potential drop (EPD) and crack mouth compliance. The use of more aggressive gradients are currently employed [3B.2-3B.4] by some researchers. These methods are not widely accepted due to the larger body of data needed to substantiate expanded guidelines by ASTM.

In an effort to determine the most suitable approach since participating companies held differing philosophies concerning the choice of gradient, a small round-robin effort was undertaken with crack geometry, C , thickness, and starting K_{max} open for investigation. Testing was divided between companies commensurate with their standard testing experience. All testing was performed at a frequency of 10 Hz on MTS servo-hydraulic test frames at room temperature. All testing was monitored using EPD, except those tests performed on specimen 8356, which were monitored with crack mouth compliance.

The CT geometry allowed multiple tests from the same specimen. A value of K_{max} was chosen for the $R = 0.1$ tests which would result in a starting growth rate below

4×10^{-6} inch/cycle. Following each shed test, the specimen was uploaded to a K_{max} corresponding to the value at the beginning of the previous test. For the K_b samples, thickness limited each specimen to a single test.

For the $R = 0.8$ tests, the same criteria for starting growth rate was used, but each participating company reached $R = 0.8$ differently. Figure 3B.2 is a graphical simulation for discussion purposes on a 0.10 inch thick K_b specimen targeting $R = 0.8$ threshold test conditions. Figure 3B.2a highlights the incremental load method which begins at $R = 0$, followed by 0.25, 0.5, and finally 0.8. Once a stress ratio of 0.8 is achieved as shown at $a/T = 0.25$, the testing mode is switched to decreasing K_{max} with a negative gradient to threshold. As shown in Figure 3B.2b, also beginning at $a/T = 0.05$, the changing gradient precrack spans the full range of stress ratios from 0.2 to 0.8. Once values of starting ($K_{max, START}$) and ending ($K_{max, END}$) maximum stress intensity, starting (R_{START}) and ending (R_{END}) stress ratio, and distance over which the change is to occur (d) is selected, a gradient can be calculated for both the maximum (C_{max}) and minimum (C_{min}) component of the loading cycle. The following equations define the relationships between these variables:

$$K_{max, END} = K_{max, START} e^{-C_{max} * \delta} \quad (3B.2)$$

$$K_{min, END} = K_{min, START} e^{-C_{min} * d} \quad (3B.3)$$

$$K_{min, START} = R_{START} * K_{max, START} \quad (3B.4)$$

$$K_{min, END} = R_{END} * K_{max, END} \quad (3B.5)$$

The advantages of method (b) over (a) are: a lower overall K_{max} is needed; it requires no manual adjustments by the test operator; less test time; and, a shorter specimen ligament is required.

The data in Figure 3B.3 was generated at $R = 0.1$ on 0.25 inch thick specimens. All CT tests were run in succession on a single specimen, while the K_b results were from two different samples. According to the tabular listing below the plot, the value of ΔK_{th} varied within a $\pm 10\%$ range. This variability is uncharacteristic for specimens tested for internal applications at both GEAE and Pratt & Whitney in titanium. In comparison with the $R = 0.8$ data which are shown in Figure 3B.4, the $R = 0.1$ data exhibited more scatter, even though tested over a similar range of test conditions and starting values.

Pippan (ARMCO iron, Fig. 3 in [3B.5]), Marci (both Ti-6Al-4V, Fig. 12c in [3B.6] and IMI 685, Fig. 13a in [3B.6]), have demonstrated more scatter in the measured value of ΔK_{th} at low stress ratios when compared with high stress ratio results. Closure mechanisms are more significant at $R = 0.1$ compared to $R = 0.8$. Closure is defined as the influence of mechanisms causing the crack tip and wake to be closed well before the minimum applied load is reached in cyclic crack growth. Results under the influence of closure mechanisms will be more sensitive to processing parameters. Material for this effort was derived from four heats, two annealing batches, and testing contributed from three established laboratories. Influence of processing parameters is offered as a possible explanation for the additional variability at $R = 0.1$.

ASTM E647 provides no recommendation concerning allowable variability. Section 11.1.2 of E647 summarizes scatter seen following testing by several laboratories on 2219-T851 aluminum removed from multiple heats and lots on valid results as $\pm 9\%$ [3B.7]. This was used as the criteria for validity. Data at $R = 0.1$ which fell into the acceptable limits ranged from 3.7 ksi $\sqrt{\text{inch}}$ to 4.5 ksi $\sqrt{\text{inch}}$ and encompasses the full population of Figure 3B.3 and all but two of the Figure 3B.5 experiments. No difference in the value of ΔK_{th} is noted based on either specimen geometry or gradient up to -30 inch^{-1} .

Applying the same conditions for validity in Figure 3B.4, results ranged from 2.1 ksi $\sqrt{\text{inch}}$ to 2.5 ksi $\sqrt{\text{inch}}$. Runs 8354C and 8354F are invalid. They are not shown since too few points were collected to plot seven-point polynomial data. Though all samples were begun at approximately the same starting K_{max} , the repeat sheds on the CT specimen at -30 inch^{-1} arrested early and fell above the upper limit. Once sample 8354C arrested prematurely, the test mode was changed to increasing gradient at a rate of $+10 \text{ inch}^{-1}$, and the crack extends by an additional 0.09 inch. The test was repeated in 8354F, and again high. As a final check, both K_{max} and K-gradient were increased. The measured value in 8354G fell within the acceptable population. The K_b samples demonstrated satisfactory response to shed rates as low as -30 inch^{-1} .

Successive $R = 0.1$ threshold tests on a single specimen monitored with the crack mouth compliance technique are shown in Figure 3B.5. Beginning at a fixed value of K_{max} , C was progressively decreased. Similar to the observations of Figure 3B.3, larger drops in load may be tolerated at lower starting K_{max} values. Now

with the gradient held constant at -20 inch^{-1} , starting K_{max} is gradually increased up to a value of $40 \text{ ksi}\sqrt{\text{inch}}$. Above $18 \text{ ksi}\sqrt{\text{inch}}$, results trend toward a premature arrest. This indicates wake effects adversely influencing results. Finally, at a fixed starting value of $40 \text{ ksi}\sqrt{\text{inch}}$, the gradient is gradually decreased, producing lower crack arrest points. The data converges within the expected population at a gradient of -5 inch^{-1} .

Mechanistically the starting stress intensity and thus the plastic zone size is producing a smaller contribution to the wake displacement field's interaction with the crack tip stress state. At higher starting stress intensity values and low negative gradients, a large plastic zone is produced. As load is shed rapidly, the influence of the plastically deformed material in the wake of the crack is in close proximity to the crack tip, thus altering the stress state at the tip. The effect is to change both the applied stress ratio and stress intensity factor. The combination of a smaller starting K_{max} value or a larger negative gradient facilitates distancing this influence zone from the crack tip stress field.

A relationship exists between the choice of starting K_{max} and K-gradient for achieving valid threshold results. Additional testing beyond the intended scope of this experiment would be necessary for defining conditions more specifically. Variables such as alternate sample geometries, test temperature, elastic properties, and starting conditions are some variables which will drive the material dependent solution.

Figure 3B.6 compares thin to thick K_b specimens tested at $R = 0.1$. As a direct comparison, no significant difference exists between the two bodies of data at threshold. When compared to the CT data, the K_b specimens lie at the low end of the range. In Figure 3B.7, thin to thick K_b specimens tested at $R = 0.8$ are compared. The data shows no clear difference. These two figures indicate no influence due to K_b specimen thickness at threshold.

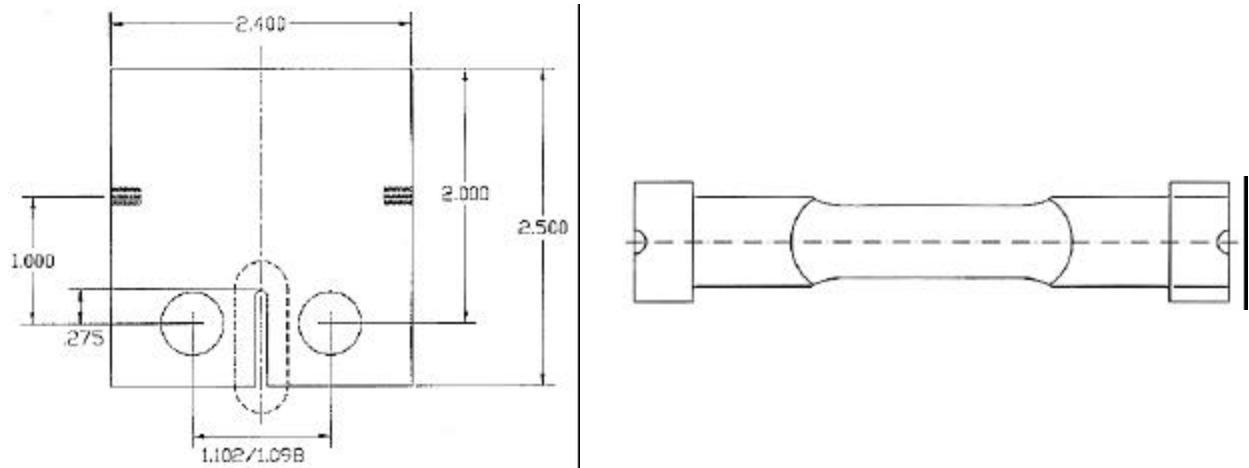


Figure 3B.1. Sketch showing both the 0.25" (0.64 cm) thick CT specimen and the button-head K_b sample. The K_b sample is available in thicknesses of 0.25" (0.64 cm) and 0.10" (0.25 cm).

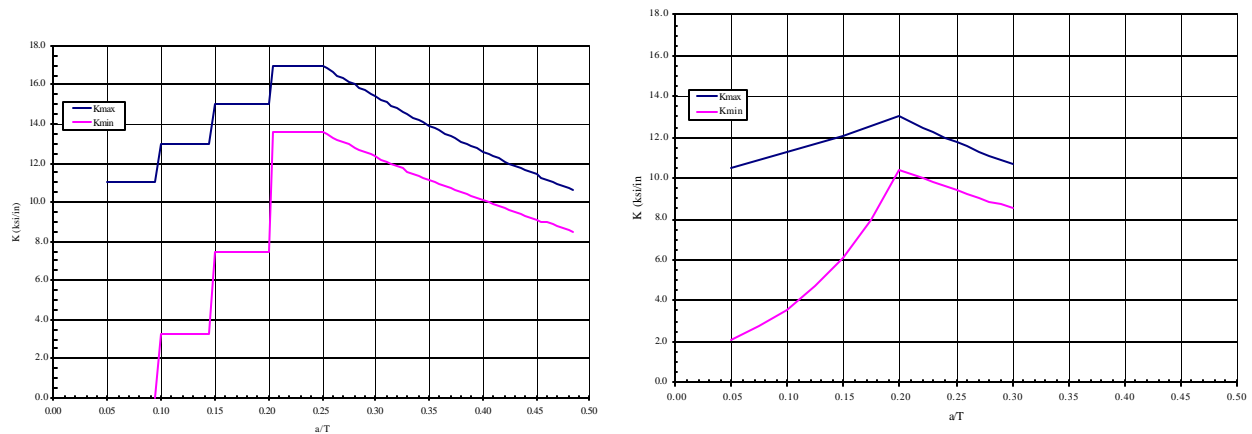
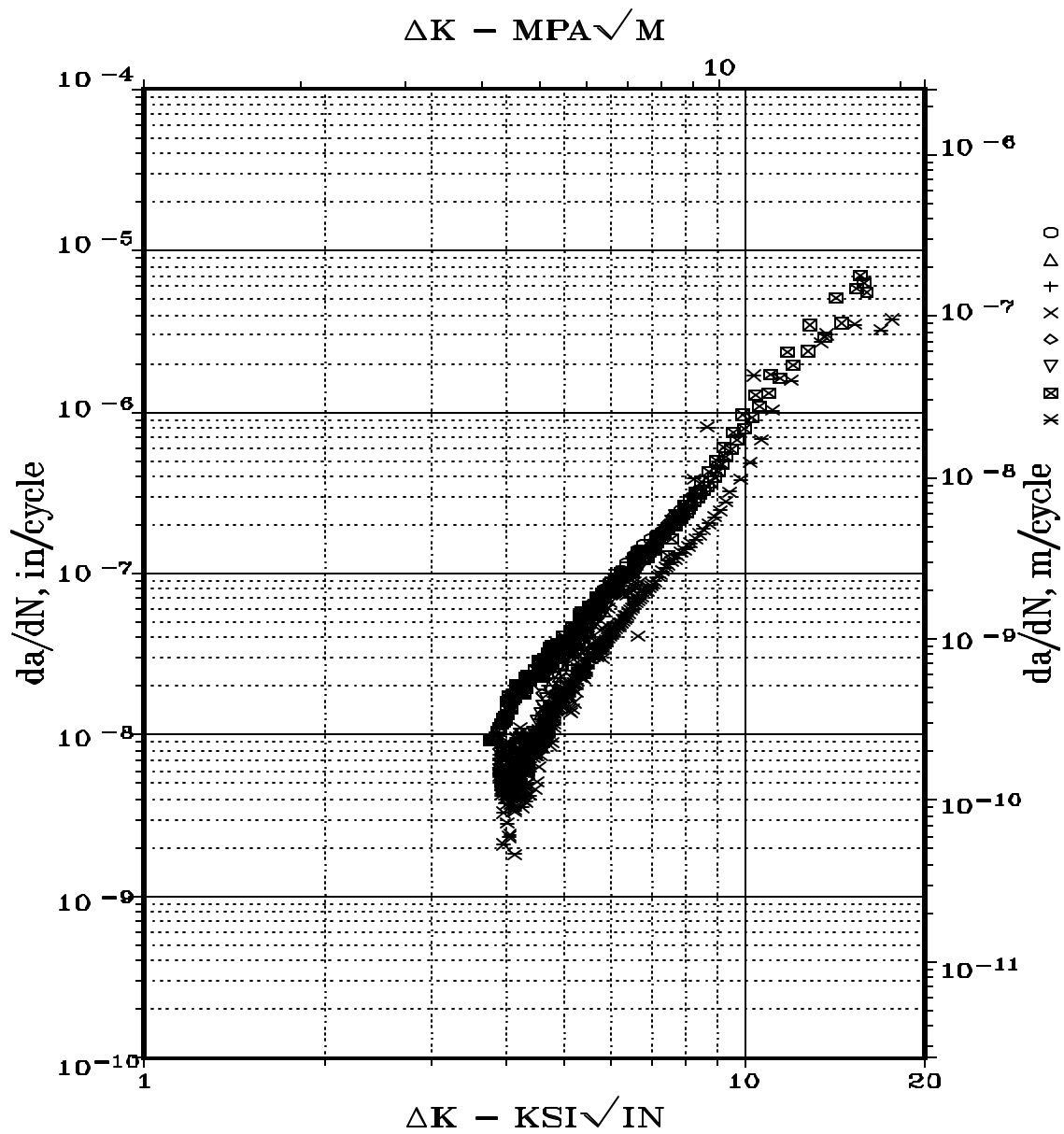
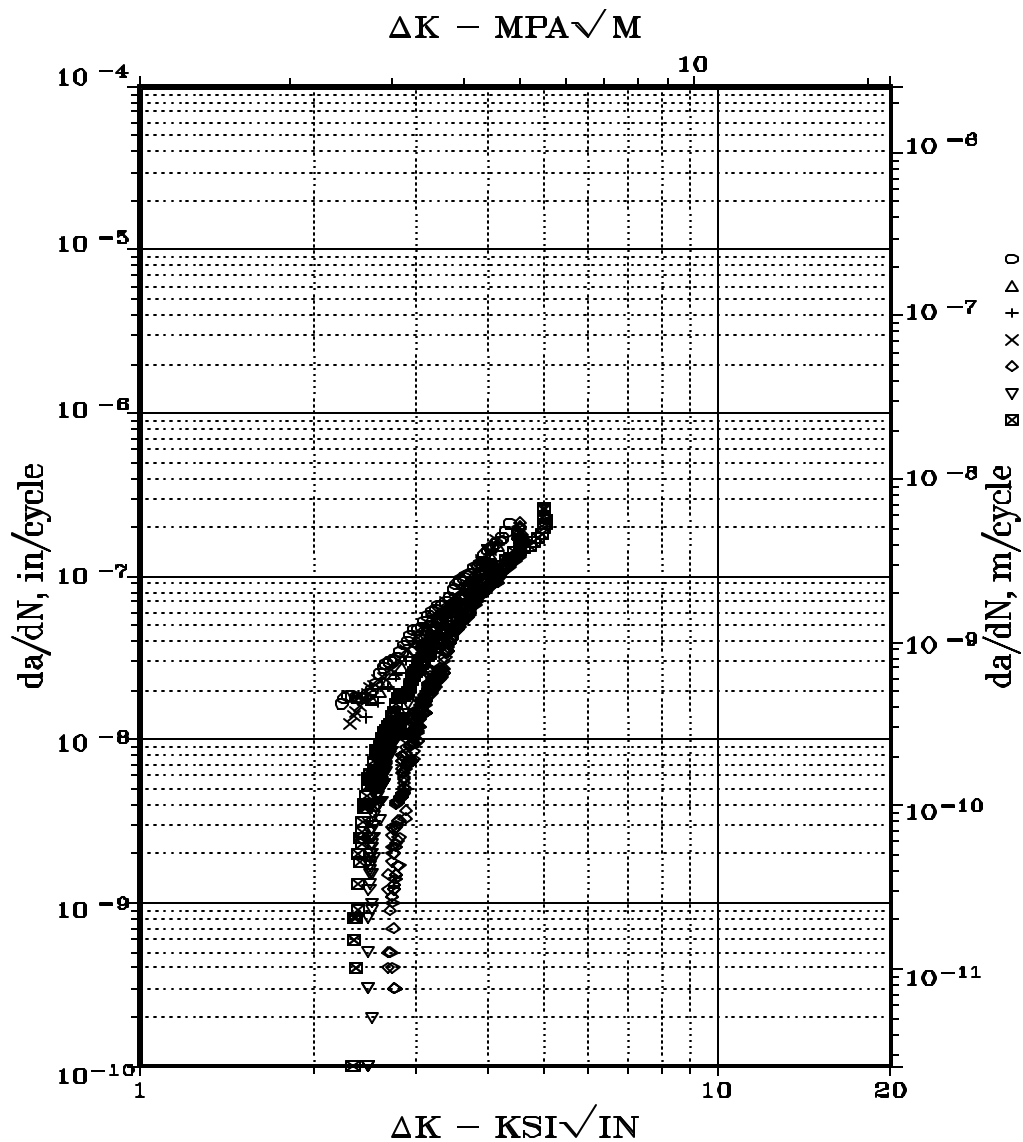


Figure 3B.2. Simulation showing how the step load (a) and changing gradient (b) precrack and test procedure for the thin K_b sample used for obtaining $R=0.8$ threshold results with a K -gradient of -20 in^{-1} .



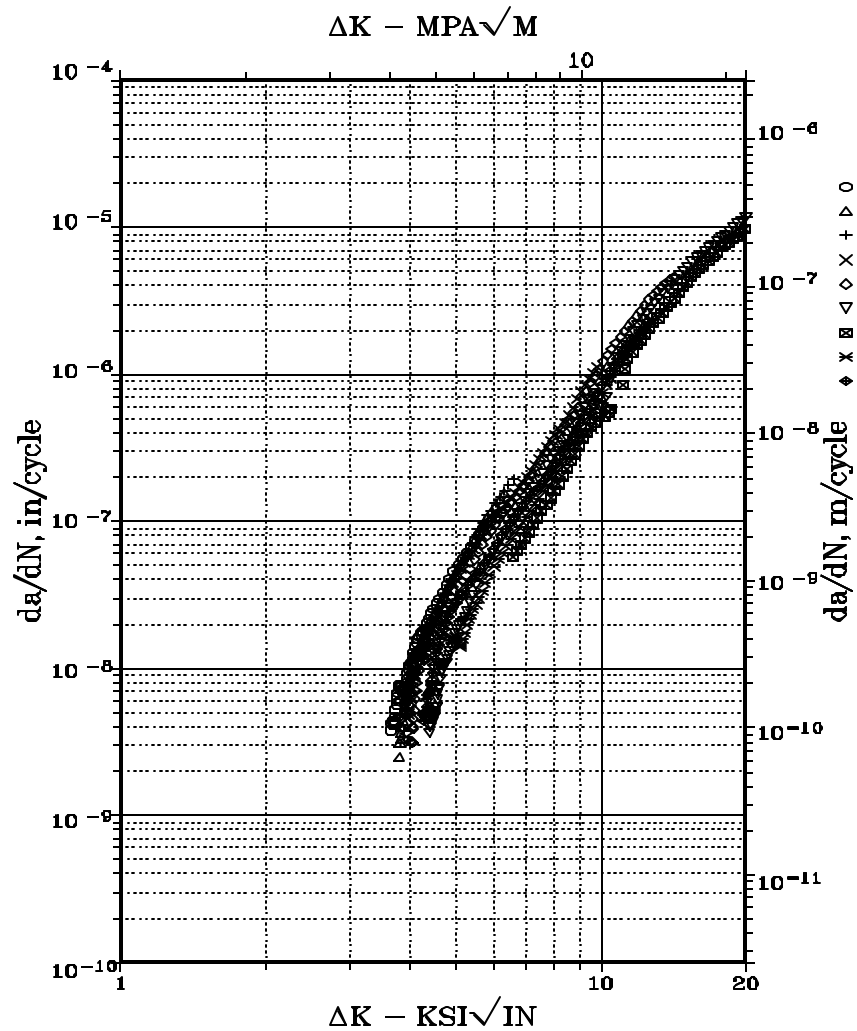
Specimen	Geometry	Shed Rate (in ⁻¹)	Starting K_{\max} (ksi√in)	ΔK_{th} (ksi√in)	da/dN_{th} (in/cycle)
O 8353	CT	-6	9.8	4.3	1.146E-8
Δ 8353A	CT	-15	9.1	4.2	4.114E-9
+ 8353B	CT	-20	8.8	4.5	2.575E-9
X 8353C	CT	-30	9.5	4.4	4.957E-9
? 8353D	CT	-30	6.7	4.2	6.816E-9
∇ 8353E	CT	-6	9.7	4.2	4.449E-9
⊠ 1121GE	K _b	-30	18.0	3.7	5.790E-9
✕ 2221GE	K _b	-10	9.1	3.9	6.170E-9

Figure 3B.3. Summary of test information, starting and ending conditions for the R = 0.1 shed work comparing specimens nominally 0.25 inch thick. The data varies about ΔK_{th} of 4.1 ksi√inch.



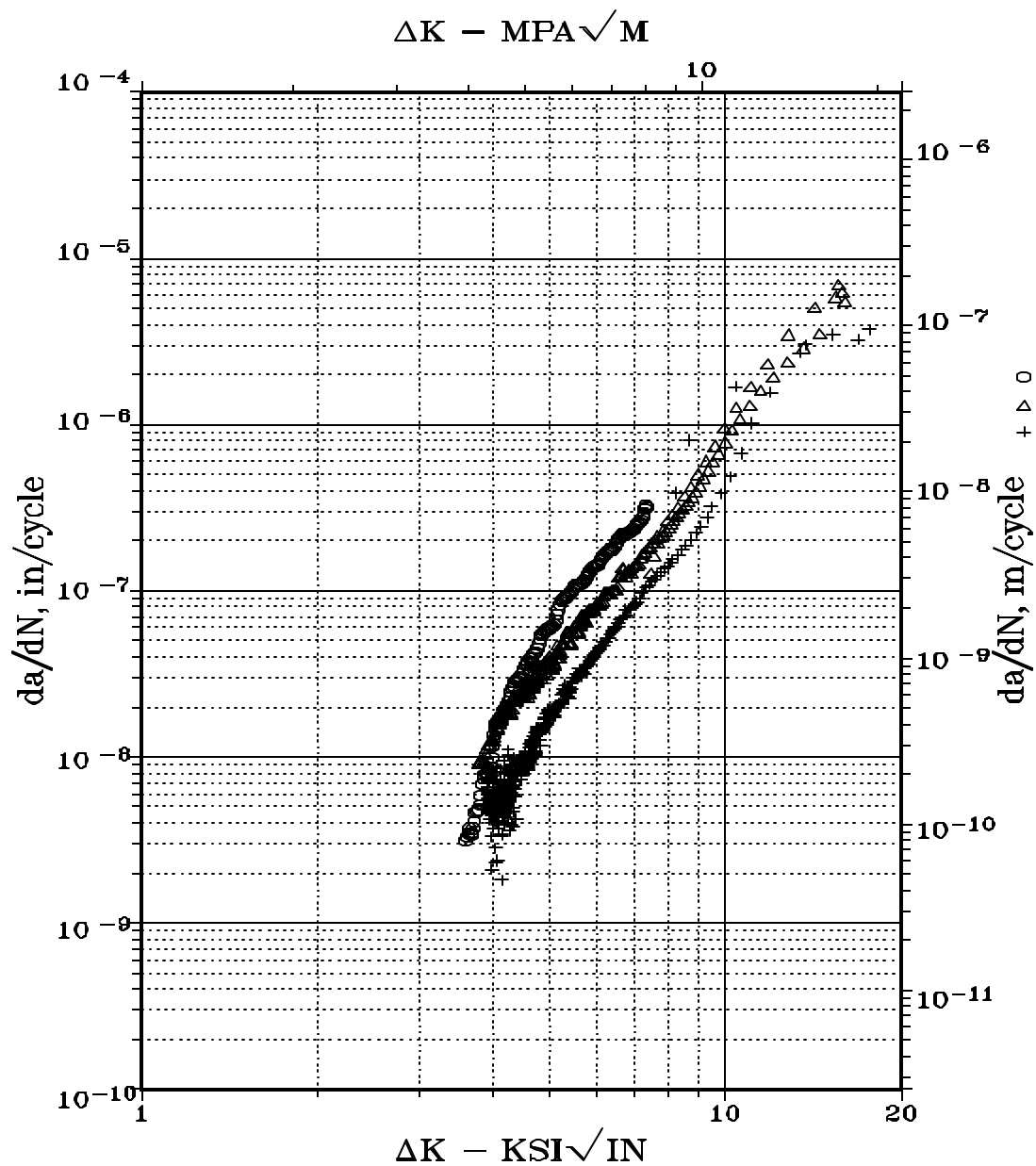
Specimen	Geometry	Shed Rate (in ⁻¹)	Starting K_{max} (ksi√in)	ΔK_{th} (ksi√in)	da/dN_{th} (in/cycle)
O 8354	CT	-7.5	22.6	2.1	9.269E-9
Δ 8354A	CT	-15	22.4	2.3	8.856E-9
+ 8354B	CT	-20	21.3	2.2	4.785E-9
8354C	CT	-30	20.6	3.5	1.104E-7
8354F	CT	-30	23.0	2.7	2.654E-9
X 8354G	CT	-7.5	22.3	2.2	6.397E-9
? 4821GE	K _b	-15	22.7	2.5	6.010E-9
▽ 9421GE	K _b	-20	20.2	2.3	2.540E-9
□ 1122GE	K _b	-30	25.0	2.1	5.000E-10

Figure 3B.4. Summary of test information, starting and ending conditions for the R = 0.8 shed work comparing specimens nominally 0.25 inch thick. The data varies about ΔK_{th} of 2.2 ksi/inch.



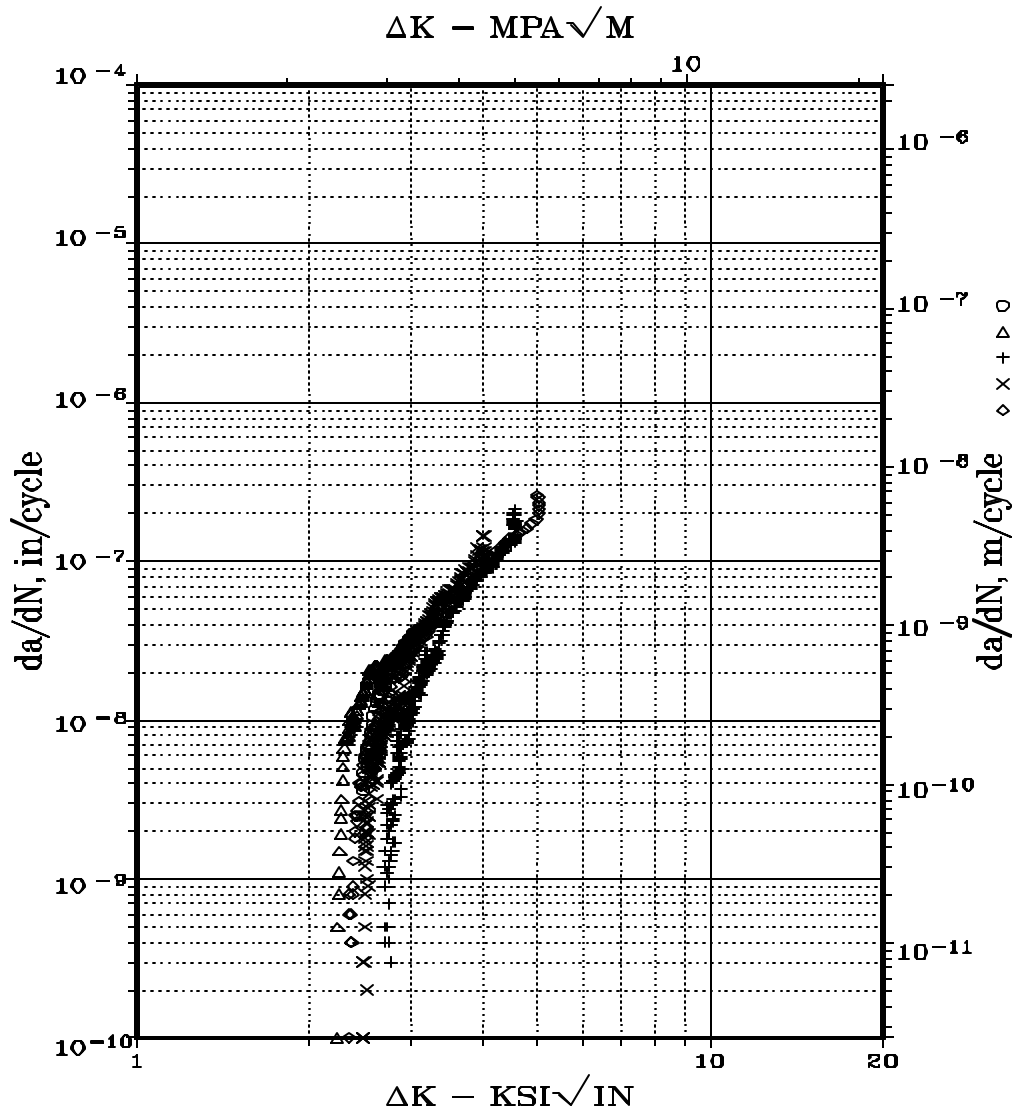
Specimen	Geometry	Shed Rate (in^{-1})	Starting K_{\max} ($\text{ksi}\sqrt{\text{in}}$)	ΔK_{th} ($\text{ksi}\sqrt{\text{in}}$)	da/dN_{th} (in/cycle)
O 8356A	CT	-10	8.0	3.7	1.941E-9
Δ 8356B	CT	-20	8.0	3.9	2.531E-9
+ 8356C	CT	-40	8.0	3.9	1.989E-9
X 8356D	CT	-20	12.0	4.0	1.628E-9
? 8356E	CT	-20	18.0	4.0	1.941E-9
∇ 8356F	CT	-20	27.0	4.4	1.318E-9
□ 8356G	CT	-20	40.0	6.3	4.607E-8
✕ 8356H	CT	-10	40.0	4.7	7.864E-9
⊕ 8356I	CT	-5	40.0	4.3	3.474E-9

Figure 3B.5. Summary of test information for the $R = 0.1$ shed work assessing the effect of: increasing gradient at low K_{\max} ; constant shed rate at increasingly higher K_{\max} ; and, decreasing gradient at high K_{\max} .



Specimen	Geometry	Shed Rate (in ⁻¹)	Starting K_{\max} (ksi√in)	ΔK_{th} (ksi√in)	da/dN_{th} (in/cycle)
O 8397	K_b - Thin	-20	8.2	3.5	9.673E-9
Δ 1121GE	K_b - Thick	-30	18.0	3.7	5.790E-9
+ 2221GE	K_b - Thick	-10	9.1	3.9	6.170E-9

Figure 3B.6. Comparison of thin to thick K_b samples at $R = 0.1$. The thin and thick have an average ΔK_{th} of 3.7 ksi√inch.



Specimen	Geometry	Shed Rate (in ⁻¹)	Starting K _{max} (ksi√in)	ΔK _{th} (ksi√in)	da/dN _{th} (in/cycle)
O 8394A	K _b - Thin	-20	17.6	2.4	1.537E-8
Δ 8395A	K _b - Thin	-20	14.3	2.2	1.564E-9
+ 4821GE	K _b – Thick	-15	22.7	2.5	6.010E-9
X 9421GE	K _b – Thick	-20	20.2	2.3	2.540E-9
? 1122GE	K _b – Thick	-30	25.0	2.1	5.000E-10

Figure 3B.7. Comparison of thin to thick K_b samples at $R = 0.8$. The thin and thick have an average ΔK_{th} of $2.3 \text{ ksi}\sqrt{\text{inch}}$.

REFERENCES

- 3B.1 Standard test method for measurement of fatigue crack growth rates, *Annual Book of ASTM Standards, E647-95a*, 1997, pp. 557-593.
- 3B.2 Hudak, Jr., S.J., Saxena, A., Bucci, R.J., and R.C. Malcolm, "Development of Standard Methods for Testing and Analyzing Fatigue Crack Growth Rate Data – Final Report," AFML TR 78-40, Air Force Materials Laboratory, Wright Patterson Air Force Base, OH, 1978.
- 3B.3 Saxena, A., Hudak, Jr., S.J., Donald, J.K., and D.W. Schmidt, "Computer-Controlled Stress Intensity Technique for Low Rate Fatigue Crack Growth Testing," *Journal of Testing and Evaluation*, Vol. 3, No. 6, 1978, pp. 167-174.
- 3B.4 Clark, T.R., Herman, W.A., and R. Jaccard, "The influence of K-Gradient and K_c max level on fatigue response during the K_c max threshold testing of V An 80 steel and Astroloy," *International Journal of Fatigue*, Feb. 1, 1997, v19 n2, 177.
- 3B.5 Pippan, R., Stuwe, H.P., and K. Golos, "A comparison of different methods to determine the threshold of fatigue crack propagation," *International Journal of Fatigue*, Nov. 1, 1994, v16 n8, 579.
- 3B.6 Marci, Gunter, "Fatigue Crack Propagation Threshold: What is it and how is it Measured?" *Journal of Testing and Evaluation*, May 1, 1998, v26 n3, 220.
- 3B.7 Donald, J.K., "Preliminary Results of the ASTM E24.04.03 Round-Robin Test Program on Low Delta-K Fatigue Crack Growth Rates," ASTM E24.04.03 Task Group Document, December 1982.

Appendix 3C

NUCLEATION AND PROPAGATION OF SMALL CRACKS

Youri N. Lenets

Honeywell

Honeywell

**Submitted
6 October 1999**

SUMMARY (ABSTRACT)

This report documents the AlliedSignal study of crack-like discontinuities and small crack growth rates via replication performed under the Air Force *Improved High Cycle (HCF) Life Prediction Program*, USAF contract #F33615-96-C-5269. As part of this effort, high cycle fatigue tests were interrupted in order to capture the nucleation of cracks and measure the growth of naturally initiated small cracks via surface replication. Growth rates were then determined for the small cracks and compared to long crack growth data both above and below threshold. Based on the data obtained in this study, the growth of small cracks was observed to occur both below long-crack threshold stress intensity factors and at relatively high rates compared to long-cracks.

INTRODUCTION

The goal of the current Air Force HCF Materials Damage Tolerance program is to improve the HCF life prediction capabilities for titanium alloy components in gas turbine engines. Since understanding the intrinsic material behavior is an important aspect of fatigue, it is necessary to understand how cracks initiate as well as how they grow.

Often associated damage modes, such as low cycle fatigue, foreign object damage or fretting, determine the size and shape of the crack along with residual stresses that may be associated with the specific damage mode. Once the linear-elastic stress intensity factor is known, standard crack growth rate curves can be used to predict if the crack will grow and how fast it will grow. Unfortunately, it has been shown that small cracks can grow at linear elastic *DK* values below threshold.

This effort was initially undertaken to provide insight and understanding into the crack nucleation process and how microstructural influences may affect nucleation. After demonstrating the ability to measure the growth of small cracks, the effort was expanded to obtain small crack growth data via the replication process.

MATERIAL AND EXPERIMENTAL DETAILS

The material used in this study was forged into simulated fan blade forgings, approximately 16 inch x 6 inch x 0.8 inch. Ti-6Al-4V, per AMS 4928, was used as the forging stock, which was preheated to 1720°F prior to forging. Forgings were solution

treated at 1710°F, fan cooled and then vacuum annealed at 1300°F for 2 hours. The microstructure of the forgings contained approximately 60% primary alpha with the remainder lamellar transformed beta (see Fig. 3C.1). The yield strength and tensile strength of specimens excised from the forgings in the longitudinal direction were 134.9 ksi and 141.8 ksi, respectively.

The specimens used in HCF testing had a nominal gage diameter of 0.2 inch and a uniform gage length of about 0.75 inch. They were excised so that the specimen axis was always parallel to the longest dimension of the forging. The specimens were low stress ground and longitudinally polished, followed by vacuum stress-relieve annealing, chemical milling and finally electropolishing to produce a mirror finish.

Tests were run on servo-hydraulic, closed-loop test frames under load control conditions at room temperature in laboratory air. The HCF tests were run at 60 Hz at a stress ratio of 0.1 and stress range of 80 ksi. During the tests, the HCF loading was periodically interrupted, and acetate replicas were taken from the gage surface of the smooth bar while under mean load. The replicas were made using 0.0013 inch thick Bioden RFA Acetyl Cellulose film and methylacetate. The replicas were subsequently examined under optical and/or scanning electron microscope in order to determine the presence and size of cracks.

The NASCRAC™ (NASA Crack Analysis Code) software was used to determine the stress intensity factor. Surface cracks were assumed to be semi-circular, so that the length of the surface crack ($2c$) was twice the crack depth (a). When compared to da/dN data, Pratt & Whitney FCG test results from specimens run at 10 - 20 Hz at a stress ratio of 0.1 that employed potential drop measurements to monitor crack extension were used.

RESULTS AND DISCUSSION

Crack Nucleation

An example of interaction between slip planes and microstructural constituents of the tested material is shown in Figure 3C.1. Higher magnification micrograph (Figure 3C.1b) shows parallel slip planes changing angle as they pass from one α -grain through the β -lamella (lighter color) and into another adjacent α -particle. At the top right corner of Figure 3C.1b, secondary cracking along a grain boundary is visible.

Two more examples of microcrack nucleation are shown in Figures 3C.2 and 3C.3 containing images of two consecutive replicas taken from the surface of the HCF specimens. One can surmise that the crack seen in Figure 3C.2b originated in transformed β -lamella and then started to propagate into the two neighboring α -grains. In another specimen, tested under identical conditions, the crack would seem to initiate at a triple point, and subsequently follow the α -grain boundary (see Figure 3C.3b).

In Ti-6Al-4V processed to contain equiaxed primary α -particle and transformed lamellar platelets, slip deformation can be controlled by either microstructural constituent. Two factors determine the extent to which a primary α -particle experiences plasticity or slip: size of the primary α -particle (determined by degree of mechanical work performed during converting and forming and by heat treatment) and orientation of the primary α -particle (determined by the orientation of the prior α -grain via the Burgers relationship). The orientation of the primary α -particle with respect to stress determines the resolved shear stress for a particular crystallographic plane and crystallographic direction. The size of the primary α -particle controls the plastic shear strain since the plastic shear strain is a function of dislocation density, Burgers vector and average length that dislocations travel. Therefore, there will be some distribution of primary α -particles that, because of their orientation, will experience slip; likewise, there will be some distribution of primary α -size where larger α -grains will experience greater plastic shear strain. When these two factors occur in the same primary α -particle, that particle will incur greater amounts of strain than other particles. In other cases, colonies of transformed lamellar platelets having the same crystallographic relationship may act as single slip systems. As with the primary α -particles, the size of the colony and crystallographic relationship of the colony with respect to the applied stress will determine the extent of slip and corresponding shear strain.

Cracking occurs when grains can no longer accommodate the shear strain that slip generates. At this point, the crack can initiate on the slip plane at an obstacle, such as a grain boundary or particle, or it can initiate along a weaker interface, such as a grain boundary. From the evidence seen during this study, both cracking modes appear possible. Surface cracks can initiate and propagate along weaker interfaces. The degree of faceting observed on fracture surfaces near nucleation sites suggests that cracks also initiate and propagate transgranularly on slip planes within the primary α -particles.

Percentage of Life Spent for Crack Nucleation and Propagation

Figure 3C.4 shows several different stages in the development of a fatigue crack naturally initiated in the smooth specimen ($\Delta\sigma = 80$ ksi, $R = 0.1$ and frequency 60 Hz) as documented via surface replication performed at uniform intervals of 15,000 cycles. Similar information gathered in the present study for five different specimens is summarized in Figures 3C.5 through 3C.9 as a relationship between number of cycles (**N**) and crack length (**2c**). Each experimental data set was fitted by a logarithmic expression of general form **N** = **m** + **k** \ln (**2c**). Numerical values for the coefficients **m** and **k** as well as for the coefficient of correlation (r^2) are given in Table 3C.1.

This information was used to obtain (by interpolation) number of cycles required to reach certain crack length (0.001 inch and 0.006 inch) in each specimen (this procedure is graphically shown in Figure 3C.5). The results of such interpolation are given in Table 3C.2 together with total number of cycles to failure recorded for each specimen under consideration. Also presented in Table 3C.2 are numbers of cycles corresponding to crack propagation from surface length $2c = 1$ mil to failure and from surface length $2c = 6$ mils to failure. The last column in Table 3C.2 represents percentage of total life of a specimen spent for crack propagation from surface length of 1 mil to failure. It can be seen that for the conditions tested the crack propagation stage can only account for 2 to 4 percent of the total life. If taken out of appropriate context, these numbers might raise the question of practical importance of the results obtained in the present study as well as any effort directed towards studying the fatigue crack propagation stage during high cycle fatigue. It should be noted, however, that in the present study only specimens that survived initial 1.5 million cycles were replicated. Therefore, more realistic comparison between crack nucleation and crack propagation stages should be based on all 15 specimens tested within the present program. Figure 3C.10 contains relevant information where very high variability of total life is evident. At the same time, crack propagation life appears to demonstrate much lower level of scatters. For example, for specimens 40-D5 and 65-B4 total lives differ by a factor of two while crack propagation lives are almost the same. The log-average total life based on all 15 specimens shown in Figure 3C.10 is 753,132 cycles, the average crack propagation life based on five specimens shown in Table 3C.2 is 67,171 cycles which gives almost 9% of the total life being spent for crack propagation.

Furthermore, in a particular case of specimen 65-B2 (see Figure 3C.10), average crack propagation life represents 53% of the total life. Finally, one should keep in mind that the above analysis is based on arbitrarily chosen criterion for crack nucleation ($2c = 0.001$ inch). In reality much shorter cracks can be observed (see, for example, Figures 3C.6, 3C.7 and 3C.9) which obviously increases the percentage of crack propagation stage in total life and justifies further investigations of the associated processes.

Propagation Behavior of Naturally Initiated Small Cracks

Another way of interpreting replication information gathered in the present study is to plot crack propagation rate da/dN vs. crack depth a (Figure 3C.11) and crack propagation rate da/dN vs. stress intensity range DK (Figure 3C.12). The following assumptions were made when converting replication information into data points presented in Figures 3C.11 and 3C.12:

- pure Mode I crack propagation;
- circular crack front shape, i.e., $a = c$ where a – crack depth and c – surface half-length;
- initial crack propagation rate (i.e., between the moment of actual crack nucleation and the moment when the crack was first replicated) was calculated as log-average of two possible extremes (da/dN_{max} – total crack extension documented in the first crack-containing replica occurred in one cycle and da/dN_{min} – total crack extension documented in the first crack-containing replica occurred during whole replication interval which in the present study was equal to 15,000 cycles);
- each da/dN value was associated with DK calculated for the average crack length recorded on two consecutive replicas taken before and after corresponding crack extension.

According to the general trend observed in Figure 3C.11, initially high crack propagation rate abruptly decreases, reaches certain minimum value and then gradually increases. This is accompanied by substantial reduction in experimentally observed scatter in crack propagation rate as the crack grows.

As mentioned above, the initial crack propagation rate (ordinate of the left point) for each specimen was calculated as a log-average of two possible extremes while all other points represent true values of this parameter. In this respect it should be pointed out that in three out of five cases (specimens 65-A3, 65-B4 and 40-D6) such calculated average shows a reasonable agreement with extrapolation based on two subsequent (true value) points. In Figure 3C.11, crack size corresponding to the minimum crack propagation rate is also compared to the average primary α -grain size. It is seen that the major trend in crack propagation behavior changes from deceleration to acceleration after the crack tip passes through the first or second primary α -grain boundary. At the same time, in one case (specimen 2) additional crack growth retardation event occurred when the crack size (depth or surface half-length) was 5 times larger than the average primary α -grain. Based on the data presented in Figure 3C.11, fatigue crack propagation behavior in the subject material can be divided into two separate stages in respect to its microstructural sensitivity. Further comparison of the results given in Figure 3C.11 and Table 3C.2 shows that microstructurally sensitive crack propagation (from $2c = 1$ mil to $2c = 6$ mils) accounts for about one half of the total crack propagation stage under the conditions studied. Similar microstructural sensitivity in fatigue crack propagation behavior can be seen in Figure 3C.12 where the results obtained are plotted as a function of stress intensity factor range, DK .

Comparison with “Long” Crack Propagation Behavior

In Figure 3C.13, the results of the present study are compared to the crack propagation behavior of “long” cracks in compact tension and surface flaw type specimens (P&W data). It can be seen that naturally initiated “small” cracks propagate well below “long” crack thresholds as determined for compact tension (CT) and surface flaw (SF) type specimens. Besides, for stress intensity range values higher than “long” crack threshold, naturally initiated “small” cracks propagate much faster than “long” cracks. Such tendency persists up to $DK \sim 10$ ksi $\sqrt{\text{inch}}$ when both sets of data merge together.

CONCLUSIONS

1. During the crack nucleation stage slip appears to occur in primary α -particles and can pass into adjacent microstructural unit.

2. Initial stage of microcrack propagation occurs both transgranularly and intergranularly.
3. Crack propagation life defined as a number of cycles required to propagate crack from 0.001 inch to failure appears to demonstrate much lower scatter than total life of the specimens tested in the present study.
4. For the conditions tested, average fatigue crack propagation life accounts for 9% of the average total life of the specimens tested. However, in respect to individual specimens, this percentage may change from 2% to 53% due to high variability in crack nucleation life.
5. Fatigue crack propagation behavior in the subject material can be divided into two separate stages in respect to its microstructural sensitivity. Microstructurally sensitive crack propagation (from $2c = 1$ mil to $2c = 6$ mils) accounts for about one half of the total crack propagation stage under conditions studied.
6. Naturally initiated small cracks were shown to propagate well below “long” crack thresholds as determined for compact tension (CT) and surface flaw (SF) type specimens.
7. For stress intensity range values higher than “long” crack threshold, naturally initiated “small” cracks propagate much faster than “long” cracks.
8. Experimentally observed differences in the fatigue crack propagation behavior between naturally initiated small cracks and “long” cracks persists up to $DK \sim 10 \text{ ksi}\sqrt{\text{inch}}$ when both sets of data merge together.

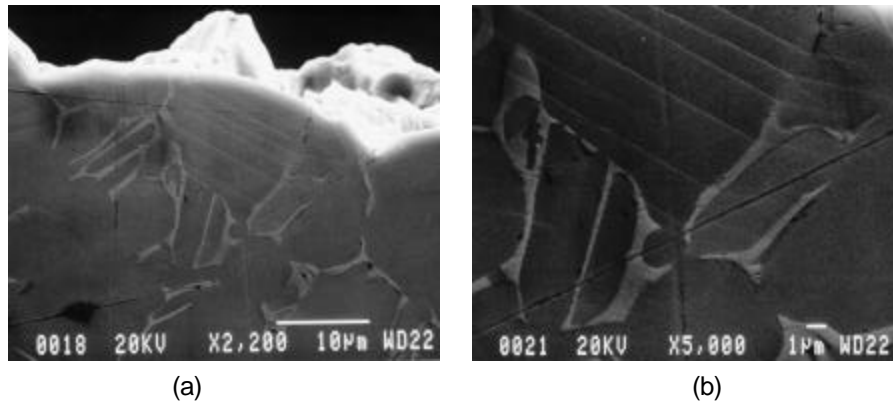


Figure 3C.1. Slip planes activity observed on the gage surface of a fatigued specimen.

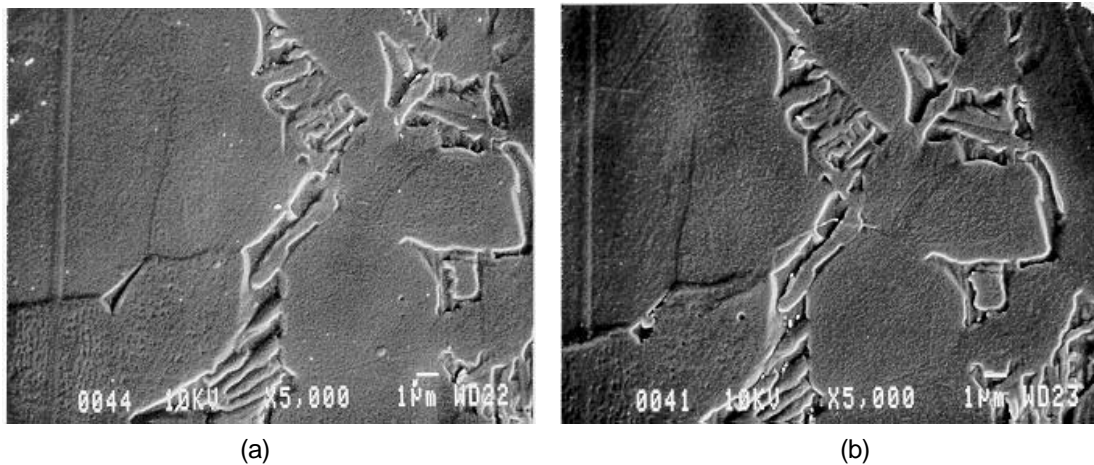


Figure 3C.2. Surface replicas taken from specimen surface during interrupted HCF tests after 2,145,000 cycles (a) and 2,160,000 cycles (b).

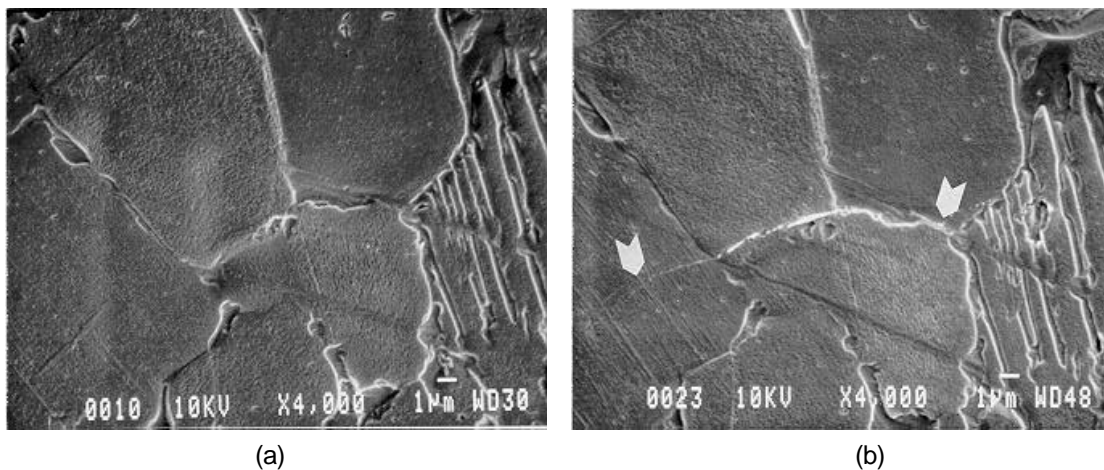
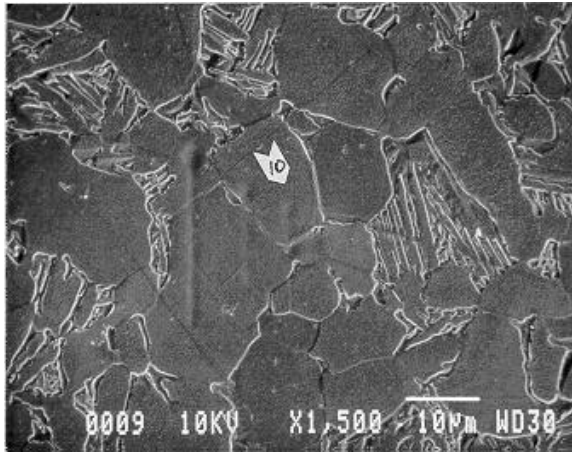
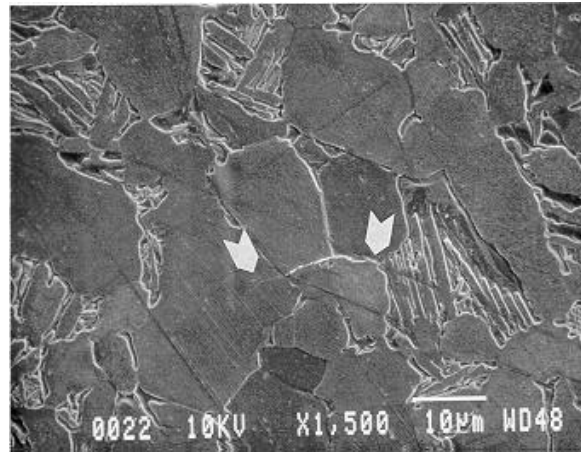


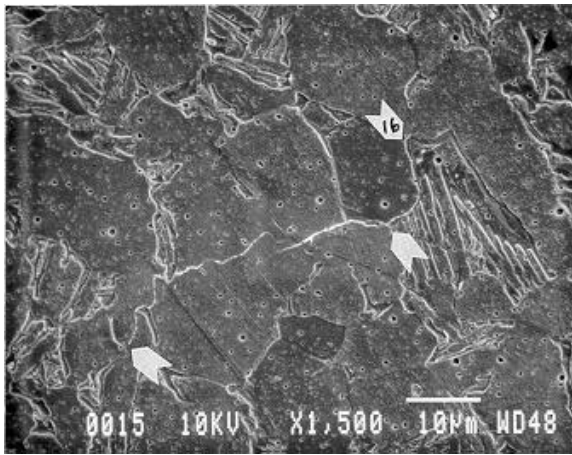
Figure 3C.3. Surface replicas taken from specimen surface during interrupted HCF tests after 1,905,000 cycles (a) and 1,920,000 cycles (b).



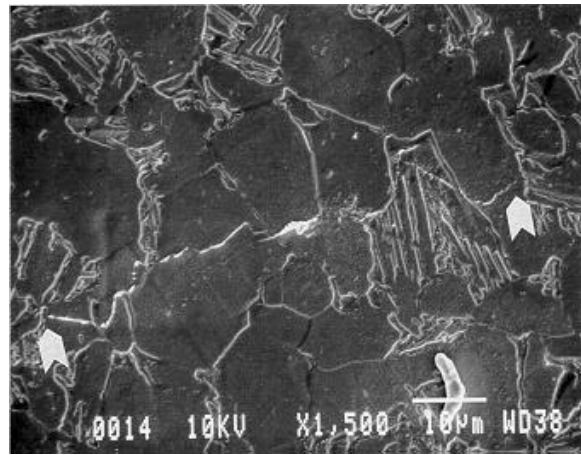
(a)



(b)



(c)



(d)

Figure 3C.4. Surface replicas taken from specimen surface during interrupted HCF tests after 1,905,000 cycles (a) 1,920,000 cycles (b), 1,935,000 cycles (c) and 1,950,000 cycles (d).

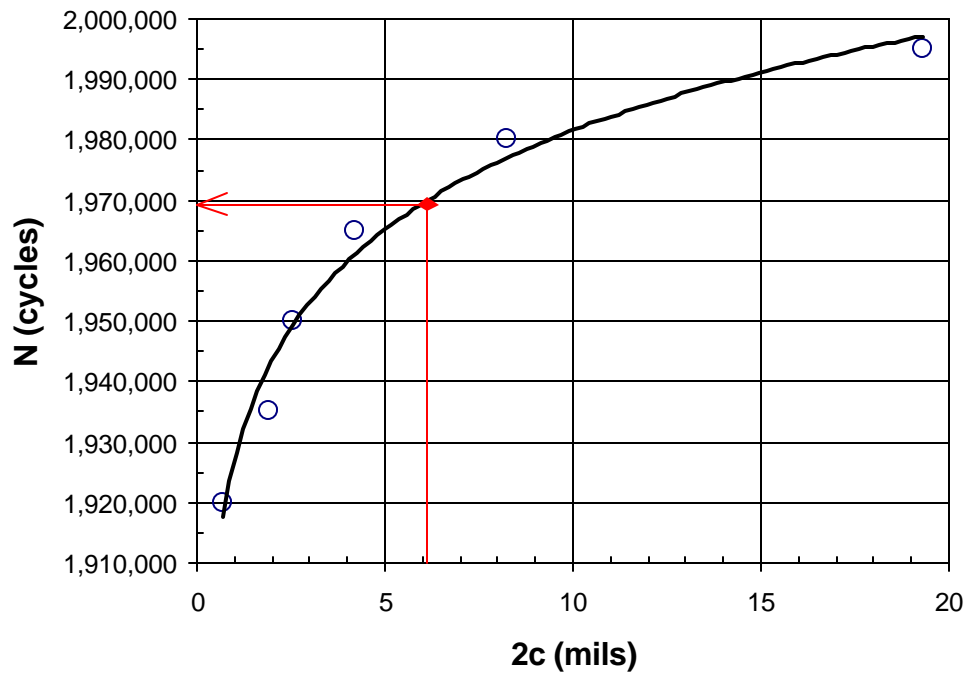


Figure 3C.5. Replication results for specimen 65-A3 and graphical representation of interpolation procedure used.

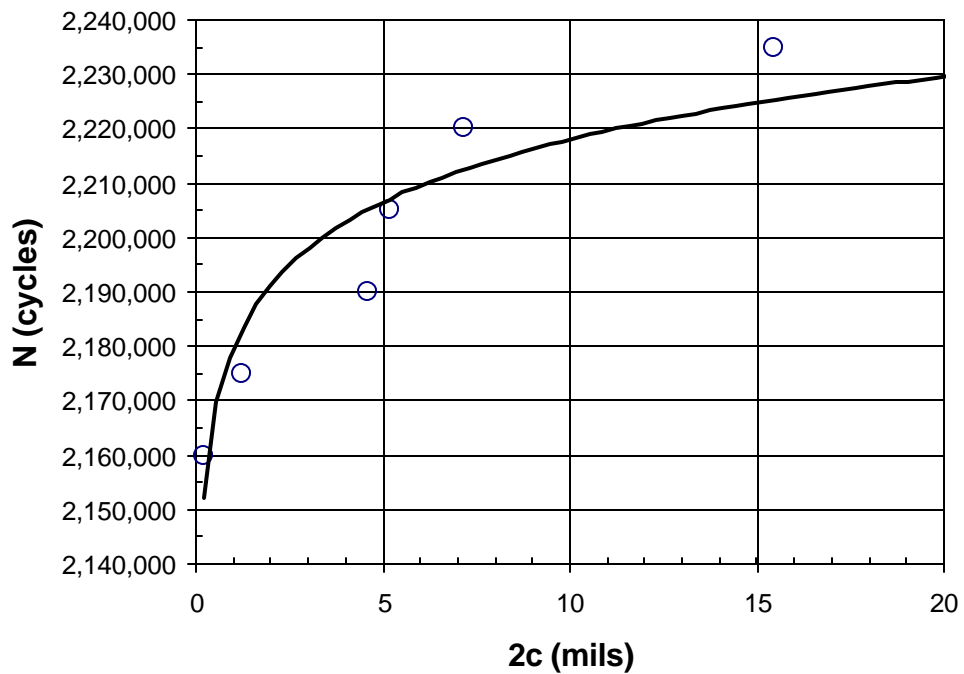


Figure 3C.6. Replication results for specimen 65-A7.

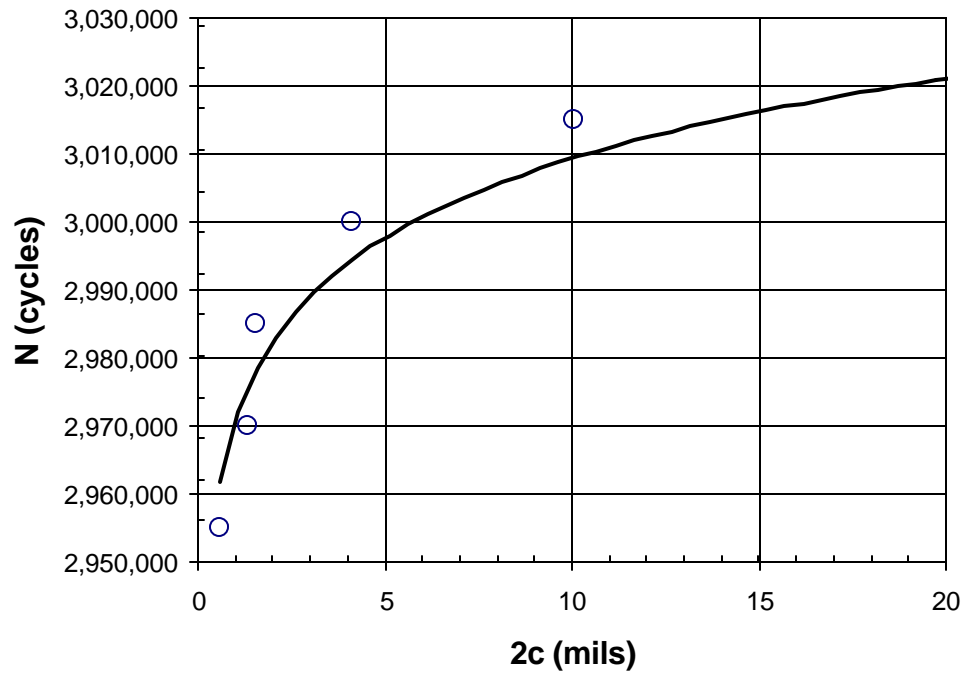


Figure 3C.7. Replication results for specimen 65-B4.

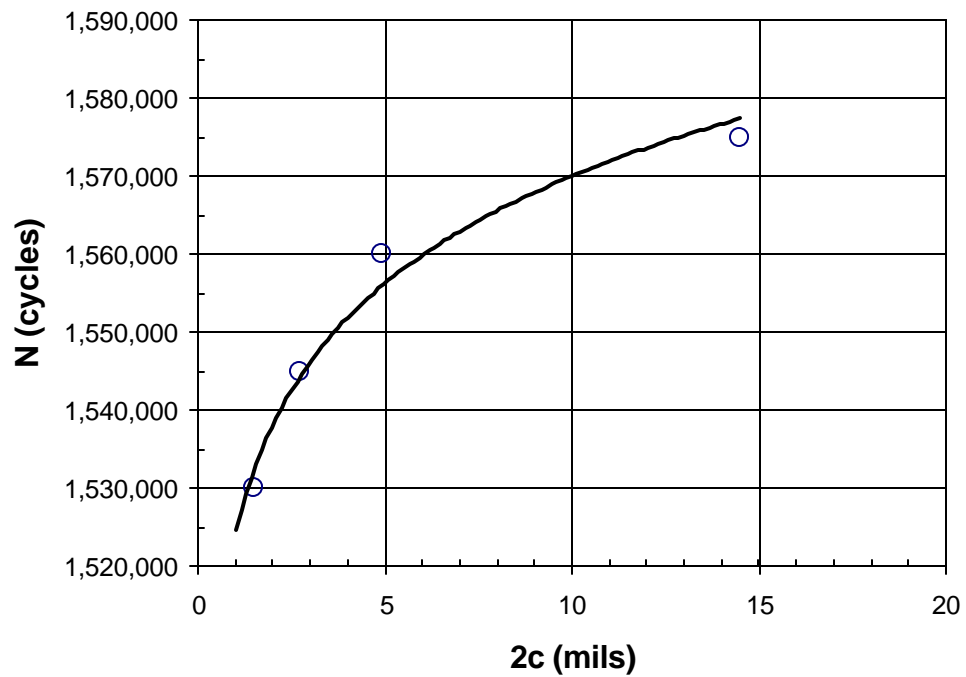


Figure 3C.8. Replication results for specimen 40-D5.

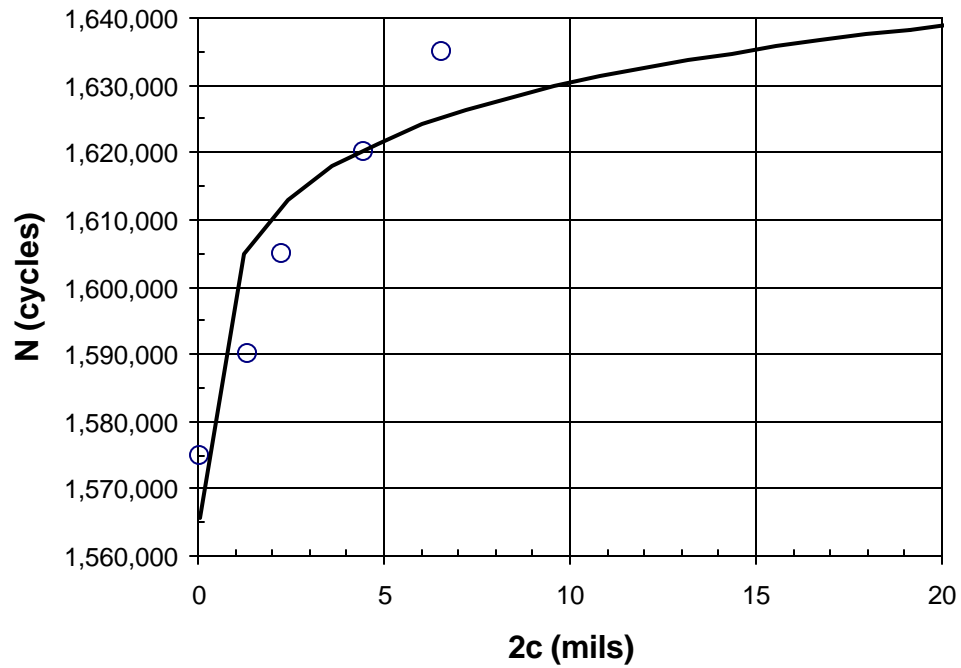


Figure 3C.9. Replication results for specimen 40-D6.

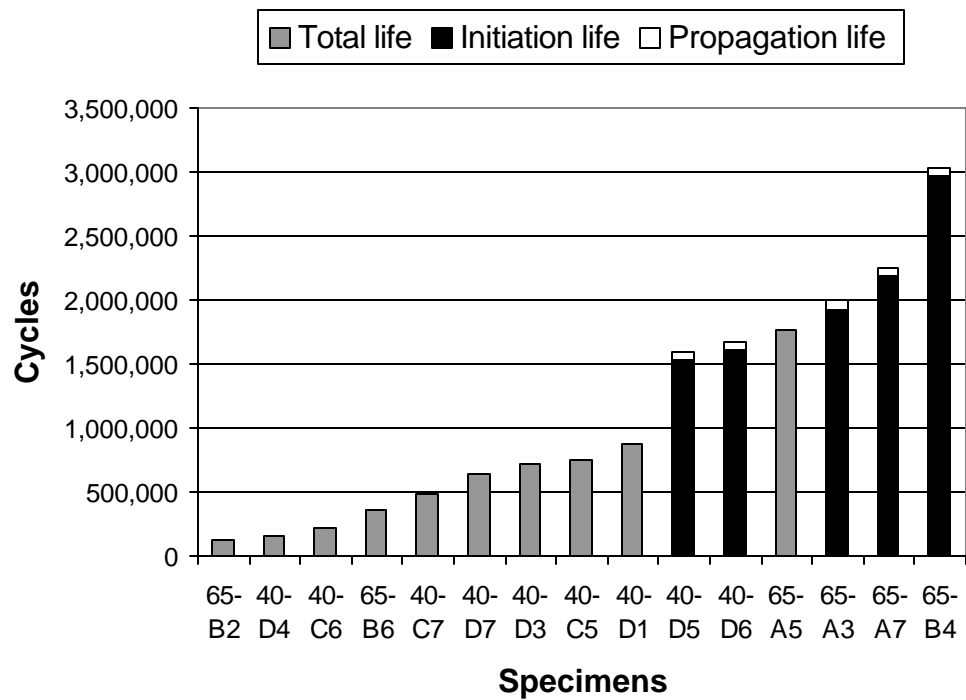


Figure 3C.10. Summary of the results obtained within the program.

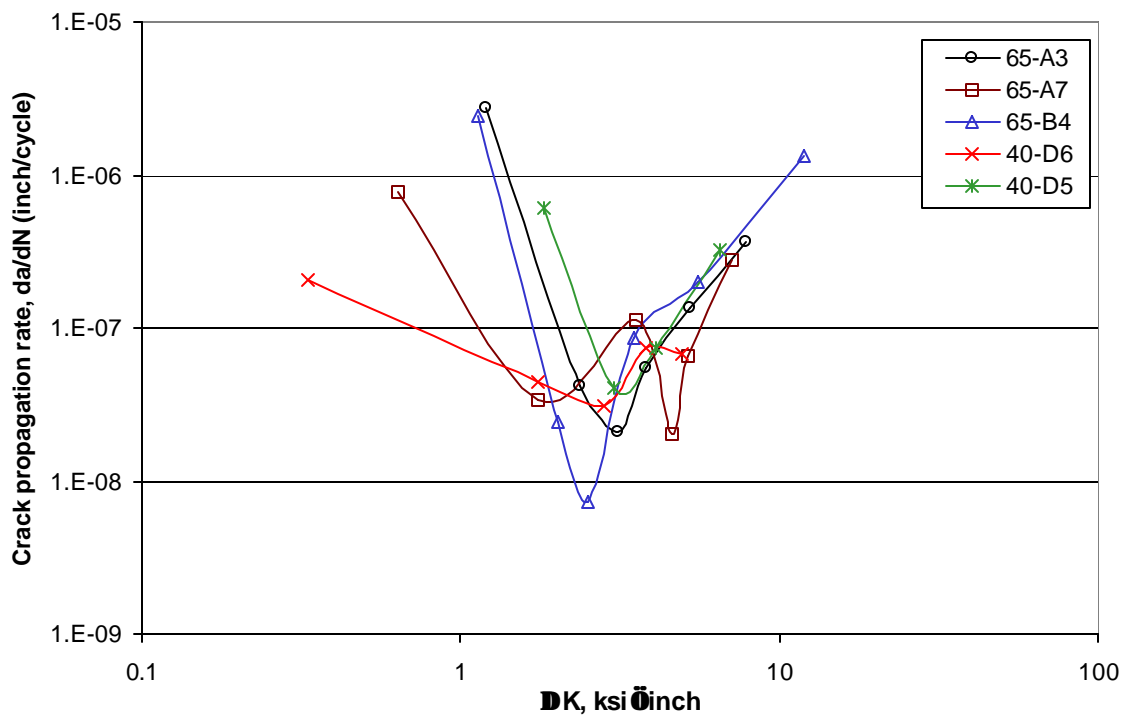


Figure 3C.11. Fatigue crack propagation rate of naturally initiated “small” cracks as a function of crack size and its relation to average size of primary α -grains.

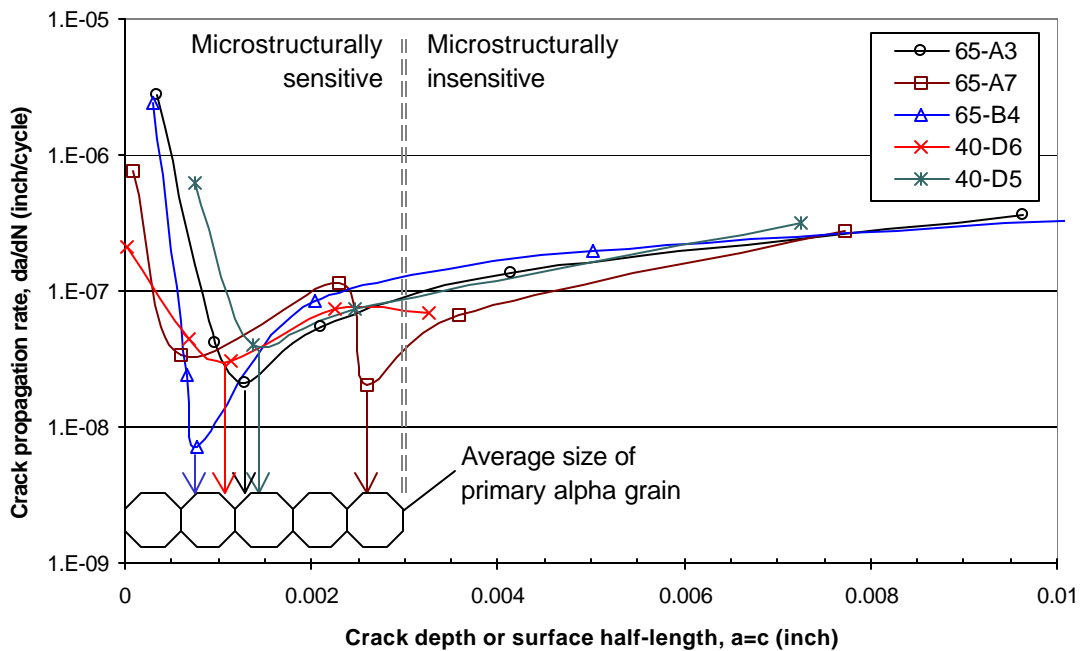


Figure 3C.12. Fatigue crack propagation rate of naturally initiated “small” cracks as a function of stress intensity factor range.

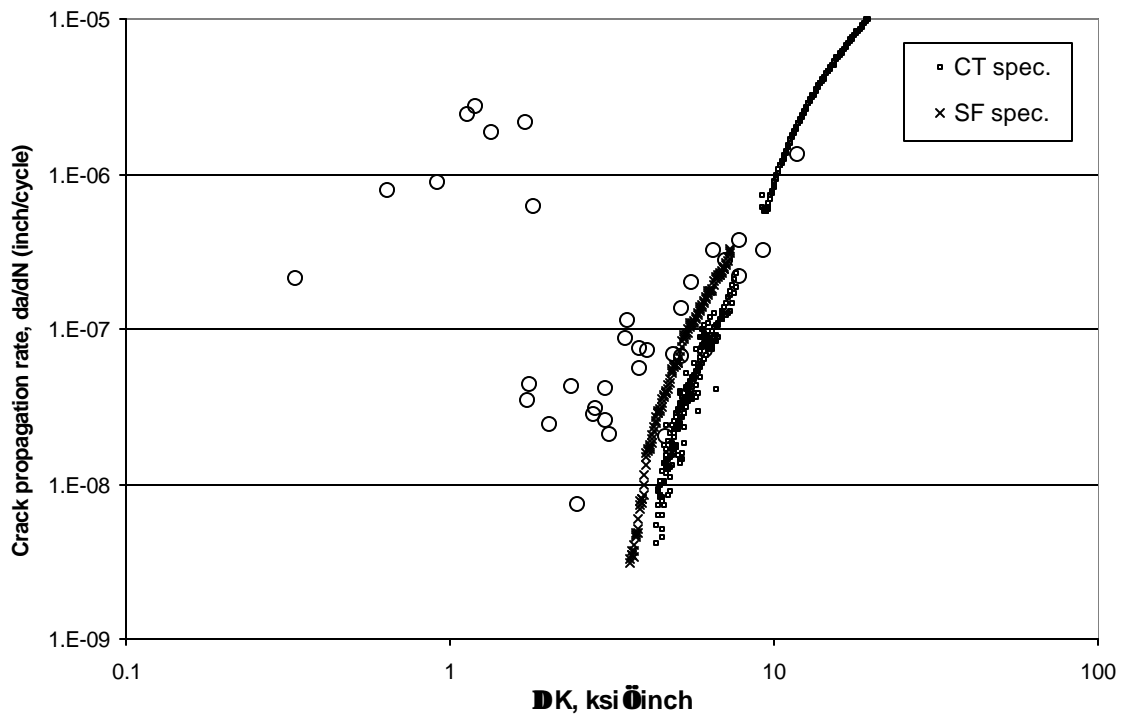


Figure 3C.13. Fatigue crack propagation rate of naturally initiated “small” cracks (circles) and “long” cracks in compact tension (CT) and surface flaw (SF) type specimens as a function of stress intensity factor range.

Table 3C.1

Specimen	m	k	r ²
65-A3	1927121	23656.124	0.9764
65-A7	2179752	16635.210	0.8706
65-B4	2970534	16864.607	0.9413
40-D5	1524289	19844.283	0.9740
40-D6	1602091	12263.847	0.9028

Table 3C.2

Specimen ID	1 mil crack	Total cycles to		Propagation from		Percent of total life spent in propagation from 1 mil to failure
		6 mils crack	Failure	1 mil to failure	6 mils to failure	
65-A3	1,927,121	1,969,507	2,005,145	78,025	35,638	3.89%
65-A7	2,179,752	2,209,559	2,248,942	69,190	39,383	3.08%
65-B4	2,970,534	3,000,751	3,032,715	62,181	31,964	2.05%
40-D5	1,524,289	1,559,845	1,587,741	63,452	27,896	4.00%
40-D6	1,602,091	1,624,065	1,665,098	63,007	41,033	3.78%

Appendix 3D

MICROSTRUCTURAL CRACK INITIATION AND GROWTH DURING THE HIGH CYCLE FATIGUE DAMAGE OF A Ti-6Al-4V ALLOY

**E.Y. Chen
L.R. Kaisand
J.A. Sutliff
S.J. Balsone**



GE Corporate Research and Development

**Submitted
1 July 1999**

ABSTRACT

The development and demonstration of a methodology for predicting the high cycle fatigue (HCF) life of titanium-base materials will provide design engineers with a tool to more accurately predict failure in gas turbine engine components, optimize designs to fully utilize a material's mechanical properties, and extend the maintenance-free life of gas turbine engines. Potential payoffs include decreased failure rates, improved system safety, reduced maintenance and spare parts cost and reduced system weight. This study aimed to advance a mechanistic understanding of fatigue crack initiation and early crack growth under HCF conditions in a $\alpha+\beta$ Ti alloy in an initially undamaged state. Effort focused on identifying the initiation and growth mechanisms of the critical cracks that govern the useful material life under HCF conditions. Experimental data was obtained from acetate replicas of fatigue specimens of a forged Ti-6Al-4V alloy tested in room temperature air in bending. An improved understanding of HCF crack initiation serves as a foundation for developing physics-based mechanistic models necessary to predict HCF life of Ti-base materials under a wide range of operational/environmental conditions. It also contributes to the technology base needed to extend the application of fracture mechanics and/or other mechanistic-based life prediction to structural problems arising from HCF, including the experimental and analytical methodologies for component life prediction under HCF conditions.

OBJECTIVE OF THIS WORK

The objective of this particular study is to develop a mechanistic understanding of crack initiation and early crack growth under high cycle fatigue (HCF) conditions in alpha-beta titanium alloys. Specific experimental objectives to be achieved include:

- 1) Characterize crack initiation and early propagation under HCF conditions in a Ti-6Al-4V alloy in an initial undamaged state;
- 2) Identify the crack initiation and growth mechanism(s) that govern the useful life of Ti-6Al-4V under HCF conditions;
- 3) Provide this information to develop physics-based models for life prediction under HCF conditions;
- 4) Comment on the potential for microstructural modifications to improve the HCF life of forged Ti-6Al-4V.

PROGRAM BACKGROUND

This study supports the U.S. Air Force and GEAE overall objective to increase the understanding of HCF failures in gas turbine engine components and to develop the technology base needed to extend the application of fracture mechanics or other mechanistic-based life prediction to structural problems arising from HCF, including the experimental and analytical methodologies for component life prediction under HCF conditions. An understanding of crack initiation and small crack threshold behavior represents a critical step in the development of a reliable life prediction philosophy for Ti alloy turbine engine components that experience significant levels of HCF. A 1992 study conducted by the U.S.A.F. Scientific Advisory Board pinpointed HCF as the single largest cause of failure for military aircraft turbine engines [3D.1].

RATIONALE FOR THIS WORK

A crack growing at 10^{-10} m/cycle would cause fatigue failure in a 20 mm thick turbine component at approximately 30 hours of operation (at 1 kHz) [3D.2]. Because of this, it becomes necessary to operate HCF-critical turbine components below the threshold stress intensity factor range, ΔK_{th} , such that crack propagation cannot easily occur. Information on ΔK_{th} are most commonly obtained from fatigue specimens containing long, through-thickness cracks already several millimeters long. In HCF, flaws leading to failure are typically tens to hundreds of micrometers [3D.3]. These flaws can be introduced by manufacturing and assembly foreign object damage (FOD), fretting, and other surface damage or overload conditions [3D.4]. For this reason, HCF design might likely be based on a small crack threshold to take into consideration the growth behavior of small cracks.

This study seeks to advance the understanding of fatigue crack initiation and early crack growth under HCF conditions in $\alpha+\beta$ Ti alloys from an initial undamaged state. This understanding provides a foundation for developing mechanistic models necessary to predict HCF life of Ti-base materials under a wide range of operational/environmental conditions. Through using a deterministic and/or probabilistic design approach, the life prediction methodology will account for the initial material damage state typical of intrinsic defects in the development of mechanistic-based concepts to predict component life under HCF conditions.

The development and demonstration of a methodology for predicting the HCF life of titanium-base materials will provide design engineers with a tool to more accurately predict failure in gas turbine engine components, optimize designs to fully utilize a material's mechanical properties, and extend the maintenance-free life of gas turbine engines. Potential payoffs include decreased failure rates, improved system safety, reduced maintenance and spare parts cost and reduced system weight.

EXPERIMENTAL DETAILS

Processing of Material and the Resulting Microstructure

The alloy studied in this work was an $\alpha+\beta$ processed and annealed Ti-6Al-4V alloy. It was supplied to GE from a set of 200 forgings specifically produced in one campaign by Teledyne Titanium for the National Turbine Engine HCF Science and Technology Program. Detailed information on the processing of this material can be found in Reference 3D.5. Table 3D.1 shows the chemical composition from the top and bottom regions of one representative bar as determined by the supplier.

Briefly summarizing the steps involved in processing this alloy, the bar stock material was forged into 41 x 15 x 2 cm plates and then air cooled. This is the standard practice for both GE and P&W fan blade forging. The material was subsequently solution treated at 925°C (1700°F) for 1 hour. The desired microstructure was bimodal containing approximately 60 vol.% primary- α and 40 vol.% lamellar colonies of $\alpha+\beta$ for optimum fatigue properties. Microstructural evaluation of one of the forged plates by Allied Signal showed that the forgings had about 52 vol.% of α_p that could vary with location as a possible result of temperature gradients as well as different levels of work. This justified the subsequent RA treatment (which is not an industry standard practice) to provide study material with no concern about location-to-location and forging-to-forging microstructural variations. Actual forged fan blades, typically, undergo only 700 to 760°C (1300 to 1400°F)/2hr mill-anneal, leading to a more elongated primary- α structure and possibly to a different crystallographic texture.

Solution treatment for the forged plates was accomplished in 4 lots with heat treat lot identification associated with each forging serial number. Heat treat lots designated 44, 46, 48 and 50 were involved. As this heat treatment is presumed to be

most important relative to traceability of the plates, Table 3D.2 indicates the distribution of forgings for each lot. The GECRD study had specimens that were machined from Forging #79, 85, 94, 99 and 126, thus involved two different heat treat lots. The cleaned forgings were then vacuum annealed at 700°C (1300°F) for 2 hours to reduce the cooling stresses from the solution treatment to stabilize the microstructure and reduce the hydrogen level at the surface. The vacuum annealing was done in two lots: Lots 1449 (pieces 110-200) and 1451 (pieces 1-16, and 18-109).

To examine die heating effects on the microstructure, four different plates were characterized in a study by the Air Force Research Laboratory (AFRL). Extensive microstructural analysis was done on one plate to statistically determine the factors such as the a_p volume fraction, possible microstructural directionality, and location-to-location variations. Based on these metallographic observations it was determined that:

- 1) The forged Ti-6Al-4V microstructure was similar for the ST, SL and LT orientations;
- 2) The Ti-6Al-4V alloy microstructure was duplex containing about 60 vol.% of equiaxed a_p ;
- 3) The microstructures of two different plates were very similar suggesting little/no die heating effects.

Since there were no significant differences in the microstructure of the plate middle sections and the far-end zones, it was assumed that there was no need to be concerned about the location where the test specimens were machined from in the plates. The microstructure was judged to be very uniform throughout the entire plate volume with only minimal location-to-location variations. In addition, since the initial forging bar stock had a highly elongated primary a -structure, the forged plate is expected to contain some crystallographic texture.

Bending fatigue specimens as shown in Figure 3D.1 were machined from the forged plates by MetcutTM Research, Inc. (Cincinnati, OH). These specimens were then low stress ground and polished. Following polishing, the specimens were stress relieved in vacuum at 700°C (1300°F) for 1 hour and chemical milled to remove about 2.5 cm (0.001 in.) from each surface in the gage. This was the standard practice used

for the fatigue specimens in the HCF program. Figure 3D.2 shows an optical micrograph of the microstructure from the surface of the gage section surface of one of the specimens. The etchant used here was a mixture of HF + HNO₃ + H₂O. For this specimen, the volume fraction of α_p was found to range between 58 to 62 vol.% for several different studied locations.

The uniaxial yield strength of the forged Ti-6Al-4V material was reported by GEAE to be about 840 MPa (122 ksi) [3D.6]. This was lower than the range of 926 to 1007 MPa (134 to 146 ksi) found by AFRL for various locations in a single forged plate [3D.5]. To measure the yield strength in 3-point bending, one of the GECRD specimens was used in a stress-strain test with a single strain gage placed on the tension side of the bend specimen. From this test, there was no evidence of yielding in bending for stress levels of up to 1030 MPa (150 ksi). Here, the modulus was determined to be about $E = 110$ GPa (16 Msi), consistent with lower-end E values found by AFRL [3D.5]. For confirmation, another strain gage was then added on the other side of the specimen, and it was placed in the hydraulic grips and then loaded in tension. When this was done, both gages showed a very sharp yield point at about 830 MPa (120 ksi). This uniaxial yield strength value was similar to that reported by GEAE for this Ti-6Al-4V alloy.

High Cycle Fatigue Testing Approach

The HCF testing methodology pursued in the GECRD work focused on bending fatigue tests in room temperature laboratory air. These tests were primarily conducted at 20 Hz (one test was conducted at 25 Hz) for one stress ratio ($R = 0.1$). Two tests were also performed at $R = 0.5$ for comparison. From these bending fatigue tests, the applied stress (S) versus number of fatigue cycles (N), or S/N , curve was obtained for comparison with uniaxial fatigue data.

Figure 3D.3 shows the 3-point bending apparatus employed for the GECRD fatigue experiments.¹ The testing equipment is automated and controlled with a computer. Given the very small loading conditions that were required for these tests, it

¹ Initial testing plans called for cantilever bending to be employed, as the fatigue specimens were designed for this type of test. It was later determined that the load levels required would be too low to be easily controlled by cantilever bending. As a result, 3-point bending was used here.

was necessary to confirm that the displacement could be controlled at 20 Hz. A strain gage was attached to the first set of specimens to measure the displacement. Strain gage preparation consisted of very light roughing of the gage section with 400 grit grinding paper in a direction parallel to the longitudinal bending stress. This is standard strain gage preparation technique. After it was determined that the displacement could be controlled with the setup, no strain gages were used in subsequent tests.

Experimental difficulties associated with generating small cracks in HCF of metallic alloys at $R = 0.1$ and $R = 0.5$ have often led researchers to try different techniques. In one corresponding HCF effort [3D.7], hourglass specimens were first fatigued uniaxially at $R = -1$ until small cracks of about 50 μm were observed. Then, testing was continued at $R = 0.1$ or 0.5. This strategy was not pursued here since the primary goal of this study was to examine the mechanisms of natural crack initiation and subsequent early growth in HCF.

Information on crack initiation and early propagation mechanisms was obtained by replicating the specimen surface with cellulose acetate film softened with acetone for a selected number of tests. Replication allowed quantitative measurements of crack length and density to be made at different stages in the fatigue life. Replication was performed for six specimens at pre-determined fatigue life intervals (e.g., 1 percent, 5 percent, 10 percent, ...) based on an initial estimated number of cycles to fatigue failure. After the replicas were made, they were vacuum-coated with gold to be analyzed in the scanning electron microscope (SEM). By using the X-Y coordinates of the SEM stage, the same specimen surface area on different replicas can be followed with respect to a common reference mark (e.g., a scratch mark). A crack is usually tracked from the last to first replica (i.e., when the crack is large it is obviously much easier to find than when it is small). In this work, replicas were typically examined at a magnification of 100 times. At this magnification, a crack of about 20 μm is readily identifiable amid the microstructural features. The light etch finish of the fatigue specimens allows features such as grain boundaries, α_p and lamellar grains to be distinguishable on the replicas, but sometimes made identifying cracks smaller than these features difficult. Therefore, for much smaller cracks, higher magnifications were required. From the replicas, cracks as small as 1 μm could be discerned using the SEM.

Electron Backscattering Pattern Procedures

To assist in the interpretation of HCF data for the Ti 6Al-4V plates, characterization of the alloy microstructure was made using the Electron BackScattering Pattern (EBSP) technique of electron diffraction in the SEM. Analysis of EBSP data can provide measurements of a material's grain size, microtexture, macrotexture, and in some cases residual plastic strain. It is well known that the mechanical properties of Ti alloys can be influenced by crystallographic texture (e.g., [3D.8, 3D.9]). In fatigue, the effect of texture can be significant [3D.10]. Primary- α in bimodal microstructures can have pronounced crystallographic texture depending on the degree and mode of deformation.

EBSP data was obtained from the surface of selected 3 point bending specimens, in the gage region, after light cleaning with ethanol and/or gas jet cleaning with a CO₂ "snow gun". Scanning electron microscopy using both secondary and backscattered electron imaging was used for preliminary examination. The instrument used was a CamScan CS44 operated at 15 kV and nominal 1 nA probe current. Figure 3D.4 shows a sample of the observed structure on the specimen gage length prior to fatigue testing.

The automated EBSP data was collected using a Channel + EBSP Analysis attached to the SEM. The specimens, due to their large size, were mounted to the top of a large, top referencing holder allowing good alignment of the plane of analysis with the X-Y translation plane of the stage. The sample/holder is tilted 70 degrees from normal incidence to the beam axis for EBSP. The probe conditions for EBSP were ~10nA probe current and 30 kV accelerating voltage. Some of the specimens were EBSP-scanned before testing while others were examined afterwards. For fatigue-tested specimens, 3 to 6 EBSP line scans were performed in the gage section away from the highest stressed region containing the critical crack (for specimens that failed). The critical crack is the crack which led to failure in the specimen.

EXPERIMENTAL RESULTS

High Cycle Fatigue Life of Ti-6Al-4V Forged Plates

The bending fatigue testing results conducted at $R = 0.1$ and 0.5 for the forged Ti-6Al-4V alloy are summarized in Table 3D.3. A total of 15 specimens were categorized into S/N (6 tests), replica (6), and EBSP + replica analysis (3) fatigue tests. The results, that include both low cycle fatigue (LCF) and HCF results, are plotted in Figure 3D.5 in

the form of a S/N curve (using stress range, ***Δs***). Comparable S/N data from Allied Signal [3D.11], obtained from hourglass fatigue specimens machined from different forging plates of the same Ti alloy, are also shown. These tests were loaded uniaxially at the same stress ratios. In Figure 3D.5, the GECRD data in bending are consistently higher than those obtained in tension for both $R = 0.1$ and 0.5 . This is expected since bending tests usually result in higher fatigue lives than uniaxial tests for the same applied stress. The $R = 0.1$ data in bending also shows significant scatter, and differences in fatigue lifetimes could be 100 times for the same stress range. These unexpected variations made it difficult to complete the bending fatigue S/N curve since it was hard to predict the expected fatigue lifetime for a given stress. The bending fatigue lifetimes for two tests at $R = 0.5$ are slightly longer than those under uniaxial loading. These results did not show the same level of scatter as at $R = 0.1$.

One of the difficulties in developing a useful database for fatigue strength of even a single Ti alloy in a single microstructural condition is the number of variables involved such as the stress/strain range, mean stress/strain, loading frequency, loading mode (bending vs. uniaxial), test environment, and surface finish condition [3D.12]. Since the specimens tested came from different forged plates, the data in Figure 3D.5 was re-plotted according to specimen lot number (Figure 3D.6) to better understand the results. The same was also done for the Allied Signal data. From Figure 3D.6, it is clear that the fatigue lifetimes for specimens from Lot #79 were inconsistent with the rest of the data. Lot #126 also had some noticeable difference for Specimen 126-1 which failed at a life ten times shorter than would be expected based on the lives of two specimens from Lot #94 tested under the same conditions. Initially, it was thought that Specimen 126-1 was simply consistent with the uniaxial Allied Signal data at $R = 0.1$. However, two other specimens from Lot #126, tested at a slightly lower stress level, had much longer fatigue lives than would be expected from the Allied Signal S/N curve. Consequently, Specimen 126-1 appeared to be a “rogue” data point. The other two Lot #126 specimens did not fail after 2 million cycles (no cracks were also observed on the replicas) because they had been tested below the fatigue limit of about 600 MPa (87 ksi) based on the S/N curve for the remaining $R = 0.1$ specimens (except Lot #79 specimens). No microstructural defect that may have led to the lower life for Specimen 126-1 was found. In contrast, the Allied Signal data indicated no fatigue

lifetime variations between three different lots at the two stress ratios. As mentioned in the previous section, although the microstructure for the forged plates is expected to be uniform from lot to lot, there may be some texture effects. Thus, EBSD was employed to examine variations in texture between the different lots.

Microstructural Crack Initiation and Early Growth in High Cycle Fatigue

From the replicas, the critical cracks leading to fatigue failure can be tracked on the surface of the specimens. Figure 3D.7 is an example of a set of replica SEM micrographs that can be obtained to track the formation and growth of the critical crack of a specimen from the surface in HCF. Replication in this HCF study of the Ti-6Al-4V alloy, however, turned out considerably more difficult to apply than in LCF. This is mainly due to the large number of fatigue cycles involved. The results of this study show that a majority of the life is spent initiating cracks, and that there are no visible surface cracks on most of the replicas. Furthermore, only a single crack (the critical crack) is ever found for each specimen replicated. This has been confirmed from fracture surface examinations of failed specimens which verified that there was only a single initiation site (grain facet-type of initiation). The existence of only a single crack could be the result of stress localization in the specimens due to testing in bending. In bending, only a small region is stressed at the maximum applied stress. No cracks were found away from the center-most gage section area.

In Figure 3D.7, the critical crack in one specimen (99-4) is seen to initiate at a slip band in an α_p particle. Intra-alpha phase initiation is commonly seen in the fatigue of $\alpha+\beta$ Ti alloys (e.g., [3D.7, 3D.13, 3D.14]). For the specimens examined here, the intense level of slip often found in LCF is not observed. In a different specimen (85-4), the critical crack appears to have nucleated at the lamellar and α_p interface/boundary (Figure 3D.8a). Interface nucleation has been reported to occur in Ti-6Al-4V under low cyclic strain levels at room temperature in the absence of detectable slip lines [3D.15]. In Figure 3D.8b, the initiation site of the critical crack for Specimen 94-3 is within a lamellar grain. This is thought to be related to an alloy partitioning effect that weakens the β phase with increasing α_p content making the lamellar more susceptible to crack initiation [3D.7]. There are not enough observations in the present work to determine if one particular site was preferred over another for critical crack initiation in bending

fatigue. The observed crack initiation mechanisms, however, are qualitatively similar with those reported in the literature for naturally-initiated LCF and HCF microcracks from smooth specimens predominantly tested at $R = -1$. The length of an initiated crack appears to be related to the length of the initiation site. For example, for slip band cracks, the diameter of the grain.

Figure 3D.9 plots the replica-measured surface crack length, a , versus the normalized number of fatigue cycles, N/N_f , for critical cracks from several specimens. As mentioned above, a major difficulty in employing replication in HCF is that there are no cracks for a majority of the fatigue life. In this study of forged Ti-6Al-4V, the HCF crack initiation regime generally ranges between 70 to 90 percent of the life but could be as low as 60 percent. In one case (Figure 3D.8a), a 15 μm crack is seen at approximately 60 percent of the fatigue life. As shown in Figure 3D.9, upon initiating the cracks grow quite rapidly. A limitation of pre-selecting the replication interval prior to starting a test is that frequently only a single replica was made in the period between crack initiation and just prior to failure. This means only one replica crack length measurement was available for an entire set of replicas. Furthermore, backtracking from a large crack to the initiation source is complicated if the crack initiated between replicas (likely if the replica interval is large). Also, there are few, readily-identifiable reference points such as large inclusions to utilize in the Ti-6Al-4V microstructure making it difficult to find small cracks (large scratches are sometimes employed, but the quality of surface finish of the specimens studied here was high). Coupled with the significant scatter in fatigue lifetimes observed in this work, it was difficult to improvise the replication process during testing by decreasing the replica interval late in the fatigue life in order to obtain more data.

From the crack length versus number of cycles (N) data, the crack growth rate can be obtained. To calculate the cyclic stress intensity factor, ΔK , the crack shape here is taken to be semi-elliptical (based on the critical crack shape seen on the fracture surface). For a surface crack in a flat bending specimen, the ΔK solution [3D.16] at the surface along the crack length is:

$$\Delta K_a = \Delta \sigma_{\text{bending}} \sqrt{\pi b} \cdot \frac{M}{\phi} SH_1 \quad (3D.1)$$

where b is crack length into the depth and M , f , S , and H_2 are constants related to the aspect ratio (b/a) and the fraction of crack depth to specimen thickness (b/t). From fracture surface measurements of the critical crack dimensions, b/a is estimated to be 1/3. Figure 3D.10 shows the log-log plot of the surface crack growth rate, da/dN , versus DK at $R = 0.1$ for three critical cracks (from three different specimens) that had sufficient replica-measured crack length data from which da/dN could be determined. The da/dN results in this study confirm that when natural cracks are small, they can grow well below the long crack-measured DK_{th} . The long crack data shown in Figure 3D.10 were obtained from different efforts [3D.2,3D.7] in the HCF program for the same forged Ti-6Al-4V alloy (different lots) using compact tension (CT) specimens (at 50 Hz [3D.2] and 30 Hz [3D.7]). Here, the long crack threshold at $R = 0.1$, taking into account the effects of crack closure (i.e., using the effective stress intensity factor, DK_{eff}), is approximately $3.7 \text{ MPa}\sqrt{\text{m}}$ ($3.4 \text{ ksi}\sqrt{\text{in}}$). The GECD data had measurable crack growth at DK values as small as $1.9 \text{ MPa}\sqrt{\text{m}}$ ($1.7 \text{ ksi}\sqrt{\text{in}}$). This is also less than the DK value of $2.9 \text{ MPa}\sqrt{\text{m}}$ ($2.6 \text{ ksi}\sqrt{\text{in}}$) below which crack growth was reported not to occur for FOD-initiated cracks [3D.2].

Mechanistically, from *limited* replica observations of growing cracks after initiation, the cracks appear to grow steadily. There are not enough replicas during the early stages of growth, however, to determine if the microcrack growth behavior was intermittent (i.e., had periods of accelerated growths coupled with periods of arrest and/or slow growth). The high volume fraction of primary α -phase results in crack propagation being predominantly through α_p or along favorably-orientated lamellae grains and α_p -lamellae boundaries perpendicular to the loading stress axis (e.g., Figure 3D.7). There are changes in crack path when a crack encounters a grain boundary due to possible crystallographic orientation differences between adjacent primary alpha grains. Little secondary cracking is observed, and for the most part the crack growth paths resemble those seen for long cracks. No instances of crack coalescence and linkages, typical of microcrack growth in LCF, are seen. This is likely because there is only a single initiated crack which rapidly grows to become the dominant crack.

Electron Backscatter Pattern (EBSP) Analysis of the Ti-6Al-4V Fatigue Specimens

The term texture normally refers to preferred orientations (“clustering” of orientations) measured over volumes/regions very much larger than the fundamental scale of the microstructure (i.e., much larger than alpha grain size diameter and alpha colony diameter). The work of Larson and Zarkedes [3D.17] suggests that the fatigue lifetimes of Ti alloys can be influenced by crystallographic texture. EBSP was employed in this study primarily to examine the microtexture of the Ti-6Al-4V fatigue specimens from different forged plates. This was pursued partially because EBSP was useful to research on dwell fatigue of *a+b* Ti-6242 where microtexture was found to play a significant role in the behavior [3D.9].

Grain Size Measurements

One mode of EBSP data acquisition involved stepping through the microstructure at 0.0005 mm to detect and characterize alpha grains along a number of test lines. This line scan data is appropriate for interpreting texture information, but also enables an analysis of grain size and colony size. Table 3D.5 shows the grain size and related measurements derived from the EBSP line scan data. The differences between the specimens are small for these microstructural parameters. The low values of α indicate low internal grain structure in all specimens and the differences observed are not significant. This is consistent with AFRL observations [3D.5].

Analysis of Macrotexture

Those orientation measurements taken over a large surface area probing a large number of individual grains form a good basis for evaluating the macrotexture in the material. That macrotexture can be described using both pole figures and orientation distribution functions (ODF). The pole figure graphically shows the distribution (in the specimen coordinate system) of specific crystallographic features – such as the {0001} plane normal. The ODF, on the other hand, gives a direct representation of Euler space – without projections. The primary features in either data representation are maxima and minima corresponding to non-random distributions of orientation – preferred orientations or crystallographic texture.

A comparison of the data from the five specimens shows that there are differences in macrotexture. These differences are somewhat easier to see in the ODFs for which different maxima are observed for some of the specimens. These are shown in Figures 3D.11. Specimens 126-2RM and 126-3RM are most similar to each other and 126-1 and 85-2 are quite similar to each other, yet lack one of the texture components found in 126-2 and 126-3. Specimen 79-4 had yet a third character different from the others. In these comparisons the absolute magnitude of texture peaks is not being strongly considered, more emphasis being placed on the patterning and the relative peak strengths.

The pole figures similarly show differences between the specimens although the structure of the peaks is not quite as clear as found in the ODF data. These are shown in Figures 3D.12. Most significant, perhaps, is the difference observed for the density of {0001} poles in the $\pm X$ direction, which would be perpendicular to the crack plane. The pole figures are just another way to look at the same data presented in the ODF.

Analysis of Microtexture

Macrotexture does not necessitate microtexture. Microtexture is the occurrence of non-random orientation distributions in local grain neighborhoods/regions involving only a relatively small number of grains. Aspects of microtexture include the size of regions having a non-random crystallographic character as well as the degree of alignment of grains in those features. Microtexture has been examined in two phase Ti6242 specimens using the EBSD technique and is associated with the primary alpha colony structure [3D.9]. In that Ti6242, there is at least an empirical relationship observed between microtexture, independent of macrotexture, and mechanical behavior has been found to be influenced by microtexture.

Again, using the 0.0005 mm linescan data, it is possible to search for colony structure in this forged Ti-6Al-4V material. It is basically an extension of the grain size analysis whereby the boundary conditions defining colonies are slightly less restrictive than those defining grains. For this analysis, an *a* colony boundary was defined as occurring where neighboring grains had more than 15 degrees misorientation of their {0001} planes. The results on the five specimens examined were very similar and indicated the essential absence of significant colony structure in this material (as

indicated by colony size, which was only ~25 percent greater than the grain size. The microtexture results are shown in Table 3D.6. In support of these numbers, orientation images (OI) that were generated from selected scans also indicate no observable colony structure, see Figure 3D.13. In the OI shown, each color represents specific clustering/range of {0001} orientations. The {0001} pole figure below the OI shows the mapping of color; this is called the icosahedral map because it is based on the division of orientations into their intersection onto each face of a colored icosahedron. Colonies of similarly oriented grains are easily revealed in an icosahedral map.

In summary, there is no indication of significant microtexture in the specimens studied. Although the strength of the macrotexture in these forged Ti-6Al-4V plates would not be classified as very strong (maximum 3 to 4.6 times random), the differences observed are significant and should be considered in interpreting differences in measured mechanical behavior.

Discussion

Influence of Texture on High Cycle Fatigue Life

It has been reported that there can be a strong effect of texture on HCF properties, sometimes even larger than that observed in LCF [3D.19]. An explanation for this has been linked to influence of primary alpha on crack initiation behavior in HCF. The secondary alpha, not being as strongly textured, contributes less to HCF crack nucleation. But, its coarseness, related to the aging temperature and cooling rate from the solution treatment, does influence early crack propagation between the nucleated sites on primary alpha particles. Hence, microcrack growth, a significant portion of the HCF life, is thought to be greatly influenced by the secondary alpha characteristics.

It has not been possible, within the scope of this study, to determine whether the texture differences observed between forging plates are responsible for the HCF lifetimes differences. The fact that Specimen 79-4 had macrotexture characteristics unlike the other specimens suggests that macrotexture may have contributed to the much longer HCF lives of Lot #79 specimens. However, while Specimens 85-2 and 126-1 had similar macrotexture and similar fatigue lifetimes, the former was loaded at a stress range of over 140 MPa higher than the latter. Furthermore, even the scatter within one lot in LCF lifetimes can be very large. For example, in IMI834 at $R = 0.1$ and

Ti-6242 at $R = -1$, fatigue lifetimes for the same alloy can vary 10 to 100 times [3D.20]. Hall [3D.13] reported that microstructural variations at different locations in a Ti-6Al-4V forging, namely vol.% of α_p (which is considered to be rather uniformly distributed in the Ti-6Al-4V alloy of this study), could result in an 90 MPa (11.5 ksi) difference in stress for HCF life of 10^7 cycles. Thus, to resolve this issue of variable fatigue lifetimes, focused experiments on the effects of macrotexture (or other microstructural properties) on fatigue lifetimes are needed. Unfortunately, these experiments are outside of the immediate objectives of the GECRD phase of the HCF Program and were not pursued further. Even more, as described above, the HCF Program has been conducted to date based on studies suggesting that there are no significant differences in microstructure between different lots of forged Ti-6Al-4V plates.

Mechanisms of Crack Initiation During High Cycle Fatigue Damage

High cycle fatigue strength of materials in an initially undamaged state is related to the ease of crack nucleation. This investigation shows that a majority of the HCF life in the studied Ti-6Al-4V alloy was spent in the crack initiation regime. This is consistent with observations by Wagner [3D.14] that up to 80 to 90 percent of life in the HCF of a Ti-6Al-4V alloy was nucleation. In contrast, the crack initiation portion of the life in LCF is generally much shorter. For example, for an $\alpha+\beta$ Ti-17 alloy tested in room temperature air under fully-reversed bending, crack initiation in LCF occurred within the first 5 to 30 percent of life [3D.20]. In a different study on forged Ti-6Al-4V, crack initiation took place within the first 5 to 10 percent of the life in LCF [3D.21]. A commonality seen between HCF and LCF is initiation by slip in α -particles. Slip band nucleation is preferred in $\alpha+\beta$ Ti alloys when coarse, elongated α_p is present and becomes inhibited with finer structures (reduced slip distance). Hall [3D.13] noted in a review of crack initiation in Ti alloys that qualitatively the nucleation mechanisms in all $\alpha+\beta$ Ti alloys are similar.

The crack initiation mechanism is controlled by the deformation behavior of the alloy [3D.12]. In turn, the deformation process is significantly affected by the characteristics of the microstructure. Deformation behavior refers to whether plastic deformation is accommodated by twinning or slip and to the nature of the slip bands. The concentration of Al in Ti alloys controls whether slip in the α -phase is planar or wavy.

Higher oxygen contents tend to cause the planar slip to intensify and become localized. In Ti-6Al-4V with a colony microstructure, slip is planar because of the Al content and the slip length is controlled by the colony size, since all plates in a colony are crystallographically aligned.

In the present study, alpha phase was generally fine (Table 3D.5), and no colony structure was identified by EBSP (Figure 3D.13). Initiation is also seen to occur at sites such as the α_p and $\alpha+b$ lamellar boundary and within the lamellar grain. Overall, there were not enough separate observations of crack initiation to determine if there was a preferential site or dominant mechanism for HCF crack initiation in this Ti-6Al-4V alloy. Each replicated specimen had only a single initiated crack, the critical crack, thus it was not possible to gather more in-depth statistics on preferred crack initiation sites without conducting additional fatigue tests. The source of the initiated cracks, however, does not appear to significantly affect the microcrack growth rates. As seen in Figure 3D.10, the microcrack growth rates for cracks from three different initiation sites were generally consistent.

Microcrack Growth Behavior in High Cycle Fatigue

The microcrack growth data obtained in this work distinguishes itself from those found in the literature as the cracks studied here were naturally-initiated at $R = 0.1$. The smaller stress range involved with testing at $R = 0.5$ and $R = 0.1$ made it more difficult to initiate and grow small cracks. This was further confirmed in that much of the microcrack growth data in metallic materials found in the literature were achieved from tests conducted at $R = -1$. The only comparable small crack data at $R = 0.1$ found in the literature for Ti-6Al-4V were those from the work of Hines et al. [3D.7]. Even here, however, small cracks were initiated at $R = -1$ first and then allowed to grow until approximately 50 μm long before fatiguing at $R = 0.1$ or $R = 0.5$.

Early crack growth can be a majority of the fatigue life in LCF. For example, in Ti-17, 40 to 70 percent of life is spent in microcrack growth since initiation takes place early [3D.20]. In contrast, the early growth stage observed for the Ti-6Al-4V alloy is just 10 to 20 percent of the life in HCF (Figure 3D.9). In terms of absolute number of cycles, this can still be a sizable length of time. This serves to illustrate the importance of designing for crack initiation resistance in HCF, and the deleterious effects of extrinsic

damage such as FOD and/or fretting in reducing the HCF properties of **a+b** Ti alloys. Once a crack or a crack-like flaw is introduced into a component, crack propagation in HCF will rapidly take place in fine grain alloys such as this Ti-6Al-4V material.

Figure 3D.14 shows the crack growth rate data at $R = 0.1$ for the naturally-initiated cracks from bending specimens of this work compared with similar results from uniaxially-loaded hourglass specimens fatigued at $R = 0.1, 0.5$, and -1 [3D.7] for the same HCF Program Ti-6Al-4V alloy. Long crack data for this material at $R = 0.1$ and $R = 0.5$ are also plotted. Microcrack growth rate data are not available from Reference 7 for **DK** values below about $2.9 \text{ MPa}\sqrt{\text{m}}$ ($2.6 \text{ ksi}\sqrt{\text{in}}$) for $R = 0.1$ since the microcracks were grown at $R = -1$ until about $50 \mu\text{m}$. However, if the $R = 0.1$ and -1 lines from this work are extrapolated for smaller values of **DK**, they overlap the GECDR results. This suggests consistency in results between both sets of microcrack growth rate data at low **DK** values. With regard to the differences in da/dN between microcracks and long cracks in Figure 3D.14, this has been attributed in part to the level of roughness at the crack front (i.e., roughness-induced crack closure). A long crack possesses a rougher crack profile than a small crack, and as the latter grows longer asperities in the crack wake combine with shear ahead of the crack tip to develop closure effects [3D.22]. Yet another common explanation for the da/dN differences is the validity of applying an elastic fracture mechanics parameter like **DK** to small cracks. The use of **DK** is questionable because when the crack size is comparable to the microstructural unit size the material cannot be considered a continuum [3D.23]. However, the use of **DK** for characterizing the crack driving force of microcracks may be appropriate if it is used only when the microcracks are growing, and not when it is the state of arrest due to factors such as microstructural obstacles and crack tip shielding [3D.24].

At higher values of **DK**, the GECDR data intersects the long crack data obtained from CT specimens [3D.2, 3D.7] between 5 to $10.5 \text{ MPa}\sqrt{\text{m}}$ (4.6 to $9.6 \text{ ksi}\sqrt{\text{in}}$). This is not the case for the microcrack data of Reference 3D.7, which does not approach the long crack data until approximately $15 \text{ MPa}\sqrt{\text{m}}$ ($13.7 \text{ ksi}\sqrt{\text{in}}$). An explanation for this is because the Paris Equation [3D.25] exponent, m , is different from each study of microcrack growth rates. Table 3D.7 shows the Paris exponent for each set of da/dN versus **DK** data plotted in Figure 3D.12. The exponent was determined by fitting the data

points or curves to a power law expression. From Table 3D.7, the exponents of the long cracks at both $R = 0.1$ and $R = 0.5$ are the largest, ranging between 4.2 to 4.8. The microcrack data in this study had the lowest exponents of 2.0 and 2.1 for $R = 0.1$. The microcracks in Reference 3D.7 had a higher exponent of 3.1 for $R = 0.1$. An explanation for the difference in m -values between these two sets of microcrack data could be the damage induced by compressive loads due to fatiguing first at $R = -1$. Another source could be differences in the stress fields from fatiguing in bending versus uniaxial loading.

The smaller Paris exponents in this study suggest that the small crack threshold will be less than those calculated by extrapolating long crack data into the threshold regime. For example, Reference 3D.2 found a lower bound threshold of $4.6 \text{ MPa}\sqrt{\text{m}}$ ($4.2 \text{ ksi}\sqrt{\text{in}}$) for long cracks in the Ti-6Al-4V forging at $R = 0.1$. Extrapolation of the GECD microcrack data gives a small crack threshold (for a crack growth rate of 10^{-10} m/cycle) of $1.1 \text{ MPa}\sqrt{\text{m}}$ ($1 \text{ ksi}\sqrt{\text{in}}$) at $R = 0.1$ for the same material. This threshold value compares well to the intrinsic threshold of $1 \text{ MPa}\sqrt{\text{m}}$ ($0.9 \text{ ksi}\sqrt{\text{in}}$) calculated in Reference 3D.2 using the approach of Weertman [3D.26]. The intrinsic threshold here represents the driving force below which dislocations can no longer be emitted from the tip of an atomistically-sharp crack. It could be defined as the theoretical lower bound for fatigue crack propagation thresholds.

Conclusions

The following are the conclusions for this investigation of HCF crack initiation and early growth in a forged Ti-6Al-4V alloy:

1. High cycle fatigue tests conducted in bending result in higher fatigue lives than under uniaxial loading at the same applied stress for $R = 0.1$ and $R = 0.5$.
2. Sixty to 90 percent of the fatigue life is spent in the crack initiation regime during HCF. Upon nucleating, the cracks grow rapidly spending just 10 to 20 percent of the life in the microcrack growth stage.
3. The critical cracks leading to fatigue failure were observed to initiate at slip bands in α_p grains, at the interface/boundary between α_p and $\alpha+b$ lamellae,

and within preferentially-oriented lamellar grains. Only a single crack was observed to nucleate in each specimen at the center of the gage section.

4. The strength of the texture in this material was not very strong. However, the differences observed are significant enough that they need to be considered when interpreting variations in the measured mechanical properties.
5. Naturally-initiated cracks in bending at $R = 0.1$ grew at DK values well below the threshold for long cracks. These cracks had a Paris exponent of about $m = 2.0$. Extrapolation of the crack growth data gives a small crack threshold of $DK_{th} = 1.1 \text{ MPa}\sqrt{\text{m}}$ at $R = 0.1$ for a crack growth rate of 10^{-10} m/cycle . This threshold value compares well to a calculated intrinsic threshold value of $1 \text{ MPa}\sqrt{\text{m}}$.

Suggestions for Future Work

A complete experimental program to develop and demonstrate a methodology for predicting the HCF life of Ti-base materials containing defects of either intrinsic or extrinsic origin using fracture mechanics or other mechanistic-based life prediction concepts must investigate the following technical issues:

- 1) the introduction and characterization of initial damage states;
- 2) the initiation of cracks from small flaws/damage;
- 3) the growth characteristics of small cracks;
- 4) the characterization of crack growth in the near-threshold regime;
- 5) the effects of crack closure;
- 6) the interactive effects of low- and high-cycle fatigue.

Experimental parameters for such a complete investigation would include: (a) temperature; (b) stress ratio; (c) frequency; (d) hold times and load history; and (e) flaw size/damage state. Also included would be a number of representative microstructural conditions, typical of those obtainable from conventional thermo-mechanical processing of alpha-beta titanium alloys, to establish the microstructure-property relationships that govern the useful HCF life of these materials.

Initial plans called for the use of surface replication in combination with the mechanical testing in hope that the specific grains associated with crack nucleation

could be examined. If the crack origin could be determined in intact specimens, then the EBSD technique would allow the exploration of possible relationships between nucleation site and orientation aspects of the microstructure, such as specific orientations of the grains, specific misorientations between crack nucleating grains and uncracked neighbors, and possibly accumulated plastic strain in the crack nucleating grains. In the present work, the intervals between taking replicas were sufficiently long that it was not possible to determine which grains were involved with nucleation in the specimens selected for EBSD. Initiation and growth to a long crack size sometimes occurred within the replica-taking interval. Likewise, large variability in lot-to-lot fatigue lifetime made it difficult to adequately employ replication. Future work can focus on improved sampling to better capture the nucleation and/or use postmortem examination of the specimen to help find the nucleation on the fracture surface and relate back to specific grains on the surface.

Acknowledgements

This work was supported by the U. S. Air Force Research Laboratory, through GE Aircraft Engines, as a part of the Advanced High Cycle Fatigue Life Assurance Methodologies Program administered by the University of Dayton Research Institute. Thanks are due to Dr. T. Nicholas (AFRL) and D. Corbly (GEAE) who served as program managers of this task, as well as Dr. R. H. Van Stone, Dr. K. Bain, Dr. D. Slavik and the GEAE HCF team who provided technical assistance and the specimens and related data. At GECD, Dr. M. F. Henry provided many useful suggestions and comments. M. E. Gilhooly and B. Cerniglia contributed expert technical assistance in mechanical testing and metallography, and S. D. Sitzman played a major role in the EBSD analysis. In addition, special thanks are due to Prof. R. O. Ritchie, B. L. Boyce, and Dr. J. O. Peters at the University of California and Dr. J. A. Hines of Technical University Hamburg-Harburg for contributing preprints of works with related small cracks data.

REFERENCES

- 3D.1 Report of the Ad Hoc Committee on Air Force Aircraft Jet Engine Manufacturing and Production Processes, U.S. Air Force Scientific Advisory Board, SAF/AQSS: the Pentagon, Washington, DC (1992).

- 3D.2 Boyce, B.L., Campbell, J. P., Roder, O., Thompson, A.W., Milligan, W.W., and Ritchie, R.O., *Int. J. Fatigue* (In press).
- 3D.3 Larsen, J.M., Worth, B.D., Annis, C. G., and Haake, F.K., *Int. J. Frac.*, 80 (1996), 237.
- 3D.4 Cowles, B.A., *Int. J. Frac.*, 80 (1996), 147.
- 3D.5 Eylon, D., Summary of Available Information on the Processing of the Ti-6Al-4V HCF/LCF Program Plates, University of Dayton, Dayton, OH (1999).
- 3D.6 Slavik, D., Private Communications, GE Aircraft Engines, Cincinnati, OH (1999).
- 3D.7 Hines, J.A., Peters, J.O., and Lutjering, G., *Fatigue Behavior of Titanium Alloys*, The Minerals, Metals & Materials Society, Warrendale, PA (In press).
- 3D.8 Evans, W.J. and Bache, M. R., *Int. J. Fatigue*, 16, 7 (1994), 443.
- 3D.9 Woodfield, A.P., Gorman, M.D., Corderman, R.R., Sutliff, J.A., and Yamrom, B., *Titanium '95 Science and Technology*, P.A. Blenkinsop, W.J. Evans, and H.M. Flower, eds., Inst. of Materials, London (1995), 1116.
- 3D.10 Peters, M. and Lutjering, G., Report CS-2933, Electric Power Research Inst., Palo Alto, CA (1983).
- 3D.11 Bellows, R.S., Muju, S., and Nicholas, T., *Int. J. Fatigue* (In press).
- 3D.12 Williams, J.C., *High Performance Materials in Aerospace*, H.M. Flower, ed., Chapman & Hall, London (1995), 85.
- 3D.13 Hall, J.A., *Int. J. Fatigue*, 19, S1 (1997), S23.
- 3D.14 Wagner, L., *Fatigue and Fracture*, Metals Handbook, Vol. 19, ASM International, Materials Park, OH (1996), 837.
- 3D.15 Benson, D.K. Grosskreutz, J. C., and Shaw, G. G., *Metall. Trans.*, 3A (1962), 1239.
- 3D.16 Newman, Jr., J.C. and Raju, I.S., Technical Note, TP-1578, National Aeronautics and Space Administration, Langley, VA (1979).

- 3D.17 Larson, F. and Zarkedes, J., Battelle Columbus Labs MCIC Report number MCIC-74-20, June 1974 (1974).
- 3D.18 Boyer, R.R. and Hall, J.A., Titanium '92, Science and Technology, F. H. Froes and I. Caplan, eds., The Minerals, Metals & Materials Society, Warrendale, PA (1993), 77.
- 3D.19 Lutjering, G., Gysler, A., and Torster, F., Metallurgy and Technology of Practical Titanium Alloys, S. Fujishiro, D. Eylon, and T. Kishi, eds., The Minerals, Metals & Materials Society, Warrendale, PA (1994), 101.
- 3D.20 Funkenbusch, A.W. and Coffin, L.F., Metall. Trans., 9A (1978), 1159.
- 3D.21 Wells, C. H. and Sullivan, C. P., Trans. ASM, 62 (1969), 263.
- 3D.22 Wagner, L. and Lutjering, G., Z. Metallk., 78 (1987), 369.
- 3D.23 Gregory, J. K., Fatigue and Fracture, Metals Handbook, Vol. 19, ASM International, Materials Park, OH (1996), 845.
- 3D.24 Chen, E.Y., Lawson, L.R., and Meshii, M., Metall. Mater. Trans., 26A, 12 (1995), 3163.
- 3D.25 Paris, P.C. and Erdogan, F., J. Basic Eng., 85D (1963), 528.
- 3D.26 Weertman, J., Mechanics of Fatigue, T. Mura, ed., American Society of Mechanical Engineers, New York, NY, AMD-Vol. 47 (1982), 11.

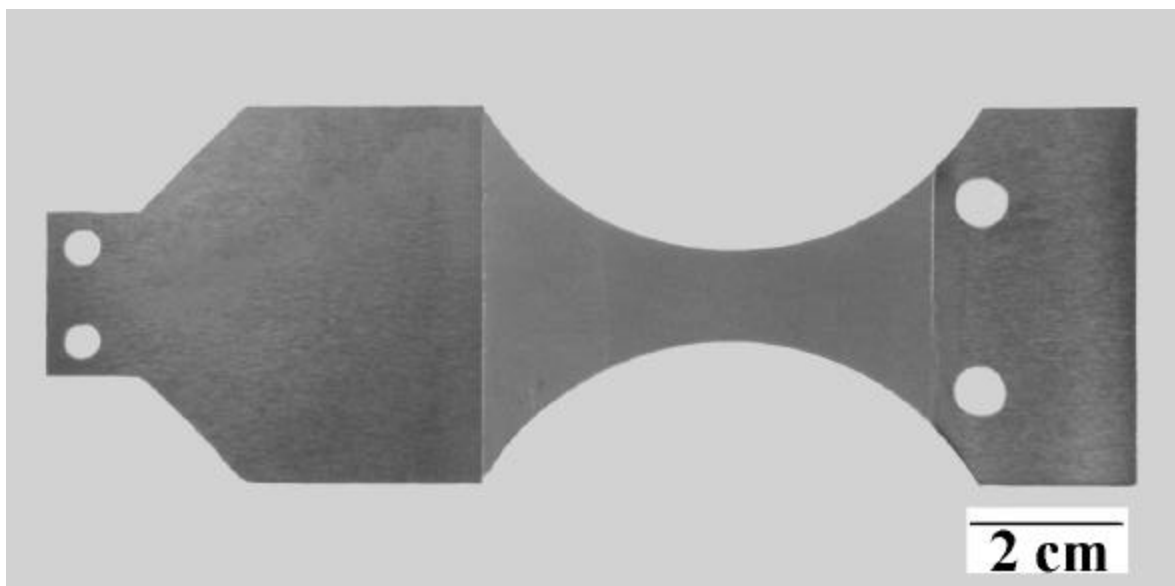


Figure 3D.1. Bending fatigue specimen design.

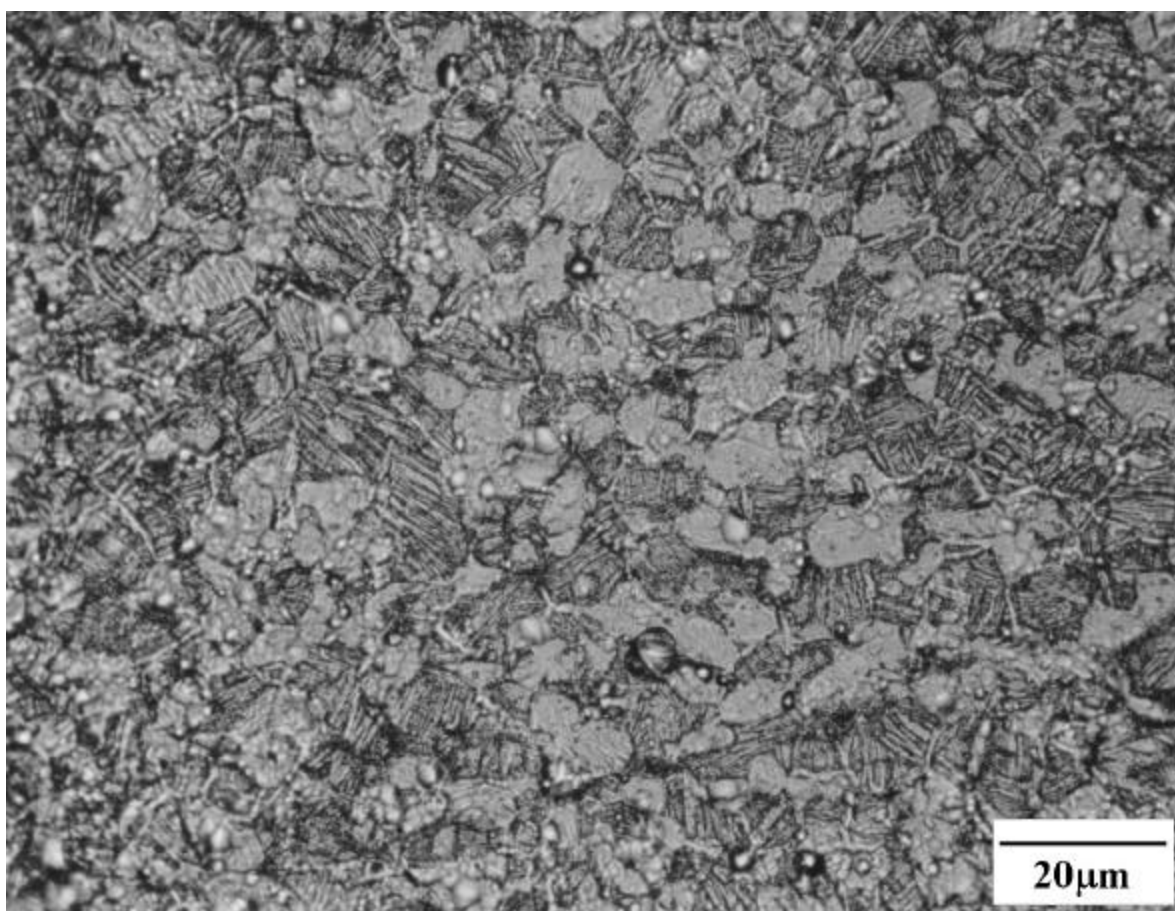
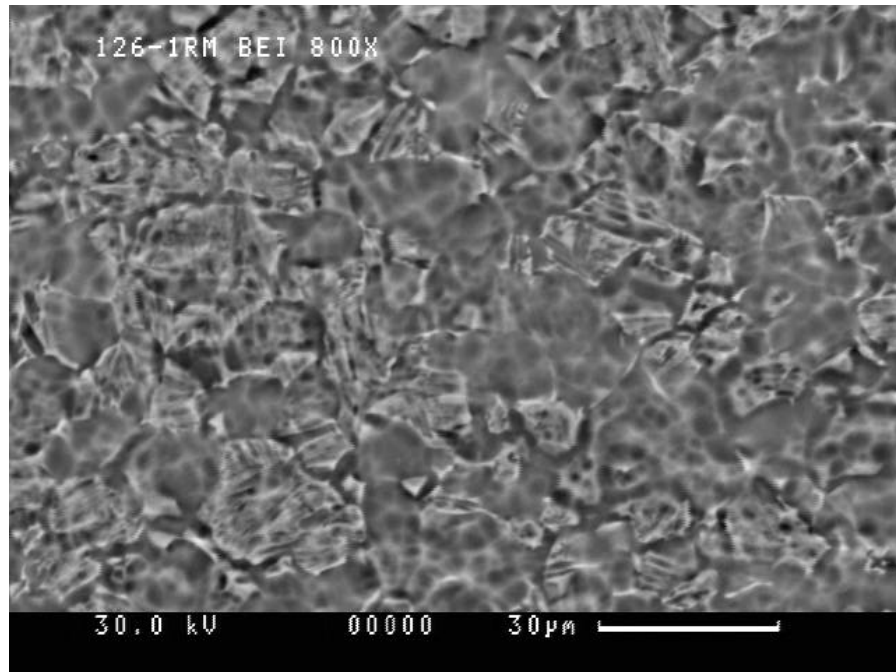


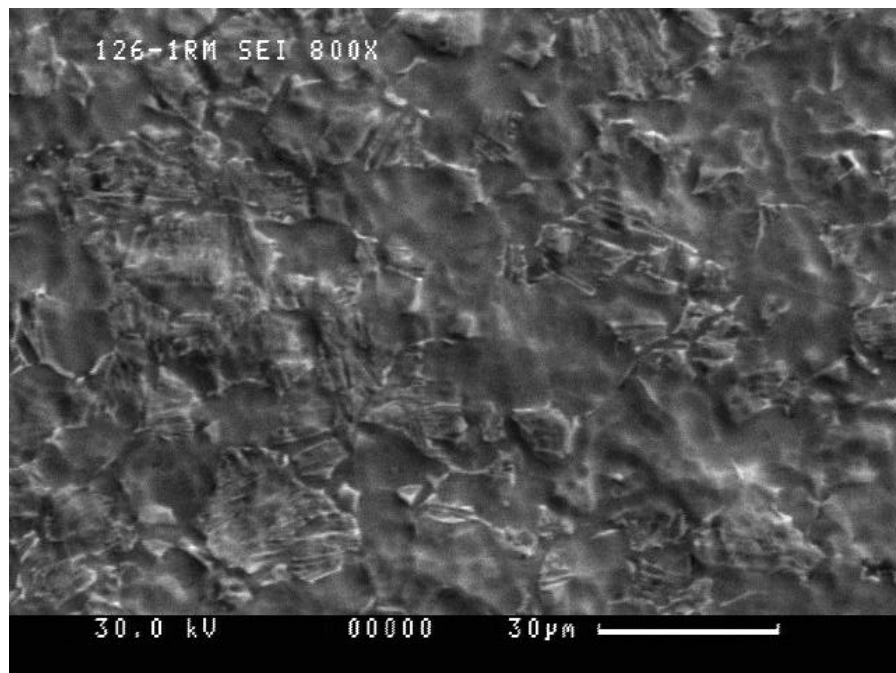
Figure 3D.2. Microstructure of the forged Ti-6Al-4V alloy as received by GECRD.



Figure 3D.3. Three point bending testing apparatus used at GECRD for HCF tests.



(a)



(b)

Figure 3D.4. Sample microstructure of the forged Ti-6Al-4V alloy as captured by the SEM for EBSD analysis: a) backscatter image and b) secondary image. Specimen 126-1 prior to fatigue testing.

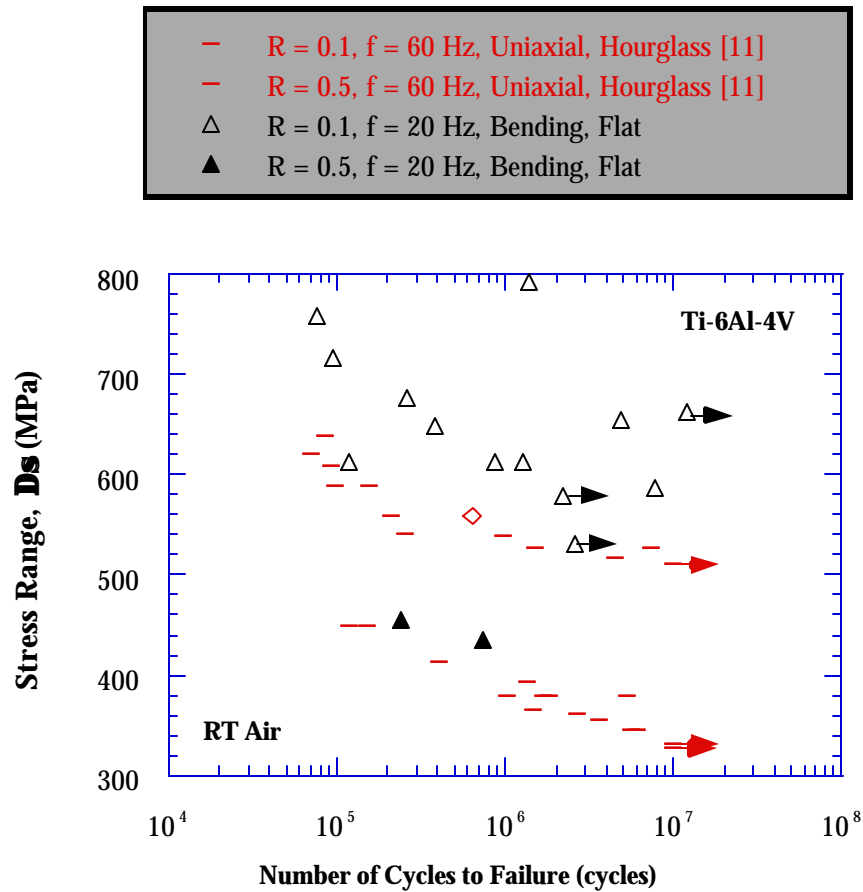


Figure 3D.5. S/N curve for high cycle fatigue of forged Ti-6Al-4V in room temperature air at $R = 0.1$ and 0.5 . Plot compares GECRD data with those for uniaxially-loaded hourglass specimens from Allied Signal [3D.11].

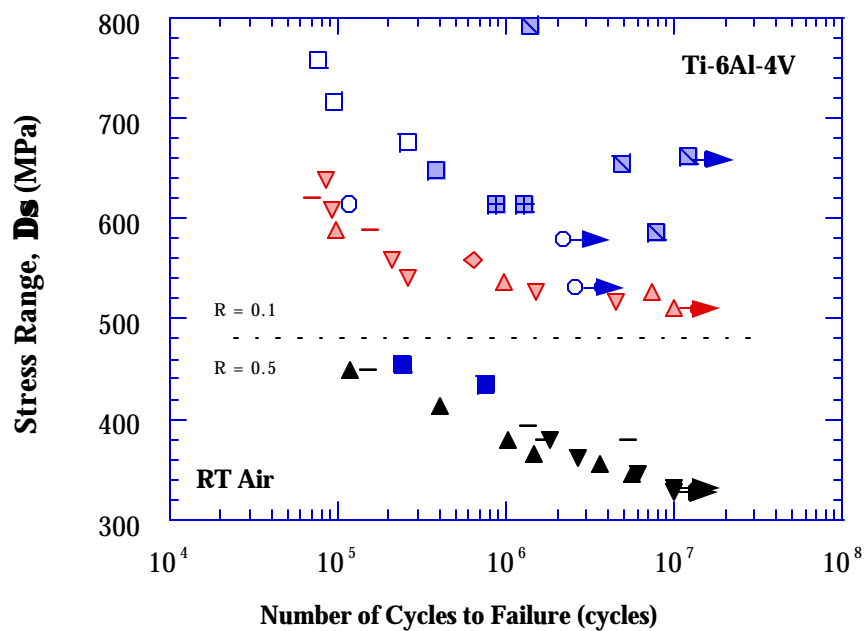
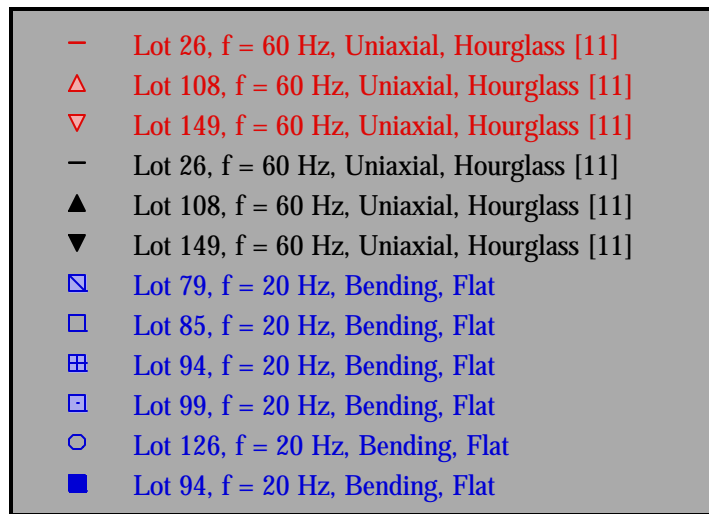
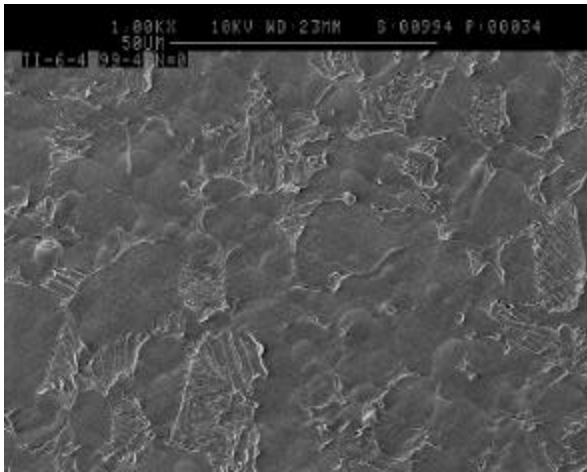
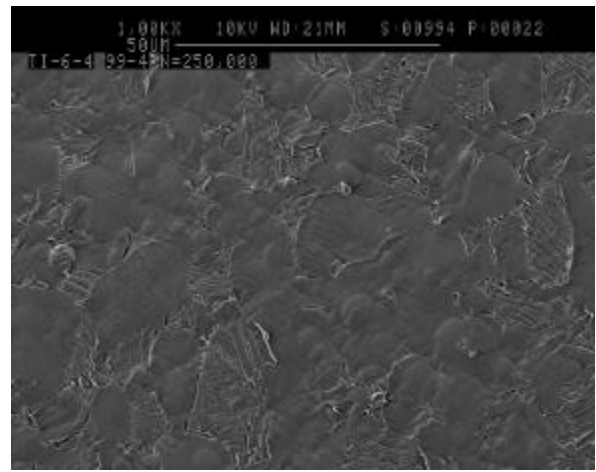


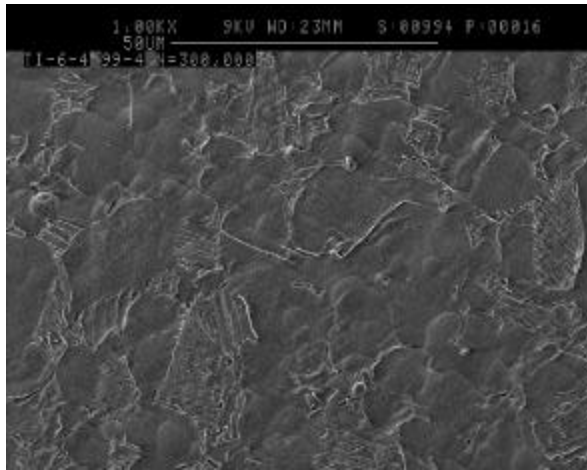
Figure 3D.6. High cycle fatigue lives of different lots of forged Ti-6Al-4V in room temperature air at $R = 0.1$ and 0.5 . Plot compares GECD data with those for uniaxially-loaded hourglass specimens from Allied Signal [3D.11].



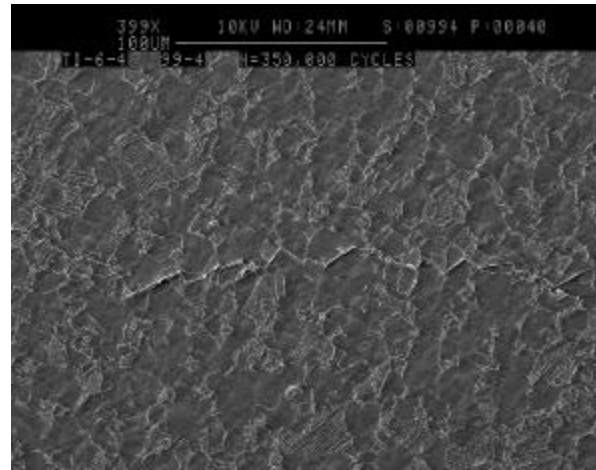
(a) $N/N_f = 0$



(b) $N/N_f = 0.65$

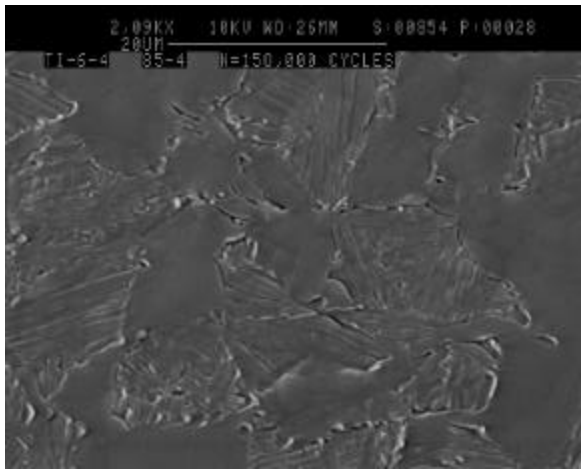


(c) $N/N_f = 0.78$

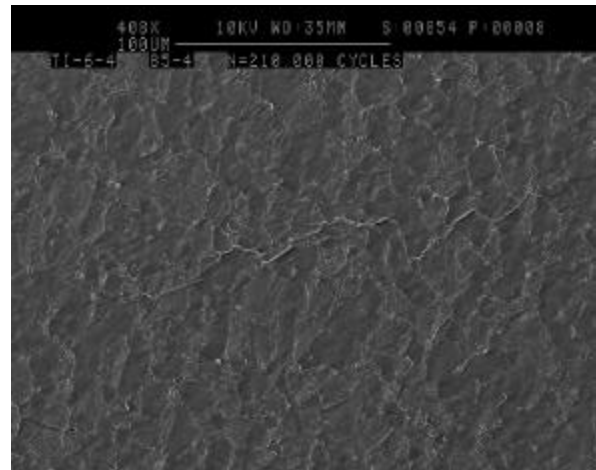


(d) $N/N_f = 0.91$

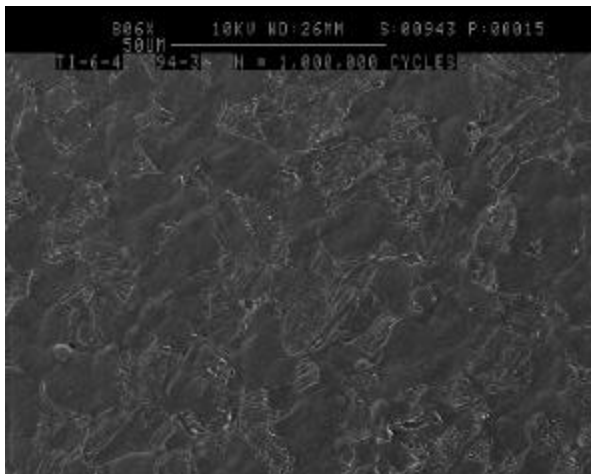
Figure 3D.7. Sequence of replica micrographs for HCF crack initiation and early growth observations in the Ti-6Al-4V forging. The crack is seen initiating by slip band formation in α_p between the replicas made at $N/N_f = 0.65$ and 0.78 . The long arrow in (a) indicates the longitudinal loading direction. Specimen 99-4.



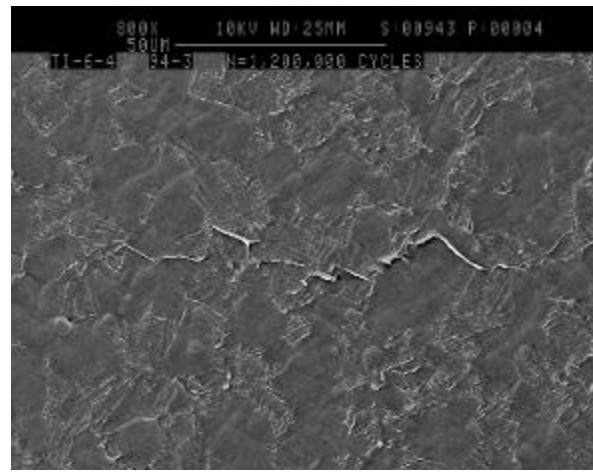
(a)



(b)



(c)



(d)

Figure 3D.8. Example of crack initiation at a) the interface between $a+b$ and a_p (Specimen 85-4) and b) within a $a+b$ lamellar grain (Specimen 94-3). Long arrows indicate longitudinal loading direction.

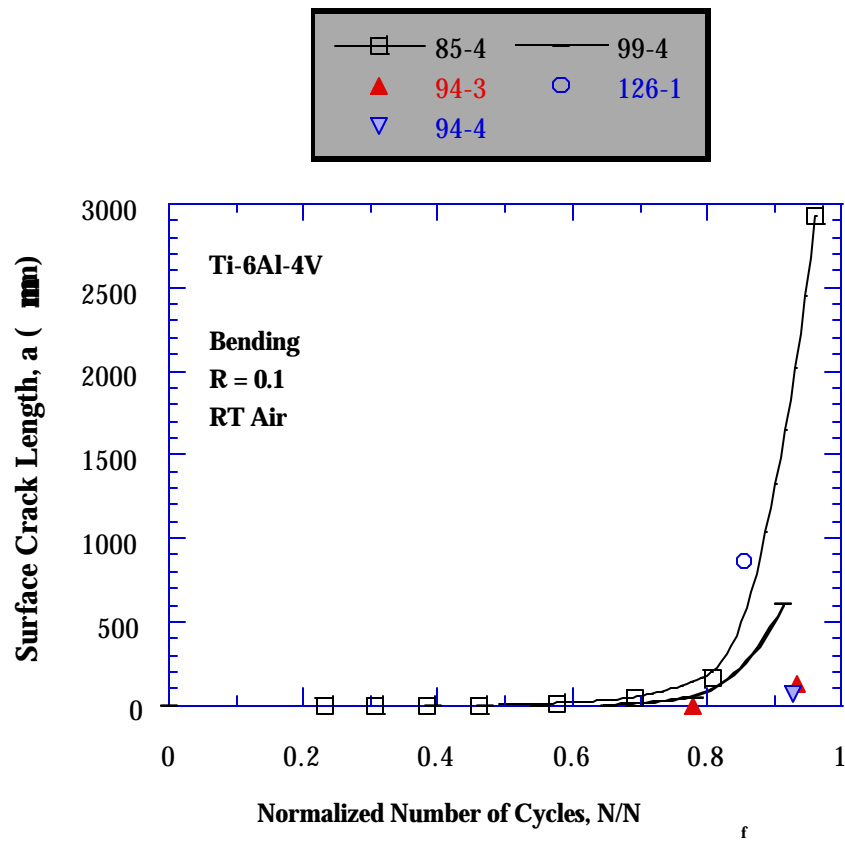


Figure 3D.9. Surface crack length, a , versus normalized number of fatigue cycles, N/N_f , for critical cracks in HCF of Ti-6Al-4V.

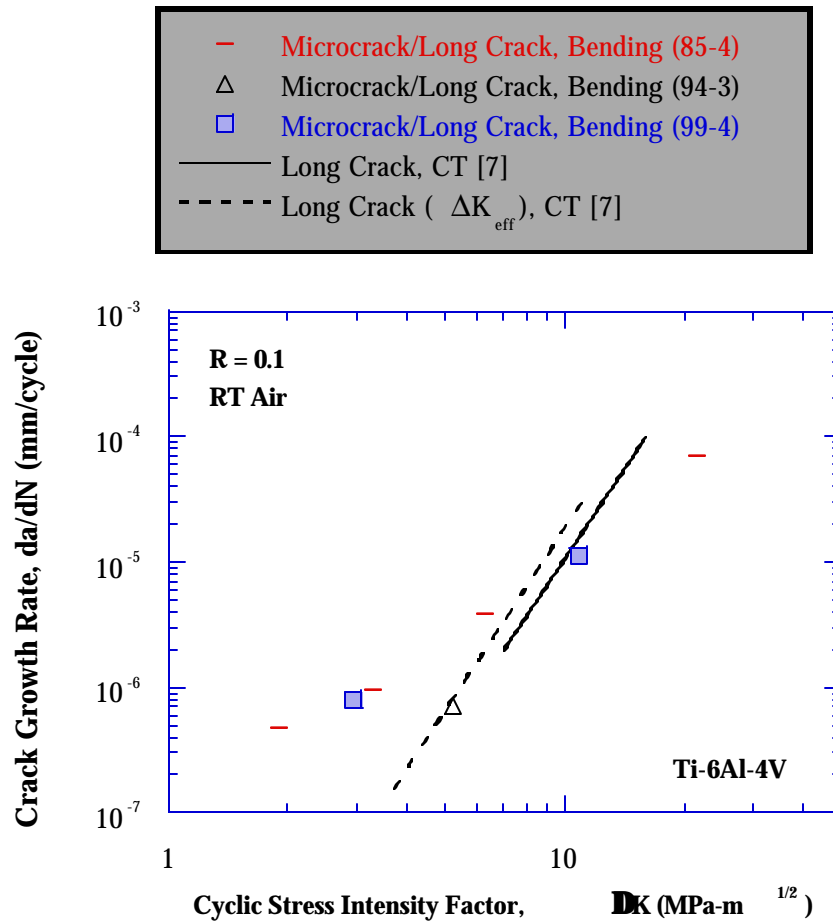
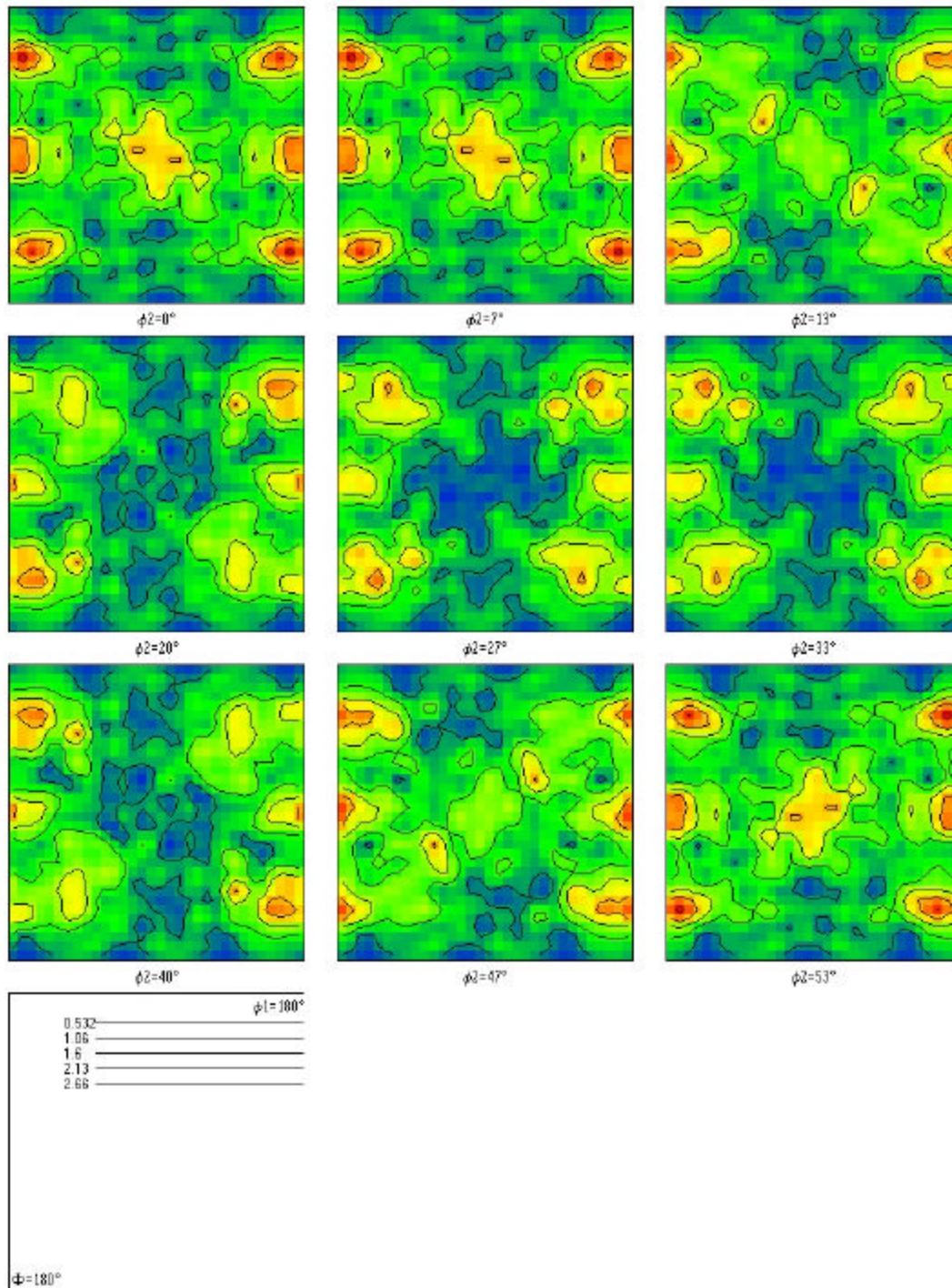
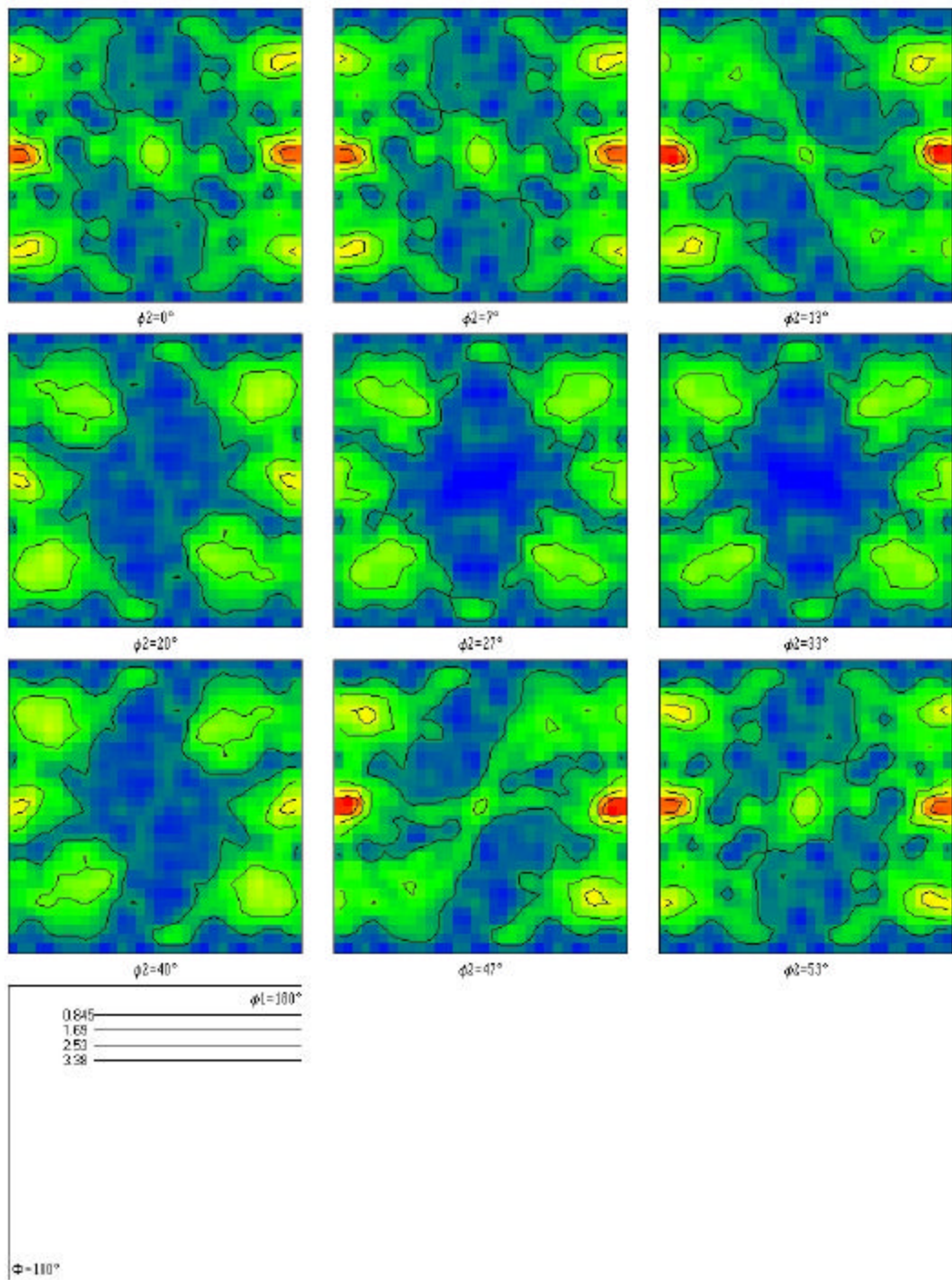


Figure 3D.10. Crack growth rate versus cyclic stress intensity factor plot for naturally initiated cracks in forged Ti-6Al-4V at $R = 0.1$. The crack growth rate results are compared with those of long cracks obtained from compact tension (CT) of the same Ti-6Al-4V material.



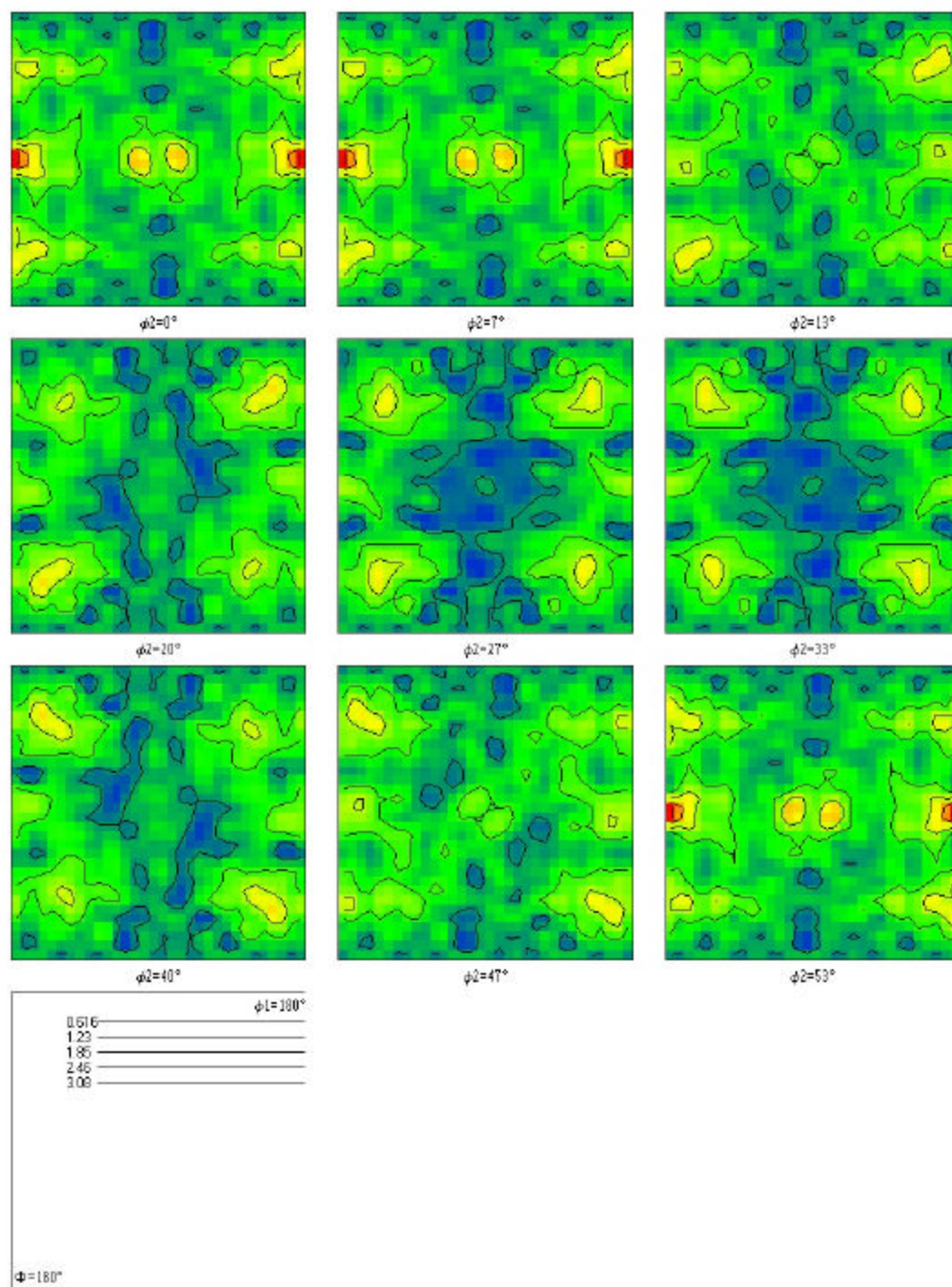
(a)

Figure 3D.11. Orientation distribution functions (ODF) obtained from EBSD analysis of the Ti-6Al-4V forging microstructure: a) Specimen 79-4, b) Specimen 85-2, c) Specimen 126-1, d) Specimen 126-2, and e) Specimen 126-3.



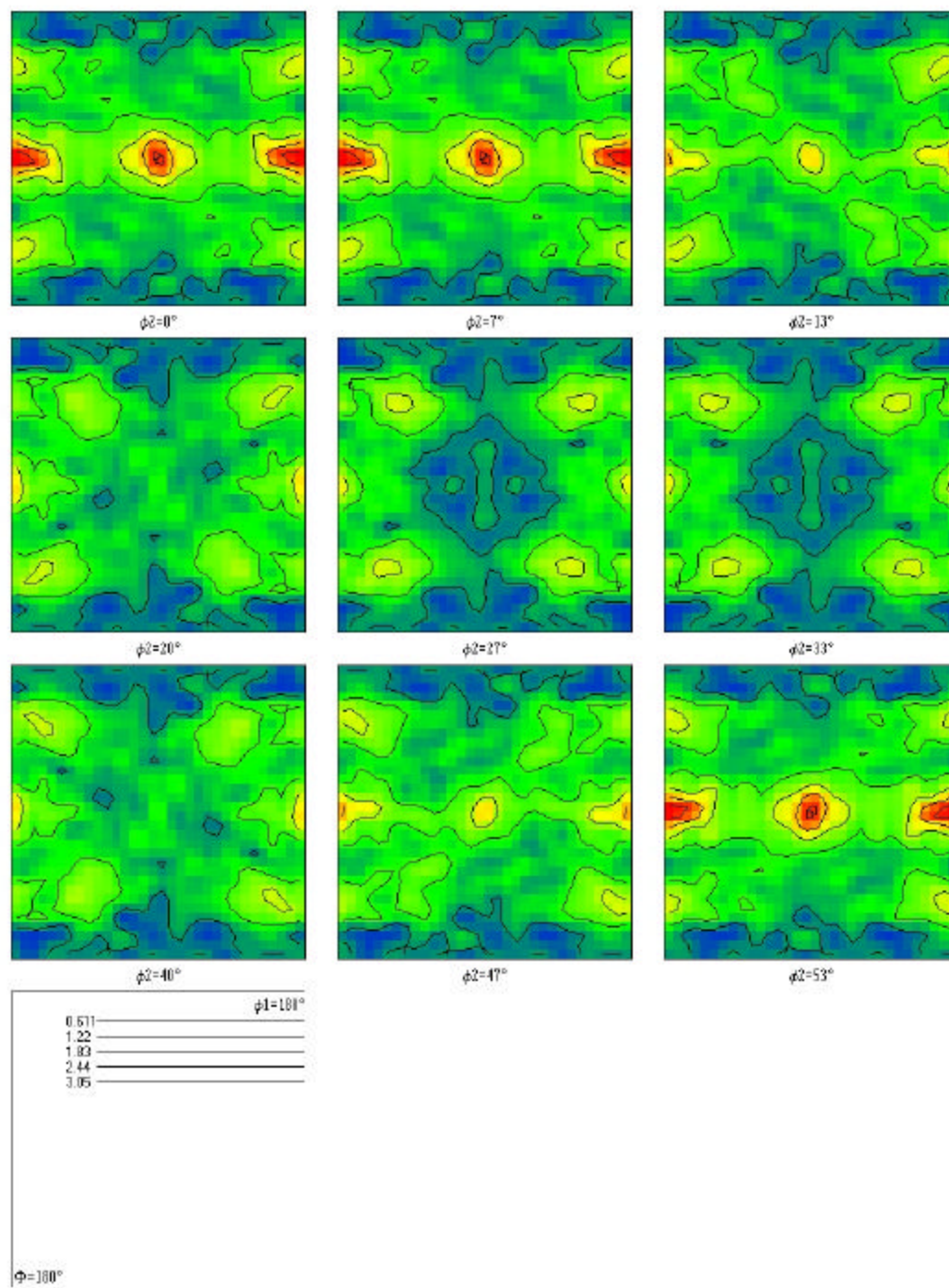
(b)

Figure 3D.11 (cont.)



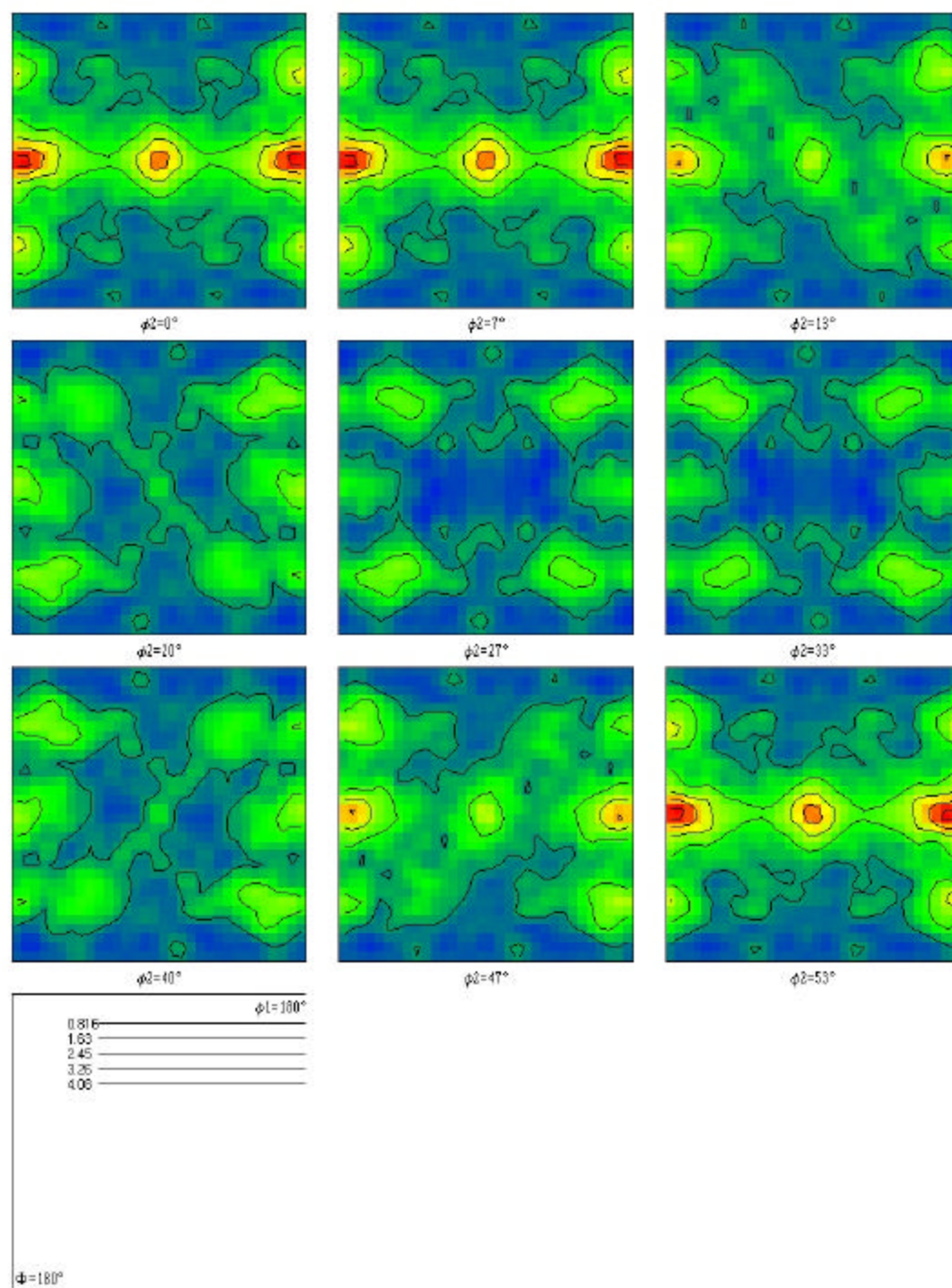
(c)

Figure 3D.11 (cont.)



(d)

Figure 3D.11 (cont.)



(e)

Figure 3D.11 (cont.)

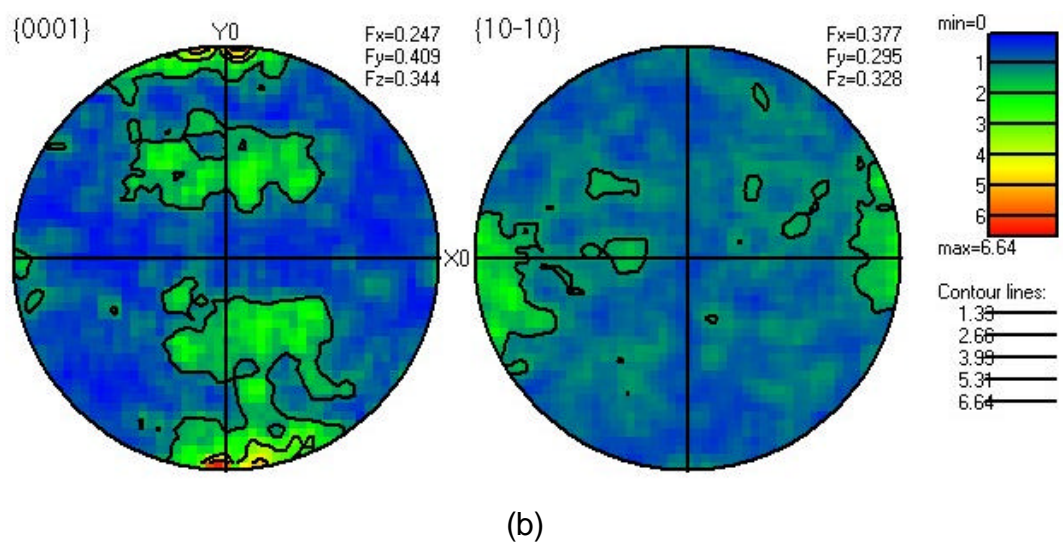
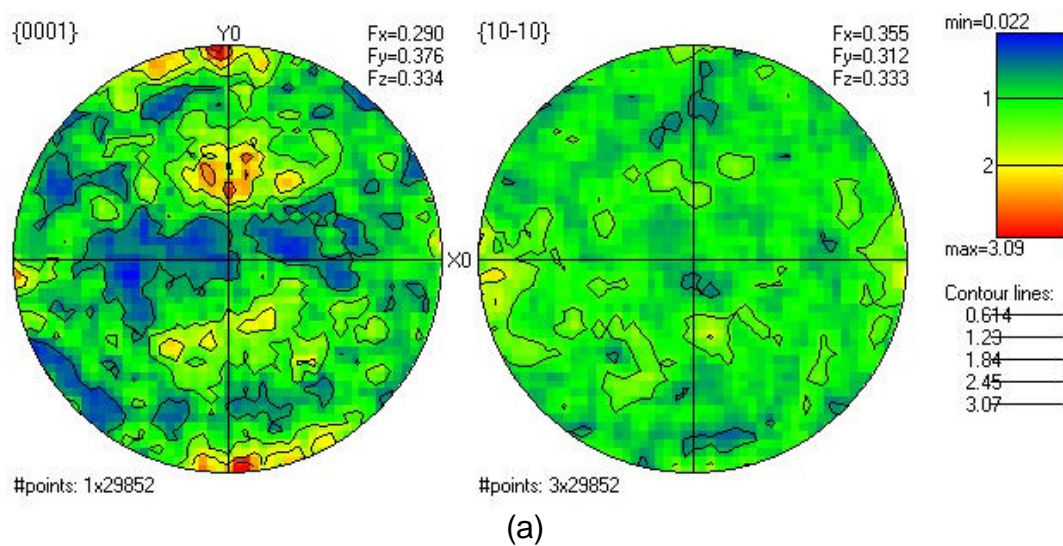
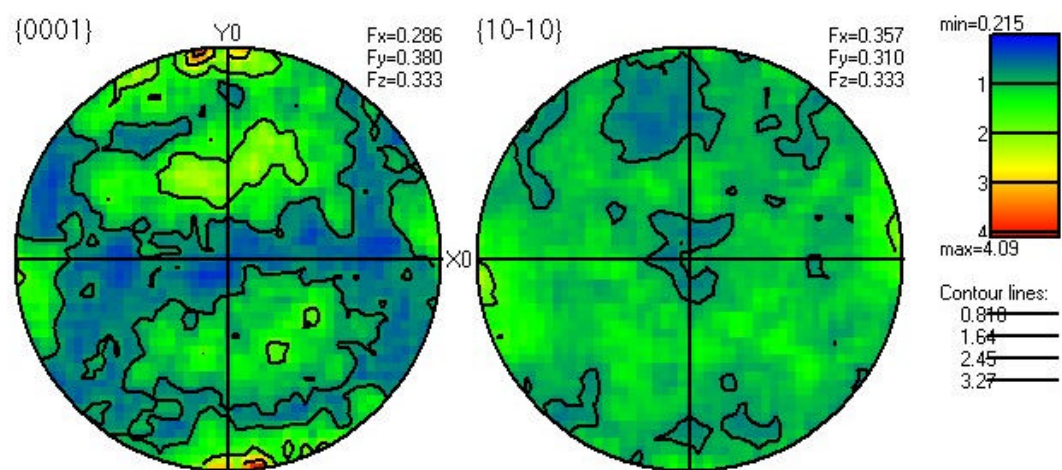
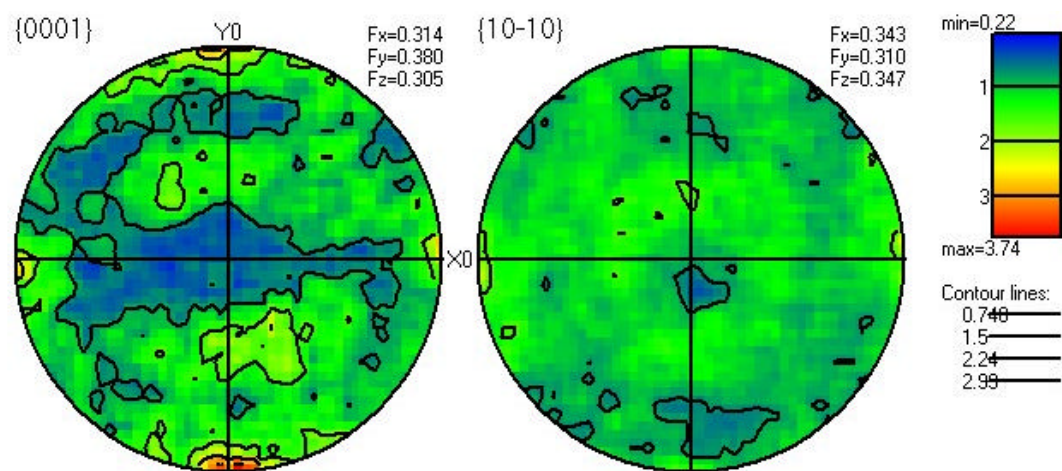


Figure 3D.12. Orientation images (OI) obtained from EBSD analysis of the Ti-6Al-4V alloy microstructure: a) Specimen 79-4, b) Specimen 85-2, c) Specimen 126-1, d) Specimen 126-2, and e) Specimen 126-3.



(c)



(d)

Figure 3D.12 (cont.)

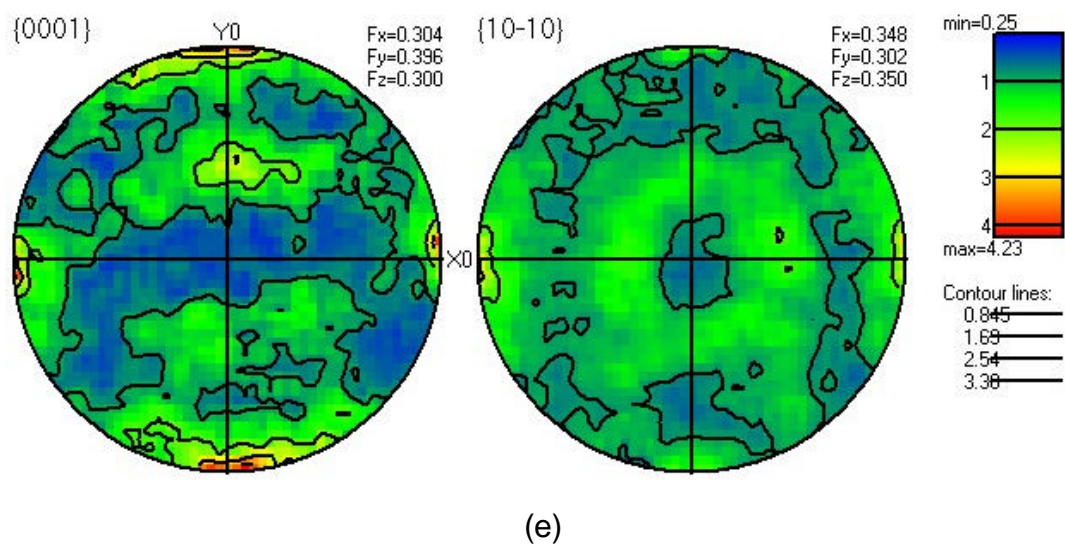


Figure 3D.12 (cont.)

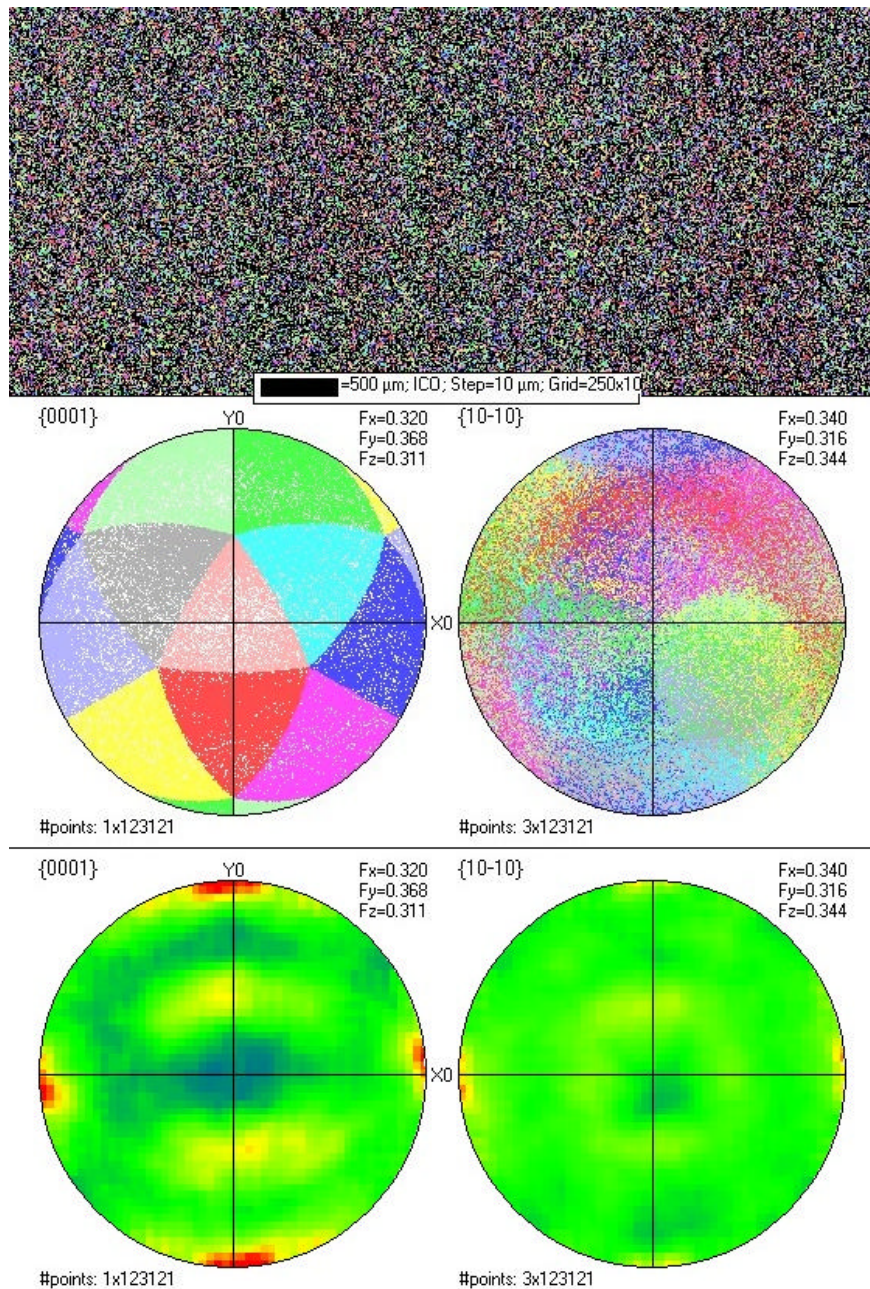


Figure 3D.13. Orientation images (OI) from Specimen 126-2 indicating no observable colony structure. In the OI shown, each colors represent specific clustering/range of $\{0001\}$ orientations. The $\{0001\}$ pole figure below the OI shows the mapping of color, or the icosahedral map.

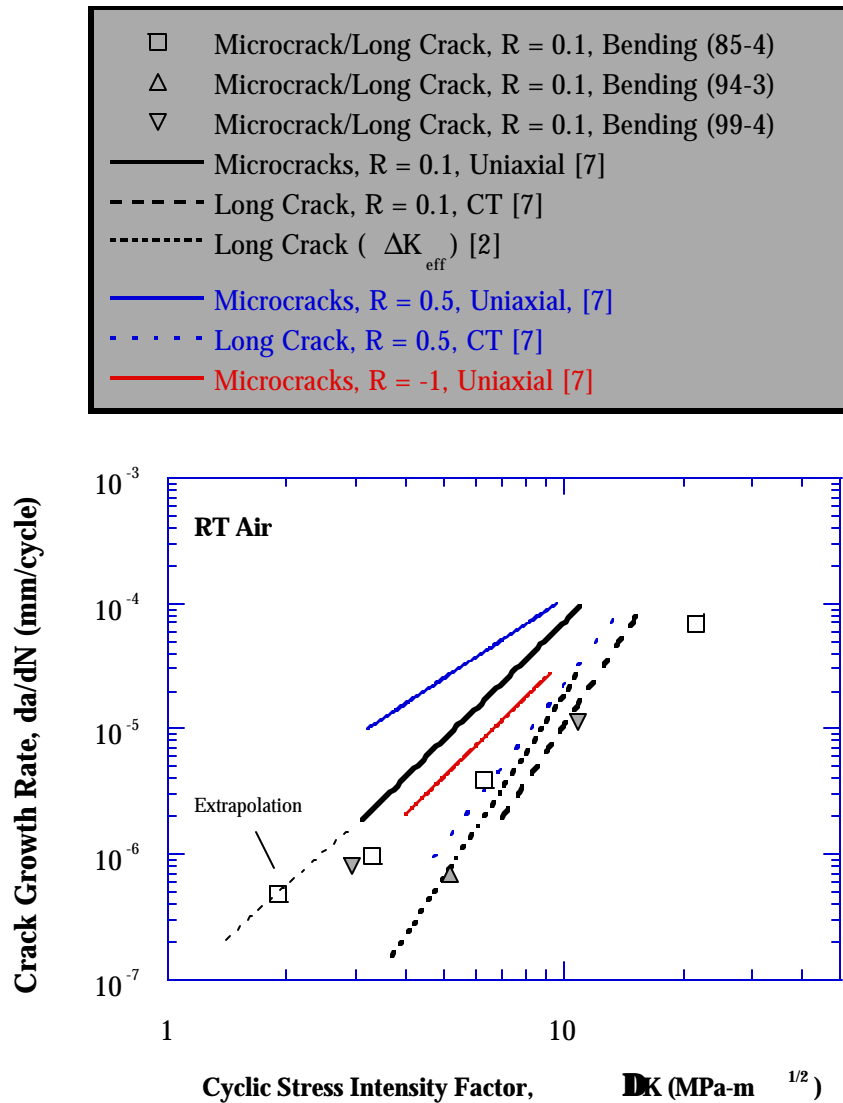


Figure 3D.14. Comparison of crack growth rates for cracks of different sizes in forged Ti-6Al-4V at different stress ratios. Data for microcracks and long cracks were obtained from the same Ti-6Al-4V material.

Table 3D.1
Chemistry of Teledyne Titanium Heat No. TE01

Element	Ti	Al	V	Fe	O	N
Top	bal.	6.27	4.19	0.20	0.18	0.012
Bottom	bal.	6.32	4.15	0.18	0.19	0.014
AMS4928	bal.	5.50-6.75	3.50-4.50	0.30 max	0.20 max	0.050 max

Table 3D.2
Solution Heat Treatment Distribution by Heat Treat Lot

Lot number	44	46	48	50
Forging #s	1-16, 18-57	58-109	110-165	166-200

Table 3D.3

Bending Fatigue Testing Results for Ti-6Al-4V in Room Temperature Air

Specimen	Frequency (Hz)	R Ratio	Life (Cycles)	Stress Range (MPa)	Stress Range (ksi)	Test Type
79-1	20	0.1	7,795,000	586	85	S/N
79-2	20	0.1	4,820,175	655	95	S/N
79-3	20	0.1	12106928+	662	96	S/N
79-4	25	0.1	1,384,536	793	115	S/N
85-2	20	0.1	77,000	758	110	S/N
85-3	20	0.1	95,000	717	104	S/N
85-4	20	0.1	260,050	676	98	Replica
94-3	20	0.1	1,283,646	614	89	Replica
94-4	20	0.1	863,034	614	89	Replica
99-4	20	0.1	383,012	648	94	Replica
126-1	20	0.1	116,743	614	89	EBSP
126-2	20	0.1	2,600,000+	531	77	EBSP
126-3	20	0.1	2,200,000+	579	84	EBSP
94-1	20	0.5	242,026	455	66	Replica
94-2	20	0.5	744,500	434	63	Replica

+ = Runout

Table 3D.4

The automated-EBSP scans made on mount 79020

Specimen	Condition	Xpoints	Ypoints	Xstep	Ystep	Objective
126-1	pre test	6	20000	500	0.5	Linescan
126-1	pre test	250	1000	10		Image
126-1	post test	45	2505	2		Image
126-1	post test	60	1670	3		Image
126-1	post test	3	20000	1250	0.5	Linescan
126-2		6	20000	500	0.5	Linescan
126-2		250	1000	10		Image
126-3		6	20000	500	0.5	Linescan
126-3		250	520	10		Image
79-4		3	20000	1250	0.5	Linescan
85-2		3	20000	1250	0.5	Linescan

Table 3D.5

Grain Size and Related Measurements Derived from EBSP Data

Name	HR	amis	%sg	all (mm)	max (mm)
1261_A	66.6	0.6	33.2	0.0059	0.0315
1261_E	64.3	0.7	39.5	0.0058	0.0330
1262_A	56.5	0.7	40.9	0.0058	0.0330
1263_A	67.0	0.7	36.5	0.0056	0.0345
85_2_A	54.5	0.7	41.8	0.0059	0.0390
79_4_A	49.8	0.6	40.5	0.0060	0.0340

HR = the percentage of locations from which indexable diffraction patterns were obtained

amis = the average intra-granular misorientation, which for some materials correlates with retained plastic strain

%sg = the percentage of grain segments exhibiting internal misorientation of at least 1 degree

all = the mean intercept length considering all boundary types having misorientation greater than 5 degrees

max = the maximum intercept length detected.

Table 3D.6

Colony size derived from EBSD data

Name	HR	amis	%sg	all (mm)	max (mm)
1261_a.rec	66.6	0.8	33.4	0.0075	0.0355
1261_E.rec	64.3	0.9	38.9	0.0077	0.0420
1262_A.rec	56.5	0.9	39.0	0.0075	0.0450
1263_A.rec	67.0	0.9	39.3	0.0074	0.0400
79_4_A.rec	49.8	0.8	40.0	0.0077	0.0580
85_2_A.rec	54.5	0.8	39.5	0.0077	0.0395

Table 3D.7

Paris Exponent for Crack Growth Rate Data of Ti-6Al-4V

Type of Crack	Stress Ratio, R	Test Type	Paris Exponent, m	Reference
Microcrack/Long Crack	0.1	Bending	2.1	This Study
Microcrack/Long Crack	0.1	Bending	2.0	This Study
Microcracks	0.1	Uniaxial	3.1	7
Long Crack	0.1	CT	4.7	7
Long Crack	0.1	CT	4.8	2
Microcracks	0.5	Uniaxial	2.1	7
Long Crack	0.5	CT	4.2	7
Microcracks	-1	Uniaxial	3.1	7

Appendix 3E

CYCLIC STRESS STRAIN BEHAVIOR

**Robert E. deLaneuville
Jerry W. Sheldon**



Pratt & Whitney

**Submitted
28 September 1999**

CYCLIC STRESS STRAIN RESULTS

Cyclic stress strain is a basic material property. Testing provides several valuable pieces of information: LCF nucleation life under predominantly strain-controlled conditions; determination of cyclic hardening or softening behavior; an understanding of whether the material is best modeled by a Neuber or Glinka hysteresis behavior; and, a model for assessing notch plasticity and yielding.

Testing was governed by ASTM E606 Standard Practice for Strain-Controlled Fatigue Testing and performed on closed-loop servo-hydraulic test machines at 20 CPM, 80°F and lab air at stress ratios of -1, 0.1, 0.5 and 0.8. Samples were prepared according to the processing specifications agreed upon for all nucleation specimens with the addition of a small population of samples peened to an intensity of 7A. A summary of test conditions and results is shown in Tables 3E.1 and 3E.2.

Using the mid life maximum and minimum values of stress and strain, a plot as shown in Figure 3E.1 can be created. The points representing the cycle peaks form a single curve described as the cyclic stress strain curve. Though the data is fit with a Ramburg-Osgood formulation, it may be thought of as close to elastic-perfectly plastic. Comparing the cyclic to monotonic results confirms that this material cyclically softens (Figure 3E.2). By looking at the high stress first cycle information from Table 3E.1 and 3E.2, the mid life stress is lower than the initial stress. Figure 3E.3 shows the total strain range versus life and reveals a significant sensitivity to fully reversed loading. Figure 3E.4 compares samples at $R = 0.1$ and -1.0 peened and unpeened with peened samples yielding longer life as expected.

Table 3E.1

Summary of the unpeened cyclic stress-strained results at strain ratios ranging from -1.0 up to 0.8. The mid life stress peaks are used to form a cyclic stress strain curve which is then compared to monotonic results. Comparing initial to mid life stress peaks indicates cyclic softening. This is confirmed by a comparison of monotonic to cyclic results.

AMS 4928 Cyclic Stress-Strain Testing of Smooth Cyl. Specimens

FML 100695, Freq. 20 cpm, Kt = 1.0, 80F

S/N	Re	Target	1st Cycle							Half Life							Cycle	N _f	Remarks
		D _e (%)	D _e (%)	D ₀ (%)	s _{max} (ksi)	s _{min} (ksi)	D _s (ksi)	s _{mean} (ksi)	E (msi)	D _e (%)	D ₀ (%)	s _{max} (ksi)	s _{min} (ksi)	D _s (ksi)	s _{mean} (ksi)	E (msi)			
10-7	-1	0.60	0.61	0.003	49.2	-52.1	101.3	-1.4	16.7	0.62	0.003	49.0	-53.0	102.1	-2.0	16.7	90,000	200,660	DNF
10-5	-1	0.80	0.79	0.004	68.6	-65.6	134.2	1.5	17.0	0.80	0.001	65.2	-70.4	135.6	-2.6	17.0	60,000	127,426	DNF
10-9	-1	0.90	0.91	0.003	76.5	-76.8	153.2	-0.1	17.0	0.91	0.003	79.2	-75.4	154.6	1.9	17.1	20,000	48,537	
34-1	-1	1.00	1.00	0.004	82.4	-84.3	166.7	-1.0	16.8	1.00	0.001	85.1	-84.9	170.0	0.1	16.7	10,000	20,199	
34-2	-1	1.20	1.20	0.069	99.9	-105.0	204.8	-2.6	18.7	1.20	0.002	101.5	-103.5	205.0	-1.0	17.1	4,000	9,700	
34-3	-1	1.30	1.30	0.003	109.3	-111.7	221.0	-1.2	17.1	1.29	0.012	105.7	-111.6	217.4	-2.9	17.0	3,000	6,737	
10-12	-1	1.40	1.38	0.036	113.8	-119.0	232.8	-2.6	17.4	1.39	0.074	112.3	-112.5	224.8	-0.1	17.1	2,540	5,319	
10-10	0.1	0.40	0.40	0.002	76.9	8.8	68.1	42.9	17.0	0.41	0.002	77.7	9.1	68.7	43.4	16.9	60,000	116,589	DNF
10-15	0.1	0.50	0.49	0.000	95.8	11.5	84.3	53.7	17.1	0.49	0.001	93.2	9.1	84.2	51.1	17.1	70,000	137,840	DNF
34-9	0.1	0.60	0.59	0.064	113.7	12.6	101.1	63.1	19.1	0.60	0.065	112.2	8.8	103.4	60.5	19.2	10,000	38,841	
34-8	0.1	0.80	0.79	0.057	137.2	6.2	131.0	71.7	18.4	0.81	0.112	114.7	-20.3	135.1	47.2	19.3	8,000	16,046	
34-7	0.1	1.00	0.99	0.020	127.5	-35.4	163.0	46.0	16.8	0.99	0.020	112.3	-50.7	163.1	30.8	16.7	5,000	9,290	
10-6	0.1	1.20	1.18	0.151	124.9	-63.2	188.2	30.8	18.2	1.17	0.125	113.5	-73.6	187.1	20.0	17.9	2,620	9,338	
10-11	0.1	1.20	1.19	0.076	140.0	-44.6	184.5	47.7	16.6	1.18	0.075	120.8	-62.2	183.0	29.3	16.6	576	9,250	
10-8	0.1	1.30	1.24	0.066	133.7	-61.6	195.3	36.1	16.6	1.25	0.085	111.7	-80.3	192.0	15.7	16.5	3,000	5,805	
10-13	0.1	1.40	1.27	0.149	131.7	-77.8	209.5	26.9	17.7	1.38	0.150	120.4	-93.6	214.1	13.4	17.4	3,000	5,210	
34-5	0.5	0.33	0.33	0.000	114.4	60.2	54.2	87.3	16.7	0.33	0.000	114.0	59.0	55.1	86.5	16.7	100,000	201,762	DNF
34-6	0.5	0.60	0.61	0.015	126.4	29.3	97.1	77.9	16.4	0.61	0.066	116.1	18.6	97.4	67.3	18.0	10,000	34,064	
10-25	0.5	0.60	0.60	0.000	135.8	32.5	103.3	84.2	16.9	0.61	0.002	115.4	16.3	99.1	65.9	16.3	25,880	50,265	
10-14	0.5	0.80	0.77	0.018	134.7	10.3	124.4	72.5	16.6	0.78	0.052	116.2	-6.2	122.4	55.0	16.9	4,317	23,045	
10-24	0.5	0.80	0.80	0.000	138.2	0.0	138.2	69.1	17.0	0.80	0.002	113.8	-16.3	130.1	48.8	16.3	5,100	26,336	
10-19	0.5	1.00	1.00	0.041	140.1	-25.9	166.0	57.1	17.3	1.00	0.050	113.4	-45.3	158.7	34.1	16.7	8,275	13,790	
10-17	0.5	1.40	1.40	0.149	139.0	-72.4	211.4	33.3	16.9	1.41	0.193	114.6	-83.7	198.3	15.5	16.3	2,800	4,802	
10-20	0.8	0.40	0.37	0.000	137.9	73.8	64.1	105.9	17.3	0.40	0.004	117.6	52.7	64.9	85.2	16.4	111,946	111,953	DNF
10-23	0.8	0.60	0.59	0.026	139.0	43.1	95.9	91.1	17.0	0.60	0.000	121.1	25.2	95.9	73.2	15.9	25,150	44,772	
10-22	0.8	0.80	0.74	0.018	140.9	20.4	120.5	80.7	16.7	0.80	0.002	118.9	-2.4	121.3	58.3	15.2	14,450	23,382	
10-21	0.8	1.00	1.00	0.103	141.8	-9.8	151.6	66.0	16.9	1.00	0.044	116.5	-26.9	143.4	44.8	15.0	7,808	13,730	

Table 3E.2

Summary of the peened cyclic stress-strained results at strain ratios of -1.0 and 0.1. The mid life stress peaks are used to form a cyclic stress strain curve which is then compared to monotonic results. Comparing mid life stress peaks with those from the unpeened results indicates no difference. Peening did extend nucleation life.

AMS 4928 Cyclic Stress-Strain Testing of Peened Smooth Cyl. Specimens

FML 100695, Freq. 20 cpm, Kt = 1.0, 80F

		Target	1st Cycle								Half Life								
S/N	Re	D _e (%)	D _e (%)	D _e (%)	s _{max} (ksi)	s _{min} (ksi)	D _s (ksi)	s _{mean} (ksi)	E (msi)	D _e (%)	D _e (%)	s _{max} (ksi)	s _{min} (ksi)	D _s (ksi)	s _{mean} (ksi)	E (msi)	Cycle	N _f	Remarks
111-1	-1	1.20	1.20	0.012	99.4	-102.6	202.0	-1.6	17.0	1.20	0.007	101.0	-99.4	200.4	0.8	16.8	110,245	110,249	D N F
10-1	-1	1.30	1.30	0.007	111.2	-104.7	215.9	3.3	16.7	1.30	0.078	103.9	-101.4	205.3	1.3	16.8	29,360	47,273	
56-1	-1	1.40	1.40	0.009	119.3	-118.5	237.8	0.4	17.1	1.40	0.142	106.3	-106.3	212.6	0.0	16.9	15,100	23,542	
111-2	-1	1.60	1.60	0.030	129.0	-136.3	265.3	-3.7	16.9	1.60	0.289	111.2	-110.3	221.5	0.5	16.9	4,100	10,244	
10-4	0.1	0.80	0.80	0.000	132.2	-2.4	134.6	64.9	16.7	0.81	0.004	106.9	-26.9	133.8	40.0	16.6	117,050	117,099	D N F
131-1	0.1	1.10	1.10	0.024	141.5	-53.2	194.7	44.2	18.1	1.10	0.049	118.6	-65.4	184.0	26.6	17.5	13,426	21,415	
10-3	0.1	1.20	1.20	0.048	137.4	-58.5	195.9	39.5	17.0	1.20	0.058	113.0	-78.9	191.9	17.1	16.8	6,300	21,119	
10-2	0.1	1.40	1.40	0.121	135.7	-76.6	212.3	29.6	16.6	1.40	0.171	111.8	-88.6	200.4	11.6	16.3	4,000	7,450	

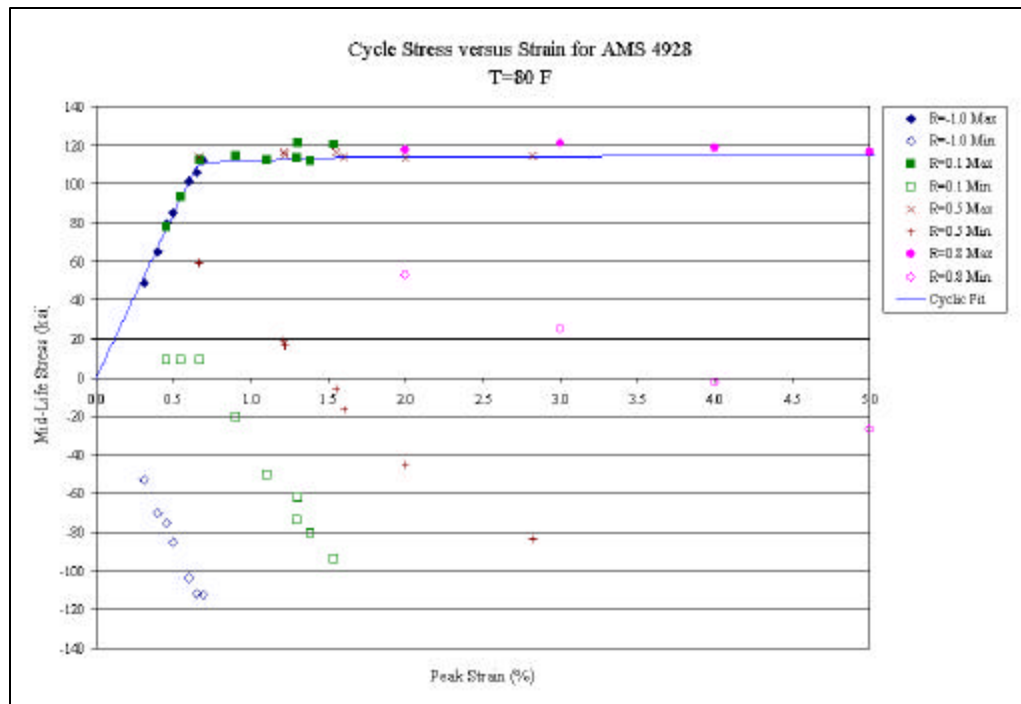


Figure 3E.1. Mid life cyclic stress strain LCF results at varying strain ratios plotted with the cyclic stress strain curve. The maximum values from multiple strain ratios form a curve fit using the popular Ramburg-Osgood formulation.

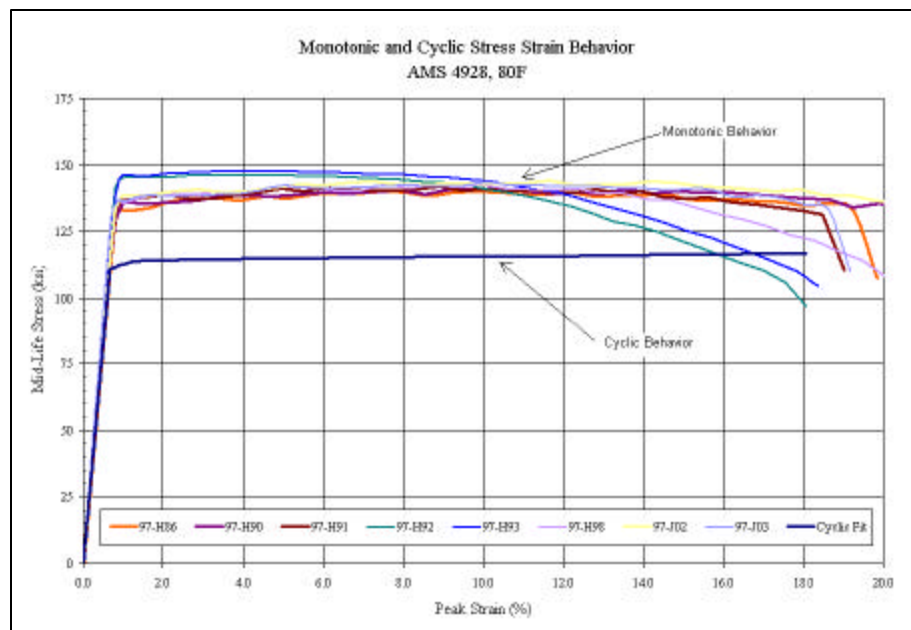


Figure 3E.2. Cyclic versus monotonic stress results indicates cyclic softening. Samples 97-H92 and 97-H93 were run significantly faster (0.0655 in/sec.) than the remaining population (0.00004, 0.00007, 0.00066 in/sec) of tensile tests.

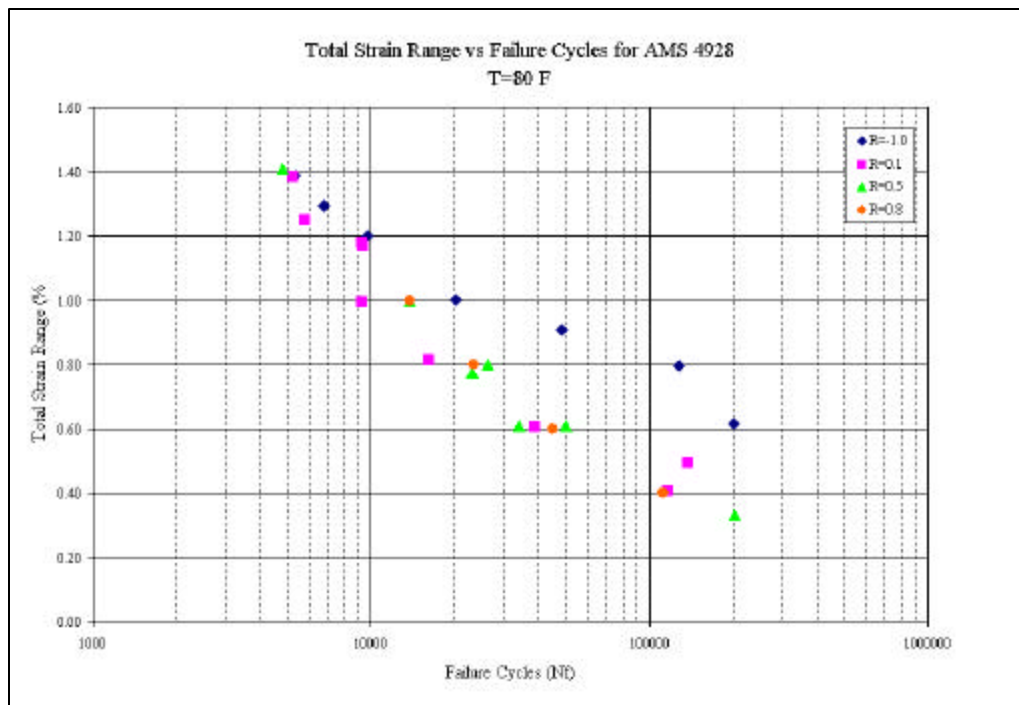


Figure 3E.3. A plot of total strain range versus life indicates the $R = -1.0$ condition is significantly different from the remaining stress ratios (0.1, 0.5, 0.8).

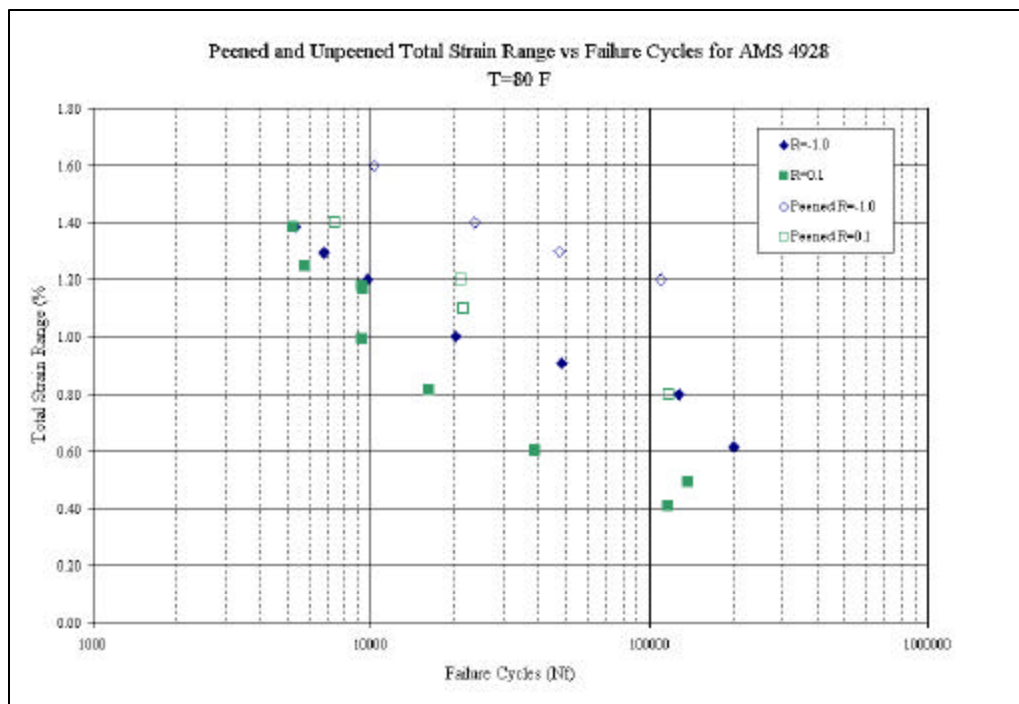


Figure 3E.4. A plot of total strain range versus life for peened and unpeened specimens at 0.1 and -1.0 demonstrates a significant benefit from peening.

Appendix 3F

EFFECT OF SPECIMEN GEOMETRY AND FREQUENCY ON HCF SMOOTH SPECIMEN BEHAVIOR

Richard Bellows

Honeywell

Honeywell

**Submitted
17 September 1999**

SPECIMEN GEOMETRY AND FREQUENCY EFFECTS

Specimen Geometry Effects

Round-robin testing was conducted at a stress ratio of 0.1 and a frequency of 60 Hz to evaluate gage geometry effects. Three different smooth bar specimens were used:

- an hourglass specimen with a nominal gage diameter of 0.165-inch and a gage radius of 1.0-inch (tested by P&W)
- a uniform gage specimen with a nominal gage diameter of 0.200-inch and a gage length of 0.75-inch. (tested by ASE, now Honeywell)
- a uniform gage specimen with a nominal gage diameter of 0.160-inch and a gage length of 0.32-inch, and (tested by GEAE)

All three specimens were tested at the 0.1 stress range, and the results were compared. The 0.200-inch gage diameter was used to evaluate the conventional versus step test results at all four stress ratios.

The results of the tests, including run-outs (suspensions), are shown in Figure 3F.1. Included with these results are curves that were determined using the Maximum Likelihood Results method. To estimate endurance limits, a censored regression analysis was used to represent the fatigue data using an equation of the form

$$\sigma_R = b (\text{Log } (N_f) - a)^{-1} \quad (3F.1)$$

where σ_R is the stress range, N_f is the cycles to failure, and a and b are parameters. Run-outs – tests that did not fail after 10^7 cycles – were used in a censored regression analysis that chose parameter values to maximize the likelihood that the experiment would have turned out the way it actually did. By using the maximum likelihood parameter method, the run-out data could be included in the determination of the endurance limit. When all tests fail (i.e., there are no run-outs), then the maximum likelihood parameter method and the ordinary least-squares method produce the same endurance limit.

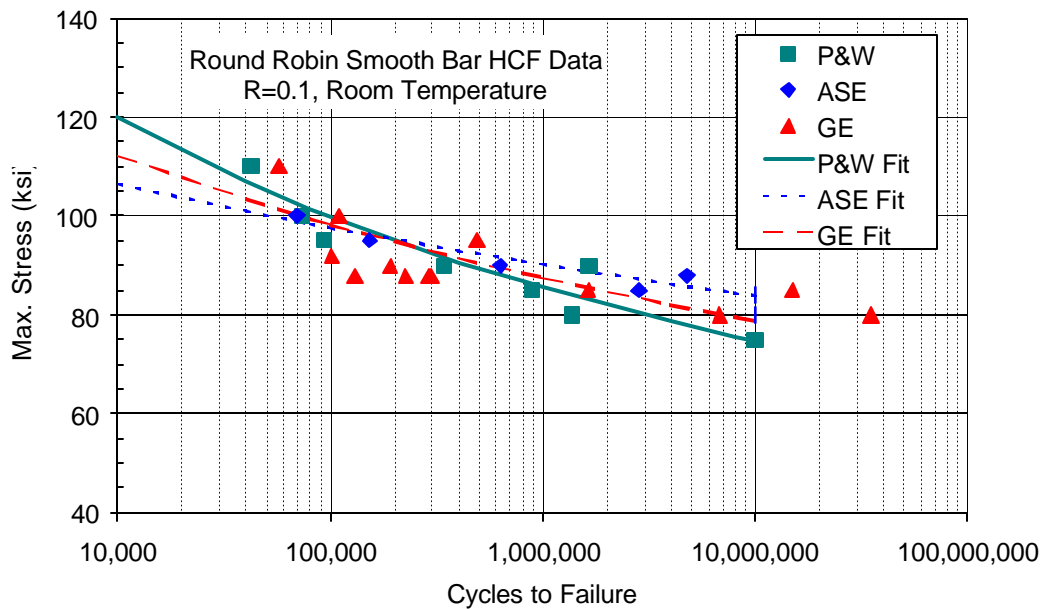


Figure 3F.1. Smooth bar fatigue data from the round-robin testing showing Maximum Likelihood Result curves.

The data was also compared without the run-out data using regression analysis. Figure 3F.2 shows only the specimens that failed and the power law curve regression curves.

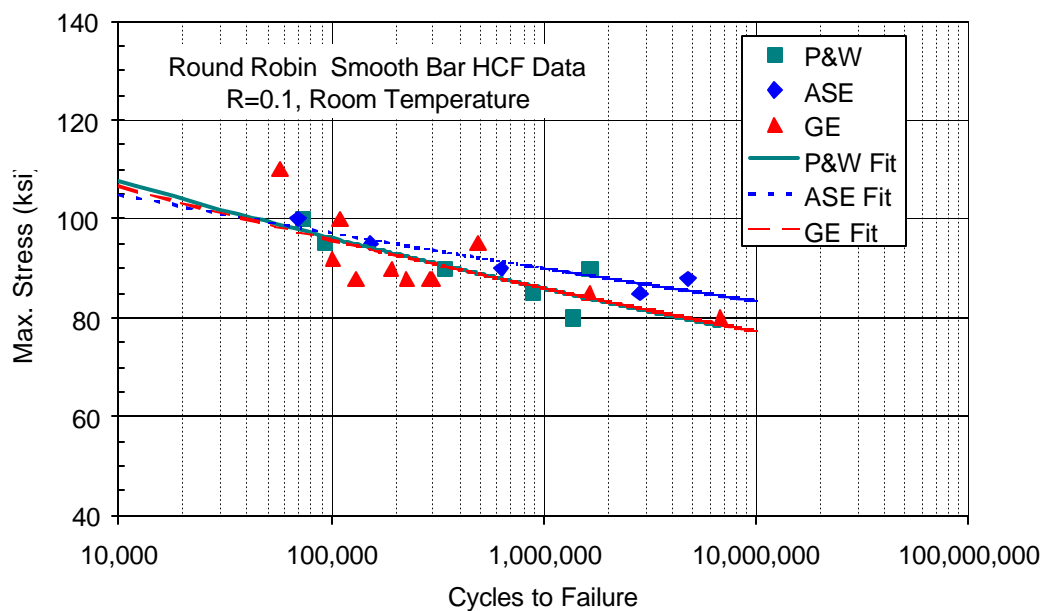


Figure 3F.2. Same data as Figure 3F.1 except the run-outs have been removed and the data are represented by regression analysis power curves.

Because different team members were responsible for testing the different specimen geometries, it is difficult to draw conclusions from the data. However, the effect of specimen geometry appears to be minimal, perhaps as a result of the homogeneity of the material. Additional testing and analysis would be required to statistically validate this position.

Frequency Effects

Smooth bars were also tested to determine the effect of frequency on total life. Frequencies of 60, 200 and 1000 Hz were evaluated at different stress ratios. The same geometry specimens that were used by different team members in the round-robin specimen testing were also used in this effort.

The comparison of 60, 200, and 1000 Hz data at the $R = -1$ condition is shown in Figure 3F.3. The comparison of 60 and 1000 Hz data at the $R = 0.1$ condition is shown in Figure 3F.4. The comparison of 60 and 200 Hz data is shown in Figure 3F.5 for the $R = 0.8$ condition.

Based on the available data, the effect of frequency on the HCF behavior appears to be minimal. The observed scatter at the 0.1 stress ratio should be further investigated to determine if test methods are responsible.

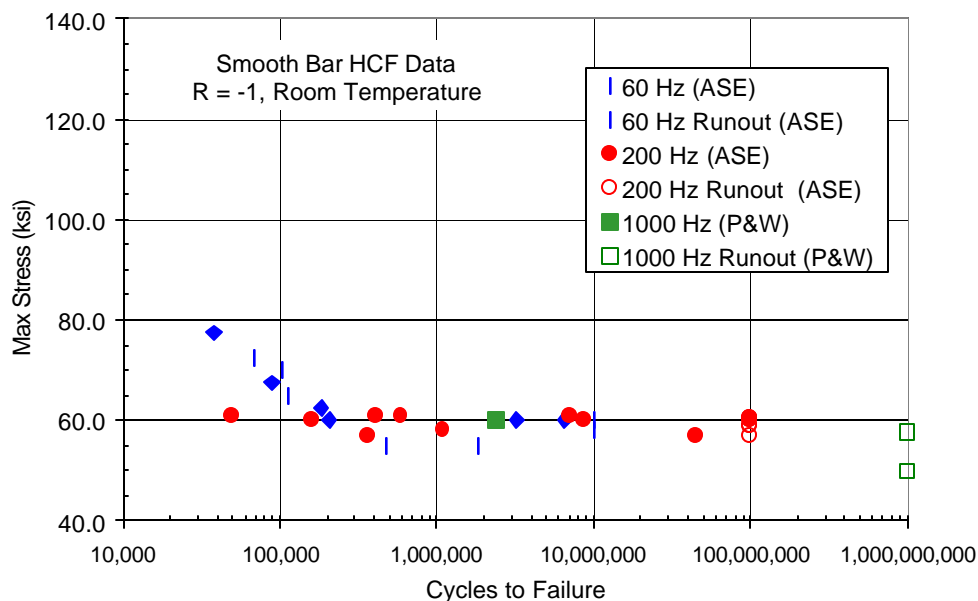


Figure 3F.3 Comparison of $R = -1$ data at three frequencies.

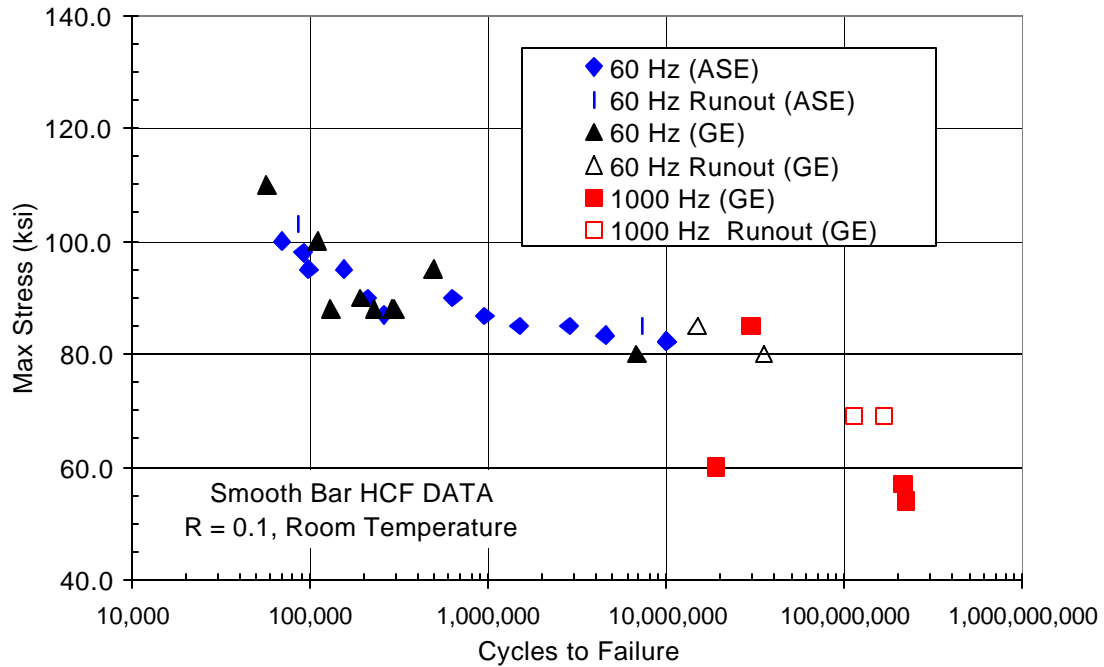


Figure 3F.4 Comparison of R = 0.1 data at two frequencies.

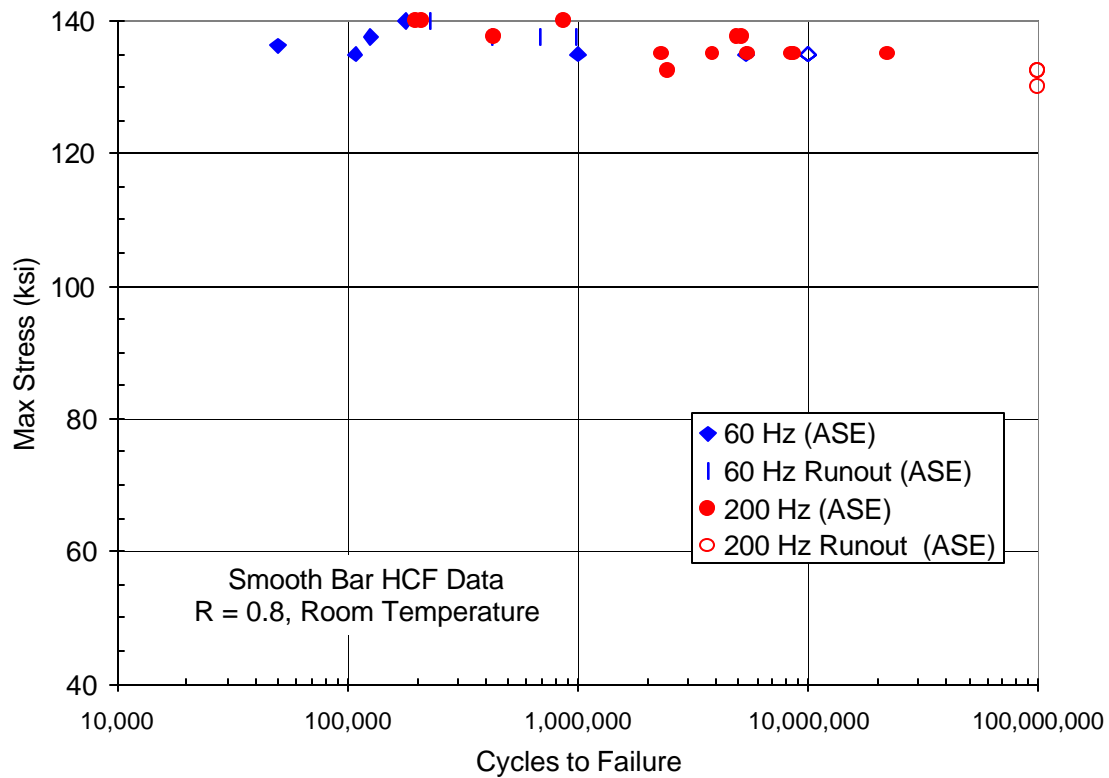


Figure 3F.5 Comparison of R = 0.8 data at two frequencies.

APPENDIX 3G

EFFECT OF SURFACE CONDITIONS ON UNDAMAGED MATERIAL HCF BEHAVIOR

Richard Bellows

Honeywell

Honeywell

**Submitted
17 September 1999**

SUMMARY

This appendix documents Surface Effects study performed under the Air Force *Improved High Cycle (HCF) Life Prediction Program*, USAF Contract #F33615-96-C-5269. As part of this effort, specimens with different surface conditions were tested under load-controlled high cycle fatigue conditions to determine the effect of surface condition on HCF endurance limit. This document contains information about the test method, test results, fracture surface and microstructural deformation.

INTRODUCTION

The goal of the current Air Force HCF materials damage tolerance program is to improve the HCF life prediction capabilities for titanium alloy components in gas turbine engines. While many HCF failures often occur simultaneously with or subsequent to other types of damage modes the influence of machining and processing on the baseline behavior of components can be an important aspect of fatigue behavior.

In order to assess the influence of surface conditions on the ensuing HCF behavior of Ti-6Al-4V components, a study was undertaken as part of the Air Force HCF program. In the study, four different surface conditions were selected for comparison to the program baseline condition. The four conditions selected were representative of either some HCF specimen surfaces or actual components. The baseline condition for the program was used to minimize the effect of surface conditions.

MATERIAL AND EXPERIMENTAL DETAILS

The material used in this study was forged into simulated fan blade forgings, approximately 16 inch x 6 inch x 0.8 inch. Ti-6Al-4V, per AMS 4928, was used as the forging stock, which was preheated to 1720°F prior to forging. Forgings were solution treated at 1710°F, fan cooled and the vacuum annealed at 1300°F for 2 hours. The microstructure of the forgings were approximately 60% primary alpha with the remainder lamellar transformed beta (see Figure 3G.1). The yield strength and tensile strength of specimens excised from the forgings in the longitudinal direction were 134.9 ksi and 141.8 ksi respectively.

Fatigue specimen blanks were excised from forgings in the longitudinal direction (with their axis parallel to the longest direction in the forging). A uniform gage specimen with a nominal gage diameter of 0.200 and a gage length of 0.75 was used for testing.

Descriptions of the baseline condition and the four surface-effect conditions are shown in Table 3G.1. Stress-relief anneal was performed at 1300F for one hour in vacuum at some point in the specimen manufacturing process to ensure a consistent metallurgical state; some specimens were stress relief annealed after machining and other specimen before machining as indicated in Table 3G.1.

Table 3G.1
The Specimen Group Descriptions

GROUP	DESCRIPTION	CODE
Baseline	Low Stress Grind + Stress Relief Anneal + Chem-mill	Baseline
I	Stress Relief Anneal + Low Stress Grind + Longitudinal Polish	SRA+LSG+LP
II	Stress Relief Anneal + Single Point Turn	SRA+SPT
III	Stress Relief Anneal + Low Stress Grind	SRA+GRD
IV	Baseline Condition + Shot Peen (A7 intensity)	BL+SP

The baseline specimens were stress-relief annealed after low stress grinding and longitudinal polishing to eliminate any residual stresses from machining and then chem-milled to remove 0.001 inch from the specimen surface in the gage section to eliminate machining marks and contamination from stress relief. Group I specimens were stress-relief annealed and then low stress ground (similar to Group III specimens) and longitudinally polished with a final polishing paper of approximately 600 grit to represent a common fatigue specimen condition. Group II specimens were stress relief annealed and then single point turned at a work speed of 50 SFPM using a carbide coated insert with a depth-of-cut of 0.010 per surface and a feed rate of 0.0035 IPR. Group III specimens were stress-relief annealed and then ground at 8-26 SFPM, with coolant, and a depth-of-cut of 0.001in/pass followed by 0.0004 inch/pass for the last 0.001 inch of material. Group IV specimens were baseline specimens that were shot peened per AMS 2432 (Computer Controlled) to an intensity of 7A +/- 1A using ASR110 cast steel shot per AMS 2431 with 100% coverage.

Prior to testing, surface roughness measurements were made on one specimen from each group with a Giddings and Lewis surface profile measurement system, capable of provide surface finish and geometry measurements accurate to 0.000005 inch over 6 inches of travel linearly and 0.0000015 inch circumferentially. Surface conditions were documented using scanning electron microscopy (SEM). Near surface microstructures were documented after testing at the -1 stress ratio (low maximum stress condition) in the gage but away from the fracture surface; longitudinal and transverse sections were nickel-plated to retain edge features and then metallographically prepared, etched with Krolls and photographed. In addition, residual stress measurements were made both before and after HCF testing (but on different specimens) to determine the depth and magnitude of surface residual stresses. Testing was performed on closed-loop servo-hydraulic test stands at 60 Hz, room temperature lab air under load control and at stress ratios of -1, 0.1 and 0.8.

RESULTS AND DISCUSSION

Surface Conditions

The results of the surface profile measurements are shown in Table 3G.2. R_a is the arithmetic average deviation from profile centerline (divided by the length of the trace); R_q is the root mean square average of R_a ; R_v is the maximum vertical valley depth from profile centerline; R_p is the maximum vertical peak height from profile centerline; and R_{max} is the vertical distance between highest and lowest points of profile. The data show that the smoothest specimens were the Group I (low stress grind plus longitudinal polish) specimens followed by the Baseline (low stress grind plus longitudinal polish plus stress-relieve anneal plus chem-mill) specimens. The roughest specimens were the Group IV (baseline plus shot peen) specimens.

Table 3G.2
Surface Profile Measurements (in μin)

	Direction	Ra	Rq	Rv	Rp
Group I SRA+LSG+LP	Axial	5.8	7.2	22.9	31.0
	Circumferential	8.7	10.5	32.0	24.3
Group II SRA+SPT	Axial	16.4	20.3	65.2	65.3
	Circumferential	6.5	8.1	25.8	19.2
Group III SRA+GRD	Axial	12.3	15.4	60.5	49.7
	Circumferential	10.0	12.6	31.1	39.1
Group IV BL+SP	Axial	45.1	57.1	143.7	258.0
	Circumferential	49.1	60.1	126.3	175.8
Baseline	Axial	9.6	12.4	58.4	52.2
	Circumferential	16.2	19.2	64.4	50.6

SEM photos of a specimen surface from each of the four groups and a baseline specimen at low (50X) and high (1500X) are shown in Figures 3G.1 and 3G.2, respectively. While the surfaces look relatively uniform at low magnification, at higher magnification, the surfaces show non-uniformity, even some tearing, laps and uneven etching (chem-milling).

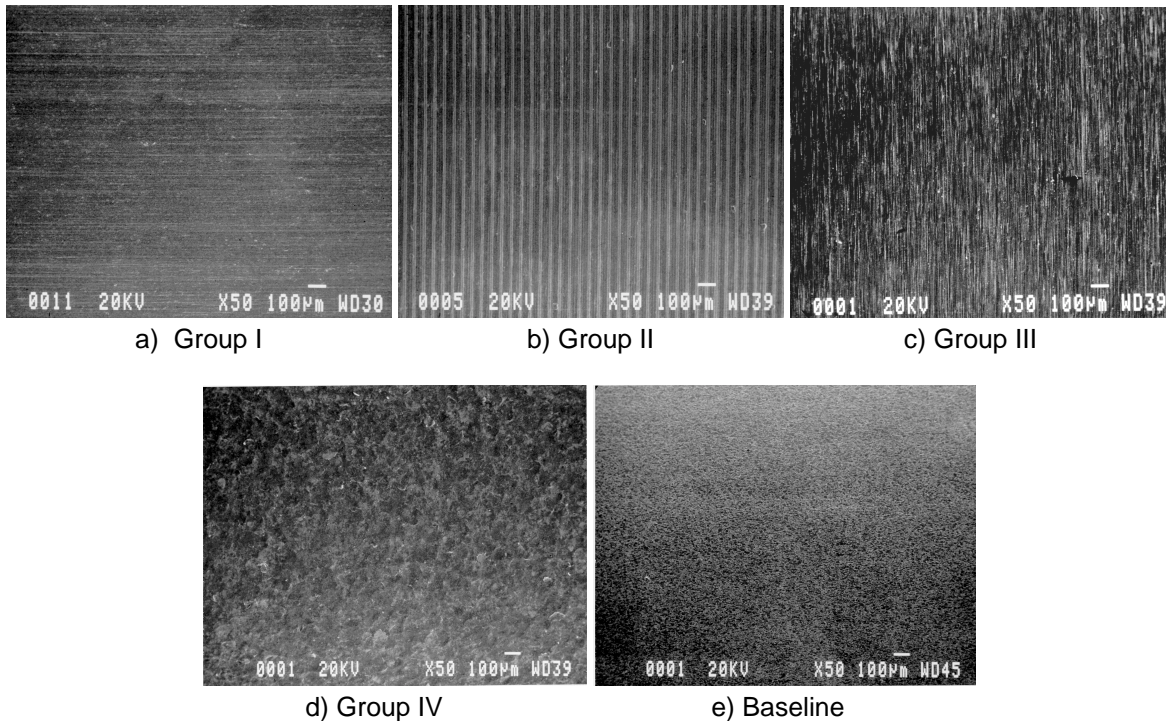


Figure 3G.1. Low magnification SEM photos of the surfaces from representative specimens (the axial direction is horizontal; the circumferential direction is vertical).

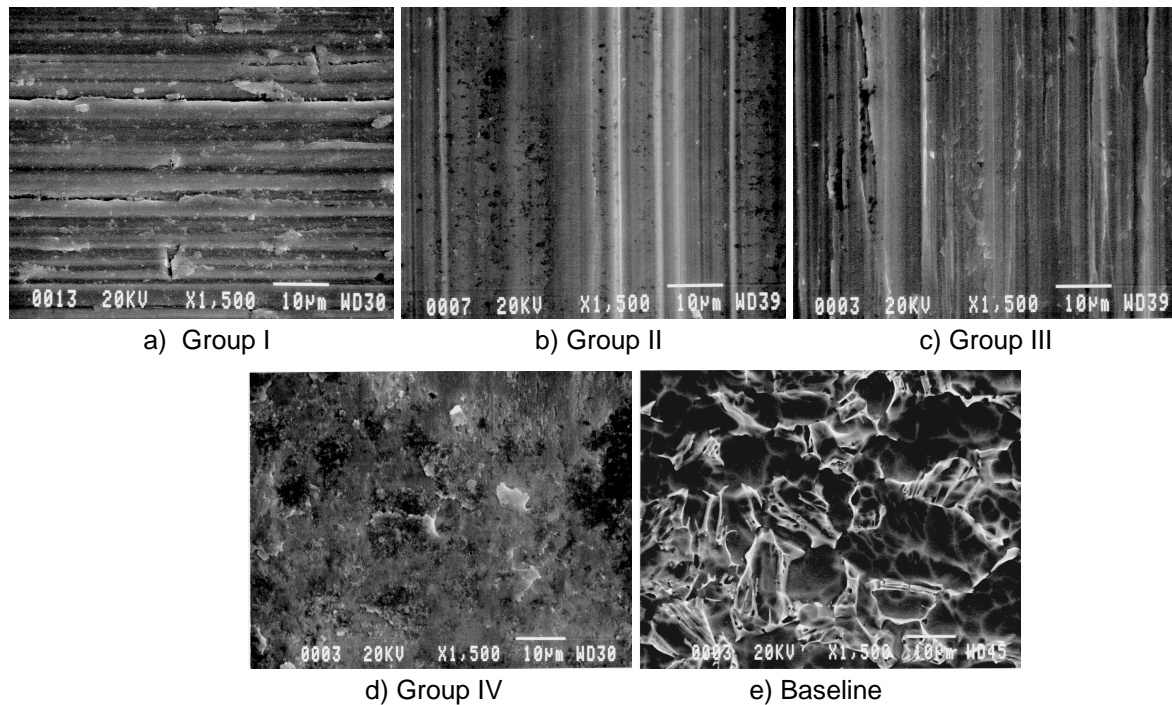
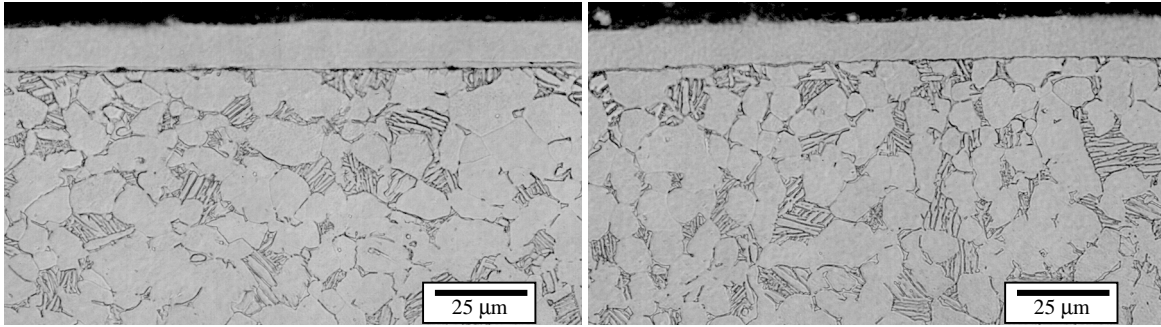
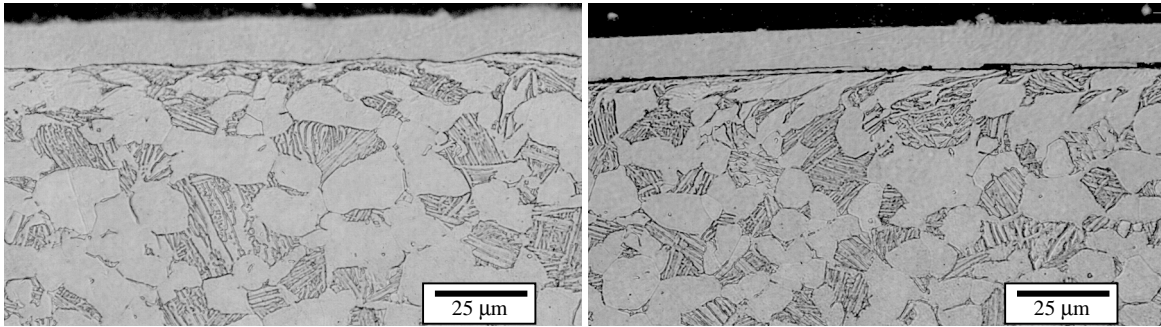


Figure 3G.2. High magnification SEM photos of the surfaces from representative specimens (the axial direction is horizontal; the circumferential direction is vertical).

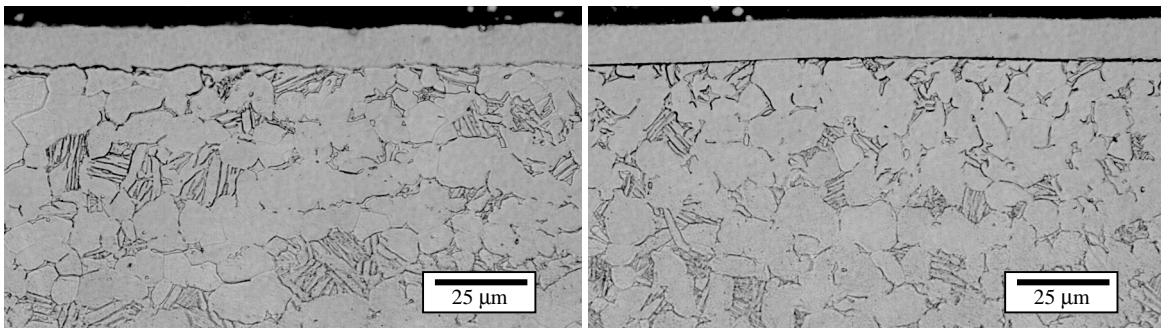
Representative longitudinal and transverse near-surface microstructures are shown in Figure 3G.3. From these photos, the heavily deformed surface of the Group II (single point turned) specimen can be seen. The other specimens show little if any visible deformation at the surface.



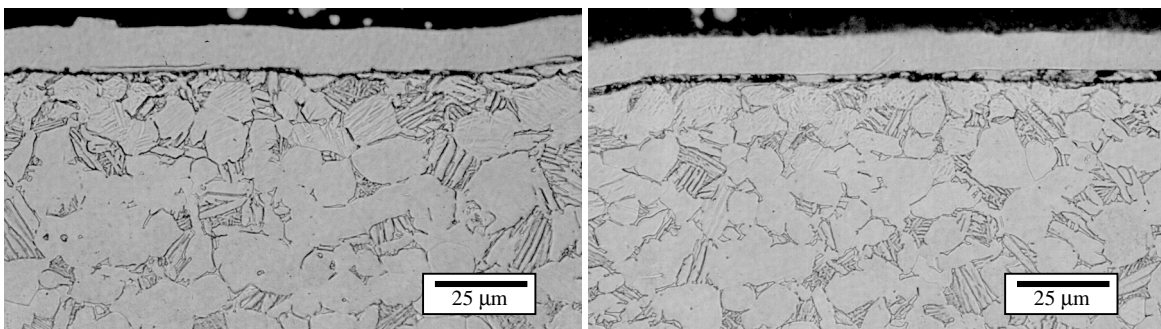
a) Group I longitudinal (left) and transverse (rights) sections



b) Group II longitudinal (left) and transverse (rights) sections



c) Group III longitudinal (left) and transverse (rights) sections



d) Group IV longitudinal (left) and transverse (rights) sections

Figure 3G.3. The near surface microstructures of representative specimens after nickel-plating.

HCF RESULTS

The test results of the specimens from the four groups are compared with the baseline results at the stress ratios of -1, 0.1 and 0.8 in Figure 3G.4, 3G.5 and 3G.6, respectively. Runouts (suspensions at 10 million cycles) are indicated by arrows. At the -1 stress ratio (Figure 3G.4), the endurance limit of the all four groups of specimens is higher than that of the baseline specimens. The greatest increase is found in both the single point turned (Group II) and shot peened specimens (Group IV), where the endurance limit appears to be increased by approximately 40 ksi.

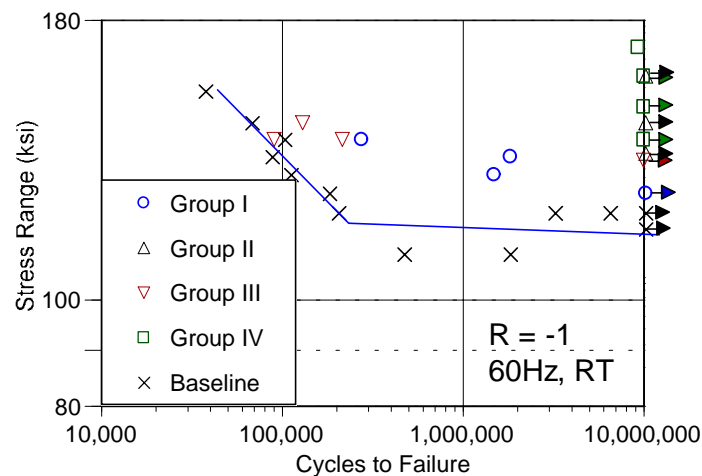


Figure 3G.4. The -1 stress ratio results.

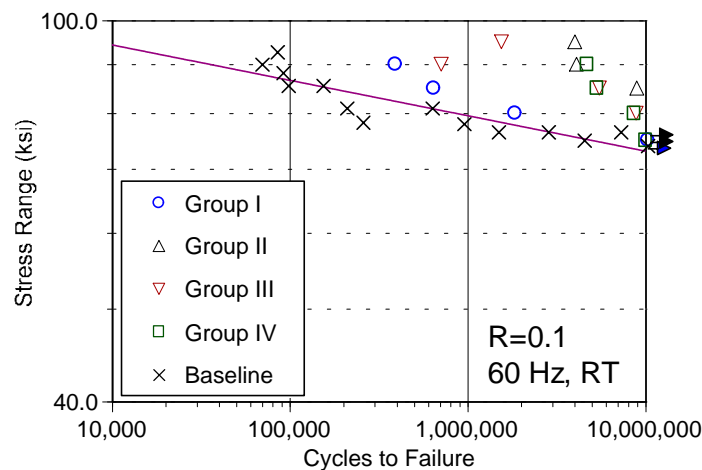


Figure 3G.5. The 0.1 stress ratio results.

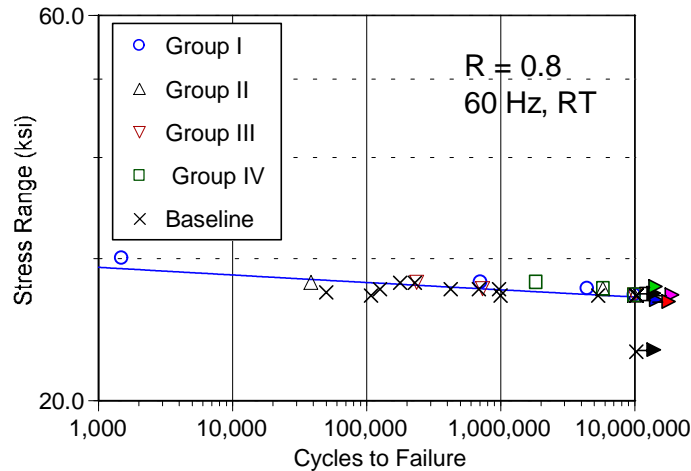


Figure 3G.6. The 0.8 stress ratio results.

At the 0.1 stress ratio (Figure 3G.5), the endurance limit of all four groups is again higher than that of the baseline specimens. The increase is similar for the single point turned (Group II) and shot peened specimens (Group IV) as well as the low stress ground (Group III) specimens. However, at the 0.1 stress ratio, the increase in the endurance limit stress range of approximately 10 ksi is less than the increase observed at the -1 stress ratio.

At the 0.8 stress ratio (Figure 3G.6), there does not appear to be any difference between the fatigue behavior of the four groups and the baseline specimens. In fact, each group of specimens had a 10 million cycle suspension (runout) at 27 ksi stress range but a failure at 27.5 ksi stress range, which is essentially the behavior of the baseline specimens (four runouts at 27 ksi stress range and four failures at the 27.5 ksi stress range).

If the maximum stress of the endurance limits are considered, one sees that the increase in endurance limits of the specimens from the four groups decreases as the maximum stress increases. For example, at the -1 stress ratio, the endurance limit for the Group II and Group IV specimens increases approximately 20 ksi maximum stress over the baseline endurance limit that is approximately 58 ksi maximum stress. At the 0.8 stress ratio, the endurance limit for all specimens, baseline included, is approximately 135 ksi maximum stress. Thus, the different surface preparation methods have less effect on endurance limit as the maximum stress of the test approaches the yield strength of the material.

RESIDUAL STRESSES

The residual stresses measured in the circumferential direction as a function of depth are shown in Figure 3G.7. While all of the specimens have compressive residual stresses, it is easily seen that the specimen with the greatest magnitude and greatest depth of compressive residual stresses is from Group IV, the shot peened specimens. The specimens from Group II and III have similar magnitudes of compressive stresses, but the Group II (single point turned) specimen has deeper residual stresses than the Group III (ground) specimen. The Group I (low stress ground plus polish) specimen, typical of many fatigue test specimens, has lowest compressive residual stresses.

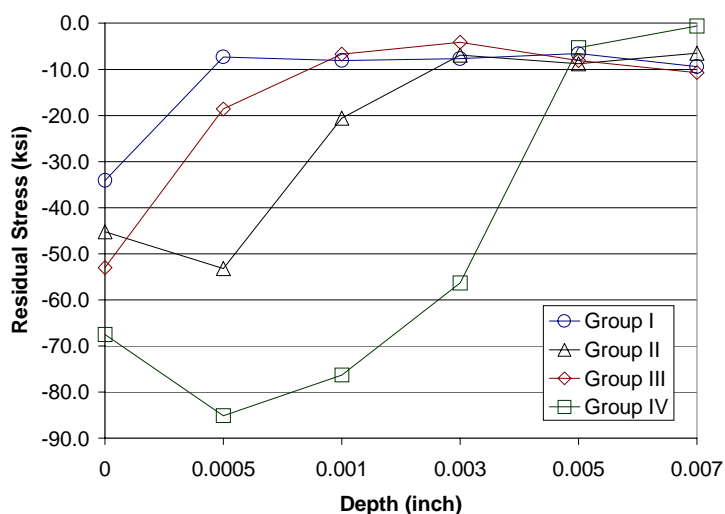


Figure 3G.7. Residual stresses measured in the circumferential direction.

The residual stresses and percent cold work at the surface of the specimens in both the axial and circumferential directions are shown in Tables 3G.3 and 3G.4. Comparison of the two tables shows that the residual stresses are similar in both directions for Group I and Group III specimens but are significantly different with the axial direction being greater than the circumferential direction in the Group II and Group IV specimens. The amount of cold work, or plastic deformation, is greatest for the IV specimens and may explain the marginal improvement at the 0.1 stress ratio.

Table 3G.3

Residual stress and cold work measurements in the axial direction

Axial	GROUP			
	I	II	III	IV
Residual Stress (ksi)	-21.4	-79.5	-59.0	-104.0
Percent Cold Work	1.5	34.3	5.5	98.5

Table 3G.4

Residual stress and cold work measurements in the circumferential direction

Circumferential	GROUP			
	I	II	III	IV
Residual Stress (ksi)	-34.1	-45.2	-53.0	-67.5
Percent Cold Work	1.0	31.1	5.4	67.3

Based on the x-ray diffraction work, it is easy to explain the relative increases in endurance limits for the four groups of specimens at the -1 and 0.1 stress ratio. As the compressive residual stresses increase, the microplasticity at the surface of specimens is retarded, and higher fatigue strengths are obtained. As cold work increases, more dislocation are generated near the surface, and these may become active at higher max stress conditions (e.g., 0.1 stress ratio). However, this does not explain the results at the 0.8 stress ratio.

Table 3G.5 contains residual stress cold work measurements taken after a representative specimen had been tested. These measurements were taken in the gage of the specimen, approximately 0.25 inches away from the fracture surface. In these results, the specimens tested at -1 and 0.1 stress ratios are similar to the results obtained on a specimen from that group prior to testing. At the 0.8 stress ratio, although the specimens from Groups I and III are similar, the specimens from Groups II and IV show a positive residual stress after testing. The results from Groups II and IV indicate that plastic yielding may have occurred during the high stress ratio tests. Since all of the 0.8 stress ratio specimens that were measured after testing were tested at the same stress range of 27.5 ksi (maximum stress of 137.5 ksi), it is interesting to note that only the Group II and IV displayed positive residual surface stresses after testing. While only one specimen per Group per stress ratio was subjected to residual stress measurements, the difference observed at the 0.8 stress ratio between Groups I and III

and Groups II and IV may lie in the magnitude of the compressive stress and the degree of cold work measured prior to testing. The higher residual compressive stresses at the surface of Group II and IV specimens would require a higher internal residual tensile stress to balance the compressive stress. This internal stress may have helped bulk yielding of these specimens. In addition, heavily cold worked structures have been identified as being more susceptible to dynamic stress relaxation, which would make yielding at the surface easier.

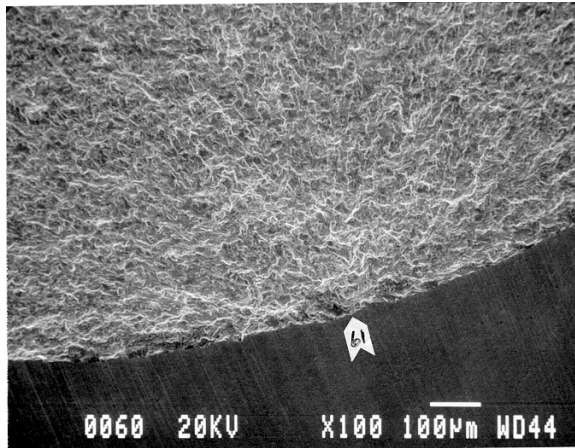
Table 3G.5
Post-test residual stress measurements

Group	I			II			III			IV		
Stress Ratio	-1.0	0.1	0.8	-1.0	0.1	0.8	-1.0	0.1	0.8	-1.0	0.1	0.8
Axial Residual Stress (ksi)	-13.6	-12.4	-20.5	-60.6	-104.4	4.7	-37.4	-33.2	-22.3	-73.3	-79.5	39.9
Circumferential Residual Stress (ksi)	-16.5	-21.0	-3.0	-28.8	-39.9	-9.2	-24.2	-47.2	-16.4	-65.7	-83.1	-9.3
Average Percent Cold Work	0.8	0.6	13.4	34.2	47.2	36.9	3.5	9.8	21.5	64.6	78.3	87.0

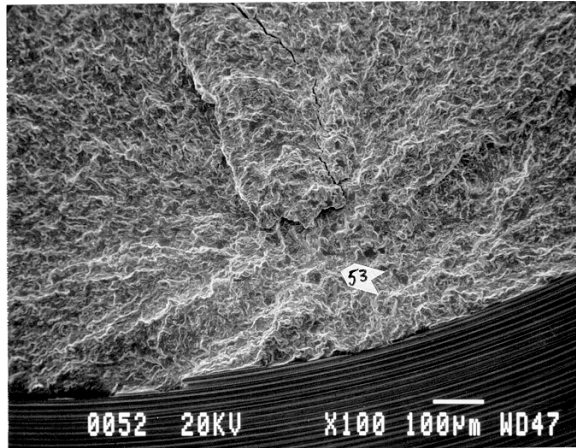
FRACTOGRAPHY

Representative specimens from the three groups were submitted for fractographic documentation.

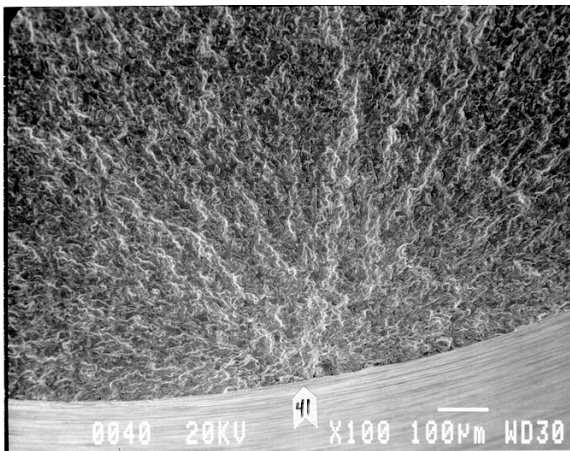
The fracture surface of one specimen from each group tested at the 0.1 stress ratio are shown in Figure 3G.8 and are discussed with respect to the previously observed fracture surface from the baseline specimens. The baseline specimens at the stress ratios of -1 and 0.1 initiated at the surface of the specimen. In the Group II and IV specimens tested at 0.1, the nucleation was subsurface (approximately 0.004 to 0.008 inch below the surface). The Group I and III specimens appear to have surface nucleations. In Group IV subsurface nucleation and Group I and III surface nucleation was true in general for the -1 stress ratio specimens as well. (Group II specimens at the -1 stress ratio were either questionable tests or runouts.) The fracture surface of the 0.8 specimens typically appeared to be ductile overload without clear nucleation sites, as was the case for the baseline specimens, with the exception of Group 1 specimen that had some facets at the identified nucleation site.



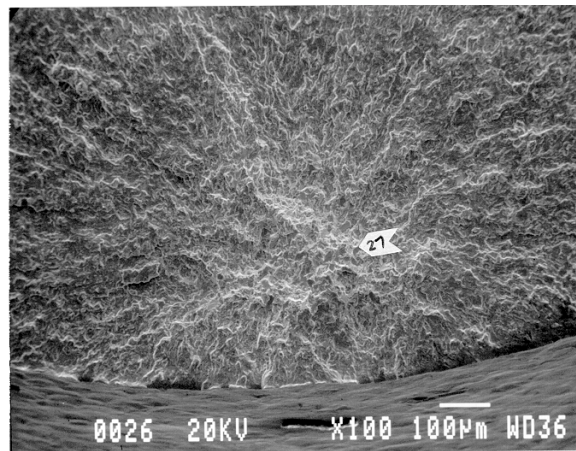
a) Group I, 80 ksi stress range, $N_f=1,848,141$



b) Group II, 85 ksi stress range, $N_f=8,942,203$



c) Group III, 80 ksi stress range, $N_f=8,873,772$



c) Group IV, 80 ksi stress range, $N_f=8,618,519$

Figure 3G.8. SEM photos of the nucleation site on the fracture surfaces of specimens tested at 0.1 stress ratio.

At higher magnifications, the nucleation sites appear to be faceted. The facets, which are on the order of the primary alpha particles (~ 0.0004 inch), tend to decrease in number away from the nucleation site.

The subsurface nucleation is expected based on the residual stress measurements. As the compressive residual stresses at the surface of the specimen offsets the applied axial tensile load, crack nucleation is not only delayed but is forced to a region where the residual compressive stresses are lower or non-existent.

CONCLUSIONS AND RECOMMENDATIONS

The surface effects study revealed the following:

- Machining and post-machining polishing and peening affects surface finish, residual stresses, and fatigue strength of Ti-6-4;
- Residual compressive stresses at the surface of specimens can increase the life of specimens;
- The increase in fatigue life of specimens by compressive residual surface stresses decreases to nil as the stress ratio changes from -1 to 0.8;
- The magnitude of compressive residual stresses are more influential in fatigue behavior than the surface roughness.

Based on the findings, the following recommendations are presented:

- Accurate life prediction models should take into account surface effects;
- Surface effects should be based on stress ratios of interest;
- Additional investigation of the effect of residual internal tensile stresses on yielding and the effect of cold work on stress relaxation should be studied.

Appendix 3H

MULTIAXIAL (BIAXIAL) FATIGUE BEHAVIOR OF Ti-6Al-4V AT 20°C

Peter Kurath
AMTEL
University of Illinois

Submitted
8 September 1999

EXPERIMENTAL PROCEDURE

The material investigated was a Ti-6-4 forged alloy on the PRDA V pedigree. The forged plate was approximately 20 mm thick. This material is utilized extensively in the front fan of gas turbine engines. Even though it is a forged plate, it is heat treated to resemble a foil microstructure. Twenty-two solid biaxial specimens were fabricated with approximate dimensions shown in Figure 3H.1.

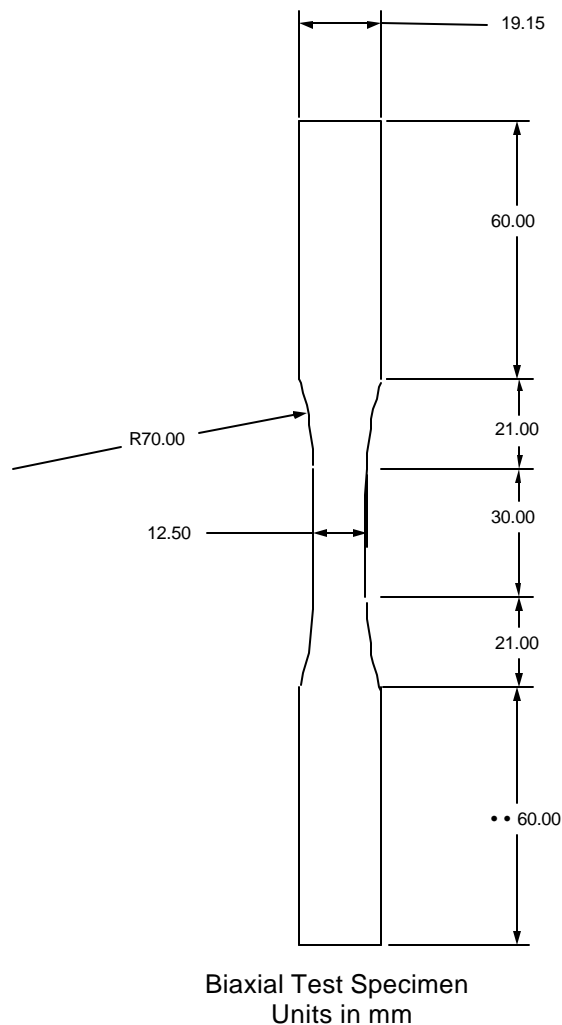


Figure 3H.1. Baseline multiaxial specimen.

Grip section diameters were dictated by the thickness of the forging. Hence, the gage section diameter of 12.5 mm was the maximum possible. The choice of a solid bar

does make analysis of plastic deformation more difficult, but a tubular specimen would have to a wall thickness of less than 1 mm for the thin walled tube approximation to be appropriate. This might have introduced torsional buckling as well as a non-representative cross section from a microstructural perspective. Grain size for this material is inferred from the PRDA V pedigree designation as are the stress relief and subsequently applied chem-milling processes. This was done in part to facilitate comparison to existing uniaxial data.

All testing was conducted on a closed loop servohydraulic tension-torsion load frame, with an axial load capacity of 445 kN and a torsional load capacity of 5000 N-m. Since anticipated maximum loads were approximately 10% of full scale, load cells were calibrated within this range, and were linear to within 0.05% of the anticipated test range. A hydraulic collet system was utilized to grip the specimens. Solid aluminum bars of the same grip diameter and length were strain gauged in accordance with ASTM E1012-93 to assure alignment of the test frame and grips. Strains were measured with a modified MTS model 632.85-xx biaxial extensometer with conical points. The modification involved strain gauging existing flexure elements to measure torsional strains. The extensometer's gage length was 25 mm and an axial full-scale calibration of 2.5%. Nonlinearity of this measurement was less than 0.2% of full scale. Torsional full-scale rotations of 5 degrees or a shear strain of approximately 4.3%, were linear to within 0.3% of full scale. Maximum cross talk between the axis was 0.5% of either full scale. This extensometer provides averaging of two locations for both axial and torsional measurements. Data acquisition and test path generation were supported by a 32-bit data acquisition/control system.

Specimen dimensions limited the maximum frequency of testing to approximately 2 Hz. Before conducting any test at the reported levels, 20 cycles of ± 10 kN axial and then ± 40 N-m torsional load were performed. This data was utilized to check both the axial and shear moduli of the specimen and insure the integrity of the extensometer before switching to strain control. These are the values reported in Table 3H.1. All test levels were initially started in strain control at 0.5 Hz. A limited number of tests were eventually switched to load control and run to failure at 2 Hz. This was only done if the stabilized cyclic deformation was linear elastic and there was no chance of introducing ratcheting by changing mode of control. This was a significant consideration in non-fully reversed tests.

Table 3H.1
UDRI-Ti-6-4 Biaxial Modulus and Path Data

Specimen ID	E* (GPa)	G* (GPa)	μ	Freq (Hz)	Path Type	N _f (cycles)	Comments
156-11/S	116.4	43.7	0.331	0.5	Ax	6,200	Axial only, R=-1
21-11/S	119.2	43.6	0.367	0.5	Tor	72,141	Torsion only, R=-1
21-6-S/L	118.3	43.4	-	1	Tor	241,250	Torsion only, R=-1
156-10/S	120.3	43.8	0.363	0.5	Tor	961,806	Torsion only, R=-1
21-7/S	117.5	43.9	0.338	0.5	Tor	24,895	Torsion only, R=0.1
156-5/S	117.6	44.1	0.333	1.0	Tor	150,293	Torsion only, R~0.1
156-4/S	120.4	43.9	0.371	0.5	Tor	151,598	Torsion only, R=0.1
156-1/S/L	116.5	43.6	0.336	0.5	Tor	814,753	Torsion only, R=0.1
21-4-S/L	120.3	43.6	0.380	1	Tor	141,229	Torsion only, R=0.5
21-1/S	119.5	43.8	0.364	0.5	Ax-Tor	67,965	Proportional Combined, R=-1
156-9/S	120.3	43.8	0.373	0.5	Ax-Tor	60,514	Proportional Combined, R=0.1
156-3/S	120.4	44.0	0.368	0.5	Ax-Tor	87,920	Proportional Combined, R=0.1
156-8/S	117.7	44.0	0.338	0.5	90-OP	111,783	R=-1 90-OP
156-2/S	119.6	43.7	0.368	0.33	Tri	38,355	Triangle path
21-2/S	119.9	43.7	0.372	0.33	Tri	43,009	Triangle path
156-6/S	118.6	43.6	0.360	0.5	Z	>19,864	Top triangle-control prob
21-9/S	120.4	43.6	0.381	0.5	Z	71,358	repeat 156-6
21-5/S	119.3	43.8	0.362	0.5	X	79,367	Bottom triangle
21-8/S	120.2	43.7	0.375	0.5	Y+	72,124	shear w/ poss epsmean
21-3/S	120.5	43.7	0.378	0.5	Y+	73,728	shear w/ poss epsmean
21-10/S	120.3	-	-	0.5	Y-	329,058	shear w/ neg epsmean
156-7/S	120.5	43.9	0.372	0.5	Y-	>24,576	shear w/ neg epsmean OVERLOAD

/L load control, /S strain control, * From low level precycling

Five circumferentially notched bars were tested. Grip and length dimensions were identical to the aforementioned biaxial specimens. Figure 3H.2 shows the details of the notch. The biaxial extensometer was utilized to monitor nominal specimen stiffness changes.

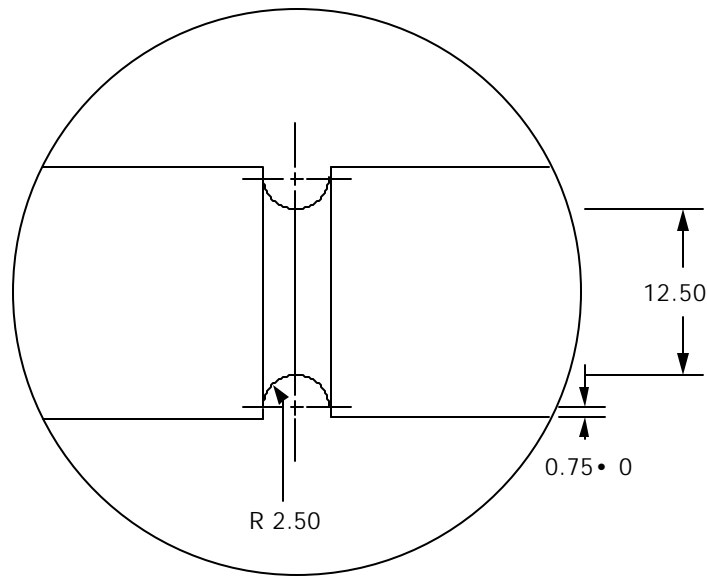


Figure 3H.2. Notched specimen details.

EXPERIMENTAL DATA

Data obtained from this smooth specimen test program is summarized in Tables 3H.1 and 3H.2. Tests are grouped with regard to type of test, not the order in which they were conducted. As previously noted, specimens were cycled at low load or torque levels prior to fatigue testing to determine the cyclic modulus. These results are summarized in Table 3H.1, and presented in a format indicative of a normal distribution in Figures 3H.4 and 3EH.5. Specimen 156-11 was a fully reversed axial test. It was initially the quality control specimen returned to GEAE after the specimens were machined. Before testing it was instrumented with a 3-element rosette strain gage to determine Poisson's ratio, and verify extensometer measurements of E and G (Note: these values are not reported). Minimal insight into specimen size compared to previous smaller uniaxial specimens was also gleaned. The next group of tests in the tables are torsion only experiments. The goal of these experiments was to ascertain if mean shear stresses influence fatigue lives. Quite a bit of mean shear stress relaxation was observed for those tests that were not fully reversed. These tests are also vital to obtain baseline constants for some critical plane multiaxial theories. Next, three proportional combined axial-torsional tests are reported. This is probably the simplest combined loading.

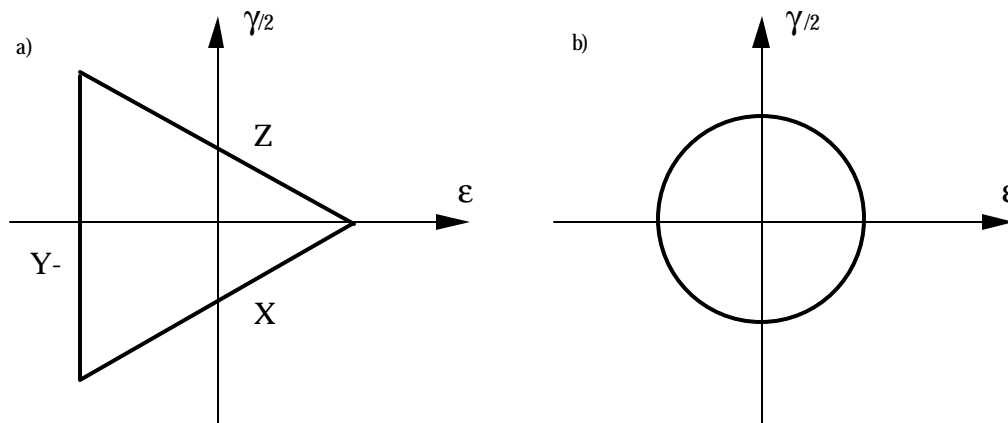


Figure 3H.3. Complex strain paths, a) Triangle Path and individual segments X, Y and Z, and b) 90 degree out-of-phase

The rest of the tests are nonproportional. One 90-degree out-of-phase test (Fig. 3H.3b) was conducted. This path has been identified by many researchers as being critical with regard to out-of-phase deformation and fatigue damage. The triangle path (Fig. 3H.3a) is another out-of-phase approximation of service conditions. The final six tests reported all consist of segments of the triangle path. Since the extrapolation of each path does not pass through the origin of strain space they are also considered to be out-of-phase. The Y+ or Y- connotation for the cyclic torsion with static axial strain indicates whether the static axial strain is positive or negative. A Y+ segment is not shown in Figure 3H.3a, but would be on the other side of the origin in comparison to the Y- segment. Both Y+ and Y- tests were proportionally loaded to the max positive shear strain when starting a test. The segments of the triangle path were also conducted so that cumulative damage of the triangle path based on the segments could be performed. The sequence of loading for the triangle path was on startup to the positive axial stress (zero shear strain), then the X leg, Y- leg and the Z leg were repeated for the duration of the test.

Table 3H.2 summarizes the deformation results. This material has a monotonic yield strength in excess of 1000 MPa, resulting in the expectation that many of the tests would incur only elastic cyclic loads. Considering plastic deformation is not difficult in the case of axial loading, but is somewhat challenging for torsional loads. The unbracketed quantities in the t_{max} and t_{min} columns in Table 3H.2 are the results of an elastic calculation based on the torque and original specimen dimensions

Table 3H.2
UDRI-Ti-6-4 Biaxial Deformation-Life Data

Specimen ID	ϵ_a^{\max} (%)	ϵ_a^{\min} (%)	γ_a^{\max} (%)	γ_a^{\min} (%)	σ_{\max} (MPa)	σ_{\min} (MPa)	τ_{\max} (MPa)	τ_{\min} (MPa)	N_f (cycles)
156-11/S	0.756	-0.751	-	-	821	-843	0	0	6,200
21-11/S	-	-	0.866	-0.868	0	0	386	-382	72,141
21-6-S/L	-	-	0.614	-0.610	0	0	266	-265	241,250
156-10/S			0.559	-0.563	0	0	249	-247	961,806
21-7/S	-	-	1.81	0.166	0	0	557 [600] (499)	-150 [-95] (-183)	24,895
156-5/S	-	-	1.21	0.090	0	0	526 [522] (494)	29.5 [27] (8.0)	150,293
156-4/S	-	-	1.36	0.150	0	0	518 [534] (458)	-13.4 [7.5] (-60)	151,598
156-1/S/L	-	-	0.958	0.086	0	0	424	40.7	814,753
21-4-S/L	-	-	1.96	0.815	0	0	567 [617] (507)	73.4 [120] (19)	141,229
21-1/S	0.312	-0.312	0.416	-0.418	365	-375	185	-187	67,965
156-9/S	0.462	0.0486	0.616	0.0550	543	57.7	276	27.9	60,514
156-3/S	0.464	0.0476	0.621	0.055	536	55.3	280	28.4	87,920
156-8/S	0.303	-0.302	0.406	-0.409	357	-355	182	-178	111,783
156-2/S	0.362	-0.373	0.471	-0.476	425 [433] (427)	-456 [-443] (-449)	204 [202] (173)	-214 [-206] (-237)	38,355
21-2/S	0.364	-0.372	0.471	-0.477	430	-454	205	-212	43,009
156-6/S	0.363	-0.361	0.476	0.004	426	-435	209	5.6	>19,864
21-9/S	0.364	-0.364	0.475	0.004	437	-446	211	9.1	71,358
21-5/S	0.365	-0.363	-0.0045	-0.475	432	-435	-4.89	-217	79,367
21-8/S	0.091	0.0893	0.666	-0.665	109	103	289	-288	72,124
21-3/S	0.090	0.089	0.666	-0.666	106	101	293	-291	73,728
21-10/S	- 0.089	-0.091	0.665	-0.664	-109	-116	282	-300	329,058
156-7/S	- 0.089	-0.091	0.663	-0.667	-110	-114	292	-294	>24,576

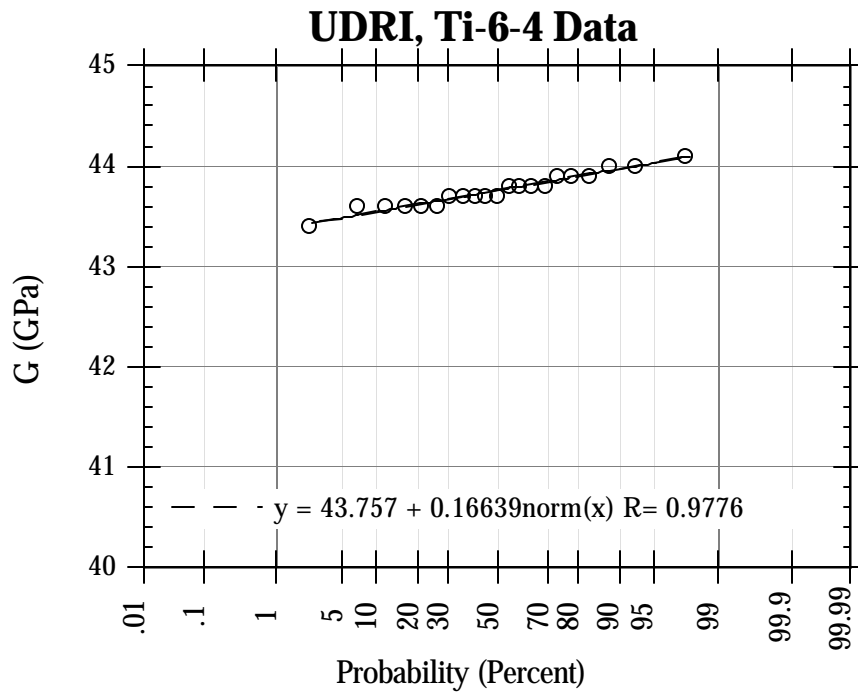


Figure 3H.4. Normal distribution of axial modulus check data.

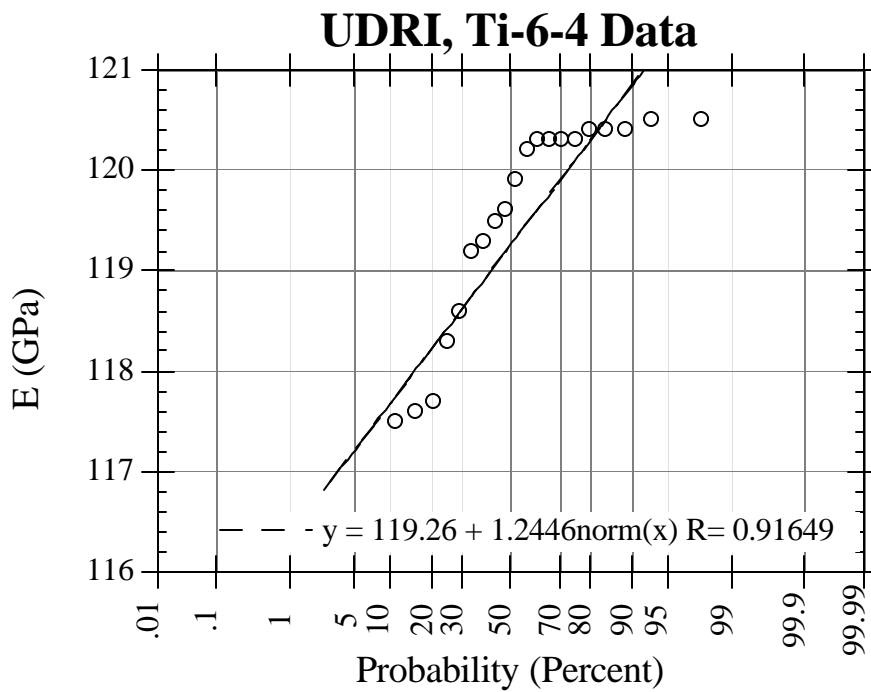


Figure 3H.5. Normal distribution of shear modulus check data.

In order to consider torsional plastic deformation it was necessary to assume a plasticity algorithm. An Armstrong-Frederick based model subsequently refined by Jiang and Kurath [3H.1-3H.5] was implemented. Even the existing uniaxial LCF data did not provide adequate data to fit the modeling constants. A uniaxial specimen was machined from remnants of the forging used for the biaxial specimens. A summary of the deformation results is shown in Figure 3H.6. Notable is the cyclic softening which occurs rapidly after the initial plastic deformation in the first cycle. Both the initial half cycle and half-life data (cycle 1024) were used to obtain two sets of plasticity constants. Note: the half-life linear elastic modulus is lower than the initial cycle value in Figure 3H.6.

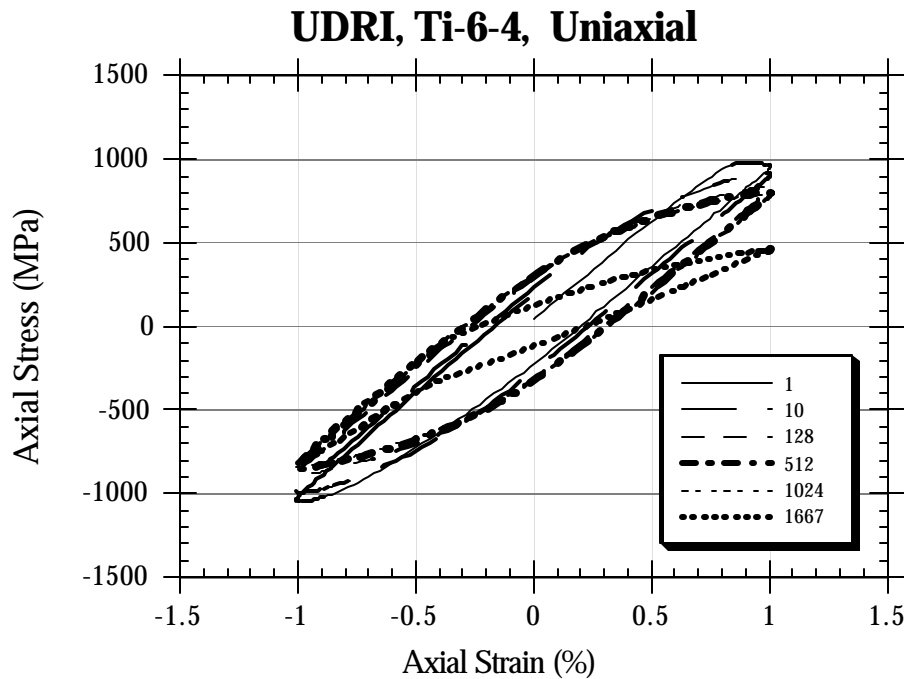


Figure 3H.6. Uniaxial deformation data.

Without laboring over the details in the derivation, the following simple procedure for determining $c^{(i)}$ and $r^{(i)}$ for an A-F type model is forwarded. Select M points from the $\sigma_a - \epsilon_a^p$ curve from the uniaxial experiment (refer to Fig. 3H.7) so that the stress range, $\sigma_{a(i)}$, and plastic strain range, $\epsilon_{a(i)}^p$, are known for any point i. Generally, half of a representative hysteresis loop is employed to represent the stress strain curve shown in Figure 3H.7. Note

that $\epsilon_{a(i)}^p$ denotes the plastic strain range and $\sigma_{a(i)}$ is the stress range corresponding to $\epsilon_{a(i)}^p$. The quantities, $c^{(i)}$ and $r^{(i)}$ are determined by the following two equations respectively,

$$c^{(i)} = \sqrt{\frac{2}{3}} \frac{1}{\epsilon_{a(i)}^p} \quad (i=1, 2, \dots, M) \quad (3H.1)$$

$$r^{(i)} = \frac{2}{3} \frac{H_{(i)} - H_{(i+1)}}{c^{(i)}} \quad (i=1, 2, \dots, M) \quad (3H.2)$$

In the previous two equations,

$$H_{(i)} = \frac{\sigma_{a(i)} - \sigma_{a(i-1)}}{\epsilon_{a(i)}^p - \epsilon_{a(i-1)}^p} \quad (i=1, 2, \dots, M) \quad (3H.3)$$

$$\sigma_{a(0)} = \sigma_y = \sqrt{3} k \quad ; \quad \Delta \epsilon_{(0)}^p = 0 \quad ; \quad H_{(M+1)} = 0 \quad (3H.4)$$

The slope between point (i-1) and point i is $H_{(i)}$ (Fig. 3H.7), and is often termed the plastic modulus. The yield stress σ_y in Equation (3H.4) is the linear elastic portion in Fig. 3H.7. The constant k is the yield stress in pure shear and is related to uniaxial loading via the von Mises criterion. The maximum stress range, $\Delta \sigma_{(M)}$, satisfies the following condition,

$$\sigma_{a(M)} = \sigma_{max} = \sqrt{\frac{3}{2}} \sum_{i=1}^M r^{(i)} + \sigma_y \quad (3H.5)$$

where σ_{max} is the maximum stress range that the model is intended to simulate. For a non-Massing material, the determination of $c^{(i)}$ and $r^{(i)}$ is more complex and involves a series of hysteresis loops, or a "step" test. The constants utilized in the plasticity model are summarized in Table 3H.3 (an $M = 10$ expansion of the backstress was utilized).

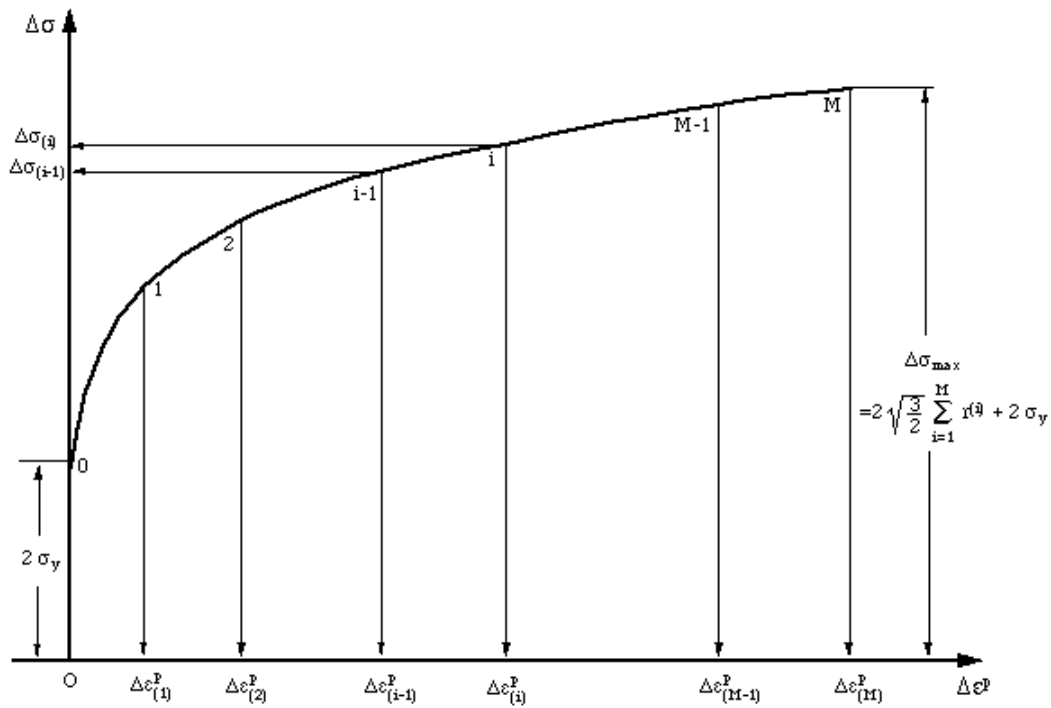


Figure 3H.7. Fitting plasticity modeling constants.

Comparison of the half-life deformation and the model is shown in Figure 3H.8. Coincidence of this data is anticipated since it was employed to fit the plasticity constants. While most of the cyclic biaxial data appears linear elastic when viewed on a cycle by cycle basis, there is appreciable plasticity on the first cycle of many $R = 0.1$ and 0.5 tests. Figure 3H.9 shows a typical torsion only test, showing experimental and analytical results. It should be noted that the y-axis on this plot is torque.

Table 3H.3
Plasticity Modeling Constants

$c^{(i)}$	$r^{(i)}$ (MPa) Cycle 1 k= 260 (MPa)	$r^{(i)}$ (MPa) Half-life k= 205 (MPa)
3265	150	127
1637	77.7	63.2
820	82.3	63.8
411	85.3	62.4
206	86.4	59.0
103	85.5	54.1
51.8	82.9	48.3
26.0	78.5	42.0
13.0	72.9	35.8
6.53	120	50.9

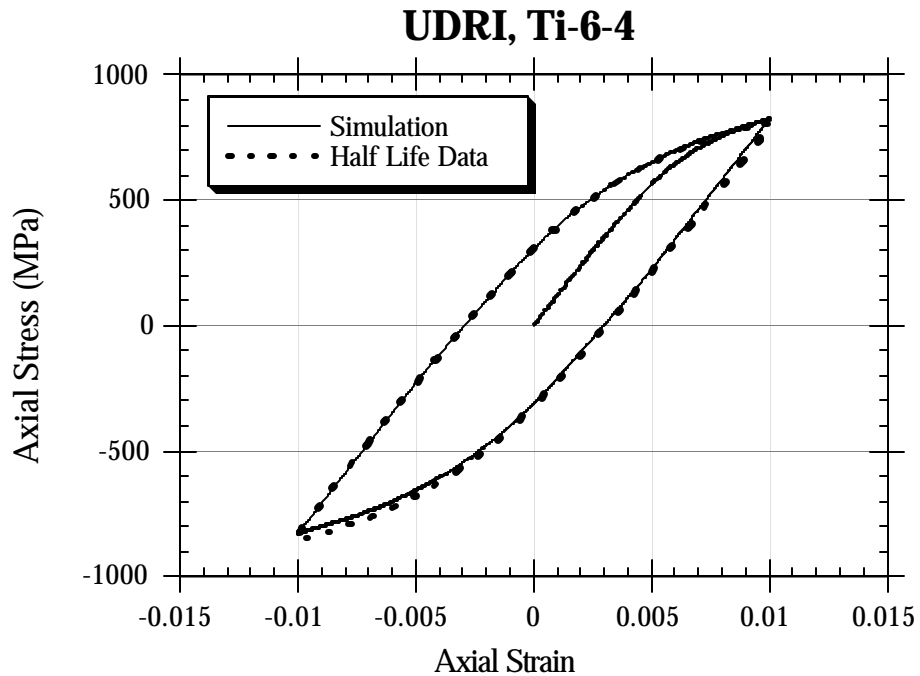


Figure 3H.8. Comparison of modeling and uniaxial data.

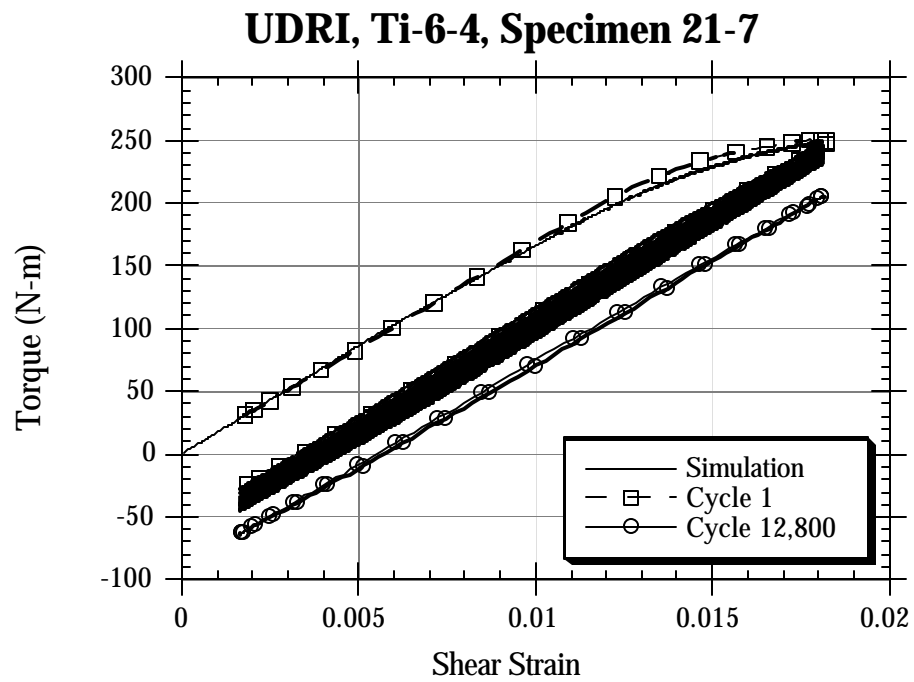


Figure 3H.9. Typical R=0.1 torsion only data.

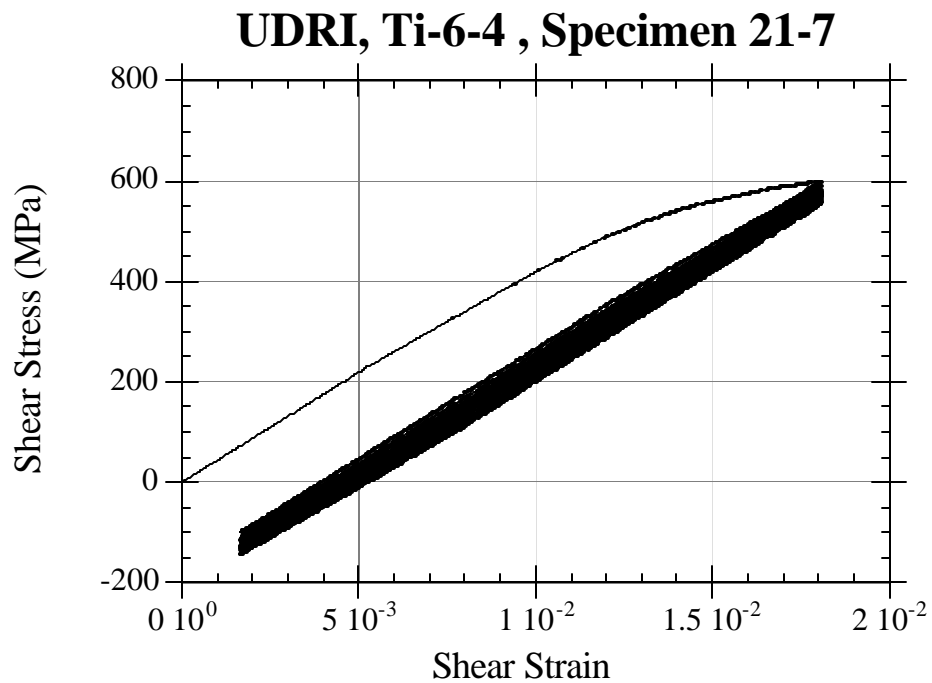


Figure 3H.10. Typical R=0.1 plasticity modeling of torsion only data.

The plasticity algorithm is run in “strain” control, and the stresses integrated to give a nominal torque. If the torque values compare favorably, the author implies that the stresses calculated are a reasonable estimate. The square bracketed stresses in Table 3H.2 were obtained from the first half-cycle properties. It should be noted in Figure 3H.9 that the mean torsional stresses appear to relax, and the plasticity model utilized has the capability of capturing this phenomenon. Within the context of the current work, half-life properties were used to calculate the stresses reported in rounded brackets. Figure 3H.10 shows the stresses calculated by the model for the test shown in Figure 3H.9. The changes in these values reflect both the changing material properties and the cyclic mean stress capabilities of the model. Where no square or round bracketed stresses are reported in Table 3H.2, plastic deformation was deemed insignificant.

LIFE PREDICTION AND DISCUSSION

The goal of the experimental program was to identify a fatigue damage parameter useful for design. While there are a multitude of fatigue damage models, two will be examined as part of this report. Other researchers are conducting a more thorough review of fatigue damage models as another facet of this program. Without undue generalization, there are basically two types of critical plane fatigue approaches: maximum principal stress or strain based and shear dominated. A modified biaxial version of the Smith-Watson-Topper (SWT) principal stress-strain based parameter (A square root and normalization of the stress by dividing by the elastic modulus is the original form proposed by Smith-Watson and Topper [3H.6]) follows,

$$\frac{\Delta \epsilon_1}{2} \sigma_1^{\max} = \text{Damage} \quad . \quad (3H.6)$$

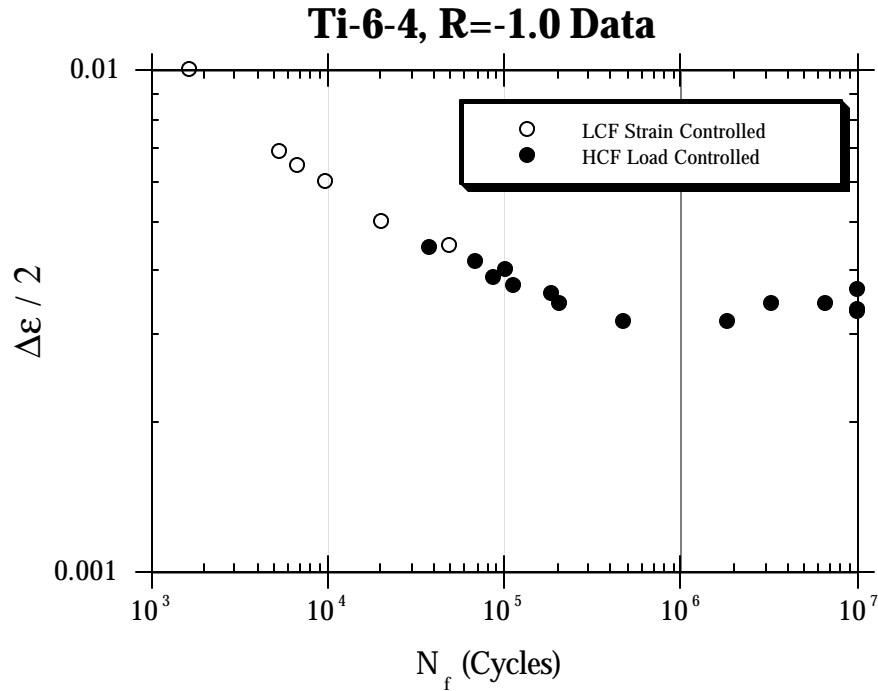


Figure 3H.11. Fully reversed uniaxial data.

For a shear-based parameter, the Fatemi-Kurath-Socie (FKS) [3H.7,3H.8] formulation was chosen.

$$\frac{\Delta\gamma}{2} \left[1 + K \frac{\sigma_n}{\sigma_y} \right] = \text{Damage} \quad (3H.7)$$

Both of the parameters are interpreted as the critical plane being that which has the highest value of damage, rather than the maximum of any individual term. This has more implications when considering Equation (3H.7) than the SWT approach. Now the equation to put on the side of the equation with “Damage” must be determined. It is useful to view the $R = -1.0$ uniaxial data (Fig. 3H.11). The approach taken in the ensuing discussion is to consider that there is no multiaxial data, but $R = -1$ uniaxial data is available.

One of the notable features is that for the limited life region of overlap, the strain controlled and load controlled tests seem to coincide. Also there is no change in slope of the strain-controlled tests where plastic deformation was noted. While most of the tests were linear elastic, the specimen in Figure 3H.6 does show appreciable plasticity. The dip between 10^5 and 10^6 cycles remains unexplained. A bilinear representation of the data will

be required, and this demarcation will not be the traditional elastic-plastic slopes associated with the strain-life approach. GEAE has also made similar observations for their damage assessment. It is useful to view the HCF data for load ratios of -1, 0.1 and 0.5 (Fig. 3H.12). A power function fit is shown on the figure for each load ratio. While the slopes are similar for $R = -1.0$ and 0.1 , there is a definite change for a load ratio of 0.5 . While $R = 0.8$ data exists it is very difficult to interpret. Further examination of the data reveals that even in the HCF regime, the $R = 0.5$ and 0.8 tests have significant plastic deformation on the first half cycle. This onset of plasticity may be significant with regard to fatigue damage. The author previously investigated a β annealed Ti-6-4 alloy [3H.9] for time dependent deformation and noted that if mechanical plasticity occurred, it triggered more time dependent plastic deformation. Hence, for this alloy and testing methodology, the onset of mechanical plasticity during the first half-cycle of high load ratio tests may increase the likelihood of ratcheting in load control (the corollary to the stress relaxation of strain controlled tests shown in Fig. 3H.9). This ratcheting may increase the fatigue damage when compared to similar amplitudes at lower load ratios. Uniaxial load or strain controlled $R = -1.0$ data is easily viewed in the context of the stipulated SWT parameter, and is shown in Figure 3H.11 with the fits employed. Viewing the data in Figure 3H.13, it is evident that a summation of the two power fits is not appropriate. A bilinear representation with a transition at somewhat greater than 10^5 cycles is the approach chosen to represent this damage parameter. In Figure 3H.14 the torsion only data is viewed with the two fits. The data seems to stay on the extrapolation of the LCF fit obtained from the uniaxial data. Finally in Figure 3H.15 all biaxial data is presented in terms of the SWT parameter. Notably the tests with the static axial strains are underpredicted by over an order of magnitude. Implications of having only $R = 0$ (or both 0.1 and -1.0) uniaxial data are minimal for fitting the SWT constants.

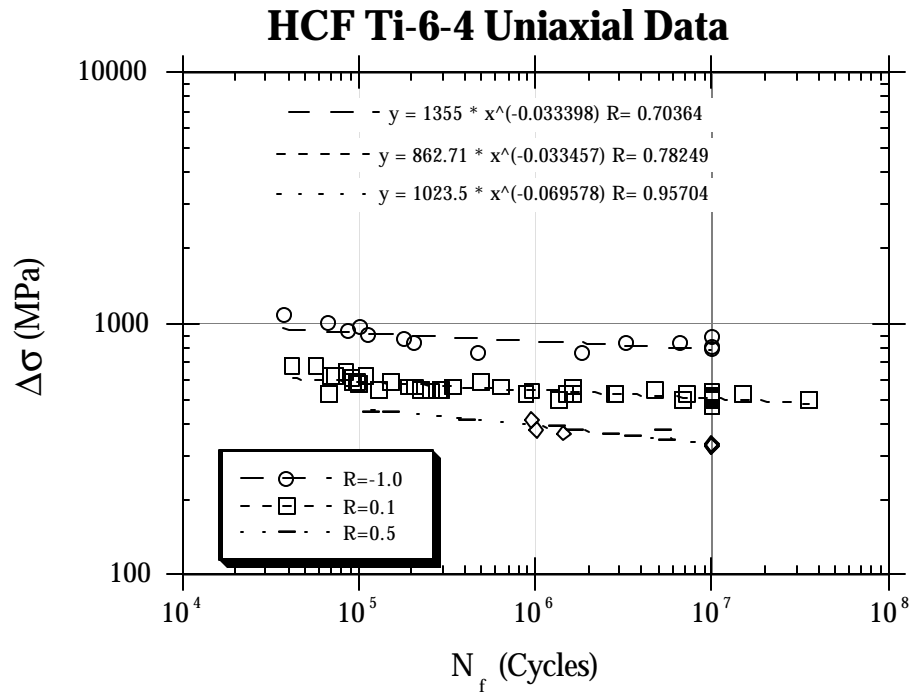


Figure 3H.12. HCF load ratio data.

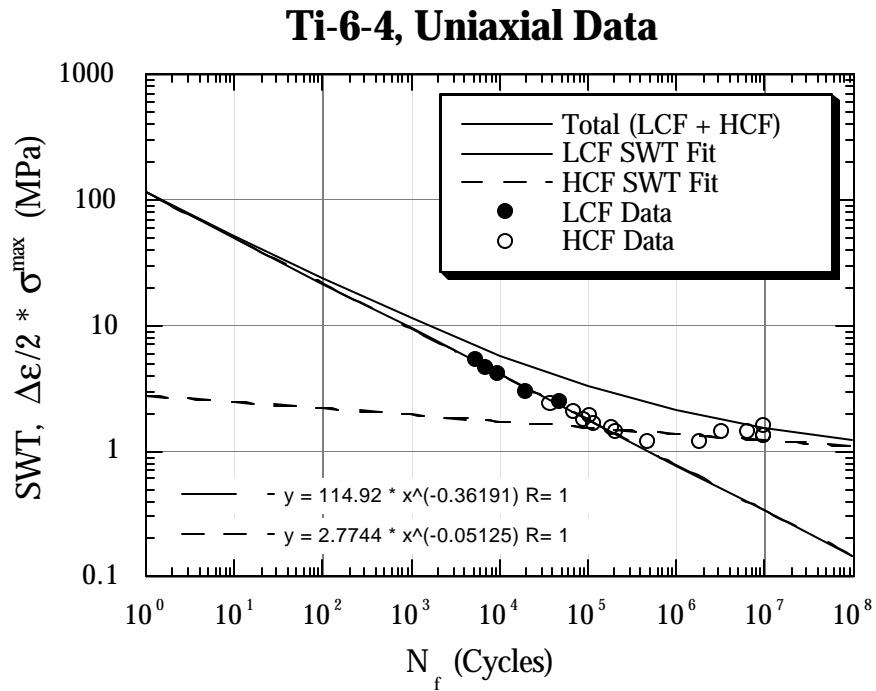


Figure 3H.13. SWT parameter constants.

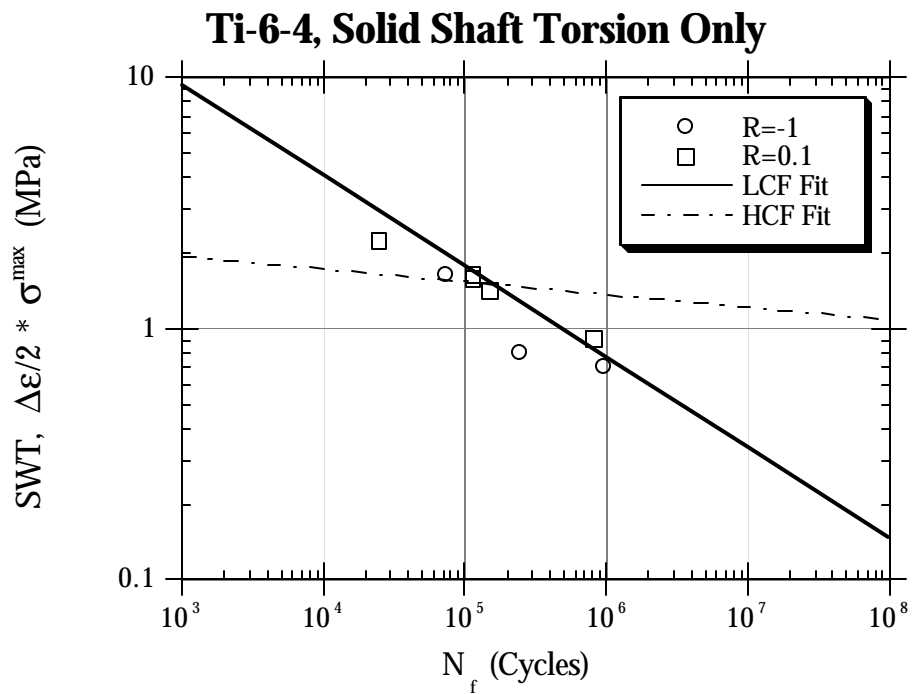


Figure 3H.14. Torsion only data.

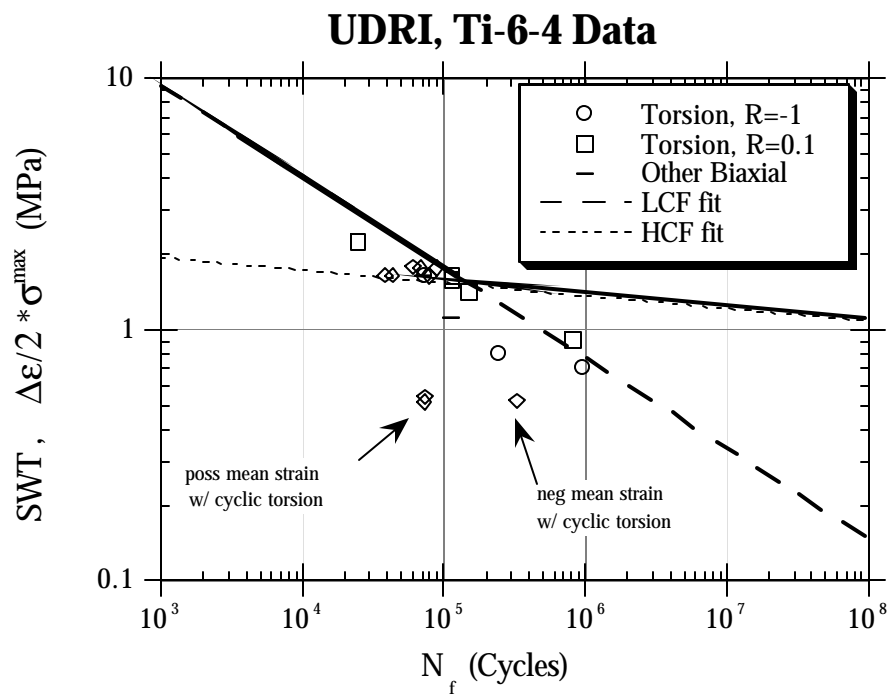


Figure 3H.15. All biaxial data for SWT parameter.

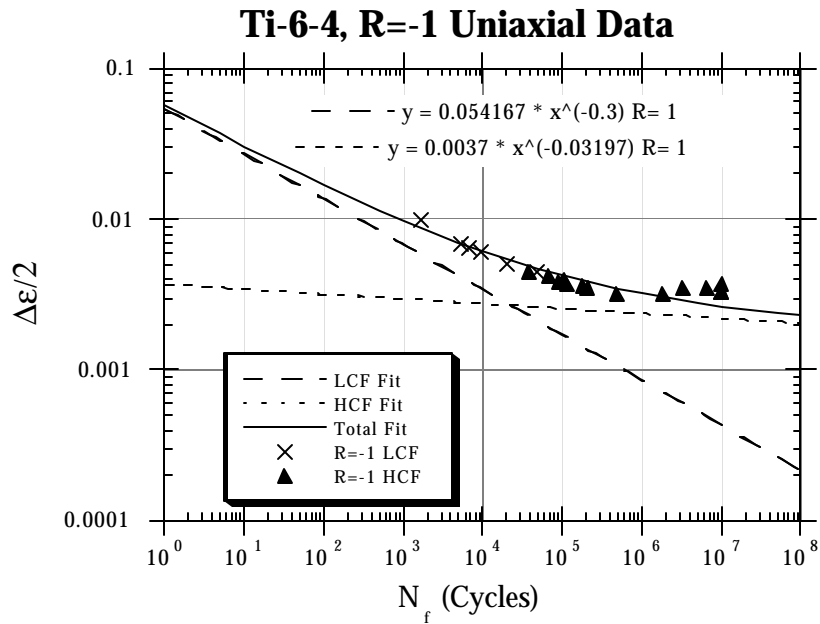


Figure 3H.16. Modified strain life fits.

Next is the shear parameter representation of the data. The exponent for the power function of the HCF curve for FKS parameter will be -0.032 (Similar to that obtained by GEAE for a modified Walker stress approach) based on the arguments forwarded in Figure 3H.12. The HCF coefficient was also based on the GEAE modified Walker stress approach (443.7 MPa). It was arbitrarily chosen to make the LCF exponent approximately an order of magnitude higher and a value of -0.3 was chosen. Fully reversed uniaxial data was viewed in this framework and an LCF coefficient was arbitrarily chosen to adequately represent the $R = -1.0$ data (Fig. 3H.16). Note that the “Total” curve passes through the data. These coefficients and exponents were viewed in the context of the traditional strain-life equation.

$$\text{Damage} = \epsilon'_f (N_f)^c + \frac{\sigma'_f}{E} (N_f)^b \quad (3H.8)$$

The FKS parameter being shear based necessitates a transformation to “torsional” based quantities. The exponents are not altered, but the coefficients are modified via an effective stress or strain criterion.

$$\tau'_f = \frac{\sigma'_f}{\sqrt{3}} \quad \gamma'_f = \frac{(1+\nu^*)}{\sqrt{3}} \epsilon'_f \quad (3H.9)$$

The quantity, v^* , was taken as 0.5 even though there is no clear elastic-plastic demarcation to the bilinearity of this curve. Representation of torsion only data appears improved with this parameter (Fig. 3H.17). Ordinarily the constant K in the FKS³ parameter would be determined comparing uniaxial and torsion only data, however this is not possible. However the representation of the data seems improved for all biaxial data as shown in Figure 3H.18. The effect of two choices of the constant, K , in the FKS parameter is depicted.

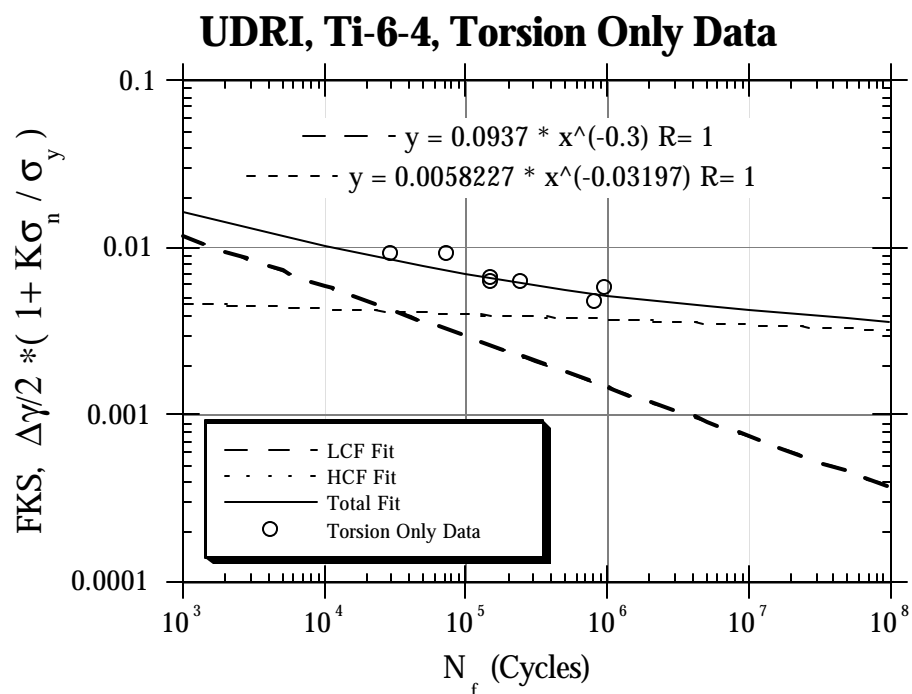


Figure 3H.17. FKS parameter representation of torsion only data.

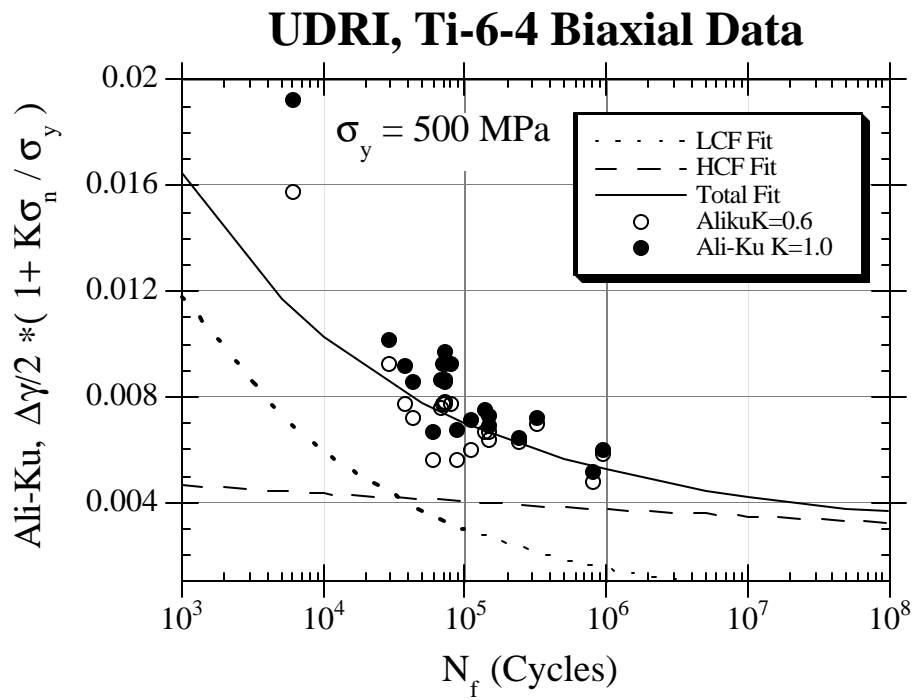


Figure 3H.18. All biaxial data with FKS parameter.

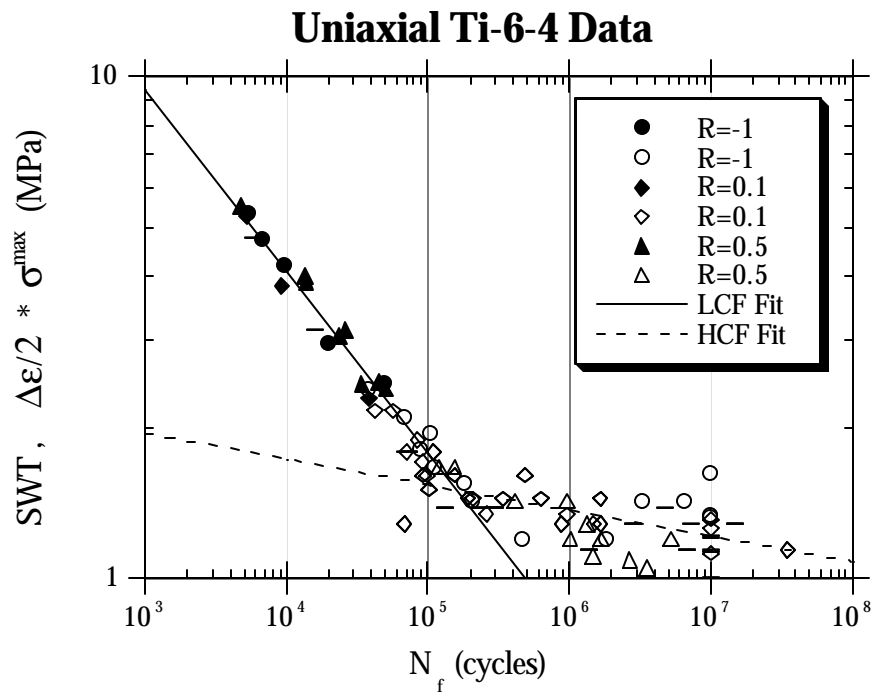


Figure 3H.19. SWT representation of uniaxial Load ratio data.

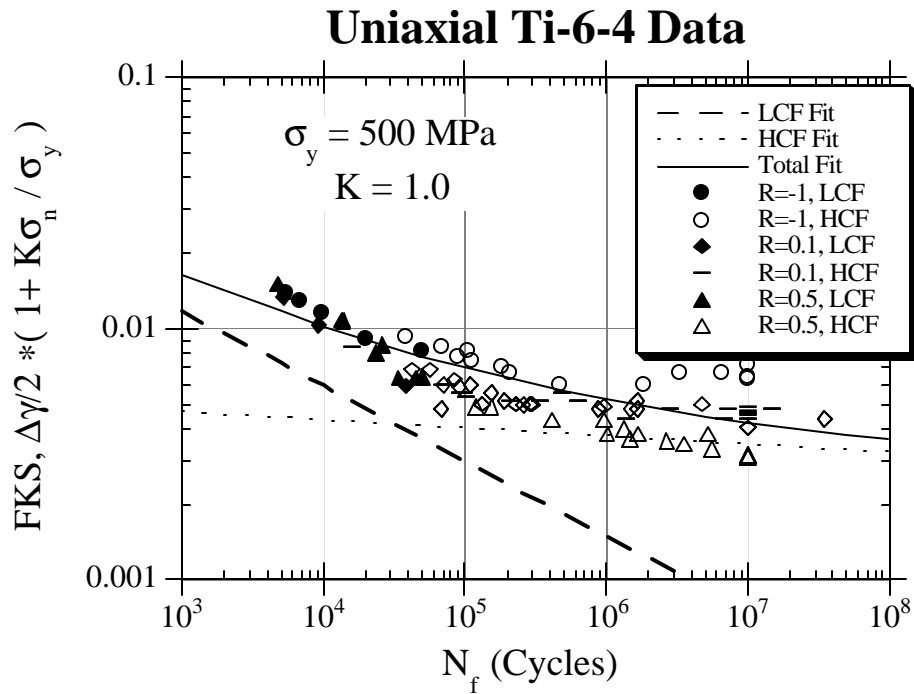


Figure 3H.20. FKS representation of uniaxial load ratio data.

In Figures 3H.19 and 3H.20 the uniaxial data including all load ratios is viewed for both parameters. The strain controlled LCF data collapses for either damage parameter. For the FKS parameter, it has been shown that K is not a constant, but dependent on life. In general it decreases at shorter fatigue lives, hence the overestimation of the data at short lives in Figure 3H.18. The value of K utilized was a guess based on previous values for an Inconel 718 and a normalized 1045 steel. Neither parameter does well for the $R = 0.5$ load controlled HCF data. This may be due to ratcheting occurring as previously stipulated. To use $R = 0.1$ or $R = 0$ uniaxial data, it may be necessary to assume some mean stress correction to calculate an “equivalent” fully reversed strain, and then fit the strain life constants. A Morrow modification is shown.

$$\left(\frac{\Delta s}{2} \right)_{R=-1.0} = \frac{\left(\frac{\Delta s}{2} \right)_{R \neq -1.0}}{\left(1 - \frac{s_m}{s'_f} \right)} \quad (3H.10)$$

This format is probably most amenable to HCF tests. A Goodman or Soderberg modification would replace σ'_f with σ_u or σ_y , respectively.

Finally, a modification of the SWT parameter utilized by GEAE was investigated using critical plane stresses and strains generated by this investigation, rather than the modified equivalent stresses.

$$Seq = 0.5 \{E \Delta \epsilon_1\}^w \{\sigma_1^{\max}\}^{(1-w)} \quad (3H.11)$$

The regression utilized was that obtained from GEAE by collapsing the type of data shown in Figure 3H.21. The results of the fitting process resulted in w from Equation (3H.11) being 0.433. The current biaxial data viewed in the context of this parameter is summarized in Figure 3H.22.

$$Seq = 7611 (N)^{-0.6471} + 65.4 (N)^{-0.03582} \quad (3H.12)$$

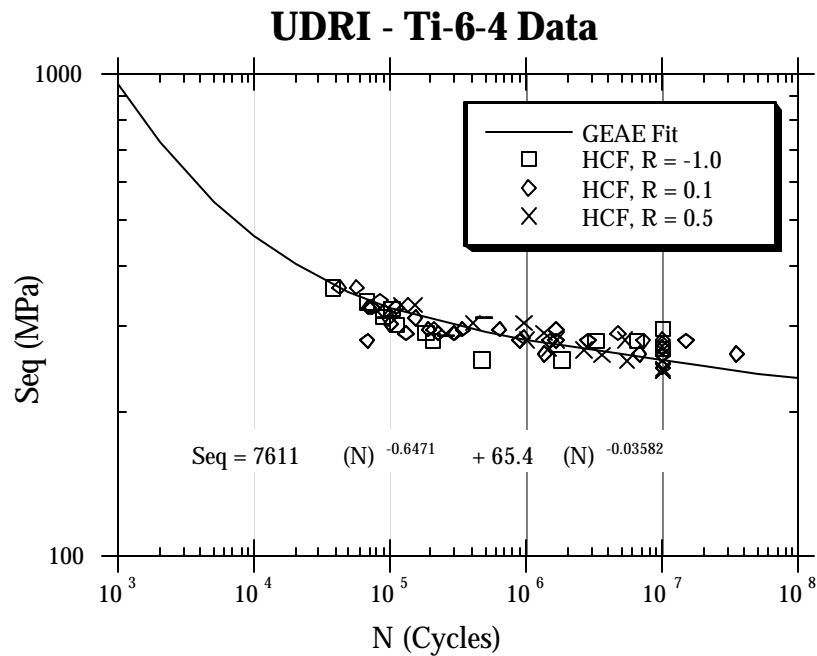


Figure 3H.21. GEAE baseline uniaxial data and regression.

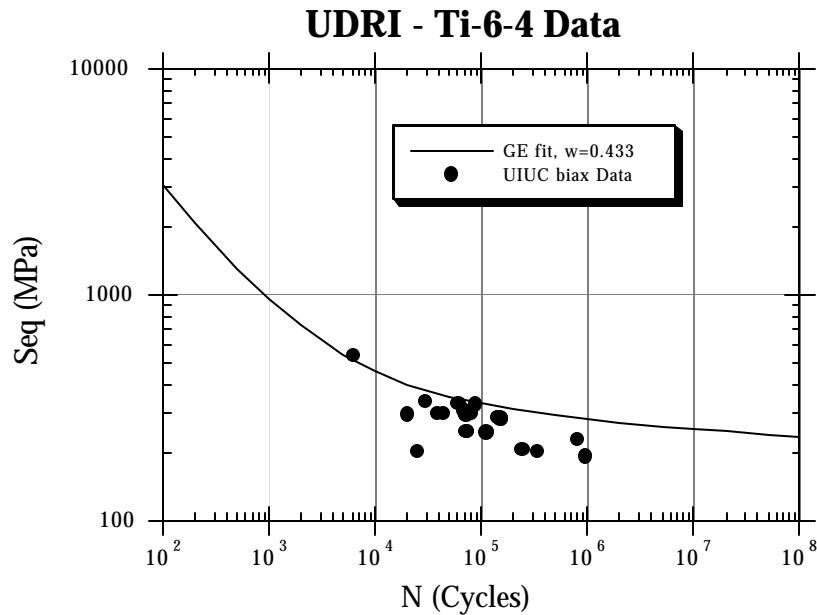


Figure 3H.22. UIUC biaxial data with GEAE damage parameter.

Finally the following table (Table 3H.4) views various data sets within the context of a lognormal distribution. The basis for comparison for these calculations was the ratio of experimental to predicted values of the damage parameter. Deviations from 1 for this methodology in a sense represent changes in loading condition. It also alleviates some of the skew inevitable when comparing experimental and predicted lives in the HCF regime where the Basquin slope is so shallow ($b \sim -0.035$).

Table 3H.4
Log-Normal Analysis of Life Prediction

Damage Parameter	Life Regime/ Data Set	Median ($N_{\text{exp}}/N_{\text{pred}}$)_{50%}	Standard Dev 1s	Standard Dev 3s
FKS, K=1.0	-1.0HCF	1.2518	0.2138	0.7575
SWT	-1.0HCF	1.0317	0.1242	0.4192
GE, Seq	-1.0 HCF	0.9862	0.0822	0.2676
FKS, K=1.0	-1.0LCF	1.1085	0.0827	0.2671
SWT	-1.0LCF	1.0061	0.0533	0.1687
FKS, K=1.0	0.5HCF	0.7583	0.0347	0.1090
SWT	0.5HCF	0.8728	0.1201	0.4120
GE, Seq	0.5HCF	1.0033	0.0425	0.1331
FKS, K=1.0	0.5LCF	0.9647	0.1921	0.6985
SWT	0.5LCF	1.0367	0.0542	0.1713
FKS, K=1.0	0.1HCF	0.9048	0.1335	0.4623
SWT	0.1HCF	0.9494	0.1018	0.3394
GE, Seq	0.1HCF	0.9936	0.0651	0.2085
FKS, K=1.0	0.1LCF	0.9758	0.2006	0.7339
SWT	0.1LCF	0.9383	0.0440	0.1381
FKS, K=1.0	All Biax	1.1336	0.1650	0.5706
FKS, K=0.6	All Biax	1.0080	0.1590	0.5561
SWT	All Biax	0.6936	0.2379	0.9862
GE, Seq	All Biax	0.8072	0.1336	0.4708

REFERENCES

- 3H.1 Kurath, P. and Jiang, Y., "Analysis of Residual Stresses and Cyclic Deformation for Induction Hardened Components," SAE Technical Paper Series No. 950707, Society of Automotive Engineers, Warrendale, PA, 15 pp., 1995.
- 3H.2 Jiang, Y. and Kurath, P., "Characteristics of the Armstrong-Frederick Type Plasticity Models," International Journal of Plasticity, Vol. 12, No. 3, pp. 387-415, 1996.
- 3H.3 Jiang, Y. and Kurath, P., "A Theoretical Evaluation of the Incremental Plasticity Hardening Algorithms for Cyclic Non-proportional Loading," Acta Mechanica, Vol. 118, pp. 213-234, 1996.
- 3H.4 Jiang, Y. and Kurath, P., "An Investigation of Cyclic Transient Behavior and Implications on Fatigue Life Estimates," ASME Transactions, Journal of Engineering Materials and Technology, Vol. 119, 1997.
- 3H.5 Jiang, Y. and Kurath, P., "Non-Proportional Cyclic Deformation: Critical Experiments and Analytical Modeling," International Journal of Plasticity, Vol. 13, No. 5, 1997.
- 3H.6 Smith, K. N., Watson, P. and Topper, T. H., "A Stress-Strain Function for the Fatigue of Metals," Journal of Materials, Vol. 5, No. 4, pp. 767-778, 1970.
- 3H.7 Kurath, P. and Fatemi, A., "Cracking Mechanisms for Mean-Stress/Strain Low Cycle Multiaxial Fatigue Loadings," Quantitative Methods in Fractography, ASTM STP 1085, B. M. Strauss and S. K. Putatunda eds., American Society for Testing and Materials, Philadelphia, PA, pp. 123-143, 1990.
- 3H.8 Kurath, P., Jiang, Y. and Fatemi, A., "Strain Path Influence on Multiaxial Deformation and Fatigue Damage," Chapter 8-2, SAE AE-14++, Society of Automotive Engineers, Warrendale, PA, To be published May 1999.
- 3H.9 Kurath, P., "Extension of the Local Strain Fatigue Analysis Concepts to Incorporate Time Dependent Deformation in Ti-6AL-4V at Room Temperature," TAM Report No. 464 UILU-ENG 84-6002 Department of Theoretical and Applied Mechanics, University of Illinois at Urbana-Champaign, (Ph.D. thesis).

Appendix 3I

FATIGUE-CRACK-NUCLEATION MODELING IN Ti-6Al-4V FOR SMOOTH AND NOTCHED SPECIMENS UNDER COMPLEX STRESS STATES

Donald Slavik



General Electric Aircraft Engines

**Submitted
28 August 1999**

ABSTRACT

Fatigue crack nucleation life models are required to predict safe stress and/or life limits for aircraft engine components. The Air Force is currently sponsoring several key programs to develop mechanistic life models. Examples for these models with comparisons to test data are given for Ti-6Al-4V. Elastic, elastic-plastic, and shear-based models are evaluated with smooth specimen fatigue tests from $10^3 \leq N_f$ (cycles) $\leq 10^9$ under variable mean loads under both strain-control and load-control conditions. Promising life models are then generalized for multiaxial stress states for evaluation with proportional and non-proportional tension-torsion fatigue tests. Finally, additional areas for life model improvement are explored by considering prediction of stress concentrations at notches from smooth specimen test results. Local notch stresses and stress gradients in the specimens are obtained from 3D elastic-plastic finite element analyses. Gradients are used to evaluate models based on: a) the peak local stress at the notch, b) stresses at a representative distance inward from the notch, and c) an average stress based on Weibull area considerations. The accuracy of the models is outlined along with a brief discussion of requirements and needs within a design system of life models for aircraft engine components.

INTRODUCTION

A number of different variables will influence the number of fatigue cycles a material can tolerate prior to fatigue crack nucleation and growth to final fracture. This behavior needs to be understood so that safe operating life and/or stress limits can be established for components in service. The needs of a lifing system for use in design further requires models that are: a) accurate and/or reasonably conservative over the entire life regime of interest, b) sufficiently general so that the methods can be used with confidence over a wide range of conditions, and c) easy to incorporate into efficient routines that can be easily used by design engineers that may not possess an expertise in fatigue life models.

The Air Force is currently sponsoring several key programs to develop mechanistic life models for aircraft engine components. This initial phase of this program has begun with testing and analysis for a single Ti-6Al-4V microstructure. The

test program goals are fairly general so that models can be evaluated over a wide range of lives ($10^3 \leq N_f \text{ (cycles)} \leq 10^9$), test type (load control and strain control), mean strains (0 to $\sim 0.9 s_{max}$), mean stresses (0 to $\sim 0.9 s_{max}$), stress state (tension, torsion, tension-torsion), stress state paths (proportional and non-proportional tension-torsion), and specimen configuration (smooth and notch geometry). Different life regimes with variable mean stresses are important when analyzing complex missions. Different stress states are important when dealing with components or edge of contact problems. (An example of the stress state for a point near the edge of contact as calculated from finite element results is shown in Figure 3l.1). Different notch geometries become important when analyzing components that are typically life-limited at stress concentrations. This test data will then be used to provide a fairly general assessment of various fatigue models used in industry and in the literature. The focus of the program will be in the long life regime, but model limitations over the entire fatigue regime examined will also be presented so that a robust life prediction model is developed.

APPROACH

Different fatigue crack nucleation models are assessed with test results in three major areas. First, the ability of the different models to correlate smooth specimen life is established under uniaxial applied stresses. Total strain-life models, elastic-plastic stress/total strain-based models, and shear-based models are considered with experiments for fatigue lives (N_f) ranging from 10^3 to 10^9 cycles. Test conditions include both load control and strain control with mean stresses/strains varying from ~ 0 to $\sim 0.9 s_{max}$. Next, the uniaxial data is used to establish constants for models that evaluate multiaxial stress states. Effective stress invariant models, a modified Smith-Watson-Topper model, and a shear-based Kurath-Fatemi-Socie critical plane model formulations are provided. Predictions from these models are then compared to multiaxial tests that include pure shear, proportional tension-torsion, and non-proportional tension-torsion stress states. Finally, additional areas for model improvements are explored by considering prediction of notched feature tests. Local notch stresses and stress gradients in the specimen are obtained from 3D elastic-plastic finite element analyses. Gradients are used to evaluate models based on: a) the peak local stress at the notch, b) stresses at a representative distance inward from the notch, and c) an average stress

based on Weibull-area considerations. The accuracy of the models are outlined along with a brief discussion of the needs within a design system of life models for aircraft engine components.

EXPERIMENTAL PROGRAM

Material

All specimens were from the Ti-6Al-4V plates in the Air Force PRDA V program. All specimens were machined, stress relieved, and chem milled to eliminate residual stresses and surface damage.

Test Procedure and Data Analysis

Uniaxial Stress State Tests: Smooth specimen fatigue tests were performed for uniaxial stress states to obtain baseline life properties. Test results including the strain range maximum stress, R-ratio ($R_e = e_{min}/e_{max}$ for strain control or $R_s = s_{min}/s_{max}$ for load control), and corresponding fatigue life for each specimen is summarized in Table 3I.1a-c. Fatigue tests performed in strain control were tested in closed loop fatigue machines at 0.333 Hz (20 cycles/minute) by Pratt and Whitney. AlliedSignal, GEAE, Pratt and Whitney or the AFRL tested fatigue tests performed in load control at 60 to 1000 Hz. Long life tests in load control were performed as step tests with life blocks (***DN***) of 10^7 or 10^9 fatigue cycles. Step tests began at a specific stress and R-ratio for ***DN*** cycles. If a step test did not fail within the specified life block, the maximum stress was increased 10% prior to performing an additional life block. This process was continued until specimen failure occurred. The advantage of this testing approach over conventional S-N methods is that all specimens will be tested to failure so that an endurance limit can be estimated with a limited number of test specimens. The failure stresses for each step tests are established based on an interpolation suggested by T. Nicholas (**REF**) based on the life of the last fatigue block and the stresses of the last two steps prior to failure.

Tension-Torsion Stress State Tests: Smooth specimen fatigue tests were performed for tension-torsion stress states to check multiaxial fatigue models. The grip section diameter of the specimen (0.75 inch) was dictated by the thickness of the forging. A tubular specimen was considered for this program but rejected given: a) a tubular specimen wall thickness of less than 0.040 inch that would be required for the

thin wall approximation would be difficult to machine and could be subjected to torsional buckling, and b) it would be difficult to ensure the chem-milled surface on the inside of a tube would be equivalent to the surface on the outside of the solid bars throughout the program. Given these considerations a solid smooth specimen bar was employed for the multiaxial test program.

The multiaxial fatigue tests were conducted on a closed loop servohydraulic tension-torsion machine with an axial load capacity of 100 kips and 44 kip-inch. Load cells were calibrated within the lower 10% of the machine maximum load capacity and found to be linear within 0.05% of the anticipated test range. Strains were measured with a modified MTS model 632-85 biaxial extensometer with conical points. The modification involved strain gauging the existing flexure elements to measure torsional strains. The extensometer gage length was 1.0 inch with a full axial calibration of 2.5%. Nonlinearity of this measurement was less than 0.5% full scale and torsional full-scale rotations of $+5^\circ$ were linear to within 0.3% of full scale. Maximum cross talk between the axis was 0.5% of either full scale. Specimen dimension and machine capabilities limited the maximum frequency of the tests to approximately 2 Hz. All test levels were initially started at low load levels to insure the extensometer was well seated on the specimen before beginning the tests in strain control at 0.5 Hz. A limited number of tests were eventually switched to load control and run at 2 Hz if the stabilized cyclic deformation was linear elastic. Torsion with variable torsional mean stresses, proportional tension-torsion, and non-proportional tension torsion stress profiles were evaluated with tests for fatigue lives from 10^4 to 10^6 cycles. Tension-torsion profiles are considered to be non-proportional when all strain components do not extrapolate linearly through zero strain. The specimen IDs, test frequency, and strain mission is given in Tables 3I.2a-3I.2b. The 90° out-of-phase profile was considered since this profile has been identified to be highly damaging for some materials (Table 3I.2b). The strain mission is provided for the 90° out-of-phase case where it is not clear which points in the mission are most damaging for the fatigue cycle.

Double-Edged Notched Specimen Tests with Axial Applied Loads: Complex geometry specimens are used to evaluate models for cases where steep stress gradients exist. The double-edged notched specimen geometry considered was flat

(0.142 inch thick by 0.236 inch wide) with 2 symmetric V-notches that are 0.071 inch deep with a 0.021 inch root radius. A number of notched bar fatigue tests was performed by the PRDA program in load control with test frequencies ranging from 60 to 1000 Hz. A single DEN specimen with a fatigue life of 10^6 for this notch geometry is used to evaluate different damage parameters as compared to different notch geometries and smooth specimens. The specimen ID #, notch configuration, and fatigue life for the selected specimen is given in Table 3I.3 (first specimen listed). Stress analysis of the specimen geometry and the finite element model is described later.

Edged Notched in the Blade tip Specimen Geometry under 4-point Bending: A specimen geometry simulative of the leading edge of an airfoil is used to further evaluate life prediction methods for more complex specimen geometries. A sharp-tip geometry with a 0.010 inch leading edge diameter was used to simulate the leading edge of a fine tip airfoil. This geometry was tested in both the unnotched and notched configurations. The notch root radius, notch root radius, and notch orientation is summarized in Table 3I.3. The 90°-notch orientation is in the normal orientation, while the 33° notch orientation is skewed. Notch configurations at the leading edge were machined into the specimens followed by a stress relief and chem-milling similar to the smooth specimen machining instructions. A blunt tip geometry with a 0.030 inch leading edge diameter was used to simulate a blunt tip airfoil. All leading edge simulation specimens were tested in 4-point bending in load control at 60 Hz with step tests ($DN = 10^6$ life blocks). Details concerning the specimen geometry and test set-up are supplied elsewhere.

STRESS ANALYSIS FOR SMOOTH AND NOTCHED FATIGUE SPECIMENS

LCF tests performed by Pratt and Whitney were used to determine the elastic modulus and the stress-strain behavior for the PRDA Ti-6Al-4V material. For this characterization, stabilized values of maximum stresses against the maximum strains are recorded for each specimen near the half-life. Test data at various R ratios with the Ramberg-Osgood correlation are shown in Figure 3I.2. The curve will be used for all subsequent elastic-plastic analyses.

Elastic-plastic analysis of the tension-torsion test specimen geometry was performed with the finite element analysis code ANSYS. One-half of the specimen gage section within the 1.0 inch extensometer attachments was modeled with a 3D-wedge sector assuming symmetry boundary conditions. Twist and axial displacement boundary conditions were applied to the model based on the strains for each specimen (Table 3I.2). The analysis focused on the tension-torsion tests that contained 2-3 key mission points. Maximum stress points were modeled assuming the Ramberg-Osgood correlation shown in Figure 3I.2. Minimum stress points were modeled assuming elastic unloading from the maximum stress point. This is directly applicable to aircraft engine components where initial plasticity is typically followed by elastic cycling conditions. Calculated stress components for the tension-torsion tests are given in Table 3I.2¹. The same approach was used to obtain maximum and minimum stresses in the notched and simulated blade tip geometries. Stresses for the double-edged V-notch specimen geometry with a 0.021 inch root radius was established with a 3D model. One quarter of the model was built with symmetry boundary conditions. A representative model of the notch is shown in Figure 3I.3. Stresses for the blade tip geometry was established with a 3D model of half of the specimen geometry with symmetry conditions. Representative models for the blade models with notches are shown in Figures 3I.4 and 3I.5. The 90° and 33° skewed notch orientation are clearly shown in Figures 3I.4 and 3I.5, respectively. The peak effective stress locations is at the notch tip away from the corners of the notch. Stresses were obtained with the boundary conditions for the test specimens that resulted in a 10⁶-fatigue life.

¹ The tension case (156-11) with cyclic plasticity is not applicable to aircraft engine components and was not considered in this analysis. The stresses for the non-proportional 90°-phase shift test (156-8) were also not available when the life analysis was completed and has also not been included in this report.

UNIAXIAL LIFE PREDICTION MODELS

Life Prediction Using Walkerized Pseudostress: Life prediction models based on the pseudostress (s_{psu}) are defined from the total strain amplitude ($\Delta\epsilon/2$) and the elastic modulus (E) as given in Equation (3I.1).

$$s_{psu} = (E\Delta\epsilon / 2) \quad (3I.1)$$

A significant advantage of the pseudostress approach is that this parameter can be obtained for specimens or components with only an elastic analysis given the maximum stress, mean stress, and plastic strain is not used for this life prediction parameter. The observed life versus the pseudostress range for specific R ratios = -1, 0.1, 0.5, and 0.8 is shown in Figure 3I.6. The observed specimen life was dependent on the pseudostress amplitude and R_e , but did not appear to depend on the test control mode or the test frequency given tests designated as HCF and LCF are continuous at each R -ratio. (Note: tests designated as HCF were run in load control at 60-1000 Hz frequencies).

The influence of the mean strain on the fatigue life can be obtained using a pseudostress with a Walker mean strain correction as given in Equation (3I.2).

$$s_{walk} = (E\Delta\epsilon / 2)(1 - R_e)^{1-m} \quad (3I.2)$$

where s_{walk} is the Walkerized pseudostress amplitude and m is a material curve fitting constant to collapse variable R_e data. This approach is still relatively easy to use for specimen or component stress analysis given the parameter is calculated from an elastic analysis only. The approach accurately predicts the trends of decreased fatigue life with increasing R_e , but does not collapse the data into a single curve over the entire life regime with a single value of m (Figure 3I.7). Walkerized pseudostress typically over-predicts the impact of R_e in the moderate and short life regime ($N_f < 10^5$ cycles) where initial plasticity is significant so that mean stresses and lives tend to be independent of R_e . The selected value of $m = 0.8$ also tends to under-predict the impact of R_e in the high life regime ($N_f > 10^5$ cycles, Figure 3I.7). These effects are drawbacks of the Walkerized pseudostress approach.

Life Prediction Using Equivalent Stress: Life prediction models are also available based on stresses and strains from an elastic-plastic analysis. An equivalent stress life prediction parameter (s_{equiv}) is defined in Equation (31.3).

$$s_{equiv} = 0.5 (E\Delta e)^w (s_{max})^{1-w} \quad (31.3)$$

where s_{equiv} is the alternating Walker equivalent stress, E is the average elastic modulus for the PRDA V material, Δe is the total strain range, and s_{max} is the maximum stress as measured on test specimens or calculated with elastic-plastic finite element stress analyses. The Walker equivalent stress exponent w is a material and temperature-dependent constant that collapses variable mean stress data into a single life curve. Given the focus of LCF/HCF life prediction for aircraft engine components is in the intermediate and long life regime, elastic cycling conditions typically dominate so that $E\Delta e \gg Ds_{psu} \gg Ds$. This can be used to establish Equation (31.4) as:

$$s_{equiv} = 0.5 (\Delta s_{psu})^w (s_{max})^{1-w} \quad (31.4)$$

This approach is essentially identical to the equivalent strain parameter that has been shown in the literature to collapse R_e data for a number of different materials. This approach: a) does require an elastic-plastic analysis, b) does not require a plastic strain range term that is typically extremely small in the life regime of interest to aircraft engine components, c) predicts a decrease in the importance of R_e on life in the short life regime. An additional advantage of this approach is that a single curve collapses test data over the entire life regime unlike the Walkerized pseudostress approach (Figure 31.8).

Life Prediction Using Shear-Based Parameter: Critical-plane life prediction models that are shear-based have also been proposed in the literature. The Kurath-Fatemi-Socie parameter in particular has shown promise for different materials over a wide range of lives for both uniaxial and multiaxial applied stress states. This parameter can be simplified for uniaxial stress states as given in Equation (31.4).

$$g_{uniaxial}^* = 0.5 (1+n) \Delta e \left[1 + K s_{max} / 2 s_{ys} \right] \quad (31.4)$$

where $g_{uniaxial}^*$ is the life parameter as proposed by Kurath-Fatemi-Socie simplified for uniaxial stress states, s_{max} is the maximum stress measured on test specimens or calculated with an elastic-plastic analysis, ν is Poisson's ratio, s_{ys} is the yield strength, and K is a material constant used to collapse multiaxial or uniaxial test data at various

R-ratios. s_{ys} was taken to be 109 ksi as established with a 0.02% plastic offset from Figure 3I.2. Poisson's ratio was taken to be 0.349 based on strain gage measurements in the elastic regime. The uniaxial data with the shear based life prediction parameter for the uniaxial data with $K = 1$ are shown in Figure 3I.9. The shear-based critical plane parameter works well in the intermediate life regime ($N_f < 105$ cycles), but generally under-predicted the influence of R_e in the intermediate to long life regime. A least square regression to establish a best-fit K and a regression through the data would be required to quantify the ability of this model to collapse smooth specimen fatigue results under uniaxial applied stresses. This was not attempted given the focus of the efforts by GEAE were on equivalent stress approach.

MULTIAXIAL LIFE PREDICTION MODELS

Modified Smith-Watson-Topper (SWT) Critical Plane Model: A number of critical plane models have been proposed in the literature for crack nucleation life prediction. The Smith-Watson-Topper parameter is one of the critical plane parameters that are defined by principal stress and strain terms. One form of the SWT parameter is given below in Equation (3I.5).

$$SWT = 0.5 \Delta \mathbf{e}_{11} s_{\max,11} \quad (3I.5)$$

where SWT is the damage metric, $\Delta \mathbf{e}_{11}$ is the total strain range normal to the critical plane, $s_{\max,11}$ is the maximum stress normal to the critical plane, and the critical plane is defined to be the plane where SWT is a maximum. Introducing a single additional adjustable constant to collapse variable R-ratio data, the SWT parameter can be modified slightly as given in Equation (3I.6).

$$SWT = 0.5 (E \Delta \mathbf{e}_{11})^w (s_{\max,11})^{1-w} = 0.5 (\Delta s_{psu,11})^w (s_{\max,11})^{1-w} \quad (3I.6)$$

This slight modification to the SWT equation is identical to the Walkerized equivalent strain amplitude given the SWT parameter is maximized along the applied stress direction for uniaxial loading. This minor modification allows the correlation established from uniaxial tests (Figure 3I.8) to be used when assessing a modified-SWT parameter for more complex stress states. Predictions using the SWT parameter identified in Equation (3I.6) with a search routine that identifies maximum SWT on all planes for the tension-torsion fatigue test results is required. Preliminary results at the

University of Illinois by Dr. Peter Kurath indicate that the SWT Equation (3I.5) or the modified-SWT parameter Equation (3I.6) significantly under-predicted the life of selected torsion and non-proportional tension-torsion fatigue tests. The model was highly non-conservative for some of these fatigue tests, making it an unlikely candidate for use in a design system for the PRDA V material if these preliminary conclusions remain.

Kurath-Fatemi-Socie (KFS) Shear-Based Critical Plane Model: A number of shear based critical plane models have also been proposed in the literature. Materials where crack nucleation is controlled by shear processes have been used to identify shear-based critical plane models. Though a number of different shear-based models exist in the literature, the Kurath-Fatemi-Socie (KFS) model has been particularly successful. The general form of the KFS model for multiaxial stresses is given in Equation (3I.7).

$$g^* = 0.5 \Delta g \left[1 + K s_n / s_{ys} \right] \quad (3I.7a)$$

where g^* is the KFS damage metric, Dg is the shear strain range on the critical plane, and σ_n is the maximum stress normal to the critical plane. Given $G Dg = Dt_{psu} \gg Dt$ initial plasticity followed by elastic cycling is the problem of interest, Equation 3I.7a can be written solely with stresses as:

$$t^* = 0.5 \Delta t_{psu} \left[1 + K s_n / s_{ys} \right] \quad (3I.7b)$$

where t^* is now the damage metric and G is the elastic shear modulus. A search routine is required to establish the critical plane for the tension-torsion test results with maximum t^* calculated for each specimen based on measured strains with the stresses established from elastic-plastic finite element analysis given in Table 3I.2. Predictions using the KFS model as compared to the correlation parameter using the uniaxial test results are required to quantitatively assess the model. The KFS parameter-life correlation from uniaxial data at variable R_e is under development.

Stress Invariant Effective Stress Life Parameters: A disadvantage of the critical plane life models lie in the need to establish the critical plane prior to calculating the life controlling parameter. This requirement is not a major factor for single cycles under uniaxial stress states, but this can be particularly computationally intensive for large missions with multiaxial stresses that may be non-proportional. Alternatively, stress

invariant life parameters instead offer an approach for life calculation that is independent of the coordinate system without the need to calculate a critical plane orientation. Stress invariant models are available within the crack nucleation code NASALIFE. The stress invariant effective stress range is defined from Equation (3I.8) as:

$$\Delta \mathbf{s}_{psu} = \frac{1}{\sqrt{2}} \sqrt{(\Delta \mathbf{s}_{xx} - \Delta \mathbf{s}_{yy})^2 + (\Delta \mathbf{s}_{yy} - \Delta \mathbf{s}_{zz})^2 + (\Delta \mathbf{s}_{zz} - \Delta \mathbf{s}_{xx})^2 + 6(\Delta \mathbf{s}_{xy}^2 + \Delta \mathbf{s}_{yz}^2 + \Delta \mathbf{s}_{zx}^2)} \quad (3I.8)$$

where \mathbf{Ds}_{psu} is the alternating pseudostress range, and \mathbf{Ds}_{ij} defines the pseudostress range for each stress component based on maximum and minimum points in the fatigue cycle. All stresses for the multiaxial tests are calculated assuming initial plasticity using constants given in Figure 3I.2 followed by elastic unloading given this is the problem of interest in life prediction for aircraft engine components. Given that the stress ranges are elastic allows Equation (3I.8) to be given on a pseudostress basis. This approach is also consistent with the analysis of the uniaxial fatigue data as given in Equation (3I.2) where $\mathbf{s}_{max} = \mathbf{s}_{mean} + 0.5\mathbf{Ds}_{psu}$.

The Manson-McKnight mean stress term used to establish \mathbf{s}_{mean} and \mathbf{s}_{max} is given as:

$$\mathbf{s}_{mean} = \frac{\mathbf{b}}{2\sqrt{2}} \sqrt{(\Sigma \mathbf{s}_{xx} - \Sigma \mathbf{s}_{yy})^2 + (\Sigma \mathbf{s}_{yy} - \Sigma \mathbf{s}_{zz})^2 + (\Sigma \mathbf{s}_{zz} - \Sigma \mathbf{s}_{xx})^2 + 6(\Sigma \mathbf{s}_{xy}^2 + \Sigma \mathbf{s}_{yz}^2 + \Sigma \mathbf{s}_{zx}^2)} \quad (3I.9)$$

where \mathbf{s}_{mean} is the mean stress, and $\Sigma \mathbf{s}_{ij}$ defines the summed stress for each stress component based on maximum and minimum points in the fatigue cycle. The Manson-McKnight coefficient ($\mathbf{b}=\mathbf{b}_{MM}$) is defined as:

$$\mathbf{b}_{MM} = \frac{(\Sigma \mathbf{s}_{xx} + \Sigma \mathbf{s}_{yy} + \Sigma \mathbf{s}_{zz})}{|\Sigma \mathbf{s}_{xx} + \Sigma \mathbf{s}_{yy} + \Sigma \mathbf{s}_{zz}|} \quad (3I.10a)$$

where \mathbf{b}_{MM} produces the sign on the mean stress term. The mean stress equation is well defined for many stress states, but the sign is poorly defined for torsional mean stress missions where small changes in the sign of first stress invariant (\mathbf{s}_{ij}) can result in large changes of the calculated mean stress. This problem is avoided with a Modified Manson-McKnight mean stress coefficient ($\mathbf{b}=\mathbf{b}_{MM+}$) defined as:

$$\mathbf{b}_{MM+} = \frac{(\Sigma \mathbf{s}_1 + \Sigma \mathbf{s}_3)}{(\Sigma \mathbf{s}_1 - \Sigma \mathbf{s}_3)} \quad (3I.10b)$$

where $\Sigma \mathbf{s}_1$ is the sum of the first principle stresses at the maximum and minimum stress points in the fatigue cycle and $\Sigma \mathbf{s}_3$ is the sum of the third principle stress at the

maximum and minimum stress points in the fatigue cycle. This result leads to the prediction that torsional mean stresses are not important in life prediction which is typically a similar conclusion drawn in the literature. The analysis of the multiaxial test results with Equations (3I.8-3I.10b) as compared to the fatigue curve as established from uniaxial test data is shown in Figure 3I.10. The multiaxial tests were not used for the life model with nearly all of the tests within the -3s regression.

NOTCHED FATIGUE LIFE PREDICTION MODELING

The final step in the development of HCF-LCF crack nucleation methods focused on life-modeling for notch geometries. These efforts focused on five different geometries where the experimental life was approximately 10^6 cycles. Different specimen and notch geometries at similar test lives are given in Table 3I.3. The average load for each specimen geometry was used to perform an elastic-plastic stress analysis for the maximum load case followed by elastic unloading. Given these cases resulted in a similar fatigue life, it is expected that the life prediction method should produce a similar damage metric. The Walkerized equivalent stress amplitudes with the Modified Manson-McKnight multiaxial model was used to evaluate feature test life models since these methods worked reasonable well for smooth specimens under uniaxial and multiaxial stress states. The Walkerized equivalent stress amplitude gradients as a function of depth below the surface of the notch from the maximum effective stress location is shown in Figure 3I.11. The stresses for both the smooth and unnotched blade geometries (sharp tip) are approximately 41ksi and constant below the surface given there is no stress concentration for these geometries. The peak local stresses for the notch geometries at zero distance are substantially higher than the stresses for the unnotched geometries with these specimens with the same measured fatigue life. This reflects the fact that higher loads are required to produce failure in the notch as compared to smooth specimens using the same s_{equiv} life metric. The predictive capability improves if an averaged s_{equiv} for elements near the surface are used as the damage metric. Yet this approach still does not significantly improve the correlation for the machined notch in the sharp tip specimen given calculated s_{equiv} is substantially higher as compared to all other geometries at a substantial distance (7 mils) in from the surface of the notch. Similarly, alternative methods did not initially offer much promise

to correlate the observed life of the machined notch in the sharp tip geometry given this geometry had the largest depth of initial plasticity and the highest stress ranges for the elastic cycling.

These difficulties led GEAE to the consideration of a weak link approach to evaluate the fatigue crack nucleation life for stress concentrations. This approach recognizes that it is less likely for a weak grain to exist at the surface of a small notch as compared to the probability of finding a weak grain on the surface of a very large notch or a smooth specimen. Weakest link approaches are routinely applied to monolithic ceramics and high strength composite fibers. This describes how the weak link approach was employed for the notched titanium specimens: The stressed surface area was evaluated as compared to volume since nearly all of the nucleation sites appeared to be on or very near the surface for the notched and smooth bar specimens.

The weak link approach begins with the assumption that the probability of survival (R_o) for a small area (ΔA_i) subject to a stress (s_i) is given by

$$[R_o(s_i)]^{\Delta A_i}$$

Therefore, the probability of survival for all of the stressed surface areas (R) is given by

$$R = \prod_{i=1}^n [R_o(s_i)]^{\Delta A_i}$$

Where,

$$\prod_{i=1}^n [F_i] = F_1 * F_2 * F_3 * \dots * F_n$$

If we take the natural log of the expression for R , we get

$$\ln(R) = \sum_{i=1}^n \ln[R_o(s_i)] \Delta A_i \quad (3I.11)$$

Assuming the probability of survival for the i^{th} area (R_o) has a two-parameter Weibull distribution, the probability for survival is given by:

$$R_o(s) = \exp \left[- \left(\frac{s}{b} \right)^a \right] \quad (3I.12)$$

where a is the shape factor and b is the scale parameter. If we substitute Equation (3l.12) into (3l.11), we get

$$\ln(R) = \sum_{i=1}^n \left[- \left(\frac{s_i}{b} \right)^a \right] \Delta A_i \quad (3l.13)$$

Since β is a constant, we can re-rewrite Equation (3l.13) such that

$$\ln(R) = \left(\frac{s_{\max}}{b} \right)^a \sum_{i=1}^n \left[- \left(\frac{s_i}{s_{\max}} \right)^a \right] \Delta A_i \quad (3l.14)$$

where s_{\max} is a constant. Now let us consider two cases (Case 1 and Case 2), and for Case 1, we can write

$$\ln(R_1) = \left(\frac{s_{\max,1}}{b} \right)^a \sum_{i=1}^n \left[- \left(\frac{s_{i,1}}{s_{\max,1}} \right)^a \right] \Delta A_{i,1}$$

or

$$\ln(R_1) = \left(\frac{s_{\max,1}}{b} \right)^a F_{S_1}$$

where

$$F_{S_1} = \sum_{i=1}^n \left[- \left(\frac{s_{i,1}}{s_{\max,1}} \right)^a \right] \Delta A_{i,1}$$

Similarly, we can write

$$\ln(R_2) = \left(\frac{s_{\max,2}}{b} \right)^a F_{S_2}$$

where

$$F_{S_2} = \sum_{i=1}^n \left[- \left(\frac{s_{i,2}}{s_{\max,2}} \right)^a \right] \Delta A_{i,2}$$

If the average lives of the two cases are the same, we can say

$$\ln(R_1) = \ln(R_2)$$

or

$$\left(\frac{s_{\max,1}}{b} \right)^a F_{S_1} = \left(\frac{s_{\max,2}}{b} \right)^a F_{S_2}$$

Rearranging this expression we get

$$s_{\max,1} = \left(\frac{Fs_2}{Fs_1} \right)^{\frac{1}{a}} s_{\max,2} \quad (3I.15)$$

where

$$Fs_j = \sum_{i=1}^n \left[- \left(\frac{s_{i,j}}{s_{\max,j}} \right)^a \right] \Delta A_{i,j} \quad (3I.16)$$

Fs_j can be calculated for any notch geometry and loading from the elastic-plastic results of the finite element analyses.

At this point, we introduce a couple small variations in the approach. We can substitute the maximum equivalent alternating stresses (Δs_{eq}) for $s_{\max,1}$ and $s_{\max,2}$ in Equation (3I.15) to get

$$\Delta s_{eq,1} = \left(\frac{Fs_2}{Fs_1} \right)^{\frac{1}{a}} \Delta s_{eq,2} \quad (3I.17)$$

where the equivalent alternating stress is calculated using a modified Manson-McKnight multiaxial model and a Walker equivalent stress model. The approach was slightly modified to use principal stresses in the calculation of the Fs term as opposed to effective stress values (Equation (3I.16)). This was done so that tensile and compression stresses on the surface would not be treated in the same manner. Equations (3I.16) and (3I.17) form the core the proposed approach and were applied to several specimen configurations.

For this evaluation, the smooth bar 10^6 equivalent alternating stress is used for the baseline. Based on the regression results from the HCF/LCF portion of the program, the average equivalent alternating stress to produce a 10^6 cycle failure in the smooth bar specimens was 40.86 Ksi ($\Delta s_{eq,1-Measured}$ to 40.86 Ksi). Fs_1 was calculated for this geometry based on the 1000 Hz smooth specimen surface area (i.e., radii regions were ignored) to produce $Fs_1 = 0.161$. Fs_2 for the other geometries was calculated using Equation (3I.16). The adjusted Walkerized equivalent stress for each geometry was modified based on the Fs value using Equation (3I.17). The results of

those evaluations are shown in Figure 3I.12. The horizontal lines represent the mean and plus and minus three standard deviations as established from smooth specimen results (Figure 3I.12). Three values of the Weibull modulus are shown. The value of 17.0 is based on the value for the distribution of all the smooth specimen data (Figure 3I.12); the value of 28.0 is based on smooth specimen results in the vicinity of 10^6 cycles; the value of 35.0 is based on the value with the best prediction for the notched tests. The Walkerized equivalent stress predictions for the notched and smooth specimen geometries improve as a damage metric for stress concentrations when this is corrected based surface area modification. Predictions of the stress concentrations are within -3s scatter bars as obtained from the uniaxial test results. The best Weibull moduli and the applicability of the approach over a larger range of life could be evaluated further by considering additional notched fatigue tests in the program.

DISCUSSION

A number of different areas of fatigue-crack-nucleation-life prediction have been evaluated and compared against Ti-6Al-4V laboratory test data. Influences of machining and residual stresses that complicate life method development have been intentionally minimized by stress relieving + chem-milling all specimens.

Method and correlation parameters were presented first developed for uniaxial stress states over a wide range of life, strain ranges, and mean stresses. Given critical locations in aircraft engine components are typically uniaxial in nature (corner location of a bolthole under tension + out-of-plane bending as an example) with an R-ratio near 0 (zero-maximum take-off stress-zero), it is typical to perform the majority of the fatigue tests under uniaxial stress states near $R = 0$ (Table 3I.1.c). However, this idealization even for uniaxial stress states does not eliminate the need for life models that are robust in nature. Non-zero minimum stresses in a fatigue cycle are routinely encountered given thermal stresses or high cycle fatigue conditions can drive minimum stresses in a fatigue cycle to values much greater than or less than zero depending on the application. And though the focus of this particular program is in the high cycle fatigue regime, the design engineer also needs models that are easy to use over the entire life regime where fatigue calculations can establish life or stress limits. Walkerized equivalent strain reasonably correlated the uniaxial stress fatigue data over the entire life regime

without a model bias when treating mean stresses, so this model was evaluated further for more complex conditions.

Specifically, models evaluated for uniaxial stress states were then generalized to account for multiaxial stress states so the models could be compared to multiaxial test data. This approach is practical and can also provide a basis to evaluate strengths and weaknesses of different models equally. It would be difficult to justify the use of a multiaxial fatigue life model that required multiaxial test data unless the predictive capabilities offered a significant improvement given multiaxial test data is relatively costly and difficult to obtain. Instead, the multiaxial tests in the program were only used to validate multiaxial models where the model constants were strictly based on uniaxial results. This approach would allow stress invariant models, a modified version of the Smith-Watson-Topper model, and shear-based critical plane models to be compared on an equal basis independent of the curve-fit or additional model constants that make direct model comparisons difficult. This approach identified a stress invariant model that could predict the influence of multiaxial stress states and could easily be programmed into a crack-nucleation-life prediction program NASALIFE for use in design. These factors should be considered as additional work on multiaxial life methods is evaluated in future work on the HCF follow-on program.

Finally, models that accounted for life prediction of feature tests were considered at a selected life of 10^6 for different notch geometries. Peak local stresses can be a fairly conservative indicator for the expected life of notched test specimens when the peak stresses were contained within a relatively small area on the specimen. Averaged stresses over small distances near the surface tend to improve the correlation, but this still did not explain the enhanced capability of specimens geometries when a very small surface area contained high stress material (fine tip notch geometry). These observations led to development of an area-weighted correction to the peak stress based on a probabilistic/weakest-link theory for fatigue. This approach would not impact the smooth specimen uniaxial and tension-torsion fatigue results where the surface stresses are constant, but it did produce a correlation for the notched test specimens with a wide array of notch configurations and stress gradients. Future work should include the evaluation of this parameter for different R-ratios and stress ranges

as well as an evaluation for more complex multiaxial stress states. These factors should be considered as additional work on notched fatigue methods is evaluated in future work on the HCF follow-on program.

CONCLUSIONS

- Different life methods that predict the influence of strain range and mean stresses on fatigue life for uniaxial stress states have been presented. The total strain range ($\Delta\epsilon$) or Walkerized pseudostress (s_{walk}) based on the total strain range and strain R-ratio are relatively easy to use in design since elastic-plastic stress analysis is not required for this parameter. However, this parameter was somewhat inferior to the Walkerized equivalent stress methods that incorporate the total strain range and maximum stress into the damage metric. Limited work was also presented comparing the Kurath-Fatemi-Socie (KFS) shear-based parameter to uniaxial test data. Additional work assessing the KFS and other shear-based parameters would provide a quantitative basis to establish if additional improvement in a life prediction correlation is possible for the uniaxial test data in the program.
- Limited results were presented comparing a modified version of the Smith-Watson-Topper (SWT) critical plane model and the shear-based KFS critical plane models as compared to a stress invariant model. An approach was presented so that multi-axial model constants are established solely from uniaxial test data. This approach is practical in nature given: a) it provides a reasonable way to compare different models equally, and b) multiaxial test data would be difficult to generate for all materials and temperatures of interest unless this was essential to improve life prediction methods. Preliminary results indicate that a SWT model modified to use the Walkerized equivalent stress correlation for baseline constants did not accurately predict life for multiaxial test results in this program. Preliminary results indicate that the predictions using the KFS and the stress invariant models were similar. An advantage of the stress invariant model is that these models allow the life to be calculated independent of a critical plane that can be computationally intensive to establish. Additional work quantifying the predictions of the SWT, KFS, and other multiaxial models as compared to the quantitative assessment given for the stress invariant model should be explored in future work. Guidelines to simplify the

determination for the critical plane would also be helpful given long mission with non-proportional stresses and varying temperature can be computationally intensive in the design environment.

- Utilizing peak stress with smooth specimen life methods can be overly conservative for life prediction for notches with stress concentrations. This observation led to an area-weighted stress correction based on a probabilistic/weakest-link theory for fatigue. This approach dramatically improved the correlation for the geometries considered that include: a) a smooth specimens, b) a sharp tip airfoil geometry, c) a sharp and blunt tip airfoil geometry with a notch. Additional work still needs to focus on utilizing the approach for a wider range of R-ratios, lives, and multiaxial stress states with an understanding of how the approach would be implemented in a design environment.

Table 3I.1a
Smooth Specimen Fatigue Results (R = -1)

Source	Test Type	R_ϵ or R_σ	freq (Hz)	$\Delta\epsilon$ (%)	σ_{\max} (ksi)	Life (cycles)
P&W	Strain Cntrl	-1.0	0.33	1.37670	112.26	5,319
P&W	Strain Cntrl	-1.0	0.33	1.29780	105.74	6,737
P&W	Strain Cntrl	-1.0	0.33	1.19780	101.50	9,700
P&W	Strain Cntrl	-1.0	0.33	1.00090	85.06	20,199
P&W	Strain Cntrl	-1.0	0.33	0.90320	79.23	48,537
Allied	Load Cntrl	-1.0	60.0	0.91879	77.50	37,767
Allied	Load Cntrl	-1.0	60.0	0.85951	72.50	68,227
Allied	Load Cntrl	-1.0	60.0	0.80024	67.50	88,303
Allied	Load Cntrl	-1.0	60.0	0.82988	70.00	103,346
Allied	Load Cntrl	-1.0	60.0	0.77060	65.00	112,506
Allied	Load Cntrl	-1.0	60.0	0.74096	62.50	183,276
Allied	Load Cntrl	-1.0	60.0	0.71132	60.00	205,774
Allied	Load Cntrl	-1.0	60.0	0.65205	55.00	474,975
Allied	Load Cntrl	-1.0	60.0	0.65205	55.00	1,834,570
Allied	Load Cntrl	-1.0	60.0	0.71132	60.00	3,247,816
Allied	Load Cntrl	-1.0	60.0	0.71132	60.00	6,553,514
Allied	Step Tst	-1.0	60.0	0.68536	57.81	10,000,000
Allied	Step Tst	-1.0	60.0	0.68761	58.00	10,000,000
Allied	Step Tst	-1.0	60.0	0.75733	63.88	10,000,000

Table 3I.1b

Smooth Specimen Fatigue Results (R = 0.5 and 0.8)

Source	Test	R_ϵ or R_σ	freq (Hz)	$\Delta\epsilon$ (%)	σ_{\max} (ksi)	Life (cycles)
P&W	Strain Cntrl	0.5	0.33	1.40000	114.60	4,802
P&W	Strain Cntrl	0.5	0.33	1.00000	113.40	13,790
P&W	Strain Cntrl	0.5	0.33	0.80000	113.80	26,336
P&W	Strain Cntrl	0.5	0.33	0.60670	116.05	34,064
P&W	Strain Cntrl	0.5	0.33	0.60000	115.40	50,265
Allied	Load Cntrl	0.5	60.0	0.38530	130.00	119,054
Allied	Load Cntrl	0.5	60.0	0.38530	130.00	152,993
Allied	Load Cntrl	0.5	60.0	0.35566	120.00	408,178
Allied	Load Cntrl	0.5	60.0	0.35566	120.00	958,757
Allied	Load Cntrl	0.5	60.0	0.32602	110.00	1,015,716
Allied	Load Cntrl	0.5	60.0	0.33788	114.00	1,340,436
Allied	Load Cntrl	0.5	60.0	0.31417	106.00	1,453,661
Allied	Load Cntrl	0.5	60.0	0.32602	110.00	1,687,437
Allied	Load Cntrl	0.5	60.0	0.31120	105.00	2,684,170
Allied	Load Cntrl	0.5	60.0	0.30528	103.00	3,569,869
Allied	Load Cntrl	0.5	60.0	0.32602	110.00	5,281,133
Allied	Load Cntrl	0.5	60.0	0.29638	100.00	5,563,469
Allied	Step Tst	0.5	60.0	0.28156	95.00	10,000,000
Allied	Step Tst	0.5	60.0	0.28204	95.16	10,000,000
Allied	Step Tst	0.5	60.0	0.28342	95.63	10,000,000
Allied	Step Tst	0.5	60.0	0.28453	96.00	10,000,000
P&W	Strain Cntrl	0.8	60.0	1.00000	116.50	13,730
P&W	Strain Cntrl	0.8	60.0	0.74000	118.90	23,382
P&W	Strain Cntrl	0.8	60.0	0.59000	121.10	44,772

Table 3I.1c
Smooth Specimen Fatigue Results (R = 0.1)

Source	Test Type	R _ε or R _σ	freq (Hz)	Δε (%)	σ _{max} (ksi)	Life (cycles)
P&W	Strain Cntrl	0.1	0.33	1.27150	120.42	5,210
P&W	Strain Cntrl	0.1	0.33	1.24220	111.71	5,805
P&W	Strain Cntrl	0.1	0.33	0.99280	112.34	9,290
P&W	Strain Cntrl	0.1	0.33	0.78880	114.74	16,046
P&W	Strain Cntrl	0.1	0.33	0.59010	112.16	38,841
P&W	Load Cntrl	0.1	0.33	0.58684	110.00	42,300
GEAE	Load Cntrl	0.1	60.0	0.58684	110.00	57,273
P&W	Load Cntrl	0.1	60.0	0.45347	85.00	67,900
Allied	Load Cntrl	0.1	60.0	0.53349	100.00	69,866
P&W	Load Cntrl	0.1	60.0	0.53349	100.00	73,000
Allied	Load Cntrl	0.1	60.0	0.54950	103.00	85,023
Allied	Load Cntrl	0.1	60.0	0.52282	98.00	91,557
P&W	Load Cntrl	0.1	60.0	0.50682	95.00	93,200
Allied	Load Cntrl	0.1	60.0	0.50682	95.00	98,046
GEAE	Load Cntrl	0.1	60.0	0.53349	100.00	109,880
GEAE	Load Cntrl	0.1	60.0	0.46947	88.00	130,942
Allied	Load Cntrl	0.1	60.0	0.50682	95.00	153,918
GEAE	Load Cntrl	0.1	60.0	0.48014	90.00	192,463
Allied	Load Cntrl	0.1	60.0	0.48014	90.00	209,277
GEAE	Load Cntrl	0.1	60.0	0.46947	88.00	227,000
Allied	Load Cntrl	0.1	60.0	0.46414	87.00	257,988
GEAE	Load Cntrl	0.1	60.0	0.46947	88.00	290,896
GEAE	Load Cntrl	0.1	60.0	0.46947	88.00	297,754
P&W	Load Cntrl	0.1	60.0	0.48014	90.00	344,000
GEAE	Load Cntrl	0.1	60.0	0.50682	95.00	491,430
Allied	Load Cntrl	0.1	60.0	0.48014	90.00	633,168
P&W	Load Cntrl	0.1	60.0	0.45347	85.00	889,000
Allied	Load Cntrl	0.1	60.0	0.46236	86.67	953,156
P&W	Load Cntrl	0.1	60.0	0.42679	80.00	1,370,000
Allied	Load Cntrl	0.1	60.0	0.45347	85.00	1,493,080
P&W	Load Cntrl	0.1	60.0	0.48014	90.00	1,650,000
Allied	Load Cntrl	0.1	60.0	0.45347	85.00	2,844,620
AFML	Load Cntrl	0.1	60.0	0.46947	88.00	4,760,000
GEAE	Load Cntrl	0.1	60.0	0.42679	80.00	6,793,930
Allied	Load Cntrl	0.1	60.0	0.45347	85.00	7,268,673
GEAE	Disc+Step	0.1	60.0	0.45373	85.05	14,922,937
GEAE	Disc+Step	0.1	60.0	0.42802	80.23	35,098,000
P&W	Step Tst	0.1	60.0	0.40012	75.00	10,000,000
Allied	Step Tst	0.1	60.0	0.42409	79.49	10,000,000
Allied	Step Tst	0.1	60.0	0.42472	79.61	10,000,000
AFML	Step Tst	0.1	60.0	0.42679	80.00	10,000,000
Allied	Step Tst	0.1	60.0	0.43865	82.22	10,000,000
Allied	Step Tst	0.1	60.0	0.44078	82.62	10,000,000
AFML	Step Tst	0.1	60.0	0.44813	84.00	10,000,000
Allied	Step Tst	0.1	60.0	0.45830	85.91	10,000,000
GEAE	Step Tst	0.1	1000.0	0.39662	74.34	10,000,000
GEAE	Step Tst	0.1	1000.0	0.45803	85.86	10,000,000
GEAE	Step Tst	0.1	1000.0	0.38435	72.04	10,000,000
GEAE	Load Cntrl	0.1	1000.0	0.32009	60.00	18,894,769
GEAE	Load Cntrl	0.1	1000.0	0.45347	85.00	29,714,022
GEAE	Step Tst	0.1	1000.0	0.37676	70.62	100,000,000
GEAE	Step Tst	0.1	1000.0	0.34890	65.40	100,000,000
GEAE	Step Tst	0.1	1000.0	0.33165	62.17	100,000,000
GEAE	Disc+Step	0.1	1000.0	0.37168	69.67	112,657,105
GEAE	Disc+Step	0.1	1000.0	0.38097	71.41	167,301,914
GEAE	Load Cntrl	0.1	1000.0	0.30409	57.00	213,209,026
GEAE	Load Cntrl	0.1	1000.0	0.28809	54.00	220,378,689
GEAE	Step Tst	0.1	1000.0	0.32033	60.04	1,000,000,000

Table 3I.2a

Smooth Specimen Tension-Torsion Fatigue Results
(stresses are calculated on the surface with finite element analysis)

Spec ID	Control	Freq (Hz)	ϵ (%)	γ (%)	σ (ksi)	τ (ksi)	Life (cycles)	Comment
156-11	ϵ ctrl	0.5	-0.756	0.000	119.1	0.0	6,200	measured stresses
			0.571	0.000	-122.3	0.0		with cyclic plasticity
21-11	ϵ ctrl	0.5	0.000	0.866	0.0	54.5	72,141	fully reversed torsion
			0.000	-0.868	0.0	-54.6		
21-6	load ctrl	1	0.000	0.614	0.0	38.6	241,250	fully reversed torsion
			0.000	-0.610	0.0	-38.4		
156-10	ϵ /load ctrl	0.5	0.000	0.559	0.0	35.2	961,806	fully reversed torsion
			0.000	-0.563	0.0	-35.4		
21-7	ϵ ctrl	0.5	0.000	1.810	0.0	65.9	30,007	R=0.1 torsion
			0.000	0.166	0.0	-36.5		
156-5	ϵ ctrl		0.000	1.210	0.0	64.2	150,293	R=0.1 torsion
			0.000	0.090	0.0	-5.6		
156-4	ϵ ctrl	0.5	0.000	1.360	0.0	65.0	151,598	R=0.1 torsion
			0.000	0.150	0.0	-10.4		
156-1	ϵ /load ctrl	0.5	0.000	0.958	0.0	60.3	814,753	R=0.1 torsion
			0.000	0.086	0.0	5.4		
21-4	ϵ /load ctrl	1	0.000	1.960	0.0	66.1	141,229	R=0.5 torsion
			0.000	0.815	0.0	-5.3		
21-1	ϵ ctrl	0.5	0.312	0.416	53.0	26.2	67,965	fully reversed tension-torsion
			-0.312	-0.418	-53.0	-26.3		
156-9	ϵ ctrl	0.5	0.462	0.616	78.4	38.8	60,514	R=0.1 tension-torsion
			0.049	0.055	8.3	3.5		
156-3	ϵ ctrl	0.5	0.464	0.621	78.8	39.1	87,920	R=0.1 tension-torsion
			0.048	0.055	8.1	3.5		
156-2	ϵ ctrl	0.33	0.362	0.000	61.5	0.0	38,355	non-proportional tension-torsion (triangular path)
			-0.373	0.471	-63.3	29.6		
			-0.373	-0.476	-63.3	-29.6		
21-2	ϵ ctrl	0.33	0.364	0.000	61.8	0.0	43,009	non-proportional tension-torsion (triangular path)
			-0.372	0.471	-63.2	29.6		
			-0.372	-0.477	-63.2	-30.0		
21-9	ϵ ctrl	0.5	0.364	0.004	61.8	0.3	71,358	non-proportional tension-torsion (top segment of triangular path)
			-0.364	0.475	-61.8	29.9		
21-5	ϵ ctrl	0.5	0.365	-0.005	62.0	-0.3	79,367	non-proportional tension-torsion (bottom segment of triangular path)
			-0.363	-0.475	-61.6	-29.9		
21-8	ϵ ctrl	0.5	0.091	0.666	15.4	41.9	72,124	non-proportional tension-torsion
			0.089	-0.665	15.2	-41.8		
21-3	ϵ ctrl	0.5	0.090	0.666	15.3	41.9	73,728	reversed torsion + mean tension
			0.089	-0.666	15.1	-41.9		
21-10	ϵ ctrl	0.5	-0.089	0.665	-15.1	41.8	329,058	reversed torsion + mean compression
			-0.091	-0.664	-15.5	-41.9		

Table 3I.2b

Smooth Specimen Results for the Tension-Torsion 90° Phase Test.
(stresses are calculated from Hooke's law with the strains and elastic moduli
to identify the full mission stresses on the specimen surface.

ID	Control	(Hz)	ϵ (%)	γ (%)	σ (ksi)	τ (ksi)	(cycles)	Comment
156-8	ϵ ctrl	0.5	0.000	0.406	0.0	25.4	111,783	90 deg phase shifted tension-torsion
			0.094	0.386	15.8	24.1		
			0.178	0.328	30.0	20.5		
			0.245	0.239	41.4	14.9		
			0.288	0.125	48.6	7.8		
			0.303	0.000	51.1	0.0		
			0.288	-0.126	48.6	-7.9		
			0.245	-0.240	41.4	-15.0		
			0.178	-0.331	30.0	-20.7		
			0.094	-0.389	15.8	-24.3		
			0.000	-0.409	0.0	-25.6		
			-0.093	-0.389	-15.7	-24.3		
			-0.178	-0.331	-29.9	-20.7		
			-0.244	-0.240	-41.2	-15.0		
			-0.287	-0.126	-48.5	-7.9		
			-0.302	0.000	-50.9	0.0		
			-0.287	0.125	-48.5	7.8		
			-0.244	0.239	-41.2	14.9		
			-0.178	0.328	-29.9	20.5		
			-0.093	0.386	-15.7	24.1		
			0.000	0.406	0.0	25.4		

Table 3I.3

Notched Configurations with Fatigue Lives of 10^6 Cycles
Used to Evaluate Fatigue Damage Metrics.

Spec ID	Notch Type	Edge Dia (in)	Notch Depth (in)	Notch root radius (in)	Orientation (deg)	Freq (Hz)	R_σ	Life (cycles)	Comment
8613	DEN	NA	0.047	0.021	90	60	0.5	1093835	double edged V-notch
48-02	sharp tip	0.01	NA	NA	NA	60	0.5	1000000	simulated blade tip, no notch, step test
70-08	sharp tip	0.01	NA	NA	NA	60	0.5	1000000	simulated blade tip, no notch, step test
75-02	sharp tip	0.01	NA	NA	NA	60	0.5	1000000	simulated blade tip, no notch, step test
11-s1	sharp tip	0.01	0.0485	0.024	90	60	0.5	1000000	simulated blade tip with notch, step test
11-s2	sharp tip	0.01	0.0482	0.022	90	60	0.5	1000000	simulated blade tip with notch, step test
11-s3	sharp tip	0.01	0.0478	0.023	90	60	0.5	1000000	simulated blade tip with notch, step test
11-s4	sharp tip	0.01	0.0485	0.023	90	60	0.5	1000000	simulated blade tip with notch, step test
22-b2	blunt tip	0.03	0.061	0.023	33	60	0.5	1000000	simulated blade tip with notch, step test
36-b3	blunt tip	0.03	0.061	0.023	33	60	0.5	1000000	simulated blade tip with notch, step test

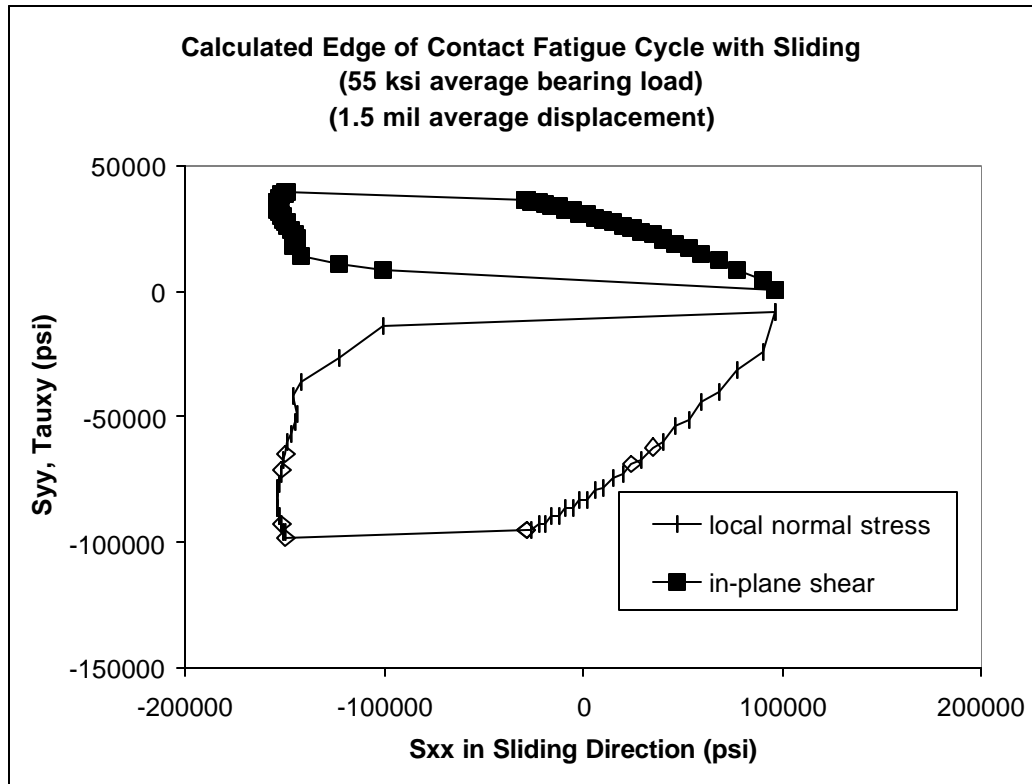


Figure 3I.1. Predicted non-proportional stress history for an edge of contact geometry with sliding.

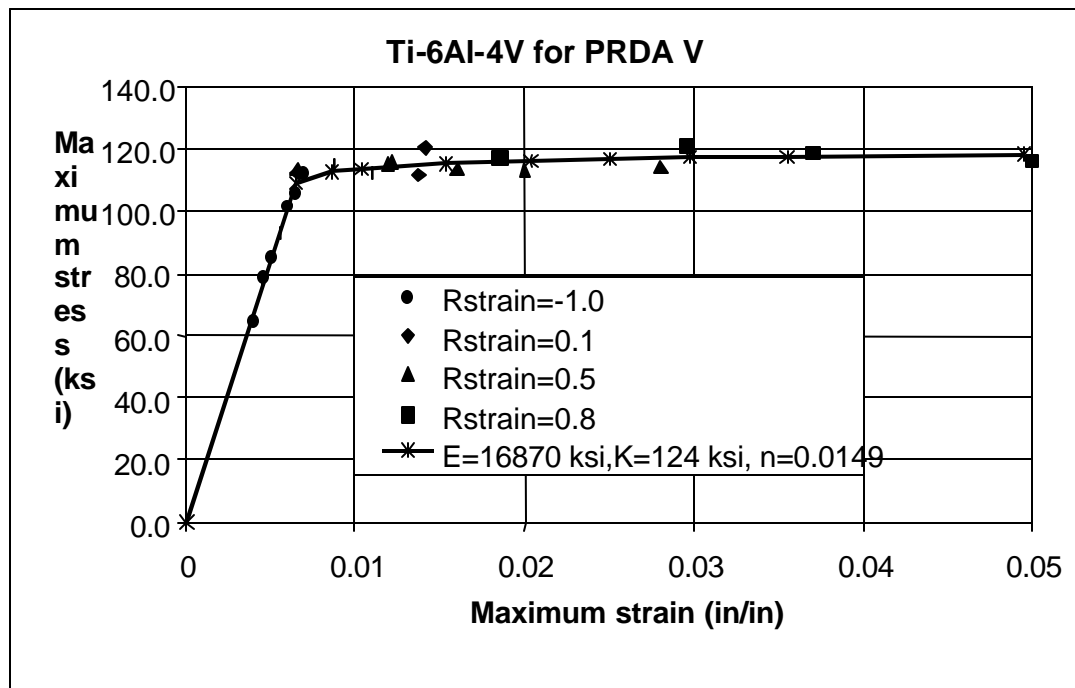


Figure 3I.2. Half-life stress-strain response for elastic-plastic finite element analysis.

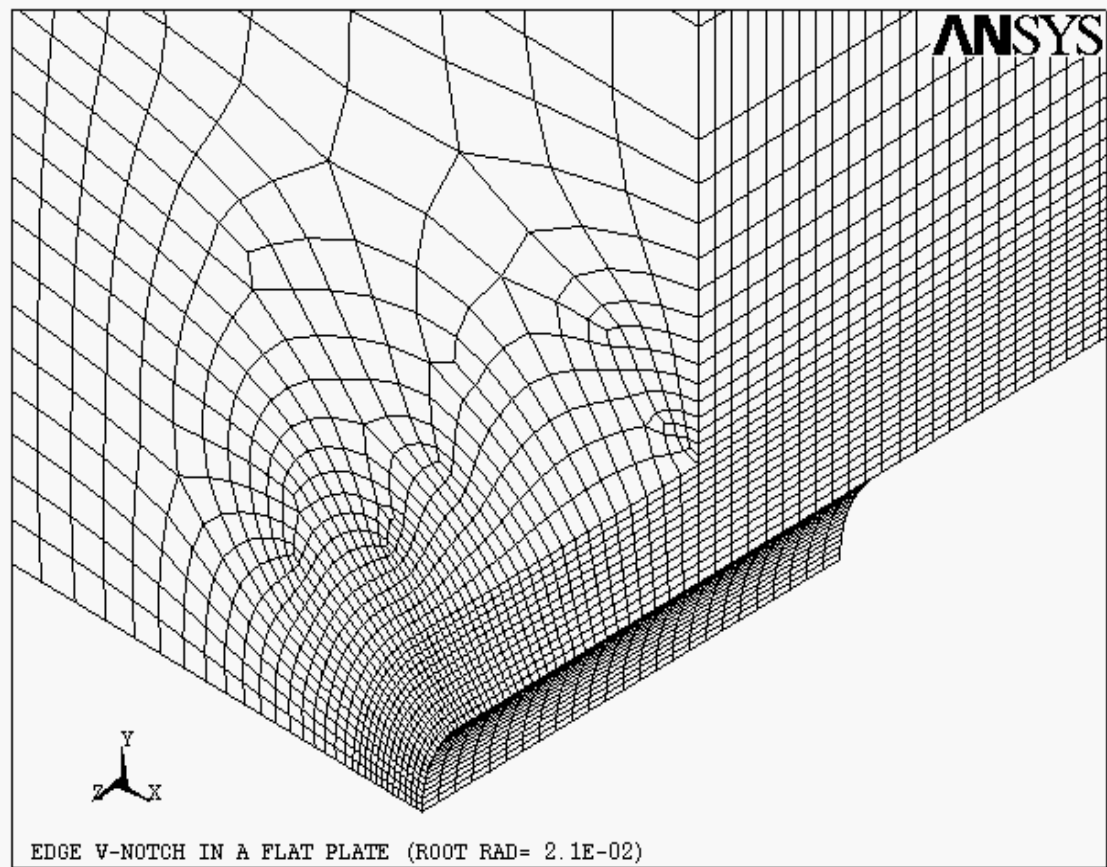


Figure 3I.3. Double edge V-notch specimen finite element model. Only one quarter of the specimen was modeled with the symmetry boundary conditions.

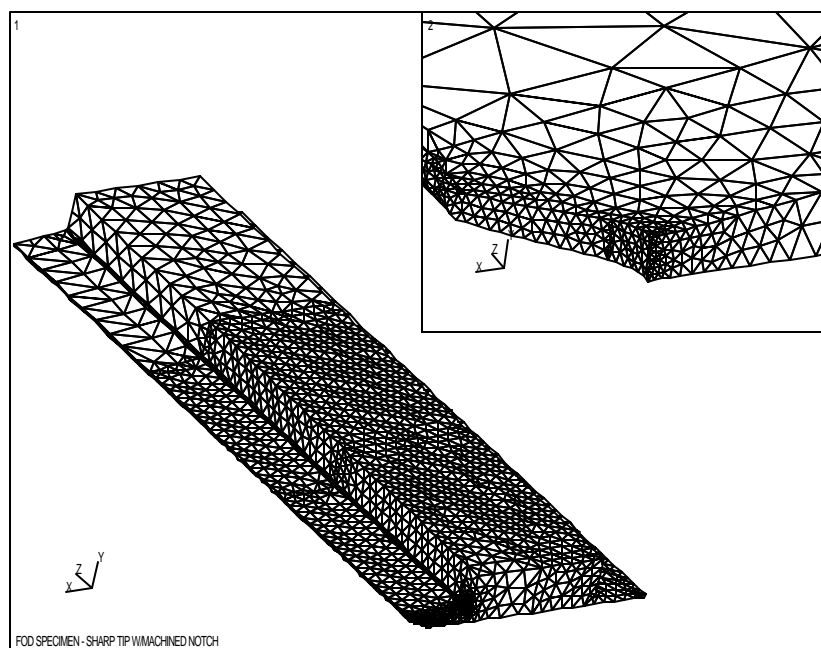


Figure 3I.4. Sharp tip specimen geometry simulative of an airfoil leading edge with a notch.

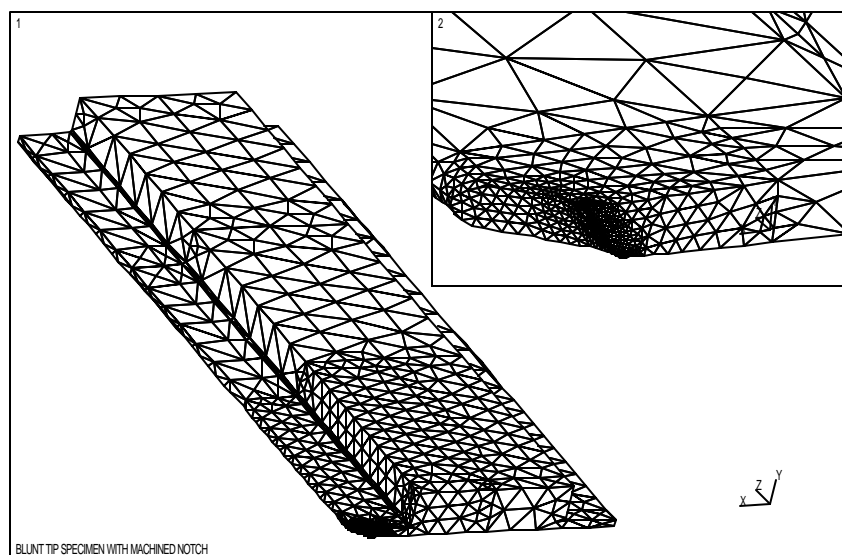


Figure 3I.5. Blunt tip specimen geometry simulative of an airfoil leading edge with a notch.

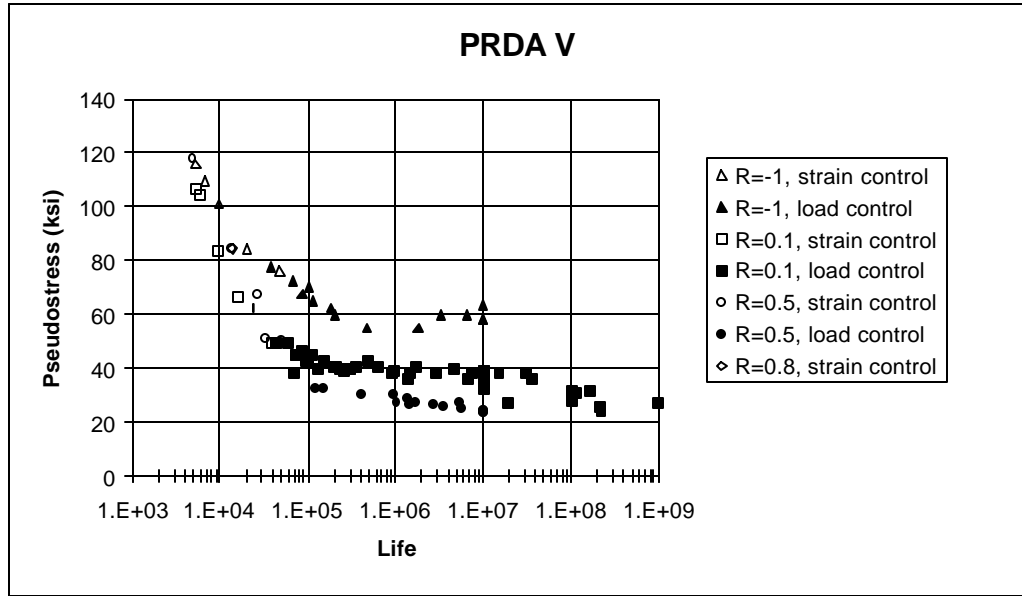


Figure 3I.6. Smooth specimen fatigue lives as a function of R-ratio as a function of pseudostress.

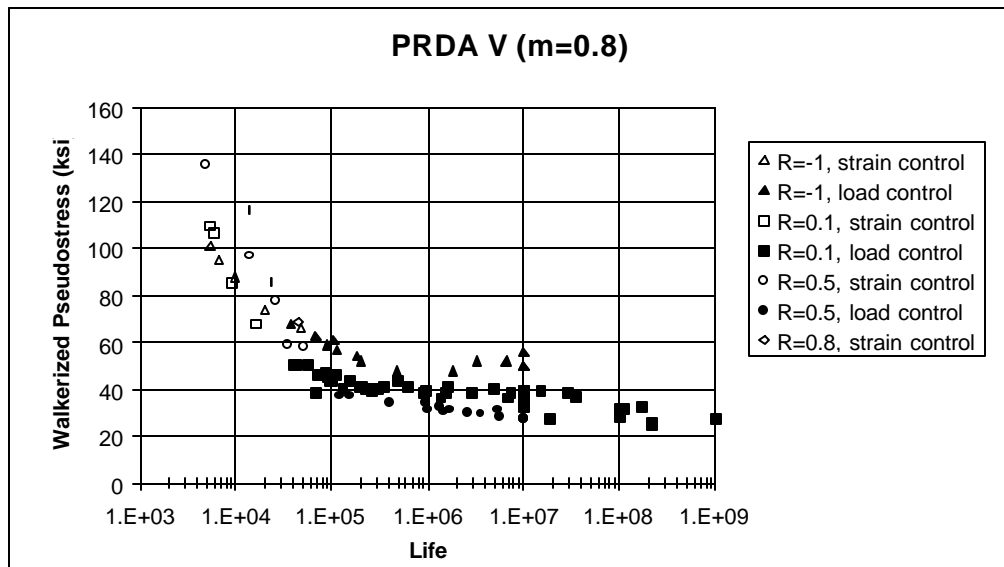


Figure 3I.7. Smooth specimen fatigue lives as a function of Walkerized pseudostress.

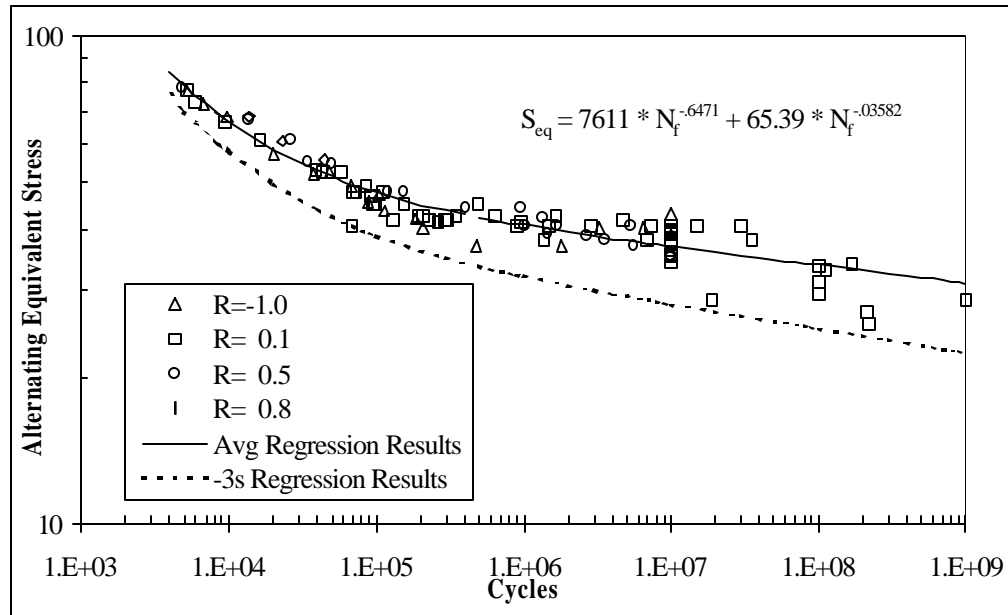


Figure 3I.8. Smooth specimen fatigue lives as a function of Walkerized equivalent stress amplitude.

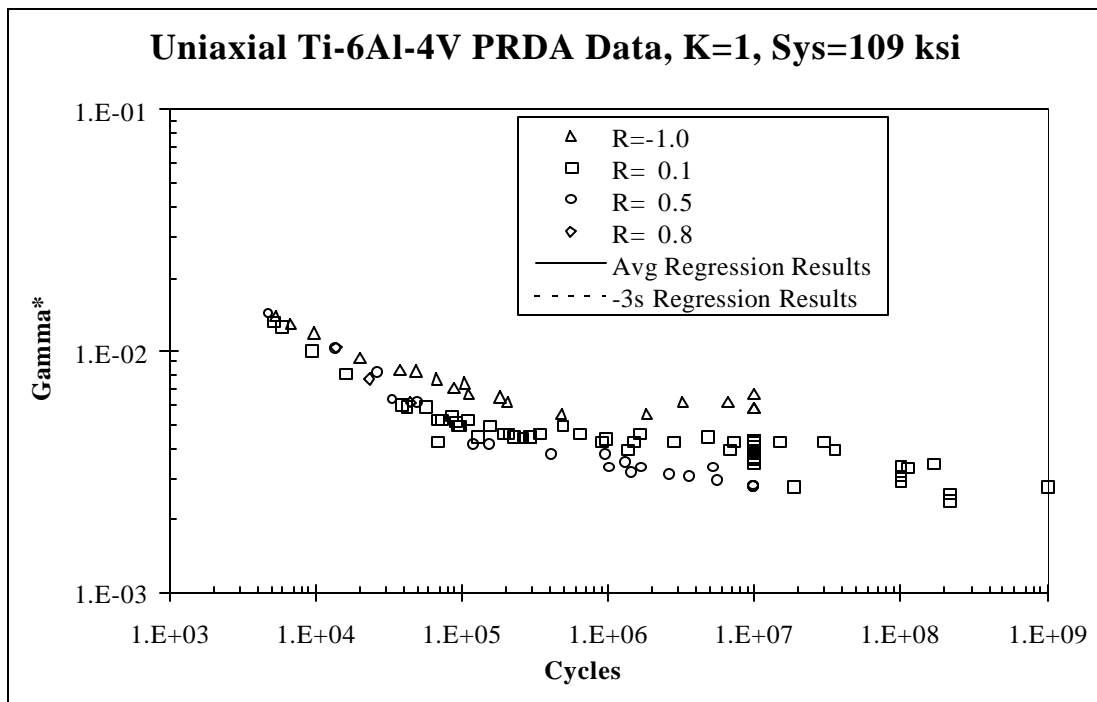


Figure 3I.9. Smooth specimen fatigue lives as a function of the Kurath-Fatemi-Socie critical plane damage parameter.

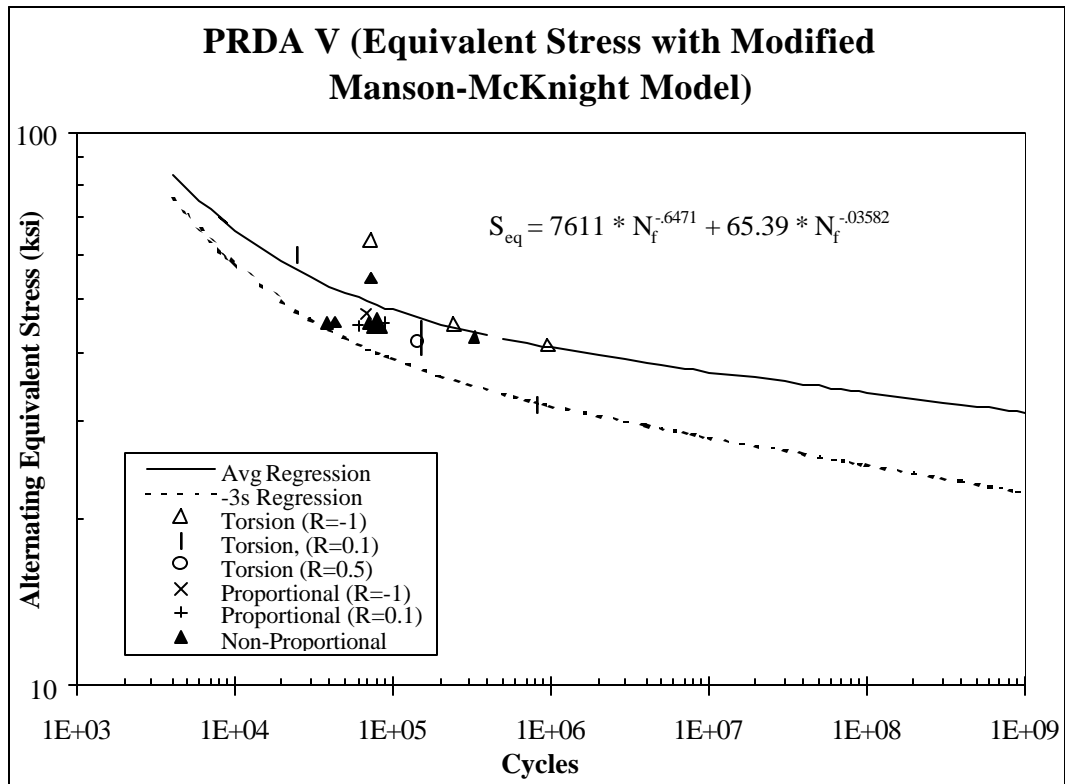


Figure 3I.10. Prediction of the multiaxial tension-torsion tests as compared to the alternating Walkerized equivalent stress with the Modified Manson-McKnight multiaxial model.

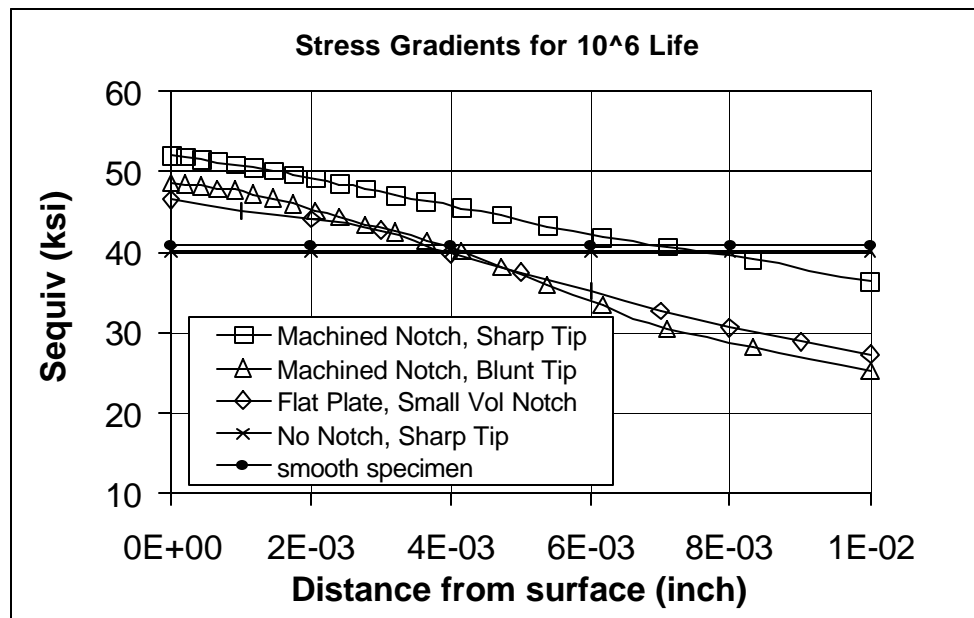


Figure 3I.11. Comparison of the Walkerized equivalent stress amplitude gradients for notched and unnotched specimen geometries with a 10⁶ fatigue life.

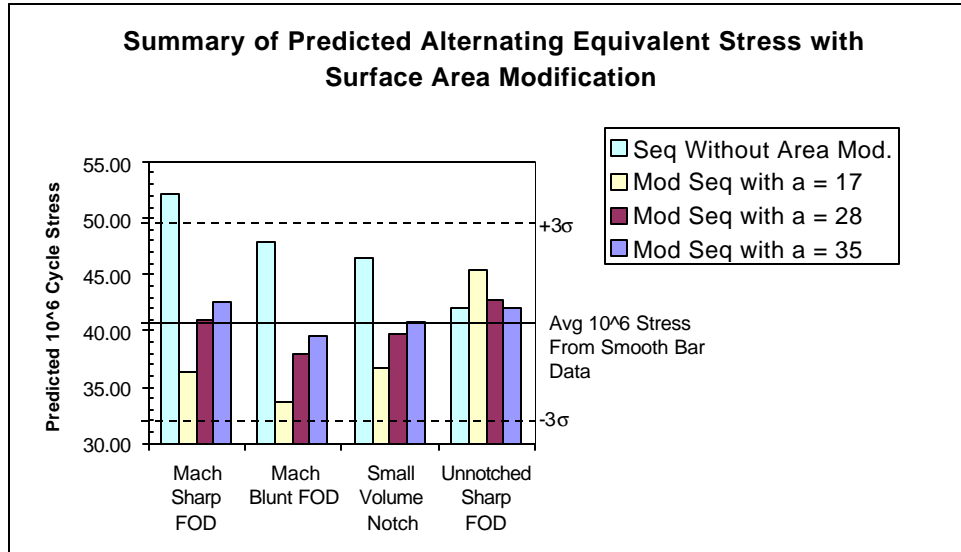


Figure 3I.12. Comparison of the predicted Walkerized equivalent stress amplitude with the Weibull surface area modification for specimen geometries with 10^6 fatigue life.

Appendix 3J

NOTCH FATIGUE

**Robert E. deLaneuville
Jerry W. Sheldon**



Pratt & Whitney

**Submitted
28 September 1999**

NOTCHED HCF FATIGUE TESTING

Two geometries were selected for notched testing. The purpose of testing two geometries was to estimate the effect of stress dieout and notch volume on nucleation life. Each sample was designed to have a nominal K_t of 2.5. The sample shown in Figure 3J.1 was used for the majority of testing. The notch tolerance is 0.021 inch \pm 0.001 inch allowing the K_t to vary between 2.45 and 2.55. The sample in Figure 3J.2 was used only at a single condition to capture the geometry effect. Exercising the tolerance on both the width in the notch direction (0.360 inch \pm 0.002 inch) and the notch radius (0.032 inch \pm 0.002 inch), K_t ranged from 2.48 to a maximum value of 2.56. Results in Figure 3J.3 demonstrate the lack of effect that both notch acuity and volume has on failure life.

Samples were processed according to the requirements set forth for all fatigue specimens. Testing was conducted using two methods, the first is the standard ASTM E466-96 for load controlled cyclic testing and the other using the step test method. Testing was performed on closed-loop servo-hydraulic test machines at 60 Hz, 80°F and lab air at stress ratios of -1, 0.1, 0.5 and 0.8.

The step test method uses a single specimen to determine the constant life endurance limit at a single stress ratio [3J.1]. This is accomplished by subjecting the specimen to a stress for a block of cycles. If failure does not occur within the block, the stress is increased by a small percentage (5% or less). This continues until failure is achieved, and the constant life endurance stress is calculated by the equation:

$$\sigma_E = \sigma_{PB} + N_f / N_{RO} (\sigma_f - \sigma_{PB}) \quad (3J.1)$$

The variables are defined according to the following:

σ_E – the constant life endurance limit

σ_{PB} – the stress from the prior block which did not fail

σ_f – the stress from final block

N_f – the cycles to failure in the final block

N_{RO} – the number of cycles considered to be a run-out

The step method has been proposed as a way to generate traditional modified-Goodman diagrams for specific conditions that can be test related (stress ratio, temperature, etc.), specimen related (surface finish, peened, etch, stress relieved, etc.), or damage mode related (superimposed low cycle fatigue, foreign object or fretting damage). The step test method can also be used in conjunction with traditional S-N curve testing to eliminate run-outs, which can be difficult to treat statistically.

To estimate endurance limits, a censored regression analysis was used to model the fatigue data using an equation of the form:

$$\sigma_R = b (\text{Log } (N_f) - a)^{-1} \quad (3J.2)$$

The variables are defined according to the following:

σ_R – the stress range

N_f – the cycles to failure

a – parameter

b – parameter

Run-outs, tests that did not fail after 10 million cycles, were used in a censored regression analysis that chose parameter values to maximize the likelihood that the experiment would have turned out the way it actually did. By using the maximum likelihood parameter method, the run-out data could be included in the determination of the endurance limit. When all tests fail (i.e., there are no run-outs), then the maximum likelihood parameter method and the ordinary least-squares method produce the same endurance limit. Results are presented in Figures 3J.4 through 3J.7. The only conditions where step testing has a clear influence on the measured endurance limit is the R = -1.0 results of Figure 3J.7. Similar results were obtained from smooth bar testing.

REFERENCES

- 3J.1 Maxwell, D.C. and T. Nicholas, "A Rapid Method for Generation of a Haigh Diagram for High Cycle Fatigue," ASTM STP 1321, 1998, T.L. Panontin and S.D. Sheppard, Editors, to be published.

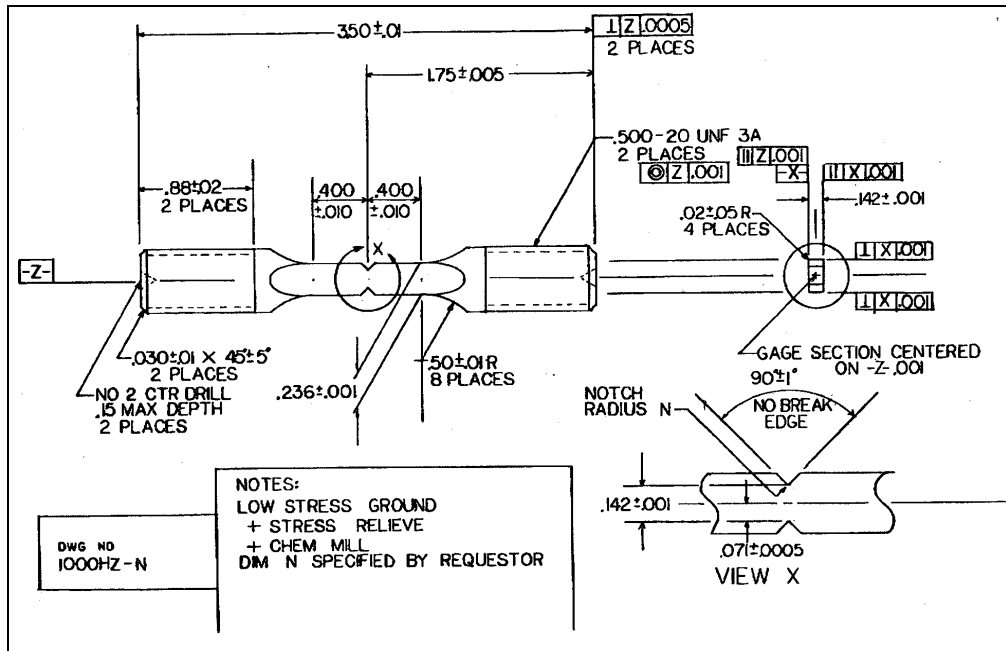


Figure 3J.1. The small volume notched fatigue specimen used for 60 Hz and 1000 Hz nucleation testing.

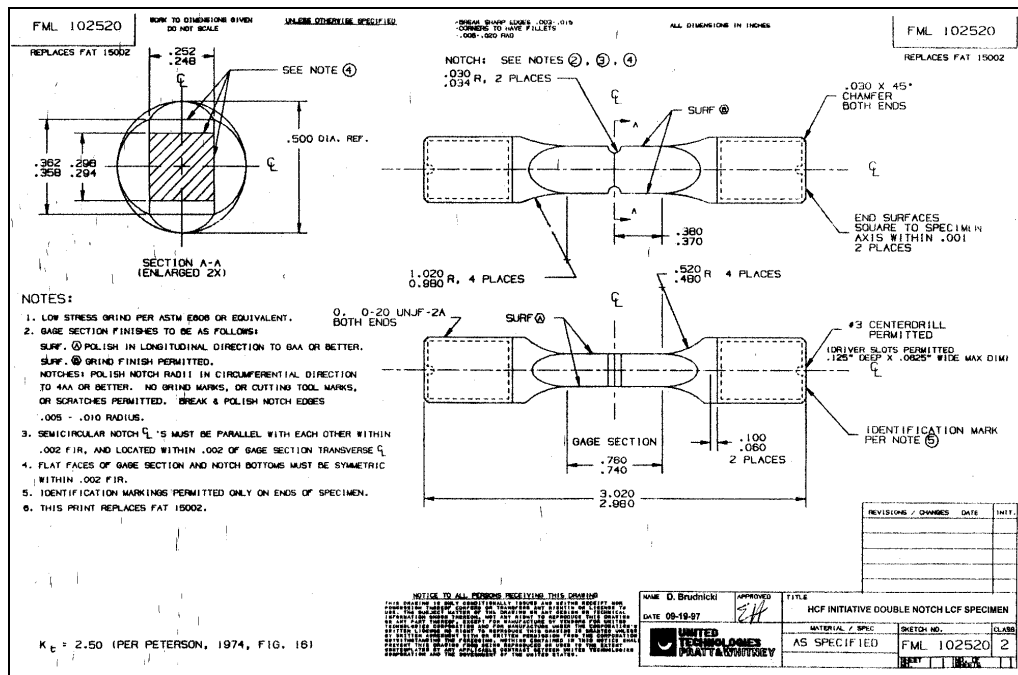


Figure 3J.2. The large volume notched fatigue specimen used for 60 Hz nucleation testing.

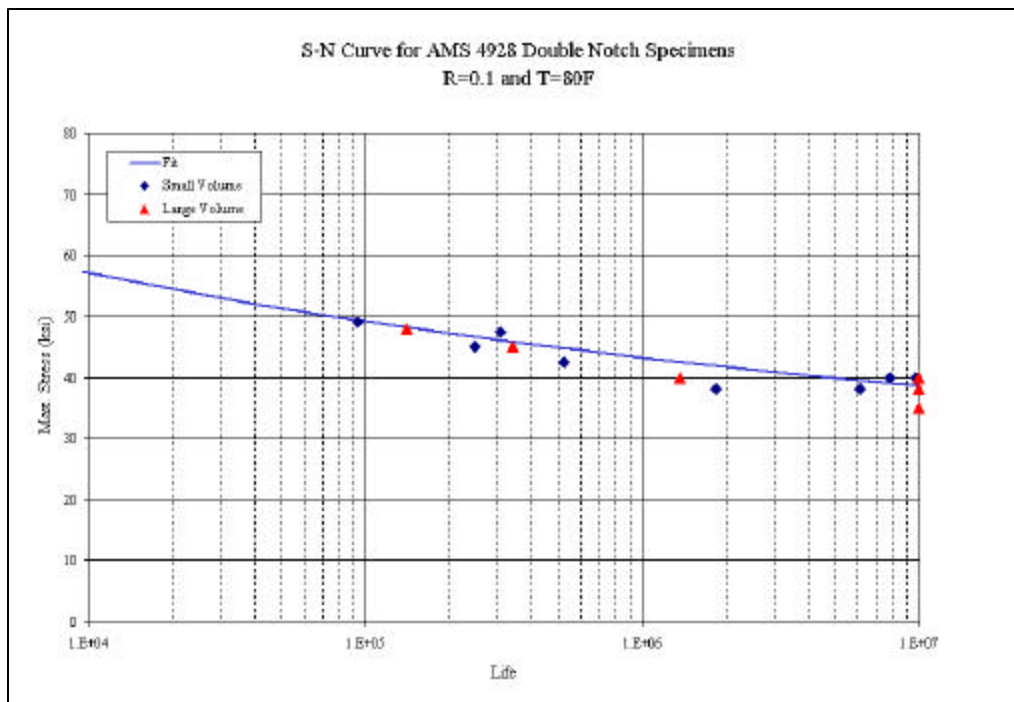


Figure 3J.3. Double notch (60 Hz, R = 0.1, 80°F) HCF results indicating no volume or notch dieout effect on nucleation life. Both geometries were nominally of K_t of 2.5.

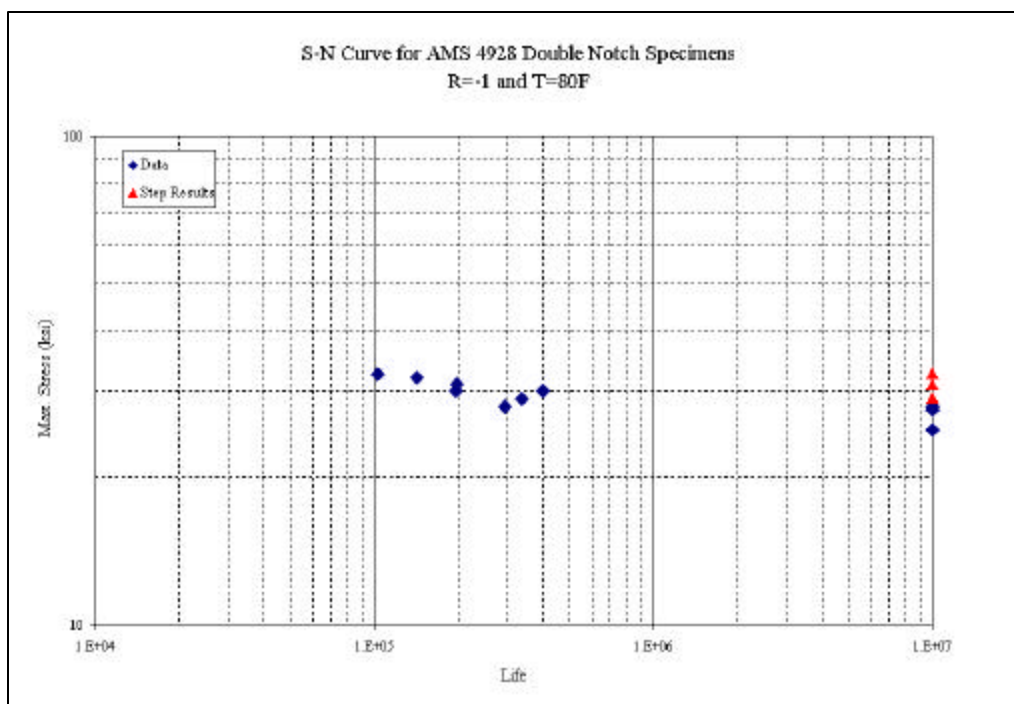


Figure 3J.4. Double notch (60 Hz, R = -1, 80°F) HCF results indicating step test results yield higher 10^7 failure lives.

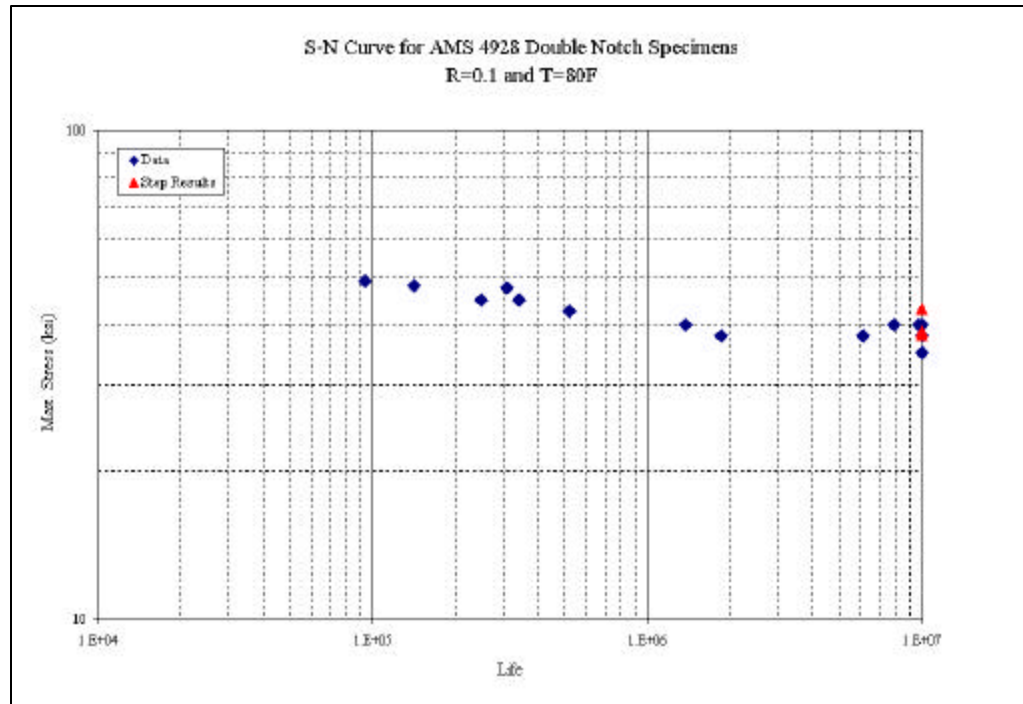


Figure 3J.5. Double notch (60 Hz, R = 0.1, 80°F) HCF results indicating step test results yield similar 10^7 failure lives compared with conventional S-N results.

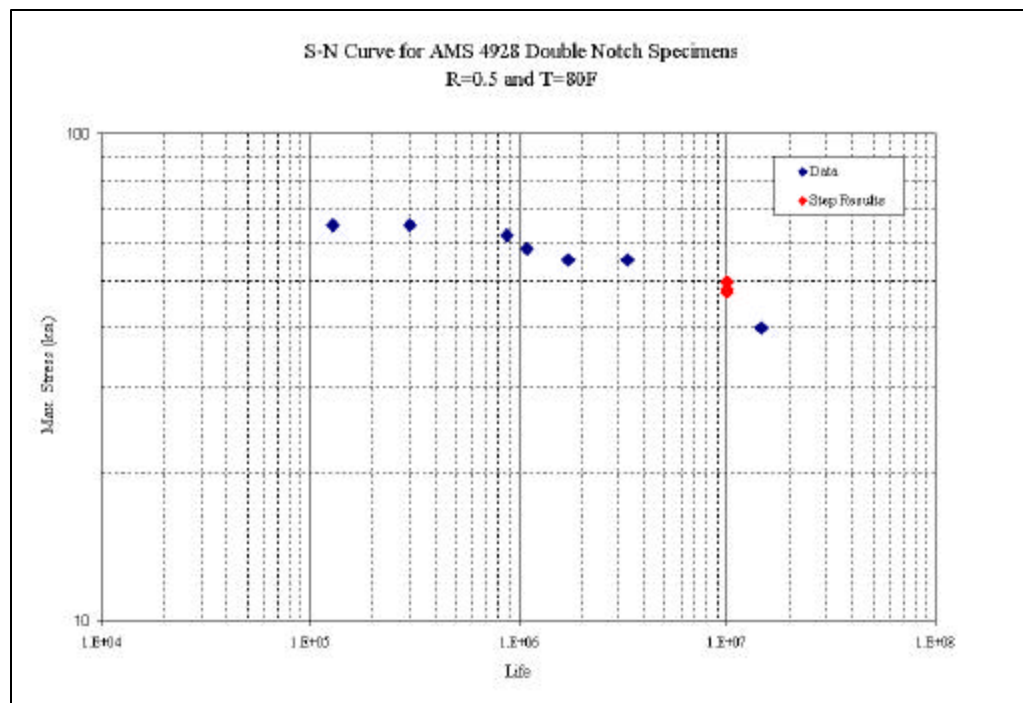


Figure 3J.6. Double notch (60 Hz, R = 0.5, 80°F) HCF results indicating step test results yield similar 10^7 failure lives compared with conventional S-N results.

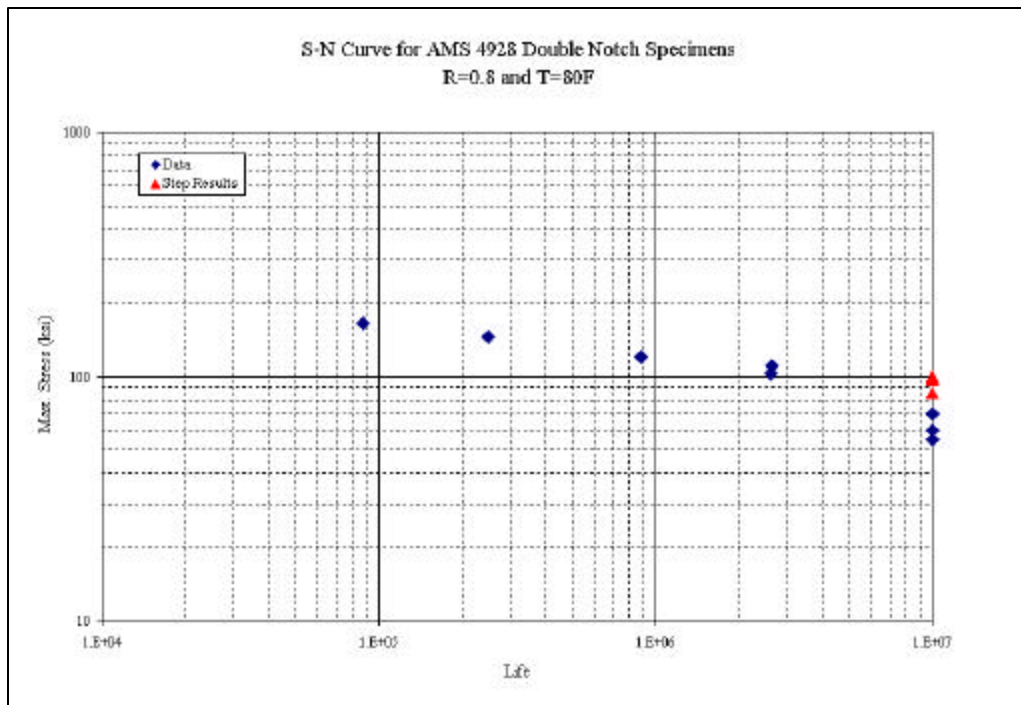


Figure 3J.7. Double notch (60 Hz, R = 0.8, 80°F) HCF results indicating step test results yield similar 10^7 failure lives compared with conventional S-N results.

Appendix 3K

FINITE ELEMENT MODELING OF NOTCHED SPECIMENS

Robert deLaneuville



Pratt & Whitney

**Submitted
28 September 1999**

FINITE ELEMENT MODELING OF NOTCHED SPECIMENS

The DEN (standard and large volume) specimens were analyzed using an ANSYS finite element analysis. Figure 3K.1 shows the finite element model that was used in the analysis of the standard DEN specimen. The details of the mesh refinement near the notch root are shown in Figure 3K.2. Figures 3K.3-3K.5 show stress results from the FEM analysis.

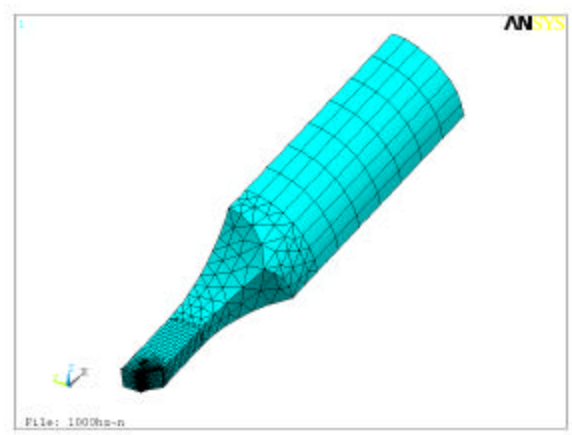


Figure 3K.1. FEM model of DEN specimen with notch radius 0.021-inch.

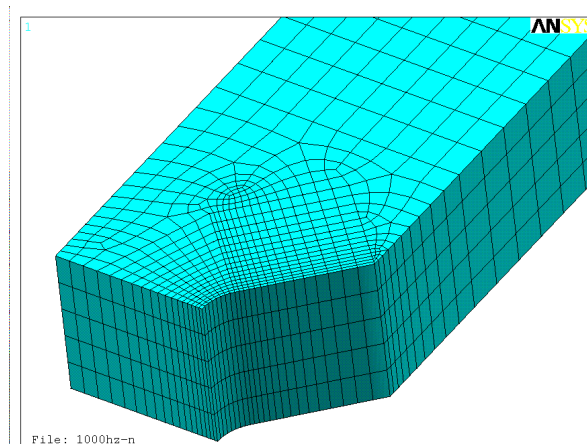


Figure 3K.2. Close-up of DEN specimen showing finite element mesh refinement near notch.

Figures 3K.3 and 3K.4 show the variation of the maximum principal stress along the notch edge and along the notch centerline, respectively. A stress concentration factor of 2.68 was calculated for the standard specimen geometry. The max principal stress varied by roughly 22% along the notch edge. Along the notch centerline the stress decreased very rapidly. For example, at a distance of roughly 2 mils from the surface, the stress was roughly 20% lower than its peak at the surface. Similar results were obtained for the large volume specimen. Tolerances for the notch radius (0.032 inch \pm 0.002 inch) and notch width (0.360 inch \pm 0.002 inch) were also considered in the analysis. The calculated K_t ranged between 2.48 and 2.56 for this specimen. These results were in agreement with GEAE results. The stress variations for the principal and Von Mises stresses for the large volume specimens are shown in Figs. 3K.5 and 3K.6.

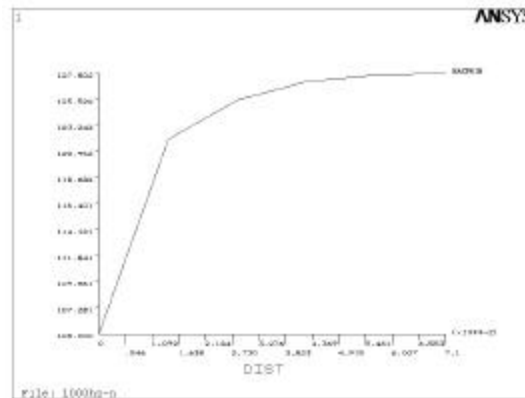


Figure 3K.3. Variation of maximum principal stress along notch edge from free edge (at DIST = 0) to centerline.

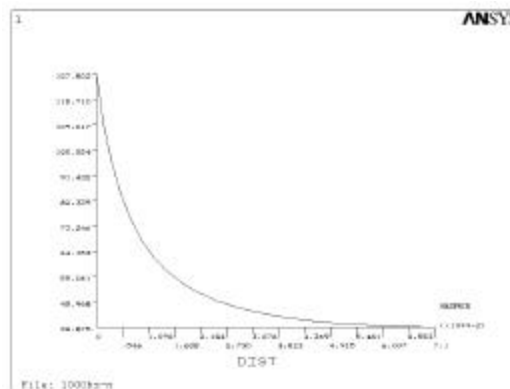


Figure 3K.4. Variation of maximum principal stress along notch centerline (free edge at DIST = 0).

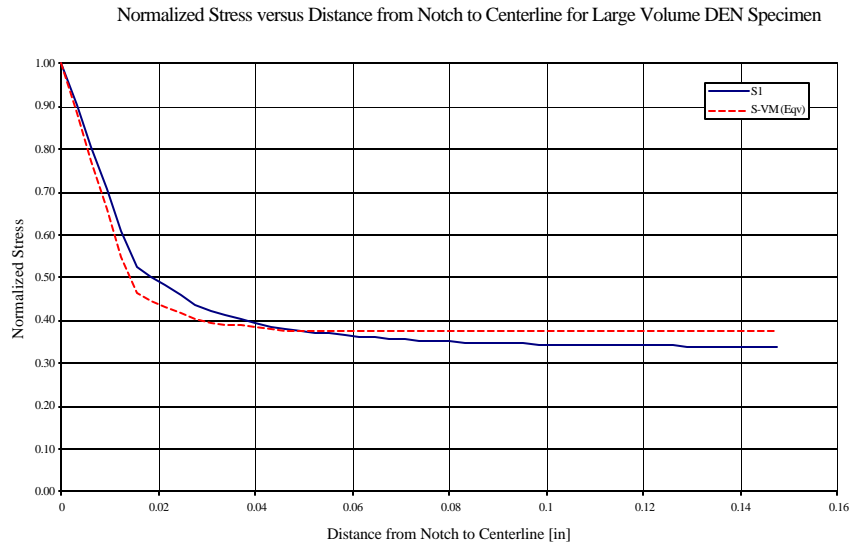


Figure 3K.5. Normalized stress versus distance from notch to centerline for the large volume DEN specimen.

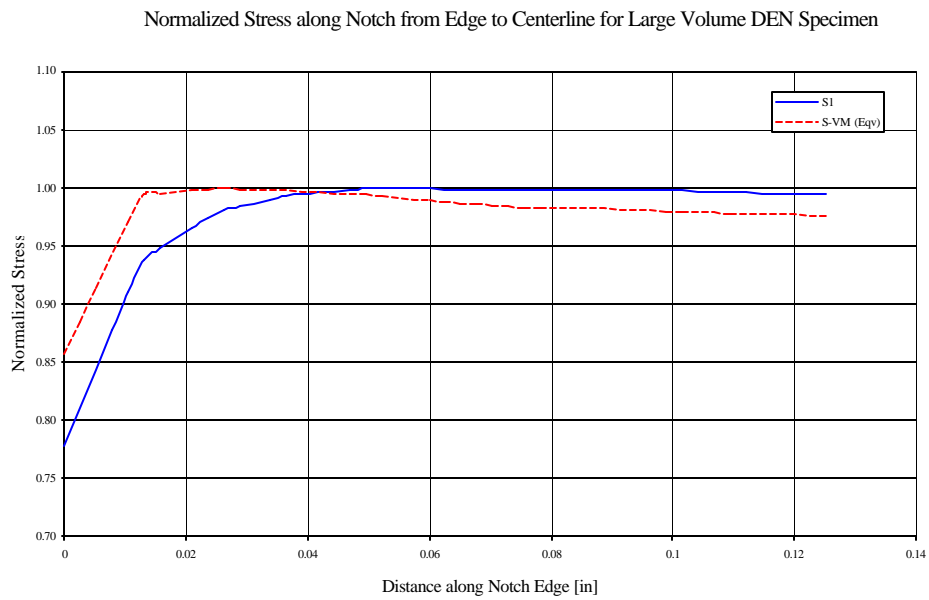


Figure 3K.6. Normalized stress along the notch from edge to centerline for the large volume DEN specimen.

Appendix 3L

OBSERVATIONS OF HCF NUCLEATION SITES USING SEM

Robert deLaneuville



Pratt & Whitney

**Submitted
28 September 1999**

OBSERVATIONS OF HCF NUCLEATION SITES USING SEM

A limited number of notched specimens tested using different R-ratios were selected for Scanning Electron Microscope (SEM) observations. As shown in Table 3L.1, an effort was made to select long and short life notched HCF specimens for SEM observations. The SEM observations are also summarized in Table 3L.1.

Table 3L.1
SEM Observations of HCF Notched Specimens

Spe3H. ID	Life	R-Ratio	Principal Stress/Max Surface Stress	Von Mises Stress/Max Von Mises Stress	SEM Observation Notes on Crack Nucleation
140-10	102,724	-1	1.00	1.00	origin at notch center, surface nucleation
140-5	198,144	-1	0.98	1.00	corner nucleation, 0.5mm from edge, surface
140-11	292,656	-1	1.00	1.00	notch center, surface nucleation
140-4	93,433	0.1	1.00	1.00	1.2mm from one edge, surface nucleation
140-8	9,722,322	0.1	1.00	1.00	1.5mm from one edge, surface nucleation, secondary cracking.
140-16	127,989	0.5	1.00	1.00	near notch center, surface nucleation, smear 20 m.
102-20	3,328,447	0.5	1.00	1.00	near notch center, surface nucleation, smeared.
123-32	88,140	0.8	1.00	1.00	near notch center, surface nucleation, yielding, secondary cracking.
102-16	2,637,889	0.8	0.99	1.00	0.6mm from one edge, near surface nucleation
140-6	10M, 716,374	-1	1.00	1.00	near notch center, surface nucleation
140-24	10M, 166,442	0.1	0.98	1.00	0.5mm from one edge, surface nucleation
123-21	10M, 2,388,074	0.5	1.00	1.00	0.9mm from one edge, surface nucleation
102-23	10M, 3,342,467	0.8	1.00	1.00	Near notch center, surface-connected nucleation

Table 3L.1 also lists the elastic principal and Von Mises stresses (normalized by the maximum stress) at the SEM observed nucleation sites. These stresses were calculated using the FEM analysis described in Appendix 3K. The maximum deviation from the peak surface stresses was 2%. Thus, in the analysis of the notched specimens, peak stresses on the surface were used for all the specimens.

Appendix 3M

ANALYSIS OF LOAD SHED EFFECTS ON FATIGUE CRACK CLOSURE DURING THRESHOLD TESTING

R. Craig McClung



Southwest Research Institute

**Submitted
31 August 1999**

ANALYSIS OF LOAD SHED EFFECTS ON FATIGUE CRACK CLOSURE DURING THRESHOLD TESTING

Background

Reliable experimental measurement of the fracture mechanics threshold is a critical component of the materials testing needed to support HCF design systems. Although many different methods for determining the threshold have been proposed, one of the most common methods in current use is the one recommended in ASTM E 647, "Standard Test Method for Measurement of Fatigue Crack Growth Rates." This method, based on research published by Saxena, *et al.* in 1978 [3M.1], steadily decreases the load range of the fatigue cycle while maintaining the chosen stress ratio, R , constant, thereby steadily decreasing the applied range of the stress intensity factor, ΔK . The stress intensity factor threshold, ΔK_{th} , is determined from the resulting FCG data as the value of ΔK corresponding to a specified slow growth rate, operationally defined in the ASTM test method as 10^{-10} m/cycle.

The ASTM method specifies the rate of load shedding in terms of the normalized K -gradient, C , such that C is limited to a value algebraically greater than -2 inch^{-1} :

$$C = \frac{1}{K} \frac{dK}{da} \quad (3M.1)$$

The relationship between ΔK and crack length, a , is therefore given by

$$\Delta K = \Delta K_0 \exp[C(a - a_0)] \quad (3M.2)$$

where ΔK_0 is the initial ΔK at the start of the load shed, and a_0 is the corresponding crack length.

Threshold tests conducted by this method, at this specified load shed rate, can be relatively slow and expensive, especially when slower cycling frequencies are required. Faster load shed rates are attractive as a means of saving time and money. Furthermore, the recommended ASTM rate of $C = -2 \text{ inch}^{-1}$ is not feasible for some small specimen geometries, such as the surface-crack tension

(Kb bar) specimen, because the crack may effectively run out of specimen before the threshold is reached.

Experience suggests that shed rates faster than those recommended by the ASTM test method can be employed without ill effect. This was observed by Saxena, et al. [3M.1] in their original work, and faster rates have been employed in the gas turbine engine industry for several years. Our HCF contractual colleagues have performed a systematic study [3M.2] of the effects of shed rate and other parameters on measured values of ΔK_{th} determined from tests on Kb and compact tension specimens of Ti-6Al-4V. They obtained nearly identical threshold values for shed rates ranging from -6 inch^{-1} up to -40 inch^{-1} at $R = 0.1$ when starting K_{max} values were less than $10 \text{ ksi}\sqrt{\text{inch}}$. At a higher stress ratio of $R = 0.8$, gradients ranging from -7.5 inch^{-1} to -20 inch^{-1} had no effect on measured threshold, although gradients of 30 inch^{-1} did exhibit distinctly higher thresholds. When initial K_{max} values were higher, ranging from 8 to $40 \text{ ksi}\sqrt{\text{inch}}$, faster shed rates also led to higher thresholds. Representative data from this study are shown in Figure 3M.1, which illustrates the increase in measured threshold with increasing initial K_{max} values for two different ASTM load shed rates. In these data, thresholds are unchanged with initial K_{max} until initial K_{max} exceeds $18 \text{ ksi}\sqrt{\text{inch}}$. The artificial elevation in threshold is more pronounced for $C = -20 \text{ inch}^{-1}$, but still occurs at $C = -10 \text{ inch}^{-1}$.

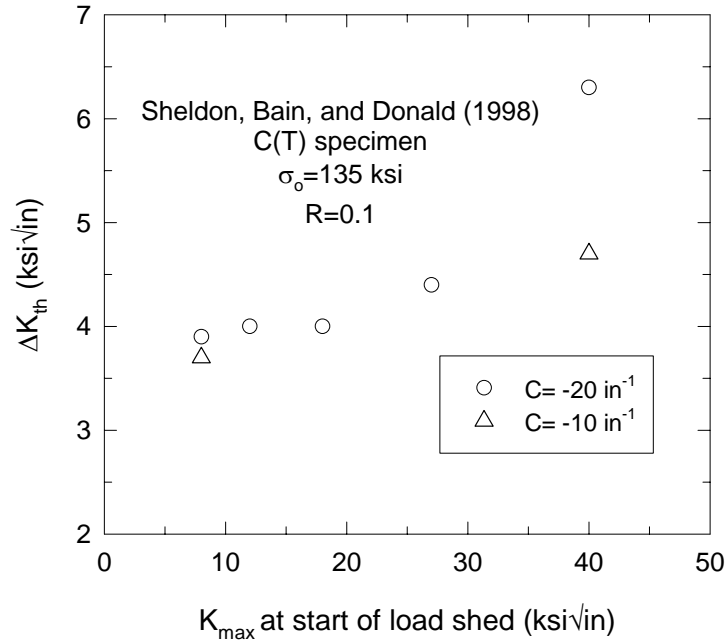


Figure 3M.1. Experimentally determined [3M.2] effect of K_{max} at start of load shed on measured threshold for different load shed rates.

It is not completely surprising that load sheds much faster than recommended by the ASTM standard can sometimes cause anomalous results. However, load sheds conducted at the recommended ASTM load shed rates can also cause difficulties when initial ΔK values are too high. Fleck [3M.3] has documented a particularly good example of this phenomenon from companion threshold tests at $R = 0.05$ with 3 mm (0.12 inch) thick compact tension specimens of BS4360 steel. Both tests employed ASTM load sheds with $C = -0.08 \text{ mm}^{-1}$ (-2 inch^{-1}). A “conventional test” with an initial ΔK value at the beginning of the load shed of $10 \text{ MPa}\sqrt{\text{m}}$ ($9 \text{ ksi}\sqrt{\text{inch}}$) gave a threshold value around $\Delta K_{th} = 6 \text{ MPa}\sqrt{\text{m}}$ ($5.5 \text{ ksi}\sqrt{\text{inch}}$). The other test, employing a much higher value of $\Delta K_0 = 51.4 \text{ MPa}\sqrt{\text{m}}$ ($47 \text{ ksi}\sqrt{\text{inch}}$), indicated a much higher threshold of $14.9 \text{ MPa}\sqrt{\text{m}}$ ($11.7 \text{ ksi}\sqrt{\text{inch}}$) (see Figure 3M.2).

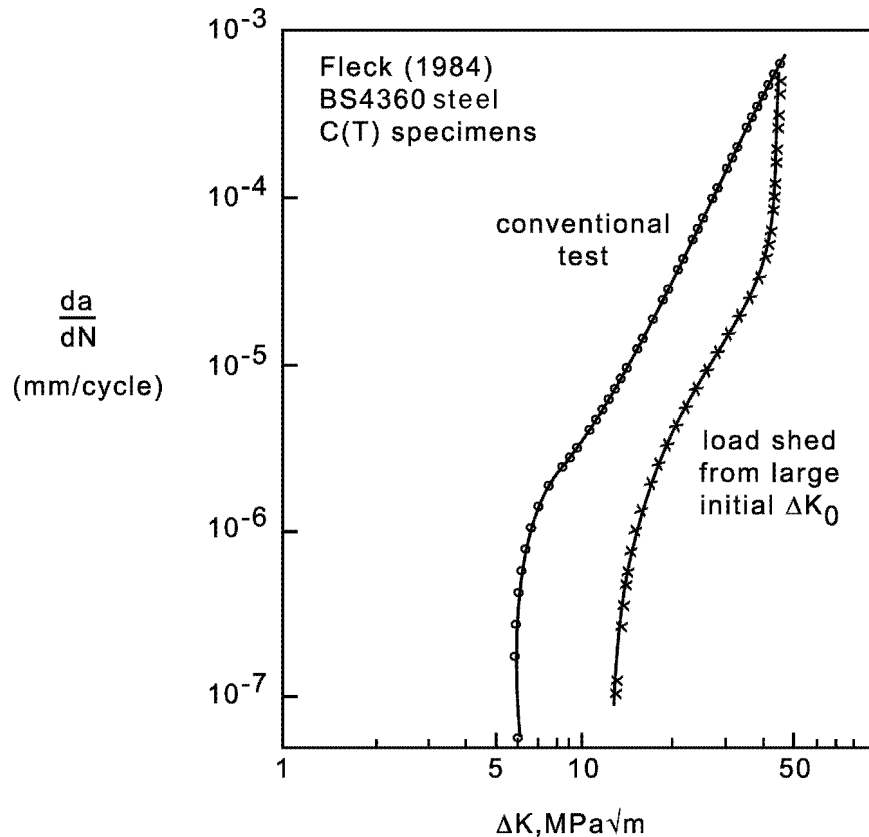


Figure 3M.2. Fleck [3M.3] FCG data for test with a conventional load shed from an initial $\Delta K_0 = 10 \text{ MPa}\sqrt{\text{m}}$ and another test with a load shed from an initial $\Delta K_0 = 51.4 \text{ MPa}\sqrt{\text{m}}$

One potential reason for the observed effects of rapid load shed and high initial ΔK on apparent threshold is fatigue crack closure. Plasticity-induced closure is dependent on the prior load history, which influences the plastic wake behind the crack as well as the residual stresses ahead of the crack. Since the prior load history in a threshold load shed has a larger amplitude than the current load history, the residual displacements behind the crack will be relatively larger, which could lead to artificially increased levels of closure. Increased closure, in turn, would reduce the effective range of the stress intensity factor, leading to threshold crack arrest at somewhat higher ΔK levels than under constant amplitude loading.

Fleck [3M.3] provided experimental evidence for this argument. He measured closure in the tests referenced previously using a crack mouth gage, back face strain gage, and replicas. As shown in Figure 3M.3, in the “conventional

test” with a load shed beginning at ΔK_0 about 10 MPa $\sqrt{\text{m}}$, the effective stress range ratio $U = (S_{\text{max}} - S_{\text{open}})/(S_{\text{max}} - S_{\text{min}})$ remained about 0.70, decreasing only very near the threshold. However, in the test where the load shed began at $\Delta K_0 = 51.4$ MPa $\sqrt{\text{m}}$, U decreased (closure increased) sharply to 0.40 as ΔK decreased to 40 MPa $\sqrt{\text{m}}$, and further decreased below 0.20 as threshold was approached. This substantial increase in closure could easily explain the sharp increase in apparent threshold.

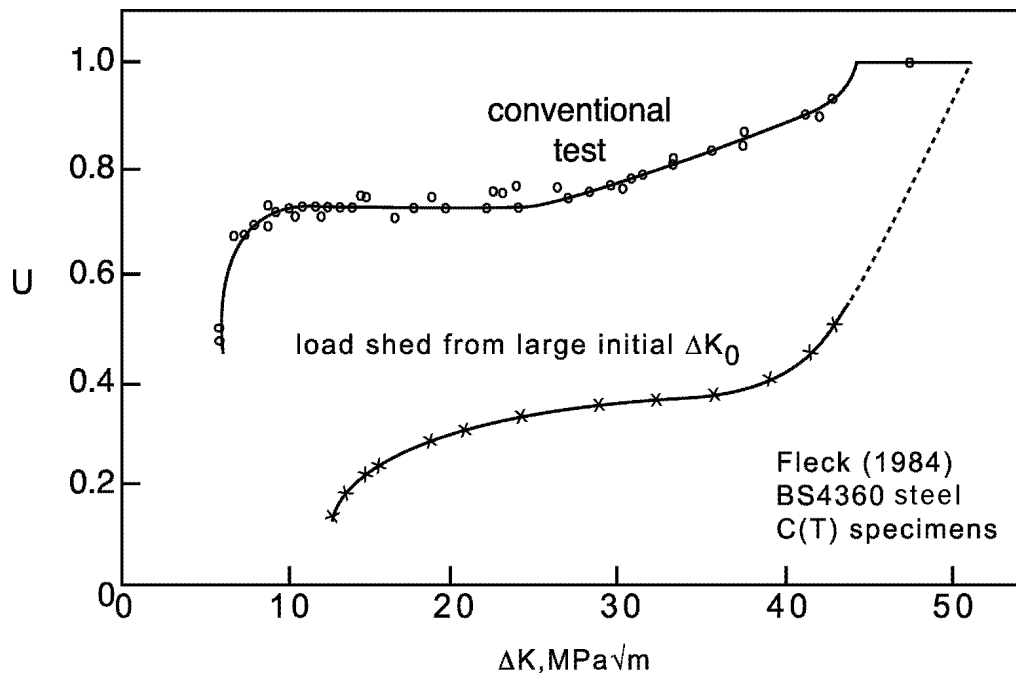


Figure 3M.3. Fleck [3M.3] crack closure measurements for test with a conventional load shed from an initial $\Delta K_0 = 10$ MPa $\sqrt{\text{m}}$ and another test with a load shed from an initial $\Delta K_0 = 51.4$ MPa $\sqrt{\text{m}}$.

The effects of threshold load sheds on fatigue crack closure behavior have been studied previously with a finite element model of a growing fatigue crack [3M.4]. The crack was first grown at a constant applied stress range until a full wake had developed and closure levels had stabilized. Then, at some predetermined crack length, stress amplitudes were reduced in accordance with Eq. 3M.2 while keeping the stress ratio constant. The closure level during the load shed simulation increased substantially to artificially high levels, which is consistent with the Fleck observations.

However, the FE model is not the ideal tool to study closure during threshold load sheds. The FE mesh along the crack line must be fine enough to capture reversed yielding at the crack tip in order to give reliable results, and this causes problems at low stress amplitudes, when plastic zone sizes become very small. The logical solution – to make near-tip elements smaller – either dramatically increases the number of elements, thereby making execution times impractically long, or requires a decrease in the length of the fine mesh region, limiting the distance over which loads can be shed. As a result, the threshold test simulations reported above addressed only the early portion of the load shed and were terminated before the applied stress intensity factor reached true near-threshold levels. Therefore, although the FE studies clearly show the tendencies for closure artifacts under some load sheds, they cannot simulate the entire load shed process.

FASTRAN Modeling

An alternative mechanics model of fatigue crack closure that is free of these limitations is one based on a strip yield crack model. Although several such models have been published, the most well-known and widely-used is the FASTRAN model of Newman [3M.5, 3M.6]. FASTRAN is an analytical crack closure model based on the Dugdale model, but modified to leave plastically deformed material in the wake of the crack. In this model, the plastic-zone size and crack-surface displacements are obtained by superposition of two elastic problems – a crack in a plate subjected to a remote uniform stress and a crack in a plate subjected to uniform stress acting over a segment of the crack surface. The FASTRAN model was developed for a central crack in a finite-width specimen subjected to uniform stresses, or through-cracks emanating from a circular hole in a finite width specimen also subjected to uniform applied stresses. The model is composed of rigid-perfectly plastic regions ahead of the crack tip and in the crack wake, and a linear elastic region elsewhere. The flow stress σ_0 in the plastic regions is taken as the average between the yield and ultimate strength of the material as a first-order approximation for strain hardening.

The primary advantages of FASTRAN are that it is much faster than the FE model, and that there are no mesh limitations on the extent of crack growth or the stress magnitudes applied. The disadvantages are that FASTRAN employs a much simpler representation of the stress, strain, and displacement fields both ahead of the crack and behind the crack (in its wake); much simpler formulations for material constitutive response and constraint; and the model is limited to two reference geometries.

FASTRAN has been used previously to study crack closure during threshold load sheds. Newman [3M.7] simulated several different threshold load shed procedures and found anomalously high levels of closure very near threshold in some cases. More recently, Newman [3M.8] employed the current version of the model, FASTRAN-II [3M.6], to investigate load shed closure behavior in more detail. A direct comparison of FASTRAN and FE simulations [3M.9] found that predicted closure levels during the load shed agreed remarkably well in the region where the two overlapped.

Based on these validations, the FASTRAN model can be used with some confidence to study how different parameters influence closure behavior during threshold load sheds. Figure 3M.4 shows results for three simulations with the same geometry, material, stress ratio, and normalized K -gradient, but different initial maximum stresses at the start of the load shed. The initial ΔK values at the start of the load shed ranged from 10.7 to 34.1 ksi $\sqrt{\text{inch}}$. The simulations show the usual stress level effect on closure before the start of the load shed. At the highest S_{max}/σ_0 value, the closure history shows a sharp immediate increase in closure when the load shed commences, followed by some decrease in closure as the load shed continues, but then a further rise in closure near the end of the load shed. At the lowest S_{max}/σ_0 value, the initial rise in closure is relatively small, and additional increases in closure are not observed near the end of the test. The final normalized closure level $S_{\text{open}}/S_{\text{max}}$ is slightly higher than $S_{\text{open}}/S_{\text{max}}$ just before the load shed, but this is to be expected; the S_{max}/σ_0 value at the end of the test is lower than at the start of the test, and the stress level effect on constant amplitude closure has already been noted.

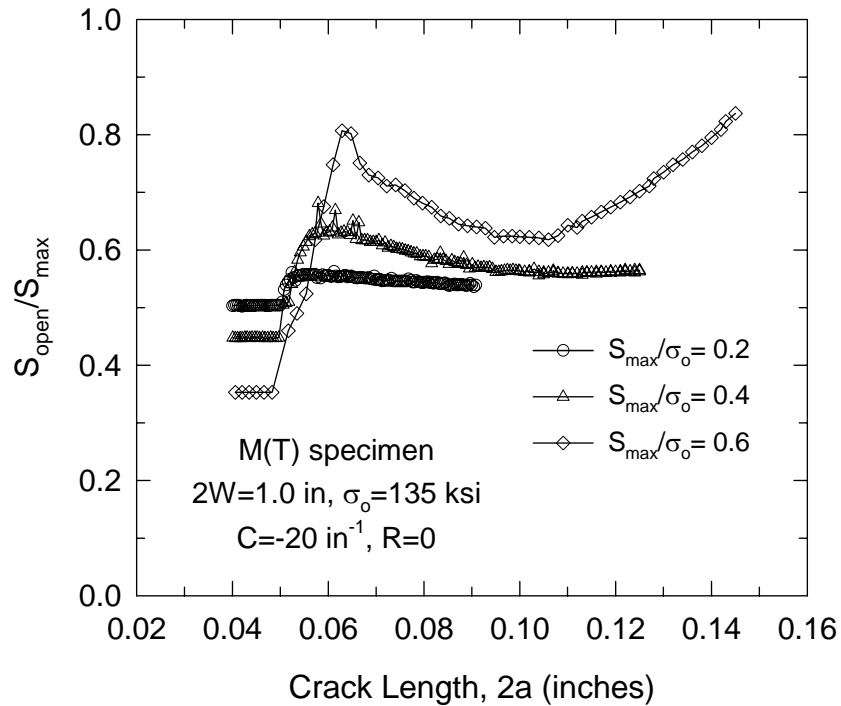


Figure 3M.4. Calculated crack opening stresses during simulated threshold load sheds for different maximum stresses at start of load shed.

Figure 3M.4 demonstrates that closure levels can change in complex ways during a threshold load shed. For the purposes of determining the FCG threshold itself, the most important closure level is probably the closure level at near-threshold values of ΔK . In this study, the value of $\Delta K = 5$ ksi $\sqrt{\text{inch}}$ was chosen as a representative near-threshold condition. In the graphs of results that follow, then, the closure behavior during a threshold load shed is characterized by the S_{open}/S_{max} value when ΔK has decreased to 5 ksi $\sqrt{\text{inch}}$, irrespective of the starting ΔK value. This provides a convenient one-parameter indication of load-shed closure.

Figure 3M.5 summarizes the results of numerous simulations for the same material, load shed rate, and a/W value, but six different specimen sizes and six different initial maximum stresses, leading to a wide range of initial ΔK values at the start of the load shed. The results demonstrate the effect of the initial ΔK

value on anomalous closure behavior during threshold load sheds. When the initial ΔK value was relatively small, the load shed had little or no effect on crack closure; the S_{open}/S_{max} value at $\Delta K = 5 \text{ ksi}\sqrt{\text{in}}$ was within a few percent of the corresponding S_{open}/S_{max} value during constant amplitude cycling at the final S_{max}/σ_0 value. As the initial ΔK increased, however, an increasing closure artifact was observed, with S_{open}/S_{max} values even approaching 1 as the initial ΔK approached $40 \text{ ksi}\sqrt{\text{in}}$. This increase was consistently observed whether the higher ΔK value was due to a larger specimen size or a higher initial stress, suggesting that initial ΔK is an appropriate correlating parameter.

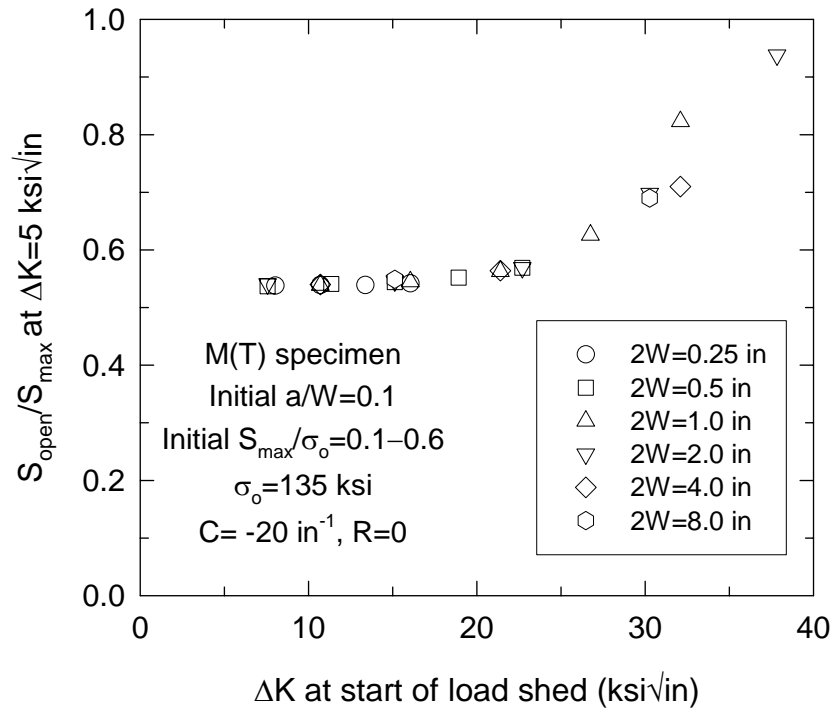


Figure 3M.5. Calculated effect of ΔK at start of load shed on crack opening stress near threshold for different specimen sizes and initial maximum stresses.

However, ΔK alone is an inadequate indication of whether or not a closure artifact is observed. The results in Figure 3M.6 demonstrate that material strength is also a critical variable. The two sets of simulations in Figure 3M.6 differed only in the material flow strength; all other loading and geometry

parameters were the same. The material with the lower flow stress exhibited closure artifacts at substantially lower values of initial ΔK .

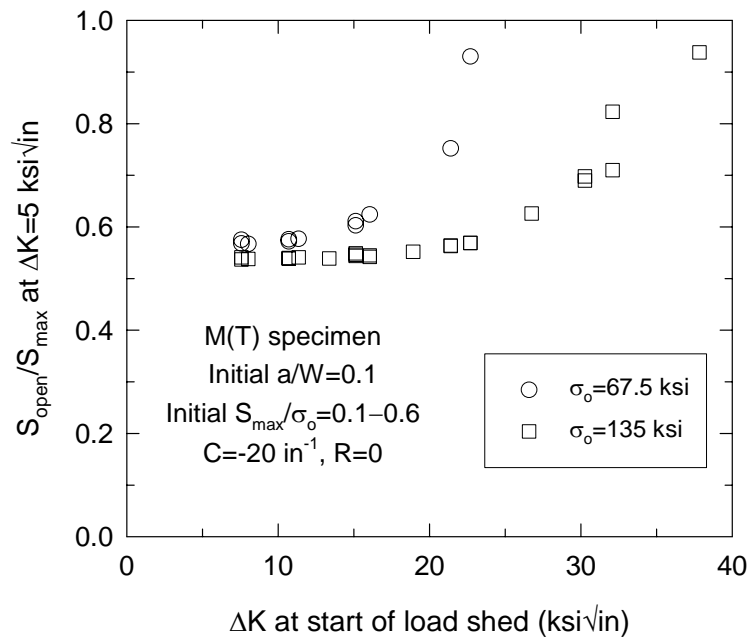


Figure 3M.6. Calculated effect of ΔK at start of load shed on crack opening stress near threshold for different material flow strengths.

All of the simulations in Figures 3M.5 and 3M.6 maintained the same value of the ASTM normalized K -gradient, $C = -20 \text{ inch}^{-1}$. The results in Figure 3M.7 show the effects of load shed rate: closure artifacts were observed at much lower initial ΔK values for faster shed rates. At the recommended ASTM rate ($C = -2 \text{ inch}^{-1}$), larger initial ΔK values could be tolerated even in this weaker material, but a closure artifact was observed eventually as initial ΔK continued to increase.

These simulation results in Figures 3M.5 through 3M.7 are entirely consistent with the experimental data shown earlier in Figure 3M.1: higher values of initial ΔK led to anomalously high closure and anomalously high thresholds, and these anomalous effects occurred at lower values of initial ΔK for faster load shed rates. No direct comparisons between the experiments and the analysis are provided because closure measurements were not reported for the

experiments, and it is not immediately obvious how to calculate the quantitative effect of increased closure on apparent threshold in the simulations. However, the analysis confirms the general conclusion of the experimental study that load shed rates of $C = -20 \text{ inch}^{-1}$ do not cause anomalous closure or anomalous threshold values if initial ΔK values are held below 20 $\text{ksi}\sqrt{\text{inch}}$.

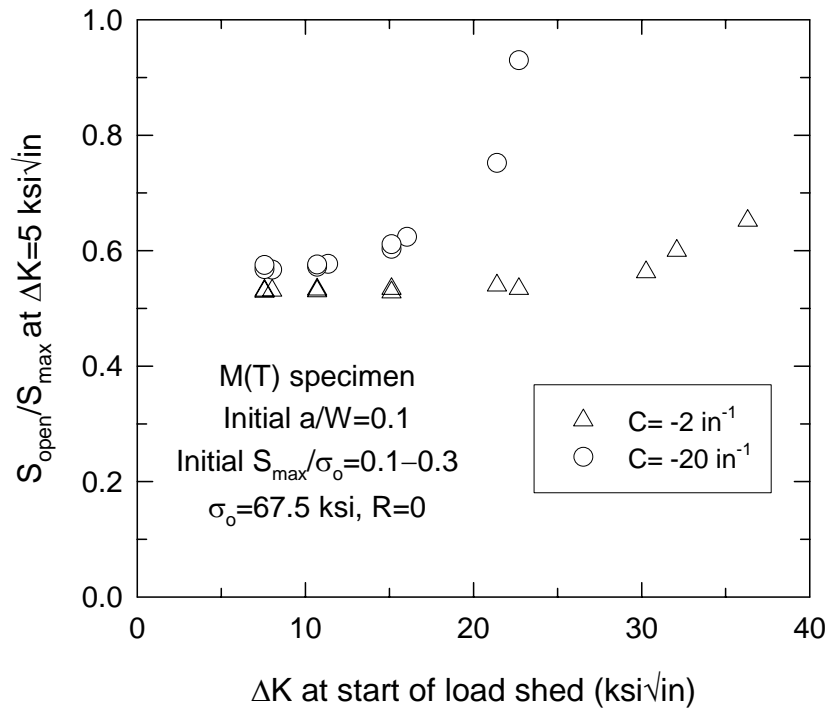


Figure 3M.7. Calculated effect of ΔK at start of load shed on crack opening stress near threshold for different load shed rates.

Several limitations of this investigation should be noted. First, all of the reported FE and FASTRAN-II results were for plane stress conditions ($\alpha = 1$ in the FASTRAN-II code). In contrast, near-threshold FCG conditions are often more nearly plane strain in nature, since loads and plastic zone sizes are small. However, additional FASTRAN threshold load shed simulations, not shown here, were conducted in full plane strain ($\alpha = 3$), where crack closure still occurs even in baseline constant amplitude behavior [3M.5]. The results were qualitatively similar, although anomalous increases in closure were somewhat less pronounced and occurred at slightly higher values of initial ΔK . The plane stress results were shown here because they illustrated the phenomena more clearly,

and because large numbers of plane stress analyses were computationally much faster than plane strain analyses. However, it should not be hastily concluded that threshold load shed closure effects are strictly a plane strain phenomenon. Thresholds may be significantly influenced by crack closure that occurs at the specimen surface, which will be more nearly in plane stress. Furthermore, remember that the most striking closure artifacts occurred very early in the load shed, when applied stresses were significantly higher and the constraint state could more nearly approximate plane stress. These artifacts may still influence closure later in the load shed after the stress state has transitioned to plane strain.

Second, these investigations were limited to plasticity-induced crack closure. Near the threshold, other closure mechanisms such as crack surface roughness or crack surface oxides may become important. However, the plasticity-induced closure mechanism is still operative near the threshold (perhaps under plane strain conditions, as discussed in the previous paragraph), and can make independent contributions to the interference of mating surfaces behind the crack tip. In other words, the contributions of different closure mechanisms may be additive, and so artificially elevated levels of plasticity-induced closure can influence the total closure level, even if the contributions of roughness- or oxide-induced closure are substantial. And again, remember that some closure artifacts are associated with the early load shed history, when applied stresses are significantly higher and plasticity-induced closure is likely of even greater relative significance.

SUMMARY AND CONCLUSIONS

1. Mechanics modeling of growing fatigue cracks indicates that closure artifacts, which would influence apparent fracture mechanics thresholds, can arise during threshold load shedding procedures.
2. Load shedding can sometimes be carried out at rates faster than recommended by the ASTM test method without introducing closure artifacts or inducing artificially high thresholds. Faster load shed rates are acceptable when values of ΔK at the start of the load shed are relatively

lower, but faster rates can cause difficulties when the values of ΔK at the start of the load shed are relatively higher. Load shedding at rates recommended by the ASTM test method can still produce closure artifacts when the initial ΔK at the start of the load shed is too high.

3. Specified values of initial ΔK at the start of the load shed are insufficient, by themselves, to determine if closure artifacts will occur. Material flow strength can also play a key role, such that weaker materials exhibit closure artifacts at smaller initial values of ΔK .
4. Safe use of the current ASTM test method requires experimentally confirmed limits on the value of ΔK at the start of the load shed, taking the shed rate and material yield strength into account. For the PRDA Ti-6-4 material and a load shed rate of -20 inch^{-1} , the initial ΔK should be kept below about $20 \text{ ksi}\sqrt{\text{inch}}$ to avoid closure artifacts.

REFERENCES

- 3M.1 Saxena, A., Hudak, S.J., Jr., Donald, J.K., and Schmidt, D.W., "Computer-Controlled Decreasing Stress Intensity Technique for Low Rate Fatigue Crack Growth Testing," *Journal of Testing and Evaluation*, Vol. 6, 1978, pp. 167-174.
- 3M.2 Sheldon, J.W., Bain, K.R., and Donald, J.K., "Investigation of the Effects of Shed-rate, Initial K_{\max} , and Geometric Constraint on ΔK_{th} in Ti-6Al-4V at Room Temperature," to be published in *International Journal of Fatigue*.
- 3M.3 Fleck, N.A., "An Investigation of Fatigue Crack Closure," CUED/C-MATS/TR.104, Cambridge University Engineering Department, 1984.
- 3M.4 McClung, R.C., "Finite Element Modeling of Crack Closure During Simulated Fatigue Threshold Testing," *International Journal of Fracture*, Vol. 52, 1991, pp. 145-157.

- 3M.5 Newman, J.C., Jr., "A Crack-Closure Model for Predicting Fatigue Crack Growth Under Aircraft Spectrum Loading," Methods and Models for Predicting Fatigue Crack Growth Under Random Loading, ASTM STP 748, American Society for Testing and Materials, 1981, pp. 53-84.
- 3M.6 Newman, J.C., Jr., "FASTRAN-II – A Fatigue Crack Growth Structural Analysis Program," NASA TM 104159, February 1992.
- 3M.7 Newman, J.C., Jr., "A Nonlinear Fracture Mechanics Approach to the Growth of Small Cracks," Behavior of Short Cracks in Airframe Components, AGARD Conference Proceedings No. 328, 1982, pp. 6.1-6.26.
- 3M.8 Newman, J.C., Jr., "Analyses of Fatigue Crack Growth and Closure Near Threshold for Large-Crack Behavior," Fatigue Crack Growth Thresholds, Endurance Limits, and Design, ASTM STP 1372, in press.
- 3M.9 McClung, R.C., "Analysis of Fatigue Crack Closure During Simulated Threshold Testing," Fatigue Crack Growth Thresholds, Endurance Limits, and Design, ASTM STP 1372, in press.

Appendix 3N

SMALL-CRACK THRESHOLD MODEL

R. Craig McClung

and

Stephen J. Hudak, Jr.



Southwest Research Institute

**Submitted
31 August 1999**

SMALL-CRACK THRESHOLD MODEL

A significant fraction of the total life of a component subjected to high cycle fatigue loading may involve the growth of very small cracks. Under some conditions, nucleation of microcracks may occur relatively early in the life. This early nucleation is more likely when other damage states, such as LCF, FOD, or fretting fatigue, act synergistically with HCF. However, larger cracks of engineering size will grow very quickly to failure under high frequency stressing once the fracture mechanics threshold is exceeded. The growth and arrest of microcracks at relatively slow rates could therefore be of appreciable significance to total life. When this occurs, an appropriate engineering description of small crack growth behavior could provide valuable input to HCF life methods.

Small fatigue cracks are known to exhibit growth rate behaviors that are different from conventional large crack behavior, under certain conditions. Small cracks may grow faster than corresponding large cracks at the same ΔK value, and they may also grow at applied ΔK values that are smaller than the large crack threshold, ΔK_{th} . The reasons for these differences are diverse and complex, but nearly all relate to a loss of either microstructural similitude (the crack is small compared to the material microstructure) or mechanical similitude (the crack is small compared to regions of plastic deformation). The literature is filled with models intending to explain and predict these anomalous behaviors.

Formulation

Life management for high cycle fatigue is fundamentally a threshold problem. The number of fatigue cycles during HCF exposure is potentially so large that design to a specific finite life is not feasible. Cyclic stresses must be held below some sort of endurance limit, and/or cyclic stress intensity factors must be held below some appropriate fracture mechanics threshold, to insure that fatal fatigue damage does not accumulate.

Under some conditions, small cracks grow at nominal ΔK values that are lower than the traditional large crack fracture mechanics threshold, ΔK_{th} . In fact, this violation of ΔK_{th} must have occurred every time an originally uncracked smooth specimen breaks under constant amplitude loading. The crack that

caused specimen failure must, at some early point in its life, have been so small ($a \rightarrow 0$) that the nominal applied ΔK was less than the nominal ΔK_{th} .

The relationship between the smooth specimen and fracture mechanics behavior is addressed by the Kitagawa [3N.1] diagram, Figure 3N.1. The Kitagawa diagram integrates the large crack threshold (ΔK_{th}), represented by the sloping line, with the traditional smooth specimen endurance limit ($\Delta\sigma_e$), represented by the horizontal line. The region on the Kitagawa diagram above either the horizontal endurance limit line or the sloping threshold line is “unsafe” in that fatigue failure is predicted to occur. The region below both lines is “safe” in that fatigue failure is predicted not to occur. The intersection of the two lines, defined as a_0 , is given by the equation

$$a_0 = \frac{1}{\pi} \left(\frac{\Delta K_{th}}{F \Delta \sigma_e} \right)^2 \quad (3N.1)$$

where, for consistency with the smooth specimen endurance limit data, $F = 1.12$ ($2/\pi$) is the geometry correction factor in the K solution for the semi-circular surface crack in the smooth specimen.

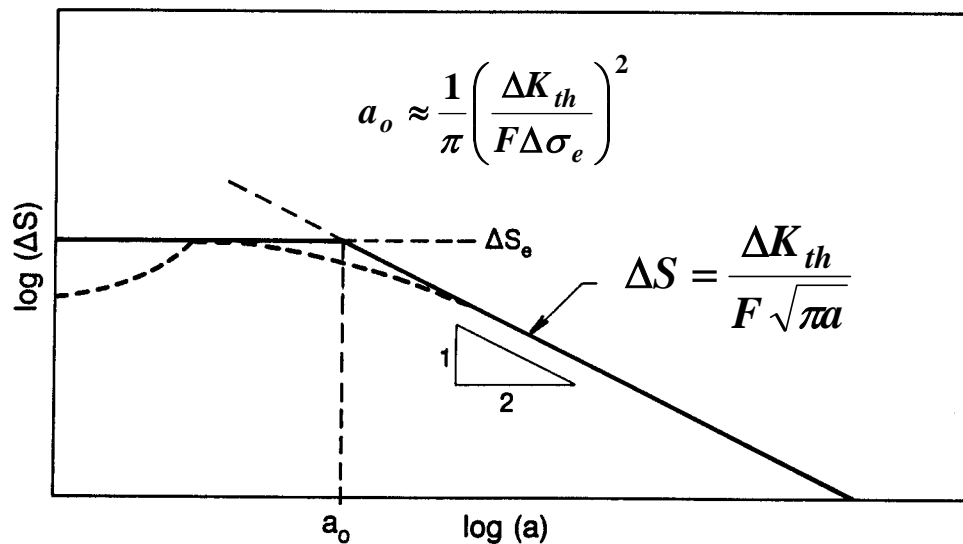


Figure 3N.1. Schematic Kitagawa diagram.

The Kitagawa diagram indicates that cracks smaller than a_0 must be able to grow at nominal stress intensity factors that are less than the large crack

threshold, since smooth specimens fail by the nucleation and growth of microcracks to failure. El Haddad [3N.2] suggested that small cracks could grow below the large crack threshold because the effective driving force of the small cracks was larger than expected from traditional large crack fracture mechanics. He proposed that the actual effective driving force was

$$\Delta K_{eq} = F(a)\Delta S\sqrt{\pi(a + a_0)} \quad (3N.2)$$

Here $F(a)$ is the crack shape and specimen/component geometry correction factor for the component of interest; a_0 is not included in $F(a)$. Note that the a_0 contribution is negligible for large values of a , but becomes increasingly significant for smaller values of a .

However, the El Haddad construction can also be interpreted as a crack-size dependent *threshold* rather than a crack-size dependent *driving force*. This crack-size dependent threshold is given as

$$\Delta K_{th}^{SC}(a) = \Delta K_{th}\sqrt{\frac{a}{a + a_0}} \quad (3N.3)$$

Although the El Haddad concept has been criticized for its apparent lack of physical justification, several researchers [3N.3, 3N.4] have independently derived similar formulations based on detailed micromechanical considerations, and these have been shown to be numerically identical to the El Haddad formulation under typical conditions. Chan [3N.3] related a_0 to dislocation pileups and Mode II shear cracks, and found satisfactory agreement with small-crack data from titanium aluminides. Tanaka [3N.4] formulated the problem in terms of a crack-tip slip band blocked by a grain boundary, and demonstrated reasonable agreement between his formulation and a variety of experimental data, as shown in Figure 3N.2. While titanium was not included in the Tanaka comparisons, Brown and Taylor [3N.5] have shown good agreement with the El Haddad formulation for a mill-annealed Ti-6-4.

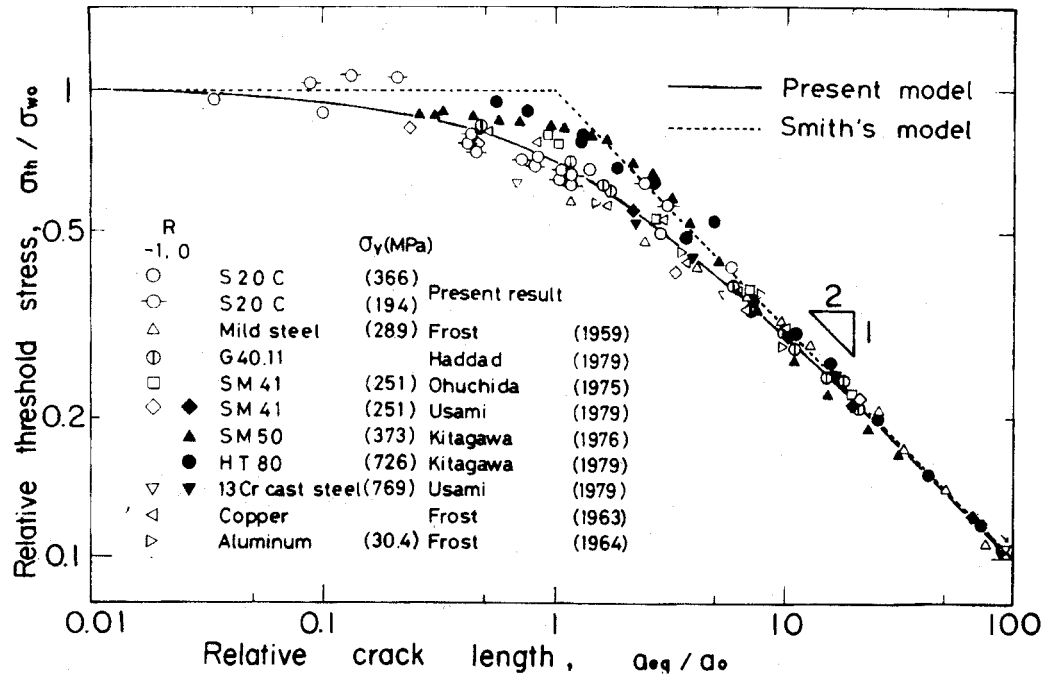
The El Haddad model is easily visualized in the context of the Kitagawa diagram. Kitagawa diagrams for the PRDA Ti-6-4 material at stress ratios of $R = 0.1$, 0.5 , and 0.8 are shown in Figure 3N.3. The endurance limit was estimated in these graphs as the approximate 10^7 cycle fatigue strength from the PRDA smooth specimen testing, and the large-crack threshold was estimated from PRDA fracture mechanics test results. The dashed curve that asymptotes to these two lines corresponds to the small-crack threshold given by Eq. 3N.3, which can also be expressed in terms of a threshold stress:

$$\Delta S_{th} = \frac{\Delta K_{th}}{F\sqrt{\pi(a+a_0)}} \quad (3N.4)$$

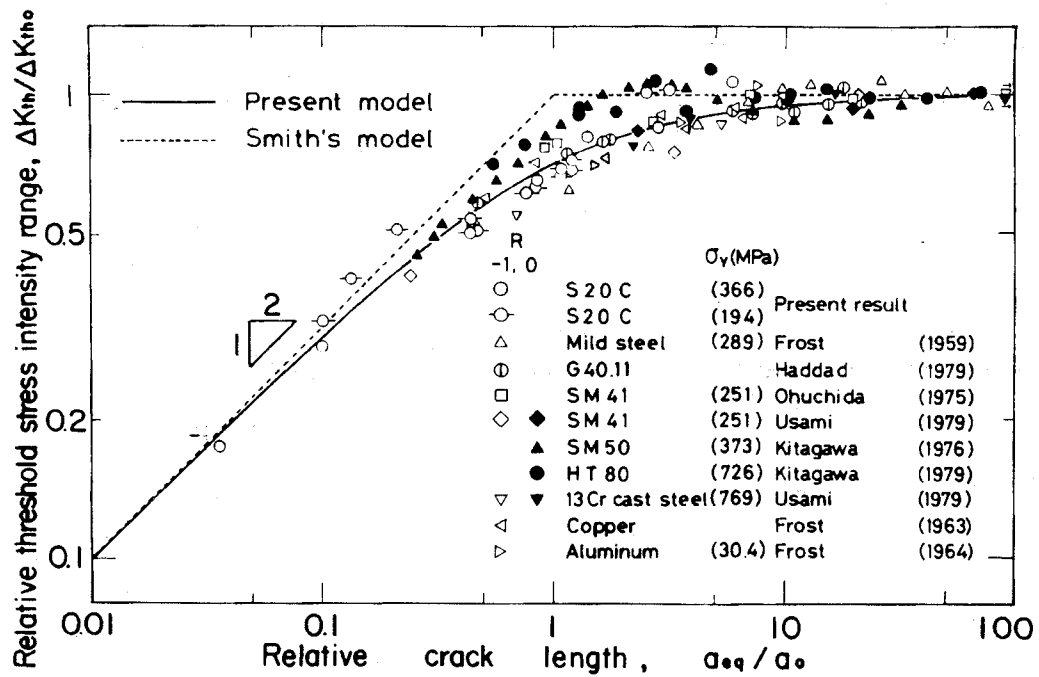
Notice that a_0 , corresponding to the intersection of the endurance limit and large-crack threshold lines, is calculated to be approximately the same for $R = 0.1$ ($a_0 = 0.0023$) and $R = 0.5$ ($a_0 = 0.0022$) and somewhat higher for $R = 0.8$ ($a_0 = 0.0049$). It is possible that this latter calculated value is influenced by time-dependent deformation at very high mean stresses in the PRDA Ti-6-4 material.

The threshold as a function of crack size is shown explicitly in Figure 3N.4 for the same three stress ratios. Perceptible decreases in threshold do not occur until crack sizes decrease well below 0.1 inch, but thresholds are about a factor of two lower than large-crack values for crack sizes on the order of 0.001 inch.

It should also be noted that the calculated value of a_0 may differ slightly depending on the design system framework in which it is generated and implemented. Different regressions of the $S-N$ data or near-threshold FCG data may result in slightly different values of $\Delta\sigma_e$ or ΔK_{th} , and different K solutions for semi-elliptical surface cracks may give slightly different F values. Furthermore, the value of $\Delta\sigma_e$ or ΔK_{th} chosen will depend on the numerical “definition” of the endurance limit or threshold. Does the “endurance limit” stress correspond to 10^7 cycles, or 10^8 cycles, or 10^9 cycles? These values may be slightly different for materials that display a continuously decreasing $S-N$ line.



(a)



(b)

Figure 3N.2. Tanaka [3N.4] comparisons of experimental data with small-crack threshold model.

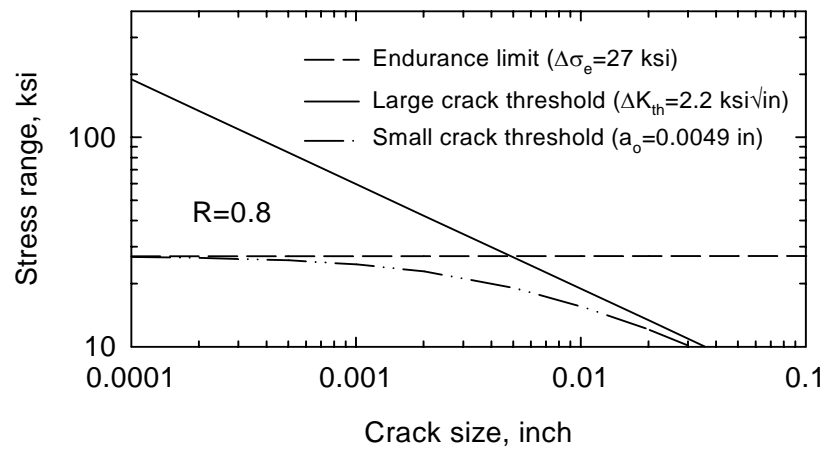
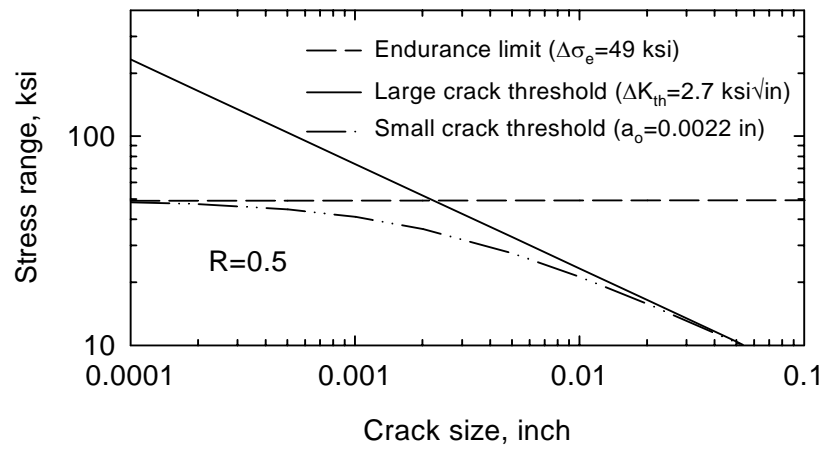
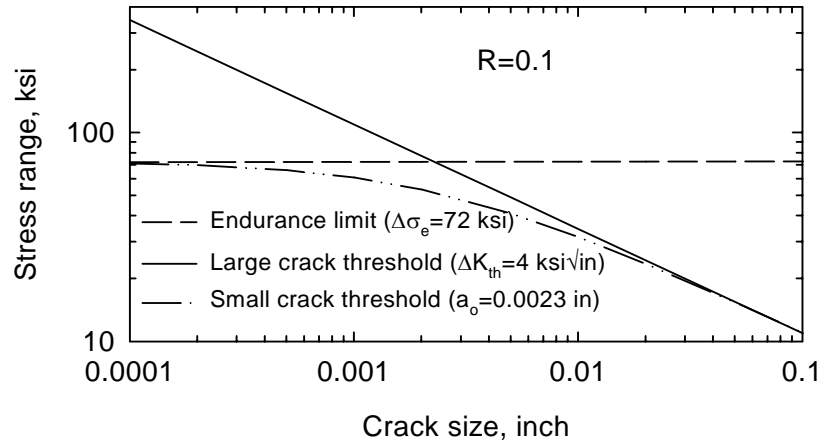


Figure 3N.3. Kitagawa diagrams for PRDA Ti-6-4 at stress ratios of $R = 0.1$, 0.5 , and 0.8 .

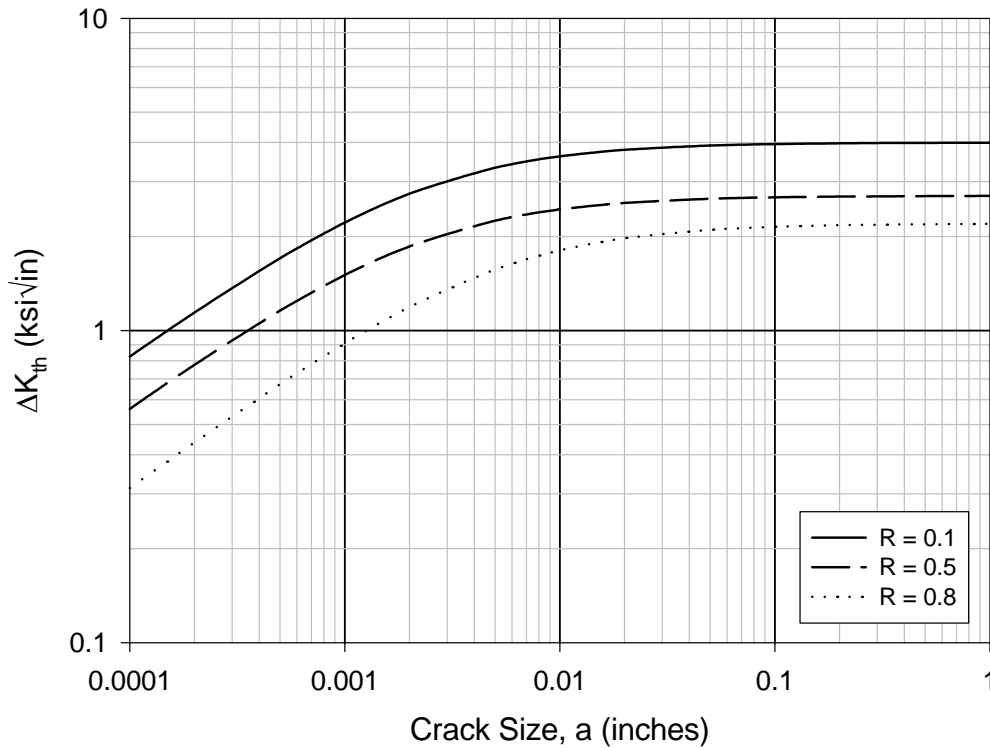


Figure 3N.4. Calculated crack-size dependent threshold for three stress ratios.

The fracture mechanics threshold value is also dependent on the specific low growth rate that is chosen to correspond to the “no growth” condition. PRDA fracture mechanics data generated by P&W for the Ti-6-4 material indicate a multi-linear da/dN vs. ΔK relationship, as shown in Figure 3N.5 for the $R = 0.1$ data. The slope of the da/dN vs. ΔK line apparently changes just above threshold, and then changes again in the vicinity of $\Delta K = 15$ ksi√inch. A closer look at representative data below $\Delta K = 10$ ksi√inch., Figure 3N.6, suggests that the da/dN vs. ΔK relationship is in fact multi-linear, and not merely continuously changing in slope in some curvilinear fashion. Furthermore, the data very near threshold appear to maintain a finite slope even at the lowest recorded crack growth rates. This observation confirms that the identified threshold value is a somewhat arbitrary function of the crack growth rate chosen to represent threshold conditions. For true HCF exposure (e.g., 10^9 cycles), thresholds may be associated with extremely slow crack growth rates (da/dN on the order of 10^{-10} inch/cycle). Therefore, it is possible that appropriate threshold stress intensity factors for HCF conditions should be slightly lower than those values that would

be assigned for LCF fatigue crack growth conditions. This would have an effect on a_0 as well.

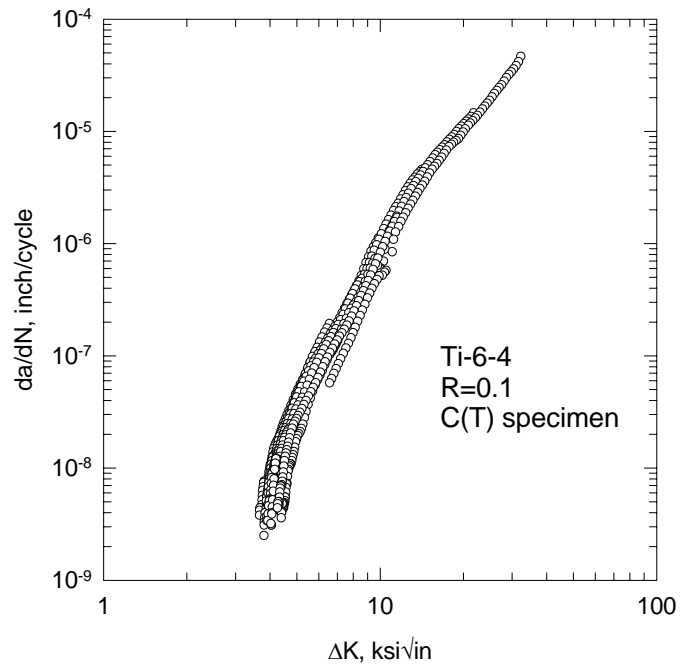


Figure 3N.5. Large-crack FCG data for PRDA Ti-6-4 at $R = 0.1$.

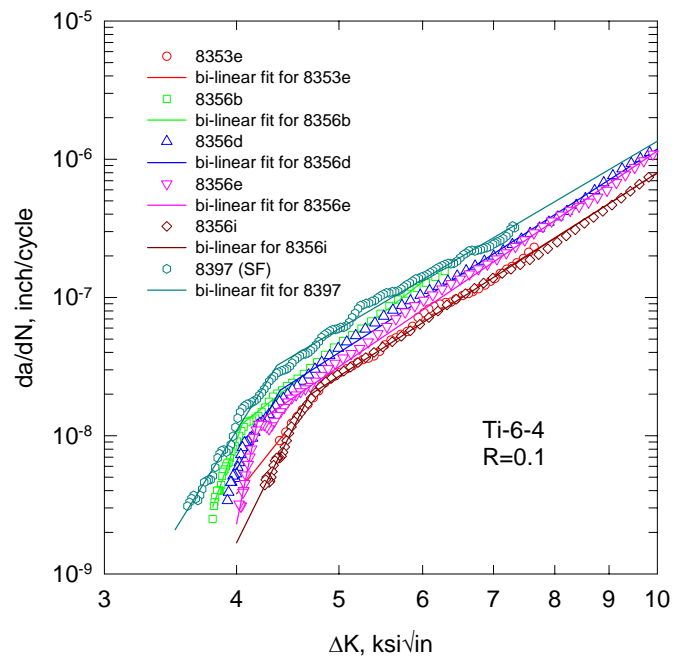


Figure 3N.6. Large-crack FCG data in the near-threshold regime for PRDA Ti-6-4 at $R = 0.1$.

The large-crack threshold can also be slightly dependent on specimen geometry. The lowest value of ΔK_{th} in the data set shown in Figure 3N.6 corresponds to the specimen with a surface crack geometry, whereas all other data in this figure correspond to compact tension geometries. Threshold values determined by GE with surface crack Kb bar specimens tended to be slightly lower than threshold values determined by P&W with compact tension specimens, especially at $R = 0.1$.

The important issue is that the small-crack construction as outlined above be carried out in a manner that is fully consistent with the existing design system for smooth specimens and large crack fracture mechanics. One of the strengths of this particular small-crack model is that it is forced to be accurate in the two limits (endurance limit and large-crack threshold behavior), and therefore serves effectively as an engineering interpolation scheme between known bounding conditions.

The proposed simple model for small-crack behavior in titanium under HCF conditions, then, is to calculate a crack-size dependent threshold according to Eq. 3N.3, where a_0 is calculated according to Eq. 3N.1. The “endurance limit” in Eq. 3N.1 is taken as the smooth specimen fatigue strength at an appropriate number of cycles, and the threshold in Eq. 3N.1 is taken as the large crack threshold at an appropriate fatigue crack growth rate.

Discussion

Other factors are also known to influence the behavior of small fatigue cracks. Cracks that are smaller than the dimension of the characteristic microstructural boundary (e.g., the grain size) are known to exhibit faster growth rates and lower thresholds under certain conditions, although crack deceleration and/or arrest may occur when the crack tip reaches the microstructural boundary. The dotted scallop just below the horizontal endurance limit line at the far left hand side of the Kitagawa diagram in Figure 3N.1 represents this type of behavior. It appears prudent to limit the applicability of Eq. 3N.3 to $a \geq D/2$, where D is the material grain size. For crack sizes smaller than $D/2$, the threshold condition may be controlled by the applied stress rather than stress

intensity [3N.3]. However, the characteristic microstructural dimension of the PRDA Ti-6-4 is extremely small (grain size on the order of 0.4 to 0.8 mils), and so cracks of this size do not appear to be of direct relevance to engineering life prediction. Future HCF efforts with alternative microstructures will require a revisiting of this issue.

Small cracks are also known to exhibit accelerated behaviors when the applied stresses are a large fraction of the material yield strength. Elevated stresses cause both a loss of similitude in the crack-tip fields and a change in levels of crack closure. However, conditions of relevance to HCF of turbine engines are primarily lower stress ranges. The endurance limit at $R = 0.1$ is on the order of half of the yield strength, and an even smaller fraction of yield at higher stress ratios. Therefore, these particular phenomena are not likely significant factors in small crack behavior for the PRDA HCF program.

The calculated values of a_0 for the PRDA Ti-6-4 given above are relatively small, indicating that the regime of small-crack effects is restricted to rather small crack sizes in this material. Figure 3N.4 suggests that the threshold will decrease from 4 ksi $\sqrt{\text{inch}}$ to 2.2 ksi $\sqrt{\text{inch}}$ or less only for cracks smaller than about 0.001 inch. However, smaller decreases in threshold are possible for cracks up to 0.1 inch in size.

THE SIGNIFICANCE OF SMALL-CRACK BEHAVIOR

A comparison of smooth specimen $S-N$ data and FCG models permits some interesting observations about the relative importance of crack nucleation and propagation in total smooth specimen lives. Smooth specimen data from PRDA testing at $R = 0.1$ are summarized in Figure 3N.7. These data include the round-robin results from three engine companies as well as selected tests from the P&W cyclic stress-strain experiments that exhibited the same $R = 0.1$ stress ratio at the half-life.

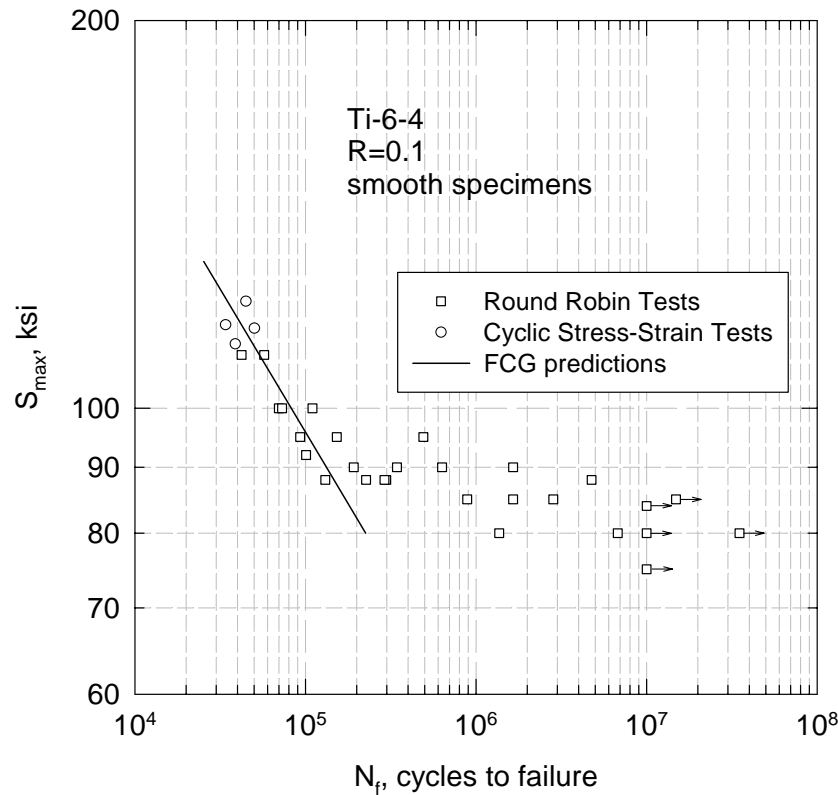


Figure 3N.7. Smooth specimen S - N data from PRDA Ti-6-4 testing at $R = 0.1$, with predicted life curve from FCG considerations.

Superimposed on these data is a predicted life curve based solely on fracture mechanics considerations. The fracture mechanics line was generated by calculating the total FCG life for a cylindrical smooth specimen geometry from an initial semicircular flaw with depth = 0.001 inches to specimen failure at crack depths on the order of 0.06 to 0.09 inches. The initial flaw depth of 0.001 inch was chosen here because of the convenient fit it provided to the S - N data, but this flaw size is comparable to the typical grain sizes of 10-20 μm (0.0004 – 0.0008 inches) in the PRDA Ti-6-4 material.

A simple single-linear Paris relationship with no threshold was assumed in this life calculation, with Paris constants taken from the linear regime in Figure 3N.6 between threshold and the $\Delta K = 15 \text{ ksi}\sqrt{\text{inch}}$ knee. Note that the threshold has been neglected because the applied stresses in this calculation are all greater than the endurance limit. According to the Kitagawa diagram (Figure 3N.1), in this stress regime no continuum fracture mechanics threshold is

operative. Neglecting the small change in slope above the 15 ksi/inch knee is of no consequence for this particular life calculation, since the great majority of the life is consumed at lower ΔK values. The specific Paris constants used in this calculation were based on the data for Specimen 8397, which is the only surface flaw specimen represented in Figure 3N.6. Compared to the compact tension specimens otherwise represented in Figure 3N.6, the surface flaw specimen experienced higher applied stresses and shorter crack lengths that were more similar to the hypothetical smooth specimen life calculations. The stress intensity factor solution employed was the SC07 solution for a thumbnail crack in a cylinder contained in the NASGRO FCG computer code.

The comparison between the fracture mechanics line and the *S-N* test data suggests that at maximum stresses above 90 to 95 ksi, the total life of the smooth specimen is dominated by crack propagation. Nucleation of a 0.001-inch, one-grain crack will not occur instantly, but will occur early enough in the total life of the specimen at these high stresses that the nucleation phase can be neglected in an engineering life calculation. At maximum stresses below 90 ksi, however, crack nucleation plays an increasingly dominant role in total smooth specimen life. For example, at 80 ksi, only about 200,000 fatigue cycles are required to grow a 0.001-inch crack to failure, but total smooth specimen lives are on the order of 10,000,000 cycles.

These observations indicate that small-crack behavior is of limited significance for total life prediction of smooth geometries under constant amplitude loading, because the crack propagation phase is a very small fraction of the total life. Furthermore, the small-crack threshold model presented earlier in this document indicates that small-crack behavior is of limited significance for traditional fracture mechanics life modeling, because the regime of important small-crack behavior occurs at crack sizes much smaller than the regime traditionally addressed by crack growth life methods. Assumed initial crack sizes in traditional damage tolerance methods are historically much larger than typical a_0 values calculated for Ti-6-4.

However, small-crack behavior may still be of great significance for HCF life modeling. Small-crack behavior will be important when microcracks can be nucleated relatively early in the design lifetime, and when their growth or nongrowth is the critical determinant of component safety. These appear to be precisely the conditions satisfied by many HCF problems. The three damage states currently under consideration – HCF/LCF interaction, FOD, and fretting fatigue – can all potentially introduce microcracks very early in the design lifetime. And, as was observed at the beginning of this document, HCF is largely a threshold problem. The potential number of fatigue cycles is so large that any non-zero crack growth rate can lead to failure relatively quickly. Component safety under HCF conditions, then, is maintained by ensuring that any microcracks that may form due to a damage state will not grow.

Therefore, the small-crack models presented here have potential applicability to all three damage states – HCF/LCF, FOD, and fretting fatigue.

SUMMARY AND CONCLUSIONS

1. A simple engineering relationship for the effect of crack size on the fracture mechanics threshold appears useful for HCF design systems. This relationship, originally proposed by El Haddad, et al. and Tanaka, et al. as a modification to the Kitagawa diagram, requires as input only conventional information about the smooth specimen endurance limit and the large crack fracture mechanics threshold. The relationship has been experimentally confirmed in the literature for a number of different materials, including titanium alloys. Confirming experimental small-crack data for the PRDA Ti-6-4 are not yet available.
2. The characteristic small-crack parameter a_0 in the El Haddad/Tanaka model was determined from PRDA baseline data to have a value of approximately $a_0 = 0.0023$ inch for $R = 0.1$ and 0.5 , and $a_0 = 0.0049$ inch for $R = 0.8$. The latter value may be artificially influenced by time-dependent deformation in the baseline tests. Calculated a_0 values may differ slightly depending on the design system framework in which they are calculated and implemented,

since a_0 functions as an interpolating parameter between the bounding values of endurance limits and large crack thresholds.

3. Crack propagation appears to consume a negligible fraction of the total life of an undamaged smooth specimen under constant amplitude loading in the HCF regime (10^7 cycles and greater).
4. The regime of anomalous small-crack behavior in the PRDA Ti-6-4 appears to be limited to crack sizes sufficiently small (on the order of 2 to 10 mils) that the small-crack phenomena is not significant for traditional large-crack damage tolerance methods based on conventional NDE capabilities.
5. Small-crack effects, and in particular the crack-size-dependent threshold, may be extremely significant for HCF life modeling in situations where damage states can potentially nucleate microcracks relatively early in the design lifetime. The growth or non-growth of these microcracks according to a fracture mechanics threshold criterion may be the principal determinant of specimen or component failure, even though the cracks are much smaller than the traditional large cracks addressed by traditional damage tolerance methods. The three damage states under study in the PRDA program – HCF/LCF interaction, FOD, and fretting fatigue – can all potentially nucleate microcracks very early in the design lifetime. Therefore, small-crack behavior appears to be highly significant for HCF life modeling, even in the fine-grain Ti-6-4 under current study.

REFERENCES

- 3N.1 H. Kitagawa and S. Takahashi, "Applicability of Fracture Mechanics to Very Small Cracks or the Cracks in the Early Stage," Proc. 2nd Int. Conf. Mechanical Behavior of Materials, Boston, MA, 1976, pp. 627-631.
- 3N.2 M.H. El Haddad, K.N. Smith, and T.H. Topper, "Fatigue Crack Propagation of Short Cracks," Journal of Engineering Materials and Technology, Trans. ASME, Vol. 101, 1979, pp. 43N.46.
- 3N.3 K.S. Chan, "Fatigue Crack Growth Thresholds of TiAl Alloys," Proc. 2nd Int. Symp. On Gamma Titanium Aluminide, D.M. Dimiduk, Y.-W. Kim, and M.H. Loretto, Eds., TMS, 1999 (in press).
- 3N.4 K. Tanaka, Y. Nakai, and M. Yamashita, "Fatigue Growth Threshold of Small Cracks," International Journal of Fracture, Vol. 17, 1981, pp. 519-533.
- 3N.5 C.W. Brown and D. Taylor, "The Effects of Texture and Grain Size on the Short Fatigue Crack Growth Rates in Ti-6Al-4V," in Fatigue Crack Growth Threshold Concepts, D. Davidson and S. Suresh, Eds., TMS-AIME, 1984, pp. 433-445.

Chapter 4

Low Cycle Fatigue Damage

4.1 BACKGROUND

4.1.1 Objective and Approach

One of this program's objectives is to determine a fan blade's HCF capabilities while under the exposure of LCF load cycles. The approach taken was to characterize this behavior through specimen testing and evaluate/refine methods (developed in Chapter 3) to predict the results of this type of behavior. Both crack growth and notch fatigue specimen tests were conducted under a combination of LCF and HCF loads. Since only notch features on a fan blade are likely to be LCF-life-limited, fatigue testing was conducted using the small-volume double-edge-notched specimen geometry described in Figure 3J.1.

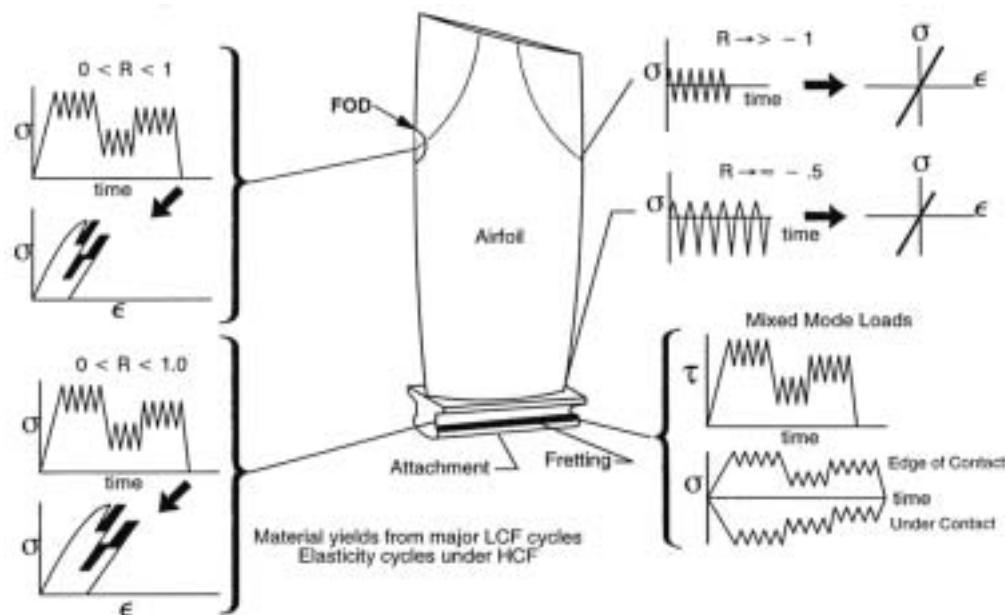


Figure 4.1. Fan blade with typical stress histories at HCF critical locations.

4.1.2 Engine LCF Histories

The fan blade in Figure 4.1 shows the exposure to LCF that is representative for that component. The highest LCF stresses are typically in the attachment region and

are concentrated at notch features or the edge of contact with the disk. The LCF state of stress can exceed the material's monotonic yield strength, but will respond elastically once the material's cyclic stress-strain stabilizes. The operational LCF stresses are typically low to near zero in a smooth airfoil, which indicates that LCF/HCF interaction is not expected to occur in smooth areas, unless a FOD notch exists. Therefore, LCF interaction with HCF fatigue nucleation is only an issue at notch (design or FOD) features; and, this typically results in higher stress ratio ($0 < R < 1$) loading conditions, as indicated by Figure 4.1.

4.1.3 Effects of LCF Cycles on Material Response

LCF cycles may yield the material in a blade notch feature, and subsequent HCF cycles will respond elastically from this yielded state of stress and strain. Characterizing and modeling this condition is a basic requirement for using local stress-strain models to predict the effects of LCF/HCF interaction. Cyclic stress-strain material property testing was conducted to provide several valuable pieces of information: LCF crack-nucleation life under predominantly strain-controlled conditions; determination of cyclic hardening or softening behavior; and a model for assessing notch plasticity and yielding.

As a first step in the process, cyclic stress-strain behavior was generated. As described in paragraph 3.3.1, mid-life maximum and minimum values of stress and strain were used to generate the data previously reported in Figure 3.16. These cyclic data were accurately modeled by the Ramberg-Osgood formulation given in that figure. It is interesting to note the curve is almost elastic-perfectly plastic. Figure 4.2 compares the cyclic Ramberg-Osgood formulation to several monotonic stress-strain curves; this comparison shows that this blade material cyclically softens.



Figure 4.2. Cyclic *versus* monotonic stress-strain results indicates cyclic softening.

4.1.4 Smooth LCF Fatigue Characterization

The baseline LCF data presented previously in Figure 3.11 show the total strain range *versus* life and indicate a dependence on mean stress. These data were generated under strain control conditions at the following strain ratios (R_ϵ): -1.0, 0.1, 0.5 and 0.8. Since most engine components are shot peened, a limited assessment was made to consider the effect of this variable. As shown in Figure 4.3, the (Intensity of 7A) peened specimen LCF testing results indicate a smooth-fatigue-life extension when compared to baseline data. This is attributed to surface compressive residual stresses, which reduce the surface mean stress levels below that anticipated for applied loading.

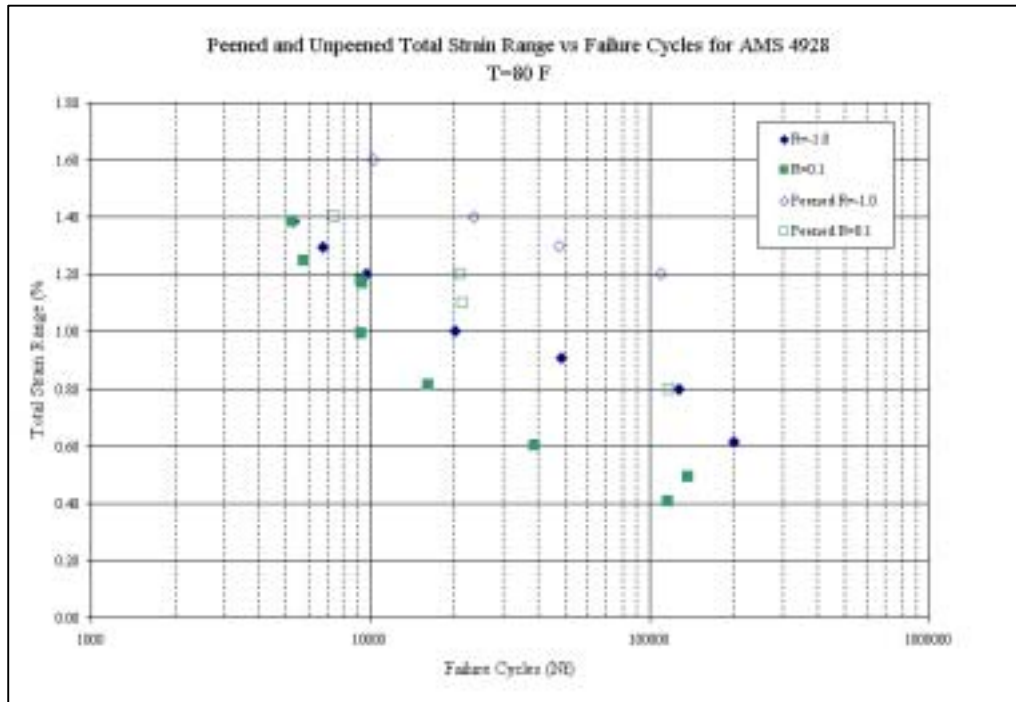


Figure 4.3. Total strain range *versus* LCF life for peened and unpeened samples at $R_{\varepsilon} = -1.0$ and 0.1 .

4.2 LCF/HCF MECHANICAL TESTING

4.2.1 Specimen Test Methods and Analysis

LCF/HCF mission testing is divided into two categories, crack nucleation and propagation. The nucleation tests used the small volume double edge notched (DEN) specimen geometry for all testing, while propagation testing was conducted on the thick Kb sample using the penny-shaped surface notch. Nucleation specimens were processed according to the requirements set forth for all fatigue specimens, while the propagation specimens saw no special surface finish. Nucleation testing was governed by ASTM E466-96 for load-controlled cyclic testing using the step-test method. Testing was performed on closed-loop servo-hydraulic test machines at 30 Hz, 80°F and laboratory air at stress ratios of 0.1 (LCF loading) followed by step blocks of either 0.5 or 0.8 (HCF loading). Propagation testing mission blocks are defined in Table 4.1. By running two different missions at $R = 0.8$, the effect of stress and number of mission blocks could be evaluated.

Table 4.1
Two-Stress-Level Mission Testing Blocks Used to Evaluate the Effect of Load Interaction

Specimen Nos.	Stress Level	Maximum Stress (ksi)	R	Repeats (cycles)	Cycles/Mission
8376, 8377	1	63.0	0.1	1	1001
Mission 1	2	63.0	0.8	1,000	
8378, 8379	1	50.0	0.1	5,000	105,000
Mission 2	2	50.0	0.8	100,000	

4.2.2 LCF/HCF Test Results

4.2.2.1 LCF/HCF Crack Propagation Results

A set of four tests were conducted to evaluate the interaction of LCF and HCF loading conditions on crack growth behavior. Two-stress-level mission testing provides an opportunity to compare the threshold measured by traditional decreasing K-gradient tests, and the threshold estimated by a measure of the effect of mission loading on crack growth. This kind of test also provides data for evaluating the adequacy of the hypothesis schematically shown in Figure 4.4.

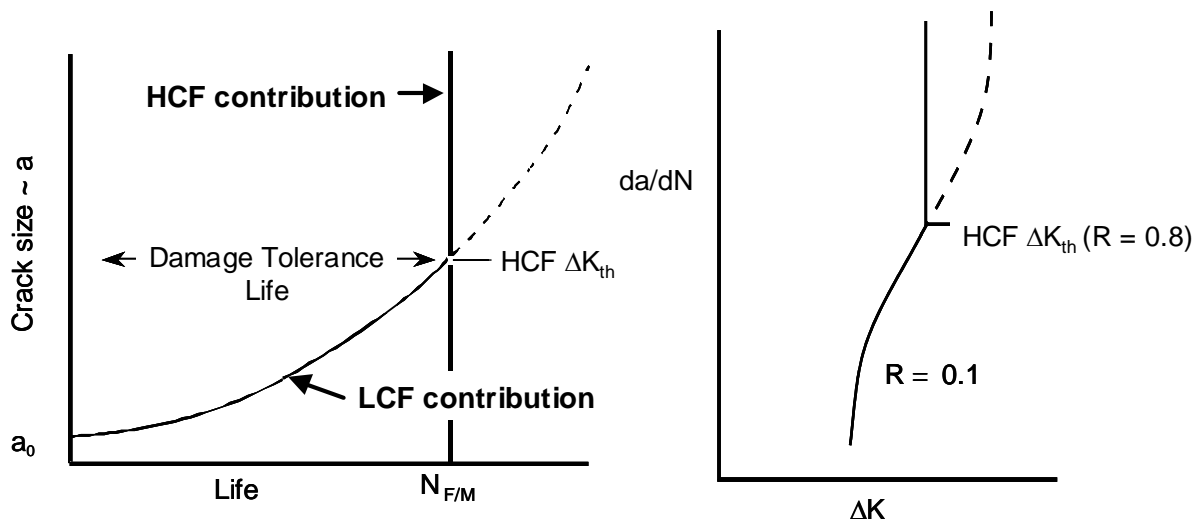


Figure 4.4 Hypothesis used to anticipate the stress intensity factor conditions associated with rapid crack growth under combined LCF/HCF loading.

The LCF/HCF crack propagation results for the 63.0 and 50.0 ksi maximum stress level missions are shown in Figures 4.4 and 4.5, respectively. For these tests, the maximum stress was chosen to propagate the crack only under the $R = 0.1$ loading condition. Furthermore, this stress level was set to ensure that the crack would not initially propagate under the $R = 0.8$ (HCF) loading condition, i.e., ΔK (for the $R = 0.8$ condition) was set below the $R = 0.8$ threshold ΔK_{th} . As the initial crack would grow under $R = 0.1$ conditions, eventually the crack would become long enough so that the $R = 0.8$ ΔK_{th} would be exceeded, and propagation from both LCF and HCF cycles would ensue.

Both Figures 4.5 and 4.6 show results that seem, at first glance, to confirm the hypothesis. As will be shown later, when these data were subjected to a threshold analysis, the results were mixed.

4.2.2.2 LCF/HCF Fatigue Test Results

A stress of 95 ksi at $R = 0.1$ for 3,000 cycles was estimated to provide a significant reduction in fatigue life. Following the initial cycling, step tests were performed beginning well below the expected endurance limit, as summarized in Table 4.2.

A stress of 95 ksi at $R = 0.1$ for 3,000 cycles was selected to provide a significant reduction in fatigue life. Following the initial cycling, step tests were performed beginning well below the expected endurance limit, as summarized in Table 4.2. Initially, the chosen $R = 0.8$ stress in sample 111-27 was too high (Figure 4.7), indicated by the short life. In the subsequent test, the endurance limit was dropped. The failure stress in both 134-33 and 134-30 was below the expected endurance limit meaning the initial $R = 0.1$ cycle debited life (resulted in reduced HCF capabilities). Conversely, in samples 123-11 and 111-26, following the $R = 0.1$ cyclic, step testing was conducted at $R = 0.5$ (Figure 4.8). Surprisingly, these values were well above the expected endurance limit for $R = 0.5$.

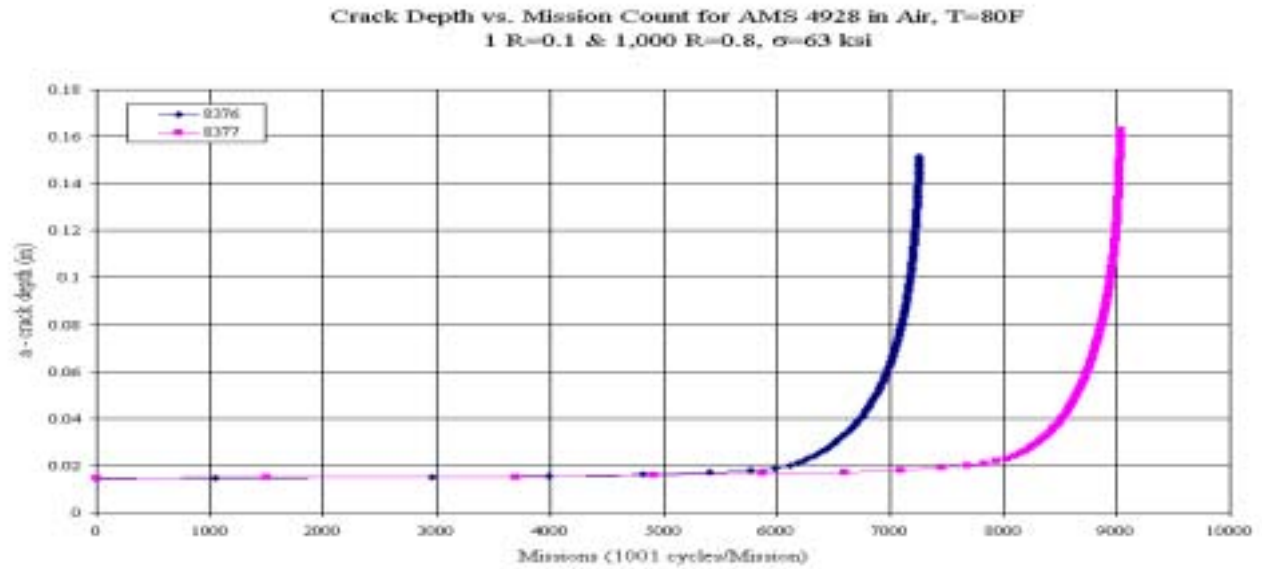


Figure 4.5. Surface crack LCF/HCF mission tests, one R = 0.1 plus 1000 R = 0.8 cycles at the 63 ksi maximum stress level mission (mission 1).

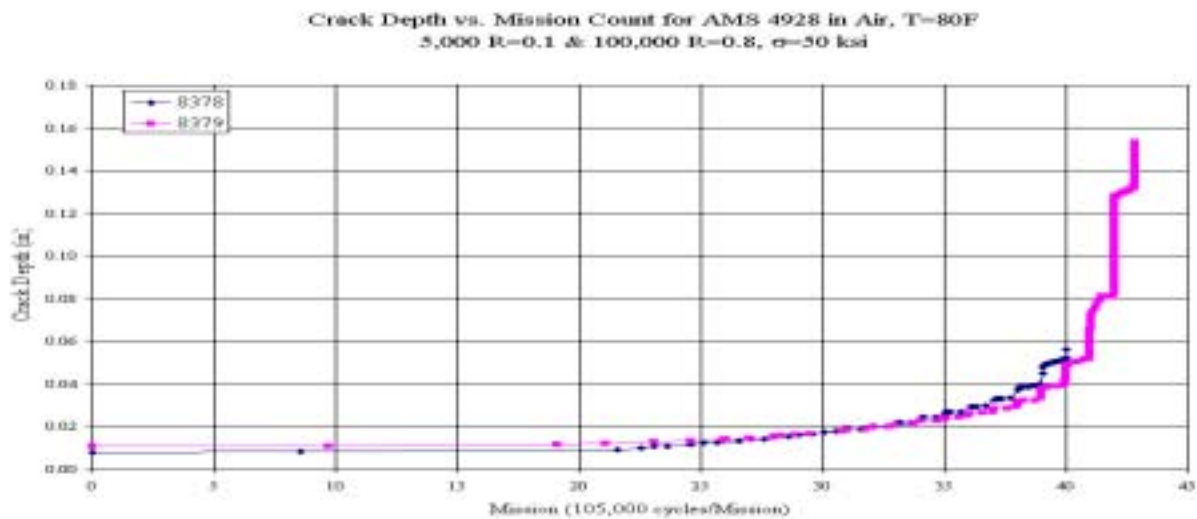


Figure 4.6. Surface crack LCF/HCF mission tests, 5,000 R = 0.1 plus 100,000 R = 0.8 cycles at the 50 ksi maximum stress level mission (mission 2).

Table 4.2
Double notch LCF/HCF Results.

Specimen ID	Run	Max Stress (ksi)	R	Freq.	N _f	Interpolated Stress	Notes
111-27	1	95.00	0.1	5 Hz	3,000	95.00	Runout
	2	95.00	0.8	30 Hz	259,132		Failure
134-33	1	95.00	0.1	5 Hz	3,000	75.68	Runout
	2	70.00	0.8	30 Hz	10,000,000		Runout
	3	73.50	0.8	30 Hz	10,000,000		Runout
	4	77.18	0.8	30 Hz	5,911,518		Failure
134-30	1	95.00	0.1	5 Hz	3,000	73.85	Runout
	2	73.50	0.8	30 Hz	10,000,000		Runout
	3	77.20	0.8	30 Hz	934,733		Failure
123-11	1	95.00	0.1	5 Hz	3,000	53.53	Runout
	2	40.00	0.5	30 Hz	10,000,000		Runout
	3	42.00	0.5	30 Hz	10,000,000		Runout
	4	44.00	0.5	30 Hz	10,000,000		Runout
	5	46.20	0.5	30 Hz	10,000,000		Runout
	6	48.50	0.5	30 Hz	10,000,000		Runout
	7	50.93	0.5	30 Hz	10,000,000		Runout
	8	53.47	0.5	30 Hz	10,000,000		Runout
	9	56.15	0.5	30 Hz	239,171		Failure
111-26	1	95.00	0.1	5 Hz	3,000	59.06	Runout
	2	48.50	0.5	30 Hz	10,000,000		Runout
	3	50.93	0.5	30 Hz	10,000,000		Runout
	4	53.47	0.5	30 Hz	10,000,000		Runout
	5	56.15	0.5	30 Hz	10,000,000		Runout
	6	58.96	0.5	30 Hz	10,000,000		Runout
	7	64.86	0.5	30 Hz	97,274		Failure

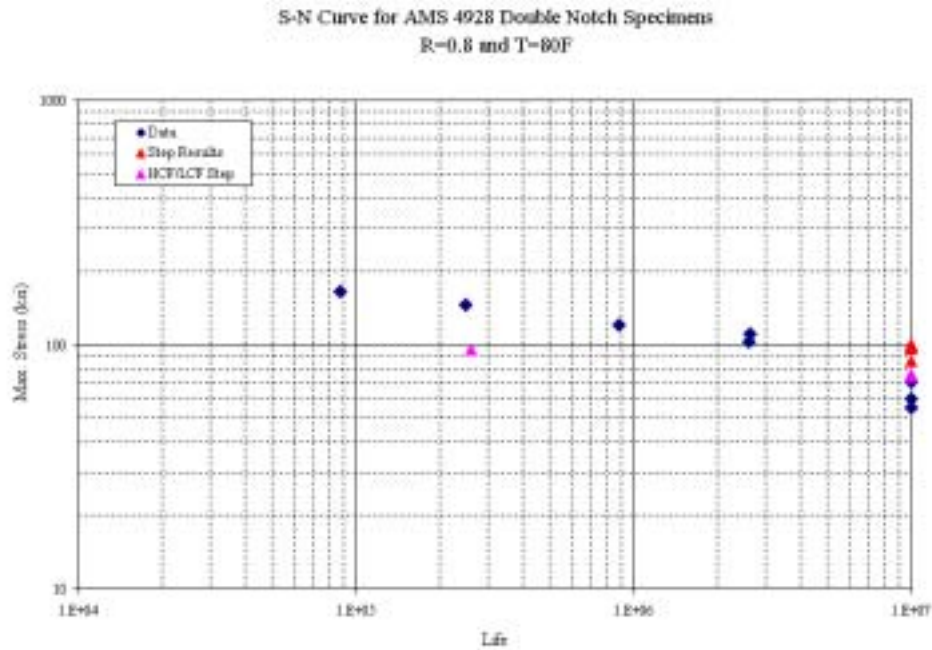


Figure 4.7. Double notch (60 Hz, R = 0.8, 80°F) HCF results indicating LCF/HCF step test results yield lower 10^7 failure lives compared with conventional S-N results and constant stress ratio step tests.

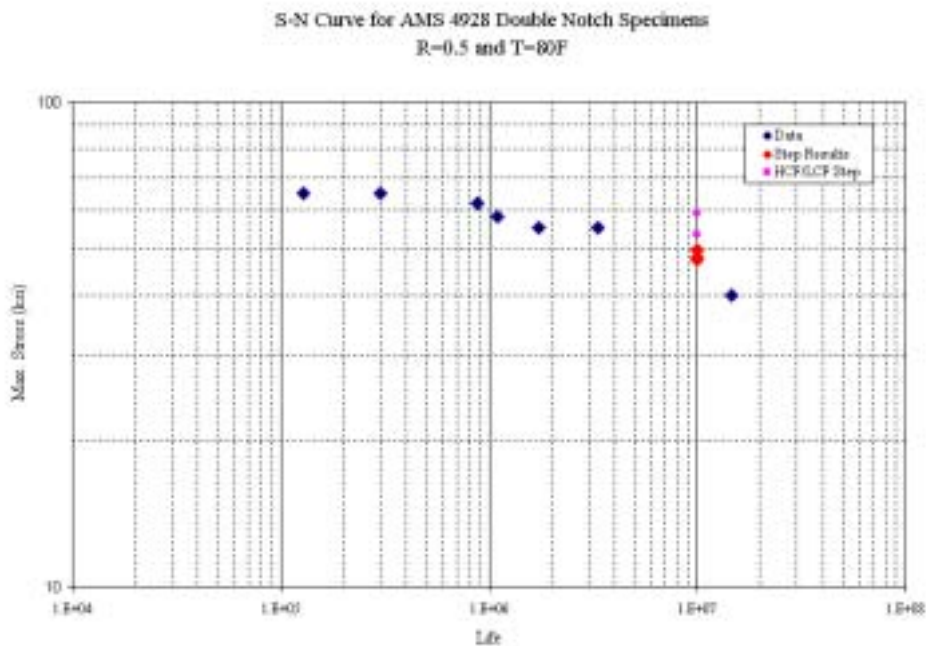


Figure 4.8. Double notch (60 Hz, R = 0.5, 80°F) HCF results indicating LCF/HCF step tests yield higher 10^7 failure lives compared with conventional S-N data and constant stress ratio step tests.

4.2.2.3 Near-Threshold Fatigue Crack Growth LCF/HCF Interaction Tests

High-resolution studies of LCF/HCF crack growth with the SwRI DISMAP system found no significant, systematic effect of periodic LCF unloads on near-threshold FCG rates under high-R HCF cycling (See Appendix 4A). This result is consistent with detailed crack-tip micro-mechanics analyses conducted under another AFOSR sponsored program, which found no significant changes in crack-tip strains or crack closure with the periodic LCF unloads^{4.1}.

4.3 LCF/HCF ANALYTICAL MODELING

4.3.1 Long-Crack Growth Models

The crack closure growth rate and threshold model described in paragraph 3.2.2.1 was used in P&W's Fracture Mechanics code to predict the propagation lives of the LCF/HCF tested Kb specimens.

The predictions for specimens 8376 and 8377 (mission 1, 63 ksi maximum stress), shown in Figure 4.9, are mildly non-conservative on lives; but, the predicted threshold of 2.2 ksi $\sqrt{\text{inch}}$ compared well to the 2.0 and 2.1 ksi $\sqrt{\text{inch}}$ values obtained for these two specimens. The results are well within the expected scatter of specimen test data for ΔK_{th} at R = 0.8.

The predictions for specimens 8378 and 8379 (mission 2, 50 ksi maximum stress), shown in Figure 4.10, are conservative on lives, but non-conservative when the exhibited (apparent) specimen thresholds of 1.2 and 1.4 ksi $\sqrt{\text{inch}}$ are compared to the predicted threshold of 2.2 ksi $\sqrt{\text{inch}}$. This threshold comparison is confusing relative to the longer than predicted specimen lives. Further evaluation is required to determine if the stress level or the use of multiple R=0.1 stress cycles caused this effect.

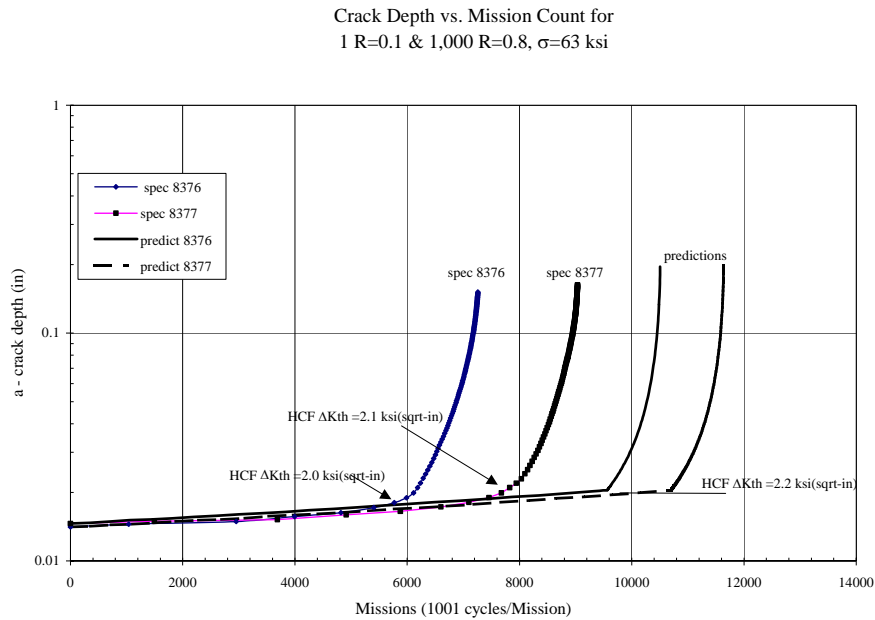


Figure 4.9. Prediction of surface crack LCF/HCF mission 1 tests, Mission 1 has a 63 ksi maximum stress and 1001 cycles per mission (one cycle of $R = 0.1$ loading followed by 1000 cycles of $R = 0.8$).

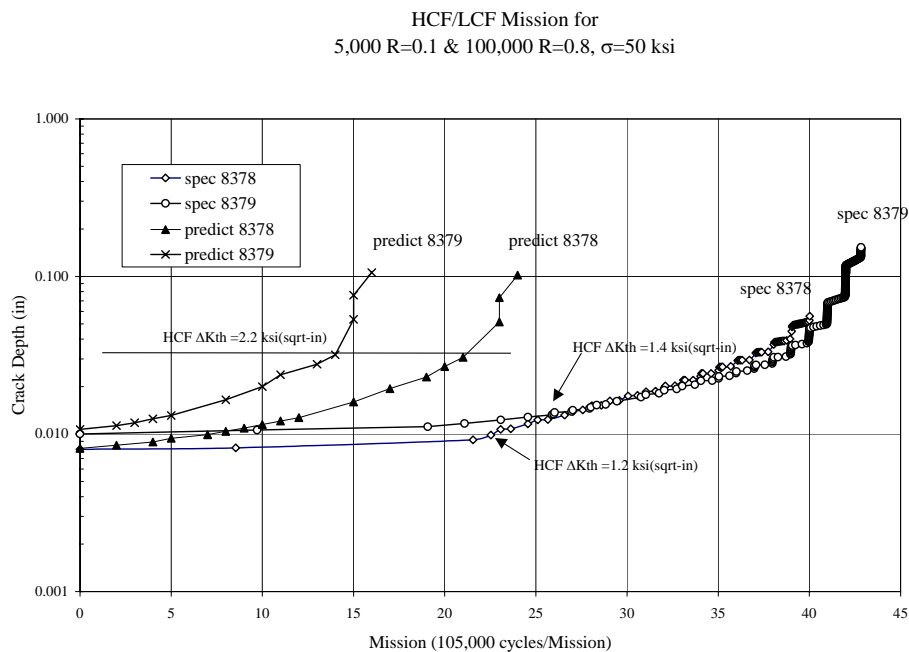


Figure 4.10. Prediction of surface crack LCF/HCF mission 2 tests, Mission 2 has a 50 ksi maximum stress (5,000 cycles of $R = 0.1$ followed by 100,000 cycles of $R = 0.8$ cycles).

4.3.2 Predictions Using Small-Crack Models

The simple small-crack model can be demonstrated by making predictions from the available PRDA baseline data. Predictions of the allowable number of LCF cycles before the HCF threshold is exceeded, as a function of the HCF maximum stress and HCF stress ratio, are shown in Figure 4.11. Here the LCF stress ratio was assumed fixed at $R = 0.1$, and three different LCF maximum stresses were explored. The same data are shown in Figure 4.12 expressed in terms of stress ranges, rather than maximum stresses. Also shown in Figures 4.11 and 4.12 are the HCF endurance limits for HCF-only cycling.

The model predicts that the HCF cycles will have little or no effect on the allowable number of LCF cycles for small HCF stresses. However, as the HCF stresses begin to approach the endurance limit for a particular stress ratio, the allowable number of LCF cycles begins to decrease, gradually at first and then more sharply with increasing HCF stress.

Note, however, that the upper limit of the allowable HCF stresses under LCF/HCF interaction is a stress that is less than the endurance limit, due to the particular construction of the model. This limiting HCF stress value corresponds to $a_{HCF} = 0.001$ inch (See Appendix 4B), since the LCF smooth-specimen data employed are consistent with a FCG life prediction from an initial crack size of 0.001 inch. The physical interpretation of this limit is that a very small number of LCF cycles can nucleate a crack of size 0.001 inch, so if a crack of this size is above the small crack HCF threshold, failure is predicted. The value of 0.001 inch itself is likely not significant, and will likely change for different smooth specimen data and fatigue crack growth models. However, there may be some physical connection between this limiting crack size and the microstructure of the material.

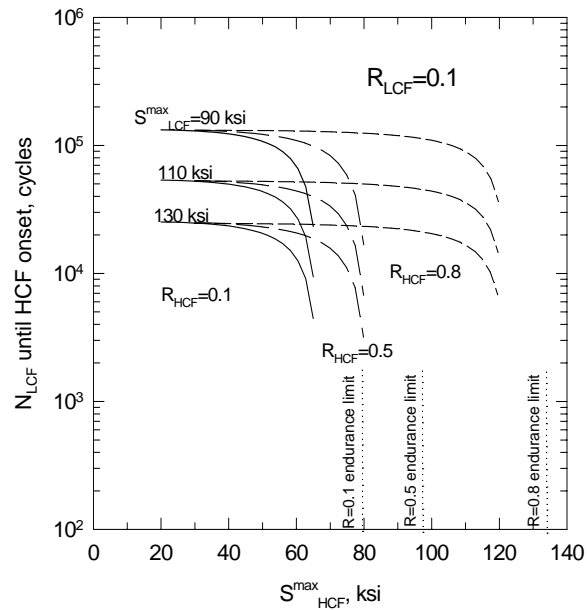


Figure 4.11. Predictions of allowable LCF cycles before HCF threshold is exceeded, based on proposed simple LCF/HCF interaction model (stress histories expressed in terms of maximum stresses).

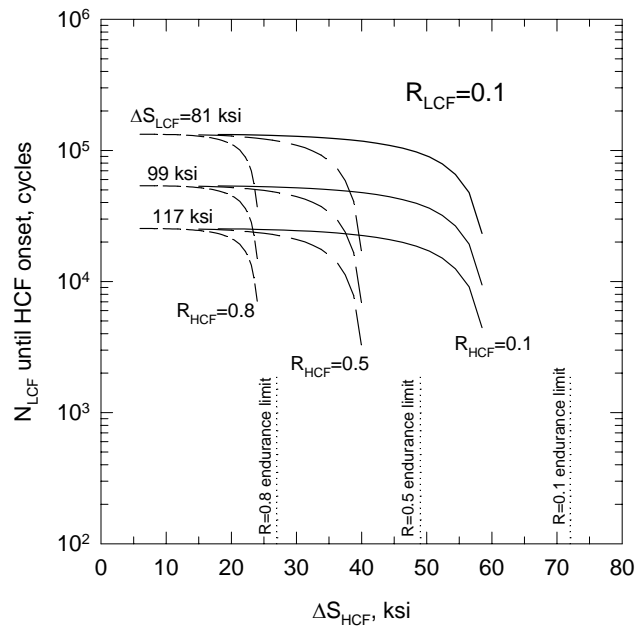


Figure 4.12. Predictions of allowable LCF cycles before HCF threshold is exceeded, based on proposed simple LCF/HCF interaction model (stress histories expressed in terms of stress ranges).

4.4 EXIT CRITERIA FOR LCF/HCF DAMAGE STATE

The exit criteria for LCF/HCF damage are expressed in terms of the distributions of the ratio of actual to predicted net maximum stresses, maximum loads and ΔK thresholds. Because of the very small number of tests that were completed, it is not sensible to address the exit criteria distributions for the LCF/HCF damage state at this time.

4.5 SUMMARY AND RECOMMENDATIONS

More effort is required to establish whether we can use long-crack fracture mechanics methodology to establish the damage sizes where HCF loading affects the behavior of LCF crack nucleation and early crack propagation. The first order estimates based on long-crack analysis methods appear to be adequate from a design prospective, but the bottom line is that insufficient small-crack and load interaction tests have been conducted to justify anything, at this time, other than a large crack hypothesis for estimating these damage sizes. Additional data and analysis are required to do the following:

- Select methods to predict onset of HCF-induced crack growth after (or with) LCF damage.
- Determine variability in notch specimen ΔK_{th} thresholds.
- Establish the nucleation threshold for notched structures.
- Establish the crack threshold for notched structures.
- Evaluate exit criteria on LCF/HCF test data.
- Implement the concepts into a design system.

4.6 REFERENCES

- 4.1 D.L. Davidson, "Damage Mechanisms in High-Cycle Fatigue," Final Report, AFOSR Contract F49620-96-C-0037, January 1999.

Appendix 4A

LCF/HCF SEM and DISMAP OBSERVATIONS

R. Craig McClung

and

David L. Davidson



Southwest Research Institute

**Submitted
31 August 1999**

HCF/LCF INTERACTIONS IN THE NEAR-THRESHOLD CRACK GROWTH REGIME

Superposition of low cycle (large amplitude) and high cycle (small amplitude) fatigue histories can prompt a variety of possible interaction effects on damage accumulation. One potential effect is an acceleration in the growth rate of cracks subjected to combined HCF/LCF cycling. The unique high-resolution experimental tools at SwRI were used to investigate this possibility.

A unique high frequency loading stage that fits within the scanning electron microscope (SEM) was used to grow the fatigue cracks. The high resolution and depth of field of the SEM allowed accurate crack length measurements and photographs of the crack tip region to be made. The loading stage allowed application of tensile vibratory loads at about 1.5 kHz. Mean tensile load was applied by a hydraulic system. Comparisons of FCG data obtained with this stage against literature data and data from other HCF researchers showed good agreement. All cracks in this particular study were grown in the vacuum of the SEM at about 10^{-7} torr. Although fatigue crack growth rates for titanium alloys are different in vacuum and air in the near-threshold regime, this environmental difference is not expected to affect the mechanisms of HCF/LCF interaction.

Fatigue cracks were initiated at small notches and grown to lengths beyond the influence of the notch. As the crack lengthened, cyclic and static loads were incrementally lowered until crack growth rates were in the 10^{-8} to 10^{-10} inch/cycle range, for stress ratios of $R = 0.6$ to 0.85 , by the time the crack was 80 to 120 mils long. All cracks investigated were large compared to the characteristic microstructural features (e.g., grain size). Cracks were found by fractography to have nearly semi-circular shapes at all crack lengths up to back face penetration. Values of ΔK for cracks growing under these conditions were in the 2 to 6 ksi $\sqrt{\text{inch}}$ range.

After obtaining low and steady crack growth rates, the mean stress was periodically removed to impose one LCF cycle. Intervals of 10^5 or 10^6 HCF cycles were used between each LCF cycle. The condition of no load was maintained for about 5 minutes before returning to the previous mean load and

continuing HCF loading. Because surface cracks were being observed, measurements were obtained at each exposed end of the crack.

The results of these exploratory tests indicated that no significant, systematic changes in near-threshold HCF crack growth rates could be attributed to the periodic LCF unloads. In some tests, the average crack growth rates during HCF cycling with periodic LCF unloads were about a factor of two or three faster than average crack growth rates during HCF cycling with no unloads. For example, Figure 4A.1 shows how crack growth rates (the slope of the crack length vs. cycles line) increased slightly as periodic unloads were introduced, and then increased again as the frequency of these unloads was increased. In other tests, however, the average crack growth rates during HCF cycling with periodic unloads were approximately the same as, or even slightly slower than, crack growth rates during pure HCF cycling. Figure 4A.2, for example, documents another test in which the slope of the a vs. N curve decreased slightly when periodic unloads were introduced. In general, linear superposition was adequate to sum the damage (crack growth) from the HCF and LCF cycles. This observation is consistent with the published research of Powell, Duggan, and Jeal [4A.1], who studied HCF/LCF interactions during the growth of large cracks in air.

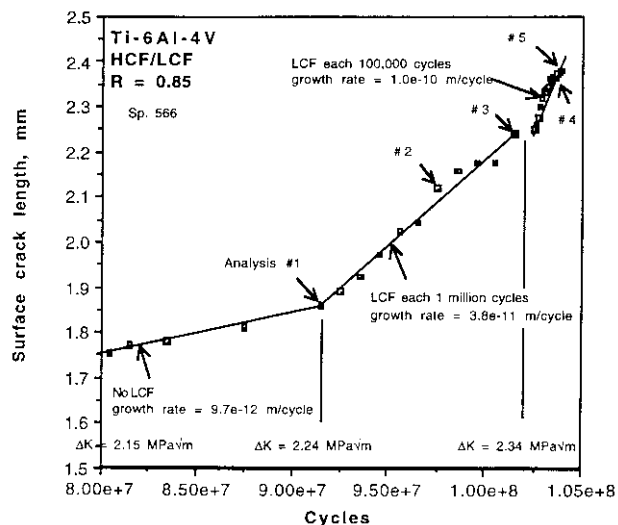


Figure 4A.1. A history of crack length changes for Specimen 566 with and without the periodic removal of mean stress (LCF). An example of increasing crack growth rates with periodic LCF.

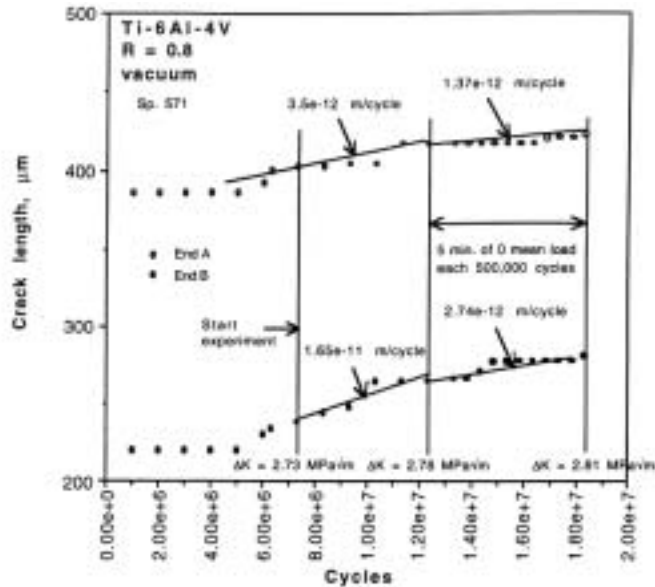


Figure 4A.2. A history of crack length changes for Specimen 571 with and without the periodic removal of mean stress (LCF). An example of decreasing crack growth rates with periodic LCF.

Davidson, in a companion AFOSR contract [4A.2], used the DISMAP displacement mapping system to characterize near-tip strains, crack closure levels, and crack-tip opening displacements during HCF cycling with and without LCF unloads. The observed crack-tip micromechanics were consistent with the earlier observations about growth rates: periodic LCF unloads did not have a systematic, pronounced effect on near-tip behavior during HCF cycling. In some cases, differences were observed, but these differences were not observed in every test. The effects of LCF unloads appear to be no greater than the normal test-to-test and cycle-to-cycle scatter in local crack-tip micromechanics.

SUMMARY AND CONCLUSIONS

1. High-resolution studies of HCF/LCF crack growth with the SwRI DISMAP system found no significant, systematic effect of periodic LCF unloads on near-threshold FCG rates under high- R HCF cycling. This result is consistent with detailed crack-tip micromechanics analyses conducted under a companion AFOSR program, which found no significant changes in crack-tip strains or crack closure with the periodic LCF unloads.

REFERENCES

- 4A.1. Powell, B.E., Duggan, T.V., and Jeal, R, "The Influence of Minor Cycles on Low Cycle Fatigue Crack Propagation," *International Journal of Fatigue*, Vol. 4, 1982, pp. 4-14.
- 4A.2 Davidson, D.L., "Damage Mechanisms in High Cycle Fatigue," Final Report, AFOSR Contract F49620-96-C-0037, Southwest Research Institute Project No. 18-8243, January 1999.

Appendix 4B

SMALL CRACK LIFE METHOD FOR LCF/HCF INTERACTION

R. Craig McClung

and

Stephen J. Hudak, Jr.



Southwest Research Institute

**Submitted
31 August 1999**

A SMALL-CRACK LIFE METHOD FOR LCF/HCF INTERACTION

The gist of the proposed LCF/HCF interaction model is that crack nucleation and early growth are due solely to the large amplitude LCF cycles. The HCF cycles become operative, and in fact dominant, in propagating the (small) crack to failure when the crack-size dependent threshold is exceeded for the small amplitude HCF cycles. The functionality of the model is to predict, for a given HCF stress range and stress ratio, and a given LCF stress range and stress ratio, when the LCF cycling will grow the small crack to this critical threshold size.

Formulation

Assumptions. Before describing the model in step-by-step detail, it is useful to acknowledge the key assumptions behind the model. Some of these assumptions are perhaps more solid than others, and in some cases the model could be extended by replacing simplifying assumptions with a more complex calculation. However, in the absence of evidence to the contrary, these assumptions are useful to build a relatively simple model for further study.

1. *Crack nucleation is caused only by LCF cycling.* The model assumes that HCF cycling does not contribute to crack nucleation at all when large amplitude LCF cycles are occurring. Based on the $S-N$ curve, the relative per-cycle damage of small amplitude HCF cycles is several orders of magnitude smaller than the per-cycle damage of large amplitude LCF cycles, and so this HCF damage is assumed to be negligible. The HCF cycles are assumed to have no synergistic effect on the LCF cycles for the crack nucleation process itself.
2. *HCF cycles do not contribute to FCG as long as ΔK_{HCF} is below the appropriate threshold.* As long as the ΔK value associated with the HCF stress amplitudes and the current crack size is less than a properly defined threshold, then no crack growth will occur during HCF cycling. All crack growth in this regime will be caused by LCF cycling. Furthermore, the HCF cycles are assumed to have no interactive effect on LCF crack growth. Limited high-resolution investigations by Davidson (described earlier in

Appendix 4A) found no systematic FCG interaction between HCF and LCF cycling for HCF cycling very near the threshold.

3. *The crack-length-dependent threshold for FCG under HCF loading (ΔK_{th}^{SC}) follows the El Haddad/Tanaka form (See Appendix 3N).* The “appropriate threshold” cited in the previous assumption is assumed to be given by the form of

$$\Delta K_{th}^{SC}(a) = \Delta K_{th} \sqrt{\frac{a}{a + a_0}} \quad (4B.1)$$

The parameter a_0 is assumed to be given by

$$a_0 = \frac{1}{\pi} \left(\frac{\Delta K_{th}}{F \Delta \sigma_e} \right)^2 \quad (4B.2)$$

which depends on the large-crack threshold ΔK_{th} and the smooth-specimen endurance limit $\Delta \sigma_e$.

4. *LCF cycling does not affect the small-crack threshold.* The El Haddad/Tanaka small-crack threshold is assumed to be itself unaffected by LCF cycling. In this formulation, there are assumed to be no LCF/HCF load interaction effects on thresholds (e.g., no overload effects).
5. *LCF crack growth (at stresses above the endurance limit) does not observe the large-crack ΔK_{th} .* In many cases, ΔK due to the large amplitude LCF cycles will be larger than the large-crack ΔK_{th} since the stress amplitudes are relatively high. However, in those cases where $\Delta K_{LCF} < \Delta K_{th}$, the failure of smooth specimens at the LCF stress amplitude (which is above the endurance limit) is taken as evidence that the large-crack threshold has been violated and does not apply. LCF crack growth below ΔK_{th} is assumed to follow the extrapolated slope of the da/dN vs. ΔK relationship immediately above threshold.

Model. The step-by-step process by which the allowable LCF/HCF exposure is determined is now given:

1. For a given HCF stress amplitude (lower than the endurance limit) and stress ratio,

- 1(a). Calculate a_0 from the large-crack ΔK_{th} and the smooth-specimen $\Delta \sigma_e$ via Eq. 4B.2.

- 1(b). Calculate the crack size a_{HCF} when the small-crack threshold is first exceeded:

$$a_{HCF} = \frac{1}{\pi} \left(\frac{\Delta K_{th}}{F \Delta S_{HCF}} \right)^2 - a_0 \quad (4B.3)$$

2. For a given LCF stress amplitude and stress ratio, calculate the number of LCF cycles required to form a crack of size a_{HCF} .

This calculation is performed in three steps:

- 2(a). Calculate the number of LCF cycles to fail a smooth specimen. This determination is typically based on conventional S-N or ϵ -N curves. This step does not require the formulation of a FCG model to predict the S-N curve from some physically meaningful initial crack size as demonstrated in the background discussion above. However, it is important that the available FCG model for LCF conditions (which will be employed in the next step) maintain reasonable consistency with the experimentally determined S-N curves. In particular, if the available FCG model gives lives that are substantially longer than the experimental S-N data, for initial crack sizes on the order of the microstructural unit size or the parameter a_0 , then the LCF/HCF model will not yield meaningful results, and something is likely wrong with either the FCG model or the experimental data.

- 2(b). Calculate the number of LCF cycles to grow a crack of initial length a_{HCF} to failure in the relevant smooth specimen geometry employed in the S-N testing. This calculation is typically based on a conventional FCG design system for LCF conditions.

2(c). *Determine the number of LCF cycles before the crack grows to a length a_{HCF} and the HCF threshold is exceeded.* Subtracting 2(b) from 2(a) performs this calculation. For sufficiently large numbers of HCF cycles, exceedance of the HCF threshold will cause rapid failure.

It should again be emphasized that this model is generic and can be integrated with any existing design system that provides information about HCF endurance limits, $S-N$ curves under LCF conditions, large-crack thresholds, and fatigue crack growth under LCF conditions. The new LCF/HCF interaction model takes these inputs and incorporates a simple relationship for the crack-size dependent threshold to calculate allowables for LCF and HCF cycles.

Predictions

The simple model can be demonstrated by making predictions from the available PRDA baseline data. Actual LCF/HCF data to evaluate the model were not available to this author at this writing.

Predictions of the allowable number of LCF cycles before the HCF threshold is exceeded, as a function of the HCF maximum stress and HCF stress ratio, are shown in Figure 4B.1. Here the LCF stress ratio was assumed fixed at $R = 0.1$ and three different LCF maximum stresses were explored. The same data are shown in Figure 4B.2 expressed in terms of stress ranges, rather than maximum stresses. Also shown in Figures 4B.1 and 4B.2 are the HCF endurance limits for HCF-only cycling.

The model predicts that the HCF cycles will have little or no effect on the allowable number of LCF cycles for small HCF stresses. However, as the HCF stresses begin to approach the endurance limit for a particular stress ratio, the allowable number of LCF cycles begins to decrease, gradually at first and then more sharply with increasing HCF stress.

Note, however, that the upper limit of the allowable HCF stresses under LCF/HCF interaction is a stress that is less than the endurance limit, due to the particular construction of the model. This limiting HCF stress value corresponds to $a_{HCF} = 0.001$ inch (see step 1(b) above), since the LCF smooth specimen data

employed are consistent with a FCG life prediction from an initial crack size of 0.001 inch. The physical interpretation of this limit is that a very small number of LCF cycles can nucleate a crack of size 0.001 inch, so if a crack of this size is above the small crack HCF threshold, failure is predicted. The value of 0.001 inch itself is likely not significant, and will likely change for different smooth specimen data and FCG models. However, there may be some physical connection between this limiting crack size and the microstructure of the material.

The model results can also be expressed in terms of allowable HCF stresses for a given LCF exposure. This formulation is illustrated in Figure 4B.3, which are actually the same results as Figure 4B.1 with the axes interchanged.

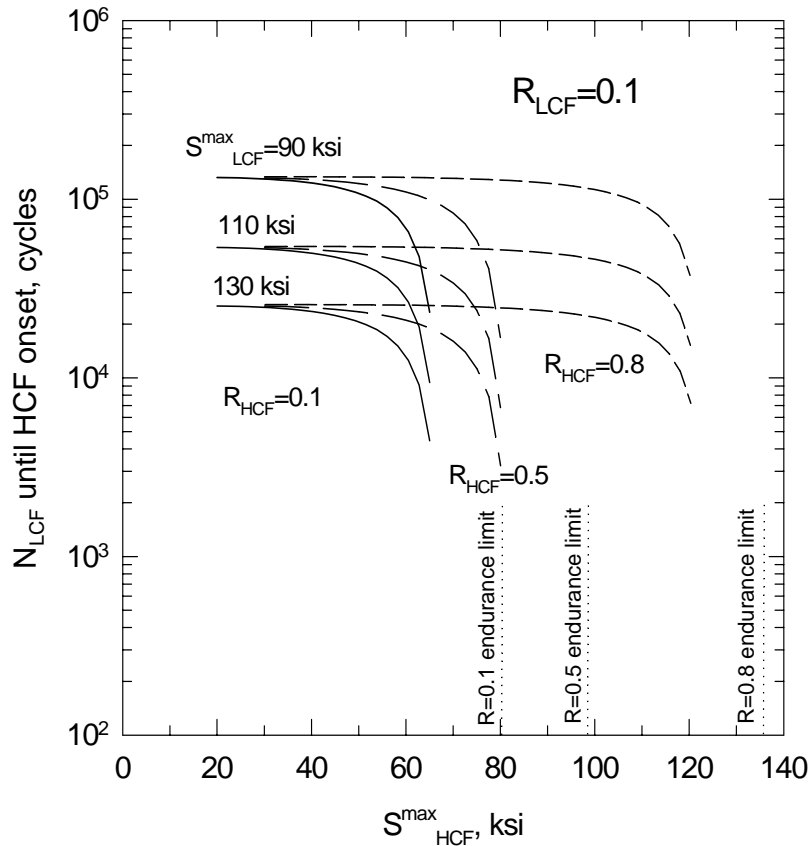


Figure 4B.1. Predictions of allowable LCF cycles before HCF threshold is exceeded, based on proposed simple LCF/HCF interaction model (stress histories expressed in terms of maximum stresses).

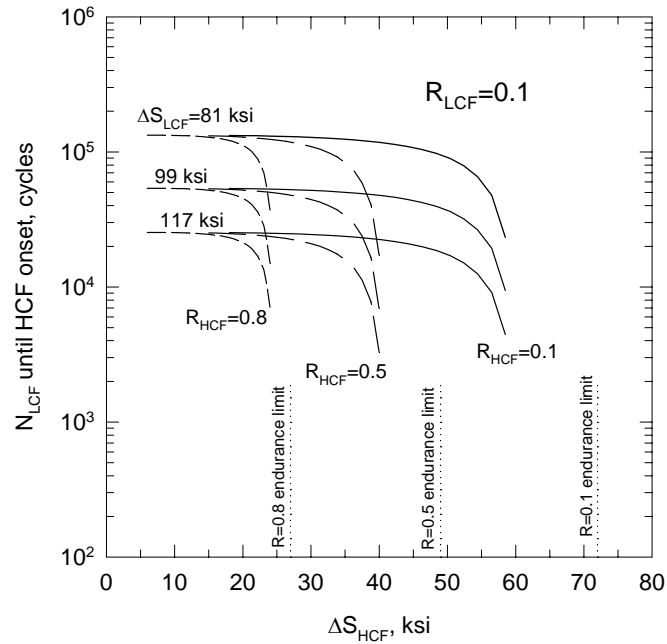


Figure 4B.2. Predictions of allowable LCF cycles before HCF threshold is exceeded, based on proposed simple LCF/HCF interaction model (stress histories expressed in terms of stress ranges).

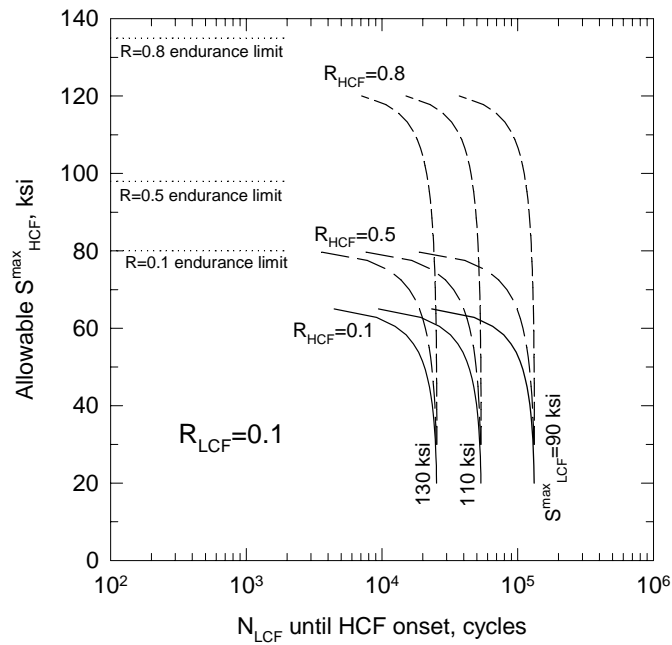


Figure 4B.3. Predictions of allowable HCF maximum stresses for various LCF exposures, based on proposed simple LCF/HCF interaction model (stress histories expressed in terms of maximum stresses).

The crack-size-dependent threshold has a pronounced effect on the model predictions. Figure 4B.4 shows the model predictions if calculation of a_{HCF} is based on the traditional large-crack threshold, and not the small-crack threshold (i.e., the a_0 term is neglected in Eq. 4B.3). Clearly, no significant smooth specimen LCF/HCF interaction effects are predicted under any conditions with this assumption.

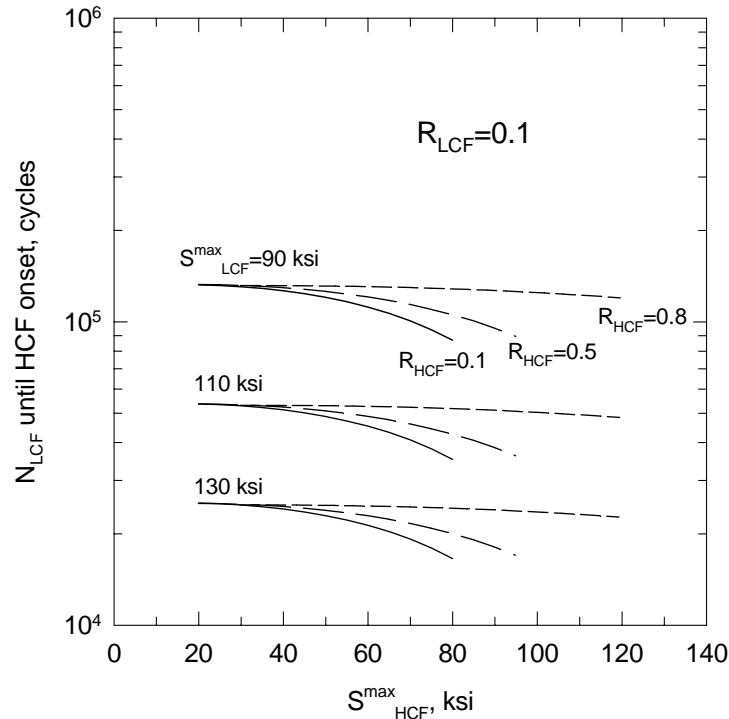


Figure 4B.4. Predictions of allowable LCF cycles before HCF threshold is exceeded, based on large-crack fracture mechanics threshold (stress histories expressed in terms of maximum stresses).

Discussion

The same model logic should be applicable to LCF/HCF interactions in notched and even FOD geometries, although the calculations would be somewhat more complex. Calculation of the threshold crack size a_{HCF} (Step 1) would require identification of the length of the small crack growing from the notch root at which the HCF stress intensity factor first exceeds the crack-length-dependent threshold as defined by Eq. 4B.1. Calculation of the number of LCF cycles required to grow a crack to this length requires an $S-N$ model for the notched

geometry (Step 2a) and a FCG design system to predict the number of cycles required to grow a crack of length a_{HCF} to failure in the notched geometry (Step 2b). Some existing FCG design systems may not adequately capture the mechanics of extremely small cracks growing at notch roots, where plastic deformation and changing crack closure levels can both be significant issues.

Presentation of a new model without prior evaluation against experimental data is always risky business. What if the model turns out to be inaccurate? The most likely sources of potential inaccuracies are the simplifying assumptions outlined earlier. One assumption of particular concern is the assumption that LCF cycling does not affect the HCF threshold. Crack closure interactions between major and minor cycles could have a substantial impact on HCF threshold behavior, especially for HCF cycles at lower stress ratios where closure could be more significant. Hopkins *et al.* [4B.1] found in a Ti-6-4 study that threshold values following overloads increased systematically with the magnitude of the overload.

The potential for overload elevation of the threshold when the LCF maximum stress is significantly higher than the HCF maximum stress is probably the most significant problem along this line. It is also possible that an LCF cycle with a substantially lower minimum stress than the HCF cycle (and perhaps the same maximum stress) could induce an underload reduction of the threshold, which would further increase the non-conservatism of the damage summation. However, since the HCF cycle in this situation will likely have a high stress ratio, and therefore exhibit minimal crack closure, it is not likely that the LCF “underload” will have a significant effect on the HCF threshold. Underload effects are typically linked to a reduction in crack closure for the minor cycles following the underload, but if closure is already minimal in the minor cycles, then there is no basis for an effect. This line of thinking is consistent with the experimental observations discussed in Appendix 4A, where occasional LCF underloads had no systematic effect on the crack tip micromechanics or the growth rates of the HCF minor cycles.

The fundamental assumption about the El Haddad/Tanaka model for crack-length dependent threshold also remains to be verified experimentally for the PRDA Ti-6-4 material. Although it seems clear that the El Haddad/Tanaka model must be correct in the two limiting extremes (smooth specimen endurance limit and large-crack threshold), the exact functional form of the interpolation between the two bounds could differ slightly from the simple formulation. In fact, experimental data for other materials do show some scatter about the El Haddad/Tanaka line, and these minor variations could have a noticeable impact on the LCF/HCF interaction predictions. However, it should be noted that limited literature small crack data for Ti-6-4 in a mill-annealed condition [4B.2] do exhibit general agreement with the El Haddad/Tanaka form.

Another issue of potential significance is the role of time-dependent deformation at high mean stresses. This appears to be a particular issue for HCF cycling at very high stress ratios in laboratory specimens, based on experimental observations to date in the PRDA program, and these deformation mechanisms are not explicitly addressed in the proposed model. This may not be an issue in actual hardware, but it could impact laboratory verification.

The current model is based on the assumption that the total HCF exposure (or the number of HCF cycles per LCF cycle) is sufficiently large that exceedance of the HCF threshold will cause failure very quickly, before a significant number of additional LCF cycles are accumulated. The model would need to be reformulated slightly to perform finite life calculations for histories in which HCF exposure is more limited in proportion to LCF exposure, so that many LCF cycles are also experienced after the HCF threshold is first exceeded. This reformulation would be straightforward.

Finally, it must be emphasized that the specific predictions of the model are dependent on the specific design system ingredients (e.g., large crack fracture mechanics life prediction system, S-N life prediction system) that are integrated into the model. The predictions shown here are based on simplistic design system elements that were developed for the purposes of illustration.

Clearly, further work would be required to validate the model experimentally. The originally planned smooth specimen LCF/HCF interaction tests were not conducted by our HCF partners in order to allocate resources to more pressing needs. A limited LCF/HCF smooth specimen test series conducted at AFRL [4B.3] found only about a 5% decrease in the $R = 0.5$ endurance limit with prior LCF exposure. However, the LCF cycles employed in that study – $R = -1$ cycles at $S_{\max} = 96$ ksi, giving an estimated 10^5 cycle lifetime—may not have been severe enough to cause early microcrack nucleation. LCF histories of greatest relevance to actual engines tend to be in the 10^4 cycle regime.

Future critical experiments may be required. The form of the model lends itself well to a number of critical experiments that explore some of the different assumptions in the model. For example, the assumption that crack nucleation is due to LCF alone could be explored by subjecting a specimen to LCF cycling alone to form cracks of size a_{HCF} , and then determining if the crack grows under HCF cycling alone.

Taken as a whole, the current model suggests that LCF/HCF interaction effects in smooth geometries may not be a severe problem. Substantial (10 - 20%) reductions in the HCF endurance limit are predicted only when (1) the LCF cycle has a high enough maximum stress to cause microcrack nucleation relatively early in life; (2) the maximum stress in the HCF cycle is similar to the maximum stress in the LCF cycle, thereby avoiding LCF overload effects that could increase the HCF fracture mechanics threshold and supercede the crack-size effect on threshold; and (3) the maximum stress in the HCF cycle is slightly less than the endurance limit. The number of situations in which all three of these criteria are satisfied may be relatively limited. However, it seems prudent to investigate further the potential for an LCF/HCF debit in the endurance limit when these three criteria are satisfied, which is likely to occur from time to time in the engine.

SUMMARY AND CONCLUSIONS

1. An engineering life method for LCF/HCF interaction has been formulated based on the assumptions that microcracks, nucleated and initially grown exclusively by the large LCF cycles, grow to failure under the influence of the small HCF cycles once the HCF cycles exceed the crack-size dependent fracture mechanics threshold. Other load interaction effects are neglected.
2. The small-crack LCF/HCF model indicates that interaction effects are insignificant until the HCF stresses approach the endurance limit. However, the model does predict a 10-20% decrease in the HCF endurance limit for relatively small numbers of LCF cycles, when the LCF cycles are sufficiently severe to cause early microcrack nucleation. LCF cycles of this severity will typically cause failure in considerably less than 10^5 LCF cycles. Furthermore, this effect could be counteracted by overload effects that may increase the small-crack threshold value when the maximum stress in the LCF cycle is considerably larger than the maximum stress in the HCF cycle. Therefore, substantially non-conservative interactions between HCF and LCF cycles may be limited to a fairly narrow range of conditions, when HCF and LCF maximum stresses are similar, HCF stresses are approaching the endurance limit, and LCF stresses are sufficiently large to cause failure in a truly low number of cycles.

REFERENCES

- 4B.1 Hopkins, S.W, Rau, C. A., Leverant, G.R. and Yuen, A. "Effect of Various Programmed Overloads on the Threshold for High-Frequency Fatigue Crack Growth," Fatigue Growth Under Spectrum Loads, ASTM STP 595, 1976, pp. 125-141.
- 4B.2 C.W. Brown and D. Taylor, "The Effects of Texture and Grain Size on the Short Fatigue Crack Growth Rates in Ti-6Al-4V," in Fatigue Crack Growth Threshold Concepts, D. Davidson and S. Suresh, Eds., TMS-AIME, 1984, pp. 433-445.
- 4B.3 T. Nicholas and D.C. Maxwell, "Evolution and Effects of Damage in Ti-6Al-4V under High Cycle Fatigue," Progress in Mechanical Behavior of Materials, Proceedings of the Eighth International Conference on the Mechanical Behavior of Materials, ICM-8, F. Ellyin and J. W. Provan, Eds., Vol. III, 1999, pp. 1161-1166.

Chapter 5

Foreign Object Damage

5.1 BACKGROUND

5.1.1 Objective and Approach

One objective of this program was to gain a better understanding of the effects of typical FOD on the HCF performance of 1st stage fan blades, and evaluate methods to predict the effects of FOD on crack nucleation and growth. The approach to achieve this objective encompasses experimental and analytical efforts. This approach began with an extensive data collection effort of in-service FOD occurrence to define typical FOD parameters that are deemed critical. Second, the durability of laboratory-simulated FOD was experimentally characterized, and the permanent deformation and residual stress from these FOD impacts were analytically predicted. Finally, the experimental FOD durability and predicted stress information was used to evaluate the life models developed in the LCF/HCF task.

5.1.2 Engine FOD History

In seeking information on the distribution of FOD sizes, shapes and occurrence rates, it was determined that very little relevant data were available throughout the engine companies. As a result, a field inspection campaign was initiated to collect such data. The first set of inspections was conducted on six (6) TF30-33 engines at the Oklahoma City Air Logistics Center in which FOD was documented on a total of 75 fan/compressor stages, encompassing in excess of 5000 blades. Most notably, the inspection was performed on complete fan and compressor modules of an engine. This ensures that the data accurately represent the distribution of FOD damage in the field rather than damaged blades specifically rejected or identified for blending.

The FOD location relative to the blade span is summarized in Figure 5.1. For each stage, the majority of the FOD appears to occur beyond 80% span. As the blade steady stresses are low in the tip region, the effects of centripetal stiffening are expected to be low as well as the global stress ratio (R) in the vicinity of most FOD events. The cumulative distribution of FOD depths appears in Figure 5.2. The measured FOD depth ranged from 0.002-inch to 0.5-inch with an average depth of

approximately 0.060-inch. This information was pivotal in defining the conditions that the HCF FOD damage state team would pursue in this program. A second study, which focused on the FOD geometry and a damage characterization of FOD that occurred in F100 fan blades, can be found in Appendix 5A.

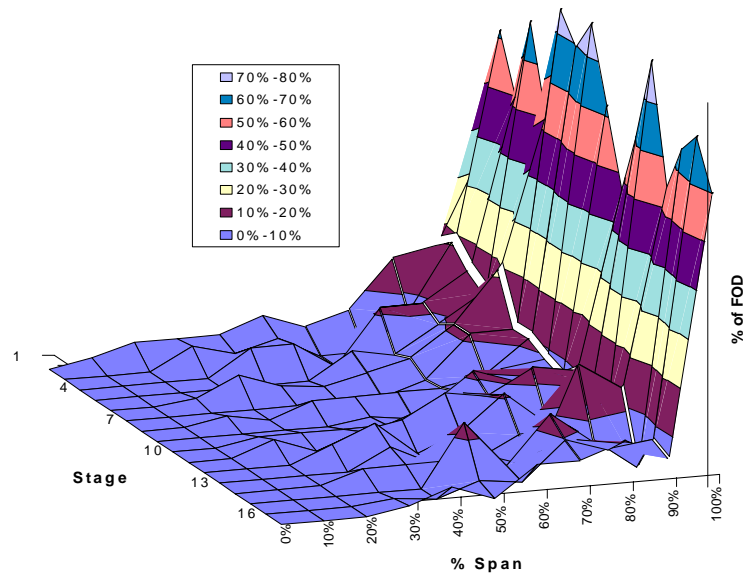


Figure 5.1. Percentage of FOD located at span locations relative to the blade tips.

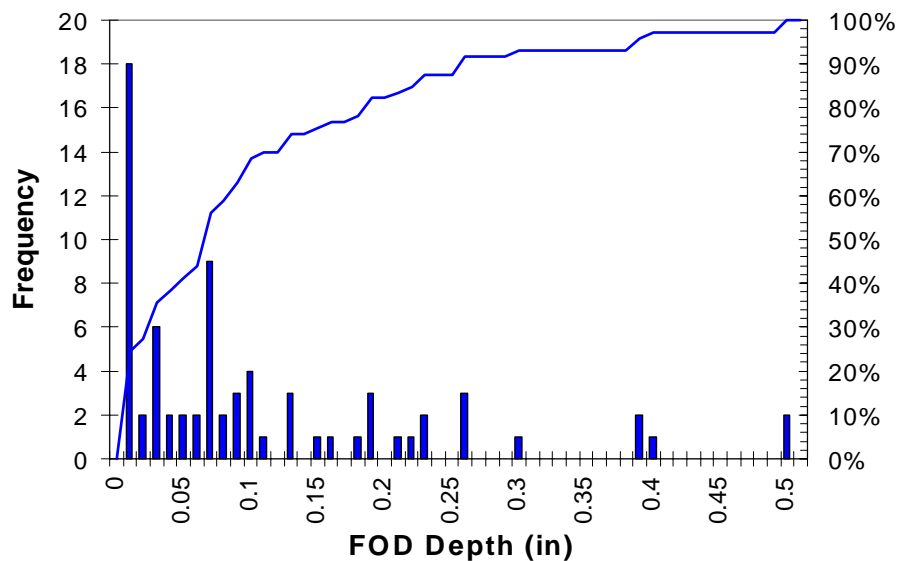


Figure 5.2. Cumulative frequency diagram of FOD depth.

5.2 FOD MECHANICAL TESTING

The typical fan blade in a large gas turbine engine is a complex airfoil with variable camber and twist. The stresses at the leading edge are the result of complex loads and moments that vary along the length of the blade due to inertial forces, pressure loads, and geometry variations. Axial loads and the flexural moment are the dominant LCF loads that control the mean stresses, while vibratory loads produce the HCF alternating stresses. The mean stresses are significantly larger than the alternating stresses in the root and mid-section regions, whereas the tip regions may contain high vibratory stresses and low mean stresses. Therefore, the stress ratio may range from $R = 0.8$ (tension-tension) near the root to $R = -1$ (fully reversed tension-compression) at the tip regions.

5.2.1 FOD Characterization/Verification – Flex Tests

The flex testing was performed on a winged specimen that can be used to simulate leading edge stresses (Figure 5.3). The artificial leading edges (sharp and blunt configurations) are far from the neutral axis so they will be highly stressed. The specimens were loaded in four-point bending with a 4.0-inch (101.6 mm) support span and a 2.0-inch (50.8 mm) loading span. Elastic stress analyses of the specimens were performed to compare the leading edge stresses of the blade to the specimens, as illustrated in Figure 5.4. Notice the stress gradients from points A to B are very similar.

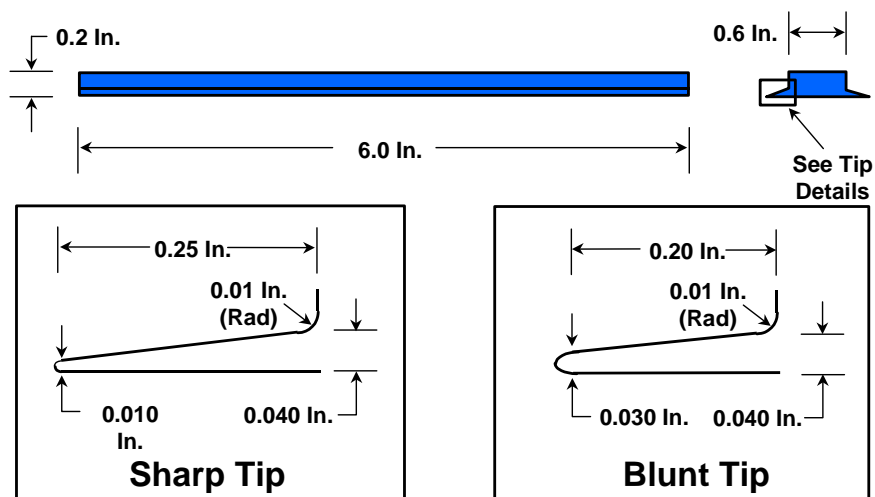
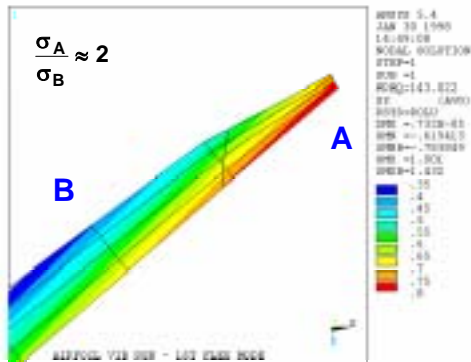


Figure 5.3. The FOD flexure specimen design.

Blade Stresses



Specimen Stresses

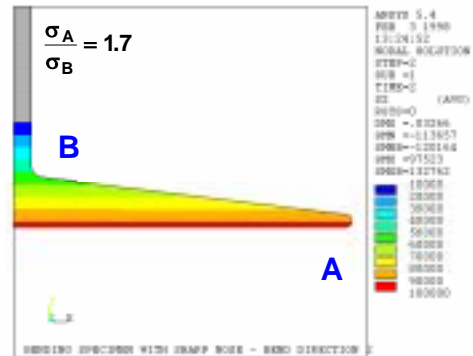
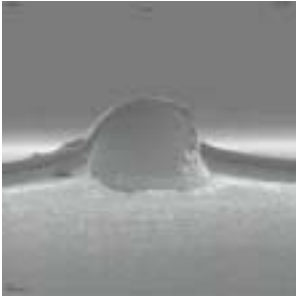


Figure 5.4. Comparison of blade and winged specimen stresses.

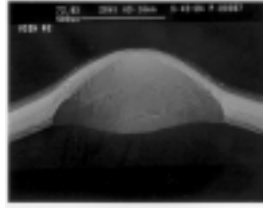
Three methods were used to simulate FOD in the winged specimens: machined notches with a 0.021-inch radius, ballistic ball impacts with 0.020 and 0.039-inch radius glass beads, and solenoid gun impacts with a chisel-point indenter (0.005 and 0.025-inch radii tips). Specimens were machined or impacted to simulate FOD nicks at 0° and 30° relative to centerline of the leading edge region on each specimen. Low-damage and high-damage target levels were set at depths of 0.005 and 0.020-inch, respectively. Figure 5.5 compares 30° notches in sharp leading edge specimens with ballistic and solenoid gun impacts. Actual notch depths ranged from 0.003 to 0.009-inch and 0.015 to 0.026-inch. An overview of this part of the test program can be found in Appendices 5B and 5C.

Loading fixtures were designed for HCF testing under tension-tension and fully reversed loading ($R = -1.0$) without measurable hysteresis effects during the loading cycle. For this program, testing rates were limited to 30 Hz due to the relatively large deflections in a flexural mode. Tests were conducted at $R = 0.5$ and -1.0 . In many cases, the electric potential drop (EPD) was monitored across the notch to identify crack nucleation. Two different welding techniques (weld-A and weld-B) and a contact pressure method were used to couple the sensing leads to the specimens.

Ballistic Impact with
0.020 Inch Radius Ball



Solenoid Gun with 0.025
Inch Radius Indentor



Solenoid Gun with 0.005
Inch Radius Indentor

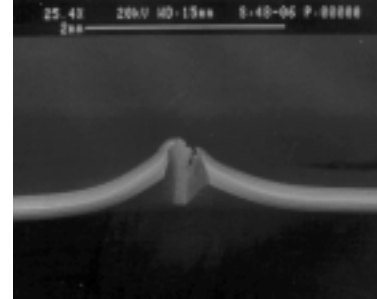


Figure 5.5. Representative FOD from ballistic and solenoid gun impacts. (Sharp LE Specimens, 30° Impacts, High Damage Levels)

A few S-N tests were conducted at constant load as a baseline, but the majority of tests were 10^6 cycle step tests, with a 10% load step. The reported stress ranges from the step tests were interpolated using the following equation:

$$\sigma_i = \sigma_{mg,j} + \frac{N_f}{10^6} (\sigma_{mg,f} - \sigma_{mg,j}) \quad (5.1)$$

where σ_i is the interpolated stress range, $\sigma_{mg,j}$ is the stress range at the previous load step, N_f is the cycles to failure at the final load step, and $\sigma_{mg,f}$ is the stress range at the final load step.

The objectives of the FOD testing on the winged specimens were to (1) compare ballistic impact results to solenoid gun impacts, (2) compare S-N tests to step tests, (3) investigate the effects of different impact parameters, and (4) provide experimental data to help verify the analytical models. Detailed test results are contained in Appendix 5C.

Figure 5.6 compares the results from the machined notches to the unnotched specimens. Figure 5.7 compares S-N results to step test results for 30° impacts with the solenoid gun. Although the step test data appears slightly lower than the S-N data, this difference is not significant, due to the relatively large data scatter. Therefore, it was assumed that S-N and step testing produced equivalent results under these conditions. Figure 5.8 presents the effect of notch depth on 10^6 endurance limit. Although again, a large amount of scatter is exhibited in the data, a few general conclusions are made. As expected, the 0.025-inch radius indentor from the solenoid

gun is not as damaging as the 0.005-inch radius indenter at comparable depths of damage. In addition, the effect of damage depth appears to plateau at the higher damage levels. Also, the ballistic impact results are not significantly different than the solenoid gun results at equivalent damage depths and impactor radii. Additional data may be required to confirm this conclusion. Figure 5.9 presents the effect of impact angle, indicating a 30° impact angle is more damaging than a 0° impact for equivalent nick depths. Figure 5.10 compares the test results for like-specimens with and without a stress relief cycle. Although these limited results do not indicate a statistically different interpolated stress range as a result of the stress relief cycle, additional testing should be conducted to confirm this conclusion. Also, indications are that EPD may influence test results; therefore, the effect of EPD monitoring on test results needs to be further investigated.

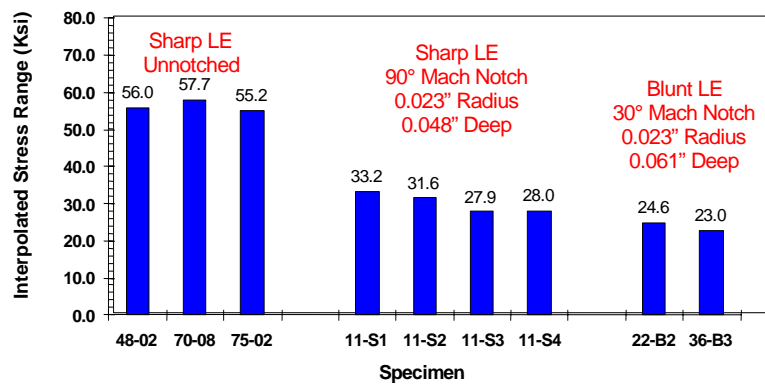


Figure 5.6. Step test results for FOD specimens with machined notches (R=0.5).

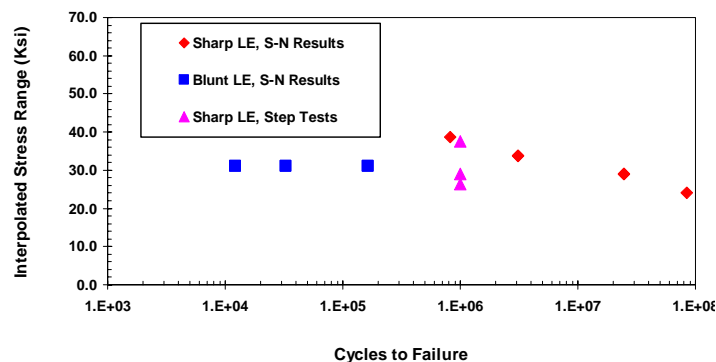


Figure 5.7. Comparison of S-N and Step Test Results (Solenoid Gun, 30° Impacts, High Damage Levels, R=0.5).

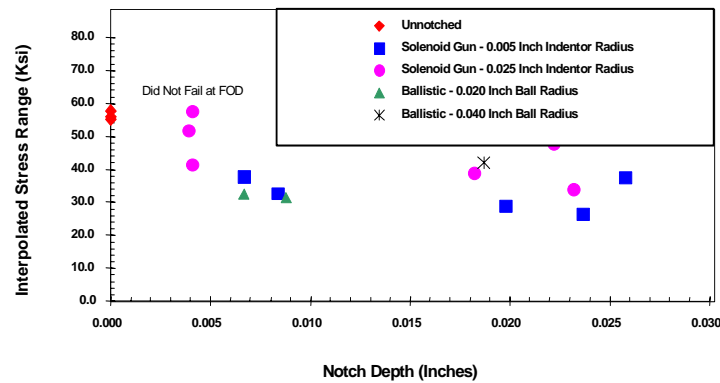


Figure 5.8. Effect of FOD notch depth and tip radius on 10^6 Step Test Durability. (Sharp LE Specimens, 30° Impact, $R=0.5$).

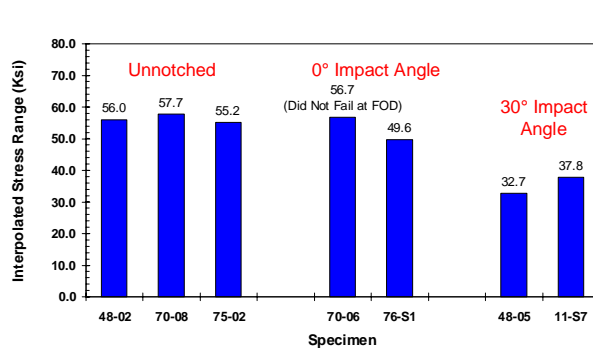


Figure 5.9. Effect of Impact Angle. (Sharp LE, Solenoid Gun, Low Damage, 0.005 inch Indentor, $R=0.5$). Step Test Results.

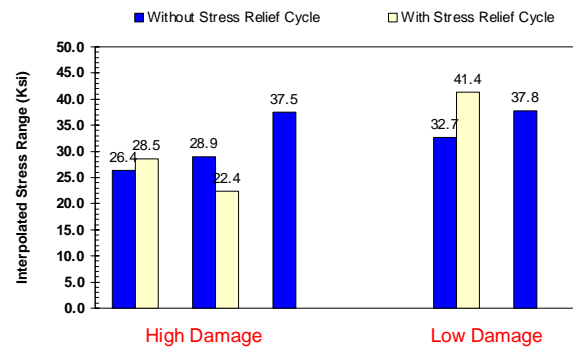


Figure 5.10. Effect of Stress Relief after FOD. (Sharp LE, Solenoid Gun, 0.005 inch Indentor, 30° Impact, $R=0.5$, No EPD). Step Test Results.

5.2.2 FOD Characterization/Verification – Axial Tests

The primary focus of the axial testing was limited to demonstrating the repeatability of impacting airfoil-like specimens using a quasi-static indentation method, and the effect on cyclic durability. This method of indentation used a standard test frame and measured the load-deflection curve, allowing the non-recoverable energy to be calculated. Repeatability was demonstrated by showing similar levels of the non-recoverable energy as well as similar debits in the subsequent fatigue life.

The airfoil-shaped specimen is based on the Air Force's diamond-like cross-section tension (DCT) specimen. Single FOD impacts were introduced to each specimen

side, resulting in two FOD notches per specimen. The indentation of the FOD event was measured using an MTS deflectometer. The non-recoverable energy associated with the FOD impacts were recorded. While some of the results appear to show good repeatability, other results show significantly different energy levels for the same depth of FOD. Additional work is required before this method can be used to calibrate the level of FOD damage imparted to specimens.

Several non-impacted and impacted specimens were tested under axial-load-control HCF conditions for comparison to baseline smooth bar fatigue data. Figure 5.11 compares the $R = -1$ and 0.5 diamond cross-section tensile (DCT or airfoil) test data with the smooth-bar baseline data. The data clearly show good agreement with smooth-bar baseline for non-impacted tests, and the negative effect that FOD has on HCF life (except for 5 mil FOD, no radius). The non-recoverable energy showed poor correlation between the energy recorded and the subsequent HCF life of impacted specimens. Additional work is needed to better understand the effect of this parameter and technique. Fractography showed that some of the nucleation sites were significantly (e.g., 0.004-inch) below the surface of the FOD impact. From the microstructural deformation observed below the FOD impact, it appears that significant cold work stresses should exist. However, these residual stresses were not measured. Additional micrographs obtained from ballistically damaged DCT specimens are presented in Appendix 5D. These micrographs support the analysis discussed in the next subsection.

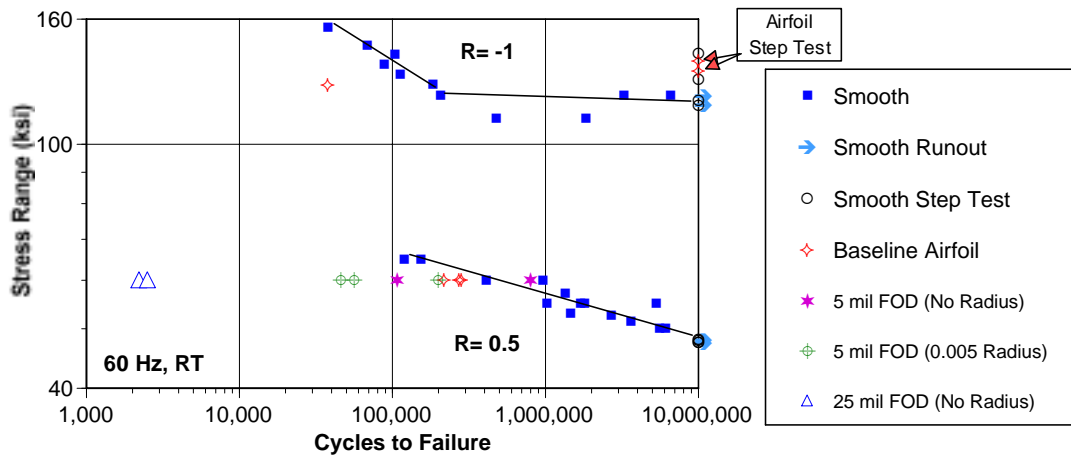


Figure 5.11. FOD data for DCT specimens versus the baseline smooth-bar data.

5.3 FOD Analytical Modeling

5.3.1 FOD Event Modeling

An analytical modeling study of leading edge FOD impact events was conducted to determine the effect of various impact parameters on leading edge damage and residual stress formation. The impact parameters investigated included leading edge radius, impact velocity, impact angle, and projectile mass and radius. MSC/DYTRAN was used for high-speed impact events and ABAQUS for low speed impact events. Both the DCT geometry, for the high-speed impact events, and the GE winged geometry, for the low-speed impact events, were studied.

The dynamic analysis modeling included rate-dependent material properties and material failure. Mesh density and material model sensitivity studies were conducted, and the analytical methods and code accuracy were confirmed with available ballistic impact test results. The DYTRAN deformation predictions correlate well with the impact test results, Figure 5.12. However, further evaluation is highly recommended to confirm the accuracy of the modeling approach.

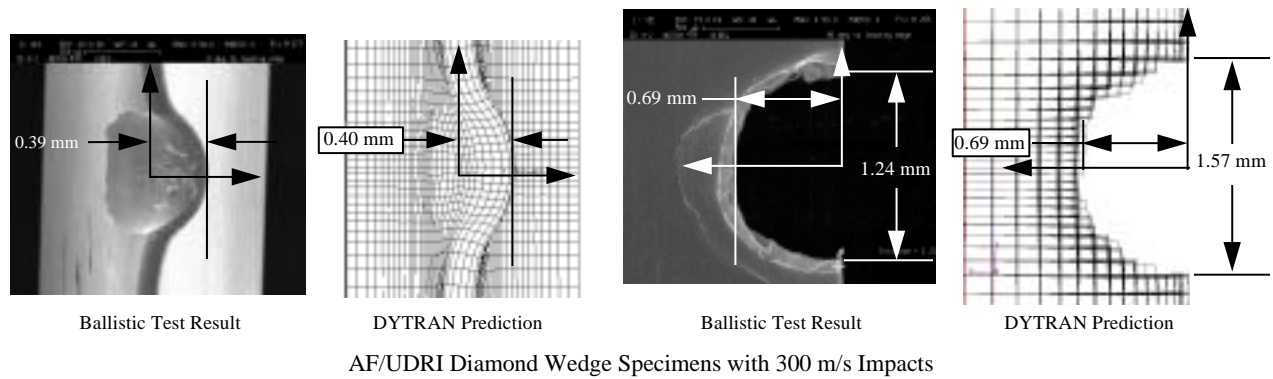


Figure 5.12. FOD impact deformation measurements and predictions

Numerous variables, and their effect on impact damage and residual stress field, have been investigated; and, the results are contained in Appendix 5E. Of particular interest is the effect of impact angle on the formation and shape of the residual stress field. Figure 5.13 shows the residual stress field chordwise through the specimen (blade) cross-section with the impact direction illustrated by the arrows. A 0° impact generates a large embedded compressive field directly behind the impact crater followed by an embedded tensile field. As the impact angle is varied, the residual stress field shifts. A high-tensile stress field is created on the entrance side of the damage site near the notch surface, and is not buffered by a large compressive field.

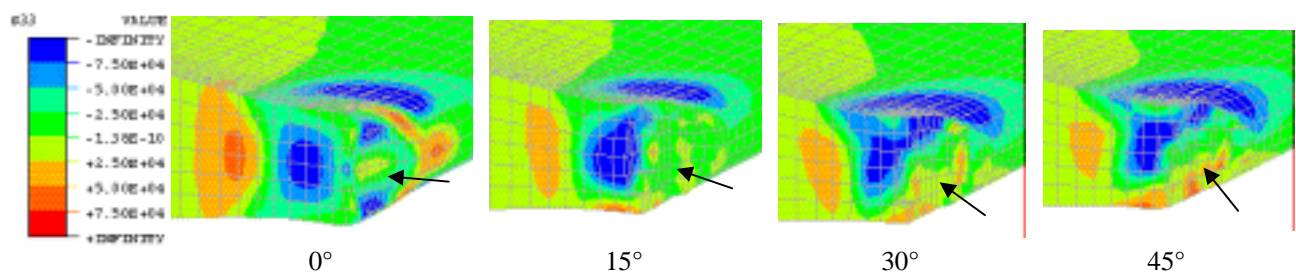


Figure 5.13. Spanwise residual stress field (ksi) for blunt edge DCT specimen impacted by 1.33 mm steel ball at 1000 ft/sec at different angles.

5.3.2 FOD Notch Stress Modeling

The influence of the residual stress in the post-impact fatigue behavior is complex, as it includes the stress itself and its interaction with the impact damage. Figure 5.14

displays three views of the 0° and 30° impact deformed leading edge of the specimen. The first shows the residual stresses at the impact site while the second view gives the stress in the specimen edge when the mean fatigue stress is applied and the residual stress is ignored. The third contour combines the applied and residual fields to obtain the true stresses in the impacted DCT bar at the mean fatigue stress.

During cyclic loading, crack propagation from a FOD-induced flaw will be controlled by both the geometry of the impact crater and the residual stress field surrounding the crater. As shown in Figure 5.14, if the residual field due to impact is ignored, the test specimen is merely a bar with a notch. However, if the residual field were included for the 30° impact, a crack would be anticipated at the maximum stress location at the intersection of the lower surface and the notch. This indicates that ignoring the residual field would lead to non-conservative stress intensity predictions.

5.3.3 Nucleation Models

Analyses of the FOD specimens using the stress invariant approach required a multi-step procedure. As a first step, the FOD damage was approximated by an angled notch with dimensions based on SEM micrographs of the failed specimens (Figure 5.15), extrapolated to the original specimen dimensions. As a result, the out-of-plane deformations were neglected. Next, the average interpolated 10^6 failure load and stress ratio were determined for a group of specimens and used to calculate the maximum and minimum loads for the FEA modeling. Figure 5.16 shows the resulting stress field for the sharp LE specimen with a low damage level. The local effective stress ($\sigma_{eff,l}$) was calculated using a modified Manson-McKnight model with a Walker model, as discussed in Paragraph 3.3.2.1. This local stress was then applied with the stressed area technique to determine an adjusted effective stress ($\sigma_{eff,a}$) that was compared to the smooth bar S-N results. Additional analytical details are provided in Appendix 5F.

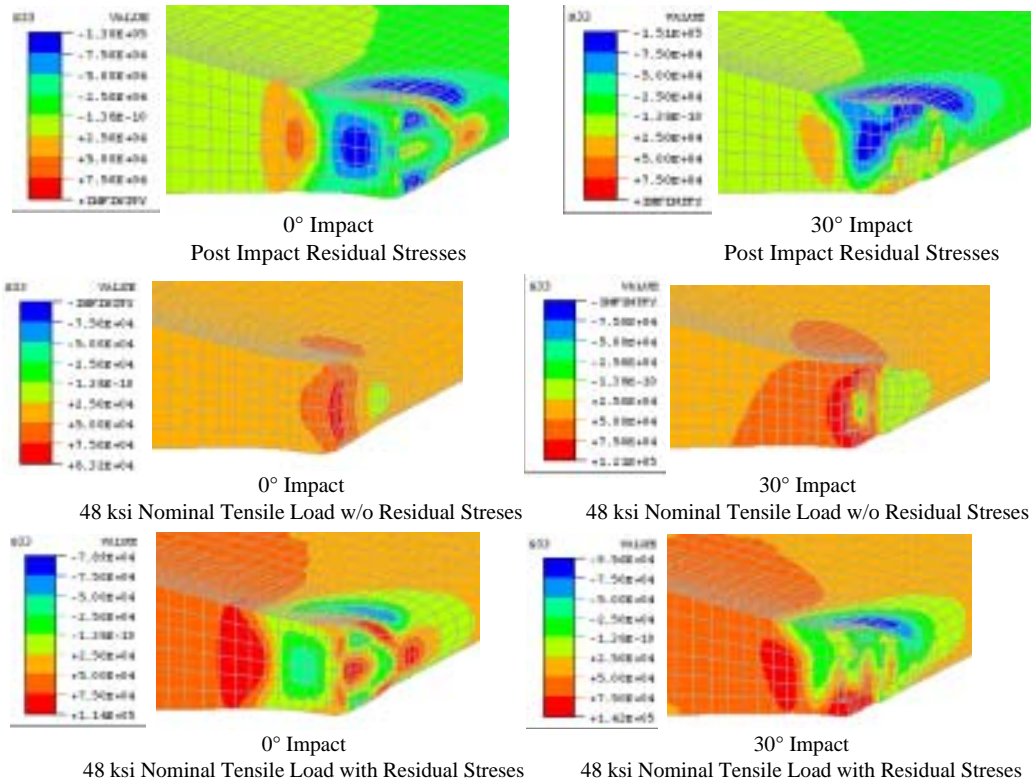
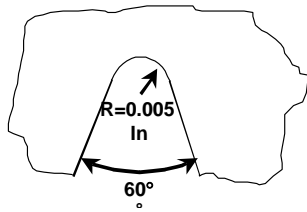


Figure 5.14. DYTRAN predictions (ksi) for blunt (0.015-inch) edge DCT specimen impacted with 1.33 mm ball at 1000 ft/sec and loaded in spanwise tension.

Six FOD cases were analyzed using the procedures described above. Table 5.1 summarizes the notch dimensions, maximum loads, stress ratios, local effective stresses ($\sigma_{eff,l}$), and adjusted effective stresses ($\sigma_{eff,a}$) for each case. Figure 5.17 indicates the predicted effective stresses are greater than the smooth bar results for most of the cases. Although, some of this variation may result from neglecting residual stress effects, additional data and specimen analyses will be required to clearly identify the sources of this variation.

Configuration A:



Configuration B:

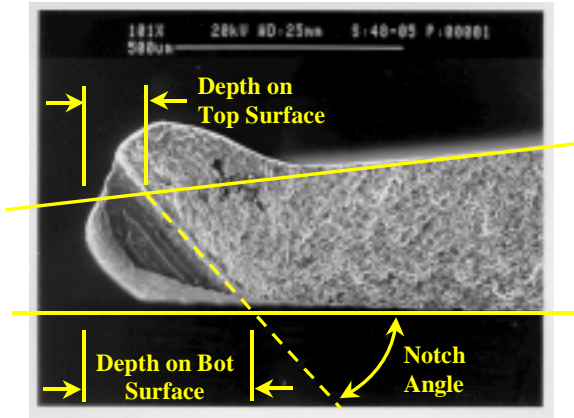
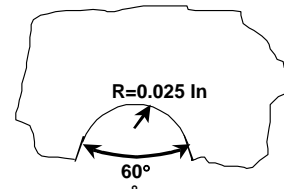


Figure 5.15 Notch Dimensions for FEM Model of Winged Specimen with FOD.

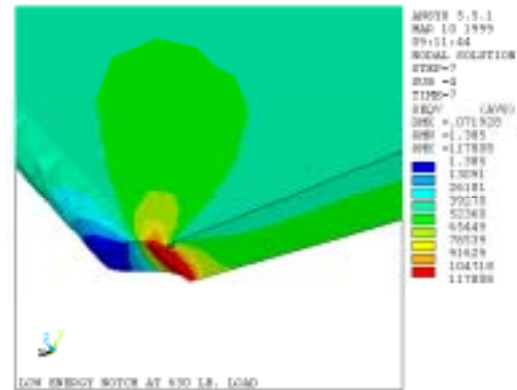


Figure 5.16. Stress contour plot from FEA of a low energy impact in a sharp LE.

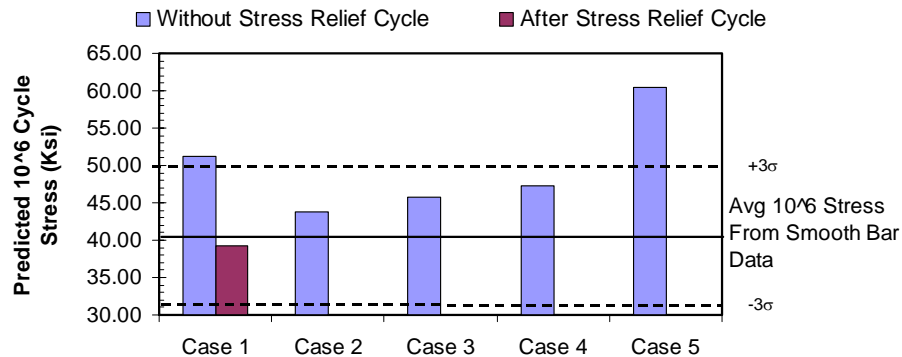


Figure 5.17. Comparison of predicted 10^6 cycle effective stress for FOD specimens to smooth bar results.

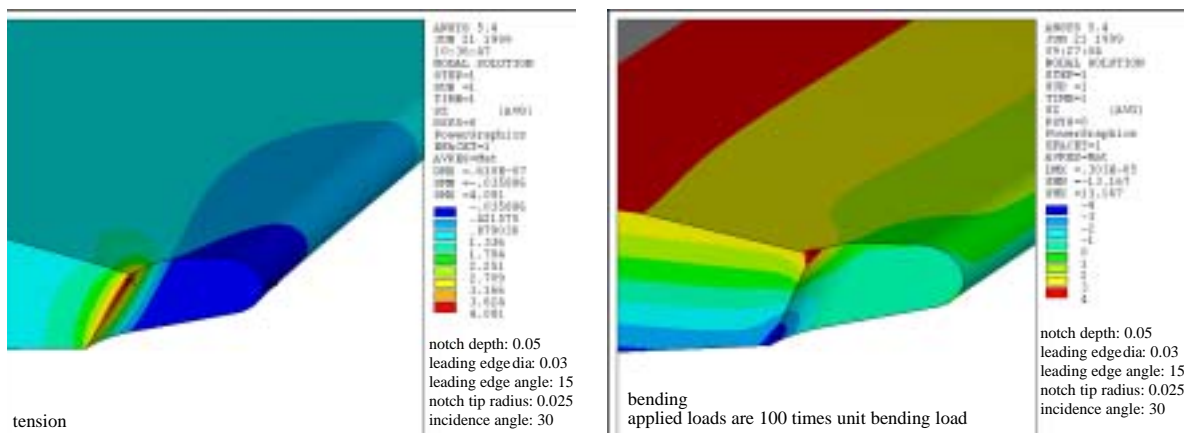
Table 5.1

Summary of FOD specimens Analyzed with Stress Invariant Models.

Case	Spec. LE Geom	Impact Angle	Simul. FOD Tip Radius	Simul. FOD Depth	Stress Relief After FOD	Notch Conf.	Notch Angle	Depth Top Surface (in.)	Depth Bottom Surface (in.)	Stress Ratio (R)	P _{range} for 10 ⁶ Cycles (lbs.)	σ_{eff} (Ksi)	$\sigma_{eff,a}$ (Ksi)
1	Sharp	30°	.005"	High	no	A	48°	.0174	0.030	0.5	278, 305, 395	69.4	51.24
1a	Sharp	30°	.005"	High	yes	A	48°	.0174	0.030	0.5	300, 236	53.1	39.21
2	Sharp	30°	.005"	Low	no	A	48°	.0053	.0143	0.5	344, 398*	60.2	43.84
3	Blunt	30°	.005"	High	no	A	48°	.0048	.0257	-1.0	492*	63.4	45.69
4	Sharp	30°	.025"	High	no	B	43°	.0180	.0300	0.5	503, 409	58.5	47.21
5	Sharp	0°	.005"	Low	no	A	90°	.0075	.0075	0.5	596, 522	66.8	60.43

*Additional tests were conducted, but the additional specimens did not reach 10⁶ cycles before failure.

A parallel effort was conducted to evaluate idealized FOD notch geometries in a parametric model to investigate the effects of various FOD and leading edge parameters on 10⁶ endurance limit stress. This effort involved predicting normalized (i.e. unit load) stress in representative FOD and leading edge geometries using ANSYS; see Figure 5.18 for representative geometry stress predictions and Appendix 5G for the complete parametric study. To validate this approach, all of the coupon specimens used in the test program were evaluated for elastic concentrated stress using strictly the results of this parametric study. An approach for notch yielding is then calculated using the Neuber local yielding approach. The final step is to calculate the SWT parameter (discussed in Paragraph 3.3.2.2) for the local FOD notch stress condition, which is used to determine cyclic life.

**Figure 5.18.** Representative geometry and ANSYS stress predictions for unit tension and bending loads.

The preceding methods were then evaluated with the coupon specimen data to assess the accuracy of the methods to determine an allowable endurance limit stress range, as discussed in Appendix 5H. In this study, the average notch-tip surface elastic-concentrated stress was used as a first order estimate to evaluate the nucleation modeling. Also, notched test data were used to determine the SWT effective notch stress capability for 10^6 cycles (65 Ksi). Figure 5.19 presents the results as a function of actual *versus* predicted stress. This method is conservative for all but three specimens, and there is significant bias between the test groups. As described in Paragraph 3.4.3.1, the stressed area can have a significant influence on cyclic capability. To account for this phenomenon, an estimate of the stress area technique (developed by GE) was used to adjust the results. This process improved the predictions overall accuracy moderately, but could not reduce the bias in the results (the stress area calculation was not performed for individual specimens), see Figure 5.20. One approach to improve the model accuracy is to add the effect of impact residual stress, but it did not seem justifiable since local notch yielding was already being predicted and the bias in the results remained.

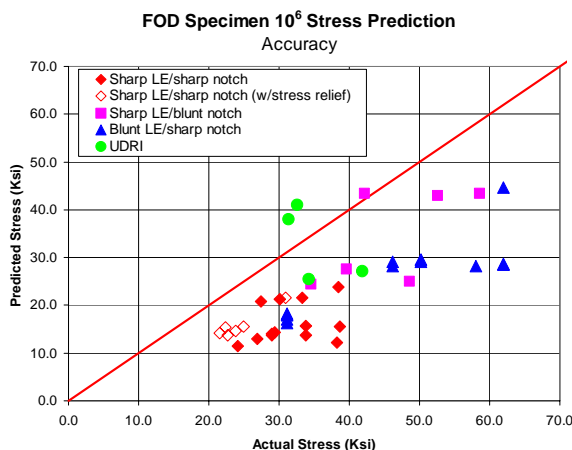


Figure 5.19. Nucleation modeling is conservative, and shows significant bias.

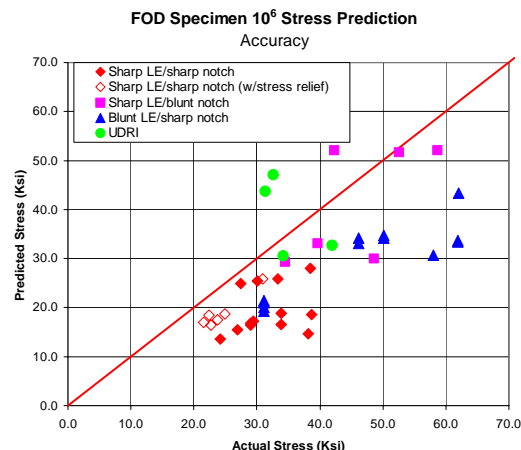


Figure 5.20. Nucleation modeling (w/stress area model) is conservative with bias.

5.3.4 Growth Models

Two fracture mechanics activities were performed to support the FOD modeling effort. First, a parametric study was conducted to compare calculated stress intensities from ANSYS to P&W fracture mechanics code solutions. The FEMs were based on the sharp LE specimen with low-damage level resulting from a 30° impact with a 0.005-inch impactor. Both through-crack and corner crack configurations were considered. Figure 5.21 shows the finite element mesh for the corner crack configuration and compares the stress intensities from the fracture code to the ANSYS solution. Results indicate the fracture mechanics code and the ANSYS solutions are comparable for a 0.005-inch corner crack. Similar results were obtained for the through-crack configuration. As a result, fracture mechanics code solutions were used for the remainder of this effort.

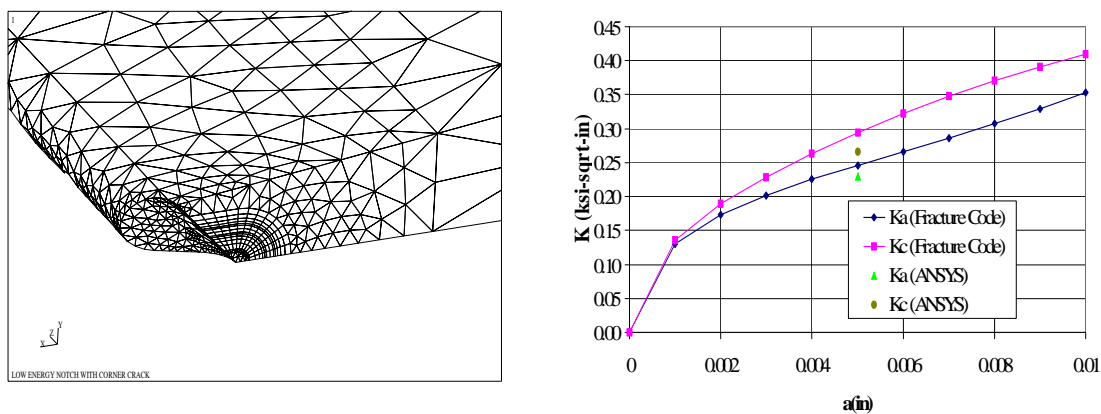


Figure 5.21. ANSYS model of a corner crack in a sharp tip FOD specimen with low damage, and comparison between predicted stress intensities from fracture code solutions and ANSYS solutions.

The second fracture mechanics activity used the fracture code to estimate the largest threshold crack sizes that would not produce crack growth. Local stresses and stress gradients were calculated from the elastic-plastic stress analyses described above, and then used to establish the maximum crack size such that predicted stress intensity factor (K) was equal to the threshold stress intensity (K_{th}). A surface crack in the center of the leading edge notch was used for these analyses based on heat-tint results of the FOD specimens. Figure 5.22 summarizes the required initial crack sizes as a function of notch depth for the five FOD specimens with residual stresses, one

FOD specimen subjected to a stress relief cycle, and the winged specimens with machined notches. Figure 5.22 indicates that an initial crack size equal to 2% of the notch depth provides a consistent metric for the three specimens without residual stresses. A consistent metric was not identified for the specimens with residual stresses due to the relatively large scatter in results.

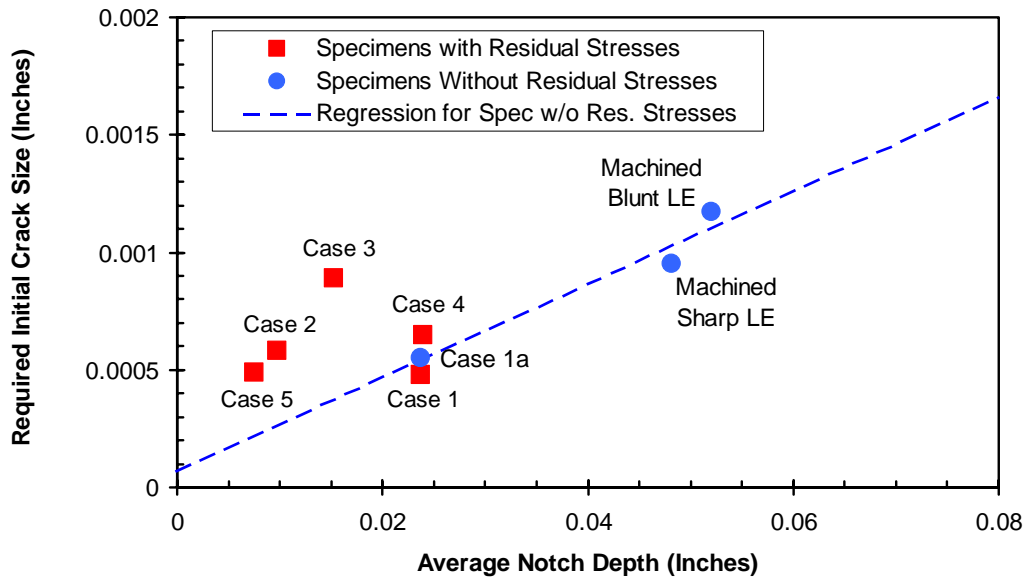


Figure 5.22. Largest initial crack sizes such that $K \leq K_{th}$ for several FOD specimens containing simulated FOD and machined notches.

As with nucleation modeling, a parallel effort was conducted to investigate K - based concepts for FOD modeling. Idealized FOD notch geometries were analyzed in a parametric model which predicts the stress intensity factor for corner cracks using the Boundary Integral Equation code FRANC3D, see Figure 5.23 and Appendix 5G for representative geometries and K versus a . To evaluate this approach, all of the coupon specimens conducted in the test program were evaluated for stress intensity for a single characteristic crack length (0.001-inch) using strictly the results of this parametric. Clearly, ΔK increases with increasing notch depth as expected, see Figure 5.24. In addition to increased ΔK , one would expect the impact or notch yielding residual stresses to also increase with notch depth. To capture this behavior, a $K_{residual}$ required to correlate ΔK for each specimen to the $\Delta K_{threshold}$ material capability model presented

in Paragraph 3.2.3.1 was calculated. The results of this study clearly demonstrate an increasing trend in K_{residual} with notch depth is required, which was then empirically fit with a polynomial equation (see Figure 5.25).

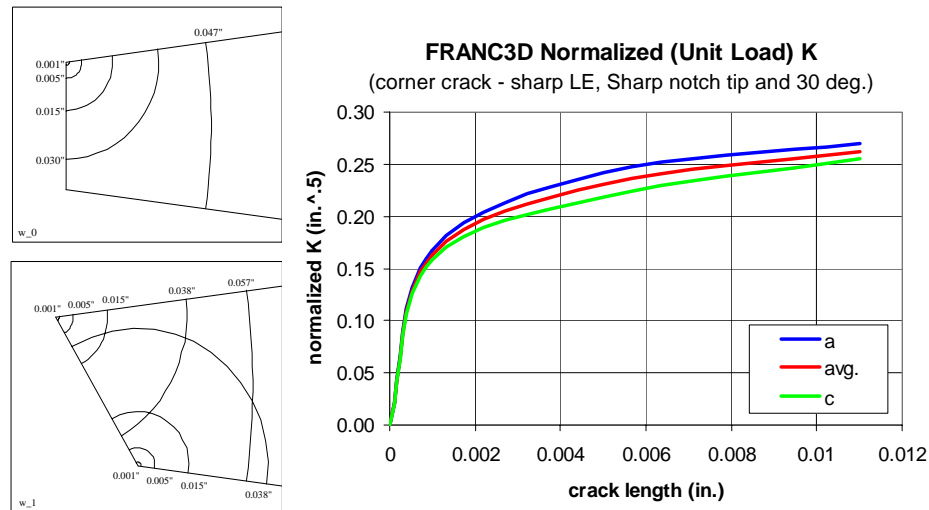


Figure 5.23. Representative geometries and K vs. a from the Stress intensity prediction parametric (normalized $K = K$ for a unit load).

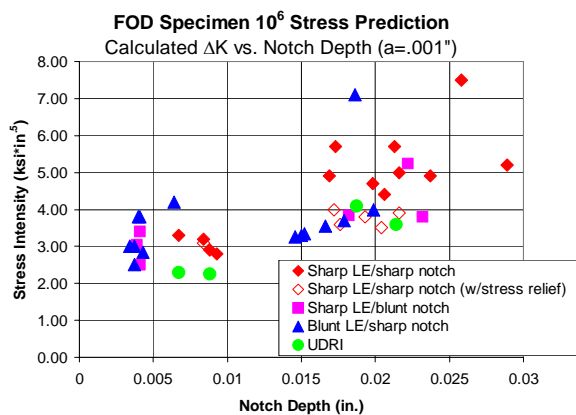


Figure 5.24. Stress intensity predictions (ΔK) vs. Notch depth (0.001-inch corner crack).

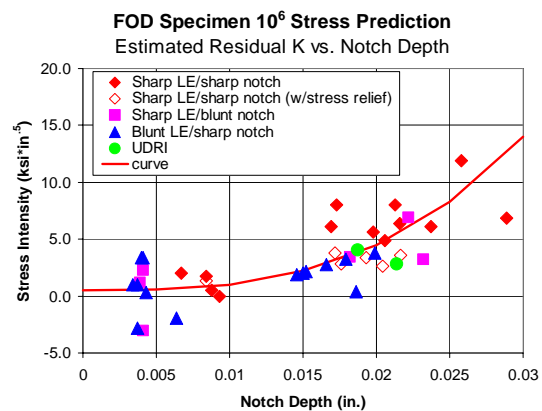
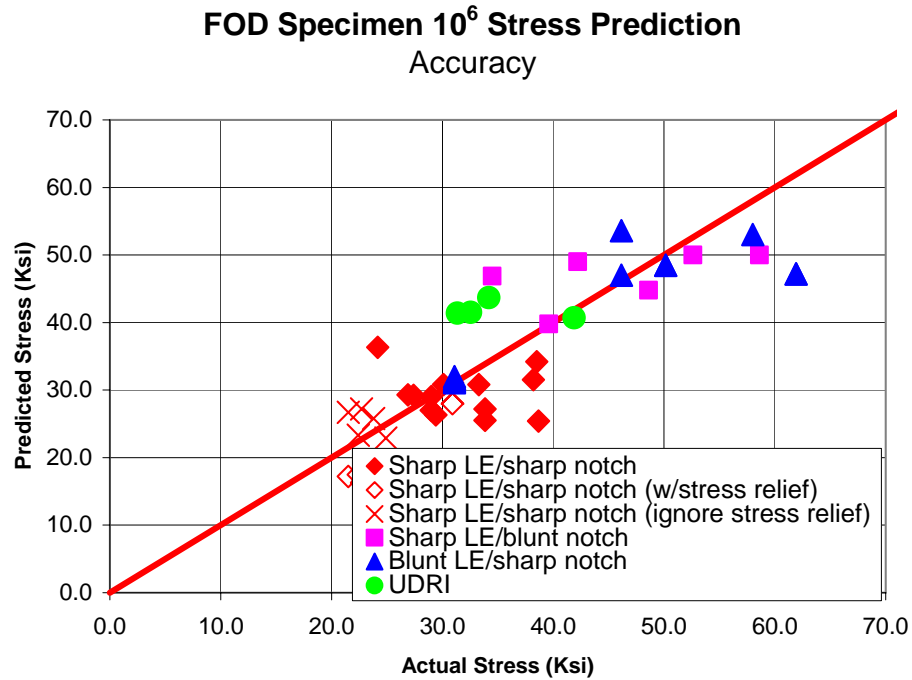


Figure 5.25. Predicted K_{residual} vs. notch depth.

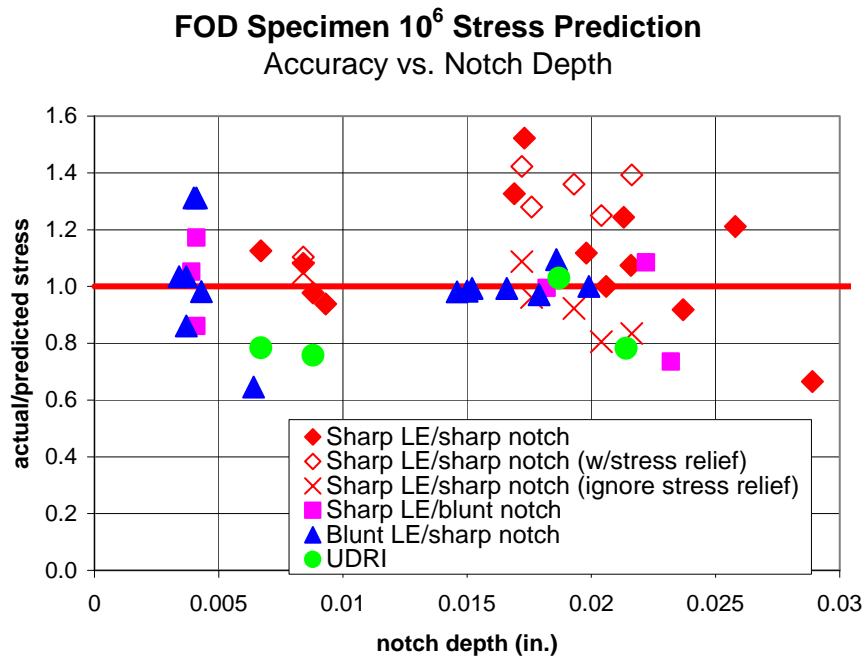
The preceding methods were then evaluated with the coupon specimen data to assess the accuracy of the methods (see Appendix 5H). Although a single characteristic crack length (0.001-inch) is used, and K is predicted from a parametric analysis, the resulting predictions are remarkably robust, as shown in Figure 5.26. Although there is large scatter in the test results, the methods predict the mean behavior reasonably well, and there is very little bias within or between any of the test groups. The exception to this statement comes for the data generated by the specimens that went through some process that resulted in stress relief at the notch tip. Predictions ignoring and accounting for full stress relaxation (i.e., $K_{\text{residual}} = 0$) span the test results, indicating that the stress relief may not zero these stresses. Although using a single crack length and accounting for K_{residual} appears to be a promising method, it has an empirical fit to a controlling parameter. It is highly recommended that K_{residual} be substantiated with notch and impact residual stress prediction methods, and correlate to a wider array of data.

5.3.5 Worst Case Notch (WCN) Model

The WCN model assumes that the lowest threshold stress for onset of HCF is controlled by whether or not microcracks can continue to grow after having been initiated early in life by FOD and/or LCF. This modified damage tolerance approach^{5.1-3} computes the threshold stress, ΔS_{th} , by equating the applied ΔK to a crack-size-dependent threshold stress intensity, $\Delta K_{th}^{sc}(a)$, which incorporates small crack effects^{5.4,5.5} as described in Paragraph 3.2.3.2 (Also see Appendix 3N). The WCN model predicts the conditions for onset of crack nucleation, as well as regimes of crack growth and arrest, or crack growth to failure (Figure 5.27). This model uses simple parametric notch-stress equations -- or, if needed, FEA -- to predict ΔS_{th} as a function of FOD-notch depth and sharpness, including residual stress effects (see Appendix 5I). Since it explicitly treats the growth and arrest of microcracks, the WCN model is also applicable to cases in which beneficial surface treatments are employed to enhance component life.



a) Actual vs. predicted stress



b) Actual/predicted vs. notch depth

Figure 5.26. Modeling which accounts for K_{residual} correlates well to data.

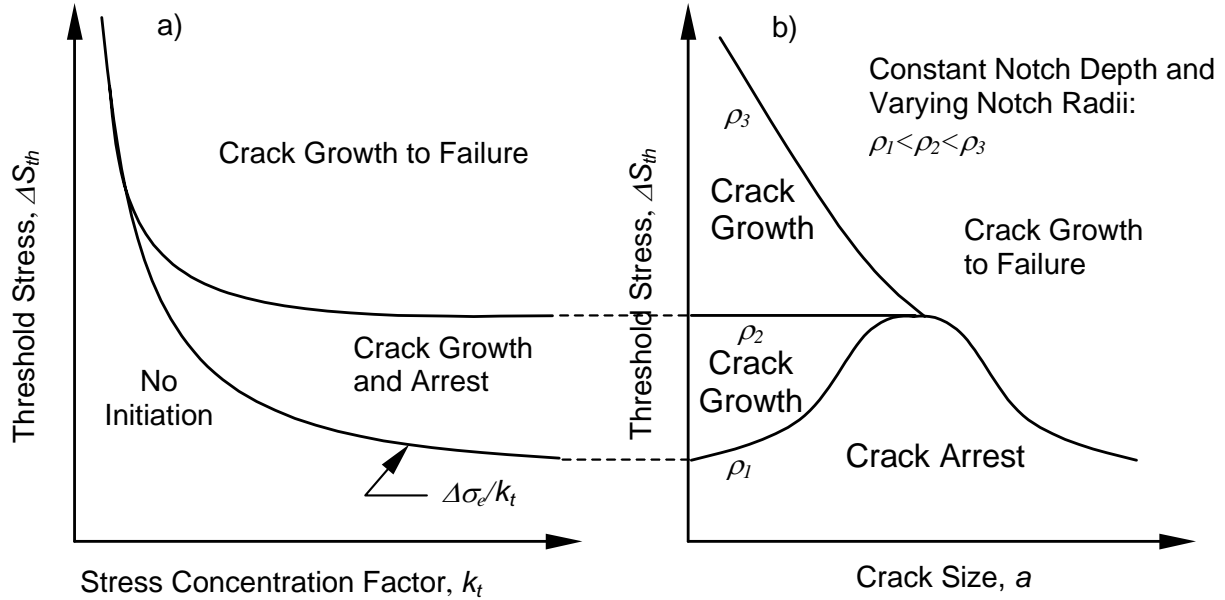


Figure 5.27. WCN model predicts crack nucleation, growth and arrest, and failure.

The general utility of the WCN model is demonstrated in Figure 5.28, where predicted ΔS_{th} values are compared with results from HCF tests on specimens with various blade leading edge configurations containing simulated FOD. The agreement between model predictions and measurements is very good, particularly considering the wide range of conditions represented in the data – including machined notches, ballistic impacts, solenoid gun impacts, as well as a range of FOD-notch depths and radii which were selected to be representative service-induced FOD in engines. In spite of these complexities, the mean behavior is predicted very well. The scatter about the mean is substantial since the impacts produced scatter in the detailed geometry of the FOD, whereas nominal geometries were employed in the analysis – as would be the case in applications of the model to design or to setting of inspection limits. The WCN model has also been shown to provide excellent predictions of literature data effects^{5,6-5,8} on steel specimens containing a wide range of notch acuity (see Appendix 5I). Thus, the WCN model appears to properly predict the influence of notch acuity on HCF behavior in a variety of engineering materials.

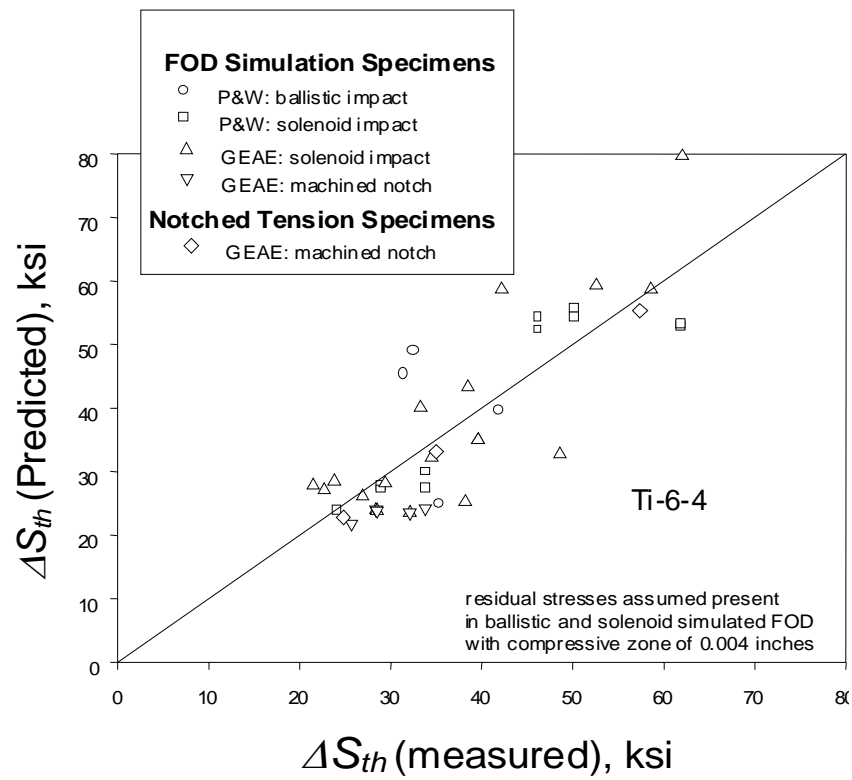


Figure 5.28. WCN model predictions versus data from FOD simulation tests.

5.4 EXIT CRITERIA FOR FOD DAMAGE STATE/DISCUSSION

5.4.1 Overview of the Requirements

The exit criteria are intended to statistically summarize the adequacy of the various life methods and to provide an approach for comparing new and existing design methods. The exit criteria for FOD modeling are expressed in terms of the ratios of actual fatigue strengths to predicted (mean) fatigue strengths and use the normal distribution to quantify the statistical parameters. The criteria are as follows:

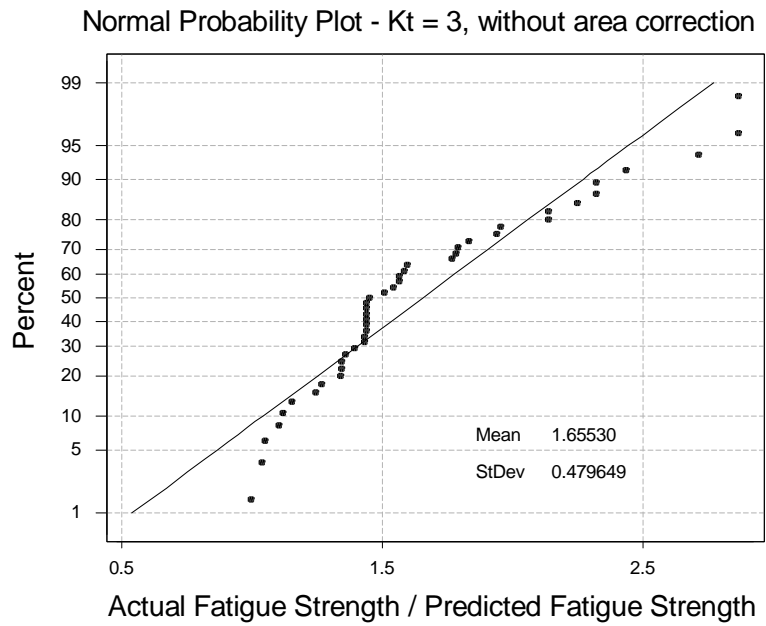
- a) The average ratio of actual to predicted (A/P) fatigue strengths be within ± 0.15 of 1.0.
- b) No significant bias shown for the test parameters.
- c) Since the standard deviation of baseline smooth A/P fatigue strengths is 0.10, the scatter of A/P values from FOD models will be less than or equal to 0.25.

5.4.2 Stress Concentration Factor Model ($K_t = 3$)

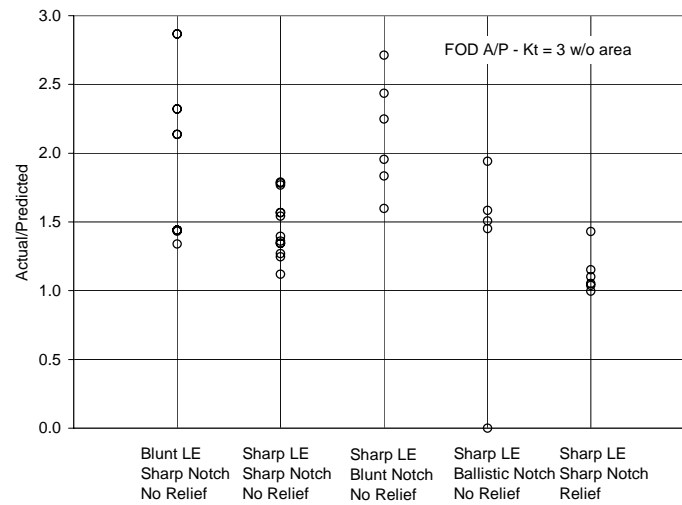
The current method for predicting FOD durability is a nucleation based, $K_t = 3$ application. The cumulative distribution of A/P values from the $K_t = 3$ model is shown in Figure 5.29a. This model had a large conservative bias of 66 percent (i.e., average A/P = 1.66) and the scatter in the A/P values (0.48) exceeds the exit criteria of 0.25. The distribution of actual to predicted fatigue strengths indicates this modeling is not appropriate for FOD predictions. Further, the effect of test condition as defined by the impacted specimens is statistically significant. This effect can be seen in Figure 5.29b that displays the A/P ratios as a function of specimen/impact type. The failure to adequately predict mean fatigue strength is attributed to the $K_t = 3$ modeling not considering other parameters which affect FOD durability, such as notch depth and tip radius.

5.4.3 SWT Model

The nucleation methods, specifically the strength estimation method with the SWT model correcting for stress area, has an average 46 percent conservative bias (i.e., average A/P = 1.46) with a composite A/P standard deviation of 0.37. The composite distribution of SWT A/P values is presented in Figure 5.30a. The SWT model predictions also did not completely account for test conditions as can be seen in

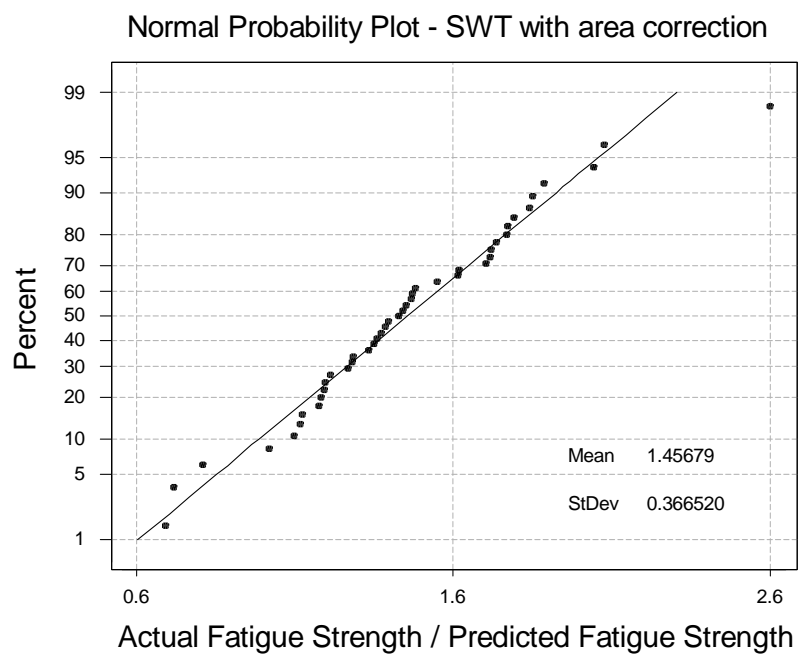


a) Normal Distribution of A/P for Composite of Test Conditions

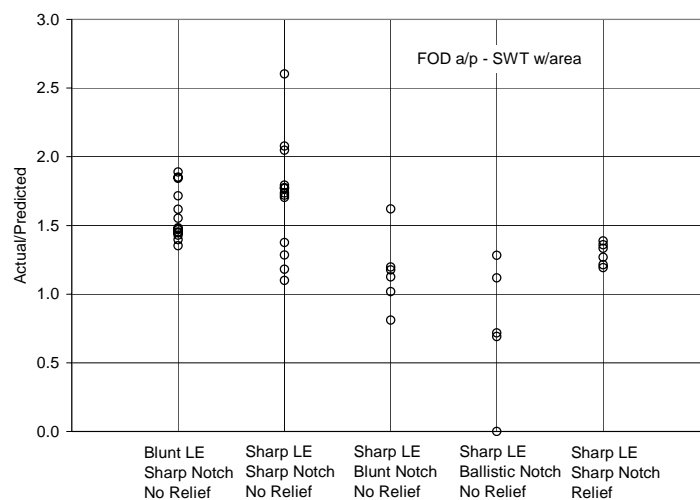


b) A/P Values for Impact Specimens

Figure 5.29. Actual/Predicted Values from $K_t=3$ Model without area correction.



a) Normal Distribution of A/P for Composite of Test Conditions



b) A/P Values for Impact Specimens

Figure 5.30. Actual/Predicted Values from SWT with Area Correction.

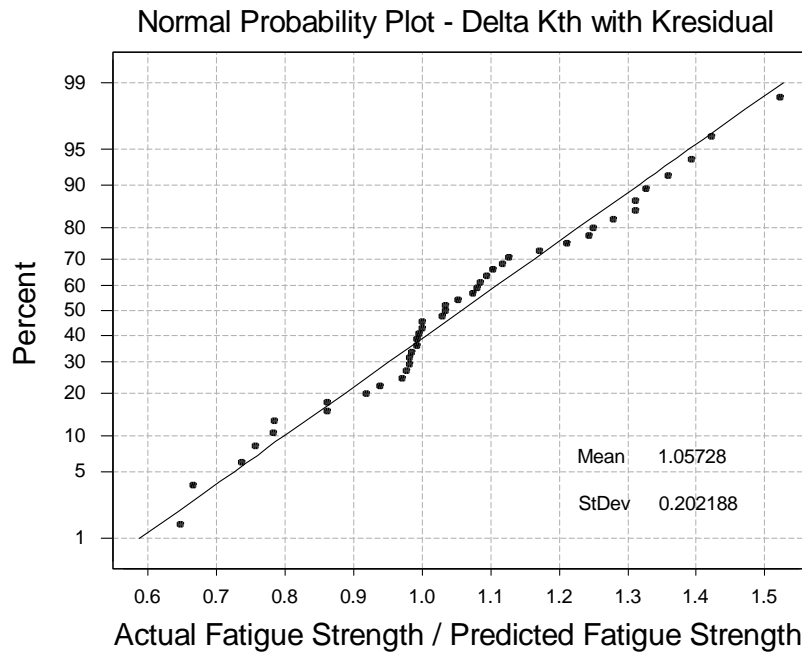
the plot of A/P values for the respective specimen sets as shown in Figure 5.30b. The same model, without correcting for stress area, has an average bias of 72 percent, the largest average bias of the three models considered. The SWT model also ignores notch acuity and stress relief.

5.4.4 Fracture Mechanics Model

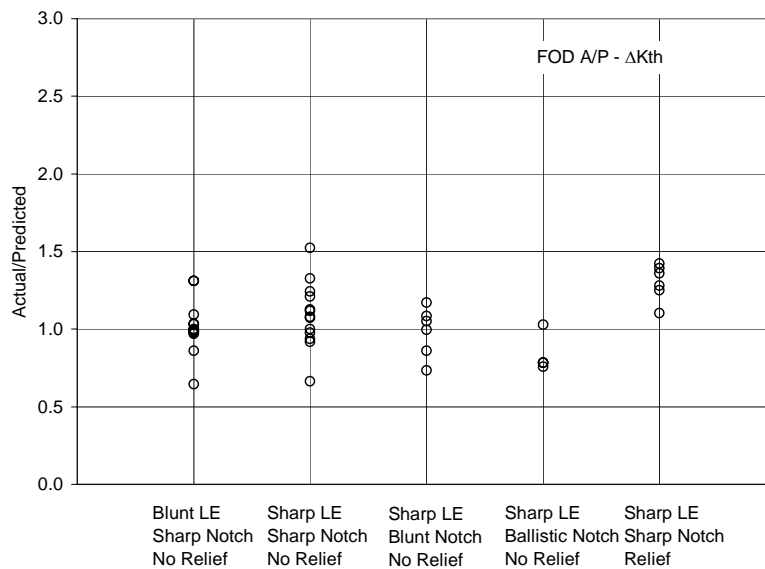
As shown in Figure 5.31a, the fracture mechanics based ΔK_{th} model with $K_{residual}$, had an average bias of 5.7 percent (average A/P = 1.057) and a coefficient of variation of 20 percent. This FOD model meets the exit criteria for bias and scatter of predictions. The normal distribution could not be rejected for the A/P values in Figure 5.31a. There was no bias introduced by the test conditions (specimens) for four of the five specimens. The specimens with sharp leading edge, sharp notch and stress relief had a statistically significant greater bias than the other four. See Figure 5.31b.

5.4.5 Worst Case Notch Model

The WCN method has a small average bias of 5.5 percent (average A/P = 1.055 as can be seen in Figure 5.32a). The standard deviation of the A/P values is 0.22. The WCN model meets the criteria for bias and scatter of predictions. The normal distribution could not be rejected for the A/P values in Figure 5.32b. The A/P ratios for the different test specimens were generally not significantly different. The only statistically significant difference was that the average bias from the sharp leading edge, machined notch, no relief specimens was greater than the average bias from the three sharp leading edge, sharp notch, and stress relieved specimens. The composite bias was not significantly different from zero.

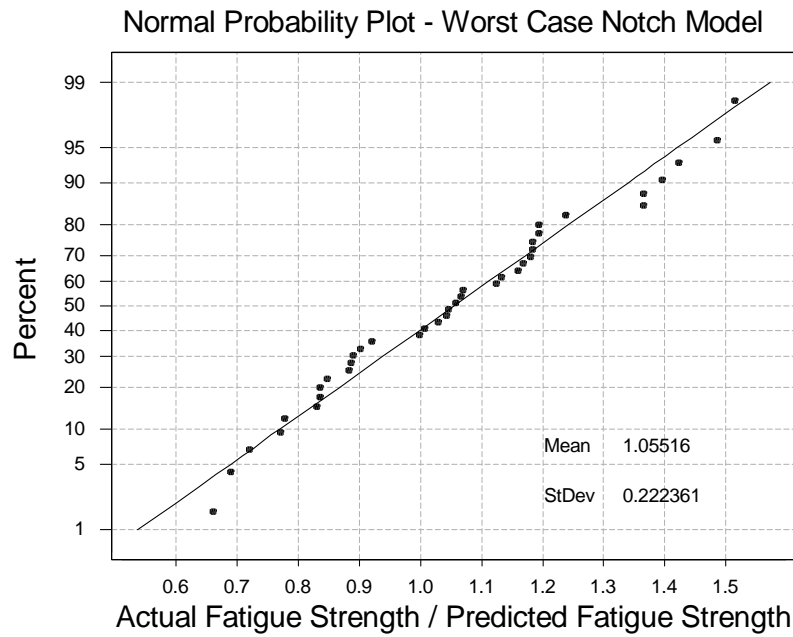


a) Normal Distribution of A/P for Composite of Test Conditions

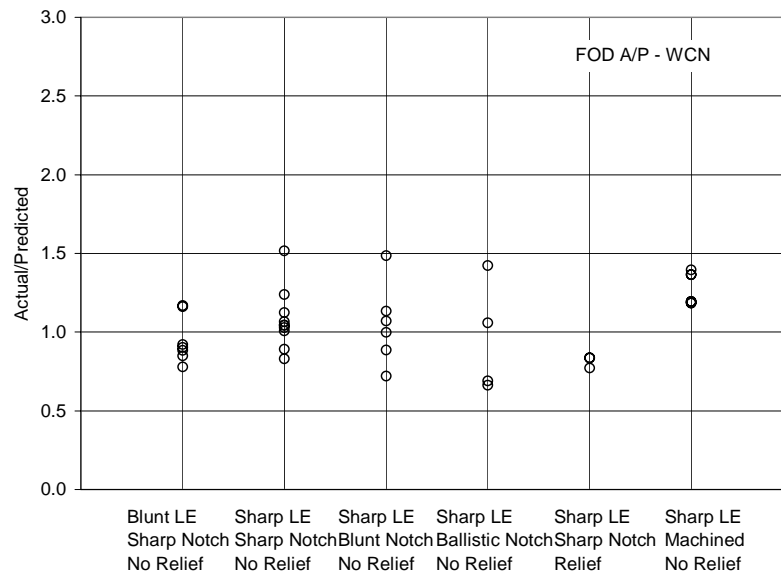


b) A/P Values for Impact Specimens

Figure 5.31. Actual/Predicted Values from ΔK_{th} with K_{residual} Model



a) Normal Distribution of A/P for Composite of Test Conditions



b) A/P Values for Impact Specimens

Figure 5.32. Actual/predicted values from WCN model.

5.4.6 Model Summary

The composite average and standard deviations of A/P values for the four models are summarized in Table 5.2. As noted above, the A/P averages and scatter from the ΔK_{th} with $K_{residual}$ and WCN models meet the exit criteria. Neither the average nor standard deviation of A/P criteria for the $K_t = 3$ and SWT with area correction models were satisfied and the predictions were dependent on the test conditions.

Table 5.2
Comparison of FOD Models

Model Parameters	$K_t = 3$	SWT	ΔK_{th}	WCN
Average	1.655	1.4568	1.0573	1.0552
Std Dev	0.4796	0.3665	0.2022	0.2224

5.5 SUMMARY AND RECOMMENDATIONS

Overall, significant progress was made in the understanding of the effect of FOD on HCF design limits and improving the ability to model the impact of FOD. The effects of leading geometries, simulated FOD methods, FOD impact parameters, and stress-ratios were investigated. Residual stresses were predicted for high-velocity ballistic impacts and low-velocity solenoid gun impacts. Stress analyses of damaged specimens were conducted, and preliminary models that predict threshold limits in the presence of FOD were evaluated. Two of the four models evaluated met the exit criteria; these were the fracture mechanics model and the WCN model.

This work will be extended under the Advanced High Cycle Fatigue Life Assurance Program (USAF Contract F49620-99-C-0007). The preliminary models will be further evaluated with the current data and then applied to a wider variety of conditions including the effects of higher temperatures and choice of different blade material. Modeling approaches will be selected based on these evaluations. In addition, the effects of residual stresses should be further investigated, and the models verified on an engine component through blade tests. Lastly, an implementation plan should be developed and initiated. These subsequent efforts will help transition the understanding and preliminary models developed under this program into turbine engine design practices that will eventually impact future fan and compressor blade designs.

5.6 REFERENCES

- 5.1 T.H. Topper and M.H. El Haddad, "Fatigue Strength Predictions of Notches Based on Fracture Mechanics," *Fatigue Thresholds: Fundamentals and Engineering Applications*, Engineering Materials Advisory Services, LTD, Warley, U.K., 1982.
- 5.2 S.J. Hudak, Jr., O.H. Burnside, and K.S. Chan, "Analysis of Corrosion Fatigue Crack Growth in Tubular Joints," *ASME Trans., Journal of Energy Resource Technology*, Vol. 107, 1985.
- 5.3 S.J. Hudak, Jr., G.G. Chell, T.S. Rennick, R.C. McClung, and D.L. Davidson, "A Damage Tolerance Approach to FOD Based on the Worst Case Notch Concept," *Proceedings of the 4th National Turbine Engine High Cycle Fatigue Conference*, Monterey, CA, February, 1999.
- 5.4 S.J. Hudak, Jr., "Small Crack Behavior and the Prediction of Fatigue Life," *ASME Trans., Journal of Engineering Materials and Technology*, Vol. 103, 1982, p. 26.
- 5.5 S. Suresh and R.O. Ritchie, "The Propagation of Short Fatigue Cracks," *International Metals Reviews*, Vol. 29, 1984, pp 445-476.
- 5.6 N.E. Frost and D.S. Dugdale, "Fatigue Tests on Notched Mild Steel Plates With Measurement of Fatigue Cracks," *Journal of the Mechanics and Physics of Solids*, Vol. 5, 1957, p.182-192.
- 5.7 N.E. Frost, "Notch Effects and the Critical Alternating Stress Required to Propagate a Crack in an Aluminum Alloy Subjected to Fatigue Loading," *J. Mech. Engr. Sci.*, Vol. 2, No. 2, 1966, pp 109-119.
- 5.8 *Metal Fatigue*, N.E. Frost, K. J. Marsh, and L.P. Pook, Clarendon Press, Oxford, 1974, pp 166-173.

Appendix 5A

CHARACTERIZATION OF SERVICE-INDUCED FOD

Stephen J. Hudak, Jr.

and

David L. Davidson



Southwest Research Institute

**Submitted
31 August 1999**

APPENDIX 5A

CHARACTERIZATION OF SERVICE-INDUCED FOD

The objective of this effort was to define the range of FOD geometries that could be produced in service. To meet this objective, SwRI asked the SA-ALC to provide examples of “typical” FOD based on their experience in inspecting and overhauling turbine engines. A total of fifty-one Ti-8-1-1 blades from either 1st, 2nd, or 3rd stage fans from F100 engines were provided to SwRI for evaluation. Thirty-one of these blades contained a total of 42 discrete FOD sites. The remaining blades were severely damaged (for example, see Figure 5A.1) and therefore were not further characterized. In general, the discrete FOD consisted of dents, tears, and notches, as can be seen by the examples in Figures 5A.2 through 5A.5. Damage was primarily to the leading edge of the blades – specifically, 40 leading-edge FOD and 2 trailing-edge FOD were observed. In two cases, the leading-edge damage consisted of FOD that had been previously blended and returned to service. A summary of the photographic documentation, as well as selected metallographic and fractographic evaluation of the FOD is given below; additional details on the FOD geometry can be found in Ref. [1].



Figure 5A.1. Five severely damaged blades showing progressive nature of the damage.

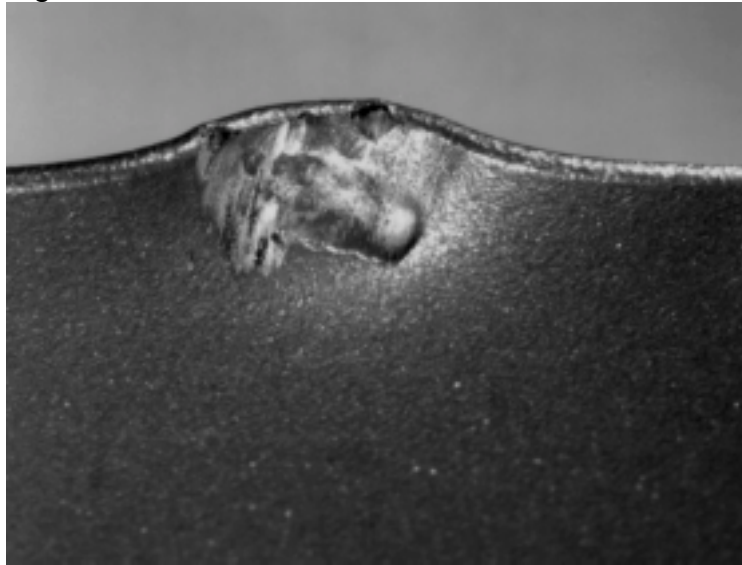


Figure 5A.2. 0.059-in dent in F100 2nd stage fan blade showing large deformation, but no cracks (10X).

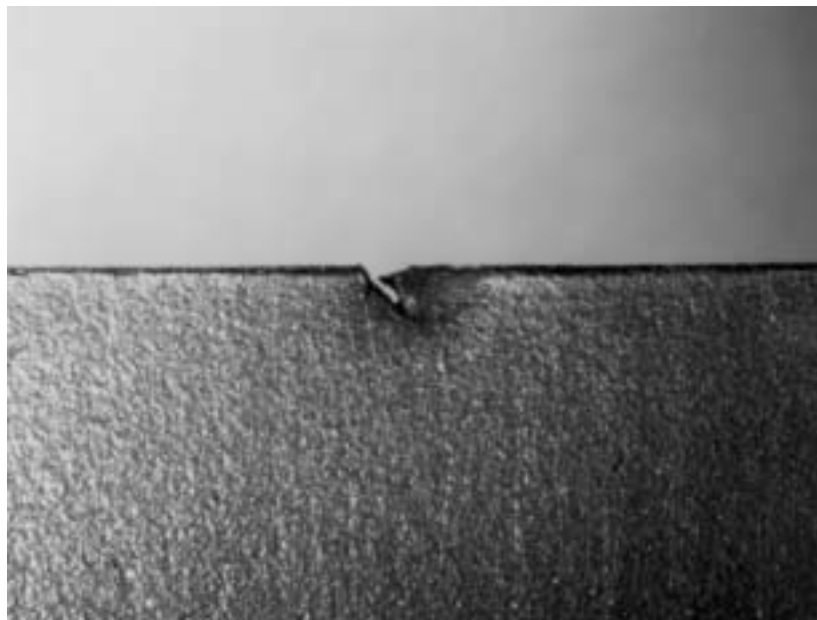


Figure 5A.3. 0.028-in.-deep tear associated with highly deformed dent in F100 2nd stage fan blade (10X).

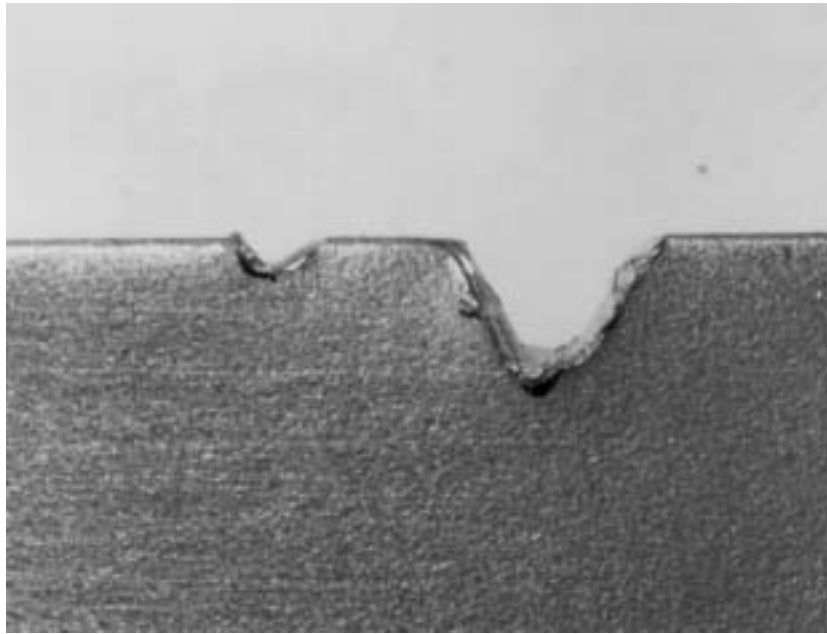


Figure 5A.4. 0.015 inch-deep semi-circular notch and 0.059-in.-deep V-shaped notch in F100 2nd stage fan blade (10X). The deformation ridge shown was only on one edge of the notch indicating that the FOD impacted the blade at an oblique angle.

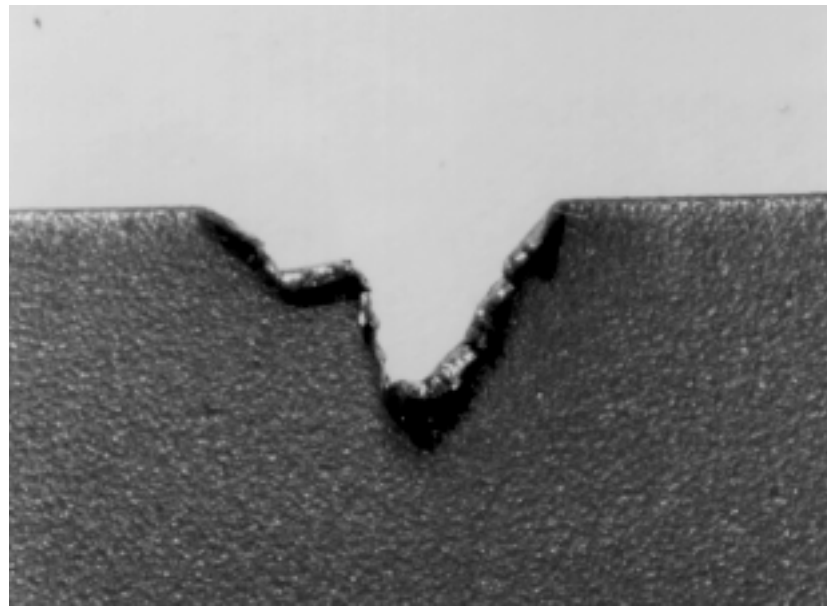


Figure 5A.5. 0.090-in.-deep V-shaped notch in F100 2nd stage fan blade. The deformation ridge shown was only on one edge of the notch indicating that the FOD impacted the blade at an oblique angle.

FOD Geometry Distributions

In order to quantify the FOD geometry, measurements of the depth and root radius of the damage were made from photographic enlargements (4X to 10X). The resulting distribution of the measured FOD depths is shown in Figure 5A.6, where it is compared with data previously obtained by Pratt and Whitney in an extensive field survey of FOD damage [2,3]. The Pratt and Whitney data are also from 1st, 2nd, and 3rd stage fan blades from F100 engines. Part of the motivation for this comparison was to determine how the SwRI-evaluated FOD compared to the larger population of FOD in service. As can be seen in Figure 5A.6 the two distributions are of very similar form – both being of the lognormal or Weibull type. These results indicated that SwRI's sample population is consistent with Pratt and Whitney's previous field survey, and thus represents a typical sampling of the FOD likely to be found in service for F100 fan blades.

Also shown in Figure 5A.6 are the serviceability limits and blend limits for F100 fan blades which are used in Jet Engine Intermediate Maintenance performed at the depots. The limits are shown as ranges since they depend on the stress level experienced in service and thus are specific to the fan stage, as well as to the location in a given blade. For example, the limits generally decrease when moving inward from the blade tip to accommodate the increasing stress near the blade platform. Blades with defects below the appropriate serviceability limit can be left in service without repair, while those between the serviceability limit and blend limit must be repaired before being returned to service. Blades requiring repairs that cannot be done within the blend limits must be scrapped. This periodic culling of blades from the overall blade population tends to remove blades with FOD depths above the blend limits thereby influencing the shape of the distribution.

It is important to recognize that FOD depth distributions are fundamentally different from crack size distributions used in classical damage tolerance analyses in that damage due to crack size progresses in a slow stable fashion throughout the life of the component, whereas FOD of any given depth can be introduced at any time in the component life, regardless of when the last inspection occurred. Thus, in developing an improved HCF design methodology, it would appear that FOD depths beyond the blend limits also need to be evaluated to ensure that they will survive to the next inspection.

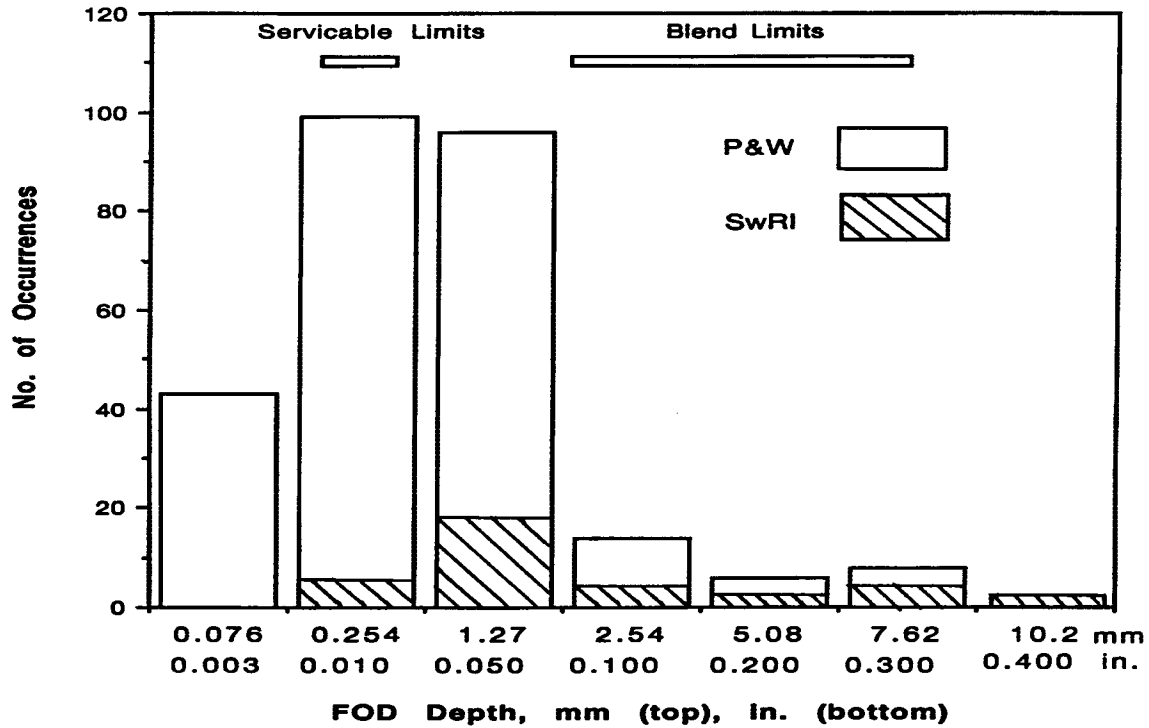


Figure 5A.6. Distribution of service-induced FOD depth from surveys of F100 fan blades conducted by SwRI and Pratt and Whitney [2,3].

The distribution of measured FOD root radii is shown in Figure 5A.7. As can be seen, this distribution is quite broad in comparison to the FOD depth distribution in Figure 5A.6. This difference in distribution shape is likely a consequence of the fact that FOD'ed blades are not generally culled from service based on the sharpness of their notch roots. An overall index of the severity of the FOD can be obtained by combining the measured FOD-root radii of Figure 5A.7 with the FOD depths of Figure 5A.6 to determine the distribution of elastic stress concentration factors, k_t , given in Figure 5A.8 [4]. These k_t values were computed using the parametric notch stress equations described in Appendix 5I. As indicated in Figure 5A.8, the average k_t is about 4, however, values of up to 10 can occur for the more severe FOD-notches.

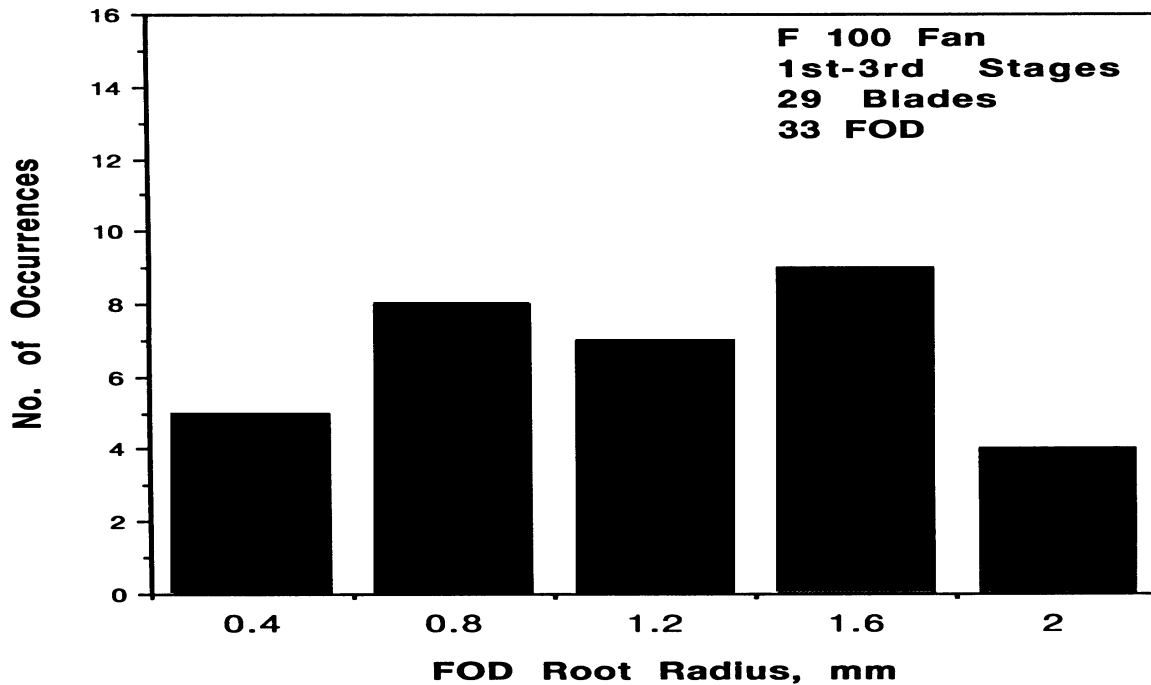


Figure 5A.7. Distribution of service-induced FOD root radii from survey of F100 fan blades conducted by SwRI.

MICROSCOPIC FEATURES OF FOD

Metallography and fractography were also performed on selected samples to characterize the FOD geometry in more detail, as well as to determine the extent of local deformation and the possible existence of cracking. Figure 5A.9 shows a V-shaped FOD along the leading edge of a blade that produced the highest stress concentration ($k_t = 10$). The rough edge on only one surface of the FOD, Figure 5A.9(a), indicates that the leading edge of the blade was impacted at an oblique angle. Although no evidence of cracking could be seen on the roughened as-manufactured and shot-peened surface of the blade, Figure 5A.9(a), a 0.008 in. (200 μm) crack is evident near the apex of the notch on a metallographically prepared section near the mid-plane of the blade, Figure 5A.9(b) and (c). The large extent of crack opening in Figure 5A.9(c) suggests that this crack was not formed by fatigue, but rather that it may have been formed during the FOD impact. To confirm this hypothesis, the crack was opened and both surfaces were examined in the scanning electron microscope. The resulting fractographs in Figure 5A.10 for several magnifications all exhibit extensive tearing of the beta phase, with small regions having necked to form tear ridges, as well as fractured alpha particles. These features are clear indications that the fracture was

caused by an overload. Conversely, no evidence of fatigue striations was found on the fracture surface. All of these observations lead to the conclusion that this fracture occurred during the FOD impact and not during subsequent fatigue cycling in service.

Figure 5A.11 shows similar results for a U-shaped FOD on the leading edge of a blade. Once again, metallographic sectioning revealed a crack emanating from the FOD, Figure 5A.11(b) and (c). However, in this instance the 0.012 in. (300 μm) crack was on the right flank of the FOD and not at the apex of the notch, in part due to the fact that this notch was not as acute as that shown previously in Figure 5A.9. The extent of crack opening and the sheared appearance of the crack near its origin, Figure 5A.11(c), suggest that this crack was also formed during the impact event.

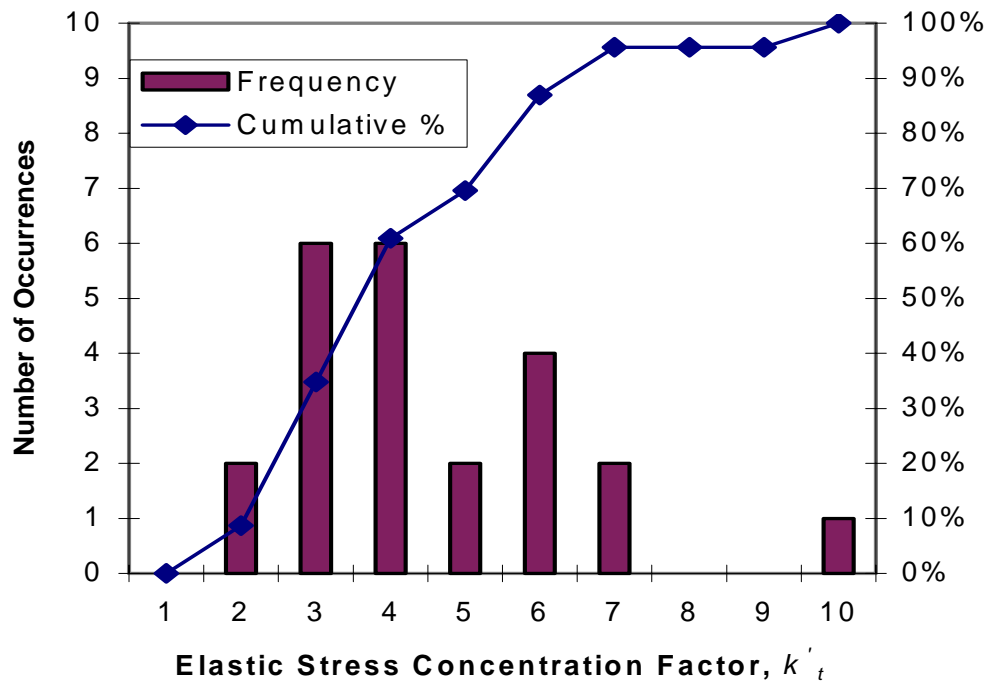


Figure 5A.8. Distribution of elastic stress concentration factors computed from FOD depth (Figure 5A.6) and root radii (Figure 5A.7) distributions using Equation (5I.6) in Appendix 5I.

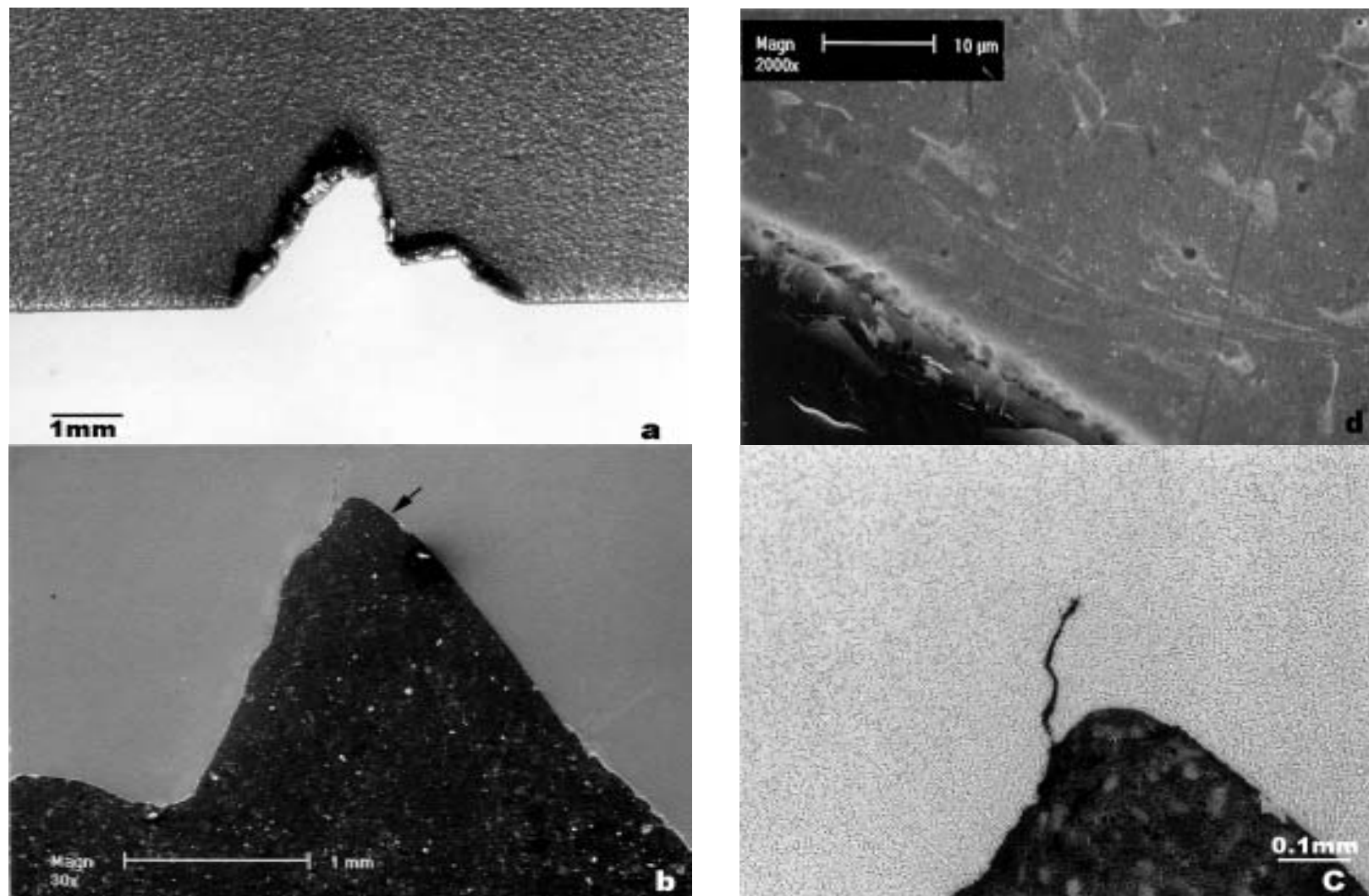
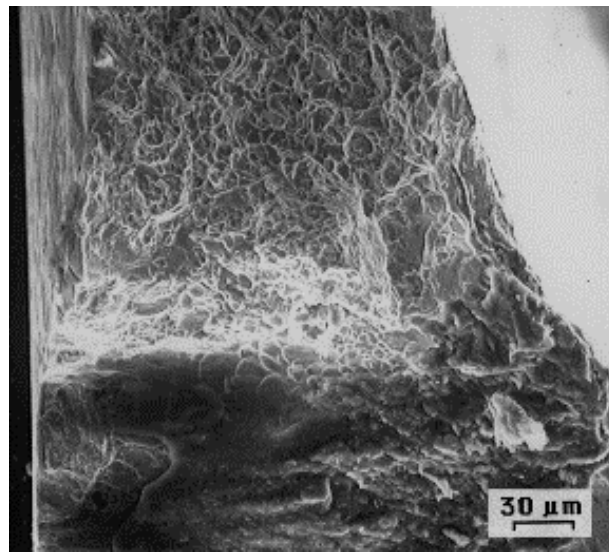
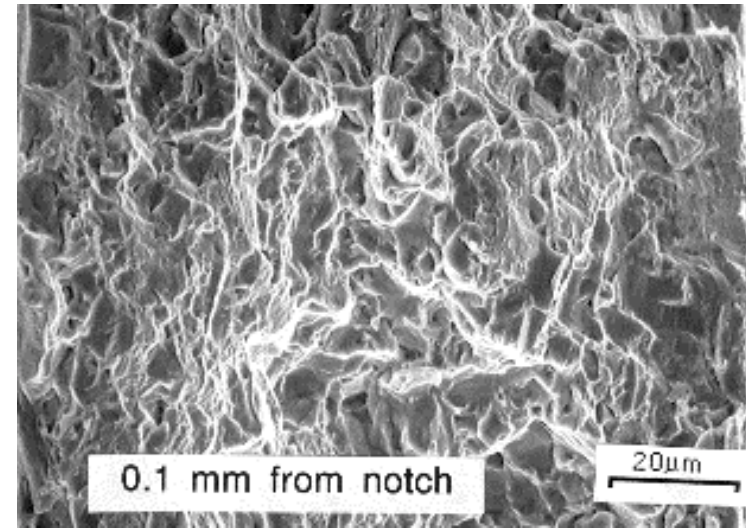


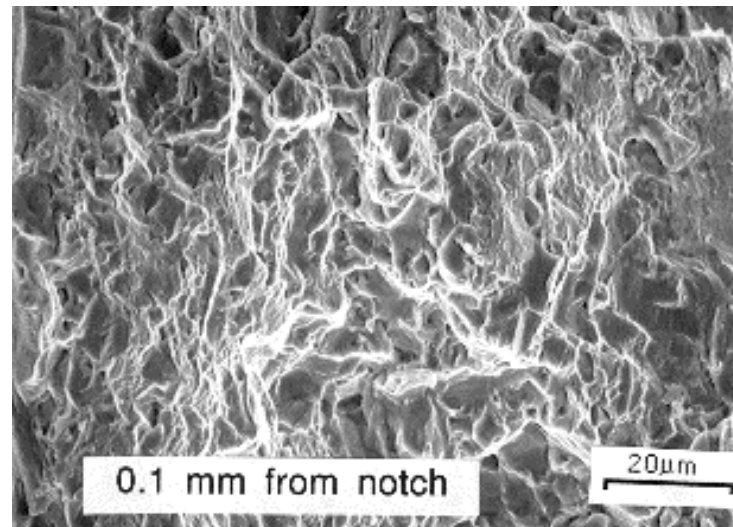
Figure 5A.9. V-shaped FOD from F100 2nd stage fan blade showing: (a) overall view of 0.090-in.-deep notch with 0.014-in. root radius, (b) close-up view of interior section showing crack near notch root, (c) magnified view of notch root showing highly deformed crack with large opening, (d) local deformed microstructure along interior section of notch indicated by arrow in (b).



(a)



(b)



(c)

Figure 5A.10. Fractograph of FOD-induced crack shown in Figure 5A.9. Tearing of beta-phase provides clear indication that the crack was formed during the FOD impact; there is no evidence of crack extension due to subsequent in-service fatigue cycling.

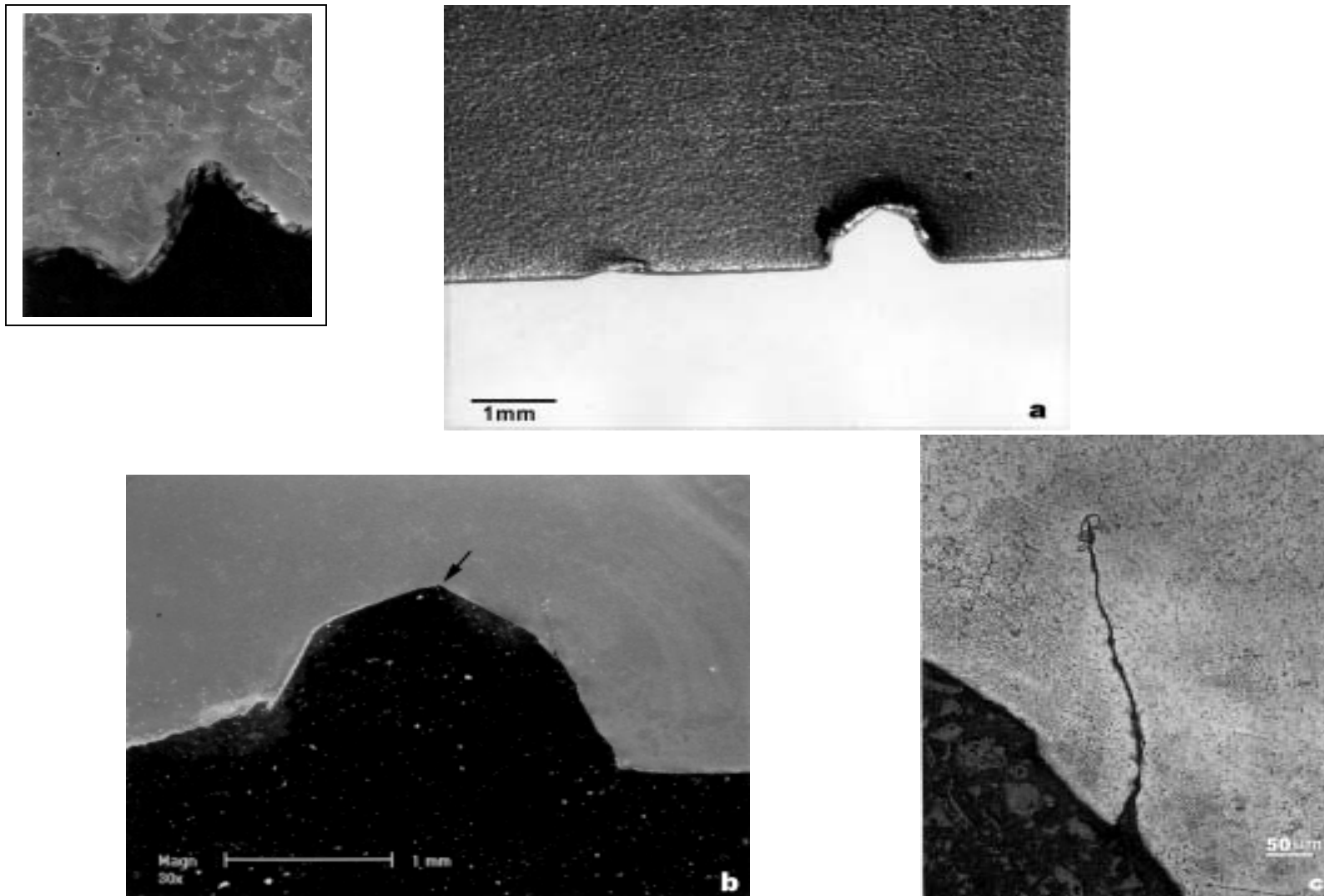


Figure 5A.11. U-shaped FOD from F100 2nd stage fan blade showing: (a) overall view of 0.046-in.-deep notch with 0.025-in. root radius, (b) close-up view of notch and crack on right flank, (c) magnified view of crack exhibiting large deformation and crack opening, (d) deformed microstructure along interior section of notch indicated by arrow in (b).

Not all FOD impacts produced cracks in these Ti-8-1-1 blades. Figure 5A.12 shows a milder FOD-notch that, upon sectioning, revealed a jagged edge with some local deformation, but no crack. Figure 5A.13 shows a FOD notch that exhibited partial spallation on the left flank and more complete spallation on its right flank, Figures 5A.13(b) and (c), respectively. The coarse, brittle morphology of the surface of the more complete spallation region is shown in Figure 5A.13(d). These features suggest that dynamic loading effects are present in at least some FOD.

The extent of microscopic deformation to the microstructure along the FOD surface is of interest because it provides information regarding the incident angle of the foreign object with respect to the blade. Metallographic results from most of the sectioned blades indicate little deformation of the microstructure – see Figure 5A.9 and Figures 5A.11 through 5A.13. Regions along the FOD surface exhibiting about 10 μm of highly deformed material can be seen in Figure 5A.9(d) and 5A.11(d); however, such highly deformed regions were rare. These observations suggest that the FOD impacted the blade at an angle to the blade centerline. Such observations are consistent with the kinematics of blade impact by foreign objects. Consequently, many of the simulated FOD testing was done at oblique impact angles with respect to the blade axis.

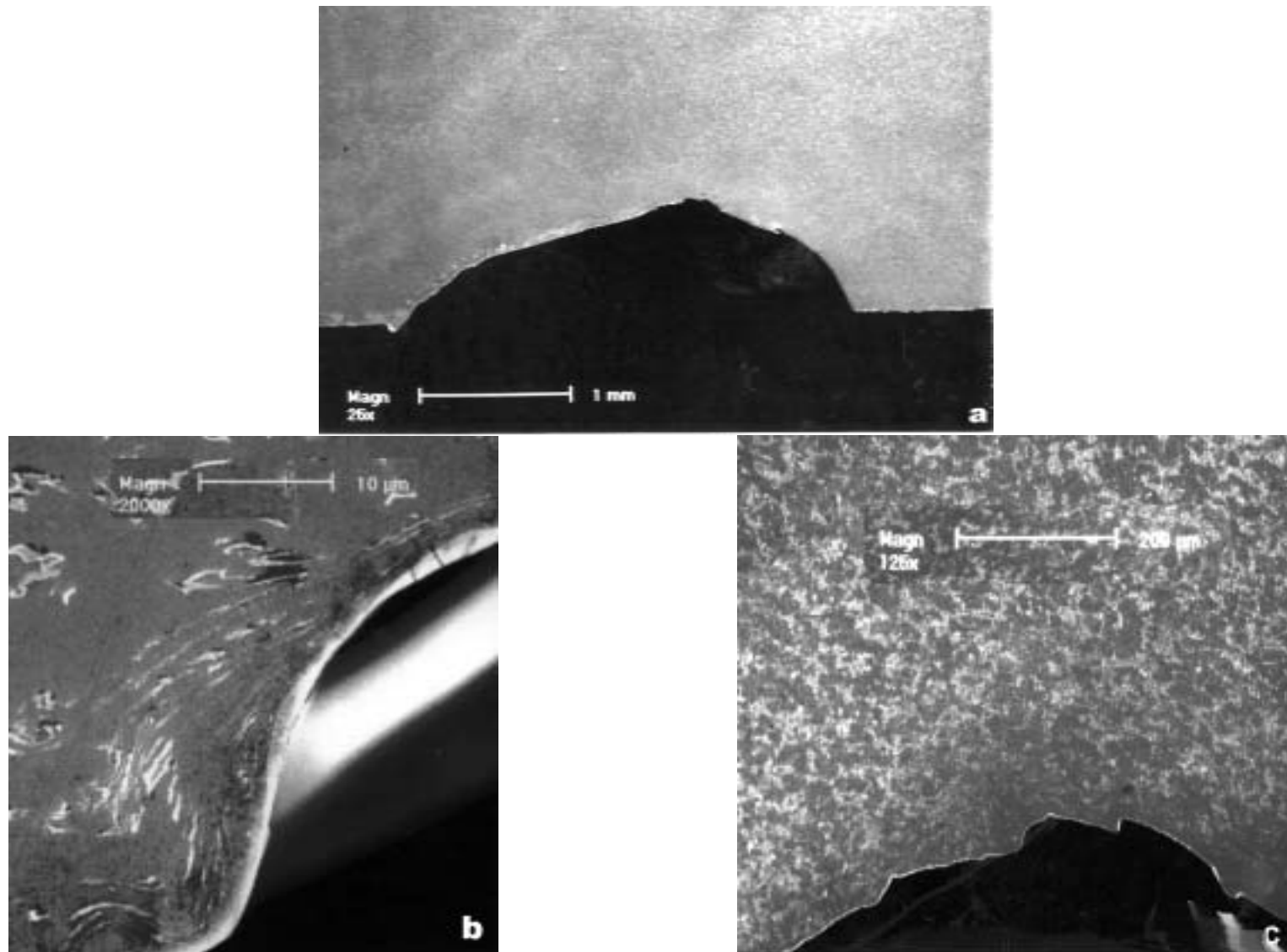


Figure 5A.12. C-shaped FOD from F-100 3rd stage fan blade showing: (a) sectioned view of 0.027-in.-deep notch with 0.065E.in.-root radius, (b) deformed microstructure on notch flank, and (c) magnified view of FOD showing irregular surface.

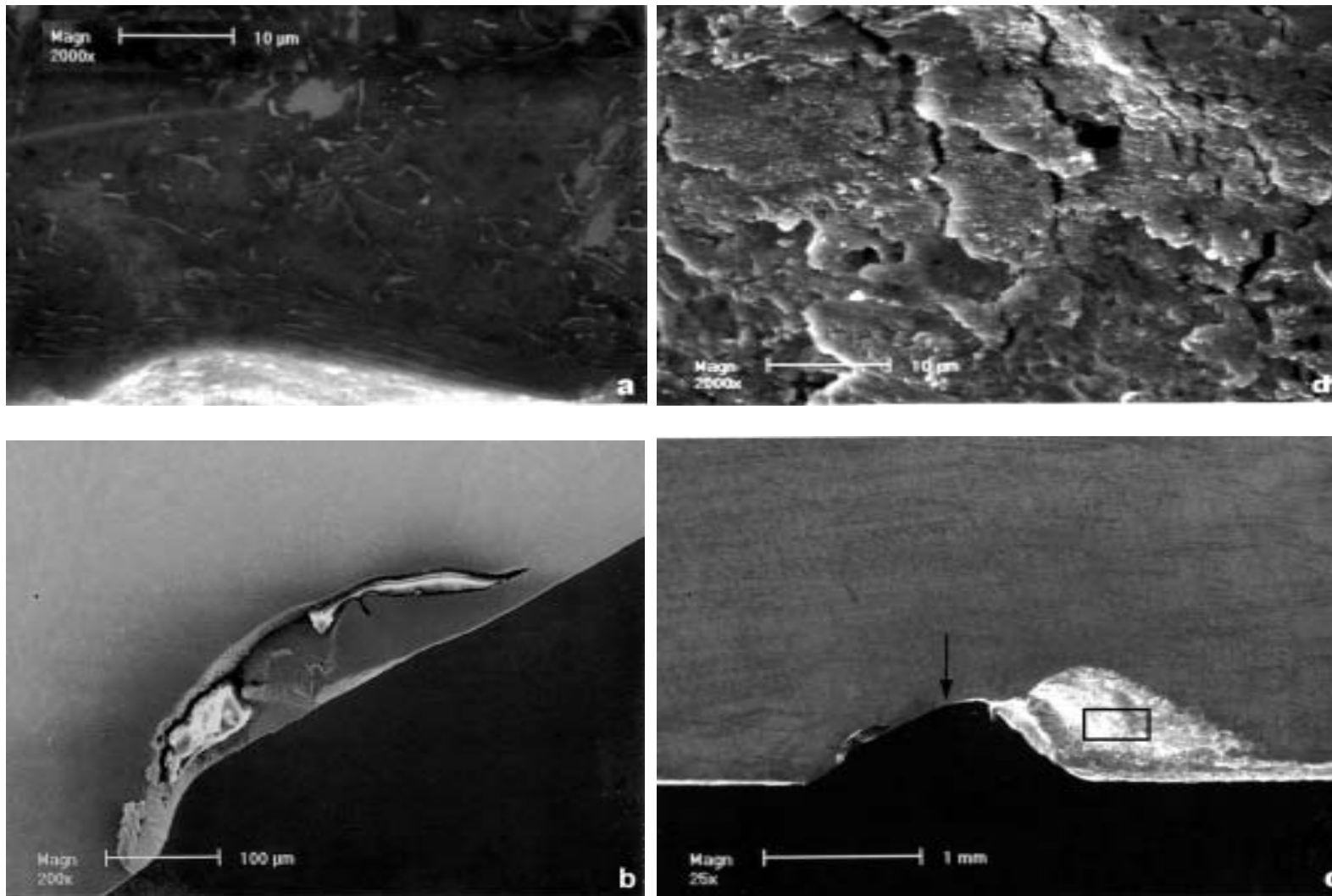


Figure 5A.13. C-shaped FOD from F-100 3rd stage fan blade showing: (a) deformed microstructure along notch flank, (b) partially spalled region on left flank, (c) micro crack at notch root (indicated by arrow), and larger spalled region on right flank, (d) brittle-looking fracture surface of spalled region highlighted in (c).

SUMMARY

A limited number of F100 FOD'ed blades were obtained for in-depth geometric and metallurgical evaluations. Several blades had FOD damage that illustrated that tears or cracks can occur during a FOD event. The SwRI geometric findings on FOD depth and radius compared well to the larger population of in-service FOD found by P&W from a field survey. The two distributions (SwRI and P&W in-service) were of very similar form – both being of the lognormal or Weibull type. These results indicated that SwRI's sample population represents a typical sampling of the FOD likely to be found in service for F100 fan blades. The estimates of the elastic stress concentration factor (k_t) were based on FOD notch depth and radius and ranged from 2 to 10.

REFERENCES

1. S.J. Hudak, Jr., R.C. McClung, K.S. Chan, G.G. Chell, and D.L. Davidson, "High Cycle Fatigue of Turbine Engine Materials," Annual Technical Report, PRDA-HCF Program, January 15, 1998.
2. F.K. Haake, G.C. Salivar, E.H. Hindle, J.W. Fischer, and C.G. Annis, Jr., "Threshold Fatigue Crack Growth Behavior," U.S. Air Force Technical Report WRDC-TR-89-4085, Wright-Patterson AFB, OH, 1989.
3. J.M. Larsen, B.D. Worth, C.G. Annis, Jr. and F.K. Haake, "An Assessment of the Role of Near-Threshold Crack Growth in High-Cycle Fatigue Life Predictions of Aerospace Titanium Alloys Under Turbine Engine Spectra," *International Journal of Fracture*, Vol. 80, 1996, pp. 237-255.
4. R.E. Peterson, "Stress Concentration Factors," John Wiley and Sons, New York, 1974.

Appendix 5B

EVALUATION OF SIMULATED FOREIGN OBJECT DAMAGE IN Ti-6Al-4V FAN BLADES

**Tom Dunyak
Robert McClain
Robert VanStone**



General Electric Aircraft Engines

**Submitted
31 August 1999**

ABSTRACT

This Appendix describes the GEAE activities under Air Force sponsorship to develop more effective techniques to evaluate and understand Foreign Object Damage (FOD) in titanium alloy Ti-6-4 airfoils. The paper will describe the types of damage to simulate, the current testing approaches, and the stress states in the blades the tests need to represent. A four point bend flex specimen will be presented which accurately represents these steady-state and vibratory stresses including the stress gradients near the leading edge of the blade. Stress states in actual fan blades and the flex specimen will be compared. A method to simulate FOD using a solenoid gun will be described, and micrographs of the damage zones will be evaluated. A detailed description of the test fixturing and preliminary results will also be presented.

Key Words: Gas Turbine Engines, Fan Blades, Foreign Object Damage, FOD, HCF.

Abbreviated Article Title: FOD Simulation.

INTRODUCTION

One of the key design drivers for fan blades in gas turbine engines is damage tolerance including foreign object damage (FOD). FOD at the leading edge of airfoils and the related HCF problem is highly complex due to:

- The random nature and type of foreign objects and the way that they interact with the leading edge of airfoils
- The overall geometry of advanced military fan and compressor airfoils with their twist and camber
- The variation of geometry along the leading edge of the airfoil
- The complicated stress states, particularly in vibratory loading, are very difficult to analyze

Due to the complexity of the problem, traditional FOD evaluation involves shaker table or siren tests with simulated FOD. However, these tests are limited to fully reversed loadings ($R = -1$) and require full scale blades. Recent work sponsored by the Air Force is developing improved test methods and mechanistic based analytical models to investigate the behavior and life of FOD'ed fan blades. These test methods and analytical models will supplement the siren tests and provide a more rigorous evaluation of FOD effects. In

addition, the test methods will enable the designer to evaluate FOD effects over the full range of loading and leading edge geometries without fabricating full scale blades. A cornerstone of this effort is the ability to accurately simulate blade stresses and FOD damage in the laboratory, and much progress has been made in these areas.

The objectives of this paper are to describe typical field issues associated with FOD and present approaches to simulate these issues with relative simple laboratory tests. The remainder of this paper is divided into six additional sections. The next section contains the results of an HCF analysis of an actual fan blade, and the third section describes a specimen design which accurately simulates the stresses. The fourth section discusses the random nature of FOD in the field, and the following section describes a method to simulate this damage in the laboratory. The sixth section describes the test configuration and preliminary results from the test specimen with simulated FOD. The final section provides a short summary. Hopefully, this information will help other investigators bypass much of the development efforts we went through and focus on the critical issues associated with FOD in aircraft engines.

GEOMETRY AND LOADING OF AIRFOILS

The typical fan blade in a large gas turbine engine is a complex airfoil with variable camber and twist (Figure 5B.1). In many cases, larger blades also contain mid-span shrouds as shown in Figure 5B.1 to enhance the stability of the blade. The stresses at the leading edge are the result of complex loads and moments which vary along the length of the blade due to inertial forces, pressure loads and geometry variations. These loads and moments are indicated schematically in Figure 5B.2. The dominant LCF loads which control the mean stresses are the axial load (F_z) and flexural moment. The dominant HCF loading which produces the vibratory stress amplitude on the leading edge is the first flex mode which is the bending vibration about the airfoil's minimum moment of inertia. As we move along the length of the blade from the root region to the tip region, the relative magnitude of the LCF loadings to the HCF loadings vary. In the root and mid-section regions, the leading edges are subject to relatively large mean stresses which significantly decrease towards the tip regions. Therefore, R-ratio effects from $R = 0.8$ (tension-tension) to $R = -1$ (fully reversed tension-compression) need to be considered. The leading edge

regions also see stress gradients due to the camber of the blade, and these gradients may be critical to accurately simulating blade stresses in a test specimen.

Figure 5B.3 presents a normalized stress distribution from a vibratory analysis of a typical fan blade. Due to the change in camber along the length of this blade, the critical stresses are located in the mid-section or lower panel of the blade. Figure 5B.4 contains a detailed contour plot of the leading edge stresses. Notice the relatively large stress gradient across the first 6.4 mm (0.25 inches) of the leading edge.

TEST SPECIMEN DESIGN

Over the past year, GEAE designed a test specimen (Figure 5B.5) which can be used to simulate leading edge stresses. The artificial leading edges are far from the neutral axis so the leading edges will be highly stressed. The specimen is loaded in four point bending with a 101.6 mm (4.0 inches) support span and a 50.8 mm (2.0 inches) loading span. This geometry was selected because it could be easily cut from flat forgings, it could have variable leading edge geometries, it could be rather easily loaded to various R-ratios or with LCF/HCF mission cycles, and the stress gradient in the leading edge could be adjusted by varying the overall height of the specimen. The initial effort focused on the sharp leading edge geometry shown in Figure 5B.5; however, blunter geometries with leading edge diameters on the order of 0.76 mm (0.030 inches) as opposed to 0.25 mm (0.010 inches) are also of interest. These bracket the range of leading edges in GEAE airfoils and will have a significantly different response to FOD with the same level of energy.

An elastic stress analysis of this specimen was performed to compare the leading edge stresses of the blade to the specimen. Figure 5B.6 contains contour plots comparing these stresses. Notice the stress gradients from points A to B are very similar. If desired, we could have matched these gradients exactly by reducing the overall 5.08 mm (0.2 inches) height of the specimen.

Due to the geometry of the specimen, the location of the neutral axis is shifted towards the bottom of specimen that contains the simulated leading edge. As a result, the peak stress actually occurs on the top of the specimen since it is farther from the neutral axis. However, the stress concentration associated with the FOD damage should move

the high stress location to the leading edge of the specimen, and produce failures in the desired location. Several tests were also conducted on specimens with tension-tension loading ($R=0.5$) at the leading edge without FOD. Under this loading, the magnitude of the stresses on the top of the specimen would be higher than in the leading edge; however, the stresses on the top specimen would be in compression which are not as damaging. In all cases, the specimen failure originated from the tension stresses in the leading edge region further validating the suitability of this specimen design.

FOD IN ACTUAL BLADES

FOD damage in actual field blades is a very complex problem which eventually needs to be addressed from a probabilistic perspective. The impact energy and impact angle relative to the centerline of the blade is highly dependent on the composition of the object (hard versus soft), mass of the object, the velocity of the object, the velocity of the aircraft, and the rotational speed of the fan. Figure 5B.7 presents simple schematic diagrams of the types of FOD observed in field blades. In general, the velocity of the aircraft and blade is significantly higher than the velocity of the particle. Therefore, the foremost portion of the blade actually hits the particle and produces a gouge or dent in the leading edge. Based on typical takeoff and fan speeds, the impact can occur at speeds as high as 300 m/s (1000 ft/sec) and typically occurs at angles of 30 to 60° relative to the centerline of the blade.

The location and depth of FOD damage also widely varies. Table 5B.1 summarizes the results of detailed inspections of over 100 engines. The inner panel corresponds to the high stress region below the mid-span shroud in Figure 5B.3, and the outer panel is the region from the mid-span shroud to the tip. Notice, all but one of the FOD nicks are less than 0.76 mm (0.030 inches). A large percentage of the nicks also occur on the inner panel where the stresses are the highest and R-ratios are approximately 0.5. In many cases, fan blades with small FOD nicks are blended or reworked in the field and reliably placed back into service. Blending techniques and blend limits will not be discussed in this paper.

Historical data indicate that a blade with a severe tear where the FOD penetrates the thickness of the blade is more severe than a smaller nick or dent which does not.

Therefore, it is convenient to point to the large tears as being representative of the FOD of concern. In almost every case, this severe level of FOD would rather easily form a crack and propagate to failure under HCF loading if that tear were located at the axial position along the leading edge with high stresses. However, the real issue is would any of the smaller nicks shown in Table 5B.1 lead to nucleation and propagation in an HCF environment. Therefore, small FOD nicks on the order of 0.13 to 0.76 mm (0.005 to 0.030 inches) in depth at impact angles ranging from 30 to 60° are the greatest concern and should be the primary focus of FOD investigations. These investigations should also focus on R-ratios near 0.5 which occur in the maximum stress regions of the inner panel; however, some testing needs to be conducted at $R=-1$ which occurs in the tip regions and to help correlate the siren tests.

FOD SIMULATION

Several techniques were evaluated at GEAE to simulate FOD in airfoils or the leading edge specimen. The most promising technique uses a solenoid gun with a chisel point indenter. The solenoid gun provides a relative high velocity impact compared to other techniques like a pendulum, and it provides much better control and repeatability than ballistic impact methods. For the tests described in this paper, the chisel point had a 0.05 mm (0.002 inch) tip radius. However, the tip radius is easily modified if desired. Figure 5B.8 contains a picture of the solenoid gun set up to impact a test specimen.

All of the specimens were impacted at a 30° angle to the centerline of the edge region as shown in Figure 5B.9. Several specimens were FOD'ed for this investigation, and Figure 5B.10 presents a micrograph of a specimen with simulated FOD damage as viewed from the bottom of the specimen. Figure 5B.11 contains a micrograph of a polished section of the damage zone. Notice, the radius of the damage zone is very sharp and should produce a high stress concentration factor (K_t). In addition, the grain structure around the damage zone does not show any indications of shear banding. A small study was conducted to evaluate other tip radii on the indenter. In all cases, the radii in the damage zone modeled the indenter radii, and we did not find any indication of shear banding under any conditions.

TEST SYSTEM AND PRELIMINARY RESULTS

HCF testing of this specimen is slightly more difficult than standard tension-tension flex fatigue testing. Tests need to be conducted at R-ratios from -1.0 to 0.8. $R = -1$ corresponds to the stress state during siren blade tests and near the tip of the blade. $R = 0.5$ represents the higher R ratios experienced in the lower part of leading edge during service, and $R = 0.8$ is more representative of the stress ratios near the root of the blade. To perform the $R = -1$ loading, a bending fixture must be capable of transferring loads through the zero point without large amounts of hysteresis. Figure 5B.12 shows a photograph of the final test configuration. In order to minimize the hysteresis in the test system, steel load pins were seated in slightly oversized machined slots which allowed the pins to roll with the deflection of the specimen. Figure 5B.13 presents load-strain traces from a strain-gaged specimen which indicates virtually no hysteresis in the loops. Subsequent tests also demonstrated no backlash in the system as the load changed between compression and tension. We also used an electric potential drop (EPD) system to monitor the crack nucleation and growth in this effort.

Once the test fixturing and instrumentation were deemed acceptable, several tests were conducted on forged Ti-6-4 specimens to validate the test method. The results of one of these tests, Specimen 03, will be discussed in detail. These results are typical of the other tests. The depth of the FOD nick in Specimen 03 was measured at 0.74 mm (0.029 inches) as shown in Figure 5B.14. The specimen was then loaded at 1156 N (260 lbf) maximum load with $R = -1$. This load produced a 175 Mpa (25.4 Ksi) nominal stress on the bottom of the specimen. The test was conducted until the crack propagated all the way across the leading edge region of the specimen. Figure 5B.15 presents the EPD results for this specimen where U_0 is the initial electric potential between two probes that span the damage zone, U is the potential after cycling, and U/U_0 represents the relative change in electric potential which can be correlated to crack nucleation or length. In this case, the specimen was removed at $U/U_0 = 1.03, 1.3, \text{ and } 1.8$ to heat tint the specimen and mark the crack locations. Figure 5B.16 summarizes the heat tint results.

Preliminary evaluation of these results indicates several key findings. First, the nominal stress level of 175 Mpa (25.4 Ksi) for failure indicated the FOD produced a local fatigue stress concentration factor (K_f) in the range of 4 based on a correlation with smooth

bar fatigue data from the same set of forgings. Second the crack initiated at approximately 79,000 cycles and propagated half way across the leading edge region by 180,000 cycles. Therefore, the actual time to failure is relatively small in an HCF environment once a crack initiates, and blade life may be controlled by nucleation as opposed to propagation. Third, the crack initiated at the lower corner of the initial damage zone and propagated in an elliptical pattern from the nucleation site. Once the crack penetrated the top surface of the leading edge region, the crack appears to be evolving from an elliptical crack into a straight through crack. At this point, additional data needs to be generated before the impact of these types of findings on the analytical models can be assessed.

SUMMARY

FOD is a critical issue in gas turbine engines. Currently, siren tests on full scale blades are conducted to assess the damage tolerance of blades subjected to simulated FOD. These tests are costly and limited in scope. Therefore, improved methods need to be developed to evaluate and predict the effect of FOD.

This paper attempted to address several of the key issues associated with FOD in fan blades. Based on field data and finite element results of actual blades, FOD nicks on the order of 0.13 to 0.76 mm (0.005 to 0.030 inches) in depth subjected to HCF loadings with $R = 0.5$ are the primary concern. However, R ratios from -1.0 to 0.8 are also important. Although FOD is random in nature, impact angles of 30 to 60° to the leading edge are expected.

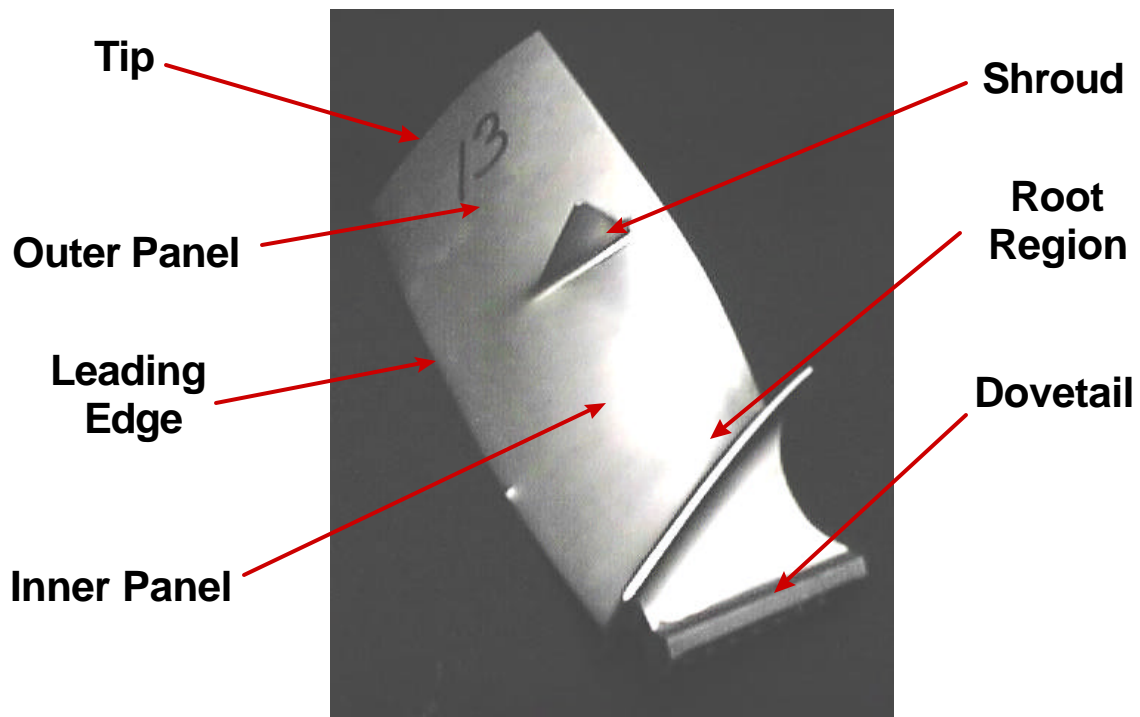
In this effort, a flexure specimen was designed which simulates the leading edge geometries and stress gradients in fan blades. In addition, a solenoid gun technique was demonstrated to simulate FOD. Test fixturing and preliminary test results were also discussed. Overall, this paper describes a small step in evaluating, understanding, and predicting the effect of FOD in fan blades. However, this information may help future investigators focus on the critical problems and bypass much of the development efforts we conducted.

ACKNOWLEDGEMENTS

The authors would like to acknowledge the US Air Force for sponsoring the majority of this effort through the University of Dayton Research Institute (UDRI) under Subcontract RI-40096X.

Table 5B.1
Results of a Detailed Investigation of FOD in Over 100 Engines
Showing Depth and Location of Damage.

<u>Depth of Damage</u>	<u>Number of FOD Nicks on the Outer Panel</u>	<u>Number of FOD Nicks on the Inner Panel</u>
0.15 to 0.25 mm (0.006 to 0.010 In)	27	7
0.25 to 0.50 mm (0.010 to 0.020 In)	7	5
0.50 to 0.75 mm (0.020 to 0.030 In)	12	0
Over 0.75 mm (0.030 In)	0	1
Total	46	13



5B. 1. Picture of a typical fan blade from a large gas turbine engine.

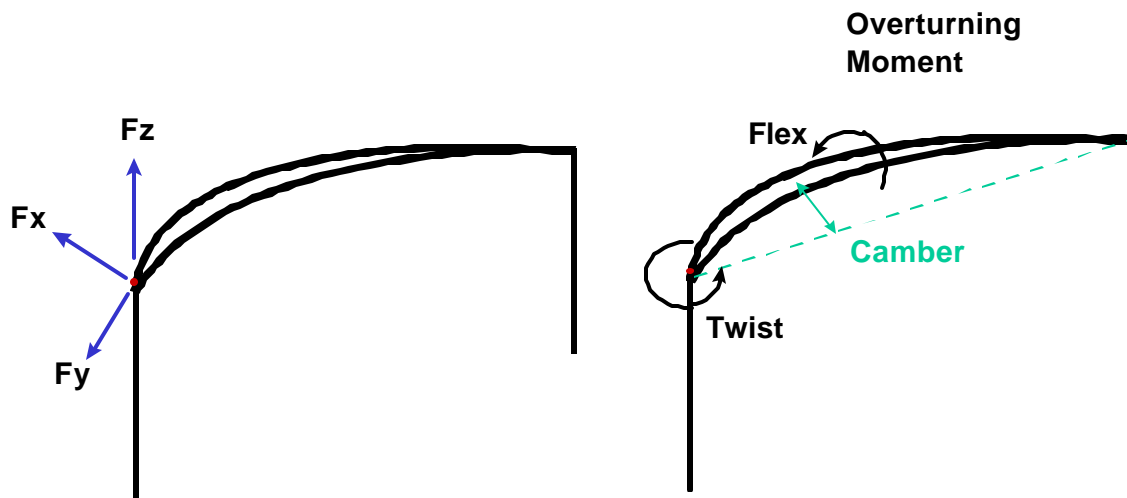


Figure 5B.2. Free body diagram of the blade loads.

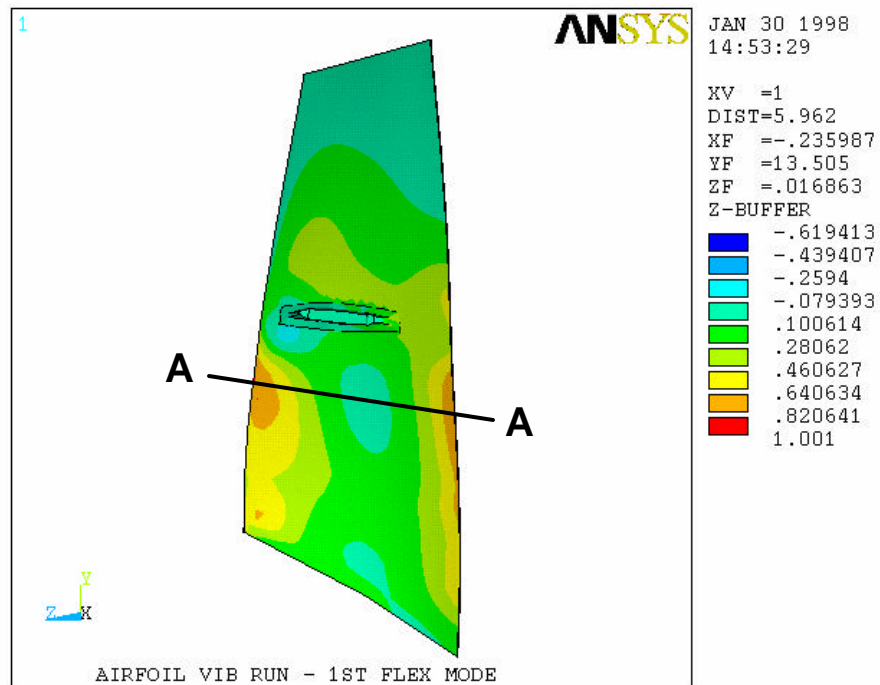


Figure 5B.3. Normalized stress distribution from a vibratory analysis of a typical fan blade.

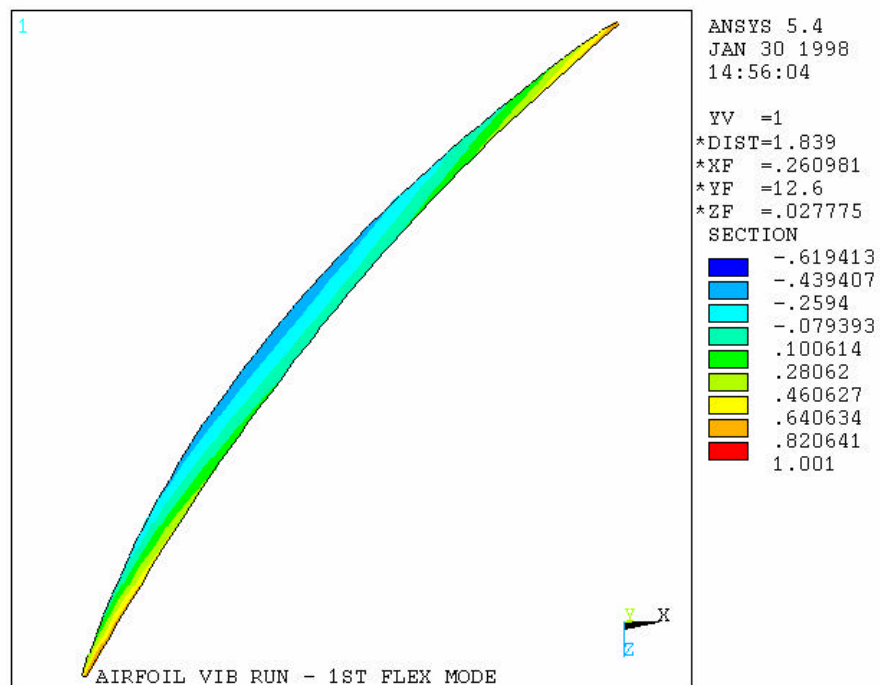


Figure 5B.4. Normalized stress distribution across Section A-A.

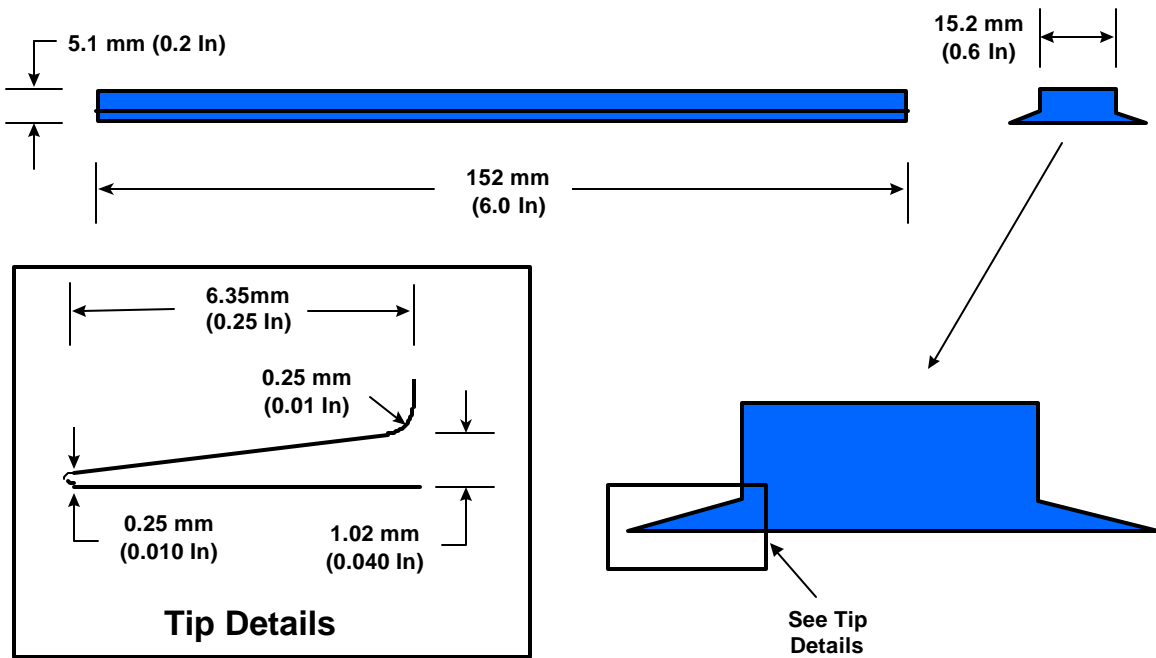


Figure 5B.5. The FOD specimen with a sharp leading edge region.

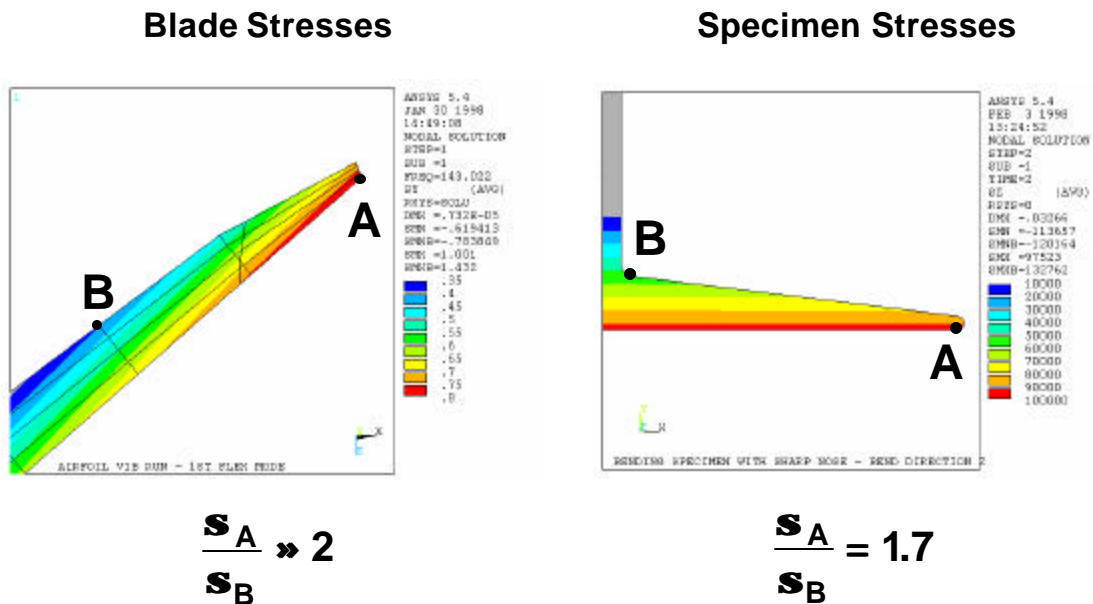


Figure 5B.6. Comparison of local leading edge stresses in the blade and the test specimen.

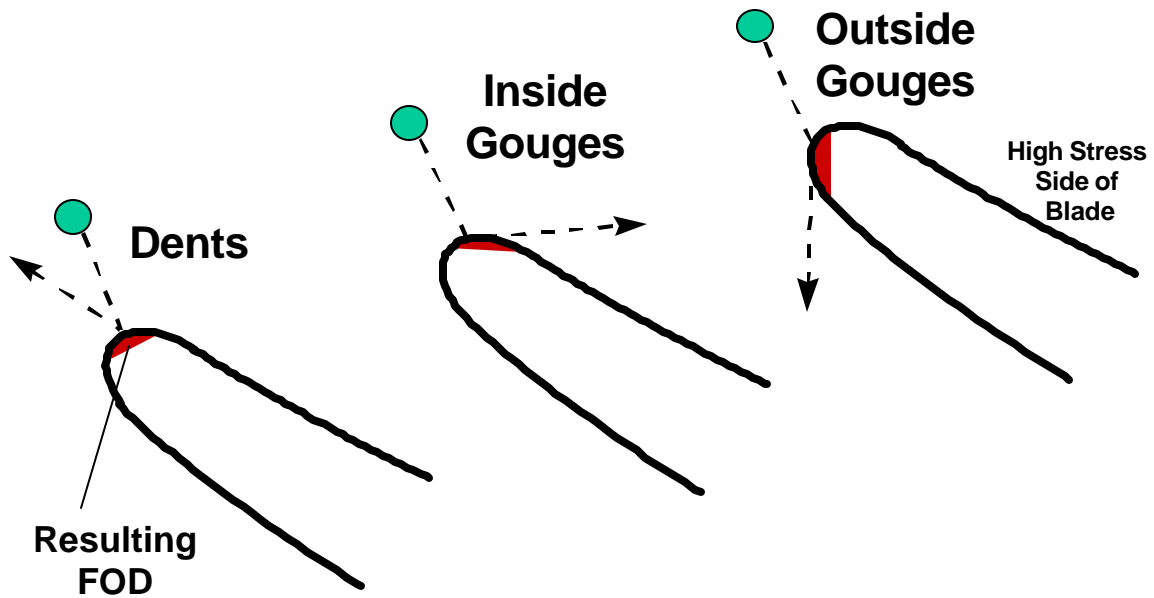


Figure 5B.7. Types of FOD observed in field blades.

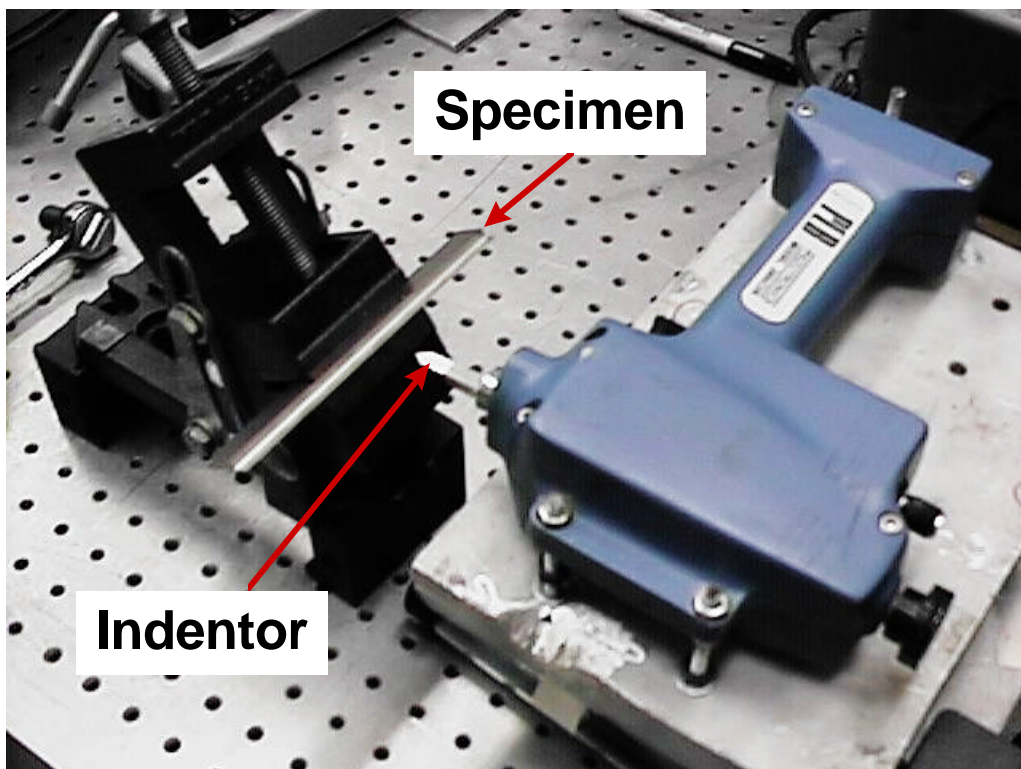


Figure 5B.8. Picture of the solenoid gun set up to FOD a specimen.

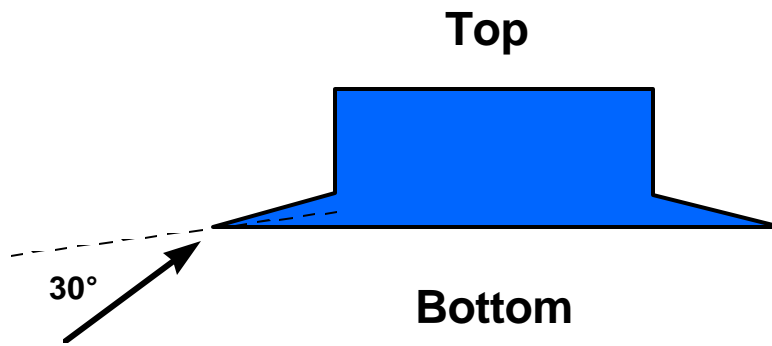


Figure 5B.9. Impact angle of FOD nicks in this investigation.

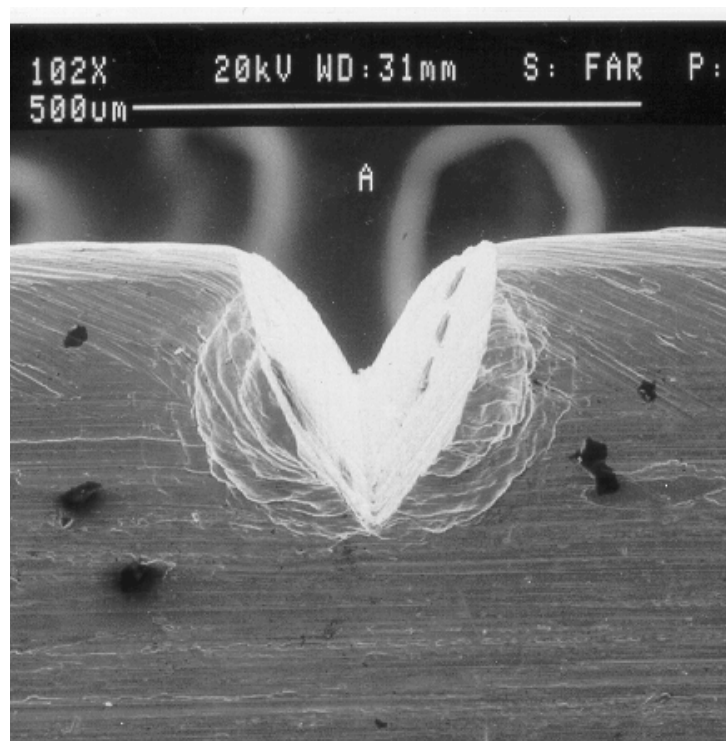


Figure 5B.10. Micrograph of simulated FOD using the solenoid gun at a 30° impact angle.

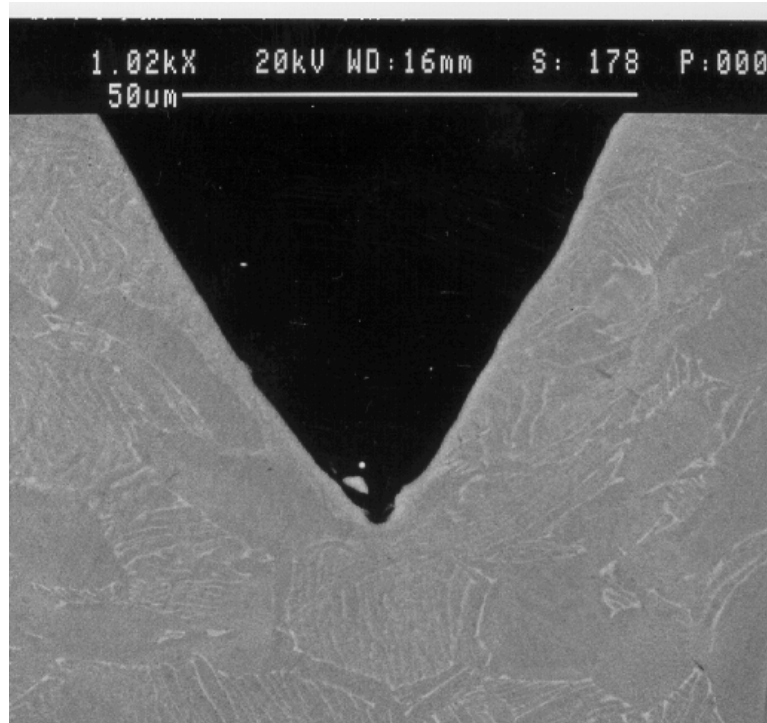


Figure 5B.11. Micrograph of a polished section of simulated FOD using the solenoid gun.

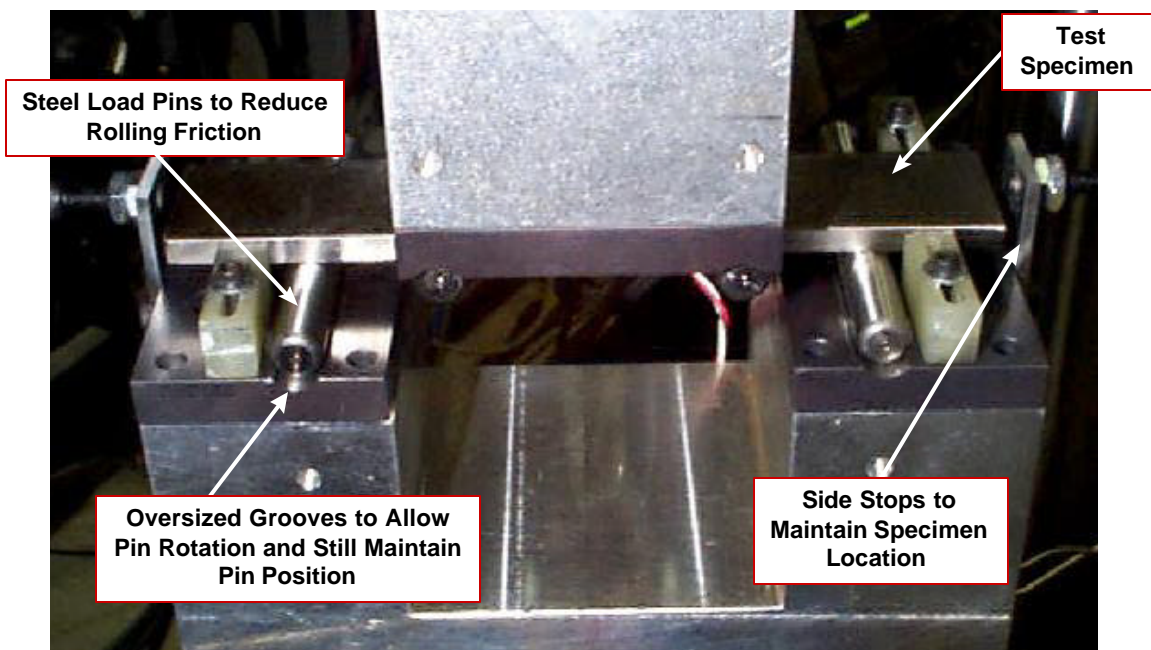


Figure 5B.12. Test fixture for the FOD specimen. Notice, portions of the fixturing which enable reverse loading have been removed to expose the loading pins and specimen.

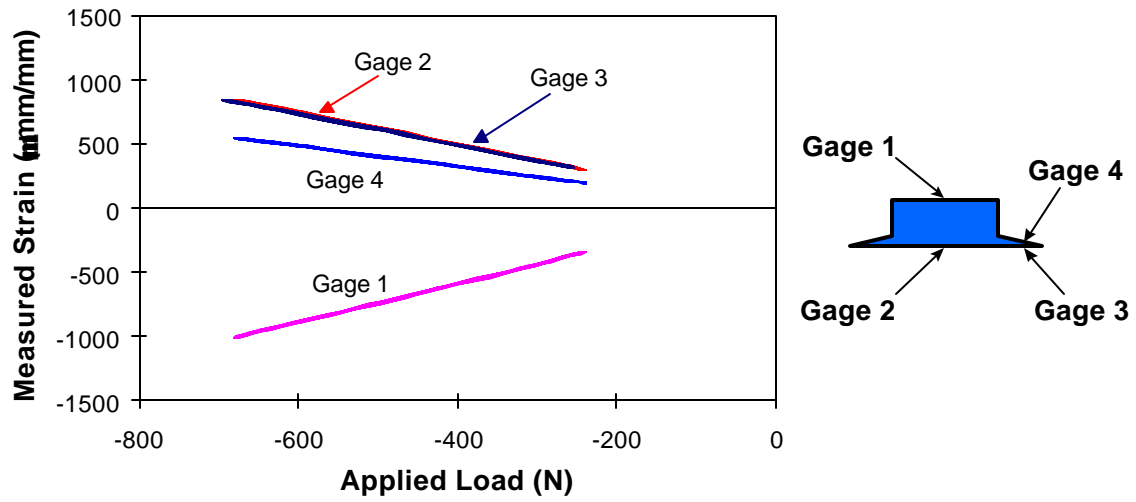


Figure 5B.13. Hysteresis loops generated using the FOD specimen fixturing.

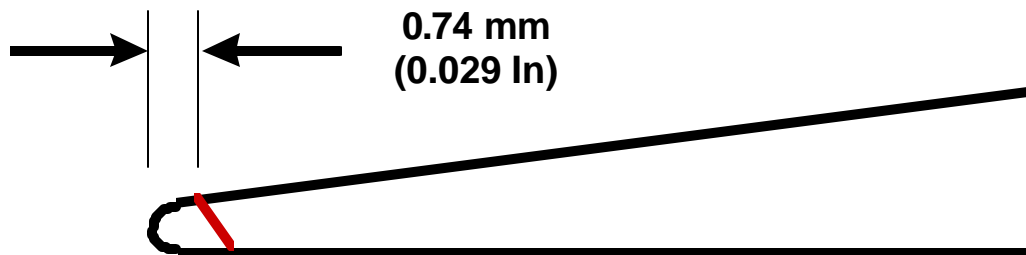


Figure 5B.14. Depth of the initial FOD nick in Specimen 03.

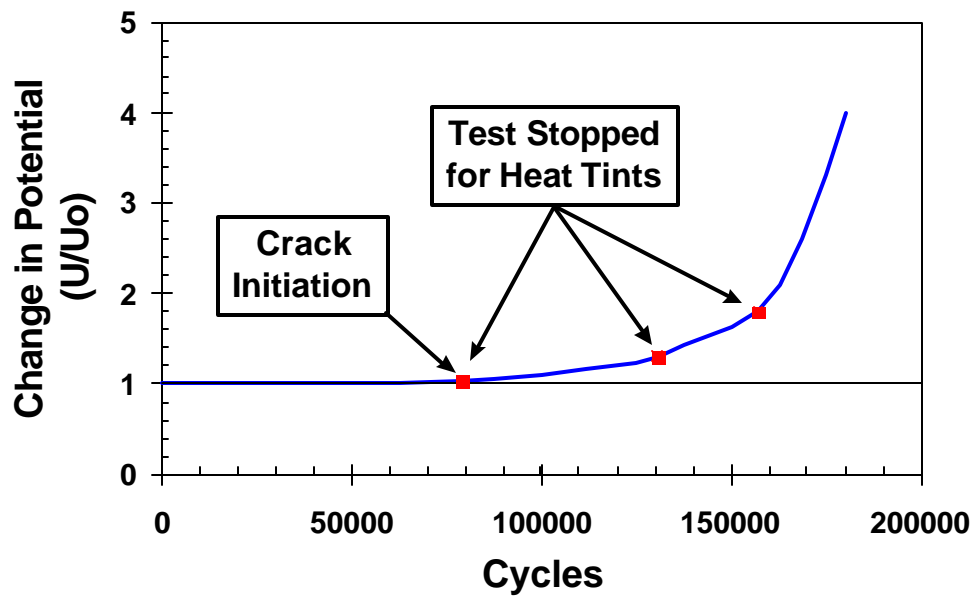


Figure 5B.15. EPD results from Specimen 03.

<u>Tint</u>	<u>U / U_o</u>	<u>Cycles</u>	<u>Conditions</u>
1	1.0347	79039	400°C / 5 Hrs
2	1.3023	130424	360°C / 3 Hrs
3	1.8011	157101	300°C / 3 Hrs

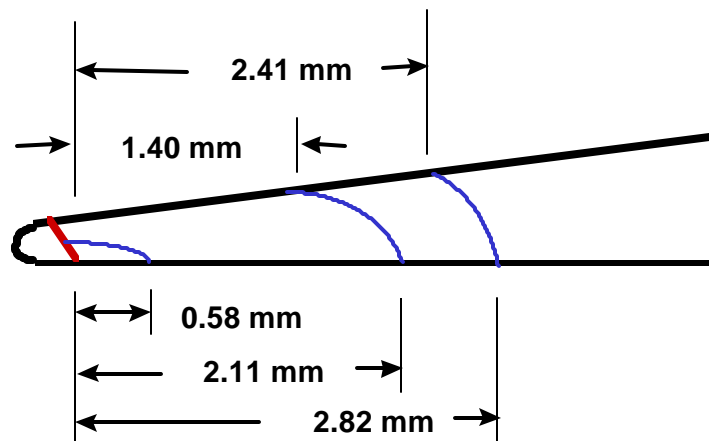


Figure 5B.16. Crack front locations as marked by the heat tints.

Appendix 5C

EVALUATION OF SIMULATED FOREIGN OBJECT DAMAGE IN Ti-6-4 FAN BLADES AND ALL TEST DATA RESULTING FROM GEAE PORTION OF PROGRAM

Tom Dunyak



General Electric Aircraft Engines

**Submitted
31 August 1999**

This appendix supplements the summary information in the final report for the FOD testing program using the winged specimen. Blade geometries and stresses are described. Detailed descriptions of the specimen geometries, specimen preparation procedures, and test fixturing are provided. The final section contains detailed test results for each specimen.

GEOMETRY AND LOADING OF AIRFOILS

The typical fan blade in a large gas turbine engine is a complex airfoil with variable camber and twist (Figure 5C.1). In many cases, larger blades also contain mid-span shrouds as shown in Figure 5C.1 to enhance the stability of the blade. The stresses at the leading edge are the result of complex loads and moments that vary along the length of the blade due to inertial forces, pressure loads and geometry variations. These loads and moments are indicated schematically in Figure 5C.2. The dominant LCF loads that control the mean stresses are the axial load (F_z) and flexural moment. The dominant HCF loading which produces the vibratory stress amplitude on the leading edge is the first flex mode which is the bending vibration about the airfoil's minimum moment of inertia. As we move along the length of the blade from the root region to the tip region, the ratio of the magnitudes between LCF and HCF loadings changes. In the root and mid-section regions, the leading edges are subject to relatively large mean stresses that significantly decrease towards the tip regions. Therefore, R-ratio effects from $R = 0.8$ (tension-tension) to $R = -1$ (fully reversed tension-compression) need to be considered. The leading edge regions also see stress gradients due to the camber of the blade, and these gradients may be critical to accurately simulating blade stresses in a test specimen.

Figure 5C.3 presents a normalized stress distribution from a vibratory analysis of a typical fan blade. Due to the change in camber along the length of this blade, the critical stresses are located in the mid-section or lower panel of the blade. Figure 5C.4 contains a detailed contour plot of the leading edge stresses. Notice the relatively large stress gradient across the first 0.25 inches of the leading edge.

TEST SPECIMEN DESIGN AND MACHINING

GEAE designed two test specimens (Figure 5C.5) which can be used to simulate leading edge stresses. The artificial leading edges are far from the neutral axis so the leading edges will be highly stressed. The specimen is loaded in four point bending with a 4.0 inches support span and a 2.0 inches loading span. This specimen can be easily cut from flat forgings. It can be loaded to various R-ratios or with LCF/HCF mission cycles, and the stress gradient in the leading edge could be adjusted by varying the overall height of the specimen.

An elastic stress analysis of this specimen was performed to compare the leading edge stresses of the blade to the specimen. Figure 5C.6 contains contour plots comparing these stresses. Notice the stress gradients from points A to B are very similar. If desired, we could have matched these gradients exactly by reducing the overall 0.2 inches height of the specimen.

Due to the geometry of the specimen, the location of the neutral axis is shifted towards the bottom of specimen that contains the simulated leading edge. As a result, the peak stress actually occurs on the top of the specimen since it is farther from the neutral axis. However, the stress concentration associated with the FOD damage should move the high stress location to the leading edge of the specimen, and produce failures in the desired location. Several tests were also conducted on specimens with tension-tension loading ($R=0.5$) at the leading edge without FOD. Under this loading, the magnitude of the stresses on the top of the specimen would be higher than in the leading edge; however, the stresses on the top of the specimen would be in compression which are not as damaging. In all cases, the specimen failure originated from the tension stresses in the leading edge region further validating the suitability of this specimen design.

Approximately 80 specimens were machined by GE and P&W according to Figure 5C.5. The GE specimens were all machined at Cincinnati Testing Laboratories (CTL), stress relieved at GEAE, and then chem-milled at Lambda Research to produce a stress free surface. The stress relief cycle consisted of a 1300°F exposure for 1 hour in vacuum. The specimens were wrapped in a tantalum foil during the stress relief cycle to help prevent alpha case formation. Go-by specimens were fabricated with each lot

of material and then metallurgically mounted to confirm an alpha case layer did not form. Several specimens contained machined notches. Figures 5C.7 and 5C.8 present the 90° notch dimensions in the sharp LE specimens and the 60° notch dimensions in the blunt LE specimens.

The P&W specimens were also machined at CTL and stress relieved at GEAE. The sharp LE specimens from forgings 54 and 189 were chem-milled at Lambda Research; whereas, the blunt LE specimens from forging 86 were not chem-milled and were tested in the stress-relieved condition. As a result, the specimens from forging 86 were slightly oversized since the chem-milling process removes 0.001 to 0.002 inches of material during the process. These specimens required a higher power setting on the solenoid gun than the chem-milled specimens to produce an equivalent notch depth.

FOD SIMULATION

Several techniques were considered to simulate FOD in airfoils or the leading edge specimen including ballistic impacts, pendulum methods, servo-hydraulic techniques, and a solenoid gun. Ballistic and solenoid gun techniques were used to FOD the winged specimens. The solenoid gun provides a relative high velocity impact compared to other techniques like a pendulum, and it provides much better control and repeatability than ballistic impact methods. In this program, the solenoid gun had a chisel point indenter with either a 0.005 inches or 0.025 inches tip radius. Figure 5C.9 contains a picture of the solenoid gun set up to impact a test specimen.

Most of the specimens were impacted at a 30° angle relative to the centerline of the leading edge region as shown in Figures 5C.10a and 5C.10b. FOD depths were measured relative to the bottom face of the specimen (Figure 5C.10c). Figure 5C.11 contains a micrograph of a polished section of a damage zone resulting from an impact with a 0.005 inches tip radius. Notice the radius of the damage zone mimics the tip radius. In addition, the grain structure around the damage zone does not show any indications of shear banding. A small study was conducted to evaluate other tip radii on the indenter. In all cases, the radii in the damage zone modeled the indenter radii, and we did not find any indication of shear banding under any conditions.

FLEXURE TEST SYSTEM

HCF testing of this specimen is slightly more difficult than standard tension-tension flex fatigue testing. To perform the $R=-1$ loading, a bending fixture must be capable of transferring loads through the zero point without large amounts of hysteresis. Figure 5C.12 shows a photograph of the final test configuration. In order to minimize the hysteresis in the test system, steel load pins were seated in slightly over-sized machined slots that allowed the pins to roll with the deflection of the specimen. Figure 5C.13 presents load-strain traces from a strain-gaged specimen which indicates virtually no hysteresis in the loops. Subsequent tests also demonstrated no backlash in the system as the load changed between compression and tension. We also used an electric potential drop (EPD) system to monitor the crack nucleation and growth on several specimens.

FOD TEST RESULTS

Table 5C.1 summarizes the test results for 53 of the specimens. The remaining specimens were used for test method development, resulted in voided tests, or were not tested. Westmoreland Mechanical Testing and Research conducted all of the testing, and all testing was performed at room temperature. Columns 8 and 9 contain the measured notch depths. “A” and “B” are listed for the specimens which contained FOD impacts on both sides of the specimens. Notice notch depths for the 30° ballistic specimens are based on a 0° measurement as opposed to 33° measurement. Column 11 lists the type of EPD monitoring used in the test. Welded EPD leads attached at GE are specified at “Weld-A”, and P&W welded leads are “Weld-B”. Based on this data EPD monitoring appears to affect the results and need to be further investigated.

Maximum stresses and stress ranges were calculated from the applied loads based on linear elastic finite element analyses of the specimens. The sharp LE specimen has a multiplier of 0.09504 to convert from load (lbs.) to stress (Ksi), and the blunt LE specimen has a 0.09272 multiplier. Stress ranges were calculated according to

$$S_{rng} = S_{max} (1 - R),$$

and interpolated stress ranges (\mathbf{s}_i) in column 21 were determined using the following equation

$$\mathbf{s}_i = \mathbf{s}_{rng,j} + \frac{N_f}{10^6} (\mathbf{s}_{rng,f} - \mathbf{s}_{rng,j})$$

where $\mathbf{s}_{rng,j}$ is the stress range at the previous load step, N_f is the cycles to failure at the final load step, and $\mathbf{s}_{rng,f}$ is the stress range at the final load step.

Column 20 lists the cycles to failure. EPD monitoring also provides cycles to nucleation where we defined cycles to nucleation as the cycle count to produce a 0.7% change in EPD voltage. The difference between nucleation and failure is approximately 200,000 cycles which corresponds to a 2% change in interpolated stress range for a 10^6 step test specimen. This difference is negligible relative to the scatter in data between samples.

Detailed specimen descriptions, FOD impact parameters, test conditions, test results, and micrographs for each specimen are provided on the following pages. The hardcopy report also contains load versus cycles plots, position versus cycles plots, EPD results (U/Uo plots), and SEM micrographs of the failed specimens. In general, load versus cycle and position versus cycle plots were not available for the specimens with EPD monitoring.

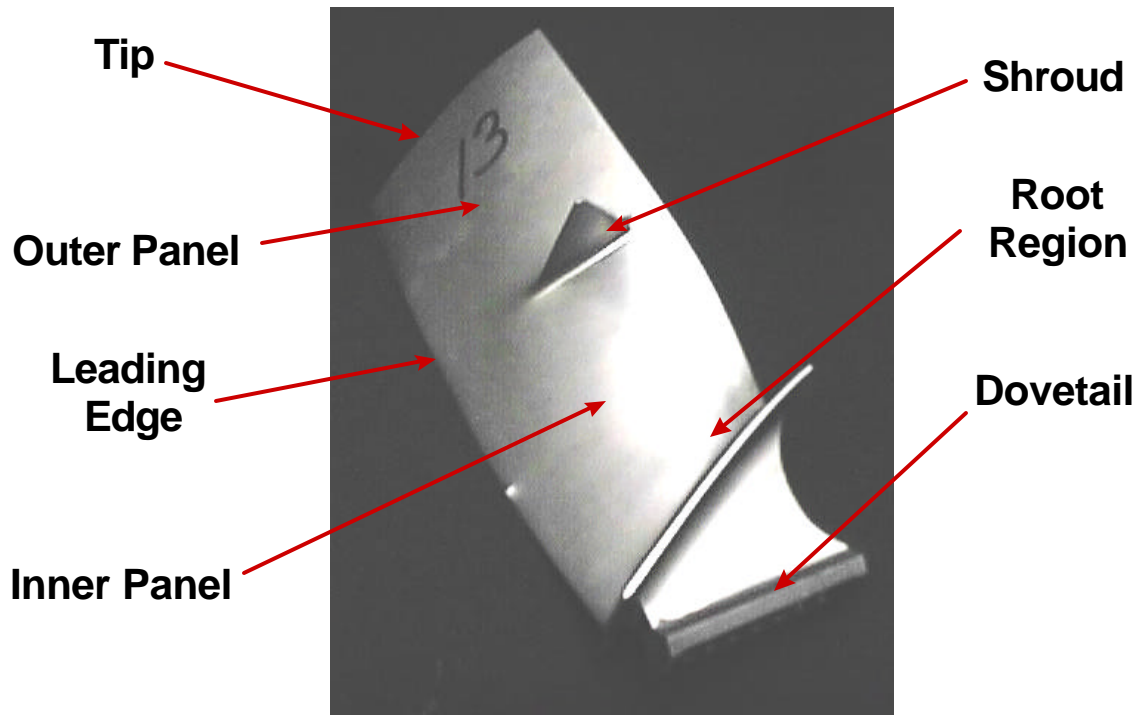


Figure 5C.1. Picture of a Typical Fan Blade from a Large Gas Turbine Engine.

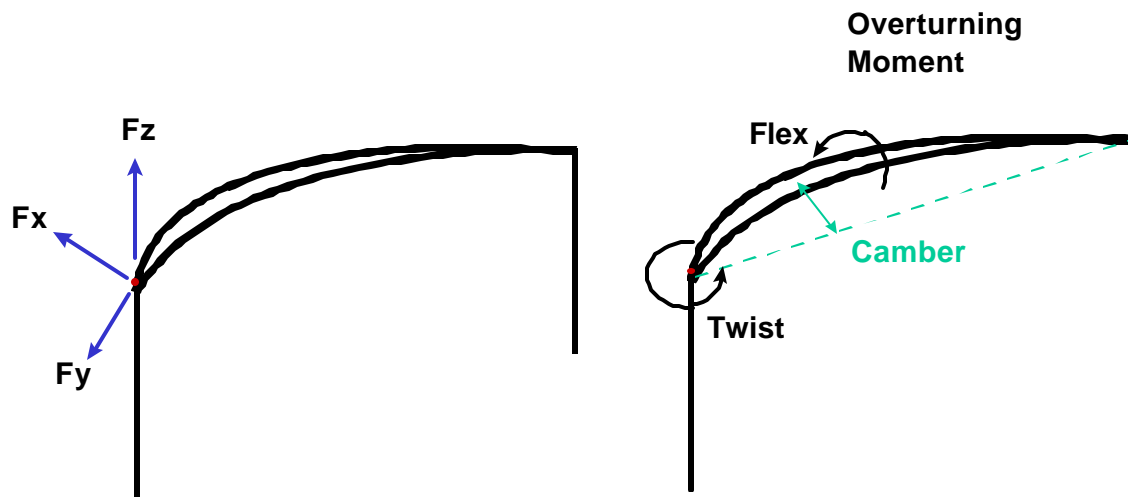


Figure 5C.2. Free Body Diagram of the Blade Loads.

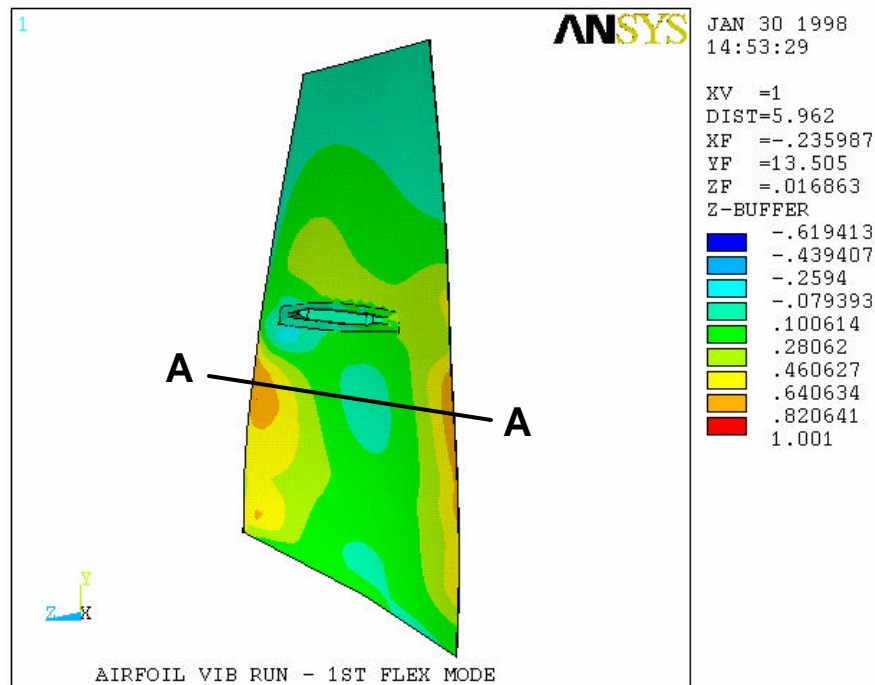


Figure 5C.3. Normalized Stress Distribution from a Vibratory Analysis of a Typical Fan Blade.

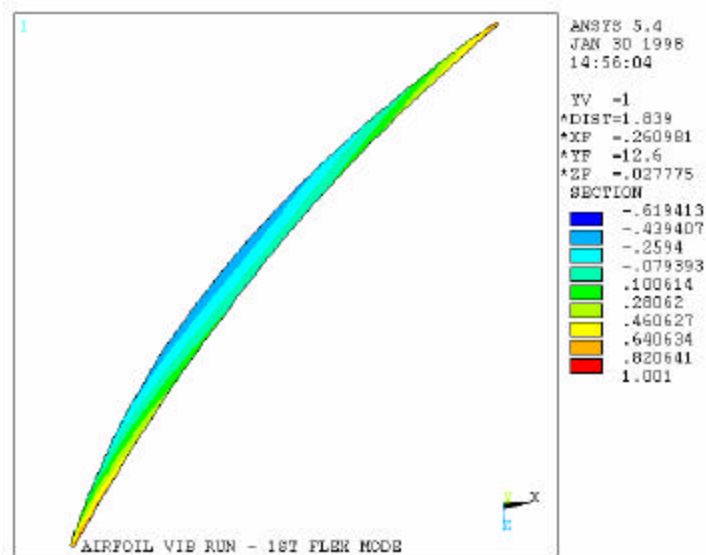


Figure 5C.4. Normalized Stress Distribution across Section A-A.

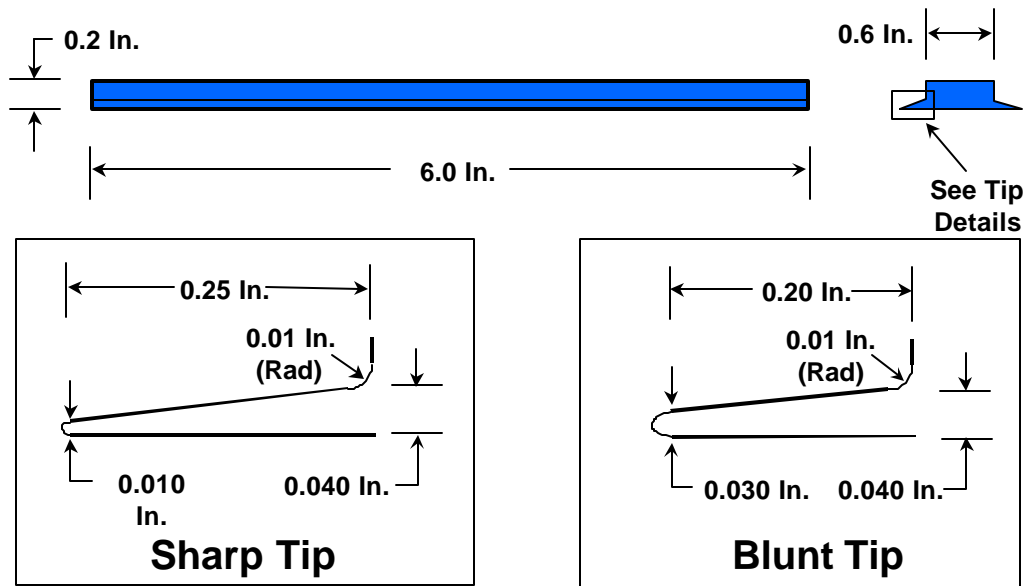
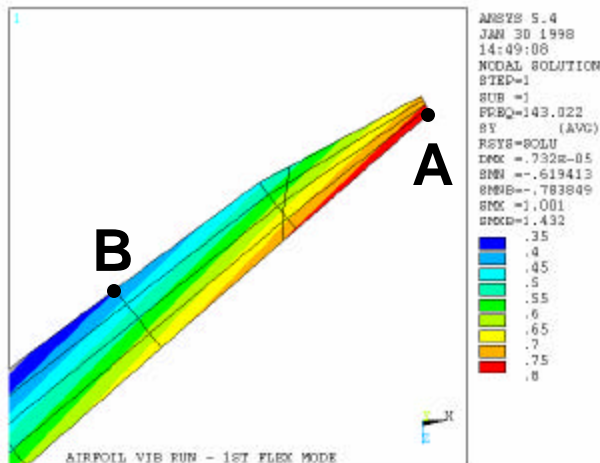


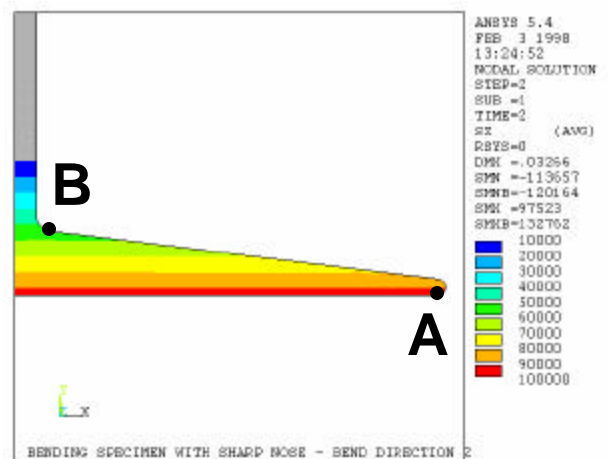
Figure 5C.5. The FOD Flexure Specimen Design.

Blade Stresses



$$\frac{S_A}{S_B} \gg 2$$

Specimen Stresses



$$\frac{S_A}{S_B} = 1.7$$

Figure 5C.6. Comparison of Local Leading Edge Stresses in the Blade and the Test Specimen.

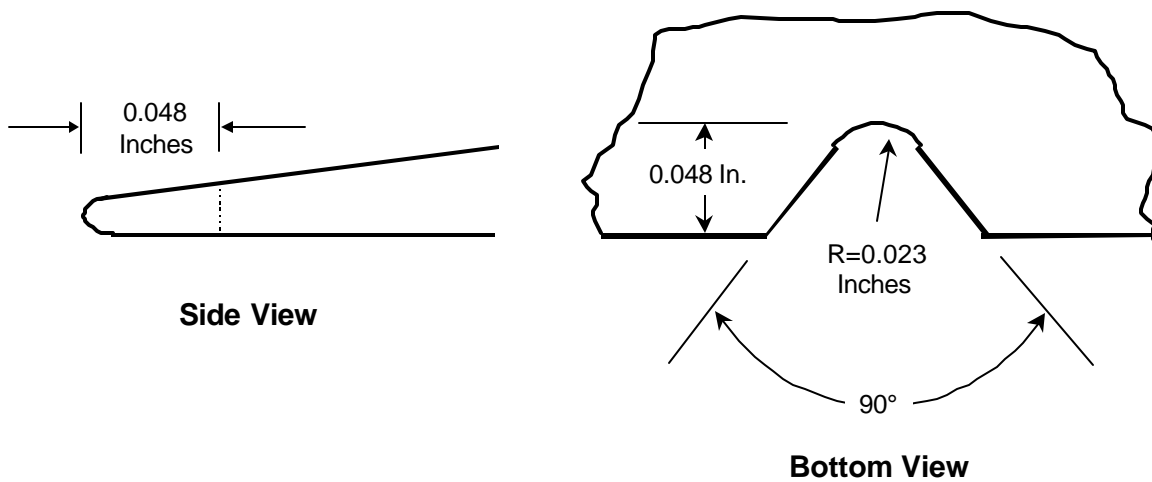


Figure 5C.7. Dimensions of the 90° machined notch in the sharp LE specimens.

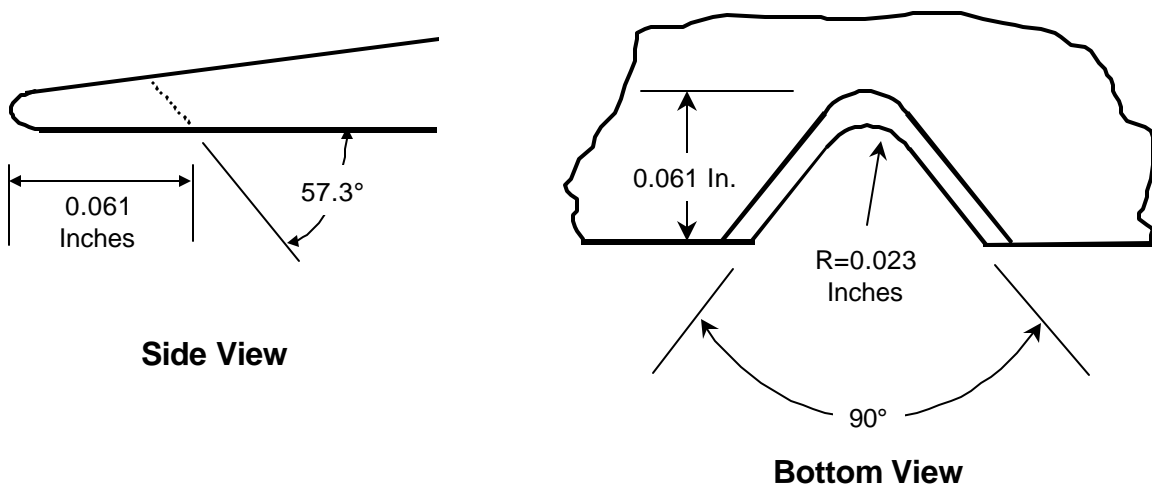


Figure 5C.8. Dimensions of the 60° machined notch in the blunt LE specimens.

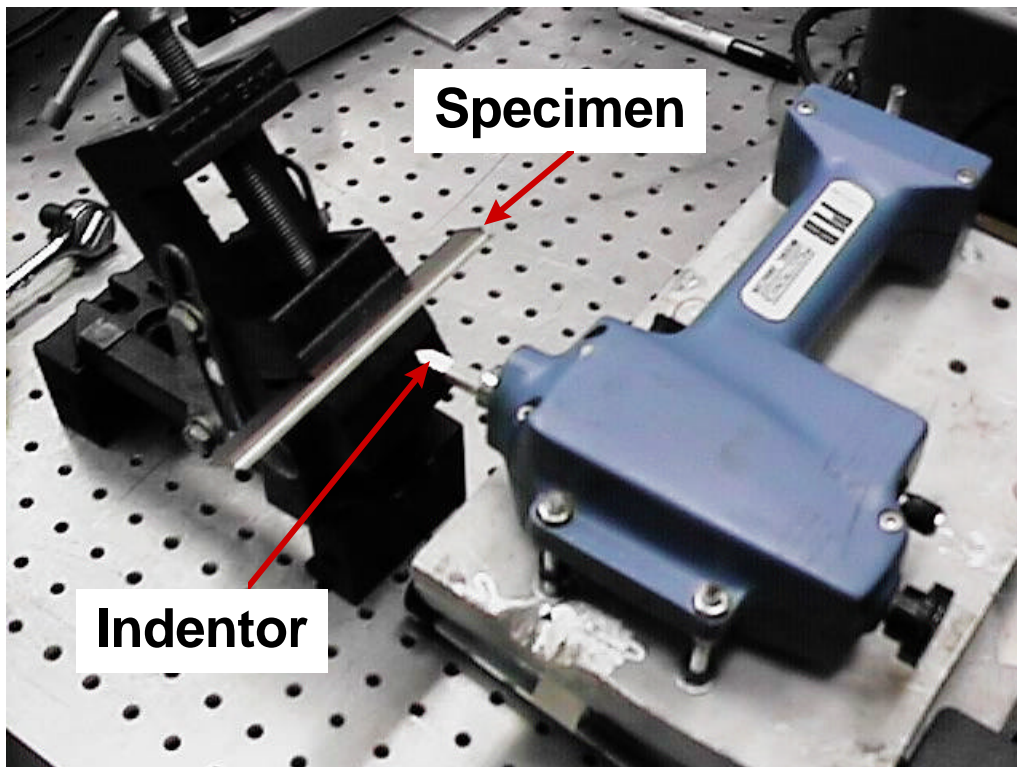
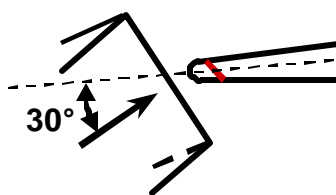
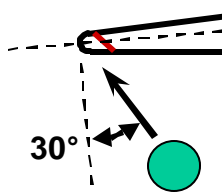


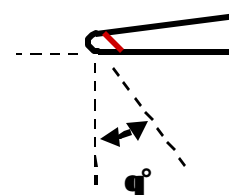
Figure 5C.9. Picture of the Solenoid Gun Set Up to FOD a Specimen.



a) 30° Solenoid Gun Impacts



b) 30° Ballistic Impacts



c) Angles for Notch Depth Measurements

Figure 5C.10. Impact Angles of FOD Nicks in this Investigation.

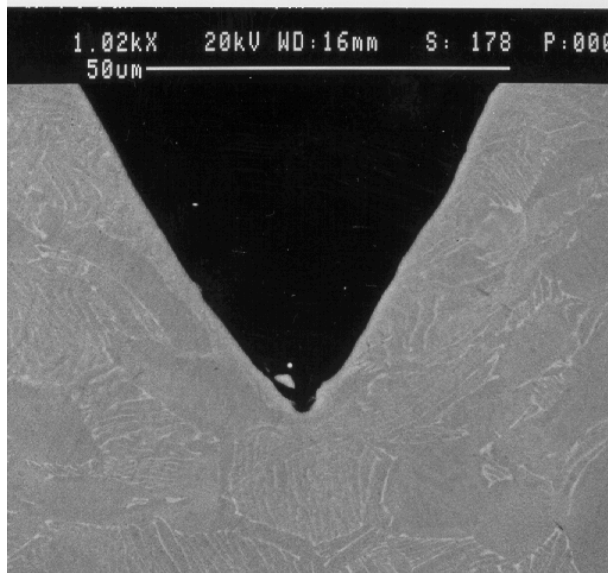


Figure 5C.11. Micrograph of a Polished Section of Simulated FOD Using the Solenoid Gun.

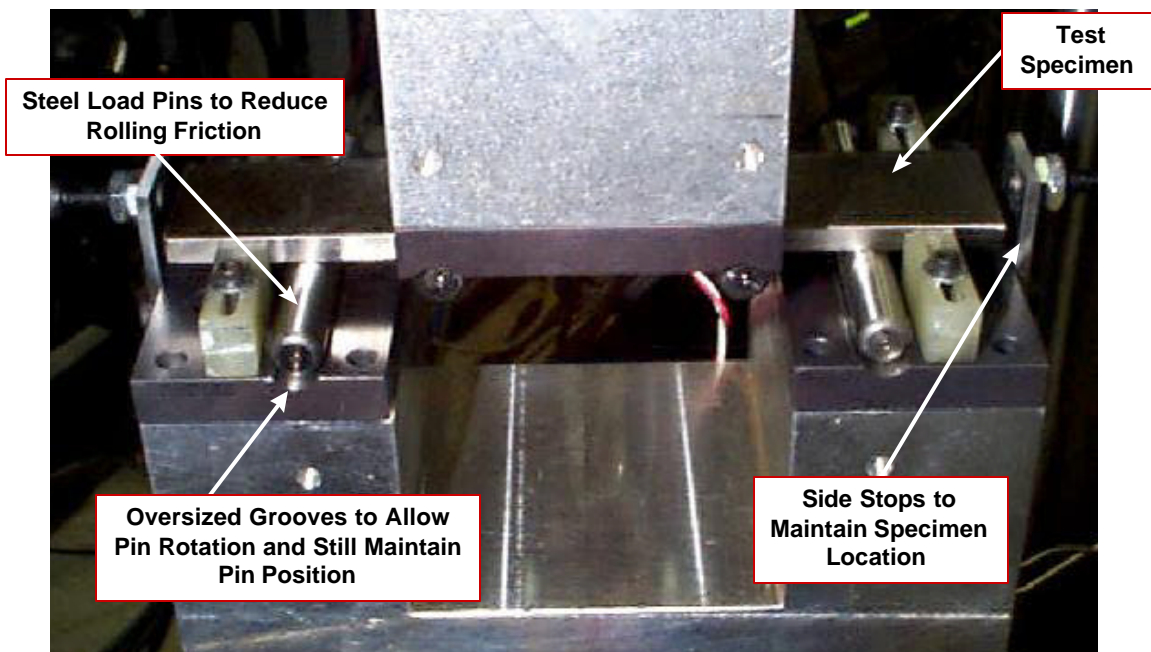


Figure 5C.12. Test Fixture for the FOD Specimen. Notice, Portions of the Fixturing which Enable Reverse Loading have been Removed to Expose the Loading Pins and Specimen.

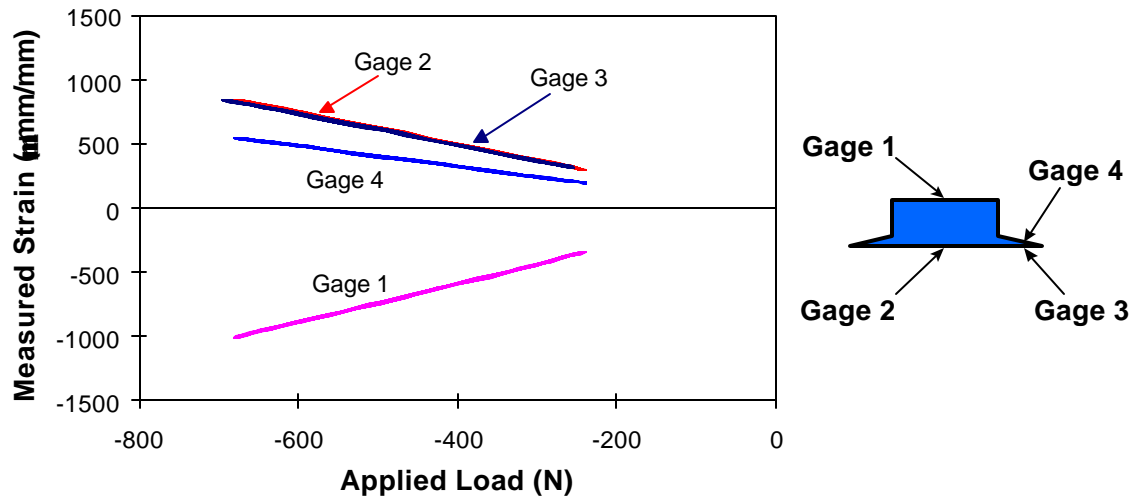


Figure 5C.13. Hysteresis Loops Generated using the FOD Specimen Fixturing.

Table 5C.1
FOD Test Results

Specimen ID	LE Diameter	Resp	Simulated FOD Technique	Notch Orient (Deg)	Notch Radius (in)	Depth on Bot Face (In)		Test Type	EPD	R Ratio	Initial Max Load (lbs)	Num of Load Steps	Cycles At Step	Load Step (Lbs)	Final Max Load (Lbs)	Final Max σ (Ksi)	Final σ Range (Ksi)	Cycles to Failure @ Max Load	Interpolated σ Range (Ksi)	Total Cycles	Comments
48-02	0.010	GE	(None)			0.0000		Step	None	0.5	1000	4	1.0E+06	50	1200	114.0	57.0	560,500	56.0	4,560,500	
70-08	0.010	GE	(None)			0.0000		Step	None	0.5	1000	5	1.0E+06	50	1250	118.8	59.4	288,964	57.7	5,288,964	
75-02	0.010	GE	(None)			0.0000		Step	None	0.5	1000	4	1.0E+06	50	1200	114.0	57.0	211,591	55.2	4,211,591	
11-S1	0.010	GE	Mach Notch	90	0.024	0.0485		Step	Weld-A	0.5	300	9	1.0E+06	10%	707	67.2	33.6	961,591	33.5	9,961,591	
11-S2	0.010	GE	Mach Notch	90	0.022	0.0482		Step	Weld-A	0.5	531	3	1.0E+06	10%	707	67.2	33.6	424,456	31.9	3,424,456	
11-S3	0.010	GE	Mach Notch	90	0.023	0.0478		Step	Weld-A	0.5	531	2	1.0E+06	10%	643	61.1	30.6	158,664	28.2	2,158,664	
11-S4	0.010	GE	Mach Notch	90	0.023	0.0485		Step	Weld-A	0.5	531	2	1.0E+06	10%	643	61.1	30.6	208,958	28.4	2,208,958	
22-B2	0.030	GE	Mach Notch	33	0.023	0.061		Step	Pressure	0.5	531	0	1.0E+06	10%	531	49.2	24.6	1,094,965	24.6	1,094,965	
36-B3	0.030	GE	Mach Notch	33	0.023	0.061		Step	None	0.5	399	3	1.0E+06	10%	531	49.2	24.6	256,459	23.0	3,256,459	
Specimen ID	LE Diameter	Resp	Simulated FOD Technique	Notch Orient (Deg)	Inpactor Radius (in)	Depth at 33° (In)		Test Type	EPD	R Ratio	Initial Max Load (lbs)	Num of Load Steps	Cycles At Step	Load Step (Lbs)	Final Max Load (Lbs)	Final Max σ (Ksi)	Final σ Range (Ksi)	Cycles to Failure @ Max Load	Interpolated σ Range (Ksi)	Total Cycles	Comments
70-03	0.010	GE	Solenoid	30	0.005	0.0088		Step	None	0.5	624	0	1.0E+06	NA	624	59.3	29.6	555,880	29.6	555,880	
75-08	0.010	GE	Solenoid	30	0.005	0.0093		Step	None	0.5	566	0	1.0E+06	NA	566	53.8	26.9	760,864	26.9	760,864	
48-05	0.010	GE	Solenoid	30	0.005	0.0084		Step	None	0.5	300	18	1.0E+06	5%	688	65.4	32.7	85,586	32.7	18,085,586	
11-S7	0.010	GE	Solenoid	30	0.005	0.0067		Step	None	0.5	483	6	1.0E+06	10%	856	81.3	40.7	232,456	37.8	6,232,456	
70-04	0.010	GE	Solenoid	30	0.005	0.0237		Step	None	0.5	300	7	1.0E+06	10%	585	55.6	27.8	455,549	26.4	7,455,549	
75-04	0.010	GE	Solenoid	30	0.005	0.0198		Step	None	0.5	300	8	1.0E+06	10%	643	61.1	30.6	417,488	28.9	8,417,488	
36-S2	0.010	GE	Solenoid	30	0.005	0.0258		Step	None	0.5	439	7	1.0E+06	10%	856	81.3	40.7	156,818	37.5	7,156,818	
11-S5	0.010	GE	Solenoid	30	0.005	0.0204		Step	Weld-A	0.5	439	1	1.0E+06	10%	483	45.9	22.9	441,250	21.8	1,441,250	
48-06	0.010	GE	Solenoid	30	0.005	0.0217		Step	Weld-A	0.5	300	5	1.0E+06	10%	483	45.9	23.0	1,030,190	23.0	6,030,190	
75-03	0.010	GE	Solenoid	30	0.005	0.0193		Step	Weld-A	0.5	439	2	1.0E+06	10%	531	50.5	25.2	576,945	24.3	2,576,945	
75-05	0.010	GE	Solenoid	30	0.005	0.0172		Step	None	0.5	439	4	1.0E+06	10%	643	61.1	30.6	260,355	28.5	4,260,355	Stress Relieved
11-S8	0.010	GE	Solenoid	30	0.005	0.0176		Step	None	0.5	439	1	1.0E+06	10%	483	45.9	23.0	745,132	22.4	1,745,132	Stress Relieved
70-05	0.010	GE	Solenoid	30	0.005	0.0084		Step	None	0.5	439	8	1.0E+06	10%	941	89.4	44.7	183,200	41.4	8,183,200	Stress Relieved
22-B1	0.030	GE	Solenoid	30	0.005	0.0065		Step	None	-1.0	248	5	1.0E+06	10%	399	37.0	74.0	377,573	69.8	5,377,573	Did Not Fail at Nick
36-B2	0.030	GE	Solenoid	30	0.005	0.0063		Step	None	-1.0	248	6	1.0E+06	10%	439	40.7	81.4	435,700	77.2	6,435,700	
36-B4	0.030	GE	Solenoid	30	0.005	0.0064		Step	None	-1.0	300	1	1.0E+06	10%	330	30.6	61.2	685,721	59.4	1,685,721	Did Not Fail at Nick
22-B4	0.030	GE	Solenoid	30	0.005	0.0184		Step	None	-1.0	225	0	1.0E+06	10%	225	20.9	41.7	306,250	41.7	306,250	
36-B1	0.030	GE	Solenoid	30	0.005	0.0170		Step	None	-1.0	225	1	1.0E+06	10%	247	22.9	45.8	959,873	45.6	1,959,873	
36-B5	0.030	GE	Solenoid	30	0.005	0.0186		Step	None	-1.0	300	0	1.0E+06	10%	300	27.8	55.6	441,838	55.6	441,838	
22-S1	0.010	GE	Solenoid	30	0.025	0.0041		Step	Pressure	0.5	439	8	1.0E+06	10%	941	89.4	44.7	282,010	41.8	8,282,010	
70-01	0.010	GE	Solenoid	30	0.025	0.0041		Step	None	0.5	439	11	1.0E+06	10%	1253	119.0	59.5	654,043	57.6	11,654,043	Did Not Fail at Nick
76-03	0.010	GE	Solenoid	30	0.025	0.0039		Step	None	0.5	941	2	1.0E+06	10%	1139	108.2	54.1	518,346	51.7	2,518,346	
11-S6	0.010	GE	Solenoid	30	0.025	0.0232		Step	Weld-A	0.5	439	6	1.0E+06	10%	778	73.9	37.0	238,312	34.4	6,238,312	
22-S2	0.010	GE	Solenoid	30	0.025	0.0222		Step	None	0.5	941	1	1.0E+06	10%	1035	98.4	49.2	687,716	47.8	1,687,716	
48-04	0.010	GE	Solenoid	30	0.025	0.0182		Step	Pressure	0.5	439	7	1.0E+06	10%	856	81.3	40.7	606,852	39.2	7,606,852	

5C-13

Table 5C.1
FOD Test Results (Continued)

Specimen ID	LE Diameter	Resp	Simulated FOD Technique	Notch Orient (Deg)	Impactor Radius (in)	Depth at 33° (In)		Test Type	EPD	R Ratio	Initial Max Load (lbs)	Num of Load Steps	Cycles At Step	Load Step (Lbs)	Final Max Load (Lbs)	Final Max σ (Ksi)	Final σ Range (Ksi)	Cycles to Failure @ Max Load	Interpolated σ Range (Ksi)	Total Cycles	Comments
70-06	0.010	GE	Solenoid	0	0.005	0.0069		Step	None	0.5	439	11	1.0E+06	10%	1253	119.0	59.5	474,176	56.7	11,474,176	Did Not Fail at Nick
76-S1	0.010	GE	Solenoid	0	0.005	0.0083		Step	Pressure	0.5	439	10	1.0E+06	10%	1139	108.3	54.1	121,452	49.8	10,121,452	

Specimen ID	LE Diameter	Resp	Simulated FOD Technique	Notch Orient (Deg)	Impactor Radius (in)	Depth at 33° (In)		Test Type	EPD	R Ratio	Initial Max Load (lbs)	Num of Load Steps	Cycles At Step	Load Step (Lbs)	Final Max Load (Lbs)	Final Max σ (Ksi)	Final σ Range (Ksi)	Cycles to Failure @ Max Load	Interpolated σ Range (Ksi)	Total Cycles	Comments
22-B3	0.030	GE	Solenoid	90	0.005	?		Step	None	0.5	439	11	1.0E+06	10%	1253	116.2	58.1	764,000	56.8	11,764,000	Did Not Fail at Nick
36-B6	0.030	GE	Solenoid	90	0.005	?		Step	None	0.5	439	8	1.0E+06	10%	941	87.2	43.6	246,868	40.6	8,246,868	

Specimen ID	LE Diameter	Resp	Simulated FOD Technique	Notch Orient (Deg)	Ball Radius (in)	Depth at 0° (In)		Test Type	EPD	R Ratio	Initial Max Load (lbs)	Num of Load Steps	Cycles At Step	Load Step (Lbs)	Final Max Load (Lbs)	Final Max σ (Ksi)	Final σ Range (Ksi)	Cycles to Failure @ Max Load	Interpolated σ Range (Ksi)	Total Cycles	Comments
189-1	0.010	PW	Ballsitic	30°	0.020	0.0067		Step	Pressure	0.5	643.1	1	1.0E+06	10%	707.4	67.2	33.6	471,945	32.3	1,471,945	
54-7	0.010	PW	Ballsitic	30°	0.020	0.0088		Step	Pressure	0.5	643.1	1	1.0E+06	10%	707.4	67.2	33.6	84,945	31.3	1,084,945	
189-4	0.010	PW	Ballsitic	30°	0.039	0.0187		Step	Weld-B	0.5	300.0	12	1.0E+06	10%	941.5	89.5	44.7	125,565	41.8	12,125,565	
189-5	0.010	PW	Ballsitic	30°	0.039	0.072*		Step	Pressure	0.5	643.1	2	1.0E+06	10%	778.2	74.0	37.0	357,968	35.2	2,357,968	Cycles to Nucleation
189-6	0.010	PW	Ballsitic	30°	0.039	0.0214		Step	Weld-B	0.5	707.4	0	1.0E+06	10%	707.4	67.2	33.6	157,243	33.6	157,243	

Specimen ID	LE Diameter	Resp	Simulated FOD Technique	Notch Orient (Deg)	Indentor Radius (in)	Depth at 33° (In)		Test Type	EPD	R Ratio	Initial Max Load (lbs)	Num of Load Steps	Cycles At Step	Load Step (Lbs)	Final Max Load (Lbs)	Final Max σ (Ksi)	Final σ Range (Ksi)	Cycles to Failure @ Max Load	Interpolated σ Range (Ksi)	Total Cycles	Comments
54-1	0.010	PW	Solenoid	30°	0.005	0.0289		S-N	Weld-B	0.5	500.0				500.0	47.5	23.8	91,892,512	23.8	91,892,512	Suspension
54-5	0.010	PW	Solenoid	30°	0.005	0.0173		S-N	Weld-B	0.5	800.0				800.0	76.0	38.0	907,797	38.0	907,797	
54-4	0.010	PW	Solenoid	30°	0.005	0.0216	0.0206	S-N	Weld-B	0.5	600.0				600.0	57.0	28.5	25,029,454	28.5	25,029,454	Initiated at FOD A
54-8	0.010	PW	Solenoid	30°	0.005	0.0169	0.0213	S-N	Weld-B	0.5	700.0				700.0	66.5	33.3	3,164,740	33.3	3,164,740	Initiated at FOD B

Specimen ID	LE Diameter	Resp	Simulated FOD Technique	Notch Orient (Deg)	Indentor Radius (in)	Depth at 33° (In)		Test Type	EPD	R Ratio	Initial Max Load (lbs)	Num of Load Steps	Cycles At Step	Load Step (Lbs)	Final Max Load (Lbs)	Final Max σ (Ksi)	Final σ Range (Ksi)	Cycles to Failure @ Max Load	Interpolated σ Range (Ksi)	Total Cycles	Comments
86-5*	0.030	PW	Solenoid	30°	0.005	0.0037	0.0034	Step	Weld-B	0.5	643.1	6	1.0E+06	10%	1139.3	105.6	52.8	19,222	50.1	6,019,222	Did Not Fail at Nick
86-8*	0.030	PW	Solenoid	30°	0.005	0.0041	0.0040	Step	Weld-B	0.5	643.1	8	1.0E+06	10%	1378.5	127.8	63.9	219,033	61.3	8,219,033	Did Not Fail at Nick
86-4*	0.030	PW	Solenoid	30°	0.005	0.0043	0.0037	Step	Weld-B	0.5	643.1	5	1.0E+06	10%	1035.7	96.0	48.0	242,857	45.9	5,242,857	Initiated at FOD A
86-3*	0.030	PW	Solenoid	30°	0.005	0.0166	0.0150	Step	Weld-B	0.5	643.1	0	1.0E+06	10%	643.1	59.6	29.8	185,830	29.8	185,830	Initiated at FOD A
86-2*	0.030	PW	Solenoid	30°	0.005	0.0199	0.0179	Step	Weld-B	0.5	643.1	0	1.0E+06	10%	643.1	59.6	29.8	278,384	29.8	278,384	Initiated at FOD B
86-7*	0.030	PW	Solenoid	30°	0.005	0.0152	0.0146	Step	Weld-B	0.5	643.1	0	1.0E+06	10%	643.1	59.6	29.8	337,398	29.8	337,398	Initiated at FOD B

* Specimen not chem-milled.

**Attachment
1
to Appendix 5C**

**Test Specimen
Photographs and Raw Data**

Specimen: 48-02, Sharp Leading Edge

Simulated FOD Conditions: Unnotched

WMT&R Report Number: 8-06498

Test Description: The test was run at an initial load of 1000 pounds, R-ratio of 0.5, and 30 Hz. The load was increased by 50 pounds after every 1,000,000 cycles until failure. This specimen was also strain gaged on top and bottom to investigate the hysteresis effects during loading. The gages were monitored at the test loads for the first 30 cycles.

Results: Final cycles: 4,560,500. Final Load: 1200 pounds.

Attached Data: Load versus cycles data, and Position versus cycles data.

Specimen: 70-08, Sharp Leading Edge

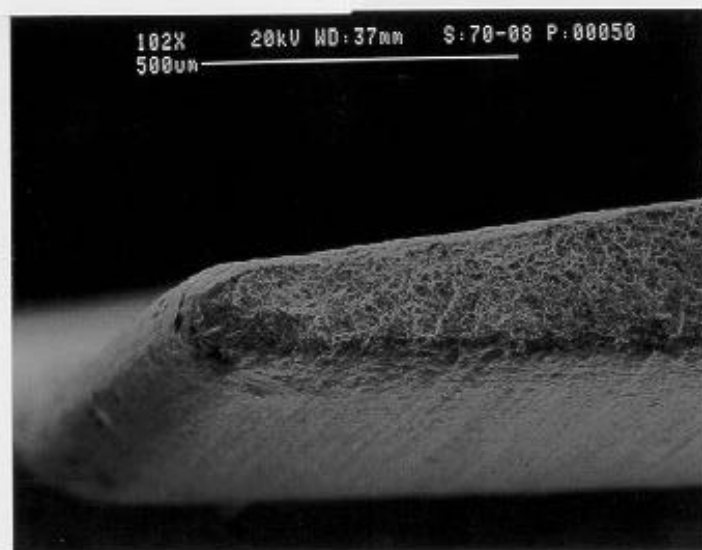
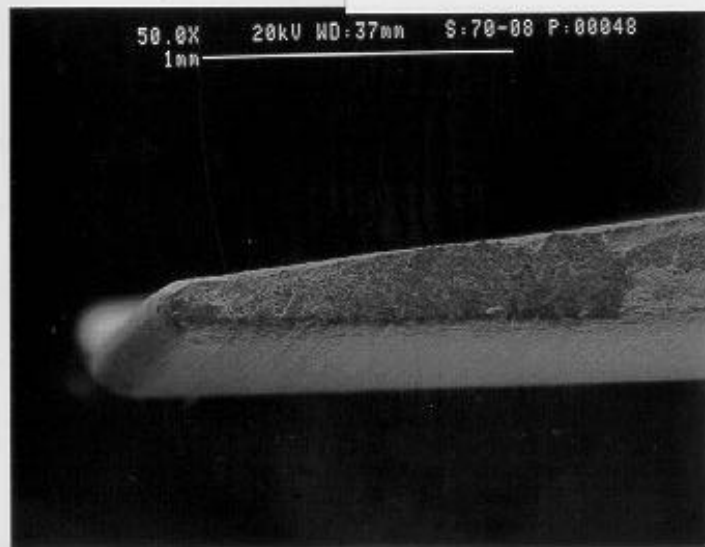
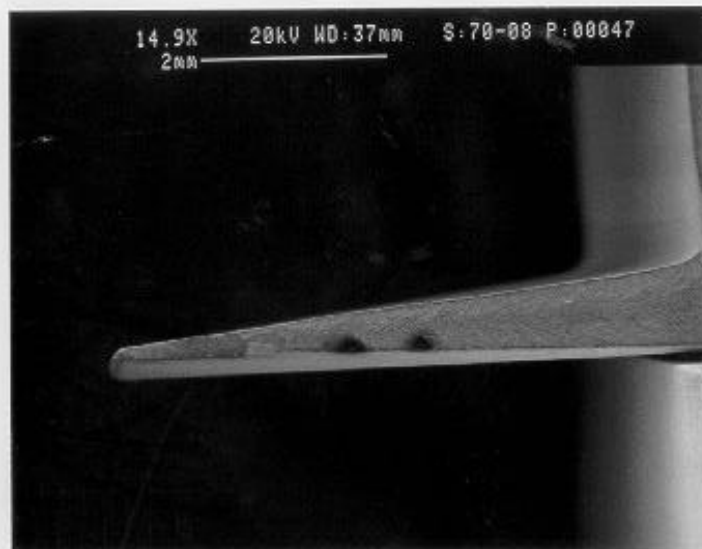
Simulated FOD Conditions: Unnotched

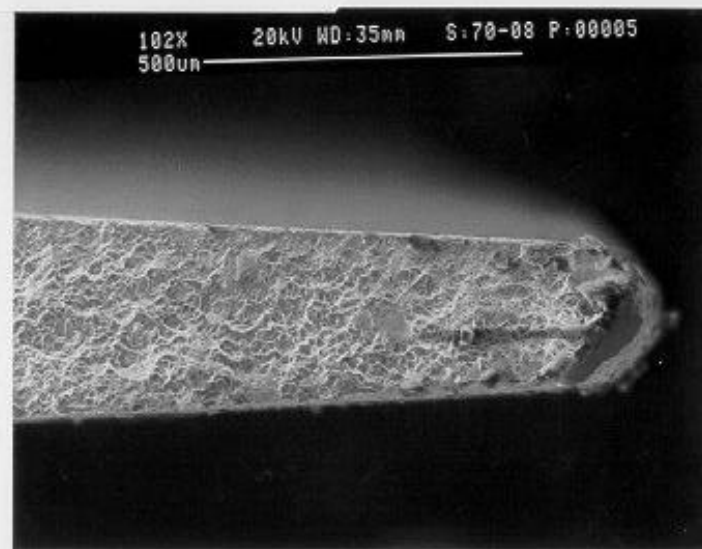
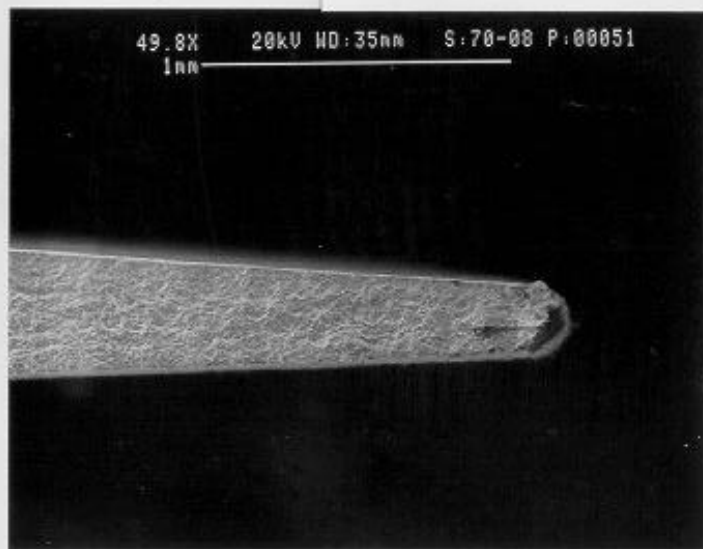
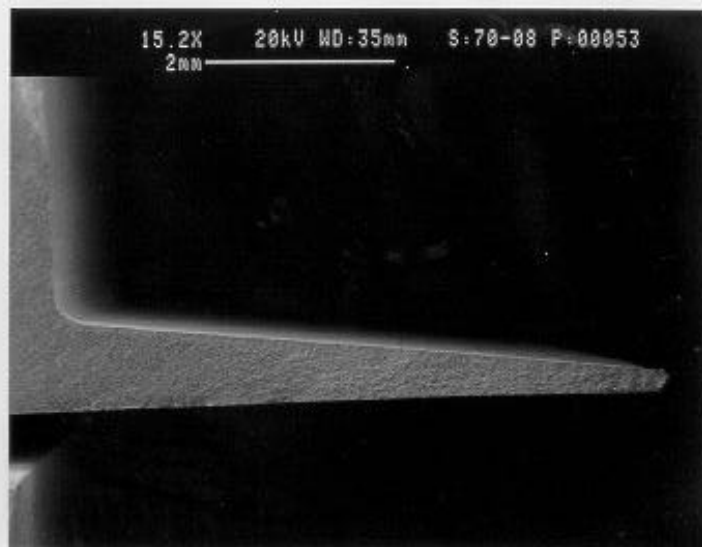
WMT&R Report Number: 8-13703

Test Description: The test was run at an initial load of 1000 pounds, R-ratio of 0.5, and 30 Hz. The load was increased by 50 pounds after every 1,000,000 cycles until failure.

Results: Final cycles: 5,288,964. Final Load: 1250 pounds.

Attached Data: Position versus cycles data, Micrographs of Failed specimens.





Specimen: 75-02, Sharp Leading Edge

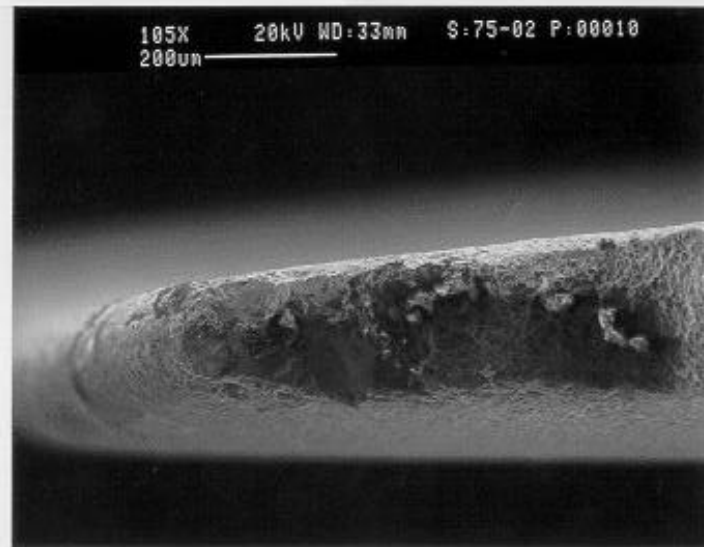
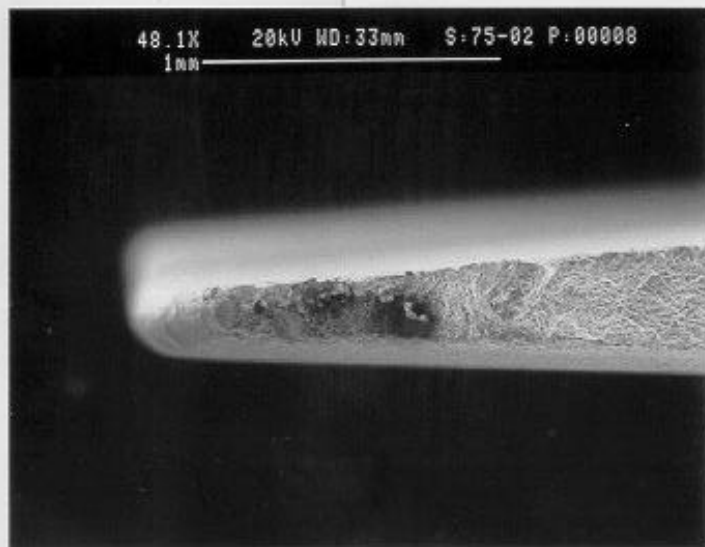
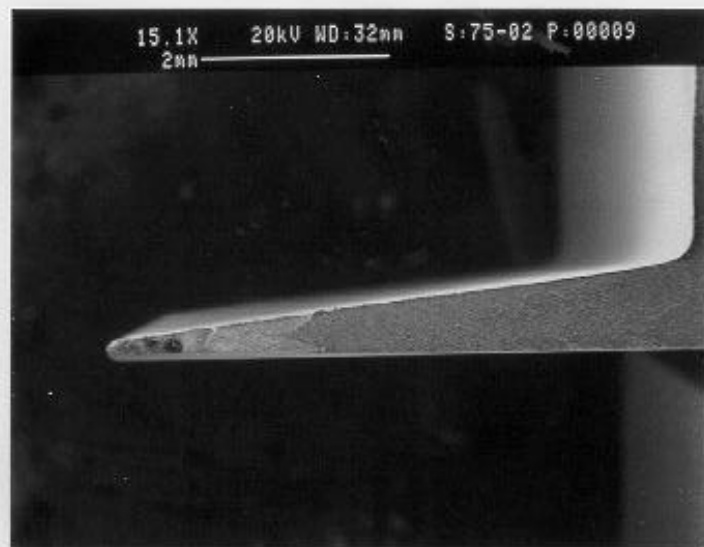
Simulated FOD Conditions: Unnotched

WMT&R Report Number: 8-13703

Test Description: The test was run at an initial load of 1000 pounds, R-ratio of 0.5, and 30 Hz. The load was increased by 50 pounds after every 1,000,000 cycles until failure.

Results: Final cycles: 4,211,591. Final Load: 1200 pounds.

Attached Data: Position versus cycles data, Micrographs of Failed specimens.



Specimen: 11-S1, Sharp Leading Edge

Simulated FOD Conditions: 90° Machined Notch

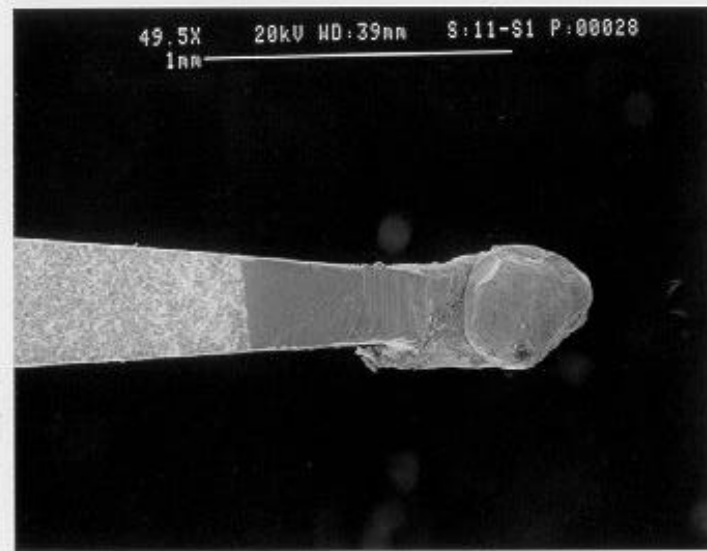
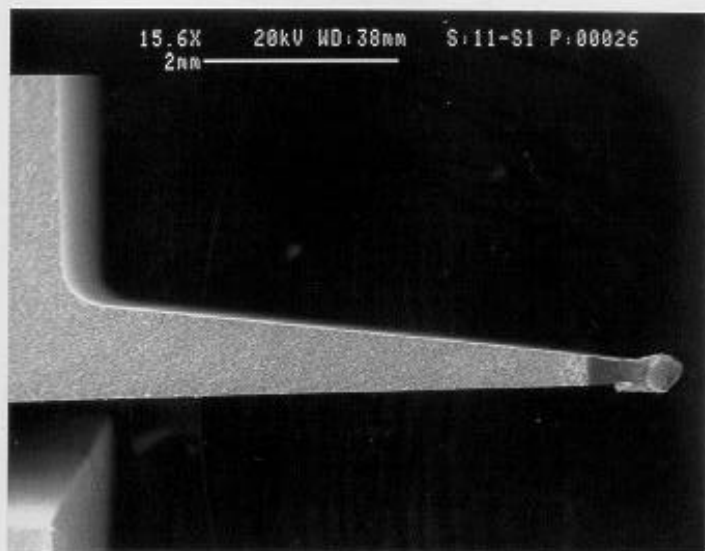
WMT&R Report Number: 8-18163

Test Description: The test was run at an initial load of 300 pounds, R-ratio of 0.5, and 30 Hz. The load was increased by 10% after every 1,000,000 cycles until failure. The specimen had welded EPD leads attached to monitor potential drop.

Results: Crack nucleation occurred at 707.4 pounds. Failure occurred at 9,961,591 cycles. EPD data:

U/Uo	Cycles	Heat Tint Data	Surface Crack Length from Heat Tint (in)	Total Crack Length with Notch (In)
1.0315	9,866,278	750°F @ 5 Hours	0.0164	0.0612
1.0501	9,869,130	680°F @ 3 Hours	0.0219	0.0667
1.2025	9,880,316	570°F @ 3 Hours	0.0515	0.0963

Attached Data: U/Uo versus cycles, Micrographs of Failed specimens.



Specimen: 11-S2, Sharp Leading Edge

Simulated FOD Conditions: 90° Machined Notch

WMT&R Report Number: 8-18163

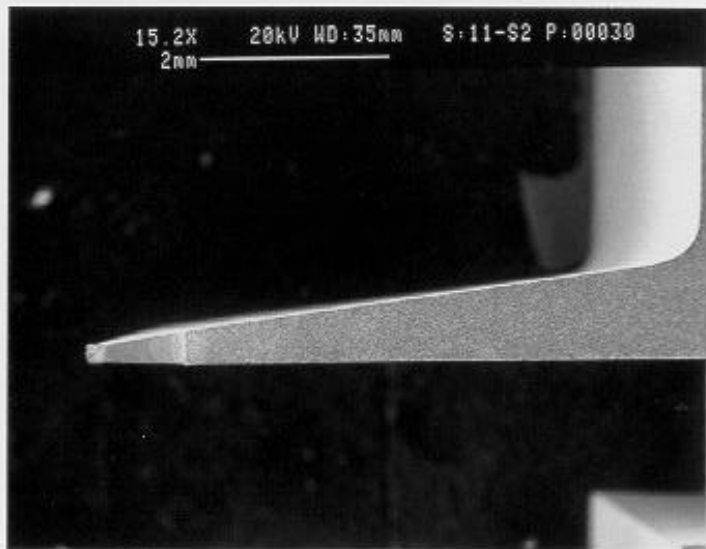
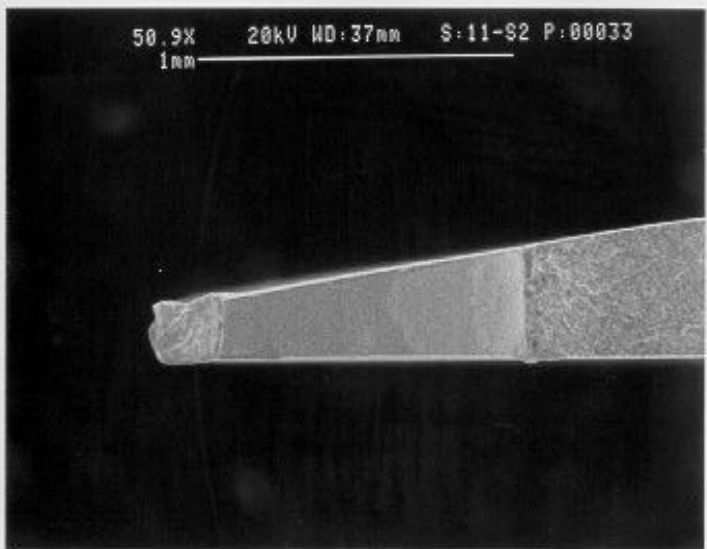
Test Description: The test was run at an initial load of 531.5 pounds, R-ratio of 0.5, and 30 Hz. The load was increased by 10% after every 1,000,000 cycles until failure. The specimen had welded EPD leads attached to monitor potential drop.

Results: Crack nucleation occurred at 707.4 pounds. 3,424,456 cycles to failure. EPD data:

U/Uo	Cycles	Heat Tint Data	Surface Crack Length from Heat Tint (in)	Total Crack Length with Notch (In)
1.0152	3,328,914	750°F @ 5 Hours	0.0076	0.0524
1.0523	3,334,743	680°F @ 3 Hours	0.0212	0.0660
1.2031	3,343,841	570°F @ 3 Hours	0.0490	0.0938

Attached Data: U/Uo versus cycles, Micrographs of Failed specimens.

5C-25



Specimen: 11-S3, Sharp Leading Edge

Simulated FOD Conditions: 90° Machined Notch

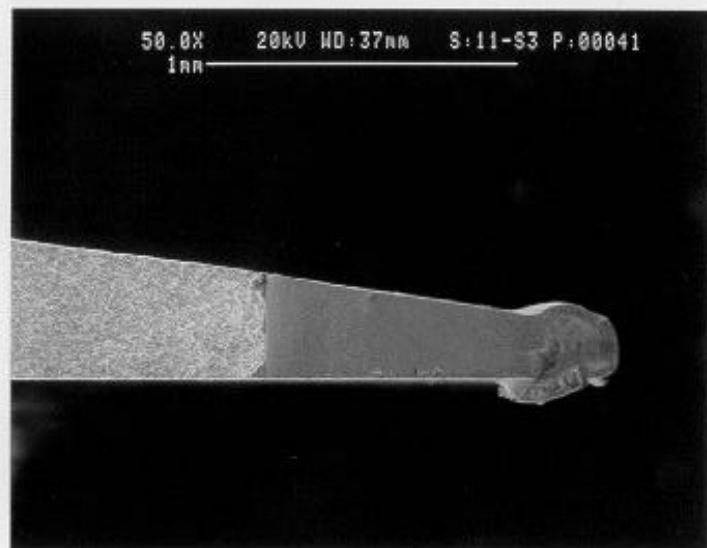
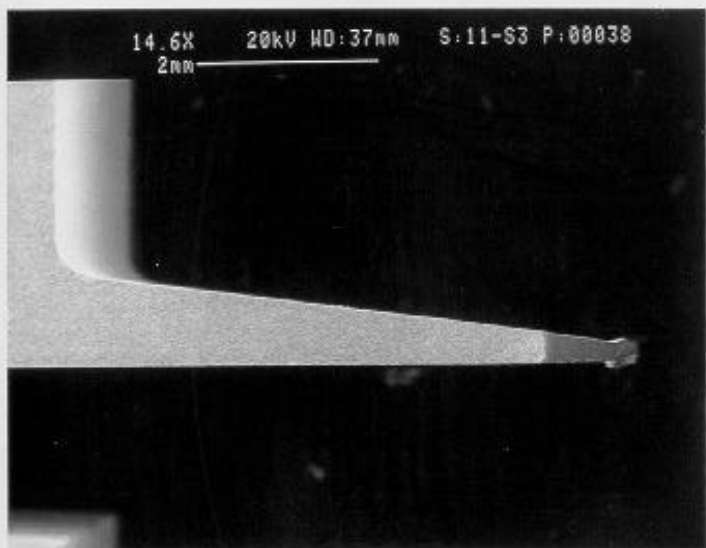
WMT&R Report Number: 8-18163

Test Description: The test was run at an initial load of 531.5 pounds, R-ratio of 0.5, and 30 Hz. The load was increased by 10% after every 1,000,000 cycles until failure. The specimen had welded EPD leads attached to monitor potential drop.

Results: Crack nucleation occurred at 643.1 pounds. 2,158,664 cycles to failure. EPD data:

U/Uo	Cycles	Heat Tint Data	Surface Crack Length from Heat Tint (in)	Total Crack Length with Notch (In)
1.0159	2,043,433	750°F @ 5 Hours	0.0123	0.0584
1.0520	2,049,172	680°F @ 3 Hours	0.0209	0.0670
1.2060	2,061,316	570°F @ 3 Hours	0.0490	0.0951

Attached Data: U/Uo versus cycles, Micrographs of Failed specimens.



Specimen: 11-S4, Sharp Leading Edge

Simulated FOD Conditions: 90° Machined Notch

WMT&R Report Number: 8-18163

Test Description: The test was run at an initial load of 531.5 pounds, R-ratio of 0.5, and 30 Hz. The load was increased by 10% after every 1,000,000 cycles until failure. The specimen had welded EPD leads attached to monitor potential drop.

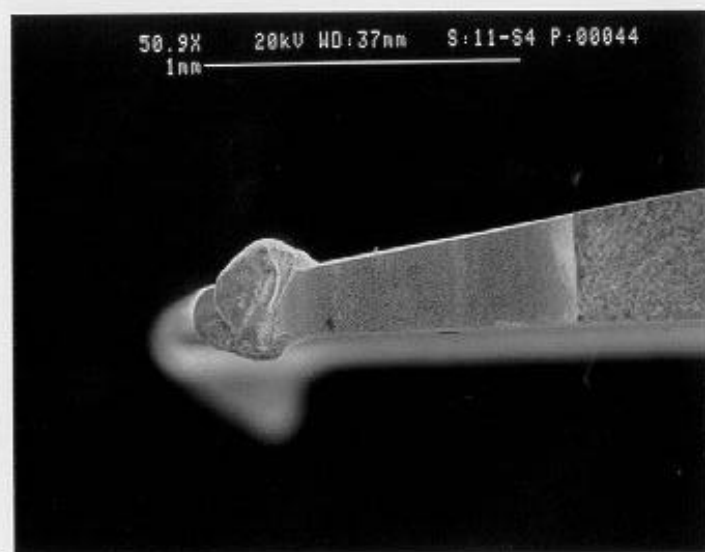
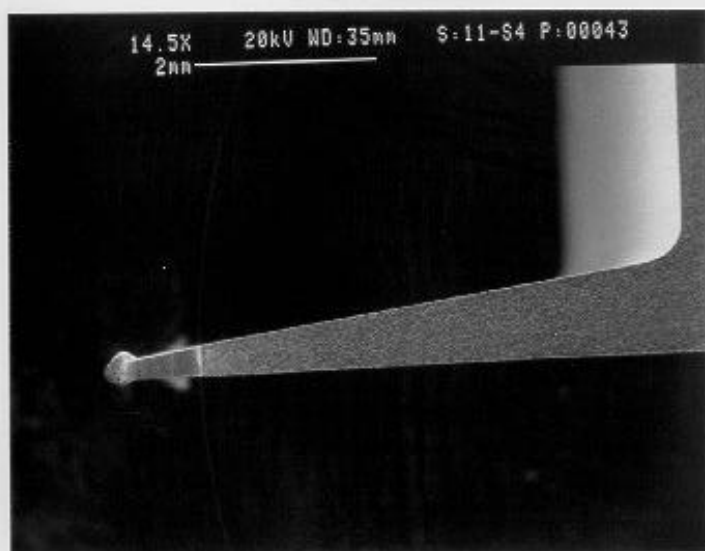
Results: Crack nucleation occurred at 643.1 pounds. 2,208,958 cycles to failure. EPD data:

U/Uo	Cycles	Heat Tint Data	Surface Crack Length from Heat Tint (in)	Total Crack Length with Notch (In)
1.0076	2,088,639	750°F @ 5 Hours	0.0125	0.0666
1.0500	2,097,390	680°F @ 3 Hours	0.0241	0.0782
1.2029	2,109,118	570°F @ 3 Hours	0.0524	0.1065



Crack Size from first heat tint:

Attached Data: U/Uo versus cycles, Micrographs of Failed specimens.



Specimen: 22-B2, Blunt Leading Edge

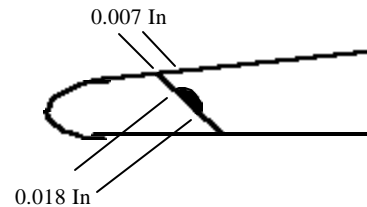
Simulated FOD Conditions: 60° Machined Notch

WMT&R Report Number: 9-04629

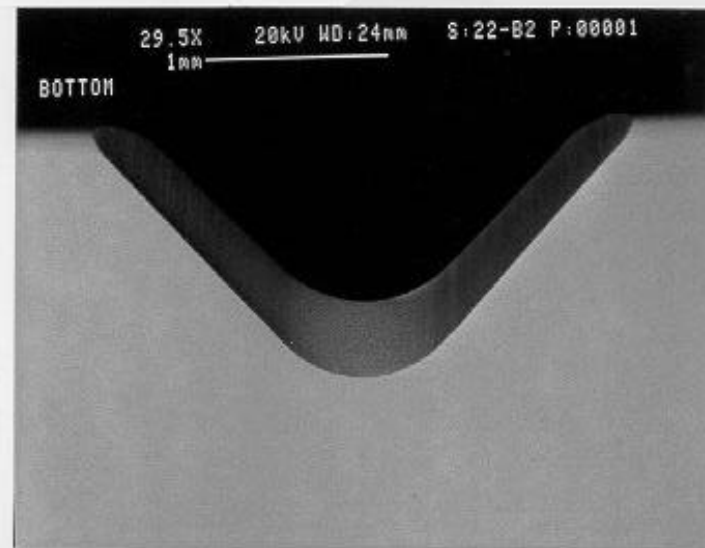
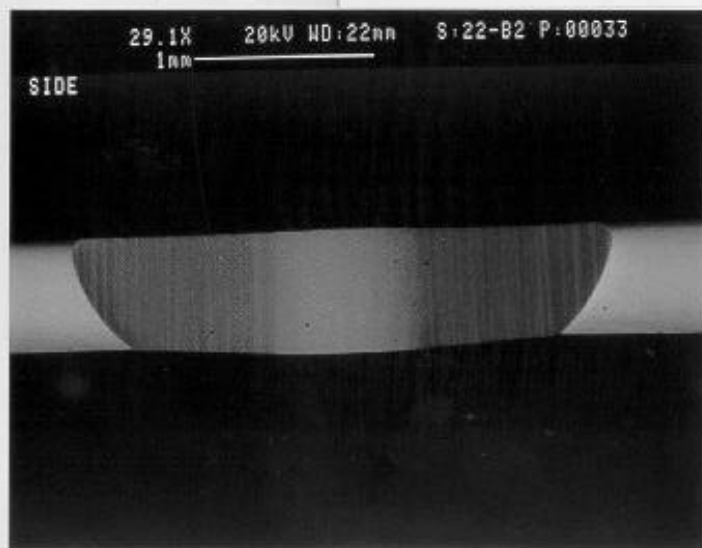
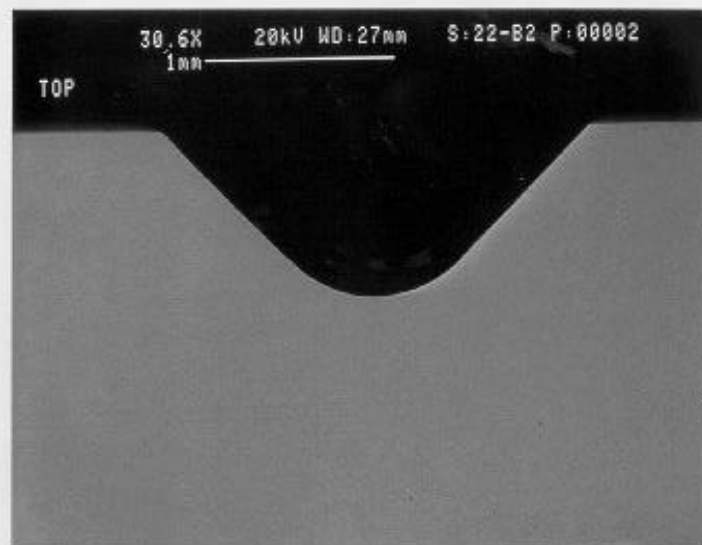
Test Description: The test was run at an initial load of 531 pounds, R-ratio of 0.5, and 30 Hz. The load was increased by 10% after every 1,000,000 cycles until failure. The specimen had pressure mounted EPD leads attached to monitor potential drop.

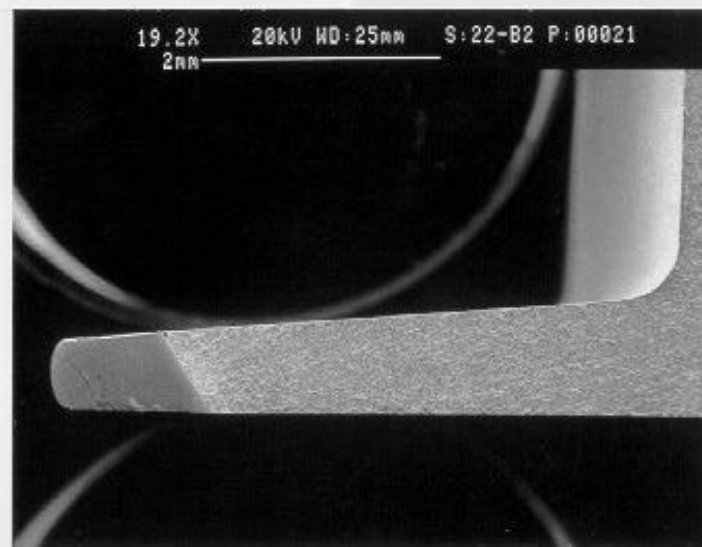
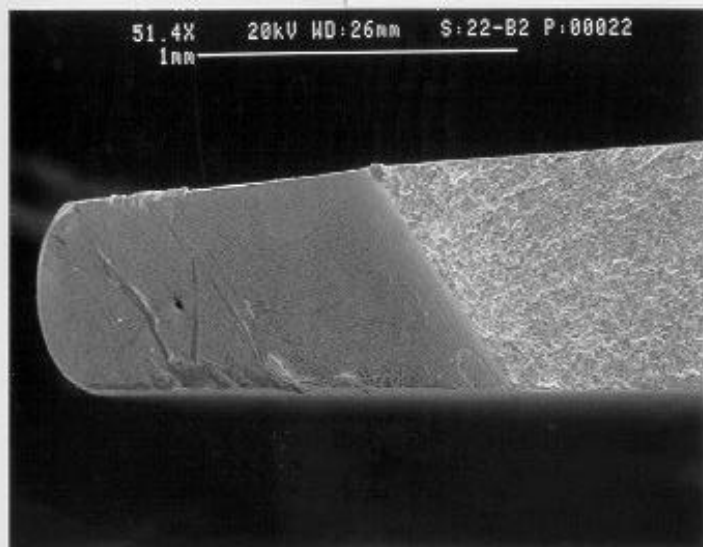
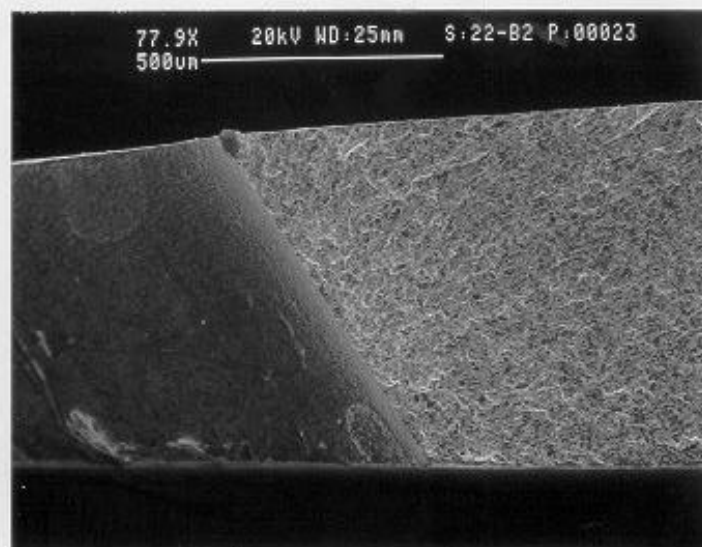
Results: Crack nucleation occurred at 531 pounds. The final cycles were 1,094,965. EPD data:

U/Uo	Cycles	Heat Tint Data	Crack Length from Heat Tint
1.0071	899,634	680°F @ 20 Hours	See Picture



Attached Data: Micrographs of Machined Notch, U/Uo versus cycles, Micrographs of Failed specimens.





Specimen: 36-B3, Blunt Leading Edge

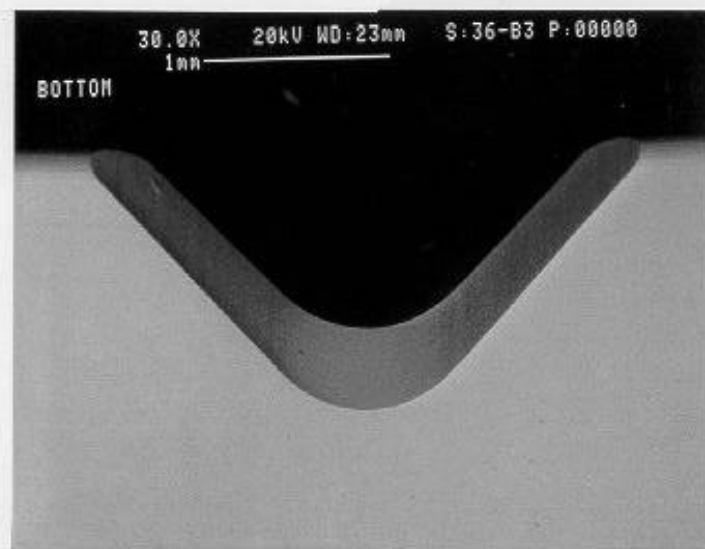
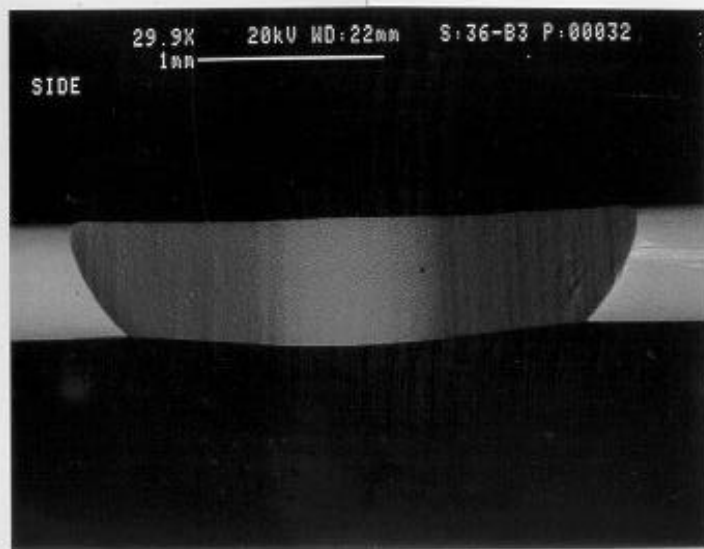
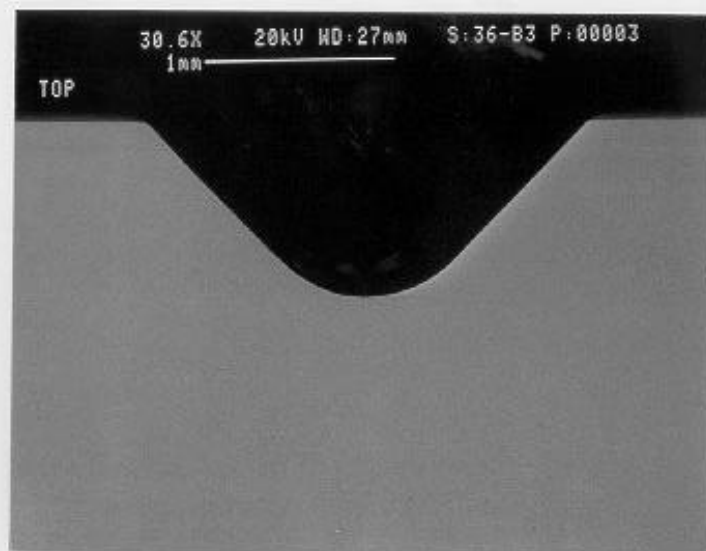
Simulated FOD Conditions: 60° Machined Notch

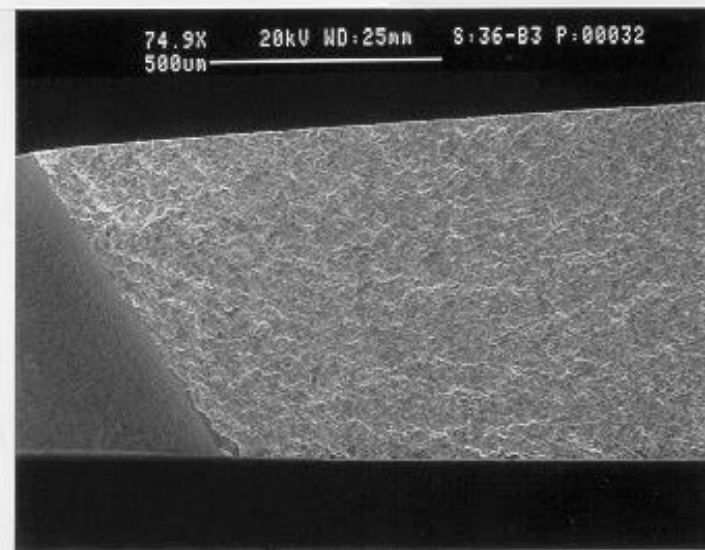
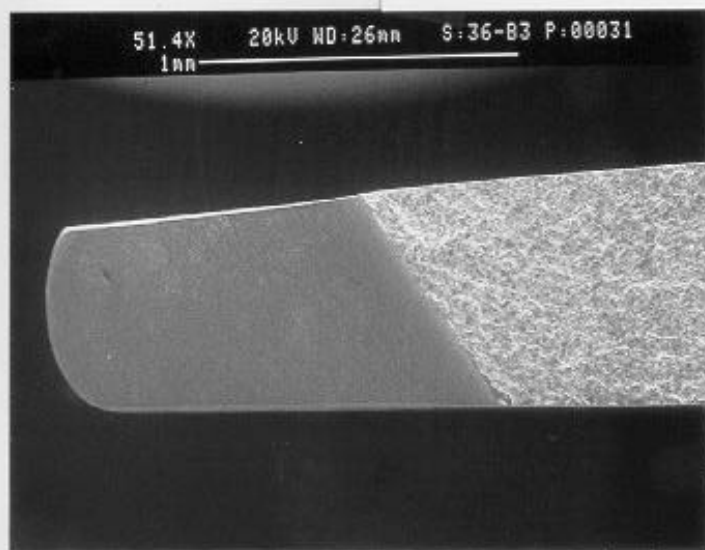
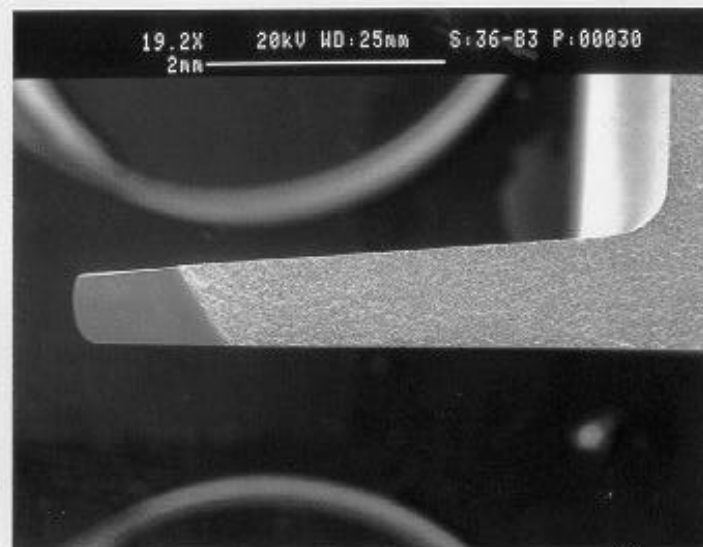
WMT&R Report Number: 9-04629

Test Description: The test was run at an initial load of 399 pounds, R-ratio of 0.5, and 30 Hz. The load was increased by 10% after every 1,000,000 cycles until failure.

Results: Crack nucleation occurred at 531 pounds. The final cycles were 3,256,459

Attached Data: Micrographs of Machined Notch, Load versus cycle plot, Position versus cycle plot, Micrographs of Failed specimens.





Specimen: 70-03, Sharp Leading Edge

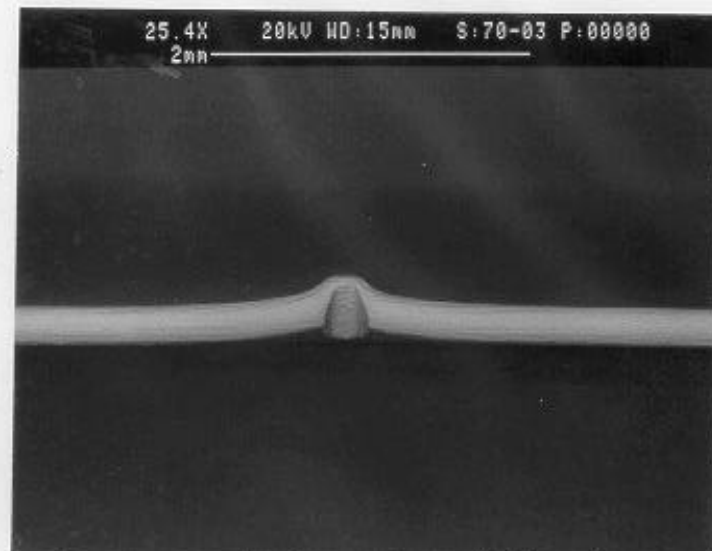
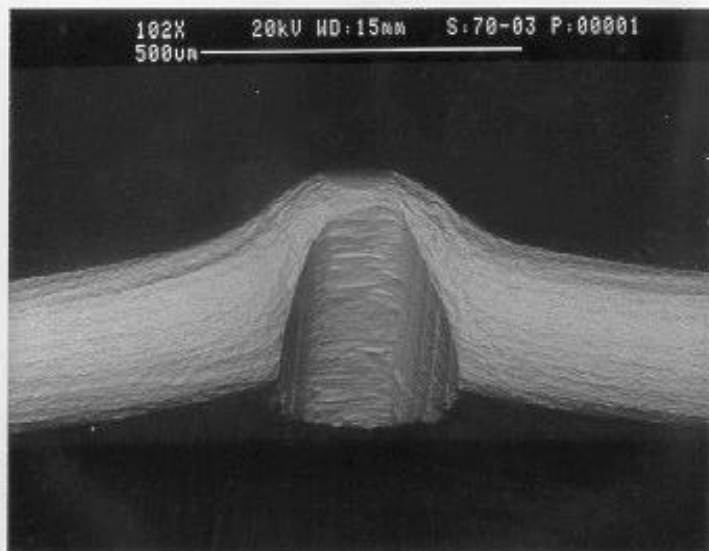
Simulated FOD Conditions: Solenoid Gun, 30° Impact angle, 0.005 inch tip radius, Low Damage Level.

WMT&R Report Number: 8-15464

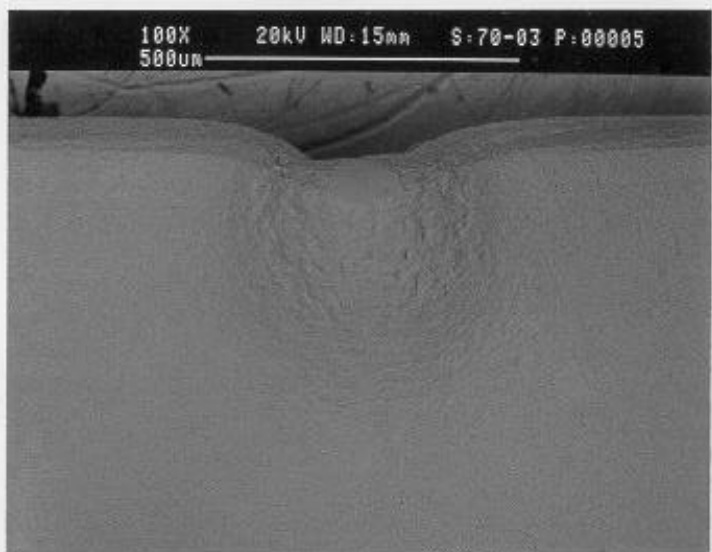
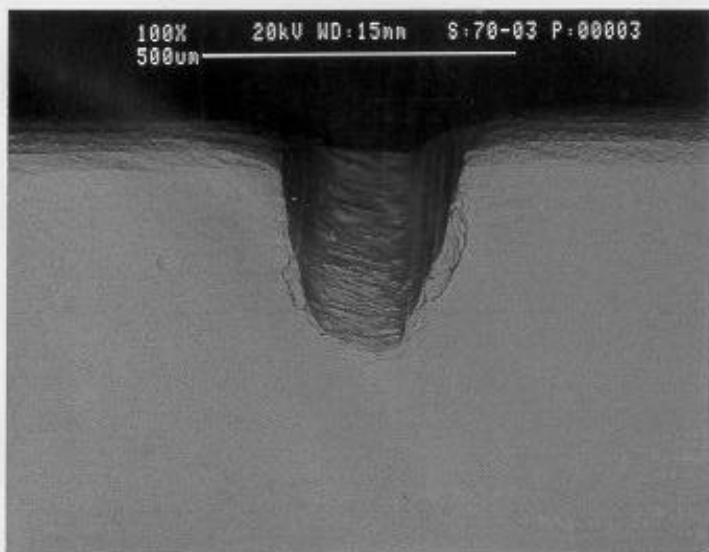
Test Description: The test was run at an initial load of 624 pounds, R-ratio of 0.5, and 30 Hz. The load was increased by 5% after every 1,000,000 cycles until failure.

Results: Crack nucleation occurred at 624 pounds. The final cycles were 555,880.

Attached Data: Micrographs of FOD'ed specimen, Micrographs of Failed specimens.

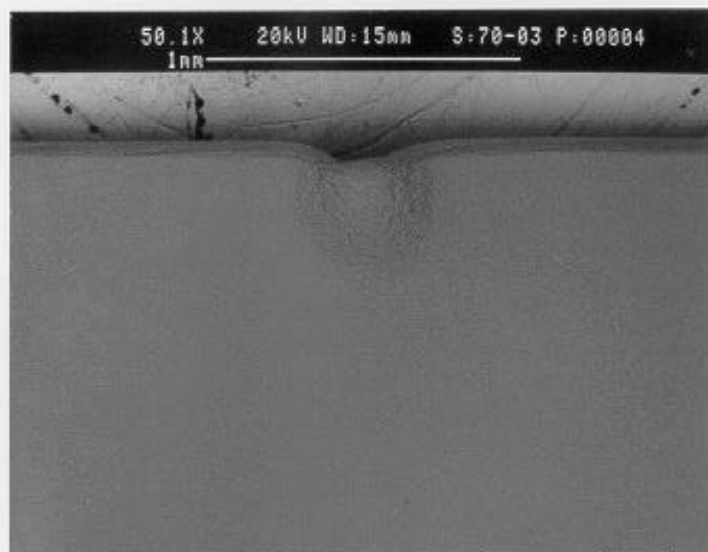
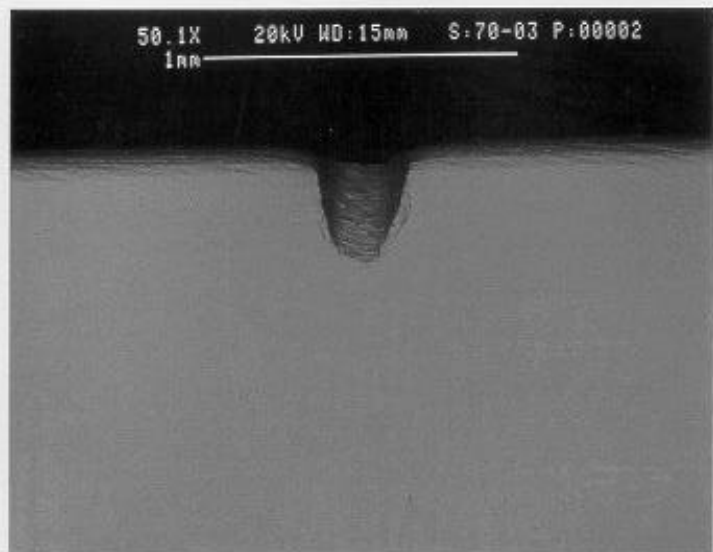


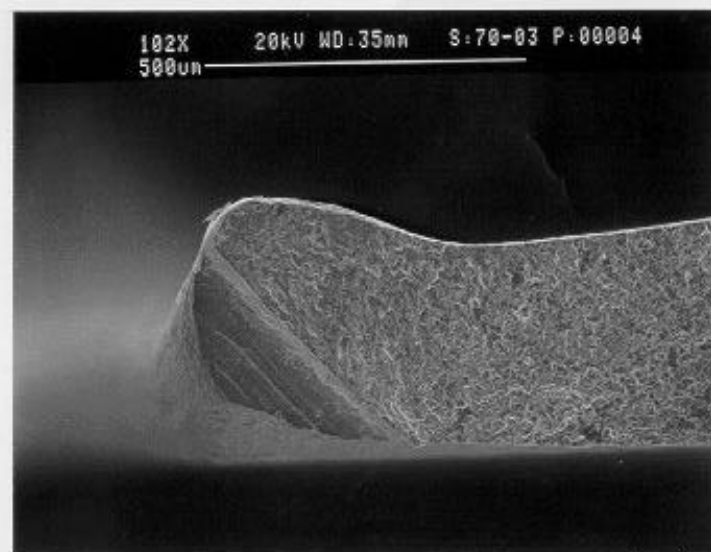
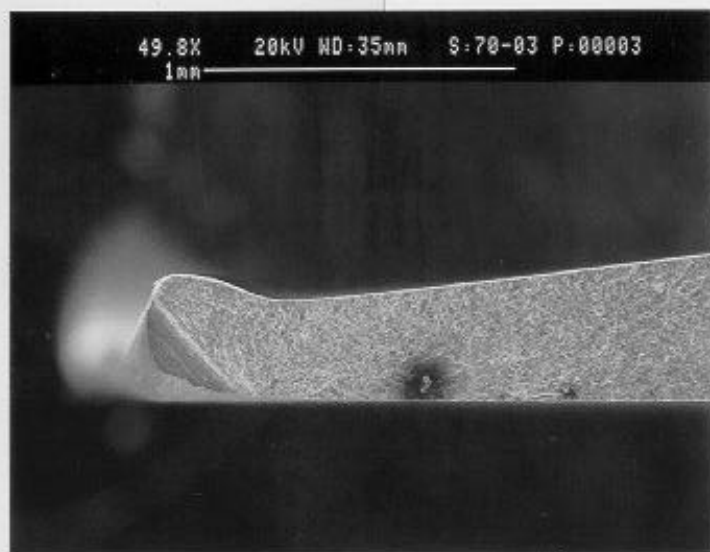
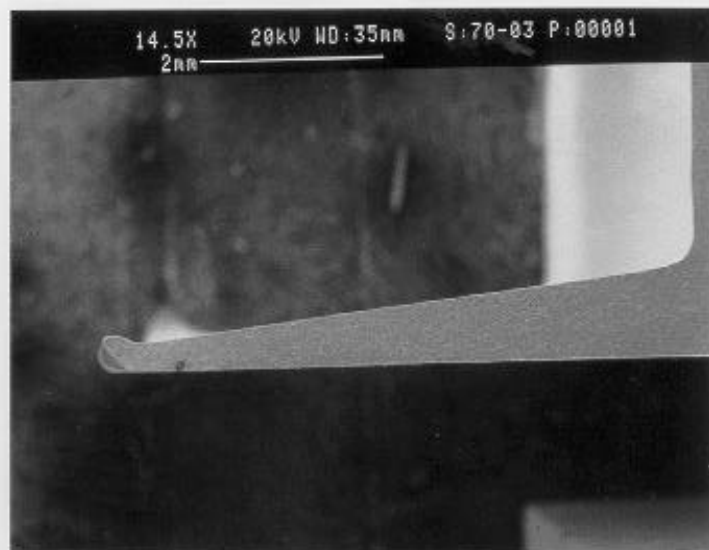
view #2



view #1

5C-38





Specimen: 75-08, Sharp Leading Edge

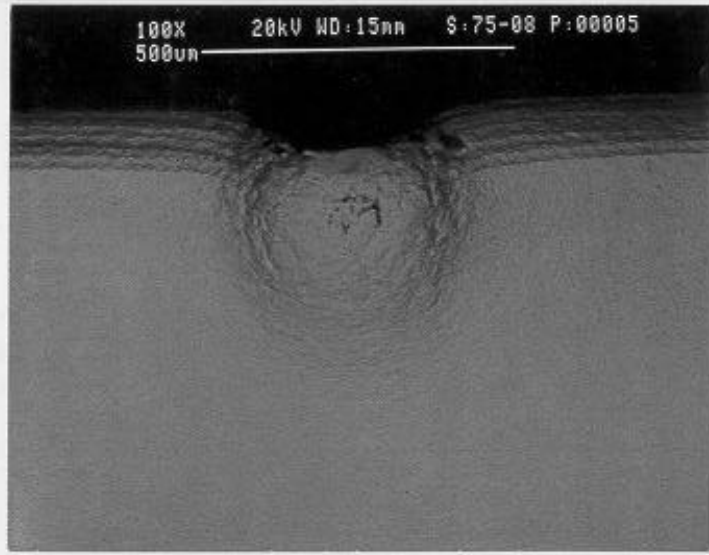
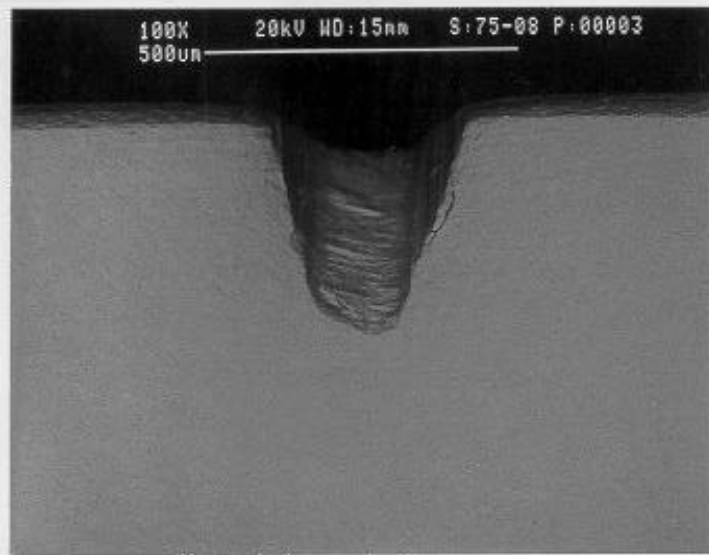
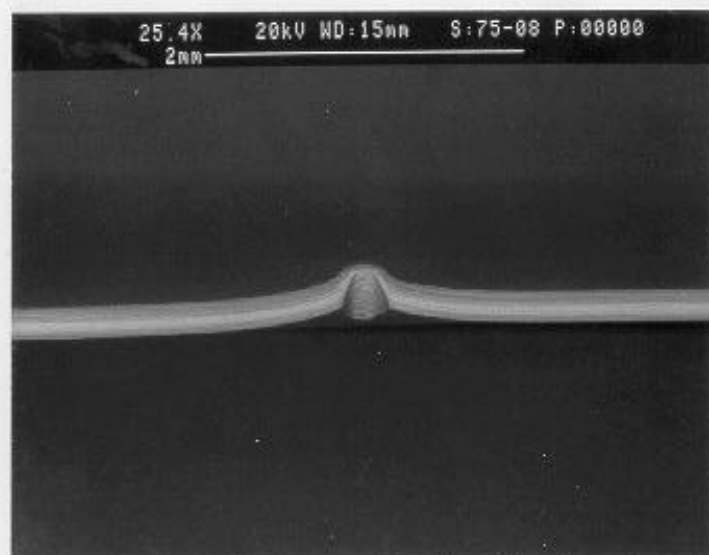
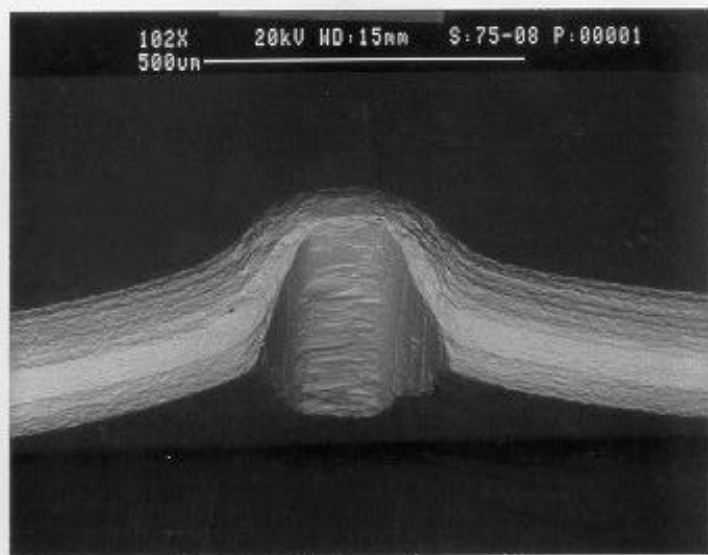
Simulated FOD Conditions: Solenoid Gun, 30° Impact angle, 0.005 inch tip radius, Low Damage Level.

WMT&R Report Number: 8-15464

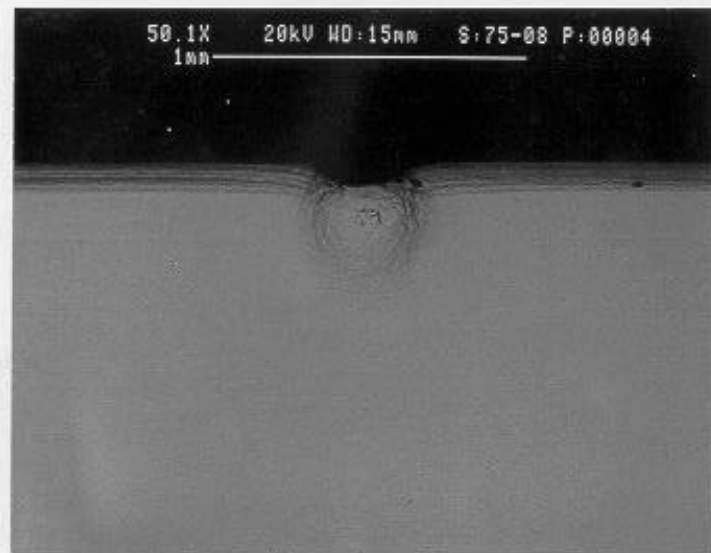
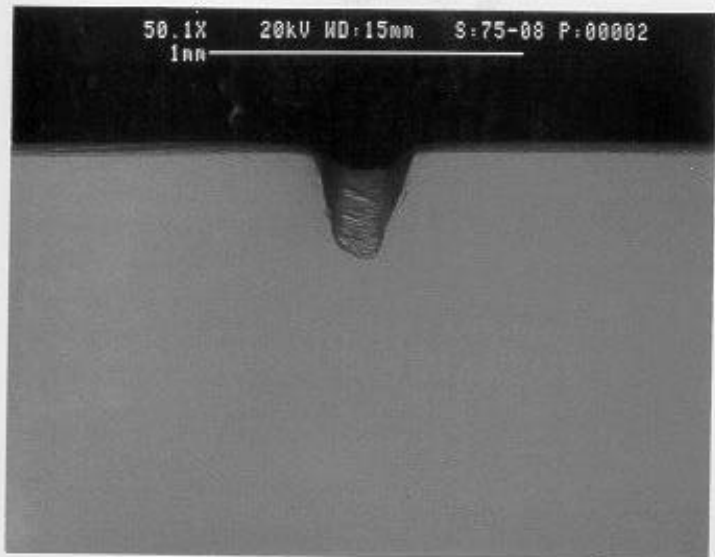
Test Description: The test was run at an initial load of 566 pounds, R-ratio of 0.5, and 30 Hz. The load was increased by 5% after every 1,000,000 cycles until failure.

Results: Crack nucleation occurred at 566 pounds. The final cycles were 760,864.

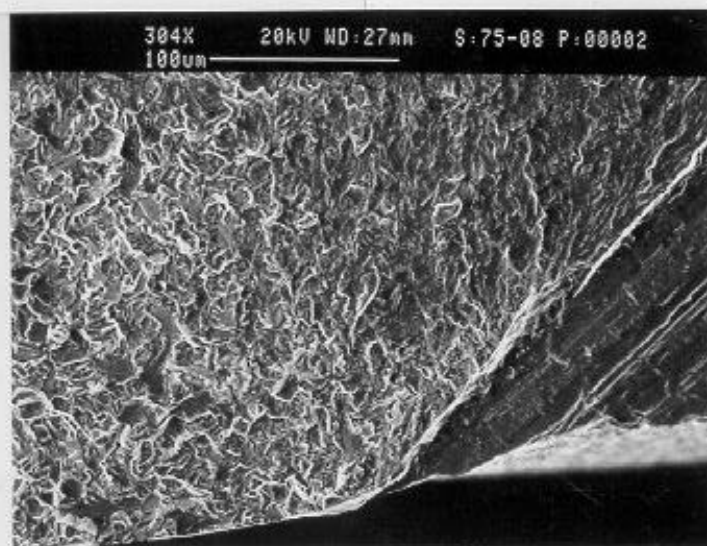
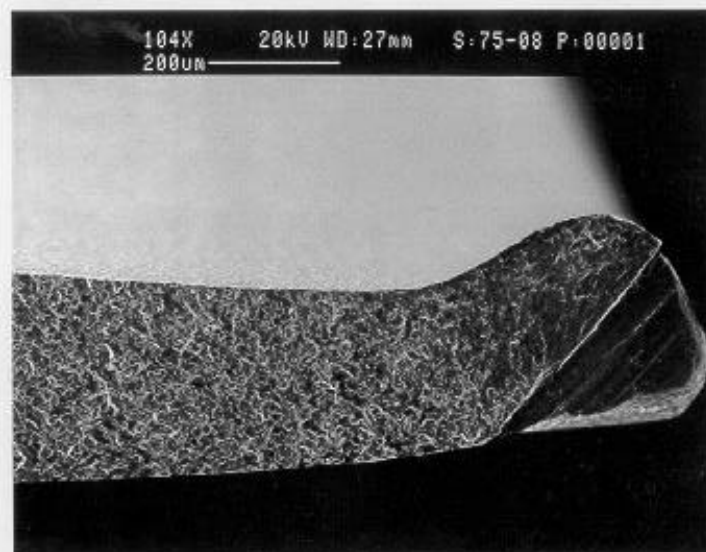
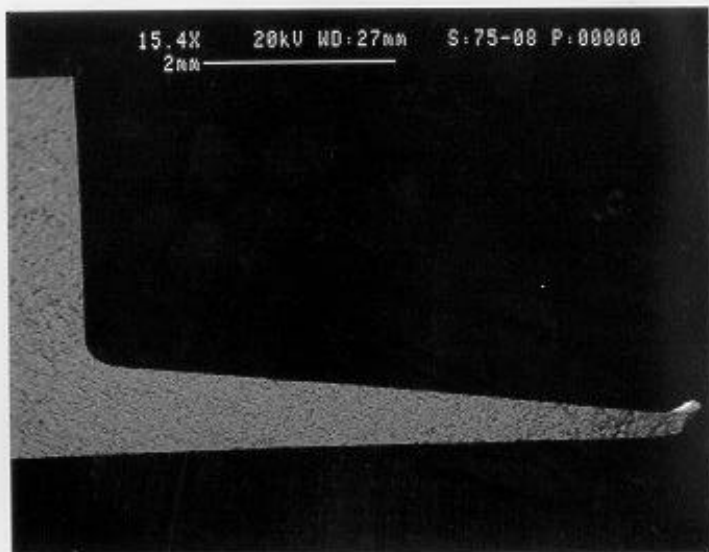
Attached Data: Micrographs of FOD'ed specimen, Load versus cycle plot, Position versus cycle plot, Micrographs of Failed specimens.



5C-42



View #1



Specimen: 48-05, Sharp Leading Edge

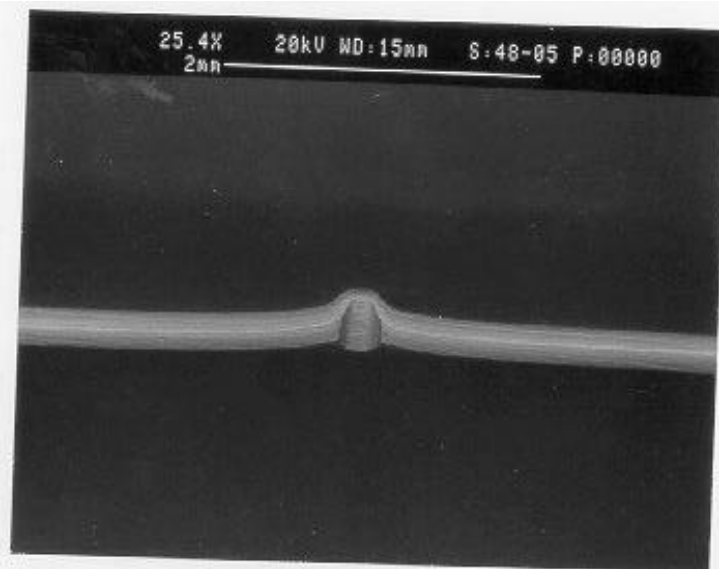
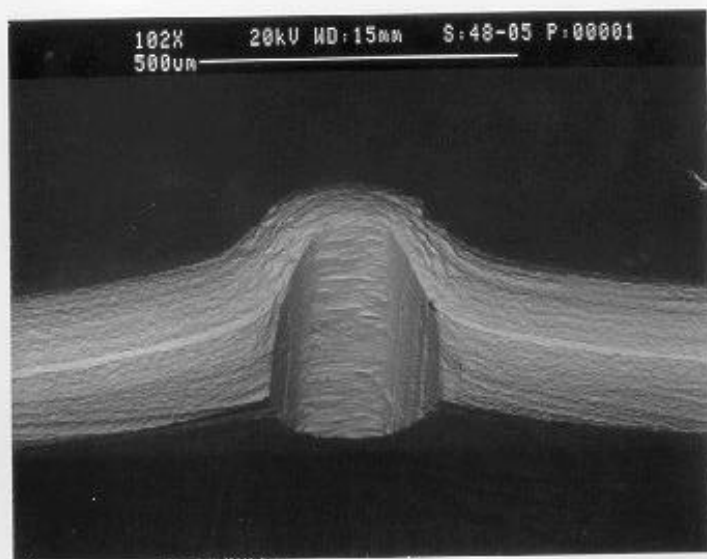
Simulated FOD Conditions: Solenoid Gun, 30° Impact angle, 0.005 inch tip radius, Low Damage Level.

WMT&R Report Number: 8-15464

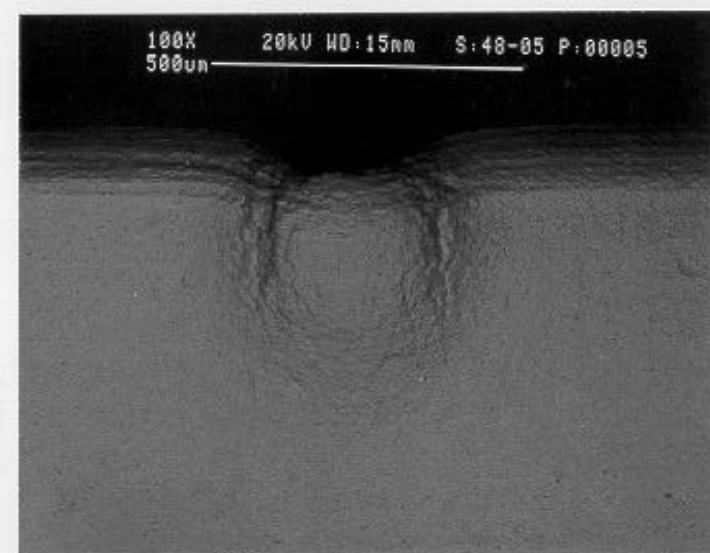
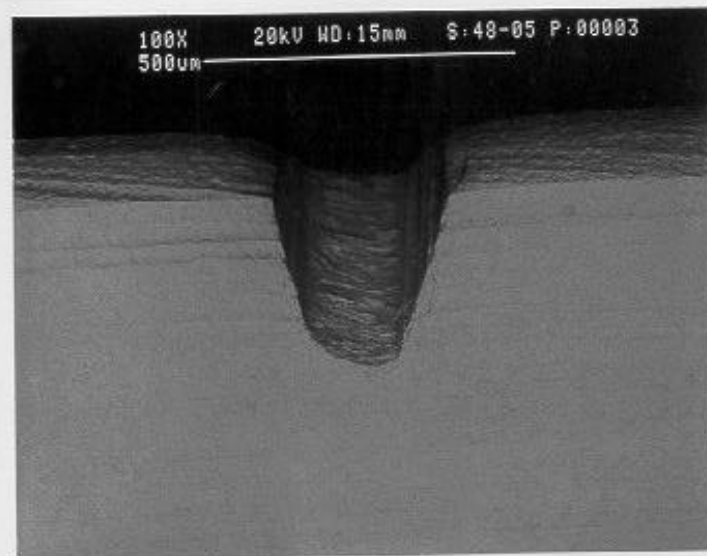
Test Description: The test was run at an initial load of 300 pounds, R-ratio of 0.5, and 30 Hz. The load was increased by 5% after every 1,000,000 cycles until failure.

Results: Crack nucleation occurred at 688 pounds. The final cycles were 18,085,586.

Attached Data: Micrographs of FOD'ed specimen, Load versus cycle plot, Position versus cycle plot, Micrographs of Failed specimens.

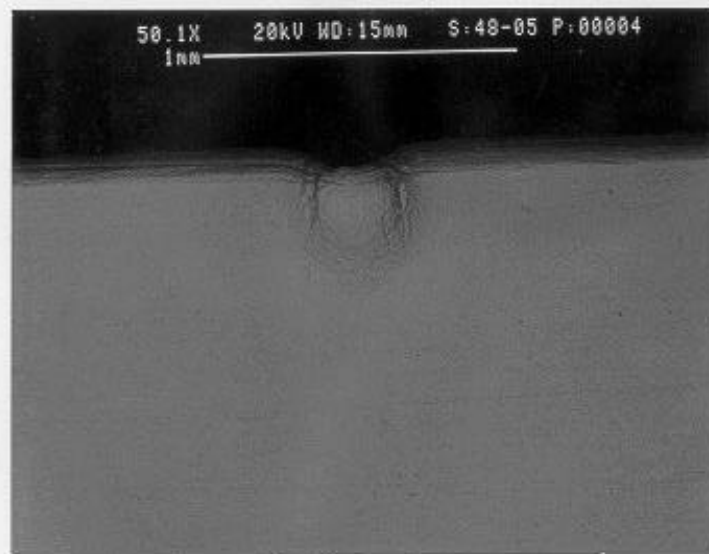
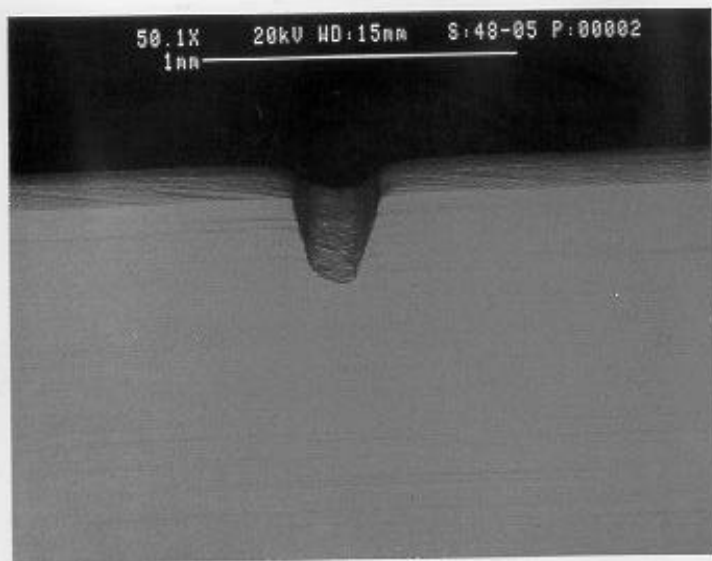


view #2

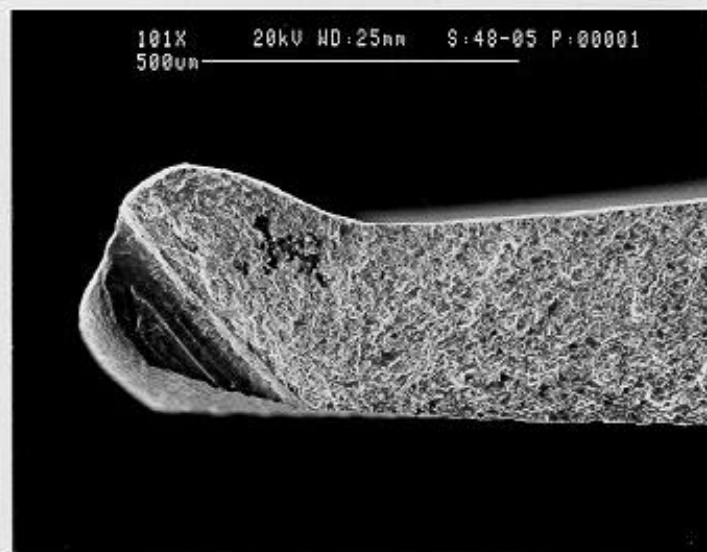
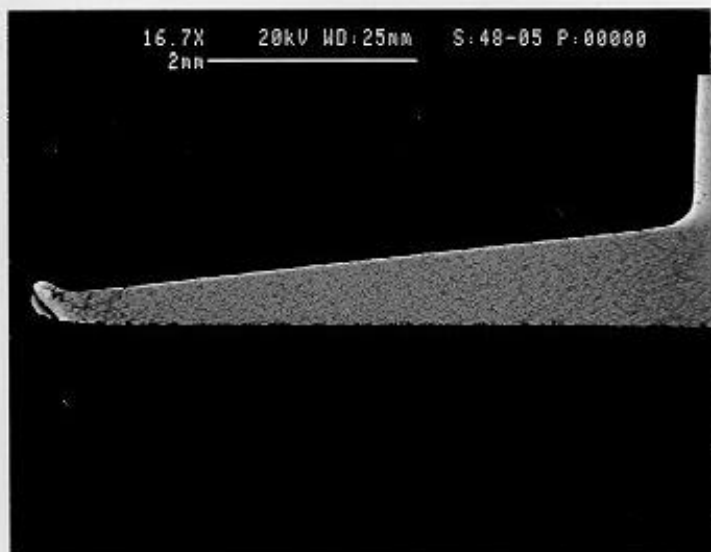


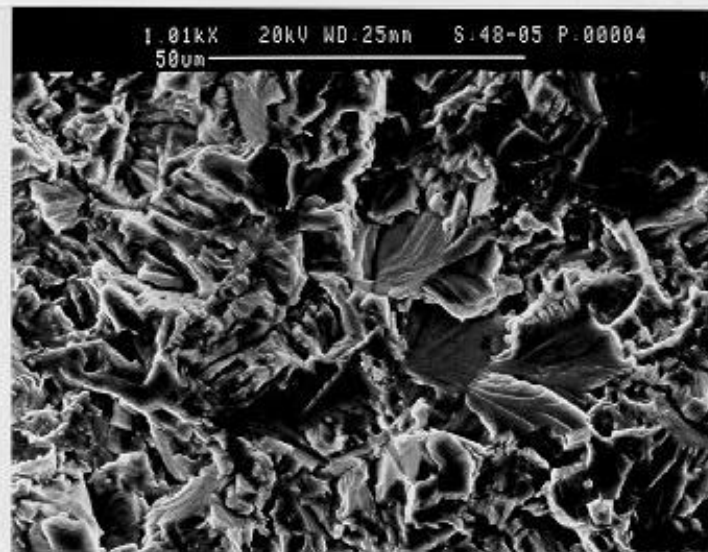
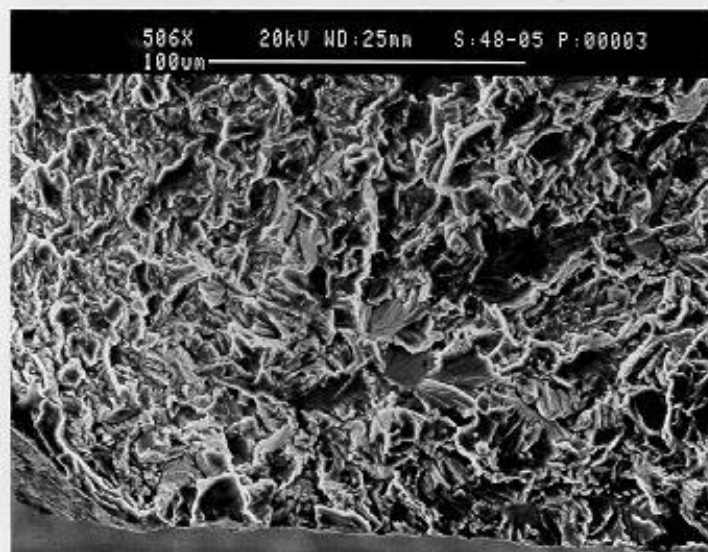
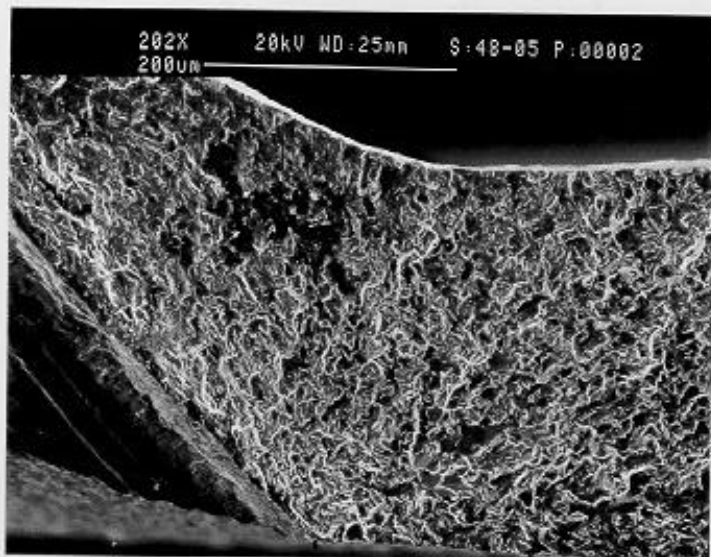
view #1

5C-46



5C-47





Specimen: 11-S7, Sharp Leading Edge

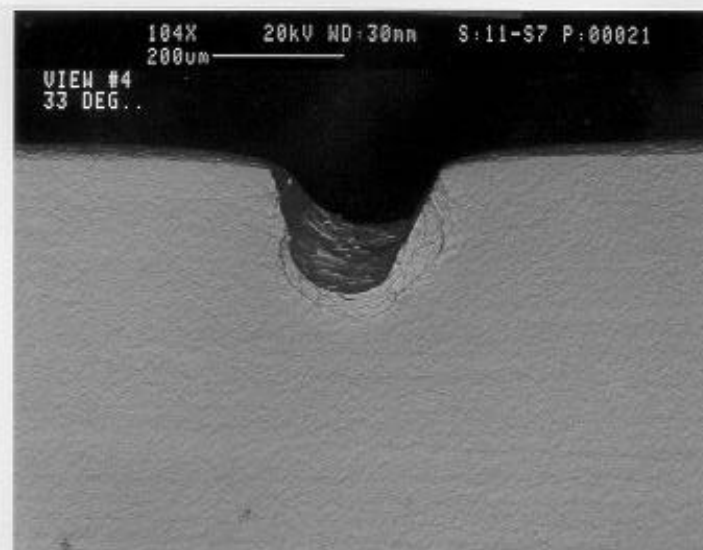
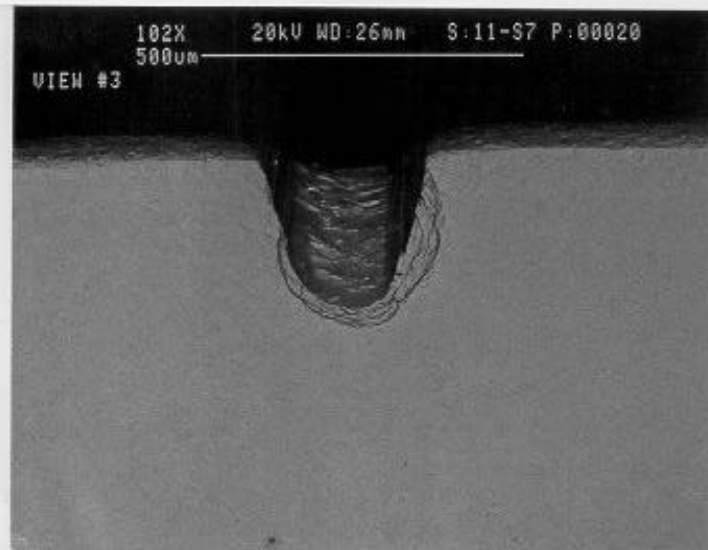
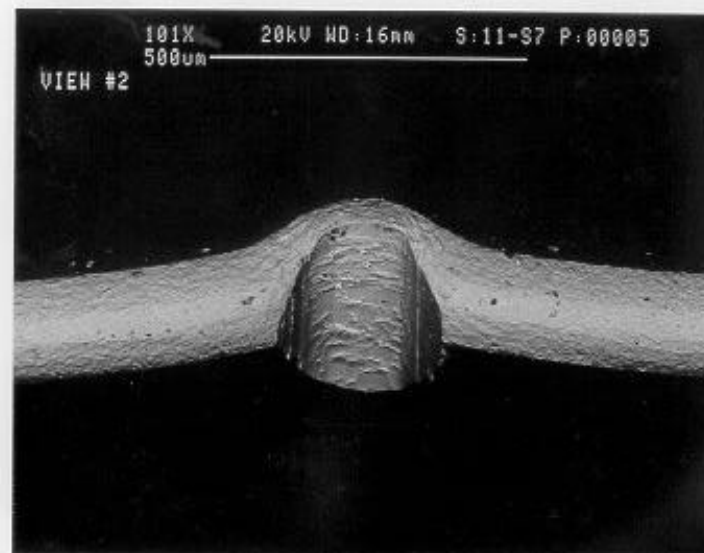
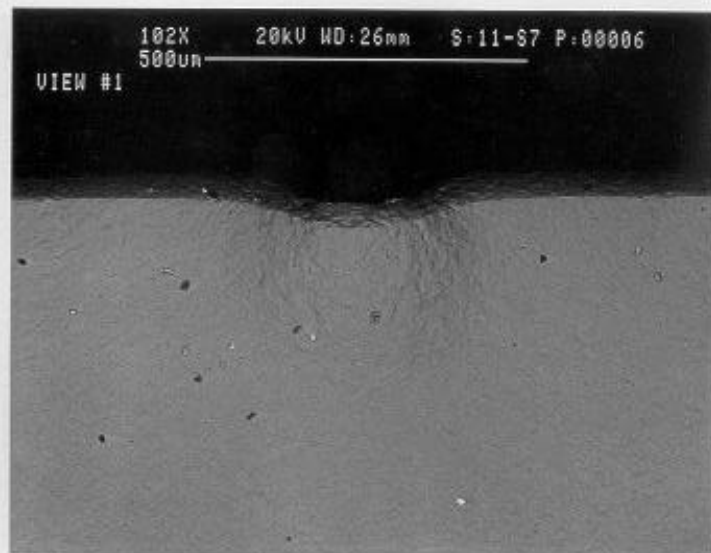
Simulated FOD Conditions: Solenoid Gun, 30° Impact angle, 0.005 inch tip radius, Low Damage Level.

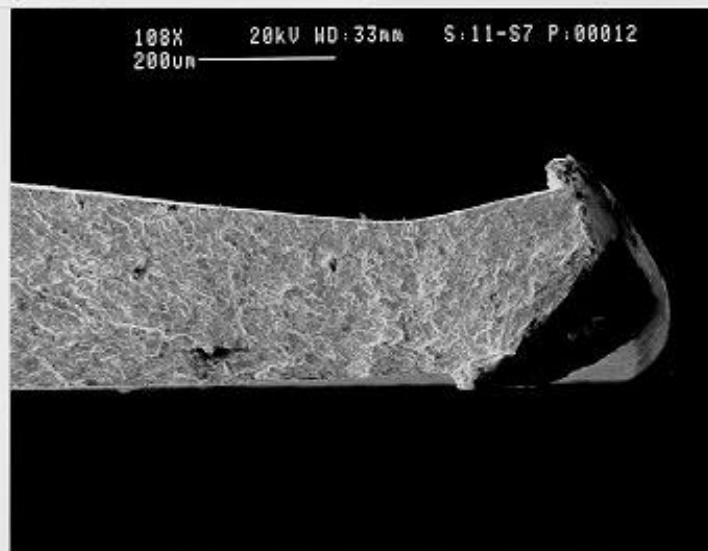
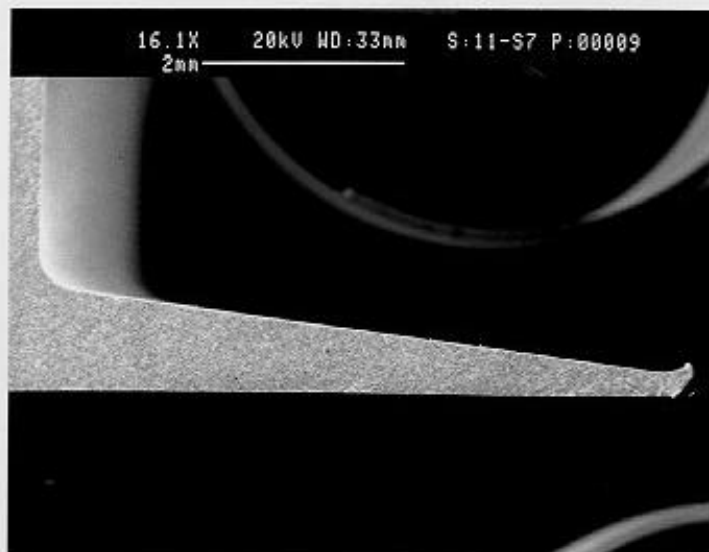
WMT&R Report Number: 9-00933

Test Description: The test was run at an initial load of 483 pounds, R-ratio of 0.5, and 30 Hz. The load was increased by 10% after every 1,000,000 cycles until failure.

Results: Crack nucleation occurred at 855.7 pounds. The final cycles were 6,232,456.

Attached Data: Micrographs of FOD'ed specimen, Load versus cycle plot, Position versus cycle plot, Micrographs of Failed specimens.





Specimen: 70-04, Sharp Leading Edge

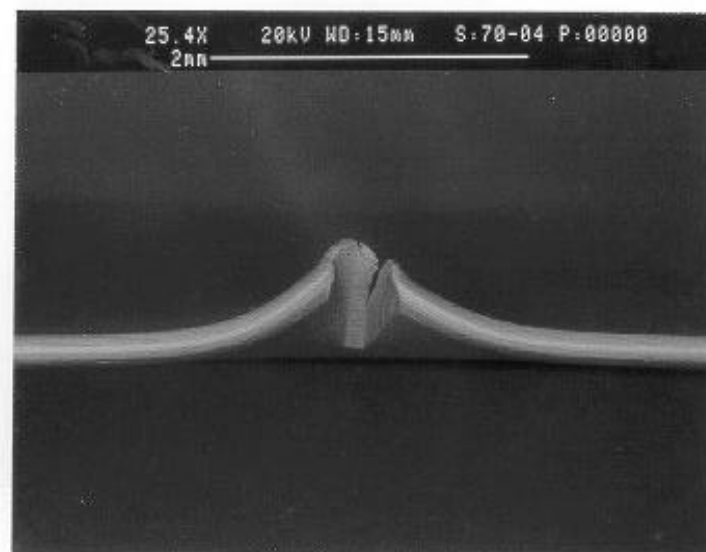
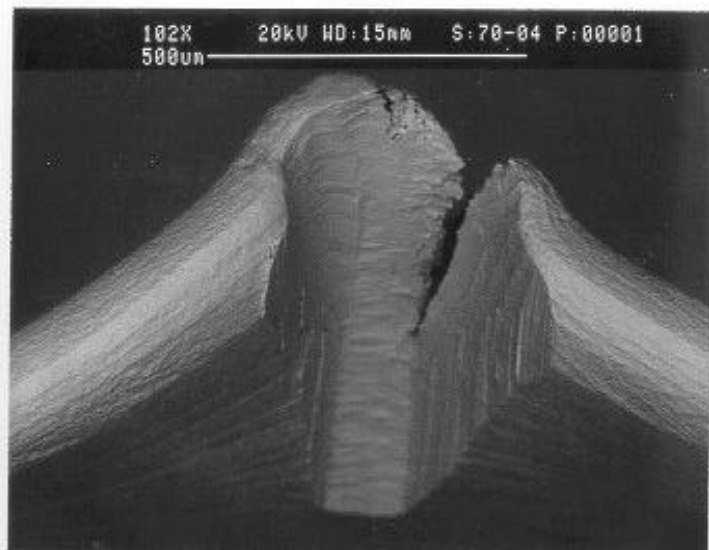
Simulated FOD Conditions: Solenoid Gun, 30° Impact angle, 0.005 inch tip radius, High Damage Level.

WMT&R Report Number: 8-15597

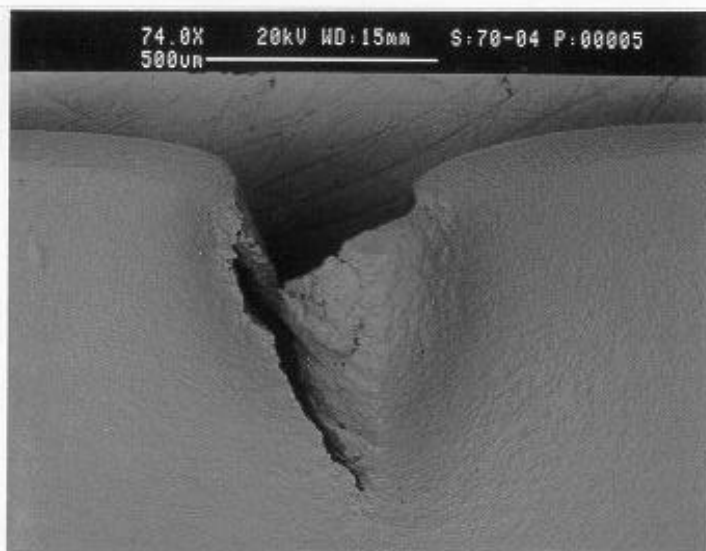
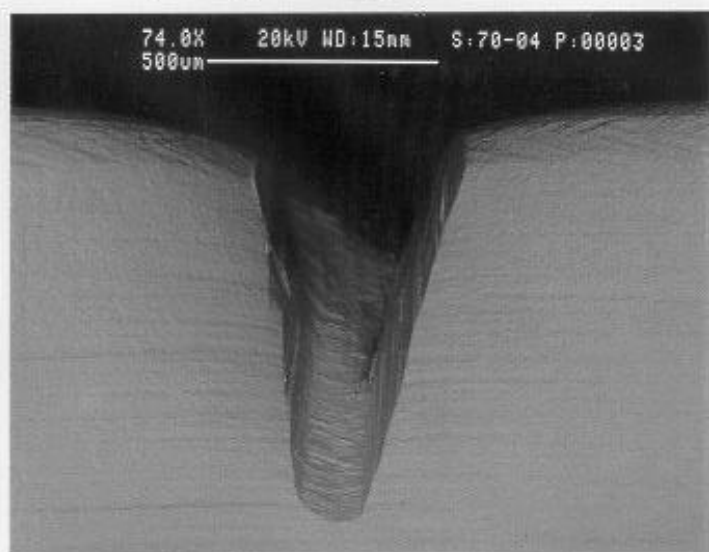
Test Description: The test was run at an initial load of 300 pounds, R-ratio of 0.5, and 30 Hz. The load was increased by 10% after every 1,000,000 cycles until failure.

Results: Crack nucleation occurred at 585 pounds. The final cycles were 7,455,549.

Attached Data: Micrographs of FOD'ed specimen, Load versus cycle plot, Position versus cycle plot, Micrographs of Failed specimens.

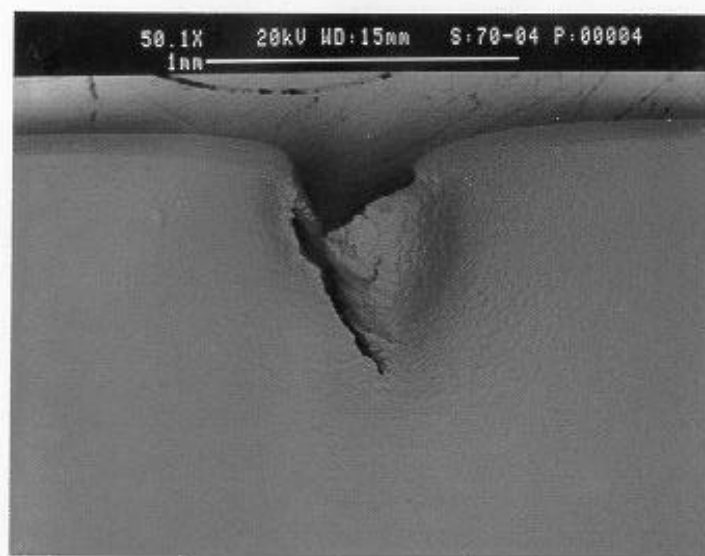
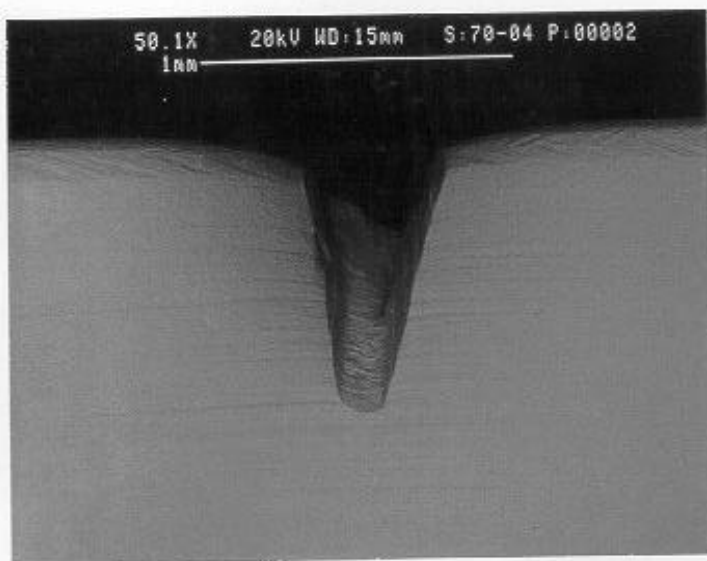


view #2

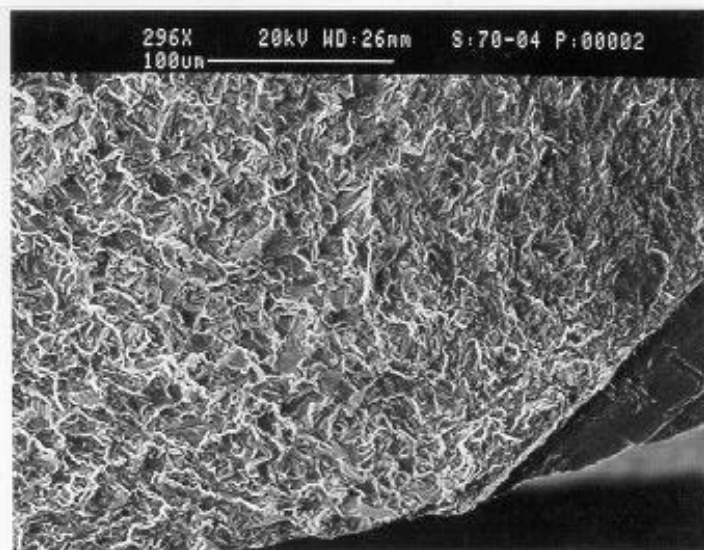
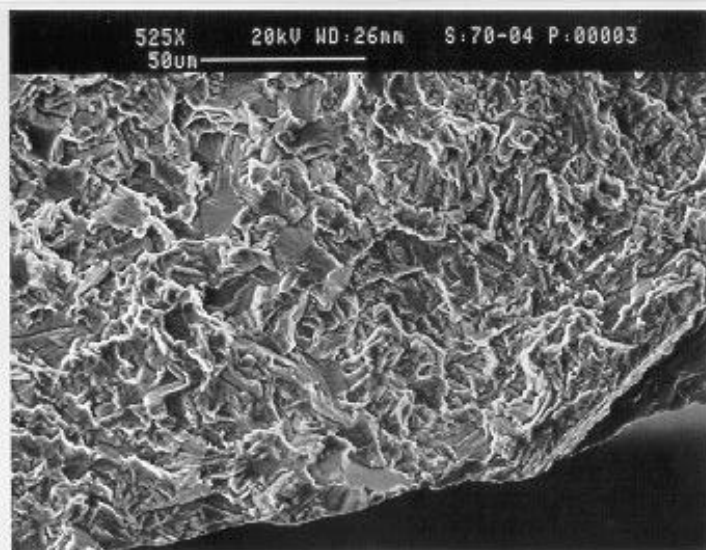
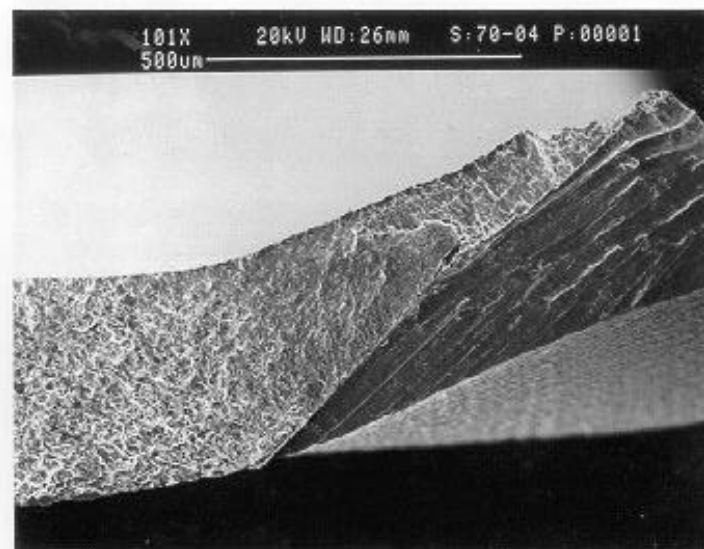
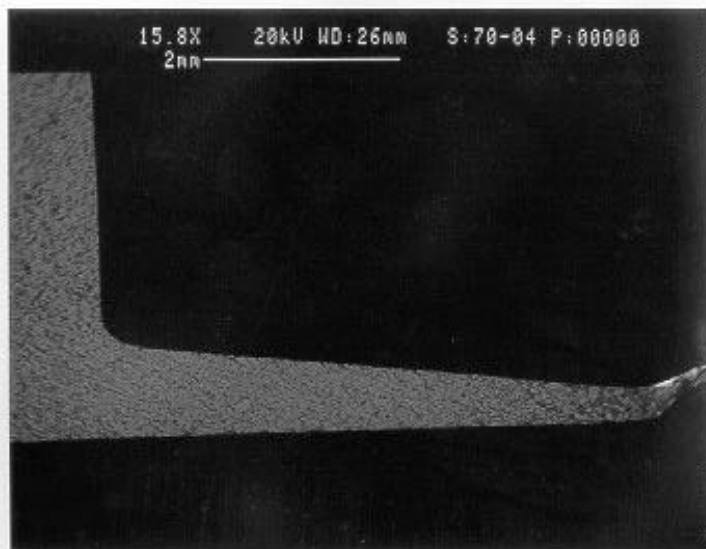


view #1

5C-54



view #1



Specimen: 75-04, Sharp Leading Edge

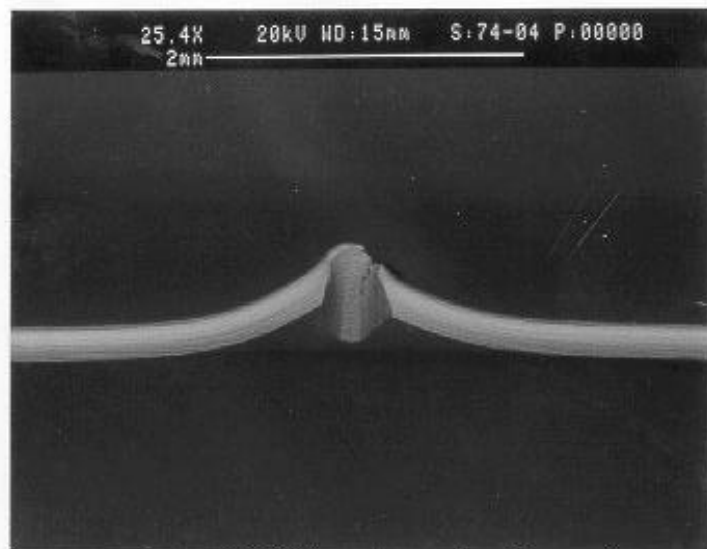
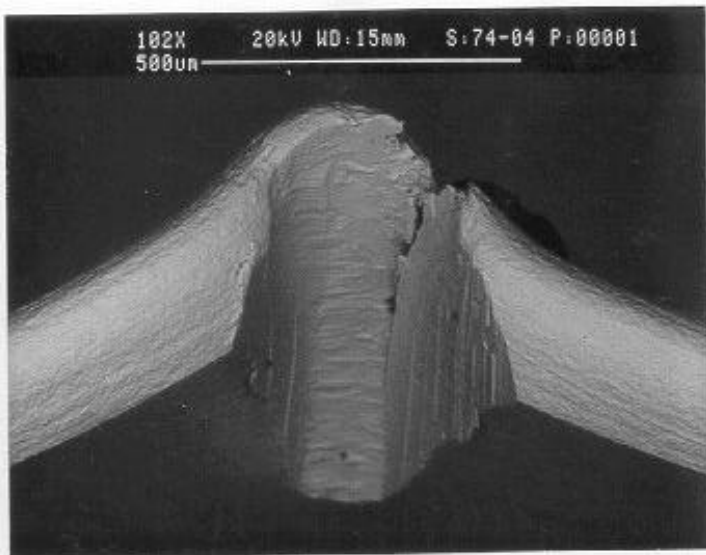
Simulated FOD Conditions: Solenoid Gun, 30° Impact angle, 0.005 inch tip radius, High Damage Level.

WMT&R Report Number: 8-15597

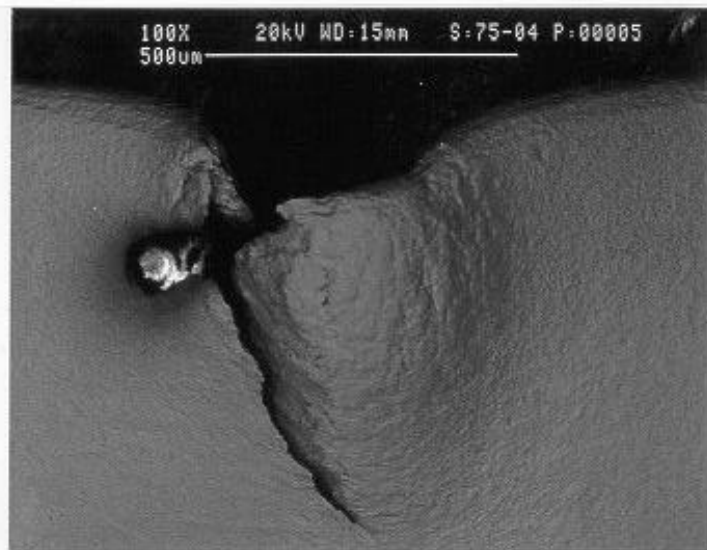
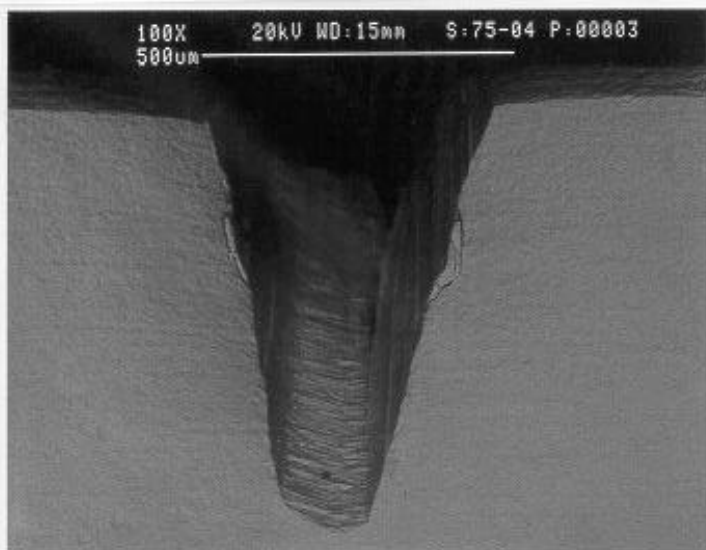
Test Description: The test was run at an initial load of 300 pounds, R-ratio of 0.5, and 30 Hz. The load was increased by 10% after every 1,000,000 cycles until failure.

Results: Crack nucleation occurred at 643 pounds. The final cycles were 8,417,488.

Attached Data: Micrographs of FOD'ed specimen, Load versus cycle plot, Position versus cycle plot, Micrographs of Failed specimens.

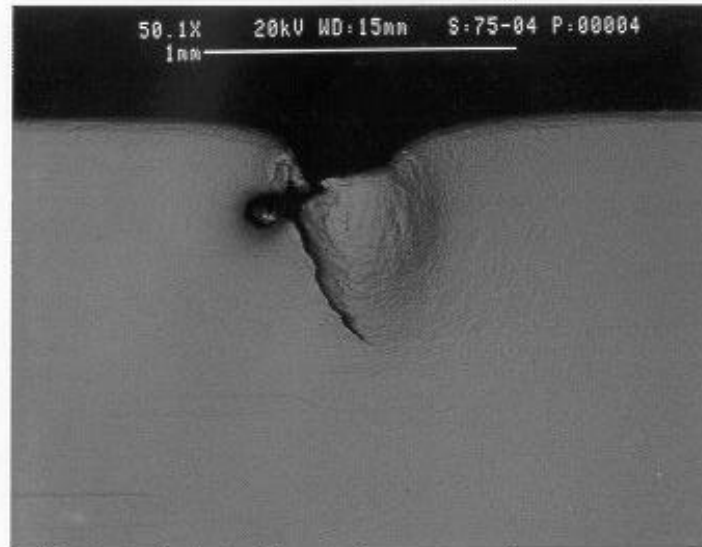
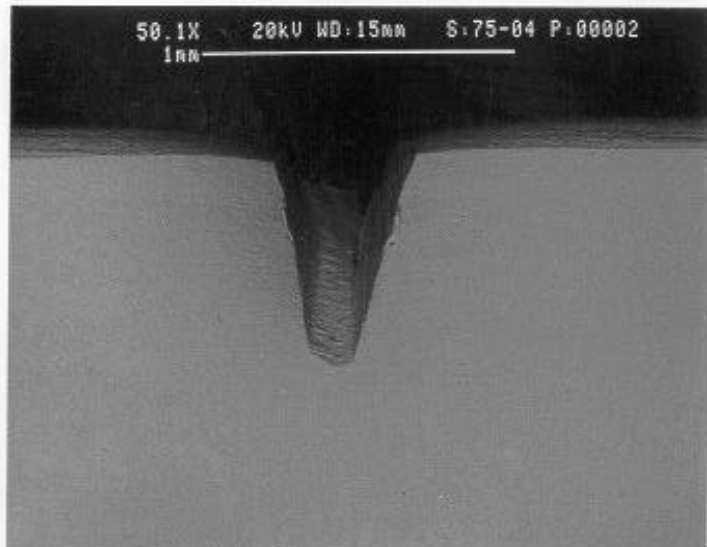


view #2

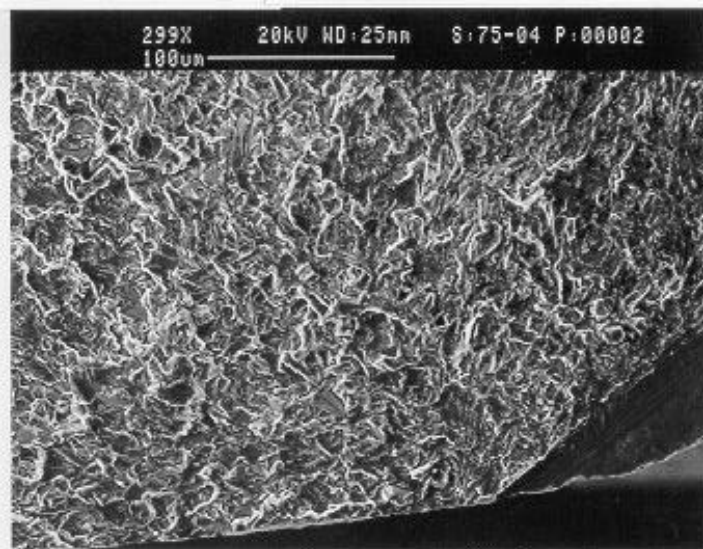
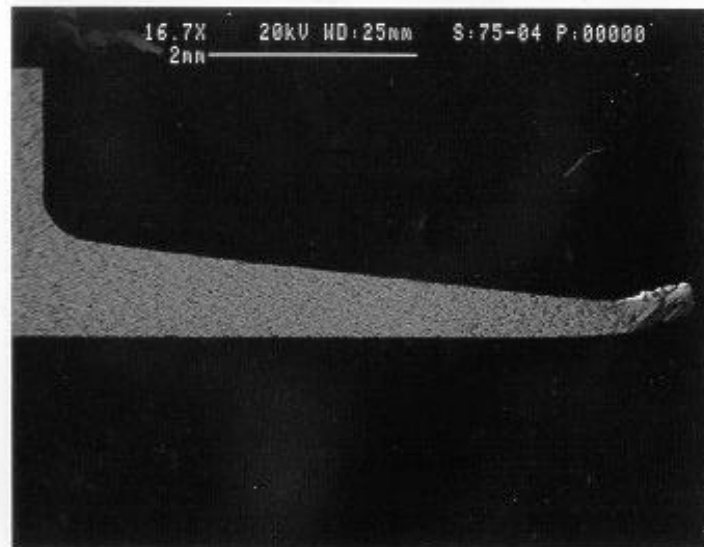
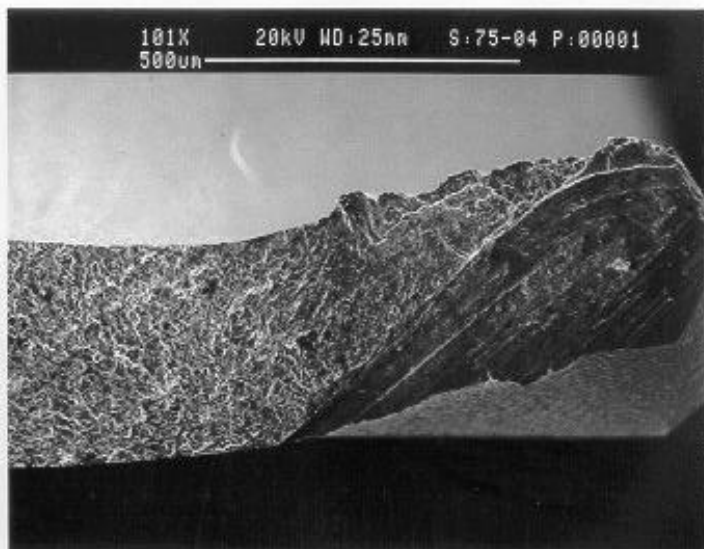


view #1

5C-58



view #1



Specimen: 36-S2, Sharp Leading Edge

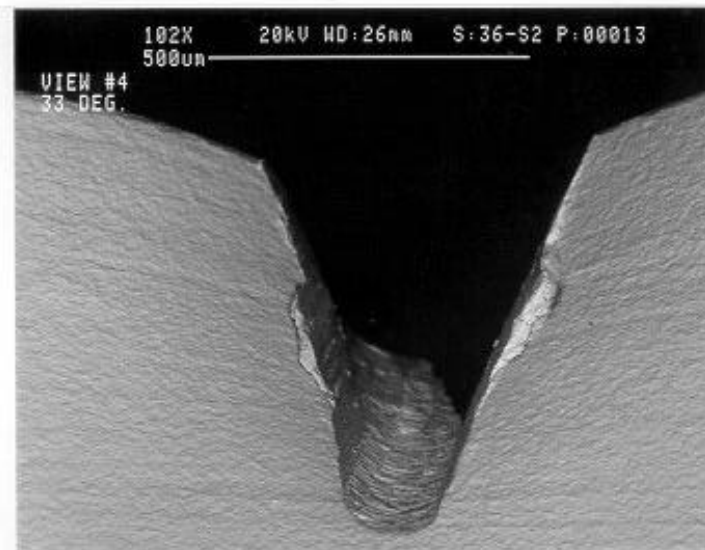
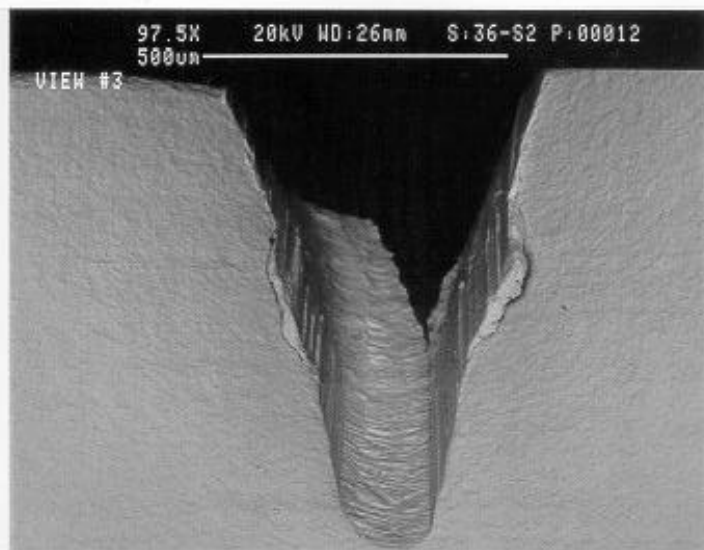
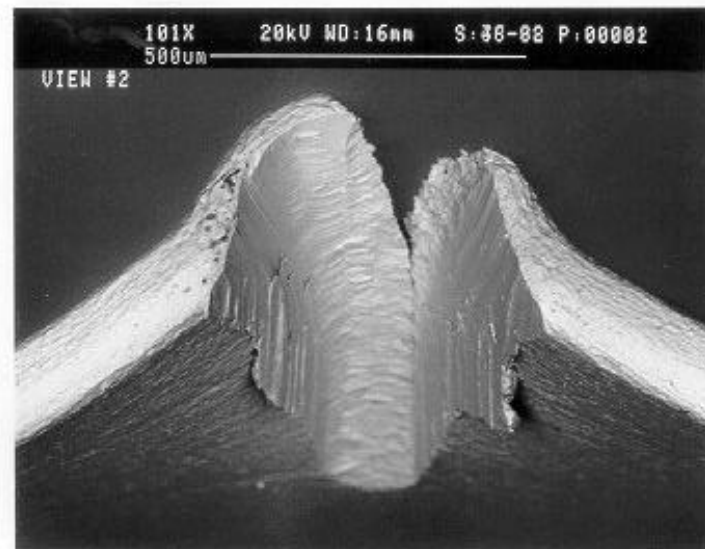
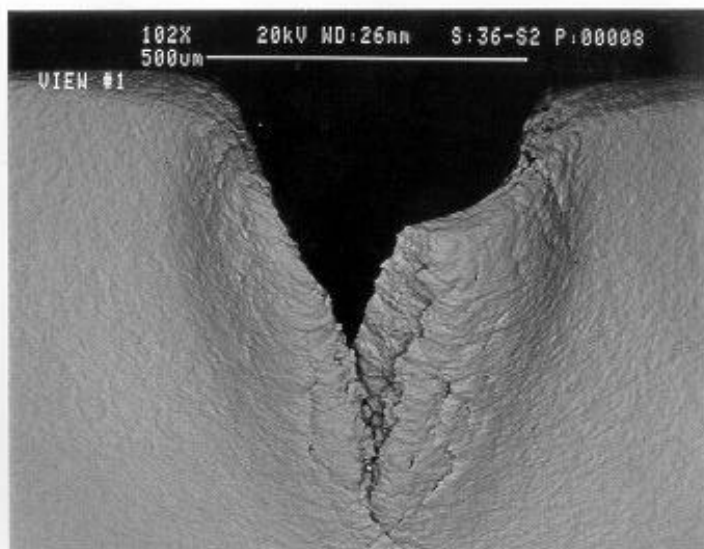
Simulated FOD Conditions: Solenoid Gun, 30° Impact angle, 0.005 inch tip radius, High Damage Level.

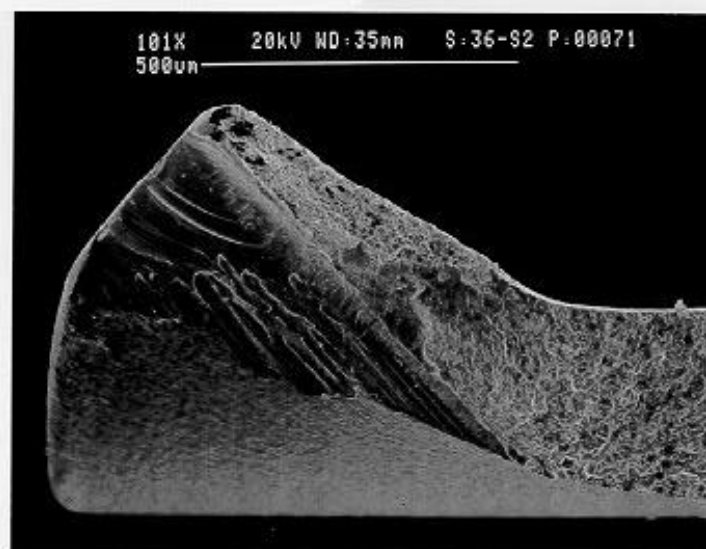
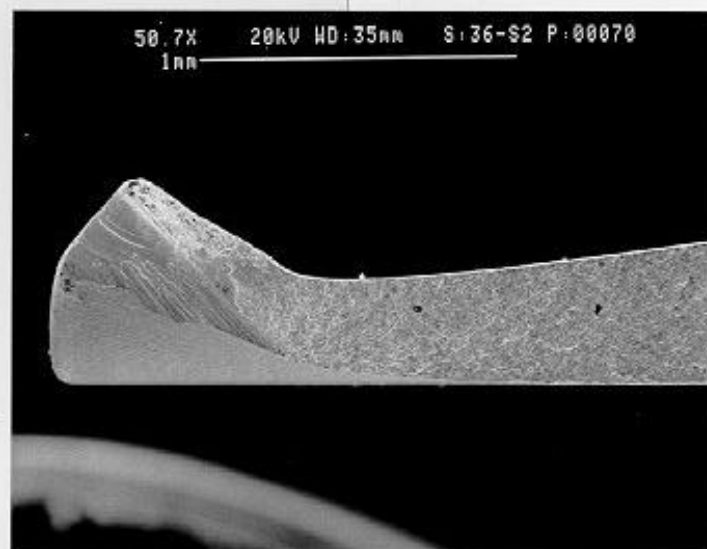
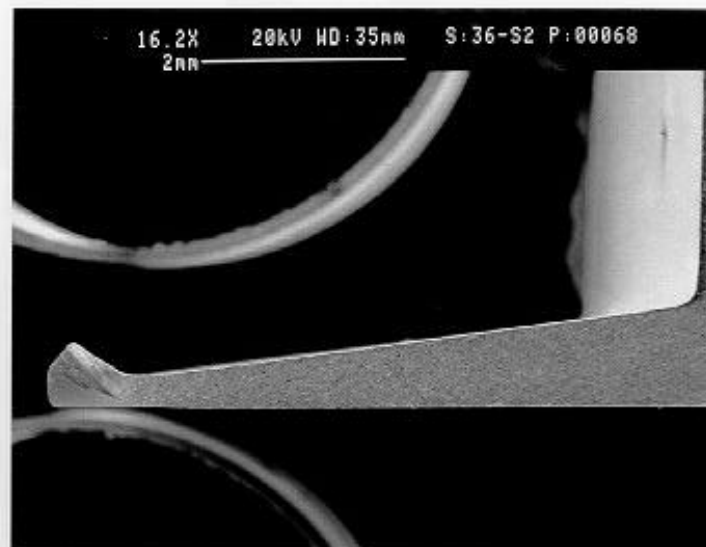
WMT&R Report Number: 9-00933

Test Description: The test was run at an initial load of 439 pounds, R-ratio of 0.5, and 30 Hz. The load was increased by 10% after every 1,000,000 cycles until failure.

Results: Crack nucleation occurred at 855.7 pounds. The final cycles were 7,156,818.

Attached Data: Micrographs of FOD'ed specimen, Load versus cycle plot, Position versus cycle plot, Micrographs of Failed specimens.





Specimen: 11-S5, Sharp Leading Edge

Simulated FOD Conditions: Solenoid Gun, 30° Impact angle, 0.005 inch tip radius, High Damage Level.

WMT&R Report Number: 9-00933

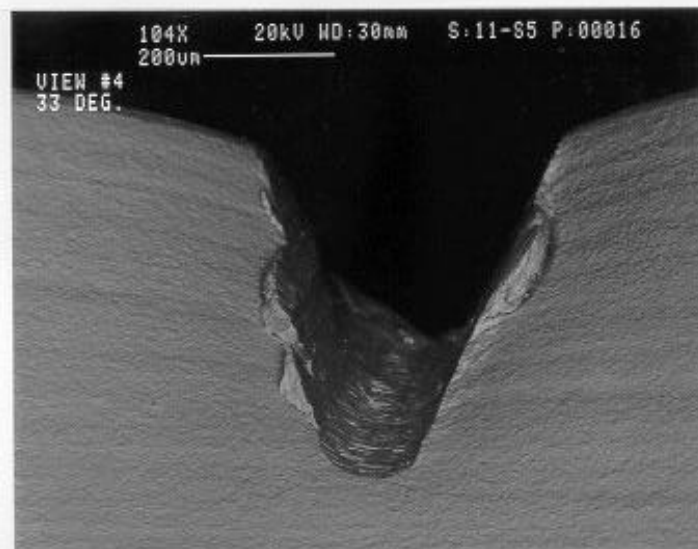
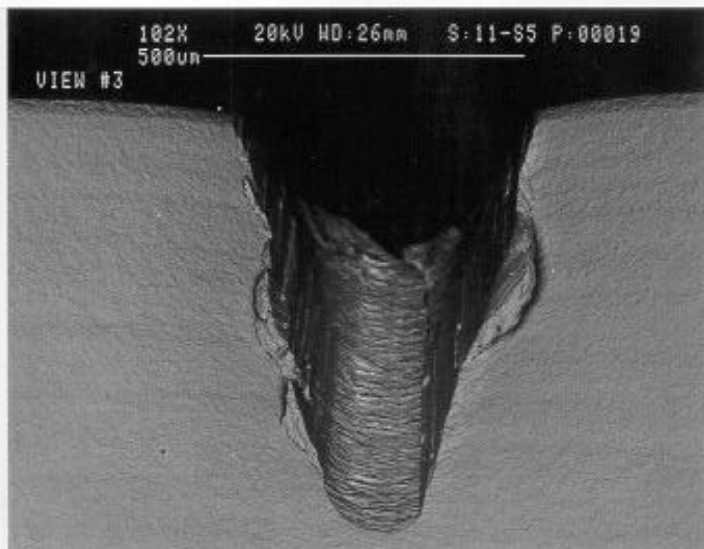
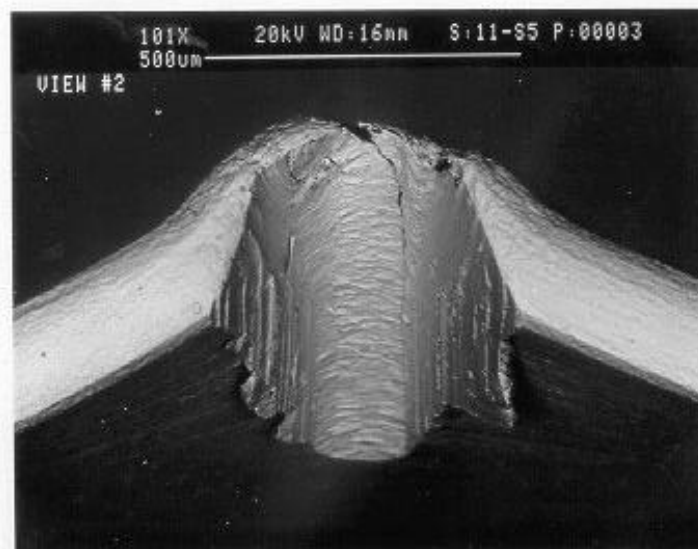
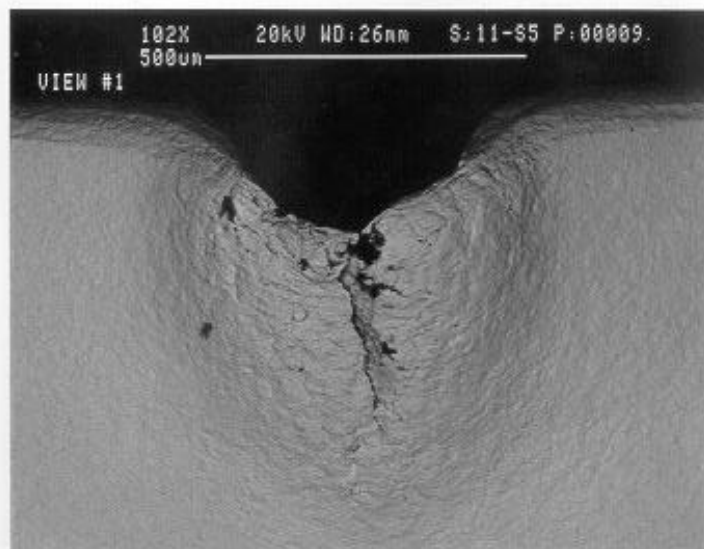
Test Description: The test was run at an initial load of 439 pounds, R-ratio of 0.5, and 30 Hz. The load was increased by 10% after every 1,000,000 cycles until failure. The specimen had welded EPD leads attached to monitor potential drop.

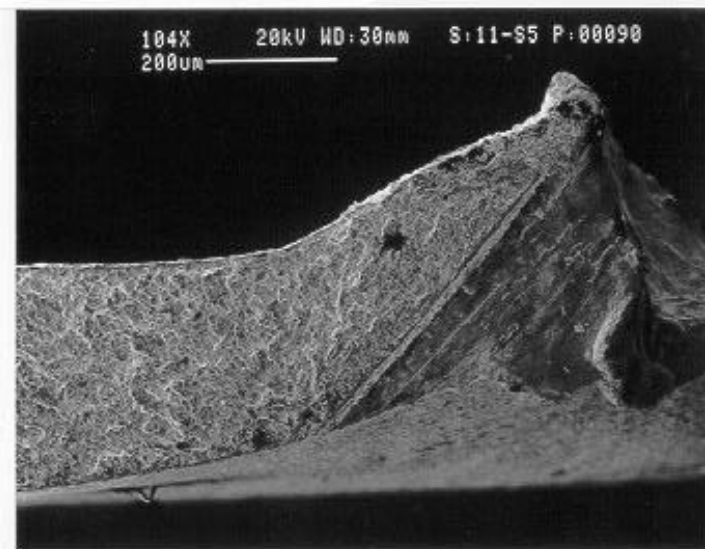
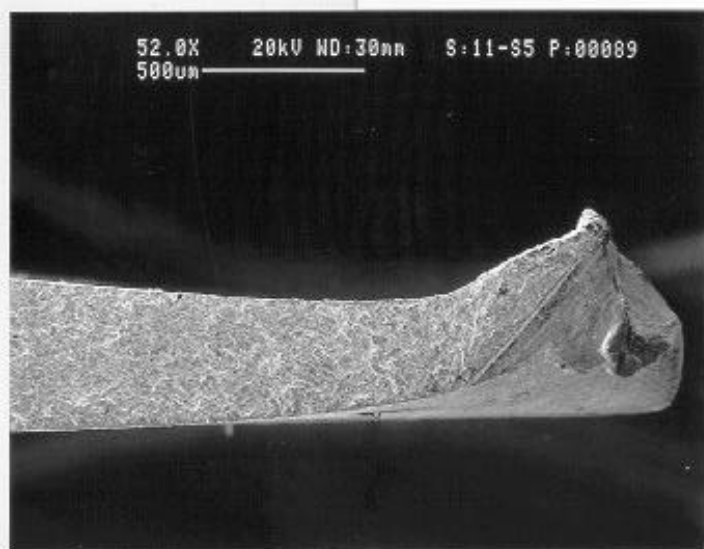
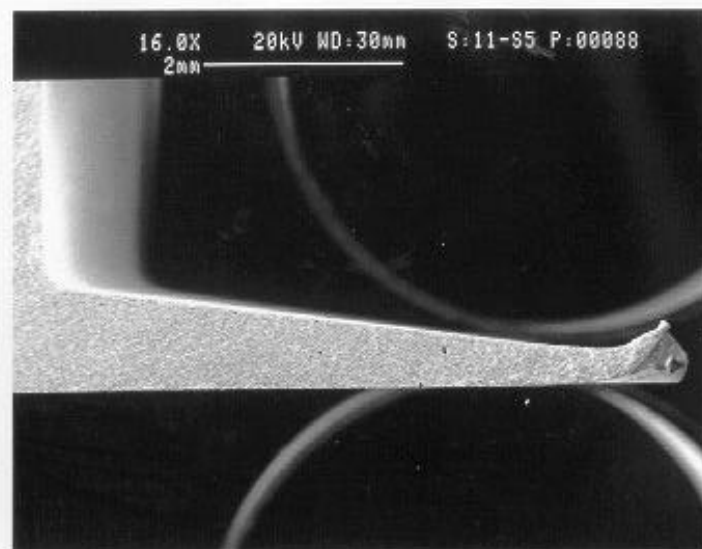
Results: Crack nucleation occurred at 482.9 pounds. The final cycle count was not reported. However, the cycle count is slightly greater than 1,441,250 based on the EPD plots. EPD data:

U/Uo	Cycles	Heat Tint Data	Surface Crack Length from Heat Tint (in)
1.0072	1,123,468	750°F @ 5 Hours	Not Visible
1.0509	1,238,041	1256°F @ 3 Hours	0.0140
1.2018	1,293,320	570°F @ 3 Hours	0.0349

The second heat tint was inadvertently conducted at 680°C instead of 680°F. Therefore, the first heat tint was not visible.

Attached Data: Micrographs of FOD, U/Uo versus cycles, Micrographs of Failed specimens.





Specimen: 48-06, Sharp Leading Edge

Simulated FOD Conditions: Solenoid Gun, 30° Impact angle, 0.005 inch tip radius, High Damage Level.

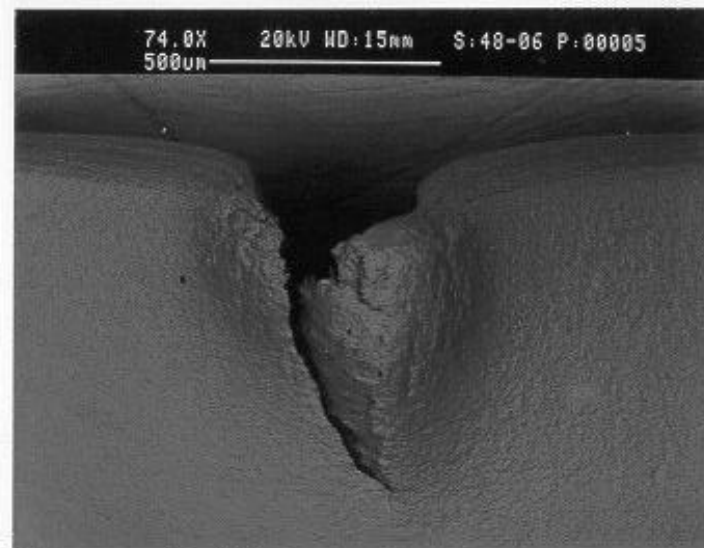
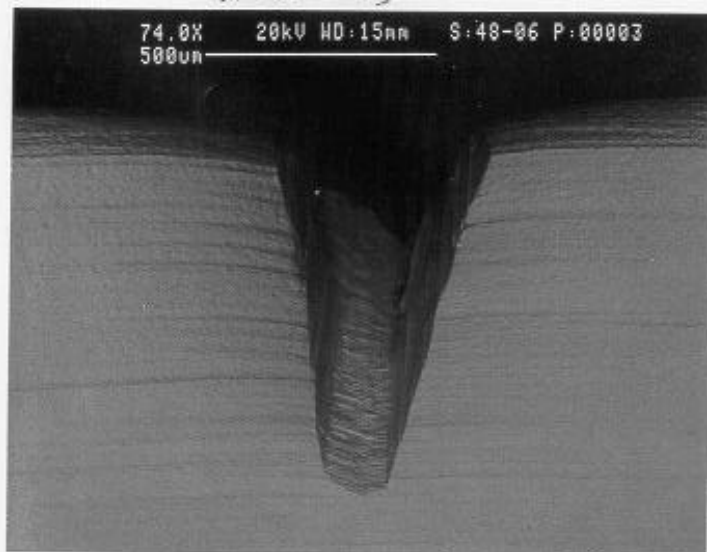
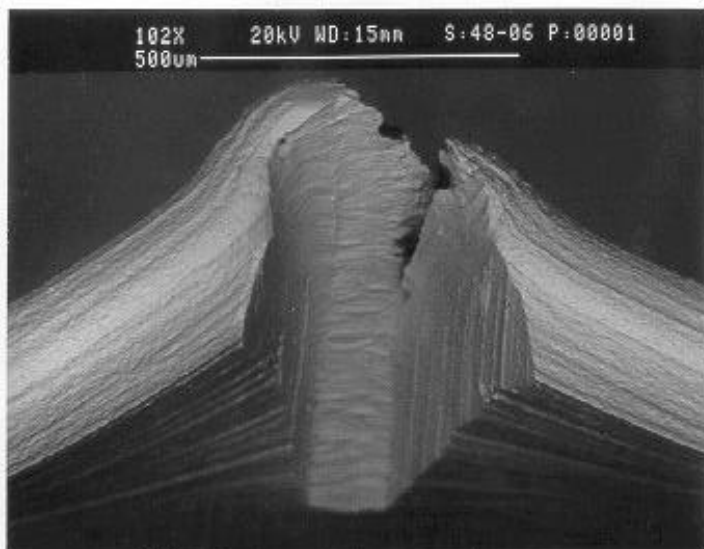
WMT&R Report Number: 8-15597

Test Description: The test was run at an initial load of 300 pounds, R-ratio of 0.5, and 30 Hz. The load was increased by 10% after every 1,000,000 cycles until failure. The specimen had welded EPD leads attached to monitor potential drop.

Results: Crack nucleation occurred at 483.2 pounds. The final cycles were 6,030,190. EPD data:

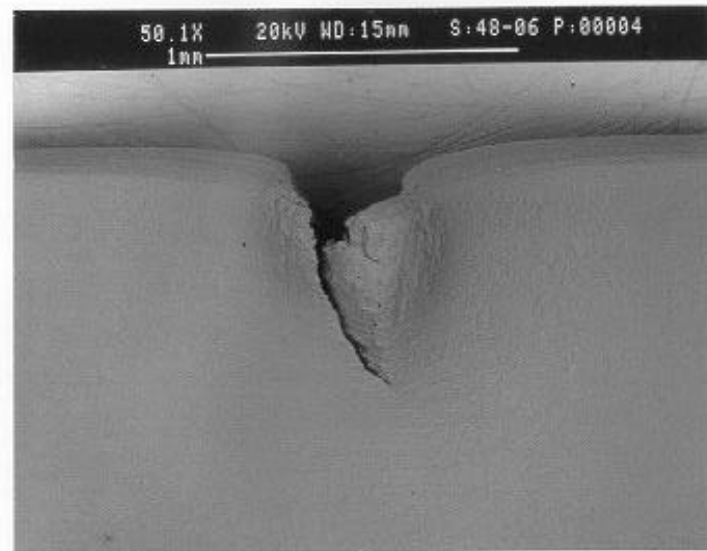
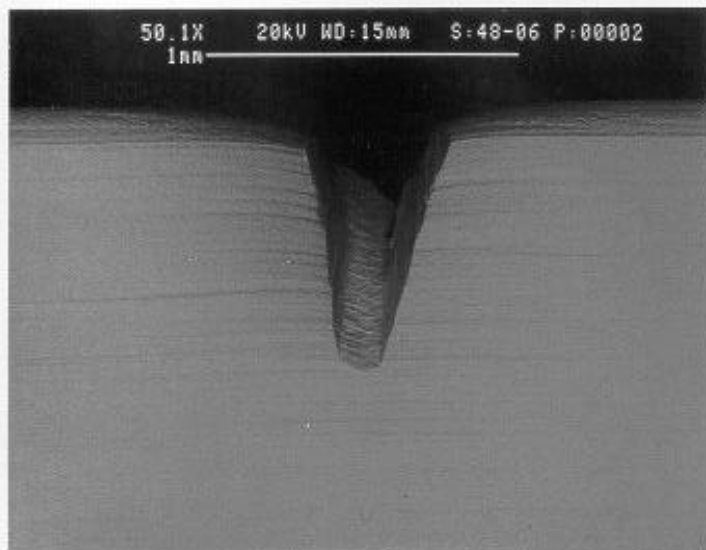
U/Uo	Cycles	Heat Tint Data	Surface Crack Length from Heat Tint (in)
1.7359	5,751,539	750°F @ 5 Hours	0.084
2.0458	5,752,430	680°F @ 3 Hours	0.100

Attached Data: Micrographs of FOD, U/Uo versus cycles, Micrographs of Failed specimens.

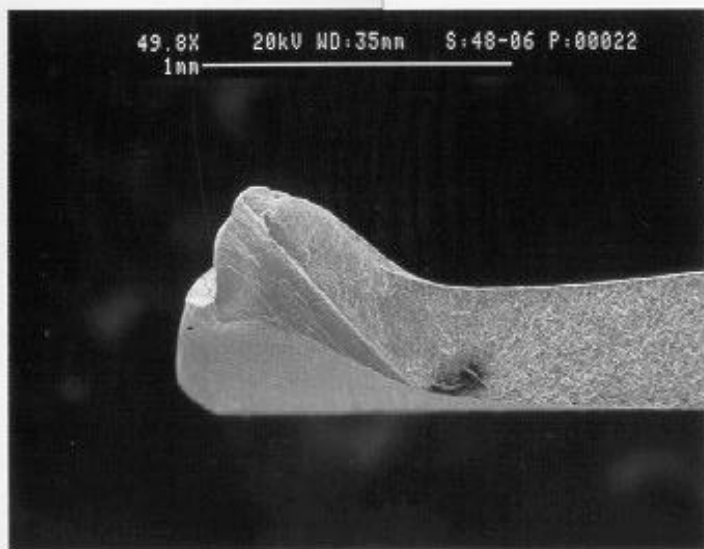
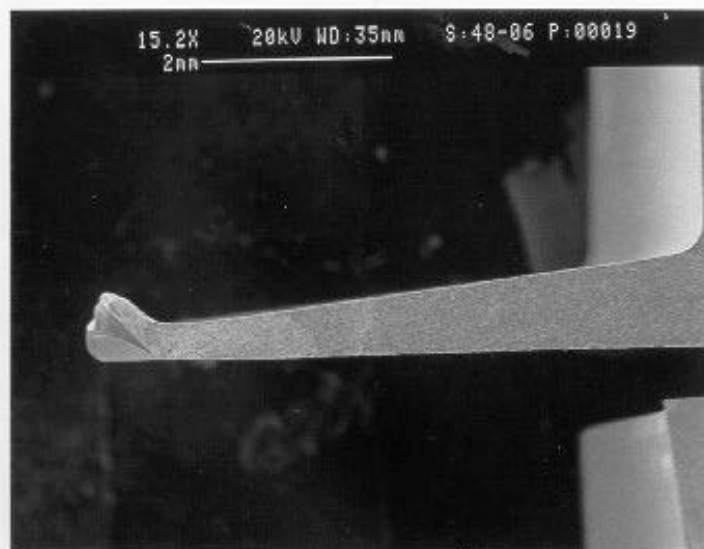


View #1

5C-68



view #1



Specimen: 75-03, Sharp Leading Edge

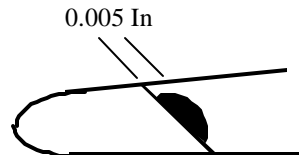
Simulated FOD Conditions: Solenoid Gun, 30° Impact angle, 0.005 inch tip radius, High Damage.

WMT&R Report Number: 9-00933

Test Description: The test was run at an initial load of 439 pounds, R-ratio of 0.5, and 30 Hz. The load was increased by 10% after every 1,000,000 cycles until failure. The specimen had welded EPD leads attached to monitor potential drop.

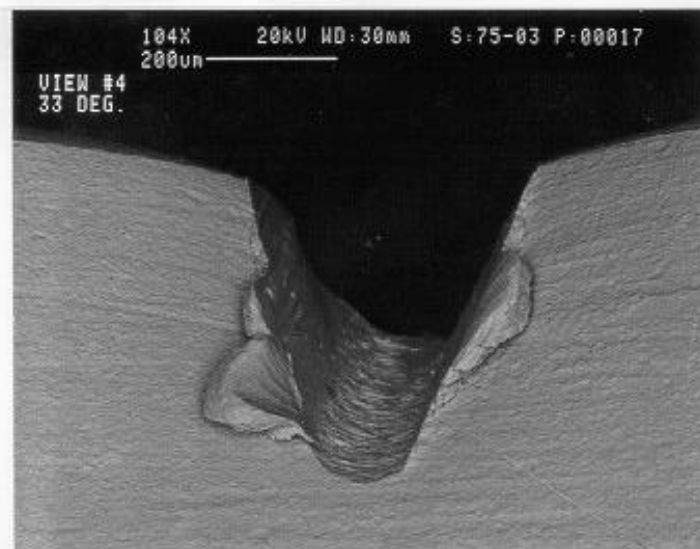
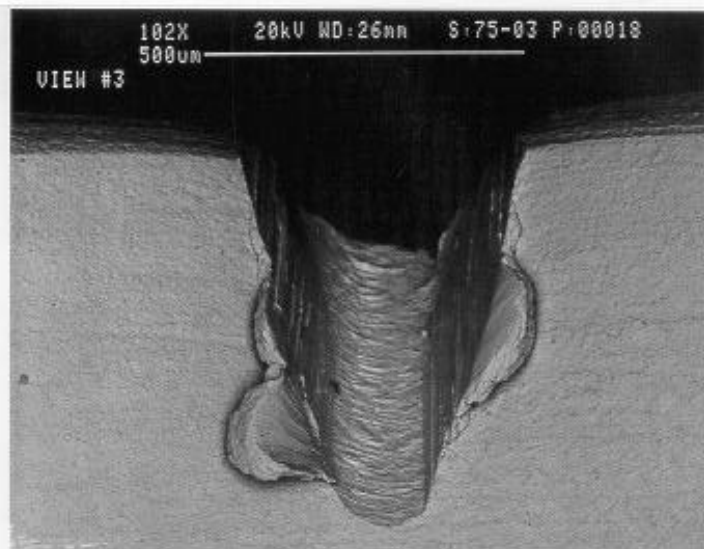
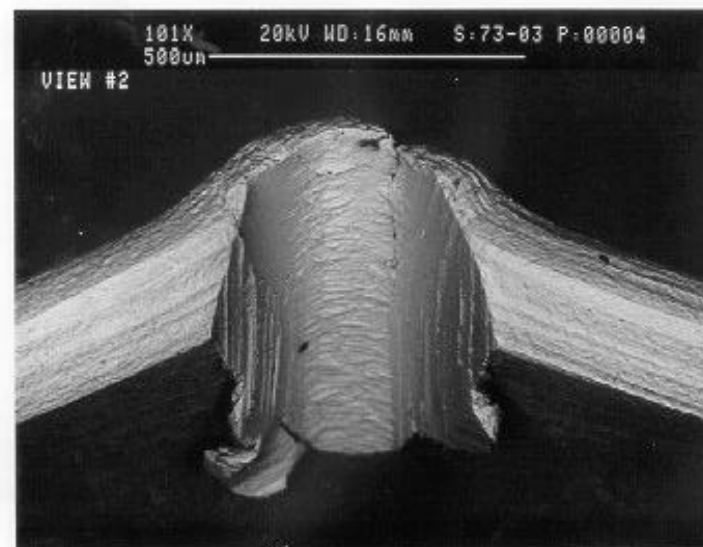
Results: Crack nucleation occurred at 531.2 pounds. The final cycle count was not reported. However, the cycle count is slightly greater than 2,576,945 based on the EPD plots. EPD data:

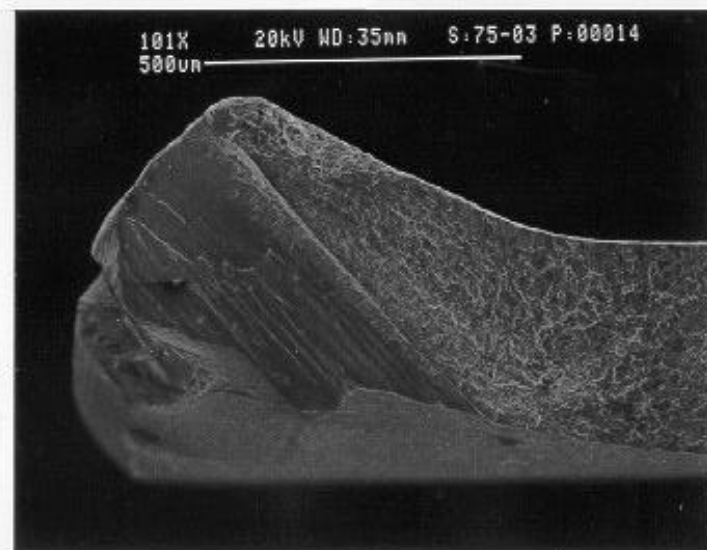
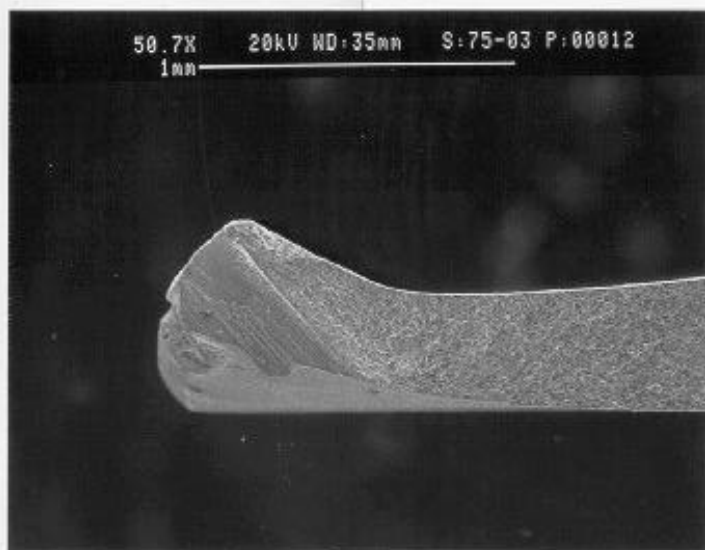
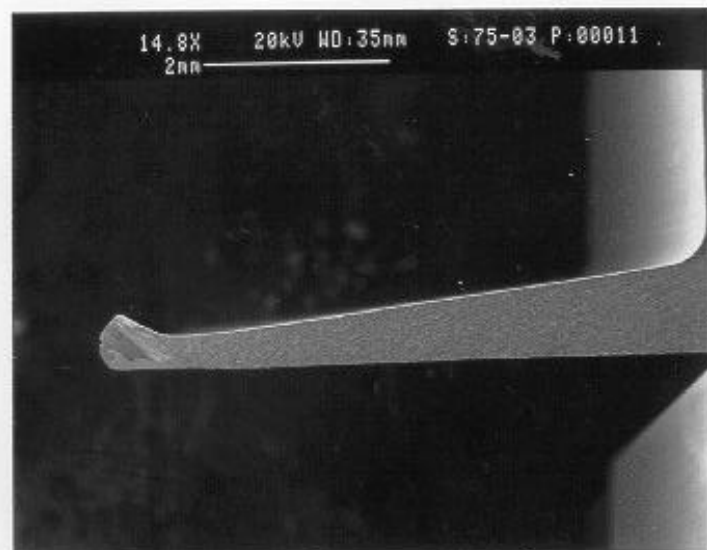
U/U _o	Cycles	Heat Tint Data	Crack Length from Heat Tint (in)
1.0150	2,197,302	750°F @ 5 Hours	0.0050
1.0496	2,288,071	680°F @ 3 Hours	0.0185
1.2003	2,351,428	570°F @ 3 Hours	0.0406



The first heat tint is as shown:

Attached Data: Micrographs of FOD, U/U_o versus cycles, Position versus cycle plot, and Micrographs of Failed specimens.





Specimen: 75-05, Sharp Leading Edge

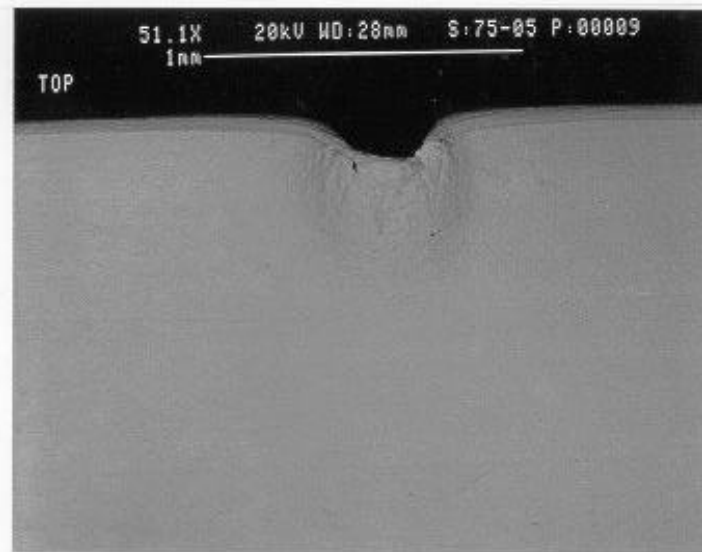
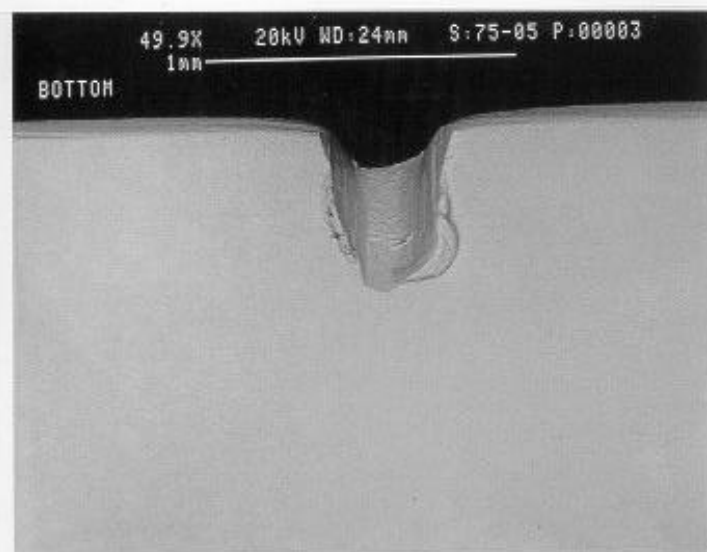
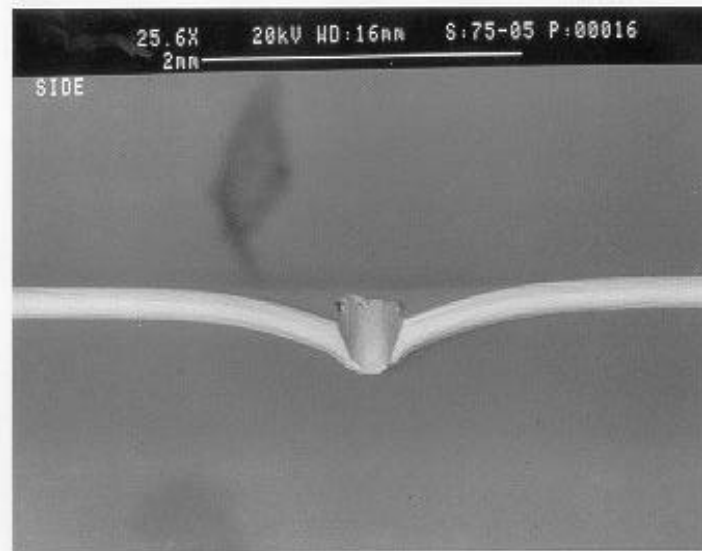
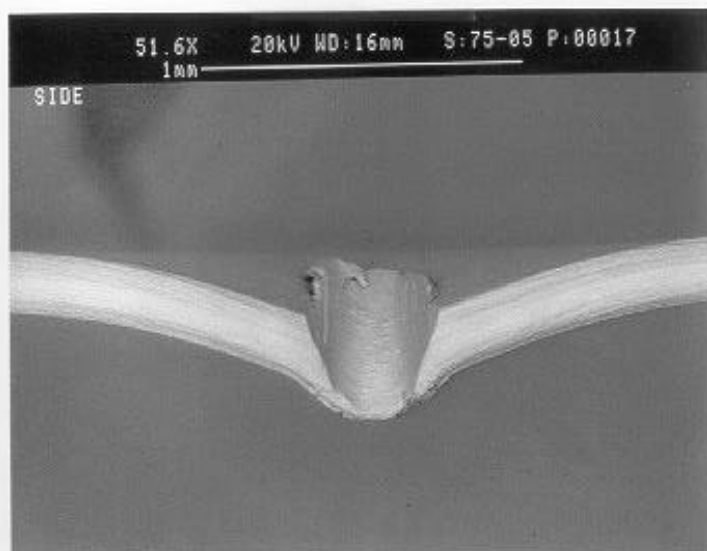
Simulated FOD Conditions: Solenoid Gun, 30° Impact angle, 0.005 inch tip radius, High Damage Level. Stress Relief Cycle (1300°F / 1 Hour with Ta wrap) after FOD.

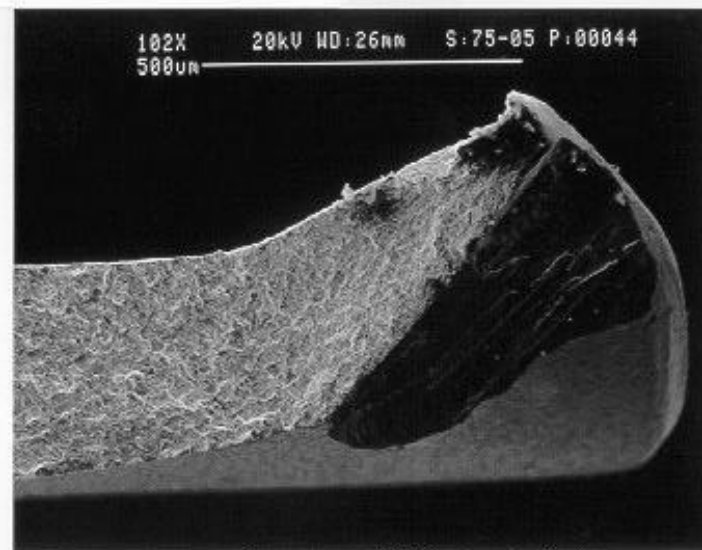
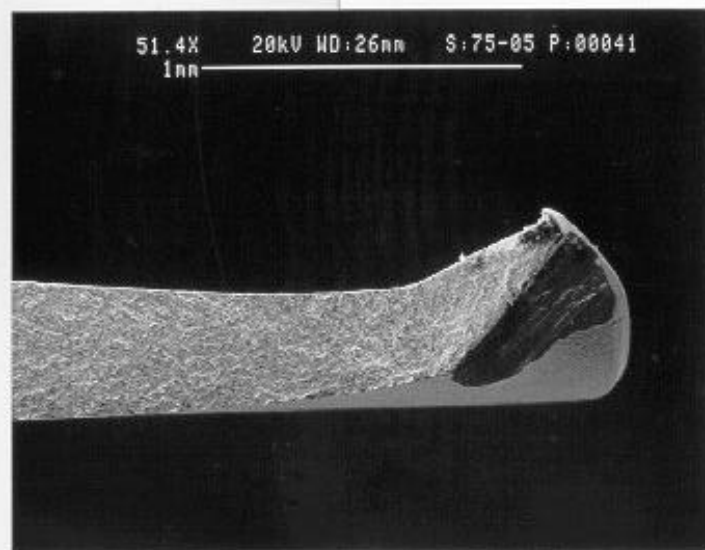
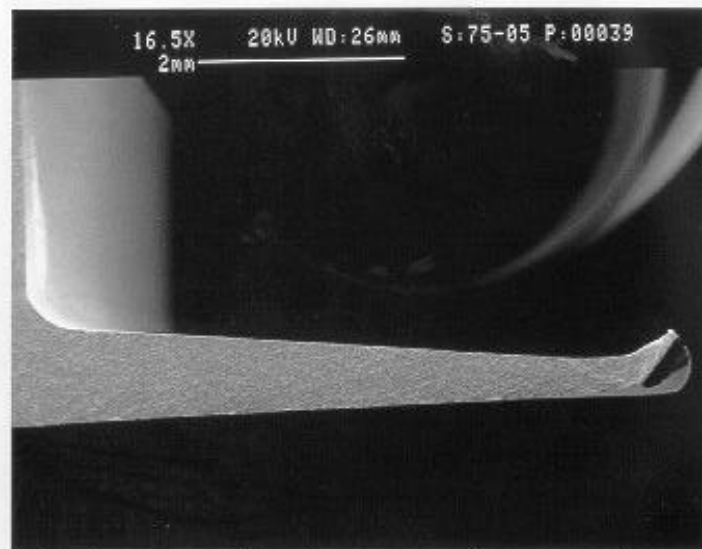
WMT&R Report Number: 9-05614

Test Description: The test was run at an initial load of 439 pounds, R-ratio of 0.5, and 30 Hz. The load was increased by 10% after every 1,000,000 cycles until failure.

Results: Crack nucleation occurred at 643 pounds. The final cycles were 4,260,355.

Attached Data: Micrographs of FOD'ed specimen, Load versus cycle plot, Position versus cycle plot, Micrographs of Failed specimens.





Specimen: 11-S8, Sharp Leading Edge

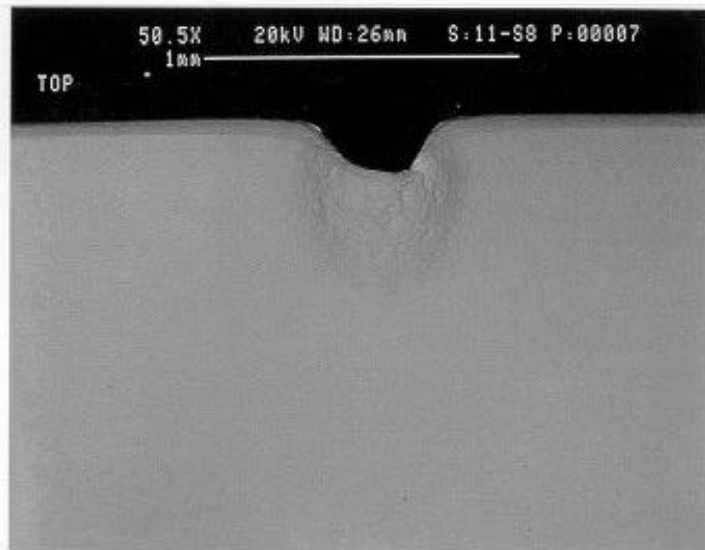
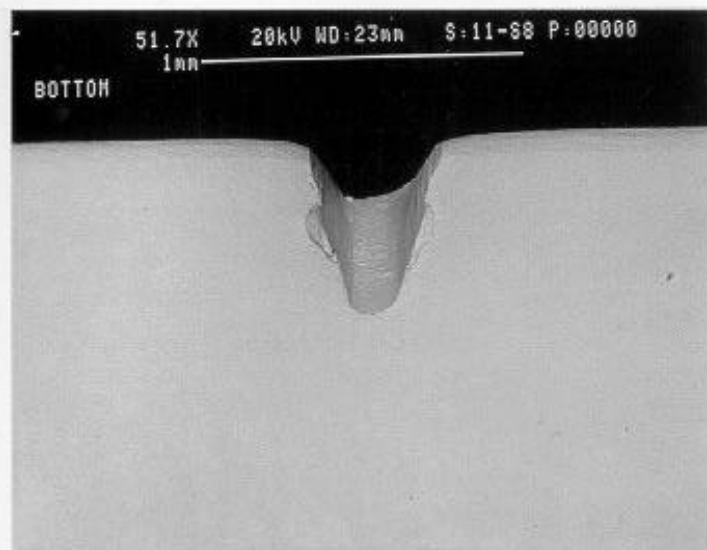
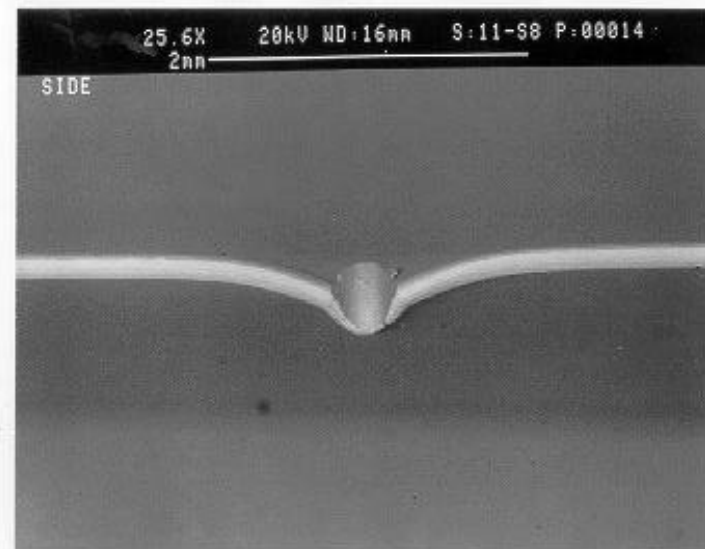
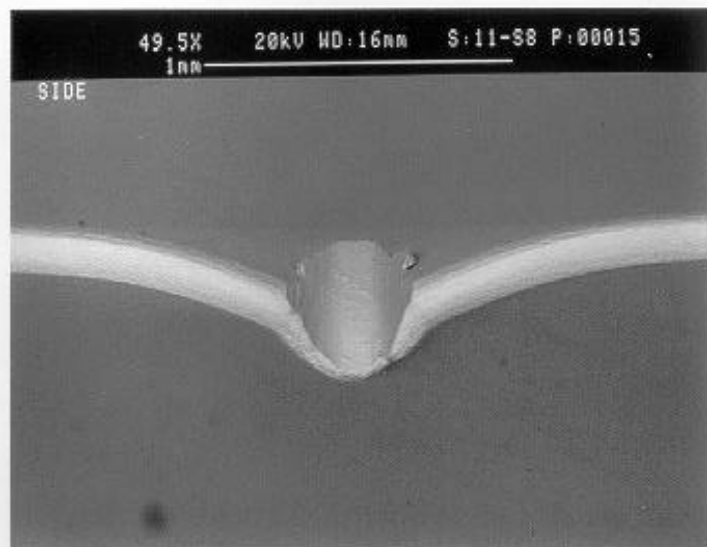
Simulated FOD Conditions: Solenoid Gun, 30° Impact angle, 0.005 inch tip radius, High Damage Level. Stress Relief Cycle (1300°F / 1 Hour with Ta wrap) after FOD.

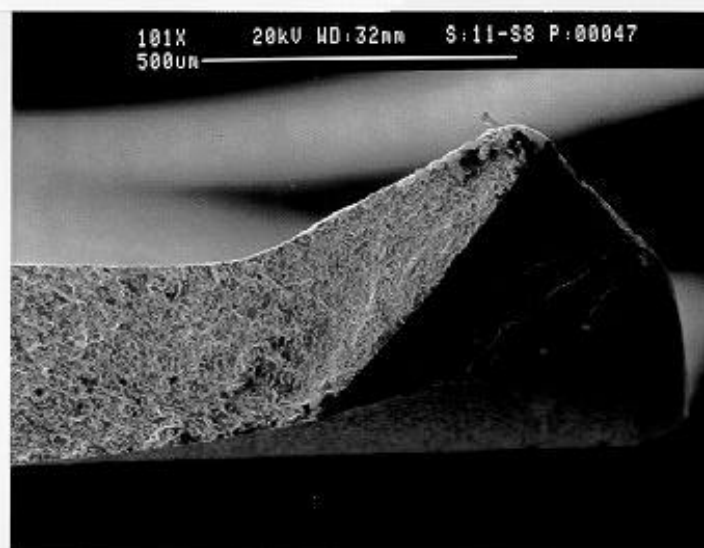
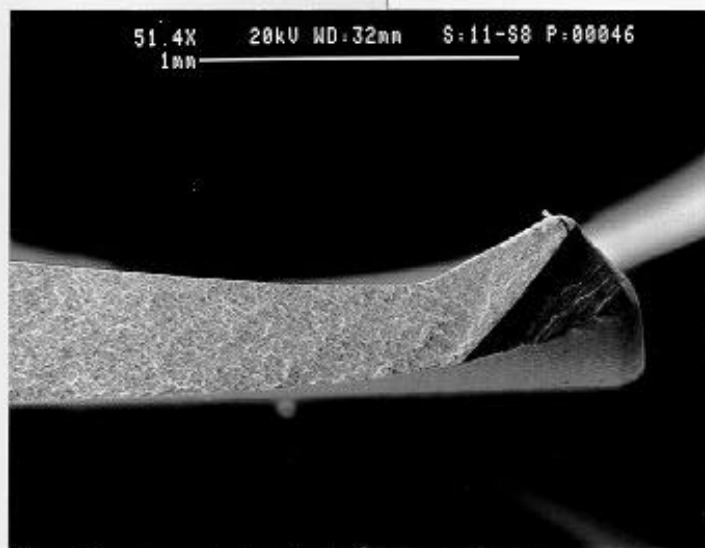
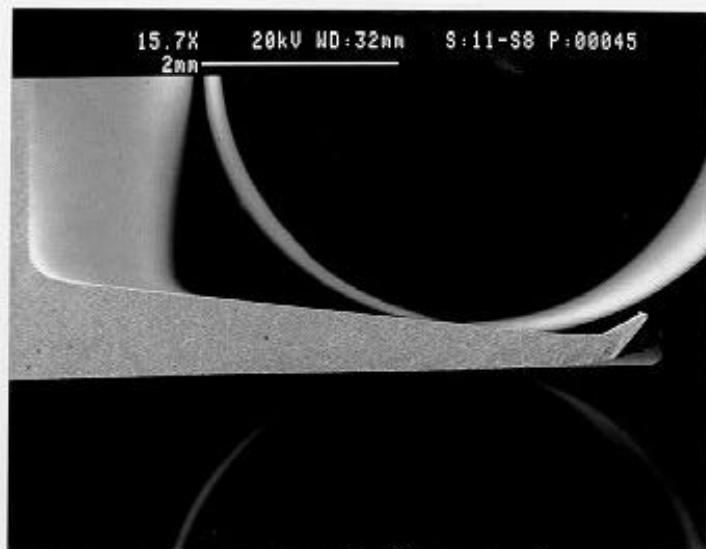
WMT&R Report Number: 9-05614

Test Description: The test was run at an initial load of 439 pounds, R-ratio of 0.5, and 30 Hz. The load was increased by 10% after every 1,000,000 cycles until failure.

Results: Crack nucleation occurred at 483 pounds. The final cycles were 1,745,132.

Attached Data: Micrographs of FOD'ed specimen, Load versus cycle plot, Position versus cycle plot, Micrographs of Failed specimens.





Specimen: 70-05, Sharp Leading Edge

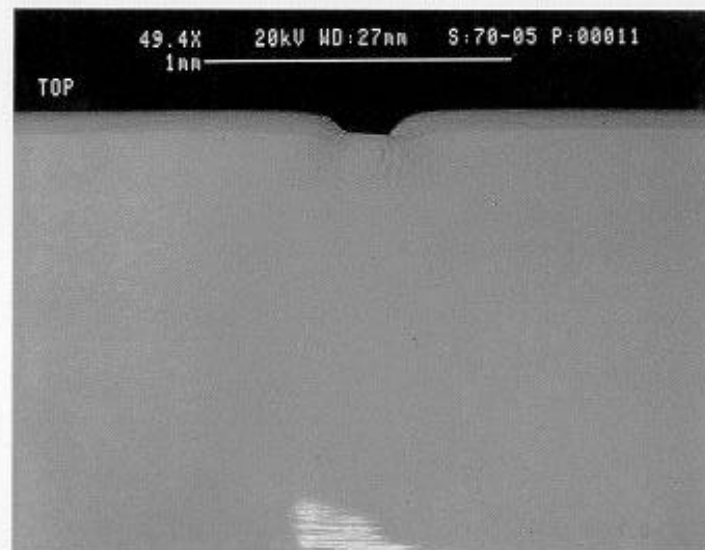
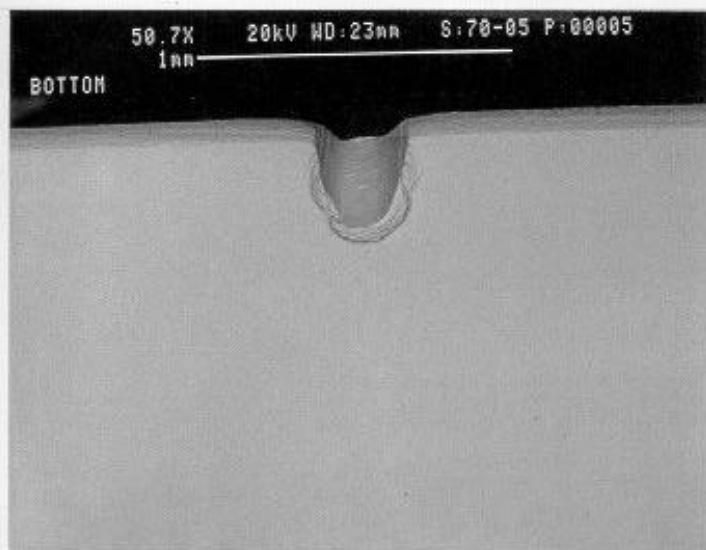
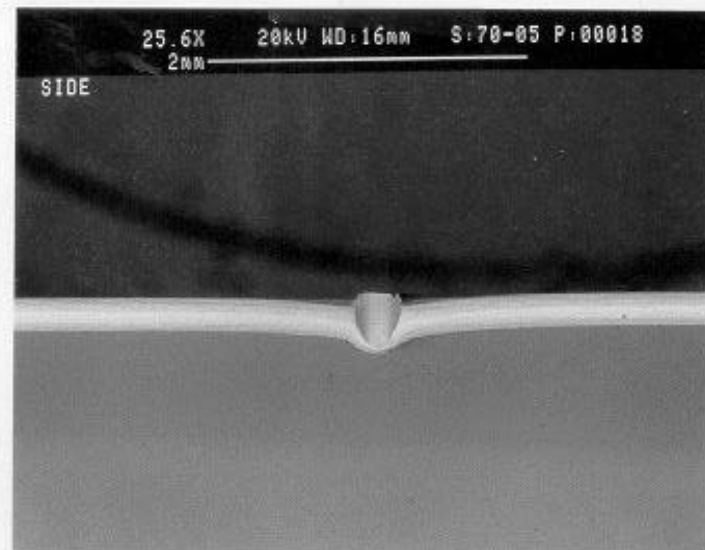
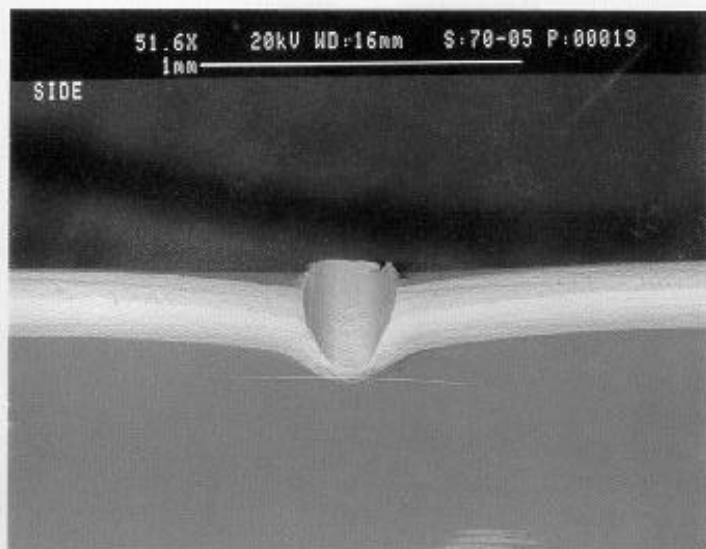
Simulated FOD Conditions: Solenoid Gun, 30° Impact angle, 0.005 inch tip radius, Low Damage Level. Stress Relief Cycle (1300°F / 1 Hour with Ta wrap) after FOD.

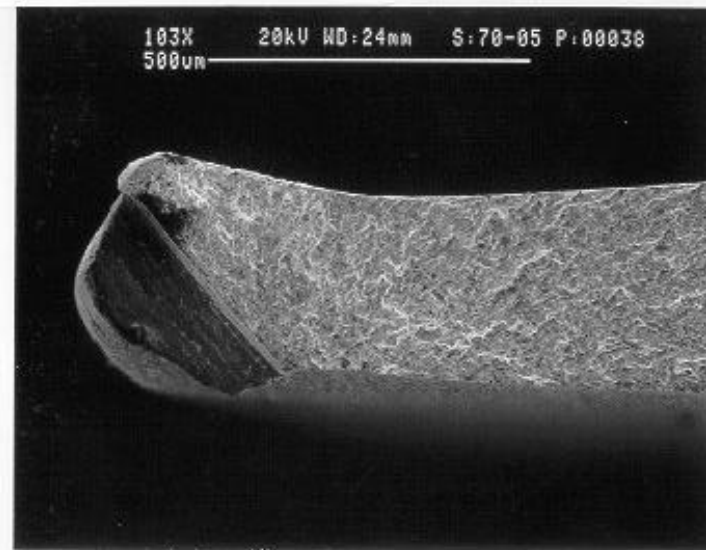
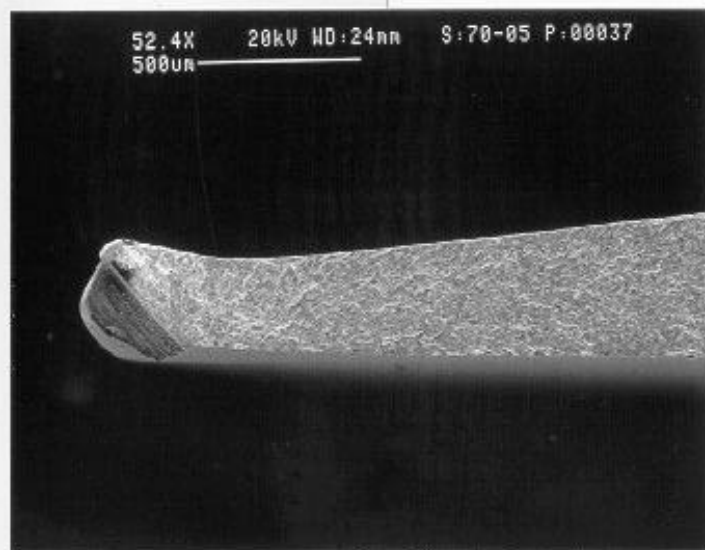
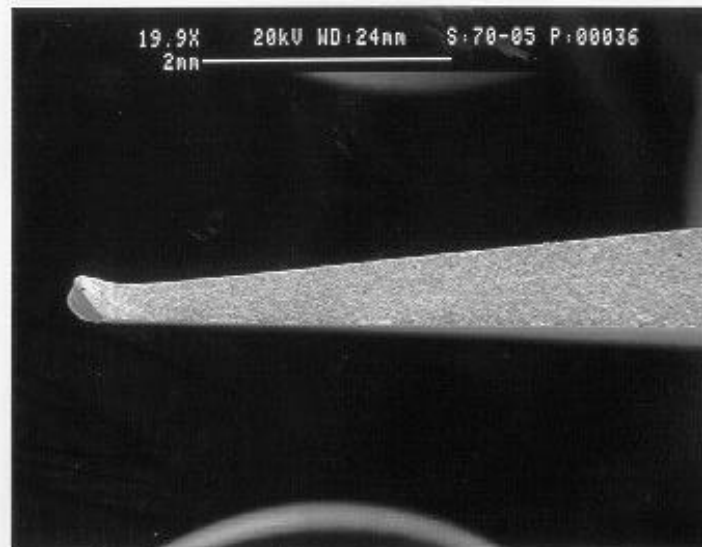
WMT&R Report Number: 9-05614

Test Description: The test was run at an initial load of 439 pounds, R-ratio of 0.5, and 30 Hz. The load was increased by 10% after every 1,000,000 cycles until failure.

Results: Crack nucleation occurred at 941 pounds. The final cycles were 8,183,200.

Attached Data: Micrographs of FOD'ed specimen, Load versus cycle plot, Position versus cycle plot, Micrographs of Failed specimens.





Specimen: 22-B1, Blunt Leading Edge

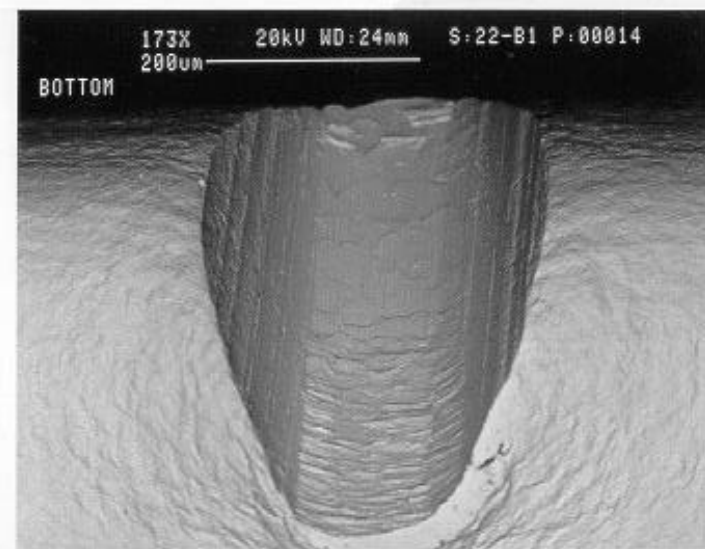
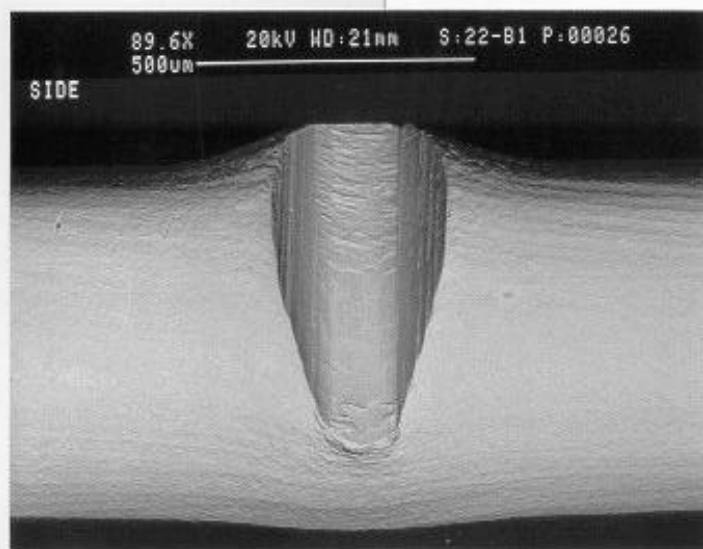
Simulated FOD Conditions: Solenoid Gun, 30° Impact angle, 0.005 inch tip radius, Low Damage Level.

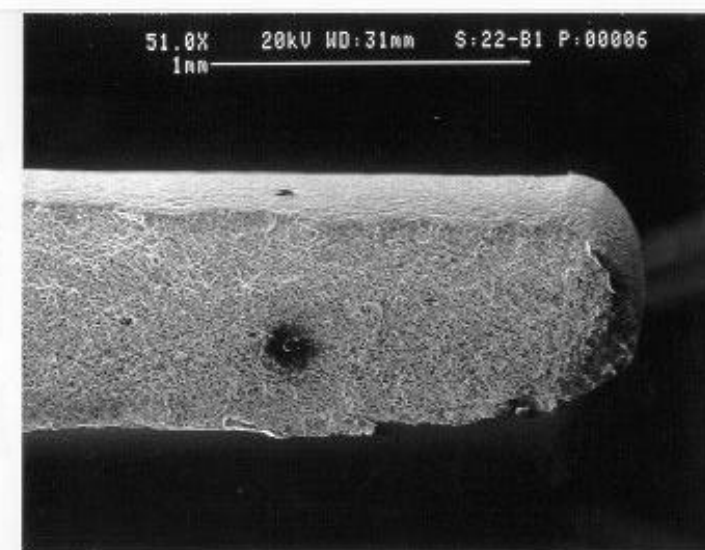
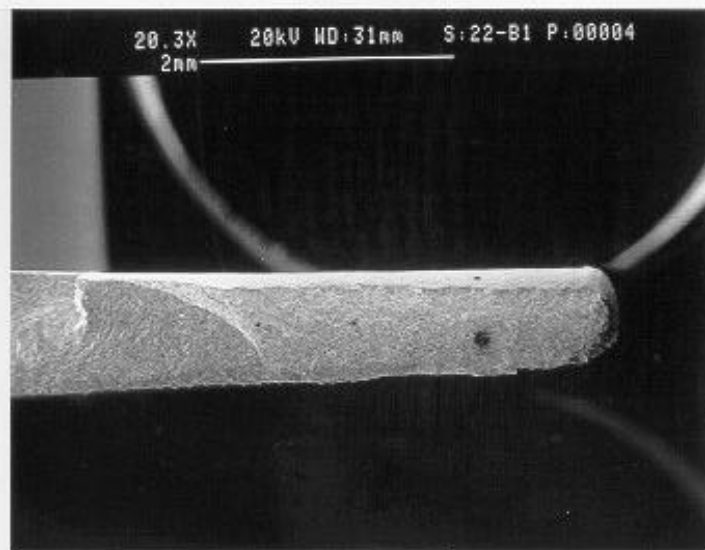
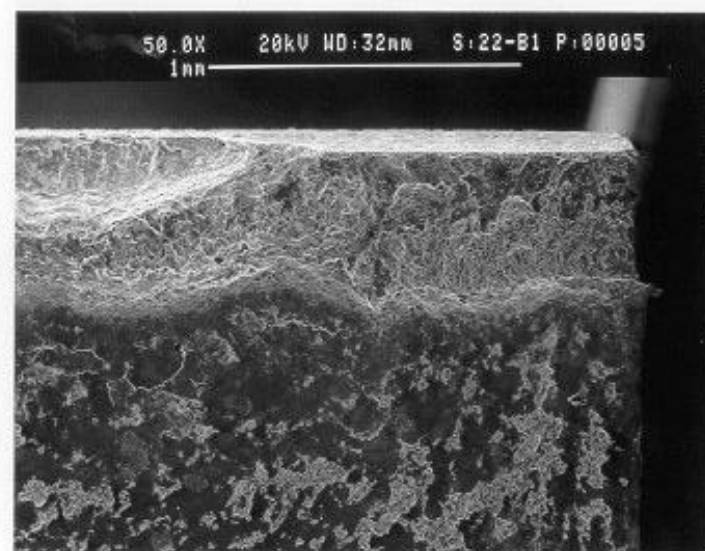
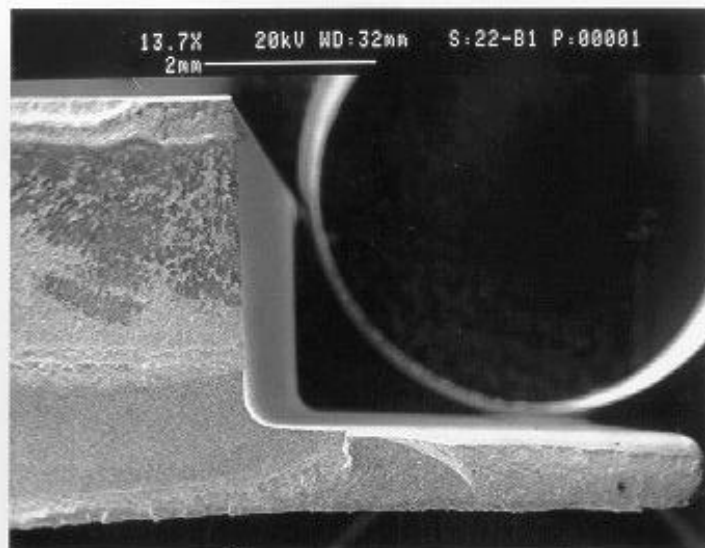
WMT&R Report Number: 9-04629

Test Description: The test was run at an initial load of 248 pounds, R-ratio of -1.0 , and 30 Hz. The load was increased by 10% after every 1,000,000 cycles until failure.

Results: Crack nucleation occurred at 399 pounds. The final cycles were 5,377,573. Specimen did not fail at FOD nick.

Attached Data: Micrographs of FOD'ed specimen, Load versus cycle plot, Position versus cycle plot, Micrographs of Failed specimens.





Specimen: 36-B2, Blunt Leading Edge

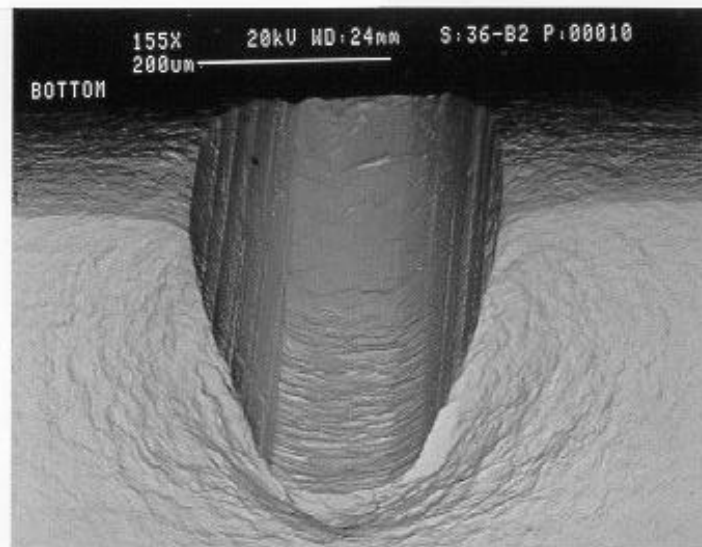
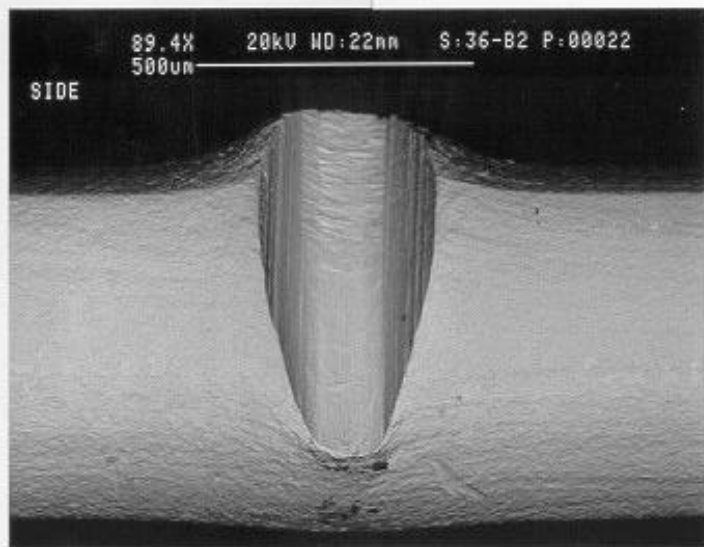
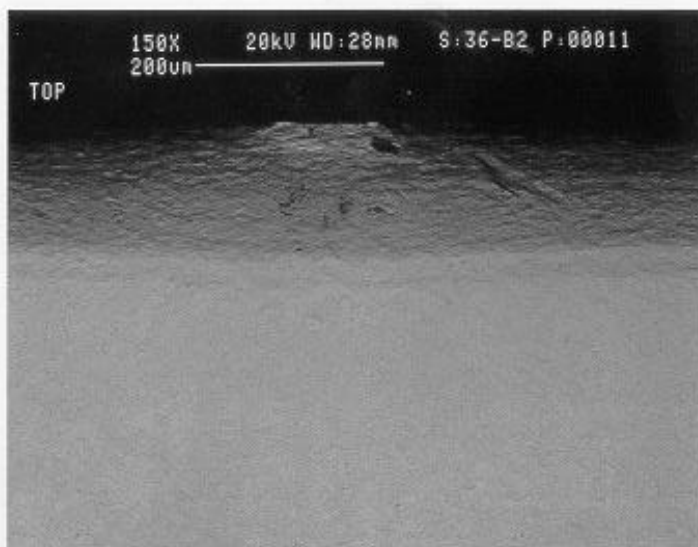
Simulated FOD Conditions: Solenoid Gun, 30° Impact angle, 0.005 inch tip radius, Low Damage Level.

WMT&R Report Number: 9-04629

Test Description: The test was run at an initial load of 248 pounds, R-ratio of -1.0 , and 30 Hz. The load was increased by 10% after every 1,000,000 cycles until failure.

Results: Crack nucleation occurred at 439 pounds. The final cycles were 6,435,700.

Attached Data: Micrographs of FOD'ed specimen and Plot of Position versus Cycles.



Specimen: 36-B4, Blunt Leading Edge

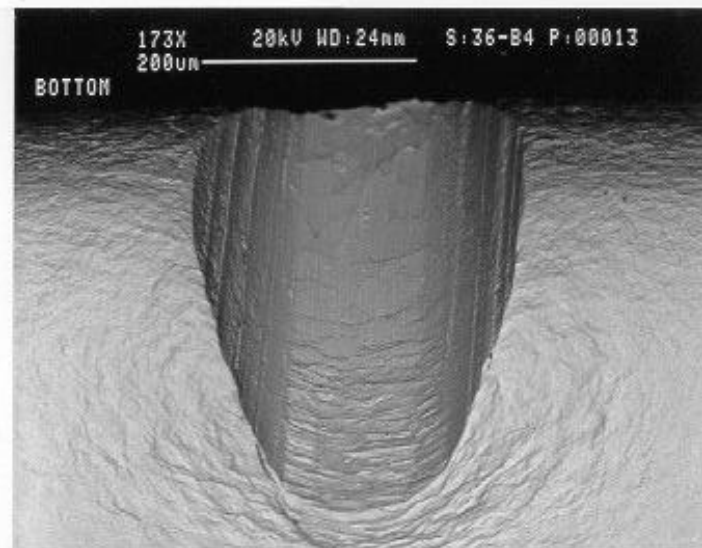
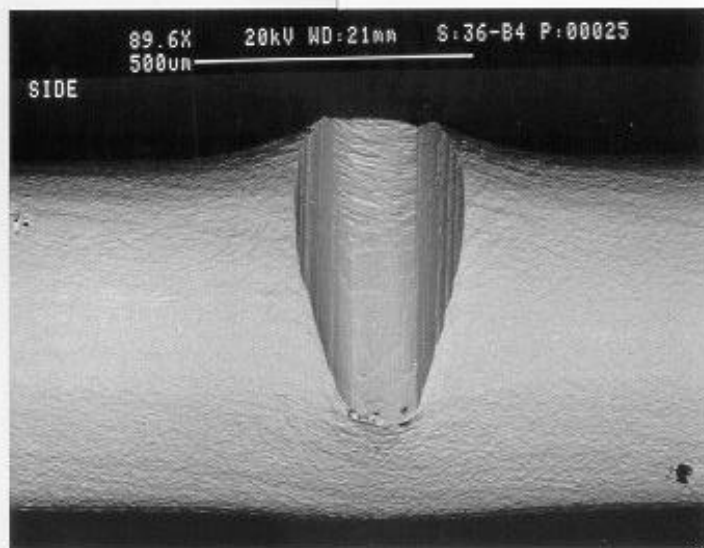
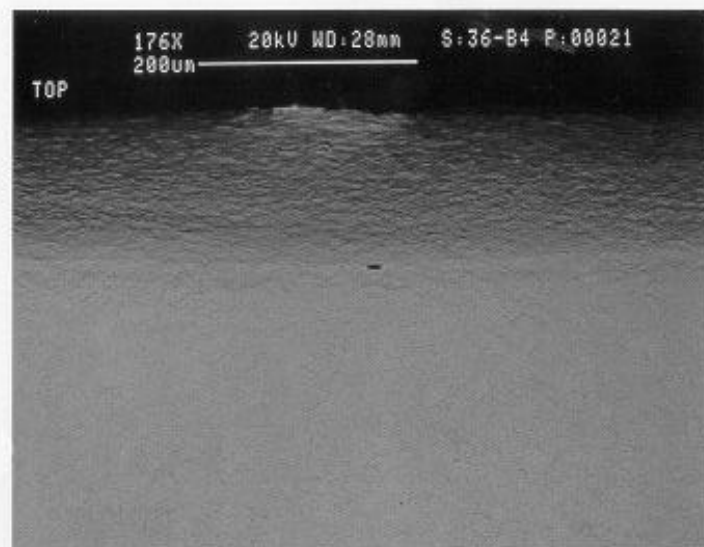
Simulated FOD Conditions: Solenoid Gun, 30° Impact angle, 0.005 inch tip radius, Low Damage Level.

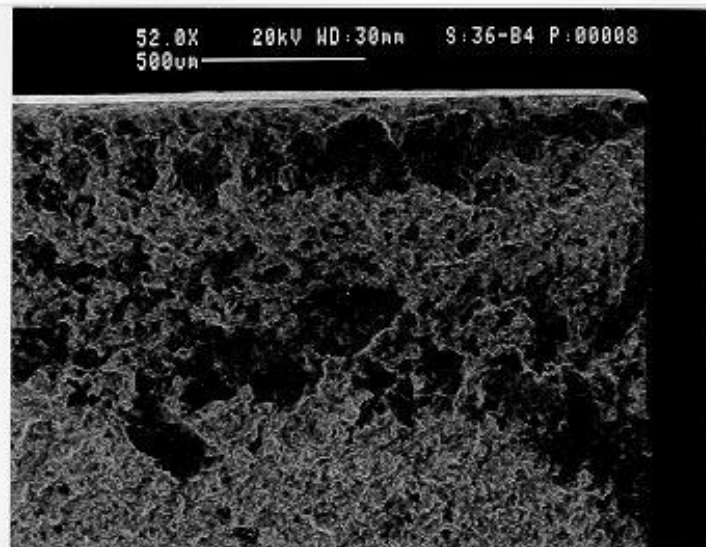
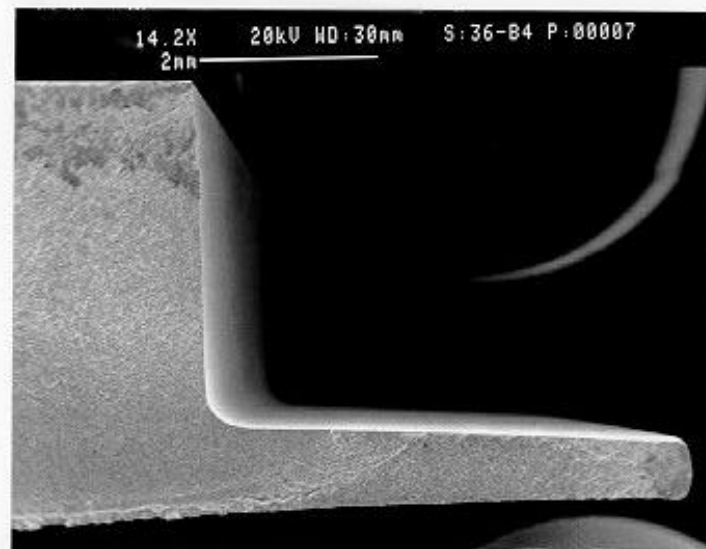
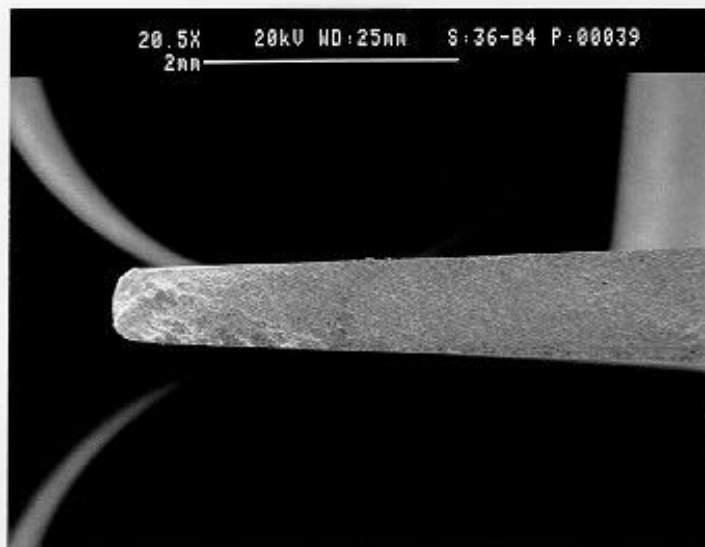
WMT&R Report Number: 9-04629

Test Description: The test was run at an initial load of 300 pounds, R-ratio of -1.0 , and 30 Hz. The load was increased by 10% after every 1,000,000 cycles until failure.

Results: Crack nucleation occurred at 330 pounds. The final cycles were 1,685,721. Specimen did not fail at FOD nick.

Attached Data: Micrographs of FOD'ed specimen, Load versus cycle plot, Position versus cycle plot, Micrographs of Failed specimens.





Specimen: 22-B4, Blunt Leading Edge

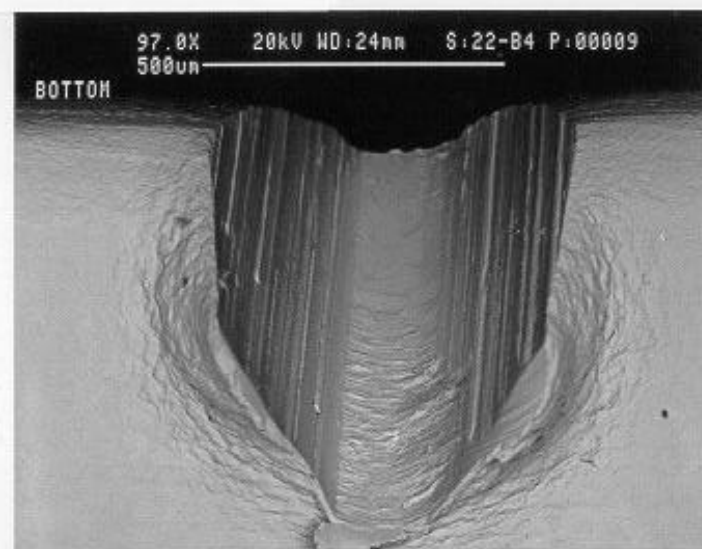
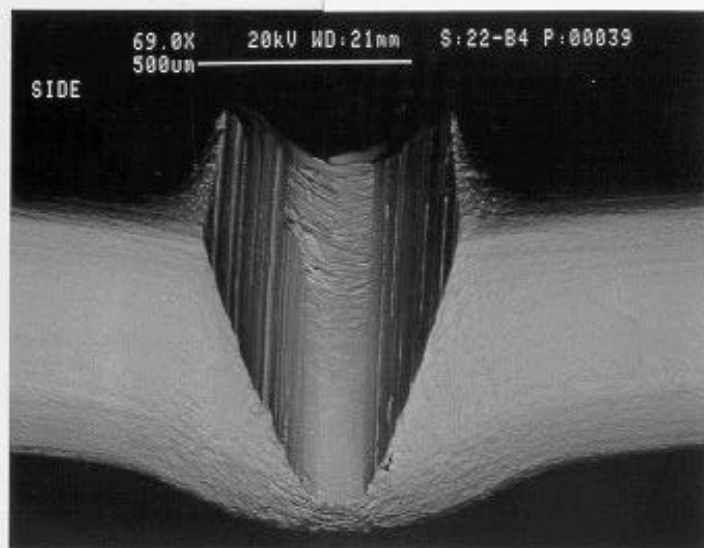
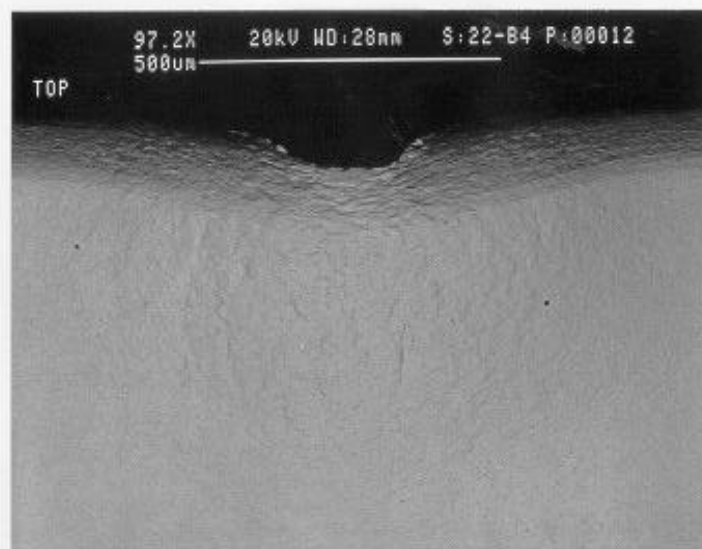
Simulated FOD Conditions: Solenoid Gun, 30° Impact angle, 0.005 inch tip radius, High Damage Level.

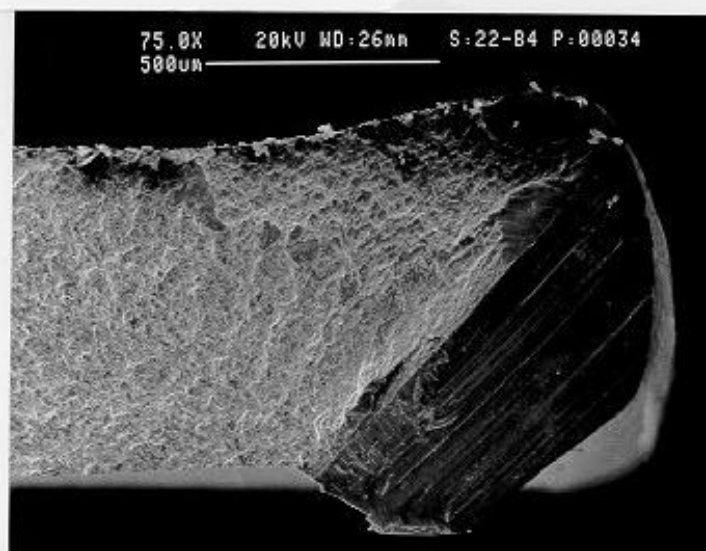
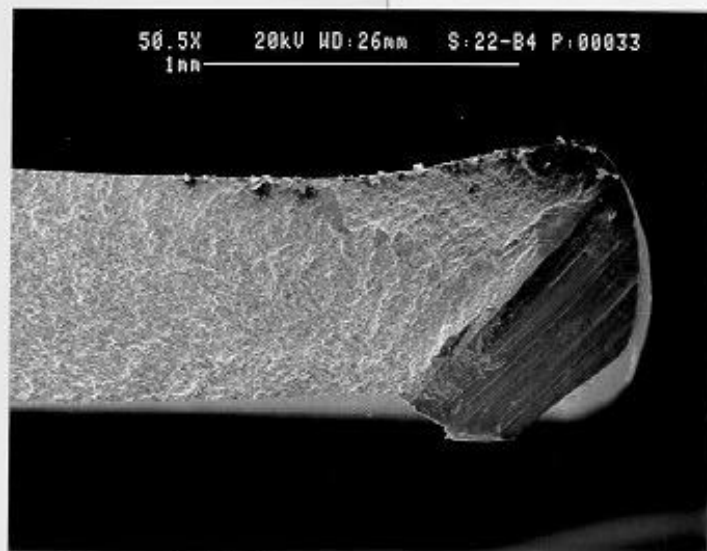
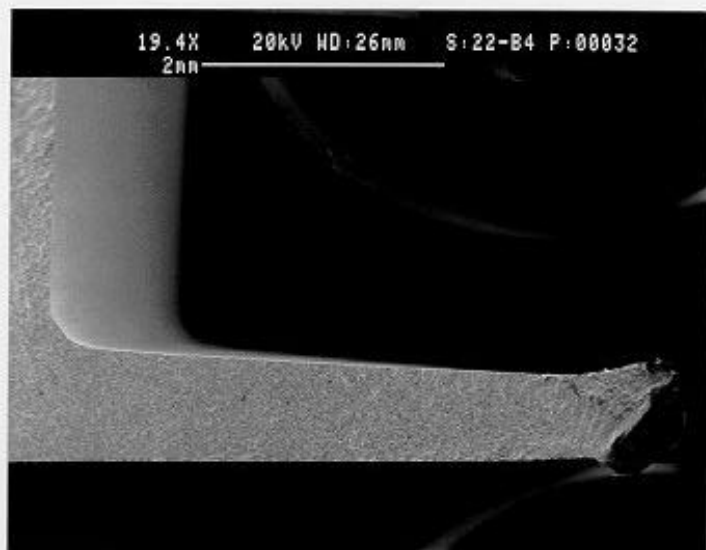
WMT&R Report Number: 9-04629

Test Description: The test was run at an initial load of 225 pounds, R-ratio of –1.0, and 30.

Results: Crack nucleation occurred at 225 pounds. The final cycles were 306,250.

Attached Data: Micrographs of FOD'ed specimen, Load versus cycle plot, Position versus cycle plot, Micrographs of Failed specimens.





Specimen: 36-B1, Blunt Leading Edge

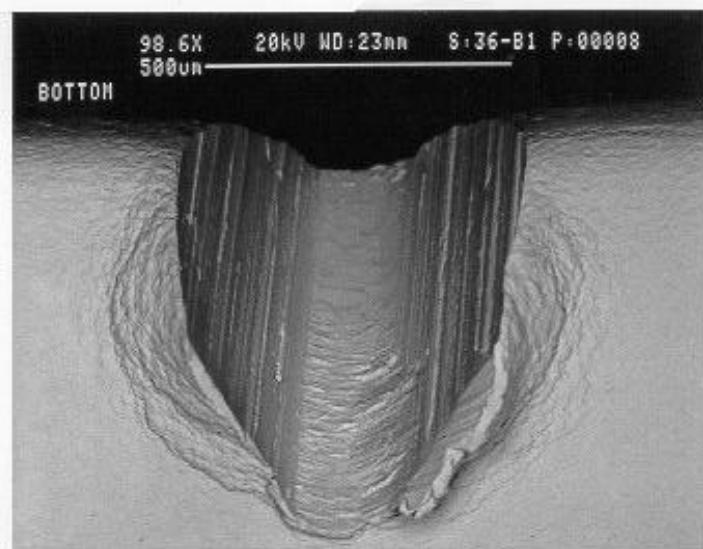
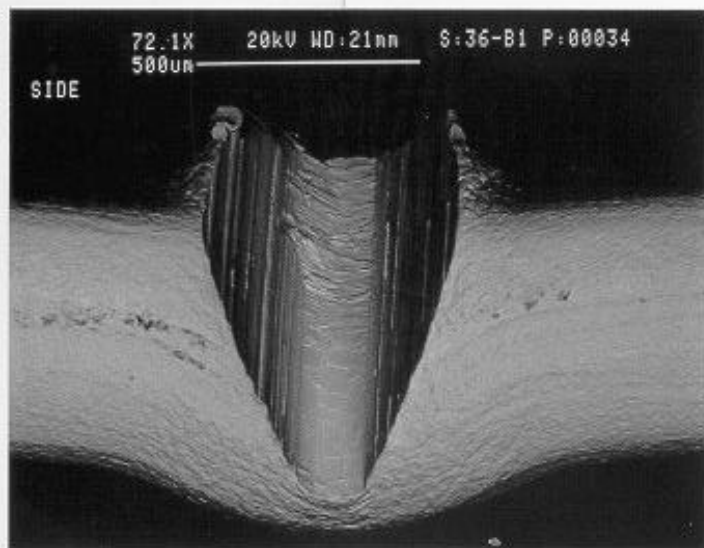
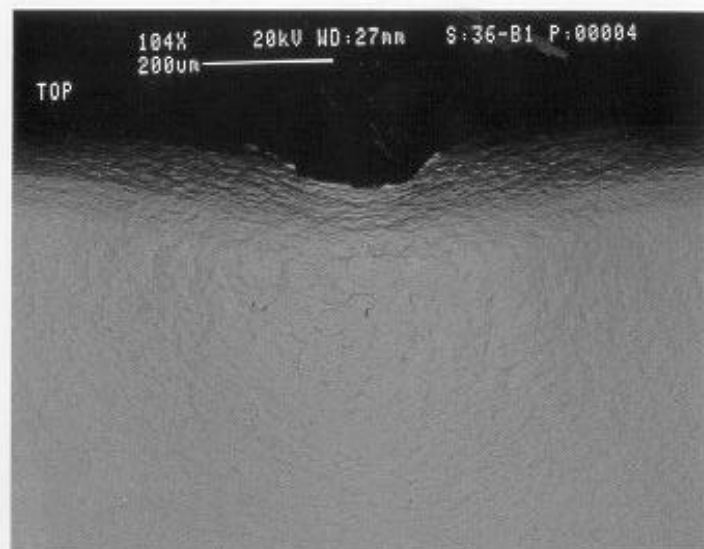
Simulated FOD Conditions: Solenoid Gun, 30° Impact angle, 0.005 inch tip radius, High Damage Level.

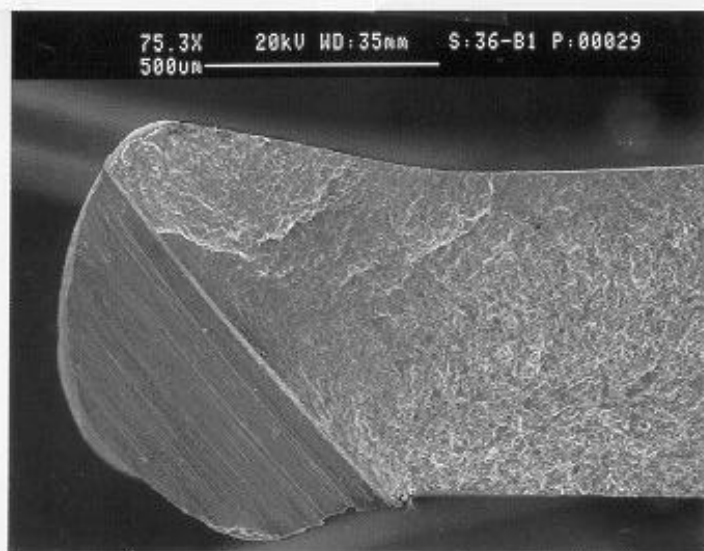
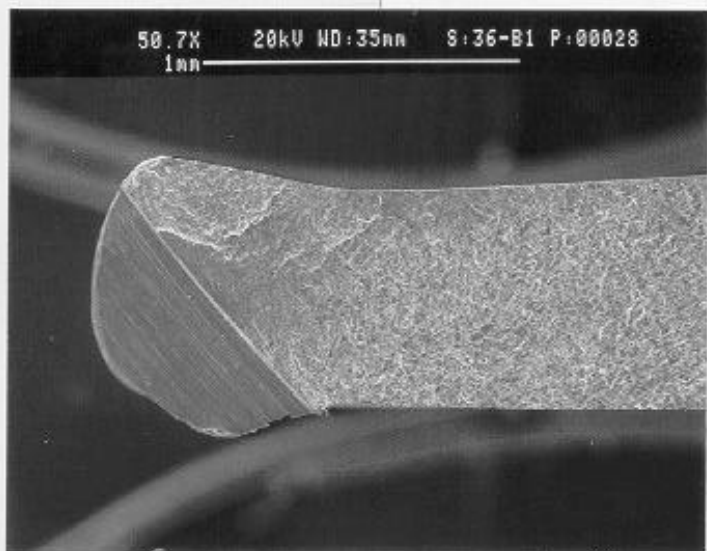
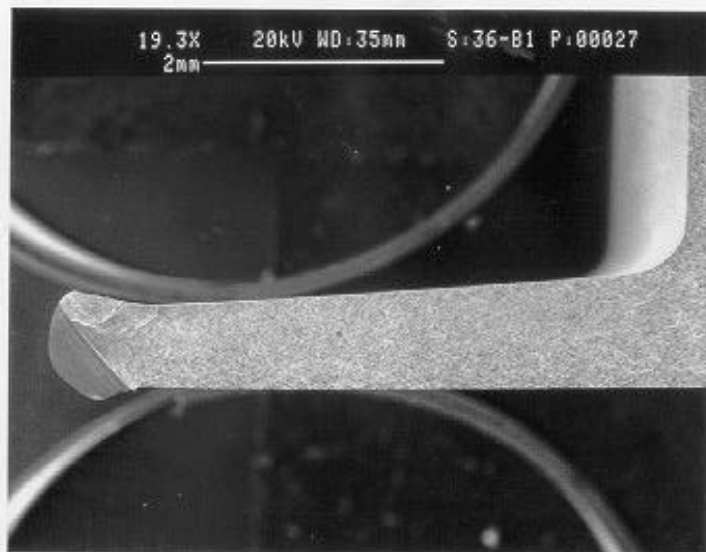
WMT&R Report Number: 9-04629

Test Description: The test was run at an initial load of 225 pounds, R-ratio of -1.0 , and 30 Hz. The load was increased by 10% after every 1,000,000 cycles until failure.

Results: Crack nucleation occurred at 247 pounds. The final cycles were 1,959,873.

Attached Data: Micrographs of FOD'ed specimen, Load versus cycle plot, Position versus cycle plot, Micrographs of Failed specimens.





Specimen: 36-B5, Blunt Leading Edge

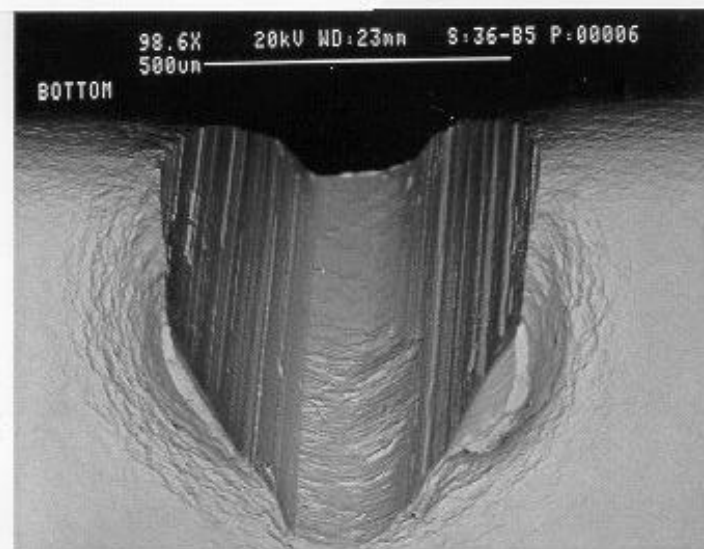
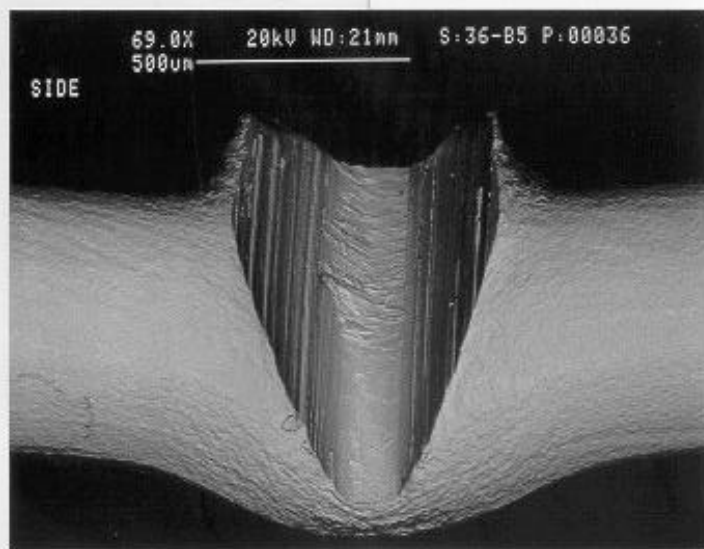
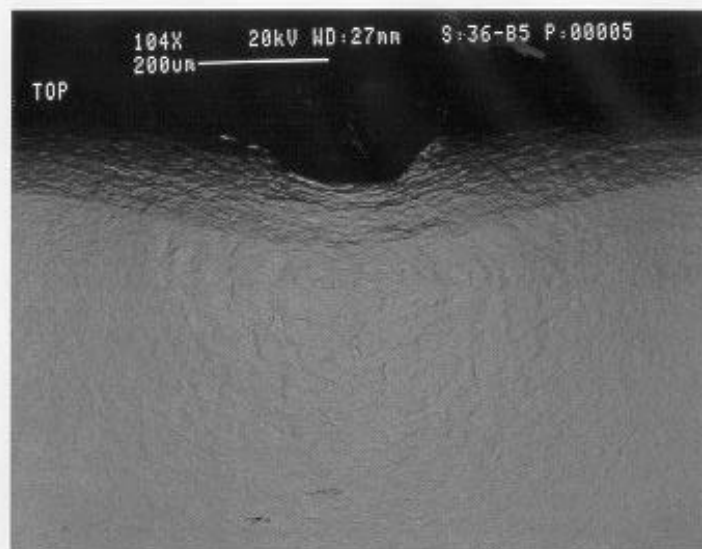
Simulated FOD Conditions: Solenoid Gun, 30° Impact angle, 0.005 inch tip radius, High Damage Level.

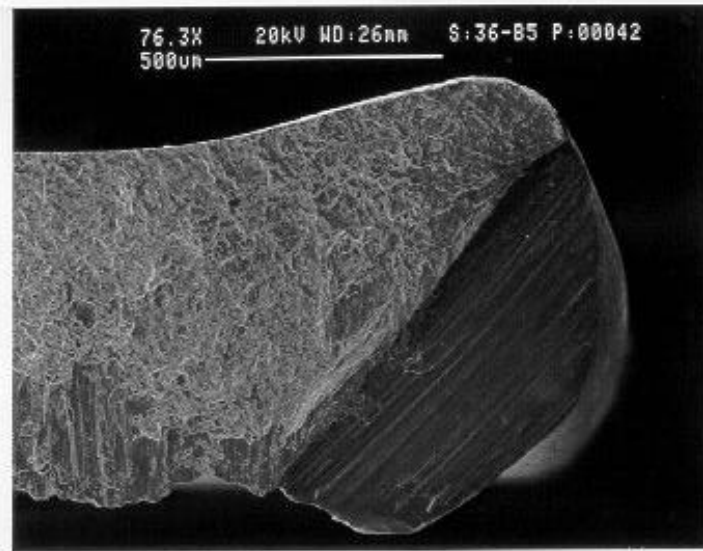
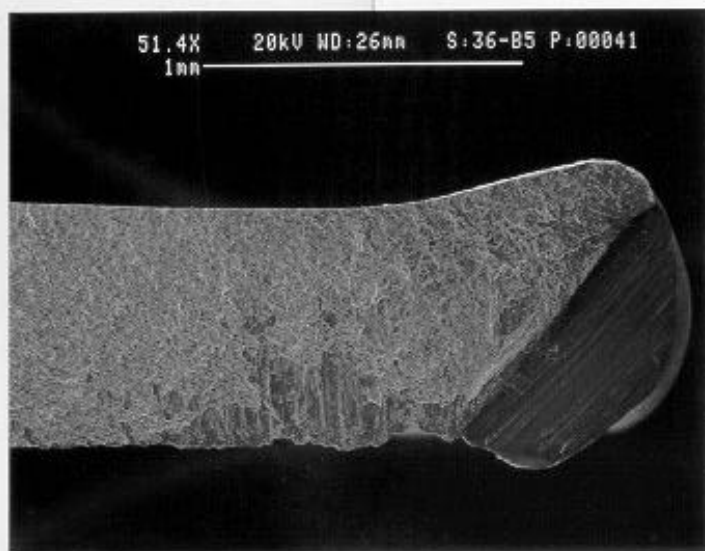
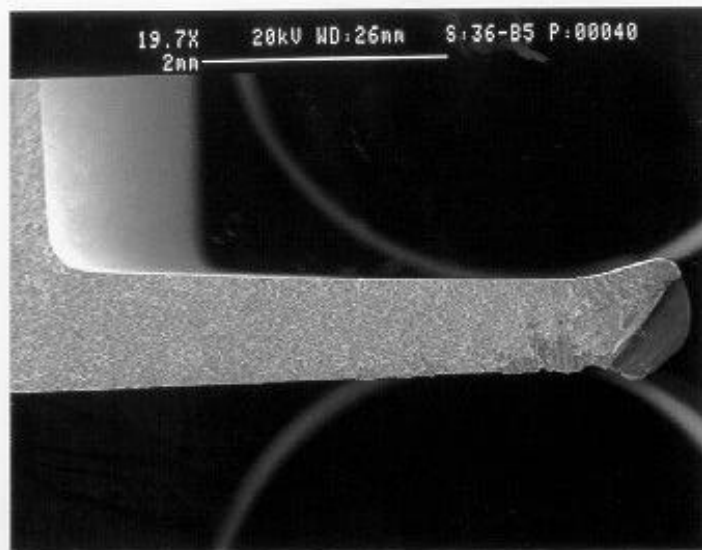
WMT&R Report Number: 9-04629

Test Description: The test was run at an initial load of 300 pounds, R-ratio of –1.0, and 30 Hz.

Results: Crack nucleation occurred at 300 pounds. The final cycles were 441,838.

Attached Data: Micrographs of FOD'ed specimen, Load versus cycle plot, Position versus cycle plot, Micrographs of Failed specimens.





Specimen: 22-S1, Sharp Leading Edge

Simulated FOD Conditions: Solenoid Gun, 30° Impact angle, 0.025 inch tip radius, Low Damage Level.

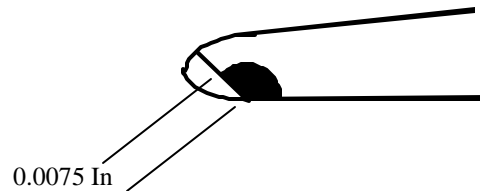
WMT&R Report Number: 9-02027

Test Description: The test was run at an initial load of 439 pounds, R-ratio of 0.5, and 30 Hz. The load was increased by 10% after every 1,000,000 cycles until failure. The specimen had pressure mounted EPD leads to monitor potential drop.

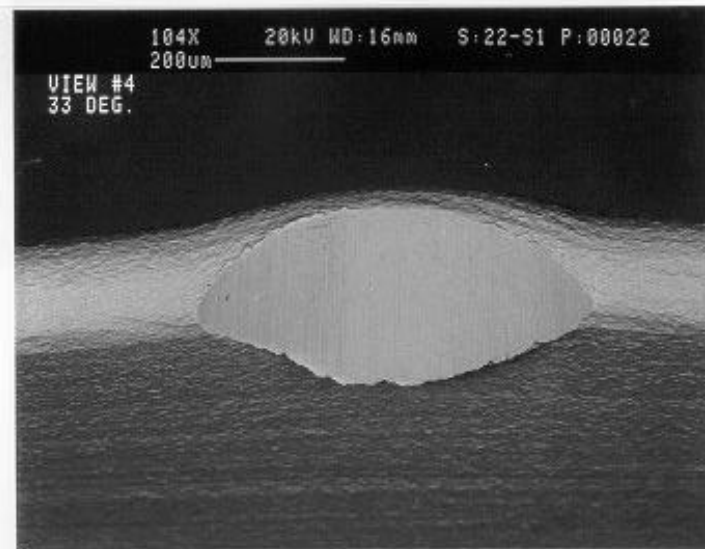
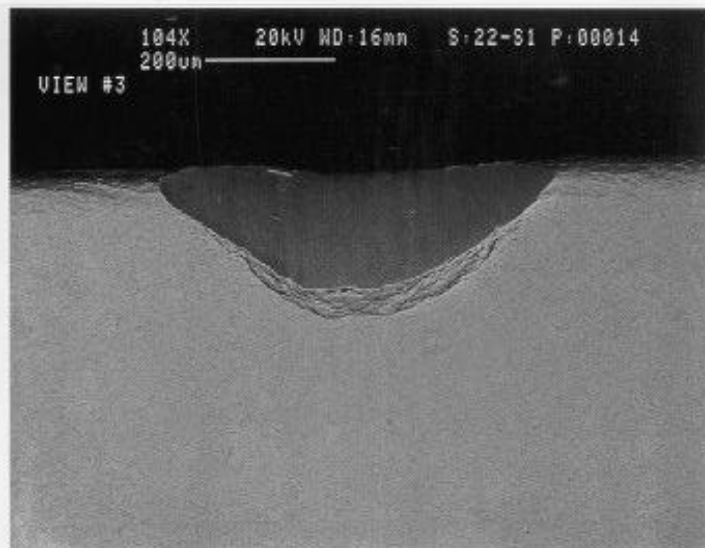
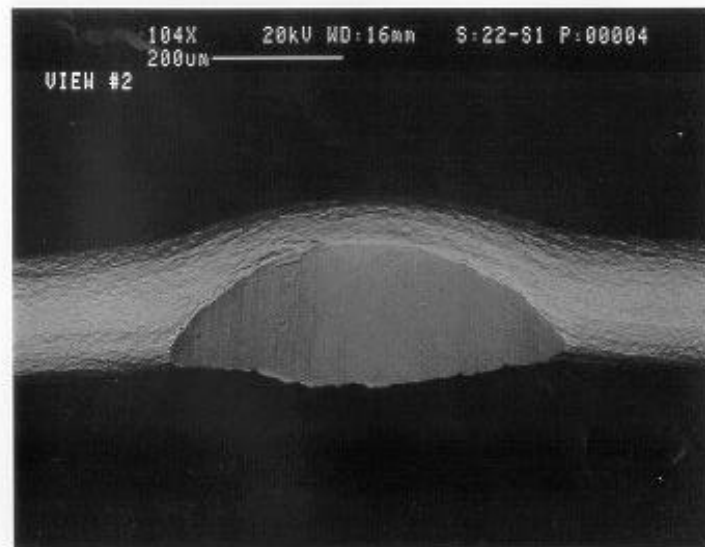
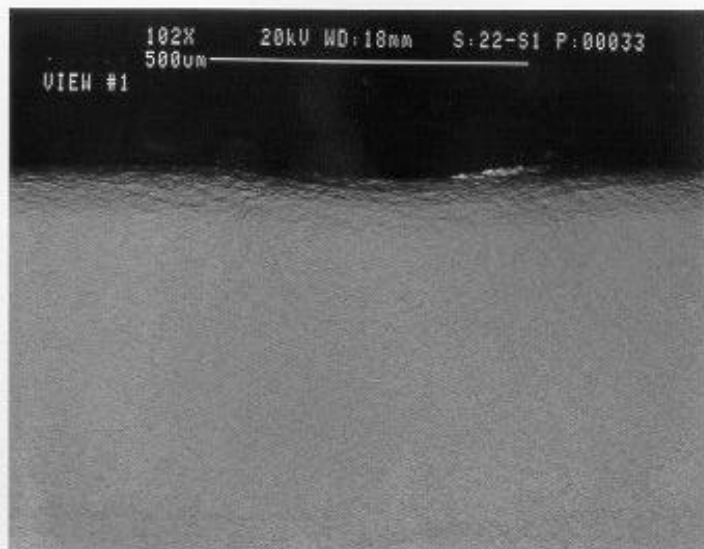
Results: Crack nucleation occurred at 941.0 pounds. The final cycles were 8,282,010. EPD data:

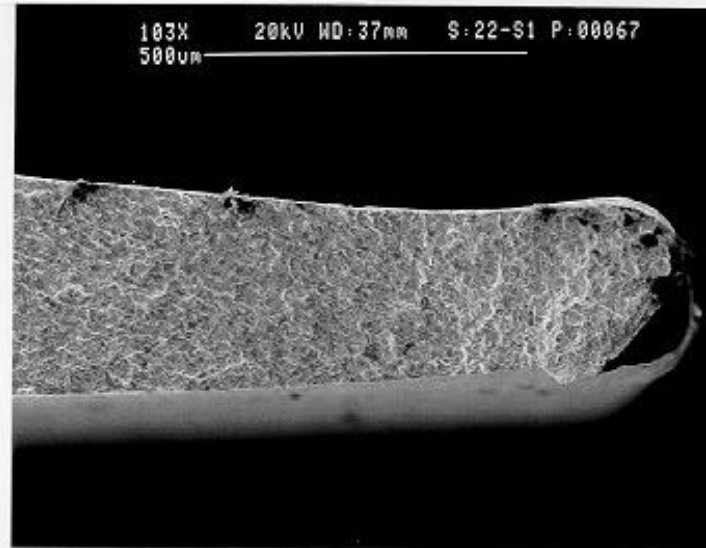
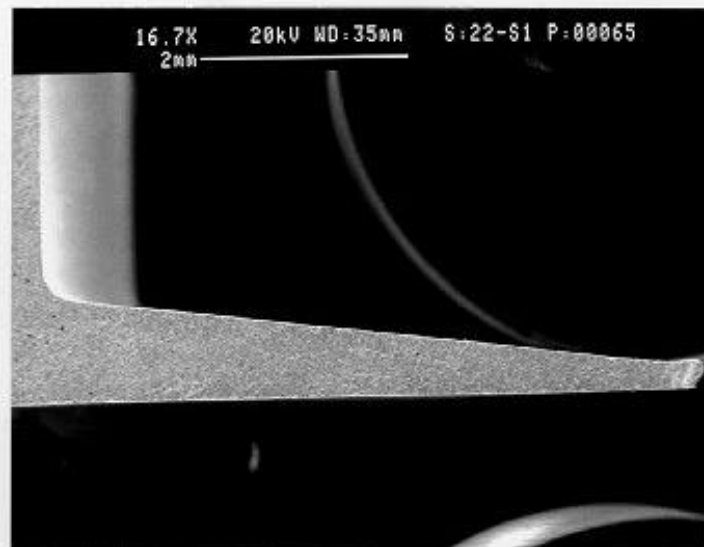
U/Uo	Cycles	Heat Tint Data	Crack Length from Heat Tint (in)
1.0070	8,193,130	680°F @ 20 Hours	0.0075

Heat Tint Results:



Attached Data: Micrographs of FOD, U/Uo versus cycles, Micrographs of Failed specimens.





Specimen: 70-01, Sharp Leading Edge

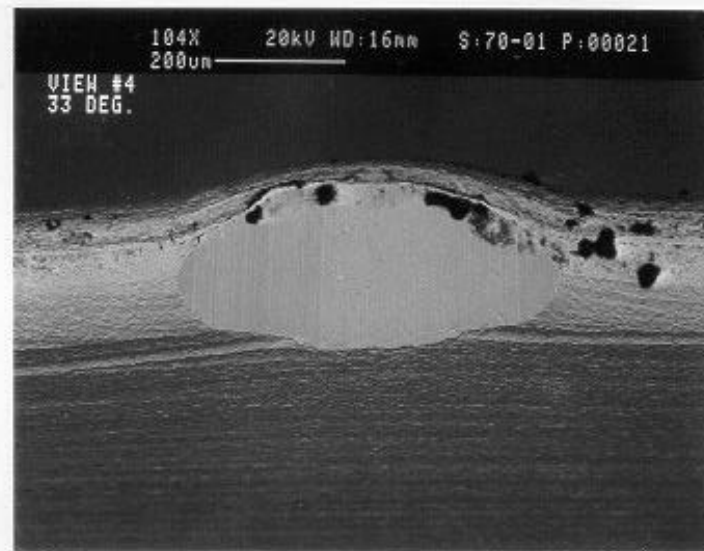
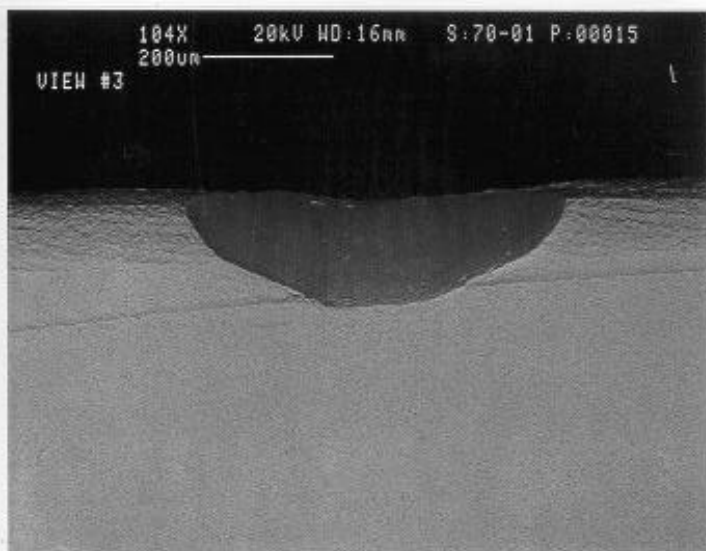
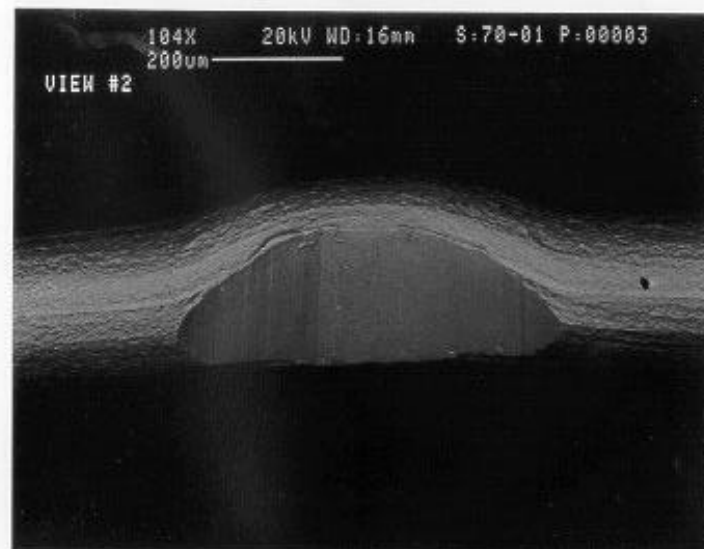
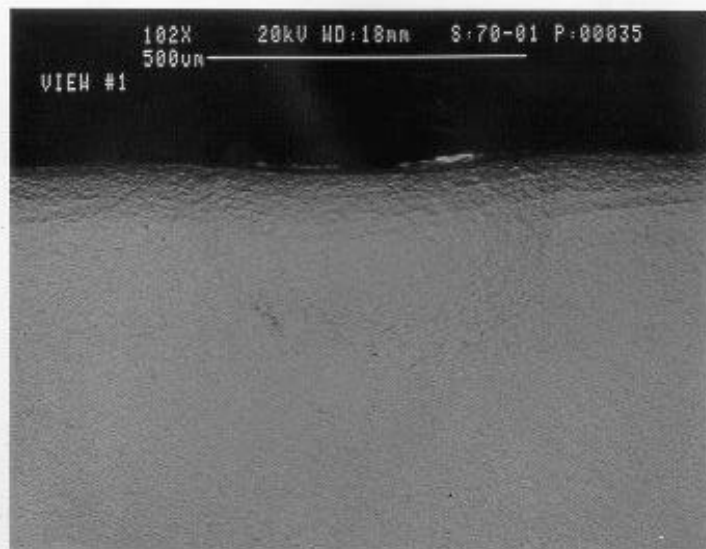
Simulated FOD Conditions: Solenoid Gun, 30° Impact angle, 0.025 inch tip radius, Low Damage Level.

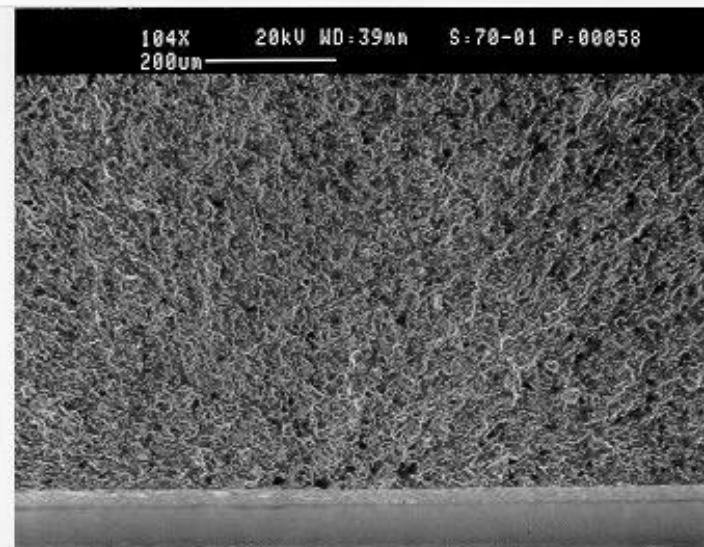
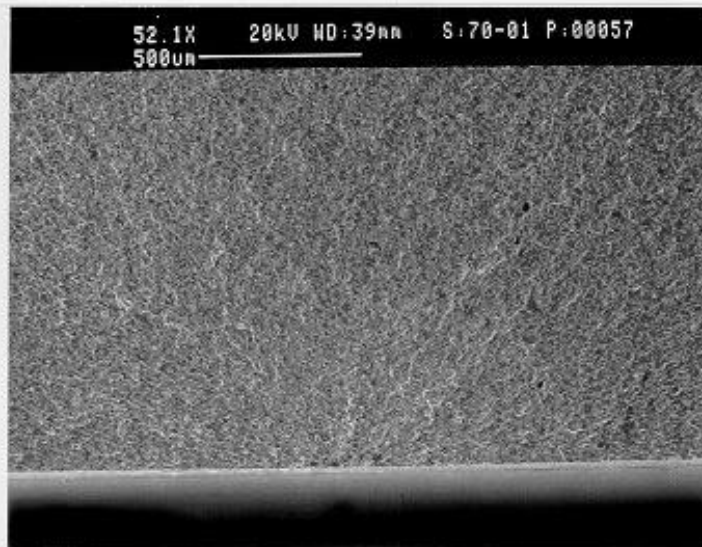
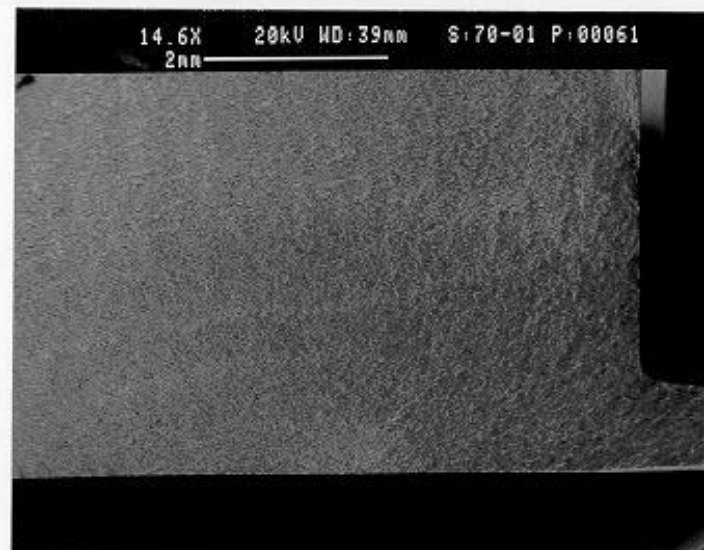
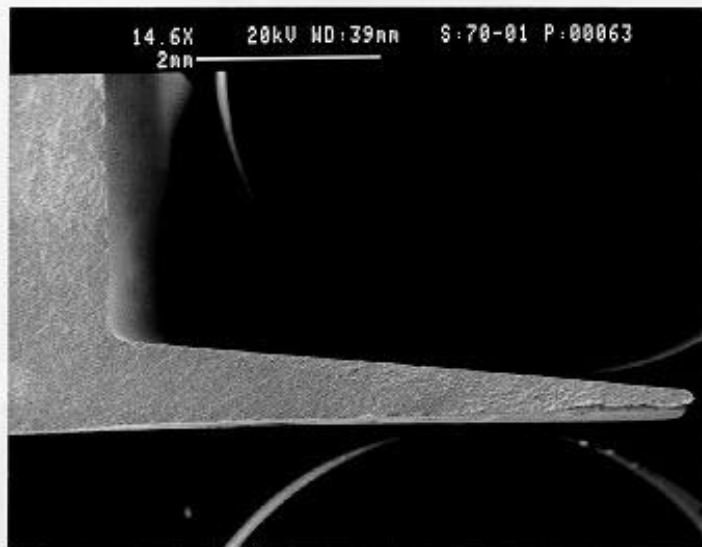
WMT&R Report Number: 9-02027

Test Description: The test was run at an initial load of 439 pounds, R-ratio of 0.5, and 30 Hz. The load was increased by 10% after every 1,000,000 cycles until failure.

Results: Crack nucleation occurred at 1252.5 pounds. The final cycles were 11,654,043. The crack did not initiate at the FOD nick.

Attached Data: Micrographs of FOD'ed specimen, Load versus cycle plot, Position versus cycle plot, Micrographs of Failed specimens.





Specimen: 76-03, Sharp Leading Edge

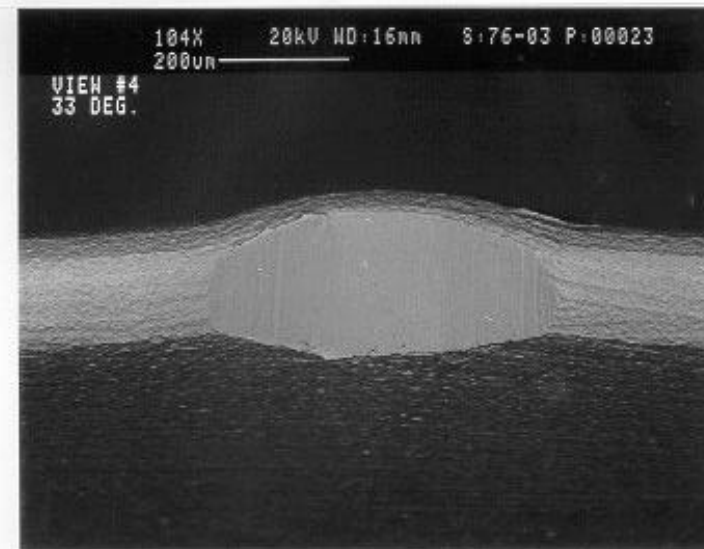
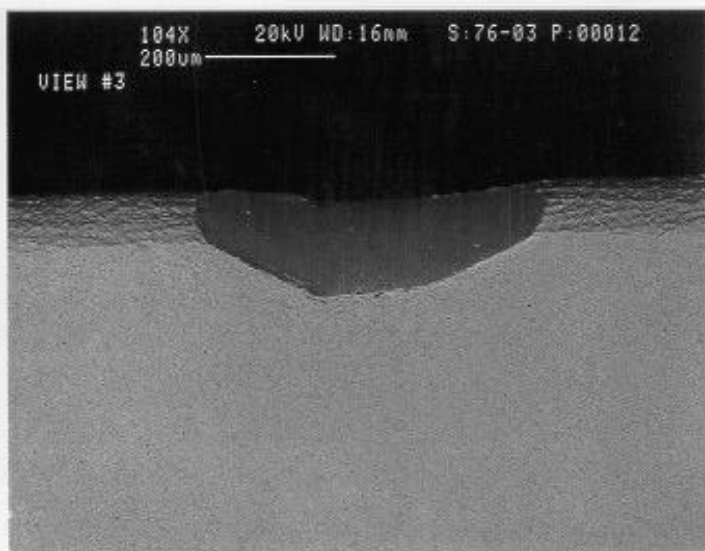
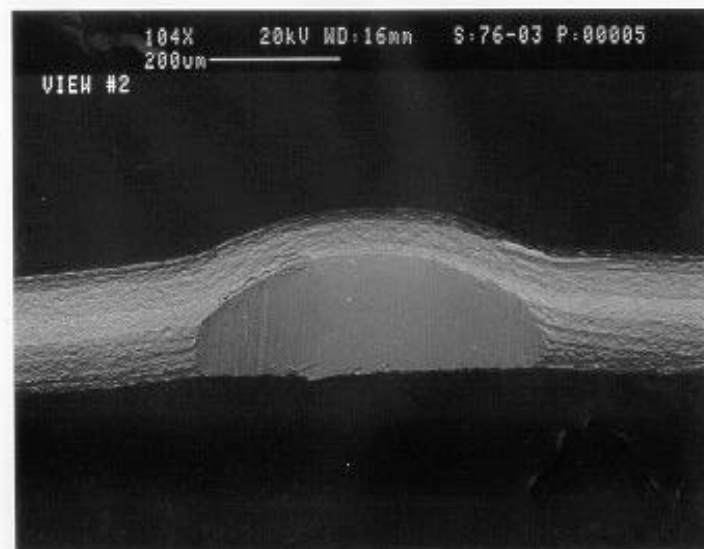
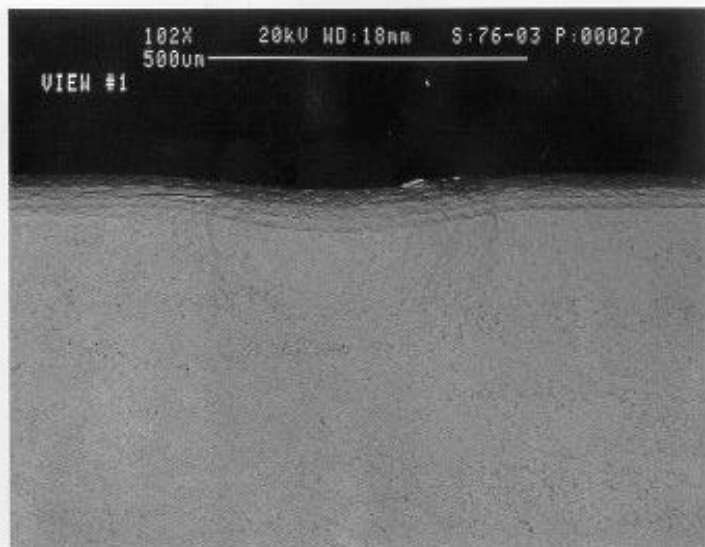
Simulated FOD Conditions: Solenoid Gun, 30° Impact angle, 0.025 inch tip radius, Low Damage Level.

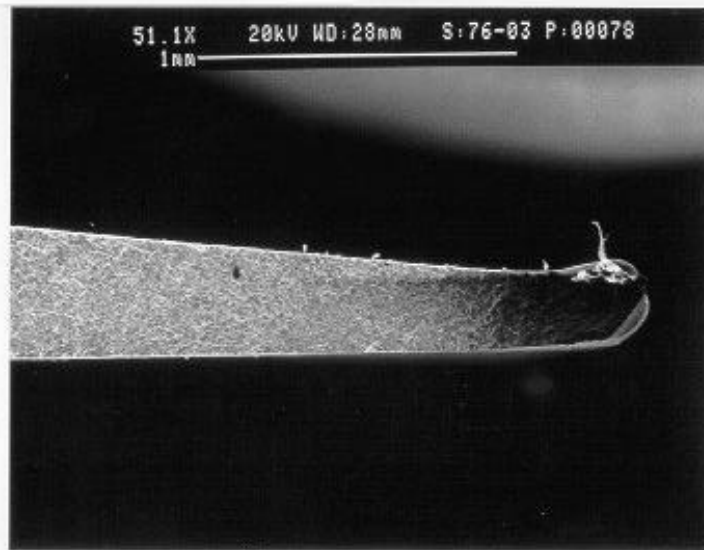
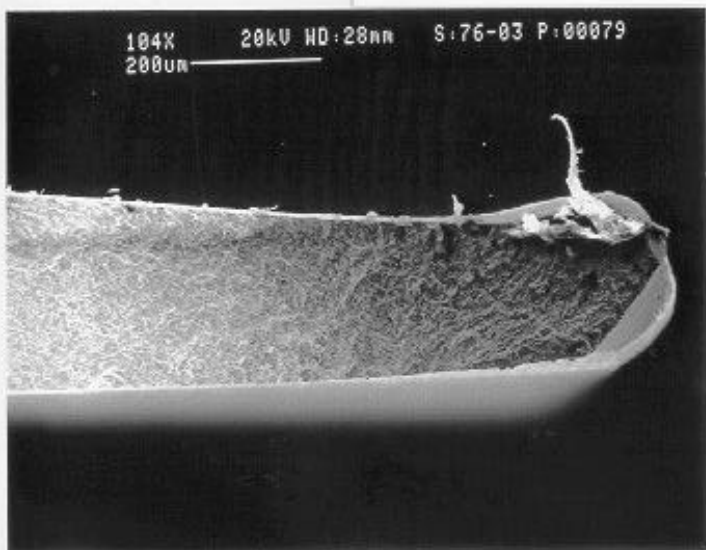
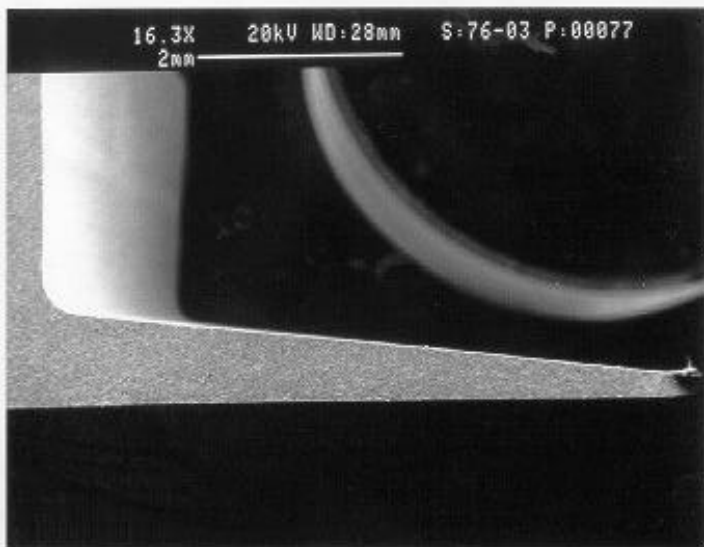
WMT&R Report Number: 9-02027

Test Description: The test was run at an initial load of 941 pounds, R-ratio of 0.5, and 30 Hz. The load was increased by 10% after every 1,000,000 cycles until failure.

Results: Crack nucleation occurred at 1138.6 pounds. The final cycles were 2,518,346.

Attached Data: Micrographs of FOD'ed specimen, Load versus cycle plot, Position versus cycle plot, Micrographs of Failed specimens.





Specimen: 11-S6, Sharp Leading Edge

Simulated FOD Conditions: Solenoid Gun, 30° Impact angle, 0.025 inch tip radius, High Damage Level.

WMT&R Report Number: 9-02027

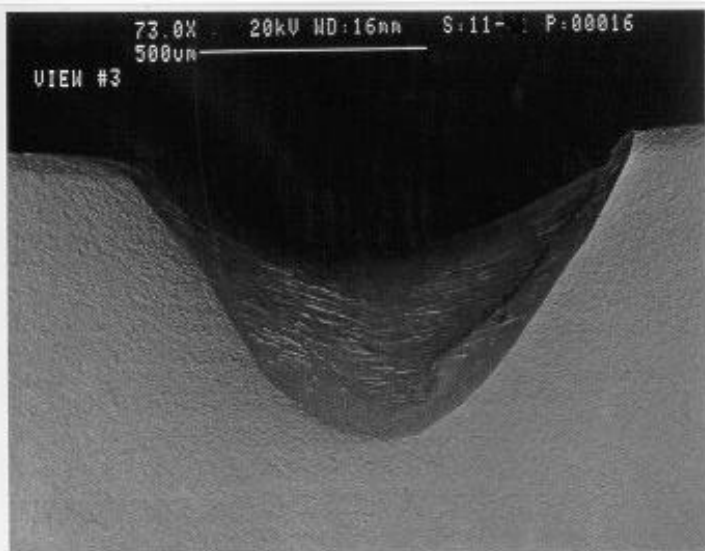
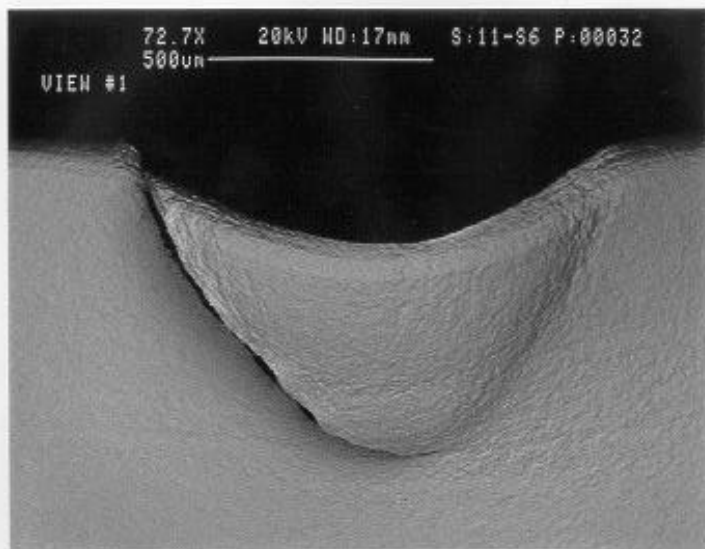
Test Description: The test was run at an initial load of 439 pounds, R-ratio of 0.5, and 30 Hz. The load was increased by 10% after every 1,000,000 cycles until failure. The specimen had welded EPD leads to monitor potential drop.

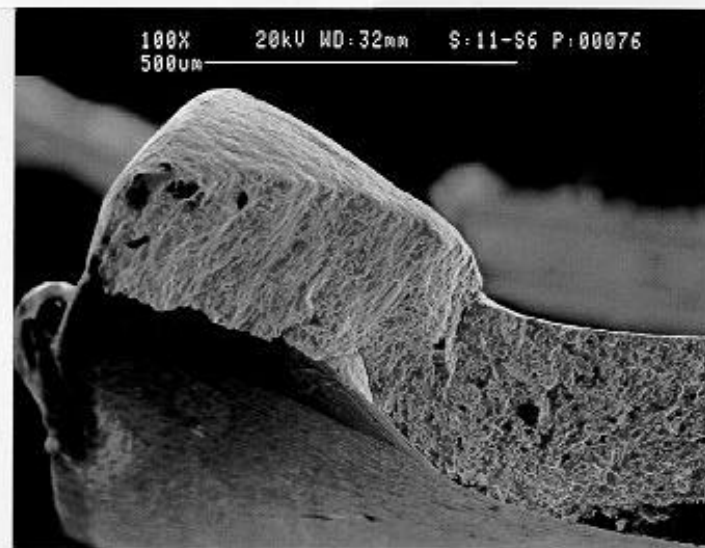
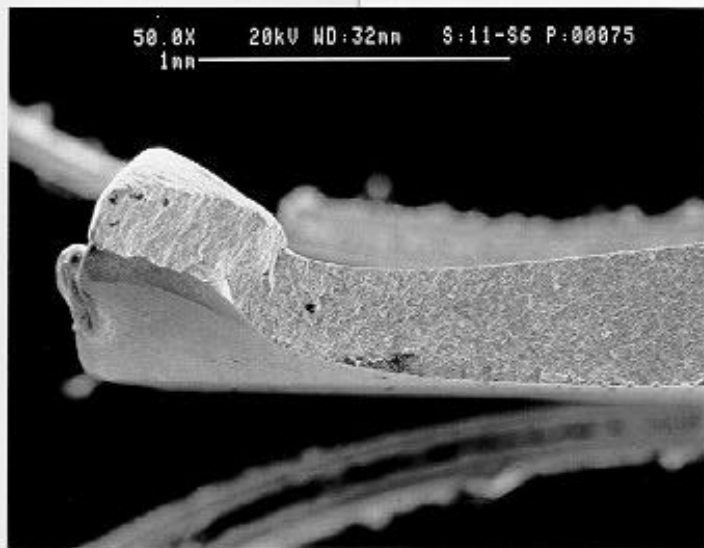
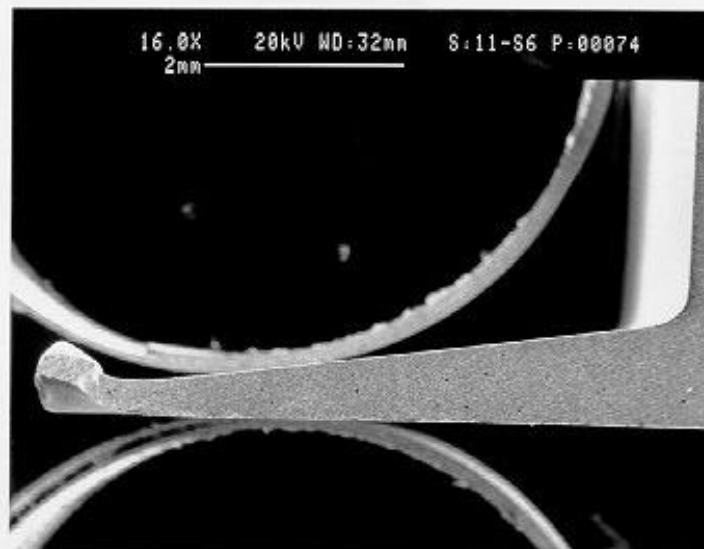
Results: Crack nucleation occurred at 777.7 pounds. The final cycles were 6,238,312. EPD data:

U/Uo	Cycles	Heat Tint Data	Crack Length from Heat Tint (in)
1.0071	6,104,549	680°F @ 20 Hours	0.0247

This specimen had unusual behavior. The U/Uo value changed every time the load was increased and then leveled out before reaching the target value of 1.007. After the U/Uo value stabilized, we would re-initialize U/Uo and then continue the test provided the new U/Uo did not reach 1.007. Once the U/Uo reached 1.007, the crack length was very long. Evaluation of the failure surface appears to indicate the crack grew from the initial crack site which resulted from the FOD.

Attached Data: Micrographs of FOD, U/Uo versus cycles, Micrographs of Failed specimens.





Specimen: 22-S2, Sharp Leading Edge

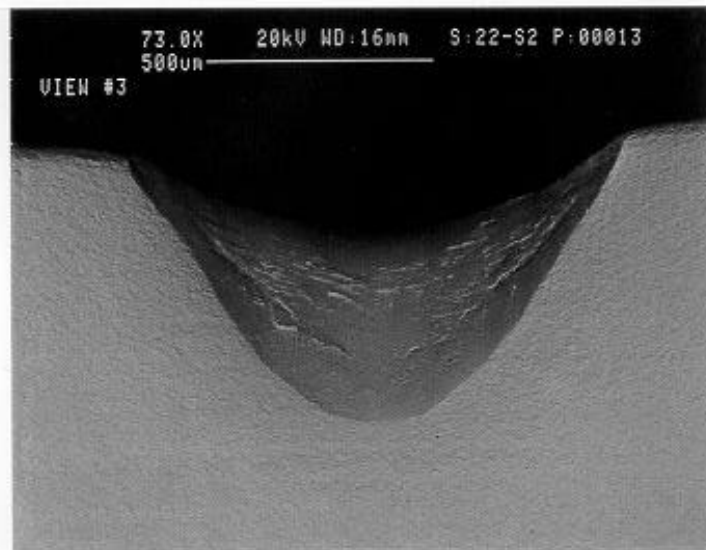
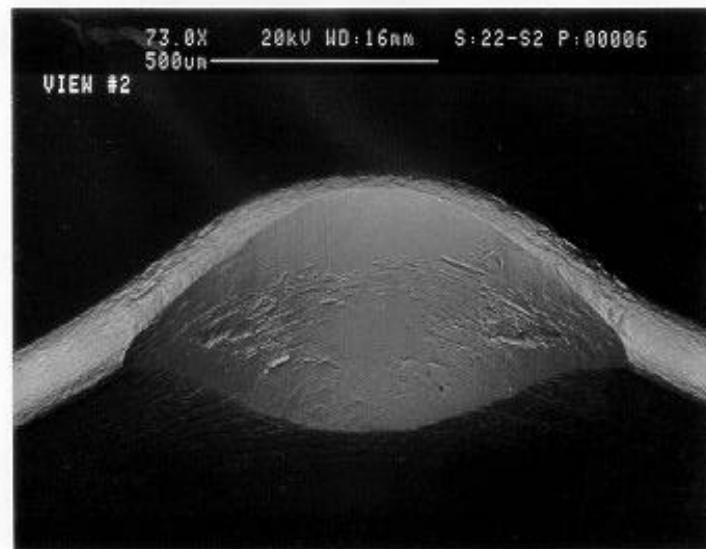
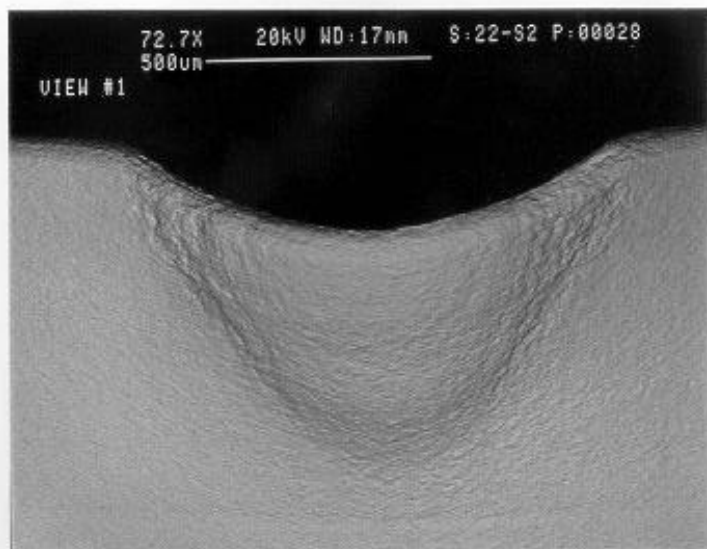
Simulated FOD Conditions: Solenoid Gun, 30° Impact angle, 0.025 inch tip radius, High Damage Level.

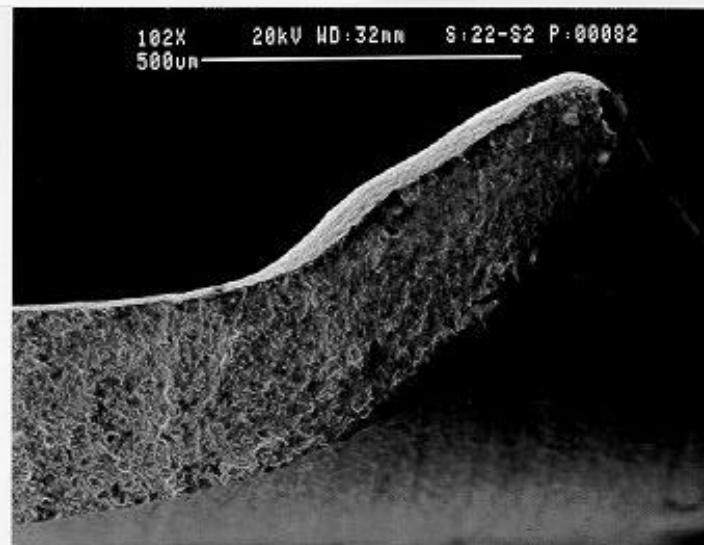
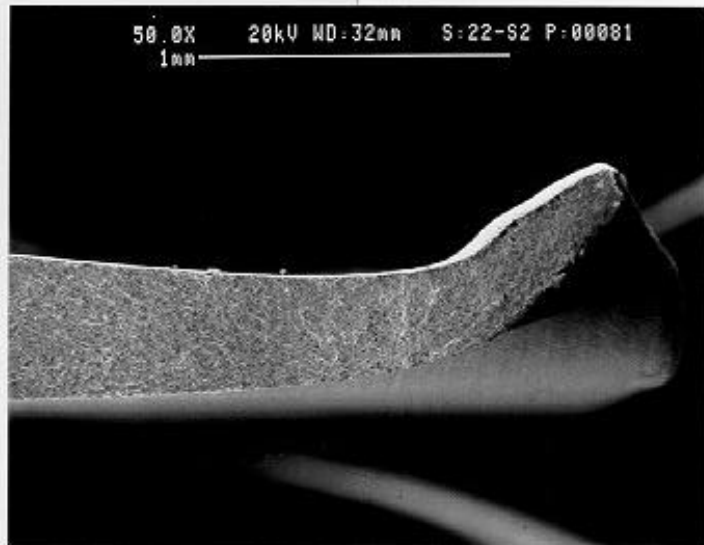
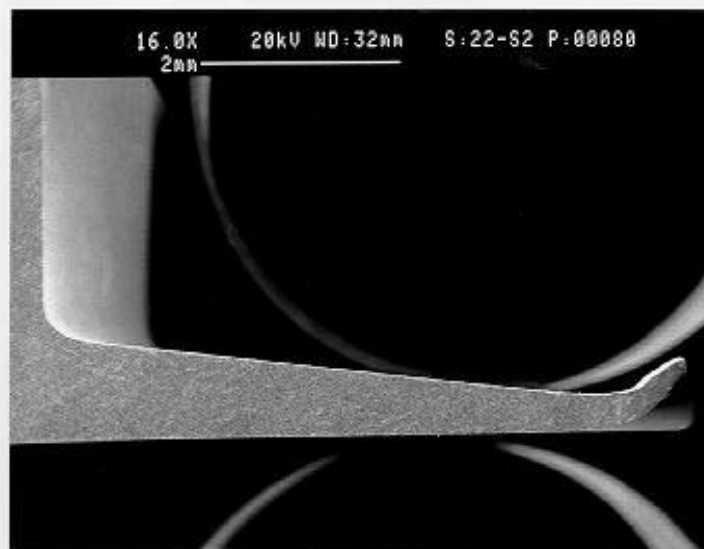
WMT&R Report Number: 9-02027

Test Description: The test was run at an initial load of 941 pounds, R-ratio of 0.5, and 30 Hz. The load was increased by 10% after every 1,000,000 cycles until failure.

Results: Crack nucleation occurred at 1035.1 pounds. The final cycles were 1,687,716.

Attached Data: Micrographs of FOD'ed specimen, Load versus cycle plot, Position versus cycle plot, Micrographs of Failed specimens.





Specimen: 48-04, Sharp Leading Edge

Simulated FOD Conditions: Solenoid Gun, 30° Impact angle, 0.025 inch tip radius, High Damage Level.

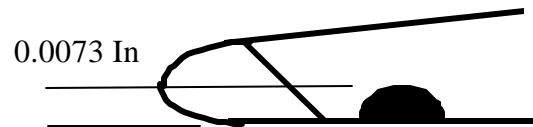
WMT&R Report Number: 9-02027

Test Description: The test was run at an initial load of 439 pounds, R-ratio of 0.5, and 30 Hz. The load was increased by 10% after every 1,000,000 cycles until failure. The specimen had pressure mounted EPD leads to monitor potential drop.

Results: Crack nucleation occurred at 855.5 pounds. The final cycles were 7,606,852. EPD data:

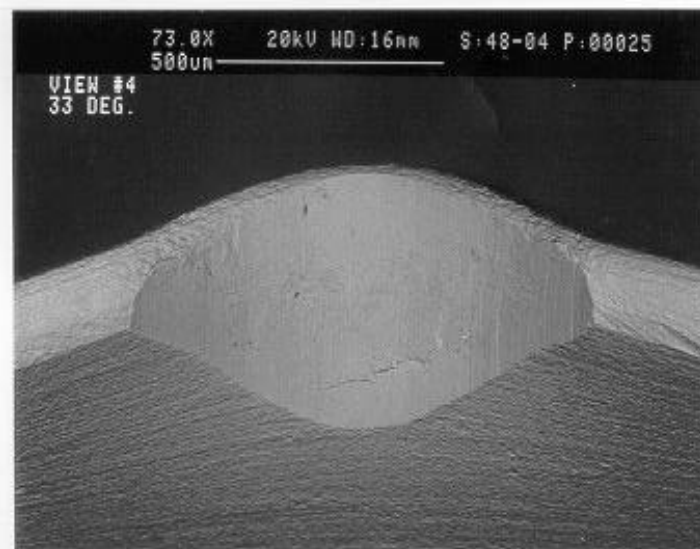
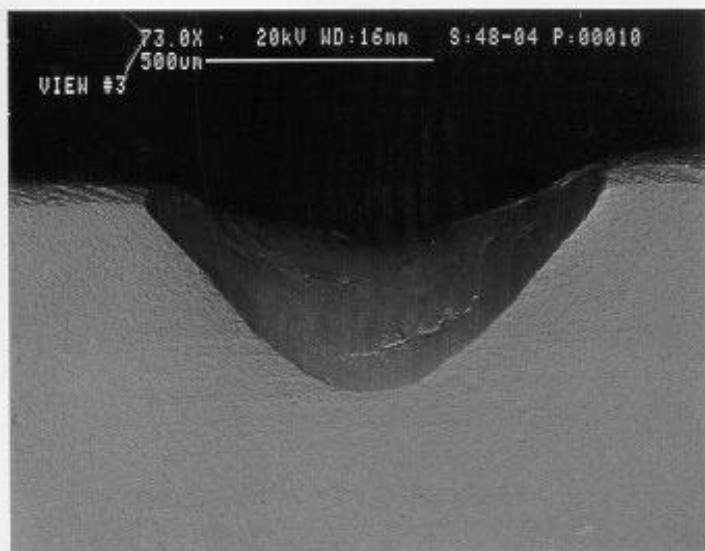
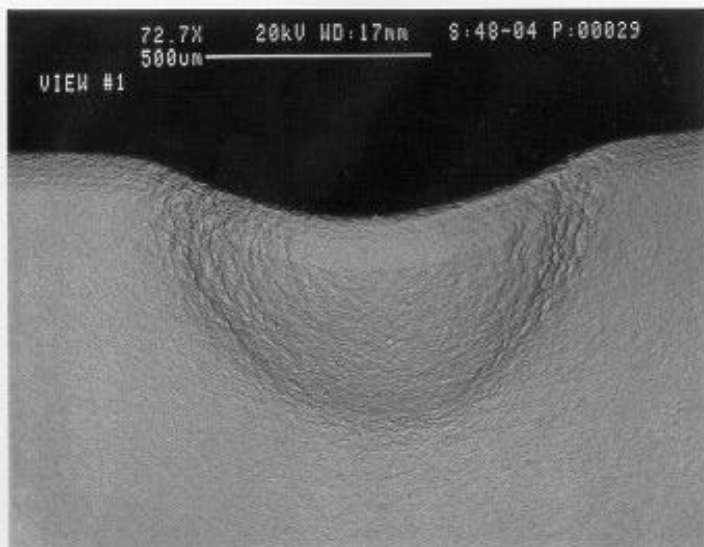
U/Uo	Cycles	Heat Tint Data	Crack Length from Heat Tint (in)
1.0072	7,527,036	680°F @ 20 Hours	0.0073

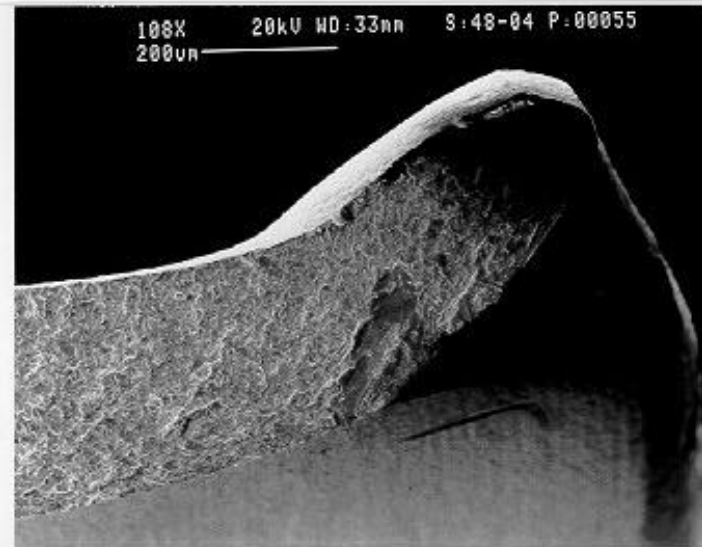
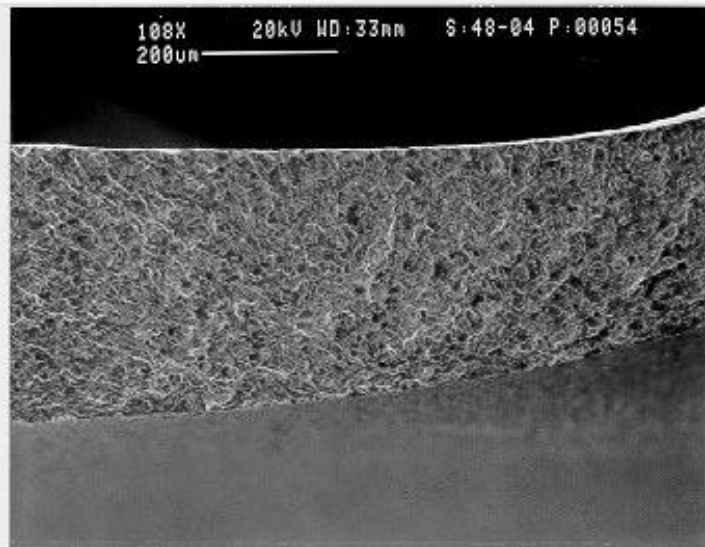
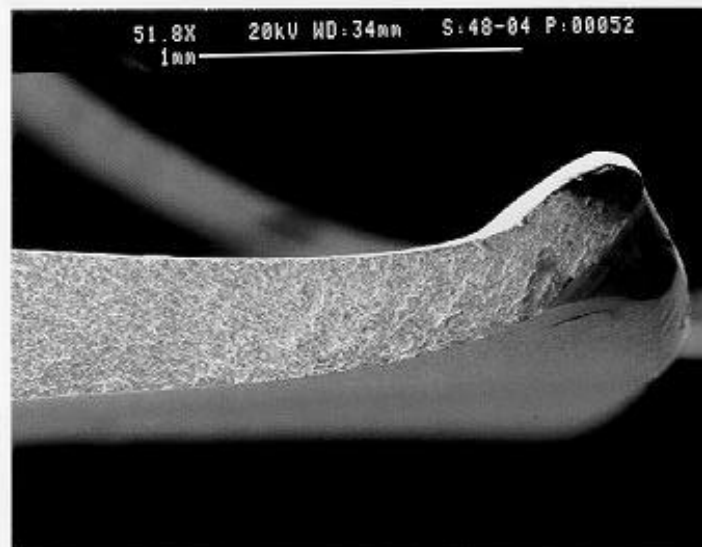
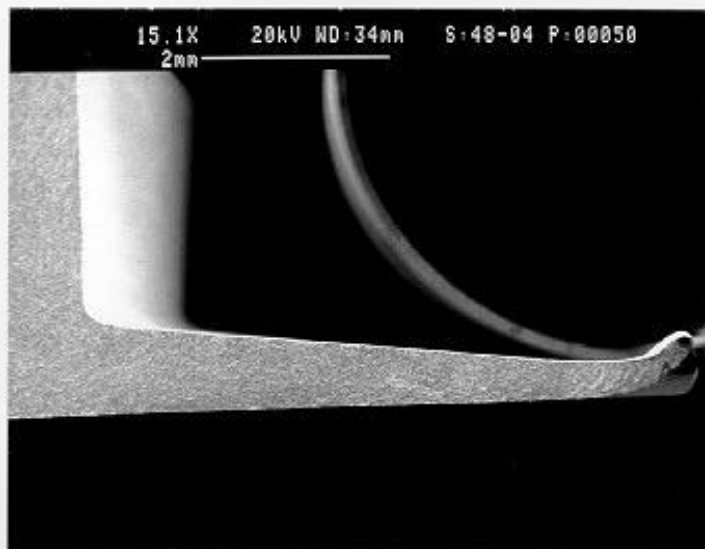
Heat Tint Results:
the



Note: The crack nucleation site was at
base of the out-of-plane deformation

Attached Data: Micrographs of FOD, U/Uo versus cycles, Micrographs of Failed specimens.





Specimen: 70-06, Sharp Leading Edge

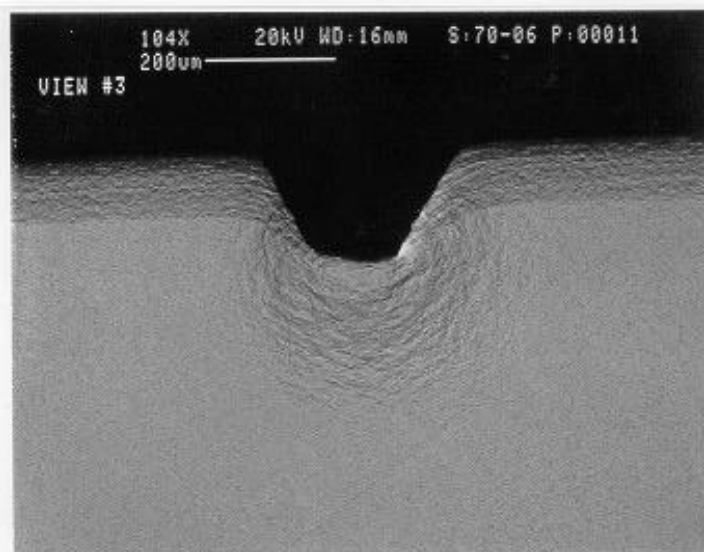
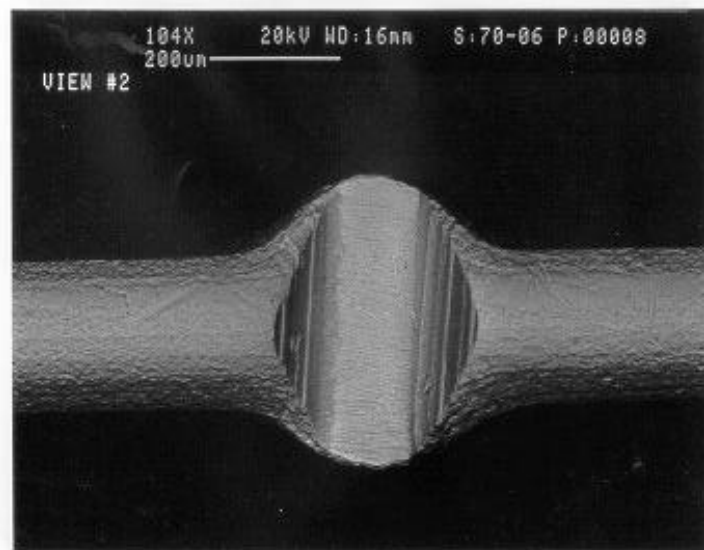
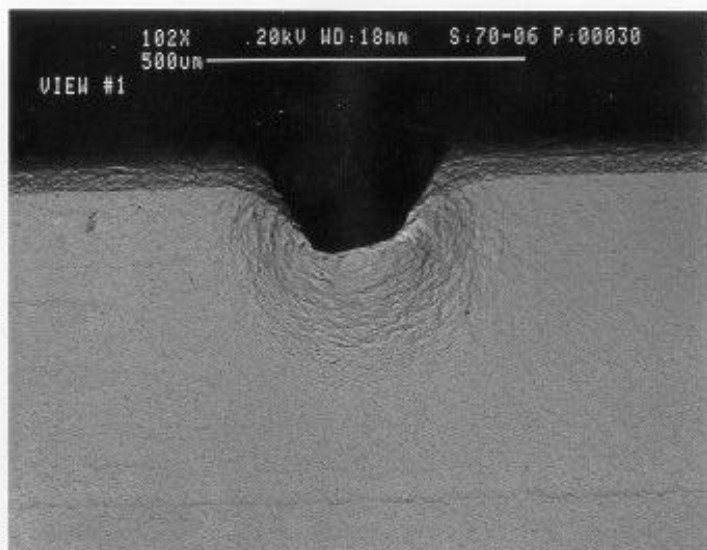
Simulated FOD Conditions: Solenoid Gun, 0° Impact angle, 0.005 inch tip radius, Low Damage Level.

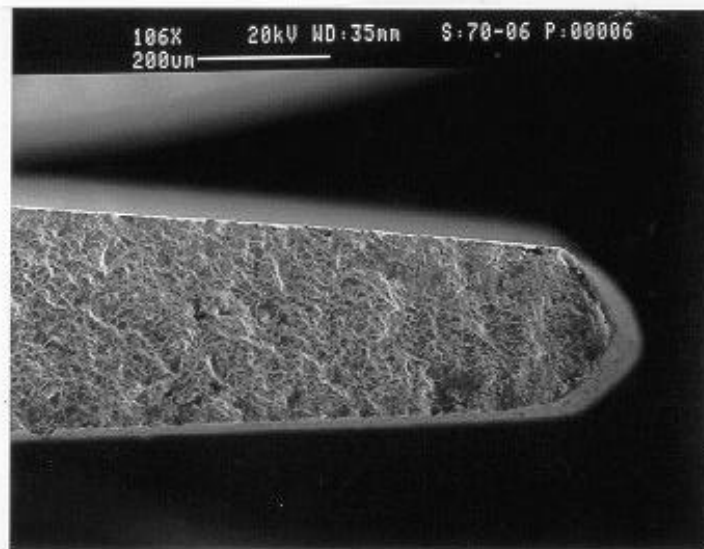
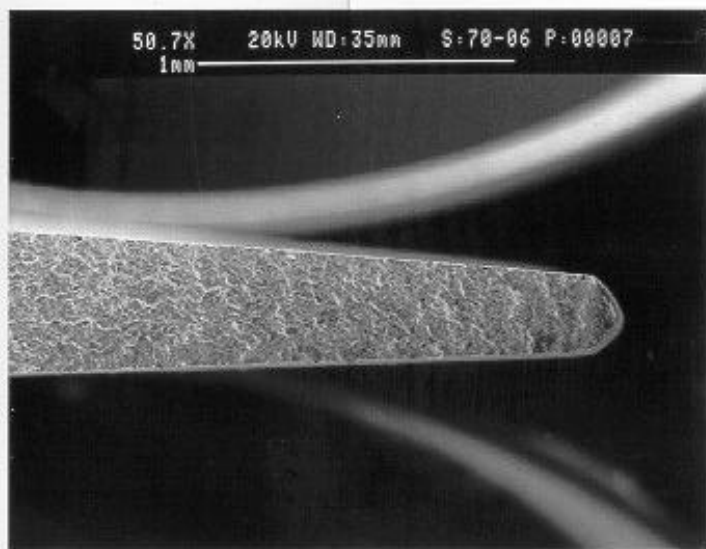
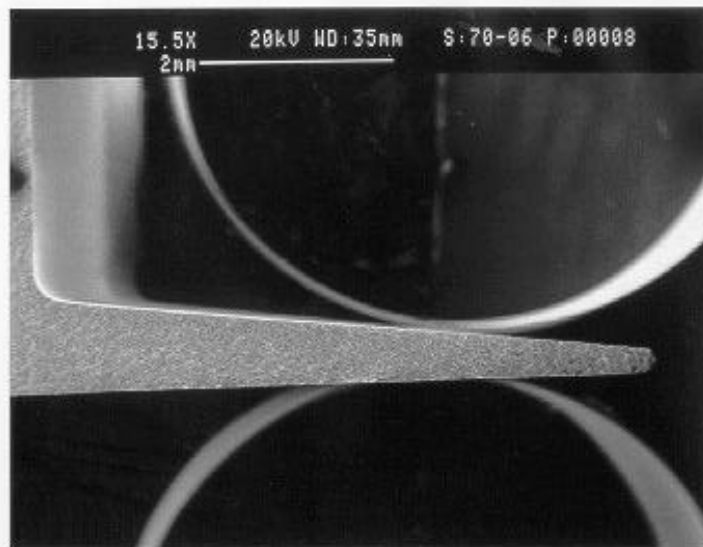
WMT&R Report Number: 9-02027

Test Description: The test was run at an initial load of 439 pounds, R-ratio of 0.5, and 30 Hz. The load was increased by 10% after every 1,000,000 cycles until failure.

Results: Crack nucleation occurred at 1252.5 pounds. The final cycles were 11,474,176. This specimen did not fail at the FOD nick.

Attached Data: Micrographs of FOD'ed specimen, Load versus cycle plot, Position versus cycle plot, Micrographs of Failed specimens.





Specimen: 76-S1, Sharp Leading Edge

Simulated FOD Conditions: Solenoid Gun, 0° Impact angle, 0.005 inch tip radius, Low Damage Level.

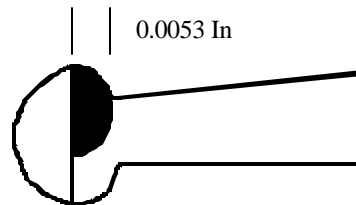
WMT&R Report Number: 9-02027

Test Description: The test was run at an initial load of 439 pounds, R-ratio of 0.5, and 30 Hz. The load was increased by 10% after every 1,000,000 cycles until failure. The specimen had pressure mounted EPD leads to monitor potential drop.

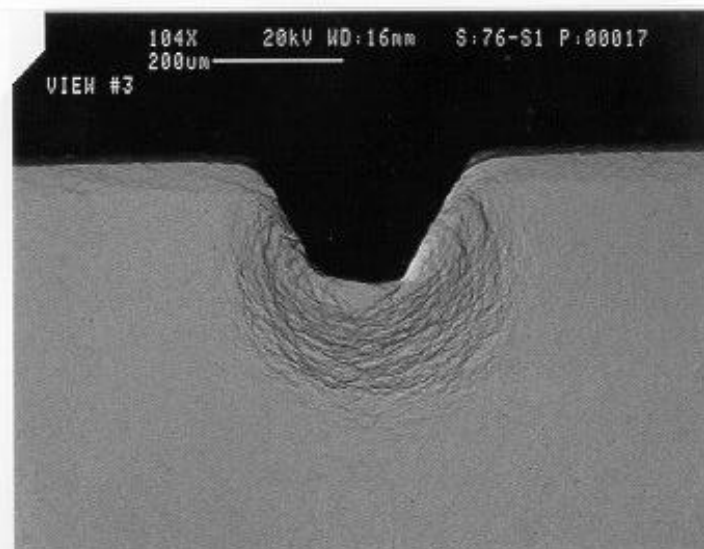
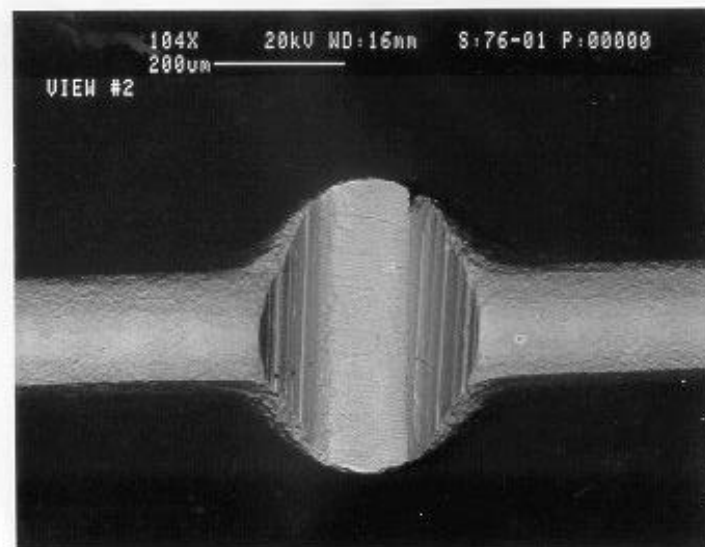
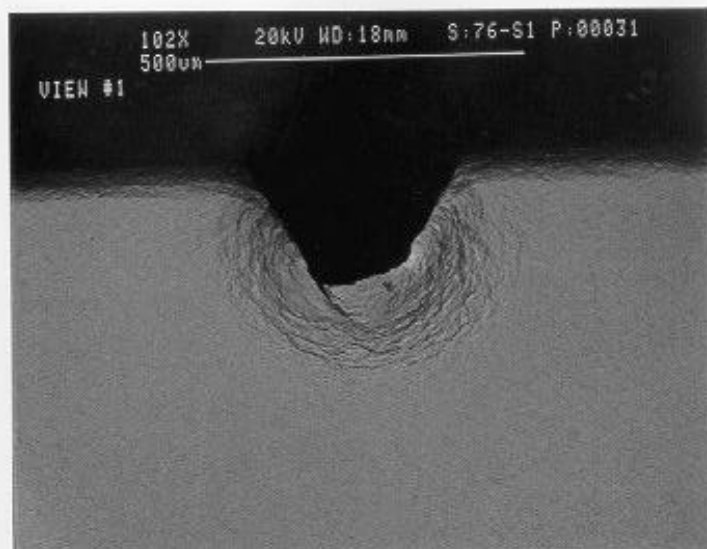
Results: Crack nucleation occurred at 1139.2 pounds. The final cycles were 10,121,452. EPD data:

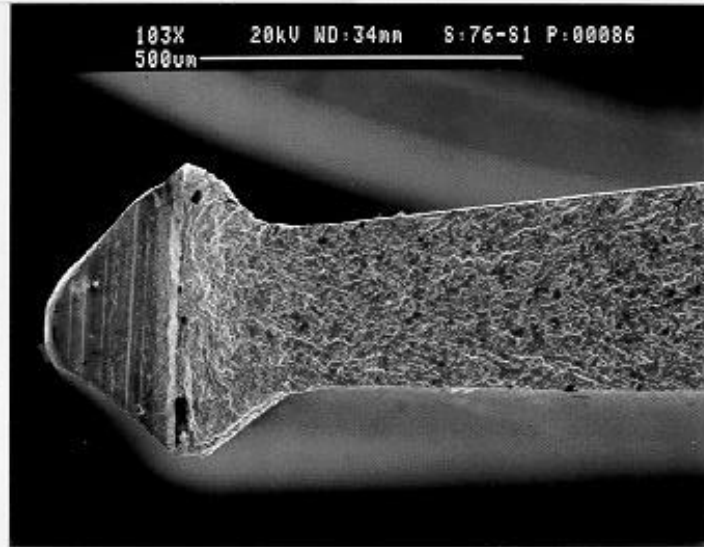
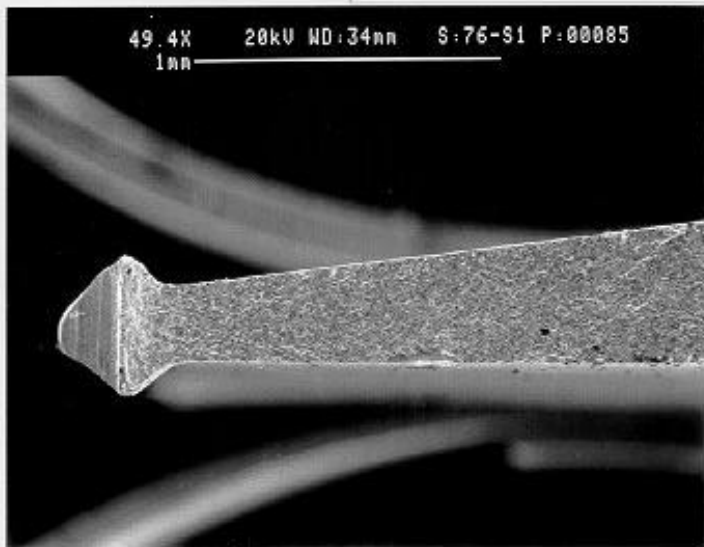
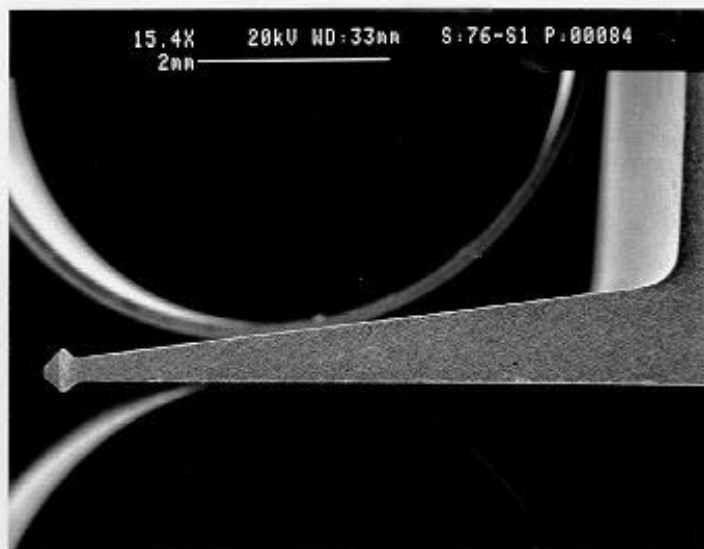
U/Uo	Cycles	Heat Tint Data	Crack Length from Heat Tint (in)
1.0071	10,078,983	680°F @ 20 Hours	0.0053

Heat Tint Results:



Attached Data: Micrographs of FOD, U/Uo versus cycles, Micrographs of Failed specimens.





Specimen: 22-B3, Blunt Leading Edge

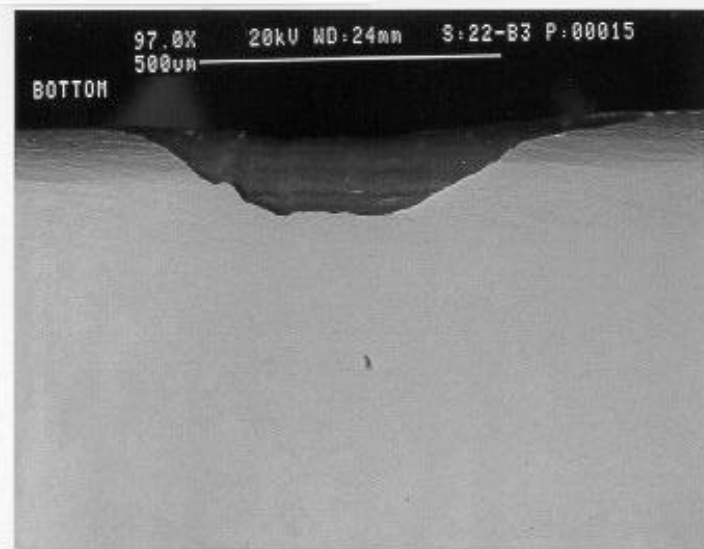
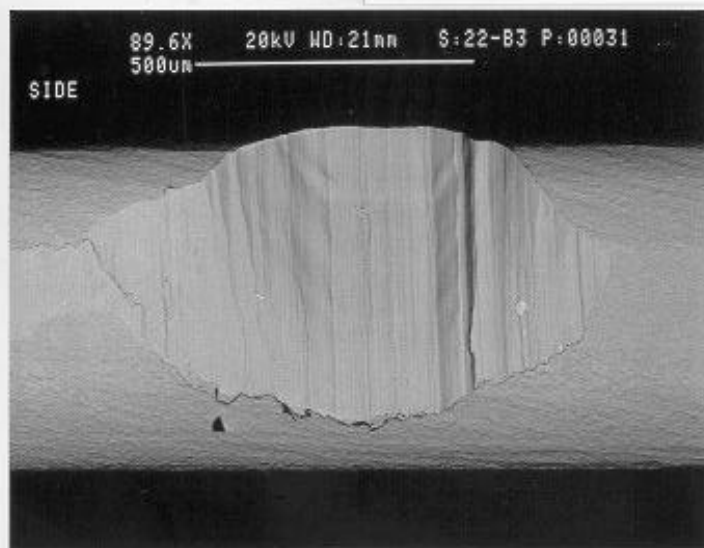
Simulated FOD Conditions: Solenoid Gun, 90° Impact angle, 0.005 inch tip radius, Low Damage Level. The solenoid gun did not give the desired impact damage. 90° impacts with the solenoid gun are not recommend for future testing.

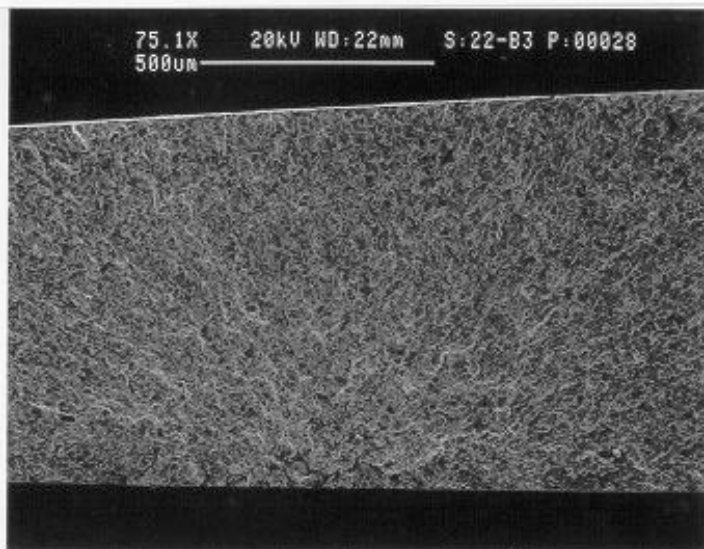
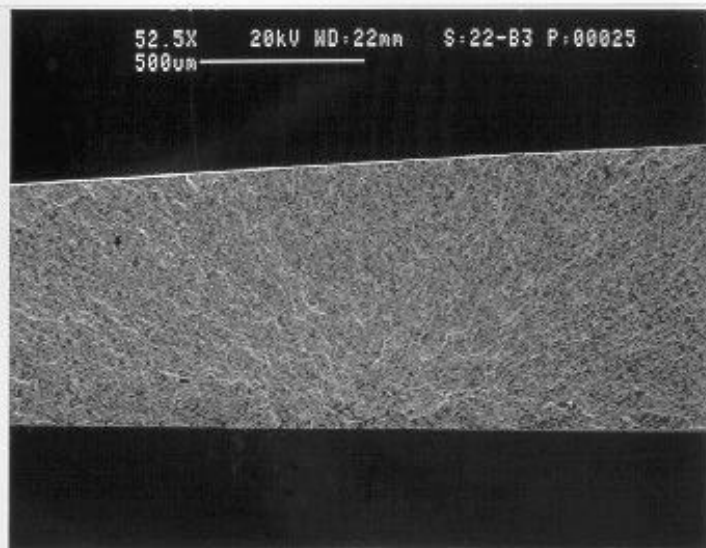
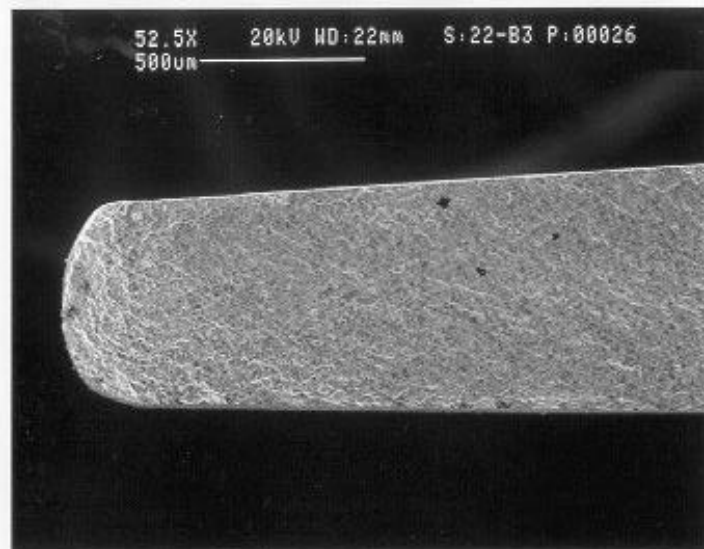
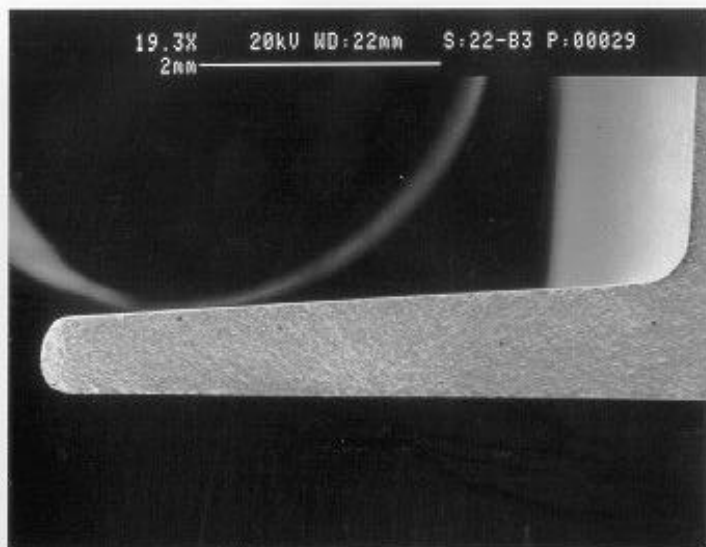
WMT&R Report Number: 9-04629

Test Description: The test was run at an initial load of 439 pounds, R-ratio of 0.5, and 30 Hz. The load was increased by 10% after every 1,000,000 cycles until failure.

Results: Crack nucleation occurred at 1252.5 pounds. The final cycles were 11,764,000. This specimen did not fail at the FOD nick.

Attached Data: Micrographs of FOD'ed specimen, Load versus cycle plot, Position versus cycle plot, Micrographs of Failed specimens.





Specimen: 36-B6, Blunt Leading Edge

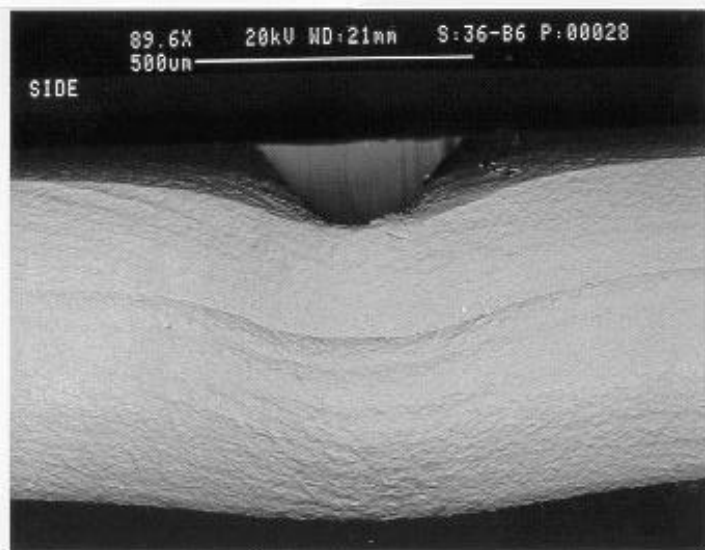
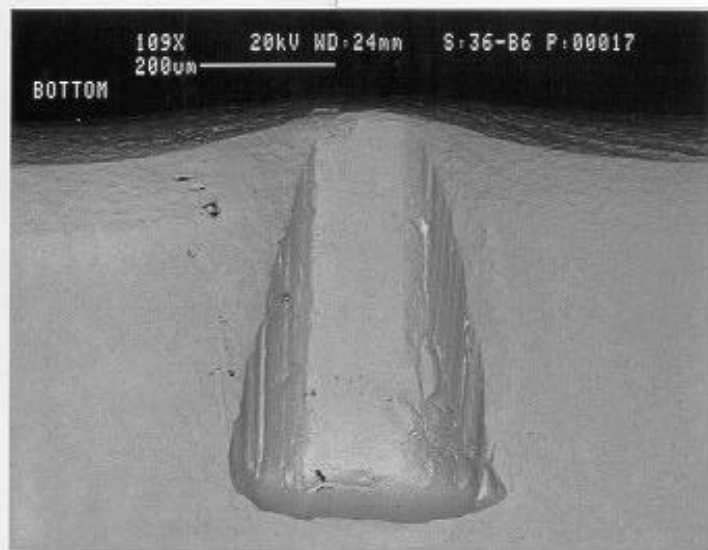
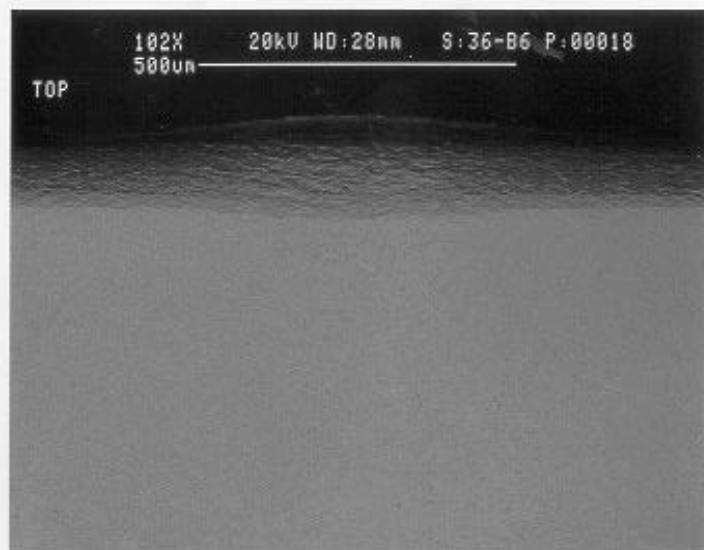
Simulated FOD Conditions: Solenoid Gun, 90° Impact angle, 0.005 inch tip radius, Low Damage Level. The solenoid gun did not give the desired impact damage. 90° impacts with the solenoid gun are not recommend for future testing.

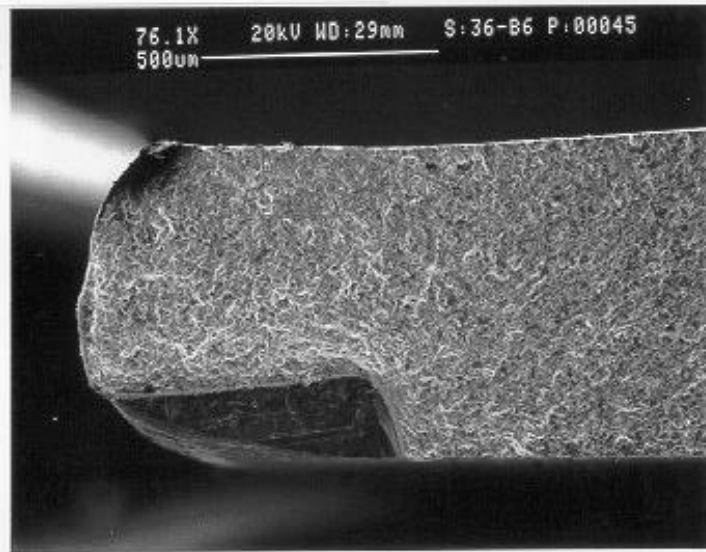
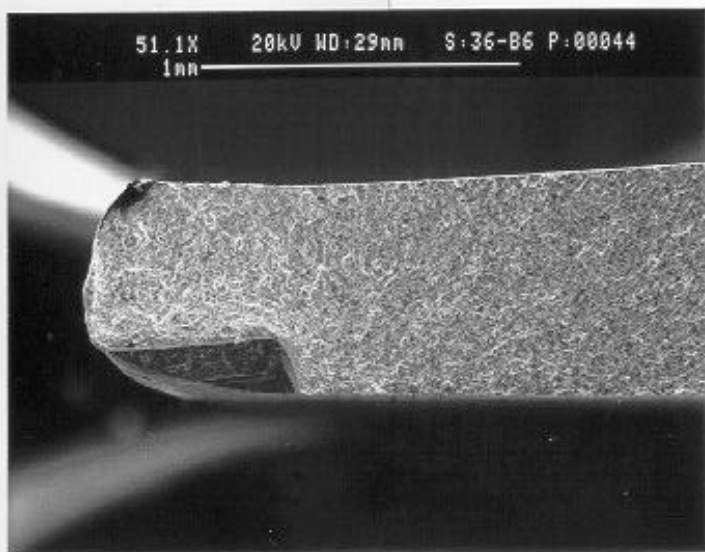
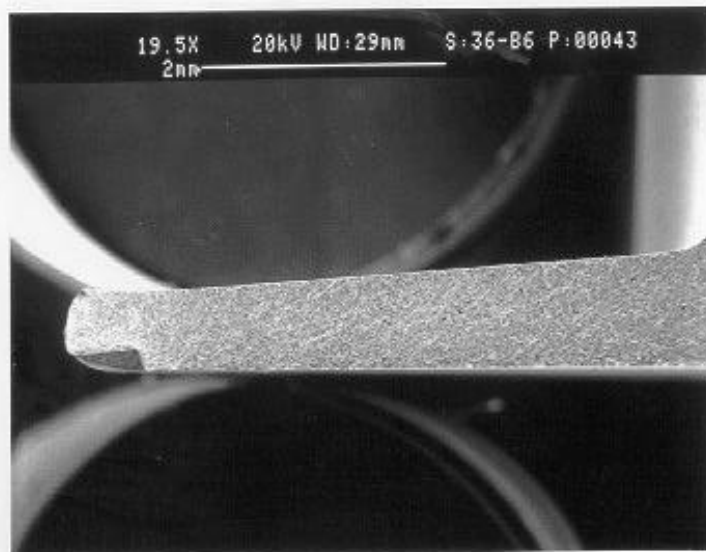
WMT&R Report Number: 9-04629

Test Description: The test was run at an initial load of 439 pounds, R-ratio of 0.5, and 30 Hz. The load was increased by 10% after every 1,000,000 cycles until failure.

Results: Crack nucleation occurred at 941 pounds. The final cycles were 8,246,868.

Attached Data: Micrographs of FOD'ed specimen, Load versus cycle plot, Position versus cycle plot, Micrographs of Failed specimens.

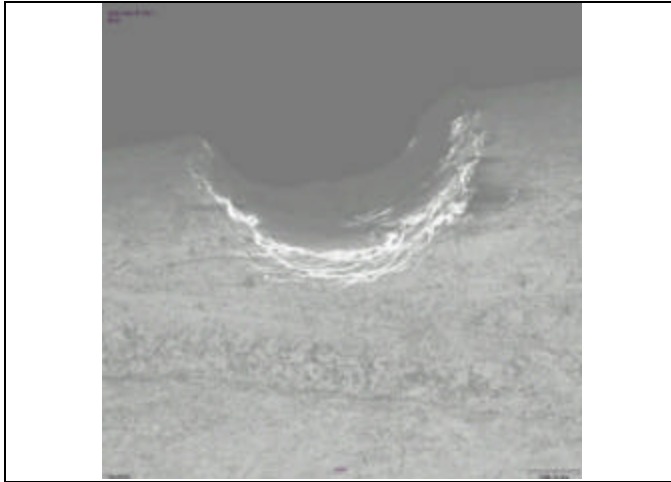




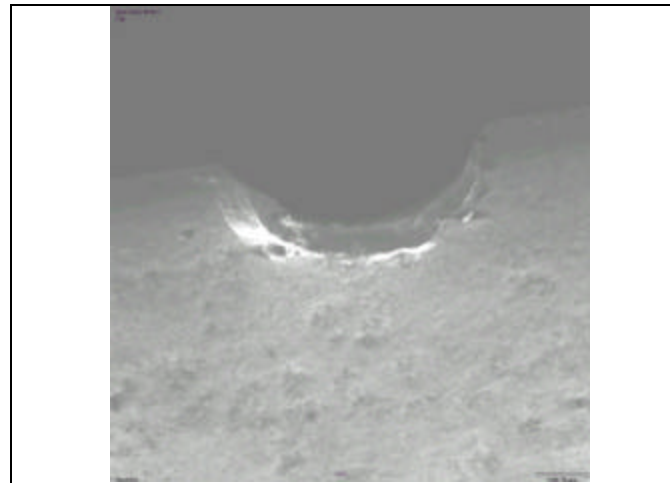
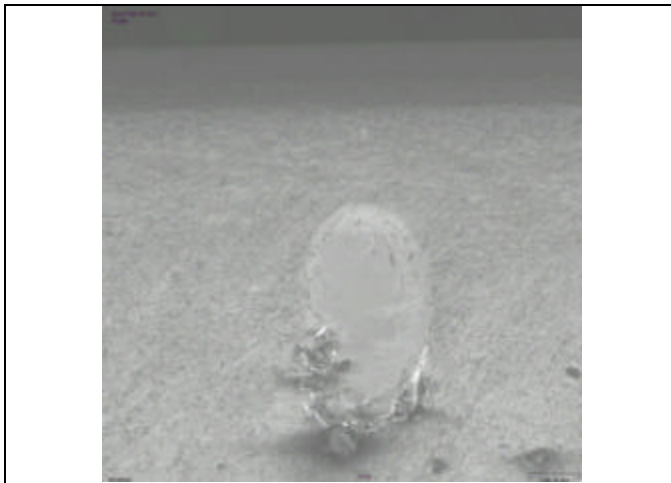
Specimen 189-01

conducted with a stress ratio of 0.5 at an initial load of 643.1 lbs and a frequency of 30 Hz. EPD was monitored throughout the test. When load did not occur after 1,000,000 cycles the load was increased 5%. Crack nucleation occurred at 707.4 lbs, and the test was continued at this load to failure. Total cycles to nucleation using a U/U_o of 1.015, 1.05, and 1.20 was 216,194.

Specimen 189-01 FOD Characterization



Side A

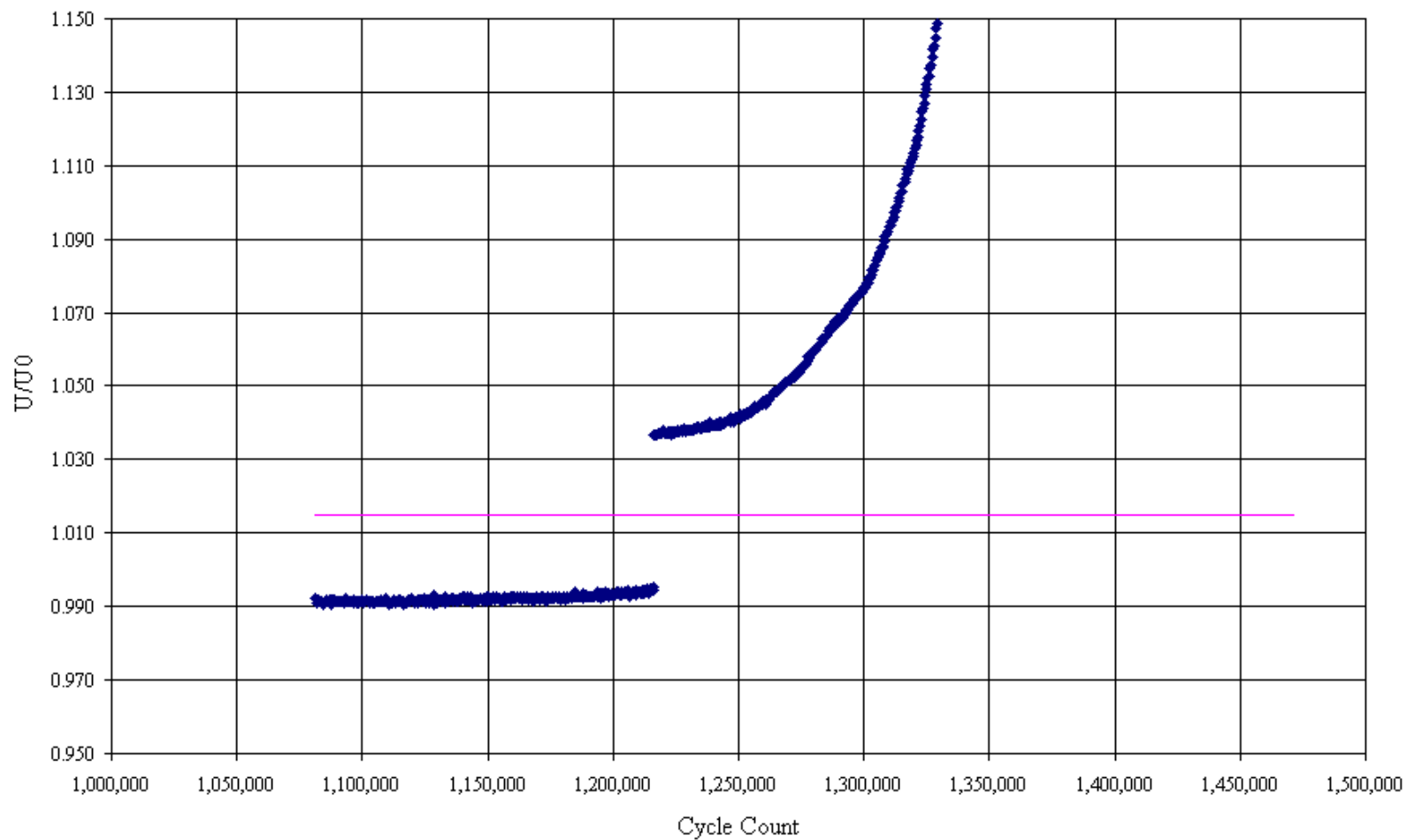


Side A

Overall picture of the EPD versus Cycle count for sample 189-01

PD behavior for FOD Sample 189-1

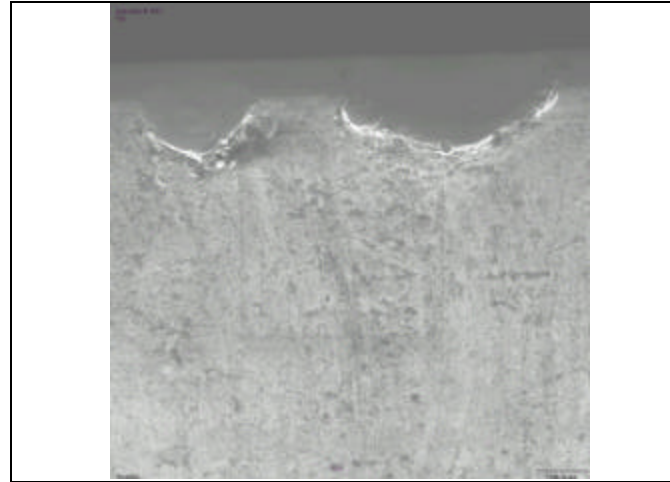
5C-131



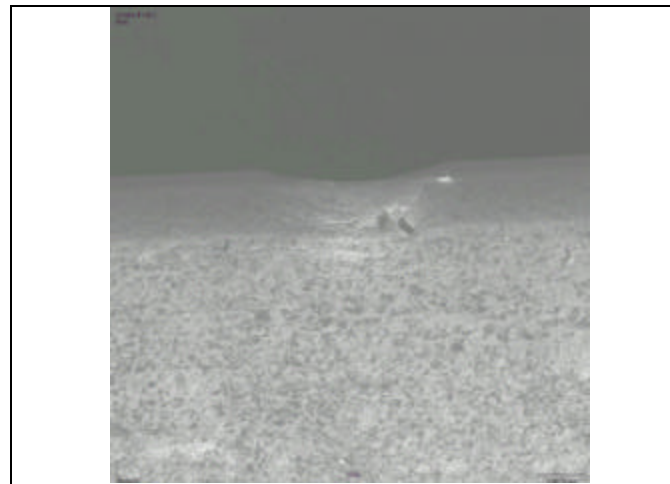
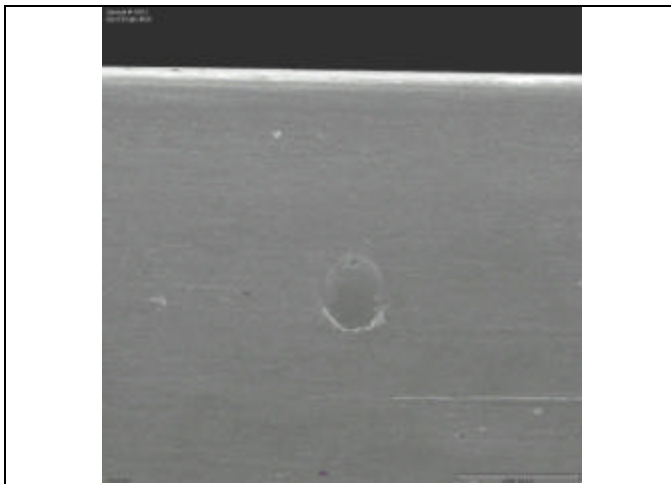
Specimen 189-02

Description: Sharp tip FOD specimen with a high energy ballistic impact at 30° with a 0.5 mm radius ball. The test was conducted with a stress ratio of 0.5 at an initial load of 300 lbs and a frequency of 30 Hz. EPD was monitored throughout the test. When load did not occur after 1,000,000 cycles the load was increased 5%. Crack nucleation occurred from the attached PD wire and was thus discontinued at 12,000,000 total cycles.

Specimen 189-02 FOD Characterization



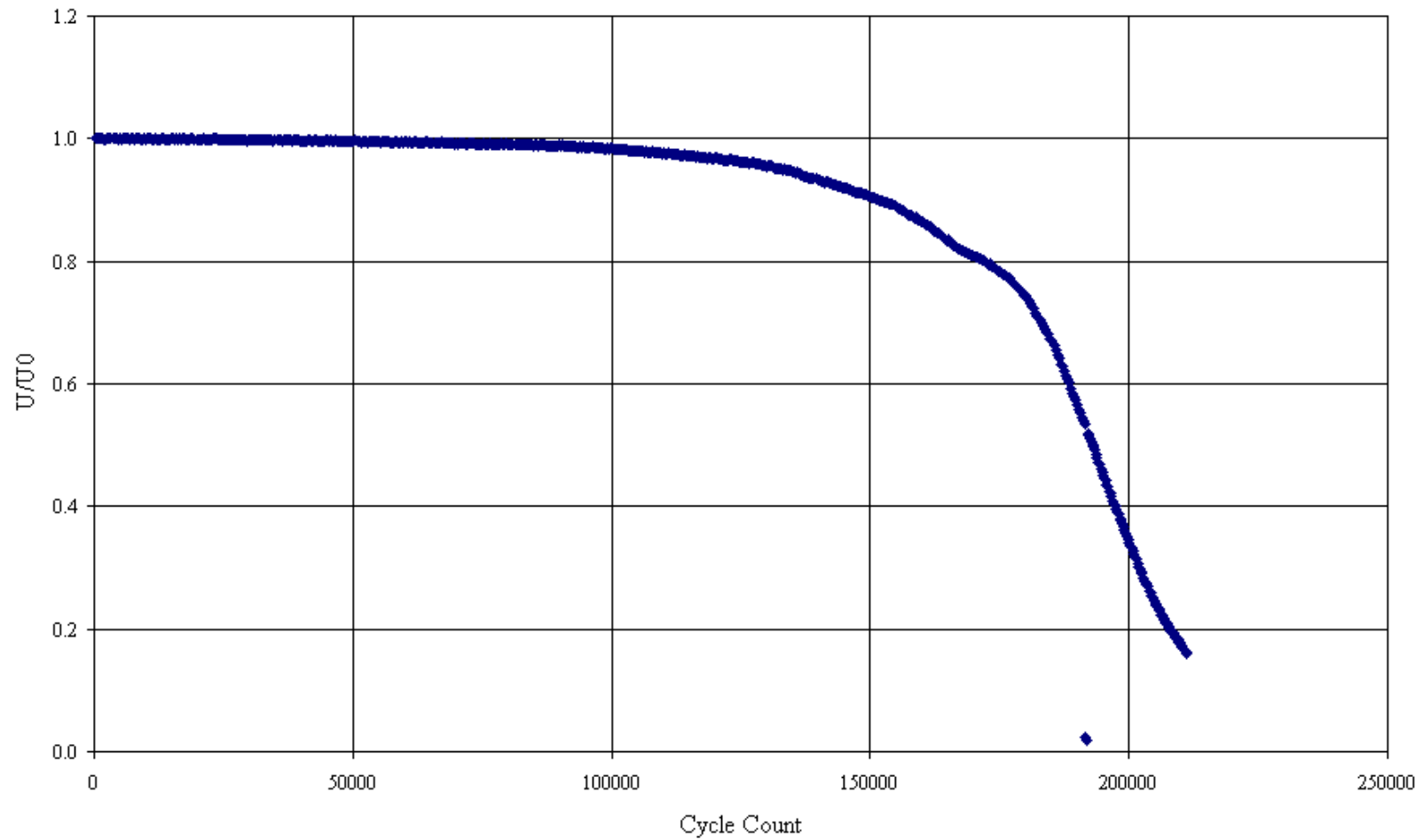
Side A



Side A

Overall picture of the EPD versus Cycle count for sample 189-02

PD behavior for FOD Sample 189-2

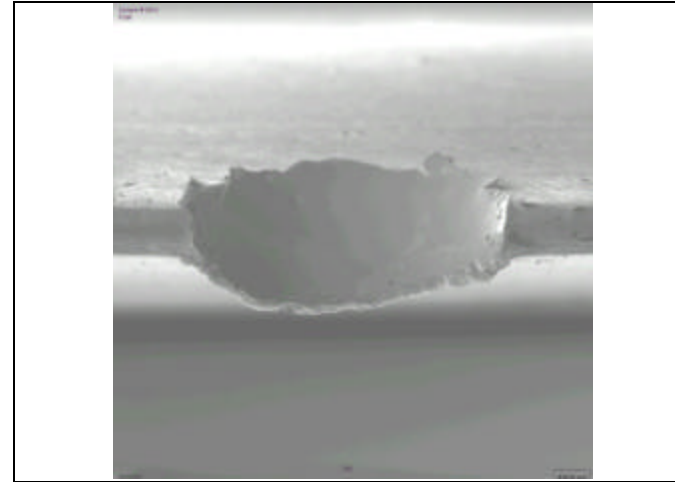
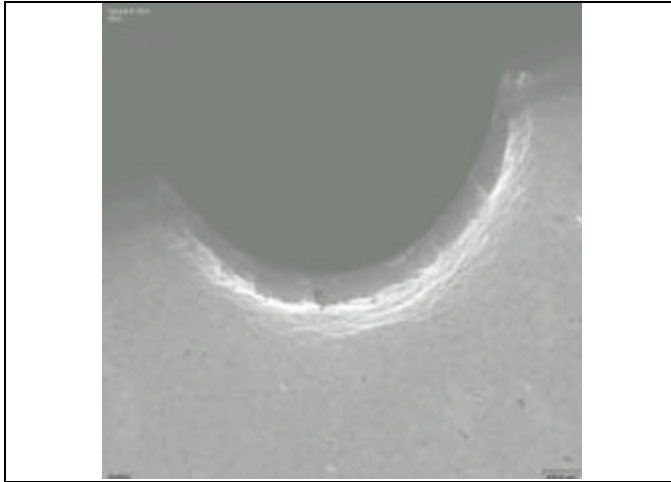


5C-134

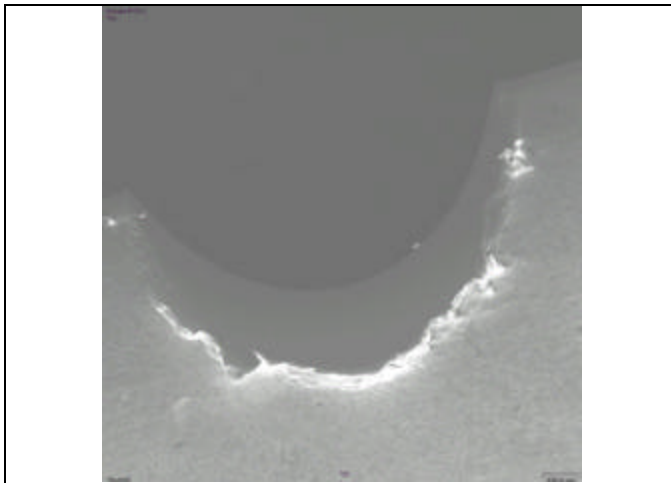
Specimen 189-4

Description: Sharp tip FOD specimen with a high energy ballistic impact at 30° with a 0.5 mm ball radius. The test was conducted with a stress ratio of 0.5 at an initial load of 300.0 lbs and a frequency of 30 Hz. EPD was monitored throughout the test. When load did not occur after 1,000,000 cycles the load was increased 5%. Crack nucleation occurred at 941.5 lbs, and the test was continued at this load. Total cycles to nucleation using a U/U_0 of 1.0075 was 125,565.

Specimen 189-04 FOD Characterization



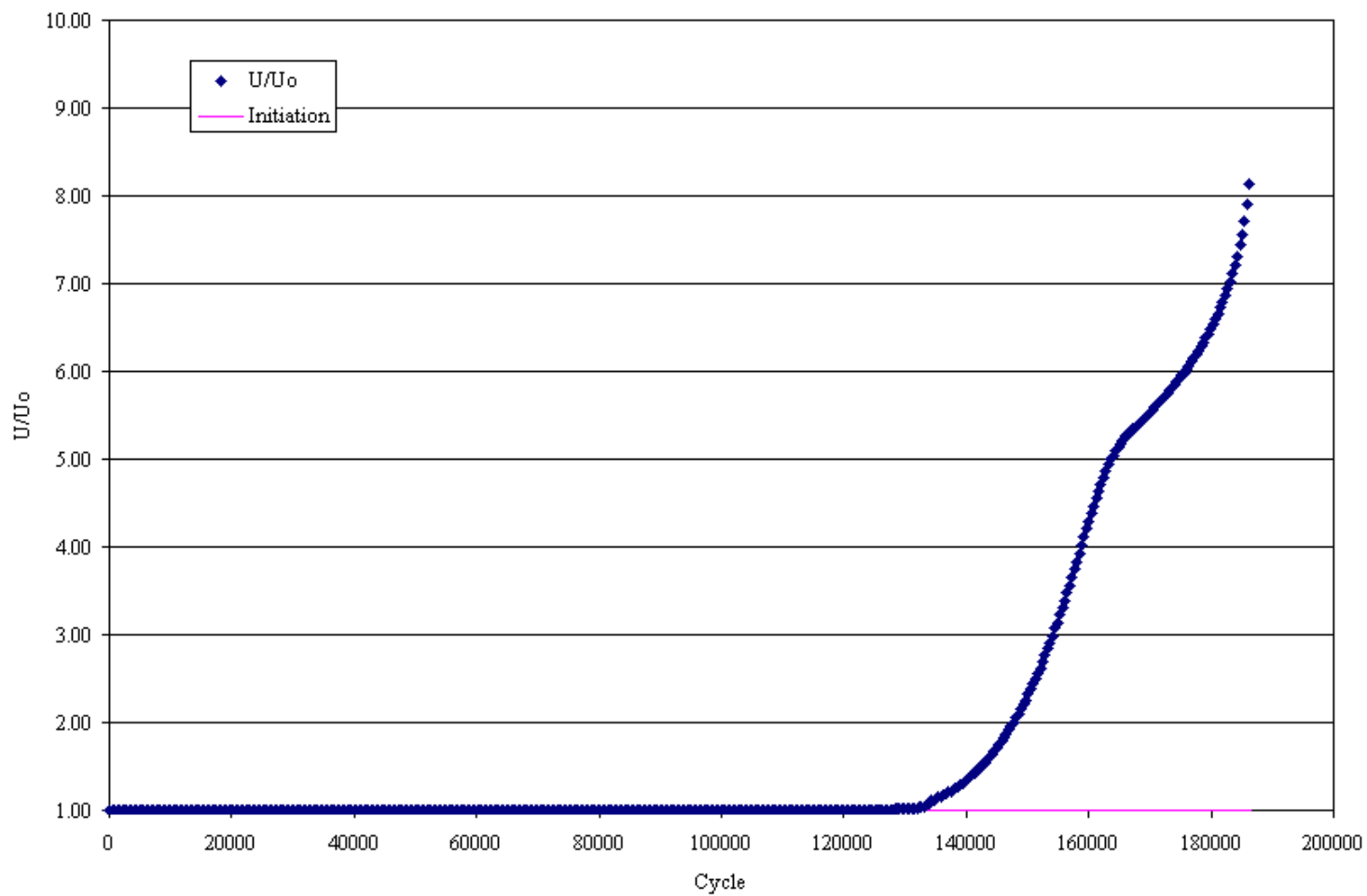
Side A



Side A

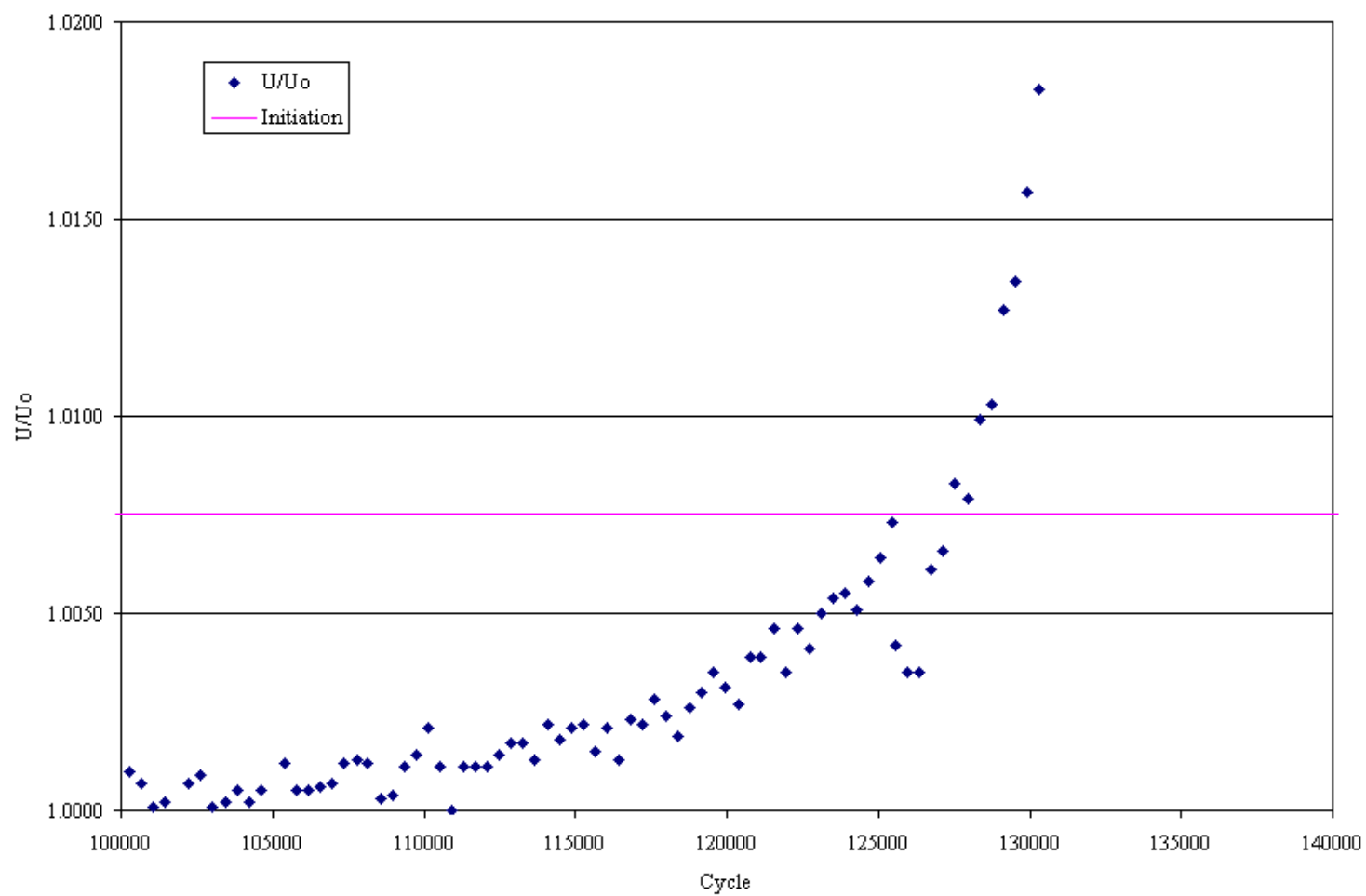
Overall picture of the EPD versus Cycle count for sample 189-04

PD Behavior for FOD Sample 189-4



Closeup picture of the EPD versus Cycle count for sample 189-04

PD Behavior for FOD Sample 189-4

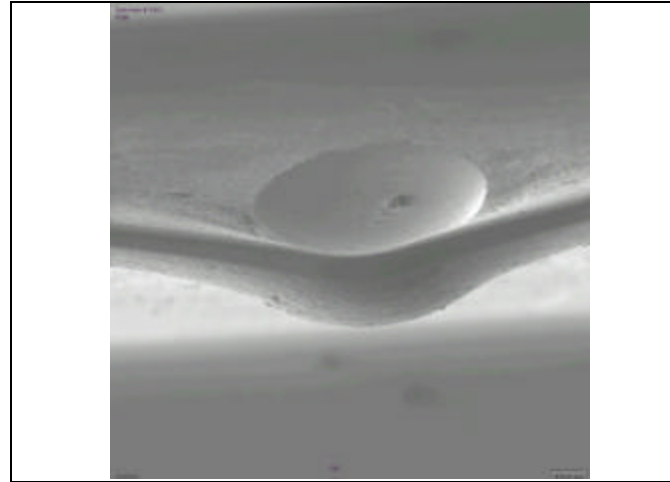
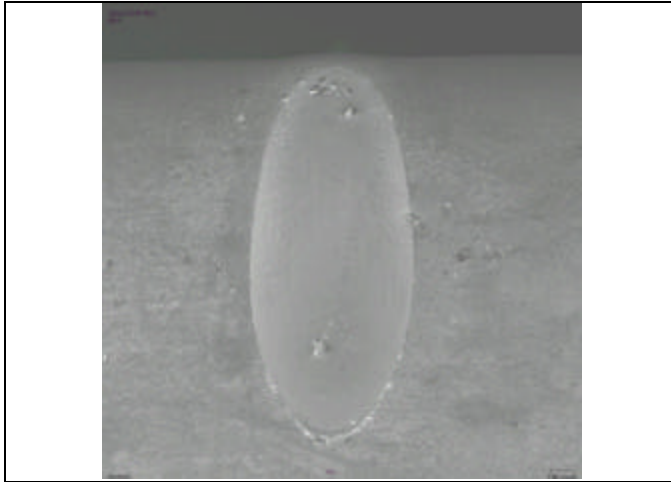


5C-138

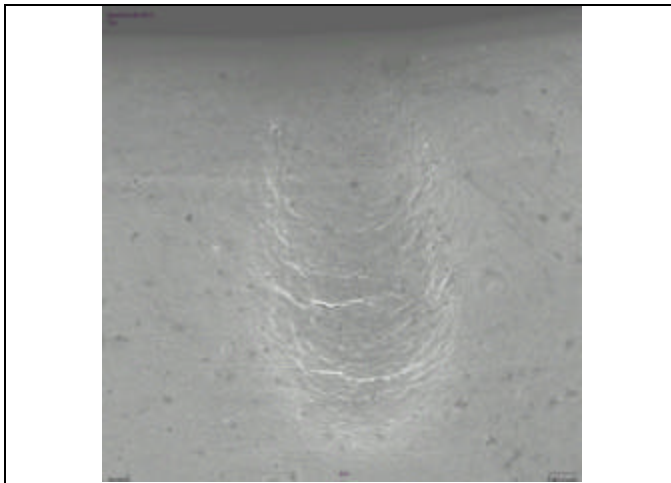
Specimen 189-05

Description: Sharp tip FOD specimen with a high energy ballistic impact at 30° with a 1.0 mm ball radius. The test was conducted with a stress ratio of 0.5 at an initial load of 643.1 lbs and a frequency of 30 Hz. EPD was monitored throughout the test. When load did not occur after 1,000,000 cycles the load was increased 5%. Crack nucleation occurred at 778.2 lbs, and the test was continued at this load. Total cycles to nucleation using a U/U_0 of 1.0075 was 357,968.

Specimen 189-05 FOD Characterization



Side A

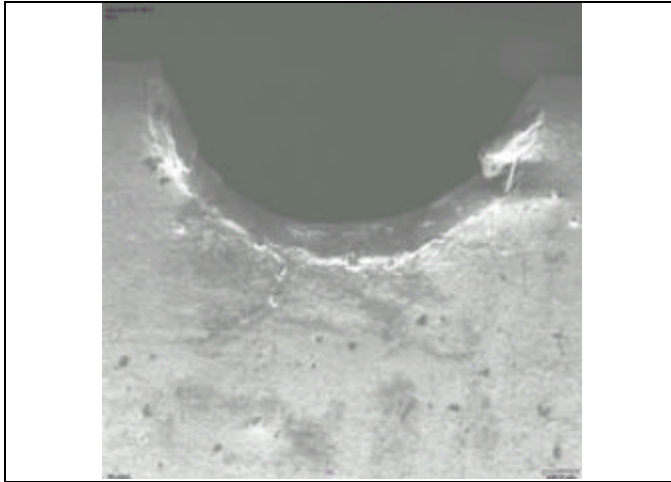


Side A

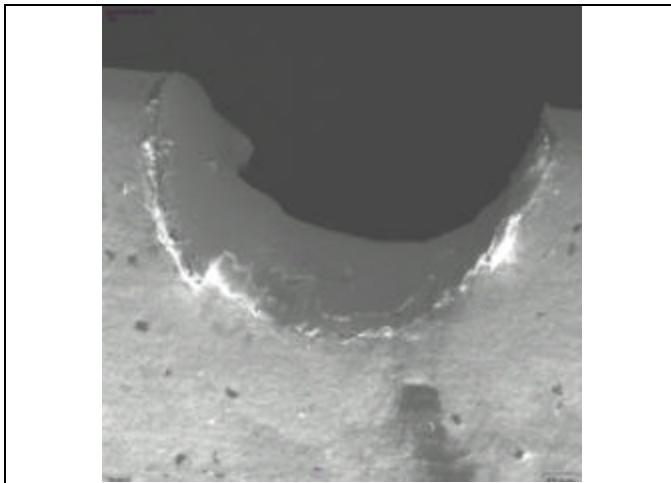
Specimen 189-06

Description: Sharp tip FOD specimen with a high energy ballistic impact at 30° with a 1.0 mm ball radius. The test was conducted with a stress ratio of 0.5 at an initial load of 707.4 lbs and a frequency of 30 Hz. EPD was monitored throughout the test. Crack nucleation occurred at 707.4 lbs, and the test was continued at this load. Total cycles to nucleation using a U/U_o of 1.0075 was 157,243.

Specimen 189-06 FOD Characterization



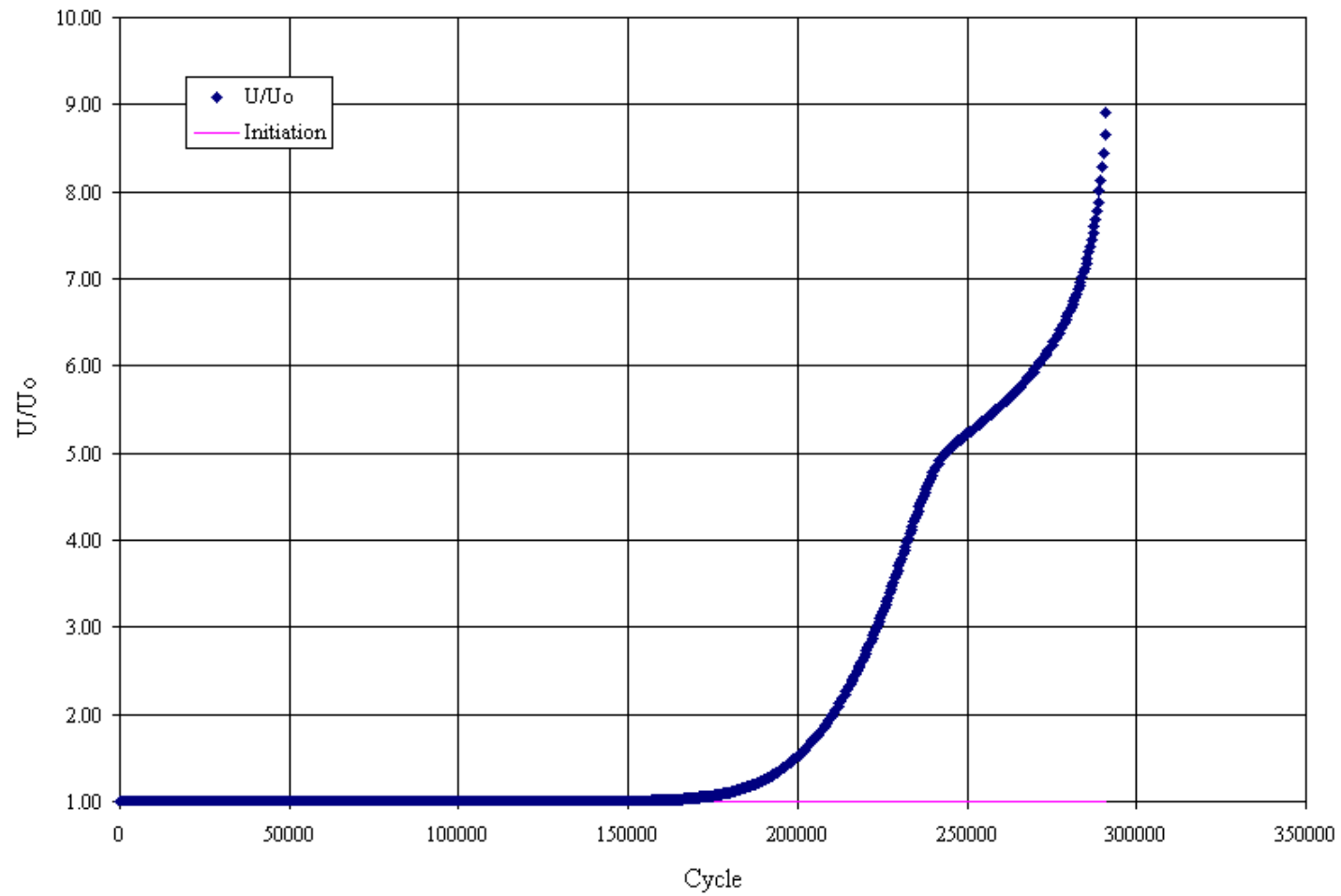
Side A



Side A

Overall picture of the EPD versus Cycle count for sample 189-6

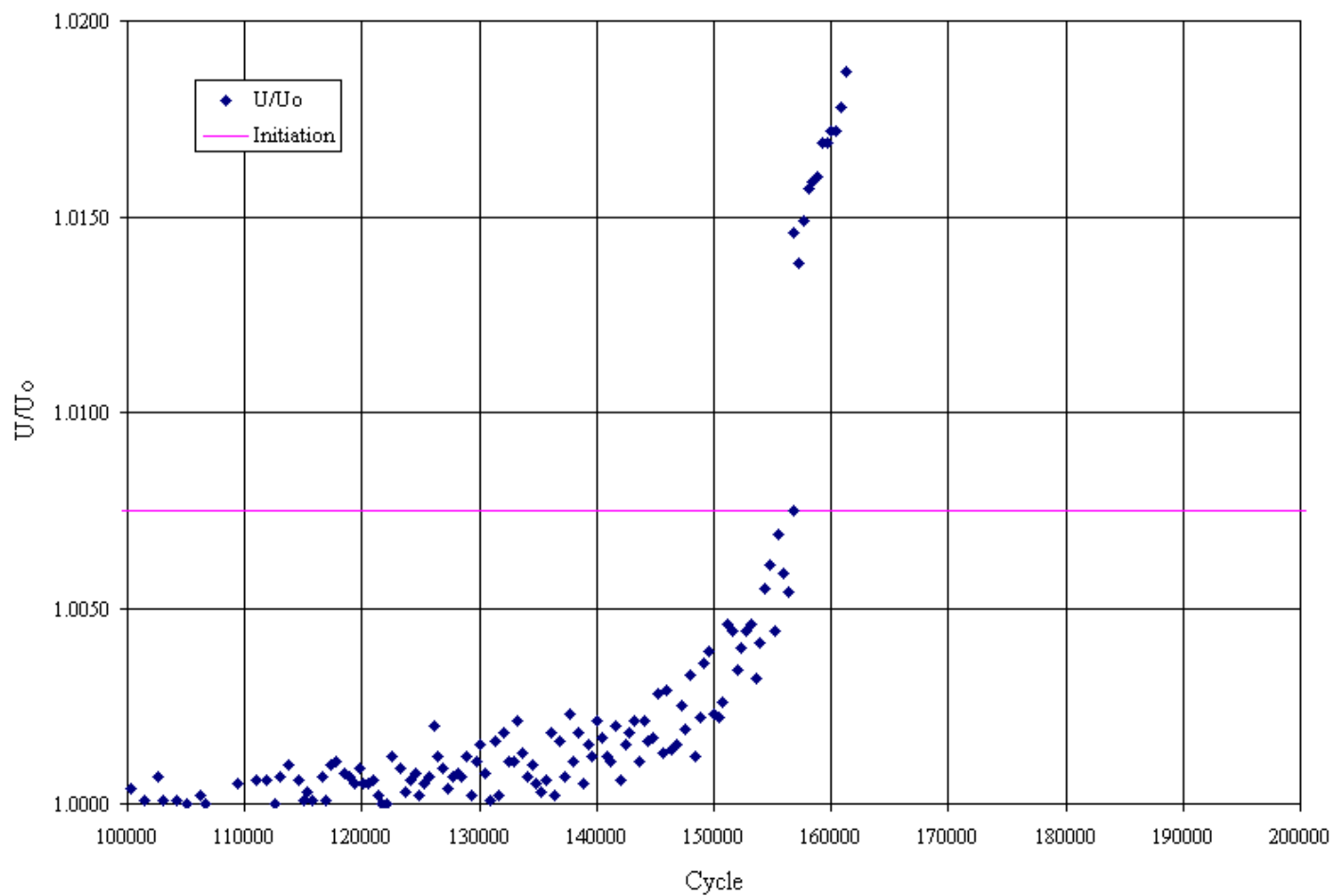
PD Behavior for FOD Sample 189-6



5C-143

Closeup picture of the EPD versus Cycle count for sample 189-06

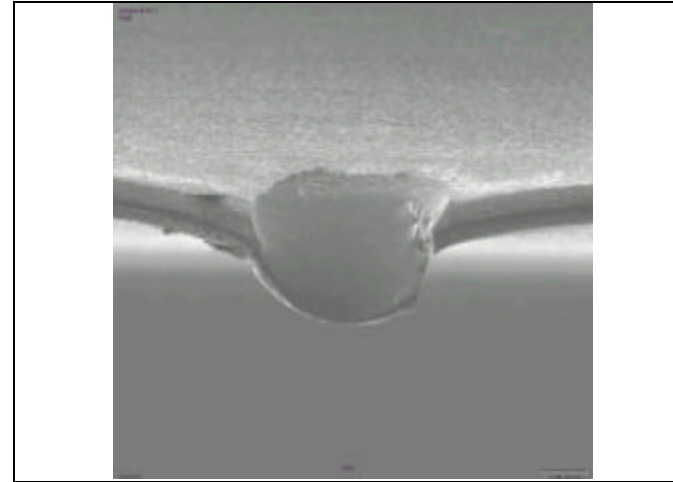
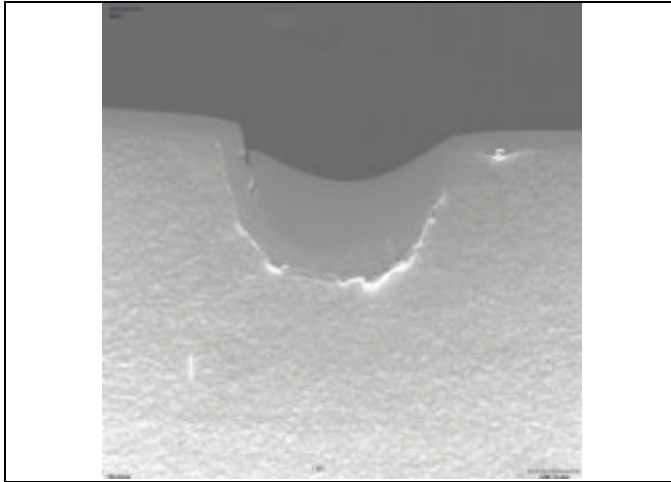
PD Behavior for FOD Sample 189-6



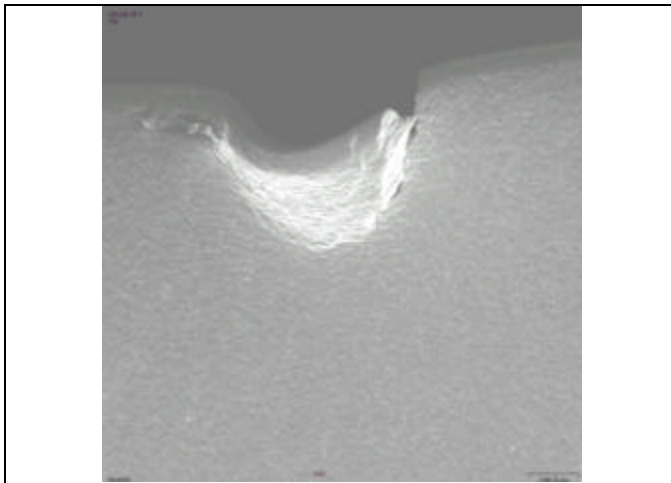
Specimen 54-07

Description: Sharp tip FOD specimen with a high energy ballistic impact at 30° with a 0.5 mm ball radius. The test was conducted with a stress ratio of 0.5 at an initial load of 643.1 lbs and a frequency of 30 Hz. EPD was monitored throughout the test. When load did not occur after 1,000,000 cycles the load was increased 5%. Crack nucleation occurred at 707.4 lbs, and the test was continued at this load. Total cycles to nucleation using a U/U_0 of 1.020 was 84,845.

Specimen 54-07 FOD Characterization



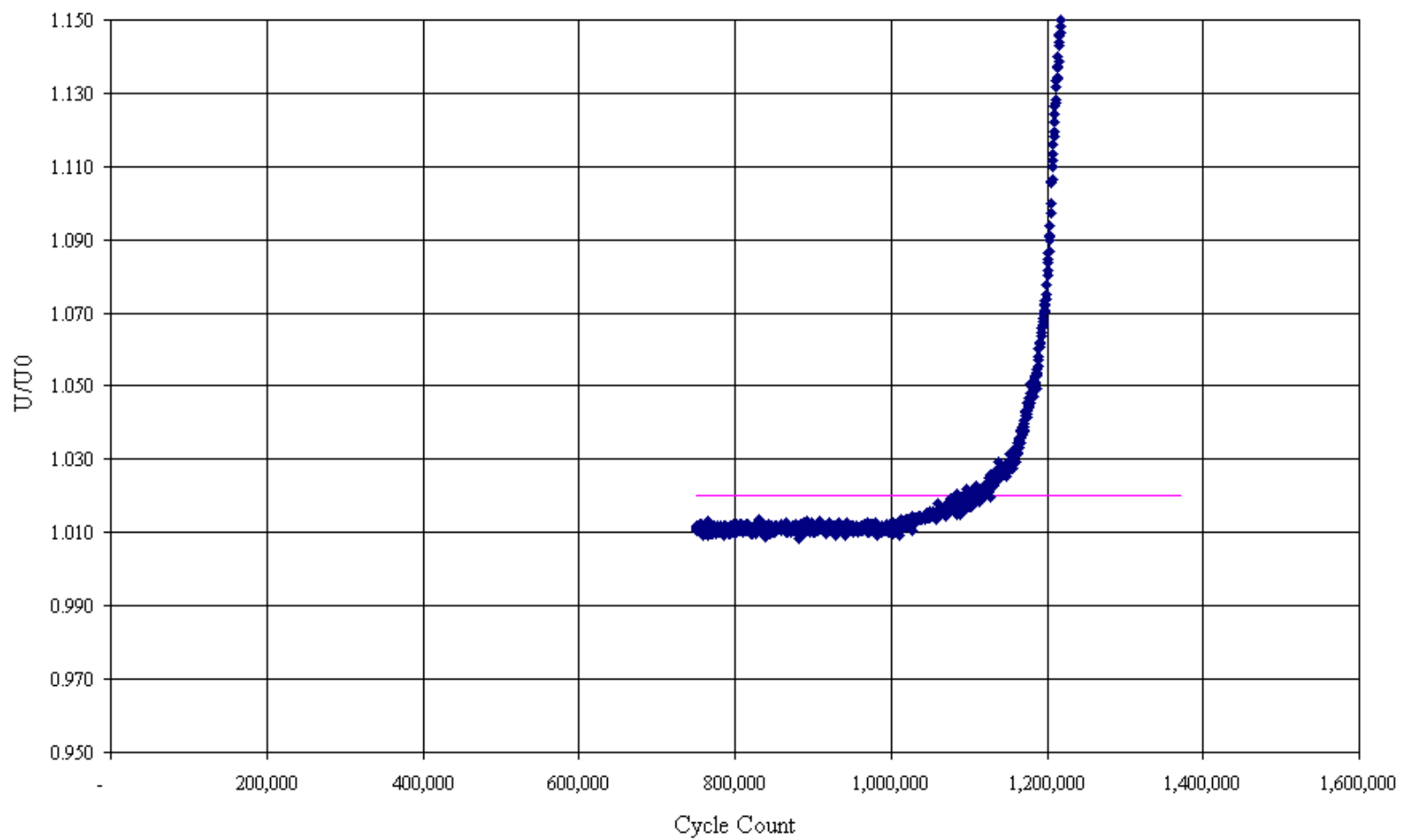
Side A



Side A

Overall picture of the EPD versus Cycle count for sample 54-07

PD behavior for FOD Sample 54-7

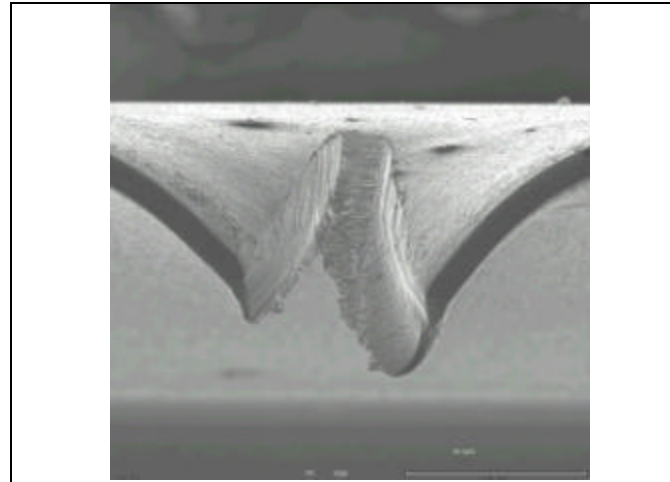
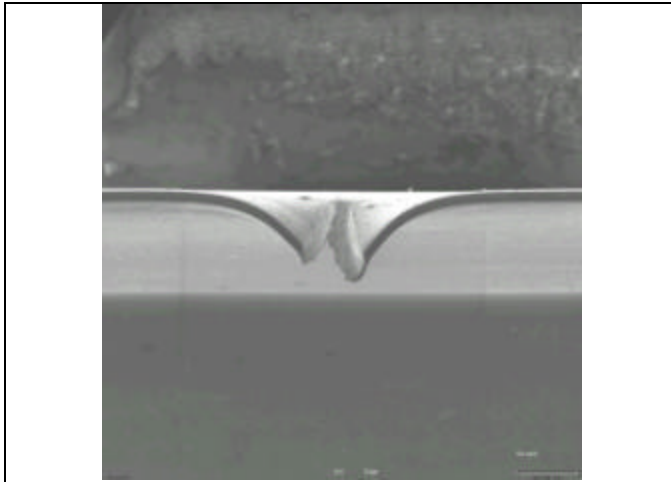


5C-147

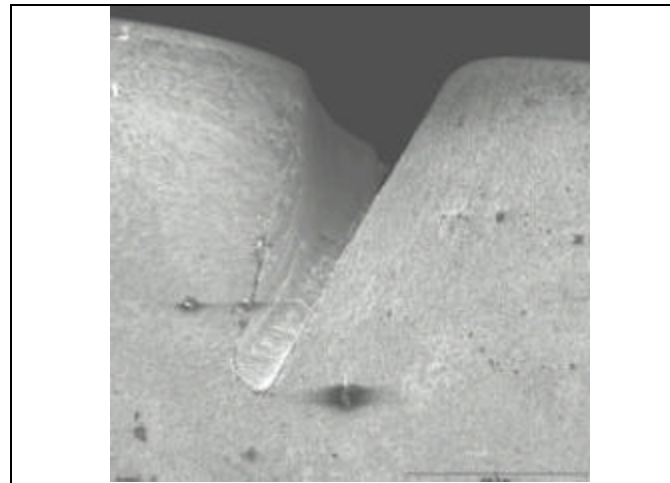
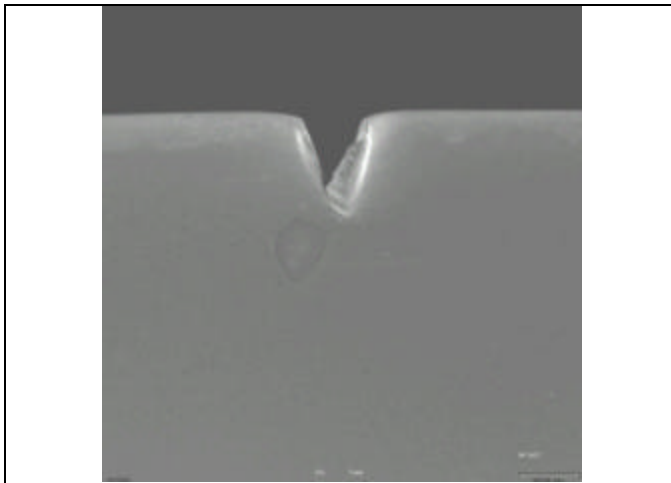
Specimen 54-01

Description: Sharp tip FOD specimen with a high energy solenoid gun impact at 30° with a 0.005 inch diameter indenter. The test was conducted with a stress ratio of 0.5 at an initial load of 500 lbs and a frequency of 30 Hz. EPD was monitored throughout the test. Crack nucleation did not occur after 91,892,512 total cycles and the test was discontinued.

Specimen 54-01 FOD Characterization



Side A

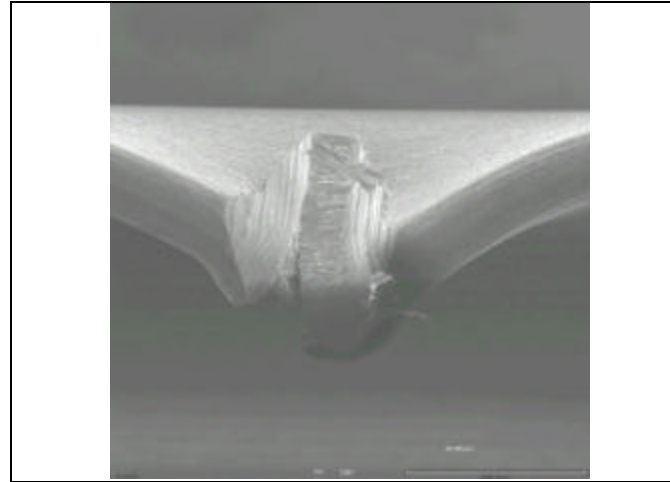
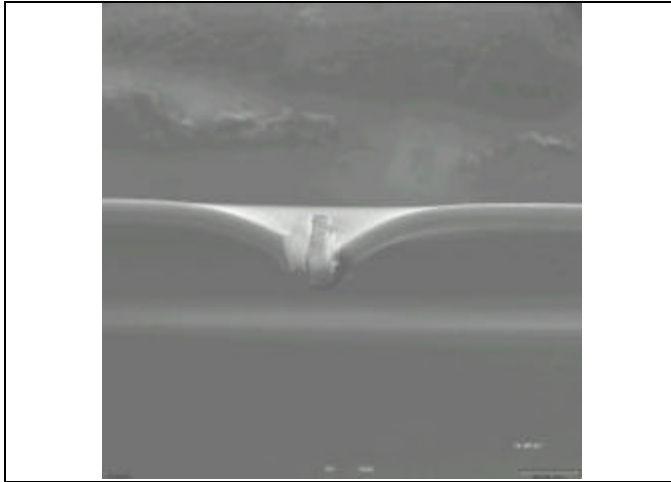


Side A

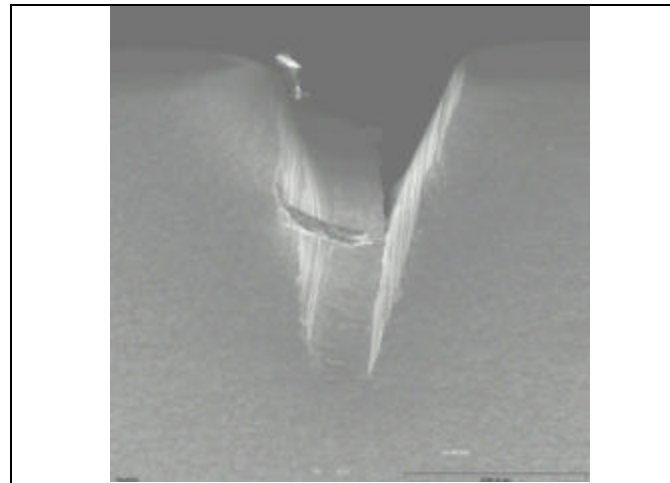
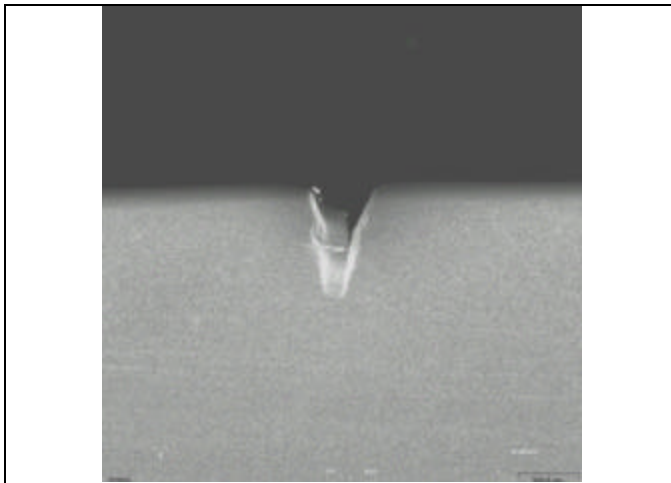
Specimen 54-04

Description: Sharp tip FOD specimen with a high energy solenoid gun impact at 30° with a 0.005 inch diameter indenter. The test was conducted with a stress ratio of 0.5 at an initial load of 600 lbs and a frequency of 30 Hz. EPD was monitored throughout the test. Crack nucleation occurred at 24,794,550 using U/U_0 of 1.0035 on the A side. The total cycles to failure was 25,029,454.

Specimen 54-04 FOD Characterization

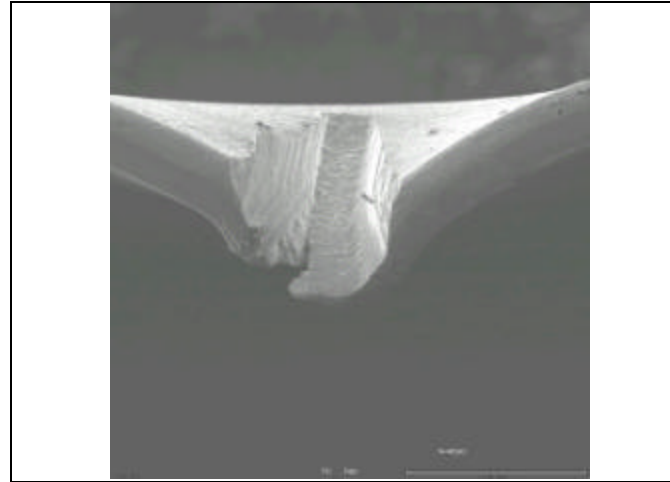
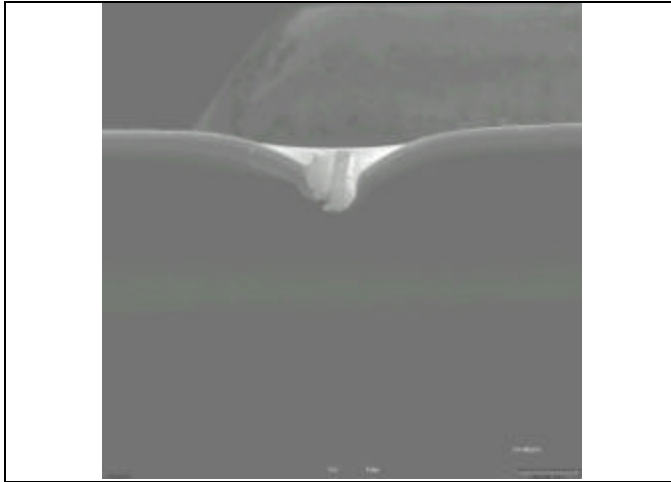


Side A

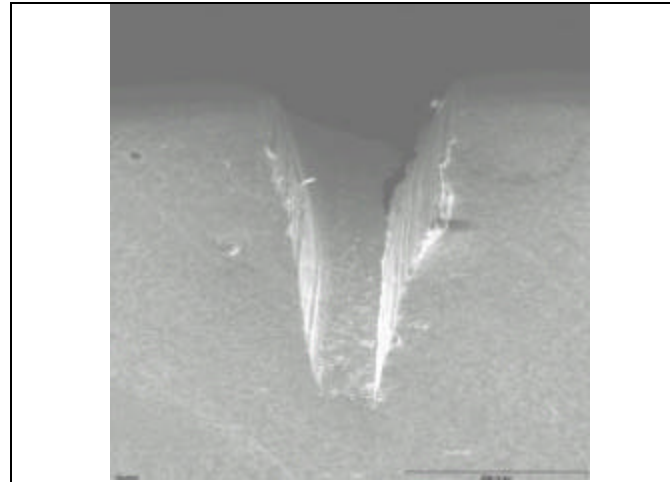
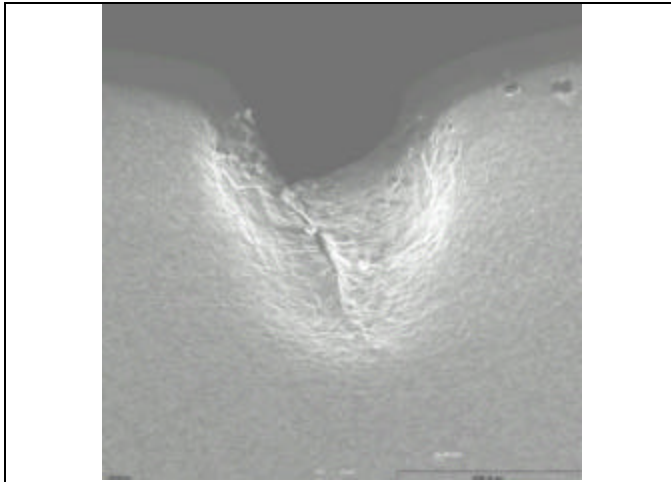


Side A

Specimen 54-04 FOD Characterization



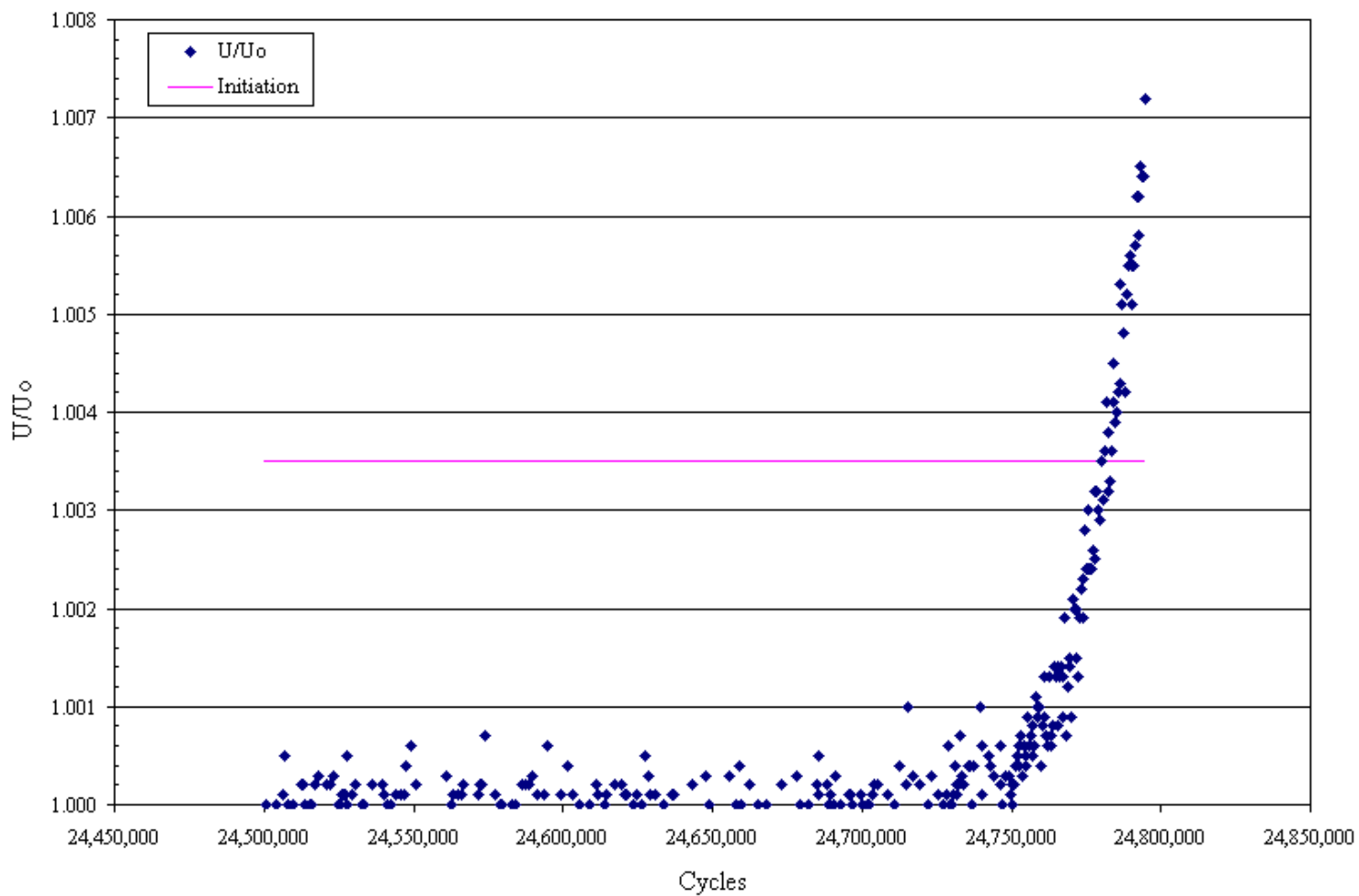
Side B



Side B

Overall picture of the EPD versus Cycle count for sample 54-04

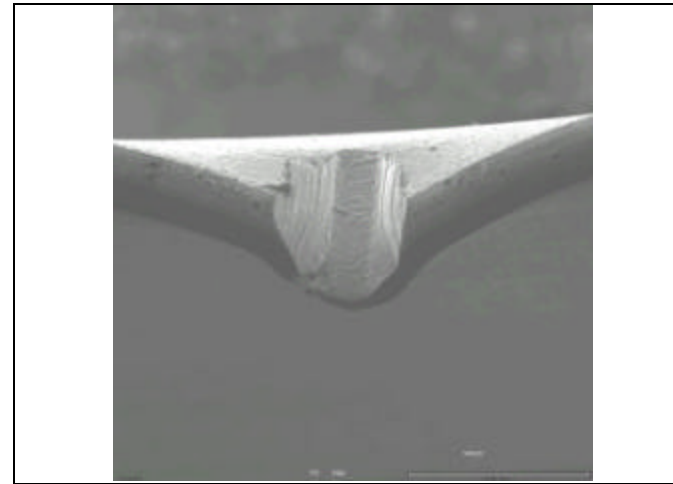
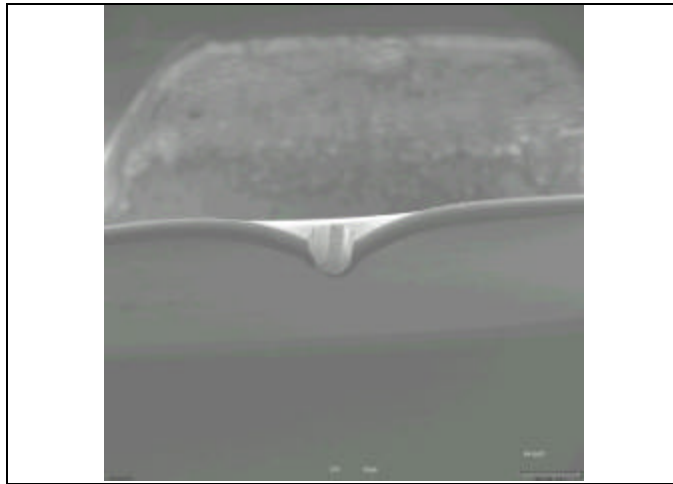
PD Behavior for FOD Sample 54-4



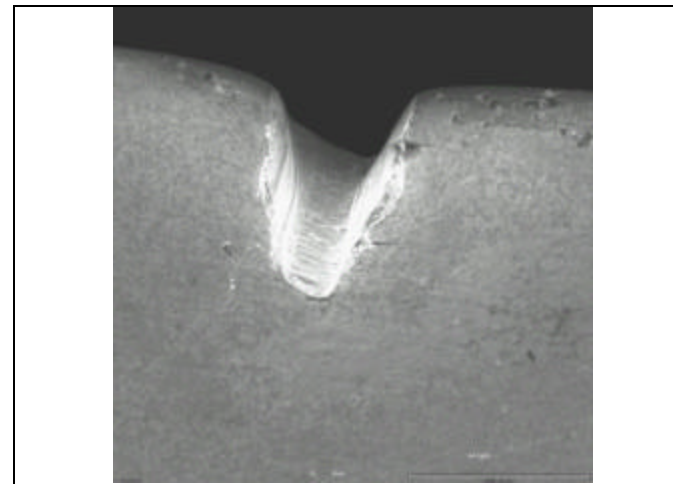
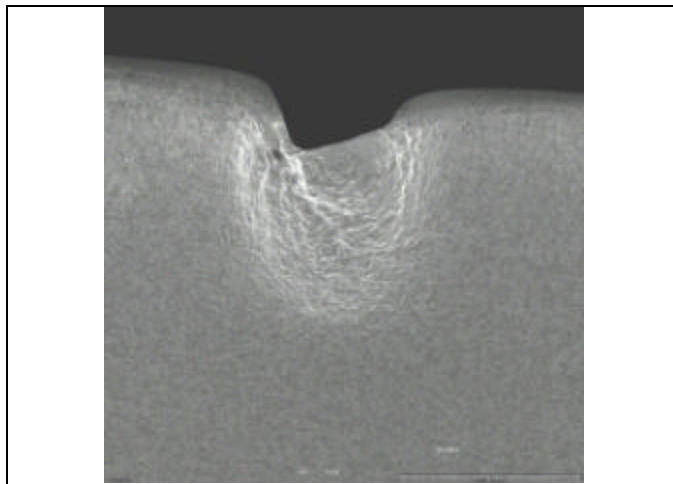
Specimen 54-05

Description: Sharp tip FOD specimen with a high energy solenoid gun impact at 30° with a 0.005 inch diameter indenter. The test was conducted with a stress ratio of 0.5 at an initial load of 800 lbs and a frequency of 30 Hz. EPD was monitored throughout the test. Crack nucleation occurred at 815,445 using U/U_0 of 1.0035. The total cycles to failure was 907,797.

Specimen 54-05 FOD Characterization



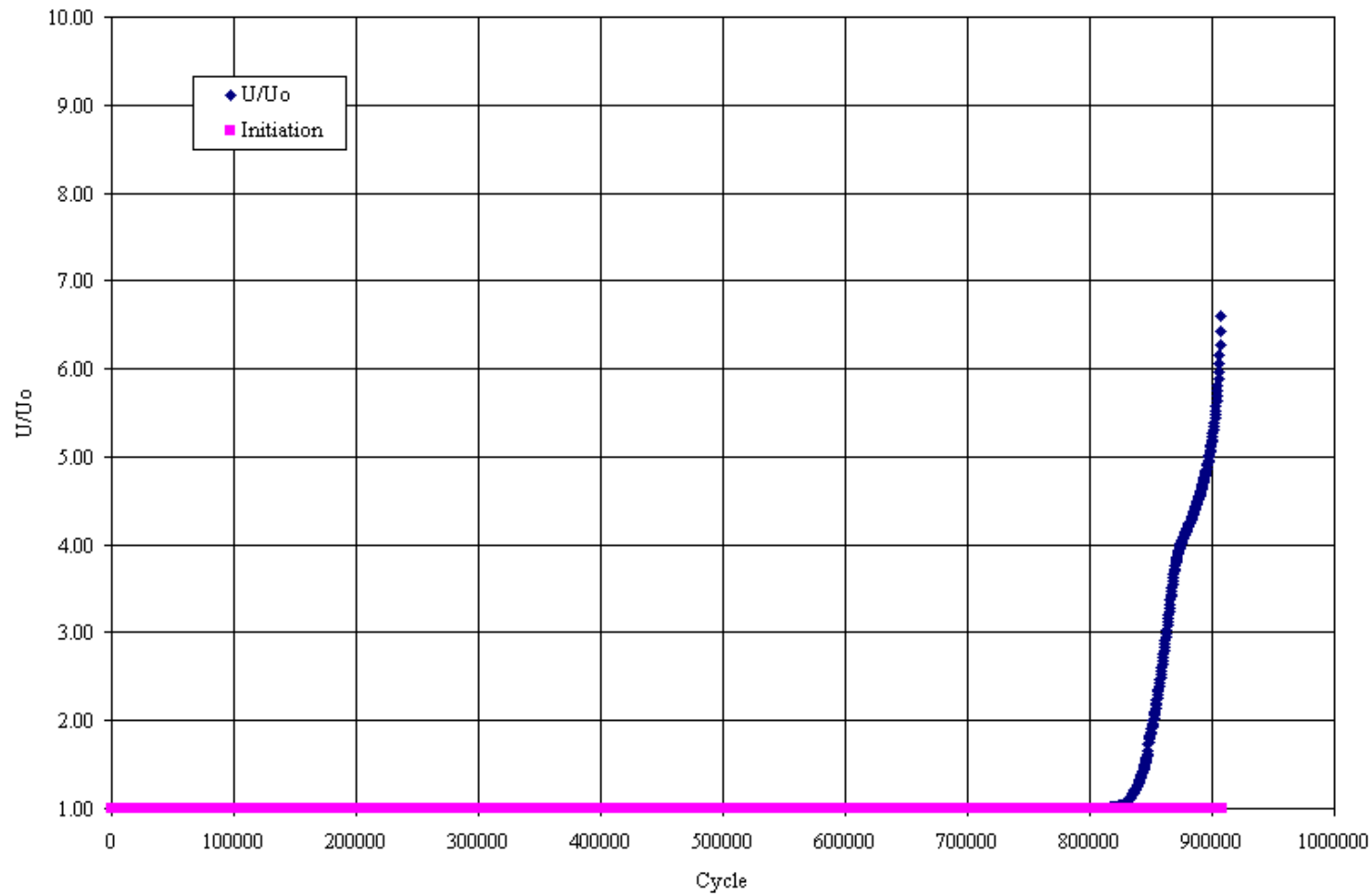
Side A



Side A

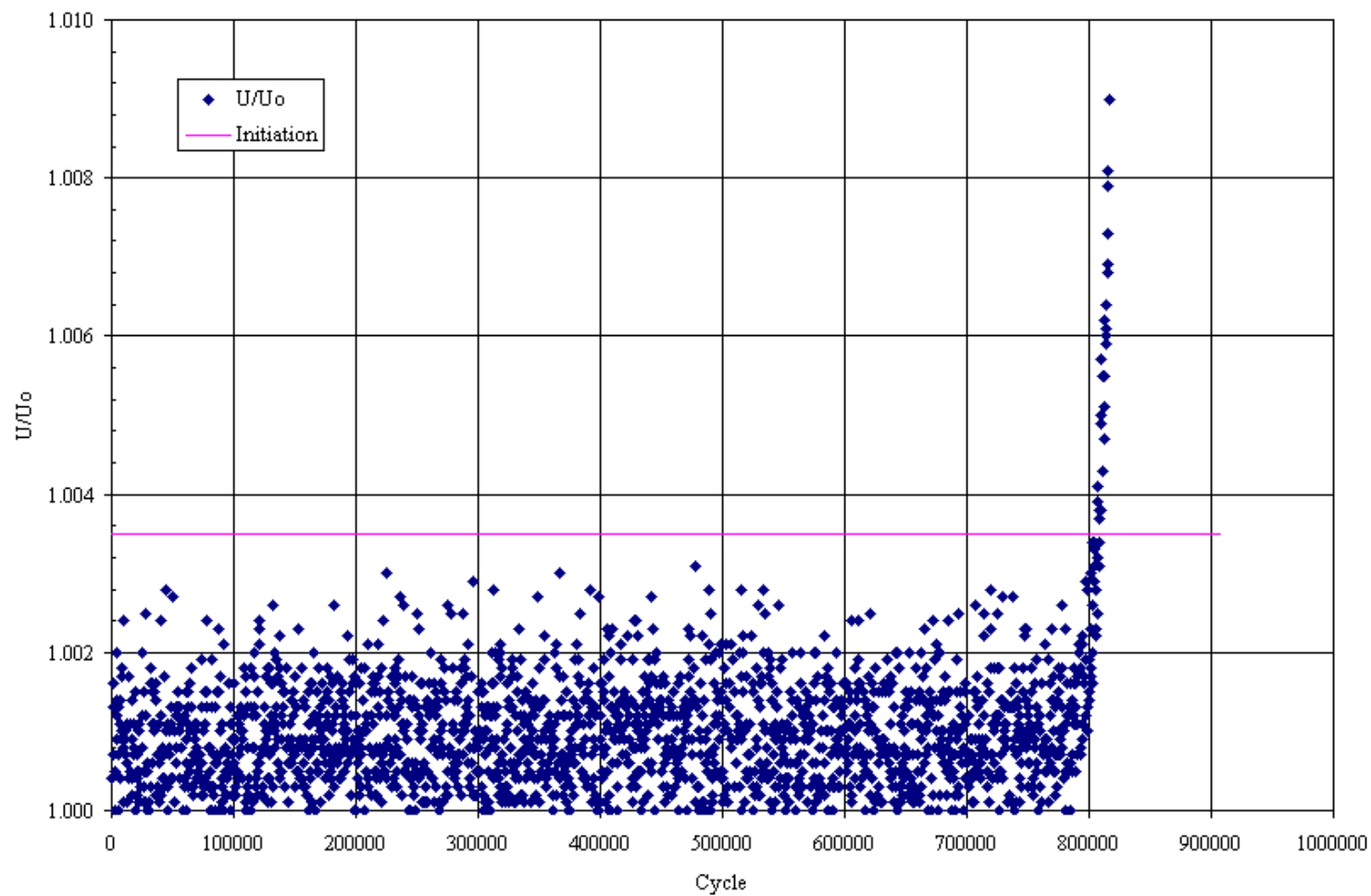
Overall picture of the EPD versus Cycle count for sample 54-05

PD Behavior for FOD Sample 54-5



Closeup picture of the EPD versus Cycle count for sample 54-05

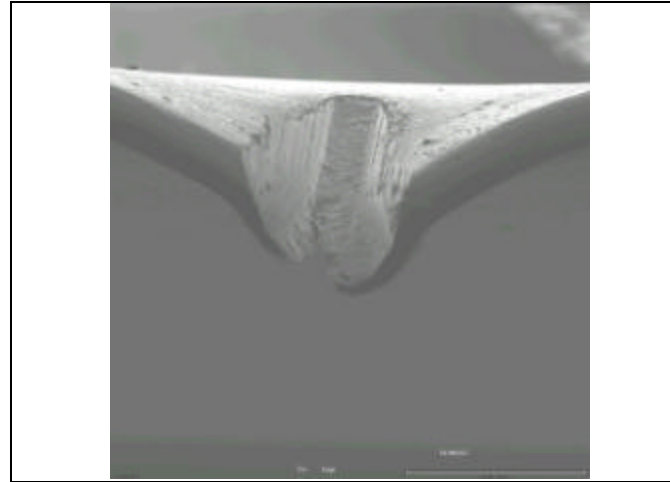
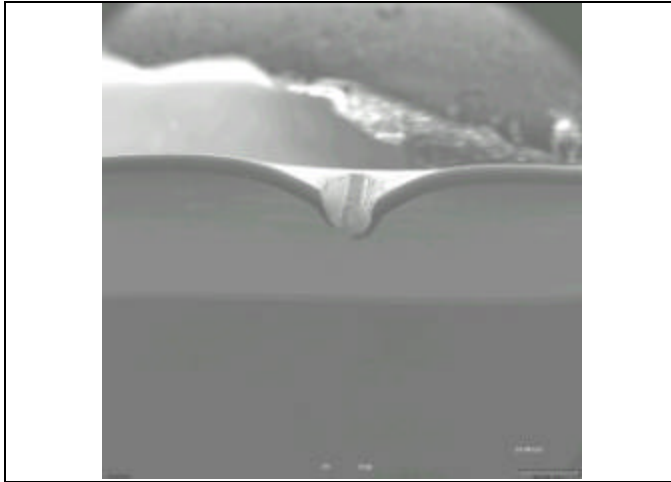
PD Behavior for FOD Sample 54-5



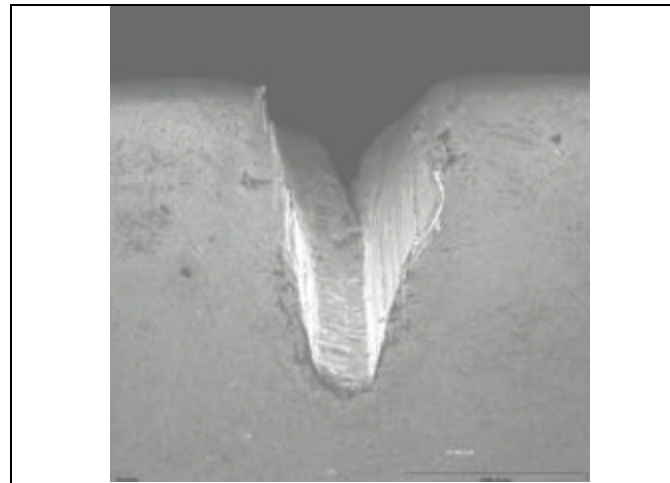
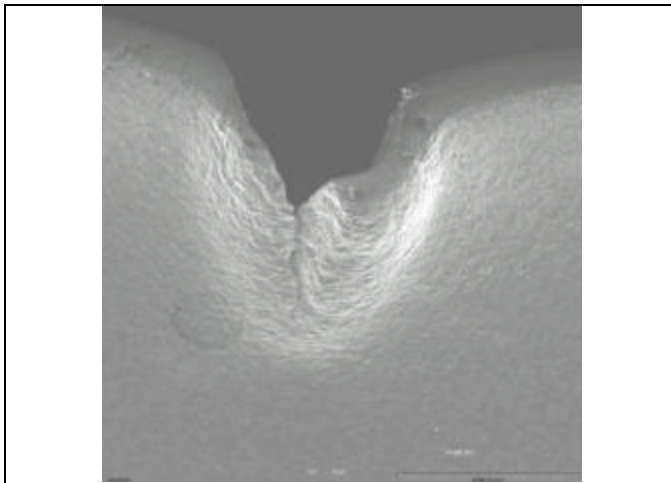
Specimen 54-08

Description: Sharp tip FOD specimen with a high energy solenoid gun impact at 30° with a 0.005 inch diameter indenter. The test was conducted with a stress ratio of 0.5 at an initial load of 700 lbs and a frequency of 30 Hz. EPD was monitored throughout the test. Crack nucleation occurred at 3,108,535 using U/U_0 of 1.0035 on the B side. The total cycles to failure was 3,164,740.

Specimen 54-08 FOD Characterization

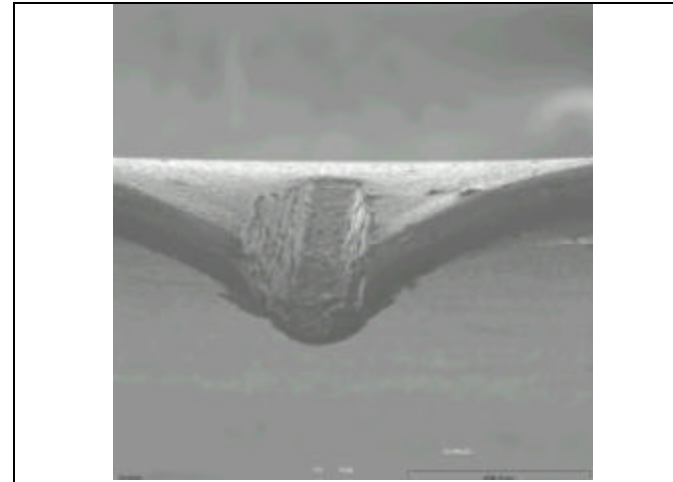
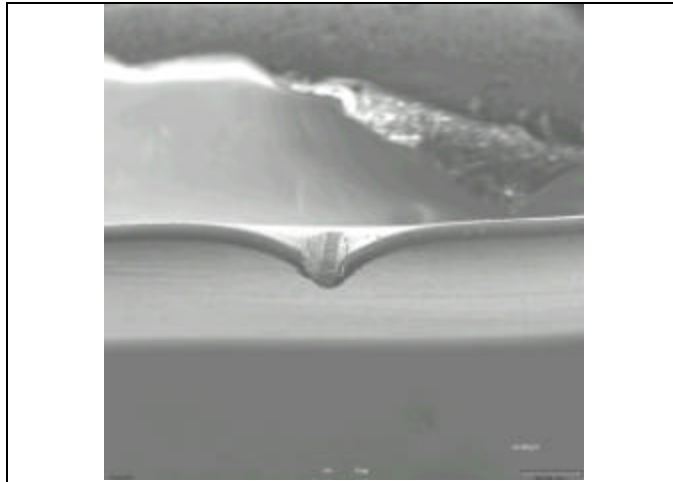


Side A

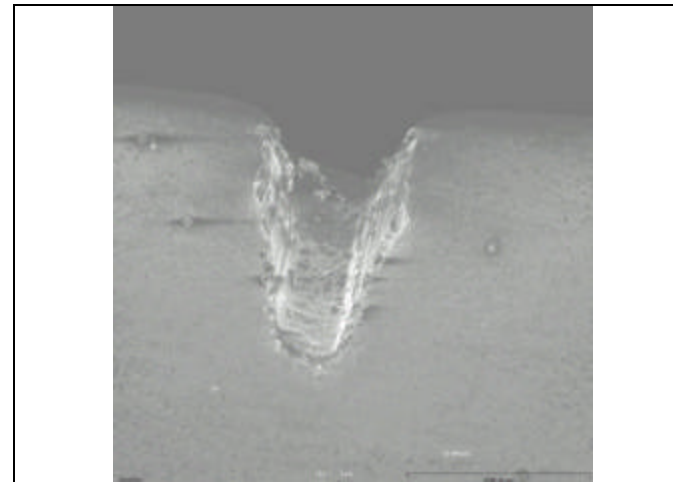
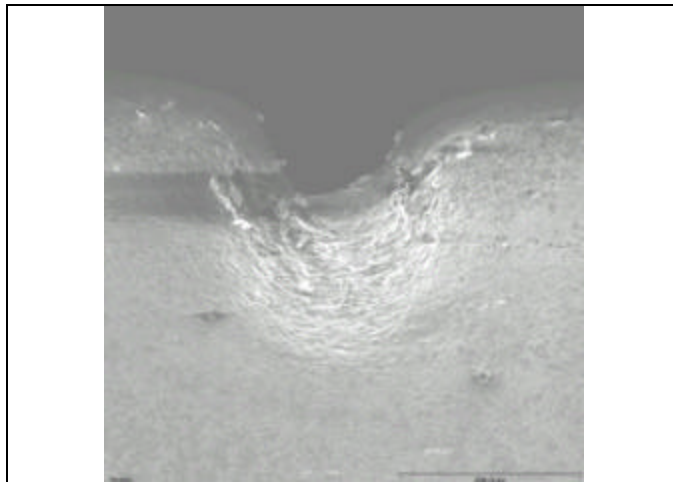


Side A

Specimen 54-08 FOD Characterization



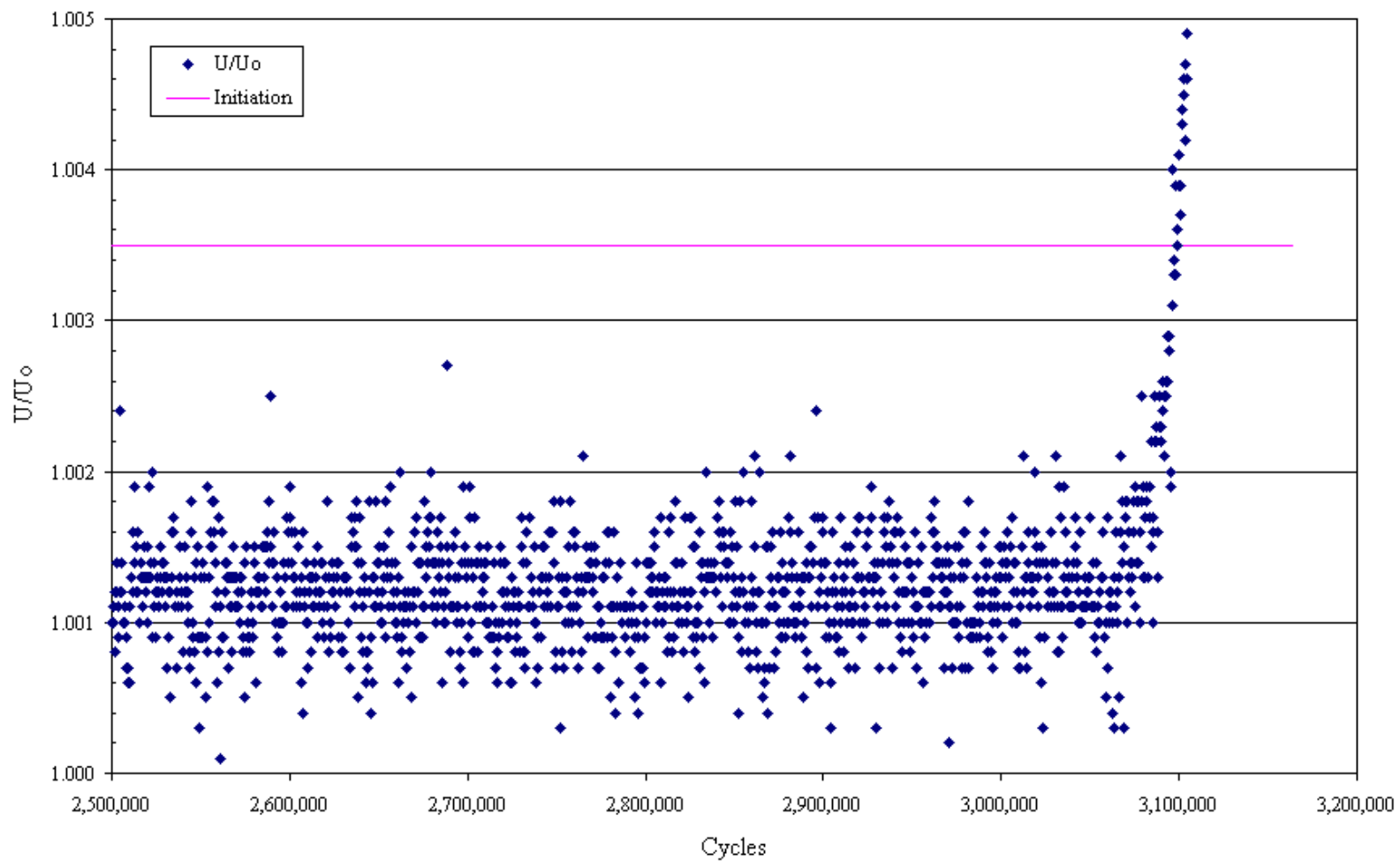
Side B



Side B

Closeup picture of the EPD versus Cycle count for sample 54-08

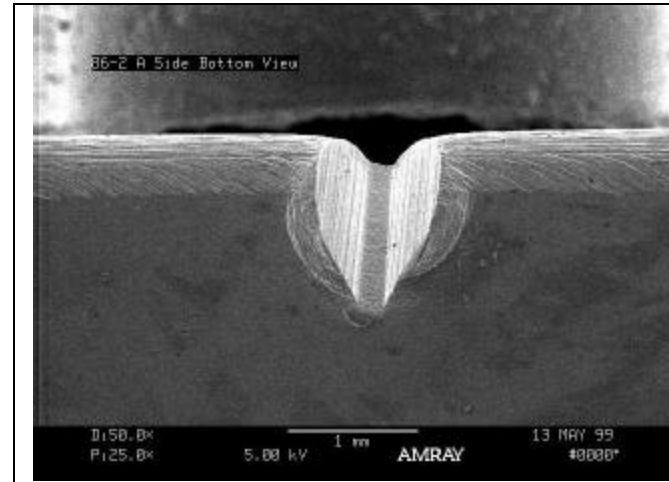
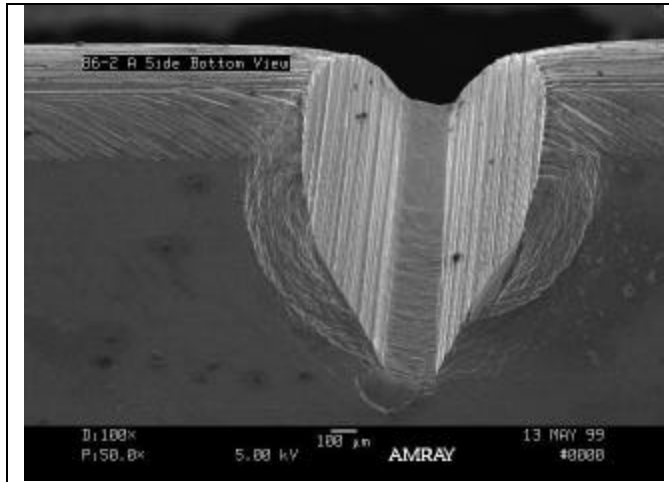
PD Behavior for FOD Sample 54-8



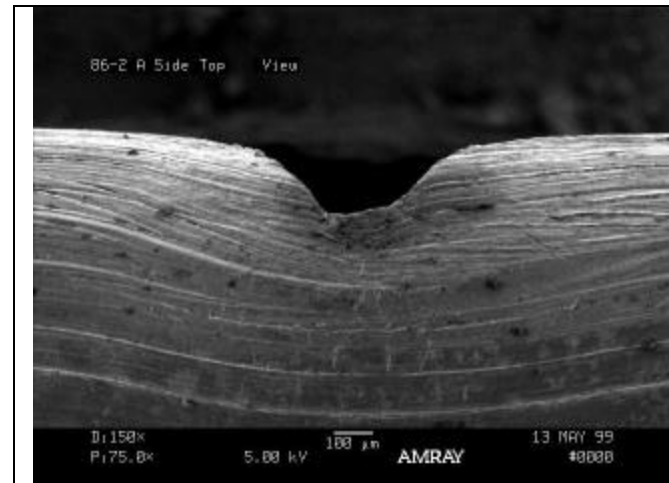
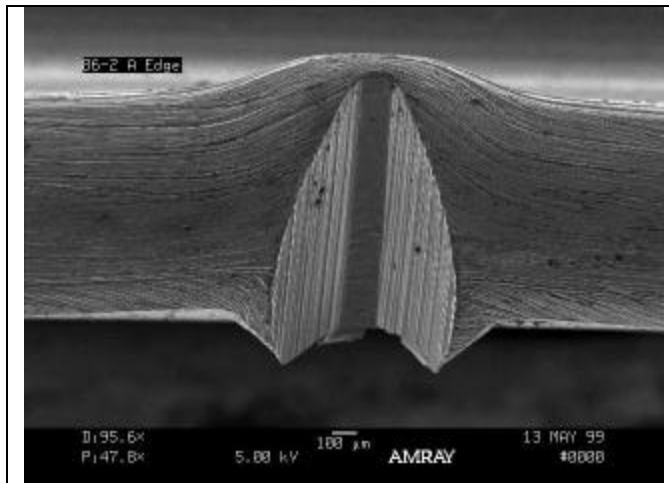
Specimen 86-02

Description: Blunt tip FOD specimen with a high energy solenoid gun impact at 30° with a 0.005 inch diameter indenter. The test was conducted with a stress ratio of 0.5 at an initial load of 643.1 lbs and a frequency of 30 Hz. EPD was monitored throughout the test. Crack nucleation occurred at 32,670 using U/U_0 of 1.0045 on the B side. The total cycles to failure was 278,384.

Specimen 86-02 FOD Characterization

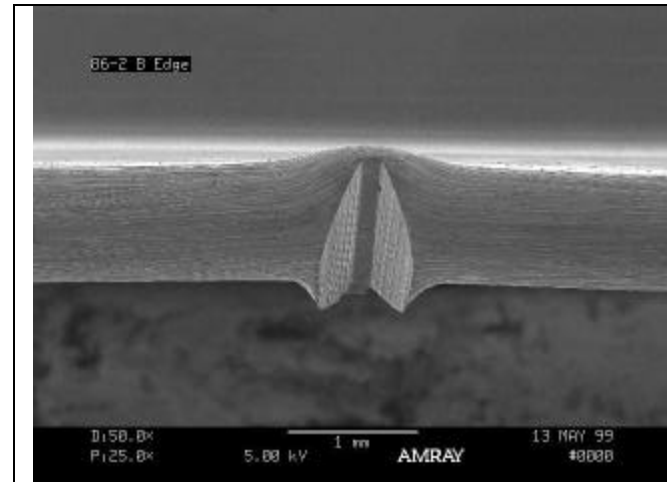
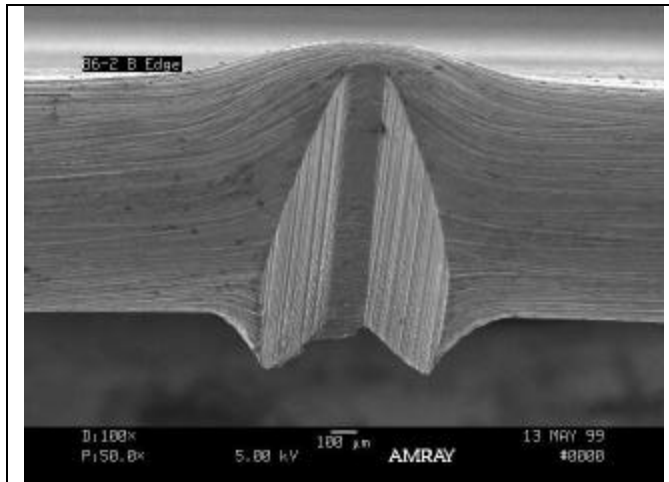


Side A

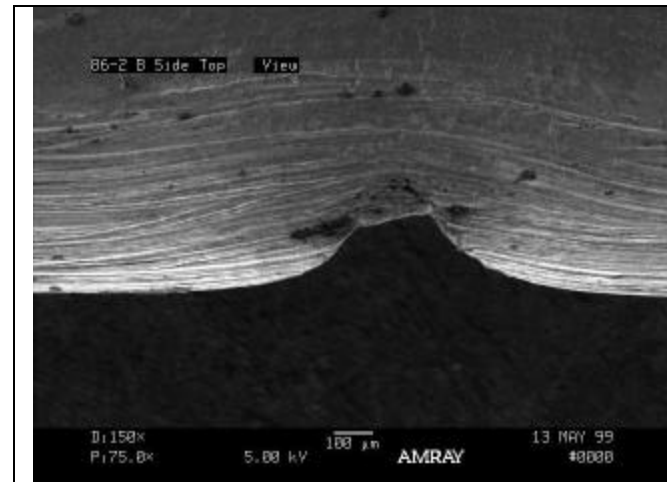
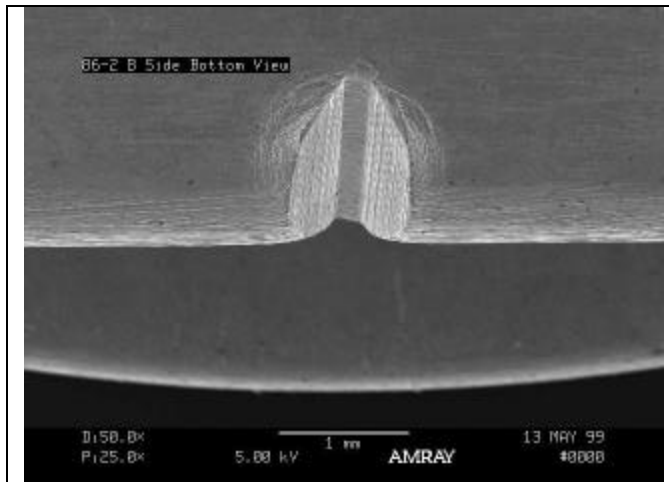


Side A

Specimen 86-02 FOD Characterization



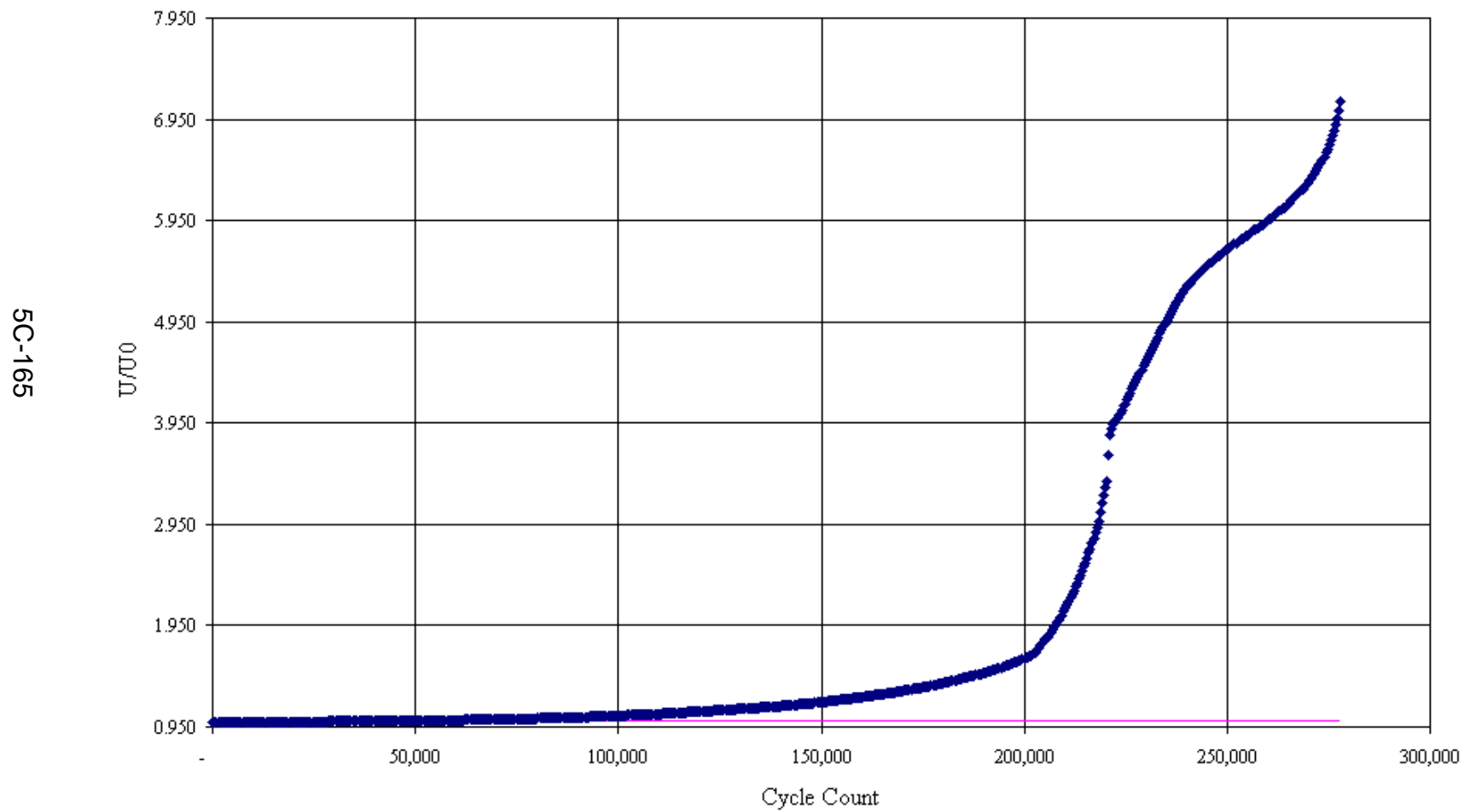
Side B



Side B

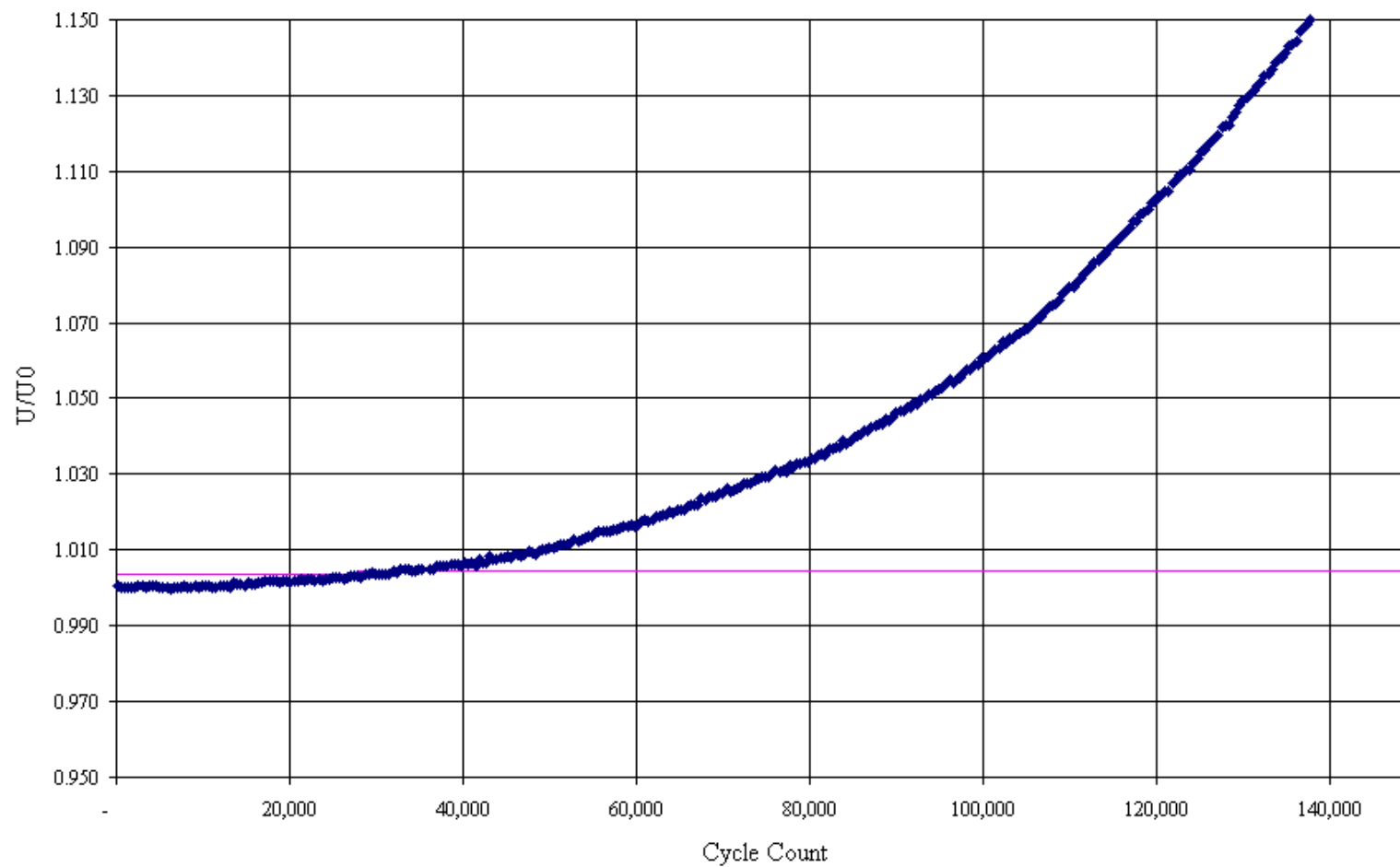
Overall picture of the EPD versus Cycle count for sample 86-02

PD behavior for FOD Sample 86-2



Closeup picture of the EPD versus Cycle count for sample 86-02

PD behavior for FOD Sample 86-2

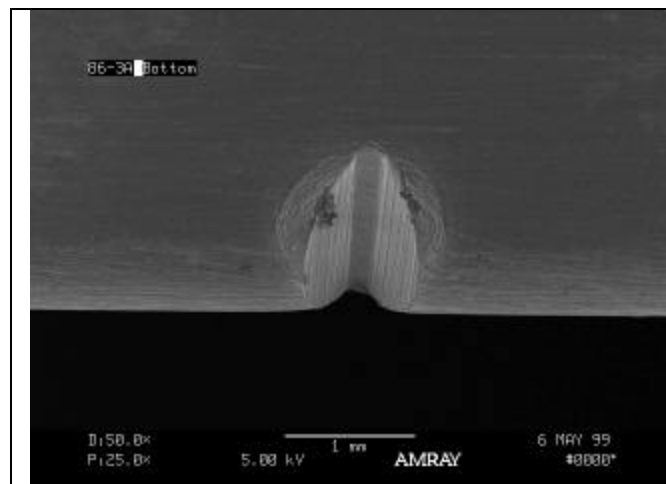
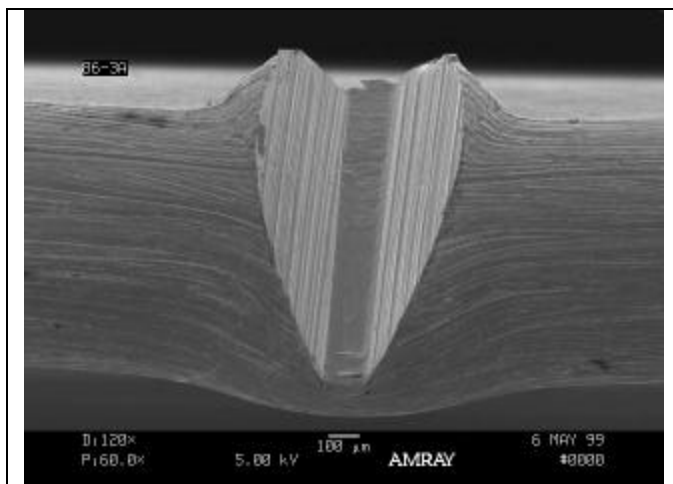


5C-166

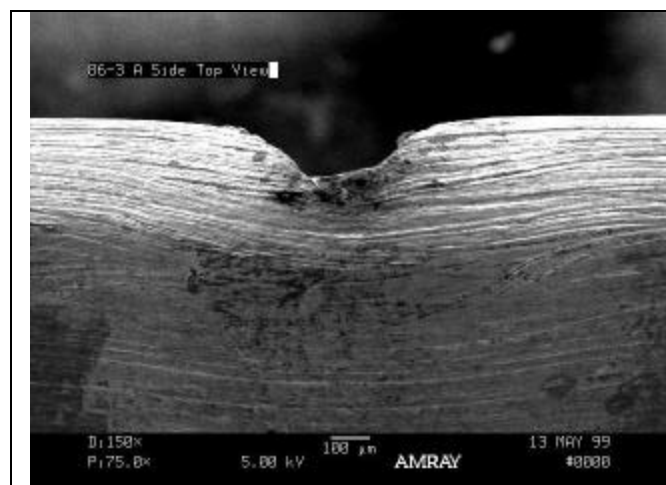
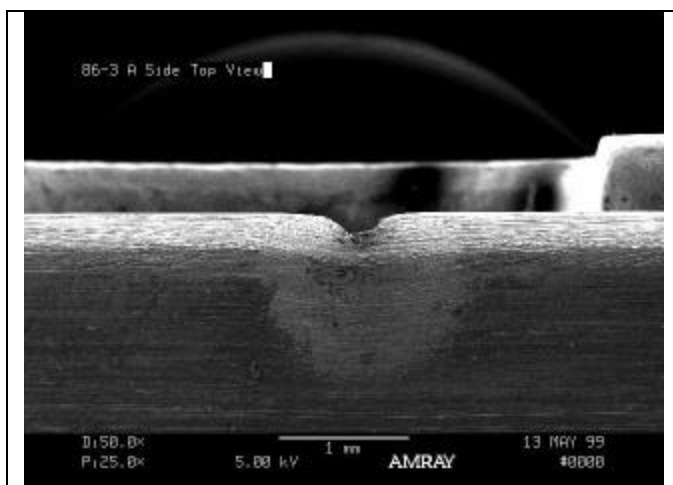
Specimen 86-03

Description: Blunt tip FOD specimen with a high energy solenoid gun impact at 30° with a 0.005 inch diameter indenter. The test was conducted with a stress ratio of 0.5 at an initial load of 643.1 lbs and a frequency of 30 Hz. EPD was monitored throughout the test. Crack nucleation occurred at 12,170 using U/U_0 of 1.0085 on the A side. The total cycles to failure was 185,830.

Specimen 86-03 FOD Characterization

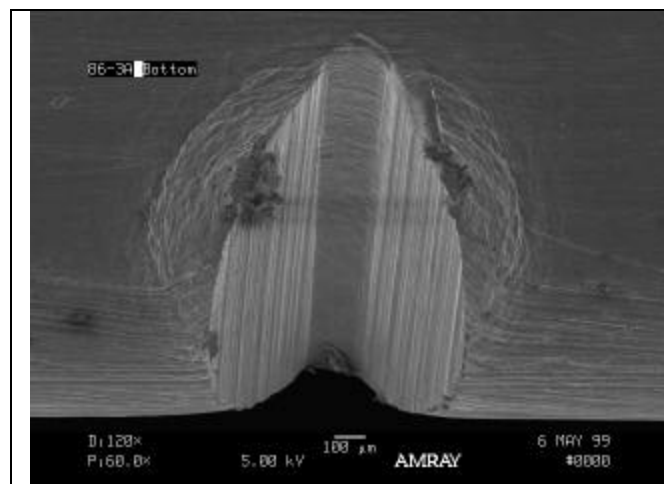
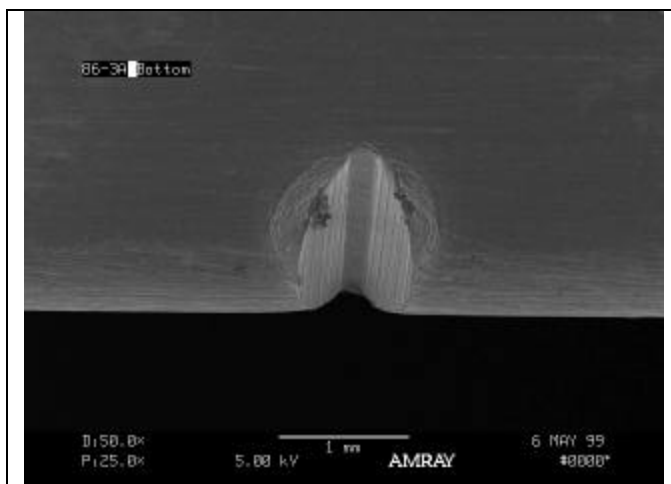


Side A

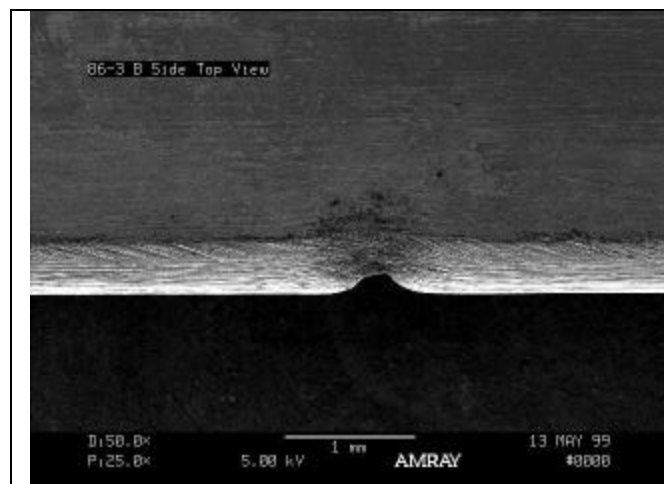
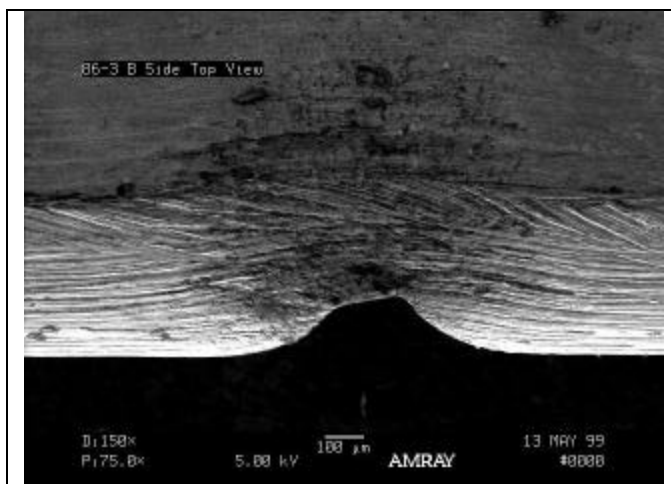


Side A

Specimen 86-03 FOD Characterization



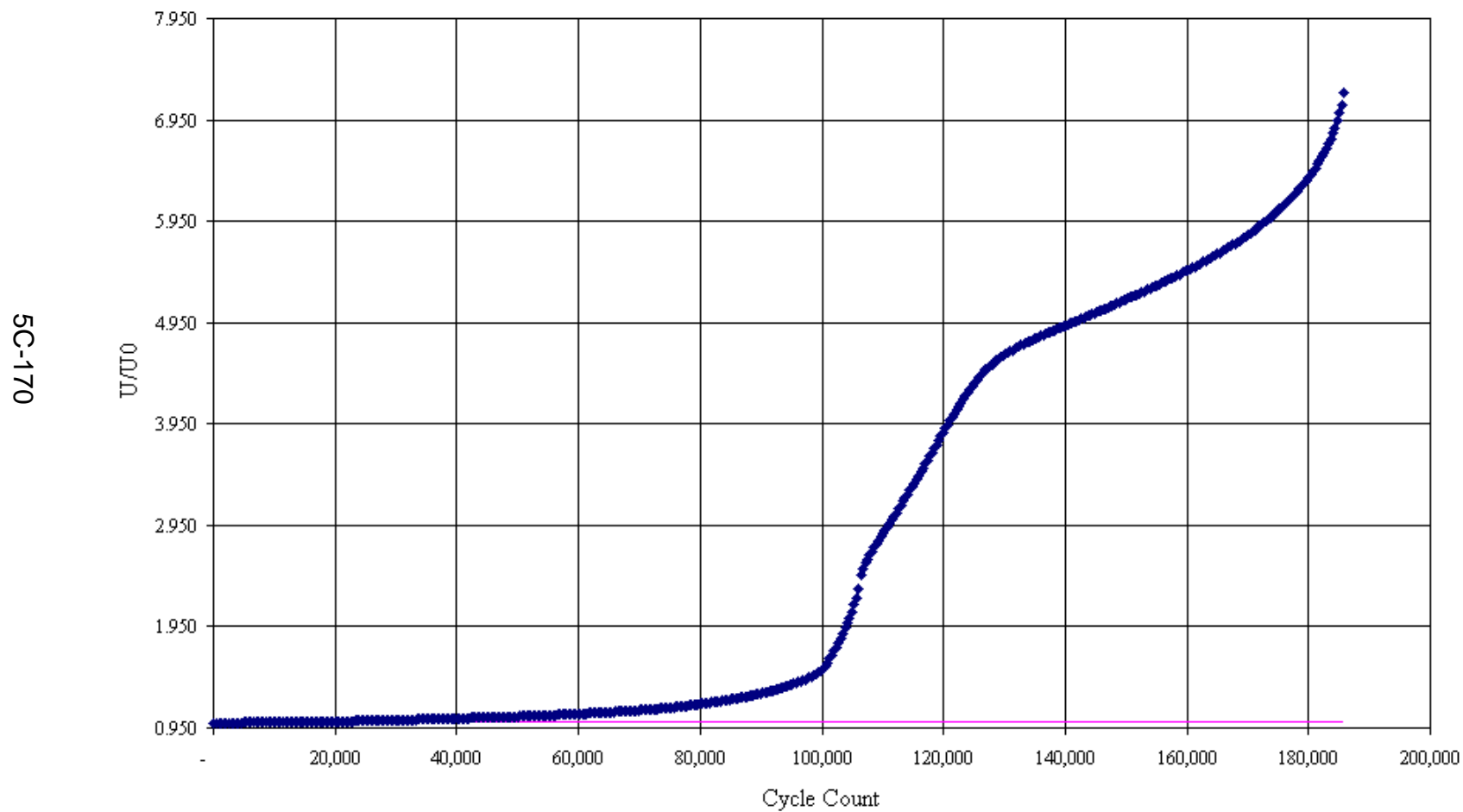
Side B



Side B

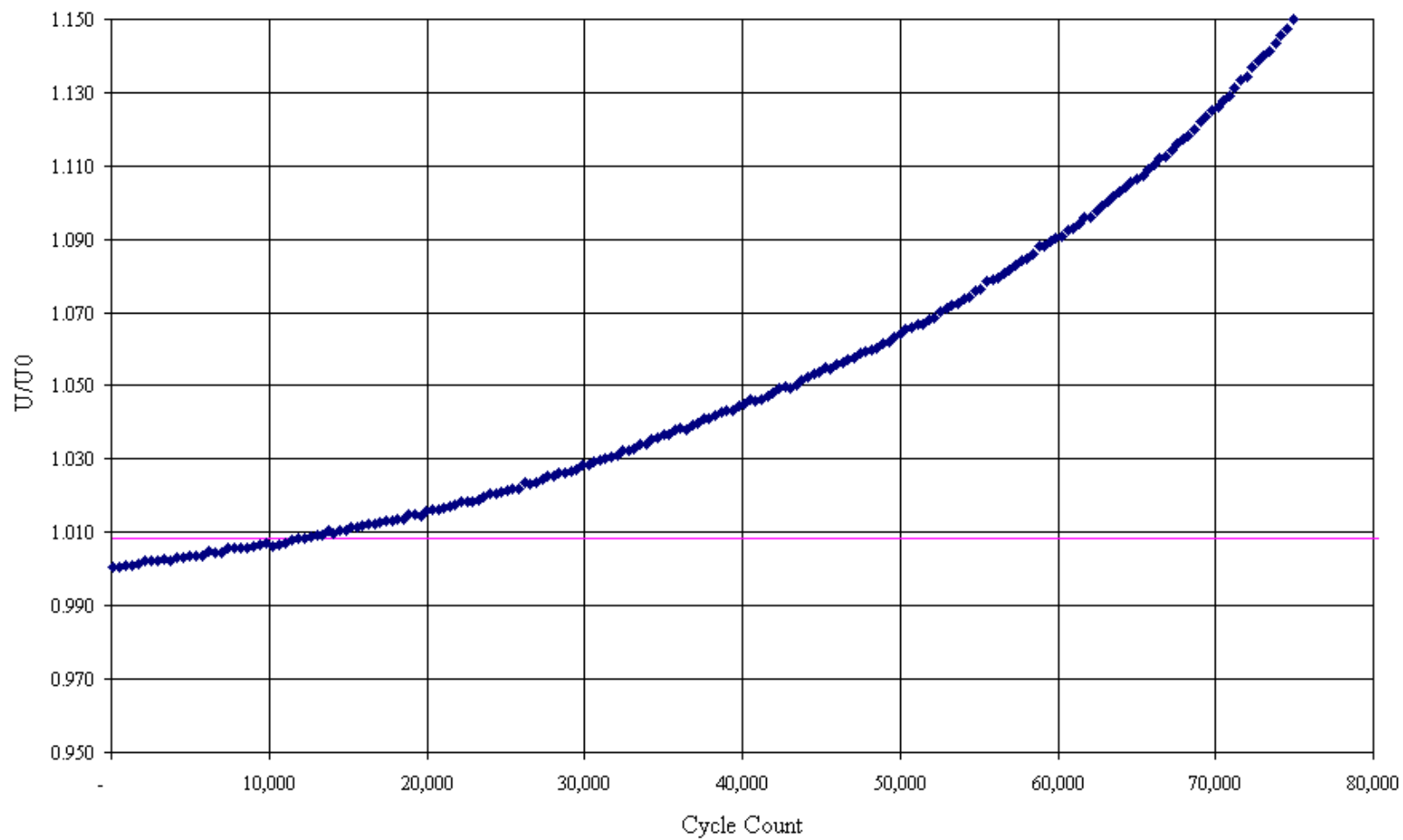
Overall picture of the EPD versus Cycle count for sample 86-03

PD behavior for FOD Sample 86-3



Closeup picture of the EPD versus Cycle count for sample 86-03

PD behavior for FOD Sample 86-3

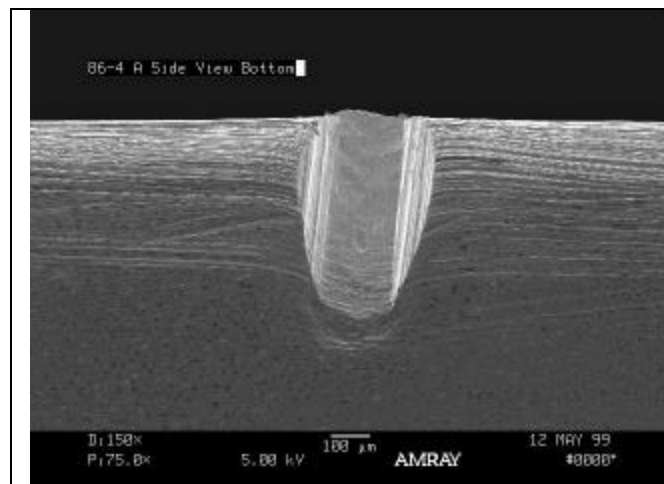
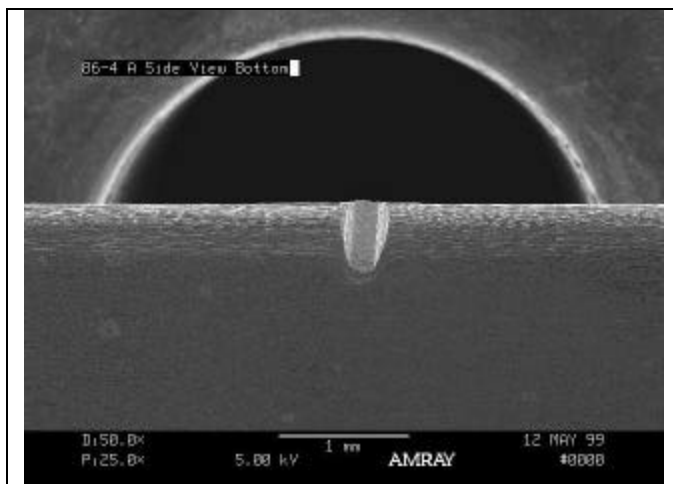


5C-171

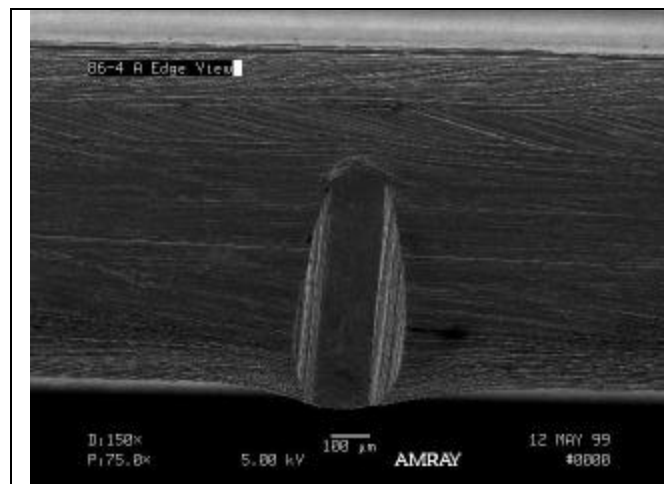
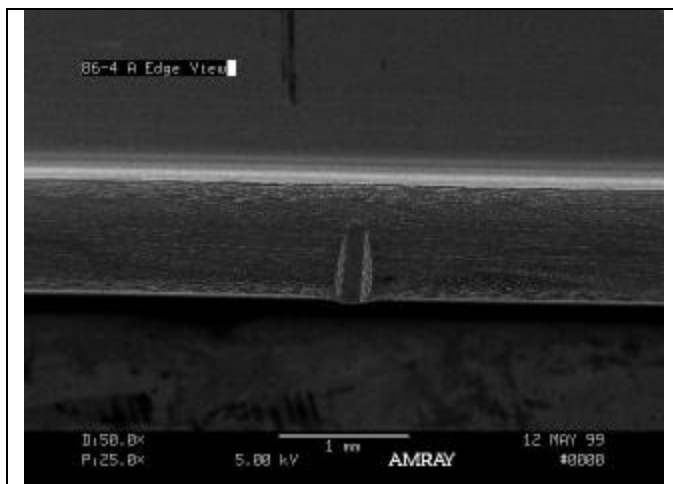
Specimen 86-04

Description: Blunt tip FOD specimen with a high energy solenoid gun impact at 30° with a 0.005 inch diameter indenter. The test was conducted with a stress ratio of 0.5 at an initial load of 941.6 lbs and a frequency of 30 Hz. EPD was monitored throughout the test. When load did not occur after 1,000,000 cycles the load was increased 5%. Crack nucleation occurred at 1035.7 lbs, and the test was continued at this load to failure. Crack nucleation occurred at 141,110 using U/U_o of 1.0085 on the A side. The total cycles to failure was 242,857.

Specimen 86-04 FOD Characterization

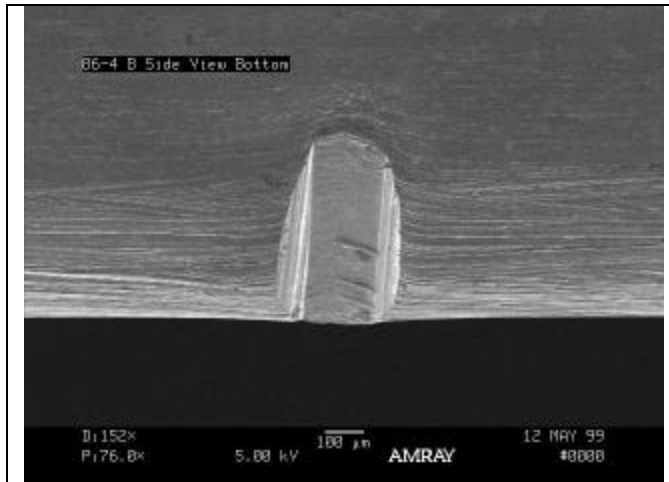


Side A

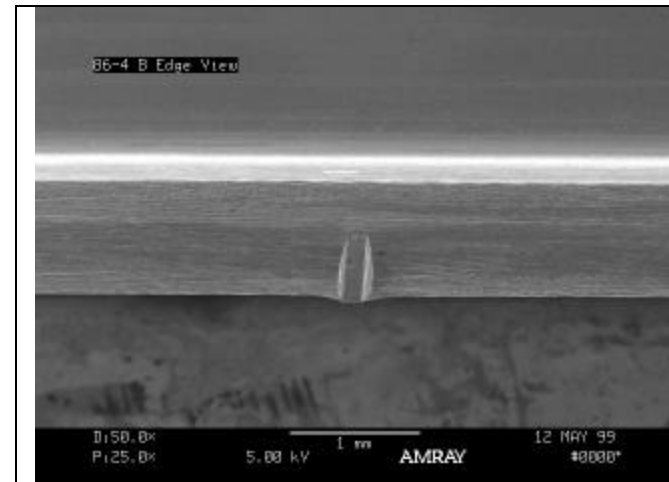
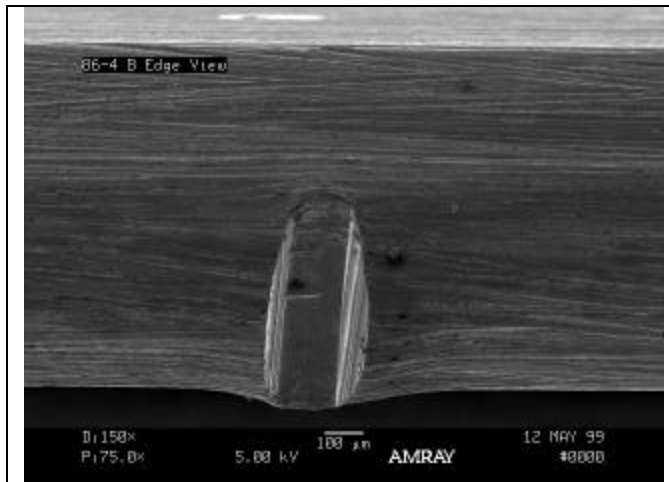


Side A

Specimen 86-04 FOD Characterization



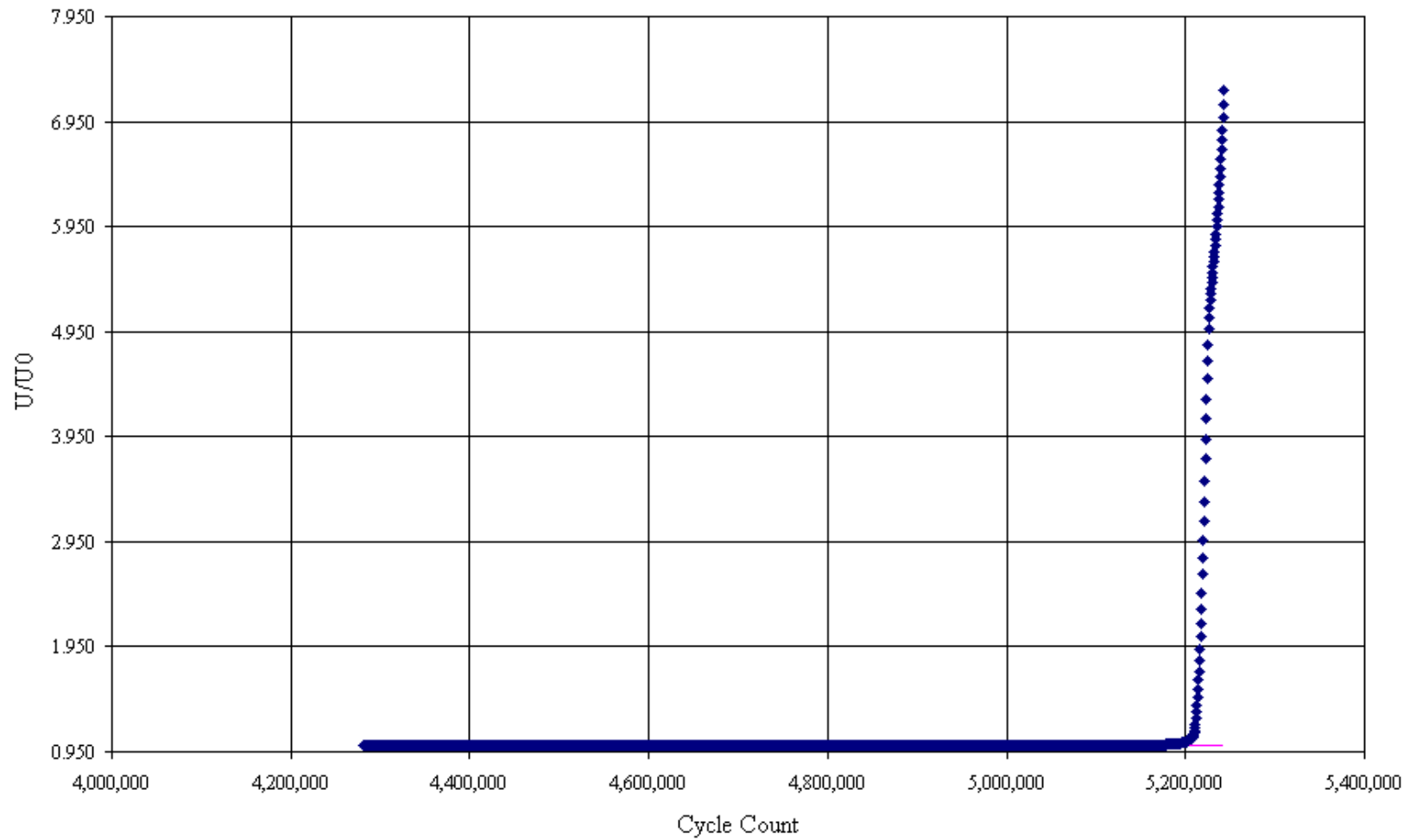
Side B



Side B

Overall picture of the EPD versus Cycle count for sample 86-04

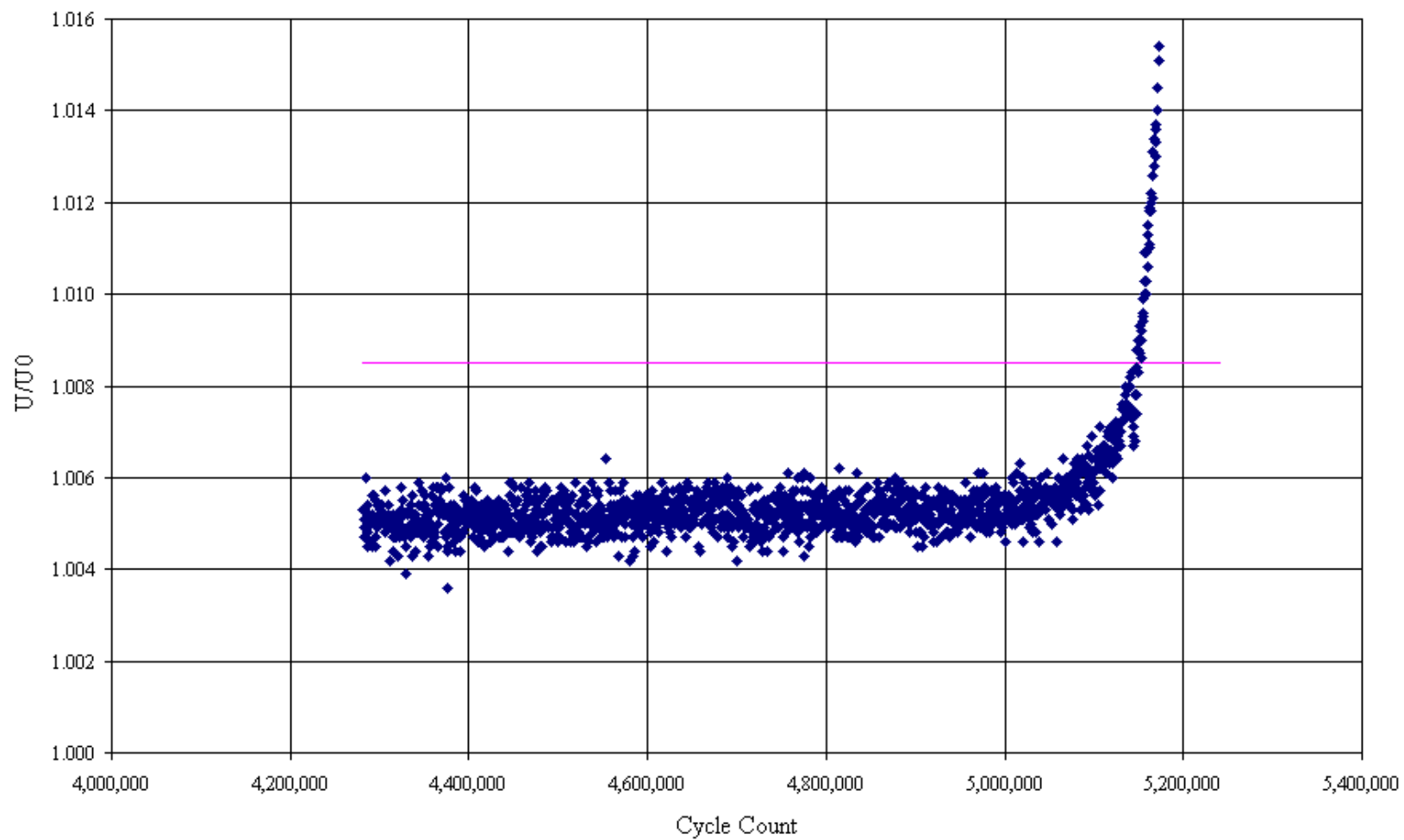
PD behavior for FOD Sample 86-4



5C-175

Closeup picture of the EPD versus Cycle count for sample 86-04

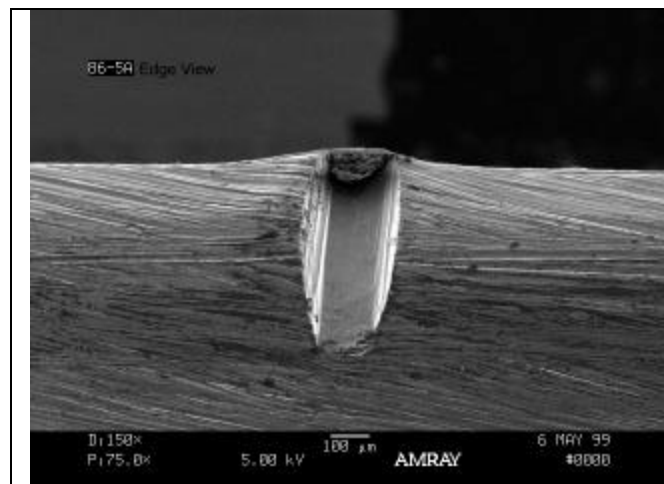
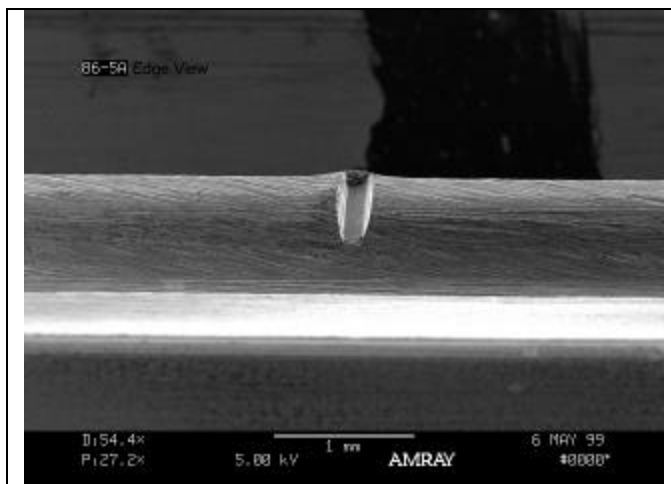
PD behavior for FOD Sample 86-4



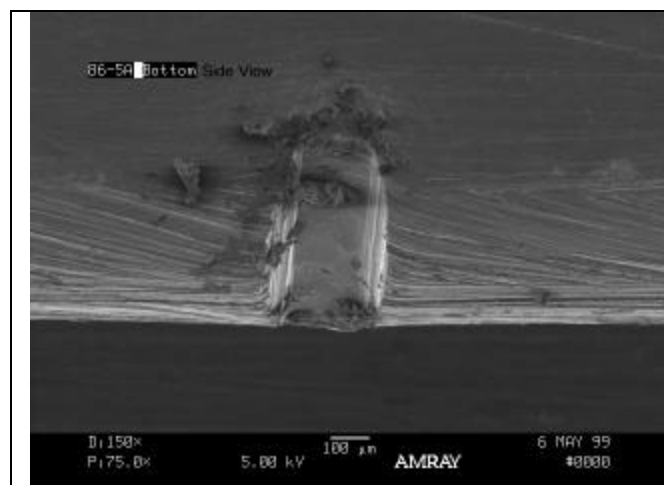
Specimen 86-05

Description: Blunt tip FOD specimen with a high energy solenoid gun impact at 30° with a 0.005 inch diameter indenter. The test was conducted with a stress ratio of 0.5 at an initial load of 1035.7 lbs and a frequency of 30 Hz. EPD was monitored throughout the test. When load did not occur after 1,000,000 cycles the load was increased 5%. Crack nucleation occurred at 1139.3 lbs, away from the intended location. The total cycles to failure was 6,019,222.

Specimen 86-05 FOD Characterization

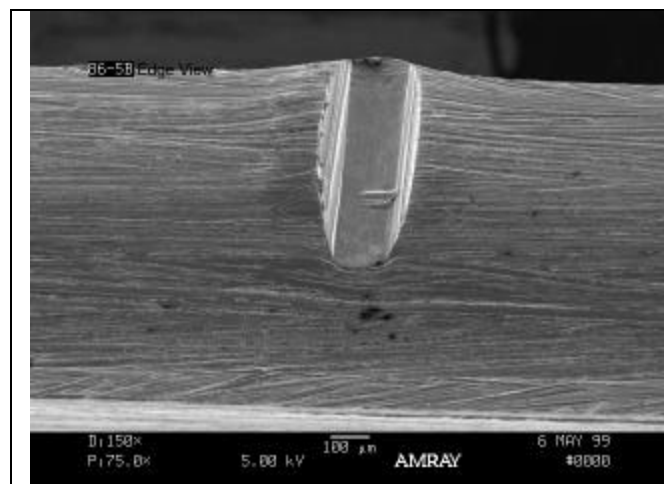
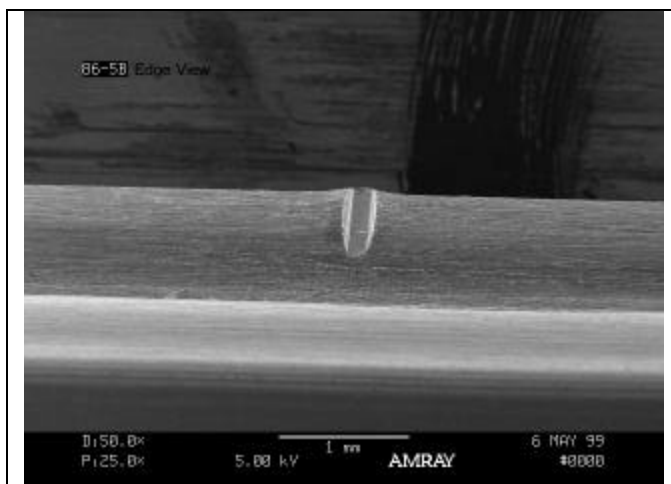


Side A

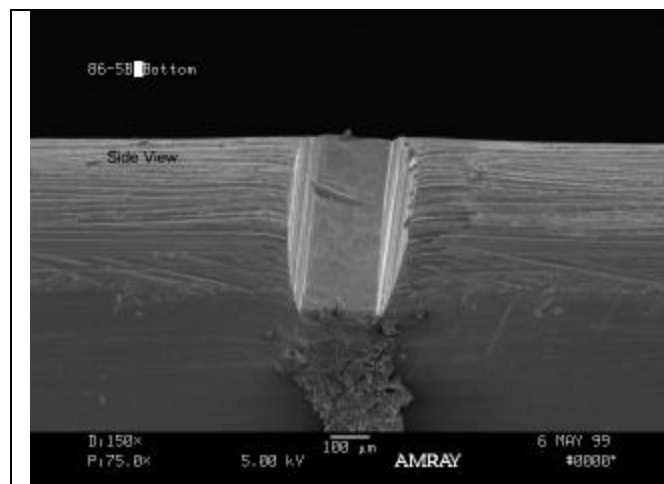
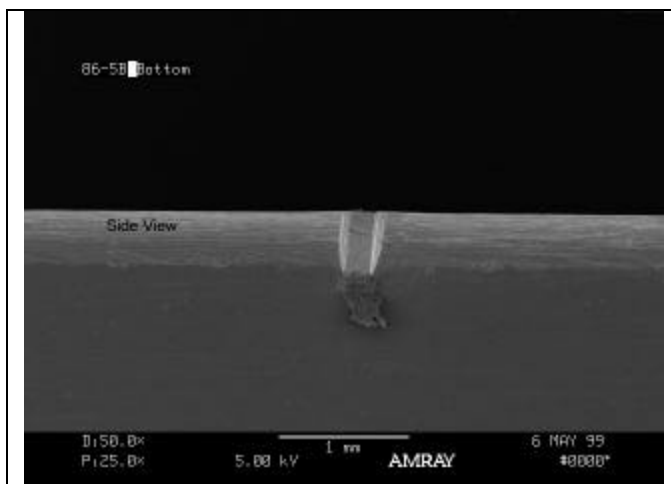


Side A

Specimen 86-05 FOD Characterization



Side B

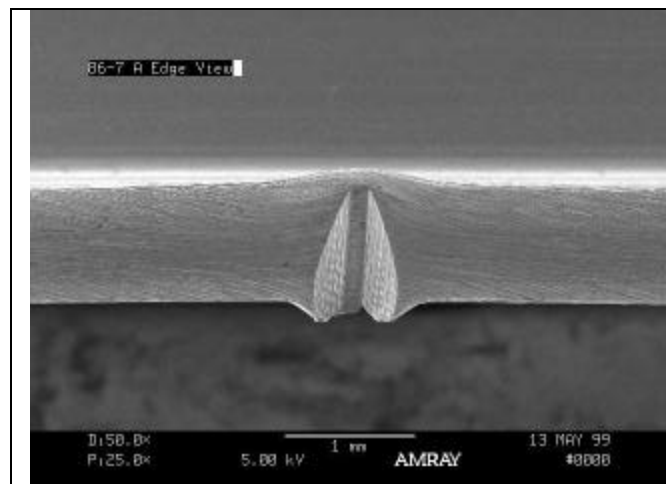
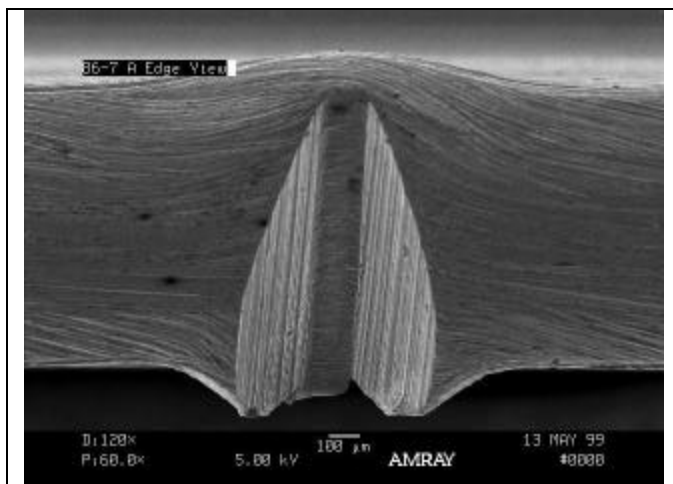


Side B

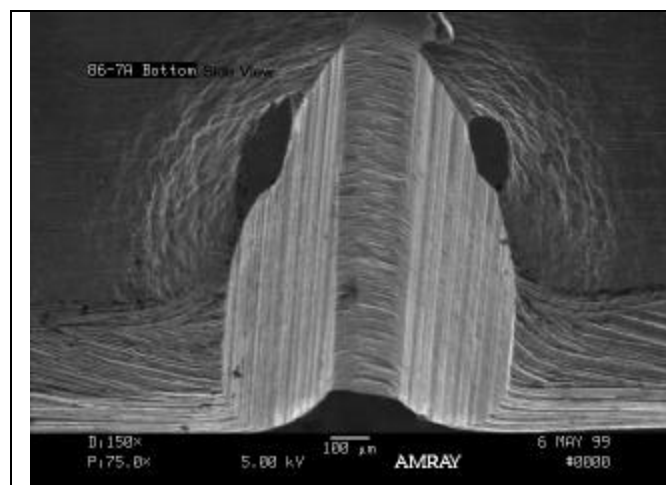
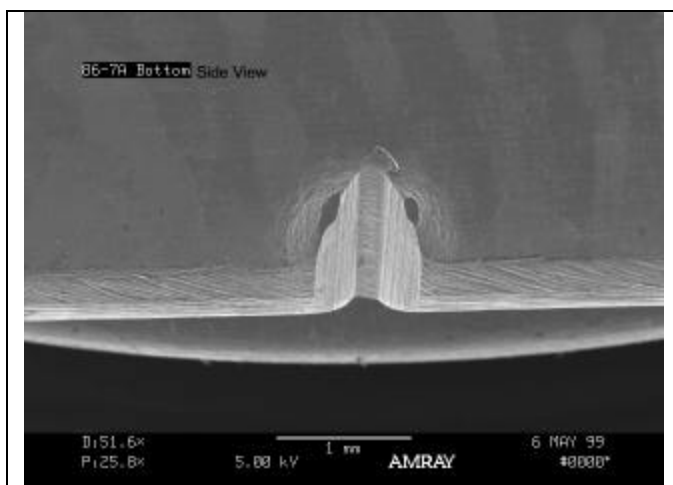
Specimen 86-07

Description: Blunt tip FOD specimen with a high energy solenoid gun impact at 30° with a 0.005 inch diameter indenter. The test was conducted with a stress ratio of 0.5 at an initial load of 643.1 lbs and a frequency of 30 Hz. EPD was monitored throughout the test. Crack nucleation occurred at 163,948 using U/U_0 of 1.0085 on the B side. The total cycles to failure was 337,398.

Specimen 86-07 FOD Characterization

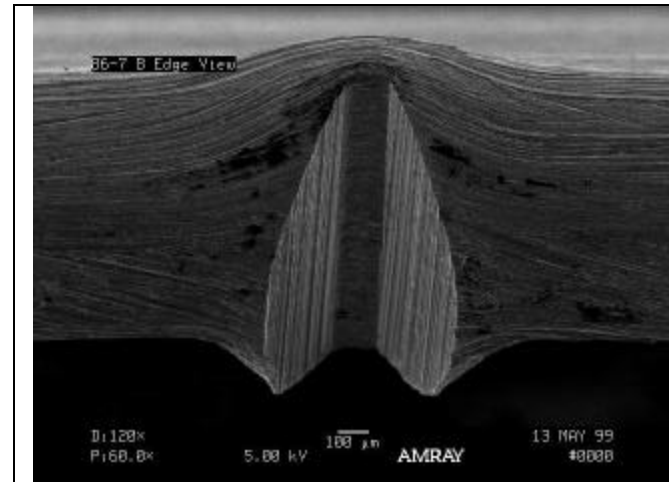
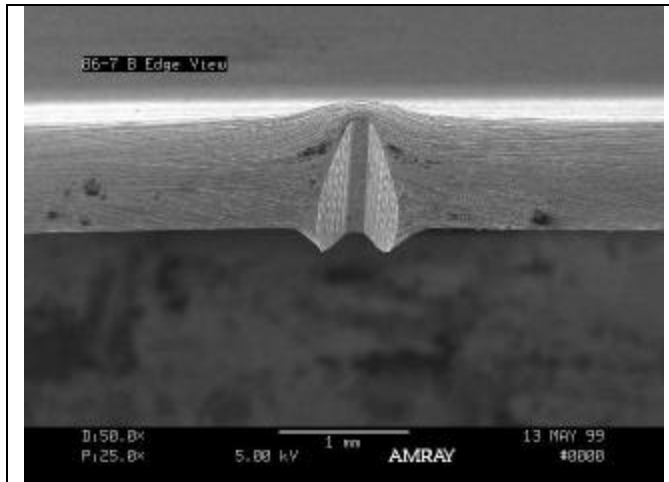


Side A

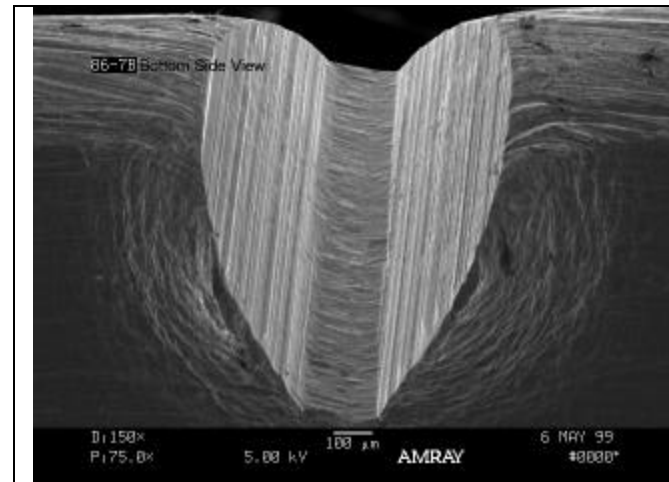
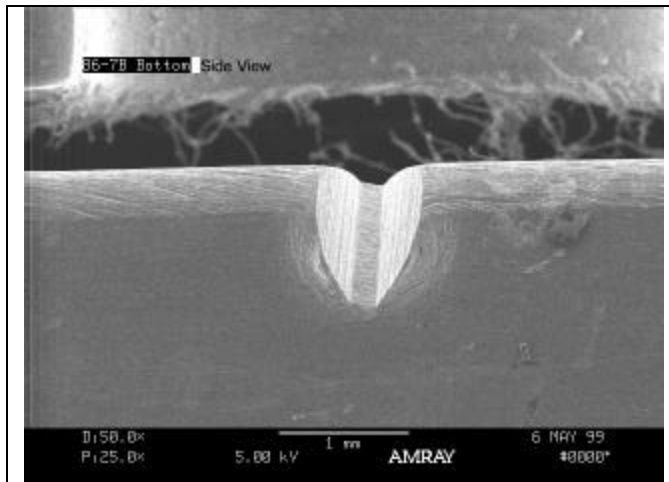


Side A

Specimen 86-07 FOD Characterization



Side B

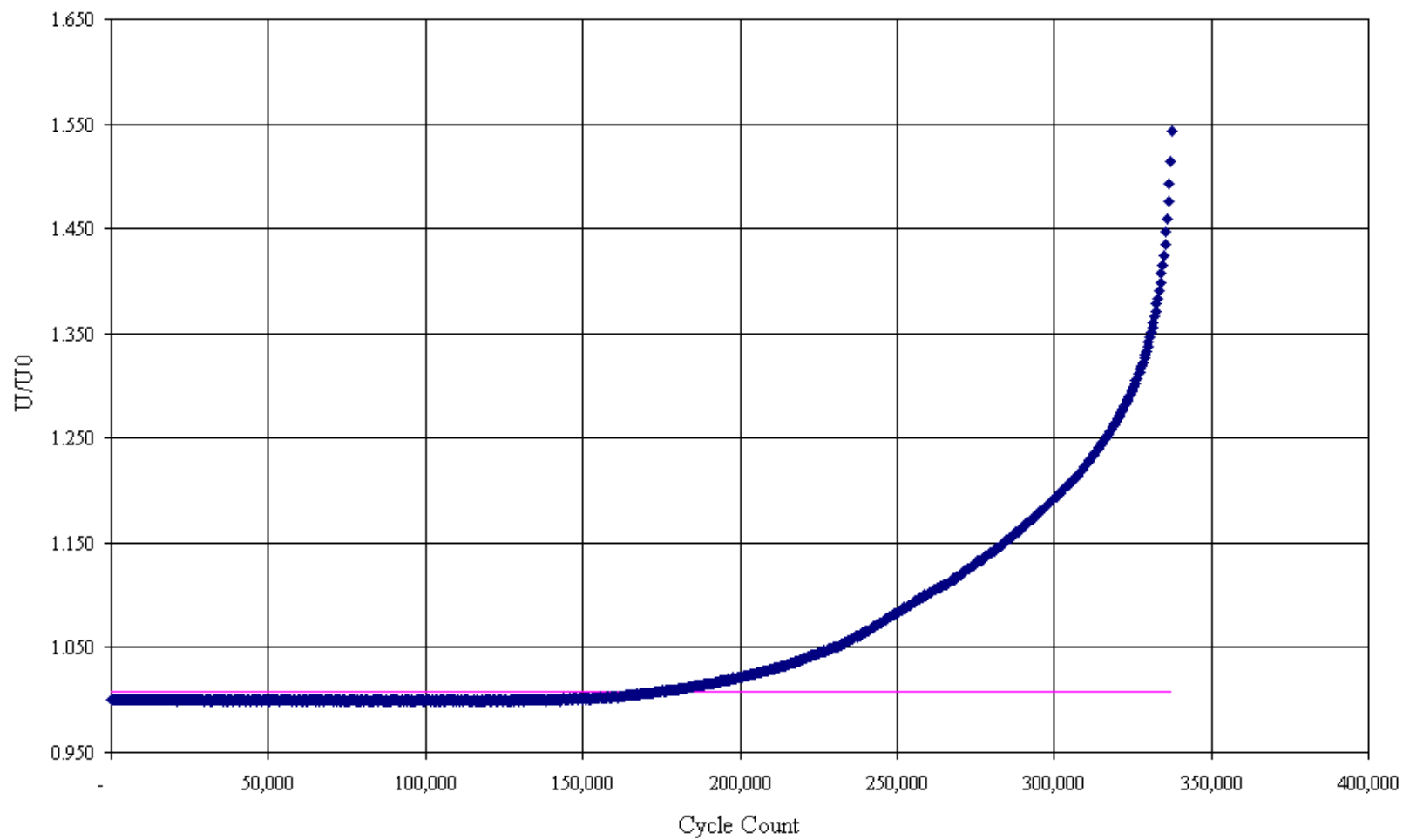


Side B

Overall picture of the EPD versus Cycle count for sample 86-07

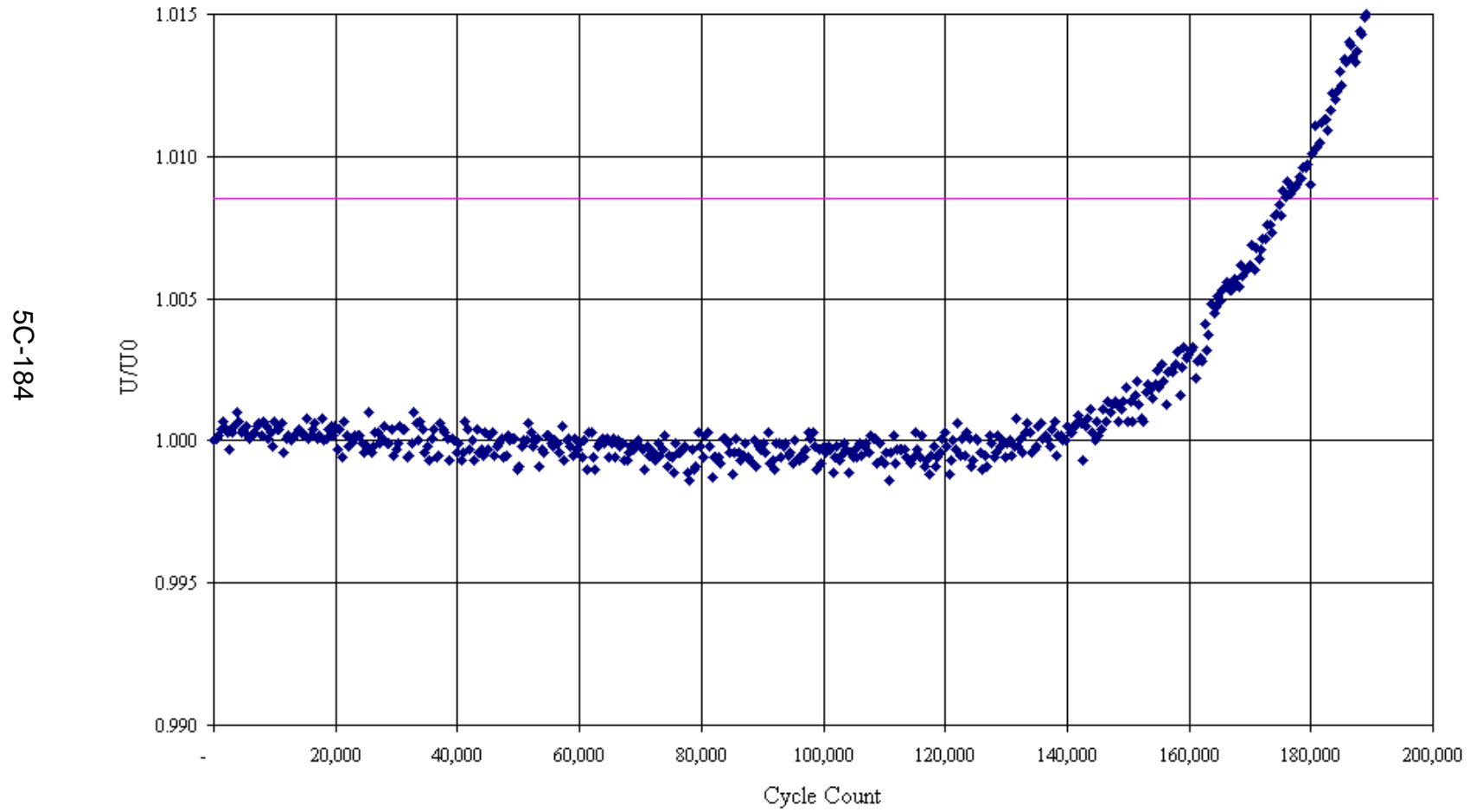
PD behavior for FOD Sample 86-7

5C-183



Closeup picture of the EPD versus Cycle count for sample 86-07

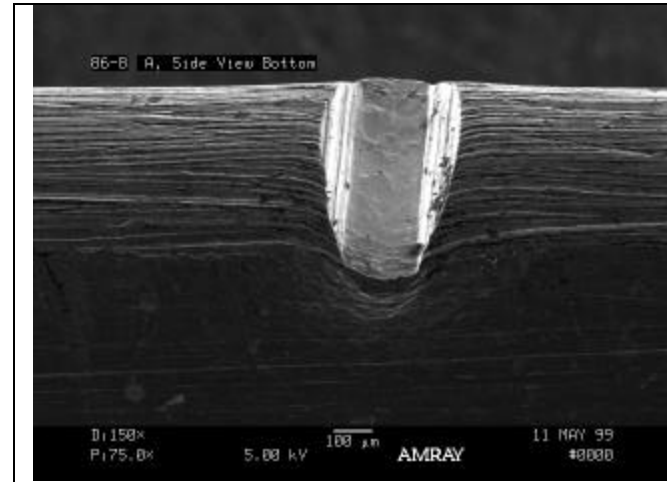
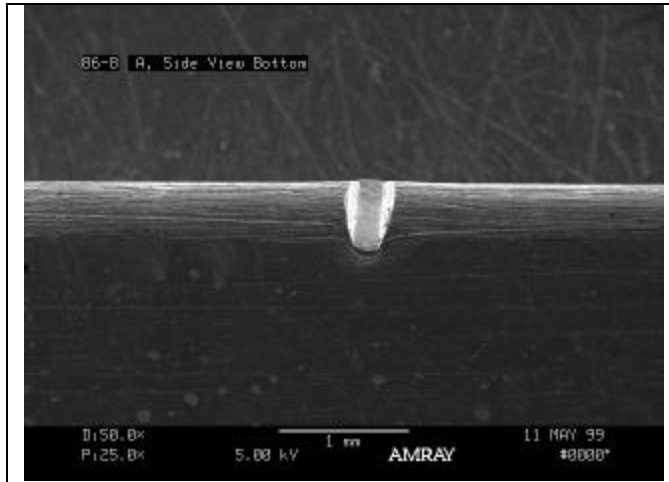
PD behavior for FOD Sample 86-7



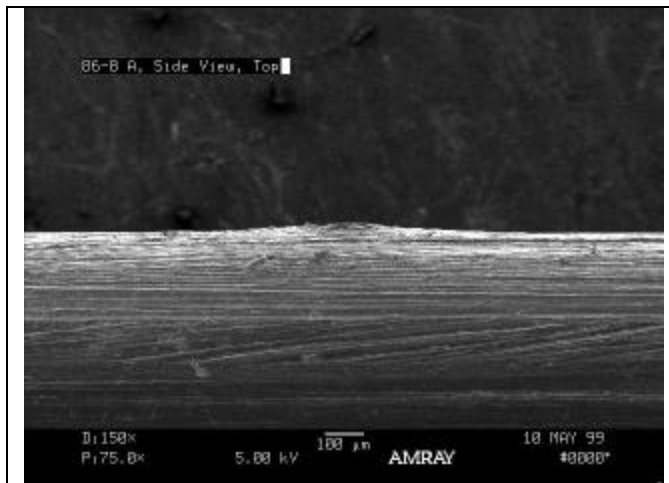
Specimen 86-08

Description: Blunt tip FOD specimen with a high energy solenoid gun impact at 30° with a 0.005 inch diameter indenter. The test was conducted with a stress ratio of 0.5 at an initial load of 1253.2 lbs and a frequency of 30 Hz. EPD was monitored throughout the test. When load did not occur after 1,000,000 cycles the load was increased 5%. Crack nucleation occurred at 1378.5 lbs, away from the intended location. The total cycles to failure was 8,219,033.

Specimen 86-08 FOD Characterization

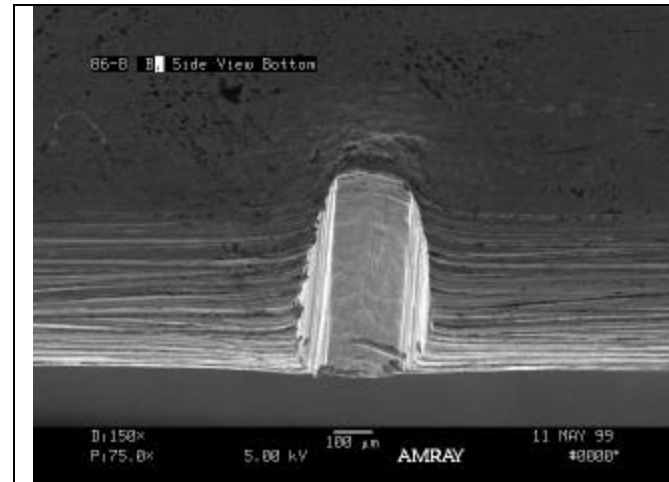
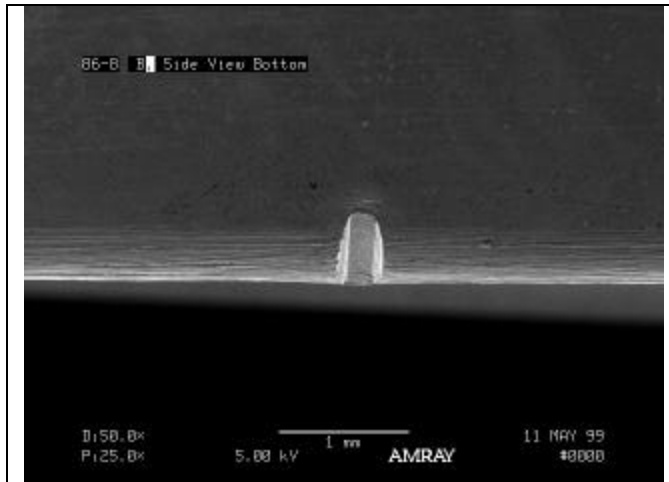


Side A

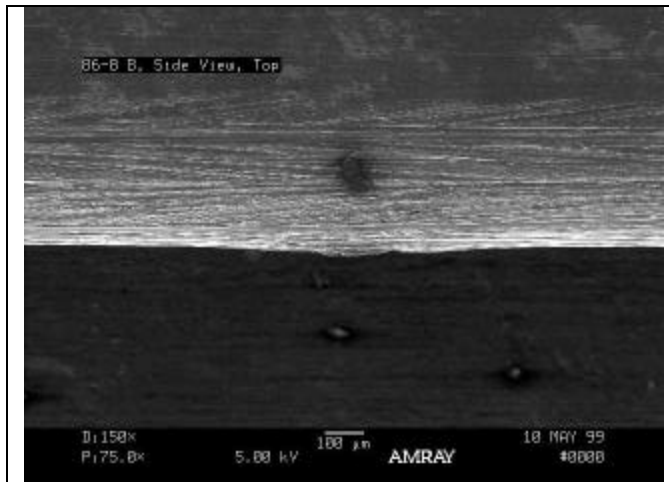


Side A

Specimen 86-08 FOD Characterization



Side B



Side B

Appendix 5D

SIMULATED FOREIGN OBJECT DAMAGE SPECIMEN PREPARATION UTILIZING BALLISTIC IMPACT



**University of Dayton
and
AFRL/ML**

SECTION ONE

**Characterization of Ballistic FOD Damage
for Analytical Model Verification
John J. Ruschau
UDRI**

SECTION TWO

**Microstructural Examination of Ballistic Impact
on Ti-6-4 Leading Edge Samples
William J. Porter
UDRI**

SECTION THREE

**FOD Impact Site Characterization Using Replication Techniques
Steven R. Thompson
AFRL
James D. Wolf
UDRI**

Section 1

CHARACTERIZATION OF BALLISTIC FOD DAMAGE FOR ANALYTICAL MODEL VERIFICATION

Researchers at the Allison Advanced Development Company were tasked to analytically model the dynamic FOD on the leading edge of Ti-6Al-4V fan/compressor blades, using DYNA3D analysis to model the ballistic impact event. To assist in this modeling, samples representative of the leading edge of typical fan blades were shot with steel spheres of various sizes and under a variety of impact conditions. The test samples that were shot were of the diamond cross-section tension (DCT) configuration, as used in several of the UDRI/AFRL FOD studies, and were machined from a single Ti-6Al-4V forged round bar. The impact conditions which were investigated are shown in Table 5D.1.

Table 5D.1

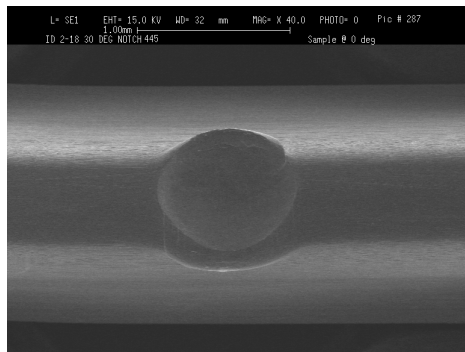
Ballistic Impact FOD Parameters for Leading Edge Specimens

Leading Edge Radius (inches)	Impact Velocity (f/s)	Ball Diameter (mm)	Impact Angle (°)
0.005	1000	1.33	0
0.015	1000	1.33	0
0.005	1000	1.33	30
0.015	1000	1.33	30
0.015	1000	0.50	30
0.015	1000	2.00	30
0.015	600	2.00	30

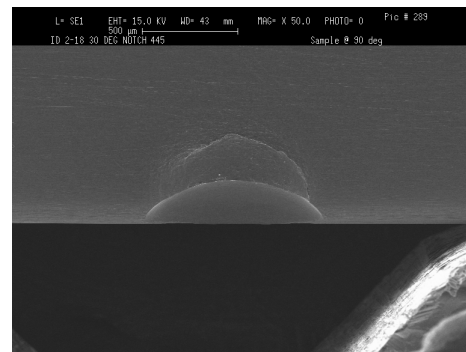
All samples were ballistically impacted by the Impact Physics Group of UDRI, using a single stage compressed gas gun. The steel ball projectiles were launched in a one-piece Lexan sabot with a cavity sized to fit the steel ball being launched. The actual steel ball was in free flight for approximately 0.75 inches (19 mm). This free flight distance permitted accurate measurement of the projectile velocity, while still facilitating

precise location of the impact. A telescopic bore scope was located behind the gun and used to sight the target and adjust trajectory.

A scanning electron microscope was used to obtain pictures of each FOD site after impact so that measurements of the damage (distortion, deformation, etc.) could be performed and used to adjust analytical model parameters as well as to verify results. Photos were taken normal and parallel to the leading edge of each of the DCT specimens. Examples of these are shown in Figures 5D.1 – 5D.12. These scaled photos were sent digitally to Allison so that detailed measurements could be made by them of the areas of concern. Results of the DYNA3D analysis with the actual FOD damage measurements incorporated in them are presented elsewhere in this report.

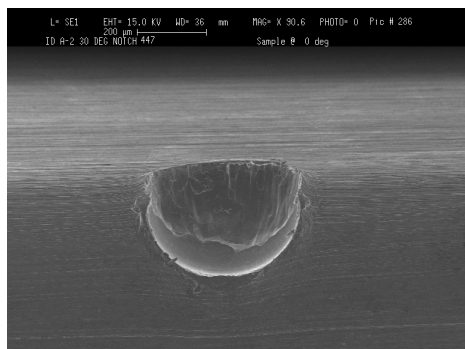


0° (normal to LE)

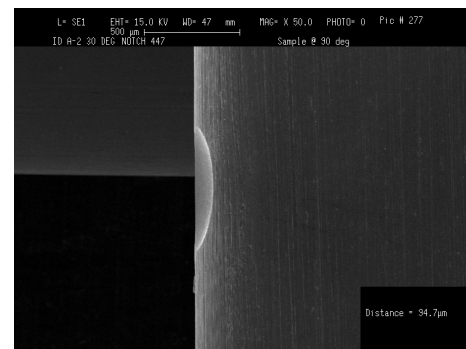


90° (parallel to LE)

Figure 5D.1. SEM photos of a 0.015" LE, 1.33mm steel ball, 600 f/s, 30° impact angle.

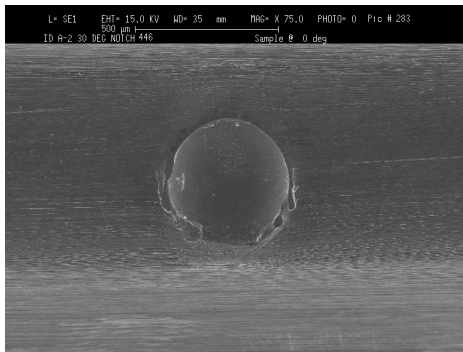


0° (normal to LE)

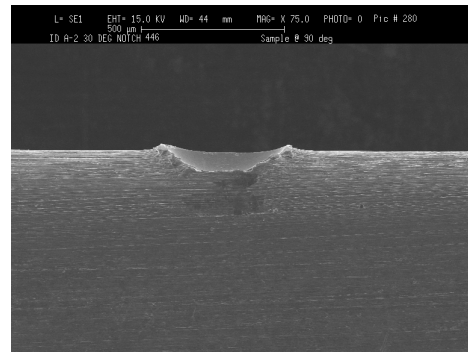


90° (parallel to LE)

Figure 5D.2. SEM photos of a 0.015" LE, 0.5-mm steel ball, 1007 f/s, 30° impact angle.

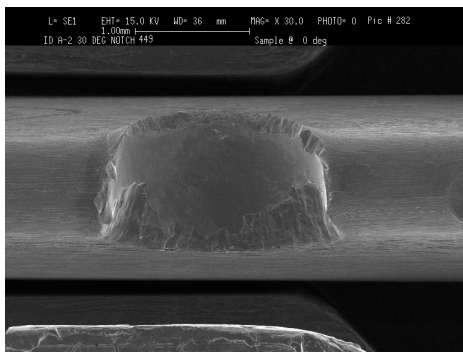


0° (normal to LE)

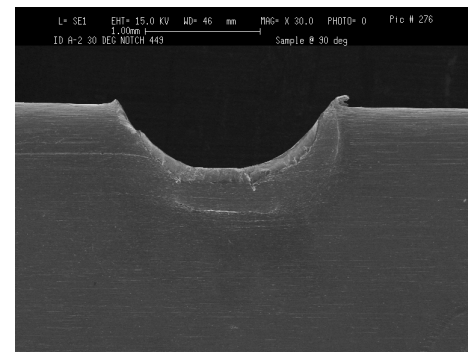


90° (parallel to LE)

Figure 5D.3. SEM photos of a 0.015" LE, 0.5-mm steel ball, 1006 f/s, 30° impact angle.

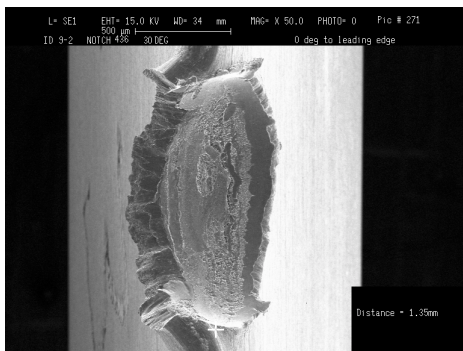


0° (normal to LE)

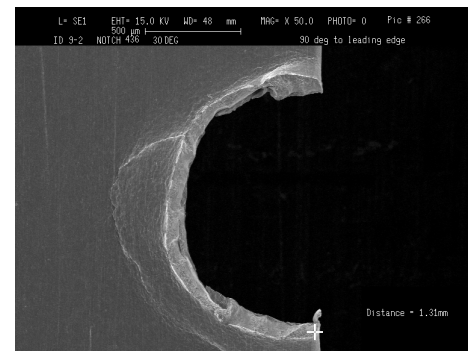


90° (parallel to LE)

Figure 5D.4. SEM photos of a 0.015" LE, 2.0 mm steel ball, 989 f/s, 30° impact angle.

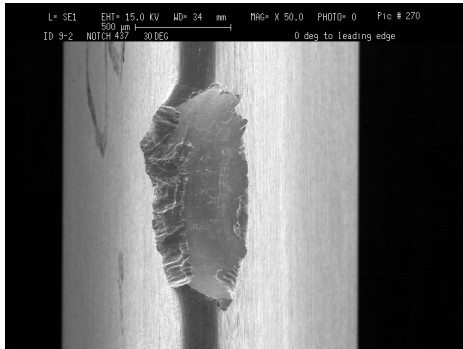


0° (normal to LE)

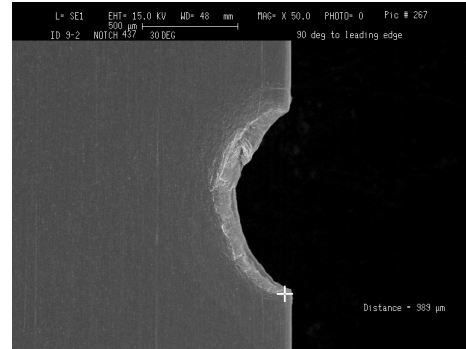


90° (parallel to LE)

Figure 5D.5. SEM photos of a 0.005" LE, 1.33 mm steel ball, 1042 f/s, 30° impact angle.

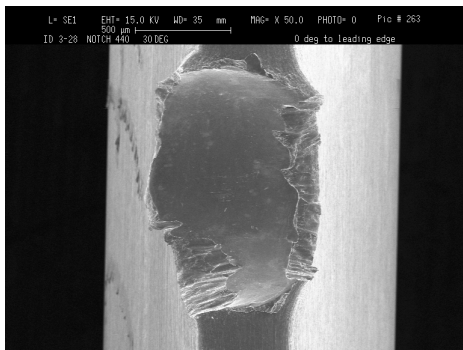


0° (normal to LE)

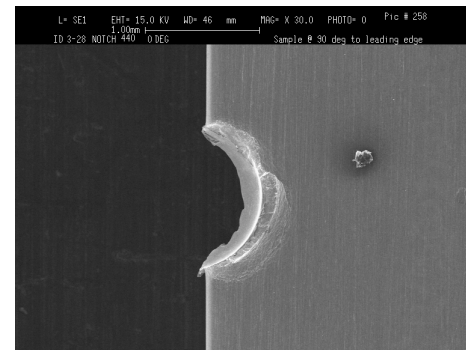


(parallel to LE)

Figure 5D.6. SEM photos of a 0.005" LE, 1.33 mm steel ball, 1040 f/s, 30° impact angle.

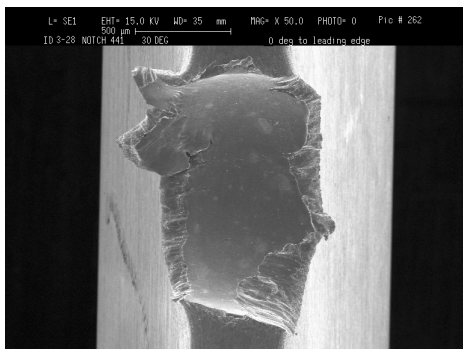


0° (normal to LE)

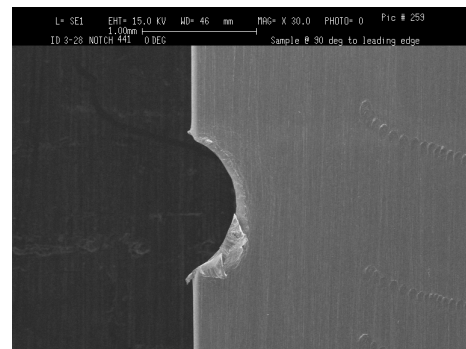


90° (parallel to LE)

Figure 5D.7. SEM photos of a 0.015" LE, 1.33 mm steel ball, 1037 f/s, 30° impact angle.

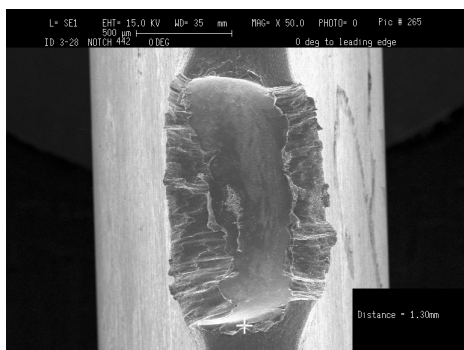


0° (normal to LE)

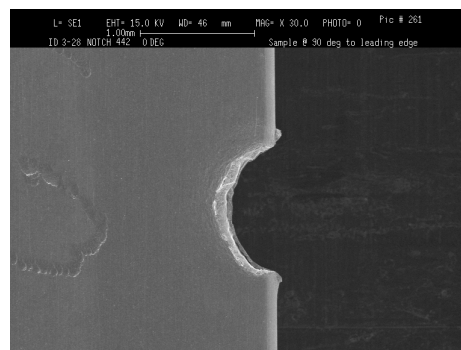


90° (parallel to LE)

Figure 5D.8. SEM photos of a 0.015" LE, 1.33 mm steel ball, 1015 f/s, 30° impact angle.

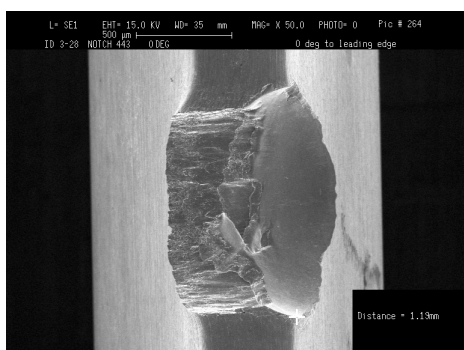


0° (normal to LE)

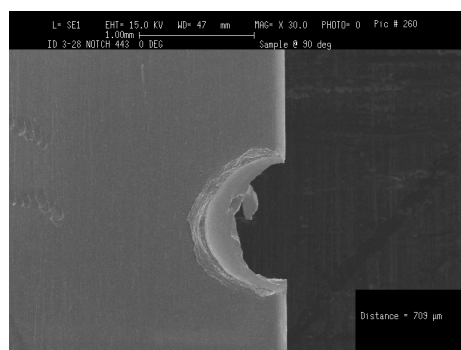


90° (parallel to LE)

Figure 5D.9. SEM photos of a 0.015" LE, 1.33 mm steel ball, 1043 f/s, 0° impact angle.

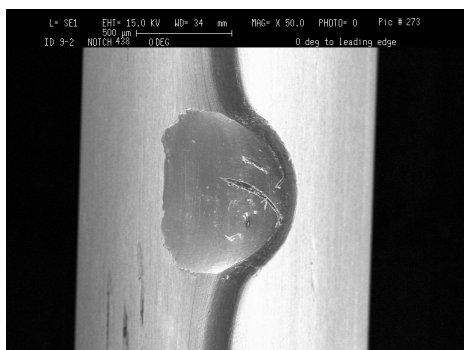


0° (normal to LE)

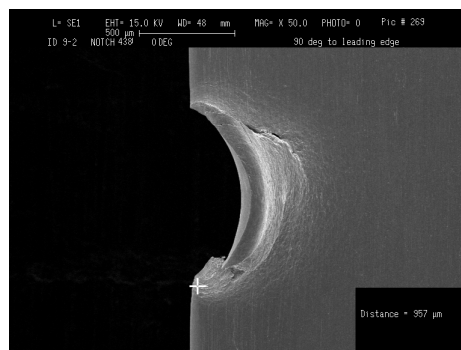


90° (parallel to LE)

Figure 5D.10. SEM photos of a 0.015" LE, 1.33 mm steel ball, 998 f/s, 0° impact angle.

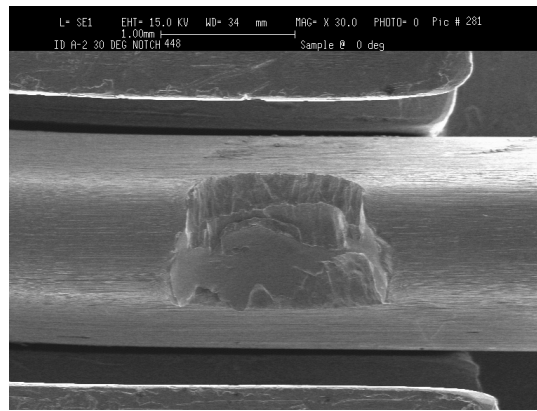


0° (normal to LE)



90° (parallel to LE)

Figure 5D.11. SEM photos of a 0.005" LE, 1.33 mm steel ball, 1042 f/s, 0° impact angle.



0° (normal to LE)

Figure 5D.12. SEM photos of a 0.015" LE, 2.0 mm steel ball, 973 f/s, 30° impact angle (no 90° view available)

Section 2

MICROSTRUCTURAL EXAMINATION OF BALLISTIC IMPACT ON TI-6-4 LEADING EDGE SAMPLES

Background

In order to understand the microstructural aspects of foreign object damage (FOD) on Ti-6Al-4V airfoils, samples representative of the leading edge section of turbine engine fan blades were impacted by spherical steel shot of various diameters and at various velocities. The microstructural damage associated with the leading edge impact sites was investigated using a serial sectioning metallographic technique and optical microscopy. Five impact sites were investigated.

Experimental Procedure

The simulated leading edge sample geometry is shown in Figure 5D.13. Though not intended for fatigue testing, the geometry of the leading edge (i.e., radius, angle, etc) are identical to that of the diamond cross-section tension (DCT) specimen used by UDRI/AFRL in numerous fatigue studies. A single 4 inch sample was impacted along its length with the impact sites distributed approximately 0.5 inches apart. Table 5D.2 contains information regarding the test conditions and approximate size of the damage sites.

The impact sites were photographed using optical and scanning electron microscopy for characterization before mounting and sectioning. The sample was then sectioned so that each impact site was isolated and subsequently molded in a metallographic mount. The samples were mounted such that sections perpendicular to the length of the original sample would be revealed. A schematic of a mounted sample is shown in Figure 5D.14. The samples were ground, polished and etched in steps ranging from 50-250 microns. Optical micrographs were taken at each step to characterize microstructural damage as a function of impact location.

The baseline microstructure of the Ti-6Al-4V material used in this study is shown in Figure 5D.15.

Results

Impact Sites

The overall appearance of the five impact sites is shown in Figure 5D.16. The width and depth of each impact site can be found in Table 5D.2.

Samples #3-0563, #3-0564 and #3-0565 showed extensive damage, with material having been removed during impact. The bulk of the separated material in #3-0563 appears to be from the incoming edge while in #3-0564 and #3-0565 the missing material is primarily from the exit side. Extensive ductile tearing of material is seen where material has been removed. The types of damage observed (removal, tearing and compression of material) are similar between these three samples, irrespective of shot size and velocity.

Samples #3-0566 and #3-0567 appear dented as opposed to having had material torn away. The damaged area in #3-0566 is much smaller than in #3-0567 even though the shot velocity in #3-0566 was much higher (934 vs. 698 f/s). This is possibly the result of a glancing shot below the leading edge in #3-0566 as compared to the direct hit in #3-0567.

Microstructure

A view of the cross sections of #3-0563 are shown in Figure 5D.17. All of the samples in the study were sectioned in a similar manner. The underlying microstructure at each section or slice was investigated using optical microscopy.

Three distinct features were apparent in all of the samples in this study. These include a deformed or compressed microstructural layer below the impact site, the presence of adiabatic shear bands, and the absence of any microcracking or delaminations. Examples of the compressed layer and adiabatic shear bands can be seen in Figure 5D.18.

The deformed or compressed microstructural layer is identified by two primary characteristics. The first is bending or distortion of the material within the transformed β grains. This distortion is shown in Figure 5D.18b where the laths making up the transformed region, which are normally linear in appearance, have been deformed or bent, losing their linearity. The other characteristic is bending or elongation of the primary α grains. Distorted or flattened primary α grains are shown below the impact surface in Figures 5D.18a and 5D.18b.

Adiabatic shear bands were found throughout the microstructure directly below the impact site. The shear bands appear to start at the surface of the impact and extended into the bulk microstructure. The angle of incidence with the impact surface was approximately 45° . The width of all observed shear bands was in the range of 1-3 μm .

Specific microstructural observations of each impact site are described below (See Table 1 for individual test details).

#3-0563

The primary alpha grains and the lamellar $\alpha+\beta$ regions are noticeably distorted to a depth of about $20\mu\text{m}$, with adiabatic shear bands and associated deformation extending to a depth of approx. $50\mu\text{m}$. Shear bands with an overall length of nearly $200\mu\text{m}$ were measured. The areas where the material was removed or 'blown away' during impact appear smooth with minimal deformation.

#3-0564

Features of this sample are similar to #3-0653 except that shear bands measure up to more than $220\mu\text{m}$ in length and extend to a depth of $100\mu\text{m}$. A situation where two shear bands terminate at approximately the same point at a depth of $100\mu\text{m}$ was observed (Figure 5D.19). As previously noted, no microcracking was observed, even in

the location of the terminating shear bands. Microstructural deformation (except for the presence of shear bands) was apparent to depths approaching 40 μ m.

#3-0565

Similar to #3-0654 except that shear bands extend to a depth of 20 μ m.

#3-0566

Microstructural deformation and shear banding extend to a depth of approx. 20 μ m.

#3-0567

Multiple shear bands observed to a depth of 125 μ m.

Summary

Five impact sites in a Ti-6Al-4V leading edge test sample were metallographically investigated. The impact sites were meant to simulate foreign object damage (FOD) that might be seen in fan or compressor blades. The impact sites were created by shooting the leading edge sample with various diameter steel balls at several velocities. The microstructural changes, aside from the scale of damage, were consistent for all specimens. The primary microstructural features due to impact damage were a compressed microstructural zone and the formation of adiabatic shear bands. No microcracking, void formation or delaminations were observed in these samples.

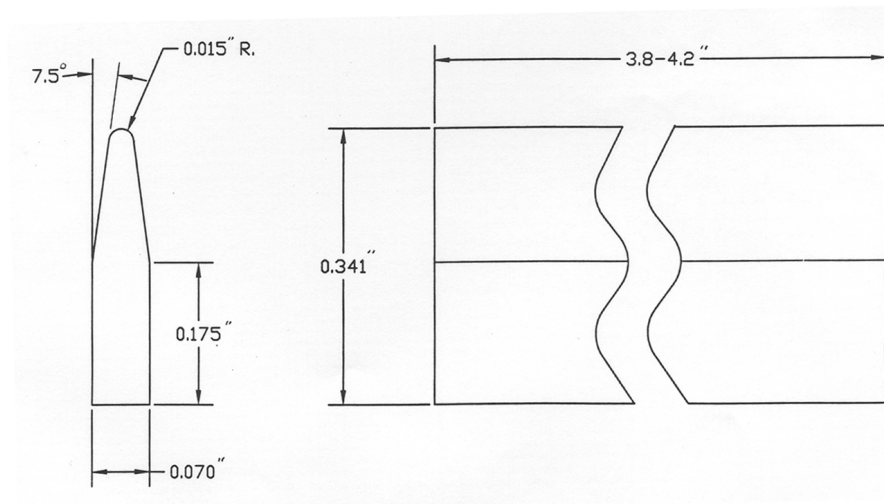


Figure 5D.13. Leading edge sample geometry.

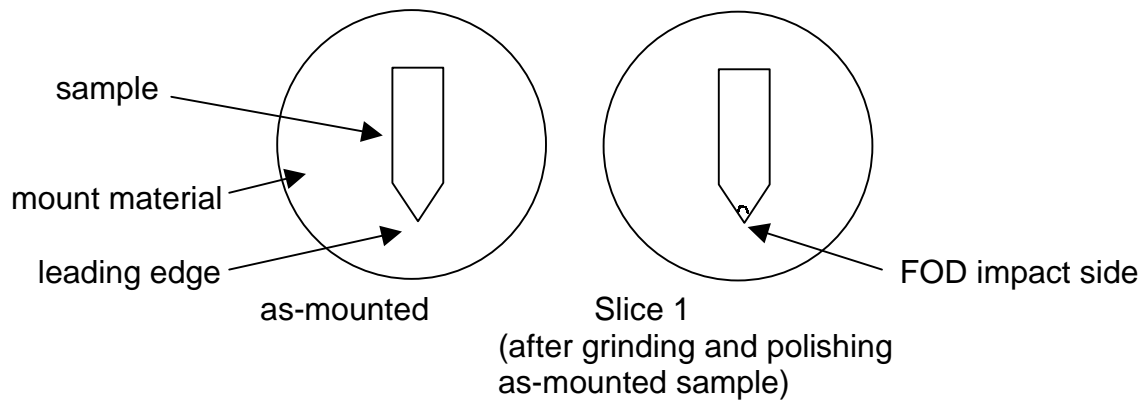


Figure 5D.14. Schematic of the metallographic mounts and sample orientation.

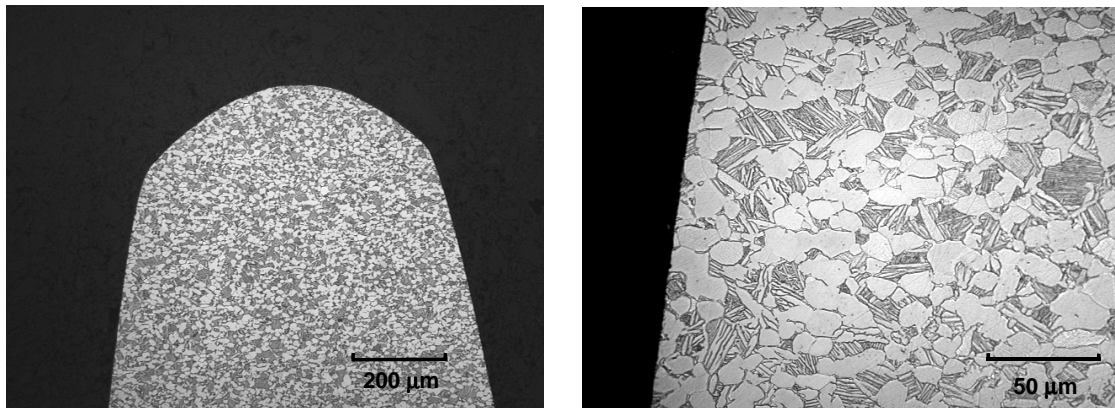
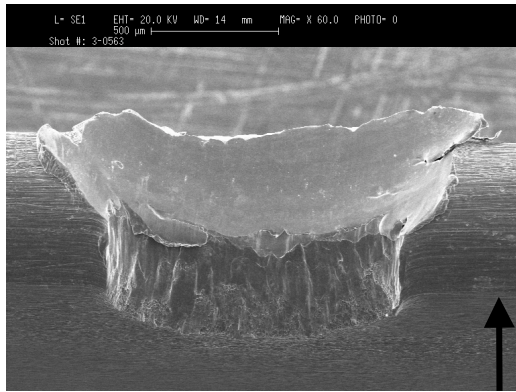


Figure 5D.15. Baseline Ti-6Al-4V microstructure.

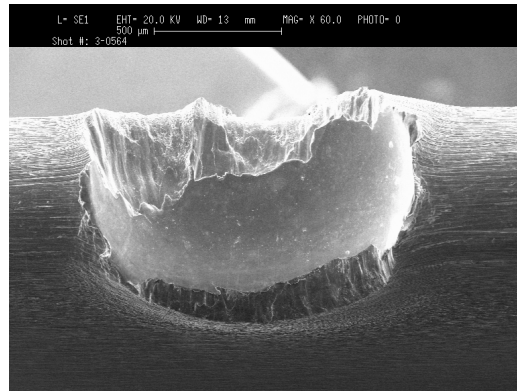
Table 5D.2

Description of Test Conditions and Impact Site Dimensions

Shot ID	Shot Velocity (f/s)	Impact Angle (°)	Shot Diameter (mm)	Width of Impact Site (mm)	Depth of Impact Site (mm)
3-0563	636	30	2.03	1.857	.350
3-0564	990	30	1.33	1.326	.520
3-0565	669	30	1.33	1.171	.420
3-0566	934	30	0.50	0.334	.030
3-0567	698	30	0.50	0.512	.080

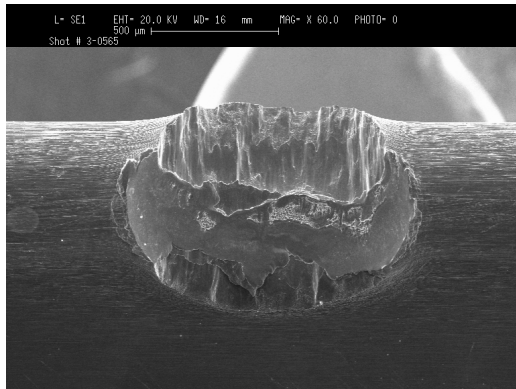


(a)

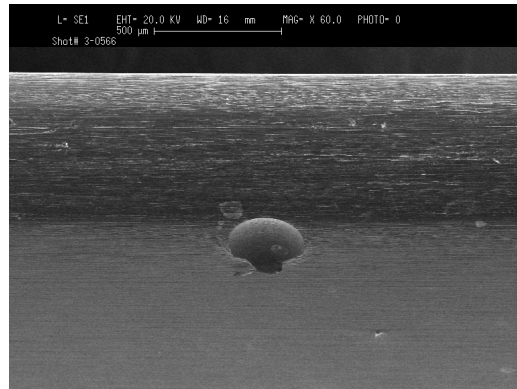


(b)

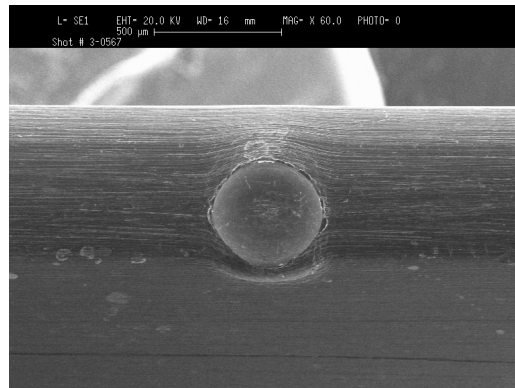
Shot
Direction



(c)



(d)



(e)

Figure 5D.16. Overall appearance of the impact sites. Shot travel was from bottom of picture (incoming) to top: a) #3-0563, b) #3-0564, c) #3-0565, d) #3-0566, and e) #3-0567.

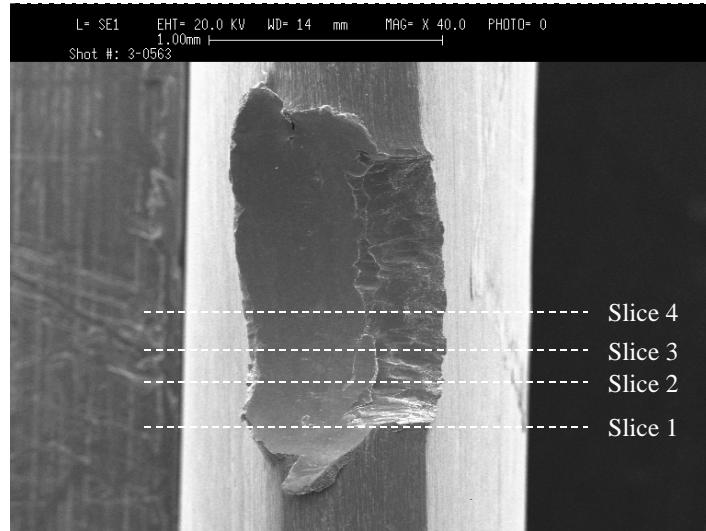
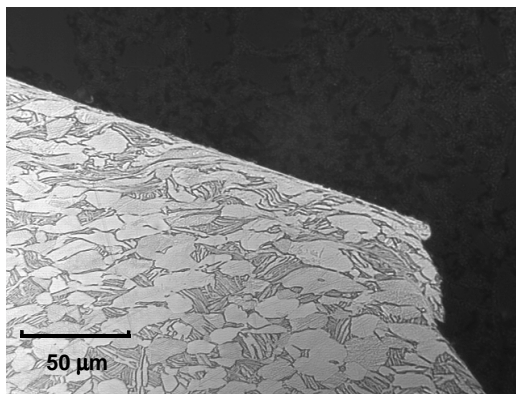
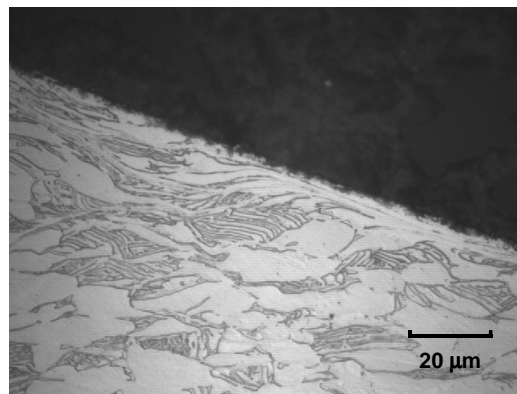


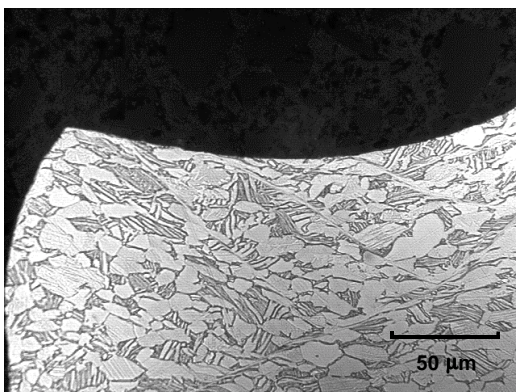
Figure 5D.17. Example of sections or metallographic slices from #3-0653. This is representative of sectioning done to all samples in this study.



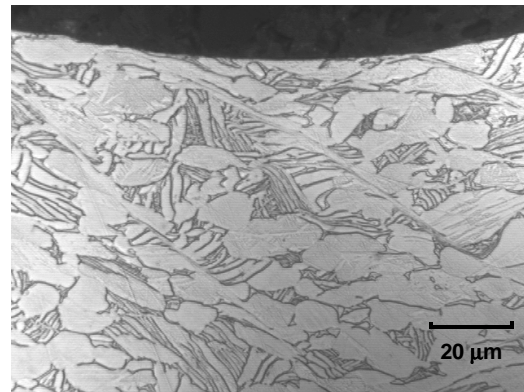
(a)



(b)



(c)



(d)

Figure 5D.18. Optical micrographs of a, b) compressed or deformed microstructure (#3-0653) and c, d) adiabatic shear bands (#3-0567). Both features were seen in all samples used in this study.

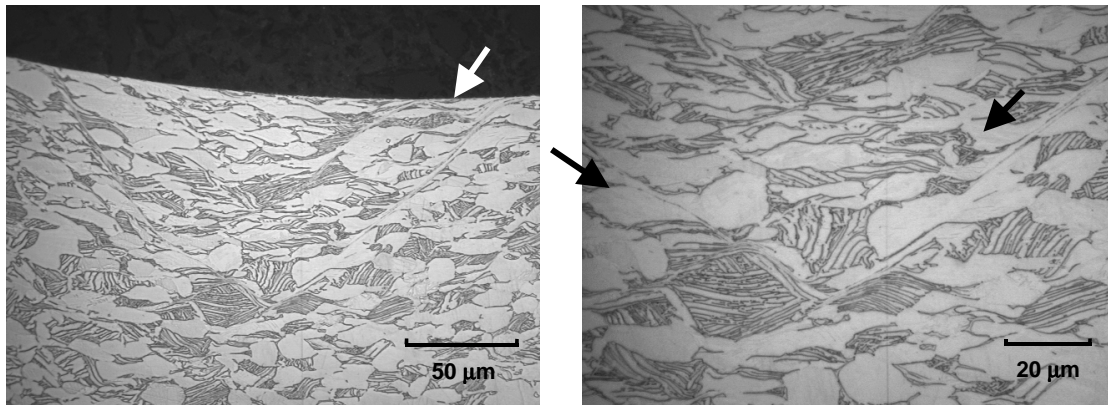


Figure 5D.19. Terminating shear bands in #3-0654.

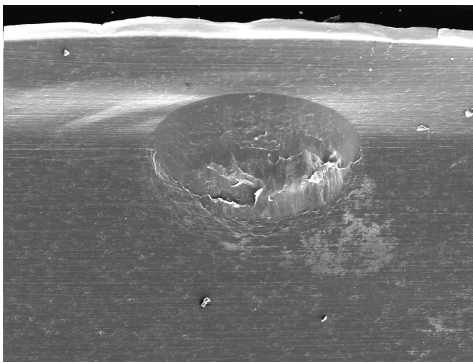
Section 3

FOD IMPACT SITE CHARACTERIZATION USING REPLICATION TECHNIQUES

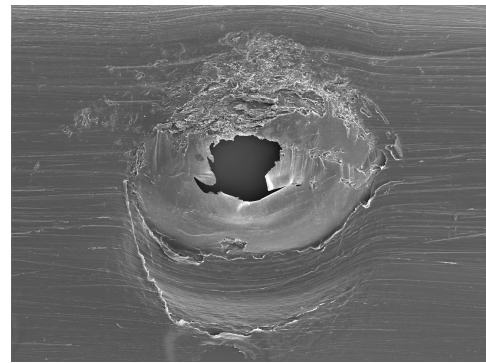
An effort was undertaken to characterize ballistic foreign object damage (FOD) sites on axial fatigue specimens prior to fatigue testing. Due to the fact that the specimens were too large to be placed into the scanning electron microscope (SEM), replication techniques were investigated as a possible characterization method. Thirteen diamond cross-section (DCT) axial fatigue specimens which had been impacted with 1 mm glass spheres were delivered to the Microanalytical Laboratory of UDRI for pre-test characterization. Each specimen had two impact sites, one on each edge. The glass spheres impacted the specimens at an angle of 30° relative to the specimen thickness plane and at a velocity of nominally 1000 ft/sec.

Because of variations in the amount of damage inflicted by the FOD impacts on the specimens, two different replication techniques were attempted. For FOD sites where the impact resulted in a “dented” surface without material removal, the standard acetate tape replication technique was employed. For sites where material had been removed, leaving a relatively deep crater with “rugged” edges an acrylic paste technique was used. Once the replicas were been made, they were placed into an SEM and photographs taken.

In some cases where the FOD damage resulted in a shallow type of indent the replication technique proved acceptable, as witnessed in Figure 5H20.a. Unfortunately, in many of the cases, neither technique was acceptable in identifying the important features which could contribute to fatigue failure. In some instances the replicas tore during removal, as shown in Figure 5D.20b. Initially it appeared as though the replication would be acceptable as a characterization technique. However these attempts were made on specimens with smoother impact site morphologies. When applied to rougher impact sites the replicas resulted in distortion, with features not always representative of the actual impact site. Thus it is apparent from this effort that the replication methods are not intended for morphologies such as those being produced by the FOD impacts.



a) acceptable



b) unacceptable

Figure 5D.20. Example of Replicas of Foreign Object Damage.

Appendix 5E

FOD ANALYTICAL MODELING – FOD EVENT MODELING

**Craig Weeks
Phillip Bastnagel
Tom Cook
Ralph Daiuto
Jim Delp**



Allison Advanced Development Company

**Submitted
31 August 1999**

DISCUSSION OF ANALYTICAL MODELING METHODS AND CORRELATION OF AIRFOIL LEADING EDGE FOREIGN OBJECT DAMAGE EVENTS

ABSTRACT

A major source of concern in the high cycle fatigue behavior of gas turbine airfoils is the introduction of damage from foreign object impact events. These events introduce damage to the airfoil leading edge and this analytical investigation will attempt to identify the effect of key parameters on this resulting impact damage. By identifying the relative influence of these parameters, airfoil designs can be better optimized to minimize impact damage. The commercial explicit finite element package MSC/DYTRAN is utilized to model hard body foreign object damage (FOD) events of titanium airfoils. The titanium airfoils are represented by tapered specimens with representative airfoil leading edge radii and are impacted with steel balls. The analysis includes rate dependent material properties and introduces material failure. The analysis methodology is correlated with impact test results prior to conducting an analytical parametric analysis. A number of variables, including airfoil leading edge radius, impactor size, speed, and impact angle are investigated to determine the effect of these variables on leading edge damage. Modeling methods and the results of analytical predictions are presented.

INTRODUCTION

In order to better understand the factors influencing high cycle fatigue (HCF) crack growth emanating from foreign object damage (FOD) impact sites in gas turbine engine airfoils, an analytical study was conducted utilizing the commercial explicit finite element code MSC/DYTRAN [5E.1]. This particular explicit finite element analysis is part of a larger analytical and experimental effort investigating the fatigue and FOD response of gas turbine airfoils. The specimen geometries contained in this analysis correspond to actual test specimens used in FOD experiments and post-FOD fatigue testing. All of the impact experiments and the corresponding analysis were conducted at room temperature (72°F/22°C). Of particular interest is the residual stress state in the airfoil after impact. These impact events can generate significant deformation and correspondingly high residual stresses. These residual stresses could play a major role in the resulting post-FOD fatigue life of the airfoils.

Characteristic materials, airfoil leading edge geometries and impact conditions representing gas turbine compressor blades were selected for the experimental and analytical programs. Titanium (Ti-6Al-4V) specimens with representative leading edge radii were impacted with steel balls at angles and velocities seen by typical compressor airfoils. A parametric analysis with impactor size, speed, angle and specimen leading edge radii was conducted with DYTRAN. The results of the analysis and the relative effects of these variables will be presented.

Two specimen geometries representing typical compressor airfoil leading edges were selected for this program and were machined for impact testing. A “sharp” edge specimen with a 0.005 inch (0.127 mm) leading edge radius (LER) and a “blunt” edge specimen with a 0.015 inch (0.381 mm) LER as shown in Figure 5E.1 were modeled. The angle of impact relative to the specimen cross-section was varied from 0° to 45° as shown in Figure 5E.2, and the impact velocity was varied from 600 ft/s (182.9 m/s) to 1200 ft/s (365.8 m/s).

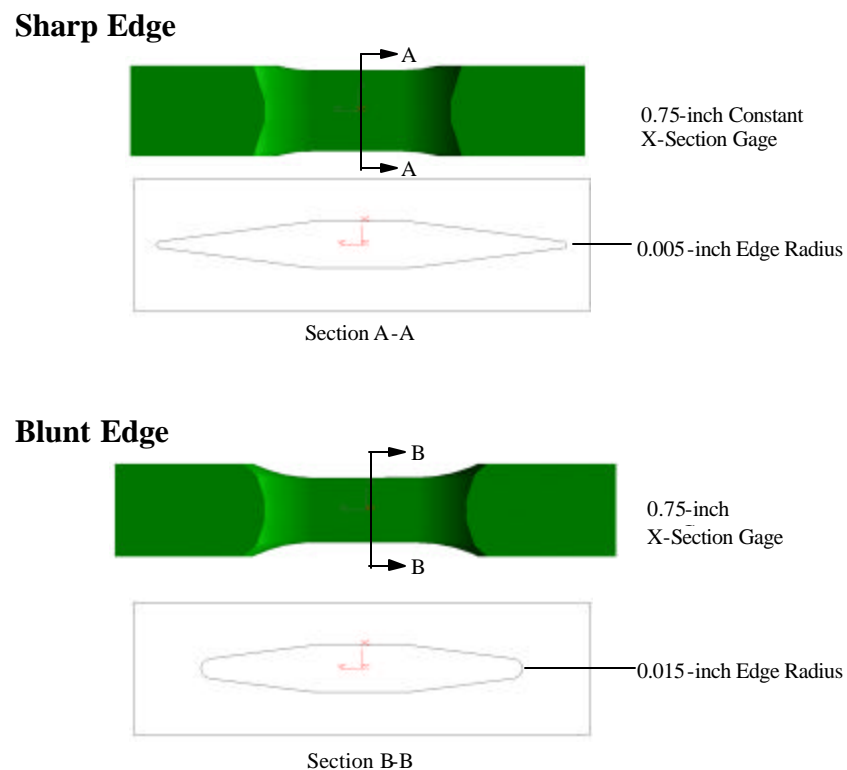


Figure 5E.1. Leading-Edge Diamond Cross-section Tension (DCT) Specimen Geometries.

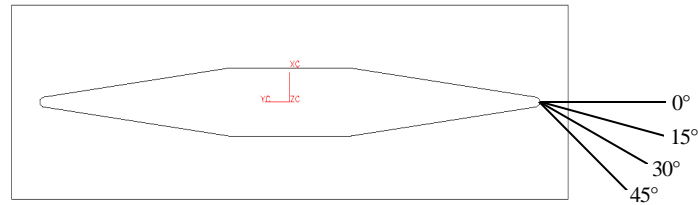


Figure 5E.2. Impact Angles.

FINITE ELEMENT MODELING

Finite element models were generated for analysis with DYTRAN. An eight noded reduced integration explicit Lagrangian brick element was used throughout the mesh for both the specimen and impacting ball. Tetrahedral and Penta elements were avoided in the mesh by utilization of an RCONN interface in the transition region between the gage section and the grip section. The RCONN interface acts as a contact surface and is used to transfer loads across surfaces with dissimilar meshes. This region is well away from the impact site and any errors introduced with this interface will have negligible effect on the predicted stress field near the impact site. Because the reduced integration element only has one integration point at the centroid of the element, hourglass controls were used to eliminate zero energy modes or “hourglassing”. The density of the mesh was weighted towards the impact site to better catch the contact between the ball and the specimen and to better predict the stress field. Figure 5E.3 shows a representative finite element mesh for a sharp edged specimen being impacted at 30° with a 0.079 inch (2 mm) diameter ball. Different specimen model meshes were utilized near the impact site for each diameter ball to keep number of elements across the length in the impact region identical for each diameter ball.

As with all finite element analysis, whether it be explicit or implicit, the density of the mesh plays a role in the stress predictions and a mesh refinement study was conducted. The specimen mesh refinement study was conducted with the ball mesh density kept constant. Figure 5E.4 shows three successively finer meshes used in this analysis to determine the relative effect and efficiency of mesh refinement.

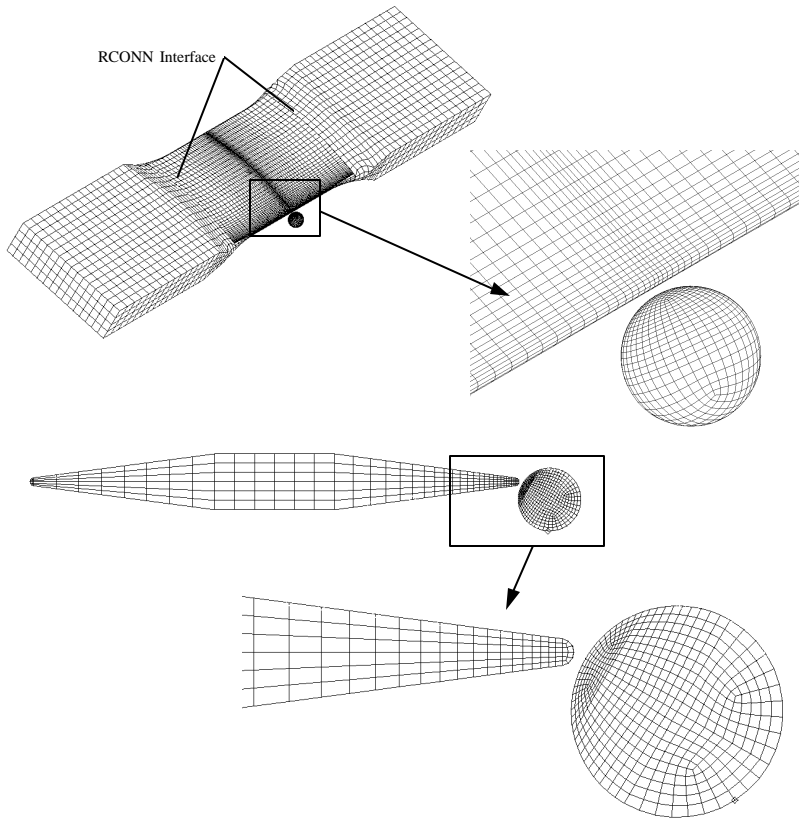


Figure 5E.3. Finite Element Model of Sharp Edge Specimen Impacted with 0.079 inch (2 mm) Ball at 30°.

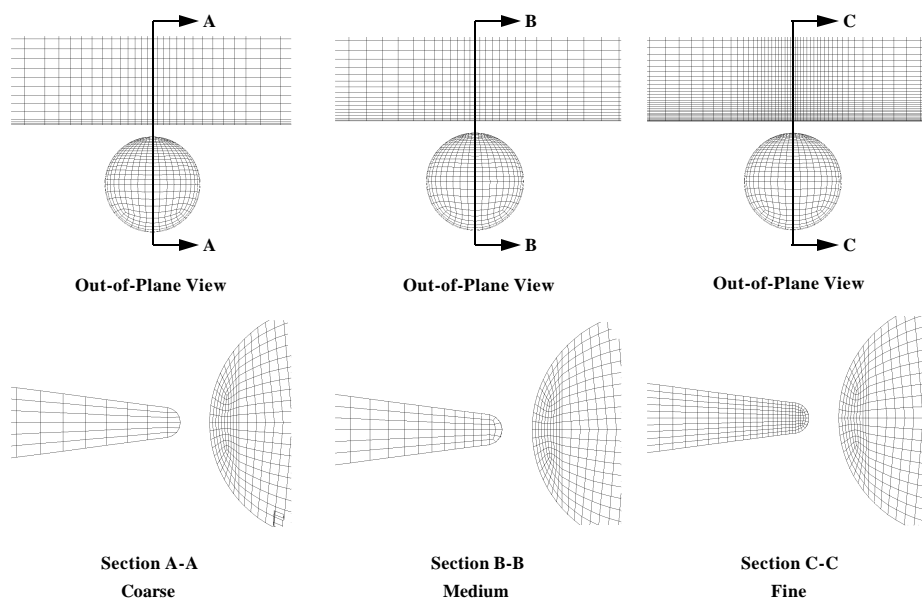


Figure 5E.4. Specimen Mesh Refinement.

Material Modeling

DYTRAN has a very large material library to describe the constitutive behavior of many types of materials. Ballistic events introduce high strain rates and titanium has been shown to be highly rate sensitive. Therefore, a strain rate dependent constitutive material model (DYMAT24) was selected for this analysis. The model allows for the modeling of a nonlinear, plastic material with isotropic hardening and the von Mises flow rule. Strain rate dependent stress-strain curves are supplied to the analysis and as the strain rate varies, the analysis calculates the appropriate stress for the specific strain rate. Although a large data base of strain rate dependent test data exists for the titanium alloy used in the HCF program, strain rate dependent tests were conducted for confirmation of the properties. Tensile specimens were taken from the same forging which supplied specimens for the ballistic experiments and the University of Dayton Research Institute (UDRI) was contracted to conduct experiments at strain rates varying from 0.0001 sec^{-1} to 1000 sec^{-1} [5E.2]. The test results were in close agreement with previous findings from other researchers. As a result of these present experiments and correlation with previous experiments, the strain rate dependent bilinear stress-strain response shown in Figure 5E.5 was used to model the material behavior. This material model has an elastic modulus of 16.6 Msi (114 GPa), a tangent modulus of (0.160 Msi) 1.1 GPa, and a quasistatic yield stress of 138 Ksi (951 MPa).

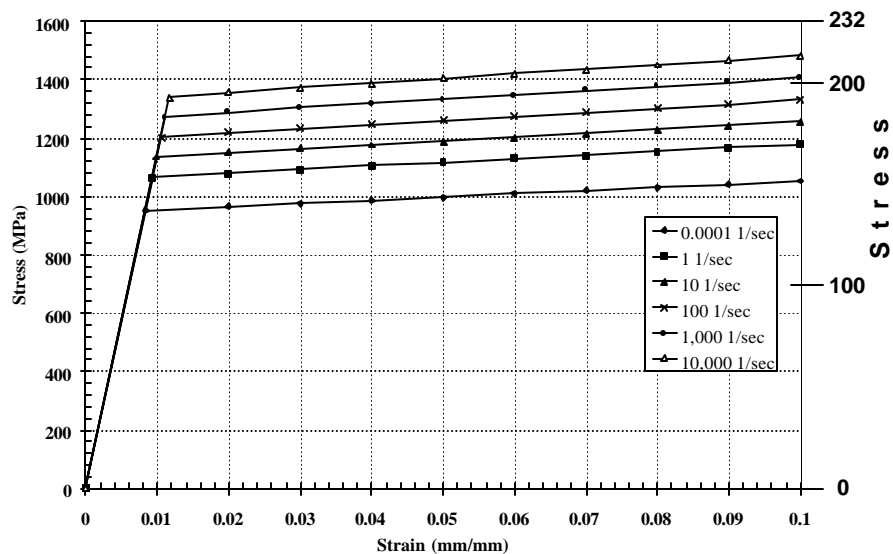


Figure 5E.5. Rate Dependent Stress-Strain Behavior Utilized in Analysis.

Material failure routines in DYTRAN are not sophisticated, and cannot accurately model crack propagation; therefore, caveats must be placed on predictions of failure. A basic material failure model based on the Von Mises yield function was selected for evaluation. This chosen material model allows for failure of the element by definition of an effective plastic strain at failure. Once the failure limit is reached, the element loses all its strength. The single effective plastic strain variable utilized does not distinguish between different modes and once the limit is reached regardless if it is tension, compression, shear, or mixed it fails. High strain rate effective plasticity is utilized in the failure criteria definition. The selection of 35% effective plastic strain was based on a combination of literature surveys and finite element correlation with impact specimens exhibiting failure. Results utilizing this material failure parameter will be presented but because of model limitations they should not be taken as absolutes and failure nucleation sites will also be predicted based on the analytical stress fields without material failure. The steel balls were modeled as linear elastic with a modulus of 29.6 Msi (204 Gpa) and a density of 0.283 lb/in³ (7832 kg/m³):

ANALYTICAL RESULTS

The analysis was first calibrated with selected ballistic experiments performed by UDRI. In addition to this experimental correlation, mesh refinement studies were utilized to calibrate the analysis to a selected mesh density. After correlation and selection of the mesh density, the parametric studies were conducted.

Experimental Correlation and Mesh Refinement Study

The experimental conditions utilized to correlate this present finite element analysis are shown in Table 5E.1. SEM photos were taken of the Diamond Cross-section Tension (DCT) tested specimens from two angles, in-plane and out-of-plane, as shown in Figure 5E.6 and these measured deflections were used to correlate the finite element analysis.

Table 5E.1
Ballistic Testing Conditions Utilized for Correlation

Test Condition	Specimen LER (Inch)	Ball Diameter (Inch)	Impact Angle	Impact Velocity (FPS)
1	0.005	0.052	0°	1042
2*	0.005	0.052	30°	1042
3	0.075	0.052	30°	600
4*	0.075	0.052	30°	1015

*Specimen exhibited large tearing and material removal

As was shown in Figure 5E.4, three different meshes were evaluated. Test Condition 1 without material failure and Test Condition 2 with material failure were used to evaluate and downselect the mesh density for the parametric studies. Figure 5E.7 shows the definition of parameters used to define the deformation and correlation with the finite element predictions. The depth and width are in-plane displacements, while the height is an out-of-plane displacement. Figures 5E.8 and 5E.9 show the relative deformation predictions for the three mesh densities as compared to Test Condition 1 and Test Condition 2, respectively. Figure 5E.8 shows the experimental results for Test Condition 1 which was experimentally intended to be an LER center impact at 0° incidence, but as can be seen in the SEM photos, the impact was not at the LER center. An offset was calculated from the SEM photos and this offset was used in the finite element model. The tearing and material removal in Test Condition 2 as shown in Figure 5E.9 did not allow an accurate measure of the “true” experimental impact site and the analysis, therefore, assumed an impact on the center of the LER.

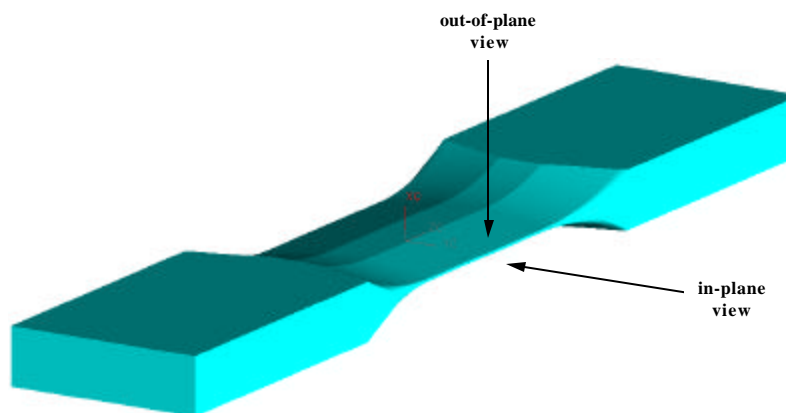


Figure 5E.6. SEM Views for DCT Specimen Photos.

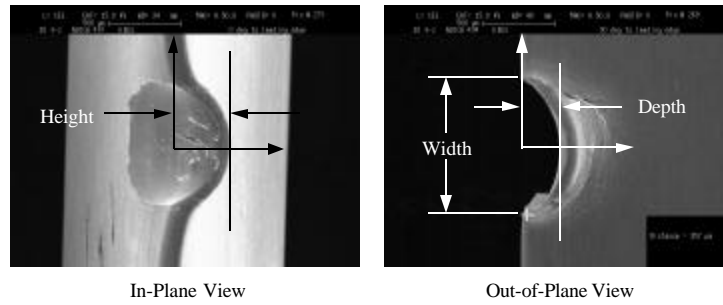
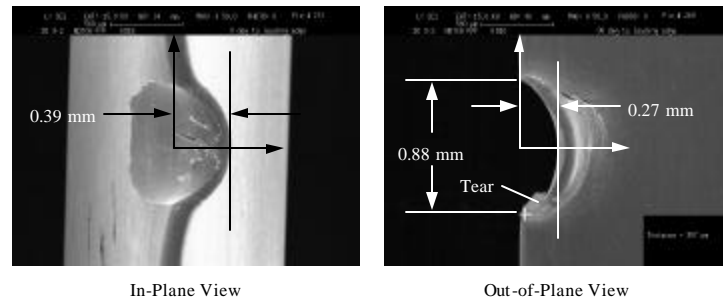
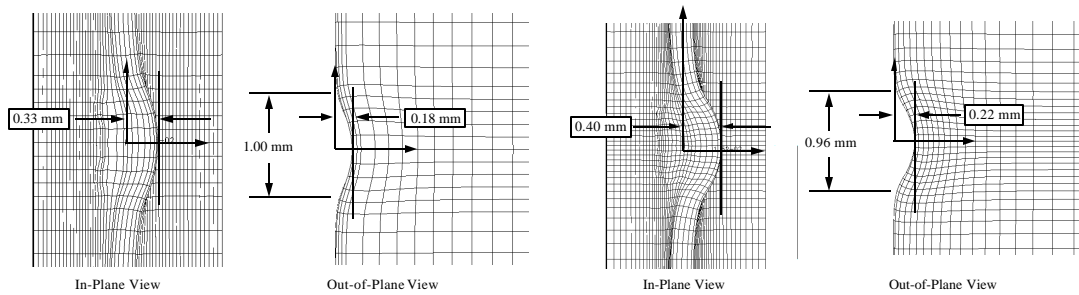


Figure 5E.7. Definition of Deformation Parameters. (1 mm = 0.039-inch)

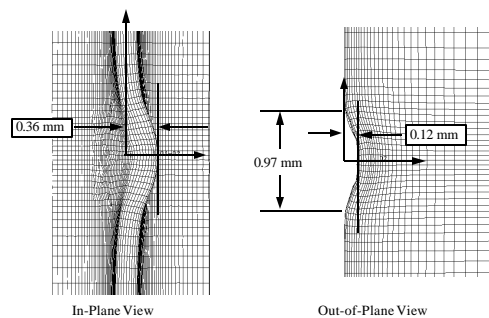


Test Result



Coarse Mesh Prediction

Medium Mesh Prediction



Fine Mesh Prediction

Figure 5E.8. Mesh Refinement Comparison and Correlation for Test Condition 1. (1 mm = 0.039-inch)

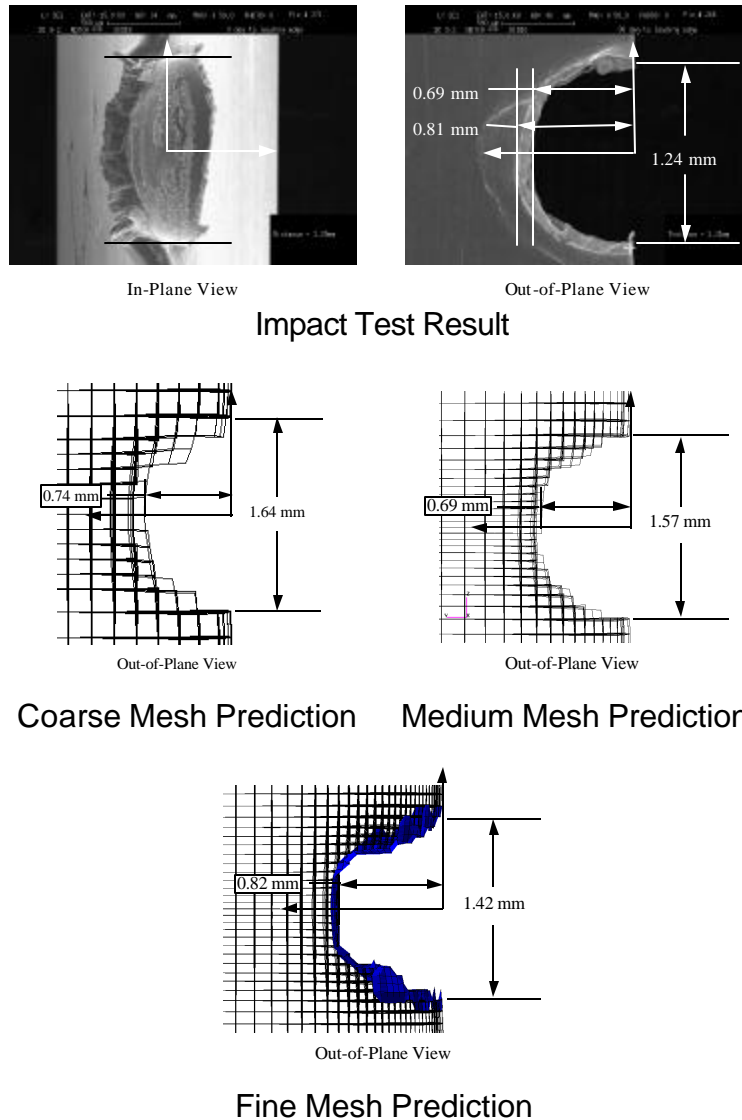


Figure 5E.9. Mesh Refinement Comparison and Correlation for Test Condition 2.
(1 mm = 0.039-inch)

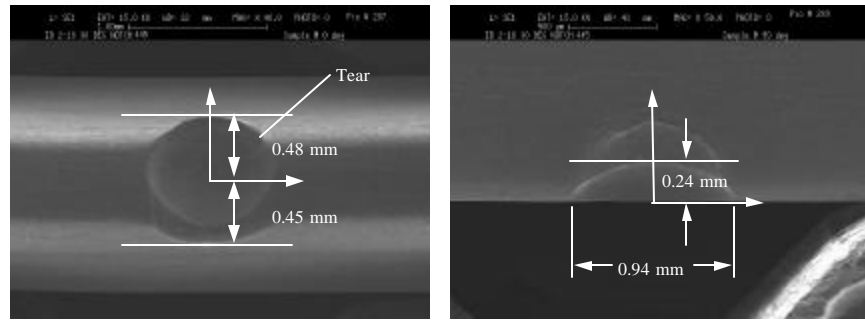
As can be seen from the analytical predictions, the medium mesh predicts the experimental results with the most accuracy. The medium mesh predicts a maximum depth of 0.009 inch (0.22 mm) vs. 0.011 inch (0.27 mm), a maximum width of 0.038 inch (0.96 mm) vs. 0.035 inch (0.88 mm) and a maximum height of 0.016 inch (0.40 mm) vs. 0.015 inch (0.39 mm) for Test Condition 1. Both the coarse and fine mesh underpredict the depth and height for Test Condition 1. It should be noted that the specimen exhibited some tearing which would cause more excessive deformation than the analysis which did not include failure.

Although the failure model is not very sophisticated, it predicts the failure remarkably well. The failure routine is based on a full element failure and partial element failure is not allowed, therefore, the mesh density (element size) will affect the failure predictions. The medium mesh finite element model with failure predicts a notch depth of 0.027 inch (0.69 mm) and a width of 0.062 inch (1.57 mm) which closely agrees with experimental results of 0.027 inch (0.69 mm) and 0.049 inch (1.24 mm). As a result of these correlations, the medium mesh was selected for the parametric studies and all further analytical results will be based on this mesh density.

Figures 5E.10 and 5E.11 show the experimental results for Test Conditions 3 and 4 as compared to the finite element predictions. As can be seen, the finite element analyses predict the deformation shapes well for both test conditions. The experimental and analytical deformation results are tabulated in Table 5E.2. It should be noted that the analysis of Test Condition 1 did not include failure and the tearing that occurred experimentally would cause the analysis to underpredict the deformation. The analytical prediction of the width was the least accurate, but it is also the most sensitive to mesh density.

Parametric Study

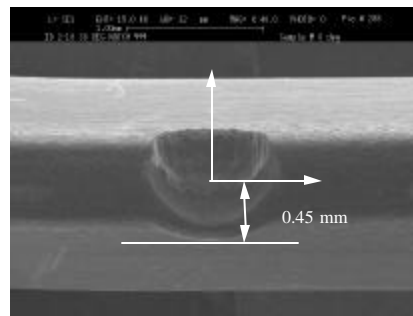
A parametric analysis was conducted to determine the relative effect of different variables on the impact response. The only variable investigated for the specimen, or blade leading edge simulation, was the LER. The two radii selected were 0.005 inch (0.127 mm) to represent a sharp LER and 0.015 inch (0.381 mm) to represent a blunt LER. Specimens with both of these LER were fabricated for impact testing. More variables were studied for the impacting ball. The ball material was kept constant during the studies, but the ball diameter (and correspondingly, mass), impact angle and impact speed were varied. The parametric variables and their analyzed values are shown in Table 5E.3.



In-Plane View

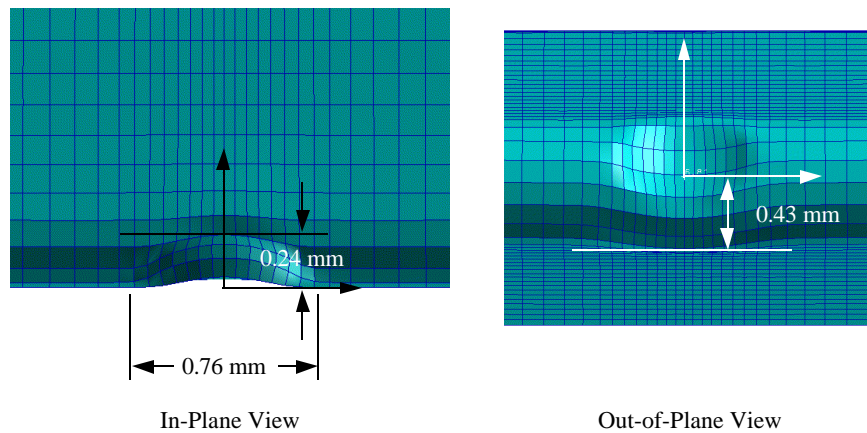
Out-of-Plane View

Impact Test 1 Result



In-Plane View

Impact Test Result



In-Plane View

Out-of-Plane View

Prediction

Figure 5E.10. SEM Photos and Measured Deflections of Test Condition 3 as Compared to Finite Element Prediction. (1 mm = 0.039-inch)

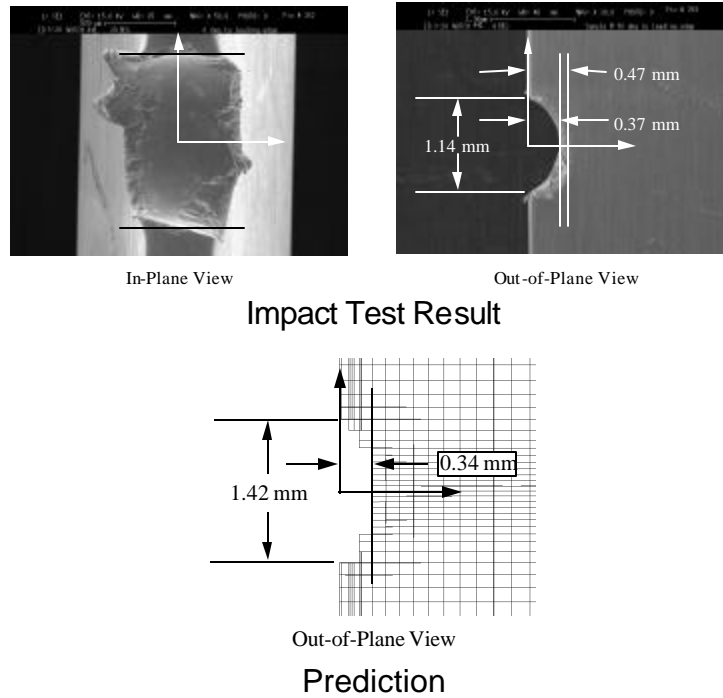


Figure 5E.11. SEM Photos and Measured Deflections of Test Condition 4 as Compared to Finite Element Prediction. (1 mm = 0.039-inch)

Table 5E.2
Experimental and Analytical Deformation Correlation

Test Cond.	Depth (mm)			Height (mm)			Width (mm)		
	Exp.	Analysis	% Diff.	Exp.	Analysis	% Diff.	Exp.	Analysis	% Diff.
1	0.27	0.22	21%	0.39	0.40	2.5%	0.88	0.96	8.7%
2*	0.69	0.69	0%	-	-	-	1.24	1.57	23%
3	0.24	0.24	0%	0.45	0.43	4.5%	0.94	0.76	21%
4*	0.37	0.34	8.5	-	-	-	1.14	1.42	22%

* Analysis with Failure

Table 5E.3
Parametric Variables and Analyzed Values

Specimen LER	Ball Diameter	Impact Angle	Impact Velocity
0.005 inch (0.127 mm)	0.020 inch (0.5 mm)	0°	600 ft/s (182.9 m/s)
0.015 inch (0.381 mm)	0.052 inch (1.33 mm)	15°	800 ft/s (243.8 m/s)
	0.079 inch (2.0 mm)	30°	1000 ft/s (304.8 m/s)
		45°	1200 ft/s (365.8 m/s)

DISCUSSION OF THE ANALYTICAL INVESTIGATION OF IMPACT INDUCED RESIDUAL STRESSES ON TITANIUM AIRFOILS

ABSTRACT

A major source of concern in the high cycle fatigue behavior of gas turbine airfoils is the introduction of damage from foreign object impact events. These events typically introduce damage to the leading edge of airfoils and if the event is severe, the event can lead to failure under subsequent cyclic loading. In service impact damage is typically measured and quantified by dent depth and crack size, while the residual stresses are not easily measured or considered in determining the health of the airfoil. This analytical investigation will attempt to determine the relative importance of the impact induced residual stress field on the behavior of airfoils subjected to continued loading. The commercial explicit finite element package MSC/DYTRAN has been used to model ballistic steel ball impact events of representative titanium airfoil leading edge specimens. The DYTRAN predicted deformation, residual stress field and effective plastic strain are then used to prestress an ABAQUS implicit finite element model of the same airfoil leading edge specimen. This damaged airfoil model is then subsequently loaded in tension and the effect of the impact induced damage is investigated. Strain energies, plastic zones and stress concentration factors will be calculated to aid in subsequent high cycle fatigue life predictions. Modeling methods and the results of analytical predictions are presented.

INTRODUCTION

In order to better understand the effects of residual stresses on factors influencing high cycle fatigue (HCF) crack growth emanating from foreign object damage (FOD) impact sites in gas turbine engine airfoils, an analytical study was conducted. Representative titanium airfoil leading edge geometries were modeled with finite elements and analyzed in a two step process. The commercial explicit finite element code MSC/DYTRAN [5E.1] was used to model the dynamic impact event, while the commercial implicit finite element package ABAQUS [5E.3] was used to model the subsequent loading after impact. The impact analysis was conducted with room temperature (72°F/22°C) material properties. The details of the dynamic analysis and an associated parametric

analysis were discussed previously. This section discusses the investigation of the impact induced residual stresses on airfoil behavior near the impact site.

In the first stage of this analysis, titanium (Ti-6Al-4V) models with representative leading edge radii (0.005 inch (0.127 mm) and 0.015 inch (0.381 mm)) were impacted with steel balls at angles and velocities seen by typical compressor airfoils. The DCT specimen geometry is shown in Figure 5E.1. The parametric analysis shown in Table 5E.3 with impactor size, speed, angle and specimen leading edge radii was conducted with DYTRAN. The angle of impact relative to the specimen cross-section was varied from 0° to 45° as shown in Figure 5E.2, and the impact velocity was varied from 600 ft/s (182.9 m/s) to 1200 ft/s (365.8 m/s).

The second stage of the analysis involved analyzing the damaged DYTRAN models with ABAQUS. The finite element models were identical in the two analyses. The effective plastic strain and full stress tensor for each element along with the nodal deformation were imported from DYTRAN to ABAQUS. The ABAQUS models were then loaded in tension along their length and the behavior near the impact site was investigated. Loading along the length of the specimen simulates the dominant spanwise loading seen by a gas turbine airfoil during engine operation. To better isolate the geometry effects from the residual stress effects, both an impact deformed model with residual stresses and an impact deformed model without residual stresses were analyzed.

FINITE ELEMENT MODELING

Finite element models of the specimens were generated for DYTRAN and the same mesh was used for the ABAQUS analysis. The DYTRAN models contained eight noded reduced integration Lagrangian brick elements. Tetrahedral and Penta elements were avoided in the mesh by utilization of an interface contact surface in the transition region between the gage section and the grip section. This region is well away from the impact site and any errors introduced with this interface will have negligible effect on the predicted stress field near the impact site. The density of the mesh was weighted towards the impact site to better predict the impact deformation and stress field. Figure 5E.12 shows the finite element mesh for a sharp edged specimen used in this analysis.

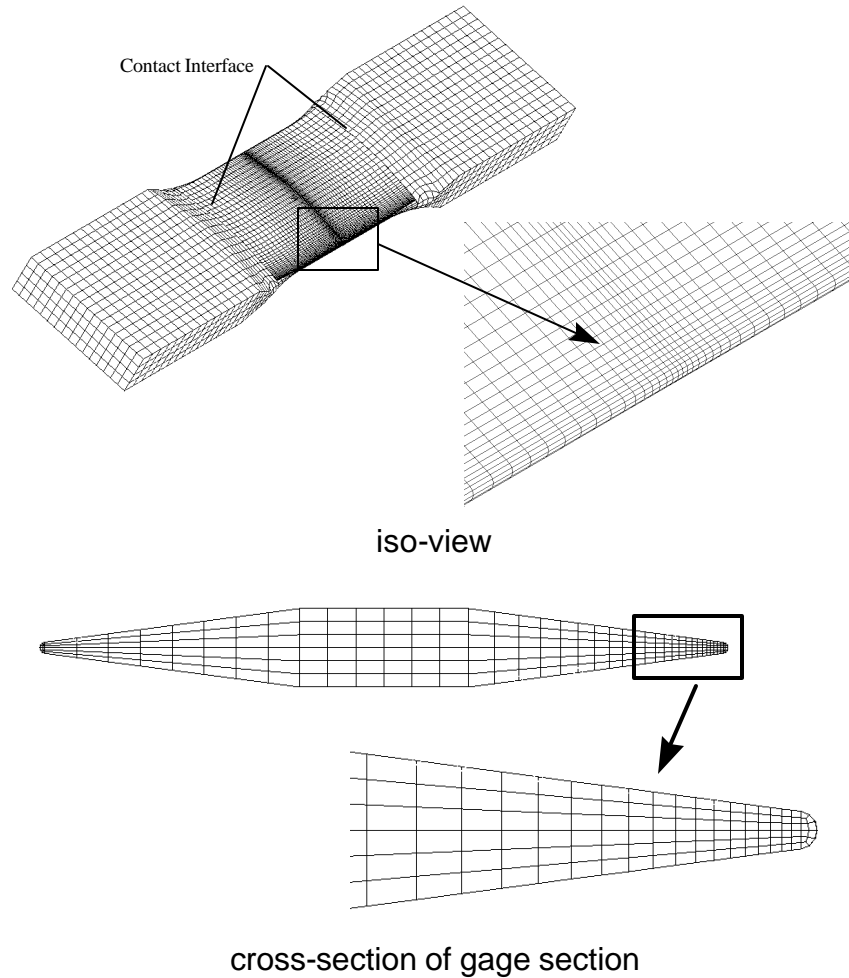


Figure 5E.12. Finite Element Model of Sharp Edge DCT Specimen.

Once the DYTRAN impact analysis was completed, the results were imported to ABAQUS. To properly define the stress state in the implicit code ABAQUS, the nodal deformations, effective plastic strain, and the full stress tensor were exported from the explicit code DYTRAN. The effective plastic strain and stresses were exported from the DYTRAN single integration point in each element to the respective ABAQUS fully integrated element and equally distributed across the eight integration points. However, prior to exporting the data from DYTRAN, one had to confirm that the plastic zone was fully formed and stable, and the stress response was fully elastic. As can be seen in Figure 5E.13, the effective plastic strain field is fully formed and stable at the conclusion of the DYTRAN analysis. The stress response was confirmed to be elastic, however the solution required damping for stabilization. Figures 5E.14 and 5E.15 show results from the same

testing condition for an undamped and damped solution respectively. Damping was introduced at a time point well beyond full formation of the plastic field (1.25×10^{-5} sec) and continued for 0.5×10^{-5} sec. A recommended damping factor based on the natural frequency of the specimen was utilized and this factor effectively stabilized the solution.

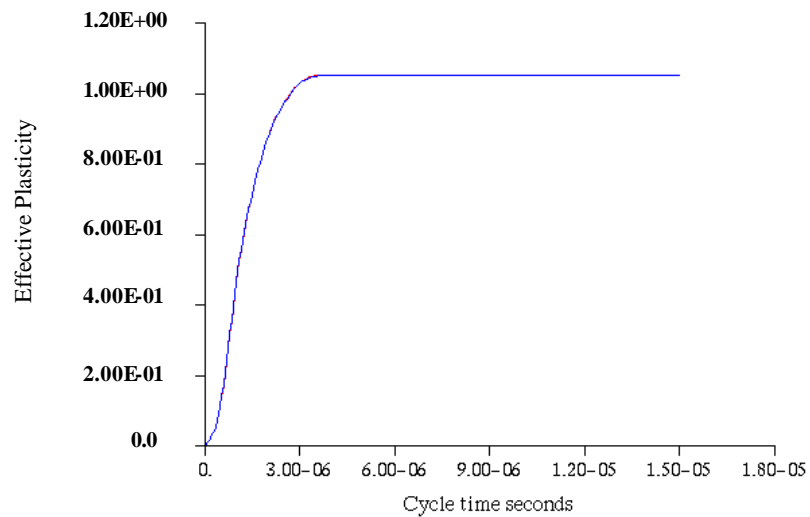


Figure 5E.13. Typical DYTRAN Predicted Effective Plastic Strain History for Element Near Impact Site.

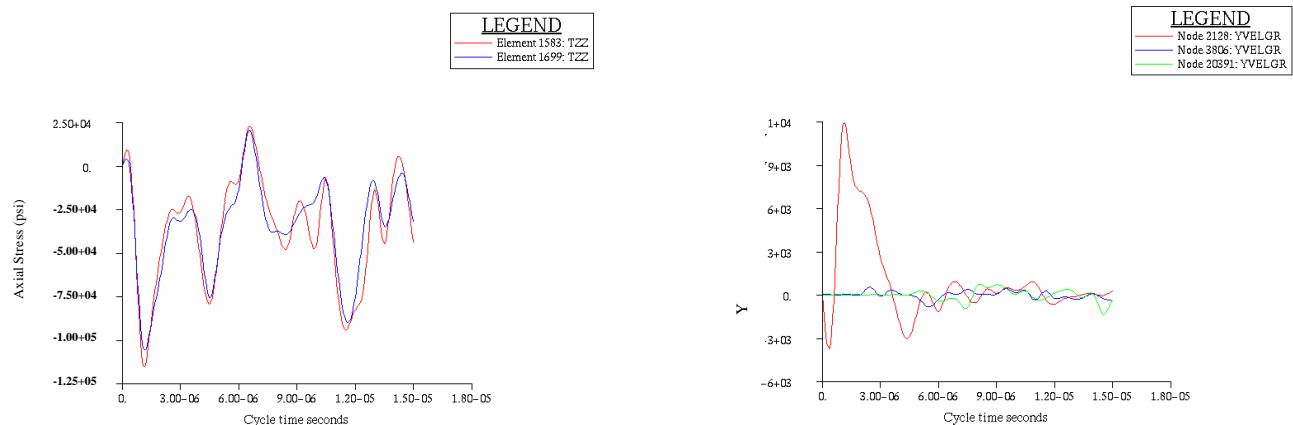


Figure 5E.14. Stress History and Velocity History Near Impact Site for Undamped Solution.

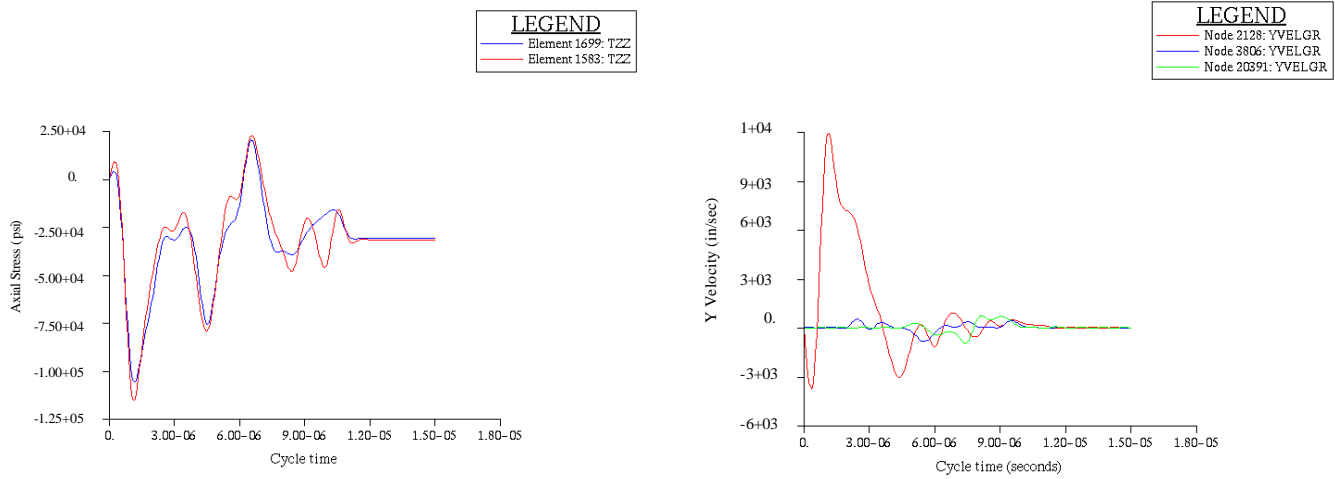


Figure 5E.15. Stress History and Velocity History Near Impact Site for Damped Solution.

ANALYTICAL RESULTS

Although a large parametric impact analysis study was conducted with DYTRAN, only DYTRAN results from selected cases will be presented in detail here. The results of the full post-impact ABAQUS analysis will be presented. The post-impact analysis investigated the effect of impact induced residual stresses by isolating geometric effects from stress field effects. This was accomplished by loading three types of models – virgin undamaged specimen, an impact damaged specimen with deformation, and an impact damaged specimen with deformation and residual stresses.

The primary variable of interest is the behavior of the stress field “normal” to the notch as it is loaded in tension along this normal direction. This loading direction represents the highly dominant spanwise loading direction of a gas turbine rotor airfoil under operation and would also be the stress component which increases or retards crack growth of a damaged airfoil. It is traditionally assumed that the impact induced residual stresses will introduce compressive stresses which would aid in retarding crack growth. Therefore, crack propagation and fatigue life calculations which do not include residual stresses would be conservative. This analysis will determine if this assumption is valid and if it is, will aid in removing some of the conservatism used in airfoil design.

Numerous variables and their effect on impact damage and residual stress field have been investigated and noted. However, of particular note is the effect of impact angle on the formation and shape of the residual stress field as shown in Figure 5E.16. Figure 5E.16 shows the residual stress field chordwise through the specimen (blade) cross-

section with the impact direction illustrated by the arrows. A 0° impact generates a large embedded compressive field directly behind the impact crater followed by an embedded tensile field. A surface crack in the crater would be retarded or stopped from propagation by the residual compressive field. The residual stress field shifts as the impact angle is varied. The high tensile stress field, created on the entrance side of the damage site near the notch surface, is not buffered by a large compressive field. A surface crack could form near the notch surface and propagate along the surface and through the airfoil.

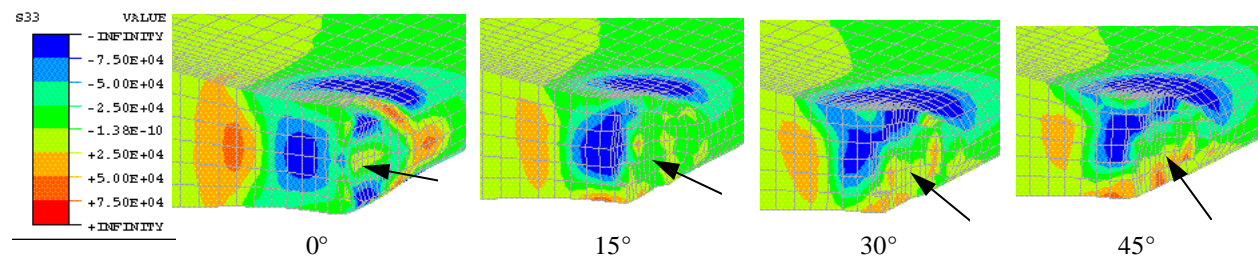


Figure 5E.16. Spanwise Residual Stress Field (ksi) for Blunt Edge DCT Specimen Impacted by 0.052 inch Steel Ball at 1000 ft/sec at Different Angles.

The influence of the residual stress in the post-impact fatigue behavior is complex as it includes the stress itself and an interaction with the impact damage. Figure 5E.17 displays three views of the 0° and 30° impact deformed leading edge of the specimen. The first shows the residual stresses at the impact site while the second view gives the stress in the specimen edge when the fatigue stress is applied and the residual stress is ignored. The third contour combines the applied and residual fields to obtain the true stresses in the impacted DCT specimen as it undergoes fatigue cycling.

During cyclic loading, crack propagation from a FOD induced flaw will be controlled by both the geometry of the impact crater and the residual stress field surrounding the crater. As shown in Figure 5E.17, if the residual field due to impact is ignored, the test specimen is merely a bar with a notch. The stress field is symmetric so a halfpenny crack would be expected to form at the base of the notch and propagate in a chordwise direction normal to the applied stress. However, if the residual field is included for the 30° impact, a crack would be anticipated at the maximum stress location at the intersection of the lower surface and the notch. This corner crack would also propagate in a chordwise direction but along the airfoil surface. A comparison of the normalized stress intensity for these different cracks at different locations is given in Figure 5E.18. This figure shows that ignoring the residual field would lead to nonconservative stress intensity predictions. Another way of viewing this is that the calculated maximum stress at the crack location is higher when the residual stress is included. Hence data generated on this specimen would, in fact, have a higher R-ratio than would be determined on the basis of the nominal stress field. Such a situation should not be used to validate the FOD lifing methodology.

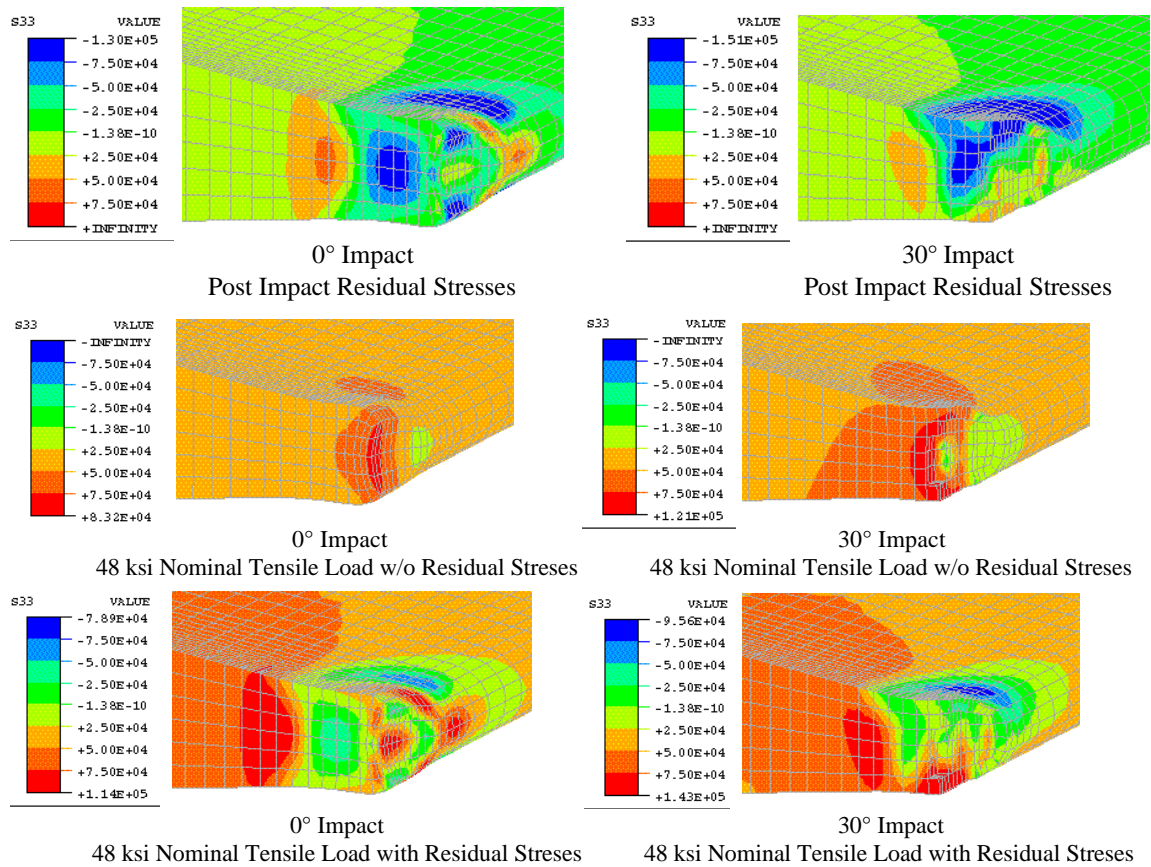


Figure 5E.17. DYTRAN Predictions (ksi) for Blunt (0.015 inch) Edge DCT Specimen Impacted with 0.052 inch Ball at 1000 ft/sec and Loaded in Spanwise Tension.

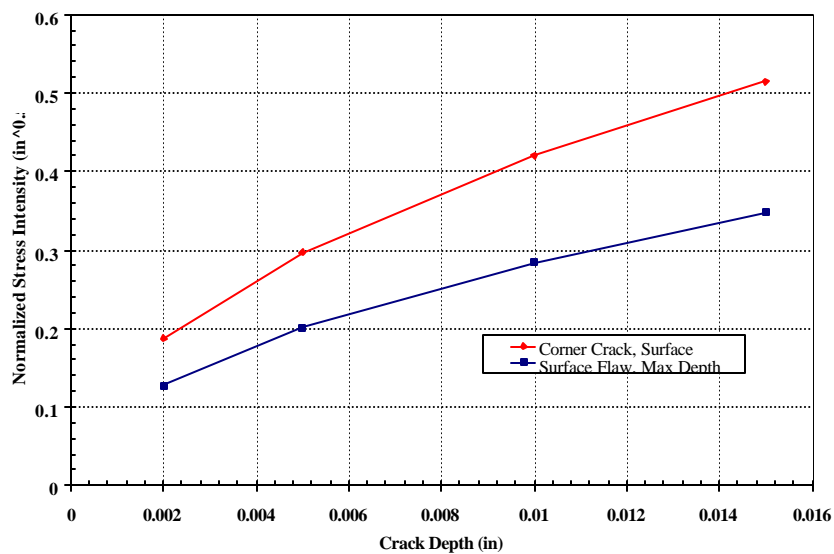


Figure 5E.18. Estimated Stress Intensity Factor for FOD Impact Cracks.

DISCUSSION OF ANALYTICAL MODELING OF GE “PIZZA-HUT” SPECIMENS

INTRODUCTION

The relative slow impact speeds of the chisel, (less than 15 ft/sec) placed the problem simulation into a difficult solution area. The event was too slow to efficiently simulate using an explicit code such as MSC/DYTRAN. Extreme material deformation, and impact conditions made an implicit solution also difficult. Initially, both implicit dynamic and explicit simulations were investigated. It was found that an explicit solution in MSC/DYTRAN would take on the order of one week while an implicit dynamic analysis in ABAQUS took 24 hours. It was decided to solve the problem using ABAQUS as a dynamic implicit solution. There was not enough time to compare a static indentation solution to the dynamic solution. Time limitations also prevented mesh density studies for the two radii specimens. Unfortunately, an implicit analysis is more sensitive to elemental distortion, and produced numeric nonconvergence problems in the 30-degree chisel impact results. These problems aside, it was felt that the overall behavior of the system was correct while the actual stress values and deflections should be looked upon as initial preliminary analysis values.

RESULTS

A similar behavior to the DCT impact specimens was noticed, that is the local tensile stress field on the initial impact side of the chisel. This would produce a local tensile field region along the surface of the blade that would allow a crack to propagate around the normally observed imbedded compressive field. A second interesting finding was the sensitivity to friction. At a low friction value of 0.2 it was noticed that the blade edge slid noticeably more along the chisel's sharp edge. Higher friction values kept the blade edge from sliding as significantly. Future GE blade/chisel impact tests should be done to determine an appropriate friction value. The results summarized assume a 0.4 coefficient of friction value. For better numerical simulation a blunt edge chisel would probably work better because it would produce less very localized elemental distortion.

REFERENCES

- 5E.1 *MSC/DYTRAN Version 4.0 User's Manual*, The MacNeal-Schwendler Corporation, 1997.
- 5E.2 Brar, N. S., Akkala, S., "Strain Rate Sensitivity of Titanium Alloy," *University of Dayton Research Institute UDR-TR-1999-00020*, March 1999.
- 5E.3 *ABAQUS/Standard Version 5.7 User's Manual*, Hibbitt, Karlson & Sorensen, Inc., 1997.

Appendix 5F

PREDICTION METHODOLOGIES FOR FOD TESTS

Tom Dunyak



General Electric Aircraft Engines

**Submitted
31 August 1999**

INTRODUCTION

The purpose of this appendix is to describe the evaluation of the various HCF prediction methods developed in this program as they were applied to the prediction of the foreign object damage (FOD) tests. This included attempts to predict the behavior of the FOD tests using both crack nucleation and propagation methods. The crack initiation methods are described in detail in Appendix 3I and will not be reviewed in significant detail here. The fracture mechanics methods are based on GEAE current state of the art methods that include the use of elastic and plastic non-linear stress gradients. The baseline material properties are taken from material tests for the PRDA material described in Chapter 3.

The focus of the FOD life method evaluations was to identify the key approaches that show promise in predicting observed behavior. The life methods focused on FOD tests that are listed in Table 5F.1. 3D elastic-plastic analysis was performed under GEAE IR&D funding for these cases. The finite element analysis procedure for the machined FOD notch geometries is described in the Appendix 3I. The finite element analyses for the FOD geometries was similarly performed at the average loads determined for the onset of cracking in multiple step tests performed for each FOD case. There was no attempt to empirically account for the FOD-induced residual stresses given these stresses were not measured independently. The figures and distributions shown in this appendix will compare the average prediction for each test condition below.

CRACK NUCLEATION

The crack nucleation method used to evaluate FOD tests was the Weibull modified equivalent stress method (see Appendix 3I). The stress analysis includes the effects of local plasticity at the notch root. The life method includes the equivalent stress model established from smooth specimen data, the modified Manson-McKnight multiaxial parameter, and the stressed area modification to the equivalent stress through the Weibull modification. The results of the FOD predictions are shown in Figure 5F.1 as a function of the maximum FOD notch depth (bottom of the wing).

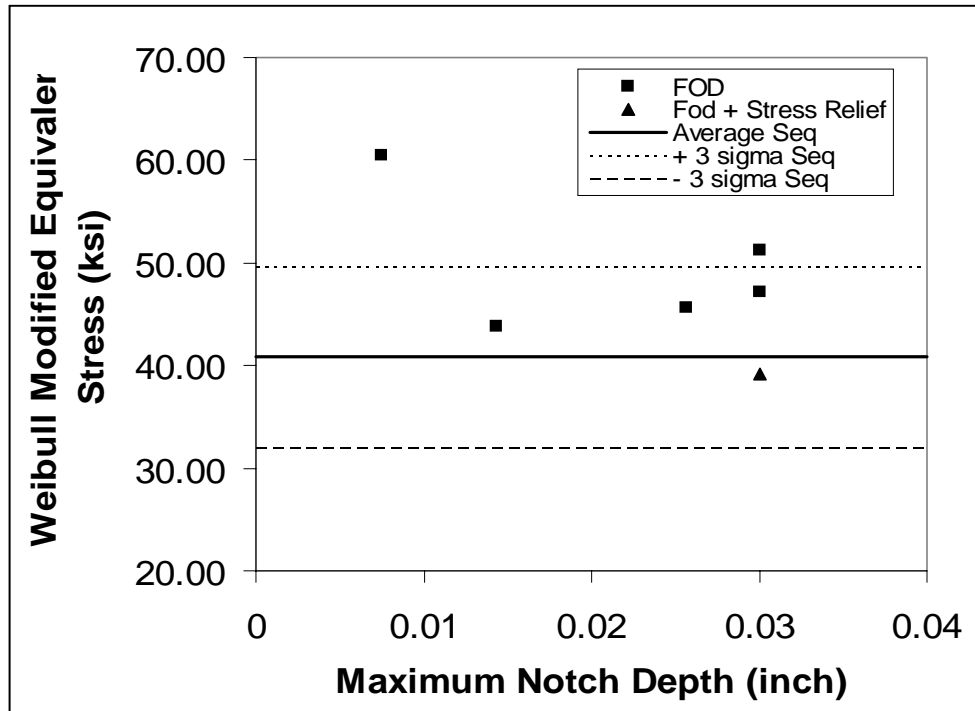


Figure 5F.1. Variation of Weibull Modified Equivalent Stress of FOD tests with maximum notch depth.

The notch depth on the bottom of the specimen was used since this can be measured relatively easily in specimens and on field hardware. Calculated S_{eq} for FOD tests without a stress relief treatment are under-estimated based on the crack nucleation life methodology for specimens with 10^6 fatigue life. Only the specimen with a stress relief to reduce residual stresses fell slightly below the average prediction. This conservative bias is expected given no benefit was taken for the compressive residual stresses induced by the FOD impact.

Probability Plot for Ti-64 HCF and FOD Tests
Weibull Distribution

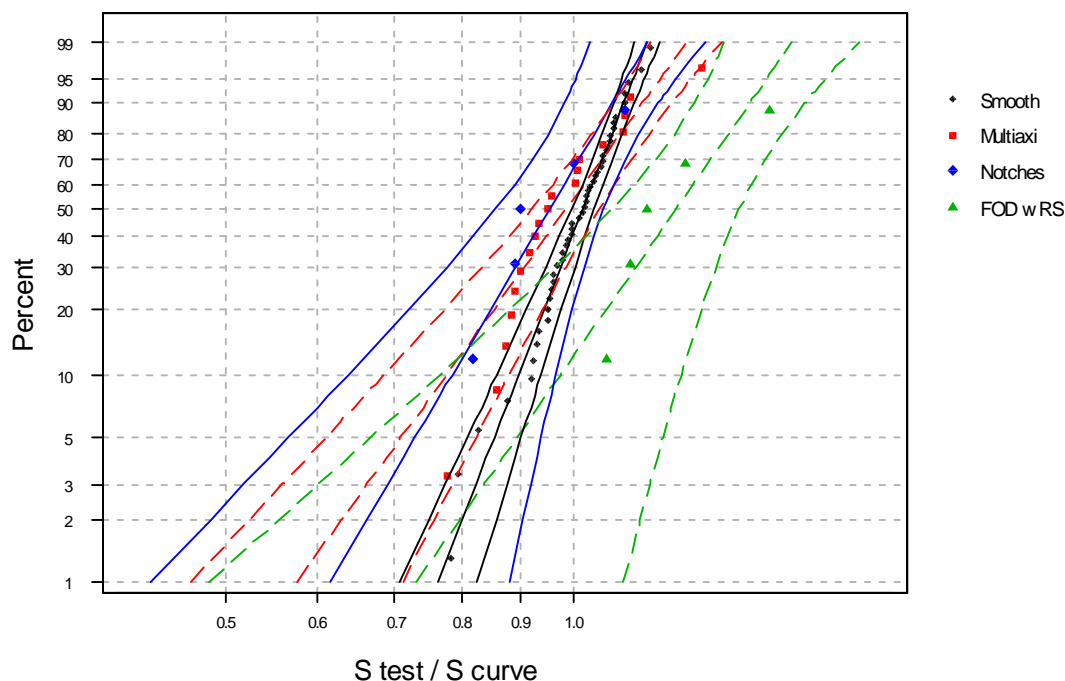


Figure 5F.2. Weibull distributions for smooth, notched, multiaxial, and FOD (with residual stress) tests.

Weibull distributions of the baseline (smooth), multiaxial, notched, and FOD tests with residual stresses are given in Figure 5F.2. The constants of the Weibull distributions are listed in Table 5F.2. The values are within 10% of the program original goals. The multiaxial and notched predictions have lower Weibull moduli than the baseline data but this may be due to the small populations of the notched and multiaxial tests. The prediction of the FOD tests with a scale factor of 1.28 is clearly conservative but the scatter (Weibull modulus) is similar to those observed for the notched and multiaxial tests. The source of the conservatism probably results from not treating the FOD-induced residual stress. This will be discussed further in the discussion section of this appendix.

FRACTURE MECHANICS MODELING

Each of the FOD tests were also analyzed with fracture mechanics (FM) models. As with the nucleation predictions, no effort was made to consider the influence of FOD-induced residual stresses. The influence of plasticity was considered with the elastic and elastic-plastic stress gradient determined from ANSYS analyses. Both the machined

notch with chem milling (minimal residual stresses) and FOD tests (FOD-induced residual stresses) were analyzed. The FM methods will be evaluated by calculating the effective K (K_{eff}) for each FOD geometry at the test loads as compared to the effective threshold stress intensity as determined from surface and compact tension tests from the PRDA and MURI program.

The first analysis performed assumed the FOD notch depth as measured from the bottom of the double wing specimen could be represented as a crack. The values of K_{eff} calculated in this fashion are shown in Figure 5F.3. The stresses used for these calculations were the stresses determined in the specimen without the presence of a notch. The ± 3 sigma range for the K_{eff} threshold stress intensity from the MURI and PRDA tests are also provided with dashed lines. This approach is extremely conservative given the smallest value of K_{eff} is more than two times the mean threshold value. This approach may be a potential way to screen FOD damage, but is too conservative to be used in a design environment.

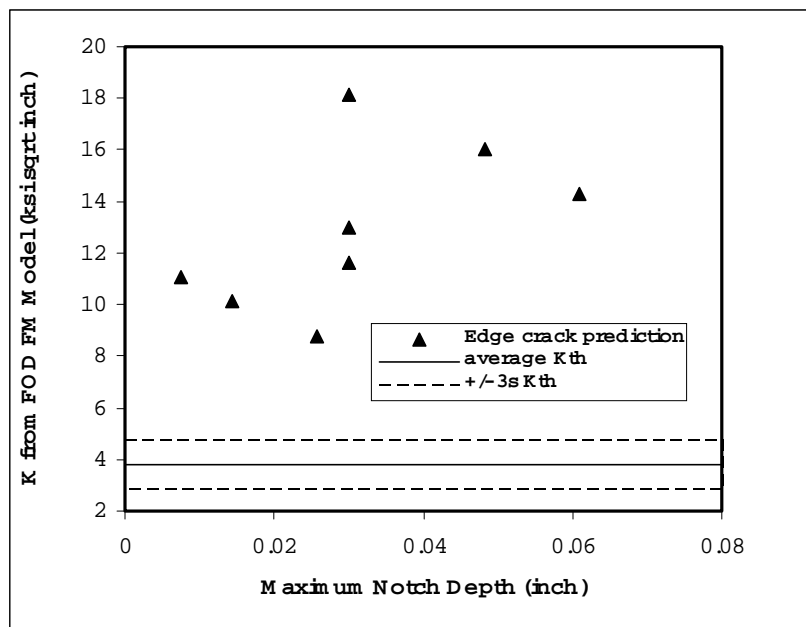


Figure 5F.3. Predicted values of K from FOD tests assuming that the crack depth equals the notch depth.

The next fracture mechanics assumption was to assume that there was an incipient crack in the FOD induced plastic zone at the tip of the FOD notch. One of the challenges here is to select the crack size and geometry to be used for this analysis. Fractographic analysis of the FOD tests showed that in most of the specimens the crack initiated near the center of the FOD notch (midway between the top and bottom surfaces of the wing with the FOD notch). For that reason, this FM evaluation used a semi-circular surface crack centered in the FOD notch. The size of the crack required for K_{eff} to equal the mean value of K_{th} was determined for each testing condition. Figure 5F.4 shows the variation of this crack size with maximum notch depth for the 3 test conditions with little or no residual stress (machined notches or stress relieved FOD notches). Note that the initial crack sizes are very small where the correlation line in Figure 5F.4 corresponds to only 1.9% of the maximum notch depth. This small value seems reasonable given the incipient crack size would be a small fraction of the FOD notch depth.

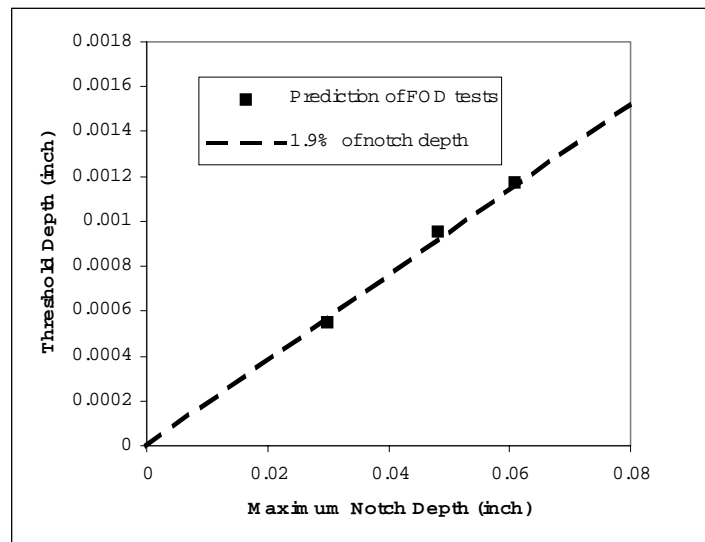


Figure 5F.4. Variation of threshold crack size in notched FOD specimens free of residual stresses with notch depth.

This value was then used to evaluate the value of K_{eff} for all the FOD conditions including those shown in Figure 5F.4 and listed in Table 5F.1. These predictions are shown in Figure 5F.5 along with the variation in baseline K_{th} from PRDA programs. Most of the data fall within the range of data, but two test points fall below the minimum value with another test point very close to the minus three sigma line.

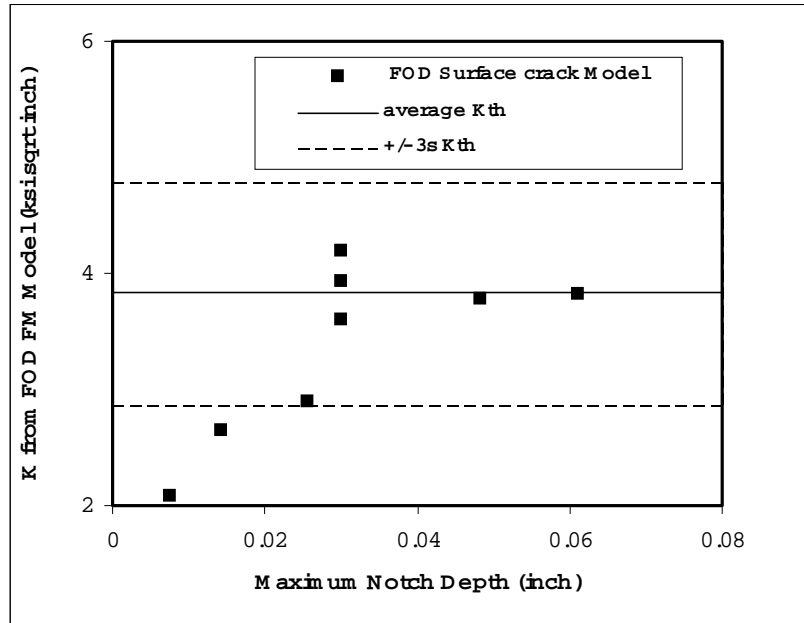


Figure 5F.5. Variation in the predicted value of K_{eff} for the FOD tests assuming an initial crack size of 1.9% of the maximum FOD depth.

This data indicates cracks have grown from FOD with residual stresses even though the incipient crack method predicts these tests to be below K_{th} . If this approach were used to predict the behavior of the tests, it would result in non-conservative allowable stress predictions. This is reinforced with the log normal distribution of K_{eff} relative the mean value of K_{th} shown in Figure 5F.6. Figure 5F.6 also shows the threshold predictions from the baseline data. As in Figure 5F.4, these data show that the values of the FOD threshold are significantly lower (non-conservative) relative to the baseline data. It should be remembered that these values do not consider any contributions of the FOD induced residual stresses.

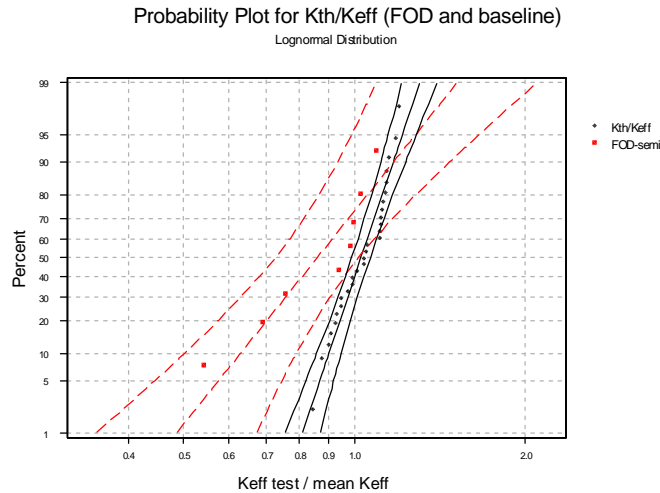


Figure 5F.6. Lognormal distributions of K_{eff}/K_{th} for baseline and FOD tests.

DISCUSSION

The methods evaluated in this appendix did not consider the potential benefits of residual stress. Comparisons of Figures 5F.2 and 5F.6 show that fracture mechanics predictions with an incipient crack tend to be non conservative (Figure 5F.6) while the crack nucleation methods are conservative (Figure 5F.2). As compressive residual stresses are considered, the predicted values of the equivalent stress and K_{eff} would decrease. This would result in the fracture mechanics methods with an incipient crack that is already non-conservative for some of the test point becoming even more non-conservative than the predictions shown in Figure 5F.5. On the basis of this analysis, it seems that a crack nucleation approach would be more appropriate than a fracture mechanics model. But before dismissing fracture mechanics (FM) methods, it is worthwhile to consider alternate ways to approach FM modeling. The results shown in Figure 5F.5 show that the region where the FM methods are the most non-conservative is at small FOD notch depths. The FM method could be forced to match the experimental crack size by increasing the initial crack depths for the shorter FOD notches. The crack size required to perfectly match the FOD results based on a FM method with K from elastic and elastic-plastic stress gradients would require an increase in the small incipient crack size by a factor of 2 to 4 for small FOD depths. The initial crack size criteria could be altered to include these factors to correlate experimentally observed

results, but the initial crack size then becomes significantly more empirical which would be increasingly suspect as applied to new FOD situations. This approach also becomes increasingly suspect given cracks were not observed at the FOD notches prior to loading.

On the other hand, the Weibull modified equivalent stress model uses minimal empiricism where all the material characteristics can be determined from the smooth HCF and LCF data (S-N, Walker exponent, and Weibull modulus). This suggests that this method would have the potential of being more applicable to a wider range of materials and loading conditions. On this basis, it appears that a crack nucleation methodology based on a Weibull modified equivalent stress seems to be a better candidate to predict the onset of HCF damage at FOD notches. However, more work needs to be performed to verify these observations, simplify, and make the equivalent stress methods useable in an engineering environment.

Table 5F.1
FOD Conditions Evaluated(*)

Indenter Geometry	Indentation Angle	Impact Energy	Impactor Tip Radius	HCF R
Sharp	30°	high	0.005 inch	0.5(**)
Sharp	30°	low	0.005 inch	0.5
Blunt	30°	high	0.005 inch	-1
Sharp	30°	high	0.025 inch	0.5
Sharp	0°	low	0.005 inch	0.5
Sharp	30°	high	0.005 inch	0.5

(*) included elastic plastic finite element, modified Weibull equivalent stress nucleation, and fracture mechanics analyses

(**) test in both FOD and FOD+ stress relieved condition

Table 5F.2
Constants of Weibull Distributions

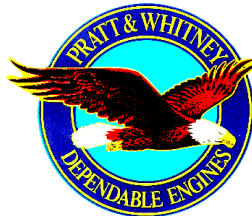
HCF test population	Scale	Shape
Smooth HCF tests	0.04545	14.7338
multiaxial tests	0.01802	7.66653
Notched HCF tests	1.00686	9.78646
FOD tests (with RS*)	1.2837	8.19846

* RS indicates FOD induced residual stress

Appendix 5G

STRESS AND STRESS INTENSITY FACTOR ANALYSIS OF SIMULATED FOD AT AN AIRFOIL LEADING EDGE

Phil Gravett



Pratt & Whitney

**Submitted
1 September 1999**

Stress and Stress Intensity Factor Analysis of Simulated FOD at an Airfoil Leading Edge

EXECUTIVE SUMMARY

This is a report on the analysis of simulated foreign object damage (FOD) at the leading edge of an airfoil. The analysis was performed by Fracture Analysis Consultants, Inc. (FAC) using the ANSYS stress analysis program and the FRANC3D crack propagation software. We would like to extend much appreciation for their dedication to this effort.

In this study, airfoils are modeled with a wedge-like geometry, and FOD is simulated with a notch. The notches are parameterized with four dimensions: notch depth, incidence angle, tip radius, and flank angle. For all analyses reported here, the notch flank angle is fixed at 60 degrees. The wedge is also parameterized with four dimensions: leading edge radius, leading flank angle, width, and half-length.

Nineteen separate geometries were considered. The dimensions defining these geometries were provided by Pratt & Whitney, and were judiciously chosen to give wide coverage of the parameter space. Two load cases were considered for all models, tension and bending.

ANSYS analyses of the nineteen geometries were performed to determine the stress distributions in the near notch-tip region. No cracks were considered in these analyses. The stress results are reported as contour images (Attachment A), Line plots of stress (Attachment B), and stress values in tabular form (delivered to Pratt & Whitney separate from this report).

For all nineteen geometries a series of hypothetical cracks growing from a "corner" of the notch root were analyzed with FRANC3D. In all, 110 crack configurations were considered. Figures showing all crack shapes analyzed are provided (Attachment C). The distribution of mode I stress intensity factors for all crack fronts are reported as graphs (Attachment D) and in tabular form (delivered to Pratt & Whitney separate from this report). Characteristic stress intensity factor values are determined. These allow a scalar value to characterize the stress intensity factor distribution for a whole crack front. These values are given in Attachment E.

Finally, plots were made showing the change in stress intensity factor for fixed crack size for a series of models that differ by one geometry parameter (Attachment F). It was found that the parameter with the greatest influence on stress intensity factor, over the parameter ranges studied, is the notch depth.

INTRODUCTION

This is a report on the analysis of simulated foreign object damage (FOD) at the leading edge of an airfoil. The analysis was performed by Fracture Analysis Consultants, Inc. (FAC) using the ANSYS stress analysis program and the FRANC3D crack propagation software.

ANSYS is a well-known commercial, general purpose, finite element package. FRANC3D is a boundary element based crack propagation simulator that incorporates solid modeling features and automatic remeshing to allow arbitrarily shaped cracks to grow in three dimensional bodies of arbitrary geometry [Gray 1990, Lutz 1990 & 1991, Martha 1993, Wawrzynek 1988, 1989, & 1991].

In this study, airfoils are modeled with a wedge-like geometry, and FOD is simulated with a notch. A typical model is shown in Figure 5G.1. The notches are parameterized with four dimensions: notch depth, incidence angle, tip radius, and flank angle. For all analyses reported here, the notch flank angle is fixed at 60 degrees. The wedge is also parameterized with four dimensions: leading edge radius, leading flank angle, width, and half-length. All parameters are illustrated in Figures 5G.2 and 5G.3. For the ANSYS stress analysis models, only one half of the wedge was modeled, with symmetry boundary conditions used on the "cut" surface in the x-y plane.

Nineteen separate geometries were considered, and were denoted w_0 to w_18. The dimensions defining these geometries were provided by Pratt & Whitney, and were judiciously chosen to give wide coverage of the parameter space. The values for the notch region parameters for all geometries are given in Table 5G.1.

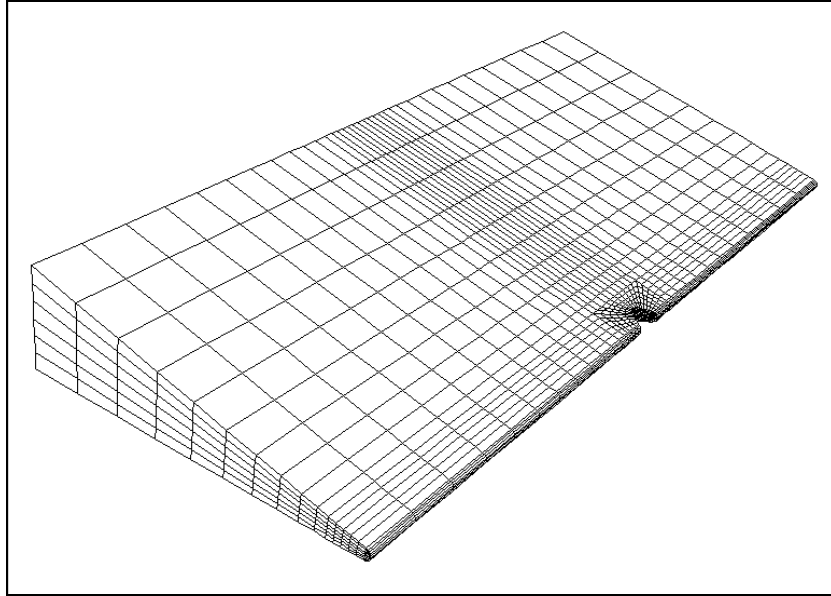


Figure 5G.1. A typical model used for the simulated FOD analyses.

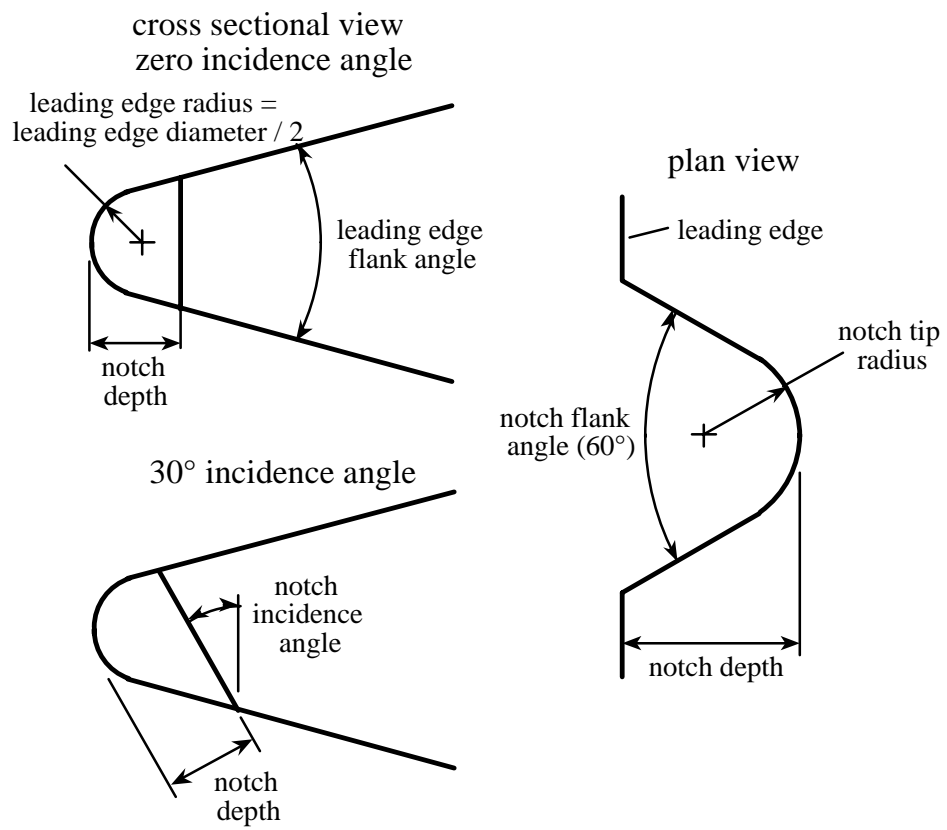


Figure 5G.2. Definition of notch and wedge parameters.

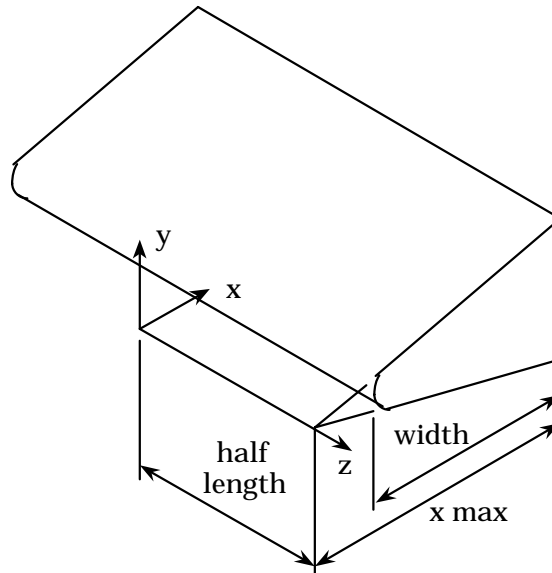


Figure 5G.3. Definition of some of the wedge parameters.

Table 5G.1
Notch Region Parameters for all geometries

	leading edge diameter (in)			leading edge flank angle (deg)			notch tip radius (in)		Damage level (in)			Impact Angle (deg)	
	0.03	0.01	0.04	3.5	7.5	15	0.005	0.025	0.005	0.02	0.05	0	30
w_0	x					x		X			x	x	
w_1	x					x		X			x		x
w_2		x				x	x		x			x	
w_3		x				x	x		x				x
w_4		x			x		x		x				x
w_5		x			x		x			x			x
w_6		x			x			x	x				x
w_7		x			x			x		x			x
w_8		x			x		x		x			x	
w_9		x			x		x			x		x	
w_10	x				x		x			x		x	
w_11	x				x		x				x	x	
w_12			x		x		x			x		x	
w_13	x				x		x		x			x	
w_14			x		x		x		x			x	
w_15			x		x		x				x	x	
w_16	x			x			x			x		x	
w_17	x			x			x			x			x
w_18	x					x	x			x		x	

The wedge width and half-length dimensions were chosen as functions of the notch depth based on 2-D studies described below. The half-length for all models was 20 times the notch depth. The width dimension was chosen to be about 18 times the notch depth, but was rounded to make the "x max" dimension a round number. The widths and half-length dimensions for the 19 geometries are given in Table 5G.2.

Table 5G.2
Wedge Parameters for all Geometries

Model	notch depth	half length	max x	width
w_0	0.05	1	1	0.900
w_1	0.05	1	1	0.900
w_2	0.005	0.1	0.125	0.092
w_3	0.005	0.1	0.125	0.092
w_4	0.005	0.1	0.15	0.079
w_5	0.02	0.4	0.4	0.329
w_6	0.005	0.1	0.15	0.079
w_7	0.02	0.4	0.4	0.329
w_8	0.005	0.1	0.15	0.079
w_9	0.02	0.4	0.4	0.329
w_10	0.02	0.4	0.6	0.386
w_11	0.05	1	1	0.786
w_12	0.02	0.4	0.6	0.314
w_13	0.005	0.1	0.3	0.086
w_14	0.005	0.1	0.4	0.114
w_15	0.05	1	1	0.714
w_16	0.02	0.4	0.8	0.324
w_17	0.02	0.4	0.8	0.324
w_18	0.02	0.4	0.6	0.500

Two load cases were considered for all models, tension and bending. For the tension case, a uniform unit traction value was applied to the ends of the wedge in the +/- z direction (Figure 5G.3). For the bending case, a linearly varying traction was applied to these faces. The traction was such that the magnitude of the traction was equal to the y coordinate. This is illustrated in Figure 5G.4. For the crack analyses, the bending load was always applied in a sense that would tend to make the crack open.

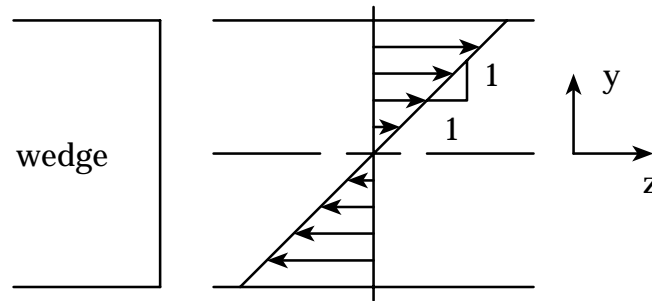


Figure 5G.4. Illustration of the tractions applied for the bending load case.

The kinematic boundary conditions used for the crack analyses (where the full wedge was modeled) are shown in Figure 5G.5. X constraints are applied over the entire "back" (maximum x) surface. Z constraints are applied to a line of nodes on the back surface with a zero z coordinate. The one node on the back surface with its y and z coordinate equal to zero is restrained in x, y, and z. There is further discussion of appropriate boundary conditions in the 2-D studies section below.

For the case of the stress analyses, symmetry is employed and only one half of the wedge is modeled. For this, z constraints are imposed on the nodes that lie on the "cut" surface, which are those with a z coordinate of zero.

A series of hypothetical cracks growing from a "corner" of the notch root were analyzed with FRANC3D. A typical crack is shown in Figure 5G.6. For all geometries, a progression of circular cracks were considered starting with an initial crack radius of 0.001 inches and ending with a crack radius that was approximately 80% of the notch tip length. For geometries where the notch incidence angle was not zero, cracks at both the top and bottom corner were analyzed. A through crack case was also considered for all models. Here the crack length was chosen to be approximately 120% of the notch tip length.

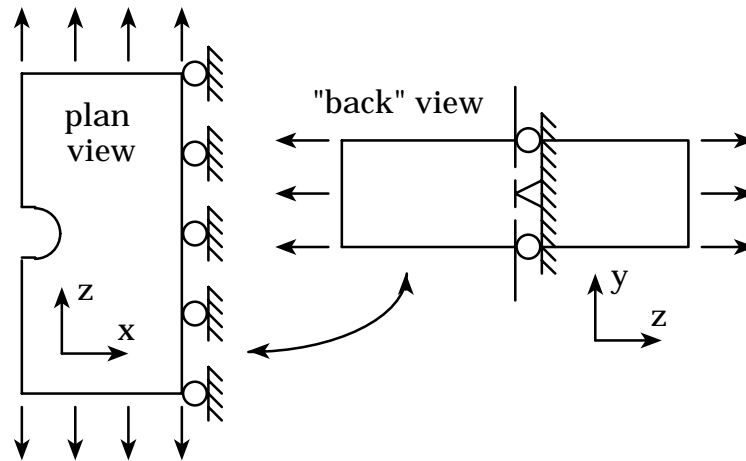


Figure 5G.5. A schematic of the kinematic boundary conditions used for the crack analyses.

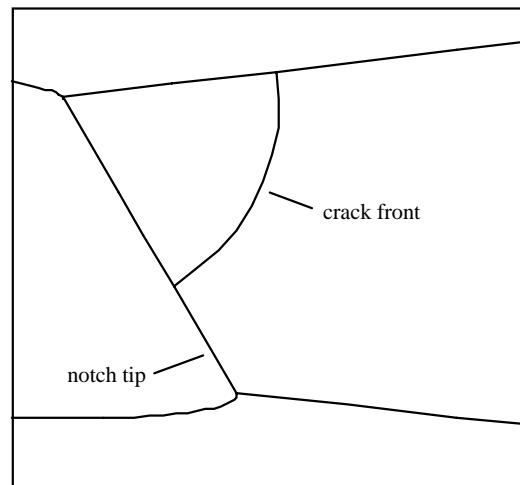


Figure 5G.6. A typical crack geometry.

Details of the analyses and results are presented in the remainder of this report. It is organized into the following sections:

- a series of 2-D studies that were performed to help determine appropriate boundary conditions and model dimensions, and to help assess the sensitivity of the stress intensity factors to the notch depth.
- the ANSYS analyses performed to determine the near notch stress distributions.
- the FRANC3D analyses performed to determine stress intensity factors.

- trends in the stress intensity factors as a function of the model parameter.
- a summary of the previous sections.

Much of the data generated is reported in the appendices. Attachment A contains contours of the stresses in the notch region. Attachment B contains similar information in x-y plot format. Attachment C contains diagrams showing the geometry of all cracks analyzed. Attachment D contains x-y plots showing the stress intensity factor distributions for all crack fronts. Attachment E contains tables summarizing the stress intensity factors for all crack fronts. Attachment F contains plots of trends in stress intensity factors as functions of model parameters.

In addition to the material in this report, the following information has been transferred to Pratt & Whitney in electronic form:

- Tables of computed stresses (all six components) in the notch front region for all models.
- Tables of the stress intensity factor distributions for all crack fronts (the data used to generate the plots in Attachment E).
- ANSYS input and results files for all uncracked models.
- FRANC3D input and results files for all cracked models.

2-D STUDIES

Before the 3-D analyses commenced, the FRANC2D program was used to perform a series of 2-D plane stress studies to help determine appropriate boundary conditions and model dimensions, and to help assess the sensitivity of the stress intensity factors (K) to the notch depth. The initial mesh used for these studies is shown in Figure 5G.7.

The model has a notch depth of 0.05 inch; the notch tip radius is 0.025 inch. The total model is 2 inch high, and about 0.9 inch wide. In these plane stress analyses only tension loading can be considered.

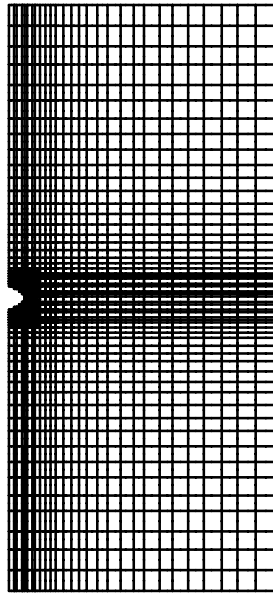


Figure 5G.7. 2D Plane stress mesh.

Remote Boundary Conditions

Two analyses were performed to assess the effect of boundary conditions used on the surface remote from the notch. The constraints used for these analyses are illustrated in Figure 5G.8.

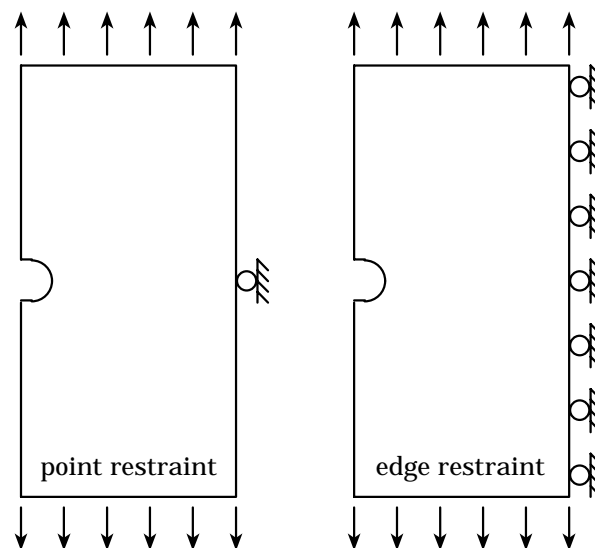


Figure 5G.8. Two types of remote boundary conditions considered.

The vertical stresses plotted along a horizontal line at the mid-point of the plates are shown in Figure 5G.9.

At the scale of Figure 5G.9 the entire width the correlation looks good. However, a careful examination of the numbers shows that in the case of the point restraint, a slight bending about the restraint is induced. This tends to increase the stresses at the notch, and reduce the stresses at the right edge. This is seen more clearly in Figure 5G.10, where this data is replotted as the percent difference between the stress values as a function of horizontal position.

To assess how such a difference in the near notch stresses would affect the stress intensity factors for cracks growing from these notches, two crack growth analyses were performed. The percent difference in the computed K is shown in Figure 5G.11 (the crack lengths are normalized with respect to the notch depth). As expected, the difference in the K for the initial crack is about the same as the difference in the stresses at the notch root. Also as expected, as the crack grows, more bending is induced, and the corresponding K are higher than those for similar length cracks where bending is restrained.

Based on these analyses, and the consideration that these simulations are to approximate the behavior of "deep chord" blades, where there will be little induced bending, the edge restraint (corresponding to surface constraints in 3-D) is used in all subsequent analyses.

Remote Model Dimensions

The width and half-length of the model shown in Figure 5G.7 was selected arbitrarily based on the experience of the analyst. The half-length is 20 times the notch depth, and the width is approximately 18 times the notch depth. The computed stress distribution for the plane stress model is examined in detail to determine if this model size is large enough such that the stress concentration effects of the notch are insignificant at the remote boundaries.

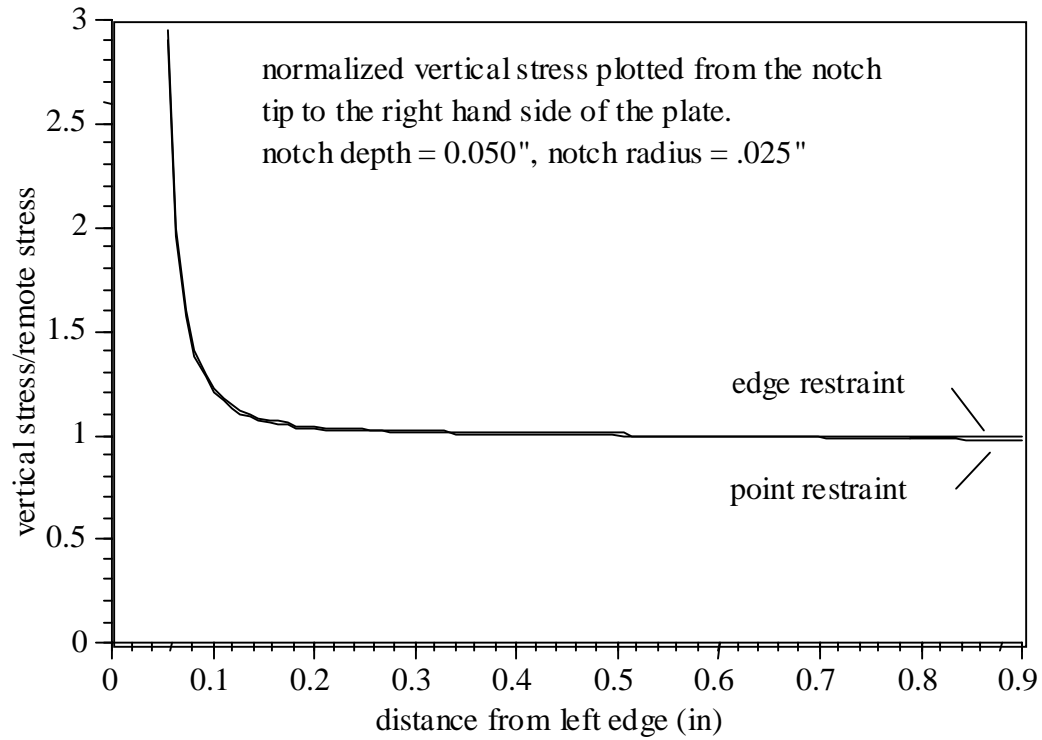


Figure 5G.9. Comparison of vertical stresses for different boundary conditions.

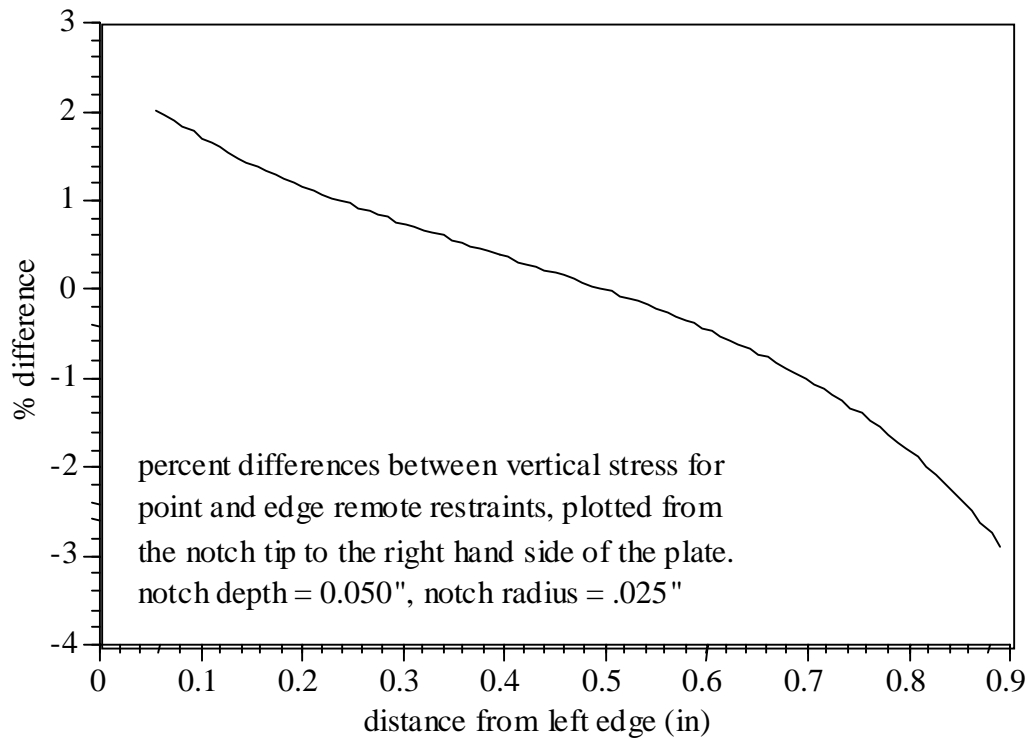


Figure 5G.10. Percent difference in vertical stresses for two sets of boundary conditions.

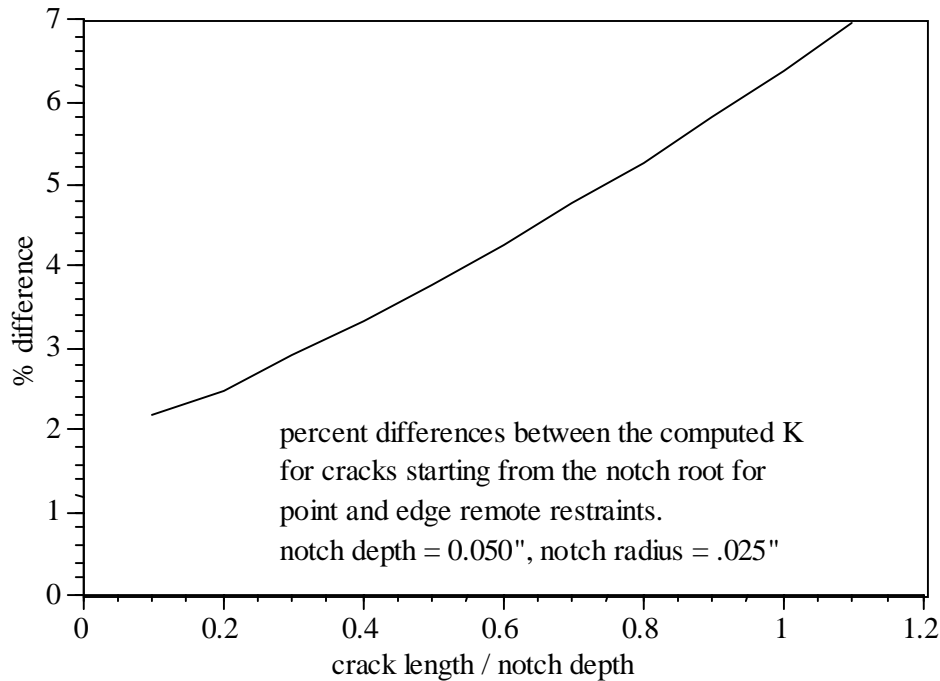


Figure 5G.11. Percent difference in computed K for two sets of boundary conditions.

Figure 5G.12 shows the vertical stresses plotted along horizontal lines for a number of different vertical locations (note that these plots show only the stresses for the left-most 40% of the model). From the figure, one can clearly see that all stress gradients have died out by the time one moves 0.9 inch in the y direction away from the notch. Therefore, it is determined that this model size is sufficient for subsequent analyses.

Notch Influence on Stress Intensity Factors

A study was performed to determine the local effect of the notch on the computed stress intensity factors. One expects that as the crack size becomes significant relative to the size of the notch, the computed stress intensity factors would approach those for a similar length crack in a model without a notch.

2-D crack growth simulations were performed for plane stress models with and without notches. The resulting computed K are as shown in Figure 5G.13.

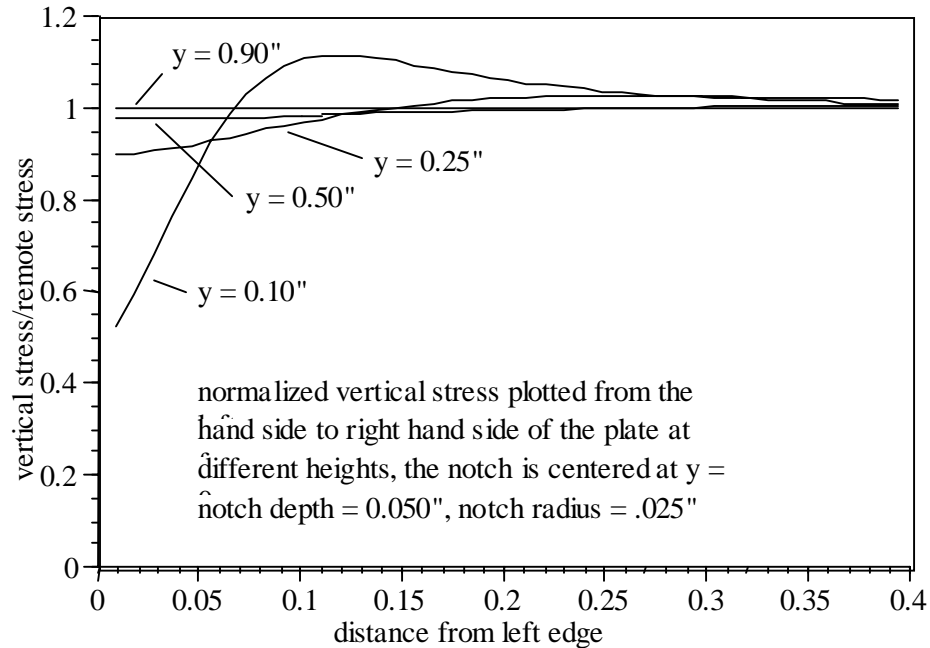


Figure 5G.12. Vertical stresses plotted from the left-hand side of the model for a number of different vertical locations.

From Figure 5G.13 one can see that the notch-solution quickly approaches the solution for no notch. To illustrate this more quantitatively, a portion of this data is replotted in Figure 5G.14. This figure shows the percent difference between the two curves (notice there is a different x-axis, the crack length has been normalized, and we consider only the portion of the no-notch solution where the crack is longer than the notch depth).

From Figure 5G.14, one can see clearly that by the time the crack length is about 1/2 the notch depth the notched and unnotched solutions have converged.

3-D STRESS STUDIES

ANSYS was used to perform stress analyses of all 19 geometries. Both tension and bending loads were considered. Images of contours showing the near notch z stress distribution were generated for all models. Typical examples of these images are shown in Figures 5G.15 and 5G.16. The images for all models are shown in Attachment A.

Note that the loads applied in the bending analyses are 100 times greater than the "unit" bending loads described in Section 1. The stresses due to these higher loads

are displayed in all the bending contour figures. However, in all other cases where stresses or stress intensity factors are reported the values already have been divided by the factor of 100.

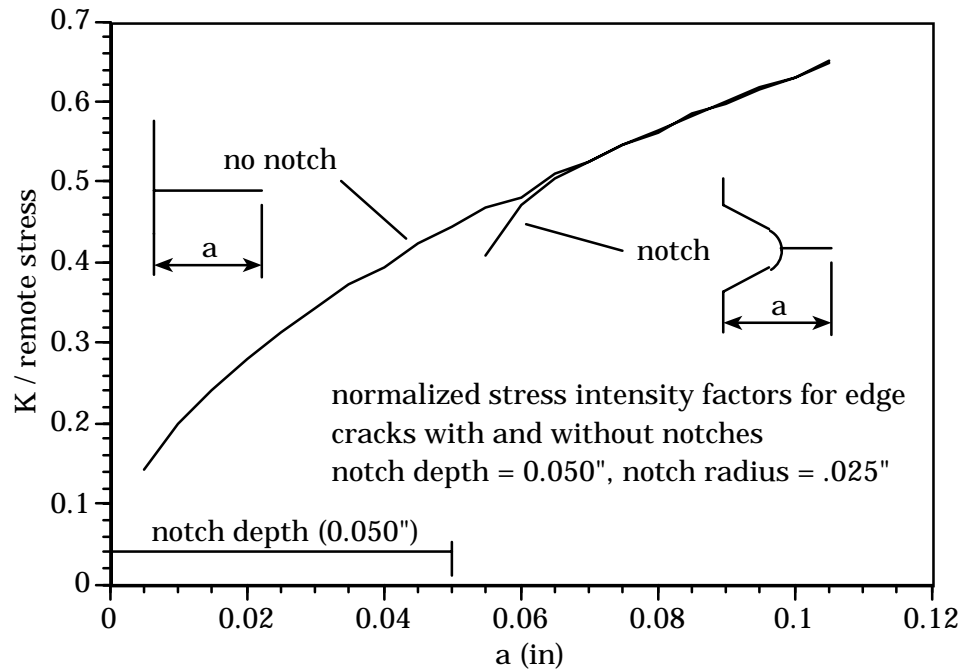


Figure 5G.13. Computed K histories for models with and without notches.

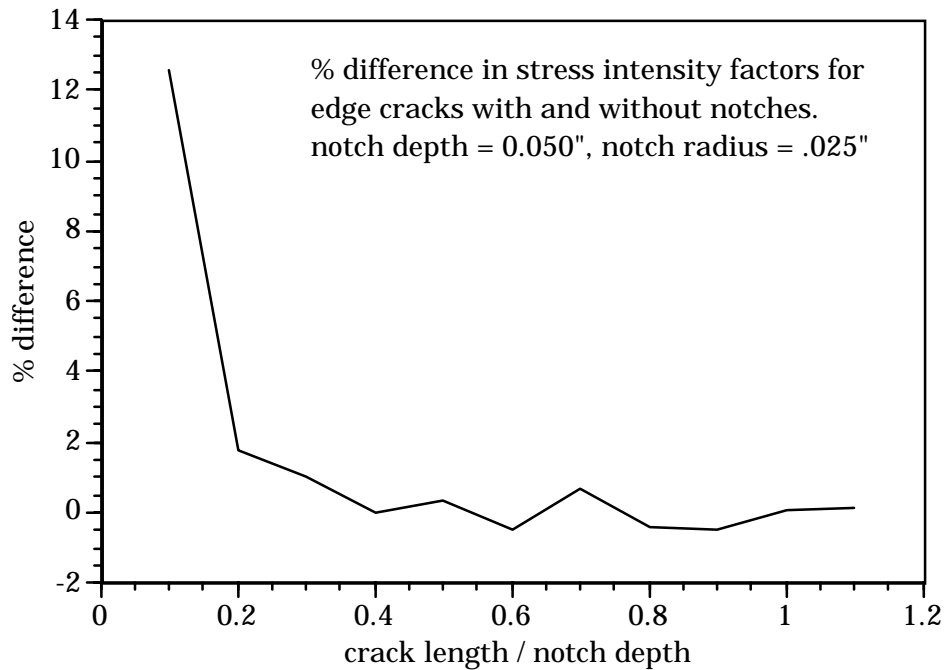


Figure 5G.14. Percent difference in K for cracks with and without notches.

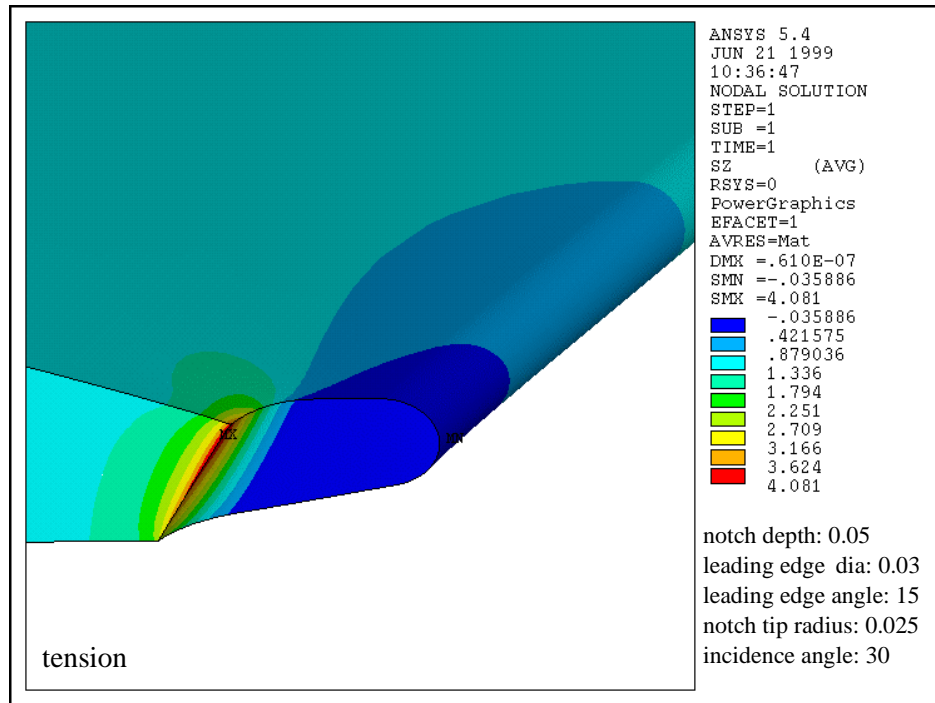


Figure 5G.15. Typical stress contour plot of z stresses for tension loading.

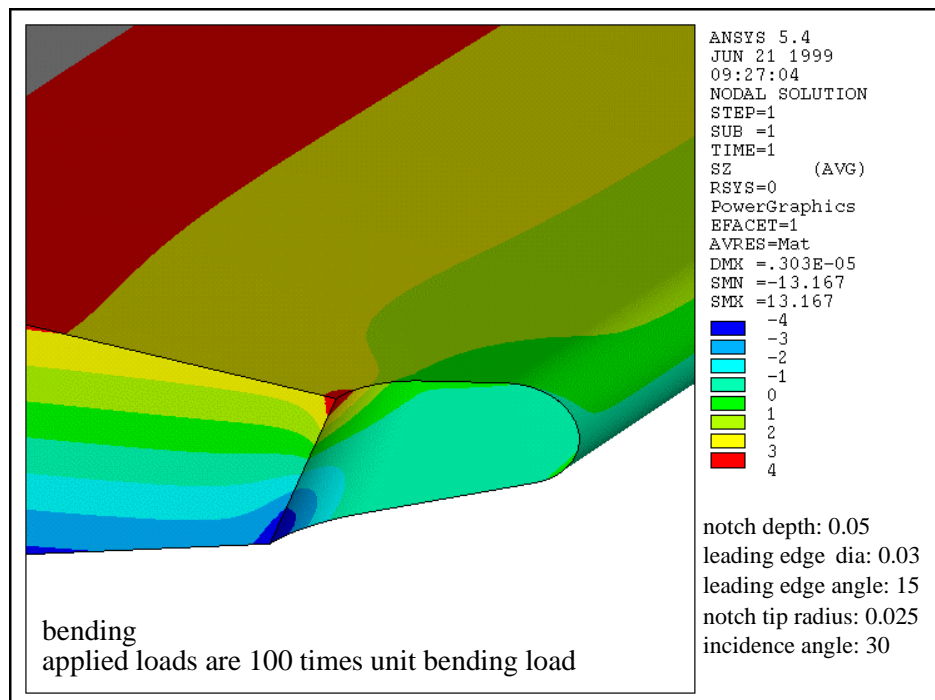


Figure 5G.16. Typical stress contour plot of z stresses for bending loading.

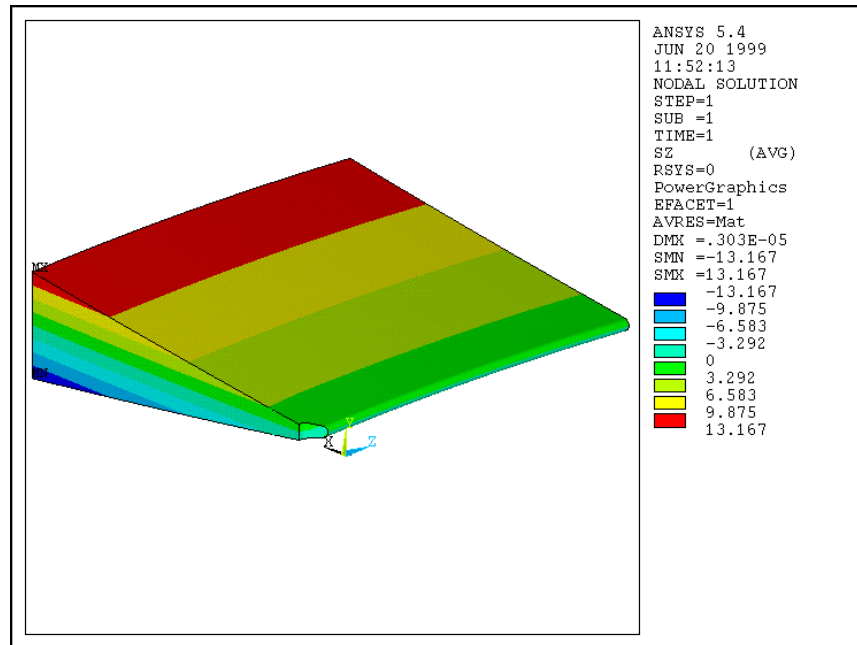


Figure 5G.17. Typical stress contour plot of z stresses on the full model for bending loading.

The contour scales in the bending images have been scaled to highlight the stress variations in the notch region. Otherwise, the relatively large remote bending stresses would "wash-out" any interesting features in the near-notch region. A typical image of the bending stress for a full model is shown in Figure 5G.17.

The near notch tip stresses are also reported as x-y plots of the z stress along various lines in the symmetry plane. Figures 5G.18 and 5G.19 show typical plots for models with a zero notch incidence angle. In this case, due to symmetry, only the 0, 25, and 50% lines are reported. For the tension case, the 75 and 100% lines will be the same as the 25 and 0% lines, respectively. For the bending case, the 75 and 100% lines will be equal in magnitude but opposite in sign (negative) of the 25 and 0% lines. Figures 5G.20 and 5G.21 show typical plots for models with a 30-degree notch incidence angle. In these cases stresses are given along five different lines. Near notch tip stress plots for all models are included in Attachment B.

For a number of models, the intersection of the notch root with the wedge surface falls on the round that makes up the leading edge of the wedge, rather than on the flats that make up the flank surfaces of the wedge. This is illustrated in Figure 5G.22.

This is true for models w_3, w_4, w_6, w_13, w_14, and w_17. In these cases, the 0% stress curve is no longer a straight line, but follows the outer surface of the wedge.

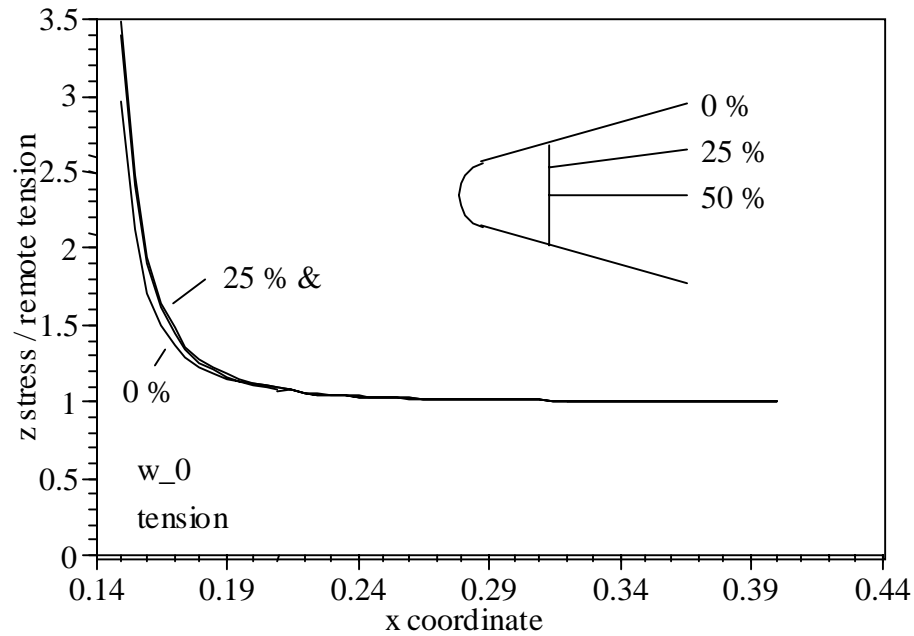


Figure 5G.18. Typical stress results for tension loading and a zero notch incidence angle.

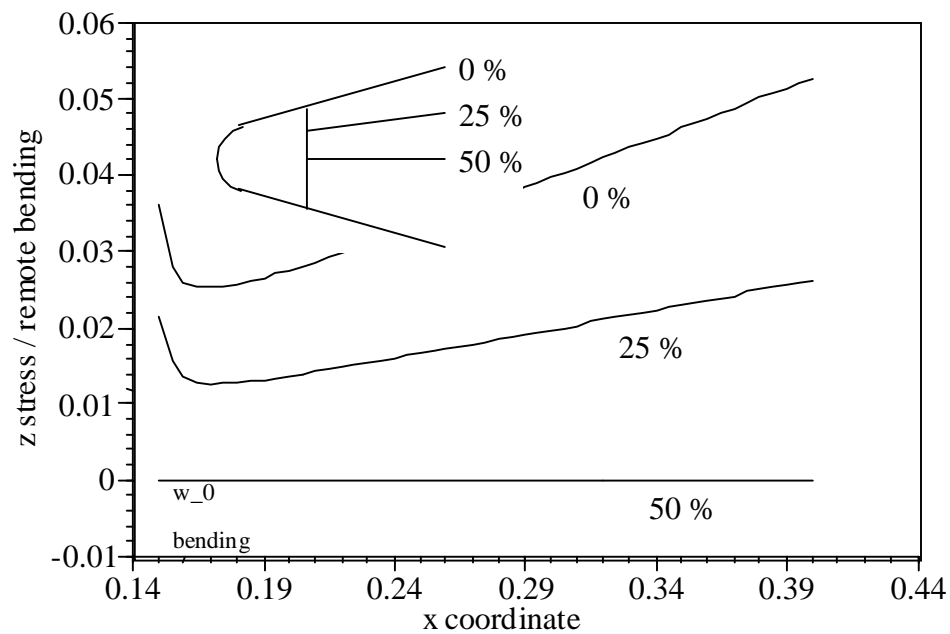


Figure 5G.19. Typical stress results for bending loading and a zero notch incidence angle.

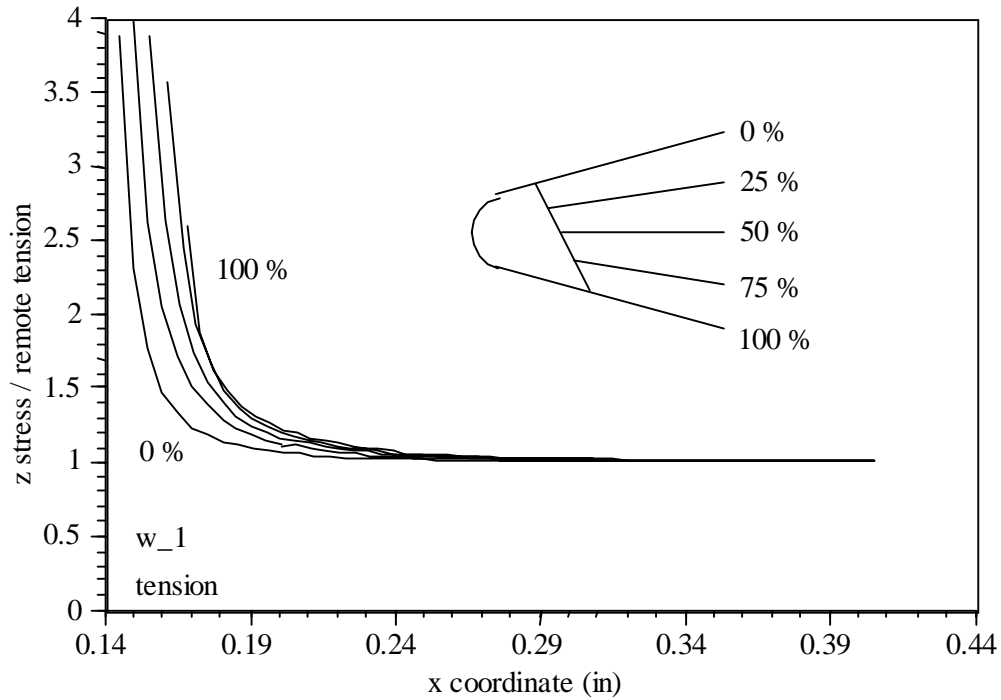


Figure 5G.20 Typical stress results for tension loading and a 30-degree notch incidence angle.

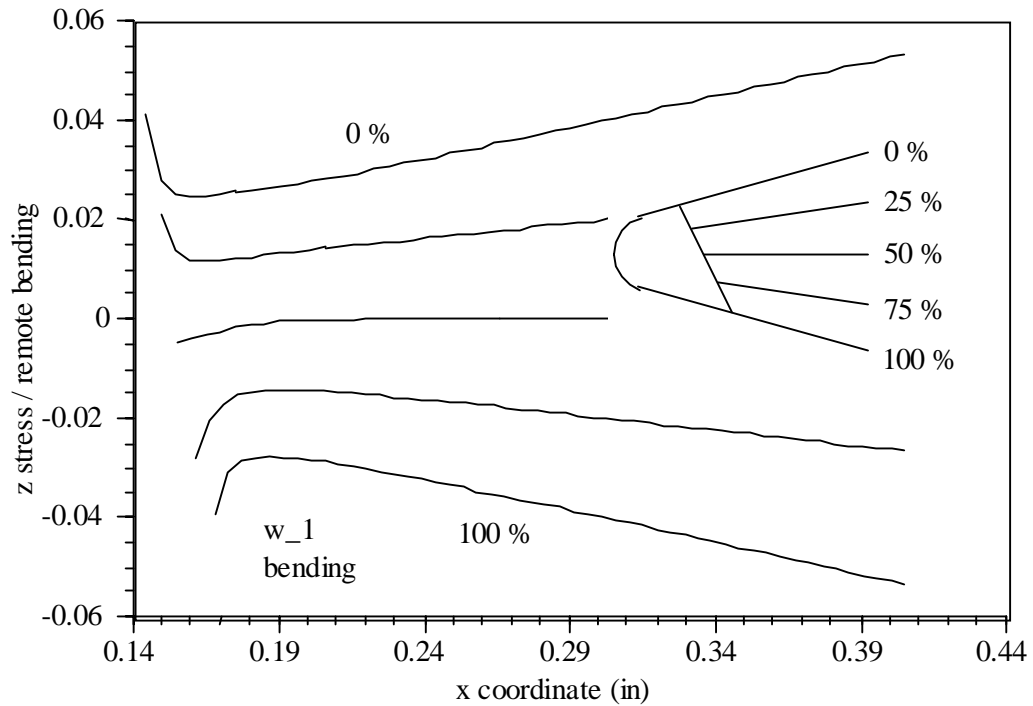


Figure 5G.21. Typical stress results for bending loading and a 30-degree notch incidence angle.

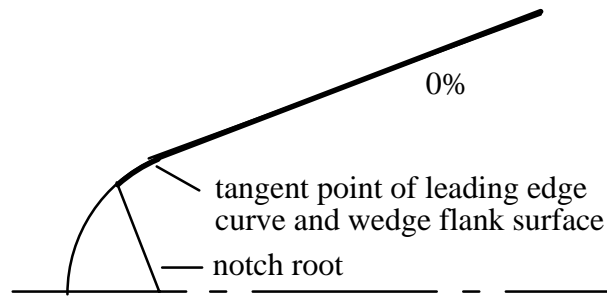


Figure 5G.22. Illustration of cases where the 0% stress line follows the surface of the model and is not a straight line.

One interesting way to view a composite of all the stress results is shown in Figures 5G.23 and 5G.24. Here the stress distributions for all 0% "lines" are plotted on one graph. The x-axis is the distance from the notch tip normalized by the notch depth. The y-axis is the local stress normalized by the remote applied stress (unity for the tension models, and the y coordinate of the line on the wedge surface for the bending case). The figures show that the effect of the notch on the stresses is very localized. All meaningful effects have died out by two notch-depths from the notch front.

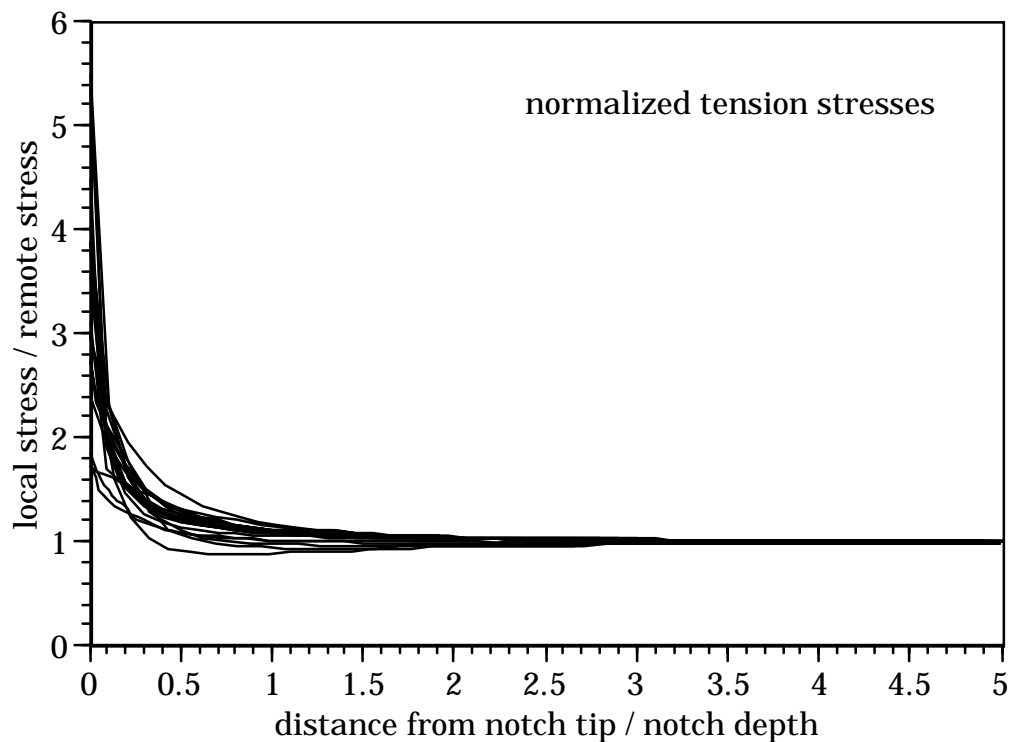


Figure 5G.23. A composite of all 0% stress lines for tension loading.

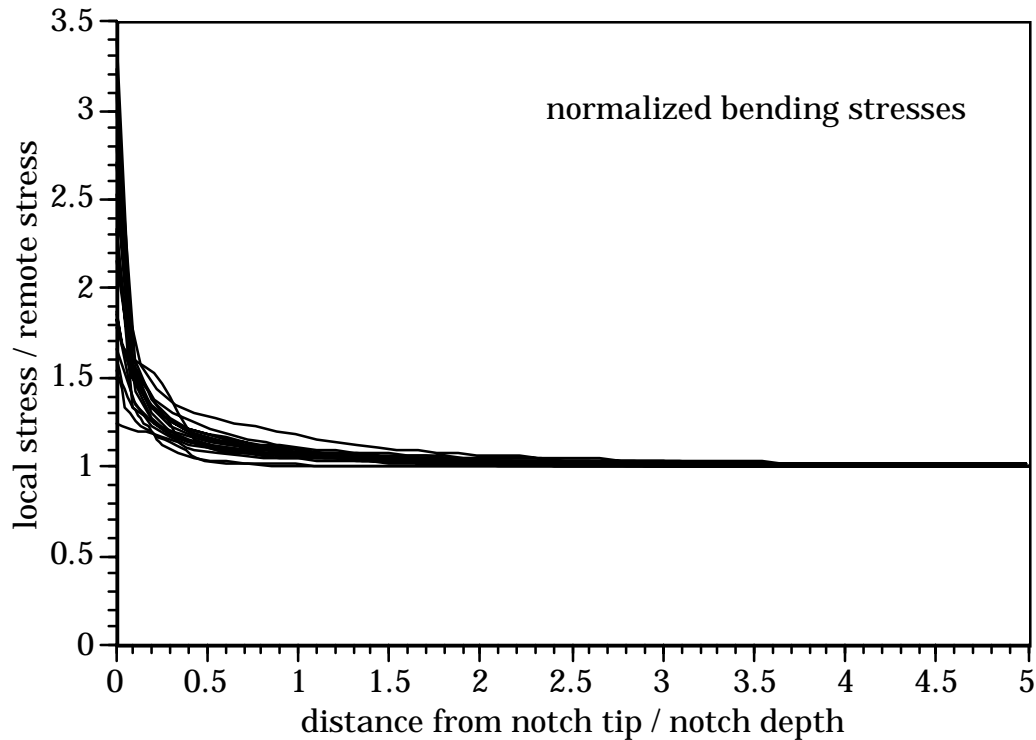


Figure 5G.24. A composite of all 0% stress lines for tension loading.

3-D STRESS INTENSITY FACTOR STUDIES

FRANC3D was used to perform a series of stress intensity factor analyses of cracks in all 19 geometries. For each geometry, a number of corner cracks were analyzed along with one through crack. The corner cracks had a circular crack front shape with the center of the circle at the point where the notch front meets the outer surface of the wedge. The radius of the circle is the reported crack size. The through crack fronts are also a portion of a circular arc. In these cases, the center of the circle is at the origin of the model coordinate system (see Figure 5G.3). For zero notch incidence angles, the reported crack size in this case is the distance from the notch front to the crack front at the center of the crack front. For nonzero crack front incidence angles, the crack size is measured from the top corner to the crack front. This is illustrated in Figure 5G.25.

The crack sizes to be analyzed for each model were selected as follows:

- For all models, corner cracks of 0.001 and 0.005" were analyzed.

- For all models, corner cracks of sizes approximately 80% of the length of the notch front were analyzed.
- At the discretion of the analyst, an additional intermediate corner crack was analyzed.
- For models with non-zero notch incidence angles, corner cracks were considered at both the top and bottom notch front corners.
- For all models, a through crack was analyzed. The crack size was taken to be approximately 120% of the length of the notch front.

In all, 110 crack analyses were performed for this study (with both tension and bending loading considered for each). The crack sizes considered are summarized in Table 5G.3.

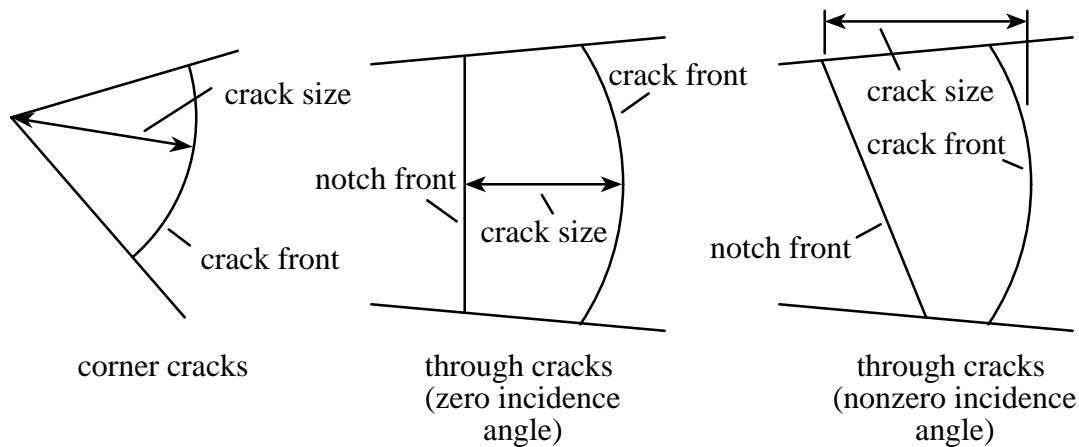


Figure 5G.25. Crack size definitions.

Table 5G.3

Summary of crack sizes considered in this study.

model	Top				through	bottom			
w_0	001	005	015	030	047t				
w_1	001	005	015	038	057t	001b	005b	015b	038b
w_2	001	005	008		012t				
w_3	001	005	009		013t	001b	005b	009b	
w_4	001	005	009		013t	001b	005b	009b	
w_5	001	005	011		017t	001b	005b	011b	
w_6	001	005	009		013t	001b	005b	009b	
w_7	001	005	011		017t	001b	005b	011b	
w_8	001	005	008		012t				
w_9	001	005	010		014t				
w_10	001	005	015	025	037t				
w_11	001	005	015	030	040t				
w_12	001	005	020	032	048t				
w_13	001	005	010	018	026t				
w_14	001	005	010	020	032t				
w_15	001	005	015	035	050t				
w_16	001	005	015	024	036t				
w_17	001	005	017	028	042t	001b	005b	017b	028b
w_18	001	005	016	025	038t				

all crack sizes in 1/1000ths of an inch

t indicates a through crack

b indicates cracks growing from the bottom corner

Typical crack fronts for a model with a zero and a nonzero notch incidence angle are shown in Figures 5G.26 and 5G.27, respectively. Crack front diagrams for all 19 models are included in Attachment C.

For the tension load crack analyses, the boundary conditions were applied in the expected way. That is, remote tension loads were applied as in the uncracked analyses. A different procedure was used for the bending analyses. The analyses were performed using linear order boundary elements. These elements do not perform well in bending. Using models with enough elements to capture the proper bending behavior would have been prohibitively expensive.

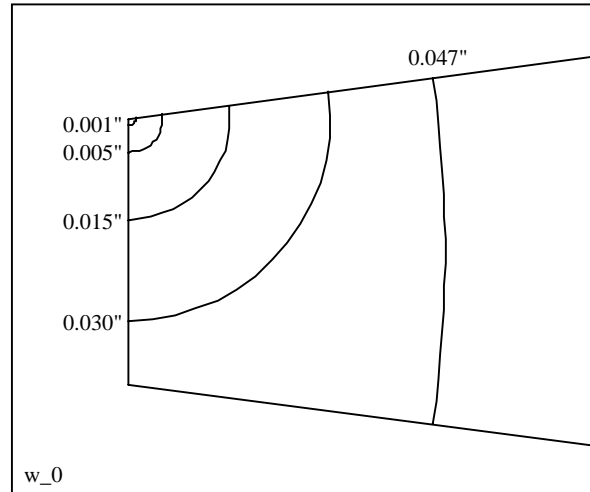


Figure 5G.26. Typical crack fronts for a model with zero notch incidence angle.

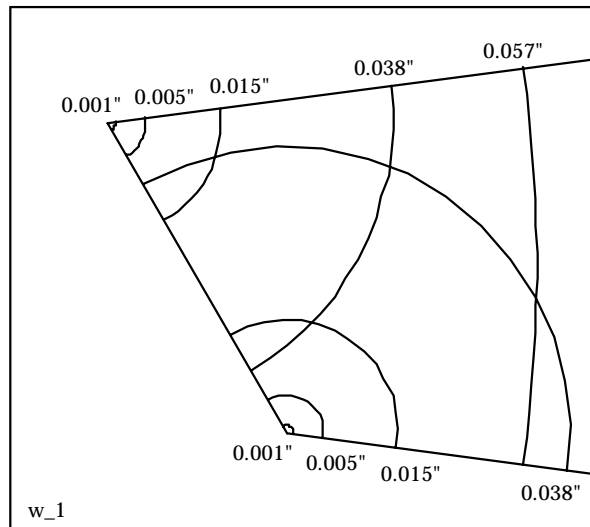


Figure 5G.27. Typical crack fronts for a model with a nonzero notch incidence angle.

To avoid excessively large models, a superposition approach was used for modeling the near crack behavior of the wedges. To understand the approach, one can imagine a "virtual" crack inserted in the uncracked ANSYS model. To keep the crack from opening, suction forces would need to be applied to the crack faces. The required forces would be exactly the "resolved" stresses in model at that point, where the resolved stresses are actually the traction, or the stress tensor times the normal to the crack face. If the crack were real, the suction forces would not exist, so those forces would need to be relaxed.

The stress relaxation is modeled with a separate, cracked (FRANC3D) model, which is otherwise unloaded. To this model one applies forces to the crack faces that are equal in magnitude to the "suction" forces, but opposite in direction (so that the crack will open). In effect, the cracked model calculates the change in deformation going from an uncracked model to a cracked model.

The "real" cracked response is the sum (superposition) of the two models. Now to determine K 's we examine the relative opening of the crack faces. The real opening is the sum of the relative crack face openings from the two models. However there is no crack opening in the uncracked model so the real K 's can be determined from the opening of the cracked model.

Typical plots of the mode I stress intensity factor distributions for tension and bending loading are shown in Figures 5G.28 and 5G.29. The K 's are plotted along the crack front starting at the notch tip and moving towards the wedge's flank surface. As can be seen in Figure 5G.29, for larger cracks subjected to bending loads, the stress intensity factors actually become negative, indicating that the crack faces want to overlap. However, in most real cases there will be a combination of tension and bending loads, meaning that the respective stress intensity factors will superimpose. If the tension loading is dominant, crack faces will remain open.

The stress intensity factor distribution plots for all analyses are given in Attachment D.

The stress intensity factor distribution is awkward to use in any predictive capacity. It is much more convenient to have one number that characterizes the stress intensity factor distribution for a given crack front. The distribution information was reduced using the following procedures:

Corner Cracks

The value of the stress intensity factors were determined for two points along the crack front arc: one 25 degrees from where the crack front meets the notch root, and the other 25 degrees from where the crack front meets the wedge flank surface. (see Figure 5G.30). These two values are then averaged to give a characteristic K value for the crack front.

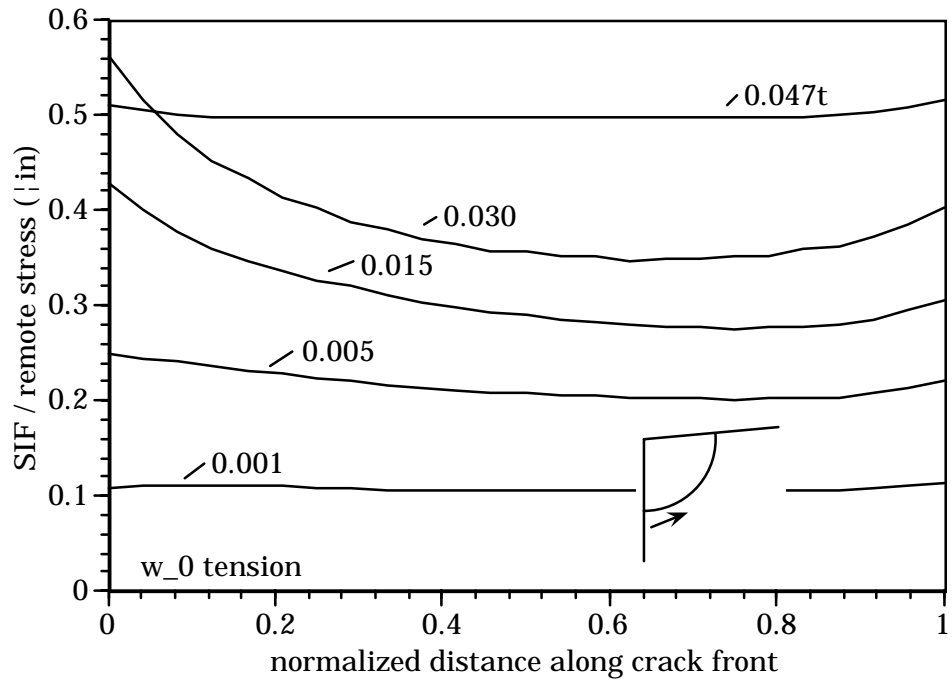


Figure 5G.28. Typical mode I stress intensity factor distributions for tension loading.

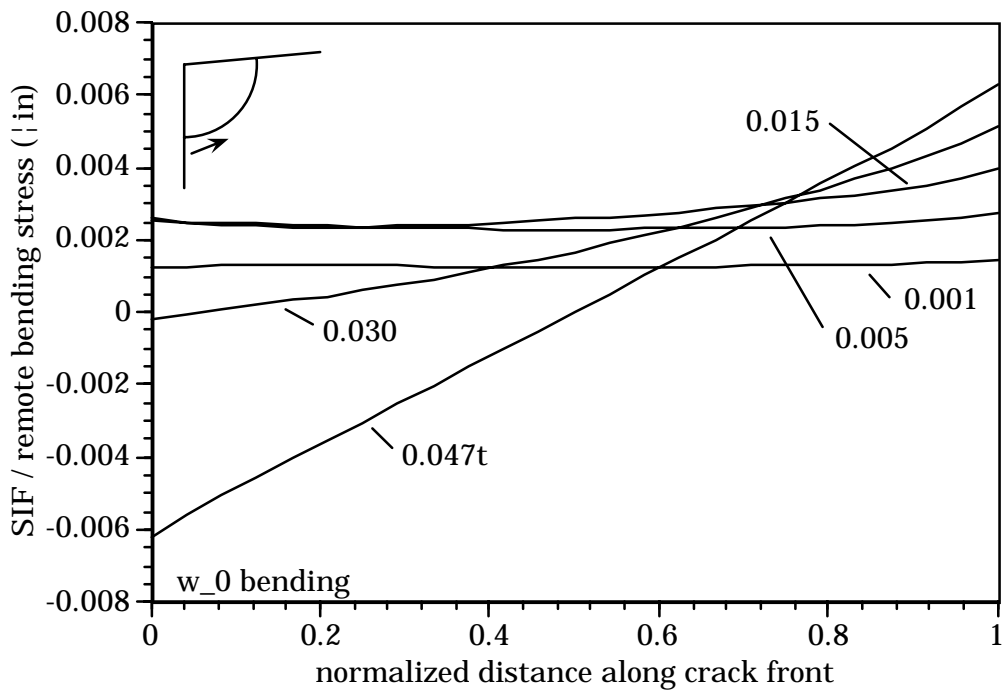


Figure 5G.29. Typical mode I stress intensity factor distributions for bending loading.

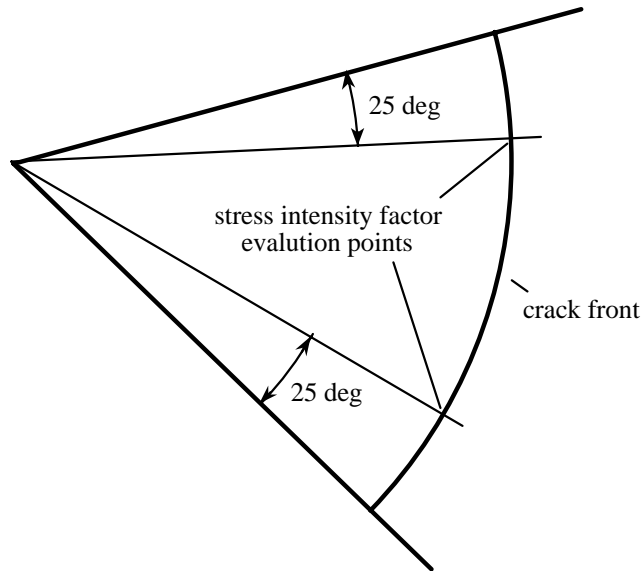


Figure 5G.30. Schematic showing the stress intensity evaluation points for corner cracks.

Through Cracks (Tension)

For through cracks in tension, the stress intensity factor at the center of the crack front was used as the characteristic K value.

Through Cracks (Bending)

For through cracks in bending, the stress intensity factors at the points where the crack fronts meet the wedge flank surfaces are used as characteristic K values. The values at the top and bottom flank surfaces are approximately equal in magnitude (within 2% for this study) and opposite in sign.

The characterizing K values for all crack fronts are given in Attachment E.

STRESS INTENSITY FACTOR TRENDS

One of the purposes of this study was to determine how the stress intensity factors for cracks growing from notch tips would change as a function of the model parameters. The actual geometries analyzed were chosen to give a large number of cases of groups of models where only one parameter changes between models. The purpose of this section is to illustrate typical trends in the relationships between stress intensity factors and model parameters. Complete plots of all matched models can be found in Attachment F.

For these comparisons, only tension loading is considered. The bending results are much more difficult to interpret because of the negative K 's for portions of some of the crack fronts, and because the shape of K distributions is much less regular with increasing crack sizes. It is anticipated that for most configurations, the tension loading will dominate.

In order to make comparisons one would like to see how the K 's for a fixed crack size vary as a model parameter is changed. However, during the analyses a variety of crack sizes were used (except for 0.001 inch and 0.005 inch cracks, which were analyzed for all geometries). To make comparisons, interpolating spline curves were fit through all the average K results. Comparisons are made by evaluating the spline at the same crack length for a group of models.

A typical comparison of computed stress intensity factors as a function of notch depth is shown in Figure 5G.31. Three models (w_13, w_10, and w_11) were selected. These differ only in their notch depth parameter; the remaining four parameters (leading edge diameter, leading edge flank angle, notch tip radius, and notch incidence angle) are the same. Figure 5G.31 shows the variation in the K 's for five different crack sizes.

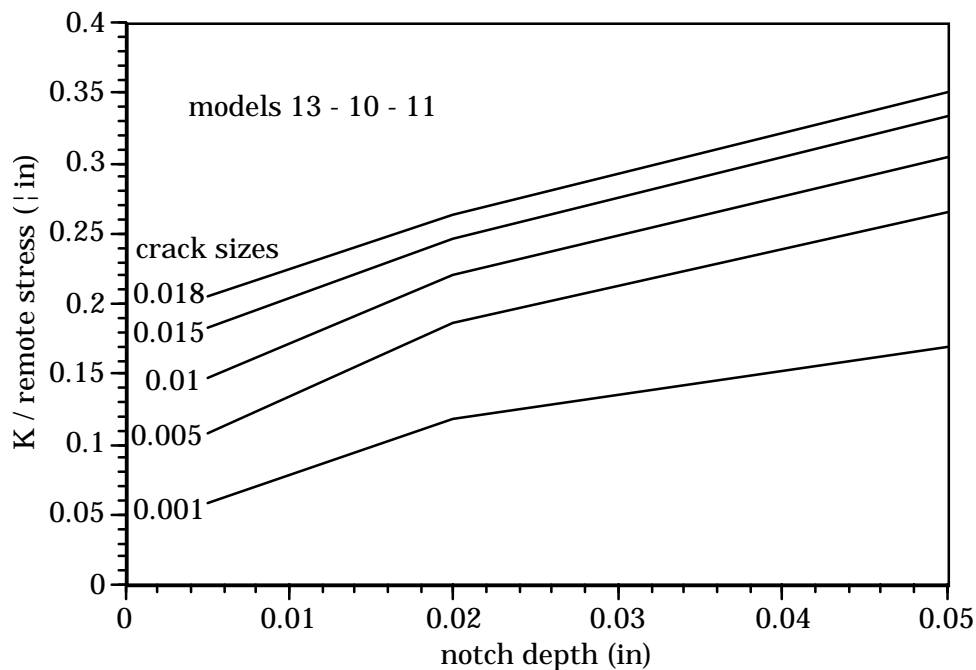


Figure 5G.31. Typical comparison of computed stress intensity factors as a function of notch depth.

One can see from Figure 5G.31 that the notch depth has a rather significant effect on the K 's. Over the range of the parameter variation (0.005 inch to 0.05 inch) one sees about 180% increase in the stress intensity factor moving from the smallest to the largest notch depth for a 0.001 inch crack. This is expected because, as can be seen in the stress plots in Attachment B, the notch depth has a dramatic effect on the near-tip stresses. For these three models, the normalized stress at the notch front corner are approximately 1.85, 3.7 and 5.4.

As the cracks get bigger, the increase in stress intensity factor is less sensitive to notch depth (about a 75% increase for 0.008 inch cracks). This is because most of the crack front has grown beyond the very high stress gradients near the notch tip, and is in a region where the stresses are more uniform among the three models.

One can also see that the variation in K is a nonlinear function of notch depth. This is not surprising if one draws an analogy to crack growth where the stress intensity factor is proportional to the square root of the crack length. While one would not expect an exact square root function here, a power-type relationship with an exponent that is less than one seems reasonable.

Figure 5G.32 shows the relationship between stress intensity factor and the leading edge diameter. In this case, one sees a much weaker dependence of K on the parameter. There is about a 17% decrease in the K over the parameter range (0.01 inch to 0.04 inch), and this relative decrease is not very sensitive to crack size. These results are what one would expect based on the stress results, which show reduced stresses in the notch tip region as the leading edge diameter is increased.

One should note that the other series of models that cover the entire parameter range (8-13-14) shows a greater effect of leading edge diameter on K (20-26%). However, in this case, on models 13 and 14 the notch tip intersects the wedge on the leading edge round and not on the wedge flank surface. This may confound comparisons.

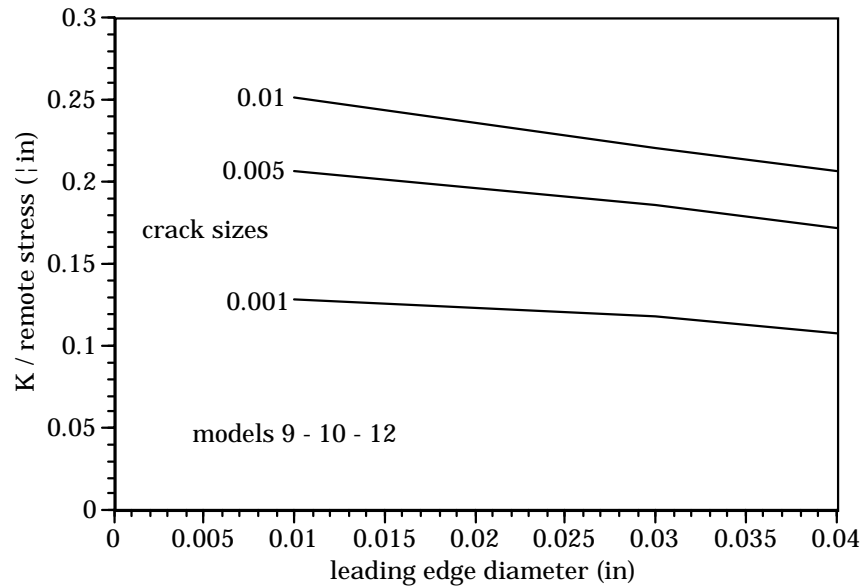


Figure 5G.32. Typical comparison of computed stress intensity factors as a function of the leading edge diameter.

Figure 5G.33 shows the relationship between stress intensity factor and the leading edge flank angle. In this case, one sees a nearly linear relationship for all crack sizes. Also the relative variation in K over the parameter range (3.5 to 15 degrees) is a relatively modest 7 to 10% for the 0.001 and 0.024 inch crack sizes, respectively.

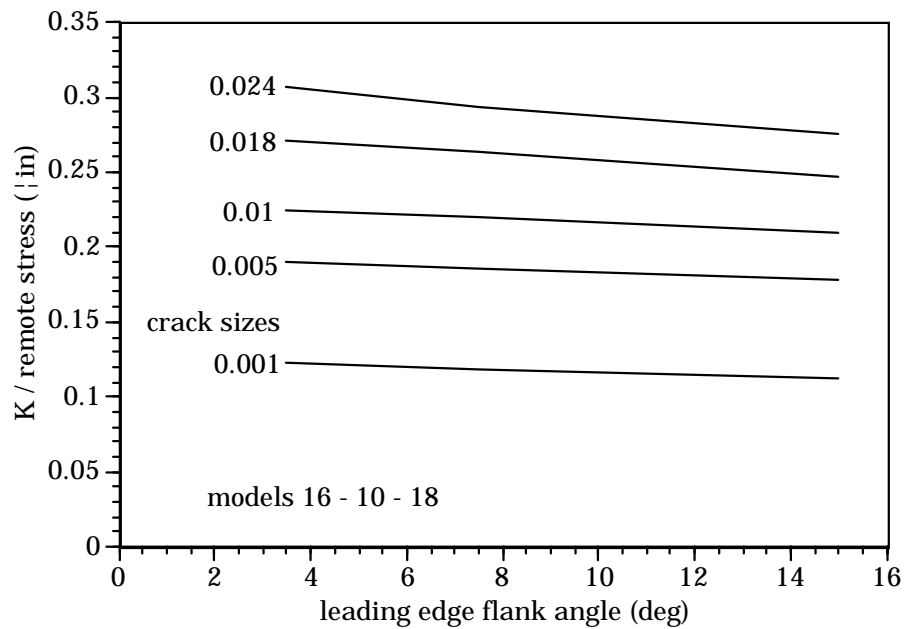


Figure 5G.33. Typical comparison of computed stress intensity factors as a function of the leading flank angle.

Only two notch tip radii were considered in the studies, 0.005 and 0.025 inch. Figure 5G.34 shows how stress intensity factor varies with this. One can see that, as expected, as the cracks get bigger, the K 's become much less sensitive to the notch tip radius. Also, even for the small cracks, the K 's are not overly sensitive to the tip radius, about 19% variation for the case shown here (however for the 5-7 case, not shown here, the variation is closer to 35%).

The final parameter was used to examine the notch incidence angle. Again, only two values were considered in the study, zero and 30 degrees. Figures 5G.35 and 5G.36 show how stress intensity factors vary with incidence angles for top and bottom cracks, respectively. In these cases the K 's are not a strong function of the angle. The biggest change in these plots is 17%. The biggest change for all models is 25%. However, most cases show a much smaller variation. An interesting trend to notice is that is that for the top cracks the curves have a positive slope for small cracks and a negative slope for larger cracks. This pattern is reversed for the case of the bottom cracks.

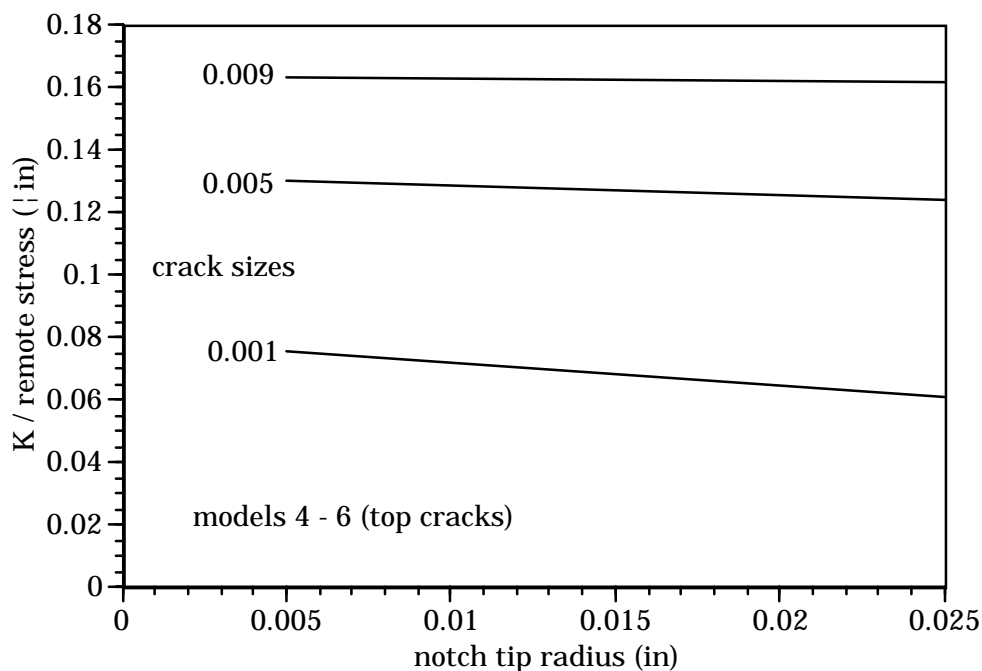


Figure 5G.34. Typical comparison of computed stress intensity factors as a function of the notch tip radius.

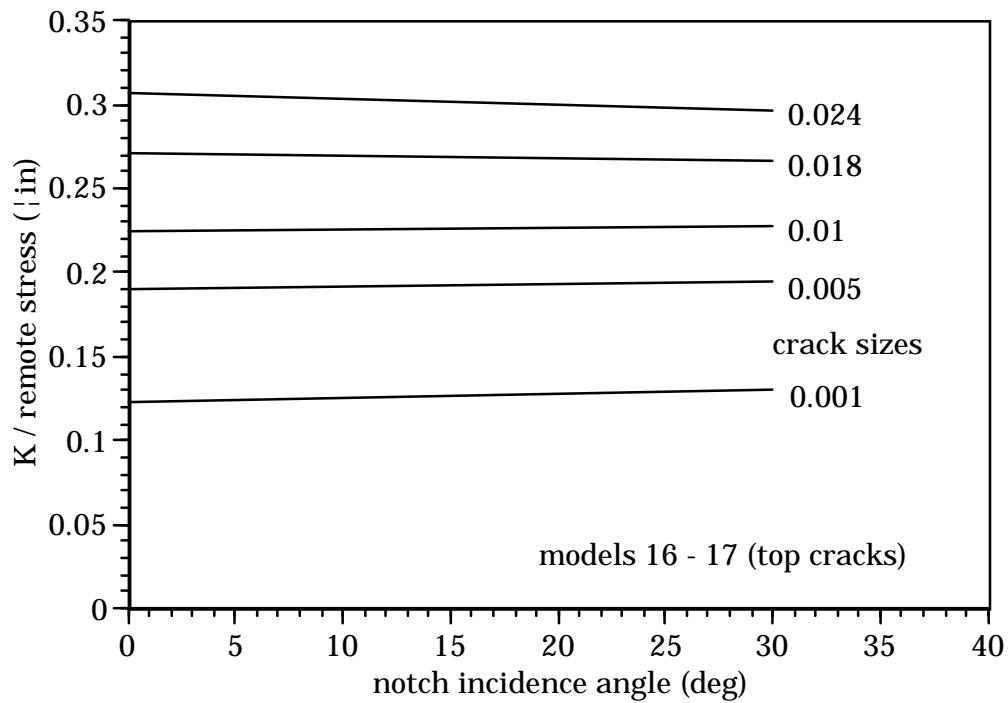


Figure 5G.35. Typical comparison of computed stress intensity factors as a function of the notch incidence angle for top cracks.

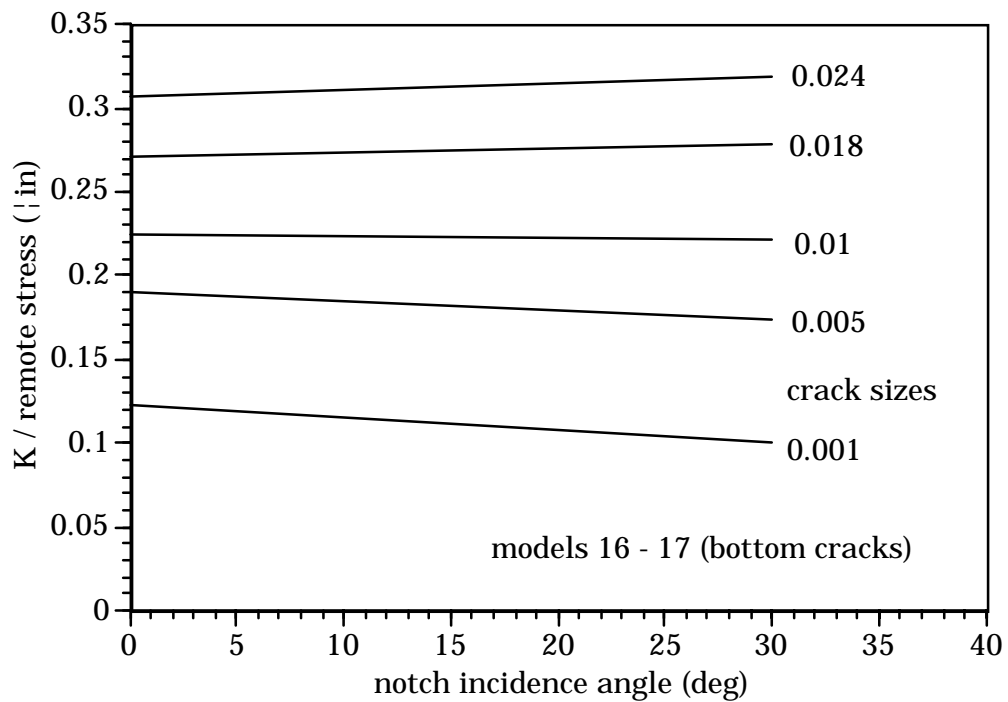


Figure 5G.36. Typical comparison of computed stress intensity factors as a function of the notch incidence angle for bottom cracks.

SUMMARY

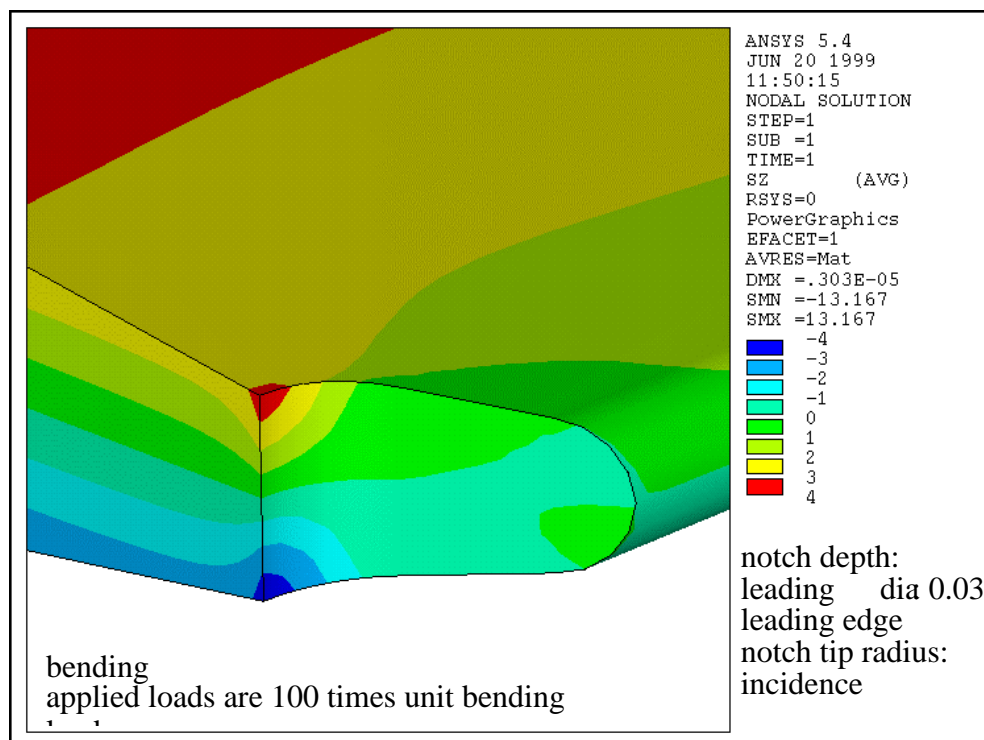
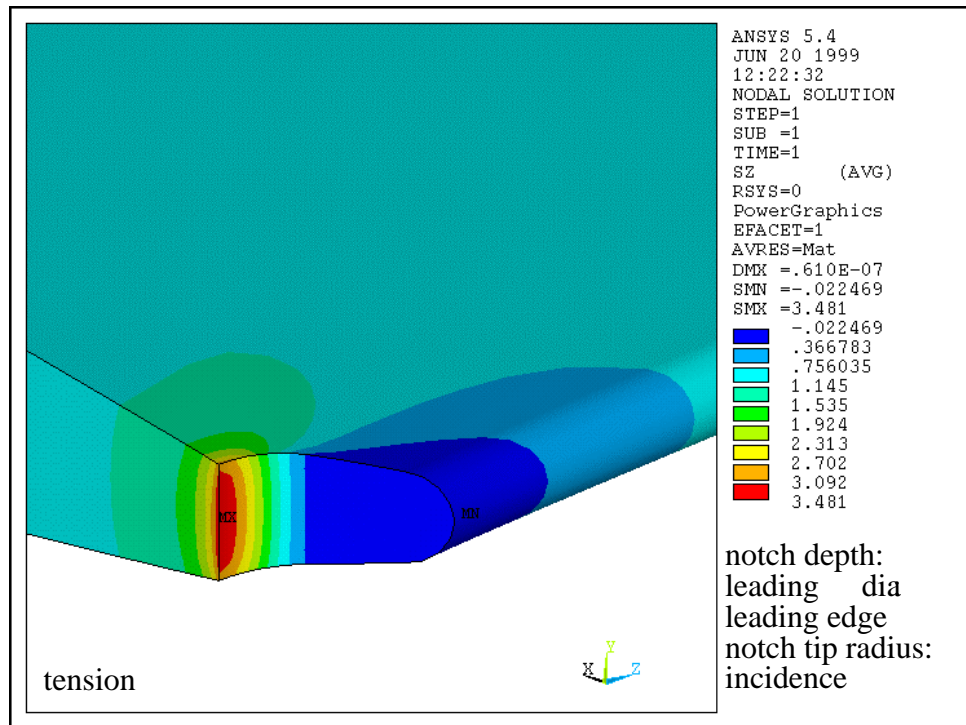
- A series of analyses were performed to simulated foreign object damage (FOD) at the leading edge of an airfoil. Airfoils are modeled with a wedge-like geometry, and FOD is simulated with a notch.
- The notches are parameterized with four dimensions: notch depth, incidence angle, tip radius, and flank angle. For all analyses reported here, the notch flank angle is fixed at 60 degrees. The wedge is also parameterized with four dimensions: leading edge radius, leading flank angle, width, and half-length.
- Nineteen separate geometries were considered. Two load cases were considered for all models, tension and bending
- ANSYS stress analyses were performed for all nineteen geometries. These analyses did not model any cracks. Stress results are given in Attachments A and B.
- A series of hypothetical cracks of various sizes growing from a "corner" of the notch root for all geometries were analyzed with FRANC3D. In all, 110 crack configurations were considered. Stress intensity factor results are given in Attachments C, D, and E.
- Trends in stress intensity factors as a function of model parameters were examined. It was found that the notch depth has the greatest influence on the stress intensity factors. These results are given in Attachment F.

REFERENCES

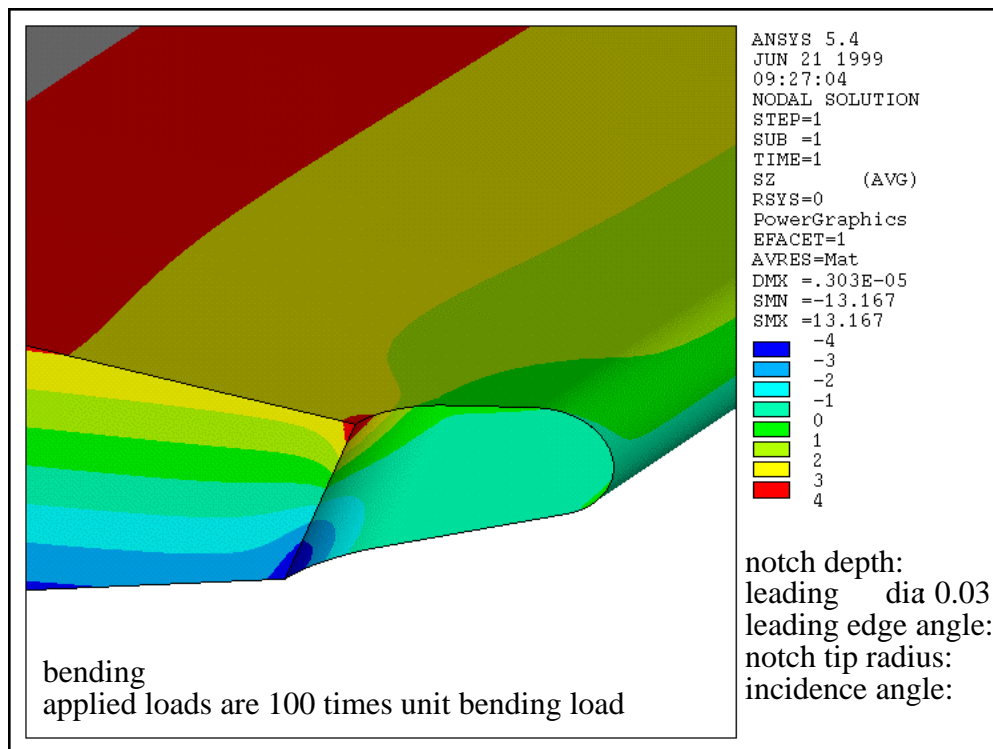
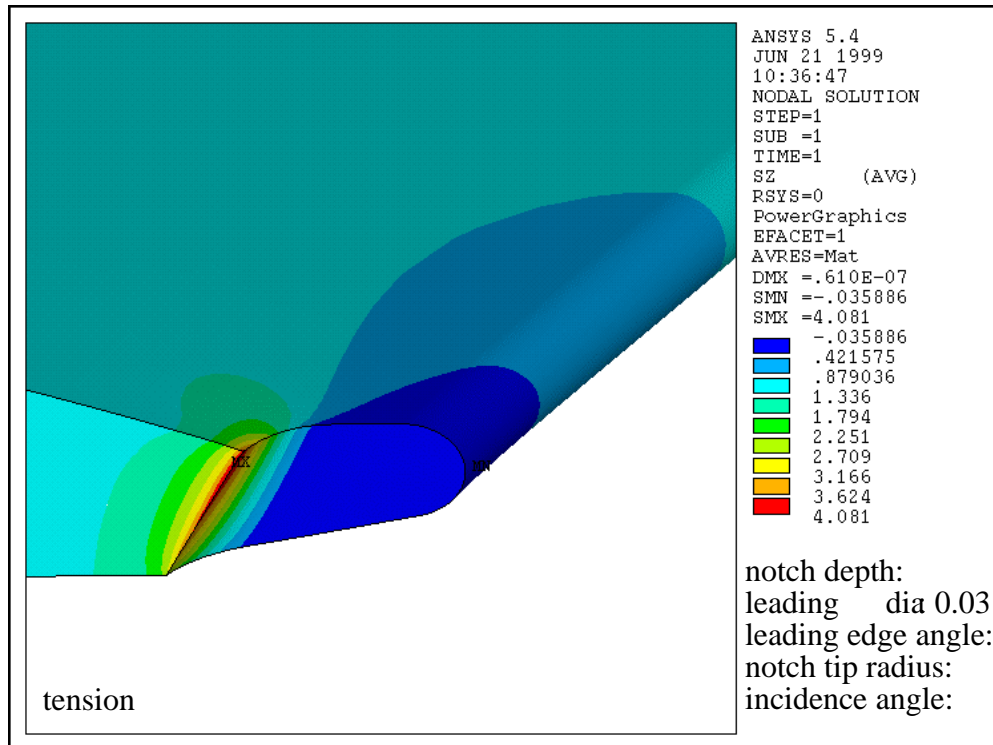
- | | |
|-----------|--|
| Gray 1990 | Gray, L.J., Martha, L.F., Ingraffea, A.R., "Hypersingular Integrals in Boundary Element Fracture Analysis," <i>Int. Journal for Numerical Methods in Engineering</i> , 29, 1990, pp. 1135-1158. |
| Lutz 1990 | Lutz, E., Gray, L., and Ingraffea, A.R., "Indirect Evaluation of Surface Stress in the Boundary Element Method", <i>Proceedings of IABEM-90: Symp. of the Int. Assoc. for Boundary Element Methods</i> , 1990. |
| Lutz 1991 | Lutz, E.D., <i>Numerical Methods for Hypersingular and Near-Singular Boundary Integrals in Fracture Mechanics</i> , Ph.D. Thesis, Cornell University, May, 1991. |

- Martha 1993 Martha, L.F., Wawrzynek, P.A., and Ingraffea, A.R., "Arbitrary Crack Representation Using Solid Modeling," *Engineering with Computers*, 1993.
- Wawrzynek 1988 Wawrzynek, P., Martha, L., Ingraffea, A.R., "A Computational Environment for the Simulation of Fracture Processes in Three Dimensions," *Proc. of the Symposium on Analytical, Numerical, and Experimental Aspects of Three-Dimensional Fracture Processes*, A. Rosakis, Editor, Berkeley, CA, June, 1988, pp. 321 - 327.
- Wawrzynek 1989 Wawrzynek, P., Martha, L., Ingraffea, A.R., "FRANSYS: A Software System for the Simulation of Crack Propagation in Three Dimensions," *Proceedings of Symposium on Discretization Methods in Structural Mechanics*. IUTAM/IJACM, H. Mang and G. Kuhn, Editors, Vienna, June 1989, pp. 273-282.
- Wawrzynek 1991 Wawrzynek, P.A., *Discrete Modeling of Crack Propagation: Theoretical Aspects and Implementation Issues in Two and Three Dimensions*, Ph.D. Thesis, Cornell University, August, 1991.

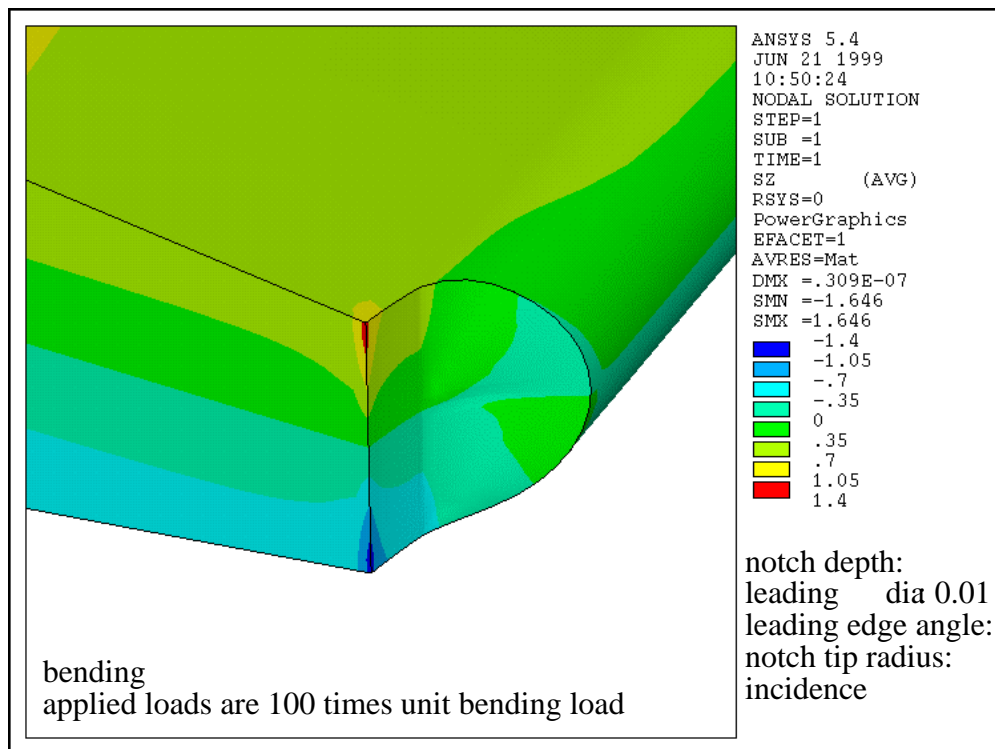
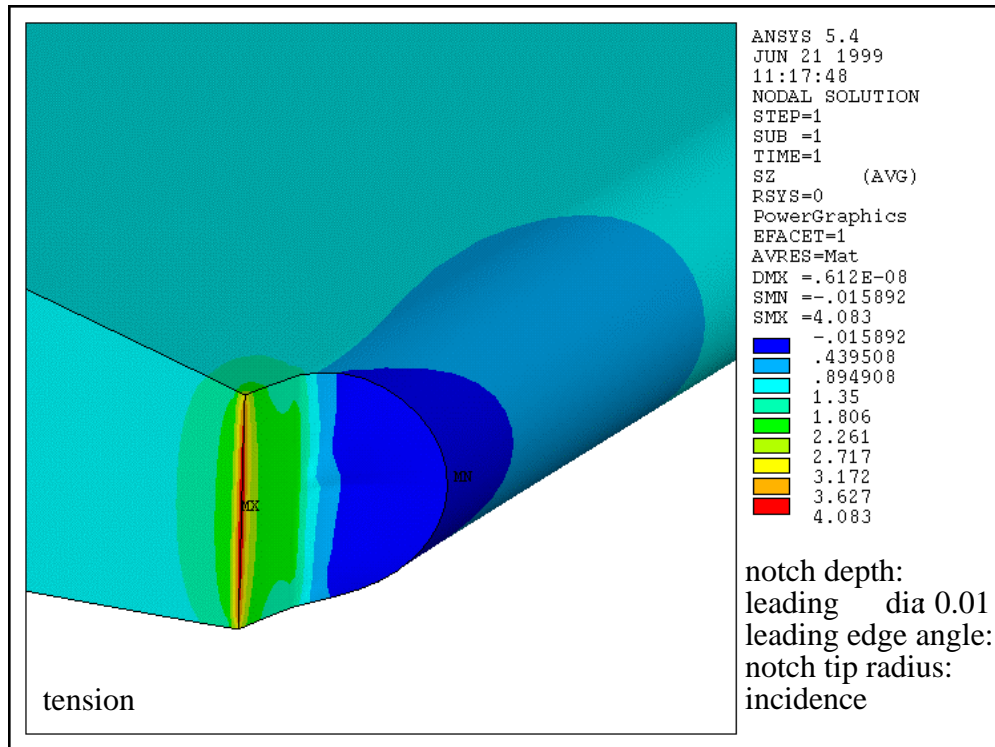
Attachment A: Near Notch-Tip Stress Contours



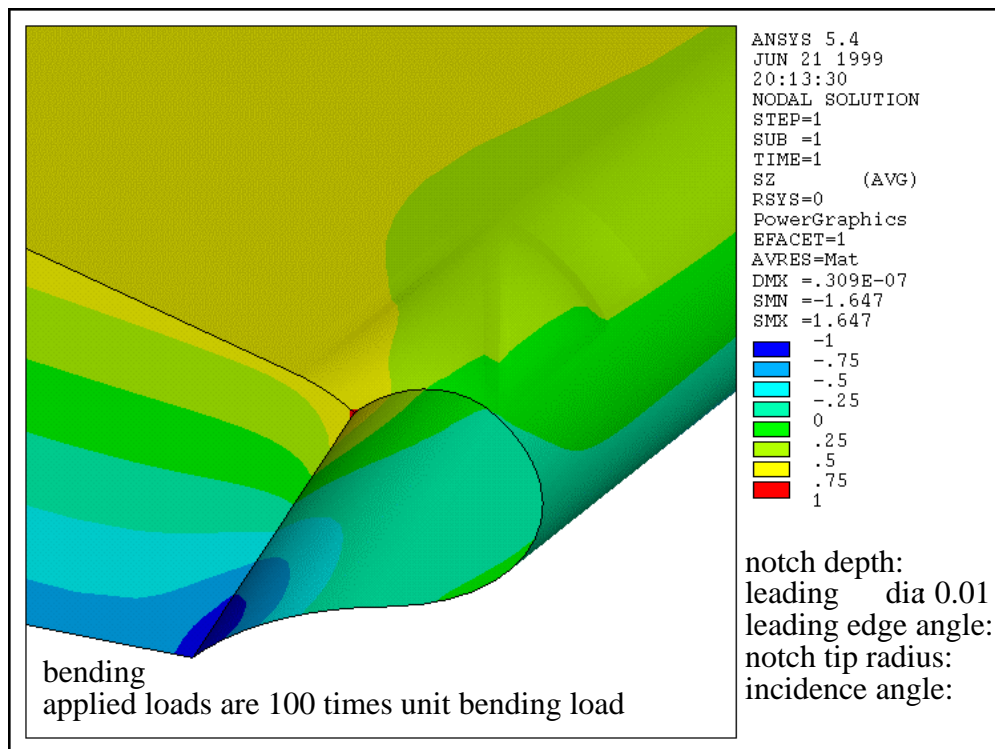
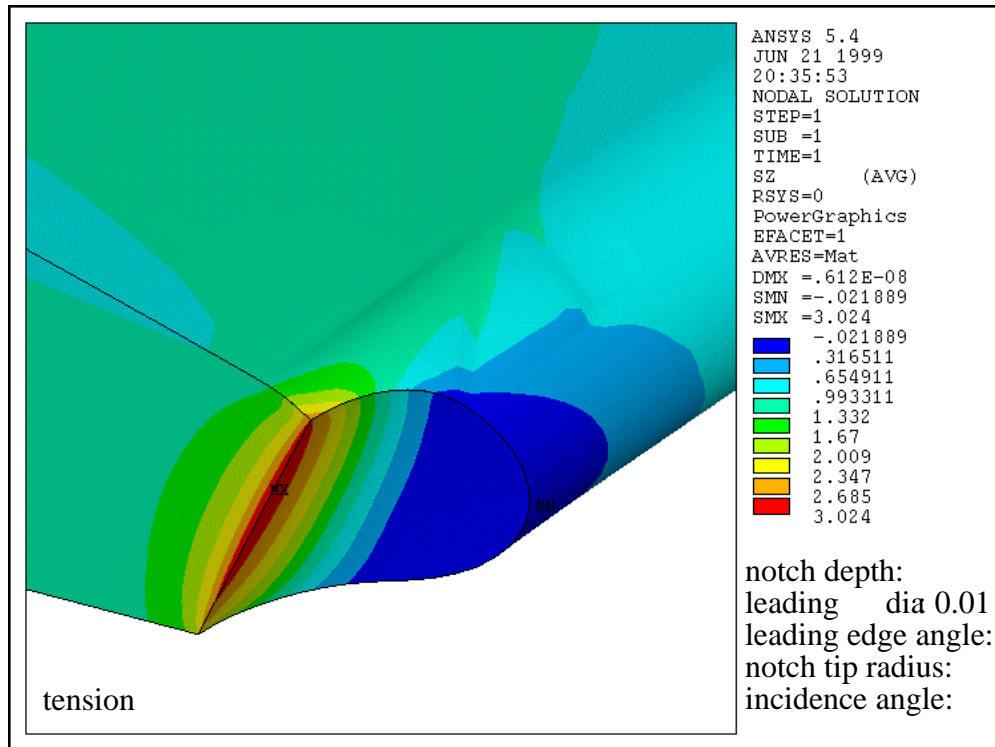
w_0



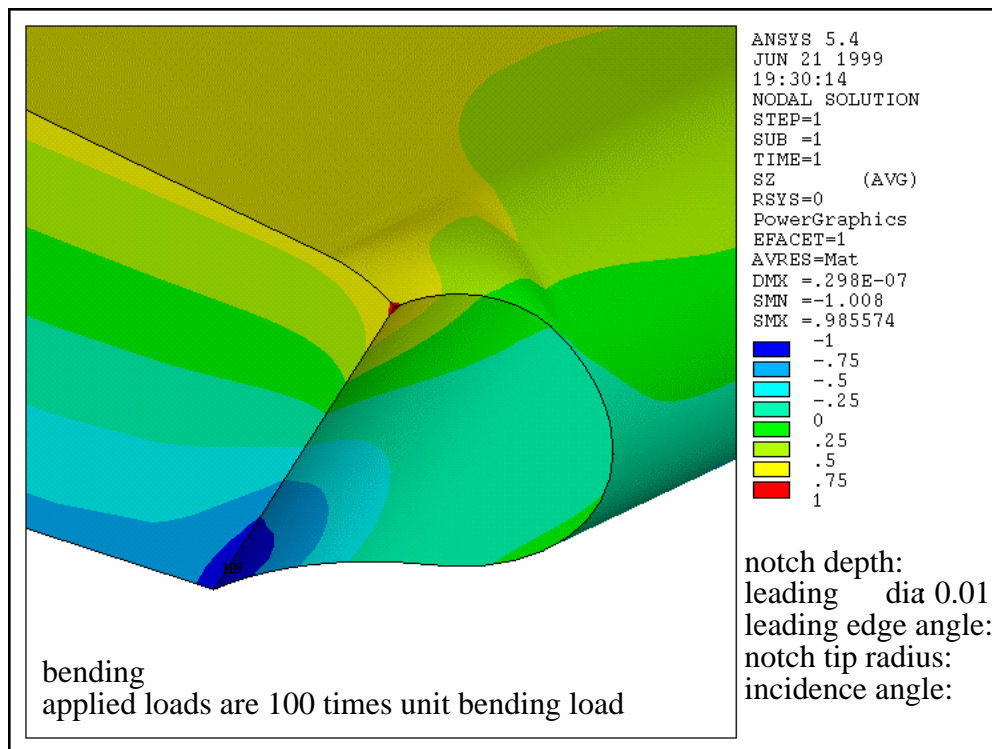
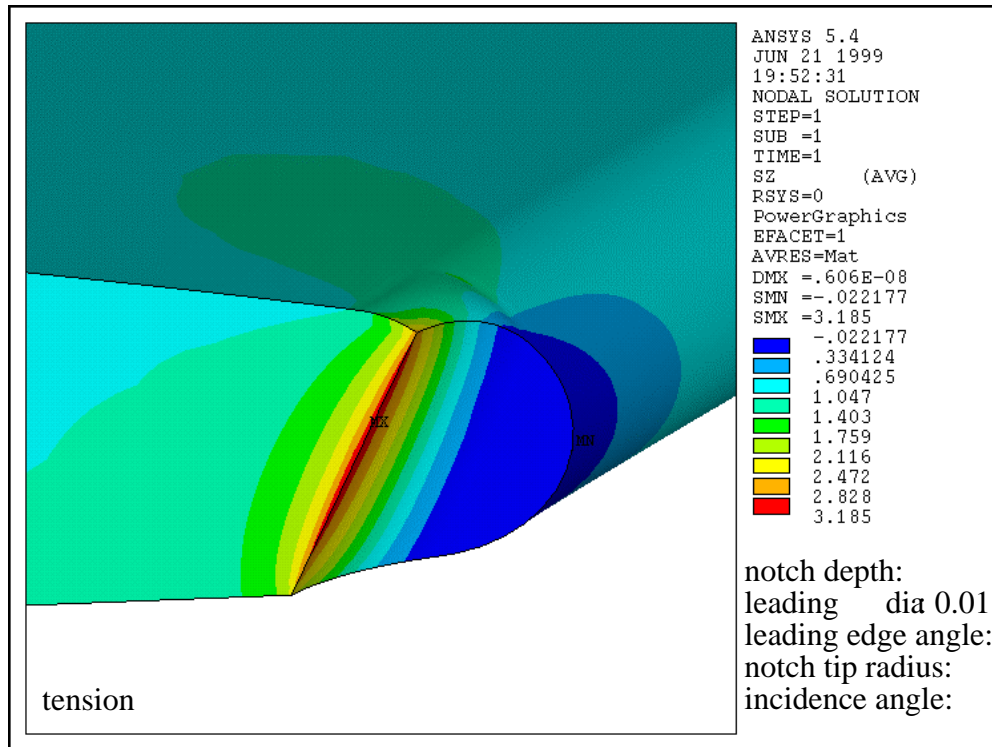
w_1



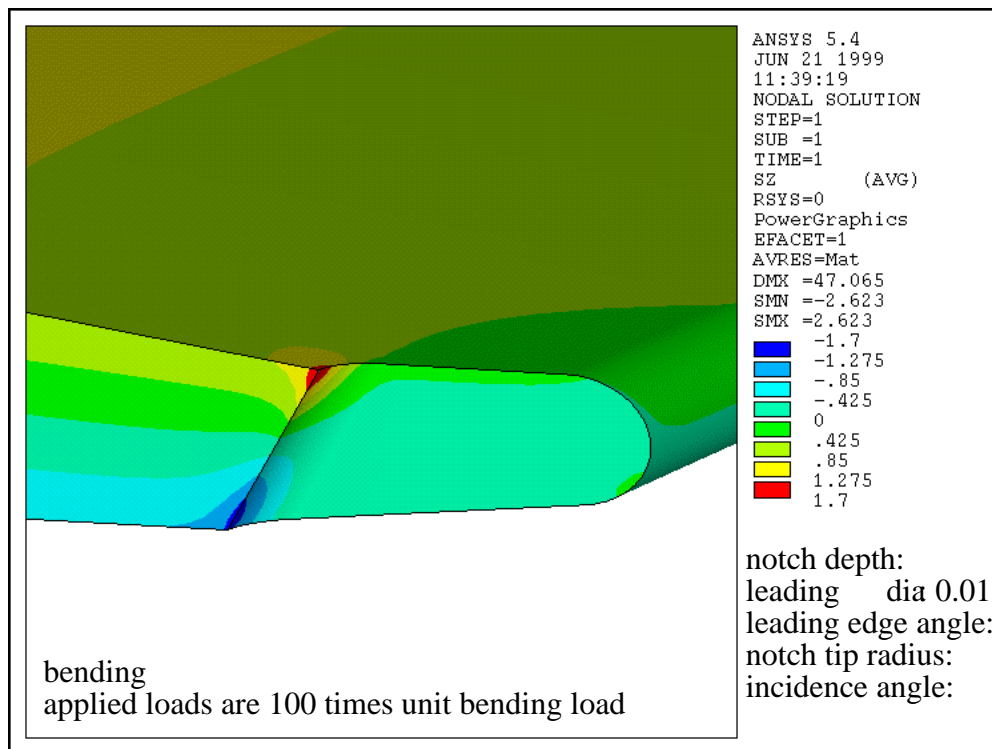
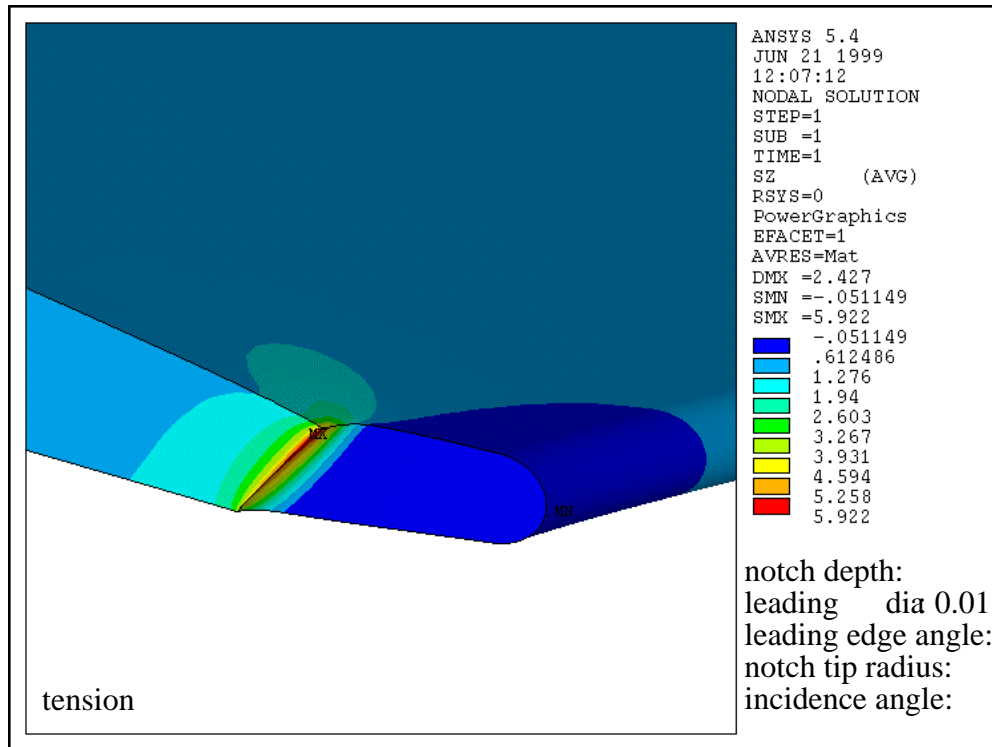
w_2



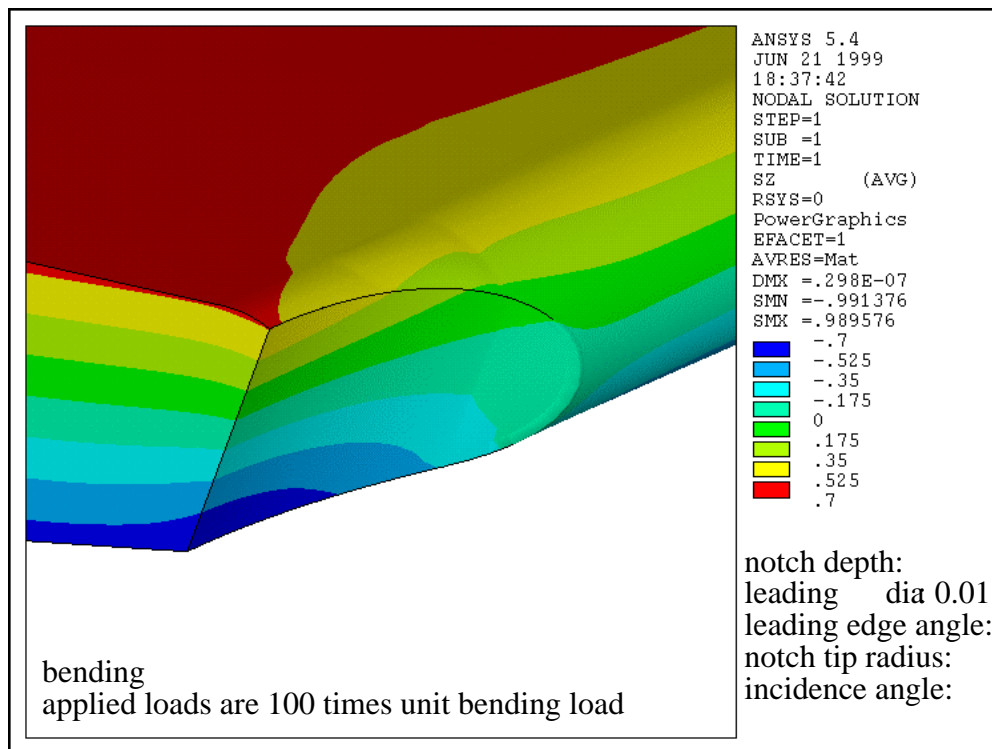
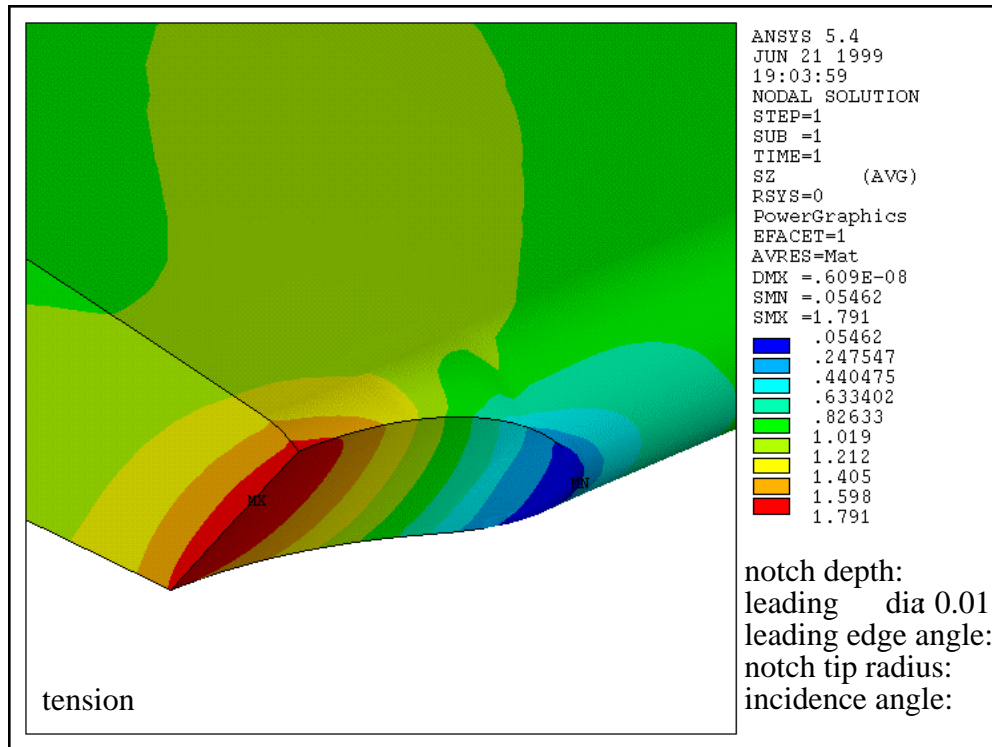
w_3



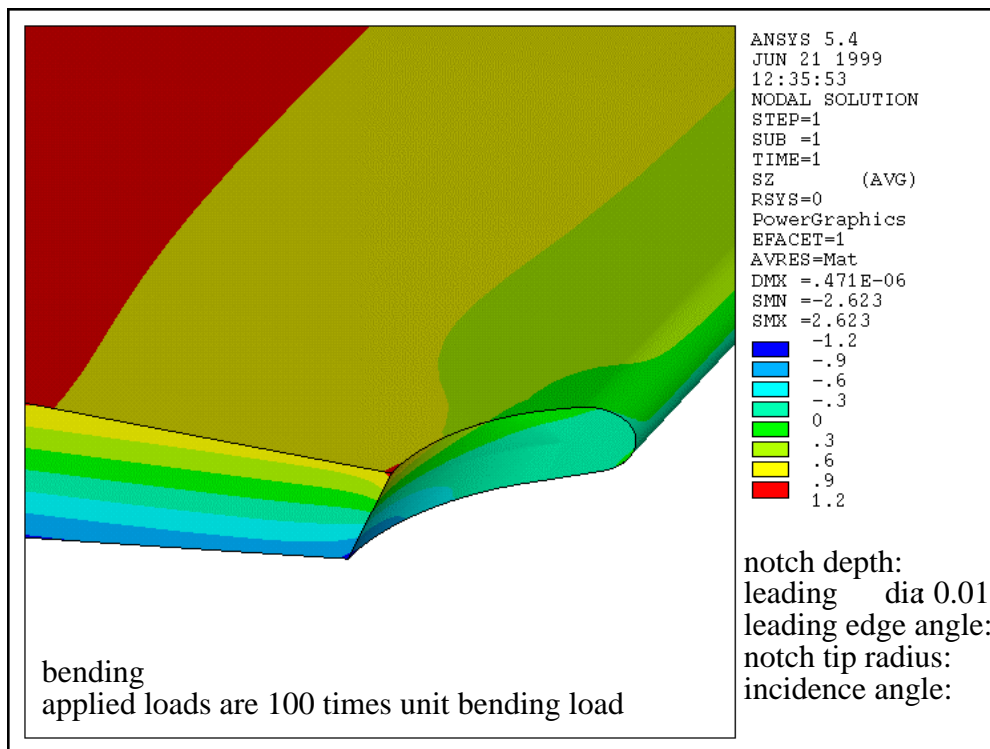
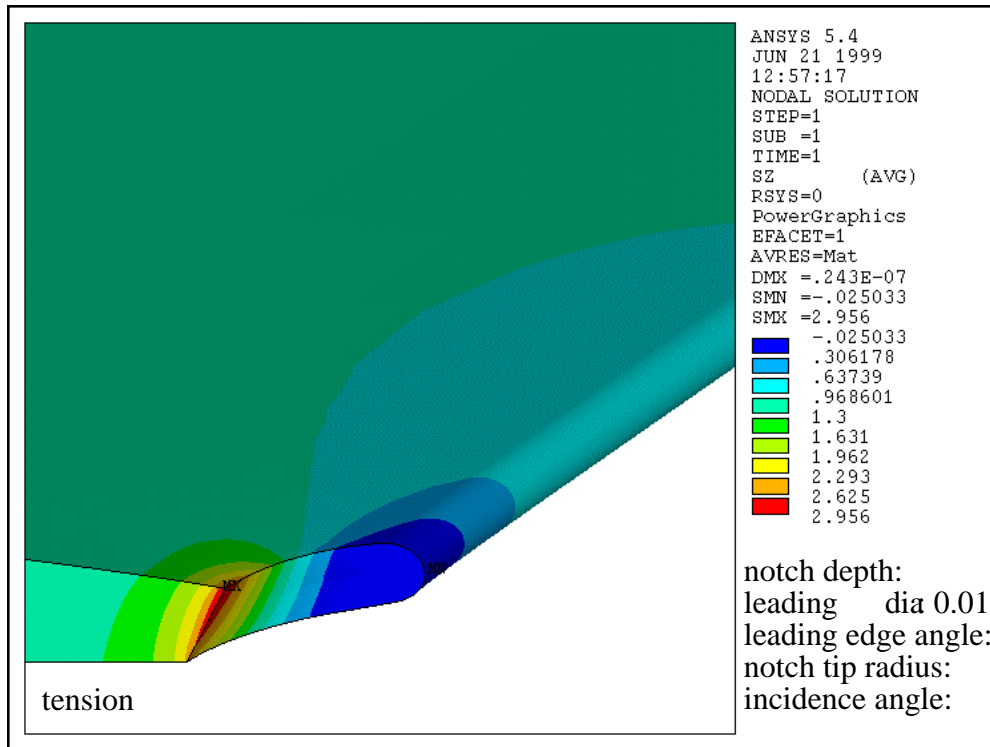
w_4



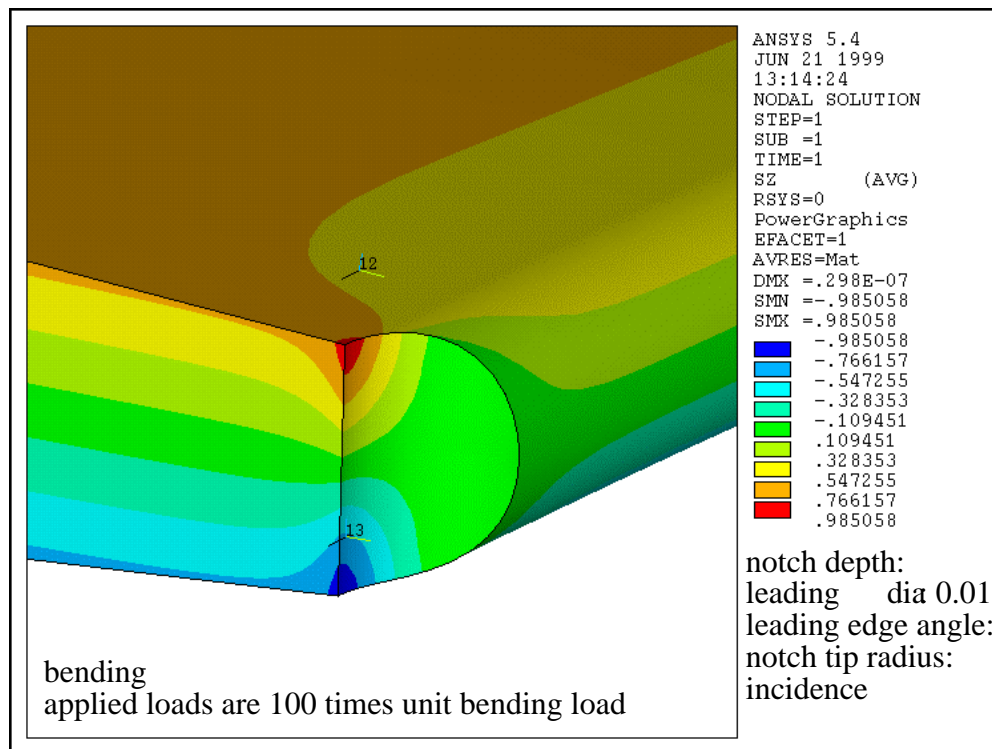
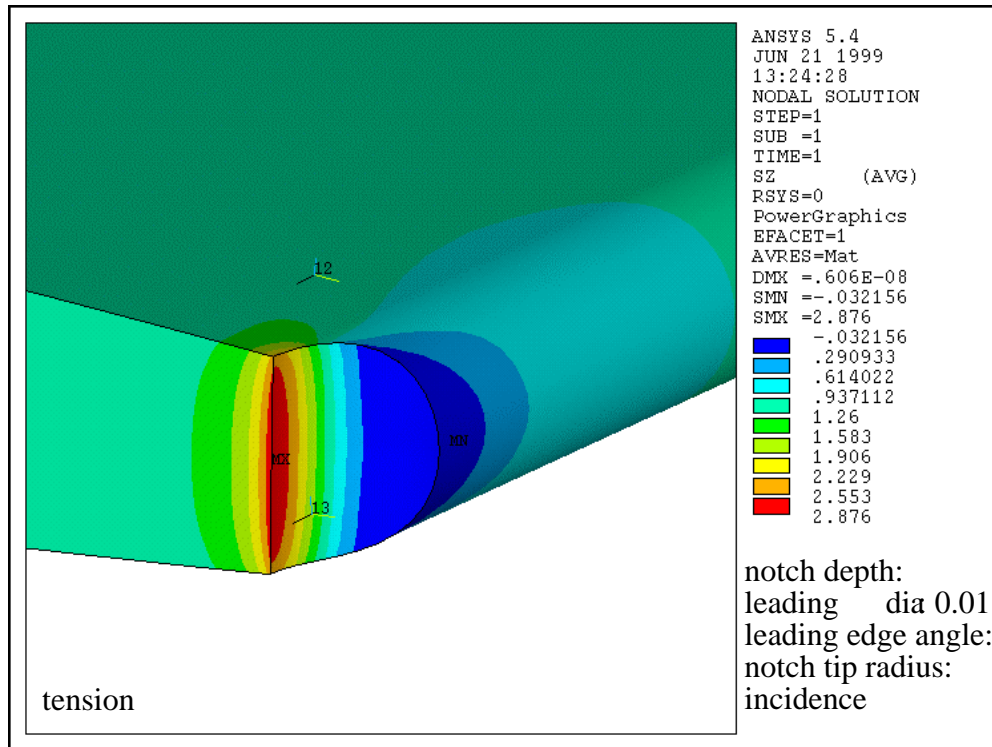
w_5



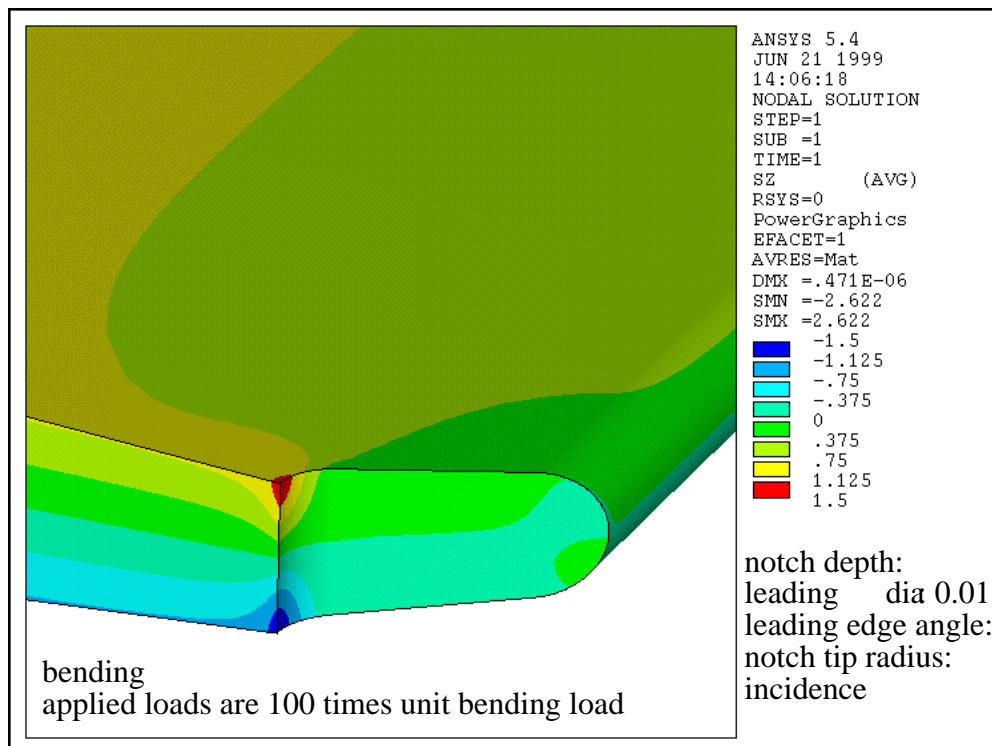
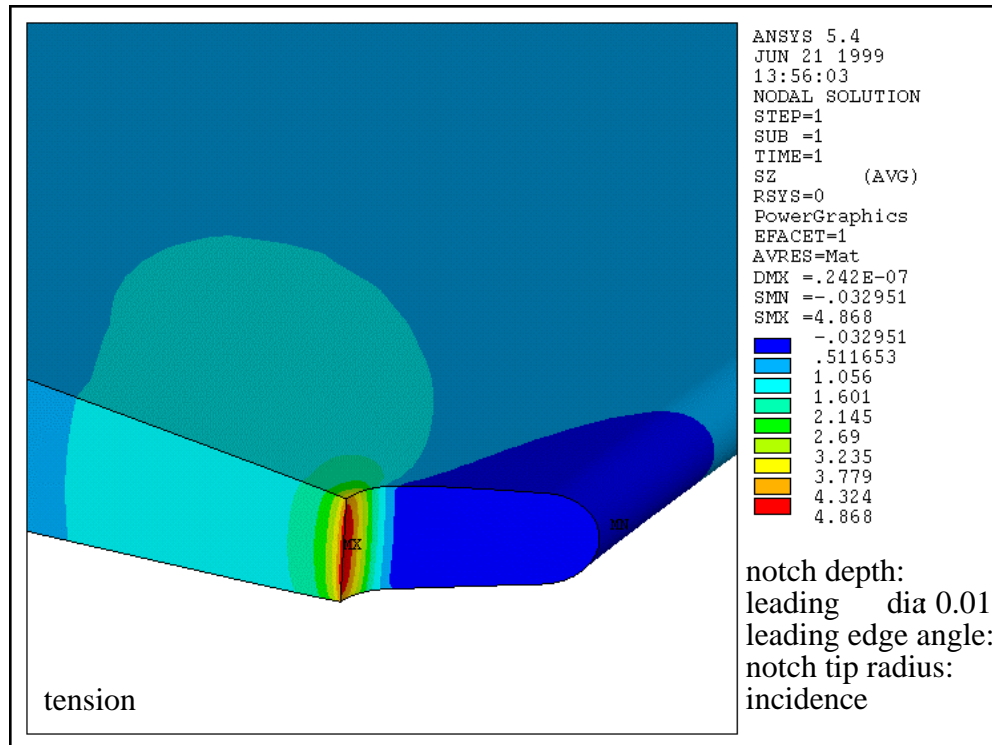
w_6



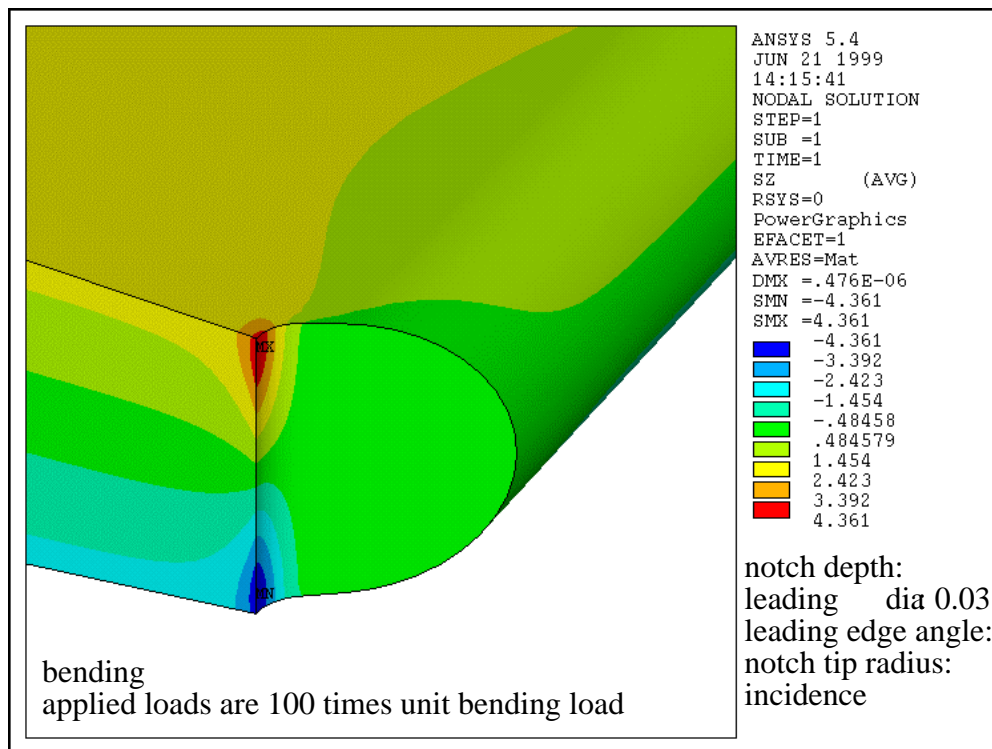
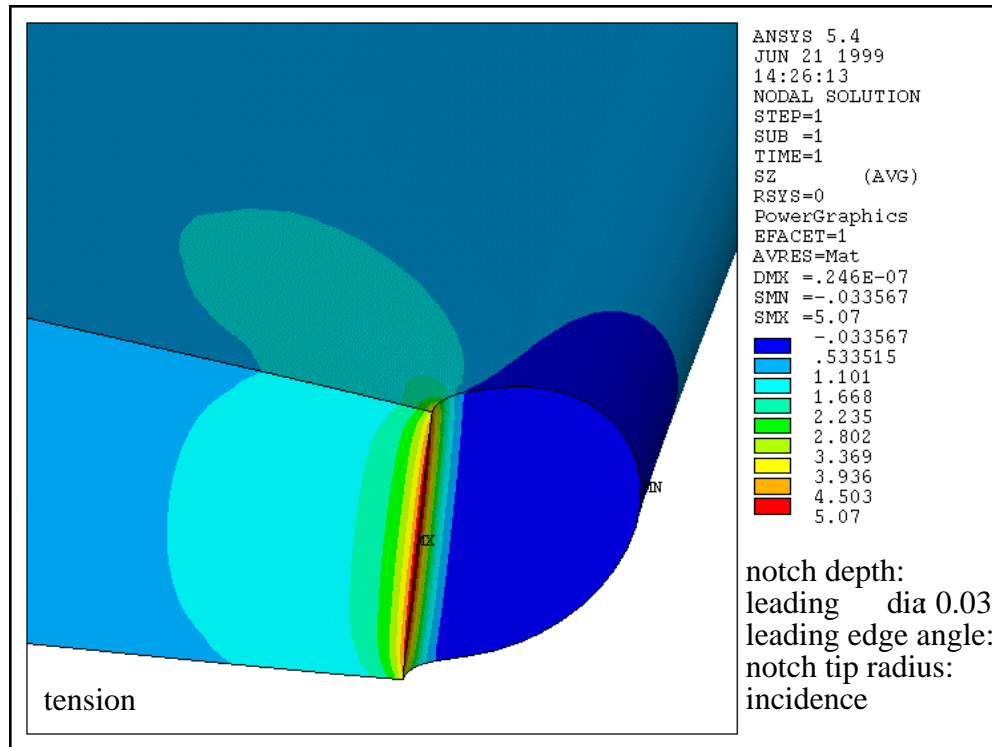
w_7



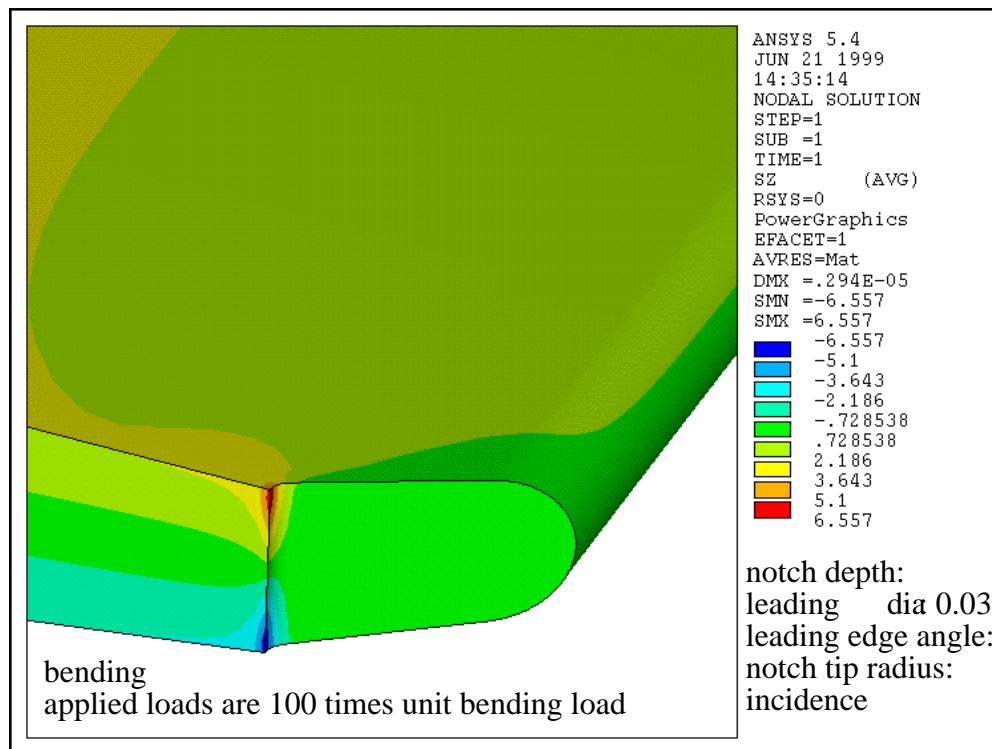
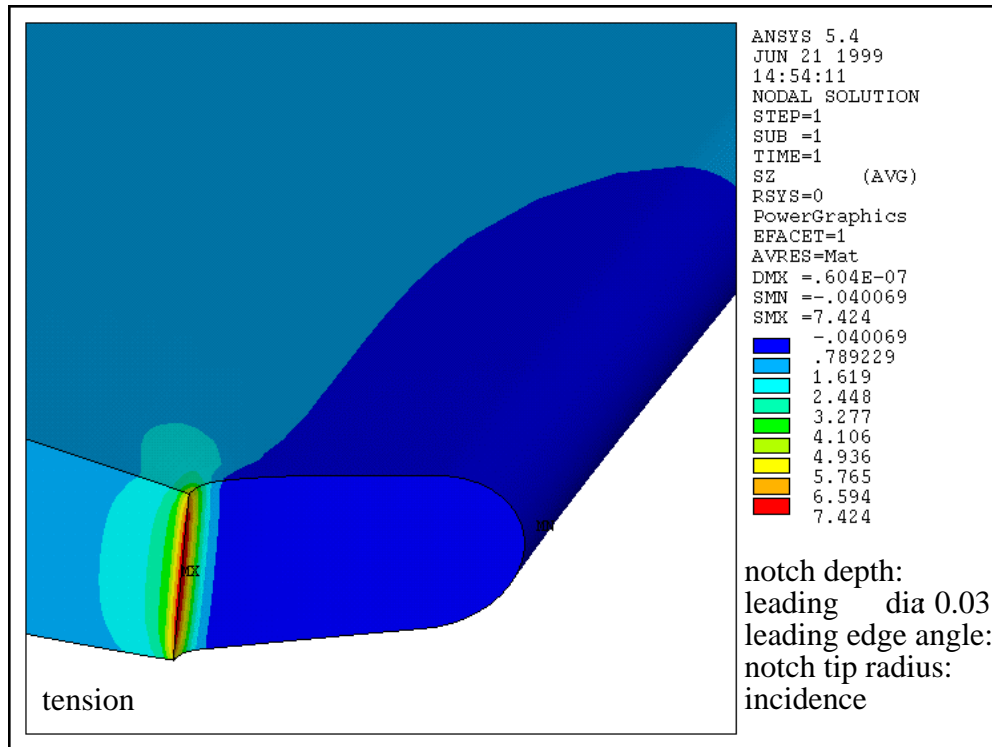
w_8



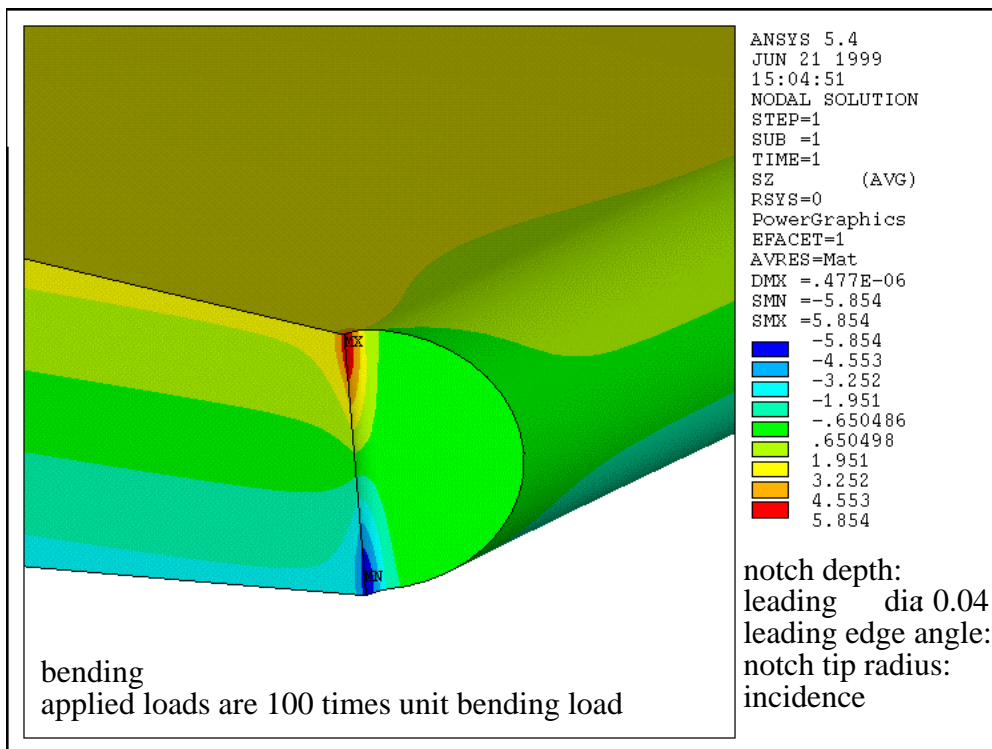
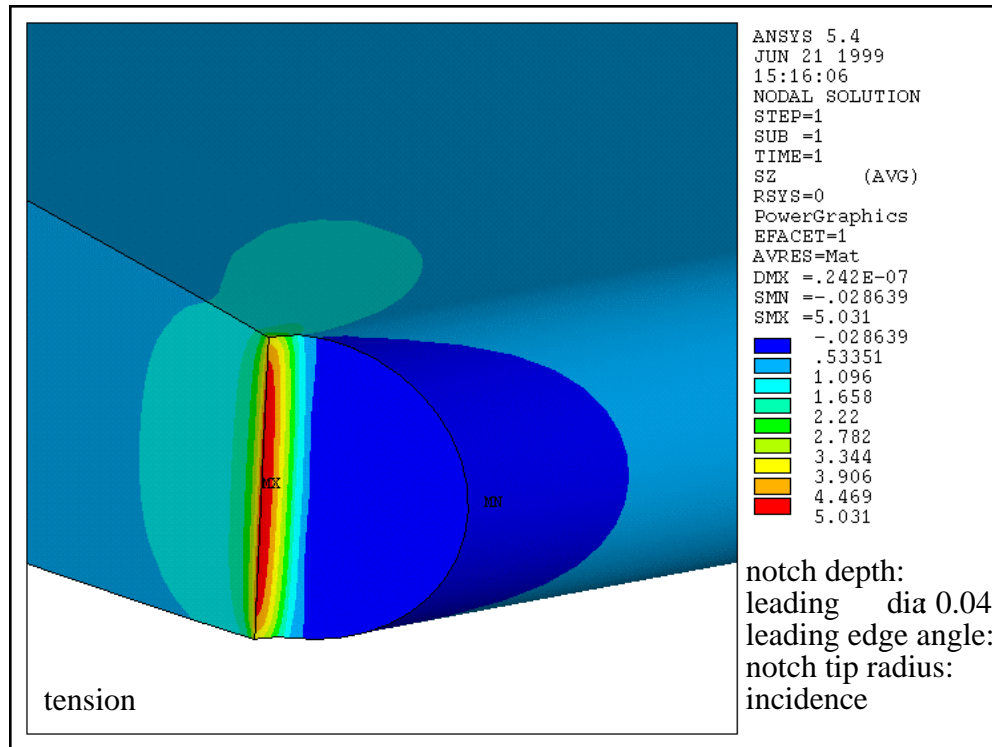
w_9



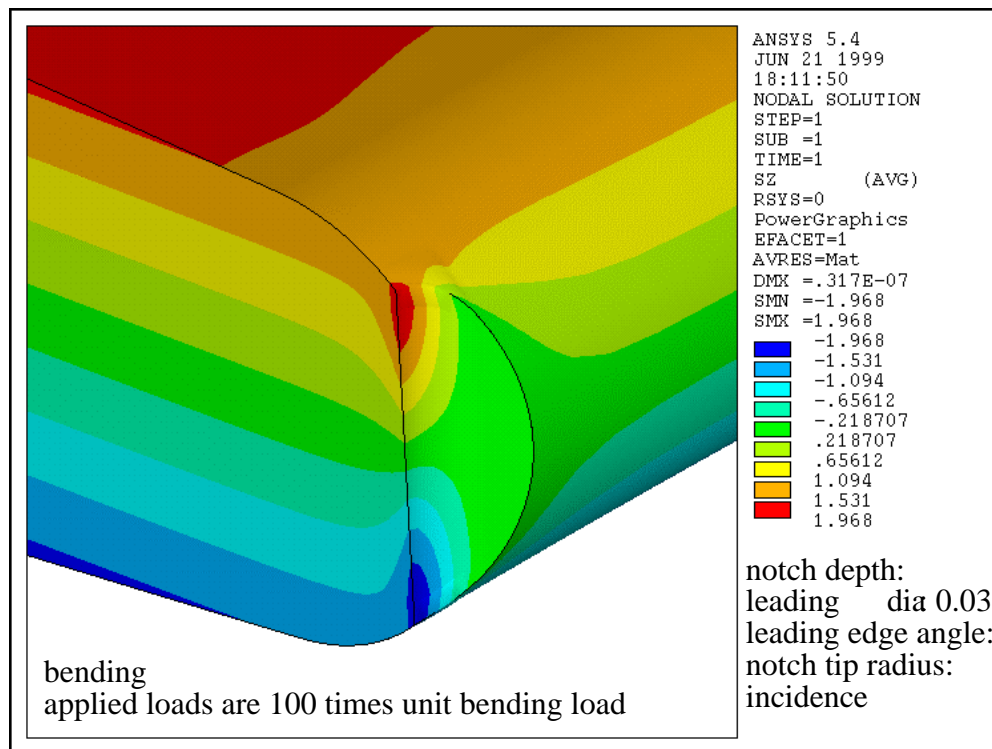
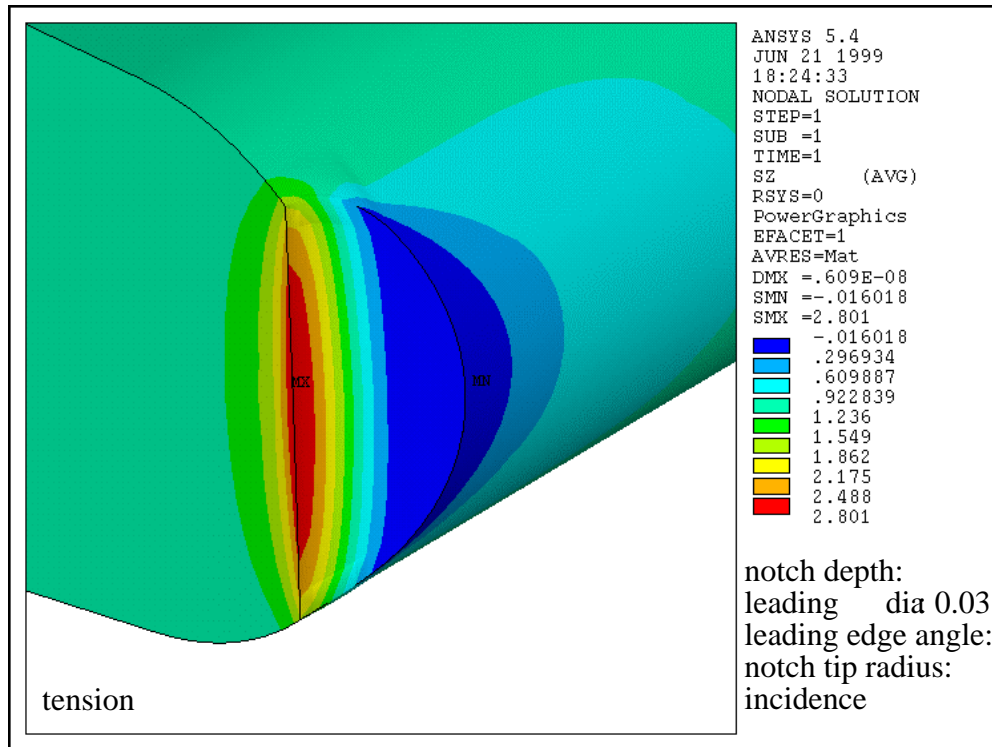
w_10



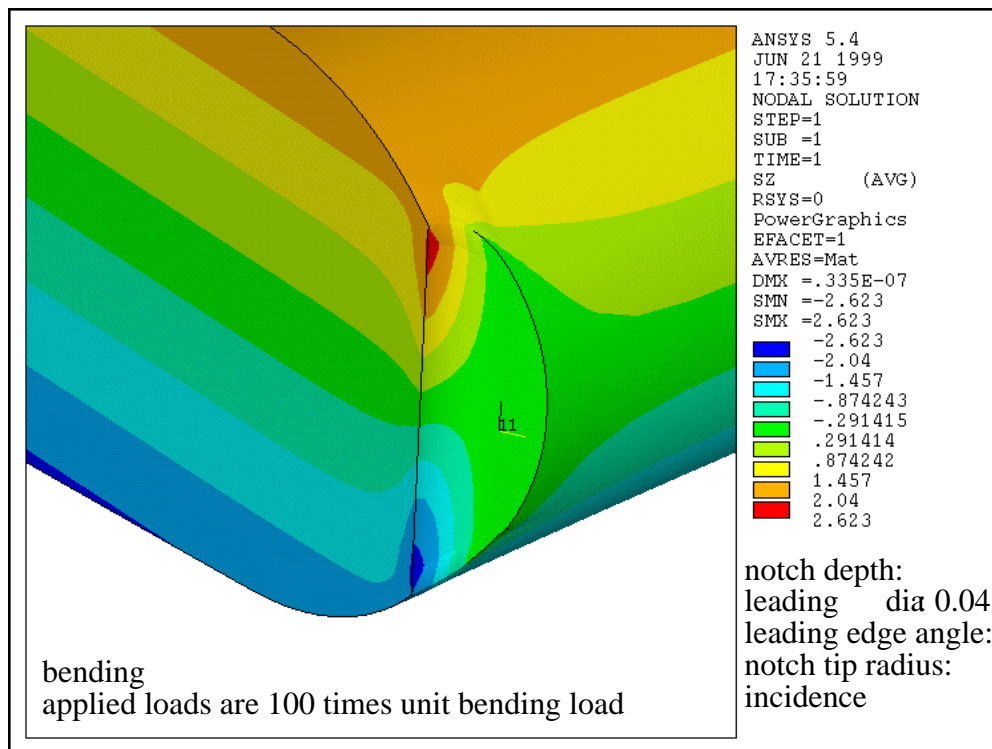
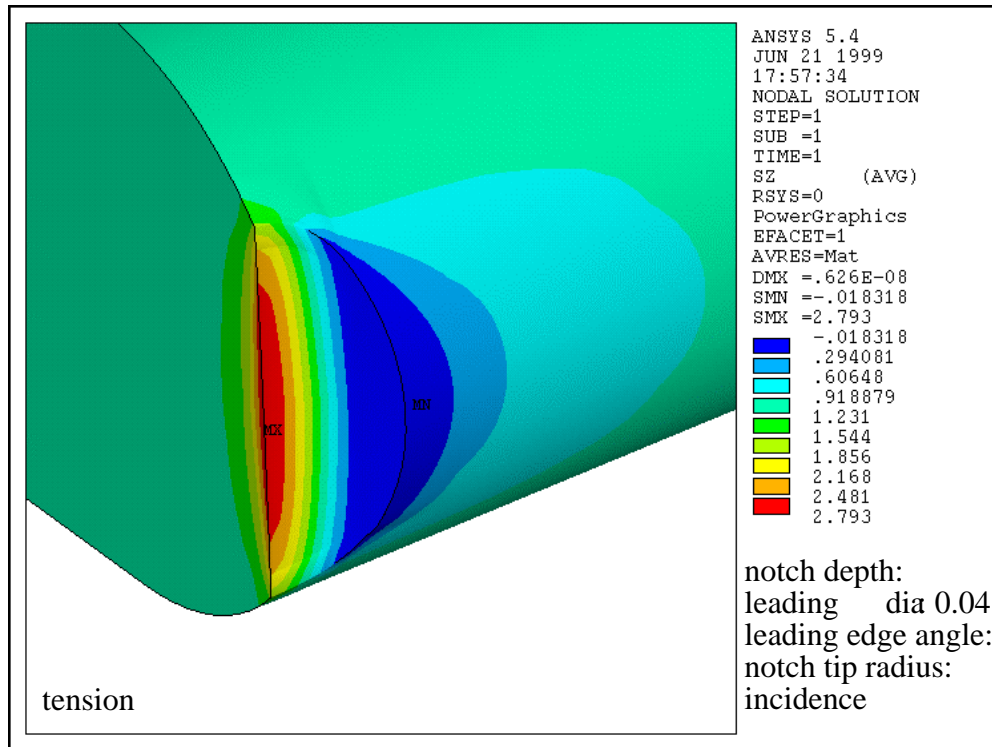
w_11



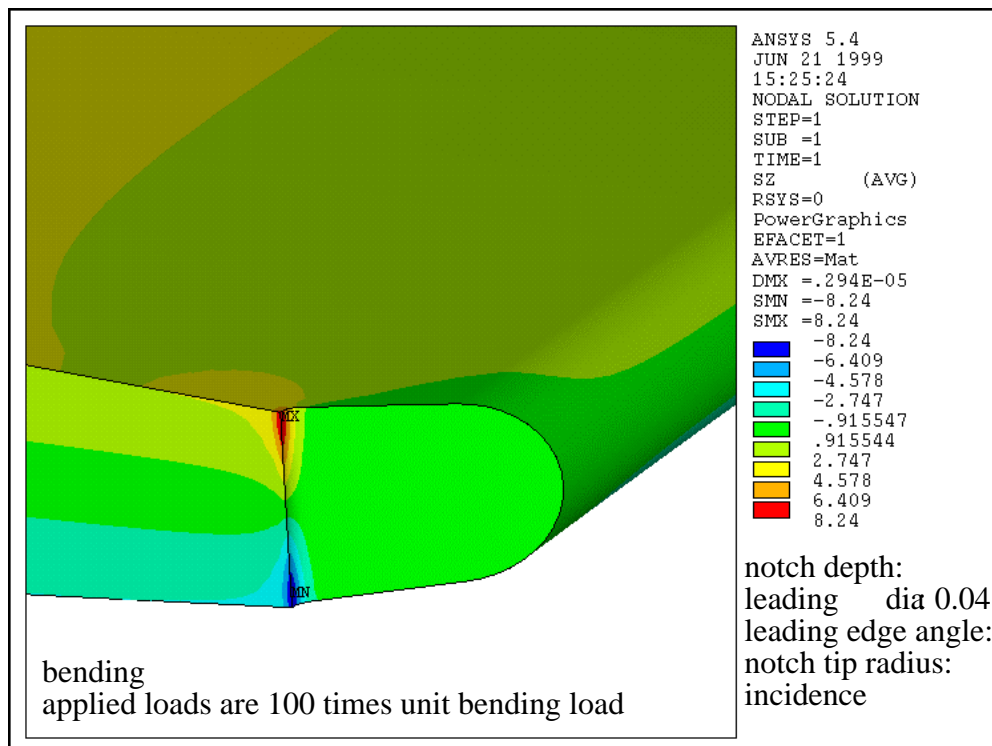
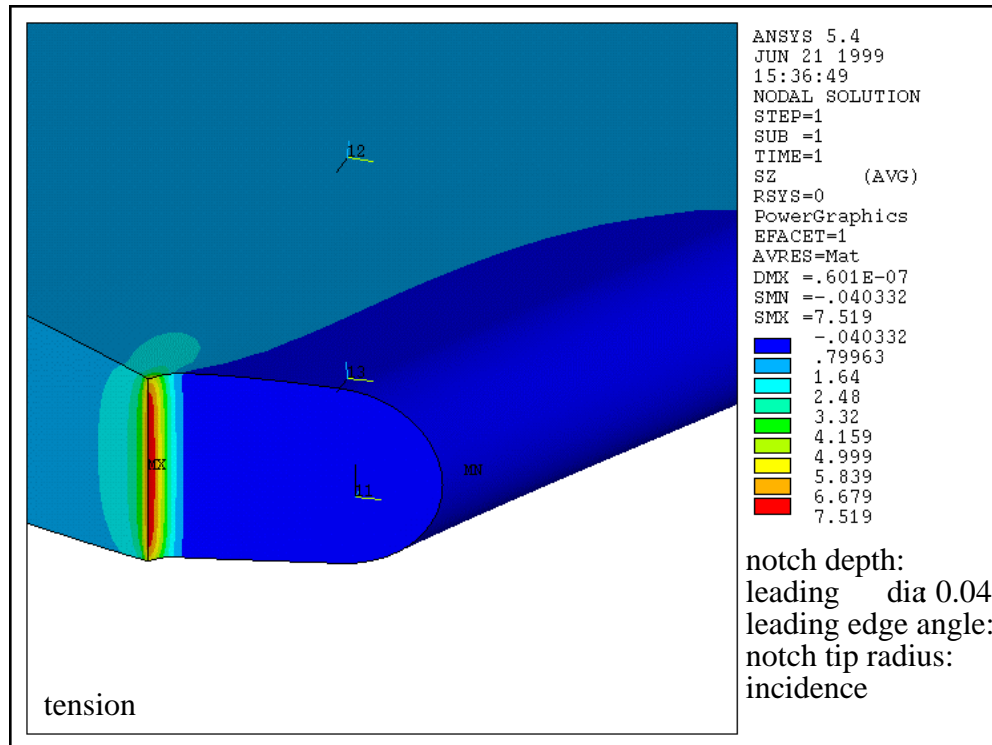
w₁₂



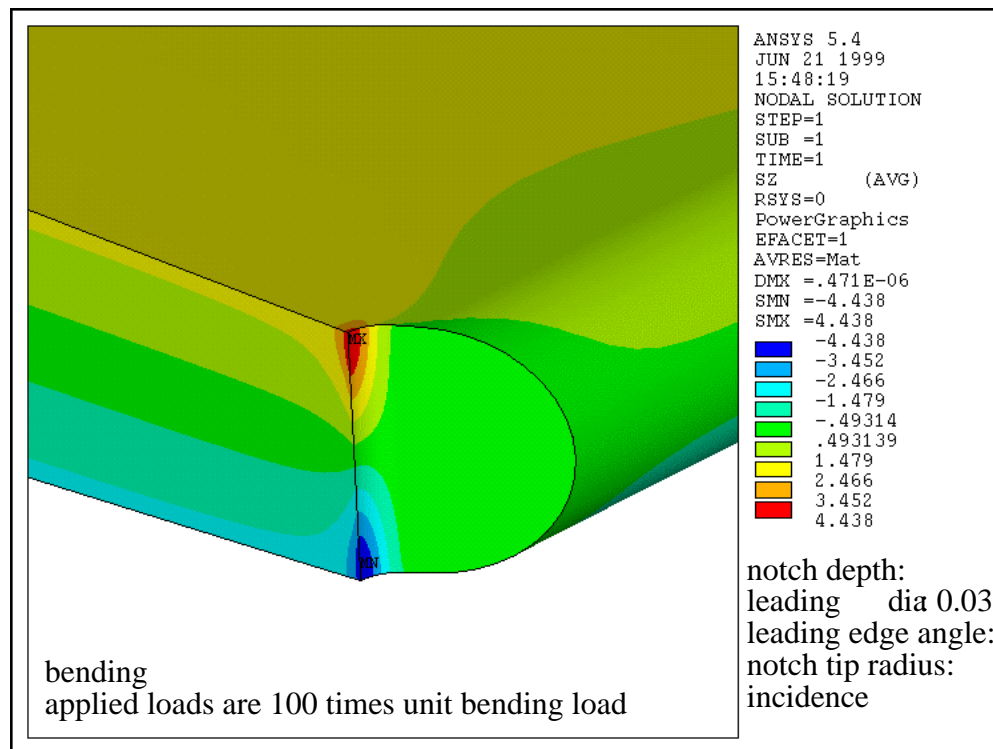
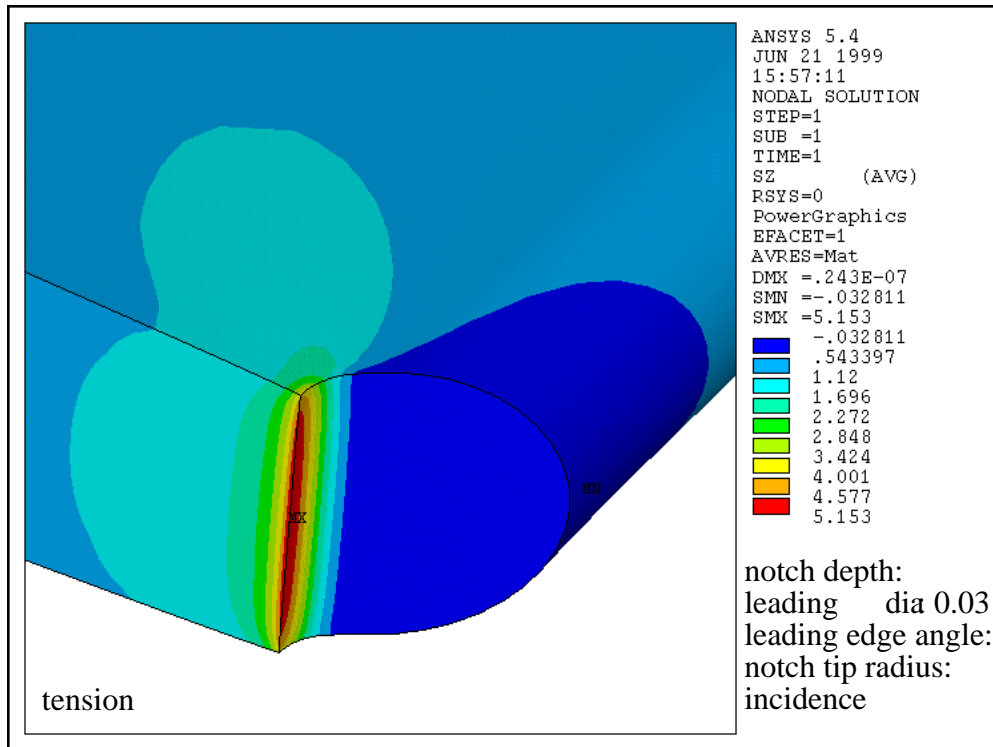
w_13



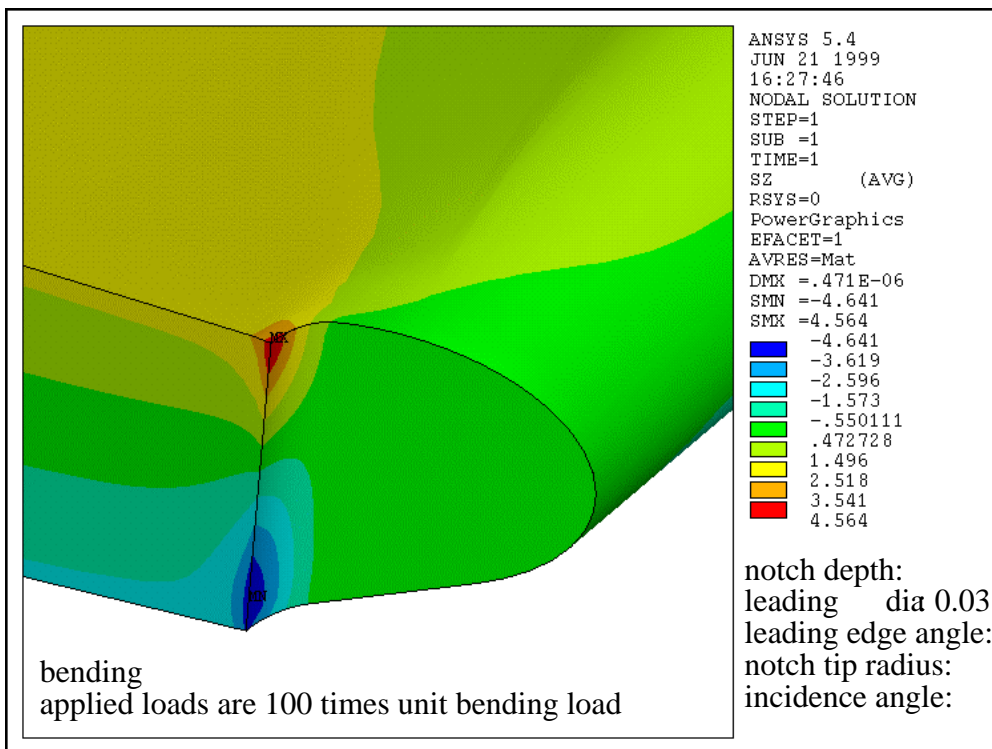
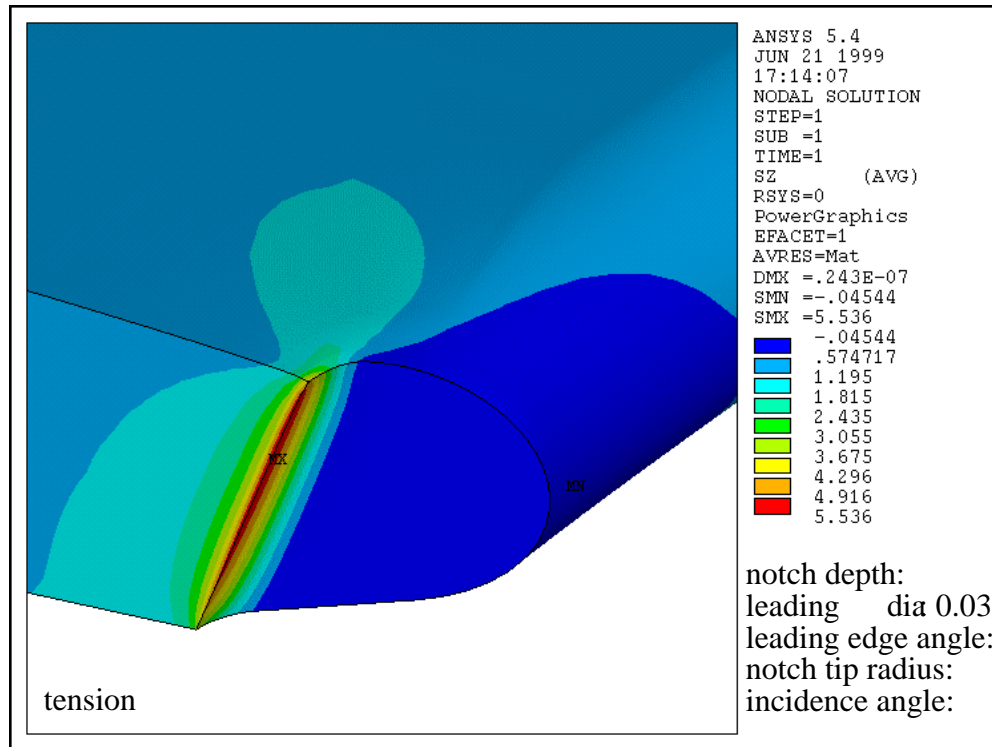
w_14



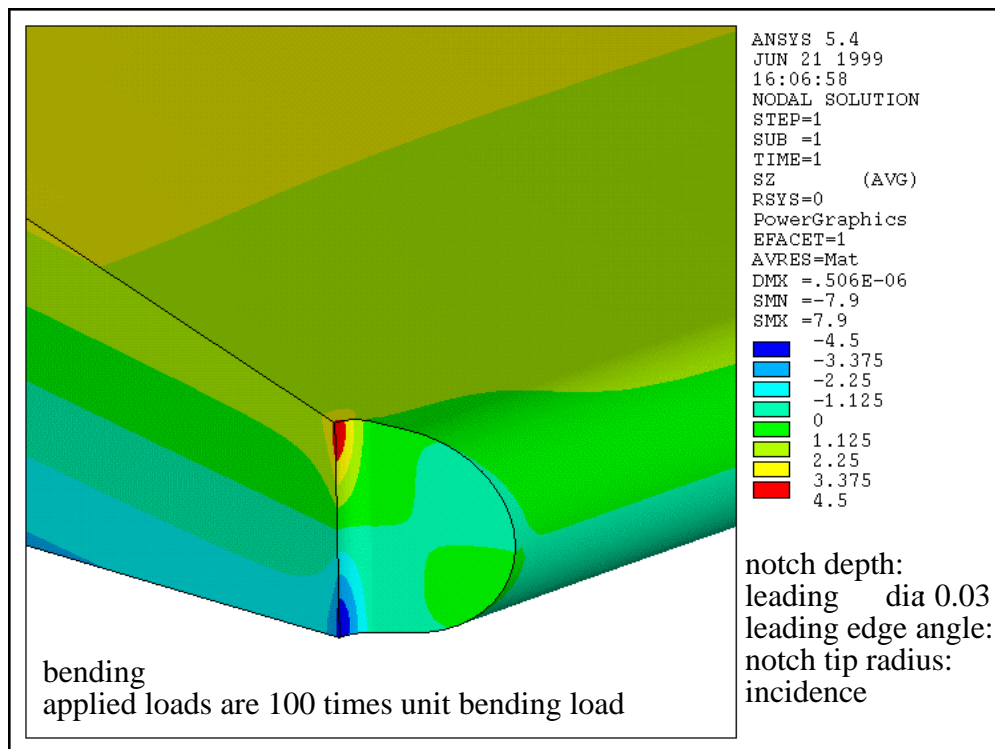
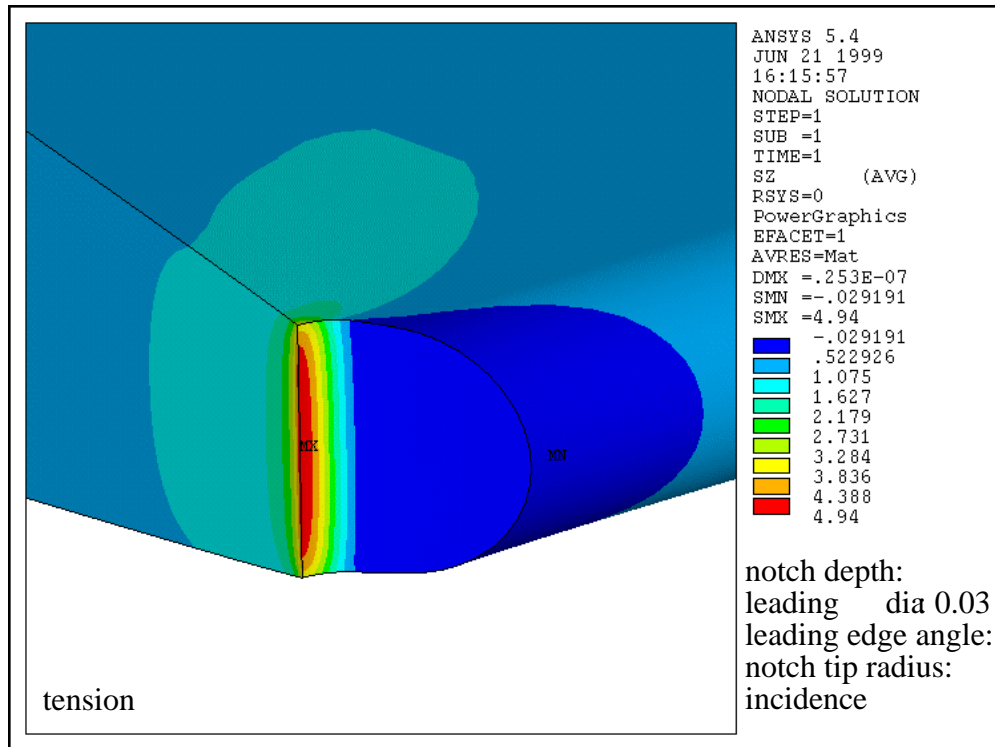
w_15



w_16



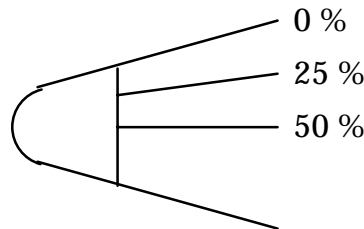
w_17



w_18

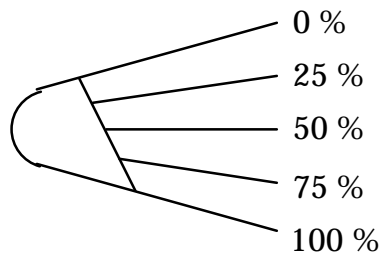
Attachment B: Near Notch-Tip Stress Plots

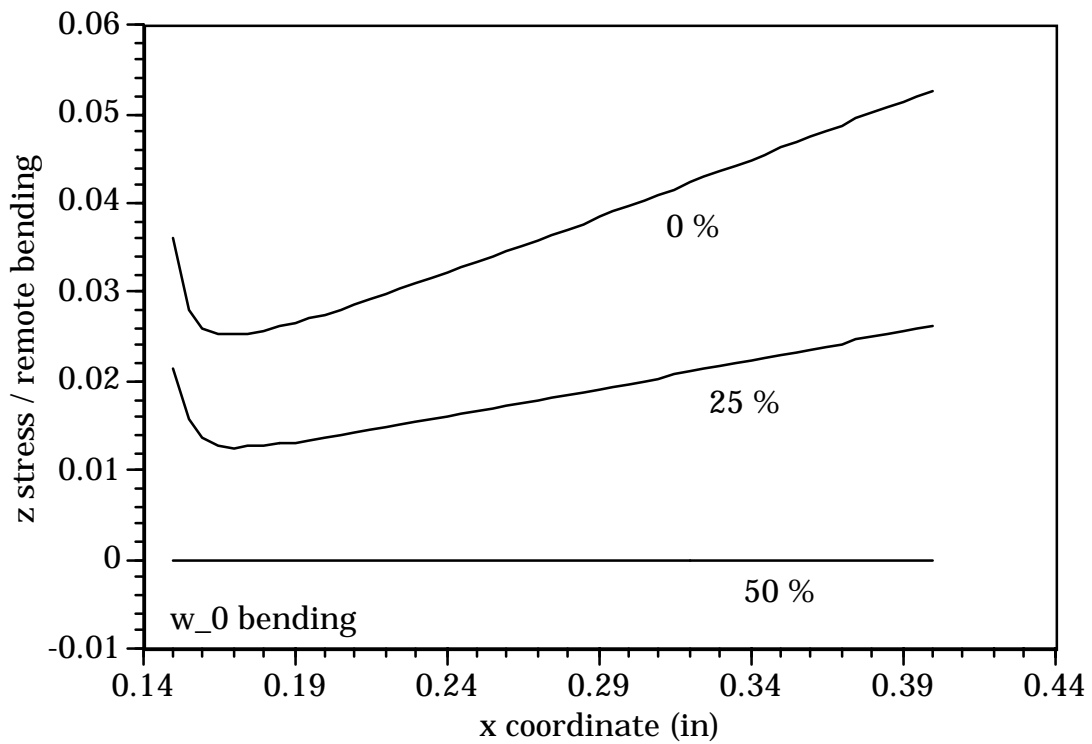
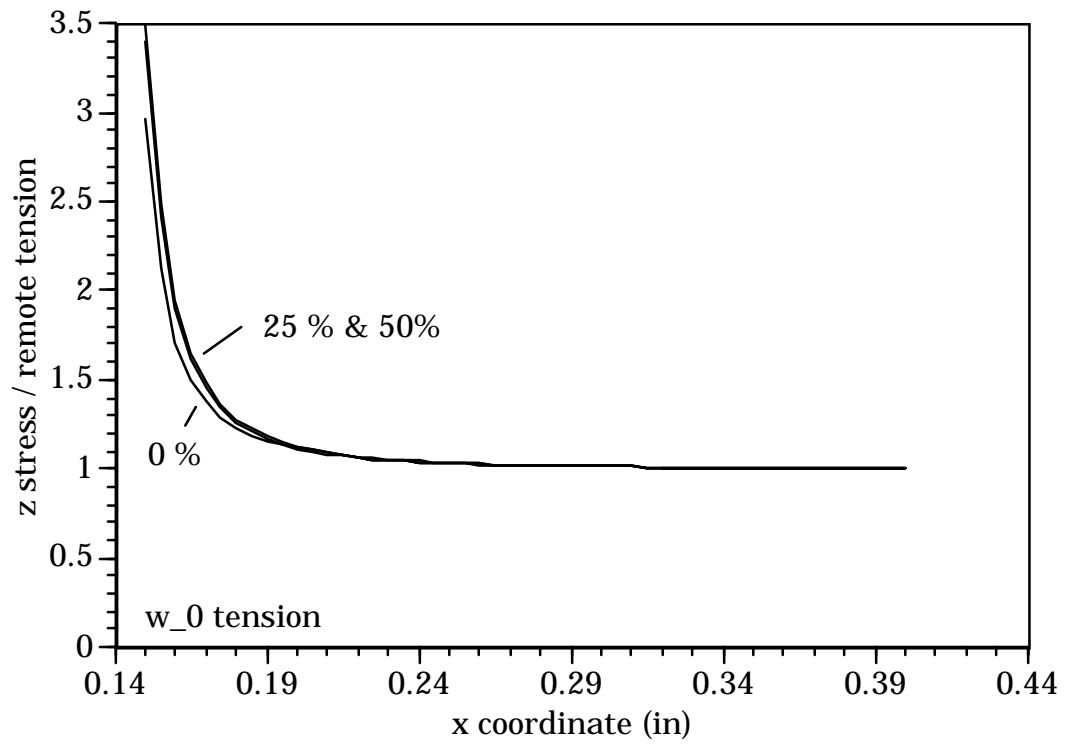
This Attachment contains plots of the z stresses along lines emanating from the notch tip. Models with a zero notch incidence angle are symmetric about a horizontal axis. In this case only the 0, 25, and 50% lines are plotted, as shown below.



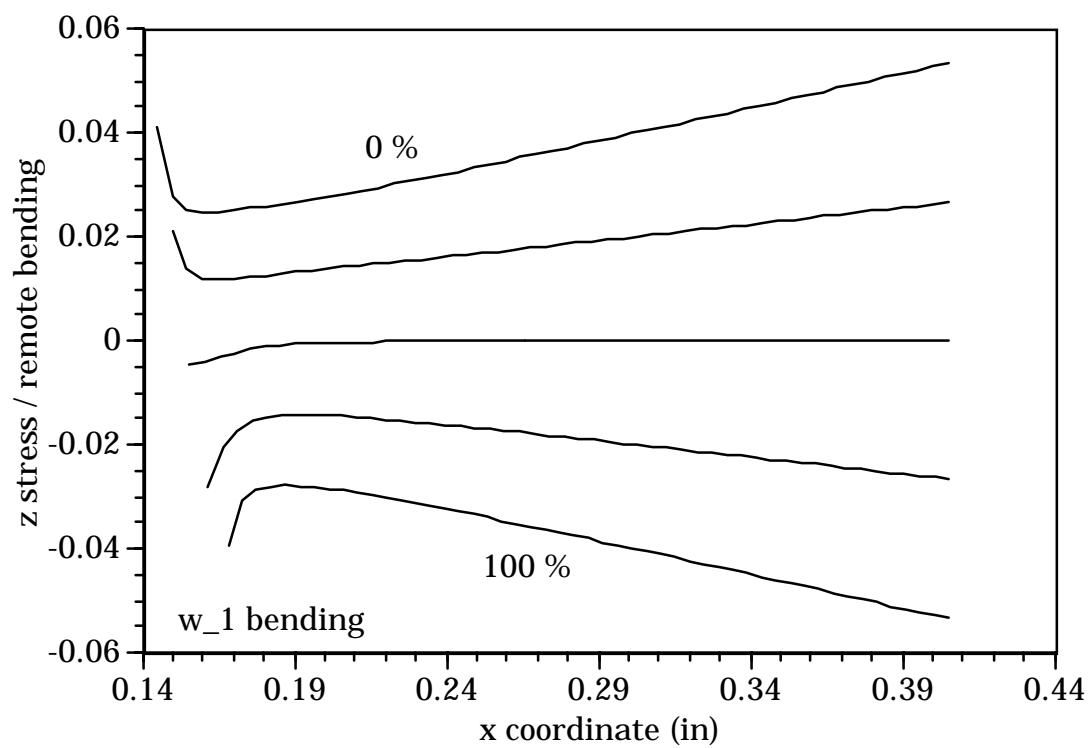
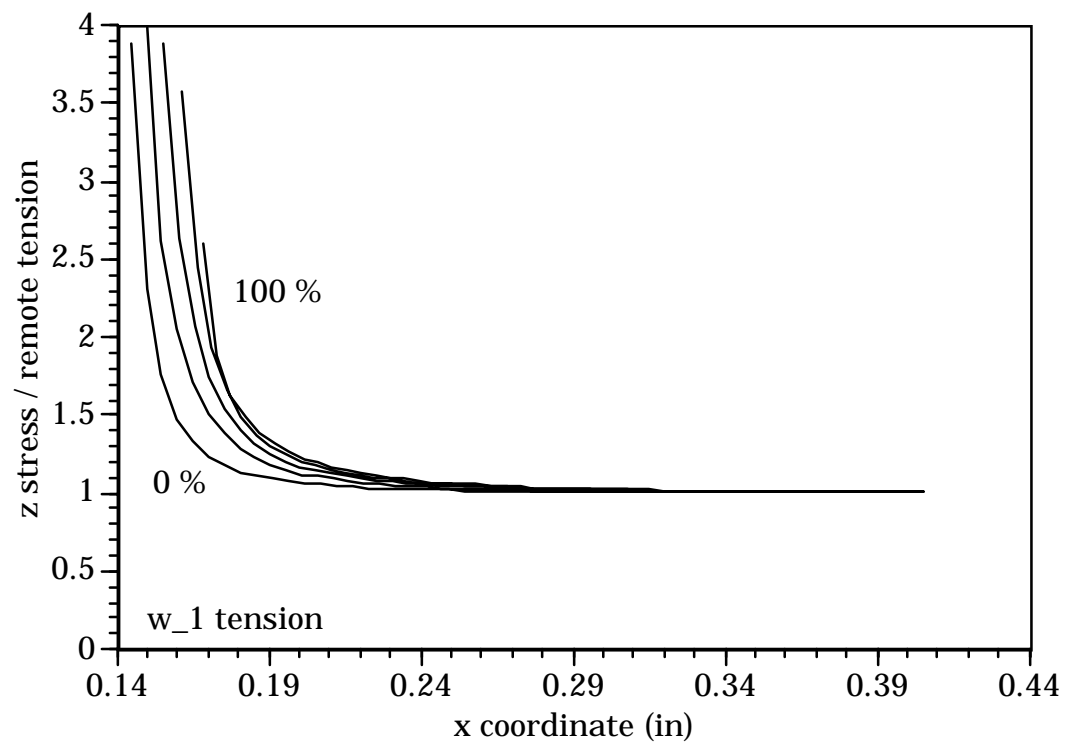
For the tension case, the 75 and 100% lines will be the same as the 25 and 0% lines, respectively. For the bending case, the 75 and 100% lines will be equal in magnitude but opposite in sign (negative) of the 25 and 0% lines.

For models with nonzero incidence angles, stresses are plotted along 0, 25, 50, 75, and 100% lines as shown here.

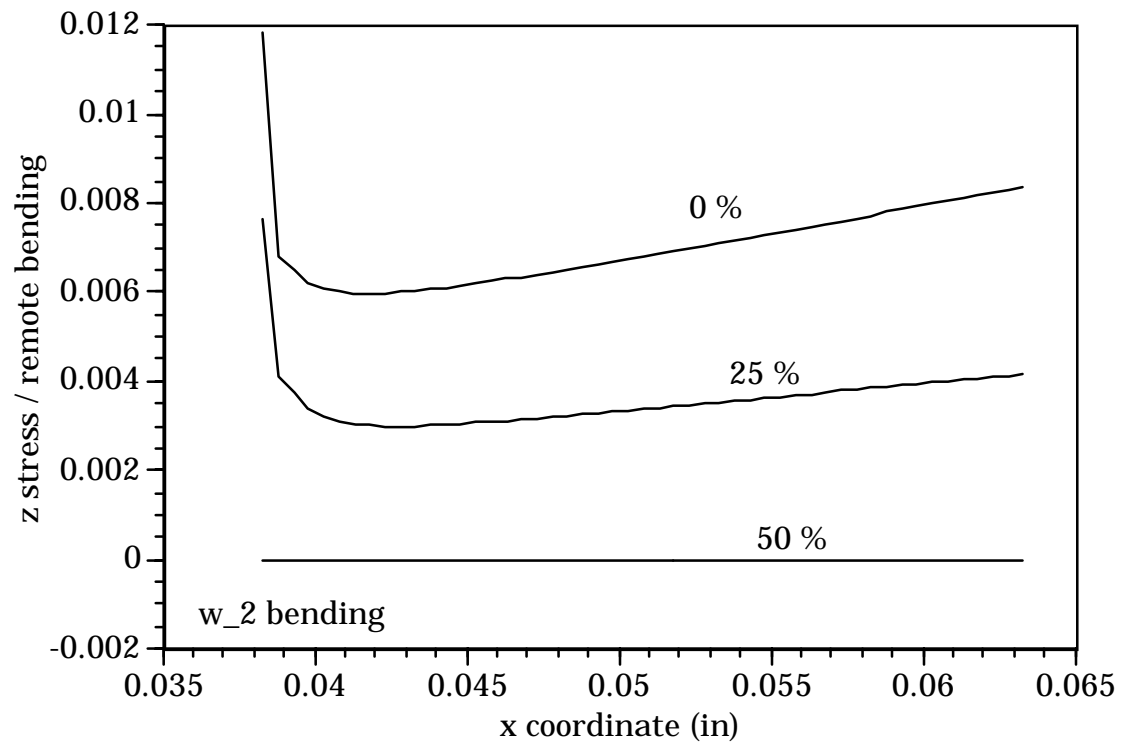
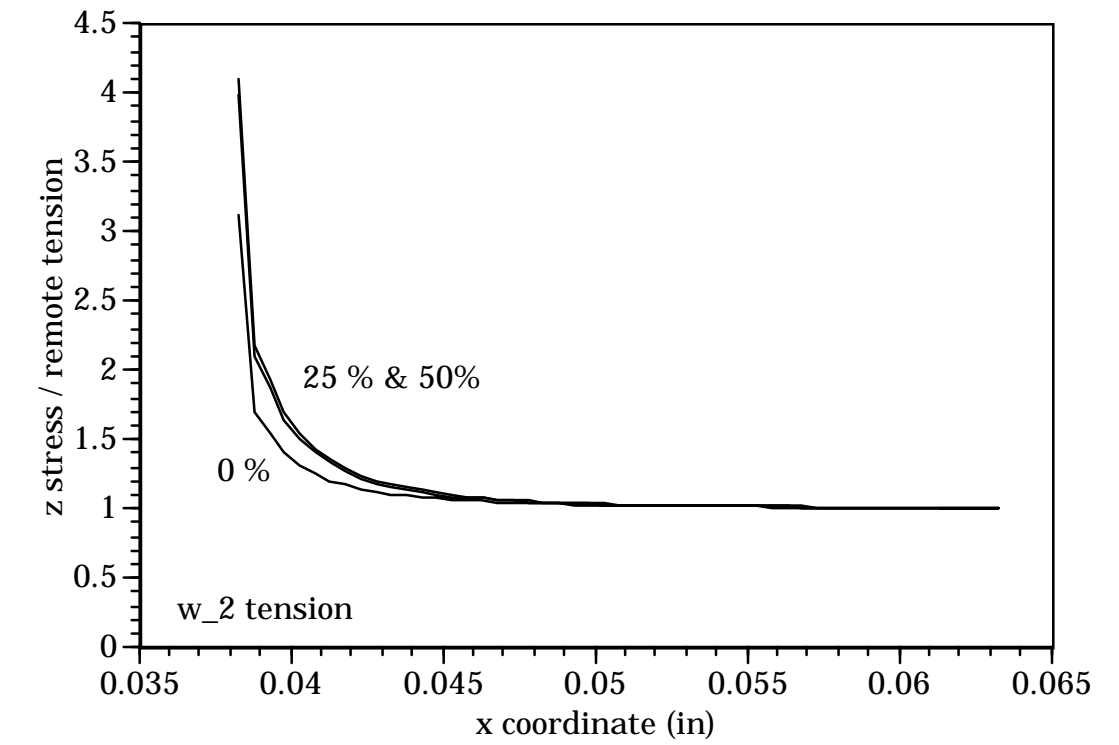




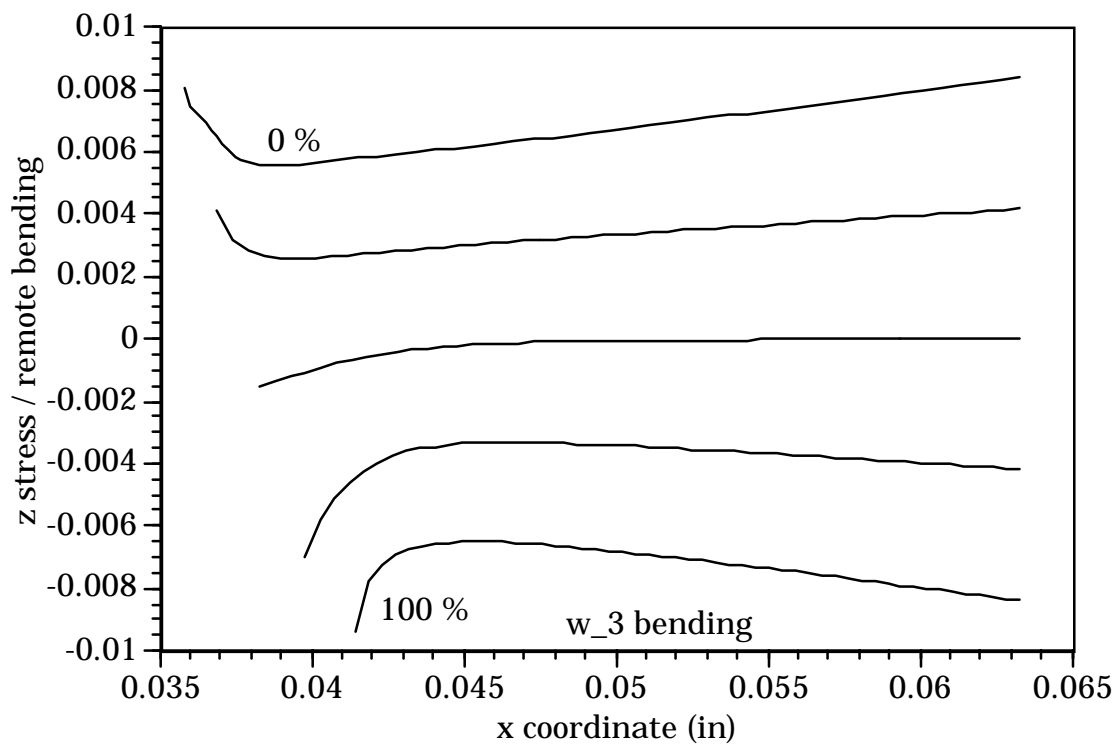
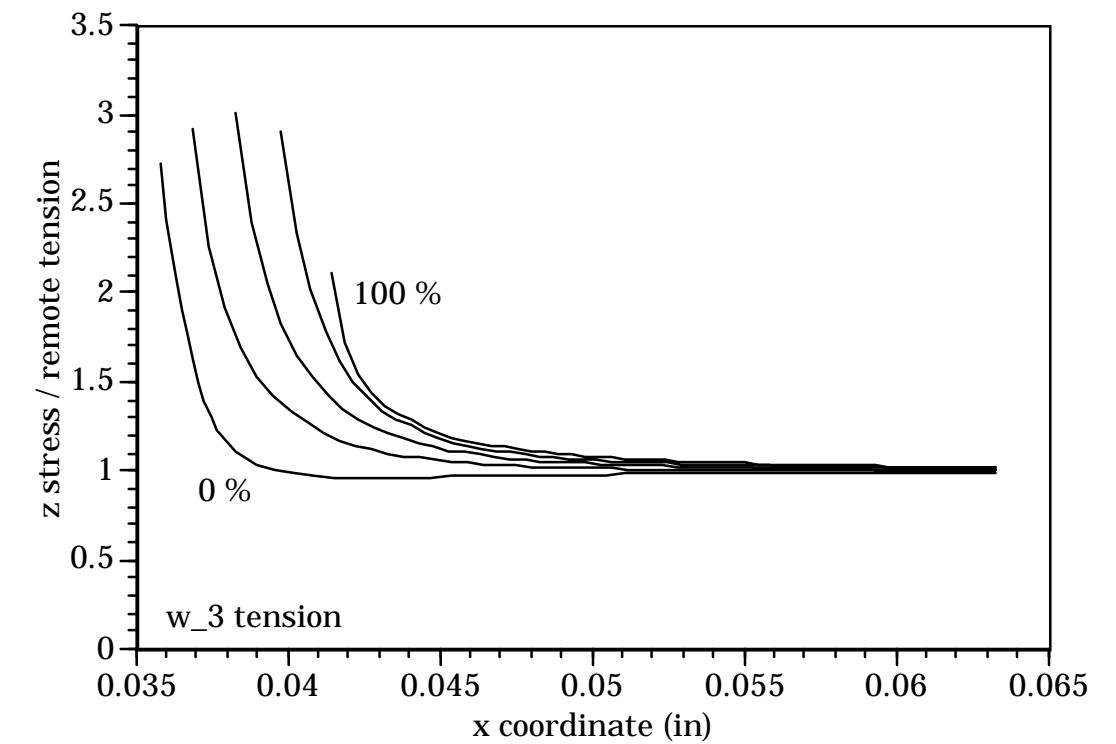
w_0



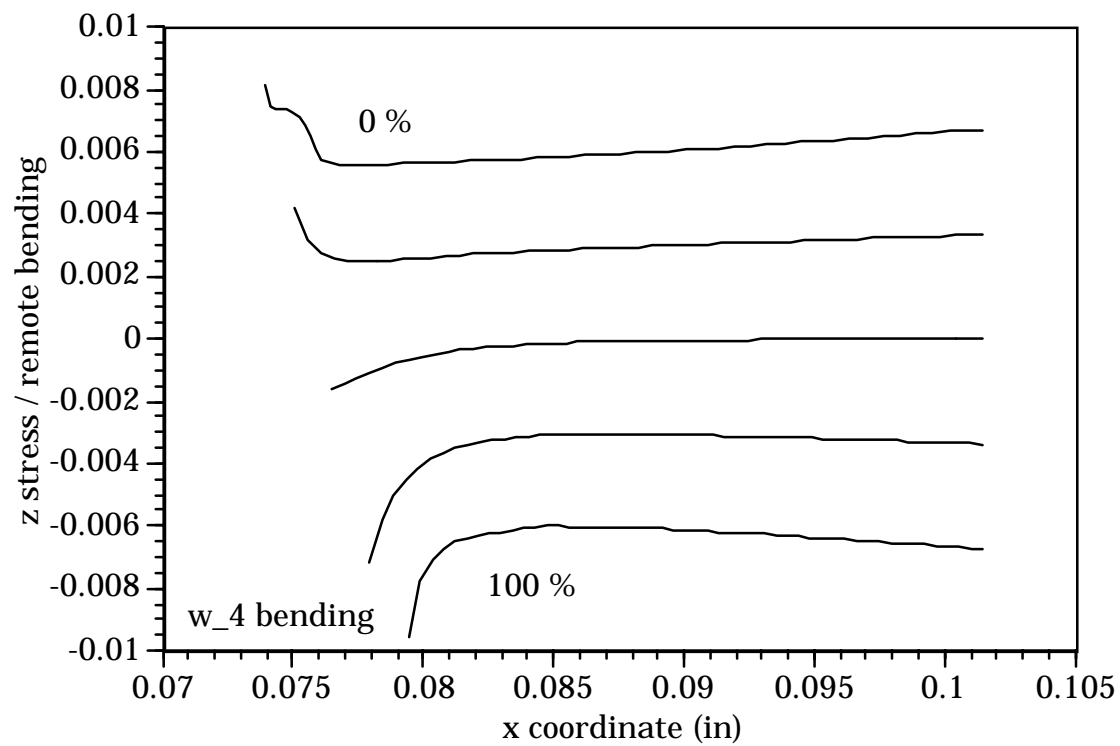
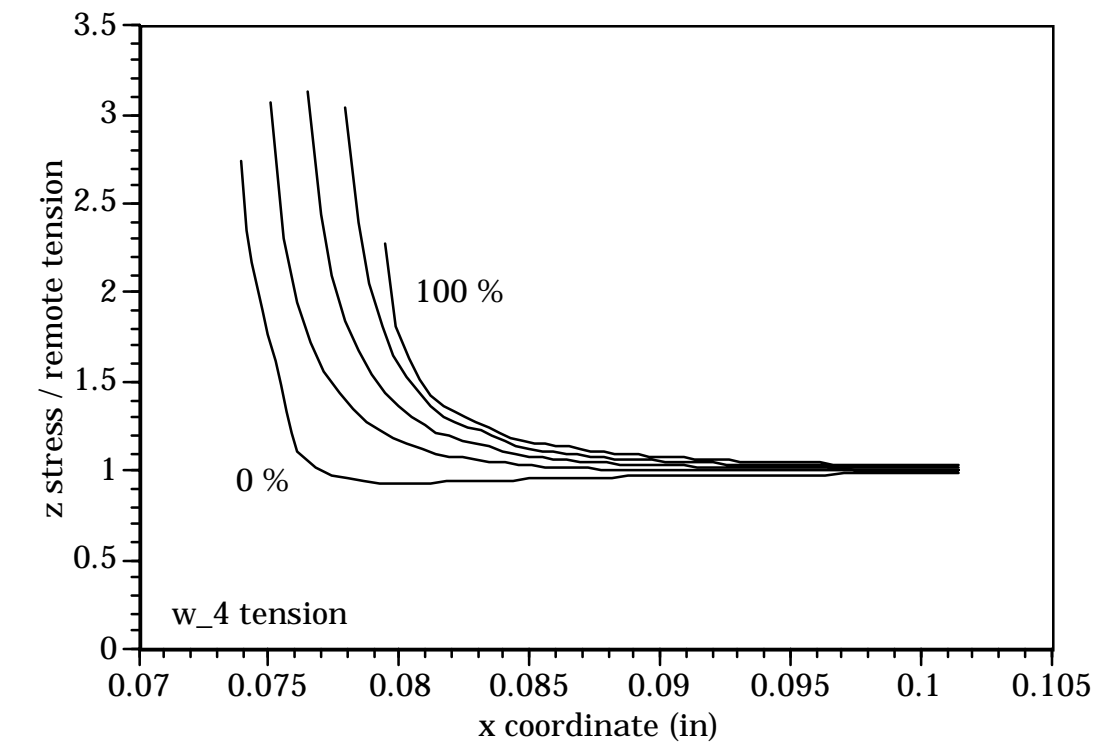
w_1



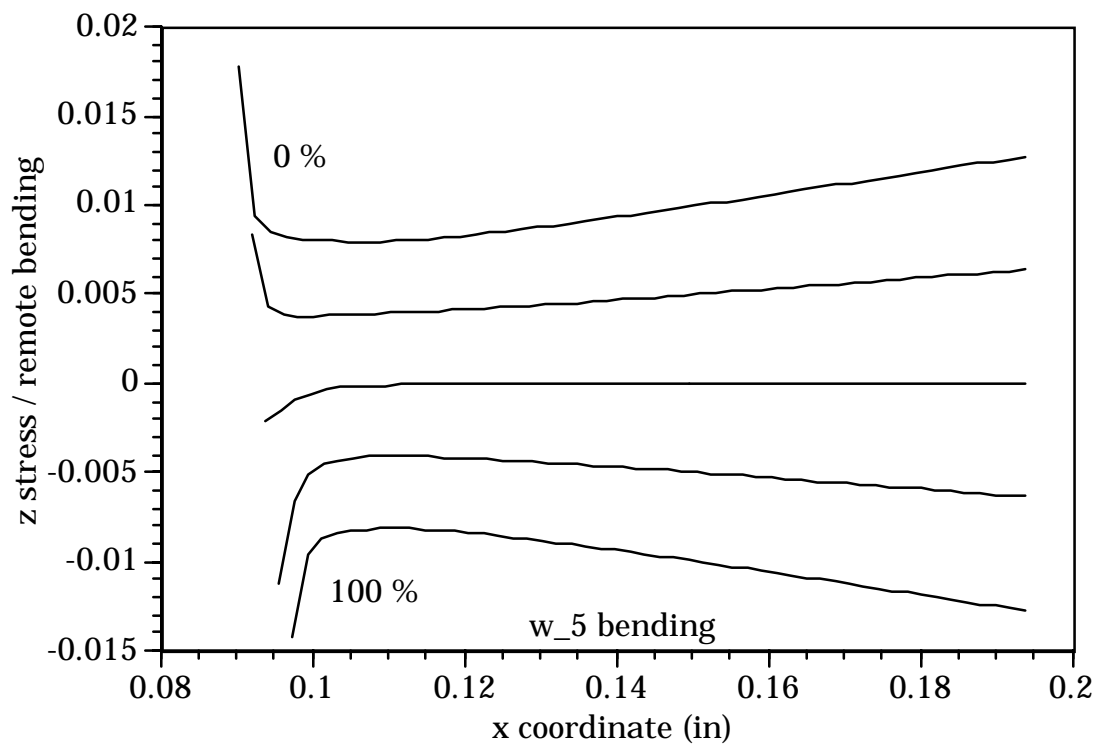
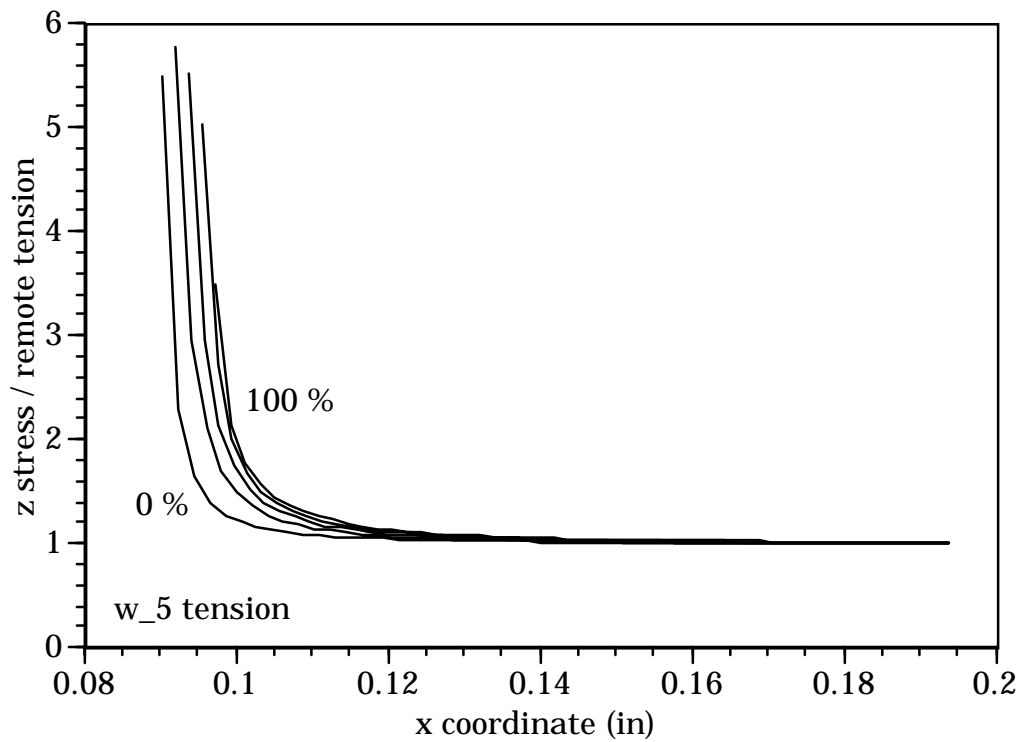
w₂



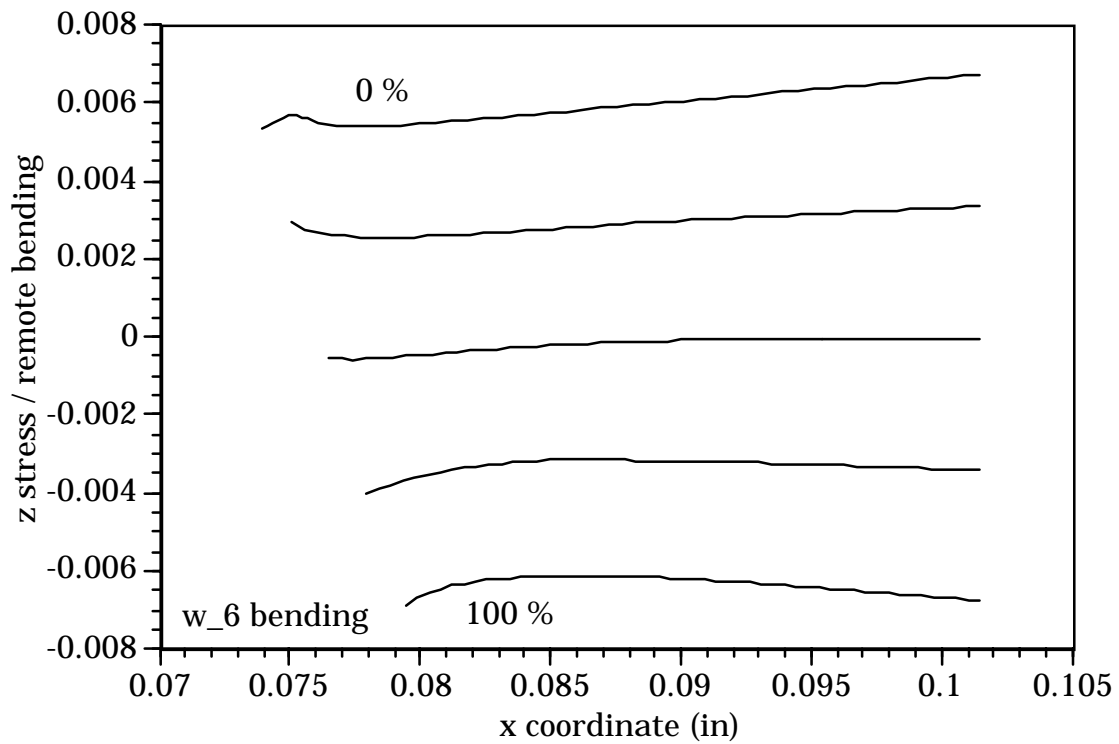
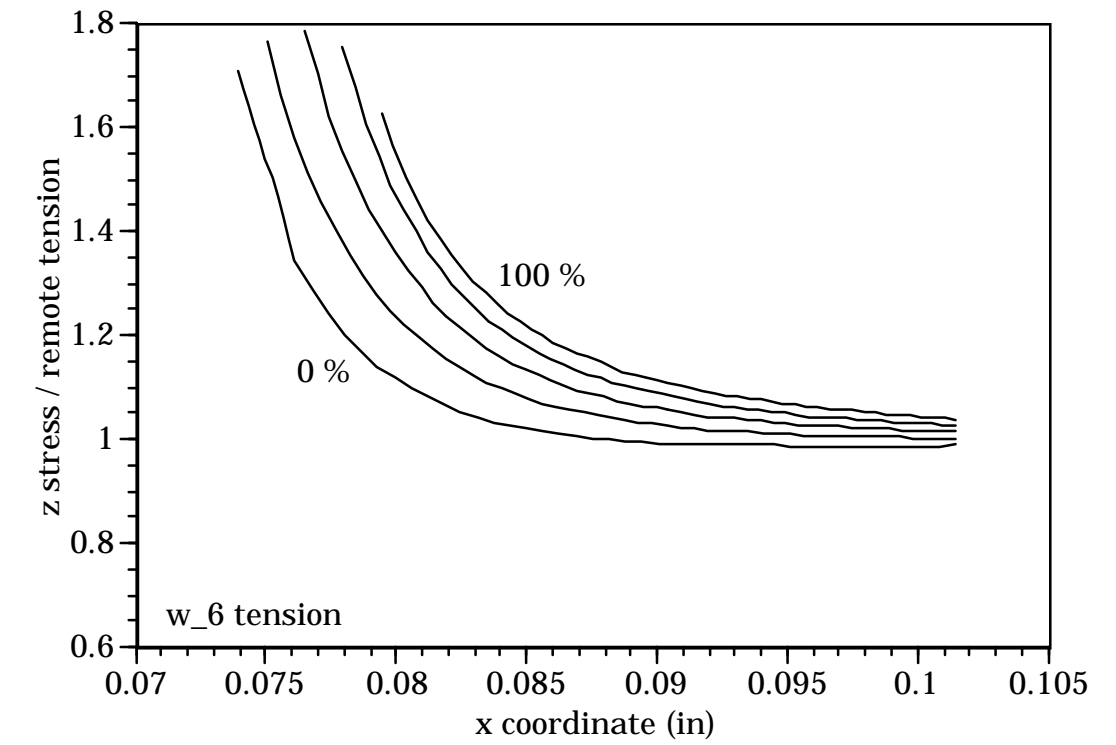
w_3



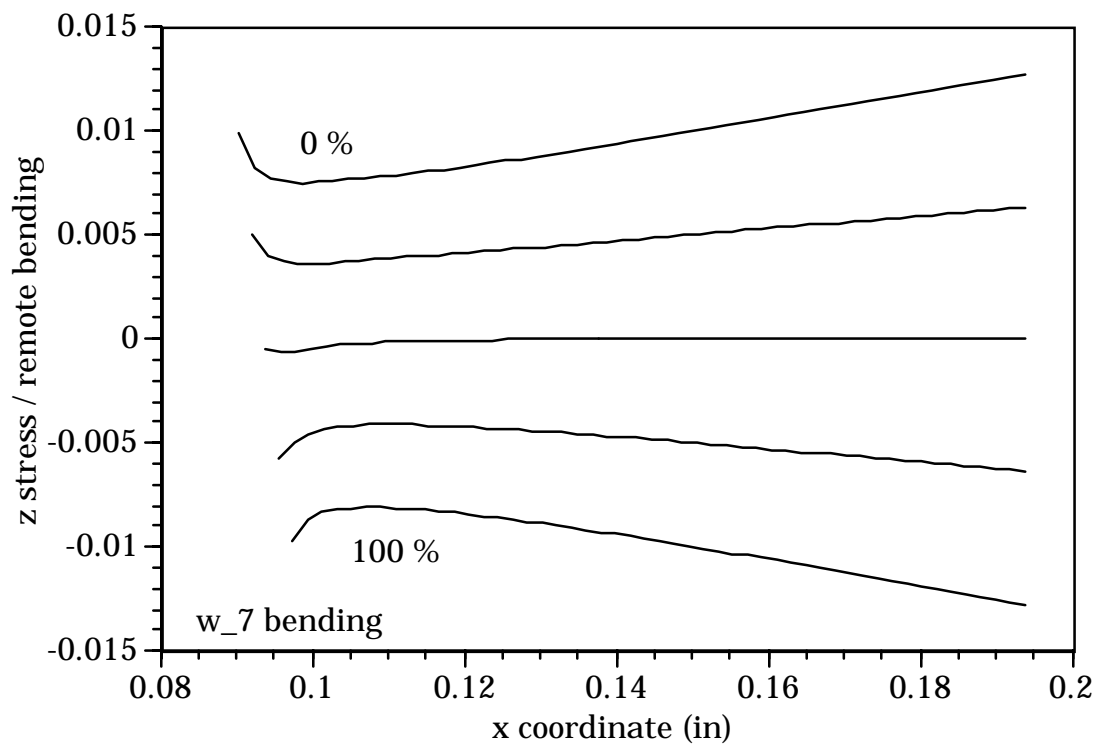
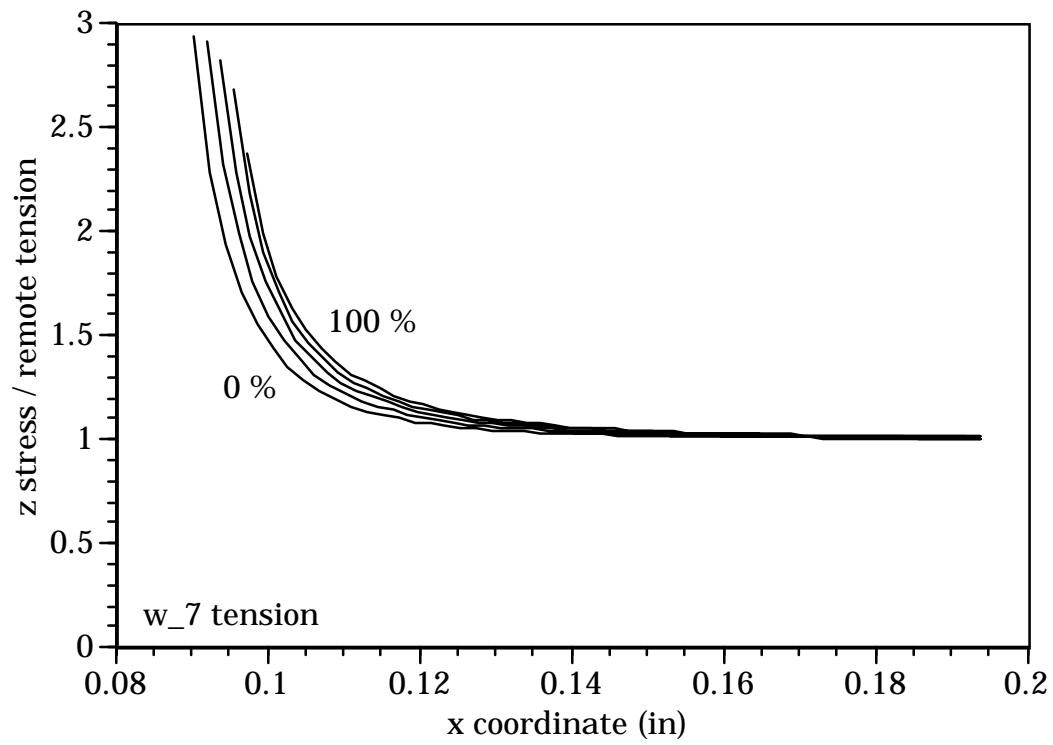
w_4



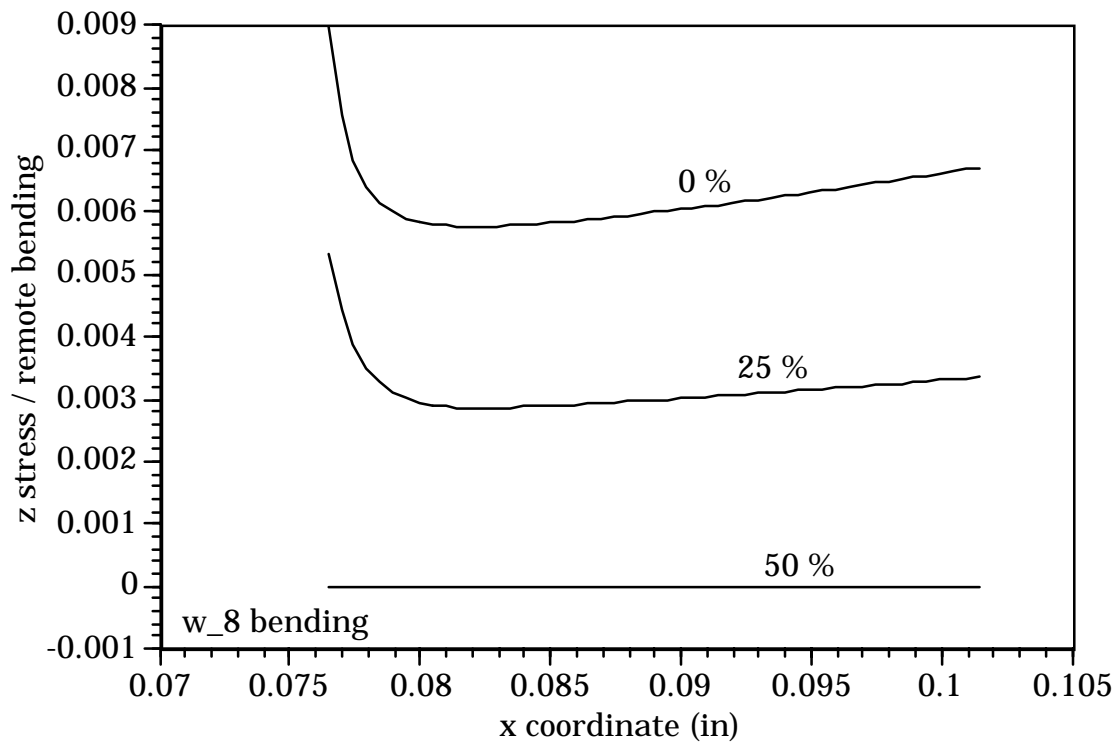
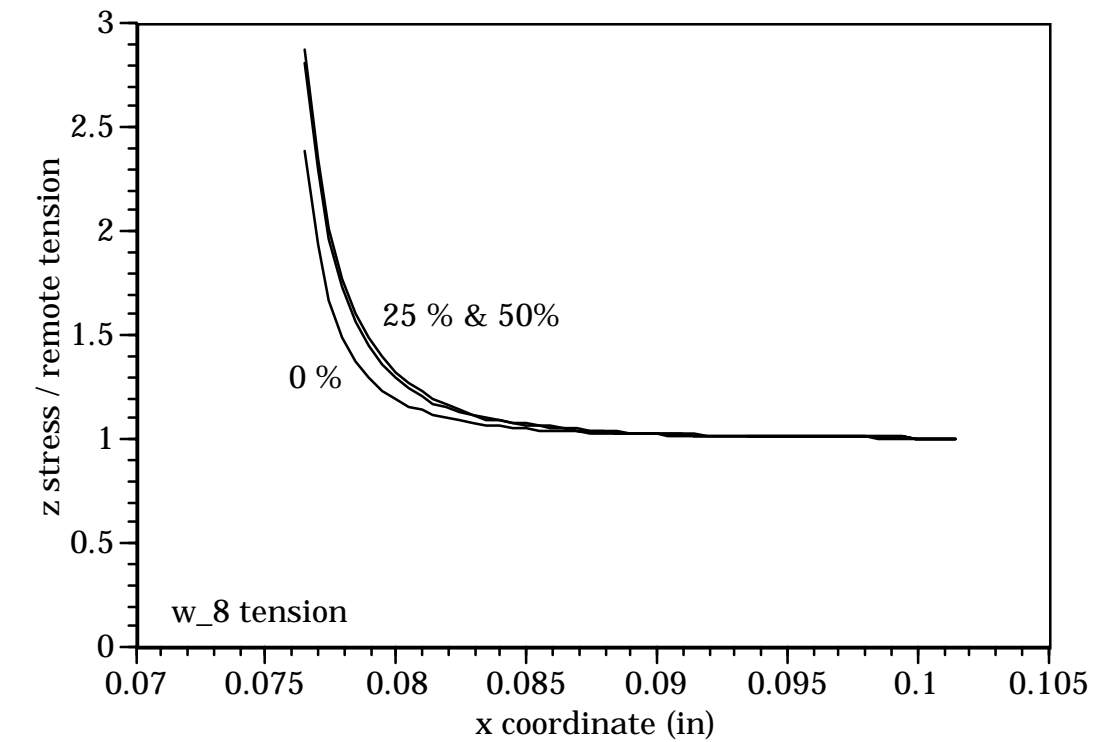
w_5



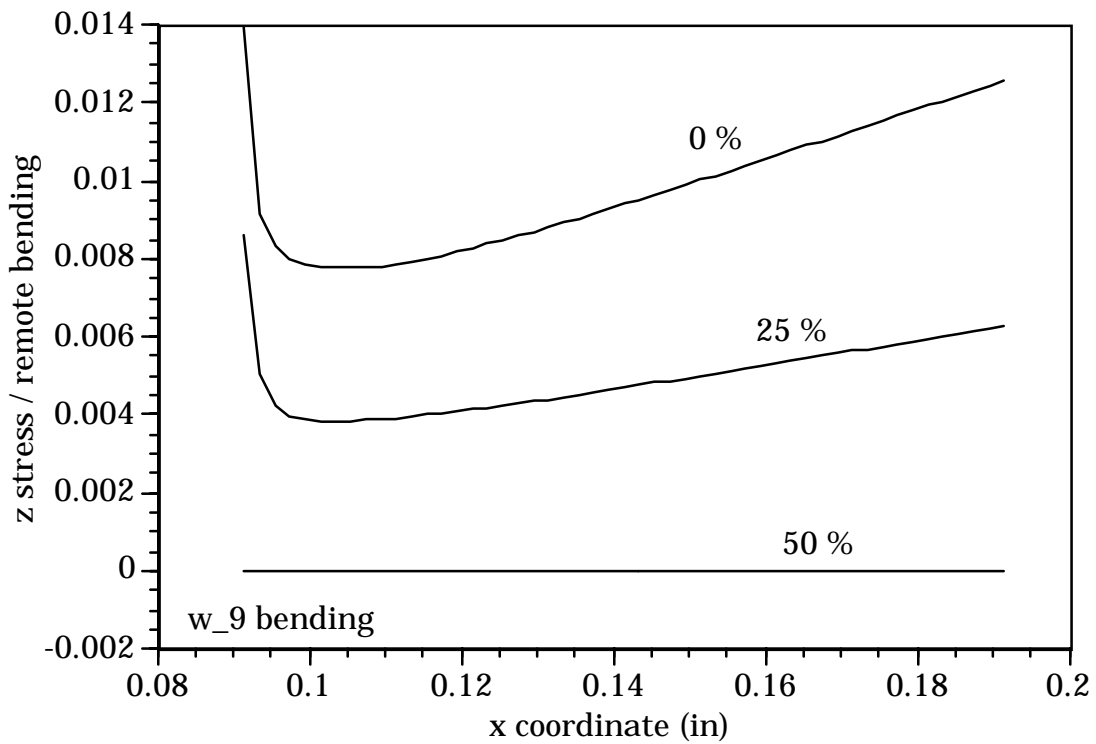
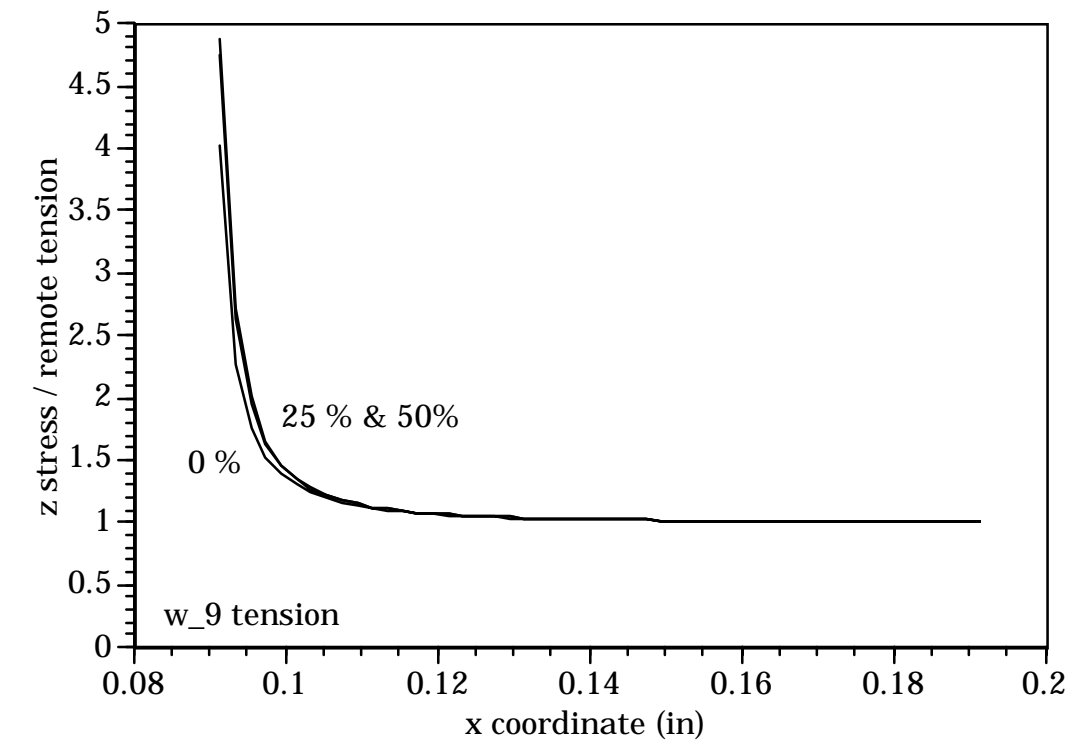
w_6



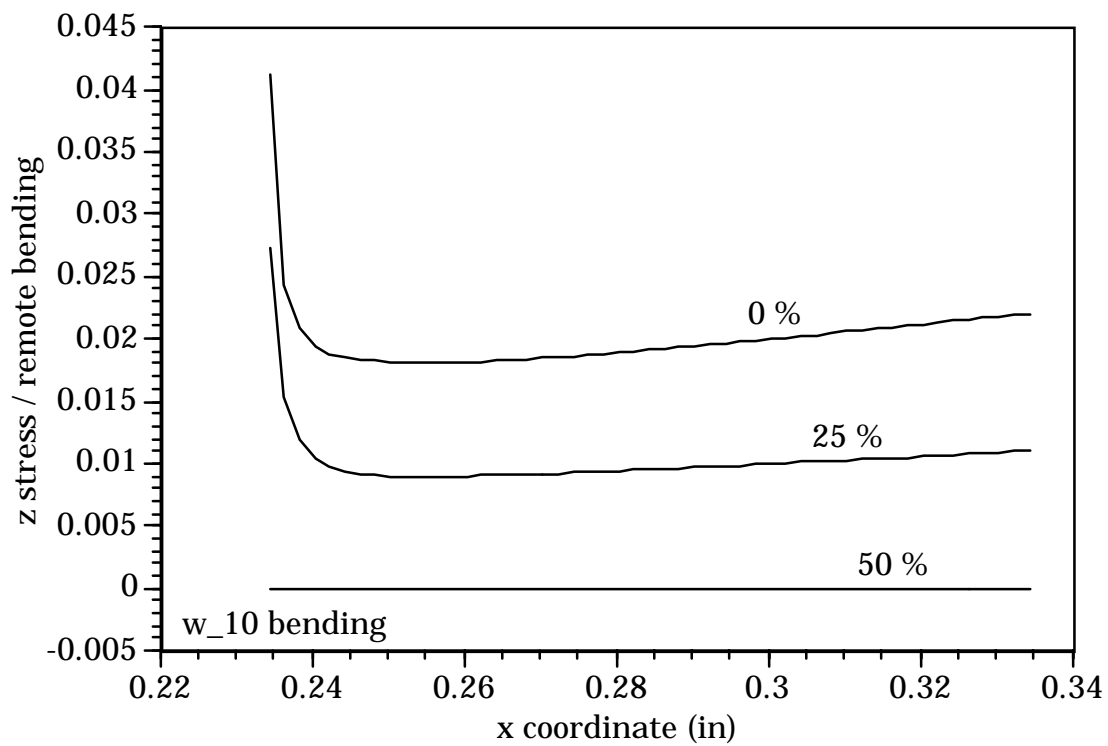
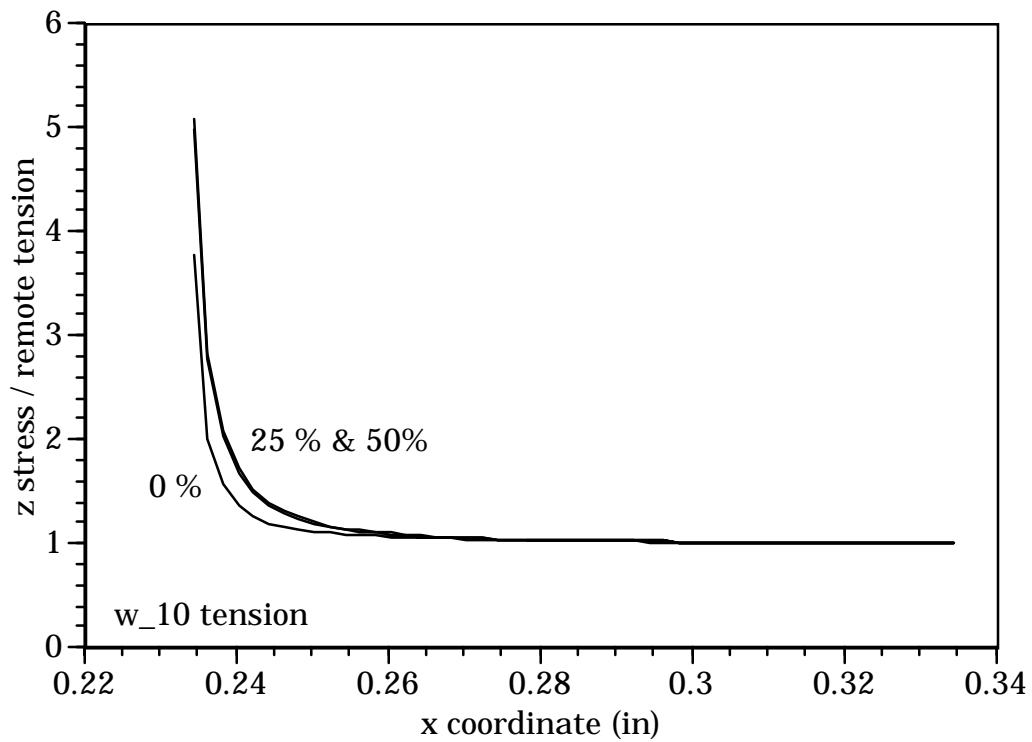
w_7



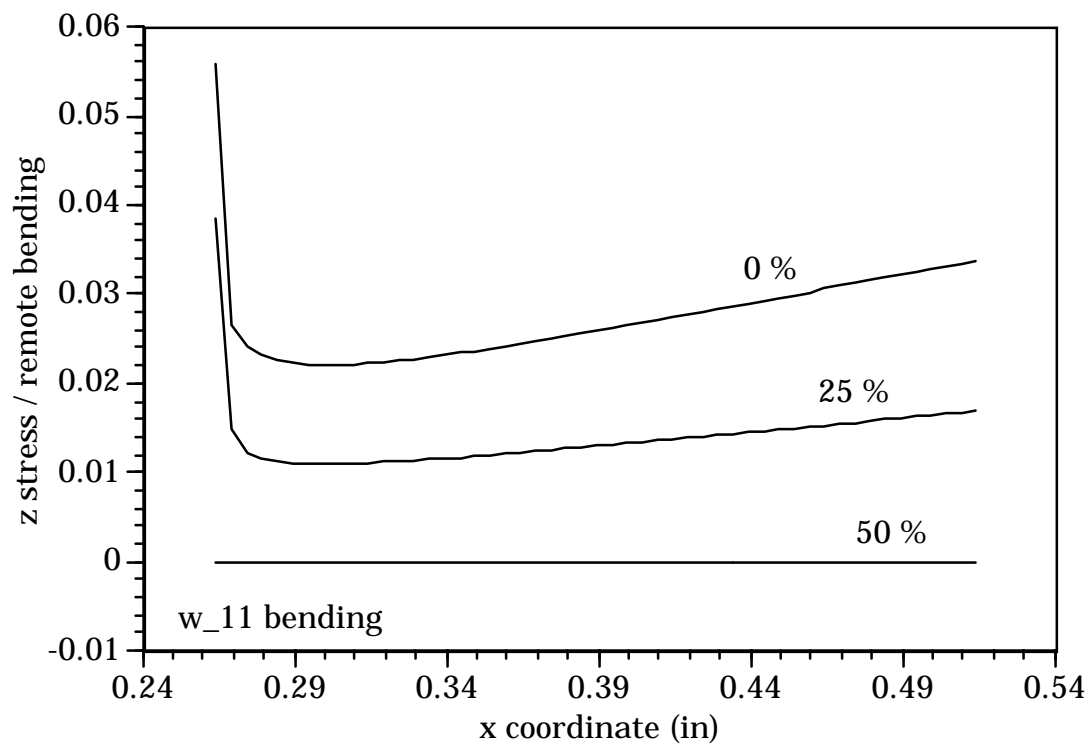
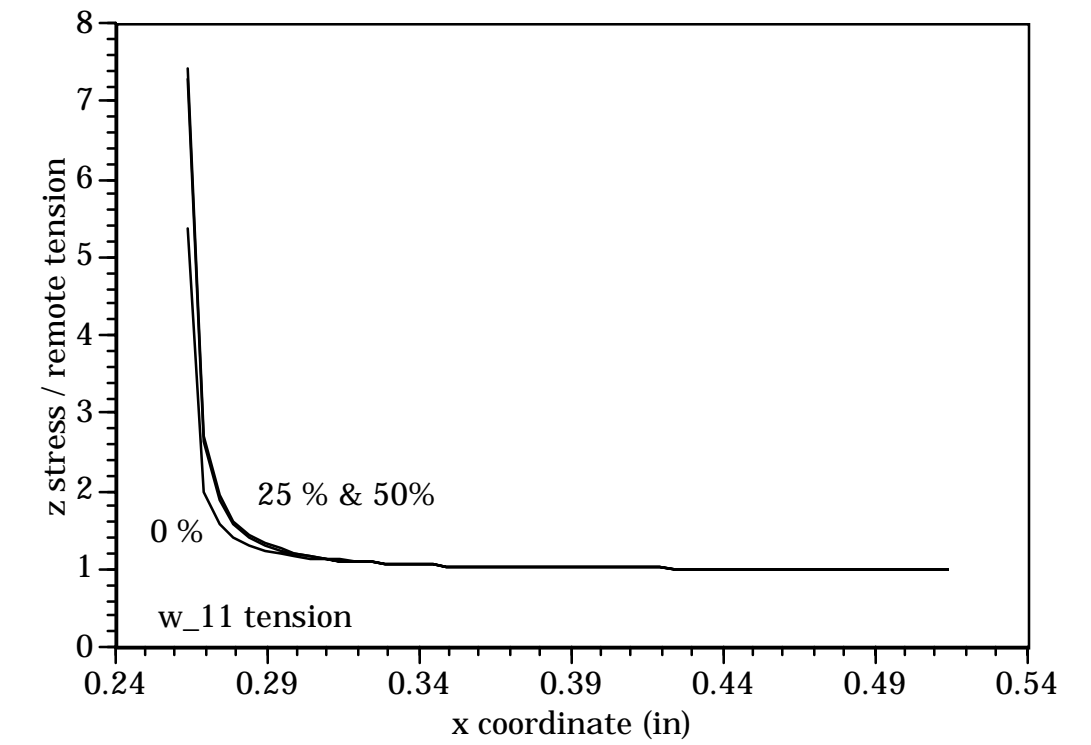
w_8



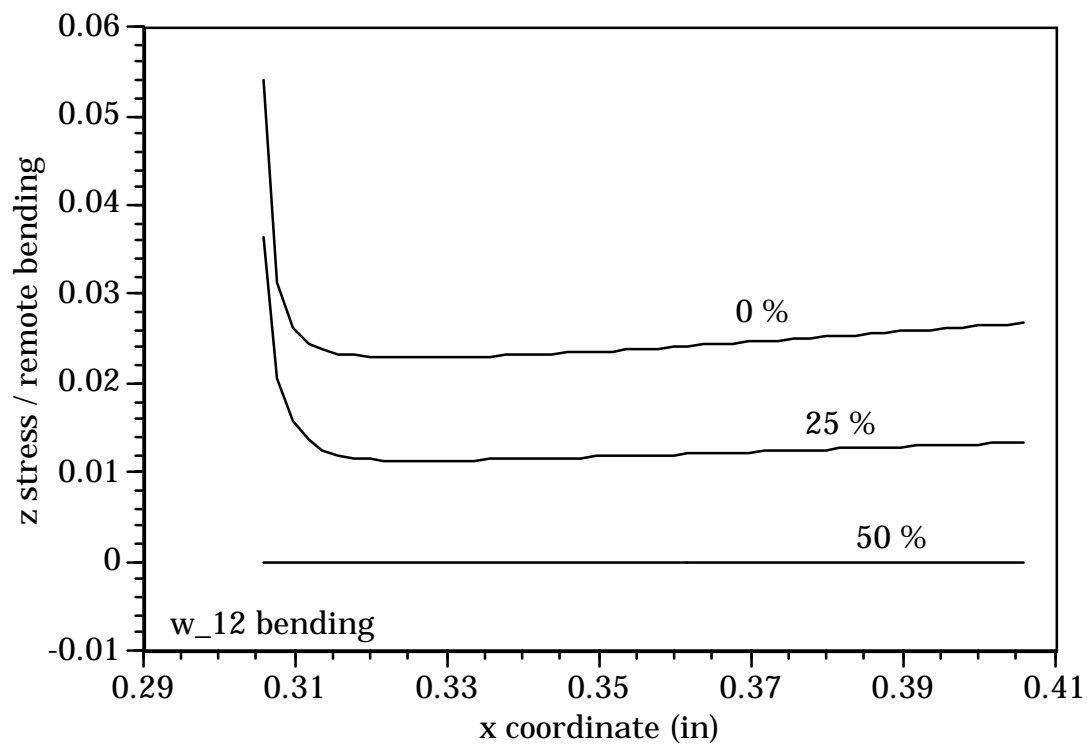
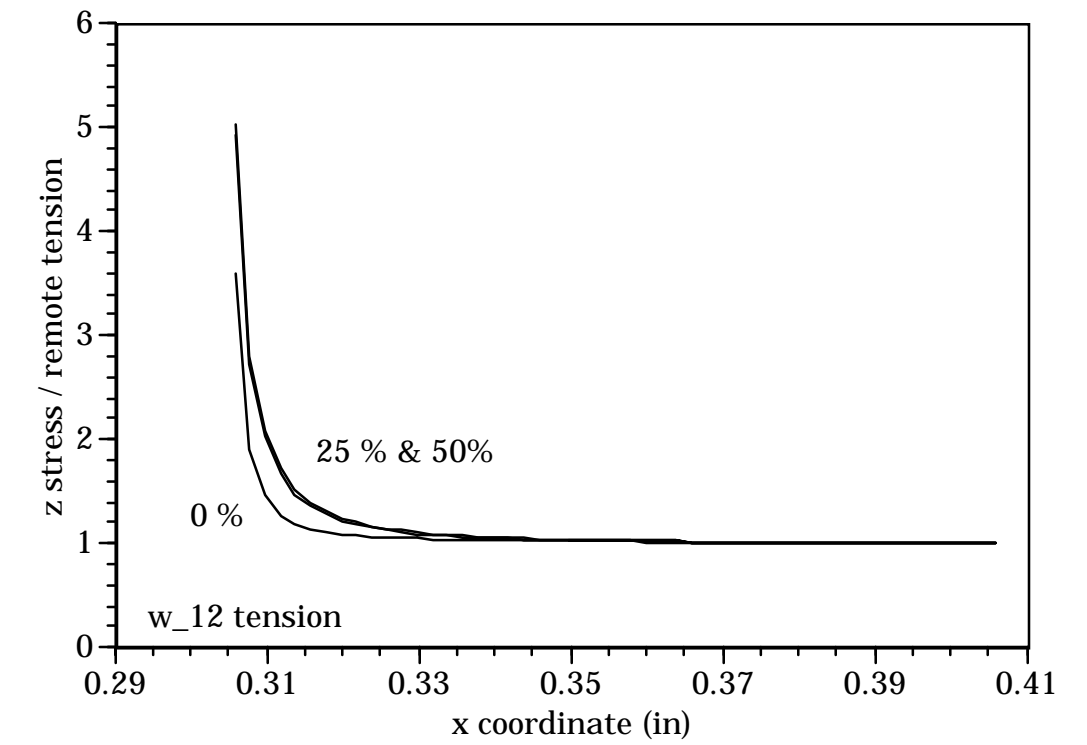
w_9



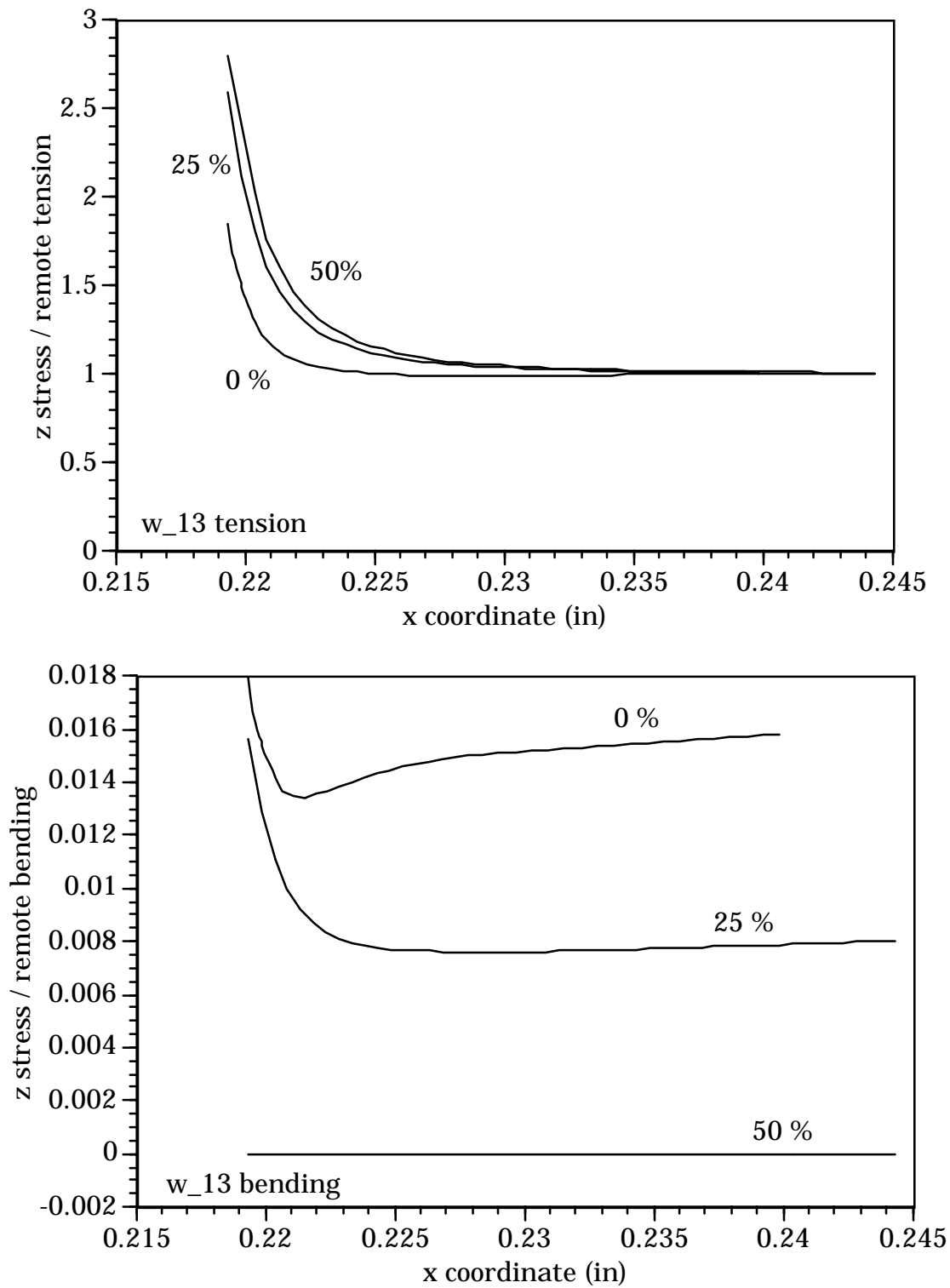
w₁₀



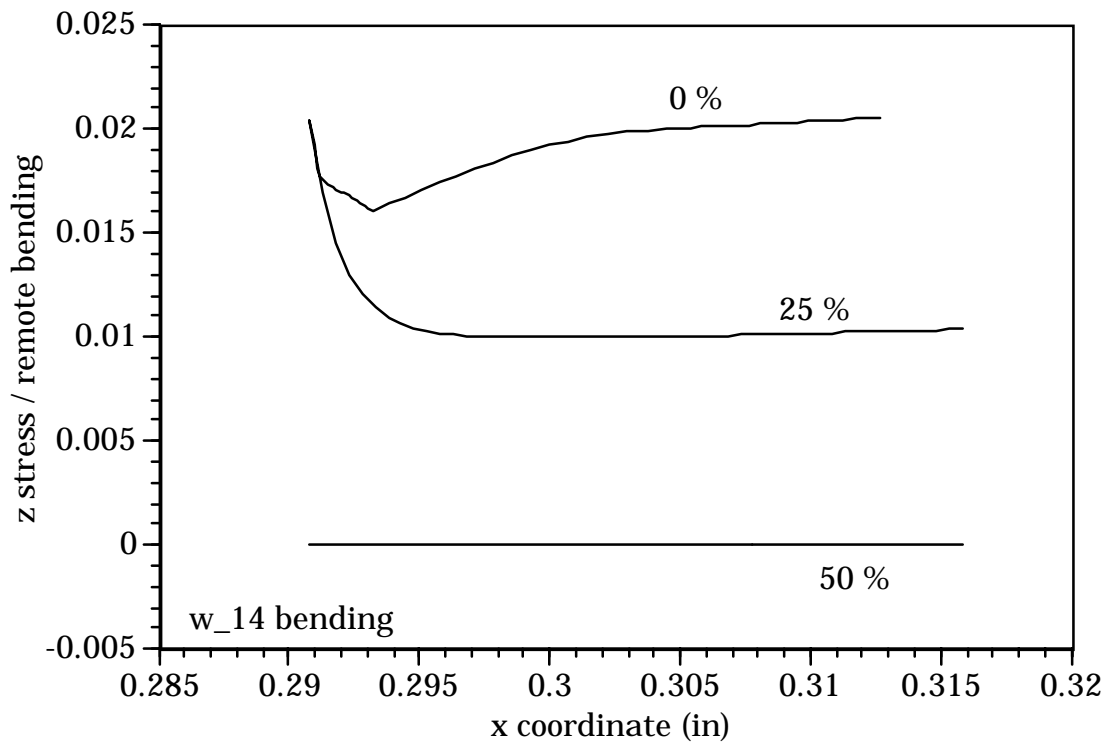
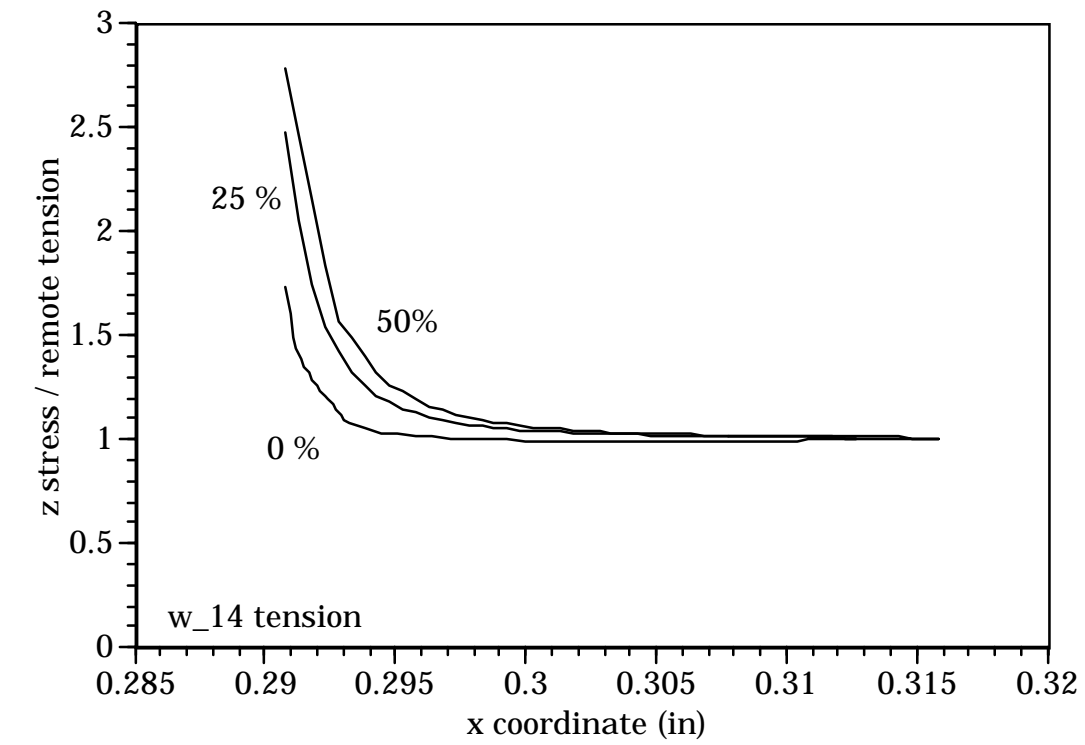
w_11



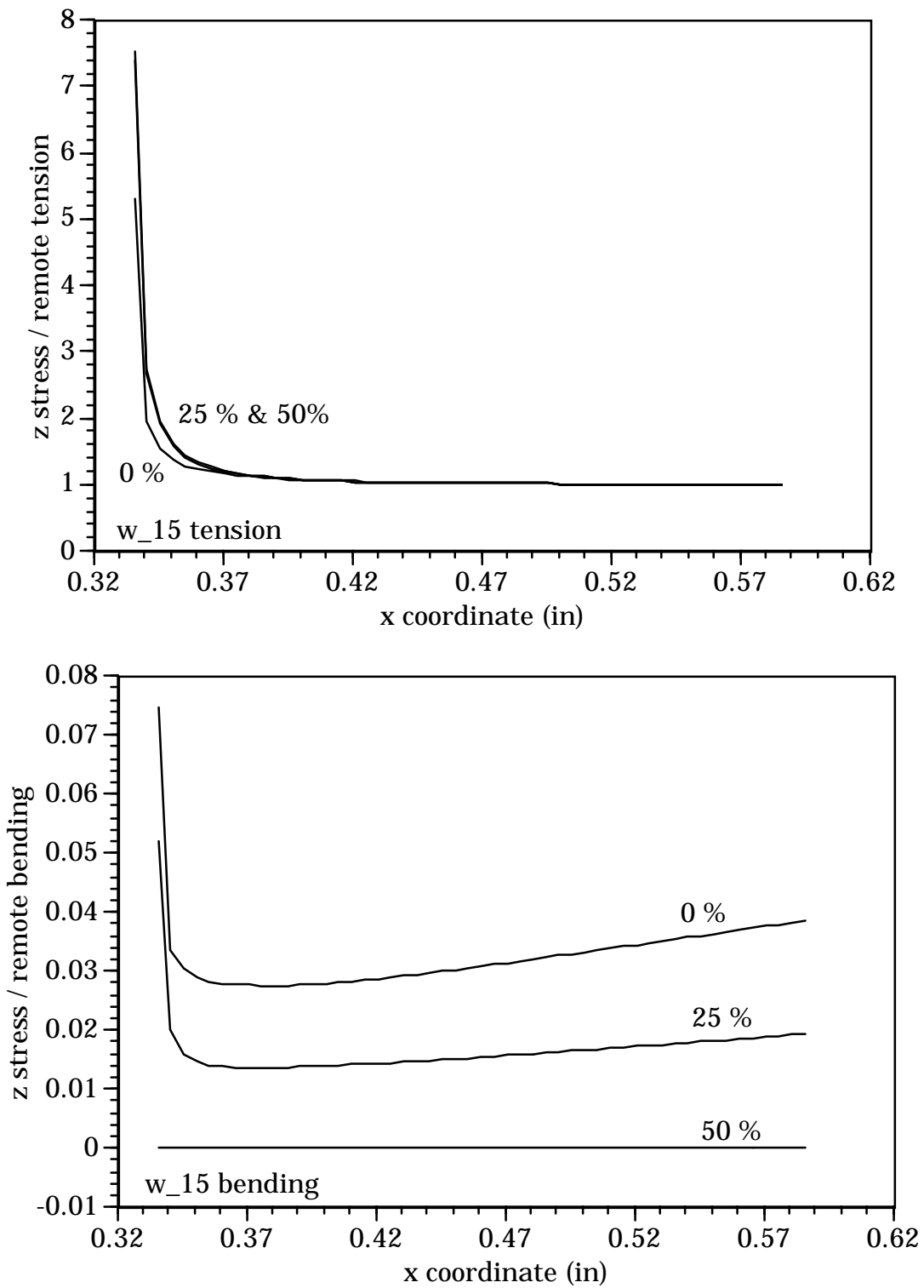
w₁₂



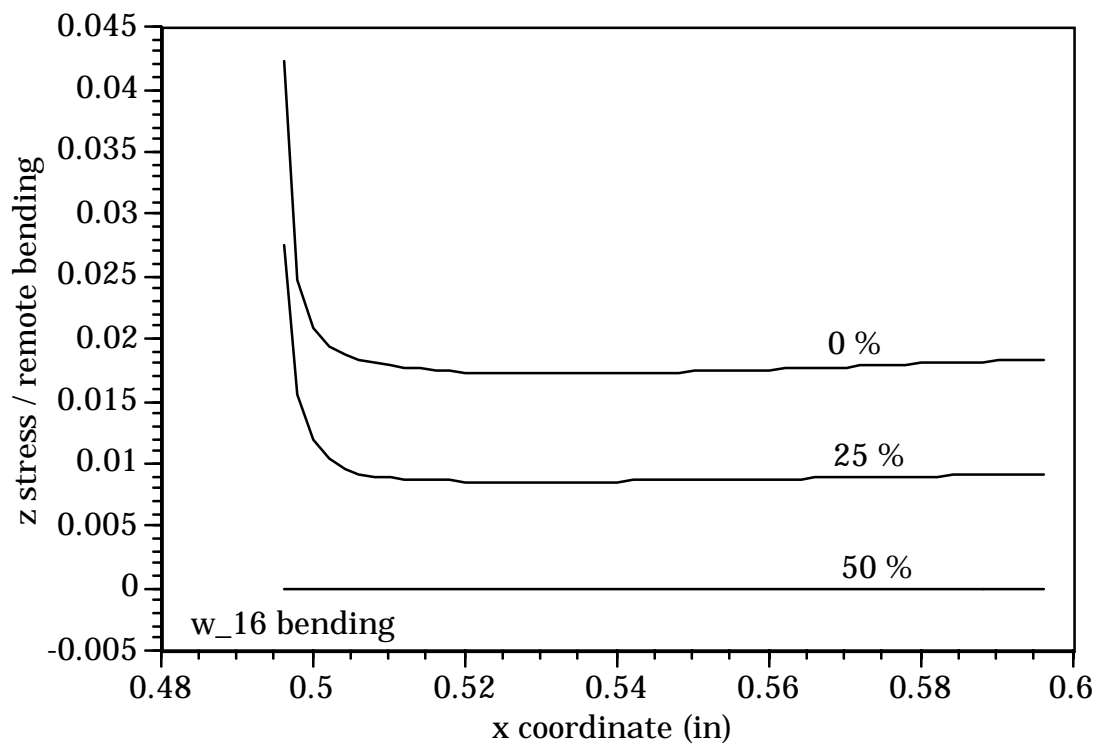
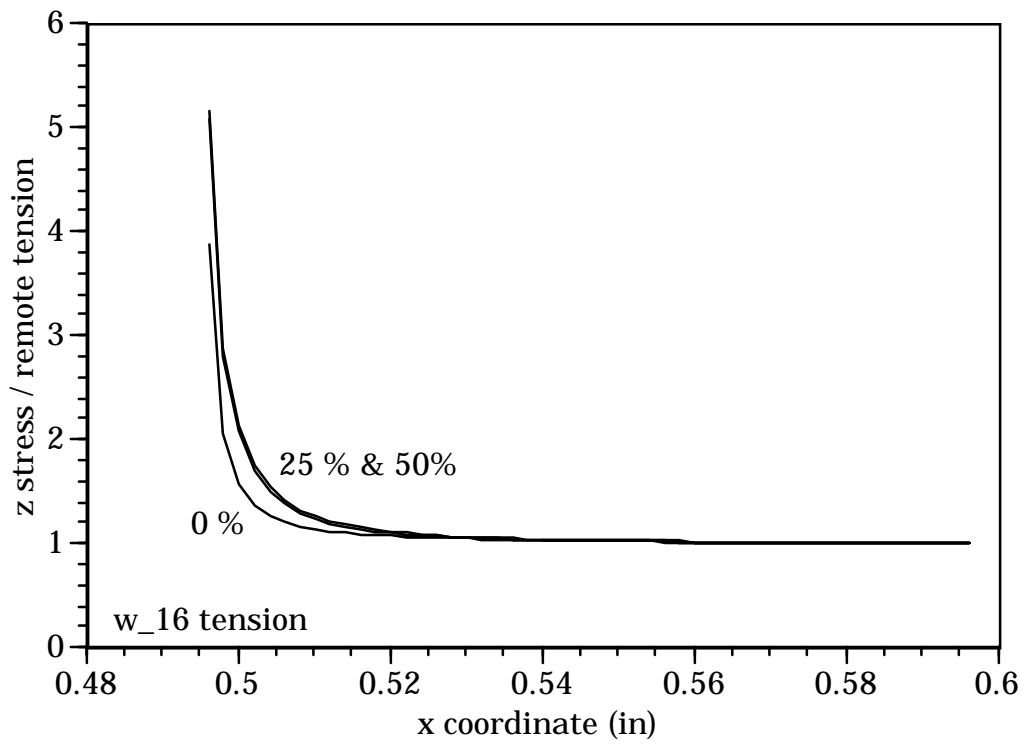
w_13



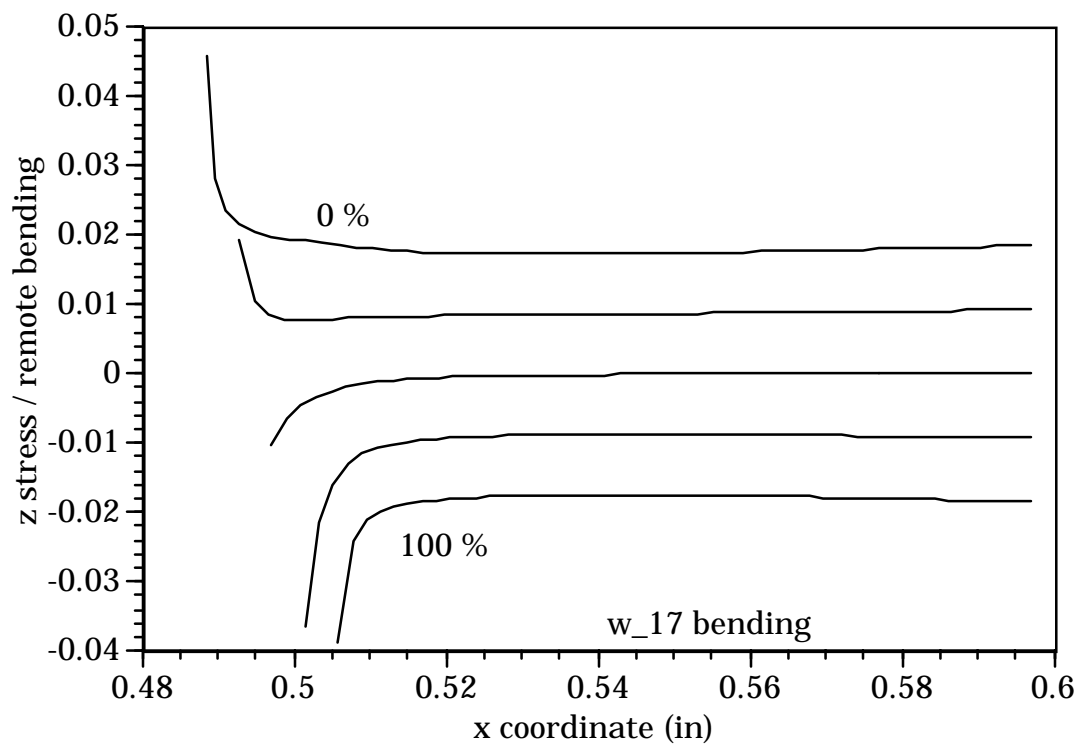
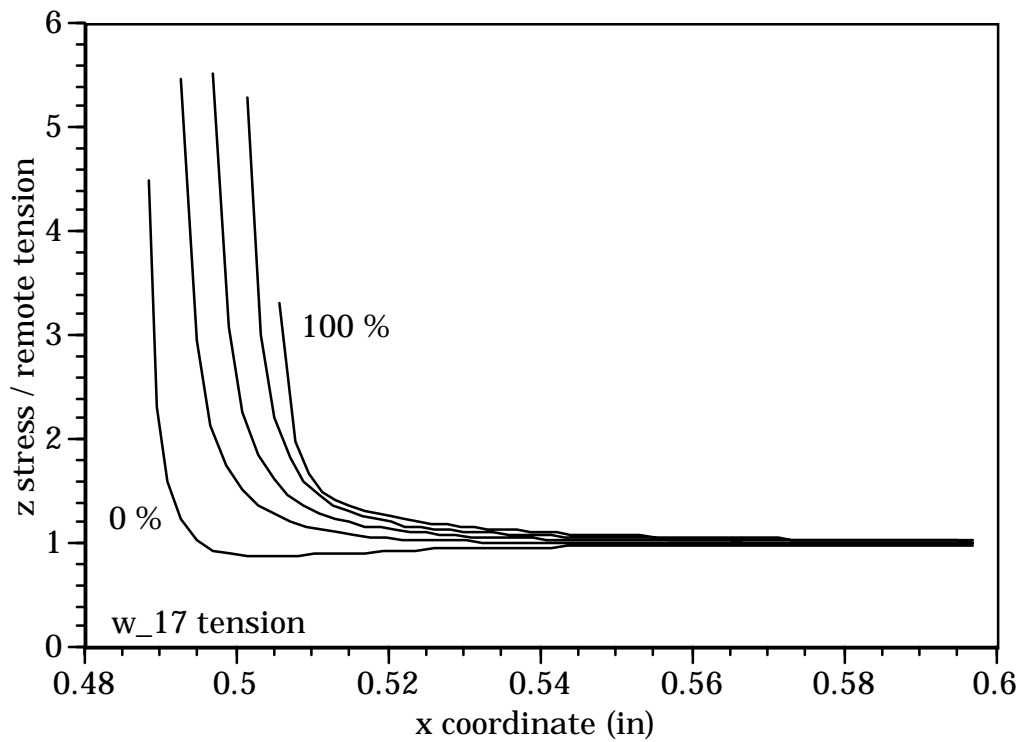
w_14



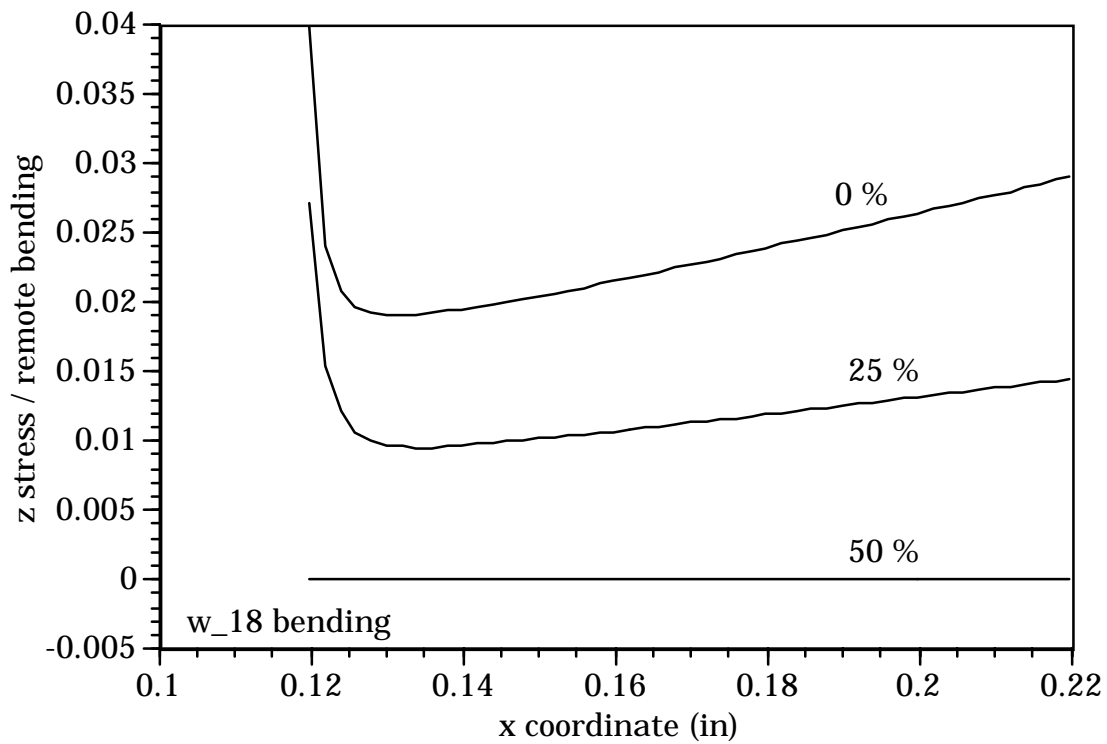
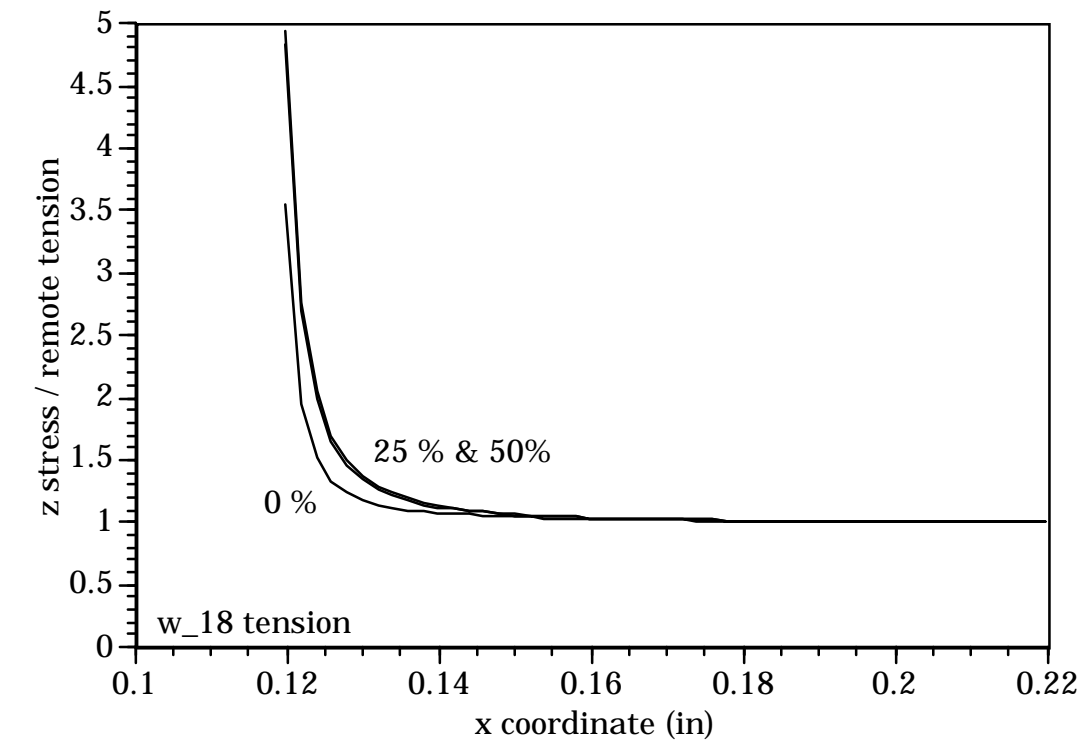
w_15



w_16

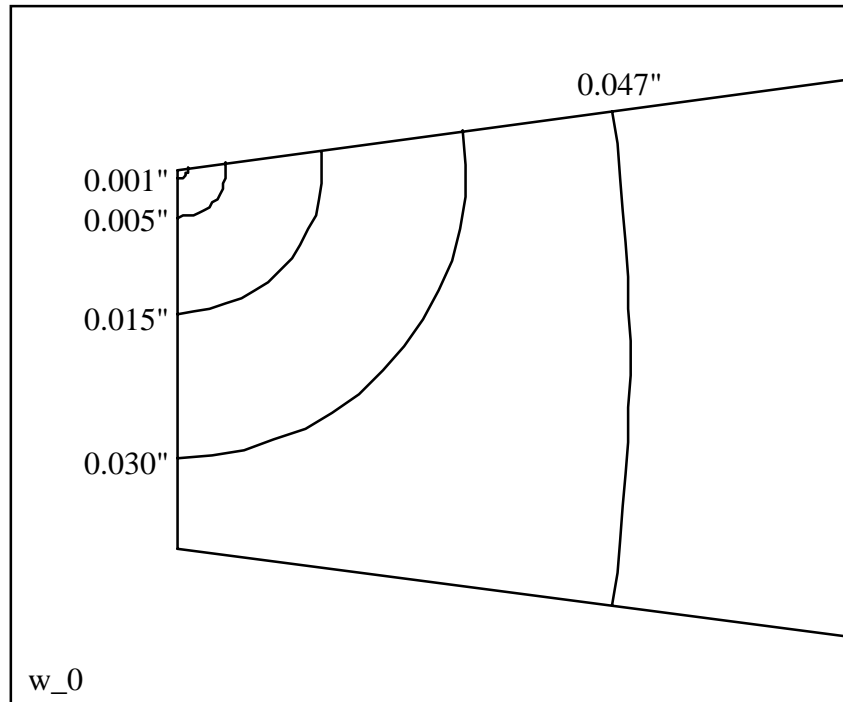


w_17

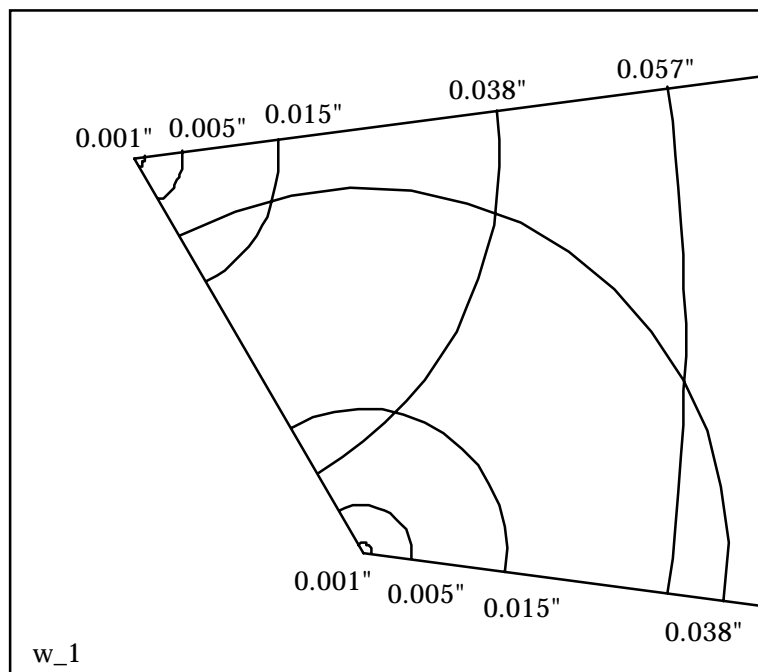


w₁₈

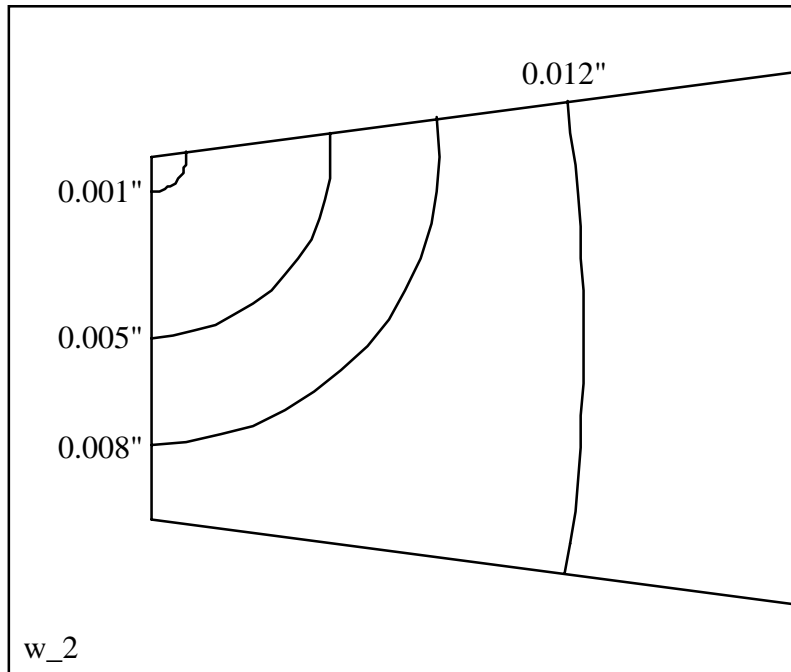
Attachment C: Crack Shape Diagrams



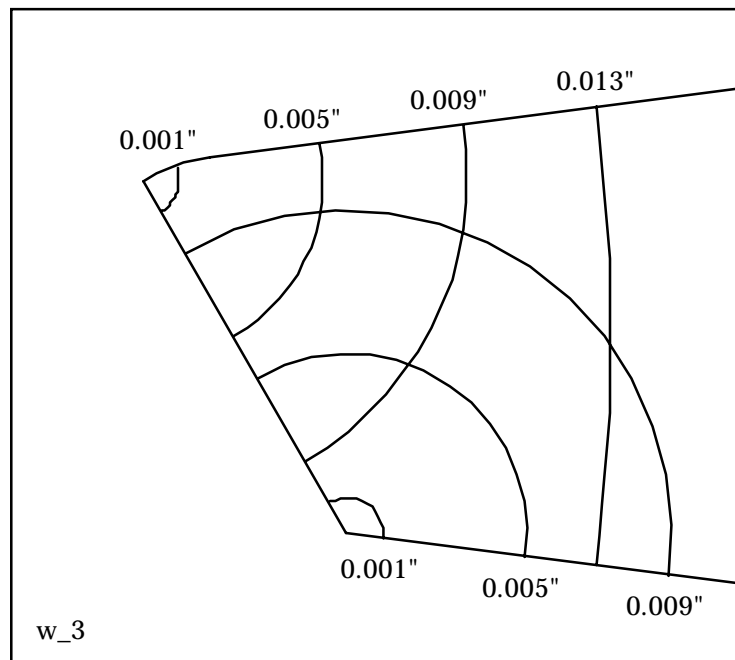
w_0



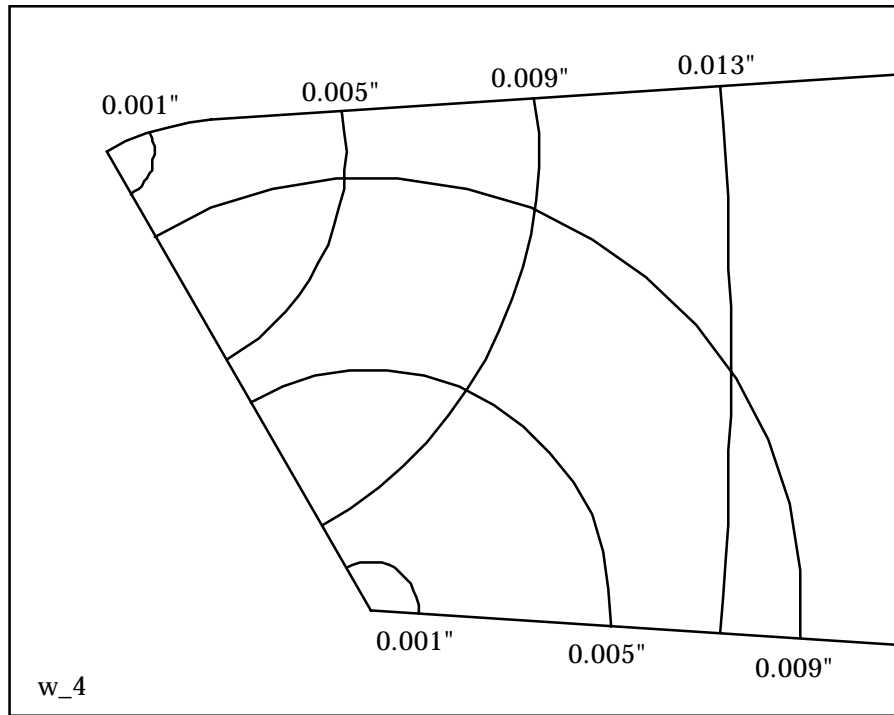
w_1



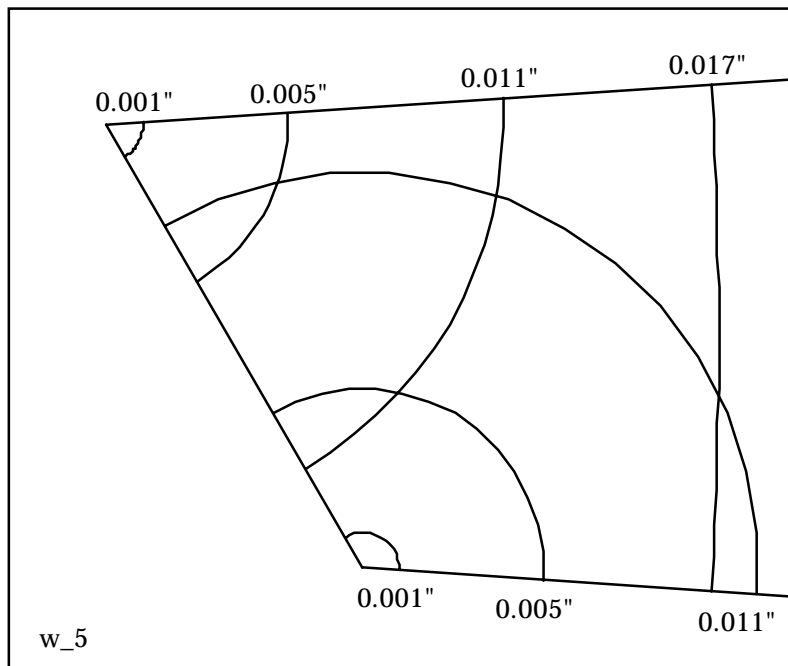
w_2



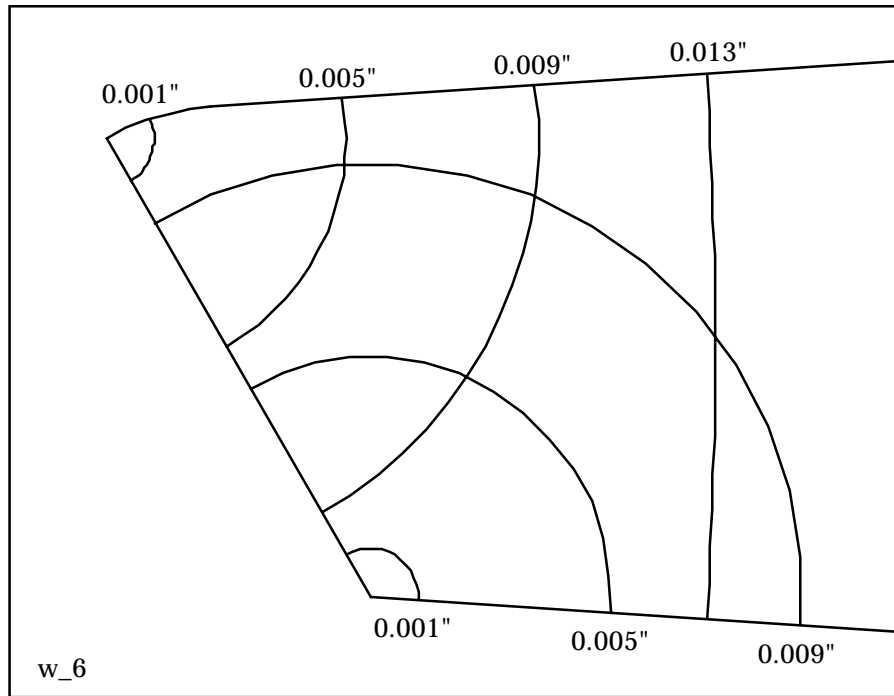
w_3



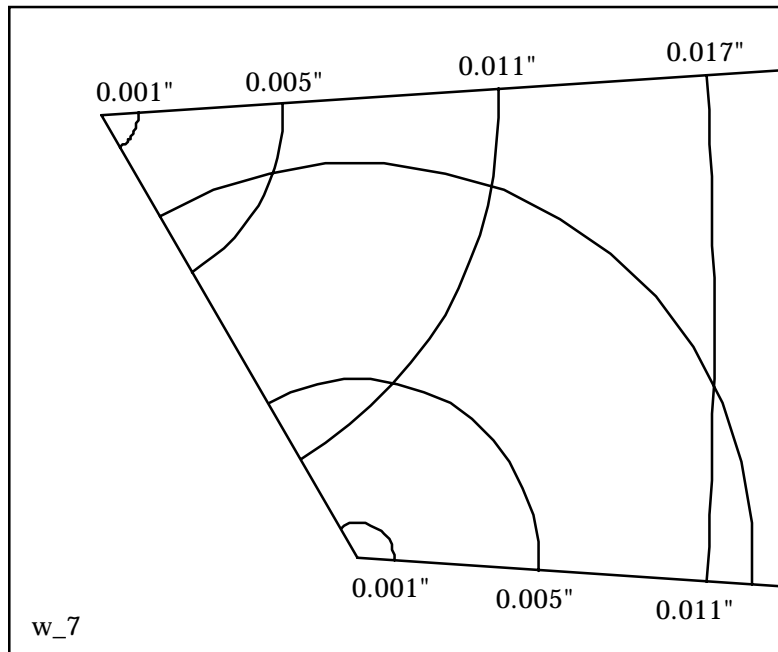
w_4



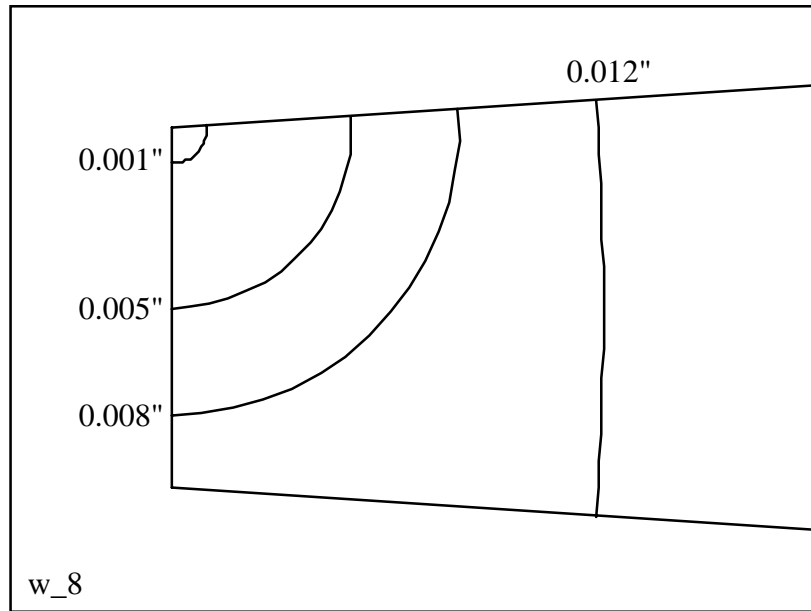
w_5



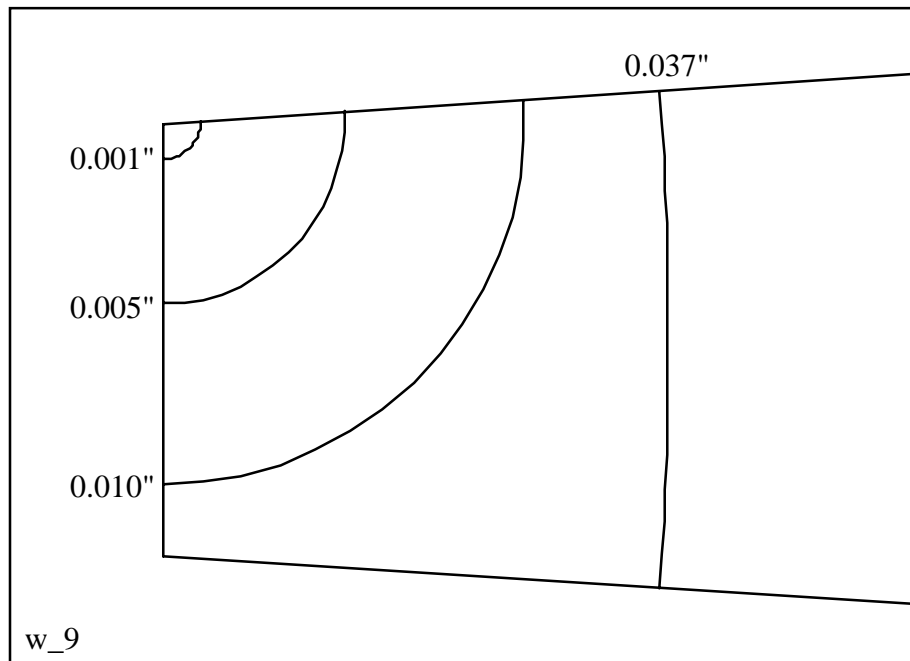
w_6



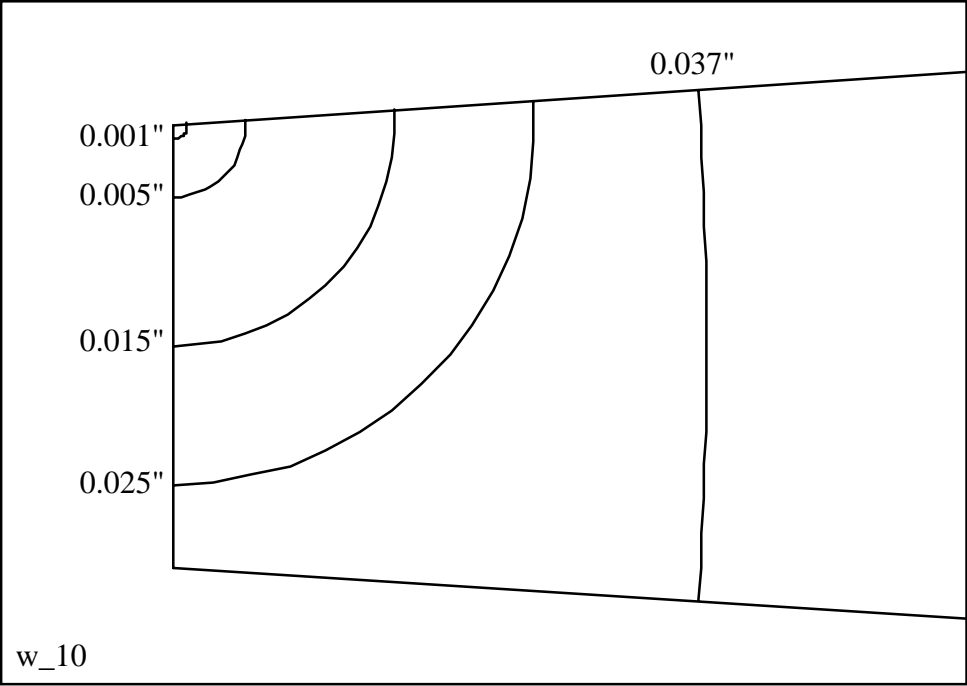
w_7



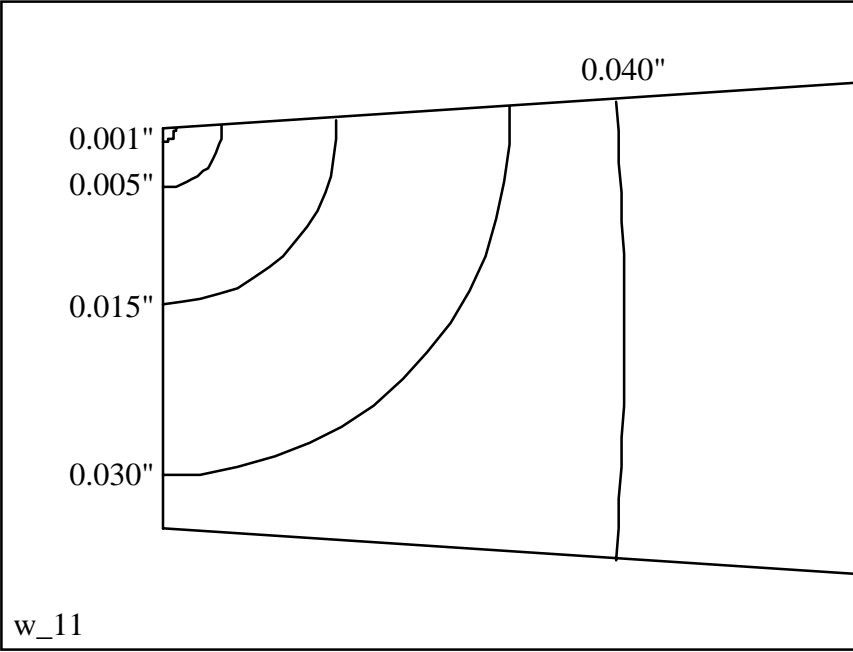
w_8



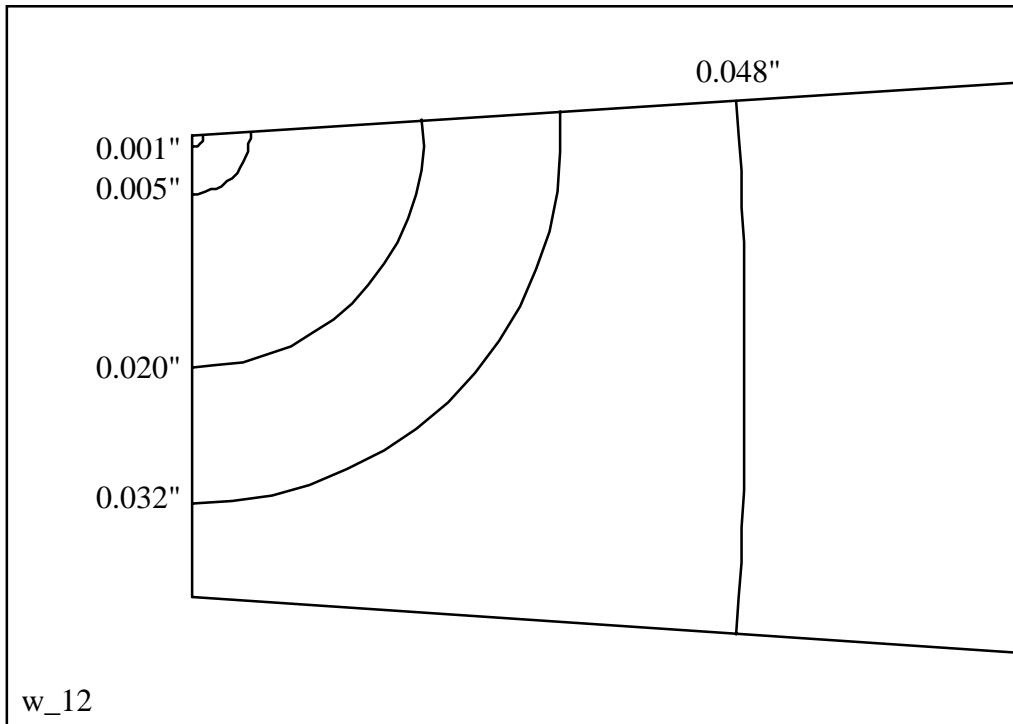
w_9



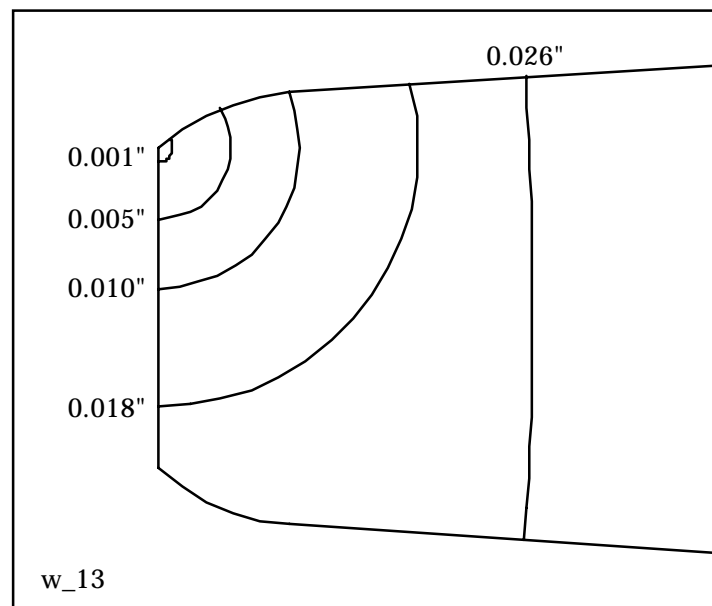
w_10



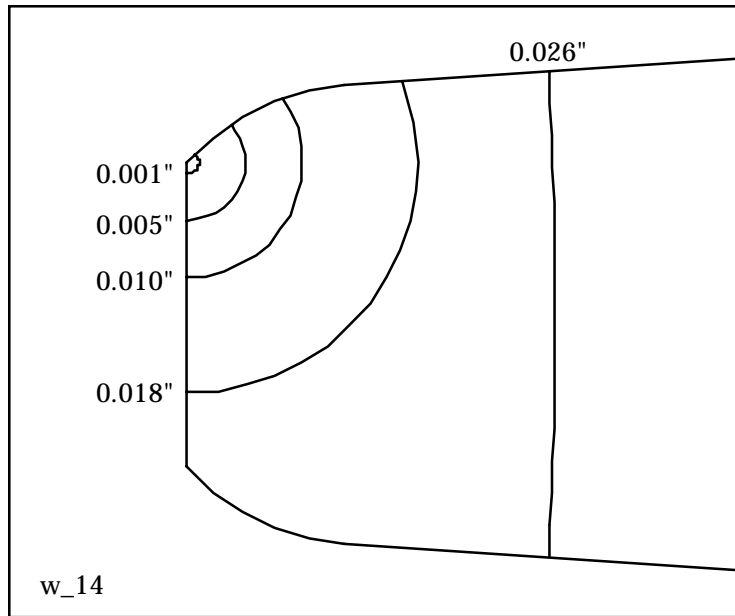
w_11



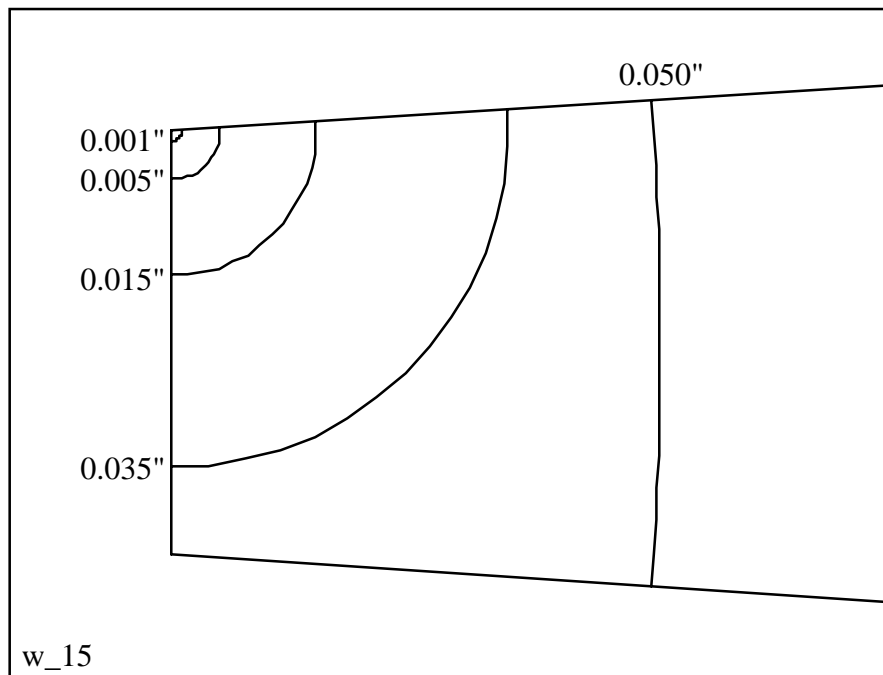
w_{12}



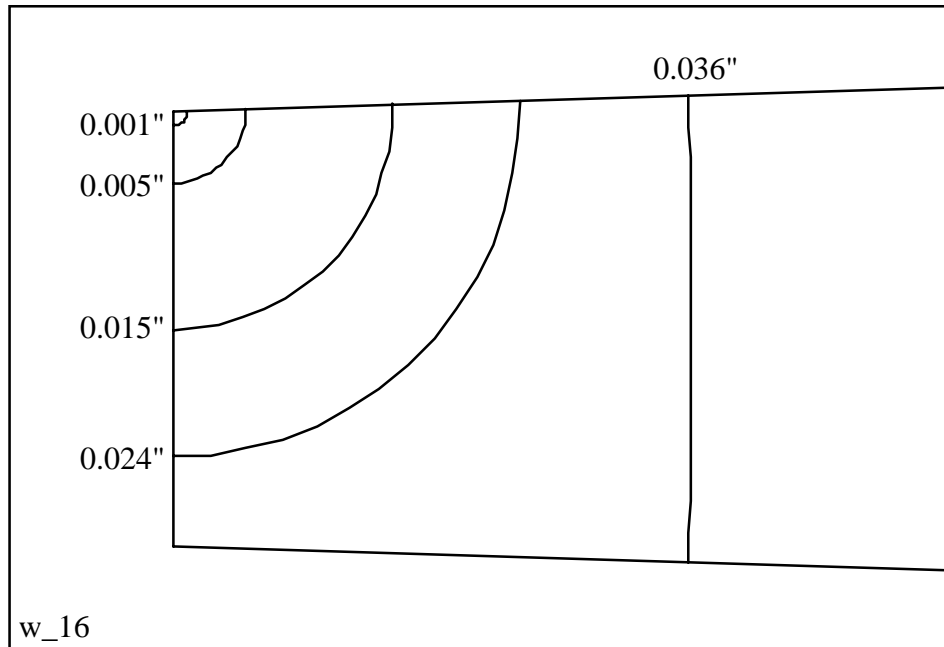
w_{13}



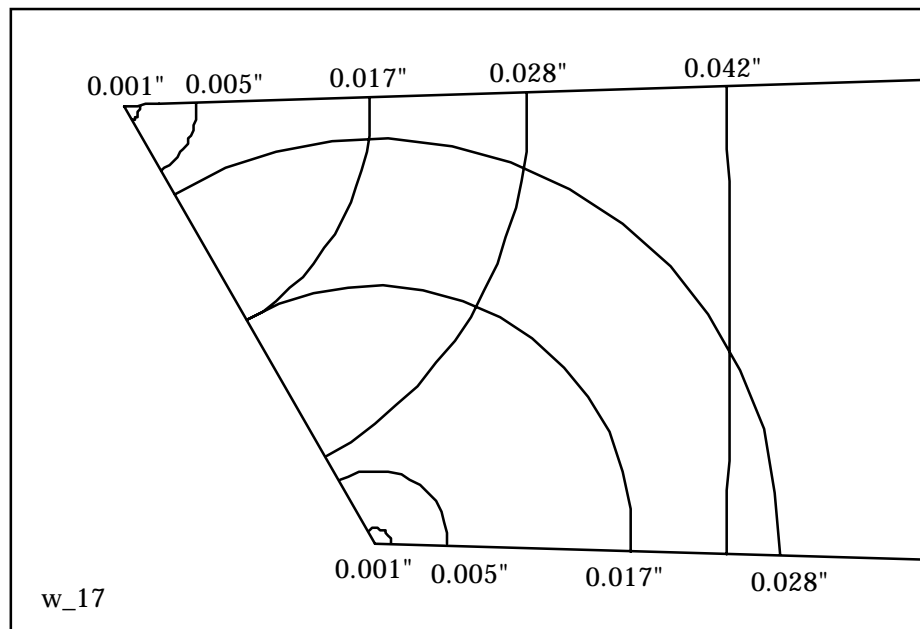
w_14



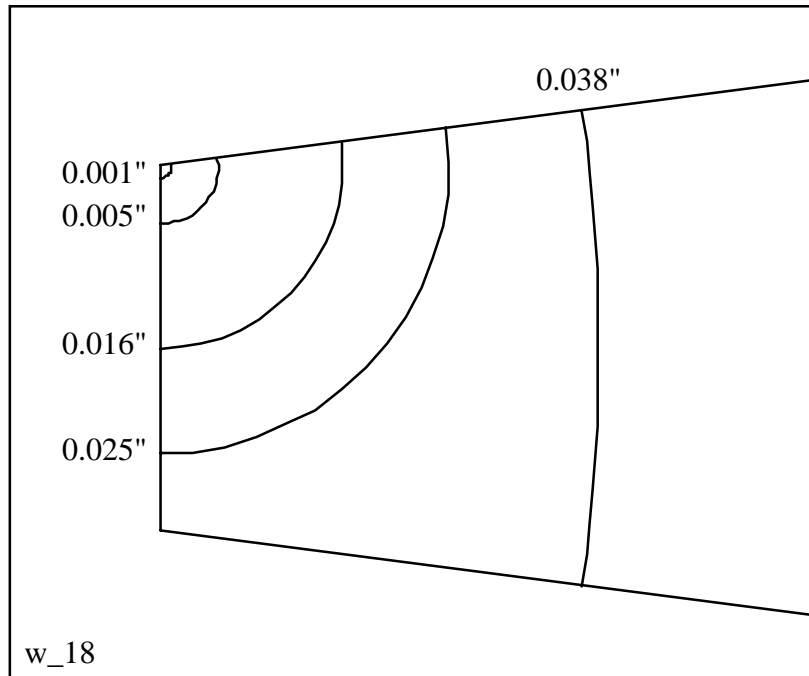
w_15



w_16



w_17

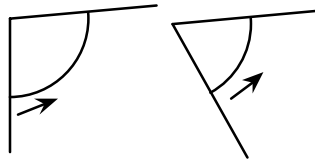


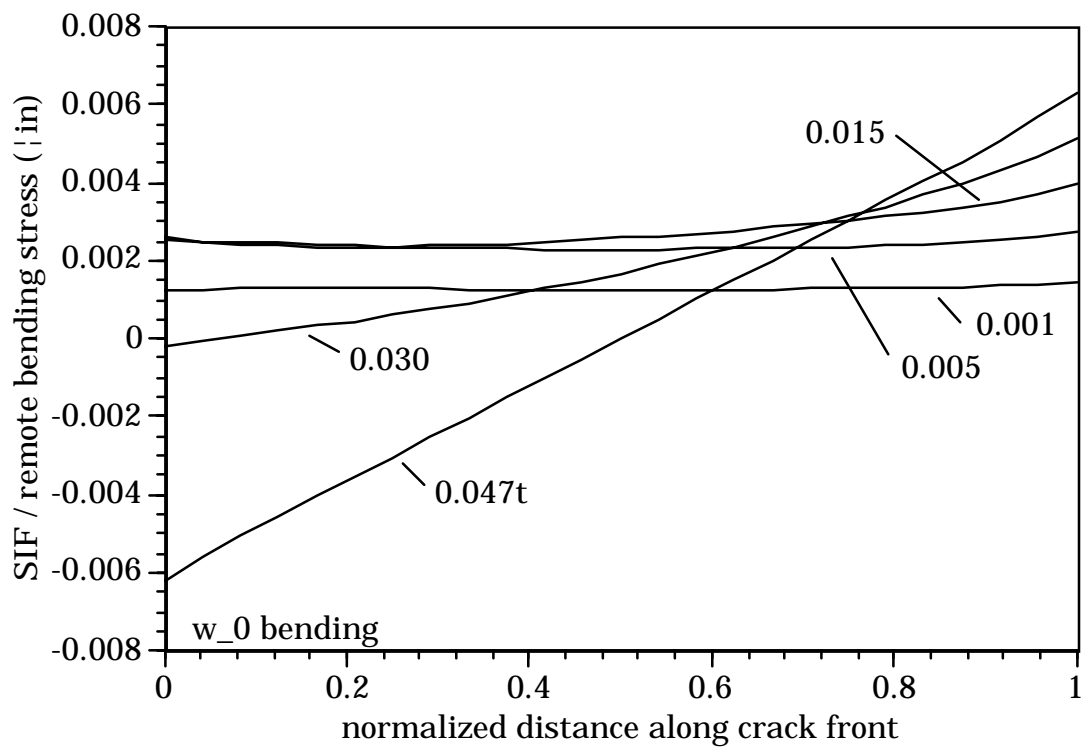
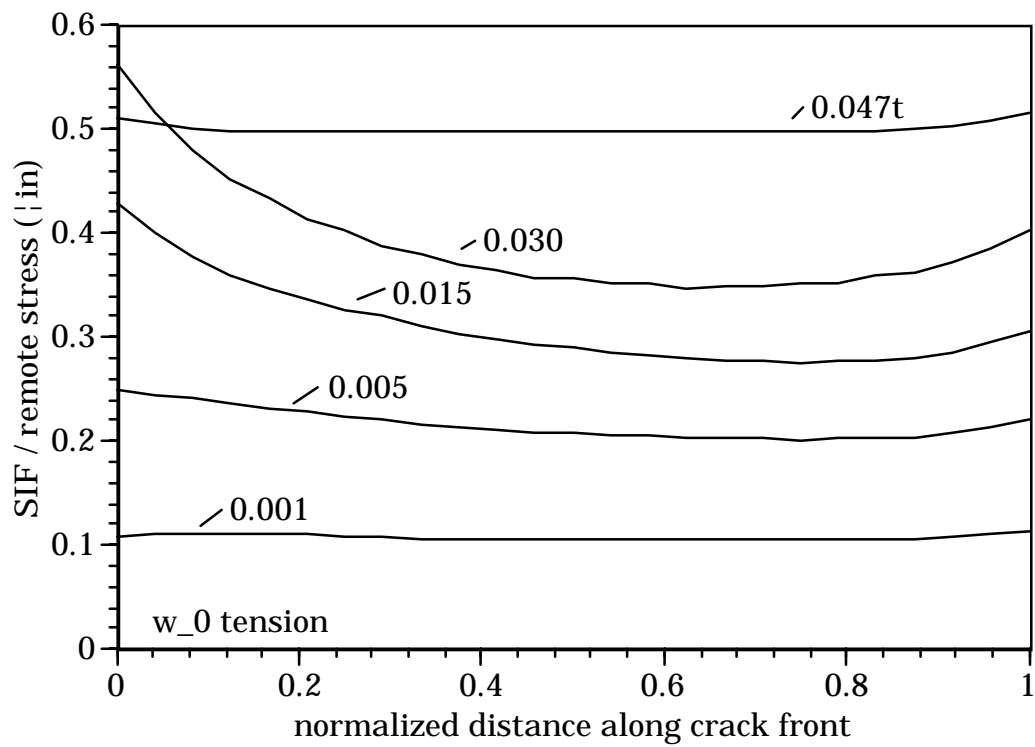
w_18

Attachment D: Stress Intensity Factor Distribution Plots

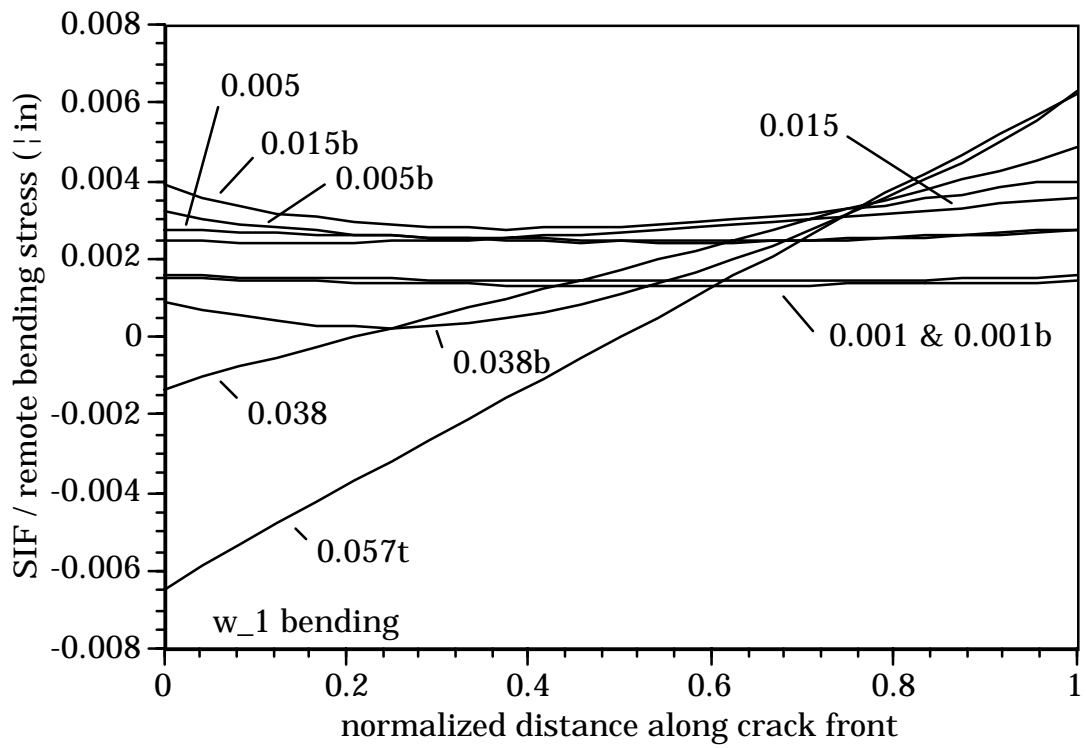
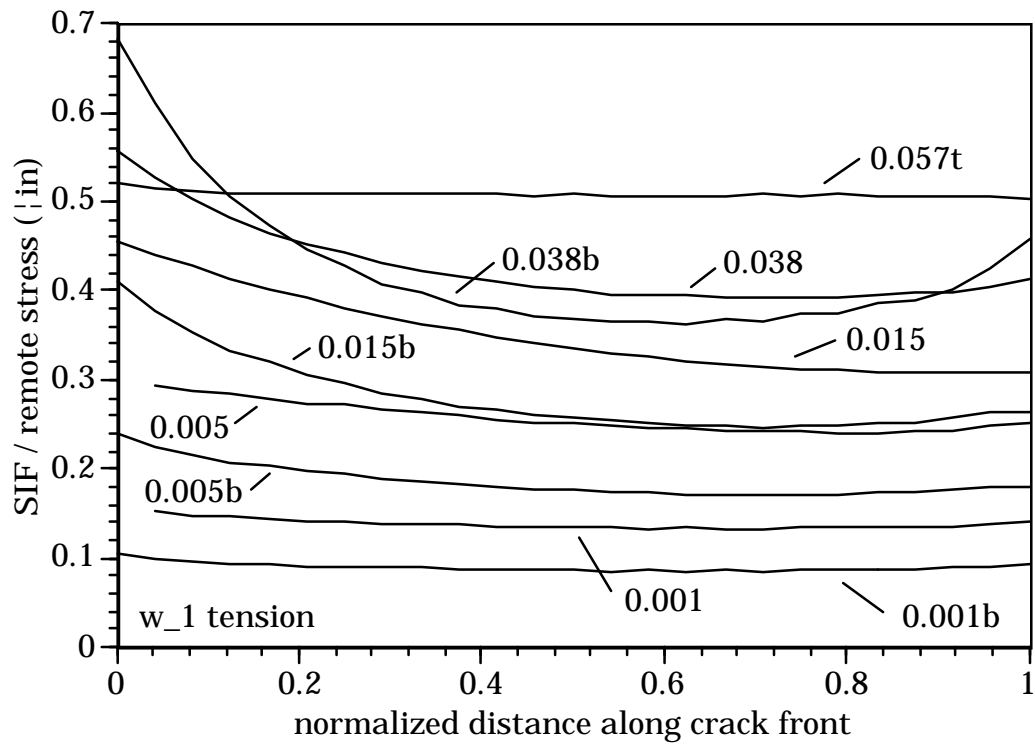
This Attachment contains plots of mode I stress intensity factors along crack fronts.

In all cases, the crack front location is normalized (from zero to one). The zero point corresponds to where the crack front breaks the surface at the notch tip. The one point corresponds to where the crack front breaks the surface on the wedge flank. This is shown schematically below.

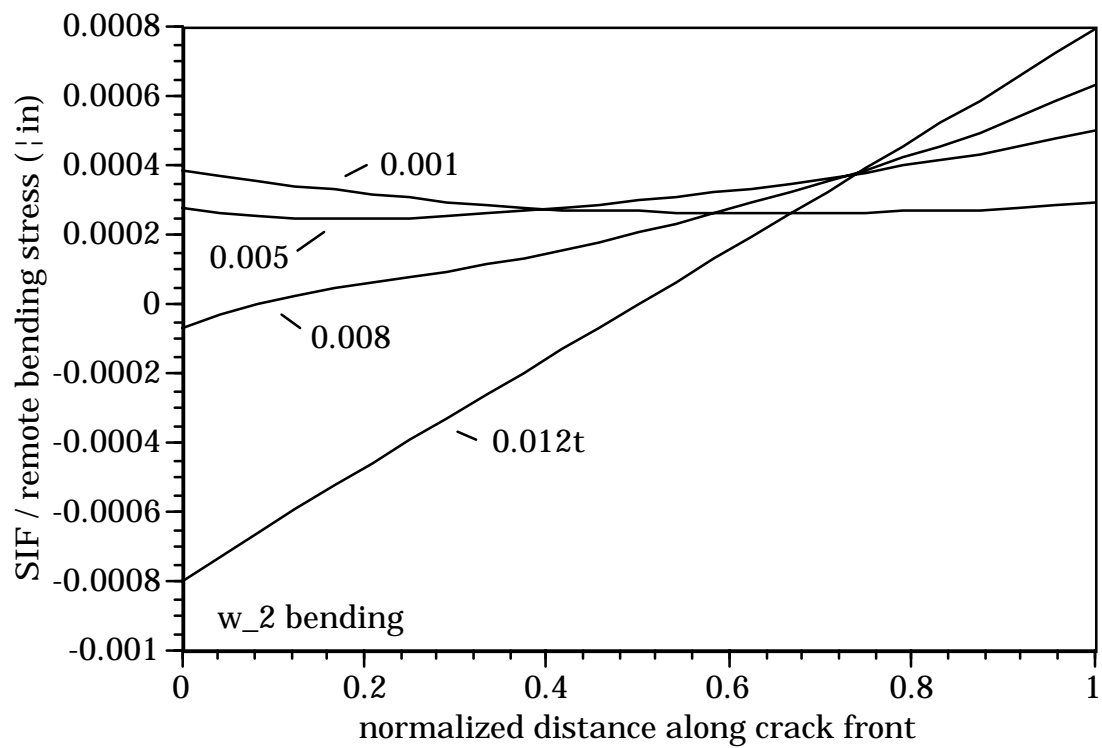
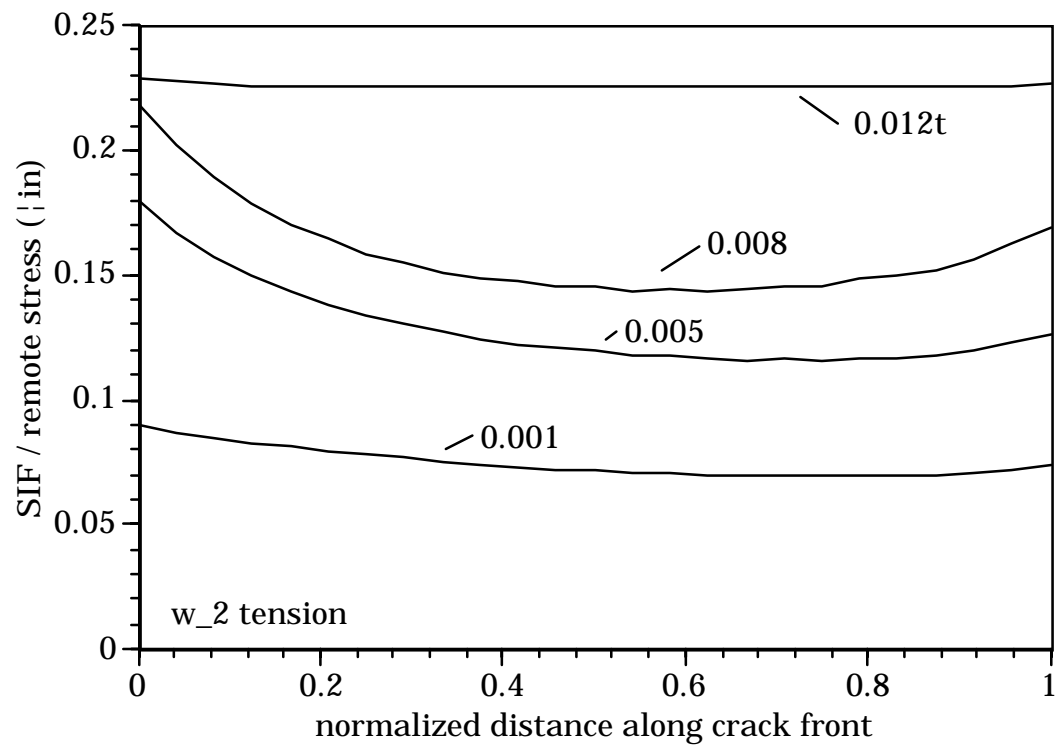




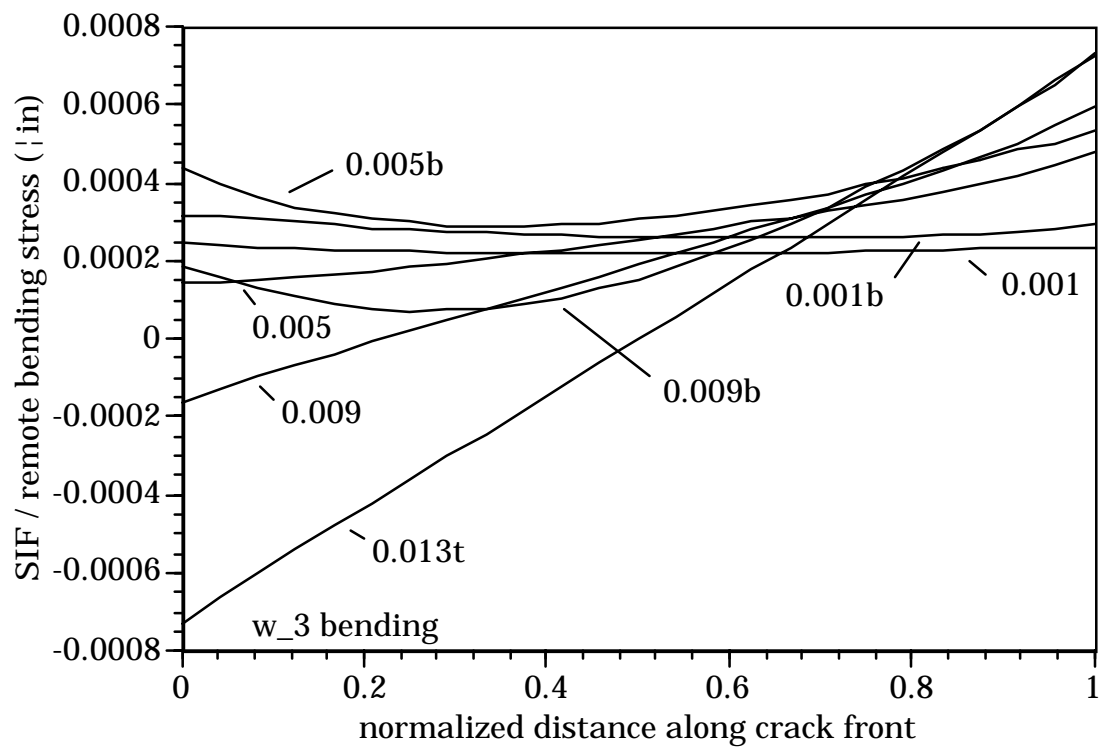
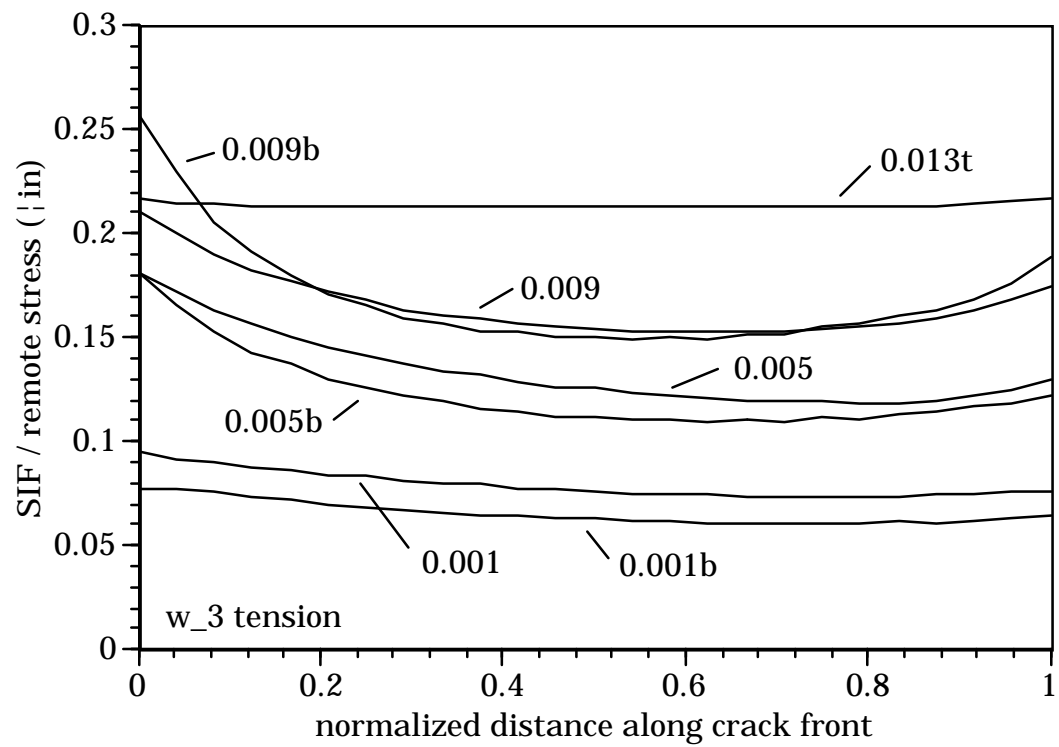
w_0



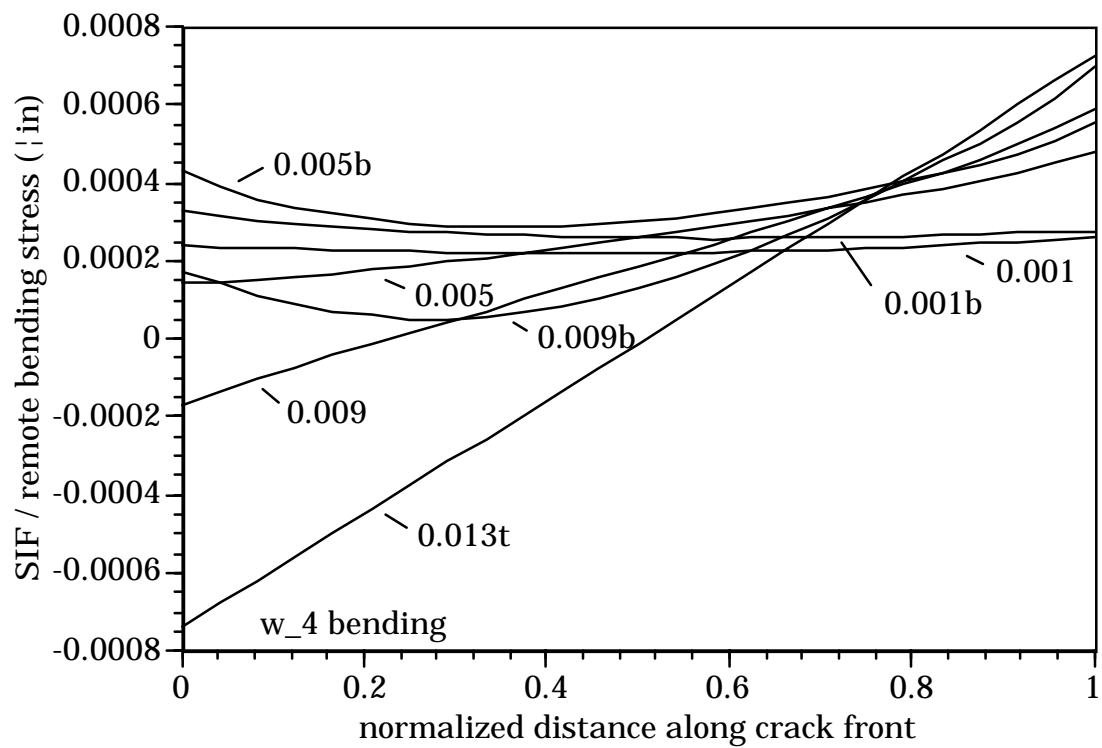
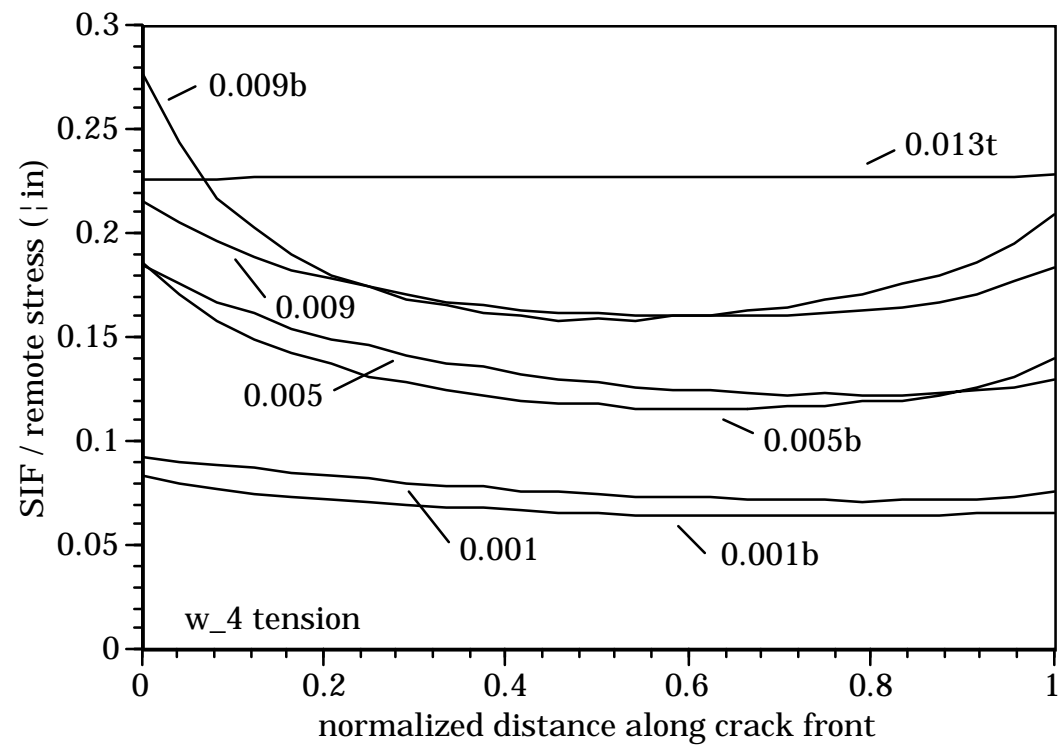
w_1



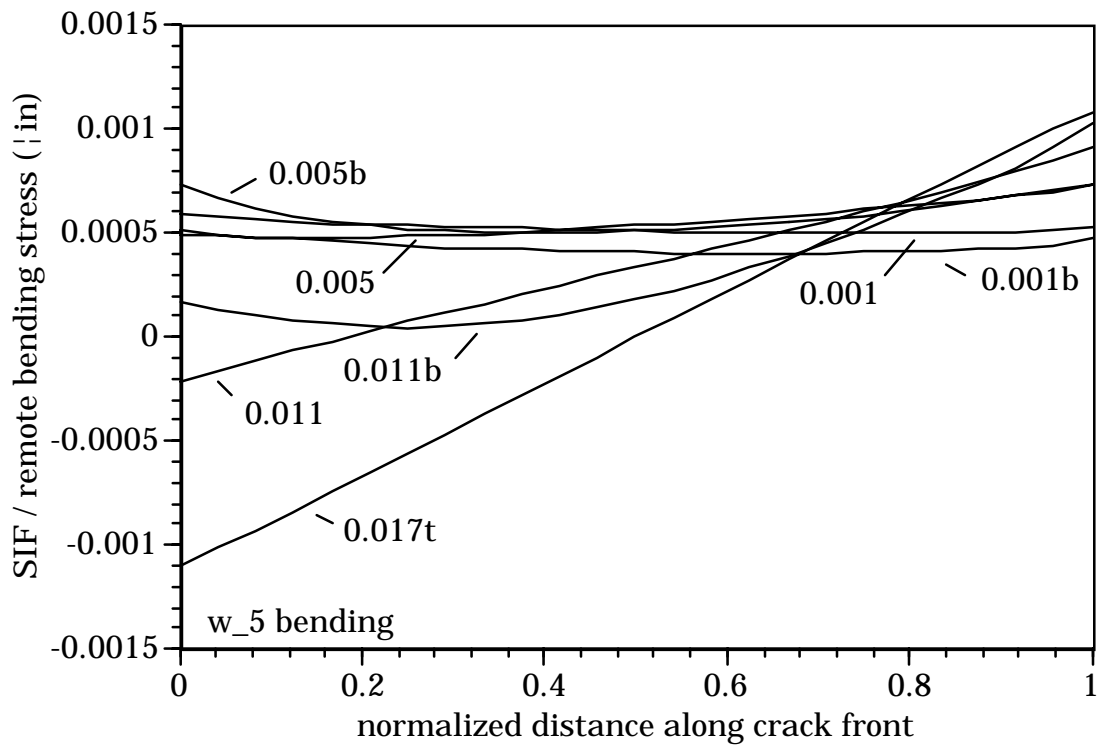
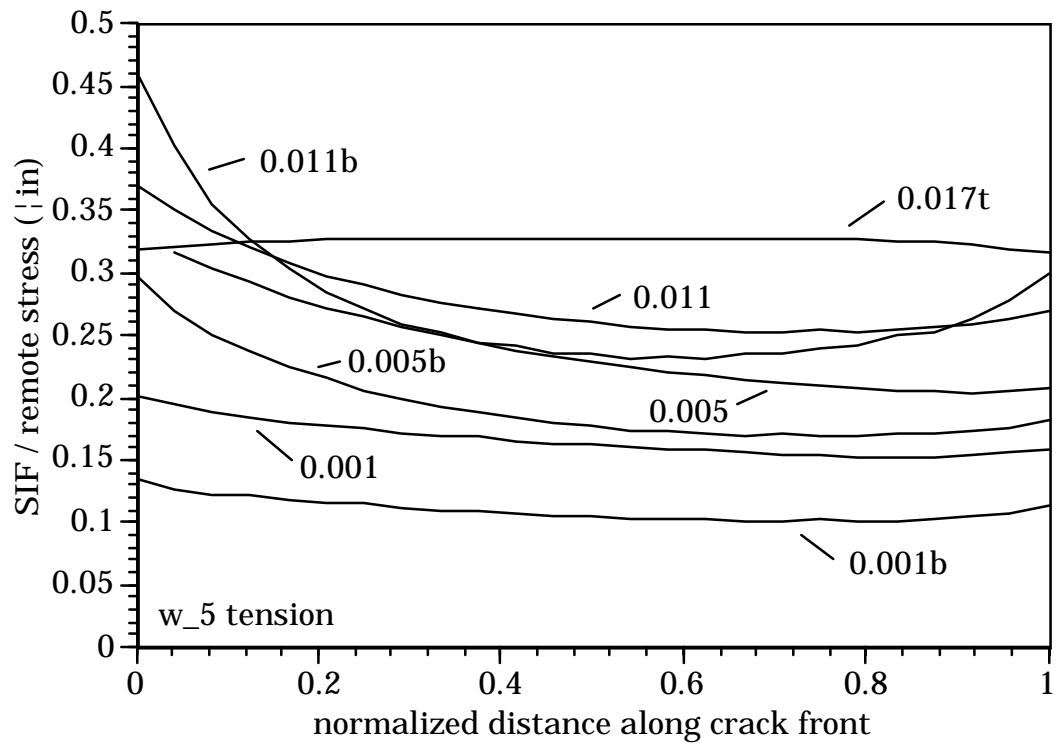
w_2



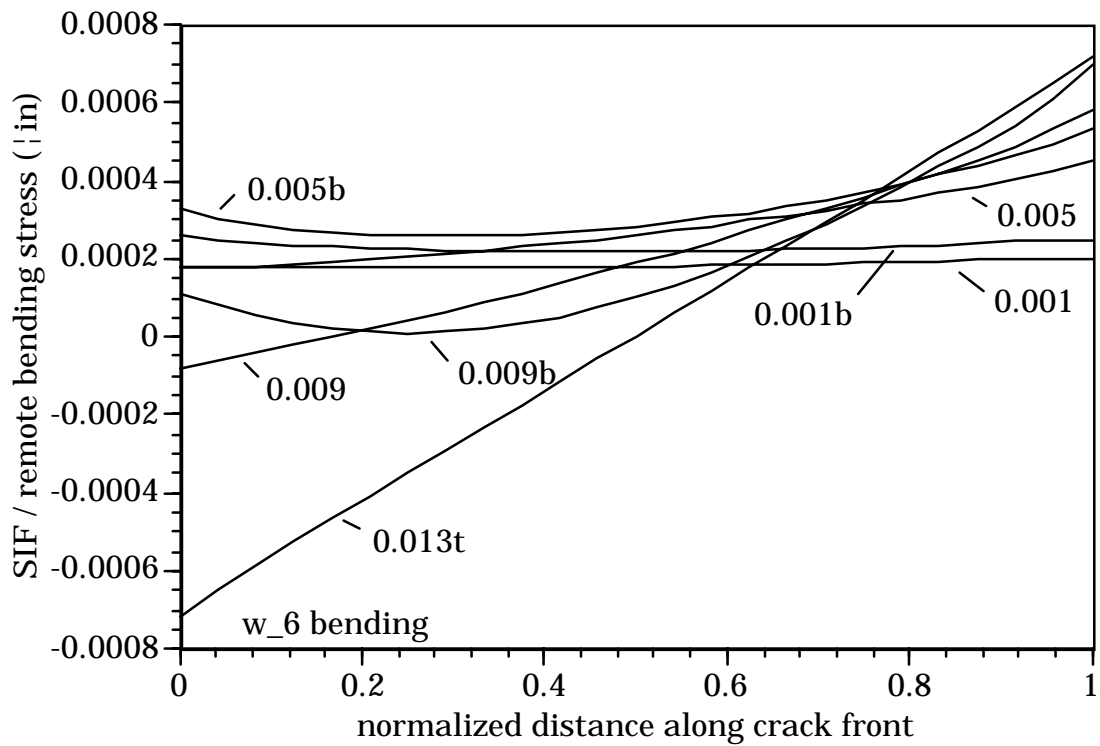
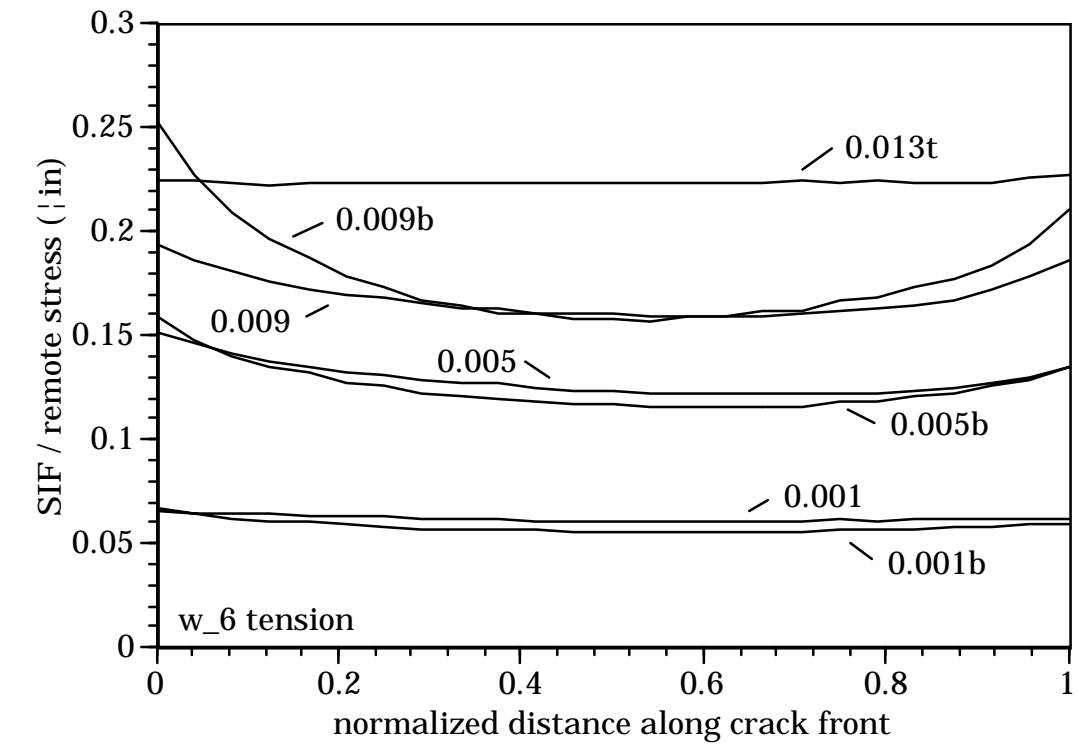
w_3



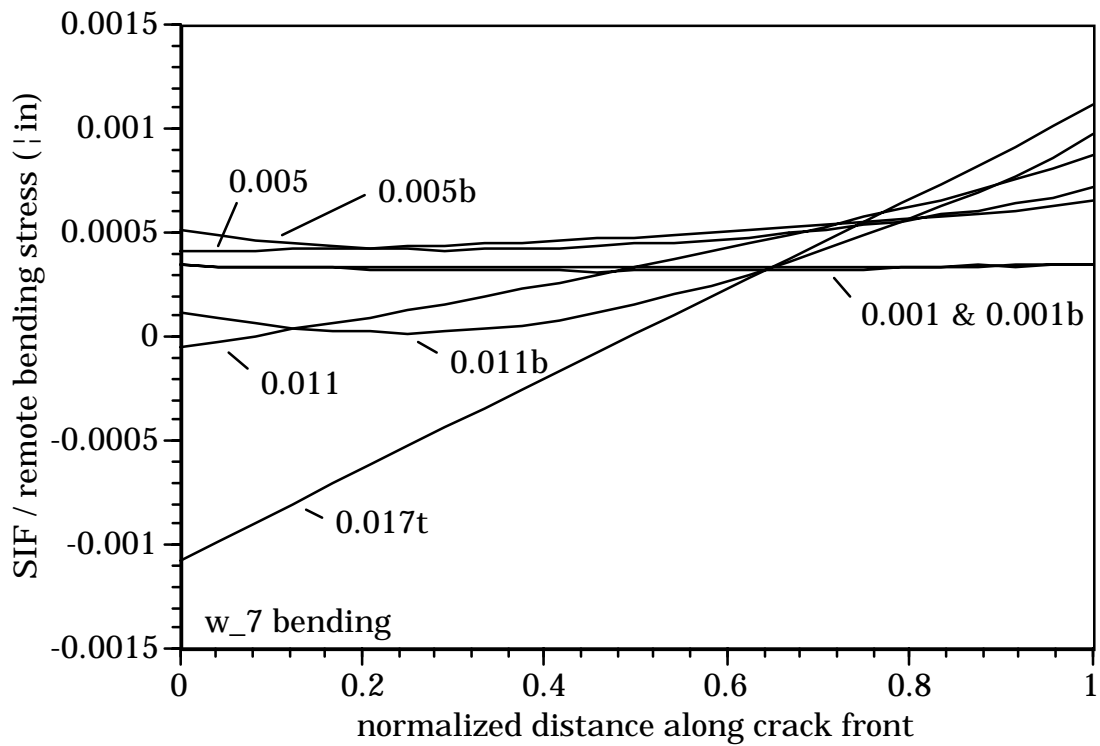
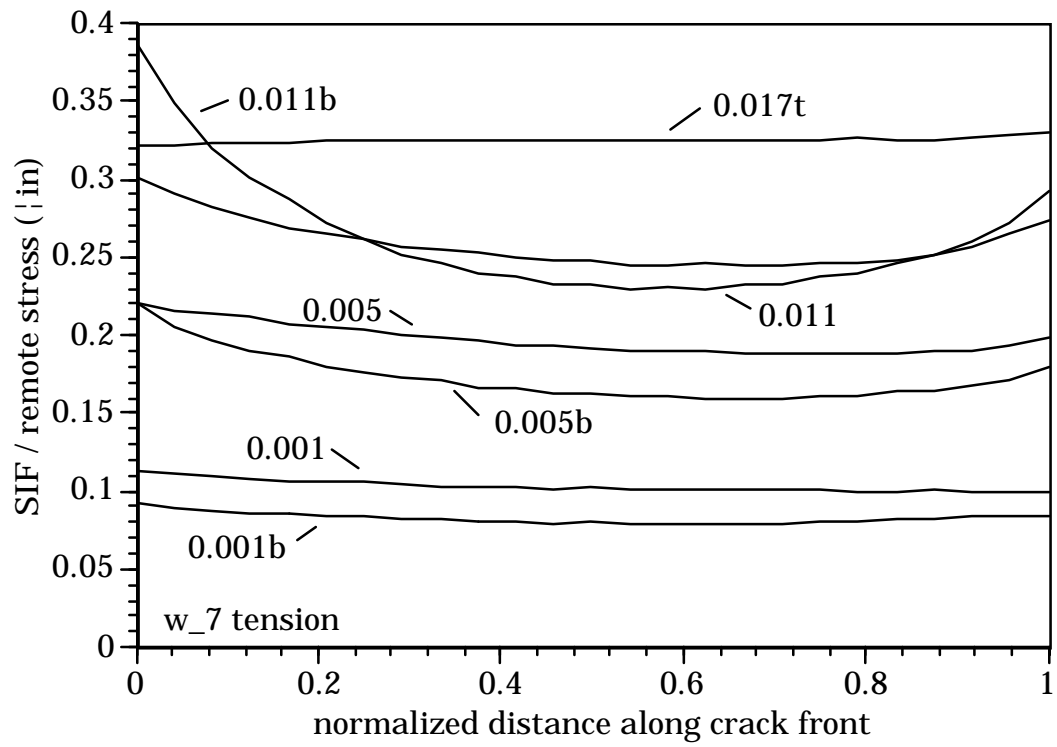
w_4



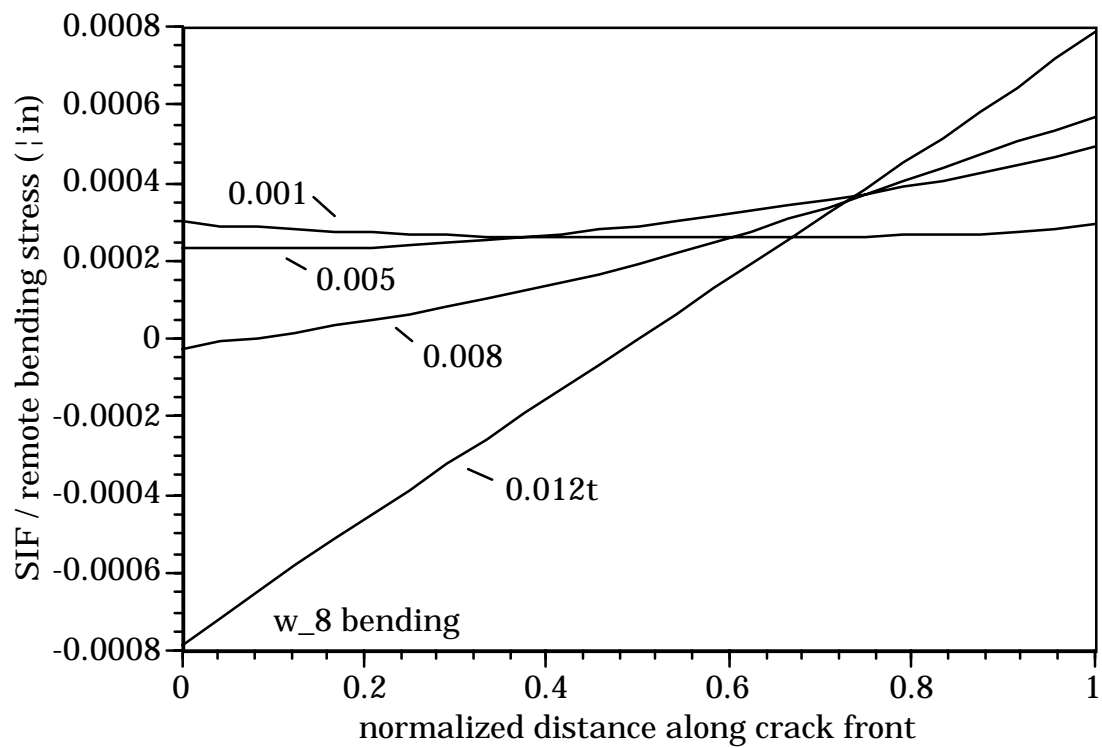
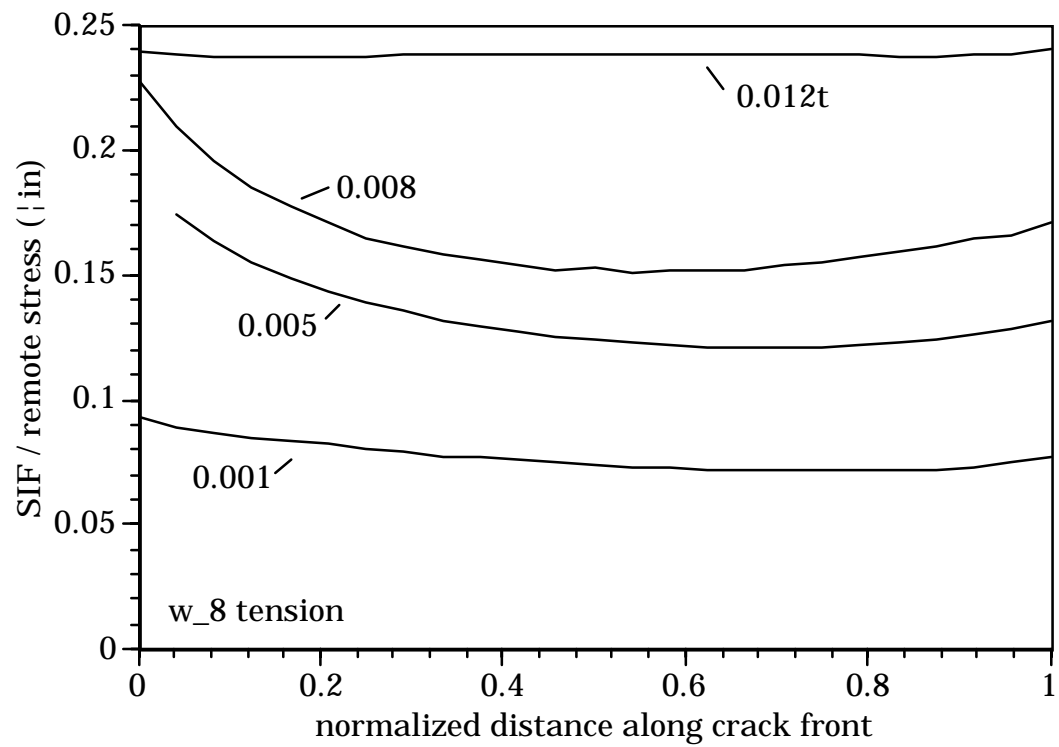
w_5



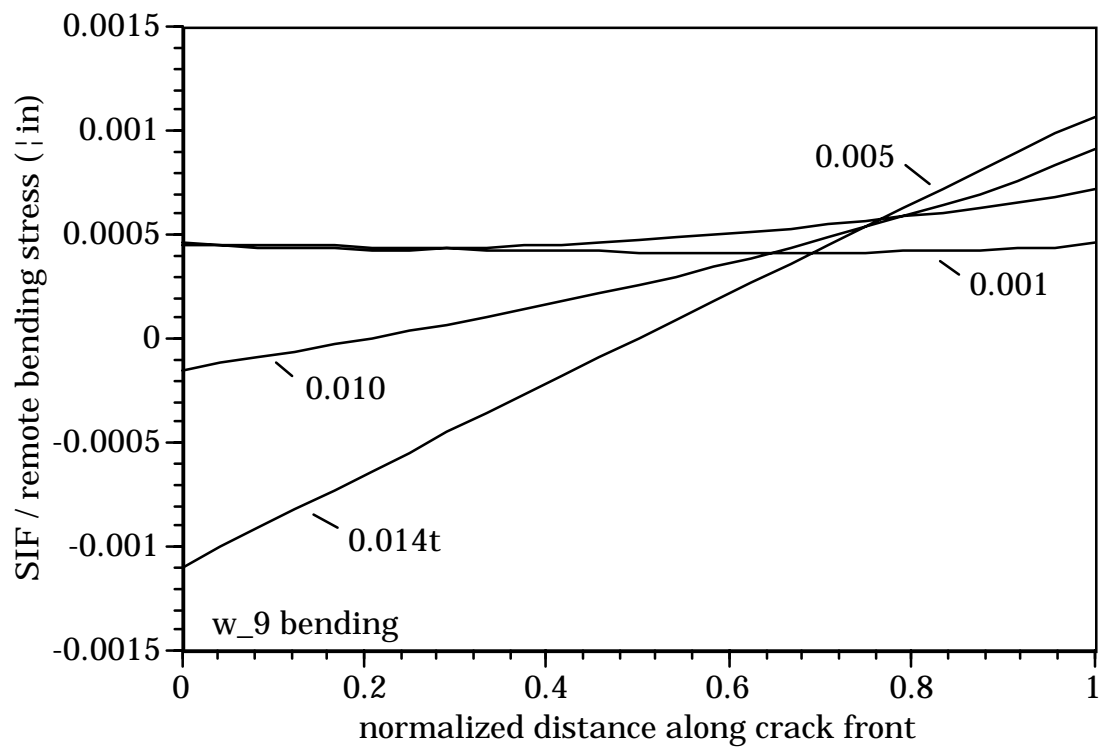
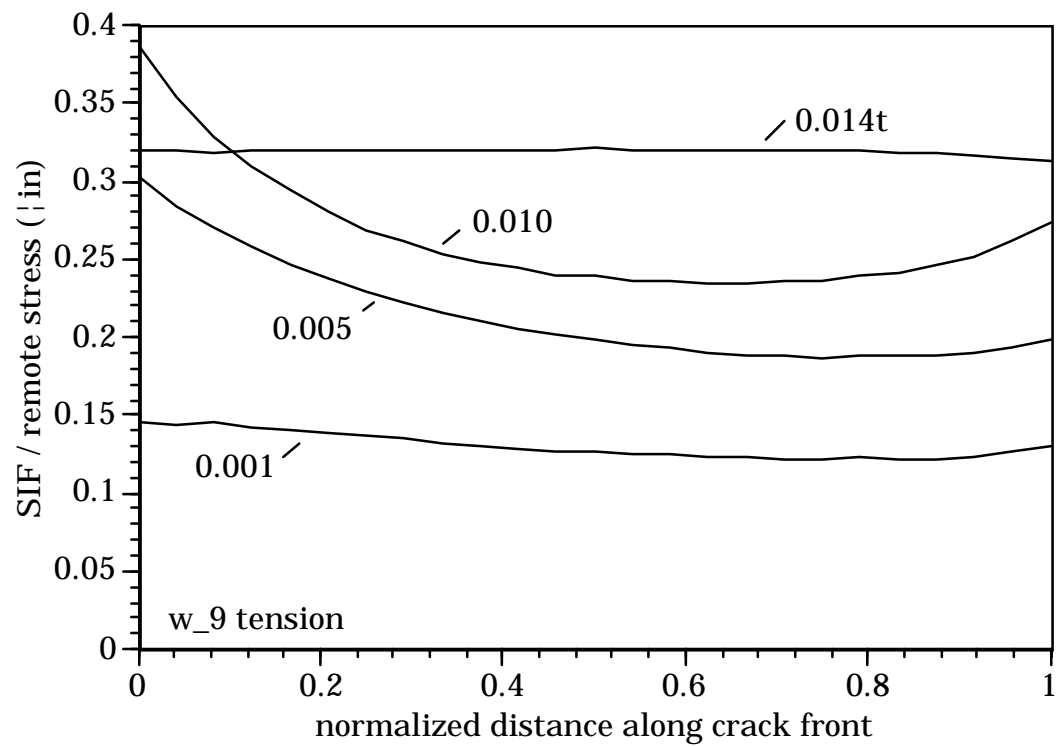
w_6



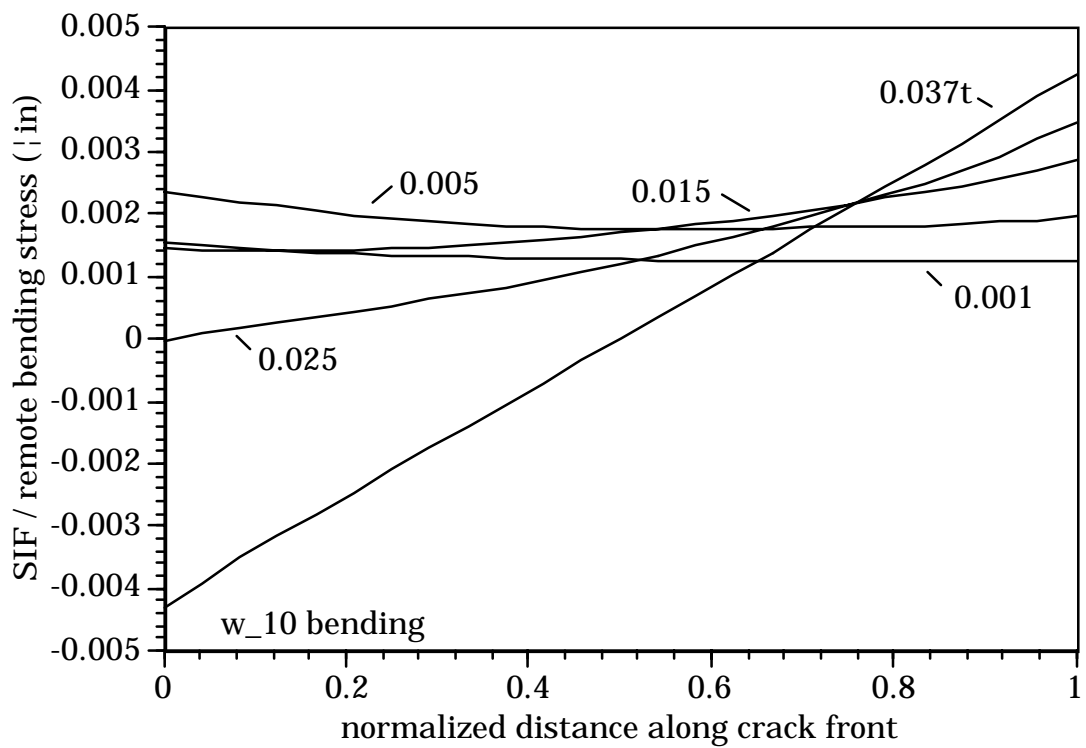
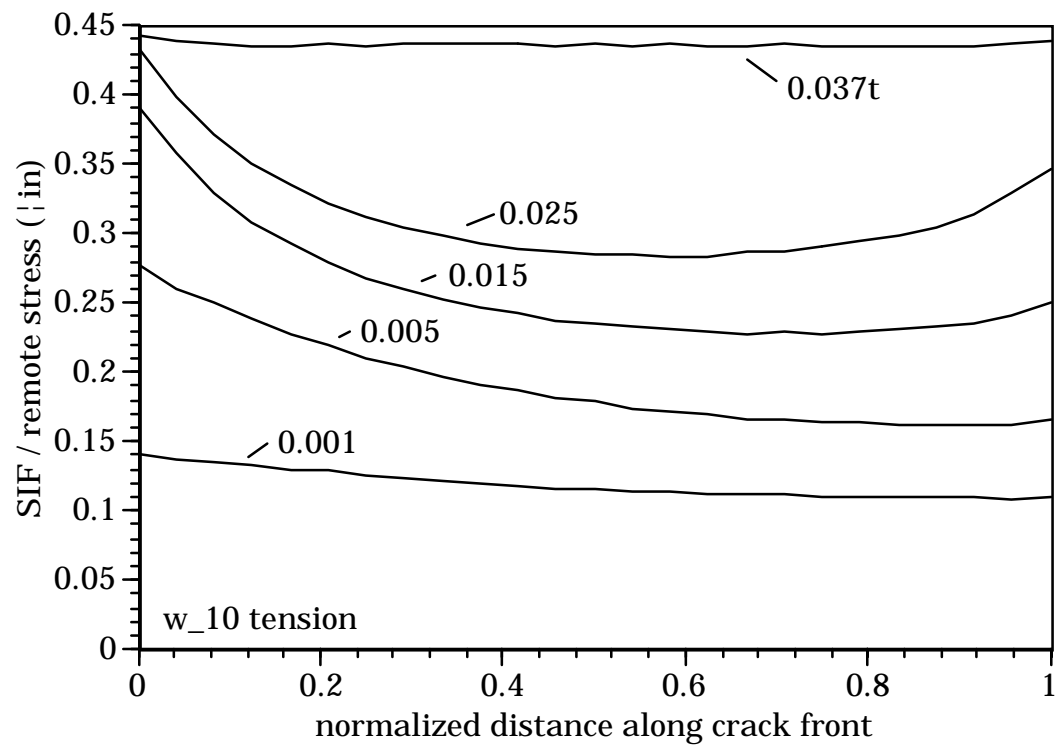
w_7



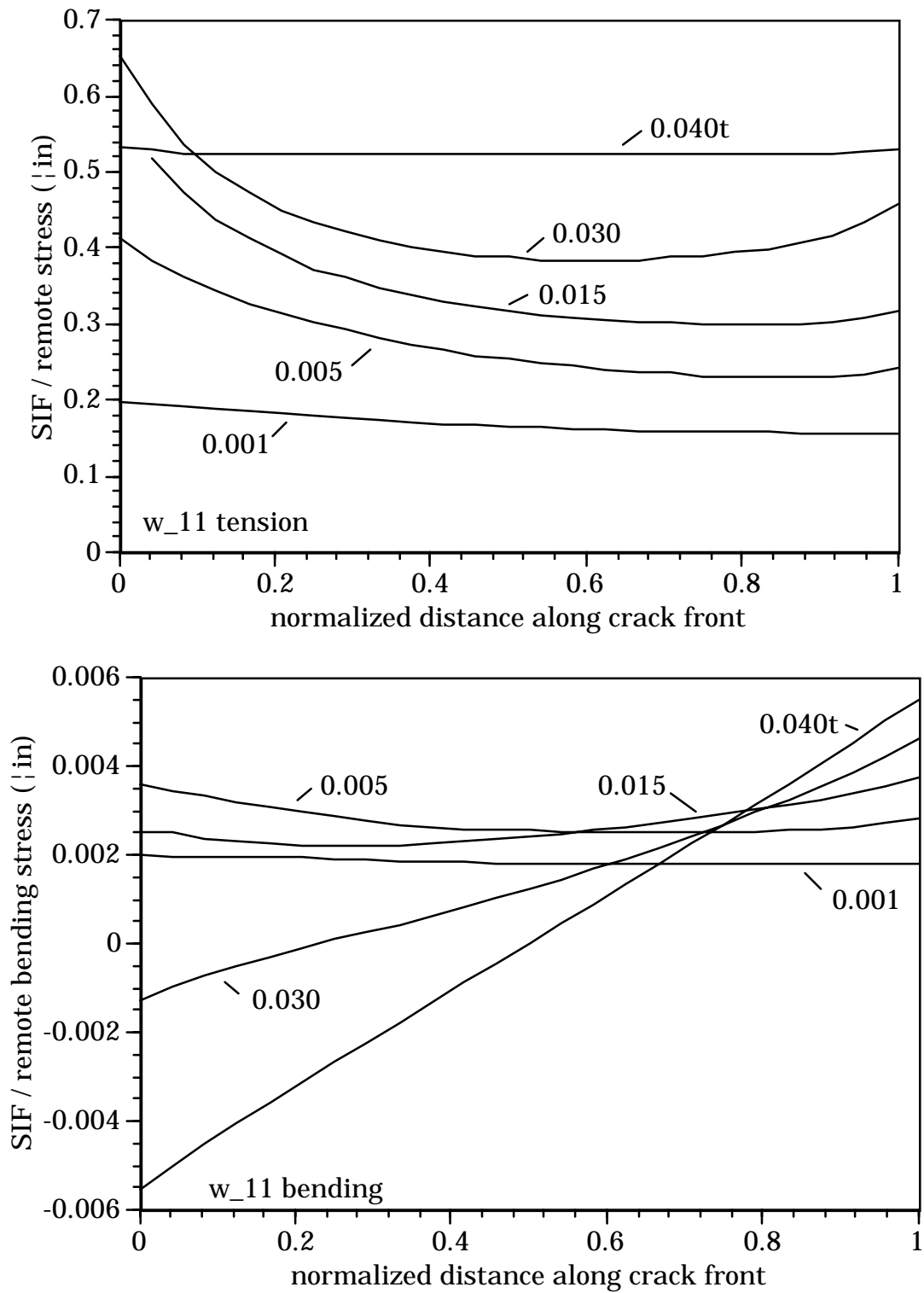
w_8



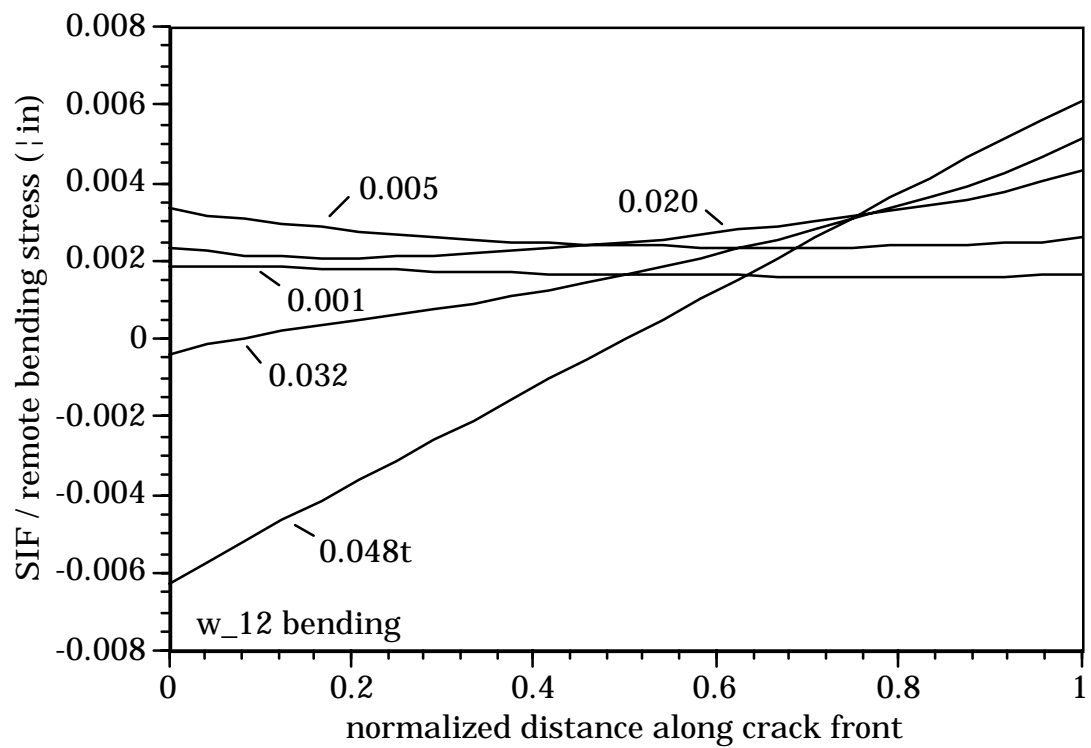
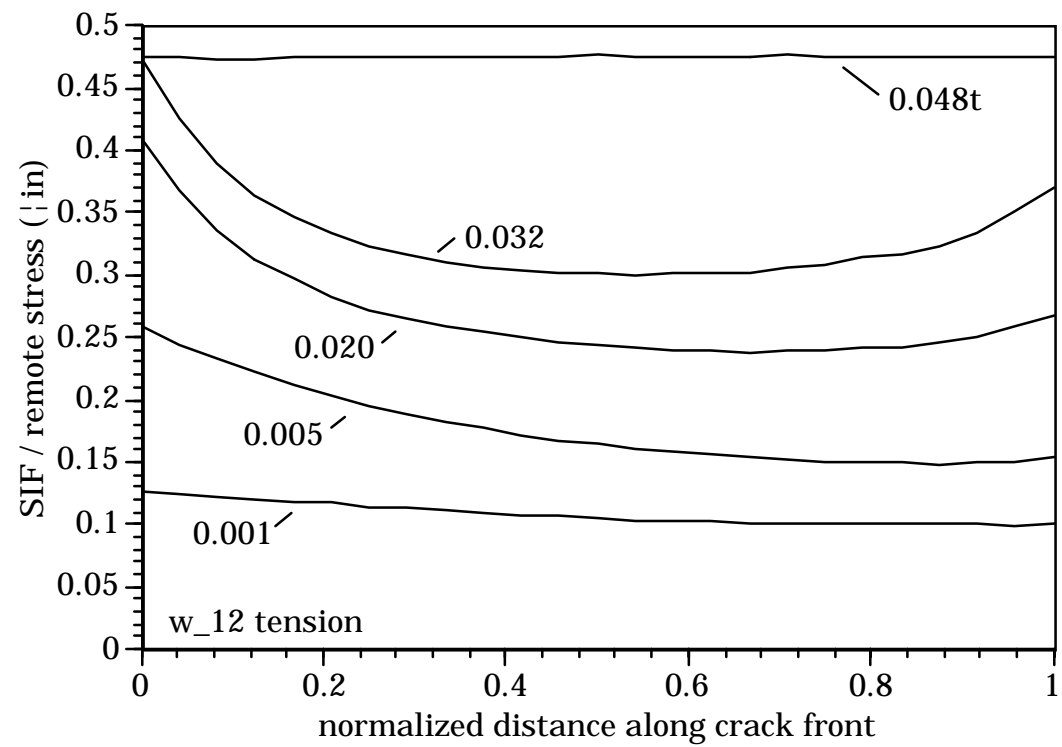
w_9



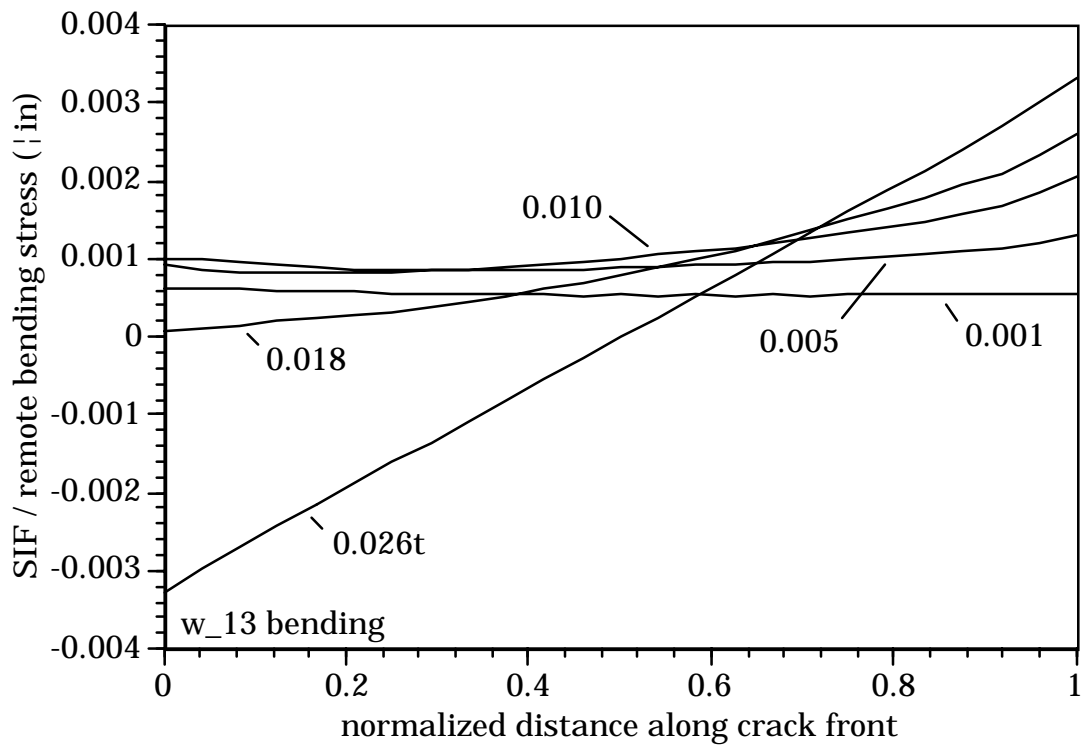
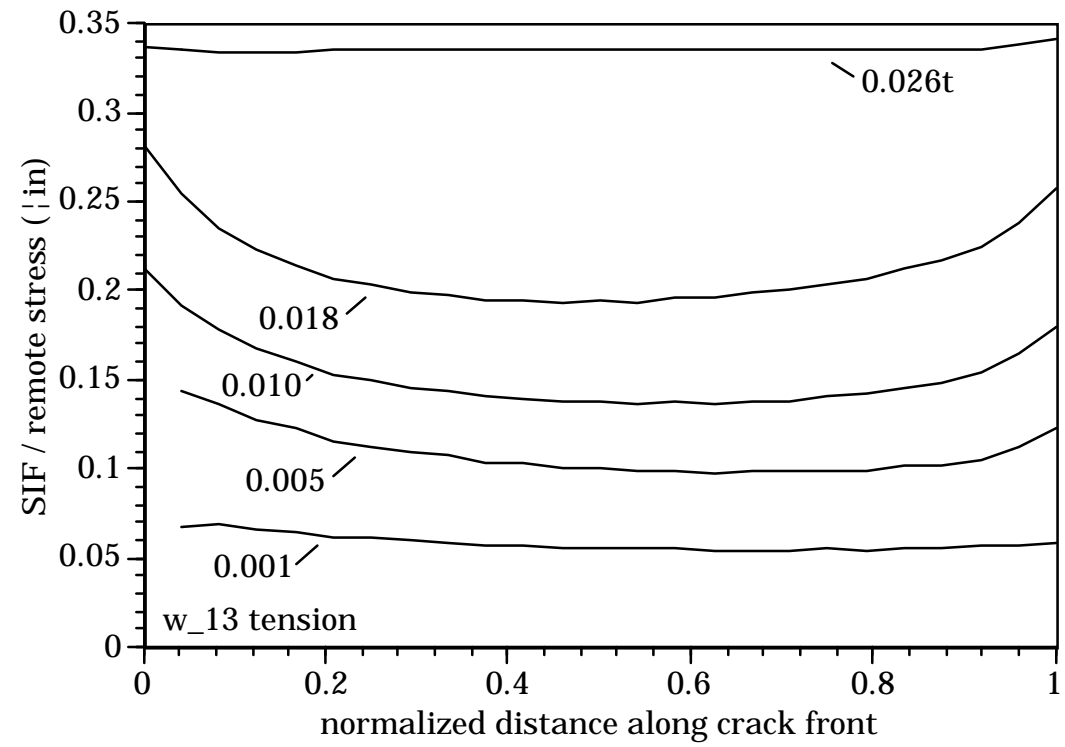
w_10



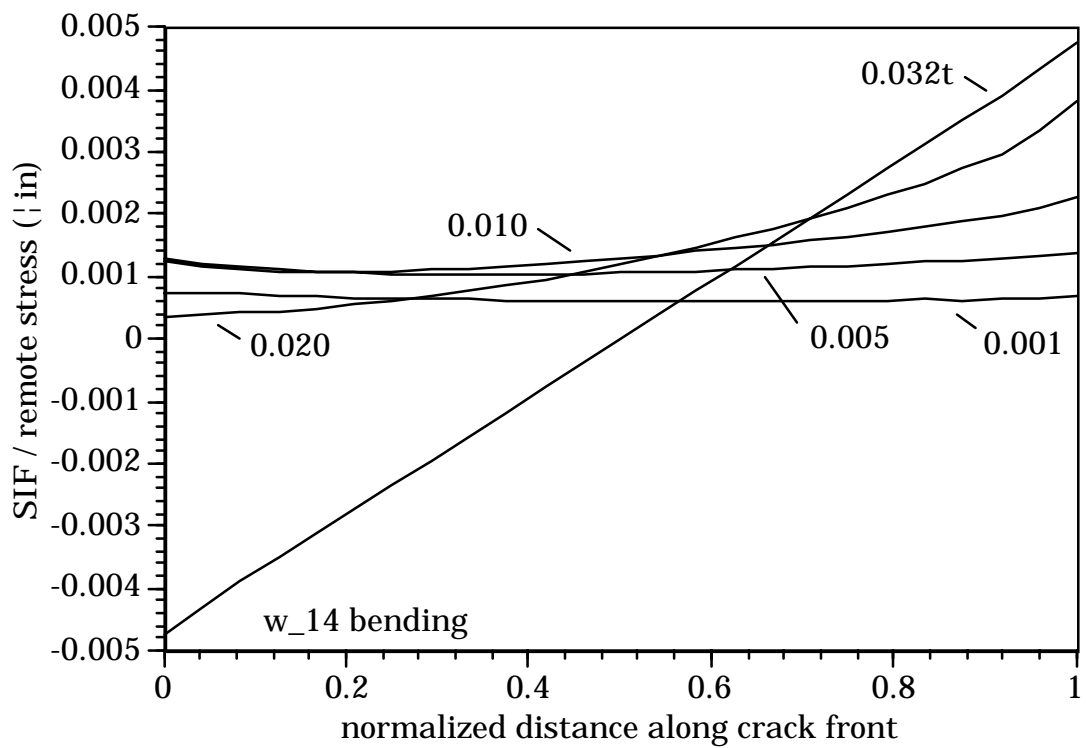
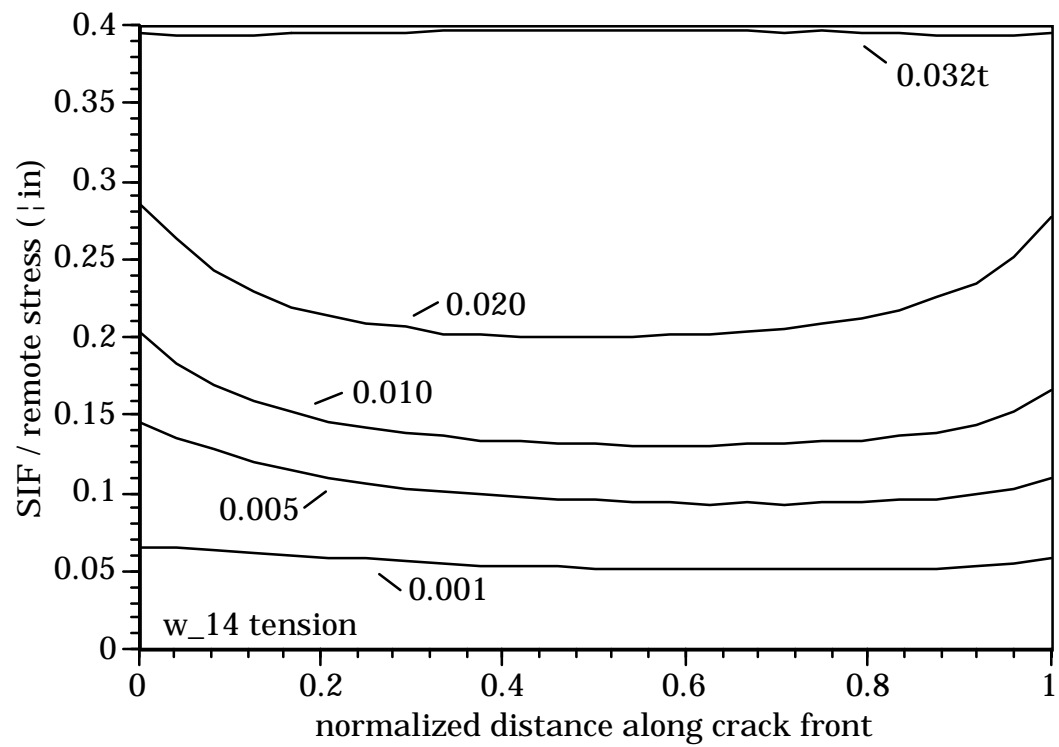
w_11



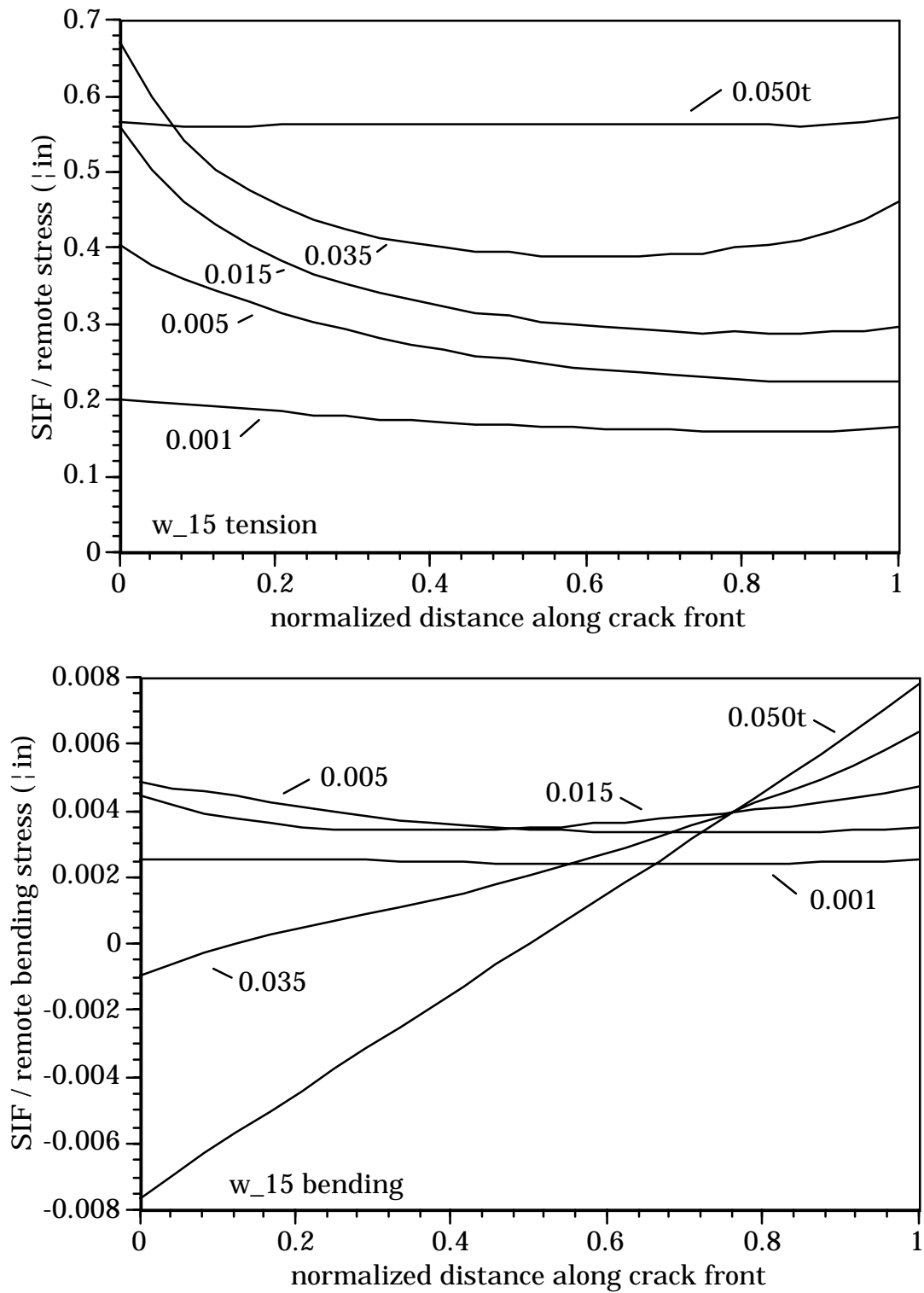
w_12



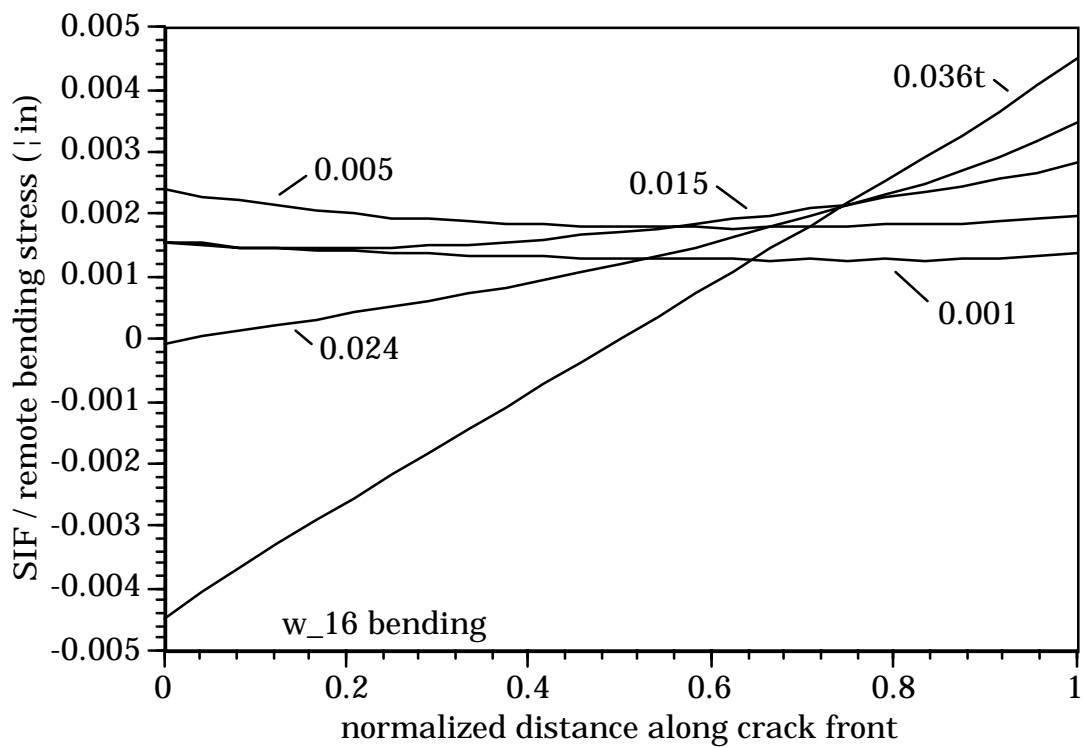
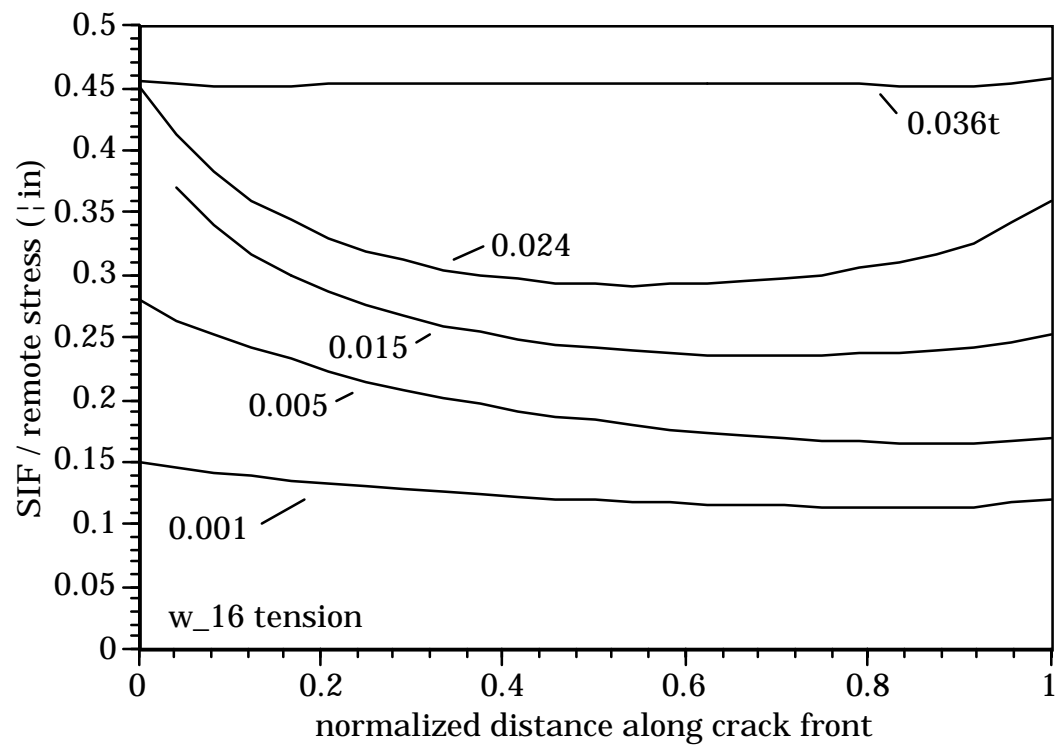
w_13



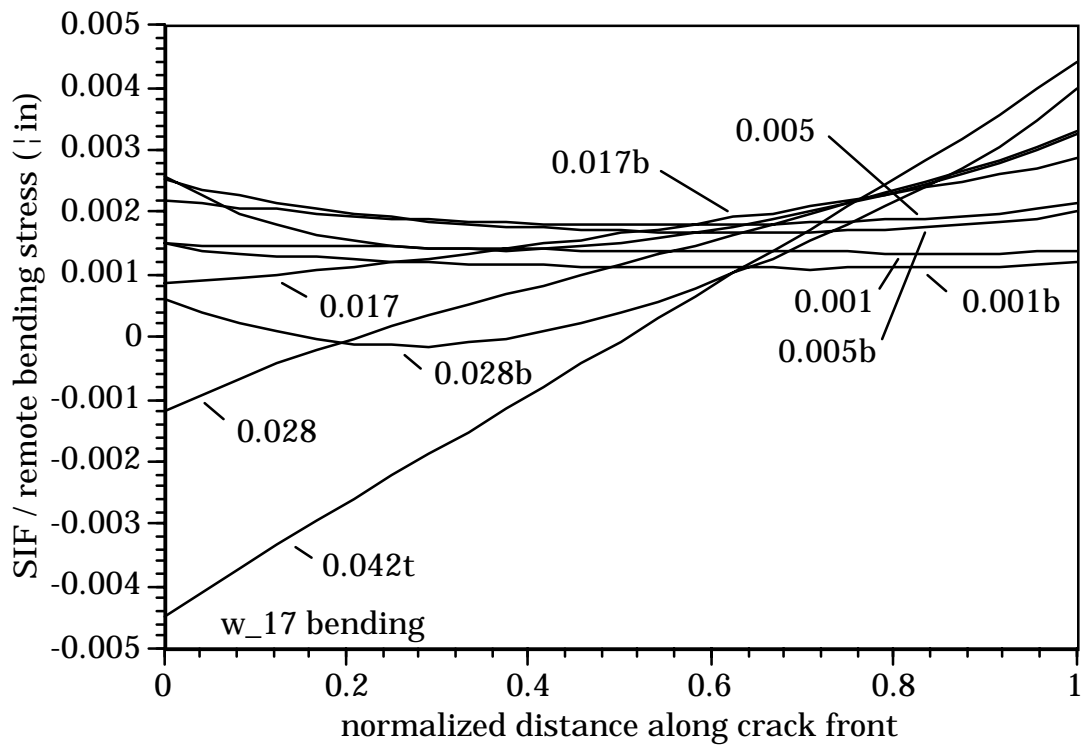
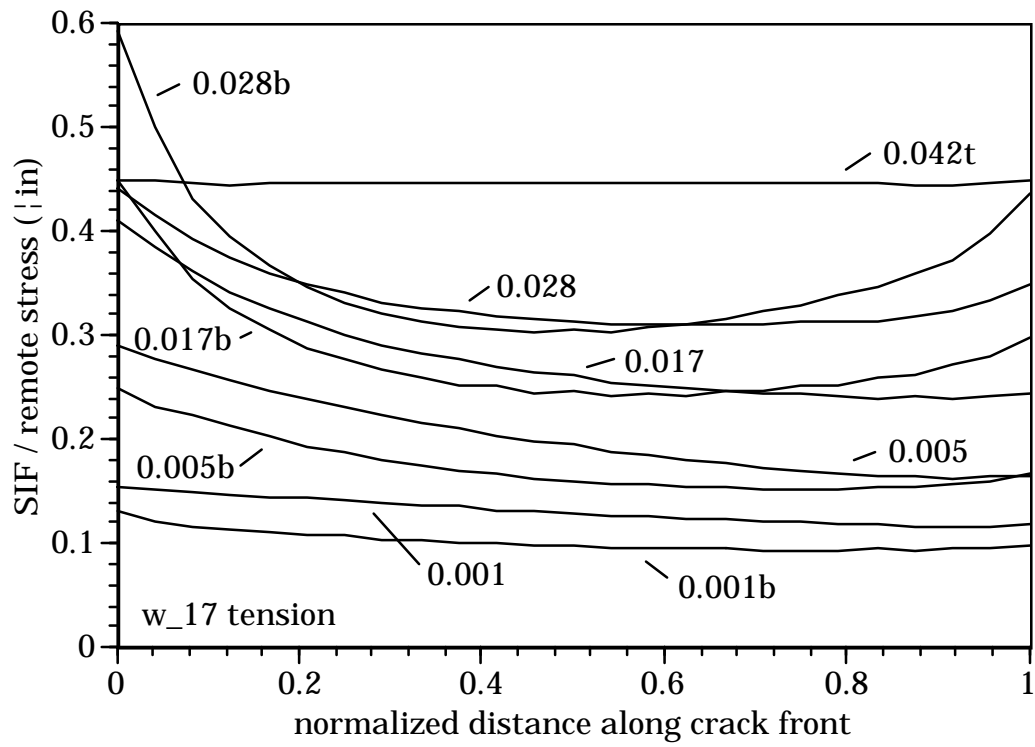
w_14



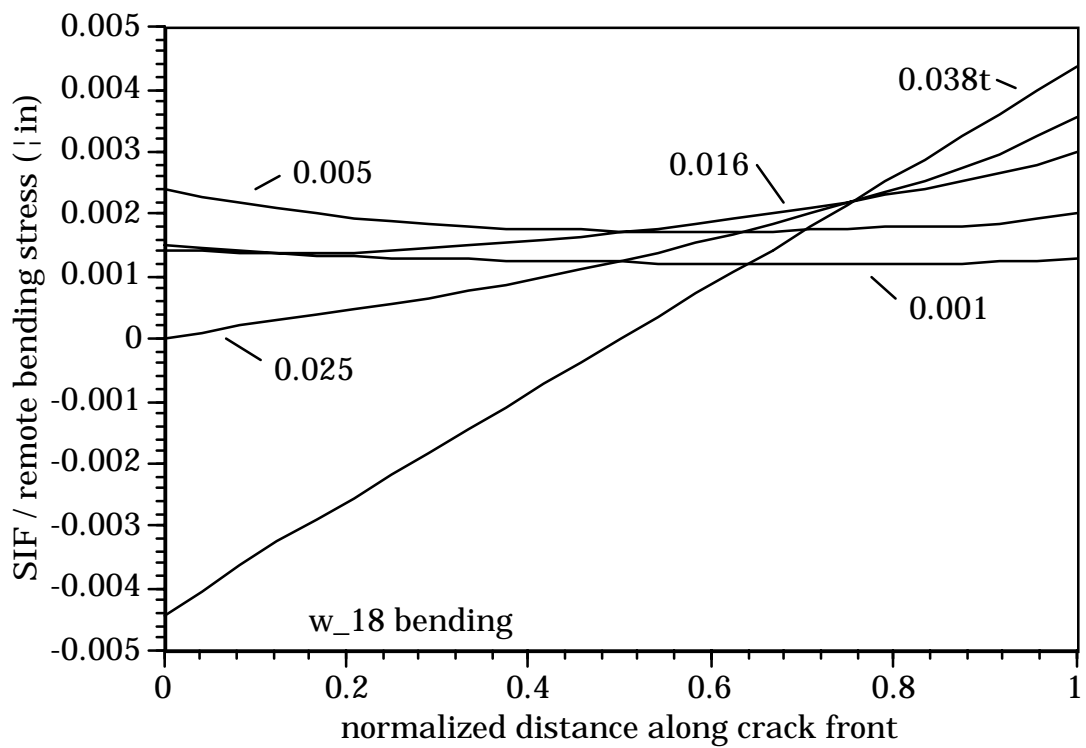
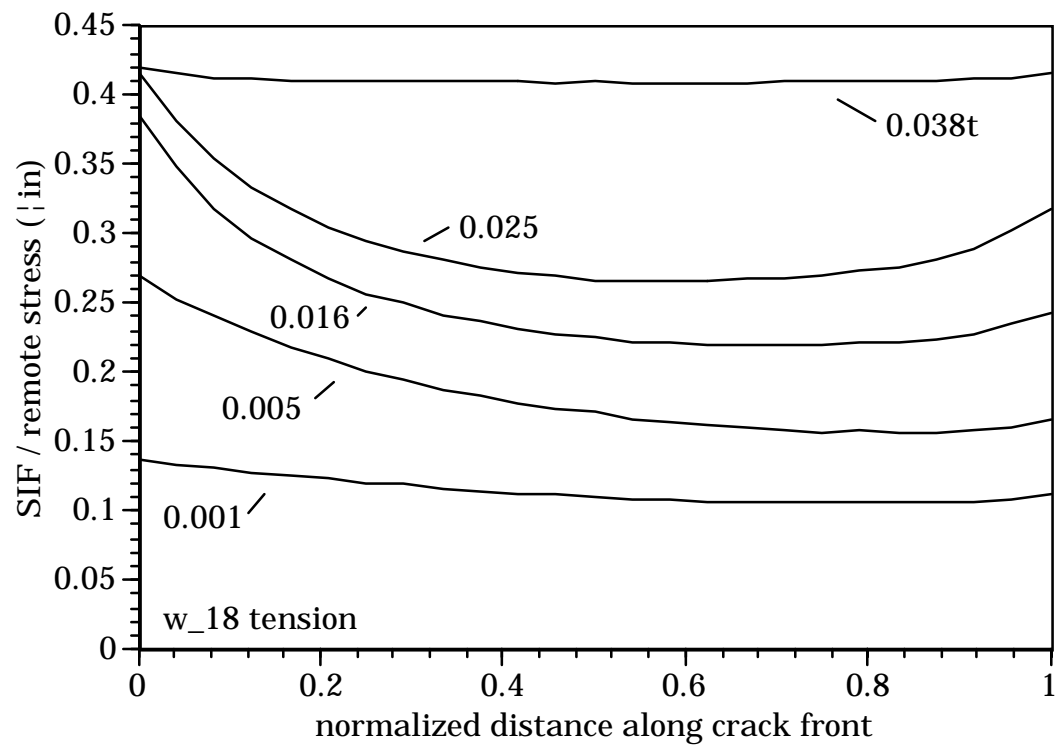
w_15



w_16



w_17



w_18

Attachment E: Stress Intensity Factor Summary

This Attachment contains the characteristic (average) stress intensity factors for all crack fronts, as explained in the body of the report.

Tension

w_0: top cracks			
a	k 25deg	k (max-25)	k average
0.001	0.108	0.105	0.106
0.005	0.223	0.201	0.212
0.015	0.325	0.276	0.300
0.030	0.400	0.352	0.376

w_1: top cracks			
a	k 25deg	k (max-25)	k average
0.001	0.137	0.134	0.136
0.005	0.260	0.245	0.253
0.015	0.356	0.321	0.339
0.038	0.418	0.394	0.406

w_1: bottom cracks			
a	k 25deg	k (max-25)	k average
0.001	0.092	0.087	0.089
0.005	0.199	0.172	0.186
0.015	0.311	0.249	0.280
0.038	0.454	0.378	0.416

w_2: top cracks			
a	k 25deg	k (max-25)	k average
0.001	0.078	0.069	0.073
0.005	0.133	0.116	0.124
0.008	0.158	0.146	0.152

w_3: top cracks			
a	k 25deg	k (max-25)	k average
0.001	0.080	0.074	0.077
0.005	0.133	0.120	0.127
0.009	0.160	0.153	0.156

w_3: bottom cracks			
a	k 25deg	k (max-25)	k average
0.001	0.070	0.060	0.065
0.005	0.132	0.112	0.122
0.009	0.173	0.158	0.165

w_4: top cracks			
a	k 25deg	k (max-25)	k average
0.001	0.080	0.072	0.076
0.005	0.137	0.124	0.130
0.009	0.166	0.160	0.163

w_4: bottom cracks			
a	k 25deg	k (max-25)	k average
0.001	0.073	0.064	0.068
0.005	0.138	0.119	0.128
0.009	0.182	0.171	0.177

w_5: top cracks			
a	k 25deg	k (max-25)	k average
0.001	0.167	0.158	0.162
0.005	0.242	0.219	0.230
0.011	0.270	0.255	0.263

w_5: bottom cracks			
a	k 25deg	k (max-25)	k average
0.001	0.116	0.101	0.109
0.005	0.217	0.170	0.194
0.011	0.288	0.244	0.266

w_6: top cracks			
a	k 25deg	k (max-25)	k average
0.001	0.062	0.060	0.061
0.005	0.127	0.122	0.124
0.009	0.163	0.160	0.161

w_6: bottom cracks			
a	k 25deg	k (max-25)	k average
0.001	0.059	0.056	0.058
0.005	0.128	0.119	0.123
0.009	0.180	0.169	0.174

w_7: top cracks			
a	k 25deg	k (max-25)	k average
0.001	0.103	0.101	0.102
0.005	0.196	0.189	0.192
0.011	0.251	0.245	0.248

w_7: bottom cracks			
a	k 25deg	k (max-25)	k average
0.001	0.084	0.081	0.082
0.005	0.181	0.161	0.171
0.011	0.274	0.241	0.258

w_8: top cracks			
a	k 25deg	k (max-25)	k average
0.001	0.080	0.072	0.076
0.005	0.138	0.121	0.129
0.008	0.164	0.154	0.159

w_9: top cracks			
a	k 25deg	k (max-25)	k average
0.001	0.136	0.122	0.129
0.005	0.226	0.188	0.207
0.010	0.266	0.236	0.251

w_10: top cracks			
a	k 25deg	k (max-25)	k average
0.001	0.125	0.111	0.118
0.005	0.208	0.164	0.186
0.015	0.265	0.228	0.246
0.025	0.308	0.289	0.298

w_11: top cracks			
a	k 25deg	k (max-25)	k average
0.001	0.179	0.159	0.169
0.005	0.298	0.233	0.265
0.015	0.368	0.300	0.334
0.030	0.428	0.389	0.408

w_12: top cracks			
a	k 25deg	k (max-25)	k average
0.001	0.114	0.101	0.107
0.005	0.192	0.151	0.172
0.020	0.270	0.239	0.255
0.032	0.321	0.307	0.314

w_13: top cracks			
a	k 25deg	k (max-25)	k average
0.001	0.063	0.055	0.059
0.005	0.117	0.100	0.108
0.010	0.152	0.141	0.147
0.018	0.204	0.205	0.204

w_14: top cracks			
a	k 25deg	k (max-25)	k average
0.001	0.060	0.052	0.056
0.005	0.112	0.095	0.104
0.010	0.147	0.134	0.141
0.020	0.211	0.211	0.211

w_15: top cracks			
a	k 25deg	k (max-25)	k average
0.001	0.180	0.160	0.170
0.005	0.298	0.231	0.265
0.015	0.361	0.290	0.325
0.035	0.433	0.393	0.413

w_16: top cracks			
a	k 25deg	k (max-25)	k average
0.001	0.130	0.115	0.122
0.005	0.211	0.169	0.190
0.015	0.271	0.235	0.253
0.024	0.315	0.299	0.307

w_17: top cracks			
a	k 25deg	k (max-25)	k average
0.001	0.135	0.124	0.130
0.005	0.208	0.182	0.195
0.017	0.272	0.251	0.262
0.028	0.319	0.310	0.315

w_17: bottom cracks			
a	k 25deg	k (max-25)	k average
0.001	0.109	0.094	0.101
0.005	0.195	0.152	0.173
0.017	0.290	0.252	0.271
0.028	0.349	0.340	0.344

w_18: top cracks			
a	k 25deg	k (max-25)	k average
0.001	0.120	0.105	0.112
0.005	0.199	0.157	0.178
0.016	0.255	0.219	0.237
0.025	0.293	0.269	0.281

tension through cracks		
model	a	k
w_0	0.047	0.497
w_1	0.057	0.508
w_2	0.012	0.226
w_3	0.013	0.213
w_4	0.013	0.227
w_5	0.017	0.328
w_6	0.013	0.224
w_7	0.017	0.326
w_8	0.012	0.238
w_9	0.014	0.321
w_10	0.037	0.436
w_11	0.040	0.525
w_12	0.048	0.476
w_13	0.026	0.335
w_14	0.032	0.396
w_15	0.050	0.562
w_16	0.036	0.454
w_17	0.042	0.447
w_18	0.038	0.409

Bending

w_0: top cracks			
a	k 25deg	k (max-25)	k average
0.001	0.001082	0.001046	0.001064
0.005	0.002228	0.002011	0.002120
0.015	0.003248	0.002762	0.003005
0.030	0.003996	0.003517	0.003757

w_1: top cracks			
a	k 25deg	k (max-25)	k average
0.001	0.001467	0.001458	0.001463
0.005	0.002537	0.002500	0.002519
0.015	0.002542	0.002876	0.002709
0.038	0.000953	0.002515	0.001734

w_1: bottom cracks			
a	k 25deg	k (max-25)	k average
0.001	0.001397	0.001352	0.001374
0.005	0.002668	0.002525	0.002597
0.015	0.002985	0.003416	0.003200
0.038	0.000268	0.003691	0.001979

w_2: top cracks			
a	k 25deg	k (max-25)	k average
0.001	0.000304	0.000264	0.000284
0.005	0.000251	0.000377	0.000314
0.008	0.000080	0.000382	0.000231

w_3: top cracks			
a	k 25deg	k (max-25)	k average
0.001	0.000220	0.000221	0.000221
0.005	0.000209	0.000307	0.000258
0.009	0.000093	0.000290	0.000192

w_3: bottom cracks			
a	k 25deg	k (max-25)	k average
0.001	0.000287	0.000265	0.000276
0.005	0.000311	0.000420	0.000365
0.009	0.000082	0.000449	0.000265

w_4: top cracks			
a	k 25deg	k (max-25)	k average
0.001	0.000223	0.000229	0.000226
0.005	0.000216	0.000310	0.000263
0.009	0.000099	0.000276	0.000187

w_4: bottom cracks			
a	k 25deg	k (max-25)	k average
0.001	0.000284	0.000264	0.000274
0.005	0.000310	0.000408	0.000359
0.009	0.000061	0.000410	0.000236

w_5: top cracks			
a	k 25deg	k (max-25)	k average
0.001	0.000521	0.000505	0.000513
0.005	0.000507	0.000564	0.000536
0.011	0.000223	0.000450	0.000336

w_5: bottom cracks			
a	k 25deg	k (max-25)	k average
0.001	0.000448	0.000407	0.000427
0.005	0.000540	0.000610	0.000575
0.011	0.000053	0.000599	0.000326

w_6: top cracks			
a	k 25deg	k (max-25)	k average
0.001	0.000177	0.000188	0.000182
0.005	0.000226	0.000303	0.000265
0.009	0.000111	0.000273	0.000192

w_6: bottom cracks			
a	k 25deg	k (max-25)	k average
0.001	0.000226	0.000232	0.000229
0.005	0.000263	0.000394	0.000329
0.009	0.000017	0.000391	0.000204

w_7: top cracks			
a	k 25deg	k (max-25)	k average
0.001	0.000332	0.000334	0.000333
0.005	0.000458	0.000509	0.000484
0.011	0.000244	0.000438	0.000341

w_7: bottom cracks			
a	k 25deg	k (max-25)	k average
0.001	0.000326	0.000331	0.000329
0.005	0.000427	0.000560	0.000494
0.011	0.000022	0.000567	0.000294

w_8: top cracks			
a	k 25deg	k (max-25)	k average
0.001	0.000268	0.000261	0.000265
0.005	0.000241	0.000366	0.000304
0.008	0.000071	0.000358	0.000214

w_9: top cracks			
a	k 25deg	k (max-25)	k average
0.001	0.000435	0.000416	0.000426
0.005	0.000432	0.000560	0.000496
0.010	0.000049	0.000518	0.000283

w_10: top cracks			
a	k 25deg	k (max-25)	k average
0.001	0.001343	0.001233	0.001288
0.005	0.001910	0.001780	0.001845
0.015	0.001453	0.002119	0.001786
0.025	0.000572	0.002071	0.001321

w_11: top cracks			
a	k 25deg	k (max-25)	k average
0.001	0.001899	0.001801	0.001850
0.005	0.002831	0.002515	0.002673
0.015	0.002214	0.002878	0.002546
0.030	0.000154	0.002584	0.001369

w_12: top cracks			
a	k 25deg	k (max-25)	k average
0.001	0.001754	0.001606	0.001680
0.005	0.002646	0.002360	0.002503
0.020	0.002120	0.003099	0.002609
0.032	0.000678	0.002969	0.001823

w_13: top cracks			
a	k 25deg	k (max-25)	k average
0.001	0.000579	0.000544	0.000561
0.005	0.000868	0.001028	0.000948
0.010	0.000818	0.001379	0.001099
0.018	0.000317	0.001528	0.000922

w_14: top cracks			
a	k 25deg	k (max-25)	k average
0.001	0.000669	0.000624	0.000646
0.005	0.001067	0.001208	0.001138
0.010	0.001072	0.001726	0.001399
0.020	0.000569	0.002218	0.001393

w_15: top cracks			
a	k 25deg	k (max-25)	k average
0.001	0.002510	0.002414	0.002462
0.005	0.003903	0.003340	0.003622
0.015	0.003440	0.003888	0.003664
0.035	0.000753	0.003732	0.002242

w_16: top cracks			
a	k 25deg	k (max-25)	k average
0.001	0.001377	0.001264	0.001321
0.005	0.001927	0.001798	0.001863
0.015	0.001477	0.002114	0.001796
0.024	0.000564	0.002034	0.001299

w_17: top cracks			
a	k 25deg	k (max-25)	k average
0.001	0.001419	0.001369	0.001394
0.005	0.001830	0.001809	0.001819
0.017	0.001457	0.001847	0.001652
0.028	0.000780	0.001535	0.001157

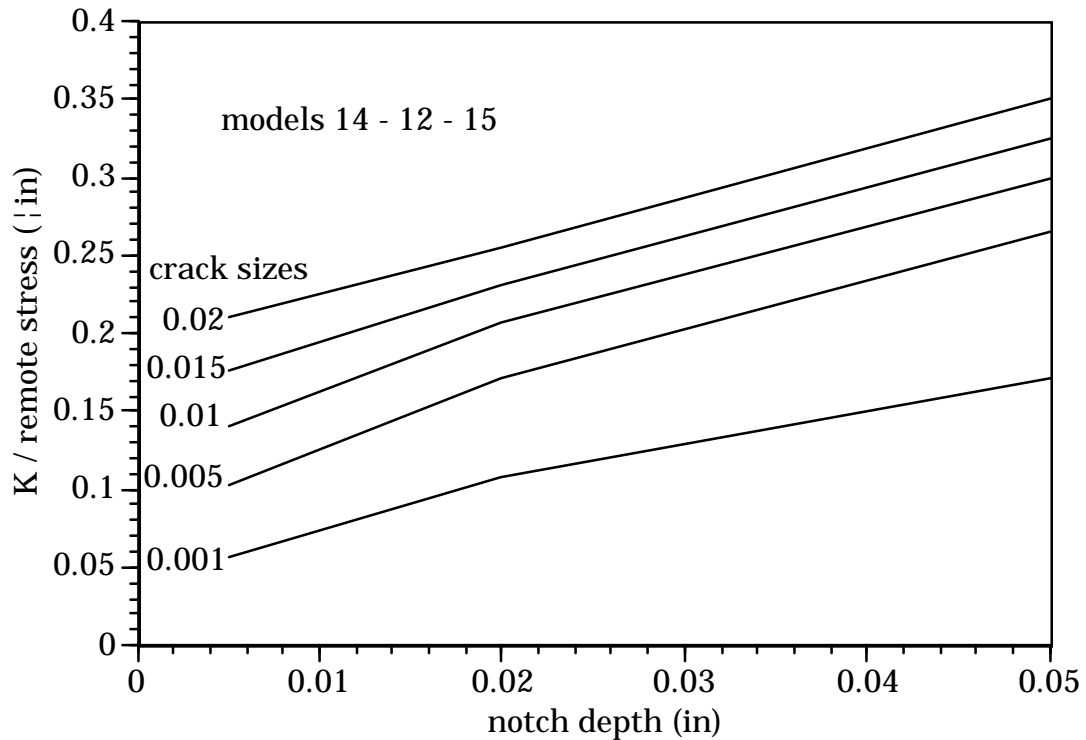
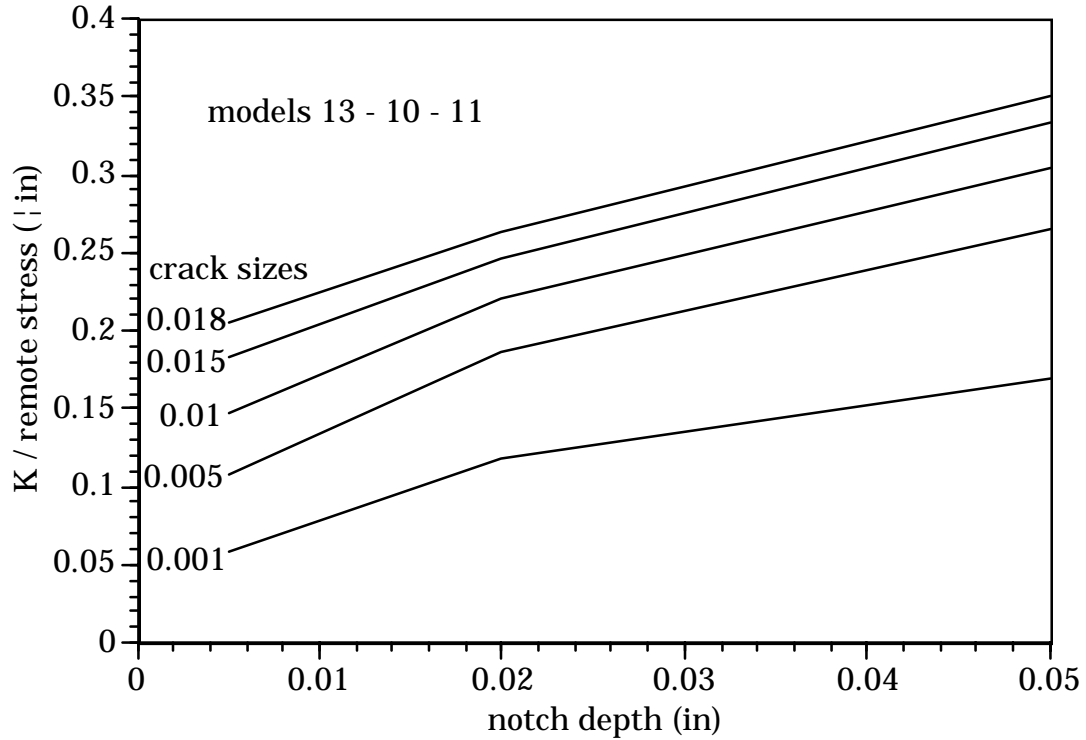
w_17: top cracks			
a	k 25deg	k (max-25)	k average
0.001	0.001243	0.001103	0.001173
0.005	0.001980	0.001731	0.001856
0.017	0.001535	0.002290	0.001913
0.028	-0.000110	0.002122	0.001006

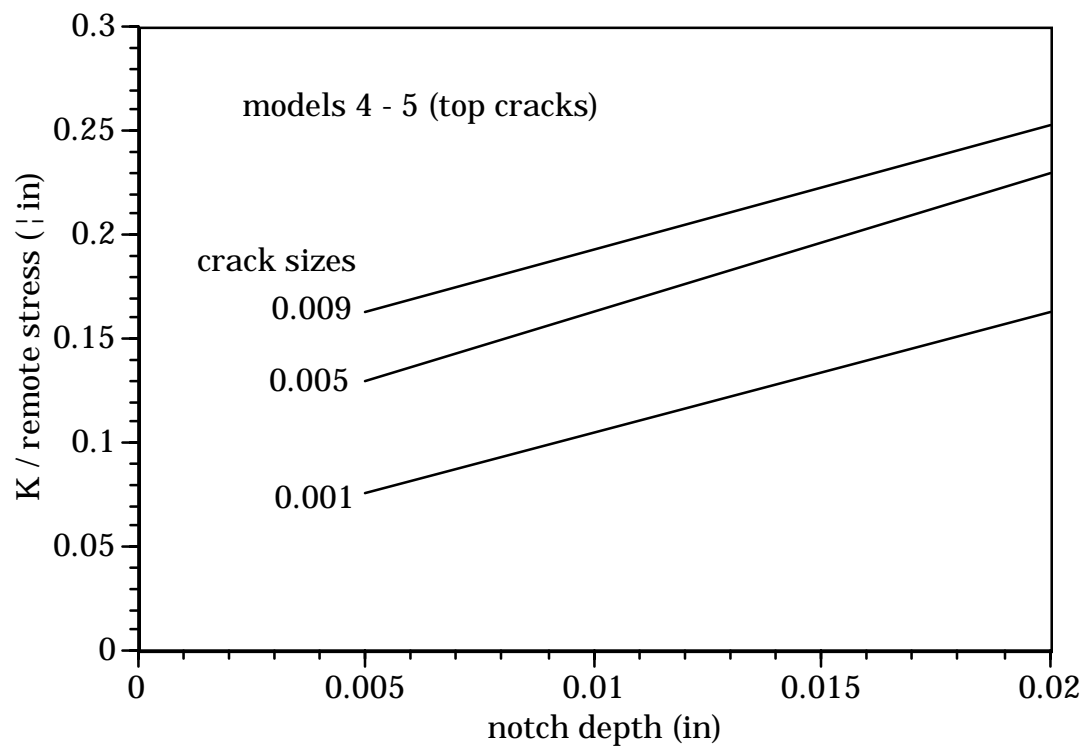
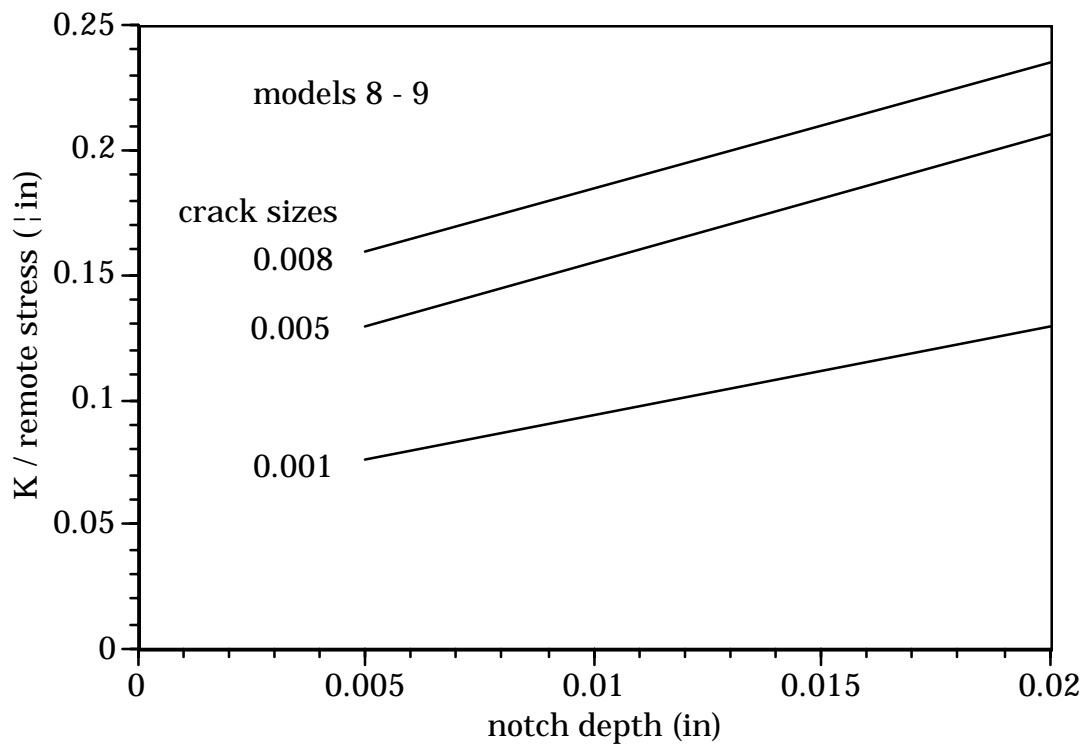
w_18: top cracks			
a	k 25deg	k (max-25)	k average
0.001	0.001304	0.001196	0.001250
0.005	0.001873	0.001748	0.001811
0.016	0.001416	0.002176	0.001796
0.025	0.000575	0.002156	0.001366

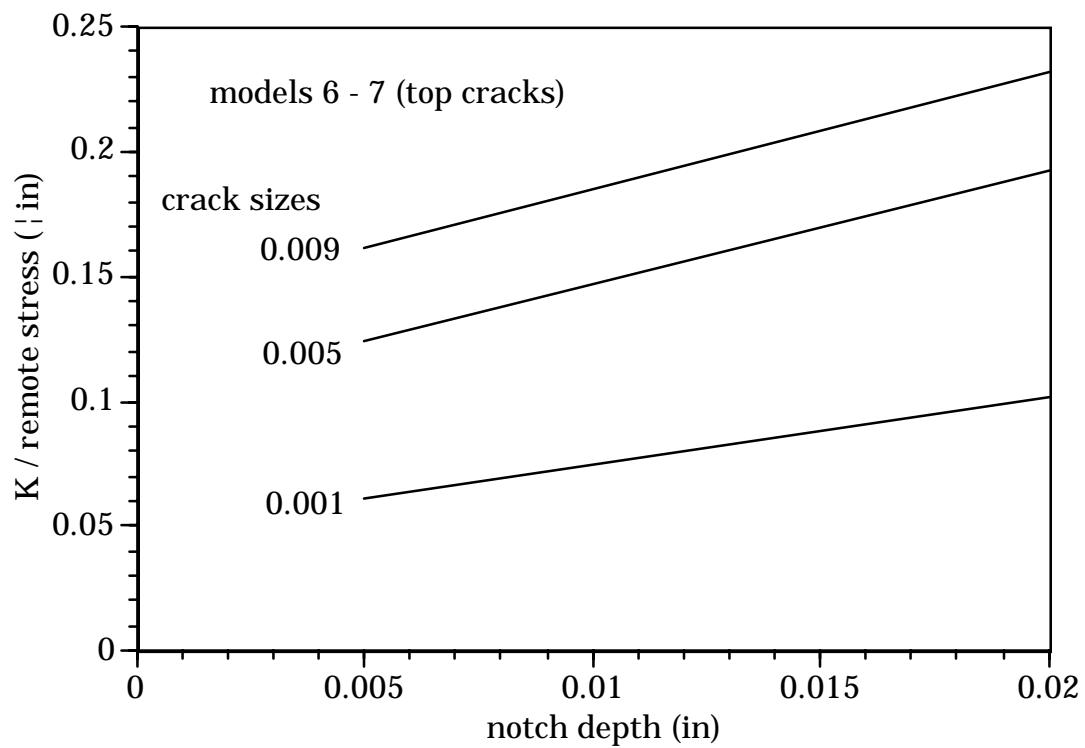
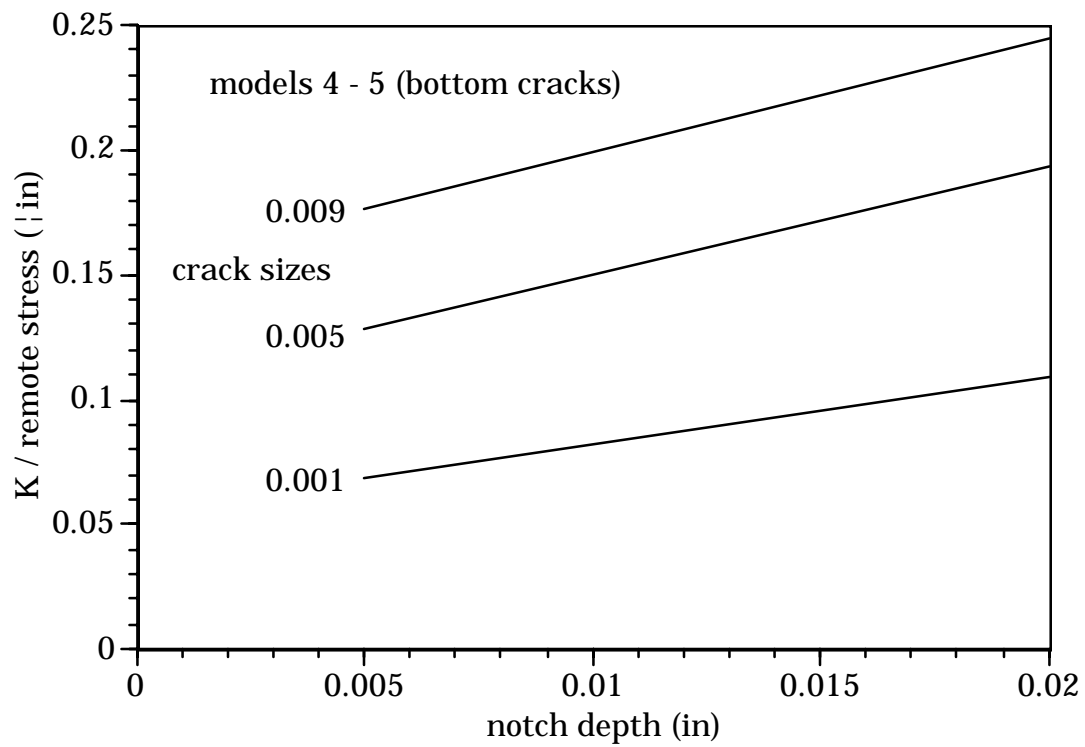
bending through cracks			
model	a	k bottom	k top
w_0	0.047	-0.006192	0.006273
w_1	0.057	-0.006472	0.006215
w_2	0.012	-0.000800	0.000791
w_3	0.013	-0.000728	0.000727
w_4	0.013	-0.000736	0.000728
w_5	0.017	-0.001102	0.001077
w_6	0.013	-0.000717	0.000719
w_7	0.017	-0.001075	0.001120
w_8	0.012	-0.000786	0.000791
w_9	0.014	-0.001098	0.001070
w_10	0.037	-0.004299	0.004251
w_11	0.040	-0.005536	0.005514
w_12	0.048	-0.006267	0.006118
w_13	0.026	-0.003266	0.003308
w_14	0.032	-0.004741	0.004735
w_15	0.050	-0.007661	0.007778
w_16	0.036	-0.004479	0.004494
w_17	0.042	-0.004502	0.004390
w_18	0.038	-0.004437	0.004379

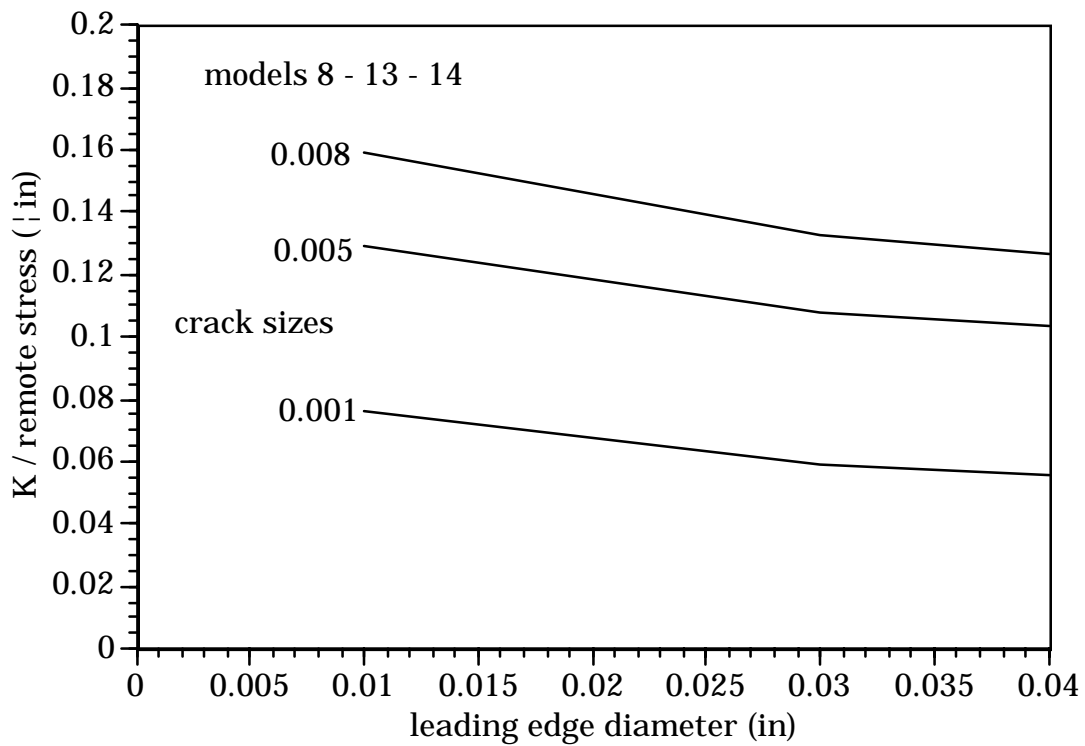
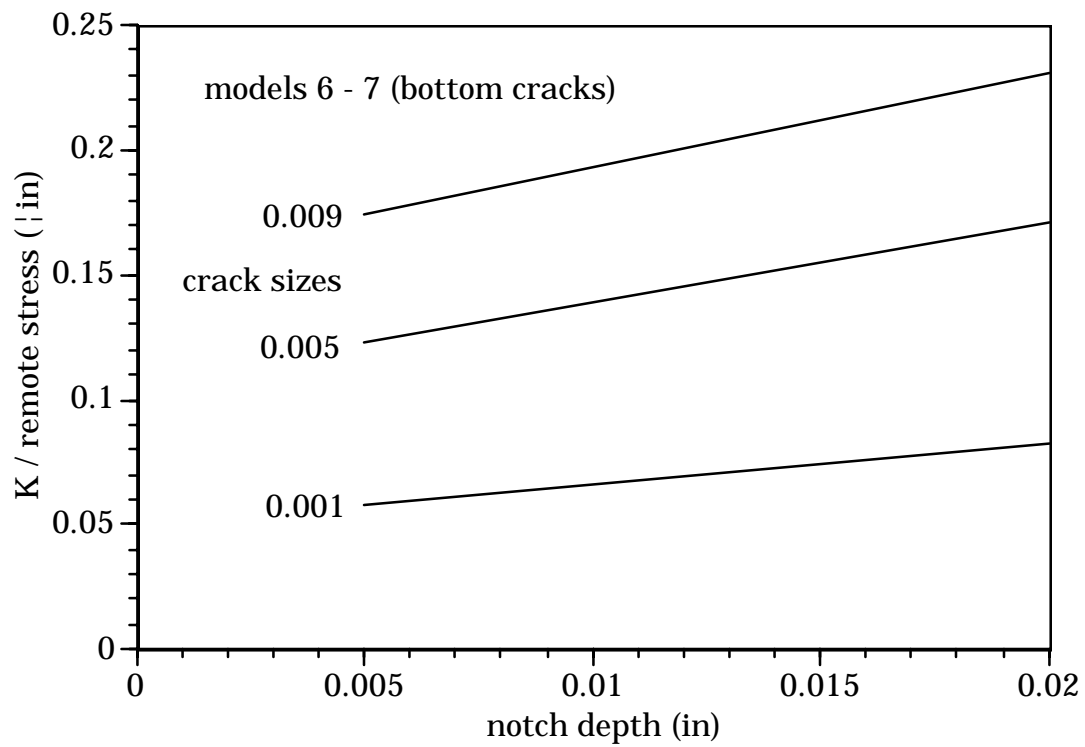
**Attachment F: Stress Intensity Factor Trends
as a Function of Model Parameters**

SIF vs. notch depth

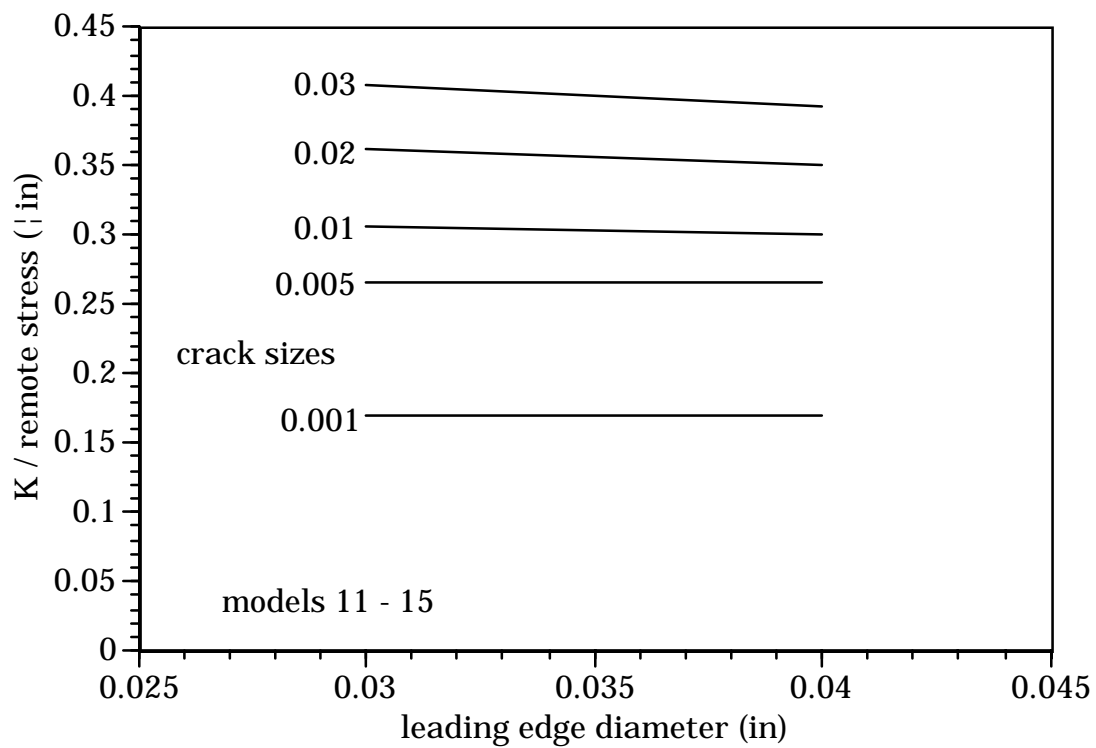
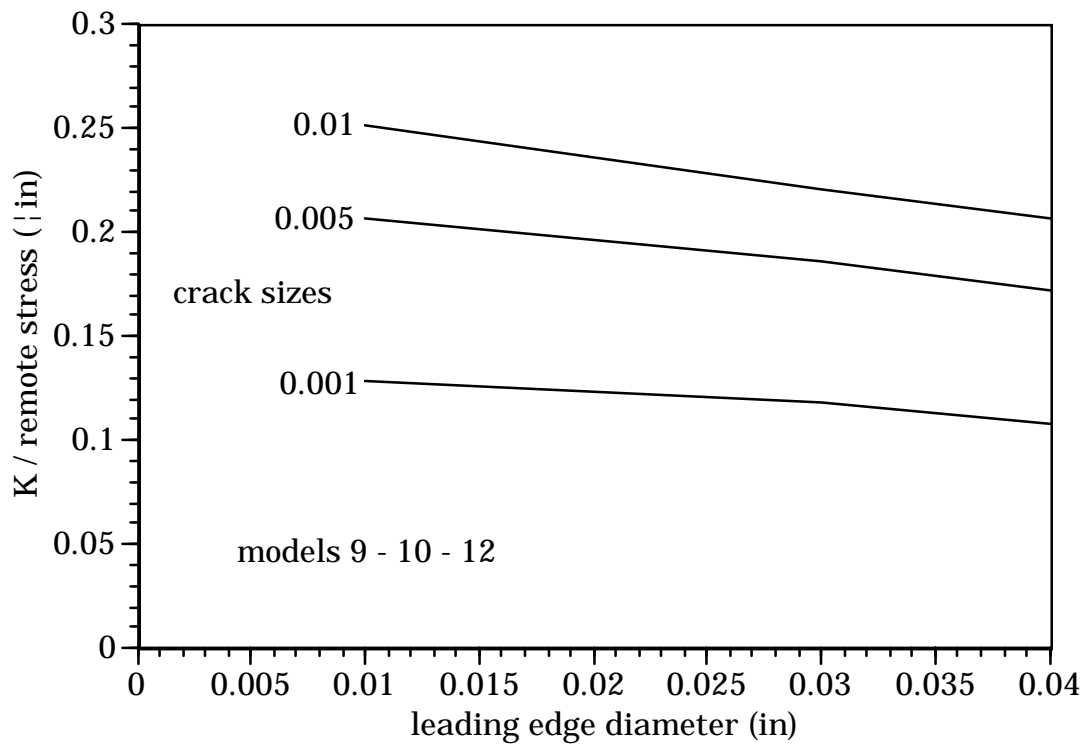


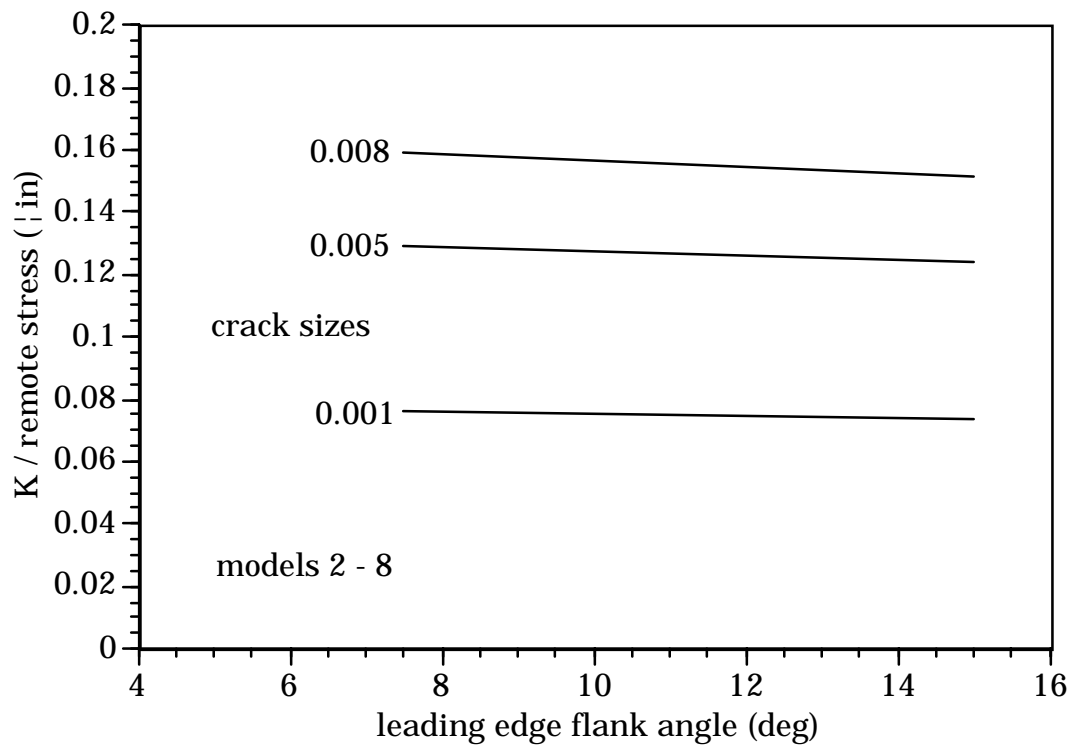
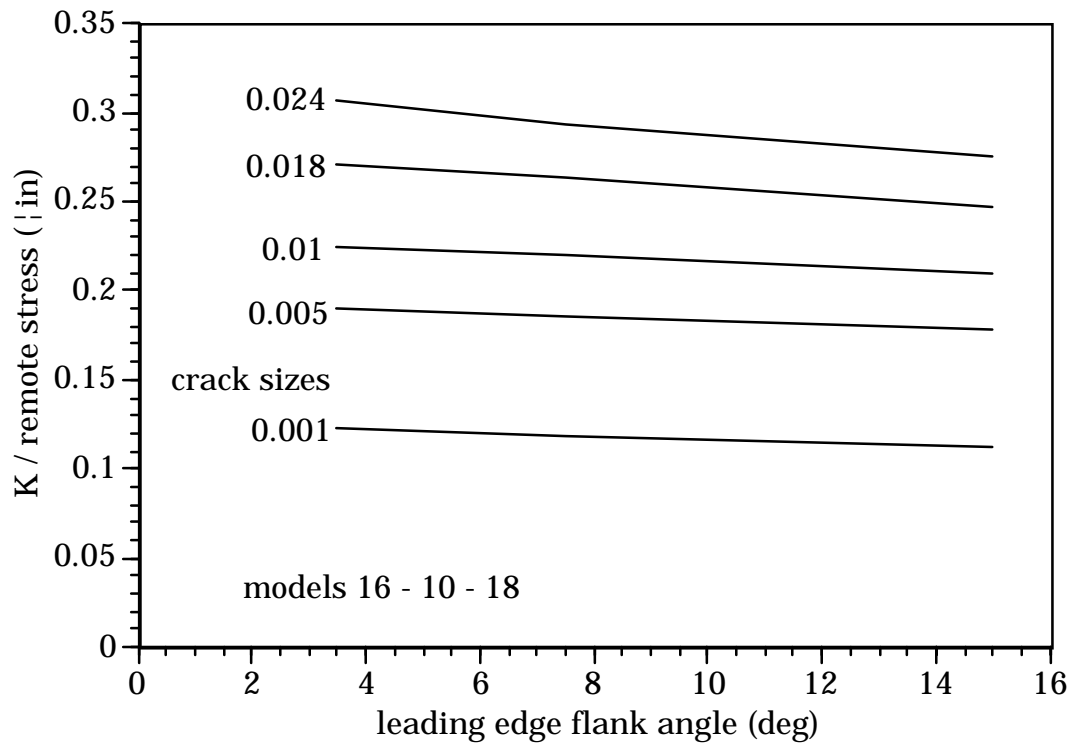




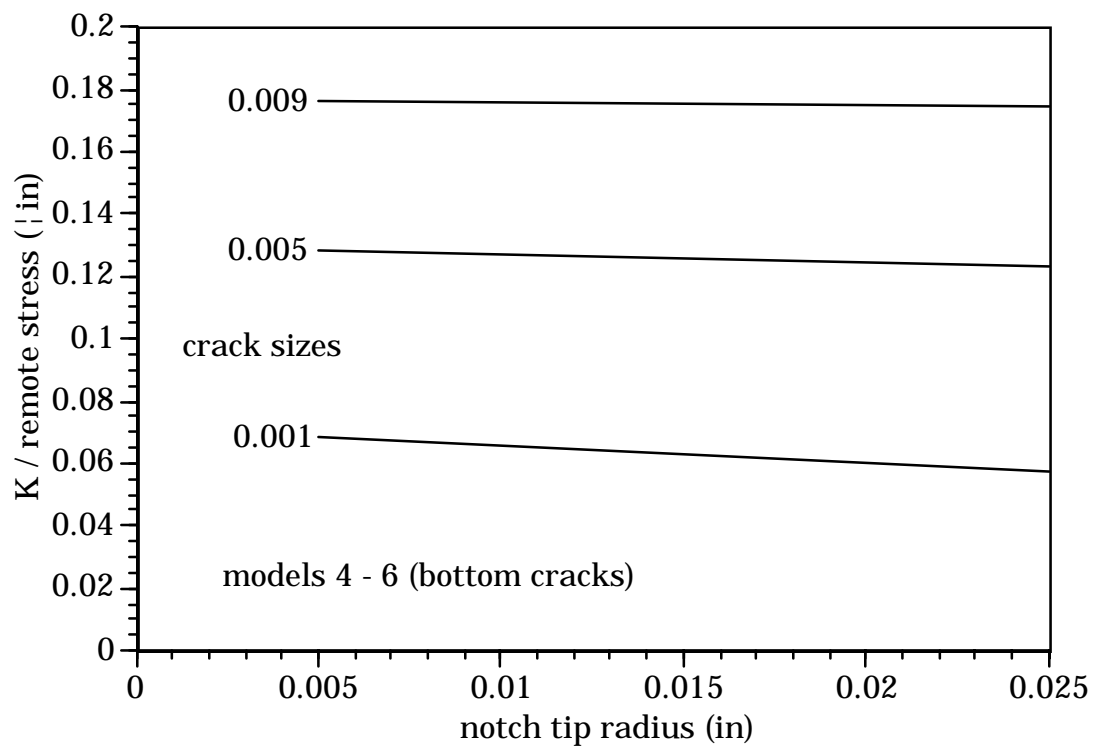
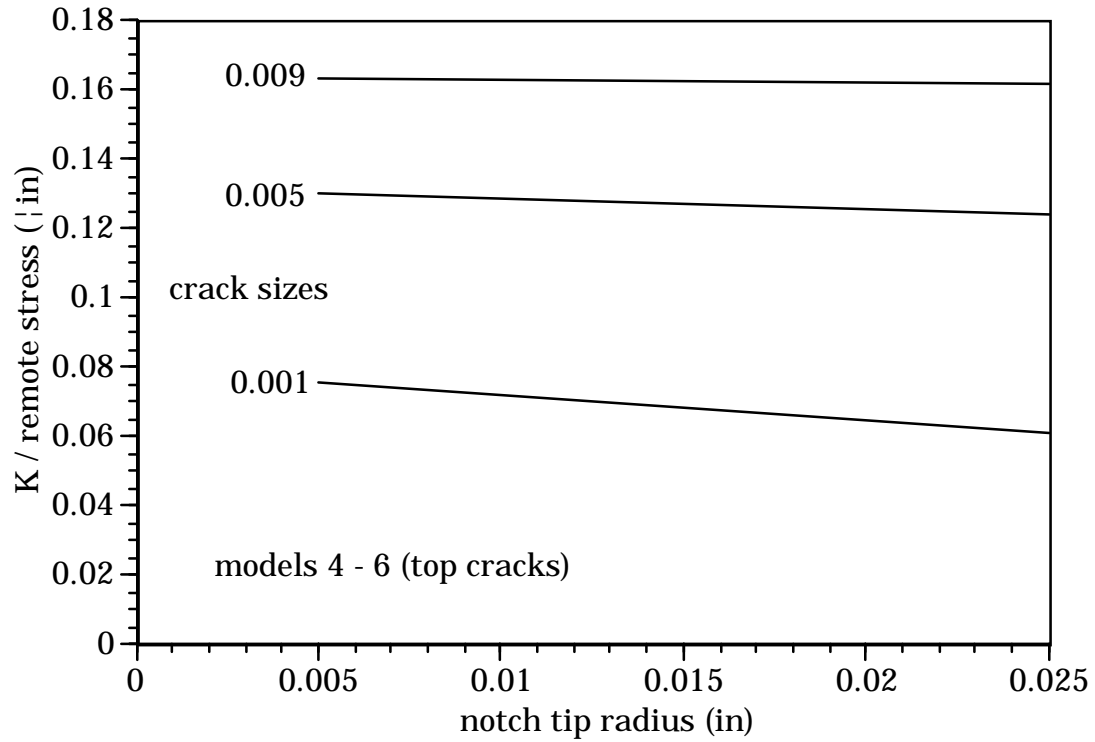


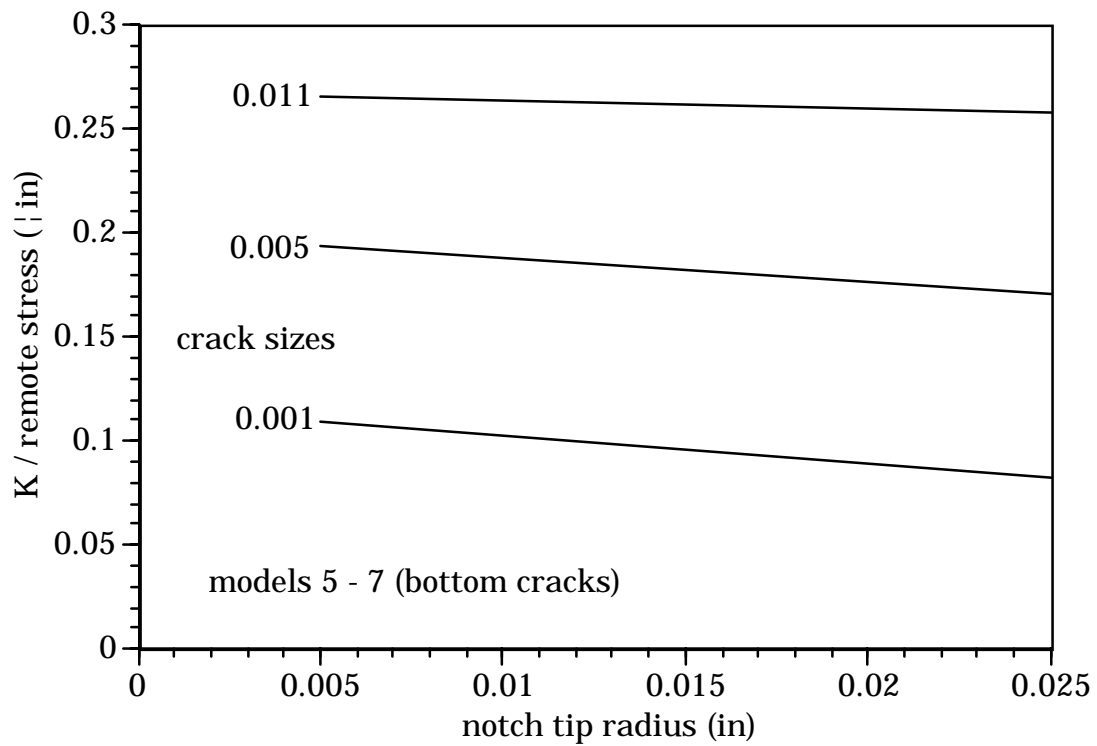
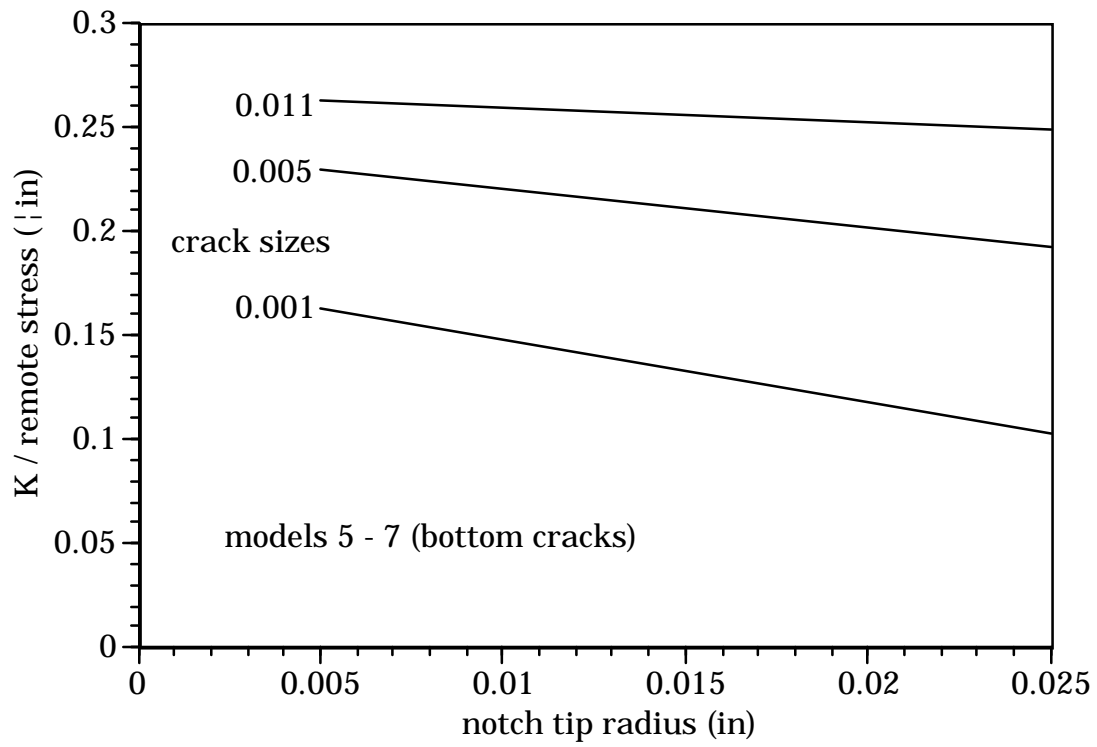
SIF vs. leading edge diameter



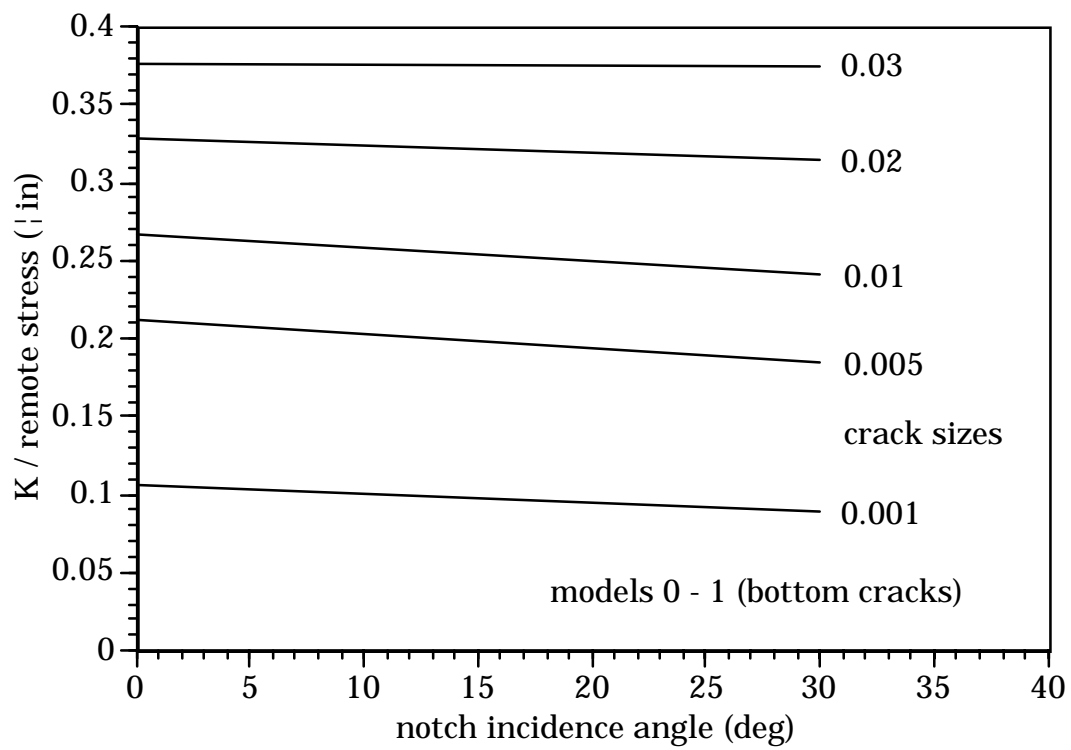
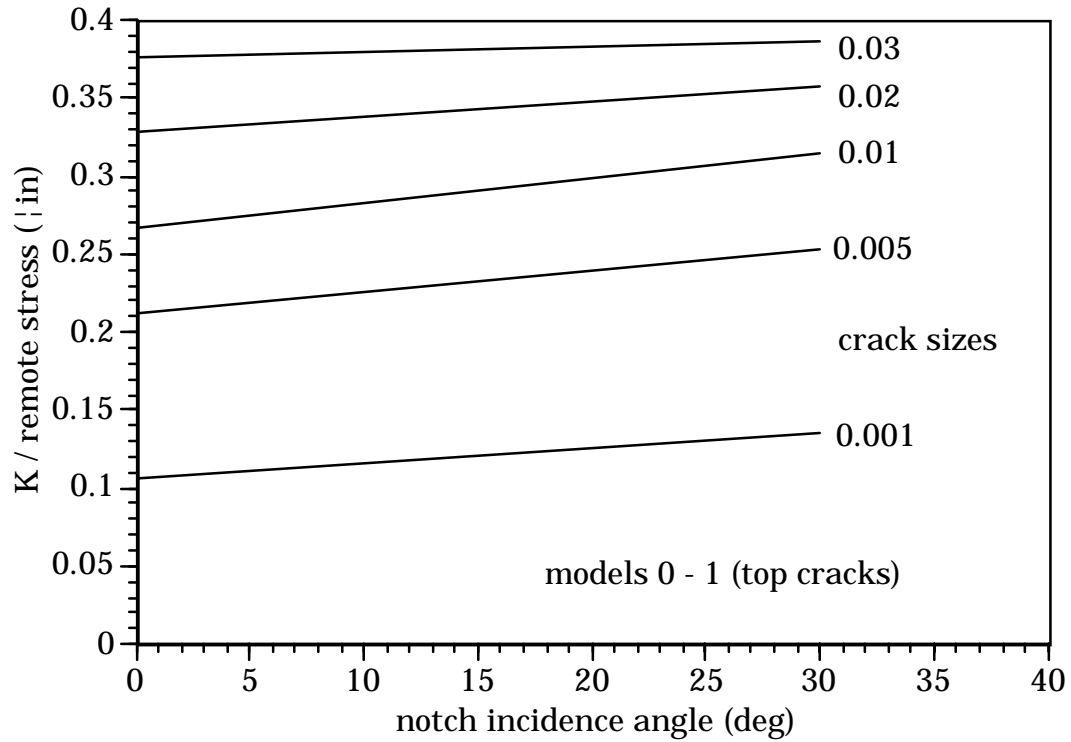


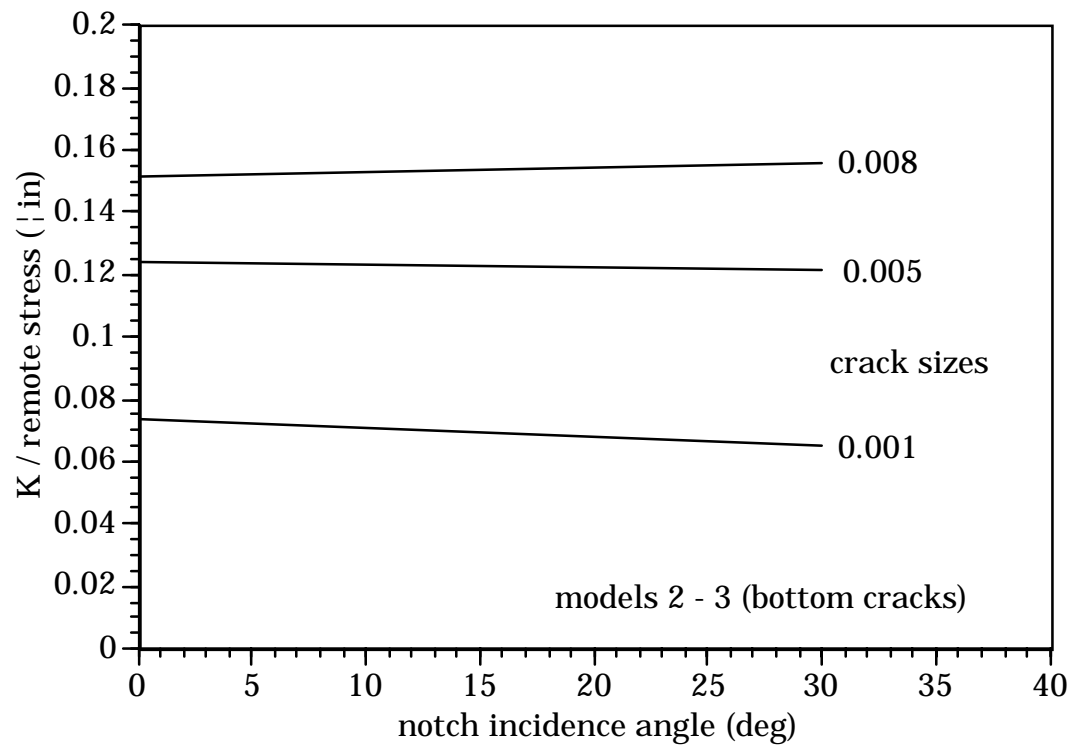
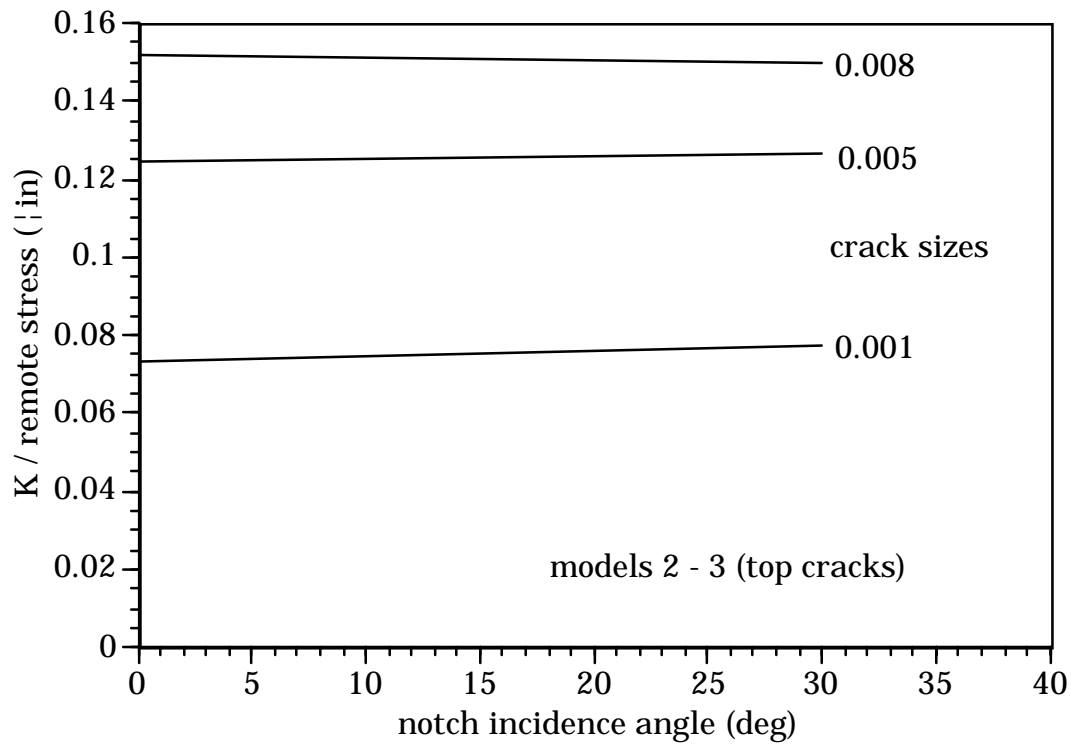
SIF vs. notch tip radius

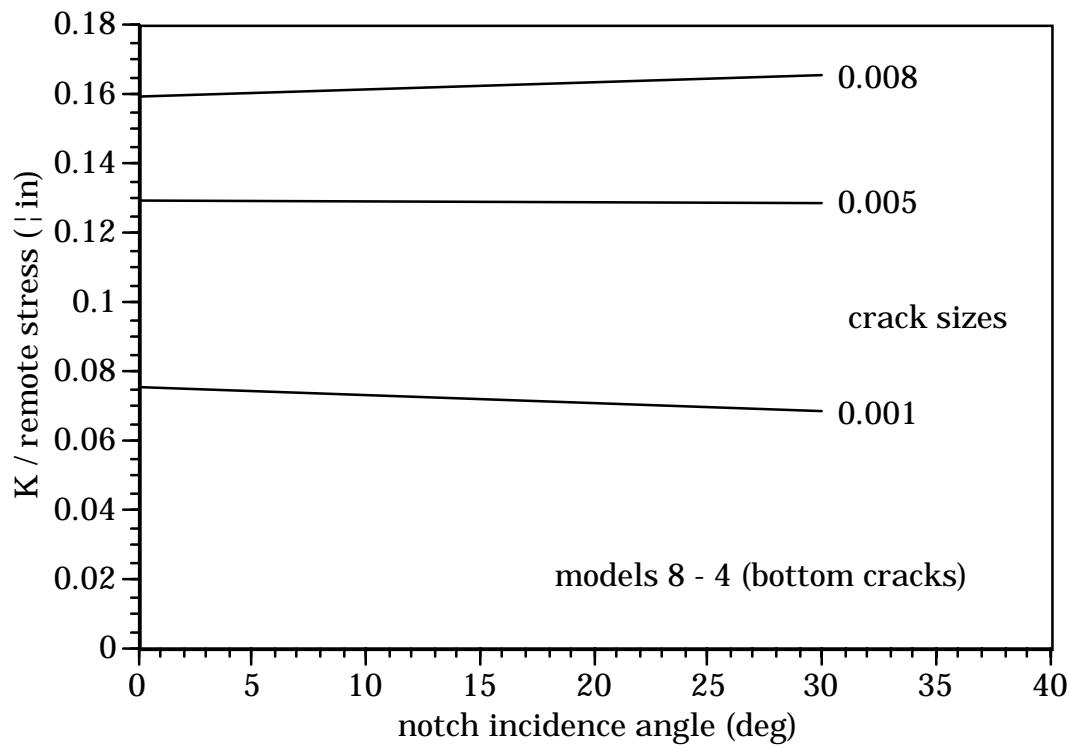
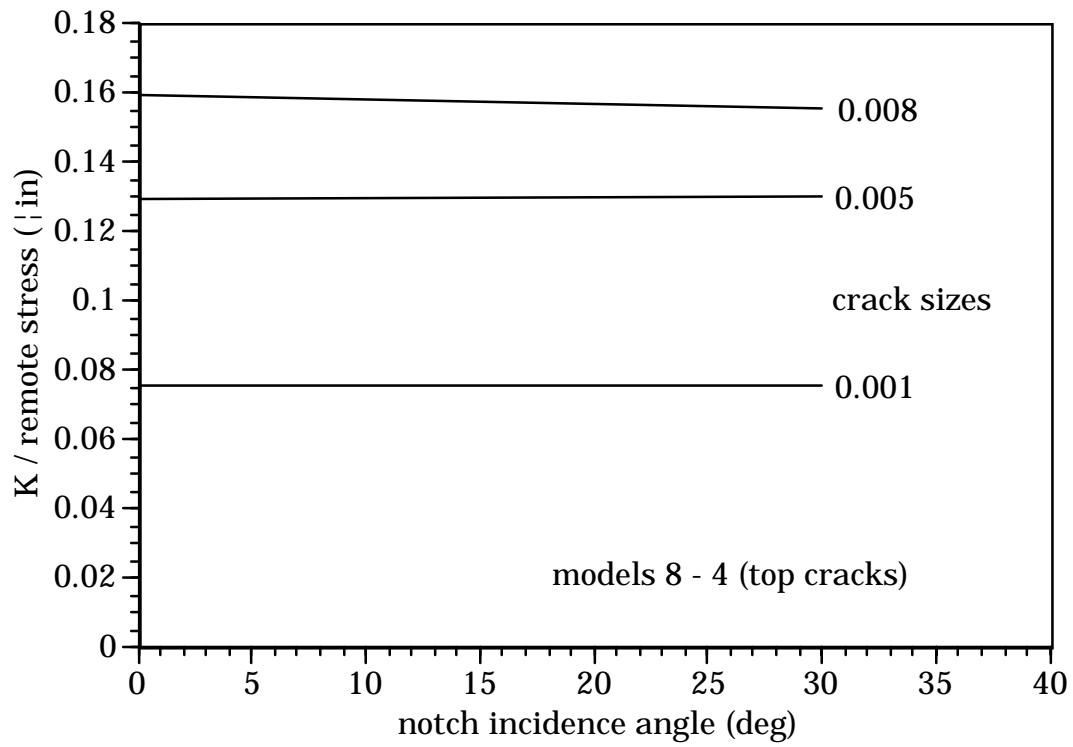


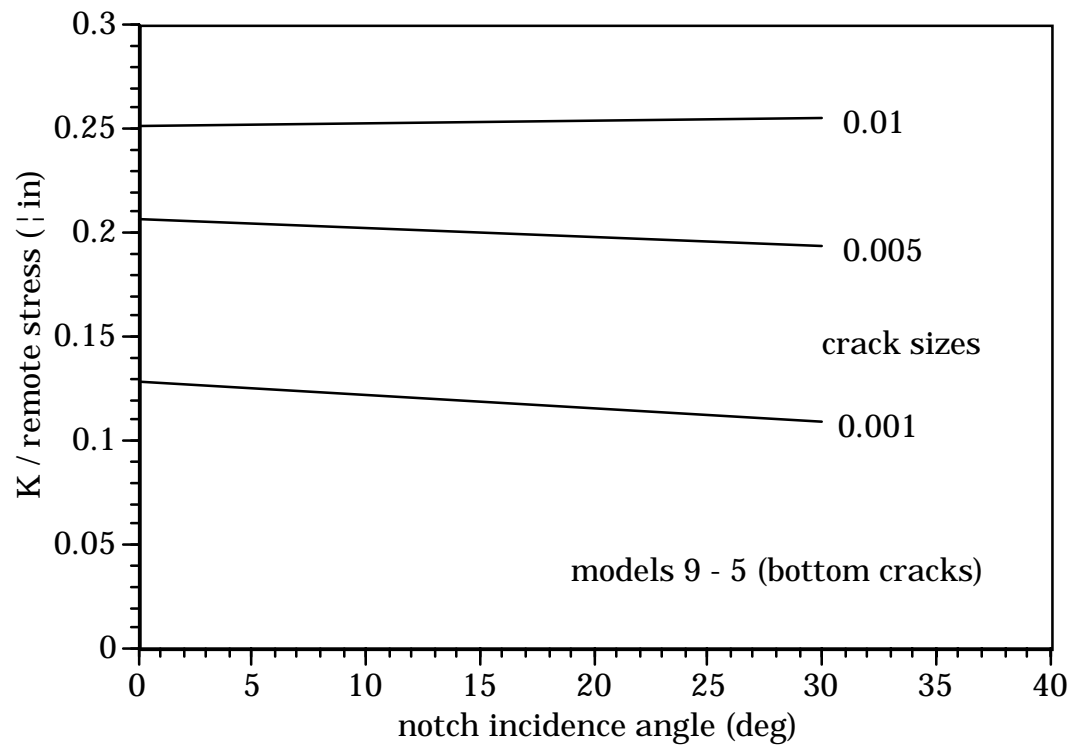
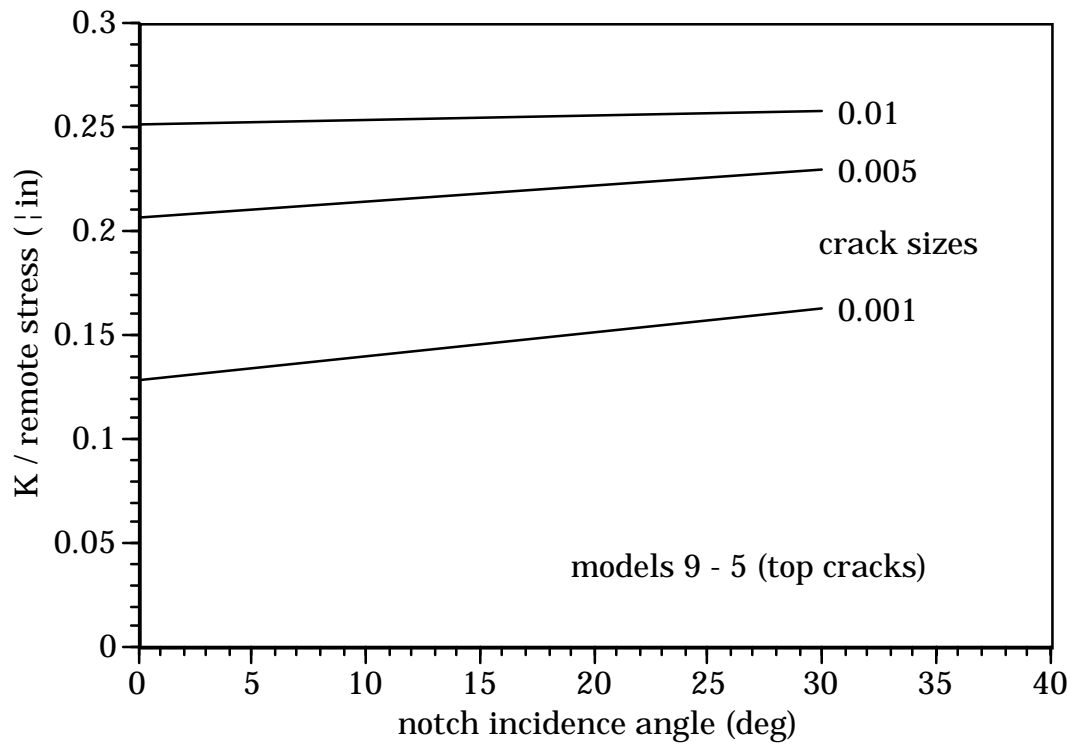


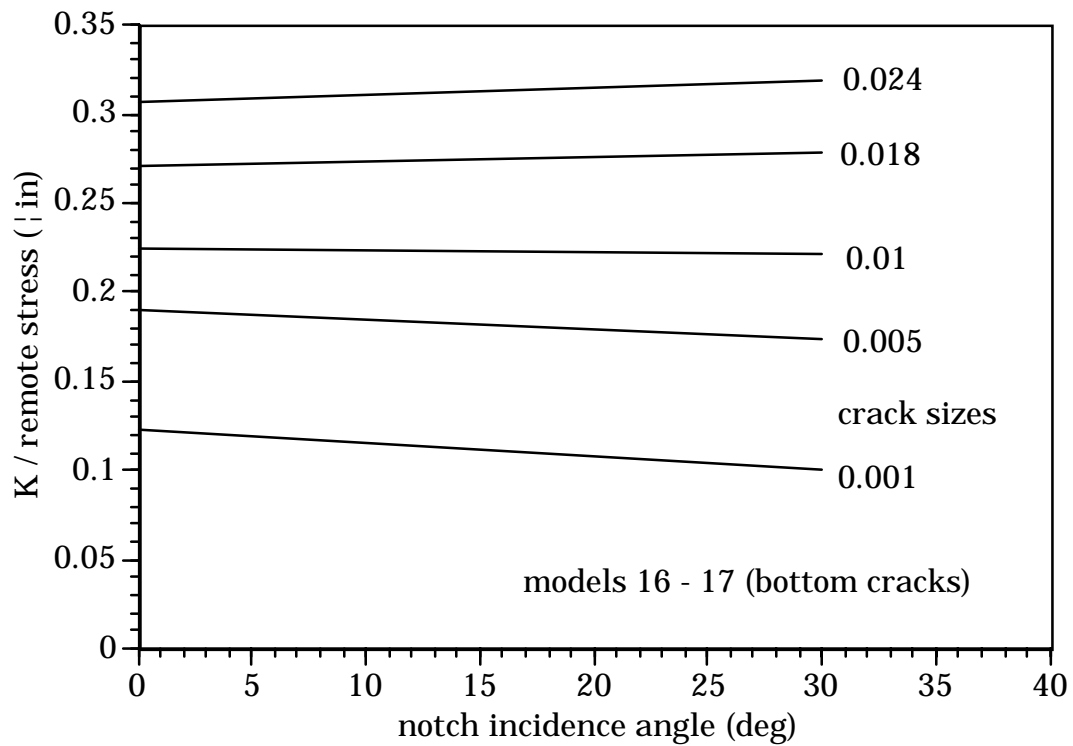
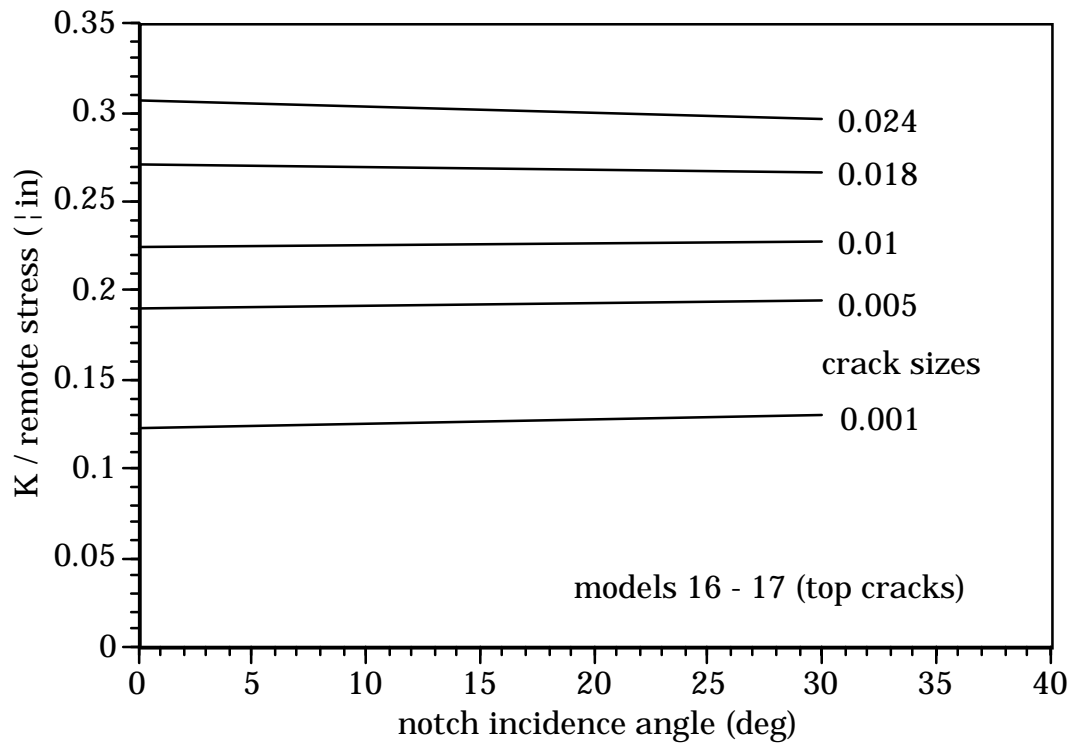
SIF vs. notch incidence angle











Appendix 5H

NUCLEATION FOD MODELING & ΔK THRESHOLD FOD MODELING

Phil Gravett



Pratt & Whitney

**Submitted
1 September 1999**

NUCLEATION FOD MODELING

The following pages contain all the calculations and material properties used to predict 10^6 cycle endurance limit stress capability for Ti-6-4 with the presence of FOD damage. Although the calculations are fairly straightforward, detailed stress and stress intensity modeling of generic leading edge and FOD notch geometries were conducted for a range of parameters which encompass the specimen conditions, see. Appendix 5G. Table “Nucleation FOD modeling calculations” contains the test conditions and prediction values for each of the specimens analyzed in this study. These calculations essentially have six steps to determine a 10^6 cycle endurance limit stress. These steps are 1) calculate normalized average notch stress for LE/notch geometry, 2) calculate elastic max stress and stress range, 3) calculate the elastic-plastic max stress, 4) calculate the Smith-Watson-Topper stress parameter, 5) compare SWT stress to material capability, 6) iterate on stress to converge on solution. The following paragraphs describe each of these steps in more detail.

1) Calculate Normalized Average Notch Stress for LE/Notch Geometry

As presented in Appendix 5G, a parametric ANSYS stress intensity analysis was conducted on LE and notch geometries which cover the specimen configurations of the test program. In this study, notch depth was varied from .005 inch to .020 inch for constant LE geometries and notch tip radius, since LE and indenter geometries are well controlled. Linear interpolation/extrapolation on notch depth is used to determine the average normalized elastic stress for the given LE/notch geometry, see the “Normalized Stress Calculations” table and plots on the following pages. Obviously, this approach will result in some error in stress predictions, but should be adequate to capture the behavior of FOD in the regime of the parametric, especially considering the amount of scatter in the test data.

2) Calculate Elastic Max Stress and Stress Range

Calculation of the elastic max stress and stress range is simply the Normalized Elastic stress times the applied stress and stress range. To predict the 10^6 cycle endurance limit stress, an initial value of stress must be selected and iterated to a solution through the remaining steps.

3) Calculate the Elastic-Plastic Max Stress

For the current analysis, local notch yielding was predicted using a simple Neuber approach. The stress-strain properties used are given in “Stress-Strain model” on the following pages. The intent of this exercise was to investigate a method and identify controlling parameters for the predictions. To gain confidence in this overall modeling technique, the residual stress trends must be evaluated and substantiated with detailed impact and/or notch yielding FEA analysis.

4) Calculate the Smith-Watson-Topper Stress Parameter

The final calculations for the modeling are to determine the SWT stress, including the effects of the notch yielding. This is simply determined by using the SWT formulation,

$$SWT = (\sigma * \Delta\epsilon/2E)^{0.5}$$

where $\Delta\epsilon/E$ equals $\Delta\sigma_{conc}$. Although the SWT nucleation parameter was used in this study, any of the nucleation methods developed in Section 3 or 4 can be applied to the FOD stresses determined above.

5) Compare SWT Stress to Material Capability

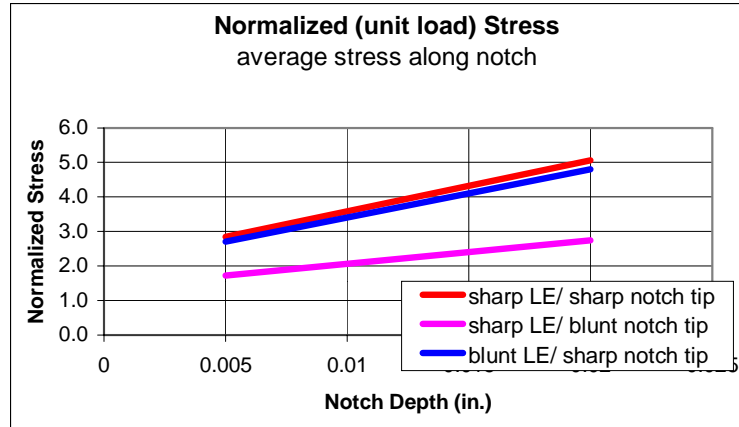
Finally, the predicted SWT stress are compared to the notched SWT material capability defined in Section 3 for 10^6 cycles. If the predicted SWT stress is above the material capability, cracks would be predicted to initiate. This step was performed for both SWT stress from notched test specimens, and a value adjusted to take advantage of the stressed area modeling performed at GEAE. This approximation increases the apparent SWT stress capability by about 9% due to the very small area of the notch.

6) Iterate on Stress to Converge on Solution

To determine the stress at which the onset of crack nucleation will occur, the applied stress must be iterated until the predicted SWT stress match the material capability.

Normalized Stress Calculations:

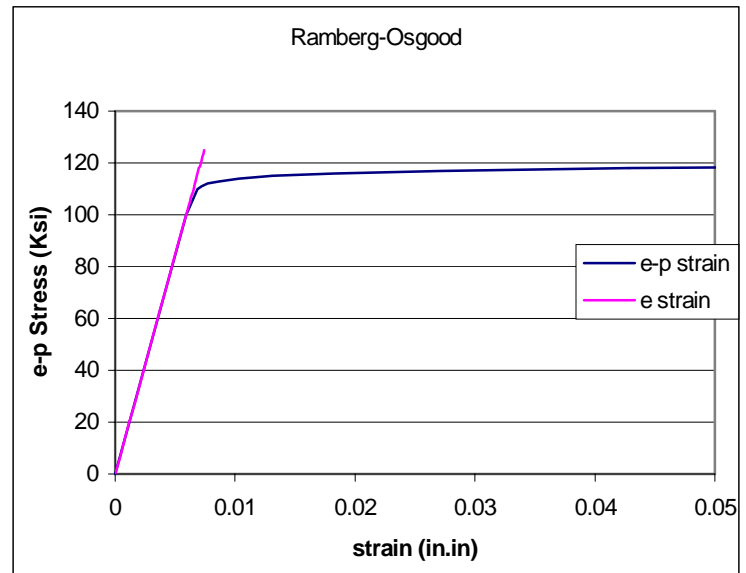
	sharp LE/ sharp notch tip	sharp LE/ blunt notch tip	blunt LE/ sharp notch tip
0.005	2.84942	1.72848	2.707395
0.02	5.05864	2.74484	4.8065



Stress-Strain Model:

Ramberg-Osgood model, $\varepsilon = \sigma/E + (\sigma/K)^{1/n}$

	stress	e-p strain
E = 16870	0	0
K = 124	100	0.005928
n = 0.0149	110	0.006843
	111	0.007171
	112	0.007719
	113	0.008659
	114	0.010299
	115	0.013181
	116	0.018256
	117	0.027181
	118	0.042836
	119	0.070201
	120	0.117843
	125	1.721825



Normalized (unit load) Stress gradients:
Sharp LE, Sharp Notch tip, 30 deg angle:
(stress along lines of constant % thickness)

FOD Notch Depth = .005							FOD Notch Depth = .020					
x	0%	25%	50%	75%	100%		x	0%	25%	50%	75%	100%
0.0000	2.746	3.063	3.121	3.040	2.278		0.0000	5.487	5.779	5.514	5.022	3.492
0.0002	2.345	2.308	2.435	2.397	1.816		0.0021	2.294	2.943	2.957	2.727	2.133
0.0005	2.168	1.948	2.089	2.056	1.630		0.0041	1.637	2.098	2.124	1.994	1.763
0.0007	2.029	1.717	1.847	1.818	1.511		0.0062	1.377	1.688	1.742	1.676	1.568
0.0009	1.900	1.551	1.673	1.652	1.427		0.0083	1.261	1.478	1.528	1.498	1.451
0.0011	1.767	1.431	1.543	1.527	1.369		0.0104	1.199	1.351	1.395	1.387	1.367
0.0014	1.624	1.342	1.444	1.431	1.339		0.0124	1.159	1.272	1.306	1.312	1.304
0.0016	1.480	1.274	1.367	1.358	1.309		0.0145	1.129	1.215	1.247	1.256	1.256
0.0018	1.340	1.221	1.306	1.309	1.279		0.0166	1.108	1.172	1.204	1.212	1.223
0.0021	1.213	1.180	1.257	1.279	1.249		0.0187	1.091	1.143	1.168	1.186	1.196
0.0023	1.112	1.147	1.215	1.250	1.219		0.0207	1.077	1.120	1.148	1.162	1.168
0.0029	1.017	1.121	1.194	1.221	1.189		0.0228	1.067	1.105	1.127	1.137	1.141
0.0036	0.976	1.098	1.174	1.192	1.167		0.0249	1.059	1.089	1.106	1.117	1.128
0.0042	0.954	1.085	1.153	1.163	1.158		0.0269	1.051	1.074	1.093	1.106	1.116
0.0048	0.941	1.074	1.132	1.133	1.149		0.0290	1.044	1.067	1.084	1.095	1.103
0.0055	0.935	1.063	1.112	1.123	1.140		0.0311	1.040	1.060	1.074	1.084	1.090
0.0061	0.933	1.052	1.091	1.115	1.132		0.0332	1.036	1.053	1.065	1.073	1.080
0.0067	0.934	1.041	1.082	1.107	1.123		0.0352	1.032	1.046	1.056	1.066	1.074
0.0074	0.936	1.030	1.075	1.099	1.114		0.0373	1.028	1.041	1.052	1.061	1.068
0.0080	0.938	1.027	1.069	1.091	1.105		0.0394	1.026	1.038	1.048	1.056	1.062
0.0086	0.942	1.024	1.063	1.083	1.097		0.0415	1.024	1.034	1.043	1.051	1.056
0.0093	0.945	1.020	1.056	1.075	1.093		0.0435	1.022	1.031	1.039	1.046	1.050
0.0099	0.948	1.017	1.050	1.068	1.089		0.0456	1.020	1.028	1.035	1.040	1.045
0.0105	0.951	1.014	1.044	1.065	1.085		0.0477	1.018	1.025	1.031	1.037	1.043
0.0112	0.953	1.011	1.039	1.061	1.081		0.0497	1.016	1.023	1.029	1.035	1.040
0.0118	0.956	1.007	1.037	1.058	1.077		0.0518	1.015	1.022	1.028	1.033	1.037
0.0124	0.958	1.007	1.035	1.055	1.073		0.0539	1.014	1.020	1.026	1.030	1.035
0.0131	0.960	1.006	1.032	1.052	1.069		0.0560	1.013	1.019	1.024	1.028	1.032
0.0137	0.963	1.005	1.030	1.048	1.065		0.0580	1.012	1.017	1.022	1.026	1.030
0.0143	0.965	1.004	1.028	1.045	1.061		0.0601	1.011	1.016	1.020	1.024	1.027
0.0150	0.967	1.003	1.025	1.042	1.058		0.0622	1.010	1.014	1.018	1.021	1.025
0.0156	0.968	1.002	1.023	1.039	1.056		0.0643	1.009	1.013	1.017	1.020	1.024
0.0163	0.970	1.001	1.021	1.037	1.054		0.0663	1.009	1.013	1.016	1.019	1.023
0.0169	0.971	1.000	1.020	1.036	1.052		0.0684	1.008	1.012	1.015	1.018	1.021
0.0175	0.973	1.000	1.019	1.034	1.050		0.0705	1.008	1.011	1.014	1.017	1.020
0.0182	0.974	0.999	1.018	1.033	1.048		0.0725	1.008	1.011	1.014	1.016	1.019
0.0188	0.976	0.999	1.017	1.032	1.046		0.0746	1.007	1.010	1.013	1.015	1.018
0.0194	0.977	0.999	1.016	1.030	1.044		0.0767	1.007	1.009	1.012	1.014	1.017
0.0201	0.978	0.999	1.015	1.029	1.042		0.0788	1.006	1.009	1.011	1.014	1.016
0.0207	0.978	0.998	1.014	1.027	1.040		0.0808	1.006	1.008	1.010	1.013	1.015
0.0213	0.979	0.998	1.013	1.026	1.038		0.0829	1.005	1.008	1.010	1.012	1.014
0.0220	0.980	0.998	1.012	1.024	1.036		0.0850	1.005	1.007	1.009	1.011	1.013
0.0226	0.981	0.998	1.011	1.023	1.035		0.0871	1.005	1.007	1.009	1.011	1.013
0.0232	0.982	0.998	1.011	1.022	1.034		0.0891	1.005	1.007	1.008	1.010	1.012
0.0239	0.983	0.998	1.010	1.022	1.033		0.0912	1.005	1.006	1.008	1.010	1.012
0.0245	0.984	0.998	1.010	1.021	1.032		0.0933	1.004	1.006	1.008	1.009	1.011
0.0251	0.984	0.998	1.009	1.020	1.031		0.0954	1.004	1.006	1.007	1.009	1.011
0.0258	0.985	0.998	1.009	1.020	1.030		0.0974	1.004	1.006	1.007	1.009	1.010
0.0264	0.985	0.998	1.009	1.019	1.029		0.0995	1.004	1.005	1.007	1.008	1.010
0.0270	0.986	0.998	1.008	1.018	1.028		0.1016	1.004	1.005	1.006	1.008	1.009
0.0277	0.986	0.998	1.008	1.017	1.027		0.1036	1.003	1.005	1.006	1.007	1.009
0.0762	1.000	1.000	1.000	1.000	1.000		0.3103	1.000	1.000	1.000	1.000	1.000

Normalized (unit load) Stress gradients:
Sharp LE, Blunt Notch tip, 30 deg angle:
(stress along lines of constant % thickness)

FOD Notch Depth = .005							FOD Notch Depth = .020					
x	0%	25%	50%	75%	100%		x	0%	25%	50%	75%	100%
0.0000	1.710	1.765	1.784	1.756	1.628		0.0000	2.941	2.912	2.821	2.680	2.371
0.0002	1.670	1.661	1.704	1.680	1.565		0.0021	2.280	2.320	2.287	2.187	1.989
0.0005	1.640	1.581	1.624	1.605	1.503		0.0041	1.940	1.991	1.975	1.900	1.779
0.0007	1.608	1.515	1.556	1.544	1.462		0.0062	1.710	1.760	1.756	1.705	1.630
0.0009	1.573	1.455	1.500	1.490	1.420		0.0083	1.548	1.595	1.599	1.565	1.522
0.0011	1.538	1.400	1.444	1.441	1.387		0.0104	1.431	1.474	1.482	1.464	1.436
0.0014	1.502	1.357	1.402	1.399	1.355		0.0124	1.344	1.383	1.394	1.387	1.370
0.0016	1.465	1.314	1.360	1.360	1.329		0.0145	1.278	1.313	1.326	1.326	1.316
0.0018	1.427	1.280	1.323	1.328	1.303		0.0166	1.228	1.259	1.274	1.275	1.278
0.0021	1.386	1.248	1.292	1.297	1.282		0.0187	1.188	1.217	1.232	1.243	1.245
0.0023	1.346	1.220	1.261	1.273	1.261		0.0207	1.156	1.185	1.205	1.213	1.212
0.0029	1.287	1.197	1.238	1.249	1.244		0.0228	1.135	1.161	1.177	1.182	1.180
0.0036	1.241	1.173	1.215	1.229	1.227		0.0249	1.117	1.138	1.149	1.156	1.164
0.0042	1.202	1.156	1.194	1.210	1.213		0.0269	1.098	1.114	1.131	1.142	1.148
0.0048	1.169	1.138	1.177	1.193	1.199		0.0290	1.083	1.103	1.118	1.127	1.132
0.0055	1.141	1.123	1.160	1.179	1.187		0.0311	1.074	1.092	1.104	1.112	1.116
0.0061	1.118	1.110	1.146	1.165	1.176		0.0332	1.066	1.081	1.091	1.098	1.103
0.0067	1.098	1.097	1.133	1.154	1.167		0.0352	1.057	1.070	1.079	1.088	1.096
0.0074	1.081	1.088	1.122	1.143	1.158		0.0373	1.049	1.062	1.073	1.082	1.088
0.0080	1.066	1.078	1.112	1.134	1.149		0.0394	1.045	1.057	1.067	1.075	1.081
0.0086	1.054	1.070	1.102	1.126	1.140		0.0415	1.041	1.052	1.061	1.068	1.073
0.0093	1.042	1.062	1.095	1.117	1.131		0.0435	1.037	1.047	1.055	1.061	1.066
0.0099	1.034	1.056	1.088	1.109	1.126		0.0456	1.033	1.042	1.049	1.054	1.059
0.0105	1.026	1.051	1.081	1.101	1.120		0.0477	1.029	1.037	1.043	1.050	1.055
0.0112	1.019	1.046	1.074	1.096	1.114		0.0497	1.026	1.034	1.041	1.047	1.052
0.0118	1.014	1.040	1.069	1.091	1.109		0.0518	1.024	1.031	1.038	1.044	1.049
0.0124	1.009	1.036	1.064	1.086	1.103		0.0539	1.022	1.029	1.035	1.041	1.045
0.0131	1.005	1.033	1.060	1.081	1.097		0.0560	1.021	1.027	1.033	1.038	1.042
0.0137	1.002	1.030	1.056	1.076	1.092		0.0580	1.019	1.025	1.030	1.034	1.038
0.0143	0.999	1.027	1.052	1.071	1.088		0.0601	1.017	1.023	1.027	1.031	1.035
0.0150	0.997	1.024	1.047	1.067	1.085		0.0622	1.016	1.020	1.025	1.028	1.032
0.0156	0.995	1.021	1.044	1.064	1.082		0.0643	1.014	1.019	1.023	1.027	1.031
0.0162	0.993	1.018	1.042	1.061	1.079		0.0663	1.013	1.018	1.022	1.026	1.029
0.0169	0.992	1.017	1.040	1.058	1.075		0.0684	1.013	1.017	1.021	1.024	1.028
0.0175	0.991	1.015	1.037	1.056	1.072		0.0705	1.012	1.016	1.019	1.023	1.026
0.0182	0.990	1.014	1.035	1.053	1.069		0.0725	1.011	1.015	1.018	1.022	1.025
0.0188	0.989	1.013	1.033	1.050	1.065		0.0746	1.011	1.014	1.017	1.020	1.023
0.0194	0.989	1.011	1.030	1.047	1.062		0.0767	1.010	1.013	1.016	1.019	1.022
0.0201	0.988	1.010	1.028	1.044	1.060		0.0788	1.009	1.012	1.015	1.018	1.020
0.0207	0.988	1.008	1.026	1.043	1.058		0.0808	1.008	1.011	1.014	1.016	1.019
0.0213	0.988	1.007	1.025	1.041	1.056		0.0829	1.008	1.010	1.013	1.015	1.017
0.0220	0.987	1.007	1.024	1.040	1.055		0.0850	1.007	1.010	1.012	1.014	1.017
0.0226	0.987	1.006	1.023	1.038	1.053		0.0871	1.007	1.009	1.012	1.014	1.016
0.0232	0.987	1.006	1.022	1.037	1.051		0.0891	1.007	1.009	1.011	1.013	1.015
0.0239	0.987	1.005	1.021	1.035	1.049		0.0912	1.006	1.008	1.011	1.013	1.015
0.0245	0.987	1.004	1.020	1.034	1.048		0.0933	1.006	1.008	1.010	1.012	1.014
0.0251	0.988	1.004	1.019	1.032	1.046		0.0954	1.006	1.008	1.010	1.012	1.014
0.0258	0.988	1.003	1.017	1.031	1.044		0.0974	1.006	1.007	1.009	1.011	1.013
0.0264	0.988	1.003	1.016	1.029	1.042		0.0995	1.005	1.007	1.009	1.011	1.012
0.0270	0.988	1.002	1.015	1.028	1.040		0.1016	1.005	1.007	1.008	1.010	1.012
0.0277	0.988	1.002	1.014	1.027	1.039		0.1036	1.005	1.006	1.008	1.010	1.011
0.0762	1.000	1.000	1.000	1.000	1.000		0.3103	1.000	1.000	1.000	1.000	1.000

Normalized (unit load) Stress gradients:
Blunt LE, Sharp Notch tip, 30 deg angle:
(stress along lines of constant % thickness)

FOD Notch Depth = .005							FOD Notch Depth = .020					
x	0%	25%	50%	75%	100%		x	0%	25%	50%	75%	100%
0.0000	2.246	2.890	3.123	3.192	2.153		0.0000	4.487	5.453	5.518	5.274	3.300
0.0021	1.219	1.182	1.308	1.407	1.157		0.0013	2.304	2.948	3.076	2.999	1.977
0.0041	0.925	1.101	1.233	1.285	1.090		0.0027	1.588	2.129	2.271	2.205	1.659
0.0062	0.839	1.085	1.160	1.207	1.084		0.0044	1.237	1.741	1.852	1.814	1.502
0.0083	0.765	1.053	1.131	1.157	1.077		0.0065	1.027	1.516	1.617	1.589	1.413
0.0104	0.738	1.030	1.099	1.114	1.073		0.0087	0.930	1.372	1.470	1.452	1.352
0.0124	0.738	1.007	1.086	1.096	1.077		0.0109	0.893	1.273	1.371	1.363	1.309
0.0145	0.750	1.000	1.069	1.081	1.081		0.0131	0.878	1.211	1.298	1.300	1.280
0.0166	0.766	0.992	1.050	1.070	1.076		0.0153	0.874	1.162	1.240	1.252	1.252
0.0187	0.785	0.984	1.045	1.064	1.070		0.0176	0.878	1.125	1.201	1.224	1.223
0.0207	0.804	0.980	1.032	1.057	1.070		0.0198	0.884	1.100	1.169	1.196	1.202
0.0228	0.824	0.973	1.026	1.045	1.069		0.0220	0.892	1.078	1.147	1.168	1.188
0.0249	0.837	0.974	1.026	1.047	1.068		0.0242	0.899	1.063	1.126	1.149	1.174
0.0269	0.850	0.977	1.019	1.046	1.068		0.0264	0.906	1.052	1.105	1.137	1.159
0.0290	0.863	0.973	1.017	1.045	1.067		0.0287	0.913	1.041	1.094	1.124	1.145
0.0311	0.873	0.972	1.017	1.044	1.070		0.0309	0.921	1.032	1.084	1.112	1.135
0.0332	0.884	0.973	1.017	1.043	1.072		0.0331	0.928	1.027	1.075	1.100	1.127
0.0352	0.894	0.975	1.016	1.043	1.071		0.0353	0.935	1.022	1.065	1.093	1.120
0.0373	0.902	0.975	1.013	1.043	1.069		0.0375	0.940	1.018	1.058	1.087	1.112
0.0394	0.908	0.974	1.013	1.042	1.068		0.0398	0.944	1.013	1.053	1.081	1.104
0.0415	0.915	0.975	1.013	1.041	1.066		0.0420	0.949	1.011	1.049	1.075	1.096
0.0435	0.920	0.976	1.013	1.040	1.066		0.0442	0.953	1.009	1.044	1.069	1.090
0.0456	0.925	0.978	1.012	1.039	1.067		0.0464	0.956	1.008	1.040	1.063	1.086
0.0477	0.929	0.979	1.012	1.039	1.066		0.0486	0.958	1.006	1.036	1.059	1.082
0.0497	0.933	0.979	1.011	1.038	1.064		0.0509	0.961	1.004	1.033	1.056	1.077
0.0518	0.936	0.979	1.011	1.037	1.063		0.0531	0.963	1.003	1.031	1.053	1.073
0.0539	0.940	0.980	1.011	1.037	1.061		0.0553	0.966	1.002	1.029	1.050	1.069
0.0560	0.942	0.981	1.011	1.036	1.060		0.0575	0.967	1.002	1.027	1.047	1.065
0.0580	0.944	0.982	1.010	1.035	1.059		0.0597	0.969	1.001	1.025	1.044	1.061
0.0601	0.947	0.982	1.010	1.034	1.057		0.0620	0.970	1.000	1.023	1.041	1.057
0.0622	0.949	0.983	1.010	1.034	1.057		0.0642	0.972	1.000	1.021	1.038	1.055
0.0643	0.951	0.984	1.010	1.033	1.057		0.0664	0.974	0.999	1.019	1.036	1.053
0.0663	0.953	0.984	1.010	1.033	1.056		0.0686	0.975	0.999	1.018	1.035	1.051
0.0684	0.955	0.984	1.009	1.032	1.055		0.0708	0.976	0.999	1.017	1.033	1.049
0.0705	0.956	0.985	1.009	1.032	1.054		0.0731	0.977	0.998	1.016	1.032	1.047
0.0725	0.958	0.985	1.009	1.031	1.053		0.0753	0.978	0.998	1.015	1.030	1.045
0.0746	0.959	0.986	1.009	1.031	1.052		0.0775	0.979	0.998	1.014	1.029	1.043
0.0767	0.960	0.986	1.009	1.030	1.051		0.0797	0.980	0.998	1.014	1.027	1.041
0.0788	0.961	0.987	1.009	1.030	1.050		0.0819	0.981	0.998	1.013	1.026	1.038
0.0808	0.963	0.987	1.009	1.029	1.049		0.0842	0.982	0.998	1.012	1.024	1.036
0.0829	0.964	0.988	1.009	1.029	1.049		0.0864	0.983	0.998	1.011	1.023	1.035
0.0850	0.965	0.988	1.009	1.029	1.048		0.0886	0.984	0.998	1.010	1.022	1.034
0.0871	0.966	0.988	1.009	1.028	1.048		0.0908	0.984	0.998	1.010	1.021	1.033
0.0891	0.967	0.989	1.009	1.028	1.047		0.0930	0.985	0.998	1.010	1.021	1.032
0.0912	0.967	0.989	1.009	1.028	1.047		0.0953	0.985	0.998	1.009	1.020	1.031
0.0933	0.968	0.989	1.009	1.027	1.046		0.0975	0.986	0.998	1.009	1.019	1.030
0.0954	0.969	0.990	1.009	1.027	1.046		0.0997	0.986	0.998	1.008	1.019	1.029
0.0974	0.969	0.990	1.009	1.027	1.045		0.1019	0.987	0.998	1.008	1.018	1.028
0.0995	0.970	0.990	1.009	1.026	1.045		0.1041	0.987	0.998	1.008	1.017	1.027
0.1016	0.971	0.990	1.009	1.026	1.044		0.1064	0.988	0.998	1.007	1.017	1.026
0.1036	0.971	0.991	1.009	1.026	1.044		0.1086	0.988	0.998	1.007	1.016	1.025
0.3103	0.986	0.998	1.008	1.017	1.027		0.3117	1.000	1.000	1.000	1.000	1.000

Nucleation FOD modeling calculations:

Test Conditions									Predictions (with area correction)						Predictions (w/o area correction)					
Spec ID	Sim. FOD Tech	LE Dia. (In)	Notch Angle	Indent Radius (in)	Depth at 33.4° (In)	Interp. σ_{range} (Ksi)	R-Ratio	Pred. Avg. notch σ_{norm}	Pred. $\Delta\sigma$ to match matl capblty (iterate)	$\Delta\sigma_{conc}$ Elastic ($\sigma_{norm} * pred \Delta\sigma$)	max. Elastic σ_{conc} ($\sigma_{norm} * pred \sigma_{max}$)	e-p σ_{max} by Neuber	SWT stress (e-p $\sigma_{max} * \Delta\sigma_{conc}/2$.5 = 70.8)	a/p	Pred. $\Delta\sigma$ to match matl capblty (iterate)	$\Delta\sigma_{conc}$ Elastic ($\sigma_{norm} * pred \Delta\sigma$)	max. Elastic σ_{conc} ($\sigma_{norm} * pred \sigma_{max}$)	e-p σ_{max} by Neuber	SWT stress (e-p $\sigma_{max} * \Delta\sigma_{conc}/2$.5 = 65)	a/p
Sharp LE/sharp notch																				
11-S7	Sol gun	0.01	30	0.005	0.0067	38.50	0.5	3.10	28.00	86.79	173.59	115.47	70.79	1.38	23.85	73.93	147.86	114.35	65.016	1.61
48-05	Sol gun	0.01	30	0.005	0.0084	33.30	0.5	3.35	25.91	86.79	173.59	115.47	70.79	1.29	21.60	72.36	144.72	116.62	64.960	1.54
70-03	Sol gun	0.01	30	0.005	0.0088	30.10	0.5	3.41	25.46	86.79	173.59	115.47	70.79	1.18	21.20	72.27	144.54	116.62	64.917	1.42
75-08	Sol gun	0.01	30	0.005	0.0093	27.40	0.5	3.48	24.92	86.79	173.59	115.47	70.79	1.10	20.80	72.44	144.88	116.62	64.992	1.32
54-8b	Sol gun	0.01	30	0.005	0.0169	33.84	0.5	4.60	18.86	86.79	173.59	115.47	70.79	1.79	15.75	72.48	144.96	116.64	65.016	2.15
54-5	Sol gun	0.01	30	0.005	0.0173	38.67	0.5	4.66	18.62	86.79	173.59	115.47	70.79	2.08	15.50	72.25	144.49	116.62	64.904	2.49
75-04	Sol gun	0.01	30	0.005	0.0198	29.40	0.5	5.03	17.26	86.79	173.59	115.47	70.79	1.70	14.40	72.42	144.84	116.62	64.983	2.04
54-4a	Sol gun	0.01	30	0.005	0.0206	29.00	0.5	5.15	16.86	86.79	173.59	115.47	70.79	1.72	14.10	72.57	145.14	116.62	65.051	2.06
54-8a	Sol gun	0.01	30	0.005	0.0213	33.84	0.5	5.25	16.53	86.79	173.59	115.47	70.79	2.05	13.80	72.45	144.90	116.62	64.997	2.45
54-4b	Sol gun	0.01	30	0.005	0.0216	29.00	0.5	5.29	16.39	86.79	173.59	115.47	70.79	1.77	13.70	72.53	145.06	116.62	65.033	2.12
70-04	Sol gun	0.01	30	0.005	0.0237	26.90	0.5	5.60	15.49	86.79	173.59	115.47	70.79	1.74	12.90	72.29	144.57	116.62	64.923	2.09
36-S2	Sol gun	0.01	30	0.005	0.0258	38.20	0.5	5.91	14.68	86.79	173.59	115.47	70.79	2.60	12.20	72.14	144.27	116.62	64.856	3.13
54-1	Sol gun	0.01	30	0.005	0.0289	24.17	0.5	6.37	13.63	86.79	173.59	115.47	70.79	1.77	11.40	72.61	145.22	116.62	65.069	2.12
Sharp LE/blunt notch																				
76-03	Sol gun	0.01	30	0.025	0.0039	52.60	0.5	1.68	51.64	86.79	173.59	115.47	70.79	1.02	43.00	72.28	144.55	116.6	64.914	1.22
22-S1	Sol gun	0.01	30	0.025	0.0041	42.20	0.5	1.67	52.05	86.79	173.59	115.47	70.79	0.81	43.50	72.54	145.07	116.6	65.029	0.97
70-01	Sol gun	0.01	30	0.025	0.0041	58.60	0.5	1.67	52.05	86.79	173.59	115.47	70.79	1.13	43.50	72.54	145.07	116.6	65.029	1.35
48-04	Sol gun	0.01	30	0.025	0.0182	39.60	0.5	2.62	33.09	86.79	173.59	115.47	70.79	1.20	27.60	72.39	144.78	116.6	64.964	1.43
22-S2	Sol gun	0.01	30	0.025	0.0222	48.60	0.5	2.89	29.99	86.79	173.59	115.47	70.79	1.62	25.00	72.35	144.69	116.6	64.945	1.94
11-S6	Sol gun	0.01	30	0.025	0.0232	34.50	0.5	2.96	29.31	86.79	173.59	115.47	70.79	1.18	24.50	72.56	145.12	116.6	65.040	1.41

Blunt LE/sharp notch																				
86-5b	Sol gun	0.03	30	0.005	0.0034	50.16	0.5	2.50	34.74	86.79	173.59	115.47	70.79	1.44	29.60	73.95	147.9	114.34	65.023	1.69
86-5a	Sol gun	0.03	30	0.005	0.0037	50.16	0.5	2.54	34.17	86.79	173.59	115.47	70.79	1.47	29.10	73.92	147.83	114.34	65.008	1.72
86-4b	Sol gun	0.03	30	0.005	0.0037	46.16	0.5	2.54	34.17	86.79	173.59	115.47	70.79	1.35	29.10	73.92	147.83	114.34	65.008	1.59
86-8b	Sol gun	0.03	30	0.005	0.004	61.91	0.5	2.58	33.62	86.79	173.59	115.47	70.79	1.84	28.60	73.84	147.67	114.34	64.974	2.16
86-8a	Sol gun	0.03	30	0.005	0.0041	61.91	0.5	2.60	33.44	86.79	173.59	115.47	70.79	1.85	28.50	73.98	147.95	114.34	65.034	2.17
86-4a	Sol gun	0.03	30	0.005	0.0043	46.16	0.5	2.62	33.08	86.79	173.59	115.47	70.79	1.40	28.20	73.98	147.96	114.34	65.037	1.64
36-B4	Sol gun	0.03	30	0.005	0.0064	62.00	-1	2.92	43.40	126.53	63.27	79.30	70.83	1.43	44.60	130.03	65.015	65.015	65.015	1.39
86-7a	Sol gun	0.03	30	0.005	0.0146	31.09	0.5	4.06	21.40	86.79	173.59	115.47	70.79	1.45	18.20	73.81	147.62	114.34	64.962	1.71
86-3b	Sol gun	0.03	30	0.005	0.015	31.09	0.5	4.11	21.11	86.79	173.59	115.47	70.79	1.47	18.00	74.00	148.00	114.34	65.046	1.73
86-7b	Sol gun	0.03	30	0.005	0.0152	31.09	0.5	4.14	20.97	86.79	173.59	115.47	70.79	1.48	17.90	74.09	148.17	114.34	65.084	1.74
86-3a	Sol gun	0.03	30	0.005	0.0166	31.09	0.5	4.33	20.03	86.79	173.59	115.47	70.79	1.55	17.10	74.11	148.21	114.34	65.092	1.82
86-2b	Sol gun	0.03	30	0.005	0.0179	31.09	0.5	4.51	19.23	86.79	173.59	115.47	70.79	1.62	16.30	73.59	147.17	114.34	64.863	1.91
36-B5	Sol gun	0.03	30	0.005	0.0186	58.00	-1	4.61	30.70	141.58	70.79	70.79	70.79	1.89	28.20	130.05	65.026	65.026	65.026	2.06
86-2a	Sol gun	0.03	30	0.005	0.0199	31.09	0.5	4.79	18.11	86.79	173.59	115.47	70.79	1.72	15.40	73.81	147.61	114.34	64.959	2.02
Sharp LE/sharp notch (w/stress relief)																				
75-05*	Sol gun	0.01	30	0.005	0.0084	30.90	0.5	3.35	25.91	86.79	173.59	115.47	70.79	1.19	21.60	72.36	144.72	116.62	64.958	1.43
75-05*	Sol gun	0.01	30	0.005	0.0172	24.90	0.5	4.65	18.68	86.79	173.59	115.47	70.79	1.33	15.60	72.48	144.96	116.62	65.010	1.60
11-S8*	Sol gun	0.01	30	0.005	0.0176	22.40	0.5	4.71	18.45	86.79	173.59	115.47	70.79	1.21	15.40	72.46	144.91	116.62	65.001	1.45
75-03	Sol gun	0.01	30	0.005	0.0193	23.80	0.5	4.96	17.51	86.79	173.59	115.47	70.79	1.36	14.60	72.35	144.70	116.62	64.952	1.63
11-S5	Sol gun	0.01	30	0.005	0.0204	21.50	0.5	5.12	16.96	86.79	173.59	115.47	70.79	1.27	14.20	72.67	145.33	116.62	65.095	1.51
48-06	Sol gun	0.01	30	0.005	0.0216	22.70	0.5	5.30	16.38	86.79	173.59	115.47	70.79	1.39	13.70	72.59	145.18	116.62	65.060	1.66
Sharp LE/Ballistic impact																				
189-1	UDRI	0.01	30	0.020	0.0067	32.55	0.5	1.84	47.08	86.79	173.59	115.47	70.788	0.69	41	75.59	151.18	112	65.061	0.79
54-7	UDRI	0.01	30	0.020	0.0088	31.35	0.5	1.99	43.70	86.79	173.59	115.47	70.788	0.72	38	75.47	150.93	112	65.008	0.82
189-4	UDRI	0.01	30	0.039	0.0187	41.90	0.5	2.66	32.67	86.79	173.59	115.47	70.788	1.28	27.2	72.26	144.52	116.6	64.907	1.54
189-6	UDRI	0.01	30	0.039	0.0214	34.20	0.5	2.84	30.56	86.79	173.59	115.47	70.788	1.12	25.5	72.41	144.82	116.6	64.974	1.34

* Specimen EPD welding caused material blueing in vicinity of notch, thus stress relief or material distress could have occurred.

ΔK THRESHOLD FOD MODELING

The following pages contain all the calculations and material properties used to predict 10^6 cycle endurance limit stress capability for Ti-6-4 with the presence of FOD damage. Although the calculations are fairly straightforward, detailed stress and stress intensity modeling of generic leading edge and FOD notch geometries were conducted for a range of parameters which encompass the specimen conditions, see Appendix 5G. Table “ ΔK threshold FOD modeling calculations” contains the test conditions and prediction values for each of the specimens analyzed in this study. These calculations essentially have six steps to determine a 10^6 cycle endurance limit stress. These steps are 1) calculate normalized elastic K ($a = 0.001$ inch) for LE/notch geometry, 2) calculate elastic K_{max} and K_{min} , 3) calculate residual K for LE/notch geometry, 4) calculate ΔK and R-ratio with residual K , 5) compare ΔK and R-ratio to material capability, 6) iterate on stress to converge on solution. The following paragraphs describe each of these steps in more detail.

1) Calculate Normalized Elastic K for LE/Notch Geometry

As presented in Appendix 5G, a parametric FRANC3D stress intensity analysis was conducted on LE and notch geometries which cover the specimen configurations of the test program. In this study, notch depth was varied from .005 inch to .020 inch for constant LE geometries and notch tip radius, since LE and indenter geometries are well controlled, see “Specimen K vs. a ” on the following pages. Linear interpolation/extrapolation on notch depth is used to determine the normalized elastic K for the given LE/notch geometry, see the Stress Intensity Calculations for $a = 0.001$ inch table and plots on the following pages. Obviously, this approach will result in some error in K predictions, but should be adequate to capture the behavior of FOD in the regime of the parametric, especially considering the amount of scatter in the test data.

2) Calculate Elastic K_{max} and K_{min}

Calculation of the elastic K_{max} and K_{min} is simply the Normalized Elastic K times the applied stress. To predict the 10^6 cycle endurance limit stress, an initial value of stress must be selected and iterated to a solution through the remaining steps.

3) Calculate Residual K for LE/Notch Geometry

For the current analysis, residual K was assumed to be solely a function of notch depth. This is a very simplistic approach to capturing the effects of residual stress local to the FOD notch by calculating the required level of residual K to calibrate the DKth based modeling. This “required” residual K was calculated for each specimen in order to match the DK calculations to the DKth material capability. When plotted as a function of FOD notch depth, there is a clear trend of residual K increasing with notch depth. A polynomial was then fit through these values to produce an overall residual K function, see “Residual Stress Intensity fit as a function of notch depth” on the following pages.

This approach does not distinguish between the probable causes of the residual stress, FOD projectile impact and local notch yielding. The intent of this exercise was to investigate a method and identify controlling parameters for the predictions. To gain confidence in this overall modeling technique, the residual K trends must be evaluated and substantiated with detailed impact and notch yielding FEA analysis. This will not only increase confidence in the methods, but will make them more robust by defining K residual as a function of LE and notch parameters.

4) Calculate ΔK and R-Ratio with Residual K

The final calculations for the modeling are to determine the local ΔK and R-ratio, including the effects of the residual K . This is simply determined by subtracting the residual K from the maximum and minimum K , and recalculating R-ratio. Since residual K will reduce the elastic K s, the local R-ratio will always be less than the applied R-ratio.

5) Compare ΔK and R-ratio to ΔK th Material Capability

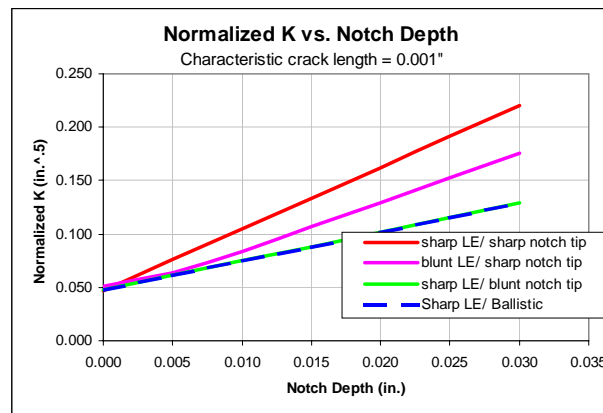
Finally, the predicted ΔK and R-ratio are compared to the ΔK th material capability defined in Section 3. If the predicted ΔK is above the material capability, cracks would be predicted to initiate.

6) Iterate on Stress to Converge on Solution

To determine the stress at which the onset of crack nucleation will occur, the applied stress must be iterated until the predicted ΔK and R-ratio match the material capability.

Stress Intensity Calculations for a = 0.001 inch:

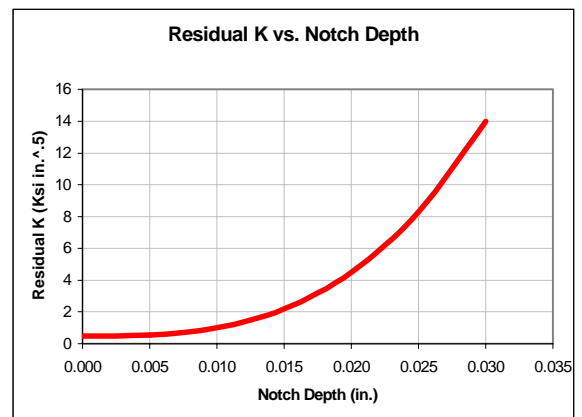
notch depth	Normalized (unit load) Stress Intensity			
	sharp LE/ sharp notch tip	sharp LE/ blunt notch tip	blunt LE/ sharp notch tip	Sharp LE/ Ballistic
0.000	0.047	0.047	0.051	0.047
0.005	0.076	0.061	0.064	0.061
0.010	0.105	0.075	0.084	0.075
0.015	0.134	0.088	0.107	0.088
0.020	0.162	0.102	0.130	0.102
0.025	0.191	0.116	0.153	0.116
0.030	0.220	0.129	0.176	0.129



Residual Stress Intensity fit as a function of notch depth:

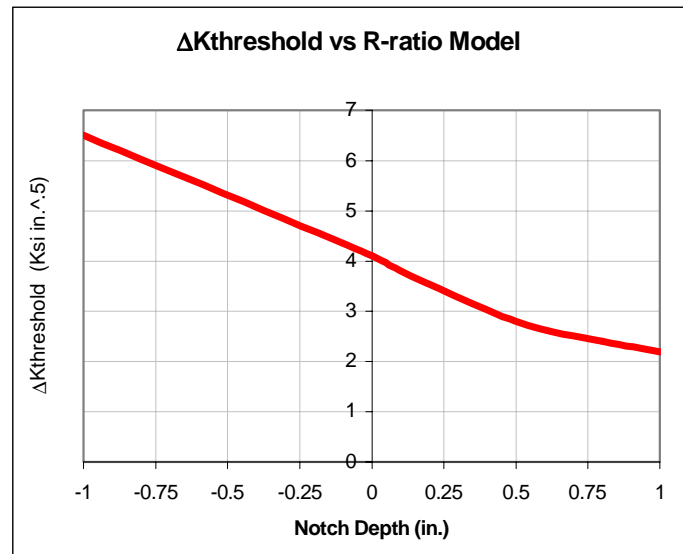
$$K_{res.} = a + b*x + c*x^2 + d*x^3$$

a =	0.5	notch depth	Residual Stress Intensity
b =		0.000	0.500
c =		0.005	0.563
d =	500000	0.010	1.000
		0.015	2.188
		0.020	4.500
		0.025	8.313
		0.030	14.000



ΔK threshold Model from Chapter 3:

R-ratio	DKth
-1	6.5
0	4.1
0.1	3.8
0.5	2.8
0.8	2.4
1	2.2



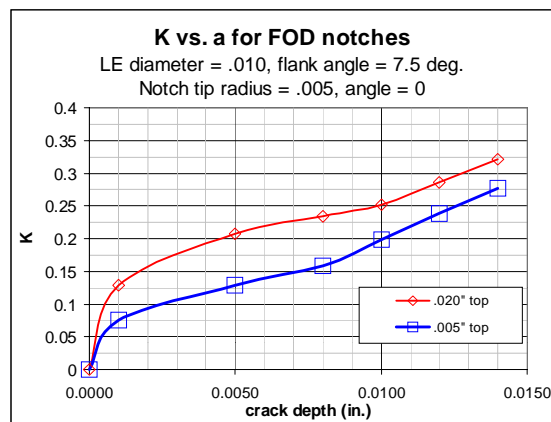
Specimen K vs. a - Sharp Leading Edge (0.010 inch dia.)

Notch Angle (0 deg.)

Notch Tip radius = .005 inch				
a	.005" top	.005" bottom	.020" top	.020" bottom
0	0		0	
0.001	0.075670		0.128883	
0.005	0.129448		0.206925	
0.008	0.159042		0.233562	
0.01	0.198597		0.251321	
0.012	0.238152		0.286054	
0.014	0.277707		0.320787	

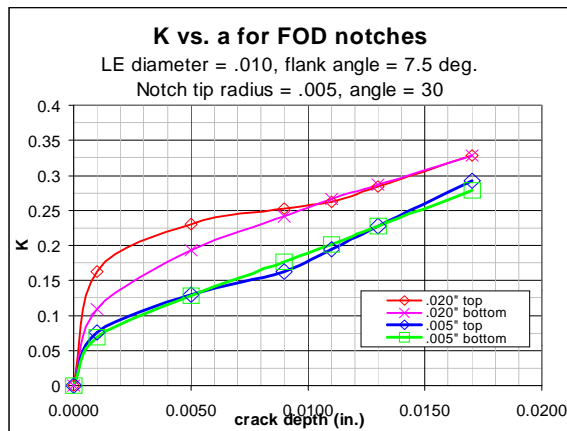
Notch Tip radius = .025 inch				
a	.005" top	.005" bottom	.020" top	.020" bottom
0				
0.001				
0.005				
0.009				
0.011				
0.013				
0.017				

TBD I BAA contract

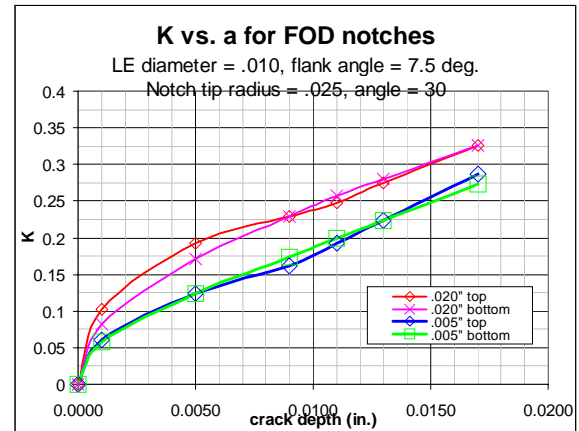


Notch Angle (30 deg.)

Notch Tip radius = .005 inch				
a	.005" top	.005" bottom	.020" top	.020" bottom
0	0	0	0	0
0.001	0.075751	0.068335	0.162452	0.108703
0.005	0.130315	0.128302	0.230348	0.193653
0.009	0.16291	0.17654	0.251829	0.241715
0.011	0.19516	0.201975	0.26257	0.265746
0.013	0.22741	0.22741	0.284370	0.286488
0.017	0.29191	0.27828	0.327972	0.327972



Notch Tip radius = .025 inch				
a	.005" top	.005" bottom	.020" top	.020" bottom
0	0	0	0	0
0.001	0.06112	0.057598	0.101988	0.082323
0.005	0.124299	0.123317	0.192246	0.170884
0.009	0.161281	0.174299	0.229607	0.228687
0.011	0.192552	0.199061	0.248288	0.257589
0.013	0.223823	0.223823	0.274076	0.280276
0.017	0.286365	0.273347	0.325652	0.325652

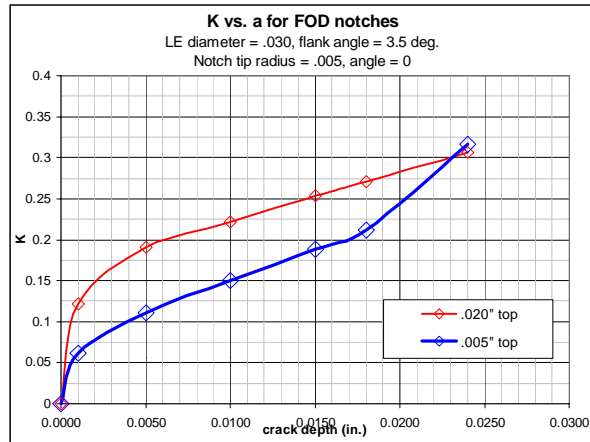


Specimen K vs. a – Blunt Leading Edge (0.030 inch dia.)

Notch Angle (0 deg.)

Notch Tip radius = .005 inch				
a	.005" top	.005" bottom	.020" top	.020" bottom
0	0		0	
0.001	0.061143		0.122131	
0.005	0.110735		0.190154	
0.01	0.150470		0.221738	
0.015	0.187894		0.253323	
0.018	0.211630		0.271181	
0.024	0.316832		0.306899	

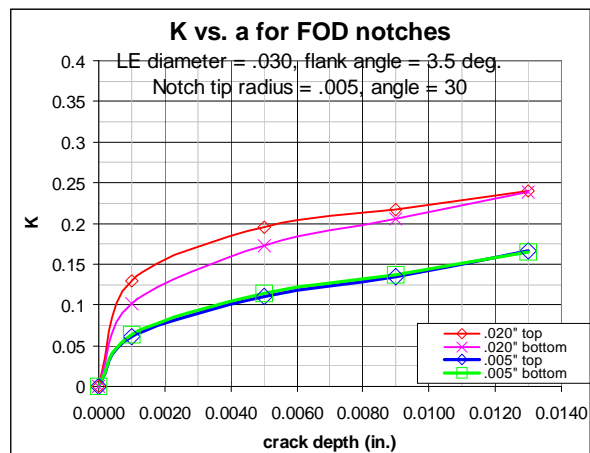
Notch Tip radius = .025 inch				
a	.005" top	.005" bottom	.020" top	.020" bottom
	TBD in BAA contract			



Notch Angle (30 deg.)

Notch Tip radius = .005 inch				
a	.005" top	.005" bottom	.020" top	.020" bottom
0	0	0	0	0
0.001	0.060478	0.063516	0.129699	0.101038
0.005	0.110404	0.114676	0.195154	0.173088
0.009	0.134804	0.136652	0.217270	0.205703
0.013	0.165986	0.165246	0.239387	0.238319

Notch Tip radius = .025 inch				
a	.005" top	.005" bottom	.020" top	.020" bottom
	TBD in BAA contract			



ΔK threshold FOD modeling calculations:

Test Conditions								Stress Predictions								
Spec. ID	Sim. FOD Tech	LE Dia. (In)	Notch Angle	Indenter Radius (in)	Depth at 33.4° (In)	Interp. σ_{range} (Ksi)	R-Ratio	K_{norm} for $a=.001$	$K_{residual} = .5 + 5e5 \cdot x^3$	$K_{max} = K_{norm} \cdot \sigma_{max} - K_{residual}$ (pred.)	$K_{min} = K_{norm} \cdot \sigma_{min} - K_{residual}$ (pred.)	Local R-ratio = K_{min}/K_{max}	Local $\Delta K = K_{max} - K_{min}$	Material $\Delta K_{threshold}$ for local r-ratio	Pred. $\Delta \sigma$ to match material capability (iterations)	Actual/predicted
Sharp LE, Sharp notch																
11-S7	Sol. gun	0.01	30	0.005	0.0067	38.50	0.5	0.0857	0.65	5.21	2.28	0.44	2.93	2.93	34.20	1.13
48-05	Sol. gun	0.01	30	0.005	0.0084	33.30	0.5	0.0961	0.80	5.12	2.16	0.42	2.96	2.96	30.80	1.08
70-03	Sol. gun	0.01	30	0.005	0.0088	30.10	0.5	0.0963	0.84	5.09	2.13	0.42	2.97	2.97	30.80	0.98
75-08	Sol. gun	0.01	30	0.005	0.0093	27.40	0.5	0.1022	0.90	5.07	2.08	0.41	2.98	2.98	29.20	0.94
54-8b	Sol. gun	0.01	30	0.005	0.0169	33.84	0.5	0.1448	2.91	4.47	0.78	0.17	3.69	3.68	25.50	1.33
54-5	Sol. gun	0.01	30	0.005	0.0173	38.67	0.5	0.1474	3.09	4.40	0.65	0.15	3.74	3.74	25.40	1.52
75-04	Sol. gun	0.01	30	0.005	0.0198	29.40	0.5	0.1599	4.38	4.03	-0.18	-0.04	4.20	4.21	26.30	1.12
54-4a	Sol. gun	0.01	30	0.005	0.0206	29.00	0.5	0.1517	4.87	3.93	-0.47	-0.12	4.40	4.39	29.00	1.00
54-8a	Sol. gun	0.01	30	0.005	0.0213	33.84	0.5	0.1684	5.33	3.83	-0.75	-0.20	4.58	4.57	27.20	1.24
54-4b	Sol. gun	0.01	30	0.005	0.0216	29.00	0.5	0.1724	5.54	3.77	-0.88	-0.23	4.65	4.66	27.00	1.07
70-04	Sol. gun	0.01	30	0.005	0.0237	26.90	0.5	0.1822	7.16	3.52	-1.82	-0.52	5.34	5.34	29.30	0.92
36-S2	Sol. gun	0.01	30	0.005	0.0258	38.20	0.5	0.1963	9.09	3.30	-2.89	-0.88	6.19	6.20	31.55	1.21
54-1	Sol. gun	0.01	30	0.005	0.0289	24.17	0.5	0.2151	12.57	3.07	-4.75	-1.55	7.82	7.81	36.35	0.66
Sharp LE, Blunt notch																
76-03	Sol. gun	0.01	30	0.025	0.0039	52.60	0.5	0.0580	0.53	5.27	2.37	0.45	2.90	2.90	50.00	1.05
22-S1	Sol. gun	0.01	30	0.025	0.0041	42.20	0.5	0.0592	0.53	5.27	2.37	0.45	2.90	2.90	49.00	0.86
70-01	Sol. gun	0.01	30	0.025	0.0041	58.60	0.5	0.0580	0.53	5.27	2.37	0.45	2.90	2.90	50.00	1.17
48-04	Sol. gun	0.01	30	0.025	0.0182	39.60	0.5	0.0972	3.51	4.22	0.36	0.08	3.87	3.86	39.80	0.99
22-S2	Sol. gun	0.01	30	0.025	0.0222	48.60	0.5	0.1080	5.97	3.71	-1.13	-0.30	4.84	4.83	44.80	1.08
11-S6	Sol. gun	0.01	30	0.025	0.0232	34.50	0.5	0.1101	6.74	3.59	-1.58	-0.44	5.17	5.16	46.90	0.74

Blunt LE, Sharp notch

86-5b	Sol. gun	0.03	30	0.005	0.0034	50.16	0.5	0.0598	0.52	5.28	2.38	0.45	2.90	2.90	48.50	1.03
86-5a	Sol. gun	0.03	30	0.005	0.0037	50.16	0.5	0.0598	0.53	5.28	2.38	0.45	2.90	2.90	48.50	1.03
86-4b	Sol. gun	0.03	30	0.005	0.0037	46.16	0.5	0.0542	0.53	5.28	2.38	0.45	2.90	2.90	53.60	0.86
86-8b	Sol. gun	0.03	30	0.005	0.004	61.91	0.5	0.0614	0.53	5.26	2.37	0.45	2.90	2.90	47.20	1.31
86-8a	Sol. gun	0.03	30	0.005	0.0041	61.91	0.5	0.0614	0.53	5.26	2.36	0.45	2.90	2.90	47.20	1.31
86-4a	Sol. gun	0.03	30	0.005	0.0043	46.16	0.5	0.0617	0.54	5.26	2.36	0.45	2.90	2.90	47.00	0.98
36-B4	Sol. gun	0.03	30	0.005	0.0064	62.00	-1	0.0677	0.63	2.62	-3.88	-1.48	6.50	7.66	96.00	0.65
86-7a	Sol. gun	0.03	30	0.005	0.0146	31.09	0.5	0.1045	2.06	4.57	1.26	0.28	3.31	3.31	31.70	0.98
86-3b	Sol. gun	0.03	30	0.005	0.015	31.09	0.5	0.1062	2.19	4.52	1.17	0.26	3.35	3.35	31.60	0.98
86-7b	Sol. gun	0.03	30	0.005	0.0152	31.09	0.5	0.1078	2.26	4.49	1.12	0.25	3.37	3.38	31.30	0.99
86-3a	Sol. gun	0.03	30	0.005	0.0166	31.09	0.5	0.1142	2.79	4.36	0.79	0.18	3.57	3.57	31.30	0.99
86-2b	Sol. gun	0.03	30	0.005	0.0179	31.09	0.5	0.1190	3.37	4.25	0.44	0.10	3.81	3.80	32.00	0.97
36-B5	Sol. gun	0.03	30	0.005	0.0186	58.00	-1	0.1224	3.72	-0.47	-6.96	14.70	6.49	-31.19	53.00	1.09
86-2a	Sol. gun	0.03	30	0.005	0.0199	31.09	0.5	0.1287	4.44	3.56	-0.44	-0.12	4.00	4.40	31.09	1.00

Sharp LE/sharp notch (w/stress relief)

75-05*	Sol. gun	0.01	30	0.005	0.0084	30.90	0.5	0.1003		5.62	2.81	0.50	2.81	2.80	28.00	1.10
75-05*	Sol. gun	0.01	30	0.005	0.0172	24.90	0.5	0.1606		5.62	2.81	0.50	2.81	2.80	17.50	1.42
11-S8*	Sol. gun	0.01	30	0.005	0.0176	22.40	0.5	0.1607		5.63	2.81	0.50	2.81	2.80	17.50	1.28
75-03	Sol. gun	0.01	30	0.005	0.0193	23.80	0.5	0.1597		5.59	2.79	0.50	2.79	2.80	17.50	1.36
11-S5	Sol. gun	0.01	30	0.005	0.0204	21.50	0.5	0.1628		5.60	2.80	0.50	2.80	2.80	17.20	1.25
48-06	Sol. gun	0.01	30	0.005	0.02163	22.70	0.5	0.1718		5.60	2.80	0.50	2.80	2.80	16.30	1.39

Sharp LE/sharp notch (ignore stress relief)

75-05*	Sol. gun	0.01	30	0.005	0.0084	30.90	0.5	0.1003	0.80	5.12	2.16	0.42	2.96	2.96	29.50	1.05
75-05*	Sol. gun	0.01	30	0.005	0.0172	24.90	0.5	0.1606	3.04	4.31	0.63	0.15	3.68	3.67	22.90	1.09
11-S8*	Sol. gun	0.01	30	0.005	0.0176	22.40	0.5	0.1607	3.23	4.26	0.52	0.12	3.74	3.75	23.30	0.96
75-03	Sol. gun	0.01	30	0.005	0.0193	23.80	0.5	0.1597	4.09	4.14	0.02	0.01	4.12	4.12	25.80	0.92
11-S5	Sol. gun	0.01	30	0.005	0.0204	21.50	0.5	0.1628	4.74	3.95	-0.40	-0.10	4.35	4.34	26.70	0.81
48-06	Sol. gun	0.01	30	0.005	0.02163	22.70	0.5	0.1718	5.56	3.79	-0.89	-0.23	4.67	4.66	27.20	0.83

Sharp LE/Ballistic impact																
189-1	UDRI	0.01	30	0.020	0.0067	32.55	0.5	0.0706	0.65	5.21	2.28	0.44	2.93	2.93	41.50	0.78
54-7	UDRI	0.01	30	0.020	0.0088	31.35	0.5	0.0718	0.84	5.10	2.13	0.42	2.97	2.97	41.40	0.76
189-4	UDRI	0.01	30	0.039	0.0187	41.90	0.5	0.0979	3.77	4.20	0.21	0.05	3.98	3.97	40.70	1.03
189-6	UDRI	0.01	30	0.039	0.0214	34.20	0.5	0.1053	5.40	3.80	-0.80	-0.21	4.60	4.60	43.70	0.78

* Specimen EPD welding caused material bluing in vicinity of notch, thus stress relief or material distress could have occurred.

Appendix 5I

DEVELOPMENT AND APPLICATION OF WORST CASE NOTCH (WCN) to FOD

G. Graham Chell

and

Stephen J. Hudak, Jr.



Southwest Research Institute

**Submitted
31 August 1999**

Appendix 5I

Foreign Object Damage (FOD)

The objective of this task was to understand and quantify the influence of foreign object damage (FOD) on high cycle fatigue (HCF) behavior, focusing on the contributions the geometric stress concentration and residual stress state produced by the FOD. This objective was pursued using a multi-step approach. First, the nature of service-induced FOD damage was characterized, primarily to identify typical FOD locations, geometries and loading modes that are likely to be encountered in fan and compressor blades. This information guided the development of parametric notch stress analysis equations that enable both the elastic stress concentration factor, k_t , and local stress distribution in the vicinity of the FOD-notches to be efficiently computed as a function of notch geometry and loading mode. Using a weight function approach, these (uncracked) stress fields were used to compute the “crack driving force” at notches in terms of the crack-tip stress intensity factor, K , including the effect of residual stresses induced by the FOD impact. Finally, in order to treat the wide-range of FOD severity that is likely to be encountered in service, a “worst case notch” concept was developed which enabled a limiting threshold stress for HCF failure to be determined. This worst case notch (WCN) model predicts the conditions for nucleation, growth and *arrest* of microcracks at the FOD-notch root. The latter is based on the crack-size-dependent crack growth threshold, and enables the threshold stress to be predicted as a function of FOD-notch depth and radius, loading mode, and magnitude and depth of residual stress.

PARAMETRIC ANALYSIS OF FOD-NOTCH STRESSES

FOD-Notch Stress Concentrations

Stress fields at notches are needed in order to assess the nucleation and growth of cracks at FOD. In this section, the stress concentration factors at notches are estimated. These estimates enable the static and cyclic stresses at the tips of FOD to be determined from stress analyses of undamaged blades, and hence threshold cyclic stresses governing crack nucleation, growth and arrest to be evaluated. Stress concentration factors also provide essential input to the analytical method described in Appendix 4B for determining stress distributions ahead of FOD. The cyclic change in

the stress distribution is needed to calculate the cyclic change in the stress intensity factor and hence the growth and arrest of cracks that emanate from the FOD.

Representation of FOD by a Single Notch

It is necessary to idealize the shape of FOD as notches with depths, b , and root radii, ρ , (see Figure 5I.1) and to assume that the thickness of the blades, B , is constant in order to derive approximate analytical expressions for the stress concentration, k'_t at the root of the damage. k'_t is defined as

$$k'_t = \frac{\text{maximum local stress } (\sigma_{\max})}{\text{gross applied stress distant from damage } (\sigma_{\text{gross}})} \quad (5I.1)$$

In the present analysis, the form of k'_t is assumed to depend on b , ρ , the width of the blade, t , and the form of the loading (e.g., force or moment), but not on the detailed shape of the damage.

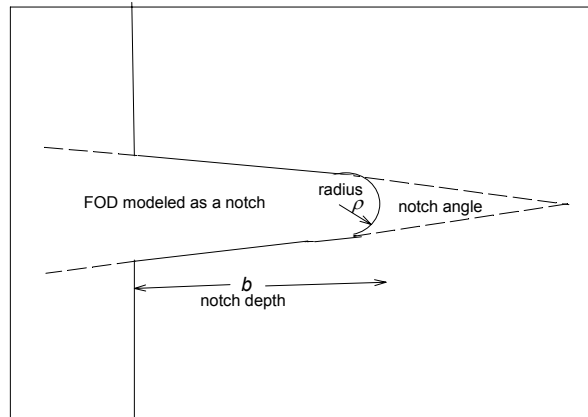


Figure 5I.1. Schematic of FOD represented as a notch with a depth (b), root radius (ρ) and notch angle.

It is possible to write expressions for k'_t in the limits of either when the root radius is very large or when it is very small. In the former case, $\rho/b \gg 1$, k'_t is given by the ratio of the net section stress to the gross stress, which can be expressed as the following area ratio:

$$k'_t \left(\frac{\rho}{b} \rightarrow \infty \right) = \frac{A(0)}{A(b)} \quad (5I.2)$$

where $A(0)$ is the appropriate area for the undamaged blade and $A(b)$ the appropriate net section area in the damaged blade. For an applied force

$$A(b) = A(0)(1 - b/t) \quad (51.3)$$

and for an applied moment and a surface notch

$$A(b) = A(0)(1 - b/t)^2 \quad (51.4)$$

In the case of a very small radius, $\rho/a \rightarrow 0$, then [1]

$$k'_t \left(\frac{\rho}{b} \rightarrow 0 \right) = \frac{2K(b)}{\sigma_{gross} \sqrt{\pi\rho}} \quad (51.5)$$

where $K(b)$ is the stress intensity factor for a crack of depth b subjected to the gross stress, σ_{gross} . Equations (51.2) and (51.5) can be combined to give approximate expressions for k'_t that are applicable for all values of the root radius, ρ .

For a surface notch, which is typical of FOD, this combination yields

$$k'_t = f \left(\frac{\rho}{b} \right) \left[\frac{A(0)}{A(b)} + \frac{2K(b)}{1.122 \sigma_{gross} \sqrt{\pi\rho}} \right] \quad (51.6)$$

where

$$f \left(\frac{\rho}{b} \right) = 1 + \frac{0.122}{\left(1 + \sqrt{\frac{\rho}{b}} \right)^{\frac{5}{2}}} \quad (51.7)$$

is a free-surface correction that appears in the stress concentration factor solution for a surface notch subjected to an uniform stressing given in reference [1], and the 1.122 is the value of the correction for a sharp crack ($\rho = 0$).

For an embedded hole the expression for k'_t simplifies to

$$k'_t = \left[\frac{A(0)}{A(b)} + \frac{2K(b)}{\sigma_{gross} \sqrt{\pi\rho}} \right] \quad (51.8)$$

In engineering applications it is common to define the stress concentration factor in terms of the net section stress rather than the gross stress. The concentration factor, k_t , defined relative to the net section stress is defined as:

$$k_t = \frac{\text{maximum local stress } (\sigma_{\max})}{\text{applied stress on net section } (\sigma_{\text{net}})} \quad (51.9)$$

$$k_t = k'_t \frac{A(b)}{A(0)} = f\left(\frac{\rho}{b}\right) \left[1 + \frac{2K(b)}{1.122\sigma_{\text{gross}}\sqrt{\pi\rho}} \frac{A(b)}{A(0)} \right] \quad (51.10)$$

The accuracy of Equations (51.6) and (51.8) can be assessed by comparing the k'_t values predicted using them with the results presented in Peterson [2]. This comparison has been done in Figures 51.2, 51.3, and 51.4 for bars containing U-shaped surface notches subjected to bending, bars containing embedded elliptical holes subjected to uniform tension, and U-shaped surface notches subjected to uniform stressing, respectively. In the figures, the x-axis shows the k'_t results extracted from Peterson [2], and the y-axis shows the corresponding predictions of Equation (51.6) (Figures 51.2 and 51.4) or Equation (51.8) (Figure 51.3). There is excellent agreement between Equations (51.6) and (51.8) and Peterson for the U-shaped surface notches and embedded elliptical holes, respectively, subjected to uniform stressing, but Equation (51.6) conservatively over-estimates by between 10% and 30% the results given in Peterson for surface notches subjected to bending.

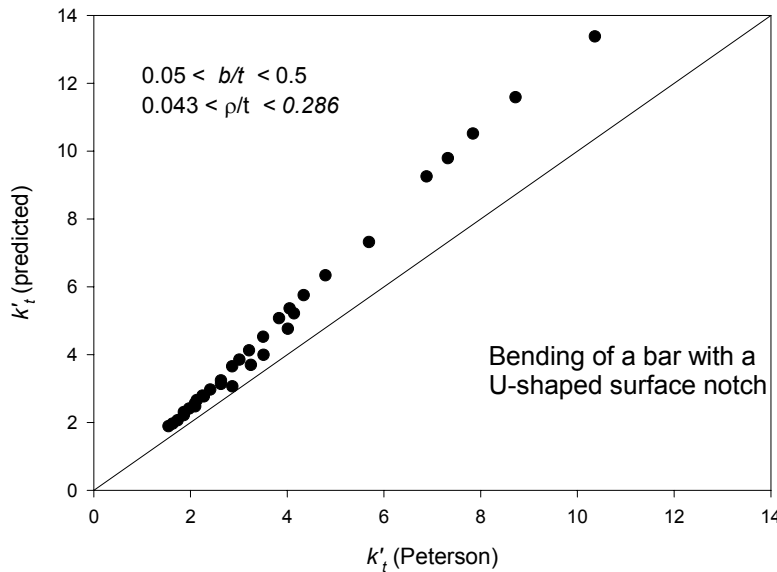


Figure 51.2. Comparison of k'_t values predicted by Equation (51.6) with the values given in Peterson [2] for surface notches subjected to bending.

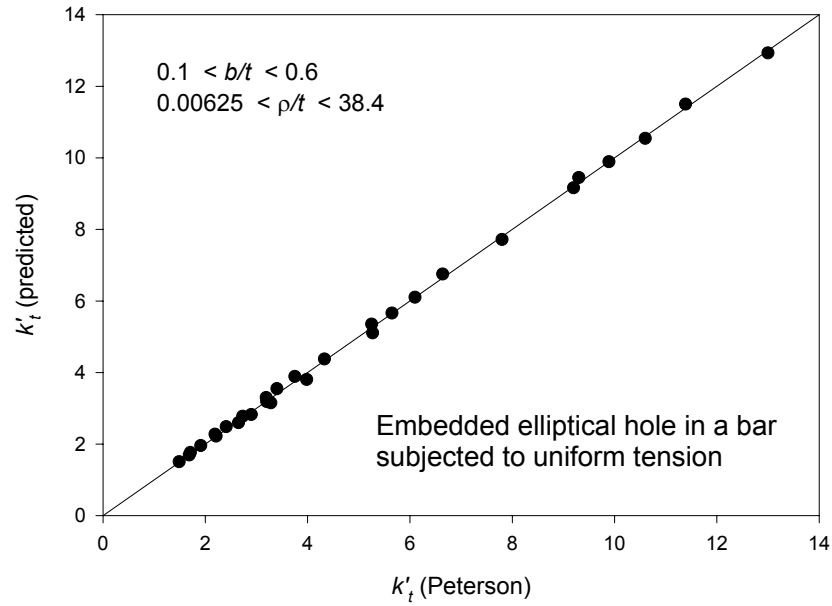


Figure 5I.3. Comparison of k'_t values predicted by Equation (5I.8) with the values given in Peterson [2] for embedded elliptical holes subjected to uniform stressing.

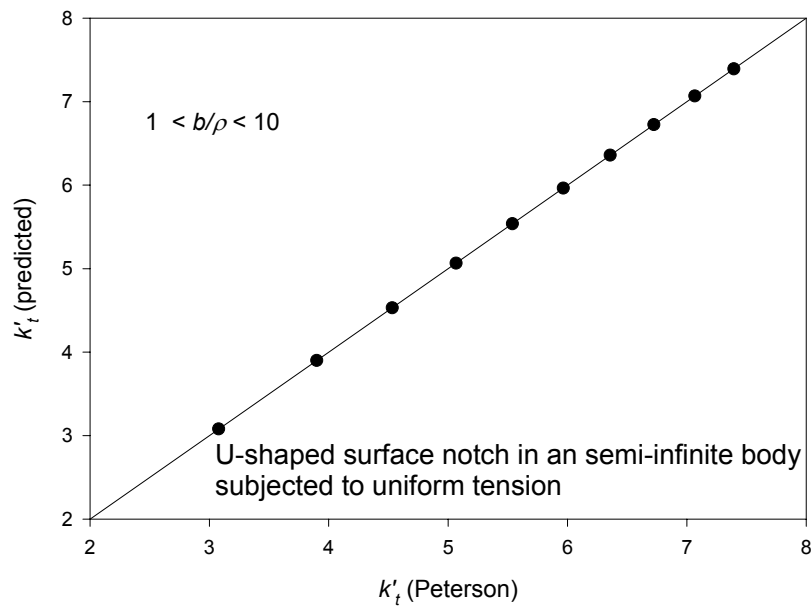


Figure 5I.4. Comparison of k'_t values predicted by Equation (5I.6) with the values given in Peterson [2] for U-shaped surface notches subjected to uniform stressing.

The foregoing results indicate that Equation (5I.6) will provide either an excellent estimate for the stress concentration factors at the roots of idealized FOD or a conservative estimate of these factors.

Effect of Flank Angle on Stress Concentration Factor

From Figure 5A.4, it can be seen that the flanks of FOD are not parallel. It is important to know what effect flank angle has on the stress distribution ahead of FOD. A schematic of the modeling of FOD by a notch and the definition of flank angle is shown in Figure 5I.1. The effect of flank angle on stress concentration factor is illustrated in Figures 5I.5 and 5I.6. The data shown in these figures were constructed using solutions given in Peterson. It can be seen that even if the flank angle is large (90°) compared to the flank angles typically encountered in FOD that the assumption that the notch behaves as a U-notch for stress modeling purposes is an acceptable one.

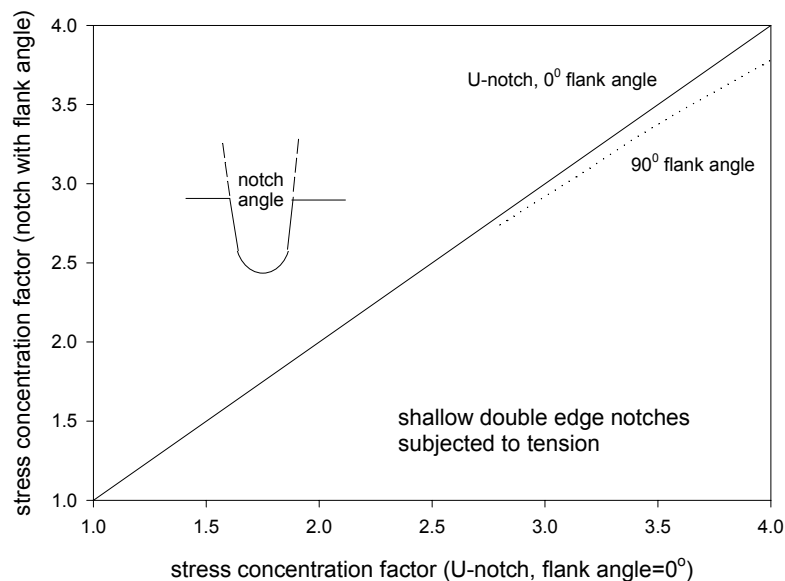


Figure 5I.5. Comparison of stress concentration factors of U-notches with zero included angle, and notches with flank angles of 90° . The data were extracted from Peterson for double edge notches subjected to remote uniform stressing.

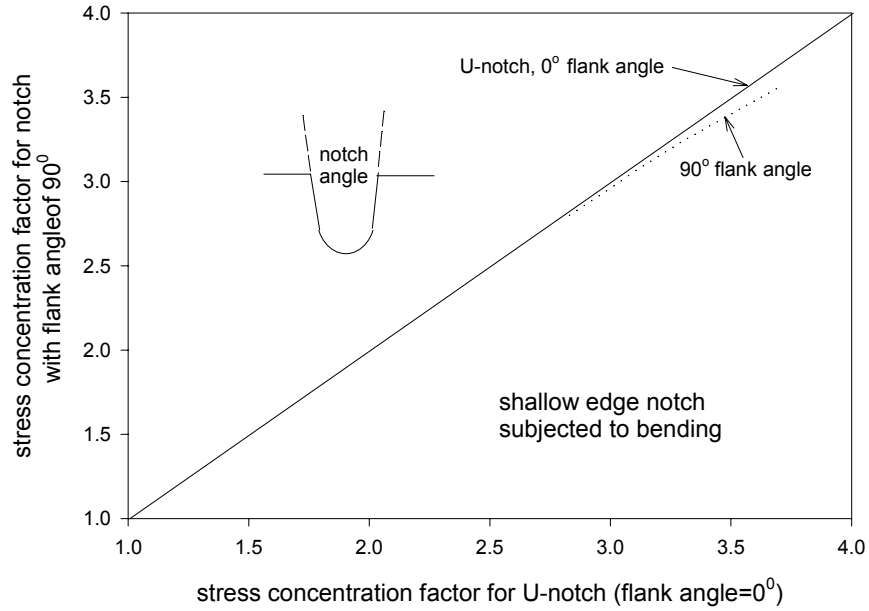


Figure 5I.6. Comparison of stress concentration factors of U-notches with zero included angle, and notches with flank angles of 90°. The data were extracted from Peterson for surface notches subjected to remote bending.

Effect of Secondary Notch-like Features on the Stress Concentration Factors for FOD

Figure 5A.12 shows that the tips of FOD are not smooth, but may be composed of secondary notch-like features. These secondary features will act as local stress raisers that should be taken into account when modeling the FOD for stress analysis purposes. To investigate the effects of secondary features on the stress distribution ahead of FOD, the FOD and secondary features are modeled as a primary notch from which a secondary notch emanates (Figure 5I.7).

The stress concentration factor for a primary notch is given by (compare Equation (5I.6))

$$k_t^{pri} = f\left(\frac{\rho_{pri}}{b_{pri}}\right) \left[\frac{A(0)}{A(b_{pri})} + \frac{2K(b_{pri})}{h\sigma_{gross}\sqrt{\pi\rho_{pri}}} \right] \quad (5I.11)$$

where, for surface notches,

$$f\left(\frac{\rho}{b}\right) = 1 + \frac{0.122}{\left(1 + \sqrt{\frac{\rho}{b}}\right)^{\frac{5}{2}}}, \quad h = 1.122 \quad (5I.12)$$

and for embedded notches

$$f\left(\frac{\rho}{b}\right) = 1, \quad h = 1 \quad (5l.13)$$

Superscripts and subscripts *pri* signify primary.

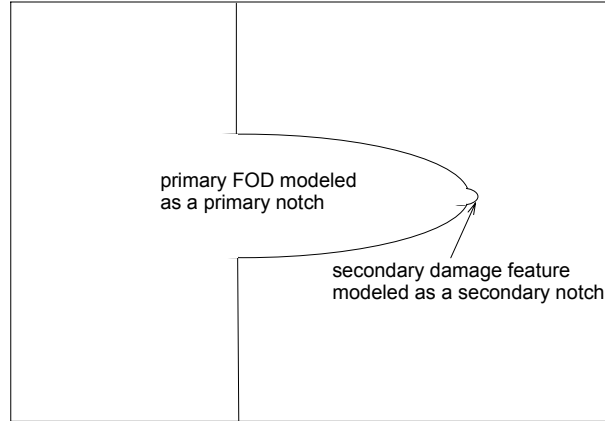


Figure 5l.7. Schematic of FOD with secondary features modeled as a secondary notch emanating from a primary notch.

If the secondary notch depth is very small compared with the root radius of the primary notch, then

$$k_t^{\text{sec}} = \frac{\text{maximum local stress at secondary notch}}{\text{maximum local stress at primary notch}} = f\left(\frac{\rho_{\text{sec}}}{b_{\text{sec}}}\right) \left[\frac{A(b_{\text{pri}})}{A(b_{\text{pri}} + b_{\text{sec}})} + \frac{2K(b_{\text{sec}})}{h\sigma_{\text{local}}^{\text{pri}} \sqrt{\pi\rho_{\text{sec}}}} \right], \quad \frac{b_{\text{sec}}}{\rho_{\text{pri}}} \ll 1 \quad \text{where} \quad (5l.14)$$

$$\sigma_{\text{local}}^{\text{pri}} = k_t^{\text{pri}} \sigma_{\text{gross}}$$

The stress concentration factor at the secondary notch for the combined primary and secondary notches subject to remote loading is

$$k_t^{\text{pri-sec}}(b_{\text{pri}}, \rho_{\text{pri}}, b_{\text{sec}}, \rho_{\text{sec}}) = k_t^{\text{pri}}(b_{\text{pri}}, \rho_{\text{pri}}) \times k_t^{\text{sec}}(b_{\text{pri}}, b_{\text{sec}}, \rho_{\text{sec}}), \quad \frac{b_{\text{sec}}}{\rho_{\text{pri}}} \ll 1 \quad (5l.15)$$

If the secondary notch depth is long compared to the root radius of the primary notch, then the stress concentration at the secondary notch tip is assumed given by the following equation for a notch of total depth $b_{\text{pri}} + b_{\text{sec}}$ with a root radius of ρ_{sec} :

$$k_t^{\text{sec}}(b_{\text{pri}} + b_{\text{sec}}, \rho_{\text{sec}}) = k_t^{\text{pri}}(b_{\text{pri}} + b_{\text{sec}}, \rho_{\text{sec}}) = f\left(\frac{\rho_{\text{sec}}}{b_{\text{pri}} + b_{\text{sec}}}\right) \left[\frac{A(0)}{A(b_{\text{pri}} + b_{\text{sec}})} + \frac{2K(b_{\text{pri}} + b_{\text{sec}})}{h\sigma_{\text{gross}} \sqrt{\pi\rho_{\text{sec}}}} \right], \quad \frac{b_{\text{sec}}}{\rho_{\text{pri}}} > 1 \quad (5l.16)$$

The validation supporting this approximation is shown in Figure 5I.8. This figure shows the stress concentration factor for semi-circular secondary notches emanating from a round hole (primary notch) plotted as a function of the radius of the secondary notch ($\rho_{sec} = b_{sec}$) divided by the radius of the primary notch ($\rho_{pri} = b_{pri}$). The long notch approximation appears to be accurate when $b_{sec}/\rho_{pri} \cong 0.15$.

Based on the short and long secondary notch solutions, the following equation is proposed for interpolating between these two extreme cases

$$k_t^{sec} = k_t^{pri-sec}(b_{pri}, \rho_{pri}, b_{sec}, \rho_{sec}) - \left(\frac{b_{sec}}{0.15\rho_{pri}} \right)^{1/2} \left[k_t^{pri-sec}(b_{pri}, \rho_{pri}, b_{sec}, \rho_{sec}) - k_t^{pri}(b_{pri} + 0.15\rho_{pri}, \rho_{sec}) \right] \quad (5I.17)$$

$$, \frac{b_{sec}}{\rho_{pri}} \leq 0.15$$

$$k_t^{sec} = k_t^{pri}(b_{pri} + b_{sec}, \rho_{sec}), \frac{b_{sec}}{\rho_{pri}} > 0.15$$

Validation for this equation is provided by Figure 5I.9 in which its predictions for an embedded round primary notch with semi-circular secondary notches are compared with the solution from Peterson.

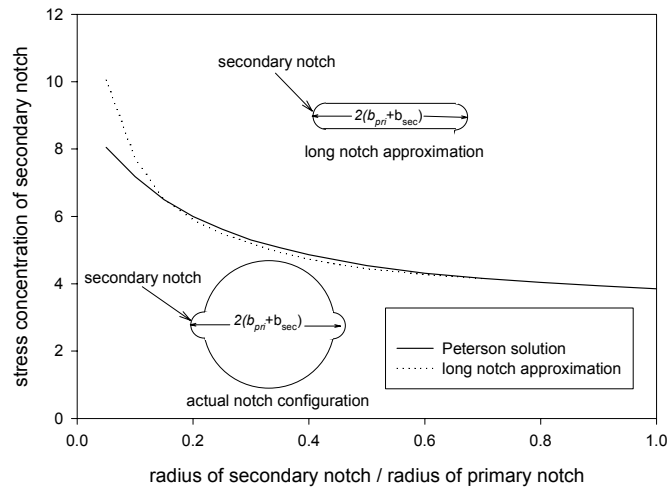


Figure 5I.8. Comparison of stress concentration factors determined according to a long notch approximation with the solution given in Peterson.

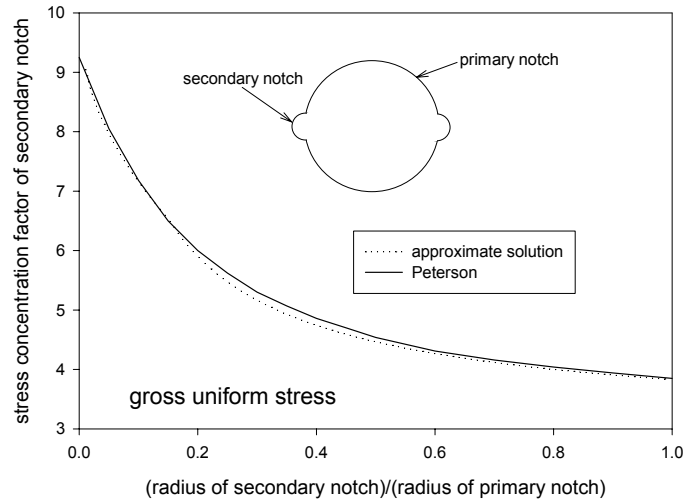


Figure 5I.9. Comparison of approximate solution for the stress concentration factor at secondary notches emanating from an embedded round notch with the solution given in Peterson.

FOD-Notch Stress Distribution

Selection of an Analytical Method for Deriving Approximate Stress Distributions

A number of investigators have proposed analytical expressions aimed at describing linear elastic derived stress distributions at notches. These methods were reviewed and short-listed to seven that were considered most appropriate for FOD applications. The seven methods selected for further studies and validation were those proposed by Amstutz and Seeger [3], Chen and Pan [4], Glinka and Newport [5], Kujawski [6], Kujawski and Shin [7], Weiss [8], and Xu, Thompson, and Topper [9].

Linear elastic finite element analyses (FEAs) were performed at SwRI on plates containing U-shaped surface notches in order to aid the selection of the most appropriate of the seven methods. Two cases were analyzed and in both of these the notch penetrated 10% through the plate width and had a b/ρ value of 2. In the first case, the plate was subjected to a uniform gross stress which resulted in a k'_t at the notch tip of 4.03, while in the second case the plate was subjected to pure bending that resulted in a k'_t at the notch tip of 3.47. These values for k'_t were used as inputs to the selected seven methods to predict the stress distributions at the notch tips. The results of these calculations, and the FEA computations, are shown in Figure 5I.10(a) and (b) for the uniform stressing and bending cases, respectively. In these figures, the stress ahead of

the notch normalized by the gross stress is plotted against the distance ahead of the notch normalized by the root radius, ρ .

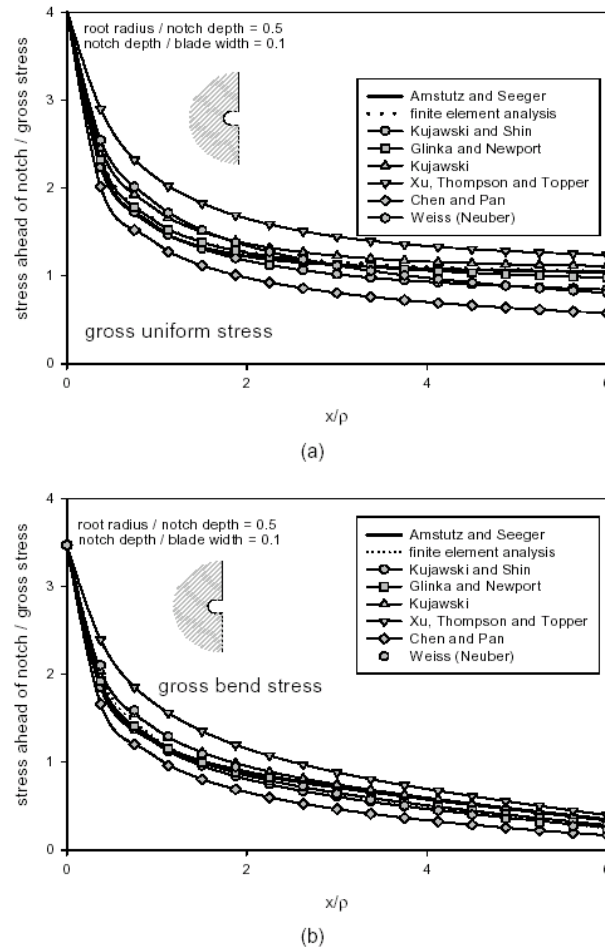


Figure 5I.10. Comparison of the results obtained using the seven selected approximate notch tip stress analysis methods with finite element results for U-shaped surface notch in a plate subjected to remote uniform stressing. The notch extends 10% through the plate width and $a/\rho = 2$, which results in a stress concentration factor, k'_t , of 4.03 for uniform stressing (a) and 3.47 for bending (b).

It can be seen from Figure 5I.10 that the two methods that best fit the FEA results are those due to Amstutz and Seeger [3] and Glinka and Newport [5]. (The method of Amstutz and Seeger was modified in the present work to allow its extension to bending based upon a technique employed by Glinka and Newport; (see the following paragraph). It was decided to adopt the Amstutz and Seeger approach in preference to Glinka and Newport as the former appeared to be the more robust method of the two. Furthermore, Amstutz and Seeger demonstrate that their approach produces stress distributions for embedded elliptical holes that are in excellent agreement with the exact solution of Xiao, Brown, and Miller [10] for $1 < k'_t < 50$.

According to the Amstutz and Seeger method, the stress distribution ahead of a notch is expressed as a function of the gross stress, σ_{gross} , the normalized distance, x/ρ , and the stress concentration factor, k'_t . In the case of bending, this approach had to be modified, and an additional function, F (which depends on b/t and x/t), was introduced into Amstutz and Seeger's formulation. This function forces the stress to zero at the neutral axis, following the recommendation in Glinka and Newport. In the present work, the neutral axis is assumed to be located at the center of the unnotched ligament. With these modifications, the stress at the tip of a notch (i.e., FOD),

$\sigma_{FOD}\left(\sigma_{gross}, \frac{x}{\rho}, k'_t, \frac{x}{t}, \frac{b}{t}\right)$, is given approximately by the expression:

$$\sigma_{FOD}\left(\sigma_{gross}, \frac{x}{\rho}, k'_t, \frac{x}{t}, \frac{b}{t}\right) = F\left(\frac{x}{t}, \frac{b}{t}\right) \sigma_{gross} \left[1 + \frac{k'_t - 1}{(1 + \Phi x / \rho)^\psi} \right] \quad (5I.18)$$

where

$$F\left(\frac{x}{t}, \frac{b}{t}\right) = 1 \quad (\text{applied remote moment}) \quad (5I.19)$$

and

$$F\left(\frac{x}{t}, \frac{b}{t}\right) = \left[1 - \frac{2x/t}{(1 - b/t)} \right] \quad (\text{applied remote moment}) \quad (5I.20)$$

$$\psi = \frac{1}{\Phi} \frac{2k'_t + 1}{k'_t - 1} \quad (5I.21)$$

$$\Phi = 0.226 + 0.394(k'_t - 1)^{3.0457}, 1 < k'_t < 2 \quad (51.22)$$

$$\Phi = 3.226 - \frac{2.706}{(k'_t - 0.9224)^{0.5018}}, 2 < k'_t < 50 \quad (51.23)$$

Application of the proposed methodology for determining approximate stress distributions at the tips of FOD requires the evaluation of k'_t using Equation (51.6), and then the evaluation of $\sigma_{FOD}\left(\sigma_{gross}, \frac{x}{\rho}, k'_t, \frac{x}{t}, \frac{b}{t}\right)$ using Equation (51.18). Validation of the methodology is presented in Figures 51.11, 51.12 and 51.13, which show the results of following this procedure together with the FEA results for surface notches subjected to uniform stressing and bending. For these particular notch configurations, Equation (51.6) predicts k'_t values of 2.86, 4.13, and 6.6 for uniform stressing and 2.65, 4.25, and 6.0 for bending, respectively, compared to the FEA results of 2.85, 4.03, and 6.7 for uniform stressing, and 2.43, 3.47, and 5.81 for bending. It can be seen from Figures 51.11(a), 51.12(a), and 51.13(a) that excellent agreement is obtained between the predictions of the proposed approach and the FEA results for the case of uniform stressing, and from Figures 51.11(b), 51.12(b), and 51.13(b) that acceptable agreement is obtained in the case of bending, with the approximate analysis providing a conservative estimate of the stress in this latter case.

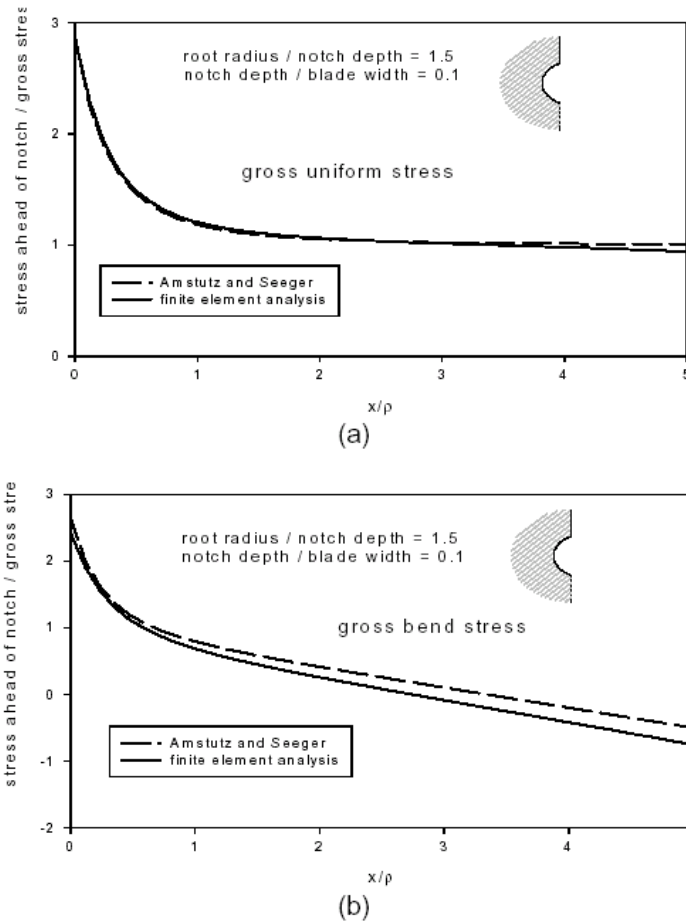


Figure 5I.11. Validation of the proposed methodology for determining stress distributions at the tips of FOD based on the Amstutz and Seeger method against finite element results for U-shaped surface notch in a plate subjected to remote uniform stressing. The notch extends 10% through the plate width and $b/\rho = 0.667$, which results in a stress concentration factor, k'_t , of 2.85 in (a) and 2.43 in (b).

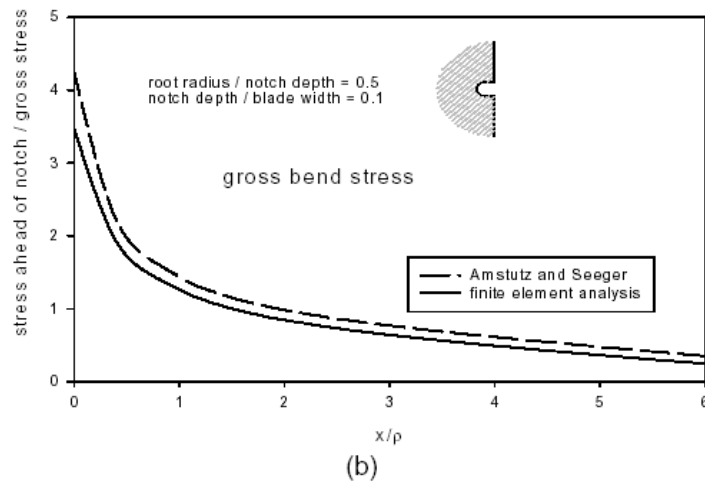
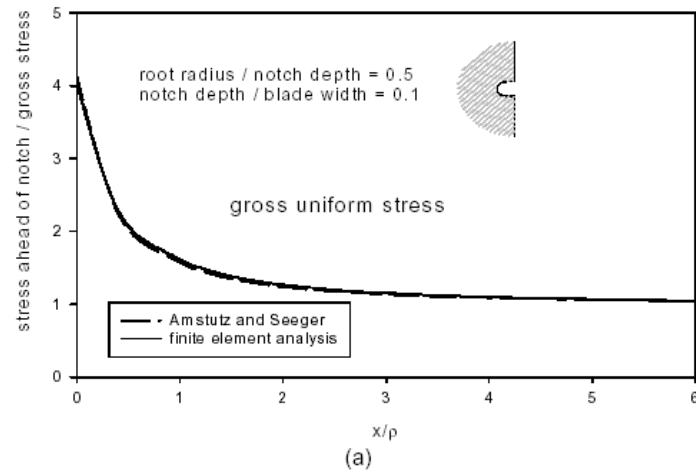
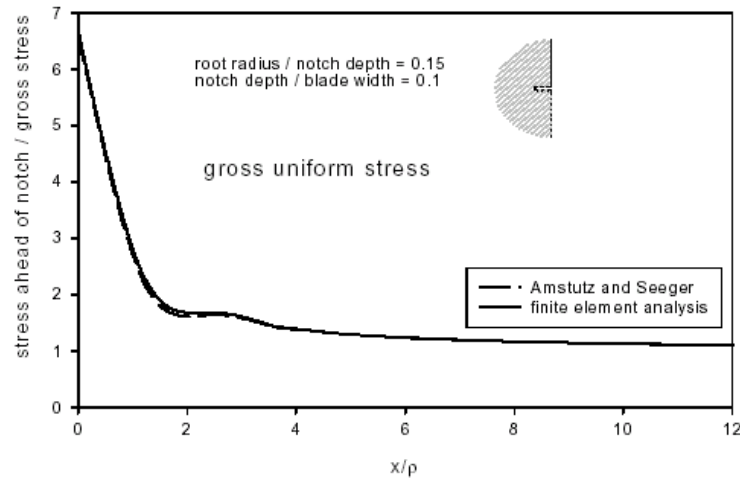
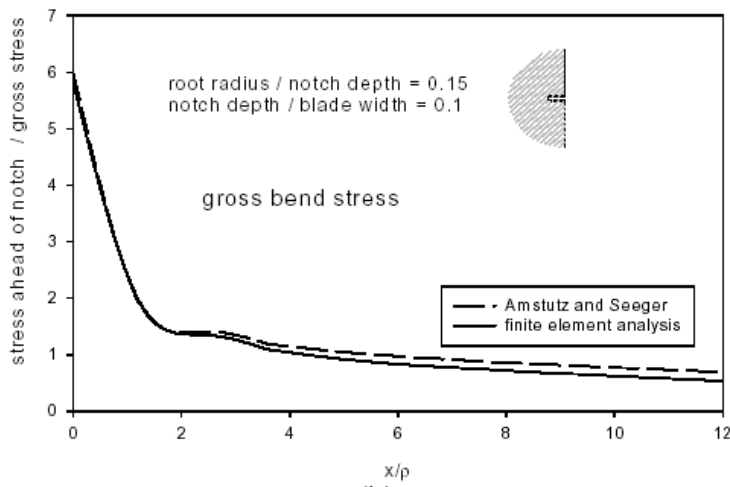


Figure 5I.12. Validation of the proposed methodology for determining stress distributions at the tips of FOD based on the Amstutz and Seeger method against finite element results for U-shaped surface notch in a plate subjected to remote uniform stressing. The notch extends 10% through the plate width and $b/\rho = 2$, which results in a stress concentration factor, k'_t , of 4.03 in (a) and 3.47 in (b).



(a)



(b)

Figure 5I.13. Validation of the proposed methodology for determining stress distributions at the tips of FOD based on the Amstutz and Seeger method against finite element results for U-shaped surface notch in a plate subjected to remote uniform stressing. The notch extends 10% through the plate width and $b/\rho = 6.67$, which results in a stress concentration factor, k'_t , of 6.7 in (a) and 5.81 in (b).

Summary of the Procedure for Evaluating Stress Distributions at the Tips of FOD

The following steps provide a procedure for implementing the approximate stress analysis method for determining the stress distributions at the tips of FOD. It is implicitly assumed in the procedure that the loading on the blade consists of a combination of forces and bending moments that can be derived from the stress analysis results for an undamaged blade.

- 1) Use Equation (5l.6) to determine the stress concentration factors, $k_t'^{tension}$, and $k_t'^{bend}$, for tension and bending, respectively, from the observed depth, b , and root radius, ρ of the FOD.
- 2) Determine the tension stress, $\sigma_{tension}$, and bend stress, σ_{bend} , from the stress, $\sigma(x)$ in the undamaged blade using the equations

$$\sigma_{tension} = \frac{1}{t} \left[\int_0^t \sigma(x) dx \right] \quad (5l.24)$$

$$\sigma_{bend} = \frac{6}{t^2} \left[\int_0^t \left(\frac{t}{2} - x \right) \sigma(x) dx \right] \quad (5l.25)$$

- 3) Determine the stress distributions, $\sigma_{FOD}^{tension} \left(\sigma_{tension}, \frac{x}{\rho}, k_t'^{tension}, \frac{x}{t}, \frac{b}{t} \right)$ and

$$\sigma_{FOD}^{bend} \left(\sigma_{bend}, \frac{x}{\rho}, k_t'^{bend}, \frac{x}{t}, \frac{b}{t} \right), \text{ at the FOD due to the tension and bend stresses,}$$

respectively, using Equation (5l.18), where $\sigma_{tension}$ and σ_{bend} , are evaluated from Equations (5l.24) and (5l.25), respectively.

- 4) The stress distribution at the tip of FOD is given by the principle of linear superposition as

$$\sigma_{FOD}^{tension} \left(\sigma_{tension}, \frac{x}{\rho}, k_t'^{tension}, \frac{x}{t}, \frac{ab}{t} \right) + \sigma_{FOD}^{bend} \left(\sigma_{bend}, \frac{x}{\rho}, k_t'^{bend}, \frac{x}{t}, \frac{b}{t} \right)$$

Stress Distributions Ahead of Secondary Notches

The following equation is proposed for evaluating the stress distribution ahead of a secondary notch based on the stress solution of Amstutz and Seeger.

$$\sigma_{FOD}^{sec} \left(\frac{x}{\rho_{pri}}, \frac{x}{\rho_{sec}}, k_t^{pri}, k_t^{sec} \right) = \sigma_{FOD}^{pri} \left(\frac{x}{\rho_{pri}}, k_t^{pri} \right) \left[1 + \frac{\left(\frac{k_t^{sec}}{k_t^{pri}} \right) - 1}{\left(1 + \frac{\phi_{sec} x}{\rho_{sec}} \right)^{\psi_{sec}}} \right] \quad (51.26)$$

where ϕ_{sec} and ψ_{sec} are the Amstutz and Seeger parameters evaluated using k_t^{sec} , and the distance x is measured from the tip of the secondary notch. This equation provides a means of interpolating between the stress at the secondary notch tip, which is determined by k_t^{sec} , and the stress distant from the tip, which is determined by the stress field due to the primary notch. (The primary notch stress field is the remote stress field acting on the secondary notch.) The predictions of Equation (51.26) for semi-circular notches emanating from an embedded round notch subjected to remote uniform tension are shown in Figure 51.14 for the case where the ratio of the secondary notch depth to the primary notch root radius is 0.05.

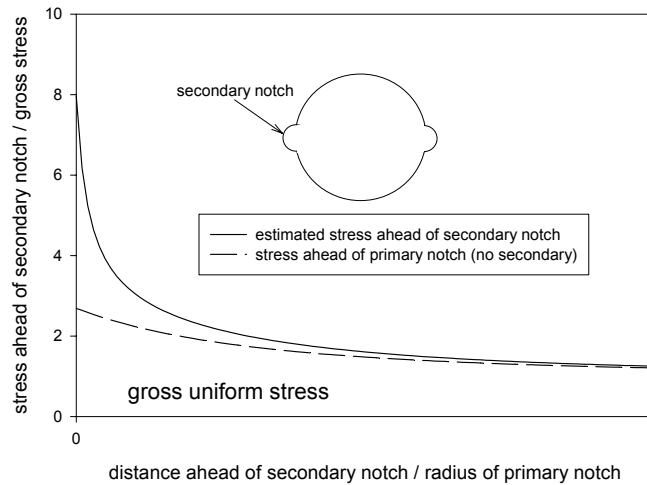


Figure 51.14. Predicted stress fields ahead of secondary semi-circular notches emanating from a primary embedded round notch and comparison with the stress field ahead of the primary notch in the absence of the secondary notches.

FOD-Induced Residual Stress

Local plastic deformation produced during FOD impact will result in a residual stress field. Although this field is likely to be very local to the surface, its influence on the nucleation and early growth of cracks could be significant, particularly in the HCF regime. Thus, any realistic treatment of HCF crack nucleation and crack growth processes should consider the influence of these residual stresses.

General features of the residual stress field are known. Specifically, the FOD impact will initially produce a large tensile plastic strain at the surface followed by elastic unloading in the material, below the surface of the FOD, resulting in a compressive stress layer at the surface. The depth of this compressive stress, as well as its magnitude, need to be determined. Evaluating these stresses is complicated by the thinness of the leading edge of the turbine blade and by the fact that most FOD impact the blade tip at some oblique angle, making the problem three-dimensional. Moreover, the size of the residual stress layer is expected to be too small for useful stress measurements to be obtained by conventional methods.

In order to better define this problem it is useful to consider a two dimensional analog. Namely, that of shot peening a large, relatively thick flat plate – this predominantly plane strain problem is often analyzed assuming the plate can be represented as a semi-infinite body. Results in Figure 5I.15 from Fathallah, et al. [11] compare the measured and predicted residual stress field for shot peening of Udiment 720 for the specific peening parameters shown. As can be seen the agreement between analytical prediction and experiment is quite good, thereby providing confidence in the analytical procedure. Also, note that the overall depth of the compressive layer is about 0.2 mm, or 0.008 in. Although shot peening involves multiple impacts to ensure full surface coverage, the energy of any given impact is considerably less than that experienced in FOD. Thus, the shot peening residual stresses in Figure 5I.15 would be expected to be a lower-bound estimate of those that are likely to result from a typical FOD impact.

Both shot peening and FOD impacts can occur at oblique impingement angles. The influence of impingement angle on the residual stresses can be estimated by considering additional results of Fathallah et. al. [11], which are given in Figure 5I.16.

These results are for the same peening parameters as those used in Figure 5I.15. As indicated in Figure 5I.16, the magnitude of the near-surface compressive residual stresses are similar in all cases, however, the depth of the compressive residual stresses below the surface decreases with decreasing impingement angle. Thus, the depth of FOD residual stresses would be expected to decrease with decreasing FOD impact angles, and would likely result in an increase in the HCF threshold stress.

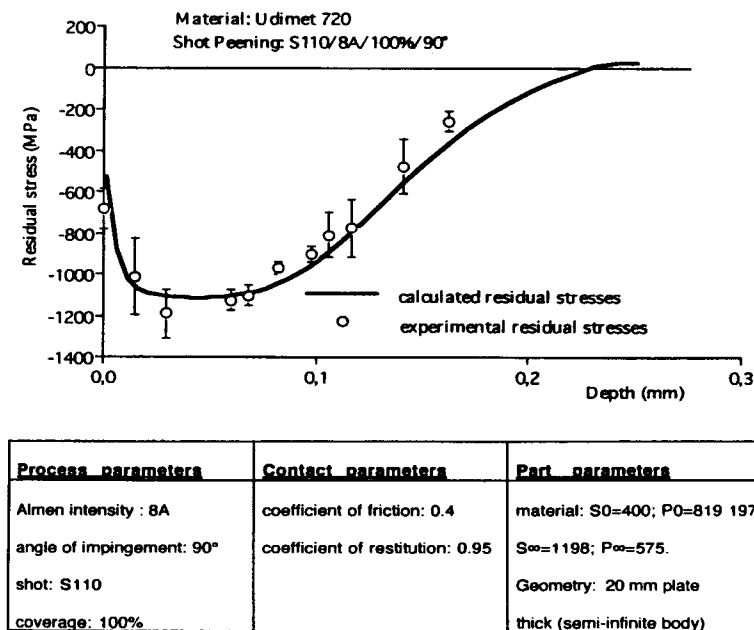


Figure 5I.15. Comparison of measured and predicted residual stresses from shot peening of Udiment 720 [from Ref. 11] (1 in = 25.4 mm, 1 ksi = 6.98 MPa).

Although the precise depth of the residual stress field, as well as the magnitude of the compressive residual stress vary somewhat with peening parameters and material hardening characteristics, the above results are generally consistent with other measurements and analyses of peening residual stresses [12], including those on Ti-6Al-4V [13]. Furthermore, elastic-plastic, axisymmetric finite element analyses of Kyriacou [14] for the case of a single impact indicate that the compressive residual stress achieves a minimum at about 0.75 to 1 times the Hertzian contact radius and that the stress remains compressive over about twice this distance.

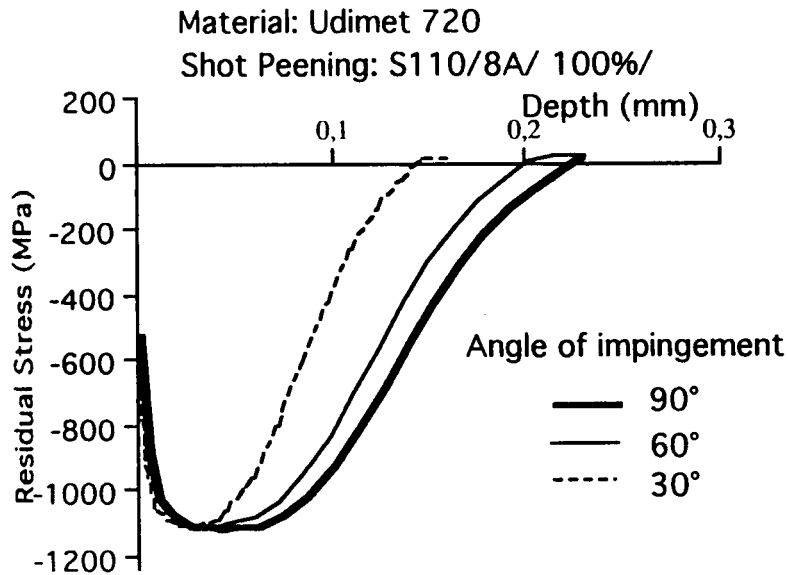
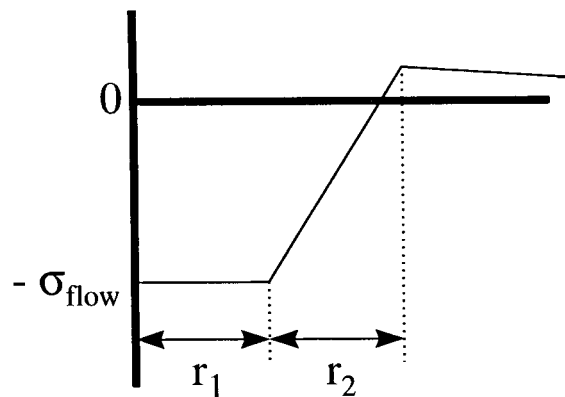


Figure 5I.16. Analytically predicted influence of angle of impingement on residual stresses from shot peening of Udimet 720 [11] (1 in. = 25.4 mm, 1 ksi = 6.89 MPa).

Based on the above results, the simple model shown in Figure 5I.17 emerges as an estimate of the residual stresses associated with FOD. The most important feature for our purposes being the depth of the compressive residual stress region, which is about 0.1 to 0.2 mm (0.004 to 0.008 in.).



$$r_1 = r_2 \text{ (Approx. 0.004 to 0.008 in.)}$$

Figure 5I.17. Idealized model of FOD residual stresses showing approximate depth of compressive stresses.

Analytical Representation of Residual Stress

The following equation is used to parametrically represent the idealized form of residual stress shown in Figure 5I.17

$$\begin{aligned}
 \sigma_{residual}(x) &= -\sigma_{flow} , \quad x \leq r_1 \\
 \sigma_{residual}(x) &= \sigma_{flow} \left[\left((1+\alpha) \frac{x}{r_1} \right) - 2 - \alpha \right] , \quad r_1 < x \leq r_1 + r_2 \\
 \sigma_{residual}(x) &= \alpha \sigma_{flow} \left[1 - \frac{x - r_2}{r_1(\beta - 2)} \right] , \quad r_1 + r_2 < x \leq r_1 + r_2 + r_3 \\
 \sigma_{residual}(x) &= 0 , \quad r_1 + r_2 + r_3 < x
 \end{aligned} \tag{5I.27}$$

where $r_2=r_1$, $r_3=(\beta-2)r_1$, $\beta=2+4/\alpha$ and α is a dimensionless parameter such that $\alpha\sigma_{flow}$ is the maximum tensile value of the residual stress. The value of β is chosen so that the residual stress is self-equilibrated (i.e., integrates to produce a net zero force). The forms of residual stress fields predicted by Equation (5I.27) for various values of α are shown in Figure 5I.18. The residual stress distribution given by Equation (5I.27) is used in the parametric study of the effects of residual stresses on threshold cyclic stress range and in the assessment of worst case notch models.

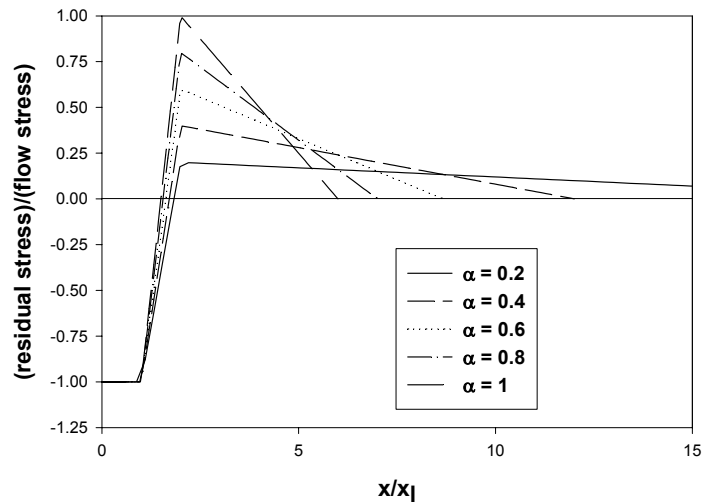


Figure 5I.18. Examples of the parametric residual stress for various values of α .

FOD Stress Intensity Factors

The stress intensity factors (SIF's) for cracks emanating from notches are needed for fatigue crack growth analysis and for determining worst case notch (WCN) scenarios that can be applied to FOD. In the present work, the SIF is calculated using the weight function approach from the stress ahead of FOD in the absence of a crack, $\sigma_{FOD}(x/\rho, \rho/b)$, where the distance x is measured from the tip the FOD, ρ is the radius of the tip, and b is depth of the FOD-notch. In general, σ_{FOD} will include a contribution from residual stresses induced during the formation of the FOD, as well as the local stress resulting from remote blade loading.

If $W_{notch}(a, x, a/\rho, \rho/b)$ is the weight function for a crack at a notch, then the SIF, $K_{FOD}(a, a/\rho, \rho/b)$, for a crack of depth, a , is given by

$$K_{FOD}\left(a, \frac{a}{\rho}, \frac{\rho}{b}\right) = \int_0^a W_{notch}\left(a, x, \frac{a}{\rho}, \frac{\rho}{b}\right) \sigma_{FOD}\left(\frac{x}{\rho}, \frac{\rho}{b}\right) dx \quad (51.28)$$

The weight function, W_{notch} , is estimated from the SIF solutions for cracks at surface notches in semi-infinite bodies subjected to remote uniform tension (Tada, Paris and Irwin [1]) using a reference solution approach. The reference SIF solutions were represented parametrically in the form

$$K_{ref, notch}\left(a, \frac{a}{\rho}, \frac{\rho}{b}\right) = \sigma_{gross} \sqrt{\pi a} F_{ref, notch}\left(s, \frac{\rho}{b}\right) \quad (51.29)$$

where σ_{gross} is the gross stress, $F_{ref, notch}(s, \rho/b)$ is a dimensionless function and $s=a/(a+b)$. W_{notch} was derived using the relationship:

$$F_{ref, notch}\left(s, \frac{\rho}{b}\right) = \frac{\int_0^a W_{notch}\left(a, x, \frac{a}{\rho}, \frac{\rho}{b}\right) \sigma_{ref, notch}\left(\frac{x}{\rho}, \frac{\rho}{b}\right) dx}{\sigma_{gross} \sqrt{\pi a}} \quad (51.30)$$

where $\sigma_{ref, notch}\left(\frac{x}{\rho}, \frac{\rho}{b}\right)$ is the Amstutz and Seeger (A&S) parametric stress equation (Equation 51.18).

The following approximate form was assumed for W_{notch}

$$W_{notch}(a, x, \frac{a}{\rho}, \frac{\rho}{b}) = 2 \left(\frac{a}{\pi} \right)^{1/2} \frac{\left(M(a, \frac{a}{\rho}, \frac{\rho}{b}) - \left[M(a, \frac{a}{\rho}, \frac{\rho}{b}) - 1 \right] \frac{x}{a} \right)}{(a^2 - x^2)^{1/2}} \quad (51.31)$$

The function M is derived by substituting Equation (51.31) into Equation (51.28) to obtain

$$M(a, \frac{a}{\rho}, \frac{\rho}{b}) = \frac{\frac{\pi}{2} \sigma_{gross} F_{ref, notch} \left(s, \frac{\rho}{b} \right) - I_2}{I_1 - I_2} \quad (51.32)$$

where

$$I_1 = \int_0^a \frac{\sigma_{ref, notch} \left(\frac{x}{\rho}, \frac{\rho}{b} \right)}{(a^2 - x^2)^{1/2}} dx \quad (51.33)$$

$$I_2 = \int_0^a \frac{\frac{x}{a} \sigma_{ref, notch} \left(\frac{x}{\rho}, \frac{\rho}{b} \right)}{(a^2 - x^2)^{1/2}} dx \quad (51.34)$$

The following analysis was used to derive parametric equations to represent $F_{ref, notch}(s, \rho/b)$ for cracks emanating from surface notches in semi-infinite bodies. For deep cracks ($a > \rho$),

$$K_{ref, notch} = \sigma_{gross} \sqrt{\pi a} F_{ref, notch}(s, \rho / b) = 1.122 \sigma_{gross} \sqrt{\pi(a + b)}, \quad \frac{a}{\rho} > 1 \quad (51.35)$$

Hence

$$F_{ref, notch}(s, \rho / b) = 1.122 \sqrt{\frac{(a + b)}{a}} = \frac{1.122}{\sqrt{s}}, \quad \frac{a}{\rho} > 1 \quad (51.36)$$

and

$$\frac{dF_{ref, notch}}{ds} = -\frac{F_{ref, notch}}{2s} \quad (51.37)$$

It is assumed that these expression for $F_{ref, notch}$ are valid when $a = \rho$ which corresponds to

$$s = s^* = \frac{\frac{\rho}{b}}{(1 + \frac{\rho}{b})} \quad (51.38)$$

In the limit $x/\rho < 1$, the stress field in the immediate vicinity of a notch can be obtained from Equation (51.18) as

$$\frac{\sigma_{ref,notch}(x \rightarrow 0)}{\sigma_{gross}} = k'_t - \frac{(2k'_t + 1)x}{\rho} \quad (51.39)$$

The following parametric equations is used for k'_t

$$k'_t = f\left(\frac{\rho}{b}\right) \left[1 + \frac{2K_{ref,notch}(b)}{1.122\sigma_{gross}\sqrt{\pi\rho}} \right] \quad (51.40)$$

where

$$f\left(\frac{\rho}{b}\right) = 1 + \frac{0.122}{\left(1 + \sqrt{\frac{\rho}{b}}\right)^{\frac{5}{2}}} \quad (51.41)$$

is a free surface correction factor given in Tada, et al. [1]. $K_{ref, notch}(b)$, for an edge crack of depth b equal to the notch depth in a semi-infinite body, is evaluated using the gross stress from the equation

$$K_{ref,notch}(b) = 1.122\sigma_{gross}\sqrt{\pi b} \quad (51.42)$$

Equation (51.39) implies that for $a/\rho \ll 1$ the $K_{ref, notch}$ solution can be written as

$$K_{ref,notch} = \sigma_{gross}\sqrt{\pi a} \left(k'_t F_0 - \frac{(2k'_t + 1)F_1 a}{\rho} \right) = \sigma_{gross}\sqrt{\pi a} F_{ref,notch}(s \rightarrow 0, \rho / b) \quad (51.43)$$

where $F_0=1.122$ is the influence function for uniform stress, and $F_1=0.6822$ is the influence function for a linear stress. Hence,

$$F_{ref,notch}(s \rightarrow 0, c / b) = (k'_t F_0 - \frac{(2k'_t + 1)F_1 b s}{\rho(1-s)}) \quad (51.44)$$

from which it may be deduced that

$$\frac{dF_{ref,notch}(s \rightarrow 0, \rho / b)}{ds} = - \frac{(2k'_t + 1)F_1 b}{\rho} \quad (51.45)$$

The values of $F_{ref, notch}$ and its derivative at $s \rightarrow 0$ and $s \rightarrow s^*$, were used to fit a cubic interpolation equation to $F_{ref, notch}$ between these two limits. Outside of this interpolated region, $F_{ref, notch} = 1.122/s^{1/2}$. The final form for $F_{ref, notch}(s, \rho/b)$ is

$$F_{ref, notch}(s, \rho / b) = (1 - \frac{s}{s^*})F_{ref, notch}(0) + \frac{s}{s^*} F_{ref, notch}(s^*) + \frac{s}{s^*} (1 - \frac{s}{s^*})^2 (F'_{ref, notch}(0)s^* - (F_{ref, notch}(s^*) - F_{ref, notch}(0))) \quad (51.46)$$

$$- \frac{s^2}{s^{*2}} (1 - \frac{s}{s^*}) (F'_{ref, notch}(s^*)s^* - (F_{ref, notch}(s^*) - F_{ref, notch}(0))) \quad , s \leq s^*$$

$$F_{ref, notch}(s, \rho / b) = \frac{F_0}{s^{1/2}} \quad , s > s^* \quad (51.47)$$

The prime indicates the derivative with respect to s .

Typical values of $F_{ref, notch}(s, \rho/b)$ as a function of s for various values k'_t are shown in Figure 51.19. These compare well with the solutions given in Tada, et al. [1].

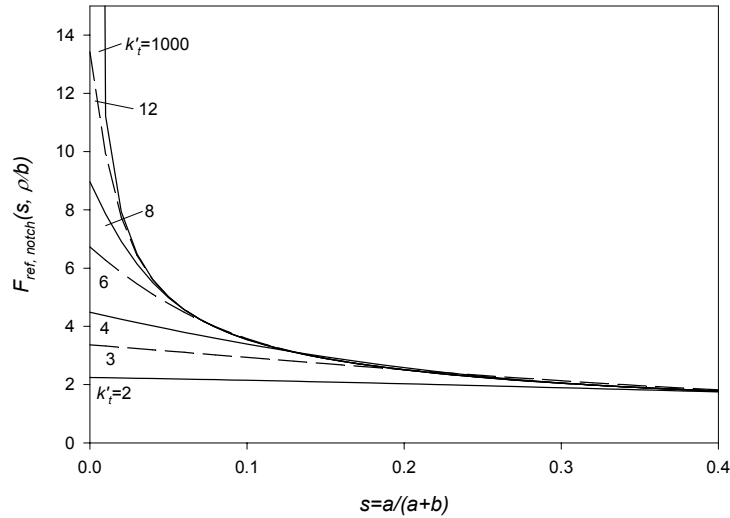


Figure 51.19. Typical solutions for the function $F_{ref, notch}$ for cracks emanating from notches in semi-infinite bodies subject to remote uniform stressing.

The foregoing analysis is for cracks at notches in semi-infinite bodies. The analysis was extended to finite-width plates and laboratory test specimens (e.g., double edge notched plates) by using the following procedure.

1. The function $F_{ref, notch}(s, \rho/b)$ in Equation (5I.35) that is used when $a/\rho > 1$ is replaced by $f_{ref}([a+b]/t)/s^{1/2}$, where f_{ref} is the appropriate function for the laboratory specimen that includes finite thickness correction terms through the ratio $[a+b]/t$, and t is the specimen thickness.
2. Equation (5I.37) is replaced by the equation
$$\frac{dF_{ref, notch}}{ds} = -\frac{F_{ref, notch}}{2s} + \frac{b}{\sqrt{s(1-s)^2}} \frac{df_{ref}}{da}$$
3. The stress concentration factor, k'_t , appearing in Equations (5I.43), (5I.44) and (5I.45) is evaluated according to Equation (5I.6).

WORST CASE NOTCH (WCN) CONCEPT

Outline of the Worst Case Notch Model

Two basic technical issues need to be considered in analyzing the influence of FOD on HCF behavior: 1) the detrimental influence of the geometric stress concentration created by the FOD “notch”, and 2) the beneficial influence of the near-surface compressive residual stresses produced by the FOD impact event.

The classical S-N approach to HCF employs the fatigue notch reduction factor (k_f) to account for the reduction in fatigue strength due to the presence of notches. However, since FOD notches can be considerably more severe than design features, it is not clear that this empirical approach can be extrapolated to the treatment of FOD. Instead, the present approach is based on damage tolerance concepts that employ fracture mechanics theory to assess the severity of FOD [15-17]. A worst case notch (WCN) model is employed, so-called because it leads to the prediction of a limiting value of the threshold stress (ΔS_{th}) for crack propagation with increasing notch severity [15-17]. The physical basis for the proposed model is consistent with observations that microcracks can grow below the traditional large-crack threshold [18-22], as well as observations that microcracks can initiate and subsequently arrest at notches [23-25]. Traditional (large crack) fracture mechanics concepts cannot explain either of these observations.

An overview of the WCN approach is shown in Figure 5I.20. The approach assumes that cracks can initiate relatively early in the life of a component due to the combined effects of the concentrated stresses introduced by the FOD and the intermittent occurrence of low cycle fatigue (LCF) loading. Consequently, it is assumed that the influence of FOD on HCF behavior is controlled by whether or not initiated cracks will continue to grow. The threshold stress defining the growth/arrest boundary is determined in the usual manner by setting the applied stress intensity factor (ΔK) equal to the threshold stress intensity factor for fatigue crack propagation (ΔK_{th}). However, a key element of the WCN model is that the latter threshold value is appropriately modified for the behavior of small fatigue cracks through the introduction of a crack-size dependence. Small crack effects and the associated conditions for non-propagation of cracks in the stress gradients of notches predicted by the WCN model provide a viable engineering solution to the problem of dealing with the large variation in FOD-notch geometry that is encountered in turbine engine blades. Initial developments along these lines have demonstrated success in treating the variation in weld-toe root radii, and their consequent effects on the HCF behavior of offshore structures [16].

Worst-Case Notch Methodology

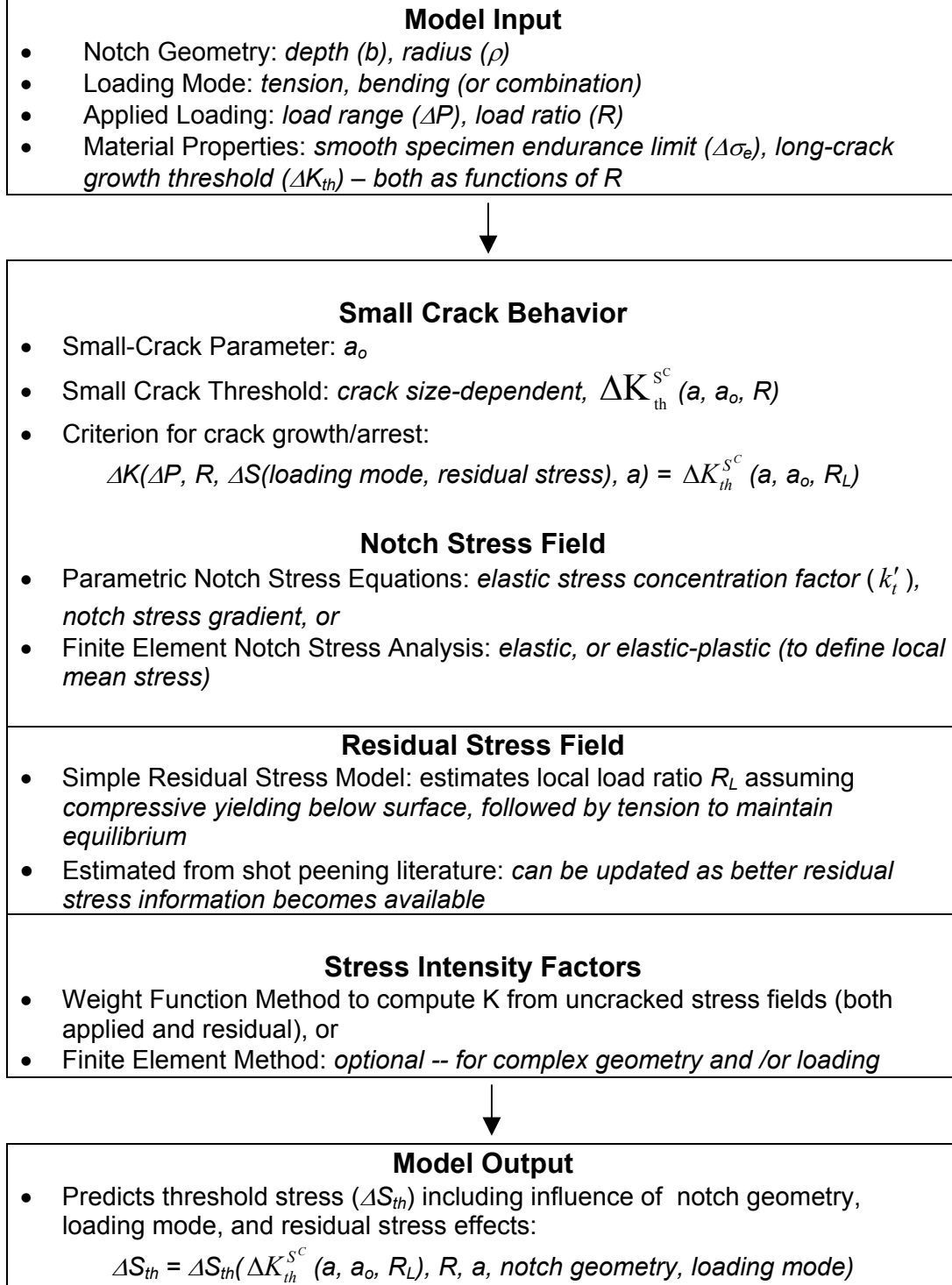


Figure 5I.20. Overview of Worst Case Notch (WCN) methodology for treating FOD.

In the present application of the WCN model, the notch stress field is estimated by parametric equations. In general, these could be replaced by results of finite-element analyses, particularly when complex geometries or loading modes are involved. A simple residual stress model is also employed to represent the beneficial effects of the near-surface residual stresses introduced by FOD. The inclusion of residual stress effects (from FOD, or any other surface treatment) is facilitated by the explicit treatment of small crack effects in the WCN model since these effects occur very local to the surface.

The WCN model enables the boundaries between crack nucleation, crack growth followed by arrest, and crack growth to failure to be defined as shown in Figure 5I.21. As indicated in Figure 5I.21(a), the nucleation boundary, given by the endurance limit divided by the elastic stress concentration factor ($\Delta\sigma_e/k'_t$), decreases continuously with increasing notch severity, whereas the boundary between crack arrest and crack growth to failure reaches a limiting value with increasing notch severity. As shown in Figure 5I.21(b), the occurrence of crack growth followed by arrest is caused by the fact that for sharp notch root radii the threshold stress (ΔS_{th}) initially increases with crack size (a) before reaching a maximum and decreasing. This behavior is the direct consequence of small crack effects and the crack-size dependent crack growth threshold. It should be noted that Figure 5I.21 is for a constant notch depth. As notch depth is increased all of the boundaries in Figure 5I.21 move to lower stresses. The WCN model predicts, among other things, the influence of notch depth and notch radius on the threshold stress. The goal of the WCN approach developed here is to quantify cyclic threshold behavior at notches in a consistent fashion that is compatible with fracture mechanics theory, and enables the technology to be employed in design.

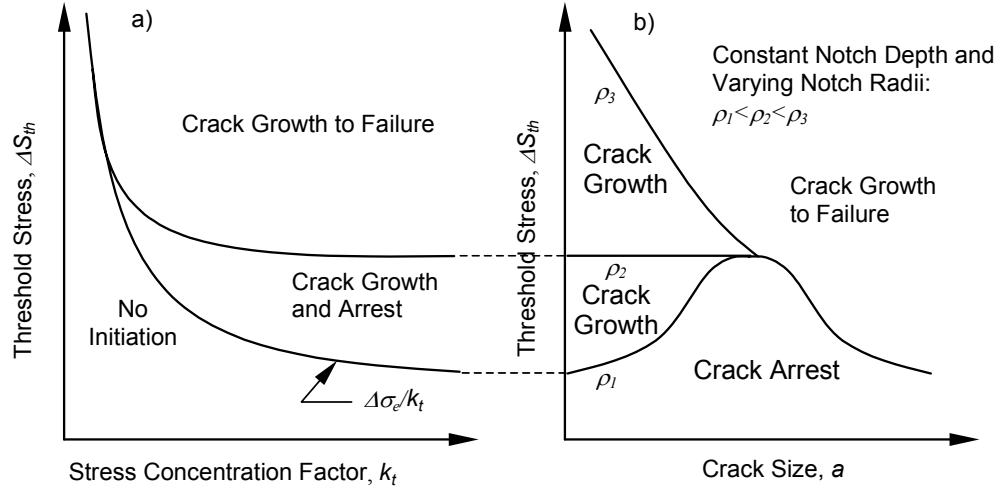


Figure 5I.21. Schematic illustration of worst case notch (WCN) concept showing regimes of threshold stresses and notch severity required for crack nucleation, crack growth and arrest, and crack growth to failure.

Estimating Threshold Cyclic Stresses using the Classical S-N Endurance Approach

In the absence of residual stresses at FOD the threshold cyclic stress ΔS_{th} for a notch with stress concentration factor, k_t' , can be estimated using the classical S-N approach from the smooth bar endurance limit, $\Delta\sigma_e$ by the equation

$$\Delta S_{th}(R) = \frac{\Delta\sigma_e(R)}{k_t'} \quad (5I.48)$$

where $R = \sigma_{min}/\sigma_{max}$ is the stress ratio, and σ_{min} and σ_{max} are the applied values of the gross stress at the minimum and maximum parts of a cycle. If residual stresses are present then a similar equation holds but the stress ratio, R , is now defined by the following equation

$$R = \frac{k_t'\sigma_{min} + \sigma_{res}}{k_t'\sigma_{max} + \sigma_{res}} \quad (5I.49)$$

where σ_{res} is the value of the residual stress at the notch tip. Equation (5I.49) can be re-expressed in the form

$$R = \frac{R_\sigma \Delta\sigma_{local} + (1 - R_\sigma)\sigma_{res}}{\Delta\sigma_{local} + (1 - R_\sigma)\sigma_{res}} \quad (5I.50)$$

where $R_\sigma = \sigma_{min}/\sigma_{max}$ and $\Delta\sigma_{local} = k'_t(\sigma_{max} - \sigma_{min})$ is the local cyclic change in stress at the notch tip. The condition for crack propagation at the notch is $\Delta\sigma_{local} \geq \Delta\sigma_e$. Hence, the stress ratio at threshold is given by

$$R = \frac{R_\sigma \Delta\sigma_e(R) + (1 - R_\sigma) \sigma_{res}}{\Delta\sigma_e(R) + (1 - R_\sigma) \sigma_{res}} \quad (51.51)$$

This equation enables R to be determined if $\Delta\sigma_e$ is known as a function of R , and hence the threshold cyclic stress to be calculated from Equation (51.48).

Estimating Threshold Cyclic Stresses Using the Worst Case Notch Model

The classical S-N approach to determining HCF does not predict the observed threshold behavior for notches with relatively large stress concentration factors. According to the fracture mechanics based WCN model, the cyclic threshold stress, ΔS_{th} , is not only a function of the FOD-notch geometry, loading mode, stress ratio, R , and material variables, but also of the depth, a , of an initiated crack, and the small crack parameter, a_o . The following equation highlights the dependence of the threshold stress on dimensional and loading parameters, as assumed in the WCN model:

$$\Delta S_{th} = \Delta S_{th}(k'_t[b, \rho], a, a_o(R), \lambda) \quad (51.52)$$

where λ is a parameter which depends on loading mode (e.g., tension or bending) and a_o is the small crack parameter suggested by El Haddad, et al. [26] given by:

$$a_o(R) = \frac{1}{\pi} \left(\frac{\Delta K_{th}(R)}{F \Delta\sigma_e(R)} \right)^2 \quad (51.53)$$

where $\Delta K_{th}(R)$ is the long crack threshold stress intensity factor range for measurable fatigue crack growth, $\Delta\sigma_e(R)$ is the smooth bar endurance limit, and F is the geometry factor for a surface crack in a smooth bar given by 1.12 for a through crack, and $1.12(2/\pi) = 0.713$ for a thumbnail crack.

Although there has been extensive debate regarding the physical significance of a_o as a material constant, it is interpreted here as a parameter which interpolates between the smooth and cracked specimen responses in terms of a crack-length-dependent, small-crack threshold stress intensity, $\Delta K_{th}^{sc}(a, a_o, R)$, given as:

$$\Delta K_{th}^{sc}(a, a_o, R) = \Delta K_{th}(R) \left[\frac{a}{a + a_o(R)} \right]^{1/2} \quad (51.54)$$

The condition for crack propagation to initiate under HCF conditions is that the applied stress intensity factor range, ΔK , equals or exceeds the cyclic threshold value

$$\Delta K \geq \Delta K_{th}^{sc} \quad (51.55)$$

Writing $\Delta K = f_n \left(\frac{a}{b}, \frac{a}{\rho} \right) \Delta \sigma \sqrt{\pi a}$, where f_n is a magnification factor that includes the effects of the crack shape and the notch, and $\Delta \sigma$ is the cyclic change in the applied gross stress, then Equation (51.54) can be re-expressed in terms of the cyclic threshold stress, ΔS_{th} ,

$$\Delta S_{th} \left(\frac{a}{b}, \frac{a}{\rho}, a, R \right) = \frac{\Delta K_{th}(R)}{(\pi [a + a_o(R)])^{1/2} f_n \left(\frac{a}{b}, \frac{a}{\rho} \right)} \quad (51.56)$$

where $a_o(R)$ is defined by Equation (51.53). In the case of remote loading,

$$R = \frac{K_{min}}{K_{max}} = \frac{(\pi a)^{1/2} f_n \sigma_{min}}{(\pi a)^{1/2} f_n \sigma_{max}} = \frac{\sigma_{min}}{\sigma_{max}} \quad (51.57)$$

and is independent of crack depth. Hence, R , remains constant during crack growth.

Equation (51.56) predicts that the behavior of ΔS_{th} as the crack grows will depend on the notch geometry. For sharp notches, the value of ΔS_{th} , predicted from Equation (51.56) will initially increase, reach a maximum value and then decrease as an initiated crack grows (compare Figure 51.21). For blunt notches, the value of ΔS_{th} is predicted to decrease monotonically with crack growth. For a given notch geometry, the threshold cyclic stress is given by the maximum value attained by ΔS_{th} as an initiated crack extends. For applied stresses greater than this maximum ΔS_{th} , cracks will initiate and grow to failure.

A Two Criteria Approach to Determining ΔS_{th}

In general, the maximum value of ΔS_{th} has to be determined numerically. However, an approximate analytical solution can be derived utilizing a two criteria approach. The two criteria are based on the observation that the classical S-N approach describes threshold behavior for blunt notches (relatively small k_t' values), and for sharp notches

(large k_t' values) ΔS_{th} is independent of k_t' (compare Figure 5I.21(a)). Here “small” and “large” are judged relative to a limiting value of k_t' , called k_w , that is derived below.

From Equation (5I.53)

$$\Delta K_{th} = F_e(\pi a_o)^{1/2} \Delta \sigma_e \quad (5I.58)$$

where F_e is a combined free-surface-shape-magnification factor for a crack initiated in a fatigue endurance test. Let the applied ΔK be given by

$$\Delta K = (\pi a)^{1/2} f_n\left(\frac{a}{a+b}, \frac{a}{\rho}\right) \Delta \sigma_{gross} \quad (5I.59)$$

where f_n is a notch-shape magnification factor. The cyclic threshold stress, ΔS_{th} is given by equating ΔK to ΔK_{th}^{sc} which, from Equations (5I.58) and (5I.59), leads to the relationship

$$\Delta S_{th} = \Delta \sigma_e \frac{F_e(\pi a_o)^{1/2}}{(\pi(a+a_o))^{1/2} f_n\left(\frac{a}{a+b}, \frac{a}{\rho}\right)} = \frac{\Delta K_{th}}{(\pi(a+a_o))^{1/2} f_n\left(\frac{a}{a+b}, \frac{a}{\rho}\right)} \quad (5I.60)$$

that defines ΔS_{th} as a function of crack depth a . Assume that the crack is deep enough so that its K can be approximated by a crack of depth $b+a$ subjected to the remote loading. Then

$$f_n\left(\frac{a}{a+b}, \frac{a}{\rho}\right) = \left(\frac{a+b}{a}\right)^{1/2} g_n\left(\frac{a+b}{t}\right) \quad (5I.61)$$

where g_n is a surface-shape magnification factor, and t is the laboratory specimen thickness. Assuming $(a+b)/t \ll 1$, then $g_n = 1.12h_n$, where h_n is a crack shape factor. In general, the cyclic threshold stress is given by

$$\Delta S_{th} = \frac{\Delta K_{th}}{\sqrt{\pi(a+a_o)} \left(\frac{a+b}{a}\right)^{1/2} g_n\left(\frac{a+b}{t}\right)} \quad (5I.62)$$

This has a maximum value when $d(\Delta S_{th})/da = 0$. Assuming that the value of g_n is insensitive to changes in a , then the maximum will occur when $a = a_w$, where

$$a_w = (ba_o)^{1/2} \quad (5I.63)$$

Crack sizes less than a_w will either not propagate or will arrest if $\Delta S_{th} < \Delta S_{th,max}$. Substituting this value for a gives

$$\Delta S_{th,max} = \frac{\Delta K_{th}}{(\pi)^{1/2} g_n\left(\frac{\sqrt{ba_o} + b}{t}\right) (\sqrt{a_o} + \sqrt{b})} \quad (5I.64)$$

Note that for cases where $\sqrt{b} \gg \sqrt{a_o}$, this equation predicts that $\Delta S_{th,max}$ will vary as $\frac{1}{\sqrt{b}}$.

It has been assumed that the SIF for a crack at a notch can be replaced by the SIF for a crack of depth equal to $b+a$ subjected to remote loading when $a \geq \rho$. This implies from Equation (5l.63) that ΔS_{th} will have a maximum when

$$\rho_w \approx (ba_o)^{1/2} = a_w \quad (5l.65)$$

Substituting this value of ρ into Equation (5l.6) then the value of $k_t' = k_w$ at which the maximum occurs is given by

$$k_w = \left(1 + \frac{0.122}{\left[1 + \left(\frac{a_o}{b} \right)^{1/4} \right]^{5/2}} \right) \left[\frac{A(0)}{A(b)} + \frac{2K(b)}{1.122\sqrt{\pi(ba_o)^{1/2}}} \right] \quad (5l.66)$$

For a shallow surface notch where $b/t \ll 1$,

$$k_w \approx \left(1 + \frac{0.122}{\left[1 + \left(\frac{a_o}{b} \right)^{1/4} \right]^{5/2}} \right) \left(1 + 2 \left[\frac{b}{a_o} \right]^{1/4} \right) \quad (5l.67)$$

Thus, the two criteria approach can be stated as follows:

- for values of $\Delta S_{th} < \Delta S_{th,max}$, the threshold cyclic stress, ΔS_{th} will have a constant value equal to $\Delta S_{th,max}$ evaluated according to Equation (5l.64),
- for $\Delta S_{th} > \Delta S_{th,max}$, it can be assumed that $\Delta S_{th} = \frac{\Delta \sigma_e}{k_t'}$.

The accuracy of the two criteria approach for notches that are subjected to only remote loading is illustrated in Figures (5l.22) and (5l.23) for notches in double edge notched plates (DENP) and circumferential round bars (CRB), respectively.

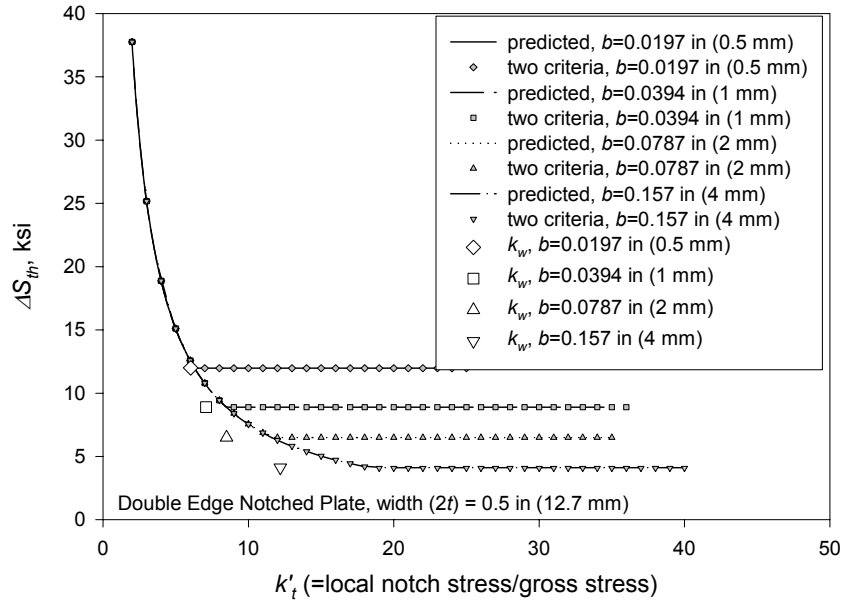


Figure 5I.22. Comparison of the predictions of threshold stresses derived from the simplified two criteria approach with the thresholds calculated using the complete WCN model for a DENP specimen. Also shown are K_w values determined from Equation (5I.66).

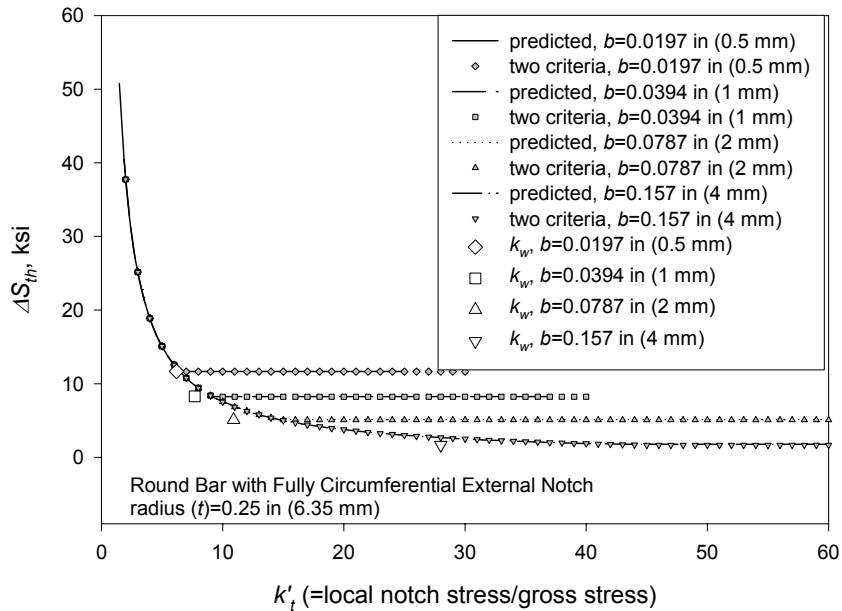


Figure 5I.23. Comparison of the predictions of threshold stresses derived from the simplified two criteria approach with the thresholds calculated using the complete WCN model for a CRB specimen. Also shown are K_w values determined from Equation (5I.66).

These figures show the threshold cyclic stresses predicted numerically for Ti-6Al-4V material properties by solving Equation (5I.56) numerically for a range of notch sizes, and the results of applying the two criteria approach. Also shown, are the limiting values of k_w predicted according to Equation (5I.66). It can be seen that the predictions of the two criteria method are in excellent agreement for all notch depths with the more precise numerically calculated values of ΔS_{th} . The estimated values for k_w are in good agreement for shallow notches with the values of k_t' at which the transition to classical S-N behavior occurs. However, the simple expression for k_w underestimates the transition value of k_t' as the notch depths become deep.

Incorporation of Residual Stresses in WCN Model

In the presence of residual stresses, the stress ratio, R , is no longer simply related to the ratio of applied minimum and maximum stresses. If $K^{res}(b, a, \frac{\rho}{b})$ is the SIF due to residual stresses, and $K_{min}(b, a, \frac{\rho}{b})$ and $K_{max}(b, a, \frac{\rho}{b})$ are the SIF's corresponding to the applied minimum and maximum remote loads, respectively, then

$$R = \frac{K^{res}(b, a, \frac{\rho}{b}) + K_{min}(b, a, \frac{\rho}{b})}{K^{res}(b, a, \frac{\rho}{b}) + K_{max}(b, a, \frac{\rho}{b})} \quad (5I.68)$$

The value of R will depend on crack depth when residual stresses are present because the value of $K^{res}(b, a, \frac{\rho}{b})$ will depend on crack depth. This dependency complicates the WCN case analysis because both the thresholds, $\Delta\sigma_e$ and ΔK_{th} , are functions of R .

Let R_σ be the R ratio determined from the remote loading, then an initiated crack will just continue to grow only if

$$R = \frac{[R_\sigma \Delta K_{th}(R) + (1 - R_\sigma) K^{res}]}{[\Delta K_{th}(R) + (1 - R_\sigma) K^{res}]} \quad (5I.69)$$

Hence, in the presence of a residual stress, calculation of the cyclic threshold stress involves the simultaneous solution of Equations (5I.56) and (5I.69). Note that, since $\Delta\sigma_e$ and ΔK_{th} both depend on R , a crack will experience different threshold conditions as it grows through a spatially varying residual stress field.

Parametric Studies Using WCN Model

Effect of Notch Depth, Notch Radius and Stress Concentration Factor on Threshold Behavior

The predicted effects of notch depth, b , notch radius, ρ , and stress concentration factor, k_t' , on threshold cyclic stress behavior according to the WCN model are conveniently summarized in Figure 5I.24. This figure shows the results of applying WCN concepts to a surface notch in a semi-infinite body subjected to remote loading. The calculated dependence of the threshold ΔS_{th} on crack depth is shown in the figure. The initiated cracks were assumed to extend through the thickness. The calculations were based on Ti-6Al-4V properties and $R = 0$ was assumed. A matrix of analyses were performed consisting of variable notch depth and notch radius such that the value of k_t' at the notches was held constant with values of 3, 5 and 7.5 as the notch depth increased. The same matrix of solutions also allows the effects of variable notch radius for a given notch depth to be studied (see inset in Figure 5I.24). The threshold value for crack propagation to failure is given by the maximum value of ΔS_{th} as the crack depth, a , increases. There are three major mechanisms that govern the predicted value of ΔS_{th} . First, when the initiated cracks are very small the value of ΔS_{th} can be determined using the classical S-N endurance approach (see Appendix 3N). This behavior is predicted by the WCN model as can be seen by setting a to zero in Equation (5I.56). For a through crack, $f_n(a = 0) = 1.12 k_t'$ and $\Delta K_{th}(R) = 1.12 \sqrt{\pi a_o} \Delta \sigma_e(R)$, and Equation (5I.56) reduces to Equation (5I.48). Second, when the initiated cracks

are very long, $a \gg a_o$, $a \gg \rho$, and $f_n = 1.12 \sqrt{\frac{a+b}{a}}$, Equation (5I.56) reduces to

$$\Delta S_{th} = \frac{\Delta K_{th}(R)}{1.12 \sqrt{\pi(a+b)}}, \text{ which is the value predicted for long cracks by standard fracture}$$

mechanics theory. Third, between the two previous limiting forms of threshold behavior, the WCN phenomenon may occur. Equation (5I.64) then predicts the maximum value of ΔS_{th} , and Equation (5I.63) predicts the crack depth at which the maximum will occur. The open symbols in Figure 5I.24 show the coordinates corresponding to these values of crack depth and threshold.

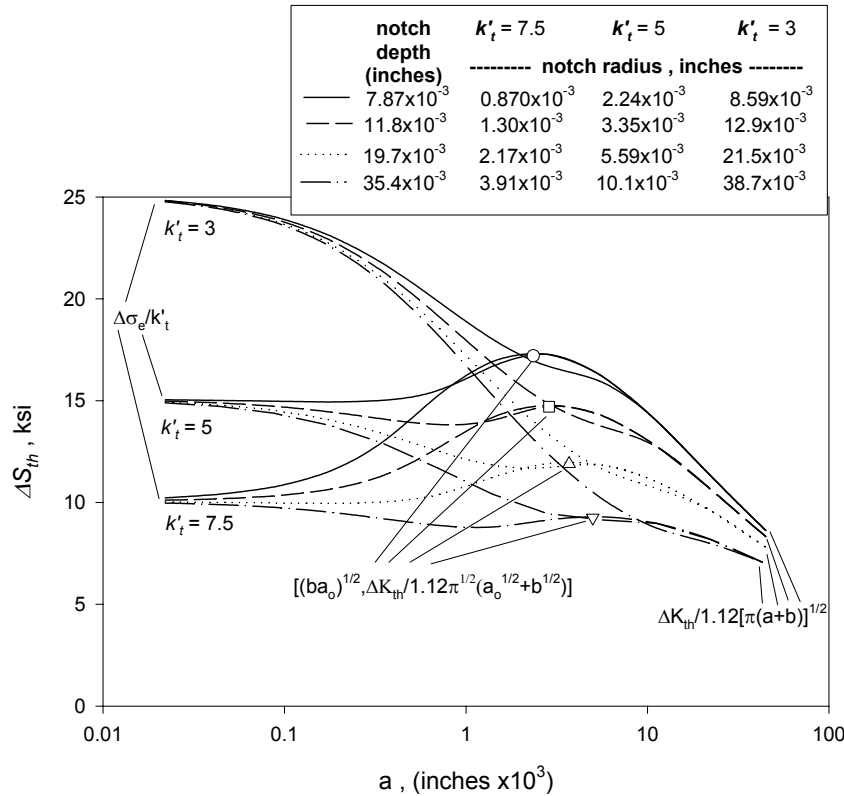


Figure 5I.24. Example of the effects of notch depth, notch radius and stress concentration factor on threshold stress behavior.

Figure 5I.24 demonstrates that there are two maximum in the values of ΔS_{th} , one corresponding to the WCN prediction, and the other to the prediction of classical S-N endurance theory. These maxima are in competition as to which value will determine threshold behavior. As can be seen from the figure, the behavior of sharp notches with relatively high k'_t values will be governed by WCN phenomenon which is controlled by a_o (which is determined from the values of $\Delta\sigma_e$ and ΔK_{th}), and the threshold stress intensity, ΔK_{th} . In contrast, the threshold stress for blunt notches with relatively low k'_t values will be controlled only by the endurance, $\Delta\sigma_e$. The two criteria approximation recognizes the competition between classical behavior and WCN behavior, and selects the highest value of ΔS_{th} predicted from applying the two approaches.

Effect of Specimen and Component Geometry on Threshold Behavior

FOD in blades is usually very shallow compared to the width of the blade and hence the WCN analysis of these notches can be performed assuming a surface notch

in a semi-infinite body. However, notches in laboratory specimens, such as double edge notched plates (DENP) and circumferential round bars (CRB), can be relatively deep compared to the thickness or radius of the specimen. In order to investigate the effects of finite geometry dimensions on the predictions of the WCN model, analyses were performed using Ti-6Al-4V material properties for deep notches ($b = 0.2$ inches) in a semi-infinite body, and DENP and CRB specimens of thickness 0.8 inches and radius 0.4 inches, respectively. The notch in the CRB was on the outside of the bar and the stress ratio, R , was taken to be 0. The results of the computations are displayed in Figure 5I.25, where the calculated thresholds are plotted against k'_t . It can be seen from the figure, that the notch in the semi-infinite body and in the DENP specimens are predicted to have very similar threshold values, even though the notch in the DENP reduces the load bearing area in that specimen by 50%. However, the predicted behavior for the notch in the CRB is significantly different from that in the other two geometries at high k'_t values, but it should be noted that in this case, the notch reduces the load bearing area in the specimen by 75%. For practical applications, particularly applications to FOD in blades, it can be assumed that the threshold behavior is independent of component geometry.

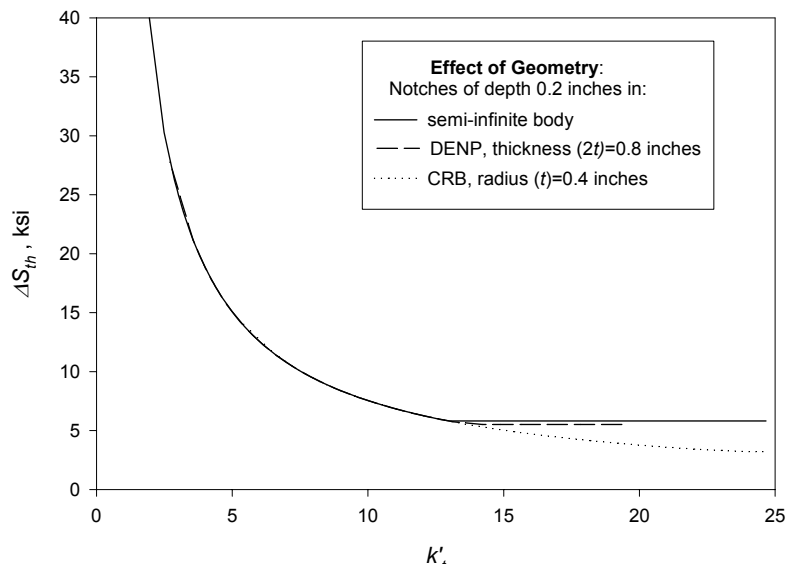


Figure 5I.25. Example of the effect of geometry on threshold stress behavior. Comparison of the WCN predicted results for a notch in semi-infinite bodies, a DENP specimen, and a CRB specimen.

Effect of FOD Residual Stress on Threshold Behavior

Figures 5I.26 and 5I.27 show the predicted effects that FOD residual stress can have on threshold behavior. The residual stresses used in the WCN calculations were based on parametric forms. These forms are functions of material flow stress, the size of the compressive stress zone, r_1 , and the magnitude of the maximum tensile stress (determined by the value of α). In the present calculations, the flow stress was taken equal to the yield stress of Ti-6Al-4V, namely 135 ksi, and two sets of WCN computations were performed in order to assess the sensitivity of the predictions to a range of assumed values for r_1 and α . A surface notch of depth 0.03 inches in a semi-infinite body was assumed. The material properties appropriate to Ti-6Al-4V were used in the calculations. Figure 5I.26 shows the predicted threshold stress behaviors for values of α ranging from 0.2 to 1 with the value of r_1 fixed at 0.00197 inches (0.05 mm). This figure also shows the threshold results for when residual stresses are absent. The effect of changing α on the residual stress profile can be seen in Figure 5I.18. It is clear that residual stresses can be significantly beneficial in raising the predicted threshold cyclic stress by over a factor of two compared with threshold values calculated for a residual stress free notch.

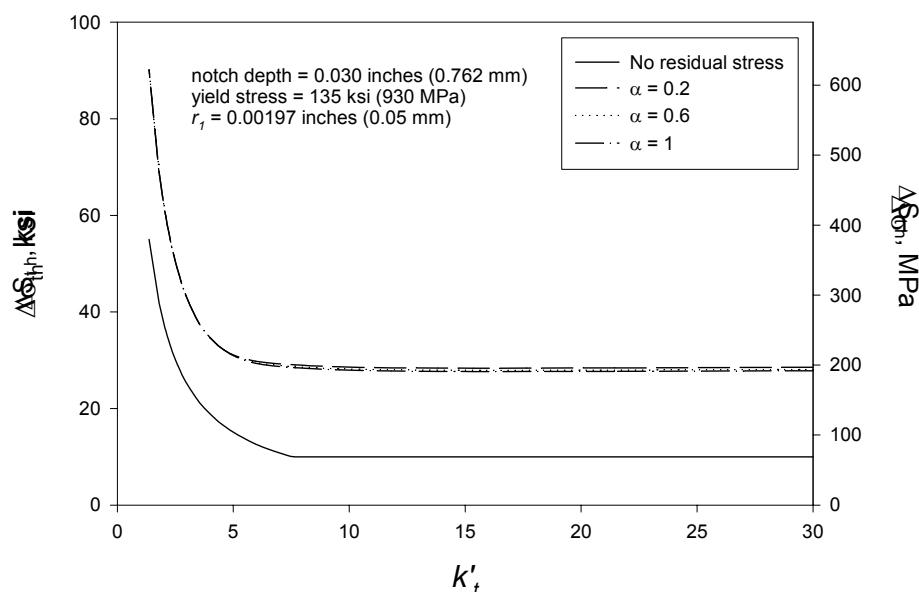


Figure 5I.26. Examples of the effects of residual stresses on threshold stresses predicted by the WCN model. The size of the compressive residual stress is fixed at 0.00197 inches, and the parameter α varies between 0.2 and 1.

The parameter, α , does not appear to significantly influence threshold behavior. Hence, as to be expected, it is the compressive residual stresses immediately adjacent to the notch that play the major role in enhancing threshold values with respect to residual stress free notches. In Figure 5I.27 are displayed predicted threshold results for the case when the value of α was fixed at 0.2, and the size of the compressive stress zone was varied between 0.000984 inches (0.025 mm) and 0.00393 inches (0.1 mm). This figure shows that there is still a large enhancement in threshold values at relatively high values of k'_t over the full range of r_1 values compared to the residual stress free notch results. The degree of this enhancement is strongly dependent on the size of the compressive zone. The larger the compressive zone, the larger the enhancement in threshold values. However, at k'_t less than about 5, the size of the compressive zone has negligible effect on threshold behavior. This is the regime where classical S-N endurance approaches are applicable, and these are sensitive only to the stress at the notch root and not to the extent of the compressive zone ahead of the notch.

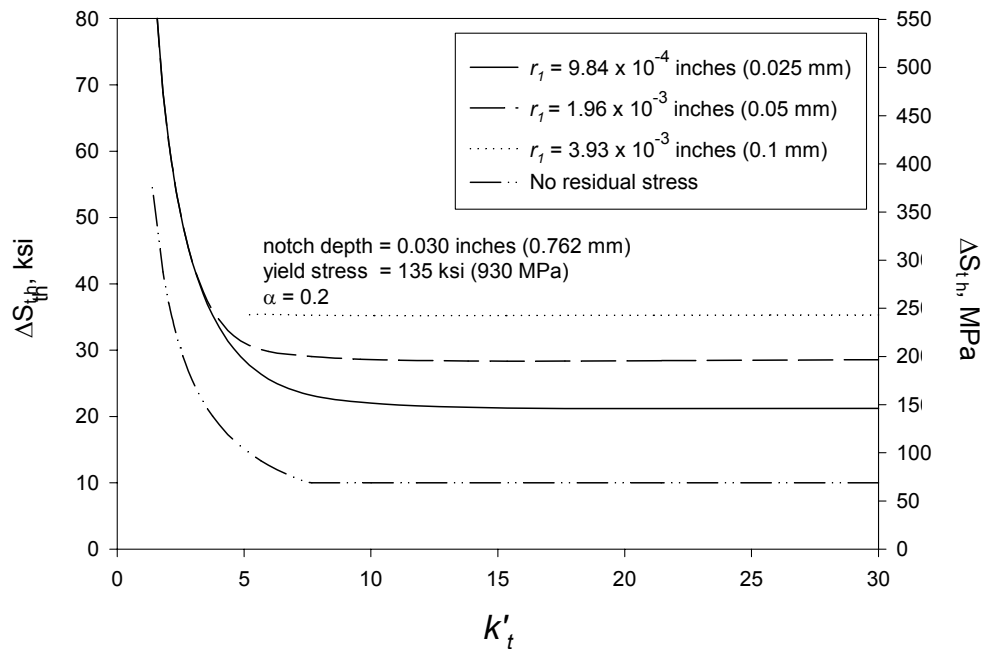


Figure 5I.27. Examples of the effects of residual stresses on threshold stresses predicted by the WCN model. The parameter α is fixed at 0.2, and the size of the compressive residual stress is varied between 0.000984 inches and 0.00393 inches.

Effect of Stress Ratio on Threshold Behavior

Stress ratio influences the endurance and the crack growth threshold. Both these quantities increase as the stress ratio, R , decreases. Therefore, it is expected that the threshold stress will increase as R decreases. This trend is borne out by the results presented in Figure 5I.28 that shows how cyclic stresses that are applied for different stress ratios affect predicted threshold behaviors calculated according to the WCN model for notches in semi-infinite bodies. It is the increase in endurance and crack growth threshold with decreasing stress ratio that provides the beneficial increase in threshold stresses when compressive residual stresses are present at a notch.

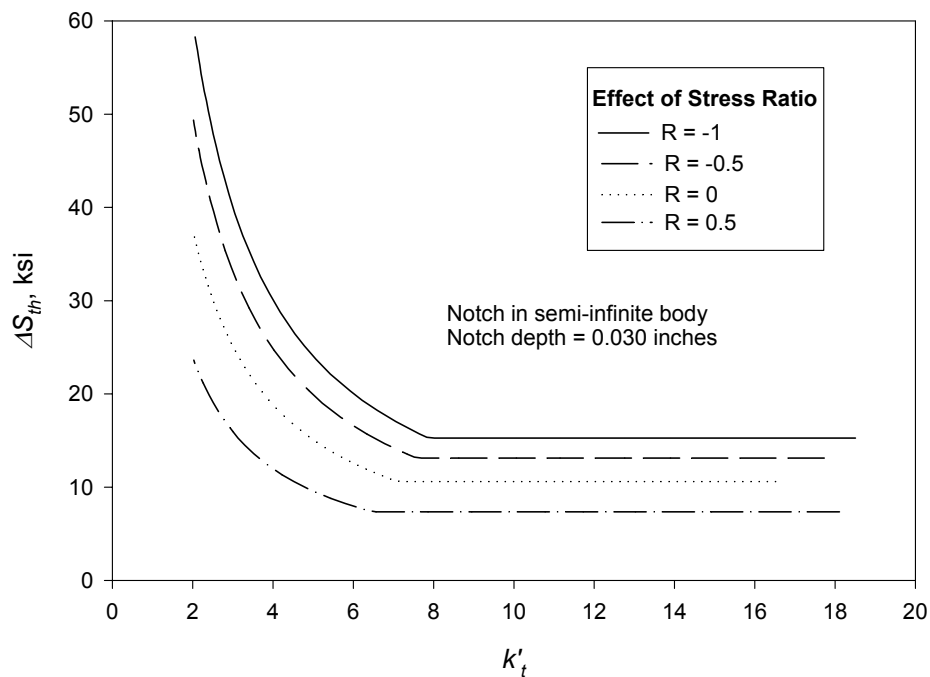


Figure 5I.28. Predicted effect of stress ratio, R , on threshold stress behavior.

APPLICATION AND ASSESSMENT OF WCN MODEL

In this section, the general validity of the WCN model is assessed by comparing predicted threshold cyclic stresses with those measured in notch tests on Ti-6Al-4V and mild steel [23,25]. In addition, the WCN model is used to predict the results of HCF tests on FOD simulation specimens of Ti-6Al-4V.

Laboratory Tests on Ti-6Al-4V

As part of the current program HCF tests were performed on double edge notched plates (DENP) for various stress ratios in order to measure the cyclic threshold stresses for Ti-6Al-4V. These data are summarized in Table 5I.1, which also details the test geometry, and the values of material properties ($\Delta\sigma_e$ and ΔK_{th}) needed to perform the WCN analysis. The values of the small crack parameter, a_o , were derived from $\Delta\sigma_e$ and ΔK_{th} using Equation (5I.53). For convenience of analysis, the $\Delta\sigma_e$ and ΔK_{th} results were curve fitted to represent the dependence of these quantities on R . The following functions were fitted to the data:

$$\begin{aligned}\Delta\sigma_e(R) &= 75.48 - 51.73R - 6.80R^2, \text{ ksi} \\ \Delta\sigma_e(R) &= 520.6 - 356.8R - 46.9R^2, \text{ MPa}\end{aligned}\quad (5I.70)$$

$$\begin{aligned}\Delta K_{th}(R) &= 3.969 - 2.19R, \text{ ksi inch}^{1/2} \\ \Delta K_{th}(R) &= 4.366 - 2.41R, \text{ MPa m}^{1/2}\end{aligned}\quad (5I.71)$$

$$\begin{aligned}\Delta K_{th}(R) &= 4.25(1-R)^{0.502}, \text{ ksi inch}^{1/2} \\ \Delta K_{th}(R) &= 4.68(1-R)^{0.502}, \text{ MPa m}^{1/2}\end{aligned}\quad (5I.72)$$

Table 5I.1
Threshold Stresses and HCF Material Properties for Ti-6Al-4V

Ti-6Al-4V: Double Edge Notched Plates (DENP): Semi-Circular Notches					
Plate thickness (t) = 0.36 inches, Notch Depth (b)=0.032 inches					
stress ratio, R	measured, ΔS_{th} (ksi)	predicted ΔS_{th} (ksi)	measured endurance $\Delta\sigma_e$ (ksi)	measured threshold ΔK_{th} (ksi inch^{1/2})	Small crack parameter* a_o (inch)
-1	57.4	55.3	120	6.1	0.000654
0.1	35	33.1	72.0	4.0	0.000783
0.5	24.8	22.8	50.0	2.7	0.000755
0.8	n/a	n/a	27.0	2.2	n/a

* a_o calculated based on through-thickness edge crack ($F = 1.12$)

The linear fit to ΔK_{th} was used in the parametric studies. The fit of ΔK_{th} to the Walker-type of equation was used in the comparison of WCN predictions with measured threshold data. Although the $\Delta\sigma_e$ and ΔK_{th} data were only fitted between $R = -1$ and $R = 0.8$, these fits were assumed for extrapolating the data

to R values as low as -3.8 when assessing the simulated FOD results reported earlier. Figures 5I.29, 5I.30 and 5I.31 show the fitted curves and the measured data values for $\Delta\sigma_e$ and ΔK_{th} .

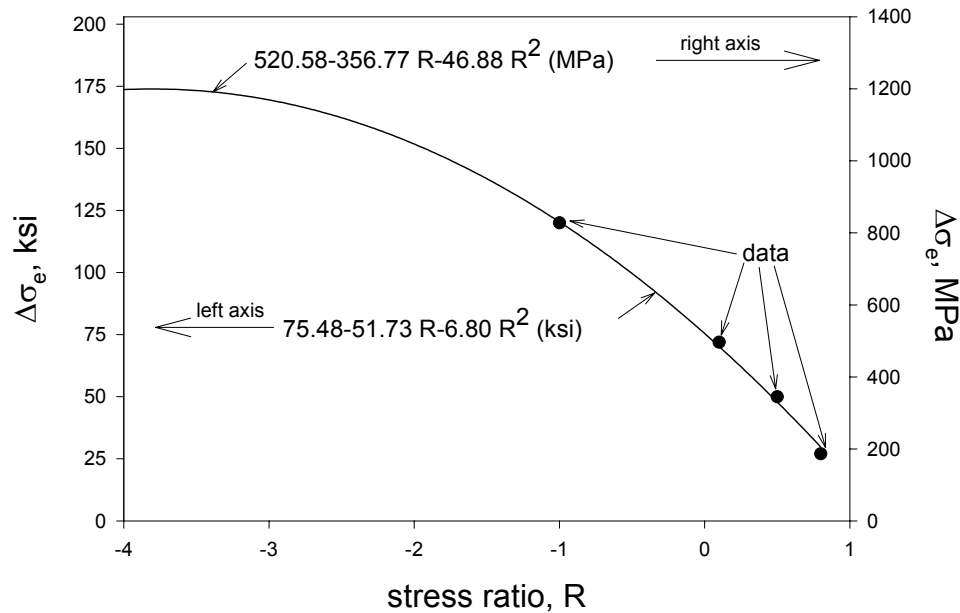


Figure 5I.29. Endurance data as a function of stress ratio, R , for Ti-6Al-4V showing baseline data and the predictions of a quadratic curve fit.

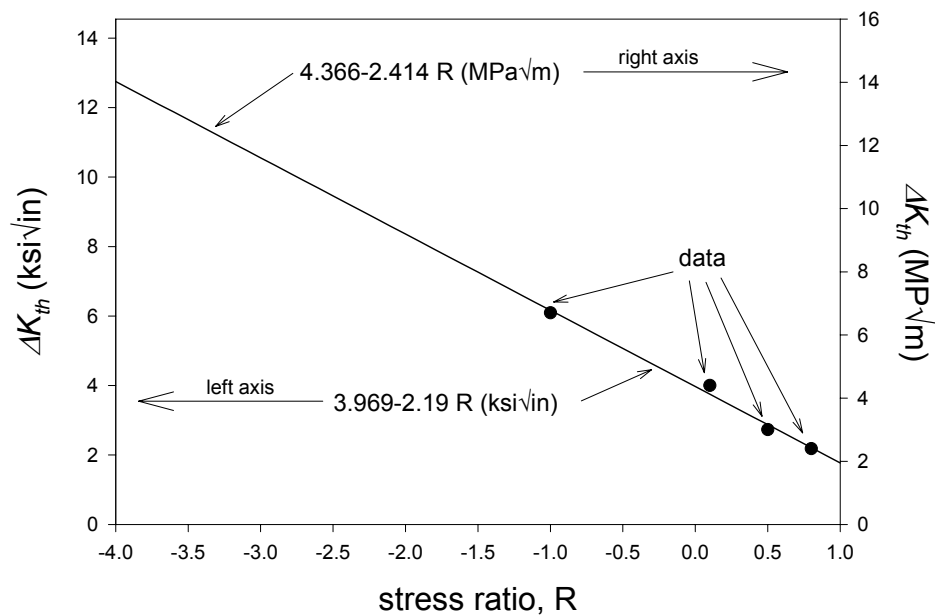


Figure 5I.30. Crack growth threshold data as a function of stress ratio, R , for Ti-6Al-4V showing baseline data and the predictions of a linear curve fit.

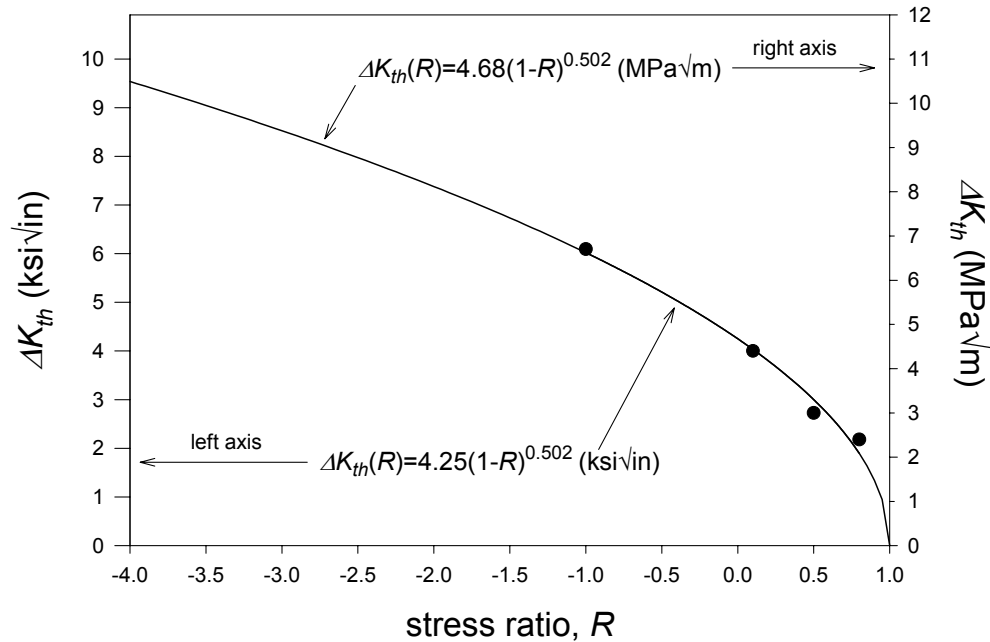


Figure 5I.31. Crack growth threshold data as a function of stress ratio, R , for Ti-6Al-4V showing baseline data and the predictions of a curve fit to a Walker type of equation.

The results of the WCN analysis are shown in Table 5I.1. Good agreement is obtained between the predictions of the WCN model and the measured values. In the analyses it was assumed that thumbnail cracks initiated and grew at the notches. The data in the table are included in the analysis results reported for the FOD simulation specimen, and in the Exit Criteria analysis.

Laboratory Tests on Mild Steel

Threshold cyclic stresses for mild steel have been generated using both double edge notched panels (DENP) and circumferentially notched round bars (CRB). The measured data and the dimensions of the notched geometries tested are listed in Table 5I.2. The measured data includes threshold values corresponding to crack propagation to failure, and thresholds corresponding to the nucleation and arrest of cracks at the notches. Although the notch depths in the DENP and CRB specimens were all fixed at 0.2 inches, the sharpness of the notches were varied to give a wide range of stress concentration factors, k_t' , and these values are also listed in the table.

Table 5I.2

Threshold Stresses for Mild Steel [25] Determined on Circumferential Round Bar (CRB) and Double Edge Notch (DENP) Specimens

Mild Steel			
Circumferential Round Bar (CRB): Radius (t)=0.846 inches, Notch Depth (b)=0.2 inches Double Edge Notched Plate (DENP): Thickness ($2t$)=2.5 inches, Notch Depth (b) = 0.2 inches			
Thresholds for Propagation to Failure			
Specimen Type	Stress Concentration Factor Based on Gross Stress k'_t	Measured ΔS_{th} (ksi)	Predicted ΔS_{th} (ksi)
CRB	2.95	35.7	30.23
CRB	3.12	30.1	28.4
CRB	5.89	18.9	16.4
CRB	7.49	16.2	16.3
CRB	11.2	16.2	16.3
CRB	15.3	16.2	16.3
CRB	17	15.7	16.3
CRB	23.8	16.2	16.3
DENP	14.8	14.5	16.3
DENP	9.77	15.7	16.3
DENP	7.33	14.5	16.3
DENP	4.75	18	18.6
DENP	2.58	26.8	34.7
Thresholds for Crack Nucleation			
DENP	14.8	45.56	41.7
DENP	9.77	60	63.1
DENP	7.33	76.66	84.1
CRB	23.8	52.22	25.96
CRBB	15.3	60	40.6

The results of applying the WCN model to the two test specimen geometries are detailed in Table 5I.2. It was assumed that through cracks initiated and propagated in the analysis. The material property values used in the WCN calculations are listed in Table 5I.3. The endurance was taken as the average of three values determined from the failure data for the three specimens that had the three smallest values of k'_t by assuming that these specimens failed in the classical S-N regime where the threshold is related to the endurance through Equation (5I.48).

Table 5I.3
HCF Material Properties for Mild Steel

Mild Steel		
Endurance, $\Delta\sigma_e$ (ksi)	Threshold, ΔK_{th} (ksi inch ^{1/2})	Small Crack Parameter, a_o (mils)
89 (average of 105, 94 and 69)	17.5	9.84

Since actual crack growth threshold data were not available for the same heat of material used in these experiments, the a_o value used in the WCN predictions was selected to give a good fit to the data, and hence ΔK_{th} was calculated from Equation (5I.53) assuming a through crack. Nevertheless, the results demonstrate the ability of the WCN model to represent the proper functional dependencies of notched HCF data over a wide range of notch severity. In addition, the WCN model agrees very well with the thresholds measured on both the DENP and CRB specimens.

The measured threshold data shown in Table 5I.2 are plotted in Figure 5I.32. Also shown on this figure are the WCN predictions for failure and crack nucleation and arrest, together with the predictions obtained from applying the classical S-N approach. It can be seen that the classical approach, which utilizes only endurance values, gives threshold predictions for crack nucleation and arrest that are in excellent agreement with the measured data but that it cannot accurately predict thresholds corresponding to failure. The predicted threshold values using the WCN model are plotted against the measured values in Figure 5I.33. It can be seen that the plotted points are evenly scattered about the one-to-one line that represents a perfect correlation between predicted and measured results.

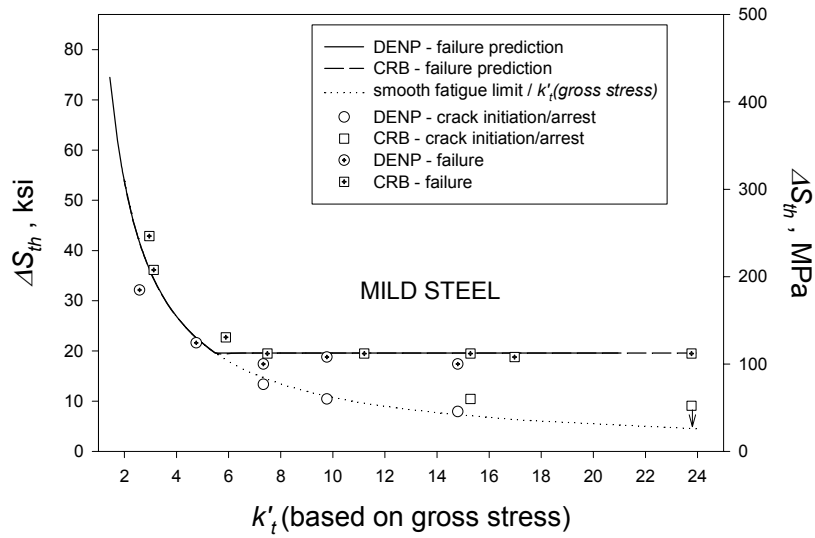


Figure 5I.32. Comparison of threshold stress predictions of the WCN model with experimental data for DENP and CRB mild steel specimens.

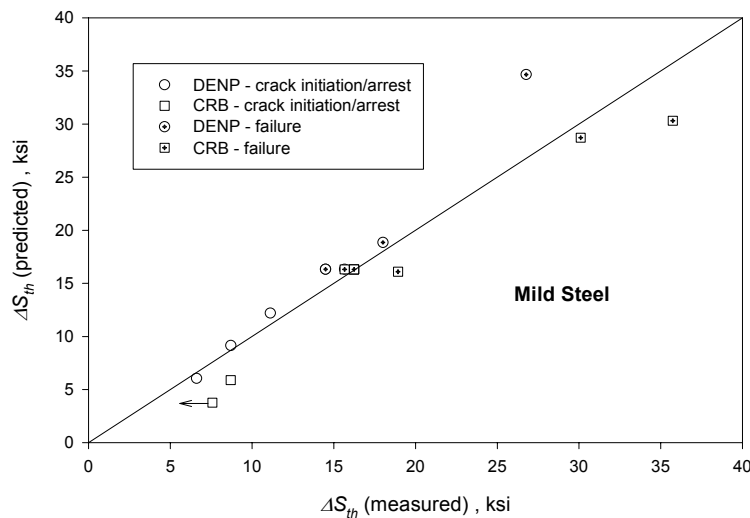


Figure 5I.33. Threshold stress predictions of the WCN model plotted against experimental data for DENP and CRB mild steel specimens. Exact agreement is signified when the data points fall on the one-to-one line.

It is of interest to plot the data shown in Figure 5I.32 in terms of the stress concentration factor based on the net section stress rather than the gross stress. This plot is shown in Figure 5I.34. It can be seen that when plotted in this way, the WCN appears to predict geometry dependent threshold behavior in the specimens with low values of k_t , and that the model also appears to give results in this regime that differ from the predictions of classical S-N endurance theory. However, these observations

are erroneous, as can be seen from Figure 5I.32, and manifest themselves only as a consequence of using the net section stress rather than the gross stress to determine the stress concentration factor.

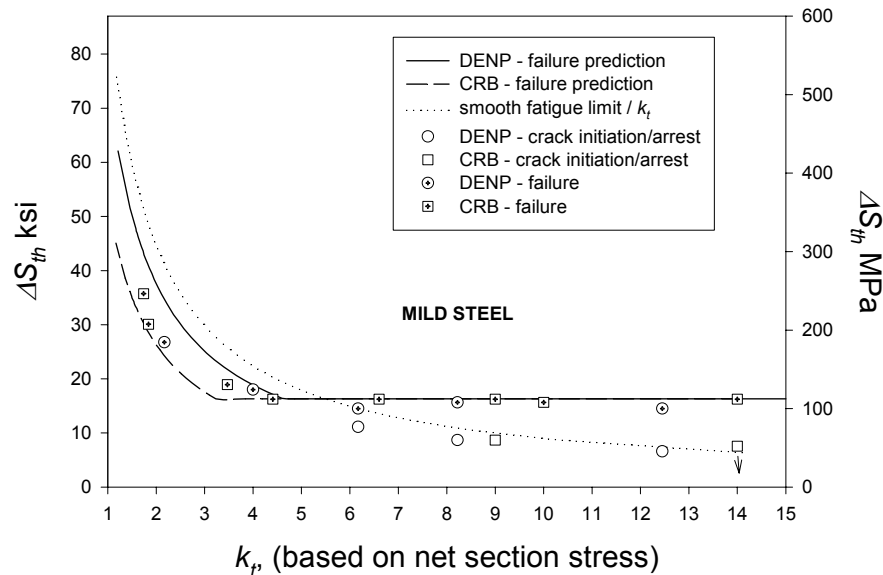


Figure 5I.34. Comparison of threshold stress predictions of the WCN model with experimental data for DENP and DRB mild steel specimens. The threshold values are plotted against the stress concentration factor of the notches based on net section stress.

Comparison of Model Predictions with FOD-Simulated Test Data

HCF tests have been performed on Ti-6Al-4V specimens containing simulated FOD created by several different methods. These techniques range from damage introduced into the blade-like leading edges of the wing specimens by high speed ballistic impacts of objects, through damage introduced at slower velocities using solenoid guns, to machined notches. It is anticipated that simulated FOD created by the ballistic and solenoid methods will produce residual stresses at the tips of the resulting notches. In addition to different methods of inducing simulated FOD the wing specimens also include data for tests performed using different impact angles, notch depths, and notch radii. Thus, these tests covered a wide range of simulated FOD conditions.

A summary of some of the simulated-FOD test results is presented in Table 5I.4. This table lists the company who performed the tests, the method used to introduce the simulated-FOD, the specimen identification number, the measured threshold stresses corresponding to 10^6 cycles, the notch dimensions and the stress ratio at which the HCF tests were performed. The specimens listed in Table 5I.4 were analyzed using the WCN model and employing the material property data for Ti-6Al-4V contained in Table 5I.1. The Walker fit to the crack growth threshold data was used in the WCN analysis. However, the endurance data were modified to take into account endurance values that were measured on notch-free wing specimens. These tests, which were performed at a stress ratio of 0.5, resulted in measured endurance values of 56.9 ksi, 58.7 ksi and 56.1 ksi, with an average value of 57.2 ksi, compared to an endurance value of 50 ksi derived from data from smooth laboratory specimens. Since it is known that measured endurance values can differ when obtained under different loading conditions (e.g. tension or bending), the curve fit to the endurance data was increased by the ratio 57.2/50.0 in the WCN analysis of the wing specimens to empirically allow for this effect. Thus the derived value of a_0 used in this analysis was based on the endurance limit measured at 10^6 cycles on unnotched leading edge “wing” specimens tested.

In order to perform the WCN analysis, it is necessary to know the stress intensity factor solution for an initiated crack (see Figure 5I.20). This can be derived from the stress field ahead of the FOD using weight function techniques. It was assumed that under HCF conditions, thumbnail cracks were initiated at the tips of the simulated FOD. Nucleation was assumed to occur at the center of notched wing sections, along the 50% through thickness line (see Figure 5I.49). Actual notched depths were used in the analysis, although nominal values of the notch radii were used – these were assumed to be equal to the impactor radii.

In the present analysis, two forms of stress field were employed. In the first, the results obtained from a limited FRANC3D-ANSYS parametric study of the stress fields ahead of the notched wing specimens were used to modify Amstutz and Seeger (A&S) stress equations. In the second, the A&S parametric equations were used as defined.

Table 5I.4
Summary of HCF Tests Performed on Wing Specimens Containing Simulated FOD

COMPANY	FOD Simulation Method	Test Data					FRANC3D-ANSYS Parameters			
		Spec. No.	Measured ΔS_{th} (ksi)	Notch Depth (mils)	Notch Radius (mils)	Stress Ratio, R	k_t	Notch Depth (mils)	Notch Radius (mils)	ID No.
GEAE	machined notch	11-S1	33.8	48.5	24	0.5	3.9	50	25	1
GEAE	machined notch	11-S2	32.1	48.2	22	0.5	3.9	50	25	1
GEAE	machined notch	11-S3	28.4	47.8	23	0.5	3.9	50	25	1
GEAE	machined notch	11-S4	28.5	48.5	23	0.5	3.9	50	25	1
GEAE	machined notch	22-B2	25.7	61	23	0.5	3.9	50	25	1
P&W	ballistic impact	189-1	32.55	6.7	20	0.5	1.7	5	25	6
P&W	ballistic impact	54-7	31.35	8.8	20	0.5	1.7	5	25	6
P&W	ballistic impact	189-4	41.9	18.7	39	0.5	2.8	20	25	7
P&W	ballistic impact	189-5	35.42	72	39	0.5	2.8	20	25	7
P&W	solenoid impact	54-1	24.17	28.9	5	0.5	5.5	20	5	5
P&W	solenoid impact	54-4a	29	20.6	5	0.5	5.5	20	5	5
P&W	solenoid impact	54-4b	29	21.6	5	0.5	5.5	20	5	5
P&W	solenoid impact	54-8a	33.84	21.3	5	0.5	5.5	20	5	5
P&W	solenoid impact	54-8b	33.84	16.9	5	0.5	5.5	20	5	5
P&W	solenoid impact	86-5a	50.16	3.7	5	0.5	2.8	5	5	13
P&W	solenoid impact	86-5b	50.16	3.4	5	0.5	2.8	5	5	13
P&W	solenoid impact	86-8a	61.91	4.1	5	0.5	2.8	5	5	13
P&W	solenoid impact	86-8b	61.91	4	5	0.5	2.8	5	5	13
P&W	solenoid impact	86-4a	46.16	4.3	5	0.5	2.8	5	5	13
P&W	solenoid impact	86-4b	46.16	3.7	5	0.5	2.8	5	5	13
GEAE	solenoid impact	48-05	33.3	8.4	5	0.5	3.1	5	5	4
GEAE	solenoid impact	11-S7	38.5	6.7	5	0.5	3.1	5	5	4
GEAE	solenoid impact	70-04	26.9	23.7	5	0.5	5.5	20	5	5
GEAE	solenoid impact	75-04	29.4	19.8	5	0.5	5.5	20	5	5
GEAE	solenoid impact	36-S2	38.2	25.8	5	0.5	5.5	20	5	5
GEAE	solenoid impact	11-S5	21.5	20.4	5	0.5	5.5	20	5	5
GEAE	solenoid impact	48-06	22.7	21.7	5	0.5	5.5	20	5	5
GEAE	solenoid impact	75-03	23.8	19.3	5	0.5	5.5	20	5	5
GEAE	solenoid impact	36-B4	62	6.4	5	-1	3	5	5	3
GEAE	solenoid impact	22-S1	42.2	4.1	25	0.5	1.7	5	25	6
GEAE	solenoid impact	70-01	58.6	4.1	25	0.5	1.7	5	25	6
GEAE	solenoid impact	76-03	52.6	3.9	25	0.5	1.7	5	25	6
GEAE	solenoid impact	11-S6	34.5	23.2	25	0.5	2.8	20	25	7
GEAE	solenoid impact	22-S2	48.6	22.2	25	0.5	2.8	20	25	7
GEAE	solenoid impact	48-04	39.6	18.2	25	0.5	2.8	20	25	7
GEAE	solenoid impact	n/a	33.8	48.5	24	0.5	3.9	50	25	1
GEAE	solenoid impact	70-04	32.1	48.2	22	0.5	3.9	50	25	1
GEAE	solenoid impact	75-04	28.4	47.8	23	0.5	3.9	50	25	1
GEAE	solenoid impact	36-S2	28.5	48.5	23	0.5	3.9	50	25	1

Table 5I.5
WCN Model Predicted Threshold Stresses Based on
FRAN3D/ANSYS for Ti-6Al-4V Wing Specimens

COMPANY	FOD Simulation Method	Spec. No.	Measured ΔS_{th} (ksi)	No Residual	Residual Stresses		
				Predicted ΔS_{th} (ksi)	Predicted $r1=0.002$ in ΔS_{th} (ksi)	Predicted $r1=0.004$ in ΔS_{th} (ksi)	Predicted $r1=0.016$ in ΔS_{th} (ksi)
GEAE	machined notch	11-S1	33.8	20.45	n/a	n/a	n/a
GEAE	machined notch	11-S2	32.1	19.82	n/a	n/a	n/a
GEAE	machined notch	11-S3	28.4	20.23	n/a	n/a	n/a
GEAE	machined notch	11-S4	28.5	20.12	n/a	n/a	n/a
GEAE	machined notch	22-B2	25.7	18.38	n/a	n/a	n/a
P&W	ballistic impact	189-1	32.55	41.17	49.16	49.16	49.16
P&W	ballistic impact	54-7	31.35	38.06	45.42	45.42	45.42
P&W	ballistic impact	189-4	41.9	33.67	39.57	39.57	39.57
P&W	ballistic impact	189-5	35.42	21.18	24.87	24.87	24.87
P&W	solenoid impact	54-1	24.17	12.46	19.77	23.99	32.33
P&W	solenoid impact	54-4a	29	14.38	22.89	27.72	36.43
P&W	solenoid impact	54-4b	29	14.1	22.43	27.18	35.8
P&W	solenoid impact	54-8a	33.84	14.18	22.56	27.34	36.01
P&W	solenoid impact	54-8b	33.84	15.61	24.88	30.08	38.95
P&W	solenoid impact	86-5a	50.16	31.67	48.92	54.44	59.63
P&W	solenoid impact	86-5b	50.16	32.56	50.21	55.62	60.21
P&W	solenoid impact	86-8a	61.91	30.61	47.34	52.98	58.5
P&W	solenoid impact	86-8b	61.91	30.86	47.72	53.34	58.63
P&W	solenoid impact	86-4a	46.16	30.12	46.62	52.3	57.96
P&W	solenoid impact	86-4b	46.16	31.67	48.92	54.44	59.63
GEAE	solenoid impact	48-05	33.3	21.4	34	40.09	48.14
GEAE	solenoid impact	11-S7	38.5	23.27	37	43.28	50.81
GEAE	solenoid impact	70-04	26.9	13.56	21.55	26.13	34.74
GEAE	solenoid impact	75-04	29.4	14.62	23.27	28.18	36.97
GEAE	solenoid impact	36-S2	38.2	13.08	20.77	25.2	33.66
GEAE	solenoid impact	11-S5	21.5	14.44	22.98	27.84	36.55
GEAE	solenoid impact	48-06	22.7	14.07	22.38	27.12	35.83
GEAE	solenoid impact	75-03	23.8	14.78	23.53	28.48	37.29
GEAE	solenoid impact	36-B4	62	61.45	79.65	79.65	79.65
GEAE	solenoid impact	22-S1	42.2	49.38	58.64	58.64	58.64
GEAE	solenoid impact	70-01	58.6	49.38	58.64	58.64	58.64
GEAE	solenoid impact	76-03	52.6	49.95	59.33	59.33	59.33
GEAE	solenoid impact	11-S6	34.5	27.19	32.2	32.2	32.2
GEAE	solenoid impact	22-S2	48.6	27.61	32.69	32.69	32.69
GEAE	solenoid impact	48-04	39.6	29.51	34.95	34.95	34.95
GEAE	solenoid impact	n/a	33.8	29.51	34.95	34.95	34.95
GEAE	solenoid impact	70-04	32.1	19.82	23.51	23.51	23.51
GEAE	solenoid impact	75-04	28.4	20.23	23.98	23.98	23.98
GEAE	solenoid impact	36-S2	28.5	20.12	23.84	23.84	23.84

The simulated FOD was formed under impact conditions and is assumed to have a compressive residual stress resulting from the impact at its tip of the parametric form. The magnitude of the compressive stress was set equal to 135 ksi, the yield stress of Ti-6Al-4V. In all the calculations, the residual stress parameter α was set equal to 0.5. The size of the compressive stress zone, r_1 , was varied, as the WCN predictions are known to be sensitive to the value of this parameter.

WCN Predictions Based on FRANC3D/ANSYS Stress Analysis

Plots of predicted versus measured threshold cyclic stresses for the Ti-6Al-4V FOD-simulation specimens are shown in Figures 5I.35 to 5I.48 for various forms of the residual stress assumed to form from impact. It can be seen from the figures that there is considerable scatter in the data. This considerable variability is believed to be a reflection of specimen-to-specimen notch variations under the impact test conditions. In addition, the spot welding used to attach potential drop leads to some of the specimens is also believed to have contributed to the data scatter. Exact agreement of the predicted and measured values would occur if the plotted data points fell on the one-to-one line. The actual predicted threshold stress values are listed in Table 5I.5. The data in Figures 5I.35 to 5I.38 include the results reported for the DENP specimens. They also include the data obtained for the machined-notched winged specimens. In both these cases, no residual stresses were assumed present in the WCN analysis.

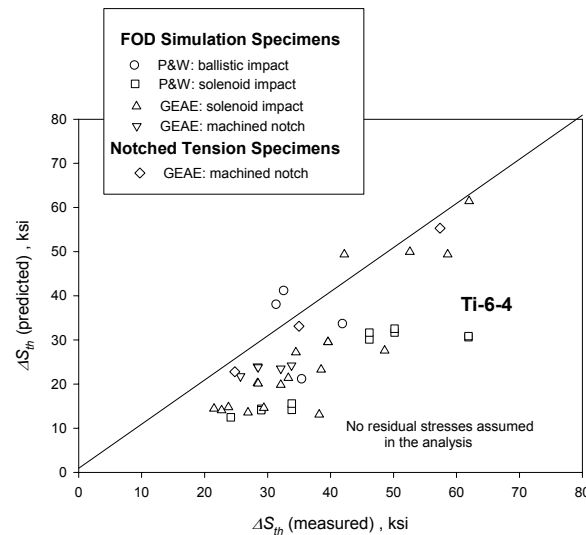


Figure 5I.35. Threshold stresses predicted using WCN model based on FRANC3D/ANSYS stress fields and ignoring residual stresses for Ti-6Al-4V. The data include simulated FOD from impact testing.

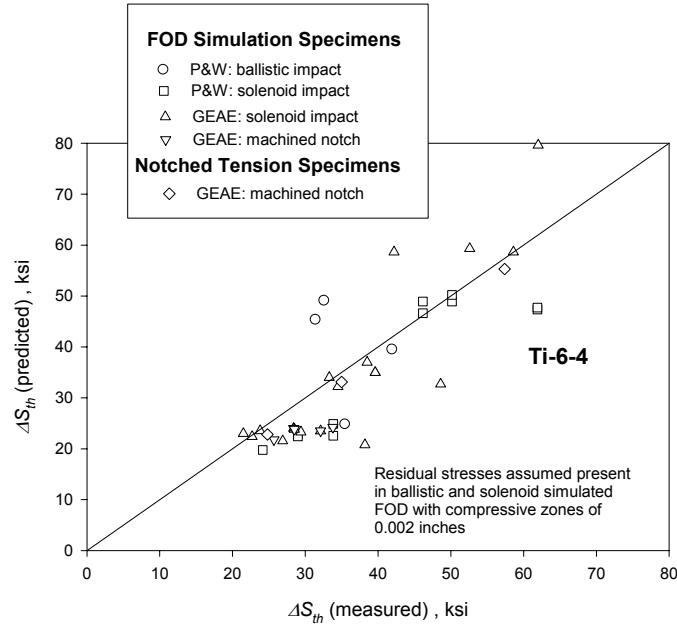


Figure 5I.36. Threshold stresses predicted using WCN model based on FRANC3D/ANSYS stress fields and assuming residual stresses with a compressive zone extending over 0.002 inches. The data include simulated FOD from impact testing.

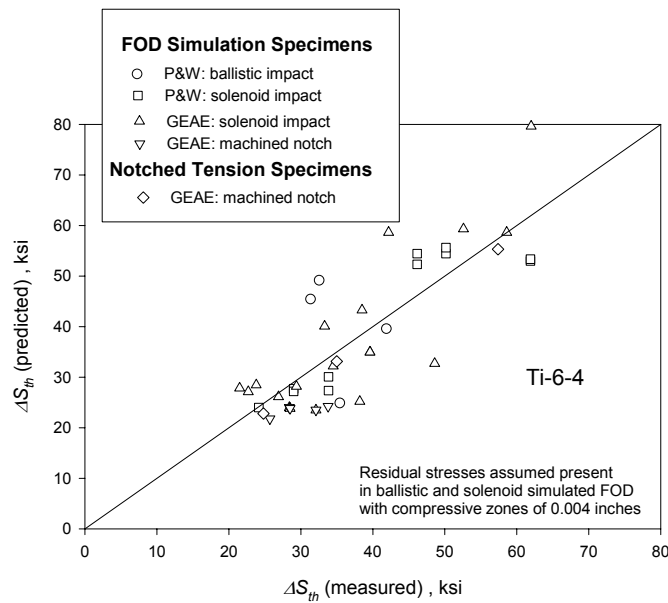


Figure 5I.37. Threshold stresses predicted using WCN model based on FRANC3D/ANSYS stress fields and assuming residual stresses with a compressive zone extending over 0.004 inches. The data include simulated FOD from impact testing.

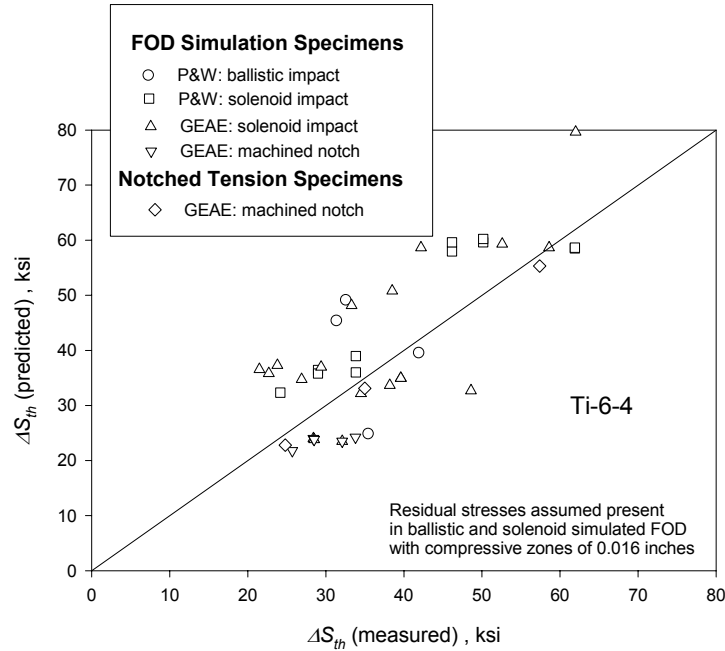


Figure 5I.38. Threshold stresses predicted using WCN model based on FRANC3D/ANSYS stress fields and assuming residual stresses with a compressive zone extending over 0.016 inches. The data include simulated FOD from impact testing.

In Figure 5I.35 the predicted WCN model results were determined assuming no residual stresses were present at the simulated FOD. It is clear that in this case, the model under-predicts the measured threshold values in the great majority of the tests. In Figure 5I.36 the results based on assuming a residual stress with a compressive zone size of 0.002 inches exists at the notch tips are shown. The introduction of a residual stress increases the predicted threshold values compared to the results derived assuming no residual stresses. However, there is still a tendency for the WCN model to under-predict the measured endurance values. Better agreement between predicted and measured threshold stresses is obtained when it is assumed that the size of the compressive stress zone is 0.004 inches (see Figure 5I.37). The assumption that the compressive zone size r_1 , is equal to 0.016 inches results in a tendency for the WCN model to over-predict the measured threshold values, as demonstrated in Figure 5I.38. These qualitative observations are reinforced by a simplified analysis of the data based on the evaluation of the arithmetic average $(A/P)_{\text{average}}$ of the ratio of actual measured threshold values (A) to predicted values (P), where

$$\left(\frac{A}{P}\right)_{average} = \frac{1}{N} \sum_{i=1}^N \left(\frac{A}{P}\right)_i \quad (51.73)$$

and N is the number of data analyzed. Evaluating the predicted and measured threshold values according to this equation for the four assumptions concerning residual stresses made above yields the results displayed in Table 51.6. Only the specimens that contained simulated FOD introduced by impact were included in this analysis.

Table 51.6
Comparison of Ratio of Actual to Predicted Threshold Values for Impact Tests on Wing Specimens. The WCN Model Predictions were Based on FRANC3D/ANSYS Stress Results

Parameter Evaluated	Characterization of Impact residual Stress			
	No residual	$r_1=0.002$ inches	$r_1=0.004$ inches	$r_1=0.016$ inches
$(A/P)_{average}$	1.59	1.12	1.02	0.92

It is concluded that the threshold results predicted by the WCN model match the average measurements provided it is assumed that the compressive part of the residual stress extends a distance of 0.004 inches ahead of the tip of the simulated FOD. This agreement is obtained in spite of the relative complexity of the notched wing specimen tests and the uncertainties associated with dynamically introducing simulated FOD. The value of $r_1 = 0.004$ inches is physically realistic and is consistent with the conclusions concerning the depth of the compressive residual stress drawn from the review on the effects of shot peening on residual stresses.

WCN Predictions Based on A&S Stress Analysis

It is important to assess the efficacy of the WCN model together with the parametric stress equations due to A&S in predicting the threshold behaviors of the FOD-simulation specimens. The reason for this evaluation is that the A&S equation has a relatively simple closed form that could easily be employed in a design analysis. Use of the A&S equation would also obviate the need to perform either FRANC3D/ANSYS three dimensional stress analyses or other alternative numerical stress analyses.

The results of applying the WCN model together with the A&S stress equation are displayed in Figure 5I.39 where the predicted threshold values are plotted against the measured values. The actual predicted threshold stress values are given in Table 5I.7. A compressive residual stress extending over a distance of 0.004 inches was assumed in the analysis of the impact tests. The agreement between the predicted and measured threshold values appears to be at least as good as the agreement obtained using stress fields based on the FRANC3D/ANSYS results (compare Figures 5I.37 and 5I.39). This is demonstrated by the fact that the value of $(A/P)_{average}$ equals 1.05 for the A&S results, compared to 1.02 for the WCN model results based on FRANC3D/ANSYS.

Table 5I.7

WCN Model Predicted Threshold Stresses Based on A&S Stress Equations, and Predictions of S-N Approach for Ti-6Al-4V Wing Specimens

COMPANY	FOD Simulation Method	Spec. No.	measured ΔS_{th} (ksi)	Predicted	
				WCN Based on A&S Equation ΔS_{th} (ksi)	S-N Approach ΔS_{th} (ksi)
GEAE	machined notch	11-S1	33.8	23.67	14.61
GEAE	machined notch	11-S2	32.1	22.99	14.16
GEAE	machined notch	11-S3	28.4	23.44	14.45
GEAE	machined notch	11-S4	28.5	23.31	14.37
GEAE	machined notch	22-B2	25.7	21.29	13.13
P&W	ballistic impact	189-1	32.55	43.63	55.95
P&W	ballistic impact	54-7	31.35	40.3	51.73
P&W	ballistic impact	189-4	41.9	38.67	45.76
P&W	ballistic impact	189-5	35.42	24.31	28.79
P&W	solenoid impact	54-1	24.17	24.59	16.93
P&W	solenoid impact	54-4a	29	28.41	19.55
P&W	solenoid impact	54-4b	29	27.85	19.16
P&W	solenoid impact	54-8a	33.84	28.01	19.27
P&W	solenoid impact	54-8b	33.84	30.82	21.22
P&W	solenoid impact	86-5a	50.16	51.75	43.05
P&W	solenoid impact	86-5b	50.16	52.9	44.26
P&W	solenoid impact	86-8a	61.91	50.32	41.6
P&W	solenoid impact	86-8b	61.91	50.66	41.95
P&W	solenoid impact	86-4a	46.16	49.65	40.94
P&W	solenoid impact	86-4b	46.16	51.75	43.05
GEAE	solenoid impact	48-05	33.3	40.15	29.08
GEAE	solenoid impact	11-S7	38.5	43.35	31.63
GEAE	solenoid impact	70-04	26.9	26.78	18.43
GEAE	solenoid impact	75-04	29.4	28.88	19.87
GEAE	solenoid impact	36-S2	38.2	25.82	17.77
GEAE	solenoid impact	11-S5	21.5	28.52	19.63
GEAE	solenoid impact	48-06	22.7	27.8	19.12
GEAE	solenoid impact	75-03	23.8	29.19	20.08
GEAE	solenoid impact	36-B4	62	77.29	63.39
GEAE	solenoid impact	22-S1	42.2	52.1	67.11
GEAE	solenoid impact	70-01	58.6	52.1	67.11
GEAE	solenoid impact	76-03	52.6	52.72	67.88
GEAE	solenoid impact	11-S6	34.5	31.47	36.96
GEAE	solenoid impact	22-S2	48.6	31.95	37.52
GEAE	solenoid impact	48-04	39.6	34.16	40.11
GEAE	solenoid impact	n/a	33.8	34.16	40.11
GEAE	solenoid impact	70-04	32.1	22.99	26.94
GEAE	solenoid impact	75-04	28.4	23.44	27.5
GEAE	solenoid impact	36-S2	28.5	23.31	27.34

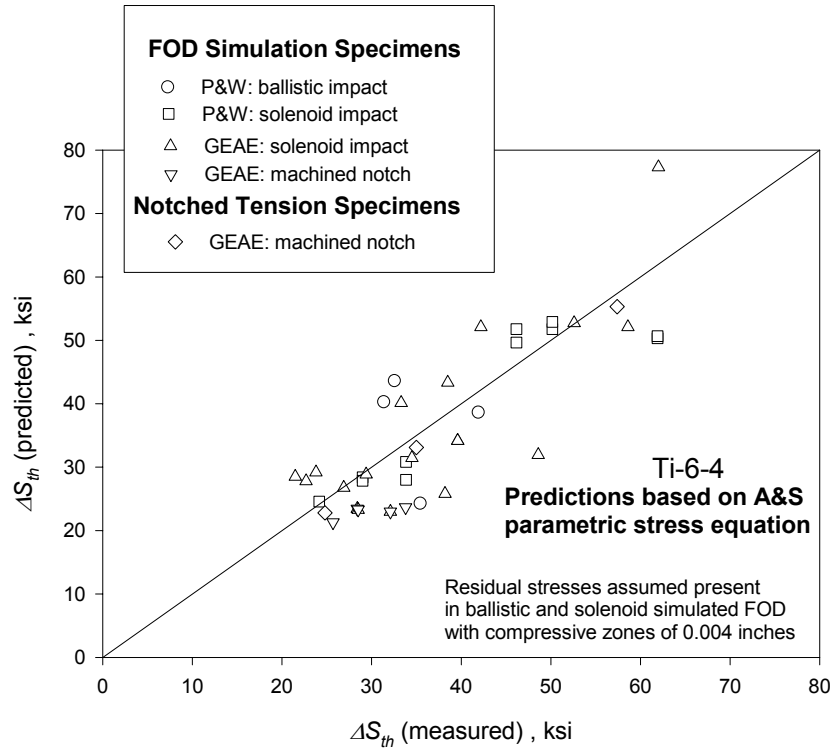


Figure 5I.39. Threshold stresses predicted using WCN model based on A&S stress equation and assuming residual stresses with a compressive zone extending over 0.004 inches. The data include simulated FOD from impact testing.

Predictions Based on Classical S-N Endurance Analysis

The application of a classical S-N endurance approach to the analysis of notched structures subjected to HCF, including the influence of residual stresses, was described previously. The S-N approach was applied to the analysis of the FOD-simulation specimens to evaluate its effectiveness, particularly since it is simple to apply and does not involve fracture mechanics calculations. In the analysis of the impact specimens, it was assumed that the residual stresses at the notch tips were equal to the yield stress of Ti-6Al-4V, namely 135 ksi. The results of the analysis are shown in Figure 5I.40 where the predicted threshold values are plotted against the measured values. The actual predicted threshold stress values are displayed in Table 5I.7. The data in Figure 5I.40 include the results for the laboratory DENP and the wing specimens that contained machine notches. It can be seen from the figure that the S-N approach tends to under-

predict the measured threshold stresses. This conclusion is supported by the fact that the value of $(A/P)_{average}$ for the impact test data was calculated to be 1.18.

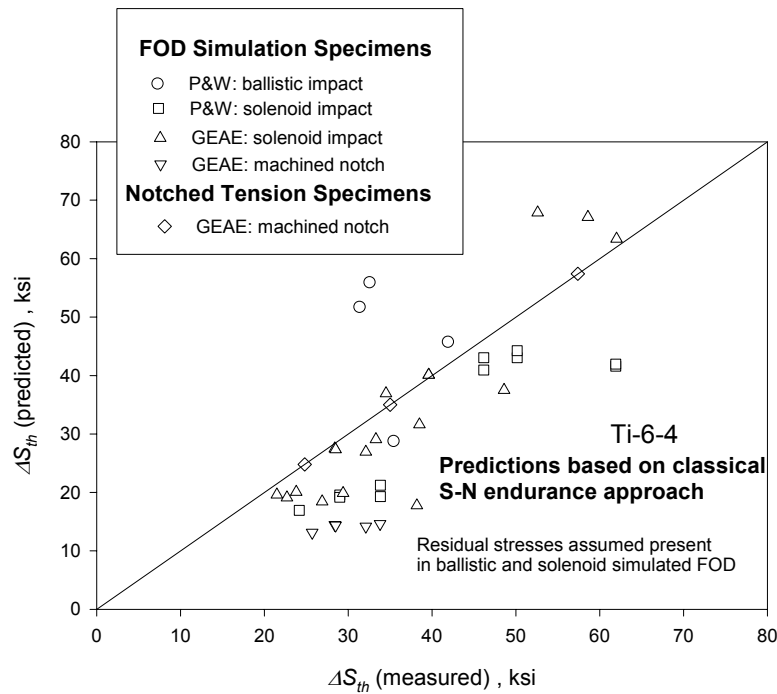


Figure 5I.40. Threshold stresses predicted using S-N endurance approach based on FRANC3D/ANSYS stress fields and assuming residual stresses. The data include simulated FOD from impact testing.

Exit Criteria Evaluation for WCN and S-N Approaches

Exit Criteria have been established for FOD model predictions of threshold cyclic stresses in order to verify that the models are acceptable in design analysis performed to establish limiting cyclic stresses that avoid damage growing to failure under HCF loading. The Exit Criteria provide a quantitative measure of the accuracy of the model, taking into account the uncertainties in the baseline data used in the calculations. The Exit Criteria for FOD modeling are that the following three conditions should be simultaneously satisfied:

- (1) The mean ratio will be within ± 0.15 of 1
- (2) No significant bias will be shown for the test parameters (Zero bias is demonstrated if the percent cumulative probability of the ratio of actual measured values (A) to predicted values (P) is 50% when $(A/P)=1$.)
- (3) The ratio (RCOV) of the coefficient of variance (COV) of the predicted results ($COV_{\text{predicted}}$) to the COV of the baseline data (COV_{baseline}) will be ≤ 2.5 where

$$\text{mean ratio} = \frac{1}{N} \sum_{i=1}^N \left(\frac{A}{P} \right)_i \quad (51.74)$$

$$COV = \frac{\text{standard deviation of } \left(\frac{A}{P} \right)}{\text{mean ratio}} \quad (51.75)$$

$$\text{standard deviation of } \left(\frac{A}{P} \right) = \sqrt{\frac{\sum_{i=1}^N \left(\left(\frac{A}{P} \right)_i - \text{mean ratio} \right)^2}{N - 1}} \quad (51.76)$$

and

$$RCOV = \frac{COV_{\text{predicted}}}{COV_{\text{baseline}}} \quad (51.77)$$

Exit Criteria for Ti-6Al-4V

The Weibull cumulative distribution functions (CDF's) for the ratio of actual to predicted threshold stresses (ΔS_{th}) are shown in Figures 51.41, 51.42 and 51.43 for the WCN model based on FRANC3D/ANSYS stress fields, the WCN model based on the A&S stress equation, and the S-N endurance approach, respectively. The baseline data used to evaluate the Exit Criteria are identified on each of the figures. Also shown, are the mean ratio and RCOV values. The following conclusions can be drawn regarding the three predictive methods:

WCN Model Based on FRANC3D/ANSYS

- This model meets the mean ratio criterion: it has a mean ratio of 1.06
- There is slight conservative bias in the predicted thresholds: this model will under-predict the average of the measured data by 6%
- This model meets the RCOV criterion: it has an RCOV of 2.05

WCN Model Based on A&S

- This model meets the mean ratio criterion: it has a mean ratio of 1.08
- There is slight conservative bias in the predicted thresholds: this model will under-predict the average of the measured data by 8%
- This model meets the RCOV criterion: it has an RCOV of 1.94

S-N Approach

- This model does not meet the mean ratio criterion: it has a mean ratio of 1.21
- There is significant conservative bias in the predicted thresholds: this model will under-predict the average of the measured data by 21%
- This model does not meet the RCOV criterion: it has an RCOV of 5.38

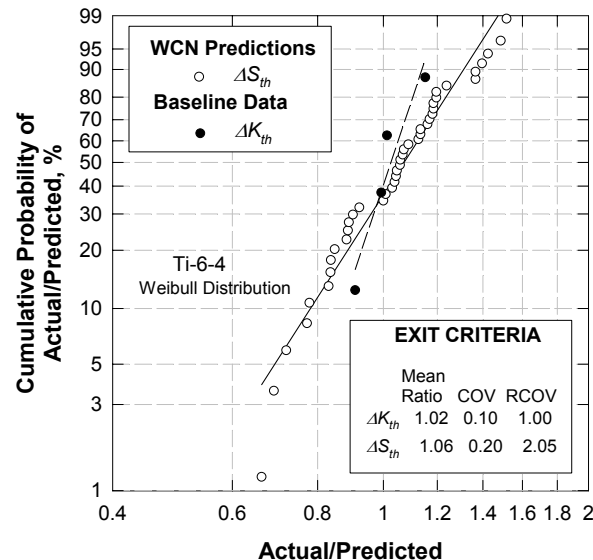


Figure 5I.41. Weibull cumulative probability distribution functions of ratio of actual/predicted results from application of the WCN model based on FRANC3D/ANSYS stress fields to Ti-6Al-4V specimens containing blade leading edges and either machined notches or simulated FOD impacts (actual data from Figure 5I.37). A compressive residual stress extending over 0.004 inches was assumed present at the notches produced by impact testing.

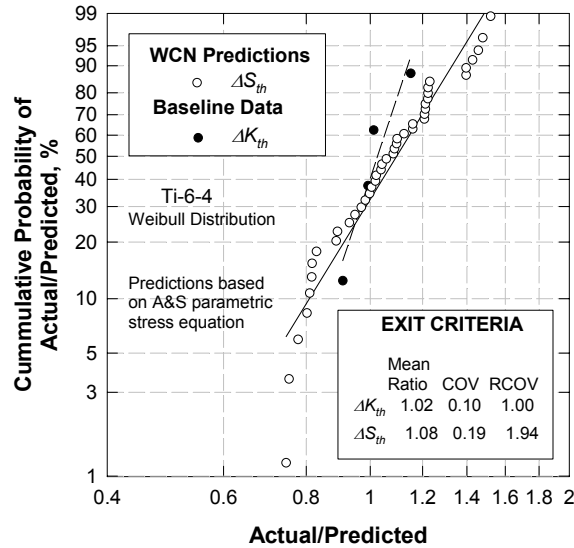


Figure 5I.42. Weibull cumulative probability distribution functions of ratio of actual/predicted results from application of the WCN model based on A&S stress equation to Ti-6Al-4V specimens containing blade leading edges and either machined notches or simulated FOD impacts (actual data from Figure 5I.39). A compressive residual stress extending over 0.004 inches was assumed present at the notches produced by impact testing.

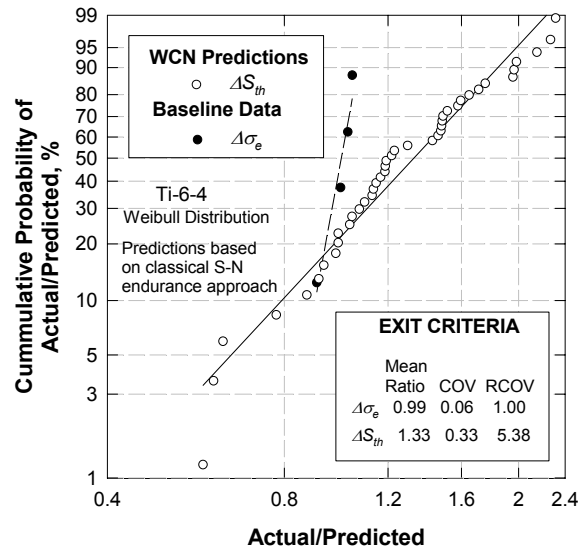


Figure 5I.43. Weibull cumulative probability distribution functions of ratio of actual/predicted results from application of the S-N endurance approach based on FRANC3D/ANSYS stress fields to Ti-6Al-4V specimens containing blade leading edges and either machined notches or simulated FOD impacts (actual data from Figure 5I.40). A compressive residual stress was assumed present at the notches produced by impact testing.

Exit Criteria for Mild Steel

Only the WCN model was analyzed for the mild steel. The Weibull cumulative distribution function (CDF) for the ratio of actual to predicted threshold stresses (ΔS_{th}) is shown in Figure 5I.44. The baseline data used to evaluate the Exit Criteria is identified on the figure. Also shown, are the mean ratio and RCOV values. The following conclusions can be drawn regarding the application of the WCN model to these data:

- This model meets the mean ratio criterion: it has a mean ratio of 0.99
- There is virtually no bias in the predicted thresholds: this model will over-predict the average of the measured data by 0.4%
- This model meets the RCOV criterion: it has an RCOV of 0.53

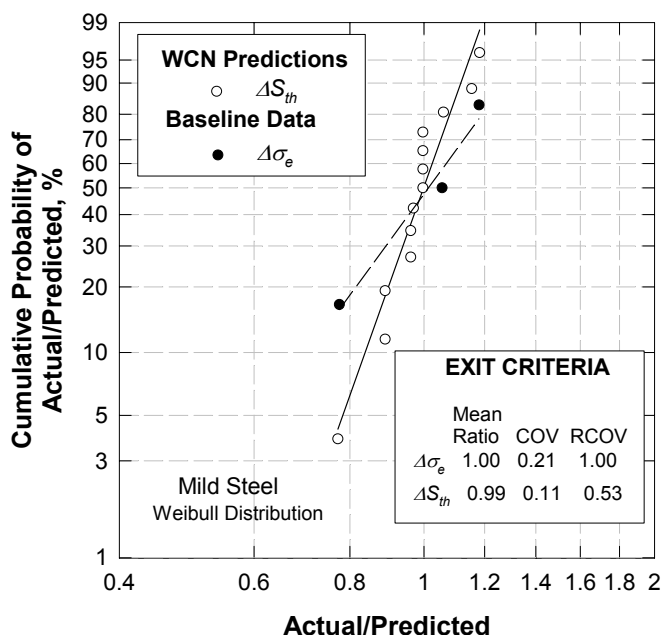


Figure 5I.44. Weibull cumulative probability distribution functions of ratio of actual/predicted results from application of the WCN model based A&S stress equation to Mild Steel DENP and CRB specimens (actual data from Figure 5I.33).

The foregoing conclusions should be interpreted in the light of the fact that only endurance data were available to analyze the mild steel test results. The values for the crack growth threshold, and hence the small crack parameter a_o , were chosen so that the model gave the best fit by eye to the measured data shown in Figure 5I.33. Even

so, the predictive capability of the model for these data, which were measured on DENP and notched CRB specimens, is impressive.

Stress Distributions Used in the Analysis of FOD-Simulation Specimens

It is necessary to know the stress distribution ahead of the FOD in order to derive the stress intensity factors needed to perform a WCN analysis. Three dimensional stress analysis of the notched winged specimens used in the impact tests to simulate FOD have been performed using the FRANC3D and ANSYS computer codes. Stress results were obtained for a range of blade and notch geometries, and object incident angles. The parameters of the notched winged specimens are listed in Table 5I.4 together with the identification number of the FRANC3D-ANSYS model considered closest to the actual notched blade geometry that was tested. As can be seen from the table, the limited FRANC3D-ANSYS solutions make it necessary to interpolate and extrapolate these in order to generate FOD stress distributions for the tested geometries. In the present analysis, the employed interpolation/extrapolation procedure was based on a simple approach that employed the Amstutz and Seeger (A&S) expression for the stress ahead of a notch. The influence of the notch geometry (depth, b , and radius, ρ) appears in this expression only through the stress concentration factor, k_t' , and the normalized distance ahead of the notch, x/ρ . It was assumed, therefore, that the A&S stress distribution would be a good representation of the FOD stress distribution in the notched wing specimens provided that the appropriate values of k_t' for the wing specimens were used in the A&S expression. Hence, if b and ρ are the actual notched specimen parameters, and b_{F-A} and ρ_{F-A} are the notched parameters from the FRANC3D-ANSYS model solutions that are nearest to the actual notched specimen, then the FOD stress is assumed given by

$$\sigma_{FOD}\left(\frac{x}{\rho}, k_t'[b, \rho]\right) = \sigma_{gross} \left[1 + \frac{k_t'[b, \rho] - 1}{\left(1 + \Phi \frac{x}{\rho}\right)^{\psi}} \right] \quad (5I.78)$$

where ϕ and ψ are defined by Equations (5I.21) and (5I.22) and

$$k'_t(b, \rho) = k'_t(b_{F-A}, \rho_{F-A}) \frac{k'_{t,A\&S}(b, \rho)}{k'_{t,A\&S}(b_{F-A}, \rho_{F-A})} \quad (5I.79)$$

where $k'_{t,A\&S}$ is given by Equation (5I.6). The accuracy of this approach can be judged by reference to Figures 5I.45 to 5I.48. These figures show the FRANC3D-ANSYS derived stress distributions for the notch models with ID's of 1, 4, 5, and 6 that have k'_t values of 3.9, 3.1, 5.5 and 1.7, respectively, and the solutions obtained from applying the modified A&S Equations (5I.78) and (5I.79). The FRANC3D-ANSYS solutions are given for three positions along the notch, corresponding to 25%, 50% and 75% through the width of the blade (see Figure 5I.49). These three positions encompass the regions of the notched wing specimens where thumbnail cracks were assumed to initiate under HCF conditions. For comparison, the stress predictions obtained from applying the unmodified A&S stress expression, that employs k'_t values derived from Equation (5I.6), are also shown in the figures. It can be seen that both the modified and unmodified approximate stress distributions are in good agreement with the FRANC3D-ANSYS stress results.

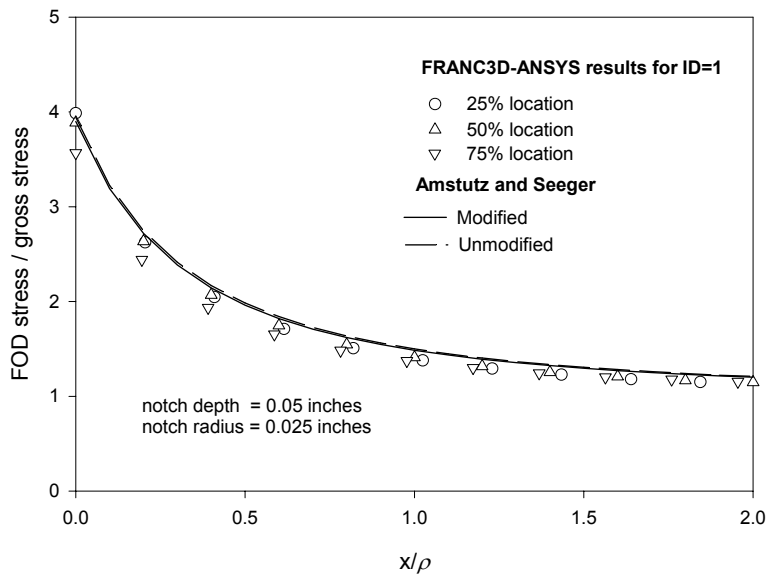


Figure 5I.45. Comparison of A&S stress distributions with the FRANC3D/ANSYS results for a notch of depth 0.05 inches and radius 0.025 inches.

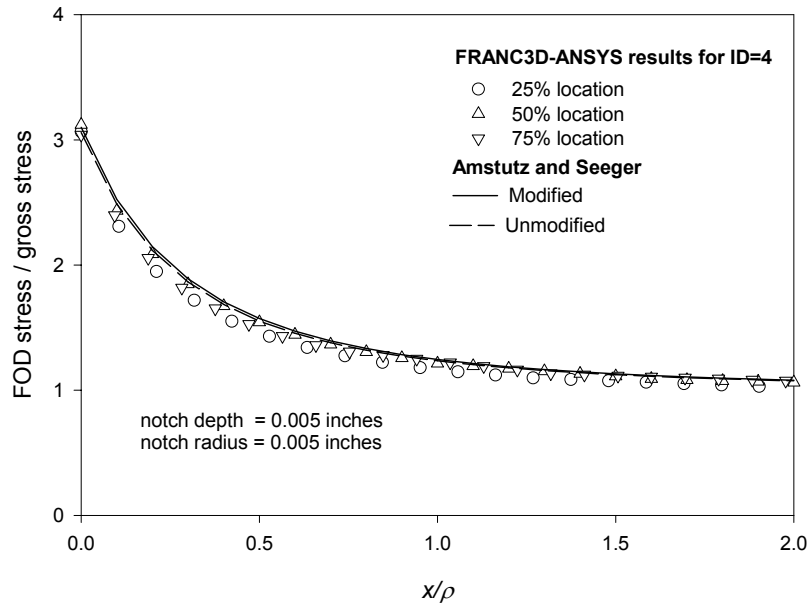


Figure 5I.46. Comparison of A&S stress distributions with the FRANC3D/ANSYS results for a notch of depth 0.005 inches and radius 0.005 inches.

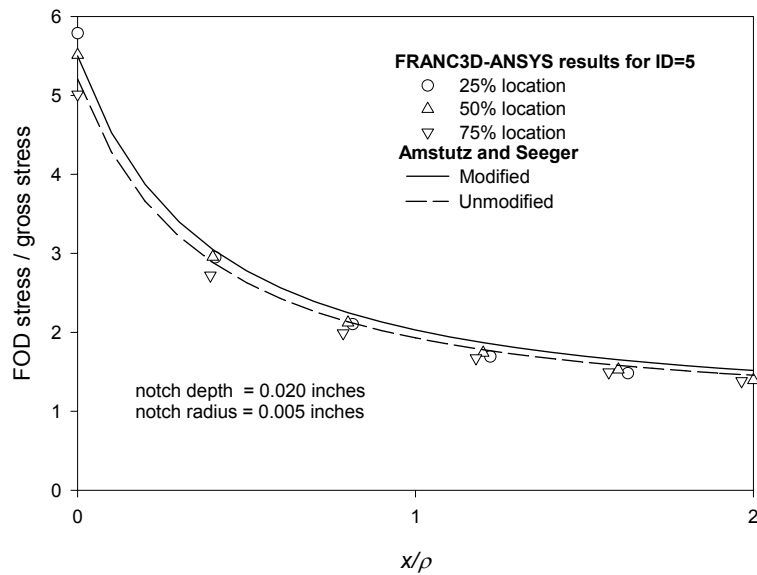


Figure 5I.47. Comparison of A&S stress distributions with the FRANC3D/ANSYS results for a notch of depth 0.02 inches and a radius 0.005 inches.

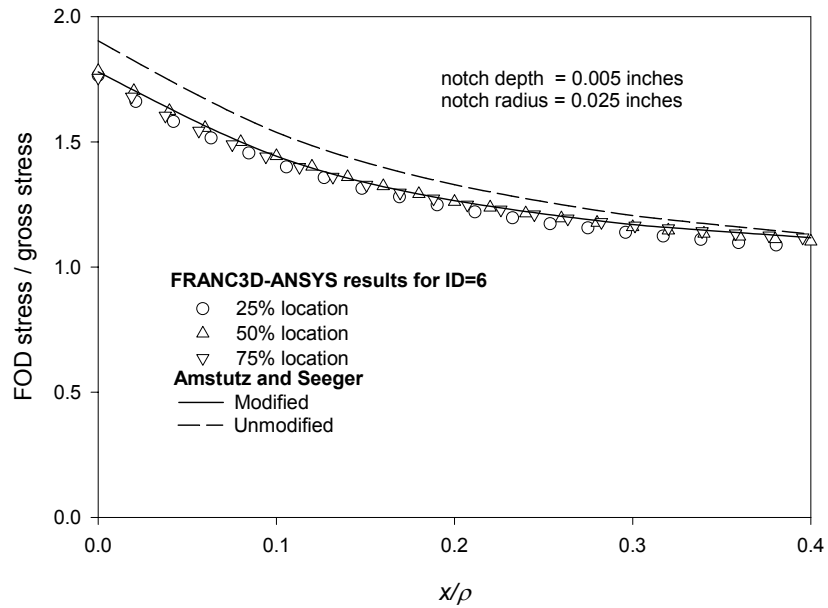


Figure 5I.48. Comparison of A&S stress distributions with the FRANC3D/ANSYS results for a notch of depth 0.005 inches and radius 0.025 inches.

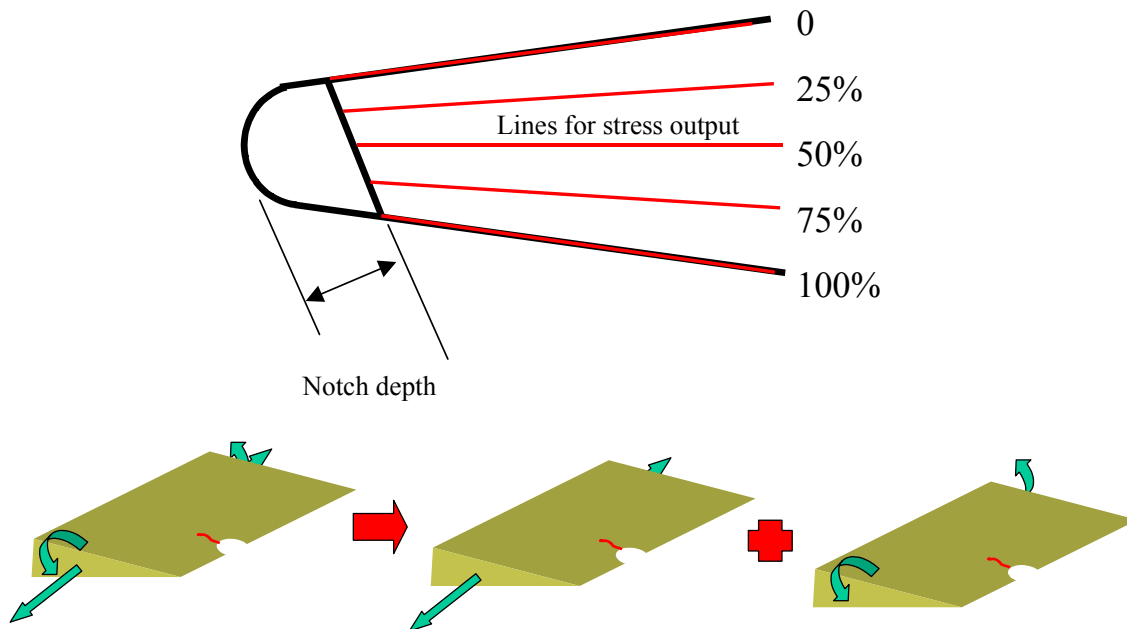


Figure 5I.49. Schematic of the FOD simulation specimens analyses using FRANC3D/ANSYS. Top figure shows the lines along which the stress distributions were determined corresponding to distances of 0%, 25%, 50%, 75% and 100% through the thickness of the leading edge of the blade.

SUMMARY AND CONCLUSIONS

A methodology for treating the influence of FOD on HCF behavior has been developed based on damage tolerance concepts and fracture mechanics theory. The approach assumes that cracks can initiate relatively early in life, particularly for severe FOD-notches, due to the combined effects of the concentrated stresses introduced by the FOD and the intermittent occurrence of LCF loading. Consequently, it is assumed that the HCF behavior of these severe notches is controlled by whether or not the initiated cracks will continue to grow. The approach is termed the “worst case notch” (WCN) approach since it leads to the definition of a limiting value of the threshold stress with increasing notch acuity. The WCN approach is also consistent with nucleation-based approaches, particularly for milder FOD-notches. A key feature of the WCN approach is that it properly predicts the nucleation, growth and arrest of microcracks at notches – an experimentally observed phenomenon that cannot be explained by classical fracture mechanics. This feature is due to the inclusion of small crack effects in the methodology, which are modeled as a crack-size-dependent threshold. Explicit treatment of the unique behavior of microcracks facilitates the inclusion of FOD-induced residual stresses in the methodology.

The WCN approach was implemented using parametric equations to define the notch stress field in terms of the elastic stress concentration factor, k_t' , and associated stress gradient. These stresses were employed to compute the crack driving force in terms of the crack-tip stress intensity factor, K , using a weight function approach. The model is capable of predicting the threshold stress as a function of FOD-notch severity, loading mode, and residual stress state. The model was verified by comparing these predicted threshold stresses with those measured in notch tests over a wide-range of notch acuity reported in the literature, as well as program data from Ti-6Al-4V specimens containing blade leading edge geometries with either machined notches or simulated FOD introduced by ballistic impacts or solenoid gun impacts. The following significant conclusions can be drawn from the verification exercise, as well as a sensitivity study with the WCN model:

- 1) The HCF threshold stress depends on both the notch depth and notch root radius and consequently cannot be uniquely defined based on k_t' alone; the

- dependence of the threshold stress on both of these geometric features is predictable using the WCN model.
- 2) For shallow notches that are of practical interest to FOD, the threshold stress is controlled by the local notch geometry and associated stress field and is independent of global specimen or component geometry.
 - 3) FOD-residual stresses can increase the threshold stress by as much as a factor of 3.5 for severe notches; the magnitude of this effect is primarily determined by the depth of the compressive residual stress field (which is assumed to be equal to the compressive yield strength) below the notch surface.
 - 4) The parametric equations developed to describe the notch stress field as a function of notch geometry and loading conditions were found to be in good agreement with results from FRANC3D/ANYSYS computations.
 - 5) WCN predictions of the HCF threshold stresses for specimens containing machined notches and simulated FOD met the exit criteria set by the HCF team.
 - 6) WCN predictions based on the parametric notch field equations and on the FRANC3D/ANYSYS computations gave nearly equivalent results and both met the exit criteria.
 - 7) Classic S-N endurance predictions of the HCF threshold stresses for specimens containing machined notches and simulated FOD did not meet the exit criteria.

REFERENCES

1. H. Tada, P. Paris, and G. Irwin, The Stress Analysis of Cracks Handbook, 2nd Edition, Del Research Corporation, 1985.
2. R.E. Peterson, "Stress Concentration Factors," John Wiley and Sons, New York, 1974.
3. H. Amstutz and T. Seeger Accurate and Approximate Elastic Stress Distribution in the Vicinity of Notches in Plates Under Tension. Unpublished results (referenced in G. Savaidis, M. Dankert, and T. Seeger, An Analytical Procedure for

- Predicting Opening Loads of Cracks at Notches, *Fatigue Fract. Engng Mater. Struct.*, Vol. 18, No. 4, pp. 425-442, 1995)
4. C. Chen and H. Pan, *Collection of Papers on Fracture of Metals*, ed. C. Chen, Metallurgy Industry Press, Beijing, p. 197 (in Chinese, referenced in Kujawski and Shin), 1978.
 5. G. Glinka and A. Newport, "Universal Features of Elastic Notch-tip Stress Fields," *Int. J. Fatigue*, Vol. 9, pp. 143 -150, 1987.
 6. D. Kujawski, "Estimations of Stress Intensity Factors for Small Cracks at Notches," *Fatigue Fract. Engng. Mater. Struct.*, Vol. 14, pp. 953 - 965, 1991.
 7. D. Kujawski, and C. S. Shin, "On the Elastic Longitudinal Stress Estimation in the Neighborhood of Notches," *Eng. Fract. Mech.*, Vol 56, pp. 137-138, 1997.
 8. V. Weiss, Application of Weibull's Statistical Theory of Fracture to Sheet Specimens. *Trans. ASME*, Paper No. 62-WA-270, 1962.
 9. R.X. Xu, J.C. Thompson, and T.H. Topper, "Practical Stress Expressions for Stress Concentration Regions," *Fatigue Fract. Engng. Mater. Struct.*, Vol. 18, pp. 885-895, 1995.
 10. S.T. Xiao, M.W. Brown, K.J. Miller, "Stress Intensity Factors for Cracks in Notched Finite Plates Subjected to Biaxial Loading," *Fatigue Fract. Engng. Mater. Struct.*, Vol. 8, pp. 349-372, 1985.
 11. R. Fathallah, G. Inglebeit, and L. Castex, "Modeling of Shot Peening Residual Stresses and Plastic Deformation Induced in Metallic Parts," *Proceedings of the Sixth International Conference on Shot Peening*, Jack Champaigne, Editor, San Francisco, CA, 1996.
 12. *Proceedings of the Sixth International Conference on Shot Peening*, Jack Champaigne, Editor, San Francisco, CA, 1996.
 13. Y. LeGuernie, J.S. Eckersley, "Peen Stress Software Selects Shot Peening Parameters," *Proceedings of the Sixth International Conference on Shot Peening*, Jack Champaigne, Editor, San Francisco, CA, 1996.

14. S. Kyriacou, "Shot Peening Mechanics – A Theoretical Study," Proceedings of the Sixth International Conference on Shot Peening, Jack Champaigne, Editor, San Francisco, CA, 1996.
15. T. H. Topper and M. H. El Haddad, "Fatigue Strength Predictions of Notches Based on Fracture Mechanics," *Fatigue Thresholds: Fundamentals and Engineering Applications*, Engineering Materials Advisory Services, LTD, Warley, U.K., 1982.
16. S.J. Hudak, Jr., O.H. Burnside, and K.S. Chan, "Analysis of Corrosion Fatigue Crack Growth in Tubular Joints," ASME Trans., *Journal of Energy Resource Technology*, Vol. 107, 1985.
17. S.J. Hudak, Jr., G.G. Chell, T.S. Rennick, R.C. McClung, and D.L. Davidson, "A Damage Tolerance Approach to FOD Based on the Worst Case Notch Concept," Proceedings of the 4th National Turbine Engine High Cycle Fatigue Conference, Monterey, CA, February, 1999.
18. S. Pearson, "Initiation of Fatigue Cracks in Commercial Aluminum Alloys and the Subsequent Propagation of Very Short Cracks," *Engineering Fracture Mechanics*, Vol. 7, 1975, pp. 235-247.
19. S.J. Hudak, Jr., "Small Crack Behavior and the Prediction of Fatigue Life," ASME Trans., *Journal of Engineering Materials and Technology*, Vol. 103, 1982, p. 26.
20. S. Suresh and R.O. Ritchie, "The Propagation of Short Fatigue Cracks," *International Metals Reviews*, Vol. 29, 1984, pp. 445-476.
21. C.W. Brown and D. Taylor, "The Effects of Texture and Grain Size on Short Fatigue Crack Growth Rates in Ti-6Al-4V," in *Fatigue Crack Growth Threshold Concepts*, D. Davidson and S. Suresh, Eds. The Metallurgical Society of AIME, 1984, pp. 435-445.
22. *Small Fatigue Cracks*, R.O. Ritchie and J. Lankford, The Metallurgical Society of AIME, Warrendale, Pennsylvania, 1986.
23. N.E. Frost and D.S. Dugdale, "Fatigue Tests on Notched Mild Steel Plates With Measurement of Fatigue Cracks," *Journal of the Mechanics and Physics of Solids*, Vol. 5, 1957, p. 182-192.
24. N.E. Frost, "Notch Effects and the Critical Alternating Stress Required to Propagate a Crack in an Aluminum Alloy Subjected to Fatigue Loading," *J. Mech. Engr. Sci.*, Vol. 2, No. 2, 1966, pp. 109-119.

25. Metal Fatigue, N.E. Frost, K.J. Marsh, and L.P. Pook, Clarendon Press, Oxford, 1974, pp. 166-173.
26. M.H. El Haddad, K.N. Smith, and T.H. Topper. Fatigue Crack Propagation of Short Cracks," ASME J. of Engr. Materials. & Tech., Vol. 101,1979, p. 42.

Chapter 6

Fretting Damage

6.1 BACKGROUND

Fretting damage in fan and compressor components is the damage created by the contact in the attachment region between fan and compressor disks and their associated airfoils. This type of attachment creates a very complex loading condition. The variables that influence fretting damage include friction, bearing loads (from centrifugal stress), and the vibration loads which are often not aligned with the axial LCF loading. It has been documented that a significant number of engine component HCF failures are attributable to the combination of fatigue and fretting damage, i.e., fretting fatigue. Approaches to avoid fretting fatigue have included shot peening for surface enhancement and the use of shims and protective coatings, but these fixes have not always been successful. Neither the mechanisms nor the mechanics of surfaces in contact subject to small cyclic sliding displacements are fully understood. The objective of this research was to develop an engineering-based understanding and predictive methodology of the fretting damage associated with attachments in titanium fan and compressor components. Carefully controlled experimental studies and companion analyses were performed to identify the key parameters that characterize the nucleation and propagation of cracks in this very complex environment.

6.1.1 Objective and Approach

The overall objective of the fretting damage effort is to develop methods that can be used by engineers in a design environment to accurately assess the potential of fretting damage in blade/disk attachments. Figure 6.1 attempts to summarize the variables that a design engineer needs to evaluate in assessing the robustness of these attachments. A key point shown in Figure 6.1 is the stick-slip region at the edge of contact. This region experiences a highly multiaxial stress state and slips a very small amount even though the bulk of the disk-blade interface is stationary. The stick - slip location is where cracks nucleate; this location is the focus of the fretting damage investigations.

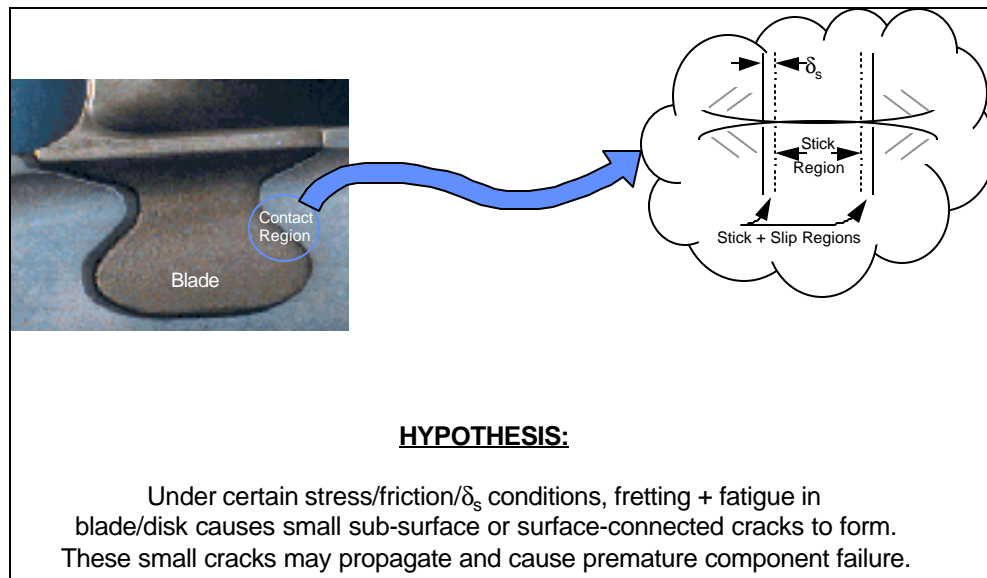


Figure 6.1. Disk blade attachment and schematic diagram of the HCF critical features in the attachment.

The approach to fretting-fatigue damage control was to develop the tools necessary to predict the localized stresses, the threshold crack nucleation stress parameter, and an appropriate crack propagation threshold level. As in the other damage states, the focus was on predicting the level of vibratory stress associated with the onset of damage in order to determine acceptable stress levels where crack nucleation and/or growth would not occur under HCF loading.

The concept of a fretting design system for engine components is shown schematically in Figure 6.2. In this system, a design engineer would perform a stress analysis of an attachment considering the LCF and HCF loadings in combination with the attachment geometry and friction conditions. The results of this analysis would include the local stresses and the stress gradients that would be used to assess the potential for crack nucleation and/or crack propagation. The designer would first assess the potential of crack nucleation for the full range of geometry, friction, and stresses/deflections experienced at this location. If cracks would not nucleate, the location would be treated as a DT location. On the other hand, if it were predicted that a crack would nucleate, fracture mechanics assessments would be performed to evaluate the potential for exceeding the crack growth threshold. Design assessments would include the effects of stress-ratio and other component surface enhancements such as

shot peening. In addition, the potential for LCF crack growth during the associated inspection interval(s) also needs to be assessed. The location would be treated as an HCF DT location if fracture mechanics assessments predict that the crack growth threshold value is not exceeded. For the cases where both crack nucleation and HCF propagation would be predicted to occur, redesign would be required to reduce the potential for HCF attachment fatigue. For design applications, the crack nucleation and propagation methods would include the use of minimum properties or of a probabilistic analysis to account for statistical variations in material behavior and loads.

The objective of the fretting damage effort is to develop the engineering tools necessary to perform the stress, crack nucleation, and crack propagation evaluations depicted in Figure 6.2. A key element of such predictions, although not addressed by this program, is the determination of the full range of vibratory modes and amplitudes experienced in the envelope of engine field operations.

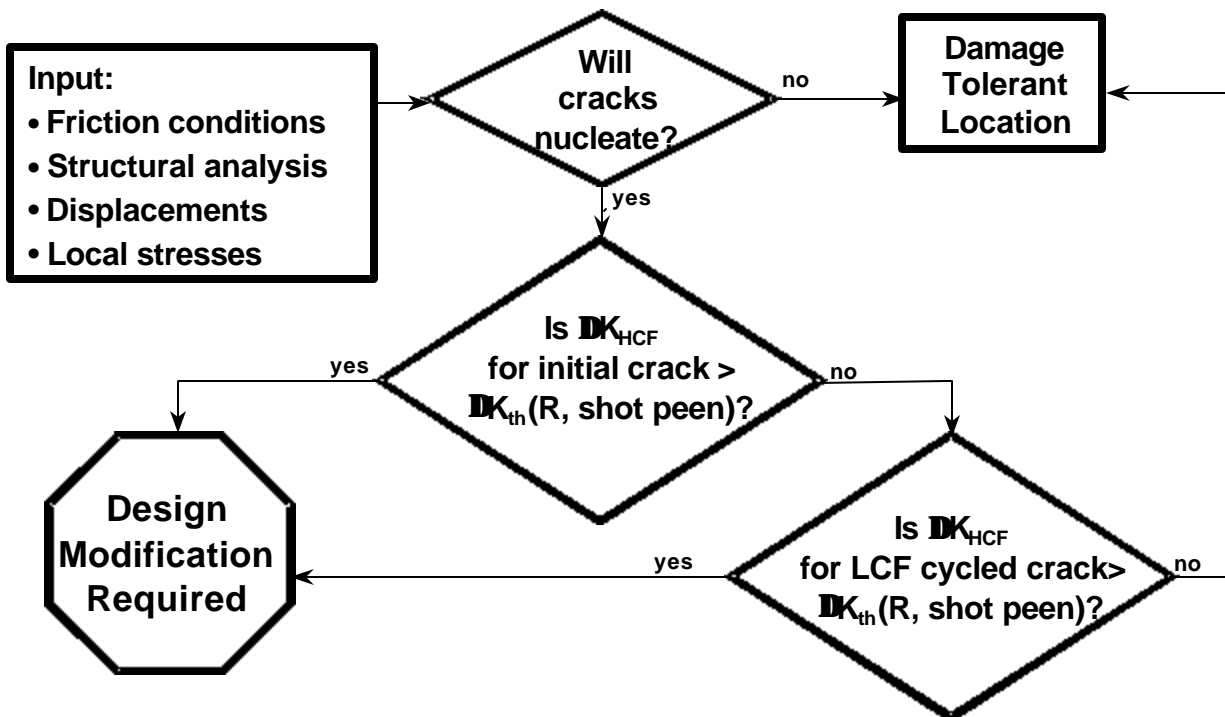


Figure 6.2. Schematic diagram of fretting design system.

6.1.2 Engine History

As mentioned in the introduction, there have been several instances of cracking in military fan and compressor attachments. These usually occur at or very close to the edge of contact in the stick-slip region previously shown in Figure 6.1. Figures 6.3 shows features typical of attachment cracking.

Figure 6.3 illustrates that fretting-fatigue-induced cracking is highly localized and that the fretted surface is rather smooth (Figures 6.3c and 6.3d). A metallographic cross section through the crack nucleation site shows that the microstructure is altered only very close to the contact surface (Figure 6.3c).

Based on surveys of GEAE and P&W engine experience, there appeared to be no special cause for fretting-fatigue events. These surveys reinforced the objective of this program, i.e., to develop engineering-based, analytical methods for predicting the nucleation and growth of cracks at attachments.

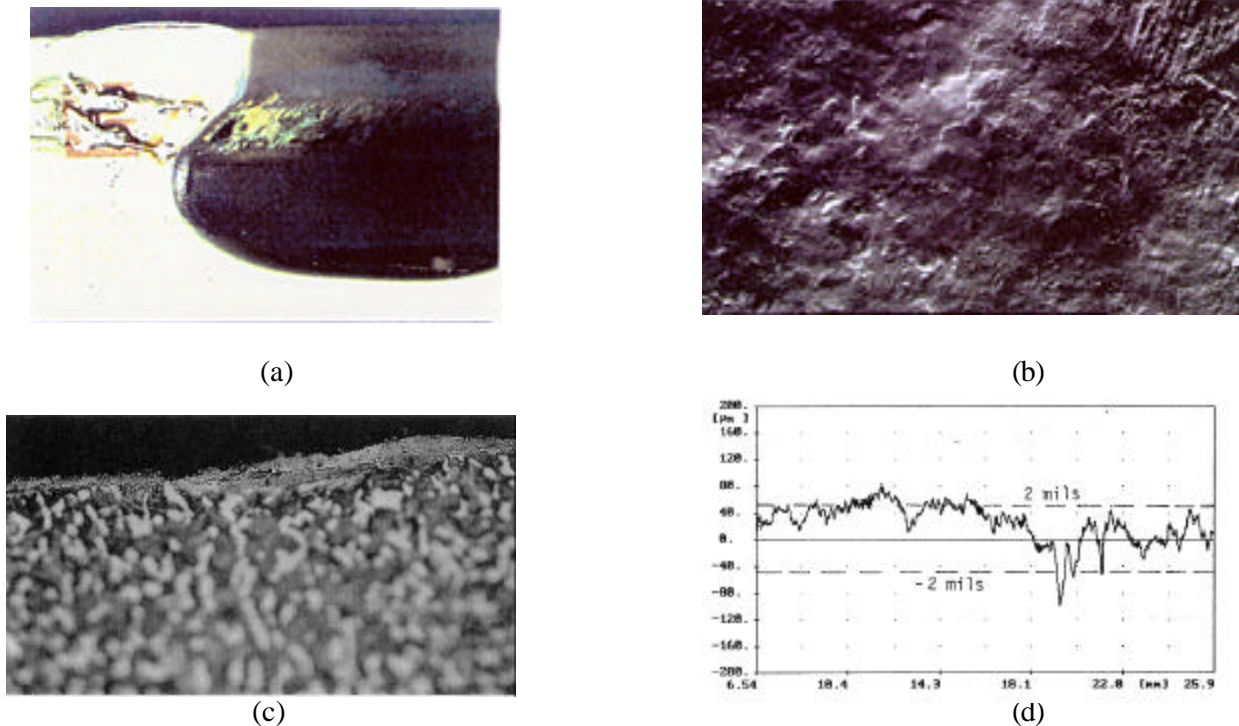


Figure 6.3. Examples of (a) fretting damage at attachments, (b) SEM micrograph of fretted surface, (c) metallographic cross-sections, and (d) laser profilometer traces of surface roughness in field hardware.

6.2 FRETTING AND FRETTING-FATIGUE TESTING

The initial parts of the experimental investigation focused on the selection of test parameters that would encompass the range of conditions experienced by engine components. These variables included fretting pad geometry, normal bearing stress ($\sigma_b = P/A$) between the fretting pad and the specimen, the relative slip distance between the pad and specimen (δ_s), and the applied fatigue stress (s_{fatigue}). These parameters are known to have a significant effect on the resulting fatigue lives of specimens in simultaneous fretting fatigue tests. The full range of parameters that were considered in this program is shown in Figure 6.4.

The initial evaluations of this type were performed by GEAE. It was shown that when δ_s exceeded 0.0015-inch, the resultant contact surface showed excessive amounts of material transfer (Figure 6.5a) and not the smoother, more benign appearance observed in components (Figure 6.5b). As a result of these observations, the maximum displacement used in subsequent tests was restricted to 0.0015-inch.

6.2.1 Evolution of Coefficient of Friction

The coefficient of friction is required for the evaluation of local stresses in fretting and fretting fatigue experiments. Friction experiments were conducted by Purdue University to study the evolution of the coefficient of friction, μ , with the number of cycles in partial slip experiments with bare Ti-6Al-4V on Ti-6Al-4V. Two types of experiments were performed. The pads used were cylindrical, resulting in a Hertzian distribution in the contact zone. In tests with cylindrical pads and constant force, the coefficient of friction increased with cycling, resulting in stabilized values of tangential force less than that required for gross sliding, so μ could not be evaluated. In the second type of test, the loading was stopped after running for a specified number of cycles. Then, without disturbing the pad/specimen contact, a waveform of increasing amplitude was applied to the specimen. The experiment was then stopped when the pad just started sliding (about 50 cycles) and the average coefficient of friction was then calculated using the maximum value of the tangential force, before the pad starts sliding. The friction experiments were conducted with two different sets of pads with radii of 5-inch and 7-inch.

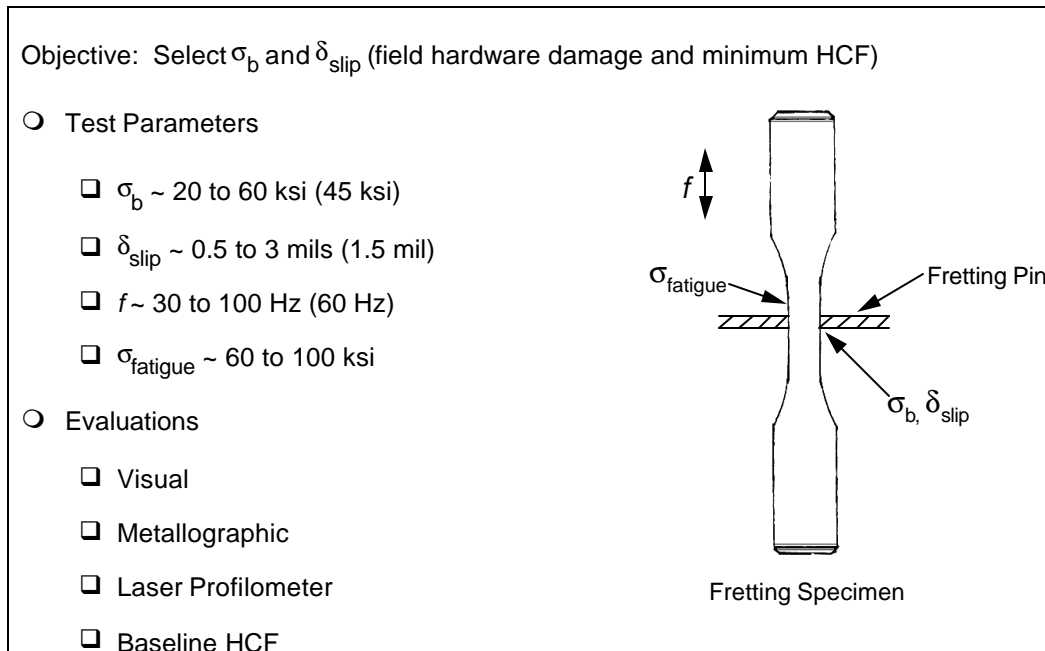


Figure 6.4. Fretting parameter selection for fretting and fretting fatigue evaluations.

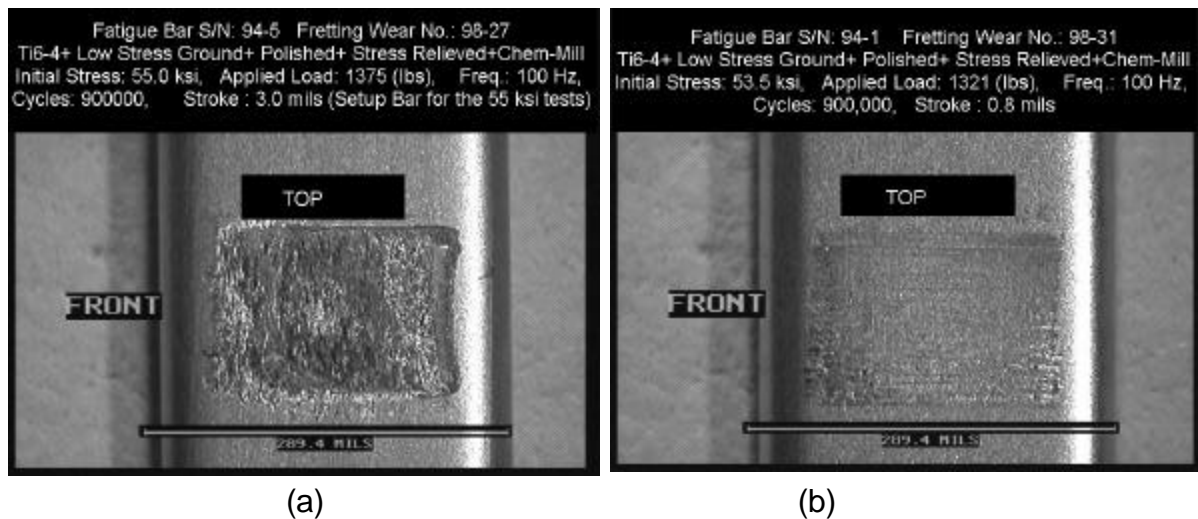


Figure 6.5. SEM micrographs showing scars from fretting specimens with (a) 0.003-inch, and (b) 0.0008-inch relative displacements.

The maximum bulk stress applied during the coefficient of friction experiments was 42 ksi. Figure 6.6 shows the results of the friction experiments. The results are similar to those measured in fretting fatigue tests with flat pads performed at GEAE.

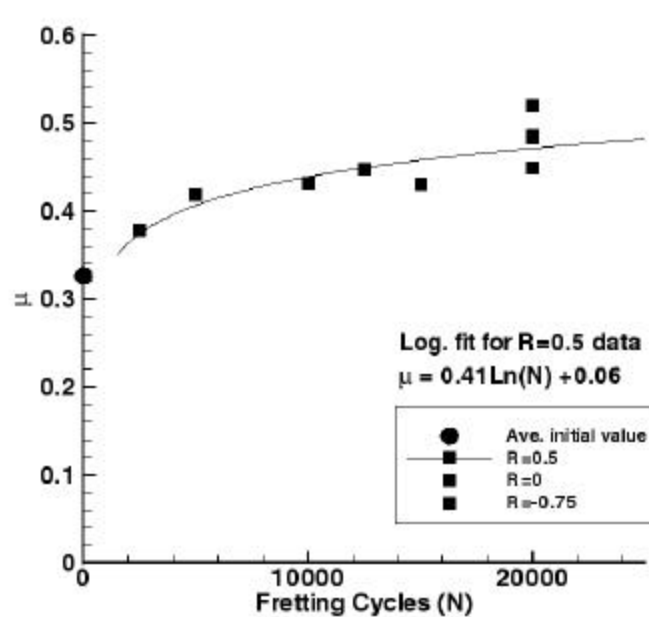


Figure 6.6. Evolution of Coefficient of friction.

Infrared thermal imaging was used to measure the temperature rise due to the frictional contact. This is a very powerful technique that can be used to measure the temperature field on the surface of a body through the measurement of the radiation emitted. This technique is particularly useful in detecting temperature changes of the order of a few degrees. Once partial slip set in, the observed frictional heating was negligible.

6.2.2 Fretting and Fretting Fatigue Experiments

GEAE, Purdue University, United Technologies Research Center (UTRC) and SwRI performed fretting and fretting fatigue experiments; the full extent of these experiments and the analyses that supported these efforts are summarized in Appendices [6A-6E](#). Each laboratory utilized different experimental techniques. The apparatus and details of these experimental techniques are described in detail in the appropriate appendices. This chapter will attempt to summarize the results and show the most important features of the results with emphasis on how the results relate to developing improved prediction capability for the onset of HCF fretting damage. Figure 6.7 compares results from R = 0.5 fretting fatigue experiments performed at UTRC with the R = 0.1 and 0.5 smooth bar tests reported in the Paragraph 3.3.1.2 (labeled as open

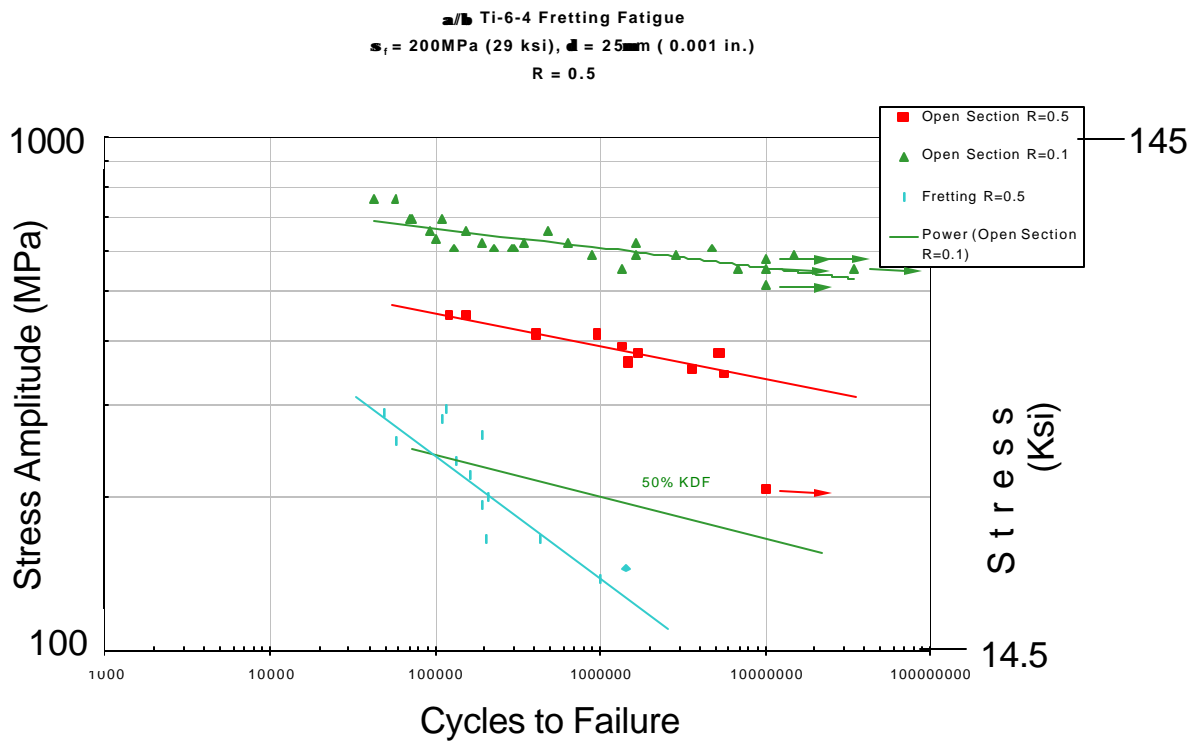


Figure 6.7. Results of selected fretting experiments performed at UTRC.

section in the figure). These results clearly illustrate the very damaging influence of fretting fatigue. The line in Figure 6.7 labeled as 50% KDF (knock down factor) is a line at half the stress amplitude of the $R = 0.5$ smooth bar trend line. This clearly illustrates the very damaging effect of fretting fatigue and that simple factors such as the 50% factor are not adequate methods for predicting the reduction in material capability as a result of fretting fatigue. Additional information on the UTRC effort can be found in Appendix 6D.

GEAE, Purdue, and SwRI all used flat pads with controlled radii in their testing programs, see Appendices 6A, 6B and 6E, respectively for details. Figure 6.8 shows an example of a pad with a 0.12-inch flat profile. These pads also had a well-controlled 0.12-inch blend radius at the region where the pad met the chamfer. This radius region covered a distance of approximately 0.023-inch. The tests conducted at Purdue used the pad geometry shown in Figure 6.8. Most of the tests performed at GEAE and SwRI used a very similar geometry except that the dimension of the flat region was reduced to 0.04-inch, but the overall width of the specimen was maintained to avoid excessive bending in the fretting pad.

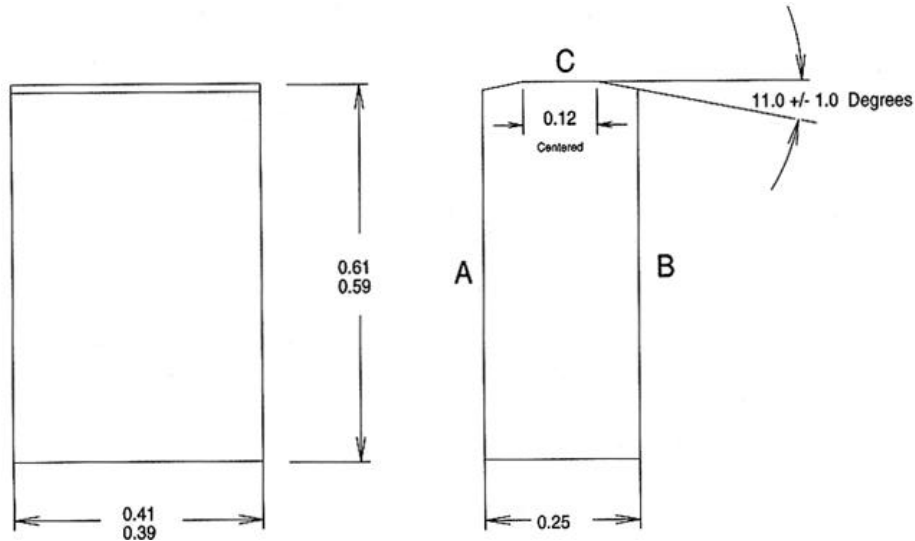


Figure 6.8. Drawing of the 0.12-inch fretting pin configuration (Dimensions in inches).

Fretting tests were performed at GEAE by controlling the sliding of a rectangular specimen relative to the pad in a very stiff system. The bearing stress was controlled using a calibrated spring system. The intent of the fretting tests was to determine the conditions necessary for the nucleation of fretting cracks. It is difficult to separate the nucleation and growth states of the crack in fretting-fatigue experiments because the cracks are generally located close to the edge of contact between the specimen and fretting pad. The fretting test matrix was based on a design of experiments concept and performed over a range of displacements (0.0005 to 0.0014-inch), bearing loads (35 to 65 ksi), surface conditions (7A shot peened *versus* not peened), and fretting cycles (40,000 to 400,000 cycles). After the completion of the fretting tests, each specimen was heat tinted and most were subsequently cycled without a fretting pad. The post fretting test used applied stresses (with $R = 0.5$) that would result in a lifetime of 10^7 cycles to failure in the absence of fretting damage. The lives of these tests are shown in Figure 6.9. Each bar in Figure 6.9 corresponds to a single test.

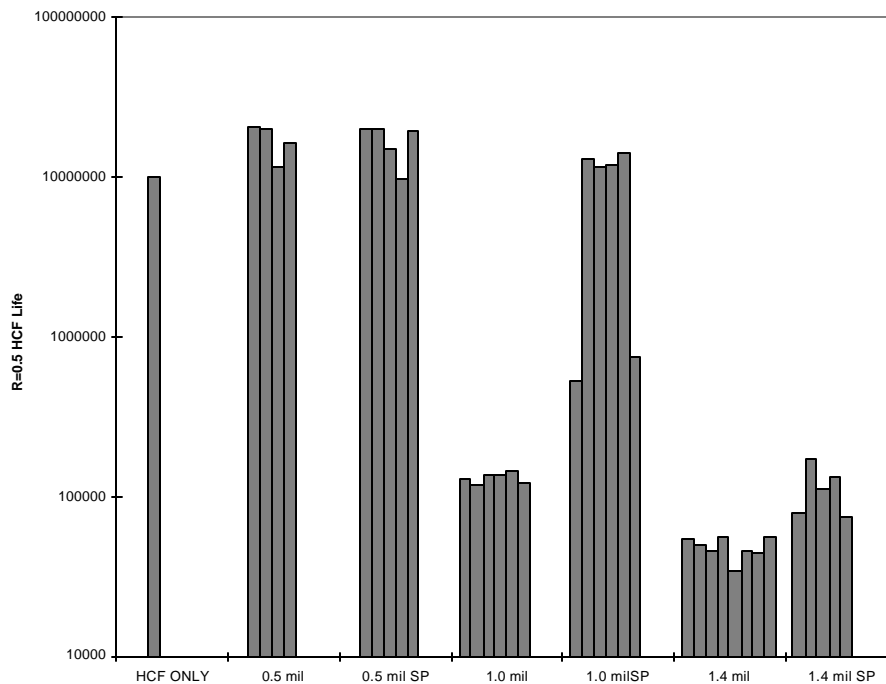


Figure 6.9. Fatigue Life results of post-fretting R = 0.5 HCF tests (SP = Shot peened).

The lives in these tests were dominated by the displacement and the surface condition. There was very little influence of fretting cycles or bearing load. For example, the two tests with low lives in the 0.001-inch displacement, shot-peened tests results were from tests with widely disparate bearing stresses of 35 and 65 ksi. Duplicate tests at these same bearing stress levels had long lives, as did the tests with bearing stresses of 50 ksi.

Post-test examination showed that no cracks nucleated at the contact regions in tests with 0.0005-inch fretting displacement. The cracks in these low displacement tests occurred away from the edge of contact, and lives all were within the scatter of the undamaged 10^7 life. Attempts to find cracks in the edge of contact region by bending followed by observation of the test specimen surface were unsuccessful. Multiple small cracks nucleated at, or very near, the edge of contact in the higher displacement tests. Shot peening had a very significant effect on the 0.001-inch displacement tests, but a very small influence on the lives of the 0.0014-inch displacement tests. The cracks

were on the order of several thousands of an inch deep with high aspect ratios. The details are reported in Appendix 6A.

The threshold stress for the nonpropagation of fretting-fatigue cracks was investigated using a high-frequency fretting-fatigue-testing machine at SwRI. Both step stress and interrupted tests were performed for various stress ranges at $R = 0.5$ and for bearing pressures of 35 and 55 ksi. All the tests were performed at 2100 Hz under load-controlled conditions. For the step stress tests, the fatigue stress ranges were increased by about 2 ksi after applying 10^7 fatigue cycles at each stress level until failure occurred. For interrupted tests, the specimen was subjected to fretting-fatigue loading for 10^7 cycles at a prescribed stress range; the test was then terminated and the specimen was examined for possible cracks nucleated by fretting fatigue. SEM metallography and fractography were performed to determine the existence of nonpropagating and propagating microcracks, as well as their respective crack lengths and depths.

Fretting scars observed on the SwRI specimens after 10^7 fretting-fatigue cycles at 35 and 55 ksi bearing pressures exhibited a benign looking appearance at low magnification. At high magnification, the fretting surfaces exhibited large amounts of oxides and smeared metal layers, as well as microcracks. The microcracks, shown in Figure 6.10a, were determined to be nonpropagating because they exhibited little or no crack opening when they were loaded to the maximum fatigue stress applied during the fretting fatigue tests. The microcracks observed on the fretting surfaces were about 0.0002 – 0.0013-inch in length for the interrupted tests. Similar to the results from other laboratories, multiple crack nucleation sites were observed on the fracture surfaces (Figure 6.10b).

Fretting fatigue experiments at Purdue University were performed to determine the crack nucleation lives of specimens under various loading conditions. The tests were conducted at room temperature. The amplitude of the axial fatigue stresses ranged from 30 ksi to 60 ksi. One set of experiments was performed with a nominal bearing stress of 55 ksi, for a remote fatigue stress with $R = 0.5$ applied at a test frequency of 10 Hz. The remaining tests were performed with 75 ksi bearing stress, a remote fatigue stress with $R = 0.0$ applied at a test frequency of 5 Hz. While most of the tests were run to failure or

runout (10^6 cycles), some tests were stopped after a fixed number of cycles to study the metallographic details of the contact surfaces.

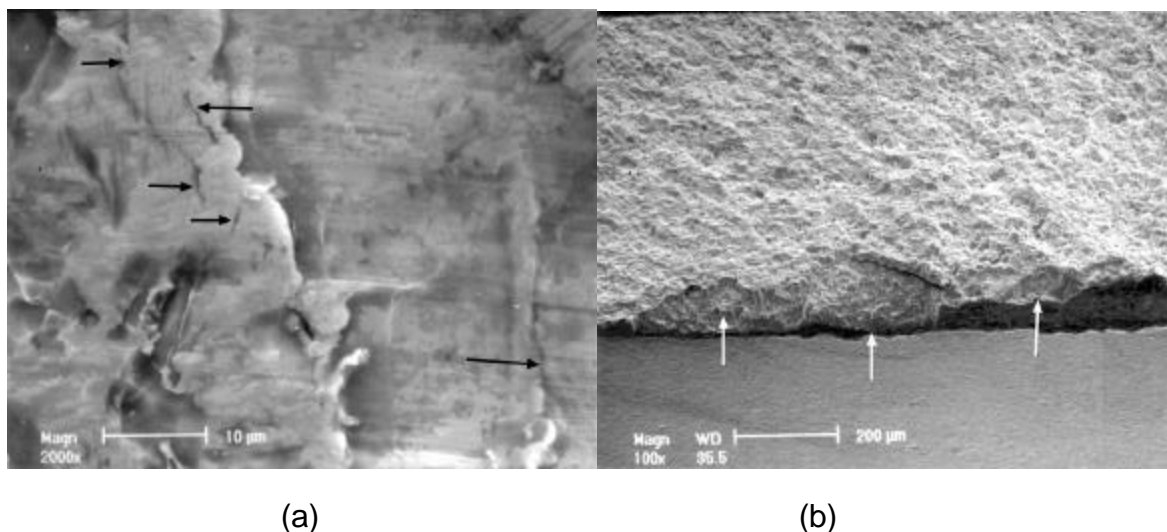


Figure 6.10. Observations of (a) nonpropagating microcracks observed on the pad-specimen contact surface after 10^7 cycles and (b) typical multiple crack nucleation sites observed on the fracture surface.

The Purdue fretting fatigue tests were performed in a specialized testing fixture in a servo-hydraulic test machine. The fixture held the pads in contact with the specimen and allowed the application of a crushing load by the pad on the specimen with the help of a hydraulic actuator. The fretting pads had the geometry previously shown in Figure 6.8. Profiles of the pads used for each individual test were taken using a surface profilometer (Talysurf) and were used as geometry inputs to obtain the stress fields associated with the contact as discussed in Paragraph 6.3.1. The details of the experiments and results are provided in Appendix 6B.

Most of the Purdue fretting fatigue experiments were run to failure, i.e., until the specimen fractured. In all these tests, failure was at the pad/specimen stick-slip location closest to the actuator where the local stress is a maximum. The cracks were observed at both the contact locations in most of the experiments. Hence, there was no preferential crack formation, thus providing confidence in the alignment of the pads. Eight of the specimens, which did not fail in fretting fatigue, were fatigue tested to failure

using a four-point bending fixture in a servo-hydraulic test machine. The growth of the dominant crack was observed and recorded using an optical microscope and a digital camera. Crack tip positions were recorded for each photo, taken after running the bending test for a certain number of cycles, and used to create a plot of the crack growth versus cycles. As with the experiments from other laboratories, many small cracks nucleated, grew, and linked up to form a large surface crack in the center. Figure 6.11 shows such a crack after 37000 cycles in the four-point bending fixture. The complete set of results can be found in Appendix 6C.

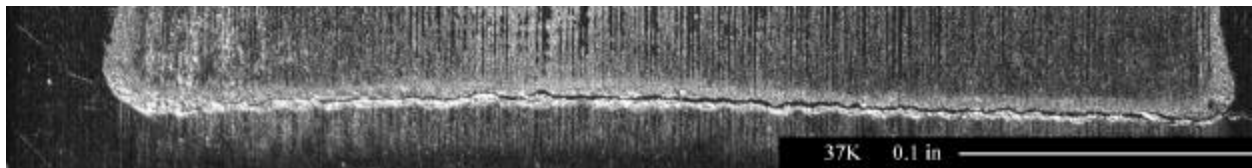


Figure 6.11. Photograph of a specimen after 37000 cycles of bending test, following a fretting-fatigue run-out.

6.3 ANALYSIS METHODS

6.3.1 Stress Analysis Methods

The local stresses at the edge of contact are very complex and require advanced analytical methods for accurate evaluation. This investigation utilized both integral equation and finite element methods.

The singular integral equation method is based on the solution representing two-dimensional, plane-strain elastic contact of similar materials with an arbitrary surface profile. A detailed description of this method and the associated equations is presented in Appendix 6B. The integral equations can be derived from classical theory of elasticity relating the slope of the contacting surfaces to the resulting interfacial tractions. The boundary conditions for this type of problem are the force and moment equilibrium conditions. In addition, the pressure must vanish at the ends of the pad. The singular integral equation can then be solved using trigonometric variable transformations. The surface normal traction can be obtained from any arbitrarily specified surface profile, normal load, and bending moment. Once the surface tractions are evaluated by this procedure, subsurface stresses can be obtained using discrete Fourier transformation techniques as discussed in Appendix 6B.

The local edge of contact stresses can also be obtained using the FEM, but FEM requires a very fine mesh to obtain a fully converged solution. Two-dimensional stress analyses were performed by GEAE for two of the experimental conditions in the GEAE fretting study using the submodeling strategy developed by Professor Sinclair and his students at Carnegie Mellon University. For these relatively simple two-dimensional models, a mesh size of 62.5 micro-inch was required to obtain a fully converged solution. Meshing to this level for a complex three-dimensional skewed disk-airfoil attachment would be a very computationally intense problem and is not well suited to an engineering or design environment. For the two-dimensional model of the experimental configuration used in the current program, the singular integral equation method gives a solution which matches very well with the solution obtained from the FEA as shown in Figure 6.12.

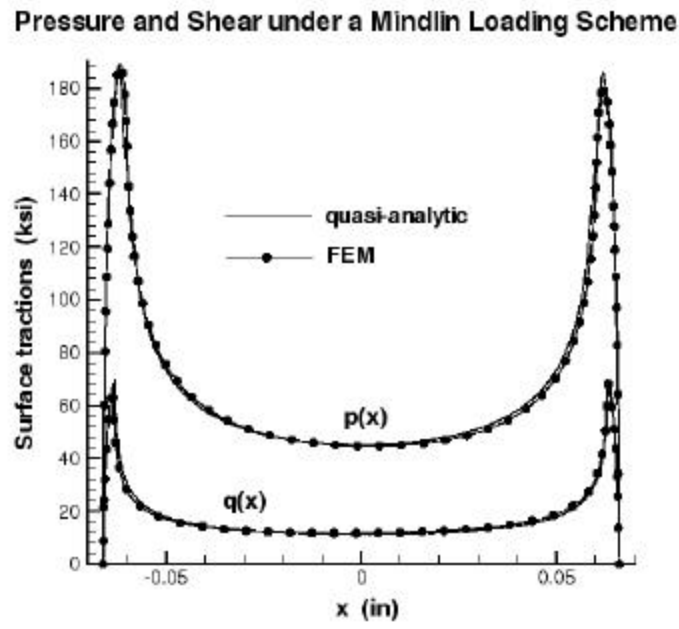


Figure 6.12. Comparison of surface normal tractions obtained from integral equation and FEM methods.

6.3.2 Predicting Crack Nucleation

Several methods were evaluated for predicting crack nucleation in the fretting and fretting-fatigue tests. GEAE evaluated stress invariant methods and Purdue University investigated use of the critical plane SWT parameter.

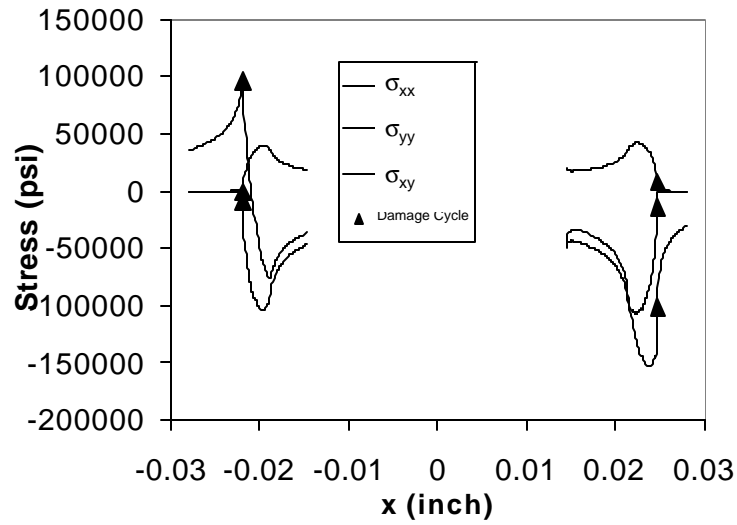
6.3.2.1 Equivalent Stress Methods

The equivalent stress methods described in Paragraph 3.3.2.1 were used to predict crack nucleation. The stress state at the edge of contact is highly multiaxial and has very steep gradients both along the contact plane and perpendicular to it. Example local stresses are shown in Figure 6.13a for the 55 ksi, 0.0015-inch displacement fretting experiment. As the fretting pad moves back and forth (in the x direction), a given position of the fretting specimen moves relative to the fretting pad. As the pad moves to the right, the axial (s_{xx}) tensile peak is just behind the left side pad and a highly compressive normal stress (s_{xx}) exists under the right side of the pad, as shown in Figure 6.13a. When the direction of the pad is reversed, the stresses are reversed and the tensile peak occurs on the right side of the pad. Therefore, it is necessary to determine the fatigue cycle associated with the fretting. This was accomplished by

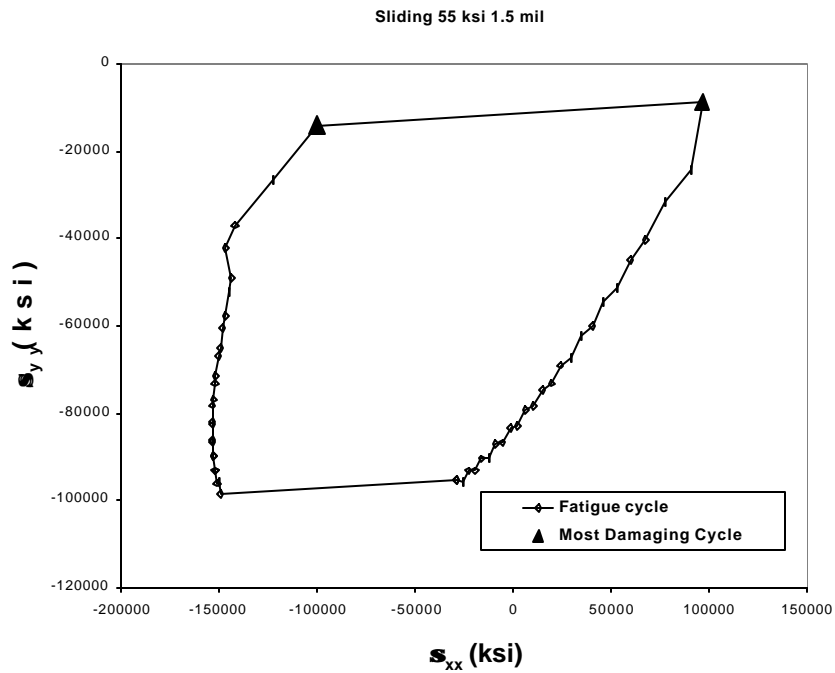
comparing the stresses at each position along the fretting specimen surface with each other point. The crack nucleation evaluation was performed using the methods described in Paragraph 3.3.2.1 (equivalent stress method with Walker mean stress model and modified Manson-McKnight multiaxial parameter). The stress pair selected as the most damaging pair is shown by the closed triangles in Figure 6.13. Figure 6.13b shows the variation in the axial and normal stresses (σ_{xx} and σ_{yy} , respectively) associated with this multiaxial fatigue cycle. One of the most interesting discoveries is that the most damaging points in the cycle are identified when the pad slides only 0.000125-inch. This discovery precluded the possibility that the fretting displacements measured experimentally affect the stress pairs that need to be used in a damage assessment. This discovery also suggests that the approach is very applicable to the partial slip situation experienced in engine hardware (Figure 6.1) as well as to the Purdue fretting fatigue experiments.

The amount of fretting displacement has a significant impact on the extent of highly stressed surface area in the fretting experiments. The stressed area is directly proportional to the relative displacement in the fretting tests. The impact of stress area was considered using the Weibull modified equivalent stress method (See Paragraph 3.4.3.1). Figure 6.14 shows the values of the Weibull modified equivalent stress for several values of Weibull modulus. The bars in the chart represent the average, $+3\sigma$, and -3σ equivalent stresses for 400,000 cycles, the upper limit of fretting cycles applied. The value of equivalent stress without Weibull corrections is above the average life value for both test conditions. When the stressed area concept is taken into account, the values of the Weibull modified equivalent stress for the 0.0005-inch displacement test is close to the fatigue minimum. The equivalent stress values (with and without Weibull modification) for the 0.0014-inch sliding condition are all above the 400,000 cycle stresses, so it is not surprising that cracks nucleated for this fretting condition. The proposed method correlates reasonably well for the two conditions modeled. This method has the characteristic of considering the local stresses through the equivalent stress methods and the fretting displacement through use of the Weibull modification. The fretting tests showed that the size of the region experiencing the high localized stresses is a very important variable that is also a key variable in other fretting work.

Sliding (55 ksi 1.5 mil)



(a)



(b)

Figure 6.13. FEM analysis of 55 ksi, 0.0015-inch fretting experiment showing (a) spatial distribution of stress components and (b) corresponding fatigue cycle.

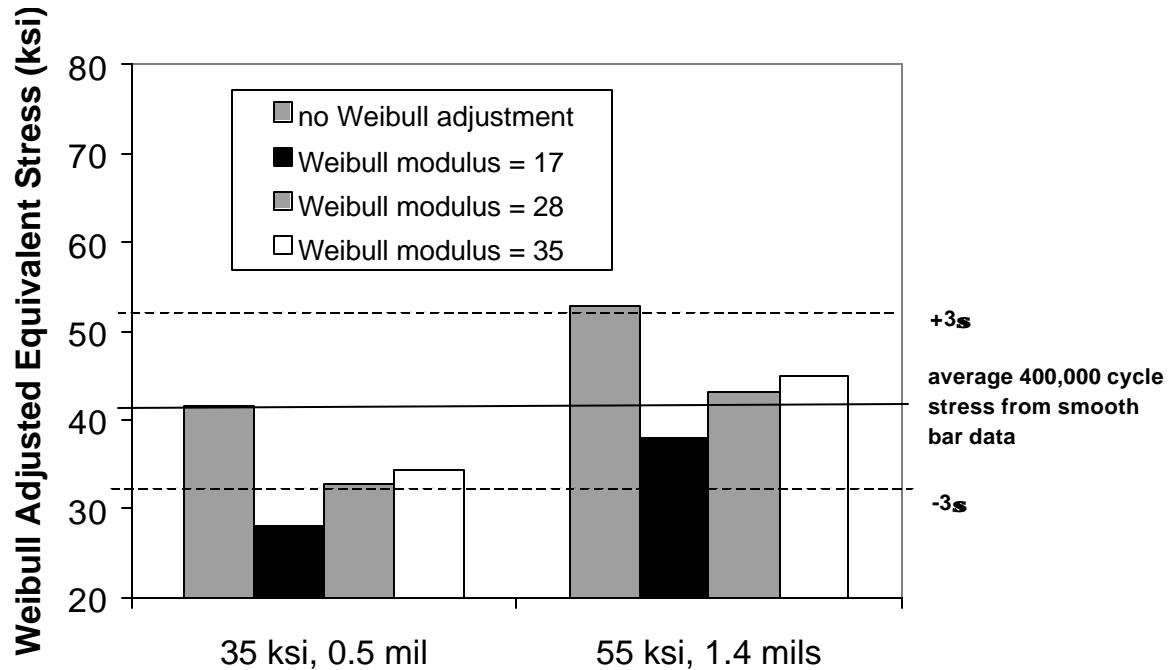


Figure 6.14. Weibull adjusted equivalent stress predictions for two fretting test conditions.

6.3.2.2 Life Evaluation Using Critical Plane Method

Researchers at Purdue University applied the SWT parameter to model crack nucleation in their fretting fatigue experiments. The SWT parameter, Γ , used for this prediction is defined as^{6.1}

$$\Gamma = \sigma_{\max} \frac{\Delta \epsilon}{2} \quad (6.1)$$

where σ_{\max} is the maximum normal stress and $\Delta \epsilon / 2$ is the normal strain amplitude. The subsurface stress field obtained from the integral equation analysis of actual profiles of each of the machined pads was used to predict the nucleation lives.

The parameter, Γ , was evaluated for all planes. The crack was assumed to nucleate at the point with maximum Γ and the orientation was given by the plane where Γ was maximum. Γ was calculated as an average over a length of 0.004-inch. The relationship between Γ and nucleation life for the titanium alloy, Ti-6Al-4V was obtained using the HCF data reported by Bellows^{6.2} (See Paragraph 3.3.1.2). Evaluation of subsurface stress fields indicated the presence of plasticity in a small region near the

contact. As a first approximation to plastic analysis, the stresses were capped at 110 ksi while evaluating the nucleation lives. The nucleation lives are presented in Figure 6.15. Though the stress-ratio of the bulk stress during the experiments is 0 or 0.5, locally in the contact region the stress-ratio is closer to -1 . Hence, the uniaxial strain-life curve given in the figure (based on data presented by Bellows^{6.2}) is for an $R = -1$. It is important to note that the fatigue curve of Bellows reflects only HCF elastic loading and not the monotonic plasticity required to predict the lower life tests. It is therefore, not very surprising that the tests with lives less than 10^5 cycles are not well predicted. This gradient averaged SWT method accurately predicts the crack nucleation lives in the Purdue fretting fatigue tests.

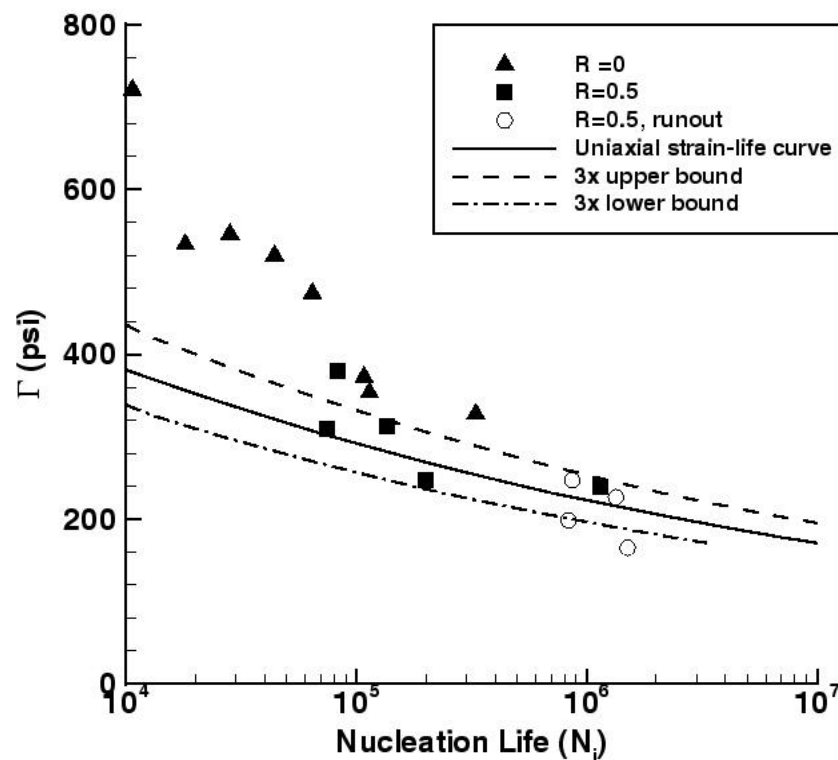


Figure 6.15. Comparison of predicted nucleation lives with experimental lives.

6.3.3 Predicting Crack Propagation Behavior

Various fracture mechanics methods were used to model the growth of cracks observed in the fretting and fretting fatigue tests. GEAE modeled the growth of the fretting cracks using conventional LEFM methods (See Paragraph 3.2.2.2) and SwRI applied the worst-case fret (WCF) model (See Appendix 6E) to a variety of the tests performed in this program.

6.3.3.1 Crack Propagation in Fretting Experiments

A fracture mechanics evaluation was performed on the GEAE fretting tests. The analysis used the HCF stresses applied during the post-fretting test (i.e., no pad contact) and crack dimensions measured from the heat tints observed during post-test fractography. The fracture mechanics analysis used the crack-growth-curve (Figure 3.8) and mean-stress-Walker exponent previously reported in Paragraph 3.2.2.2. The crack dimensions are shown in Figure 6.16 along with fracture mechanics predictions of the crack sizes which would result in lives of 48,000, 110,000, and 130,000 cycles. As shown previously in Figure 6.9, tests with 0.001- and 0.0014-inch displacements applied to unpeened test specimens resulted in lives that ranged from 40,000 to 200,000 cycles. Figure 6.16 also shows lines representing the threshold condition for peened and unpeened surfaces. The peening predictions were made with a Ti-6Al-4V shot-peen-fracture mechanics model created at GEAE prior to this contract and made available to interpret this data. The crack sizes observed in the lower life conditions (0.001-inch unpeened, 0.0014-inch both peened and unpeened) agree fairly well with the fracture mechanics predictions. One of the most interesting points is that the 0.001-inch unpeened condition fell on the curve based on this program's Ti-6Al-4V threshold values. The trend line for the threshold including the effect of shot peening is above the observed crack size. This suggests that fretting can nucleate cracks that will not grow when K is below the fracture mechanics threshold. This type of fracture mechanics evaluation must take credit for the beneficial effect of shot peening and is supportive of the design methodology schematically shown in Figure 6.2.

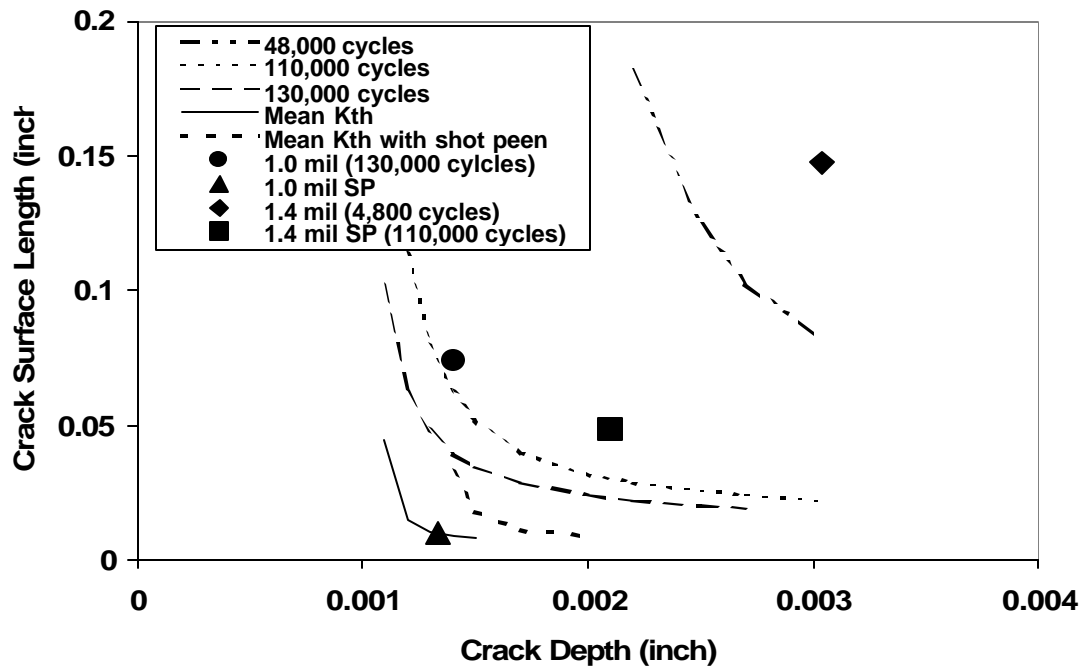


Figure 6.16. Comparisons of crack sizes observed in fretting specimens with fracture mechanics predictions.

6.3.3.2 WCF Model Predictions

A fracture-mechanics-based life-prediction methodology has been developed for treating high-cycle fretting fatigue. This approach is based on the WCF concept, which is analogous to the WCN concept used in FOD modeling (Paragraph 5.3.5). The underlying assumptions of the worst-case fret approach are: (1) the highly concentrated stresses under contact surfaces are likely to induce fretting-fatigue cracks relatively early in life, and (2) the high-cycle fatigue life can best be predicted on the basis of the nonpropagation of these fretting-fatigue cracks. Development of this crack nonpropagation-based method involved developing analytical tools for computing the contact stress field, the stress intensity factor, K , solutions for the fretting-fatigue cracks, and a life-prediction scheme based on a crack nonpropagation criterion for small cracks.

An overview of the WCF methodology is presented in Appendix 6E. The contact stress field for two flat surfaces under fretting fatigue was analyzed via an integral equation technique^{6.3}. The local fretting stress field of the uncracked body was

then utilized to obtain the Mode I and II stress intensity factors for an arbitrarily oriented fatigue crack using a continuum dislocation formulation^{6.4}. Based on the stress intensity factors, the limiting threshold stress ranges for the nonpropagation of fretting-fatigue cracks were predicted on the basis that fretting-fatigue cracks are either: (1) large cracks that arrest at a stress intensity range below the large-crack growth threshold, or (2) small cracks that exhibit a crack-size-dependent growth threshold and propagate at stress intensity ranges below the large-crack threshold (see Paragraph 3.2.3.1). For crack nucleation, the threshold stress is predicted on the basis that the stress range due to fretting fatigue equals the endurance limit for the same stress ratio.

A significant predictive capability of the WCF model is the treatment of both nucleation and propagation of small cracks. Figure 6.17 shows the predicted threshold stresses for fretting crack nucleation, nonpropagation, and propagation to failure as a function of bearing pressure for Ti-6Al-4V subjected to gross slip conditions ($\Delta Q \geq \pm \mu P$ with $\mu = 0.5$, where μ is the coefficient of friction and P is the bearing load). The crack nucleation boundary was computed by setting the local fretting stress at the edge of contact equal to the endurance limit at 10^7 cycles for $R = -1$, which is the stress ratio at the edge of contact. As seen in Figure 6.17, the crack nucleation stress decreases rapidly with increasing bearing pressures. At or above 16 ksi bearing pressure, the local fretting stress is sufficiently large to nucleate fatigue cracks without the aid of a cyclic bulk stress. Under this circumstance, the limiting HCF stress is controlled by the nonpropagation of small cracks. The calculated crack nonpropagation boundary is in good agreement with experimental data generated at UTRC and SwRI. The SwRI data, which were generated under partial slip conditions, have been adjusted for gross slip based on the UTRC data, which were generated under gross slip conditions. This was done so the data could be plotted on the same figure. The GEAE data, which were obtained from fretting tests, i.e., without an applied cyclic bulk stress, are shown at $\Delta S = 1$ ksi because of the logarithmic axis. The local fretting stress at the contact edge is predicted to be less than the yield strength, 135 ksi, for bearing pressures less than 55 ksi. Thus, local yielding under the fretting pad is expected only when the bearing pressure exceeds 55 ksi.

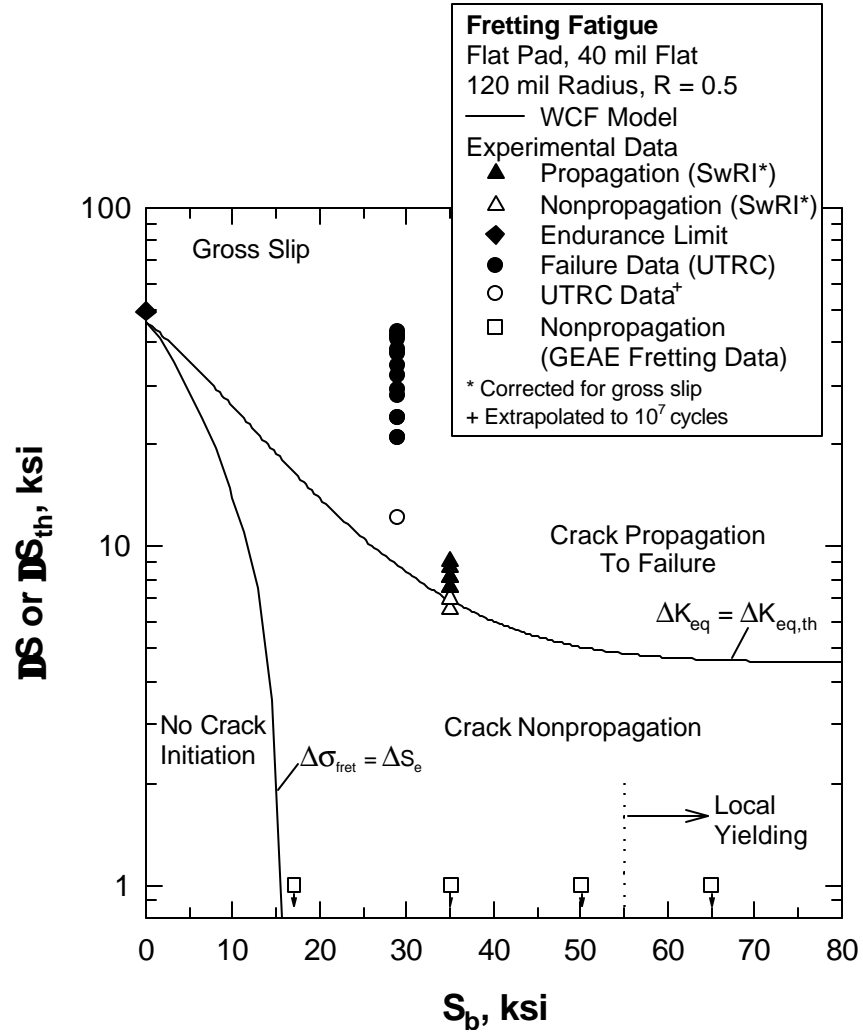


Figure 6.17. Predicted threshold stresses for crack nucleation, nonpropagation and propagation to failure compared to fretting fatigue data (UTRC and SwRI) and fretting data (GEAE).

6.4 EXIT CRITERIA

6.4.1 Overview of the Requirements

The exit criteria are intended to statistically summarize the adequacy of the various life methods and to provide an approach for comparing new and existing design methods. The exit criteria for fretting modeling are expressed in terms of the ratios of actual fatigue strengths to predicted (mean) fatigue strengths and use the normal distribution to quantify the statistical parameters. The criteria are as follows:

- a.) The average ratio of actual to predicted (A/P) fatigue strengths be within ± 0.15 of 1.0.
- b.) No significant bias shown for the test parameters.
- c.) Since the standard deviation of baseline smooth A/P fatigue strengths is 0.10, the scatter of A/P values from fretting models will be less than or equal to 0.25.

Two of the models presented in this chapter were compared against sufficient data to justify an exit criteria evaluation. One model is based on the total life approach that utilizes the SWT mean-stress parameter (G) averaged over a depth of 0.004-inch to estimate initiation life, and the other is the Kitagawa approach that is based on the WCF model and utilizes small crack modeling to estimate threshold behaviors.

6.4.2 SWT Model

The SWT parameter (G), discussed in Paragraph 6.3.2.2 and in more detail in Appendix 6B, was calculated for all the Purdue experimental fretting-fatigue data (Γ_A) and compared for the value of the parameter (Γ_P) determined for the estimated initiation life (associated with a crack of 0.004-inch deep). The complete set of results compared was presented in Figure 6.15, (Also see Table 6B.7 in Appendix 6B). Figure 6.18 compares the A/P ratios, i.e., (Γ_A / Γ_P) using the normal cumulative distribution for the SWT parameter. As can be seen from the figure, the mean A/P ratio is 1.182 and its standard deviation is 0.270. For this model, the mean estimate is very conservative and outside the desired range, while the scatter is only slightly larger than desired.

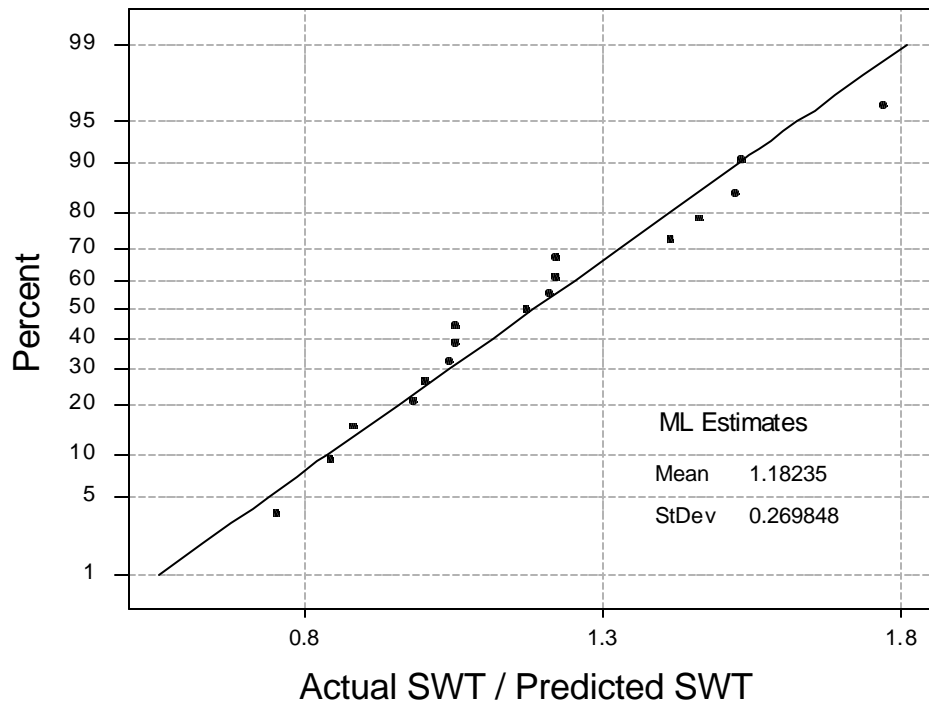


Figure 6.18 Normal cumulative distribution of A/P values of the SWT parameter for fretting-fatigue crack initiation (0.004-inch deep cracks).

6.4.3 WCF Model

The WCF model was discussed in Paragraph 6.3.3.2 and in more detail in Appendix 6E. The WCF model was used to calculate estimates of the threshold axial stress range for a mix of fretting and fretting fatigue tests conducted at SwRI, GEAE, Purdue, and UTRC during this program. Table 6E.2 in Appendix 6E lists the test data and stress range estimates that were compared to determine the A/P ratios. As noted in this table, life data from Purdue were extrapolated from 10^4 - 10^6 to 10^7 to estimate the threshold stress levels. Figure 6.19 compares the A/P ratios for the axial stress ranges, where it is shown that the mean A/P ratio is 1.102 and the standard deviation is 0.406. For this model, the mean A/P is moderately conservative and within the desired range, but the scatter is substantially larger than desired.

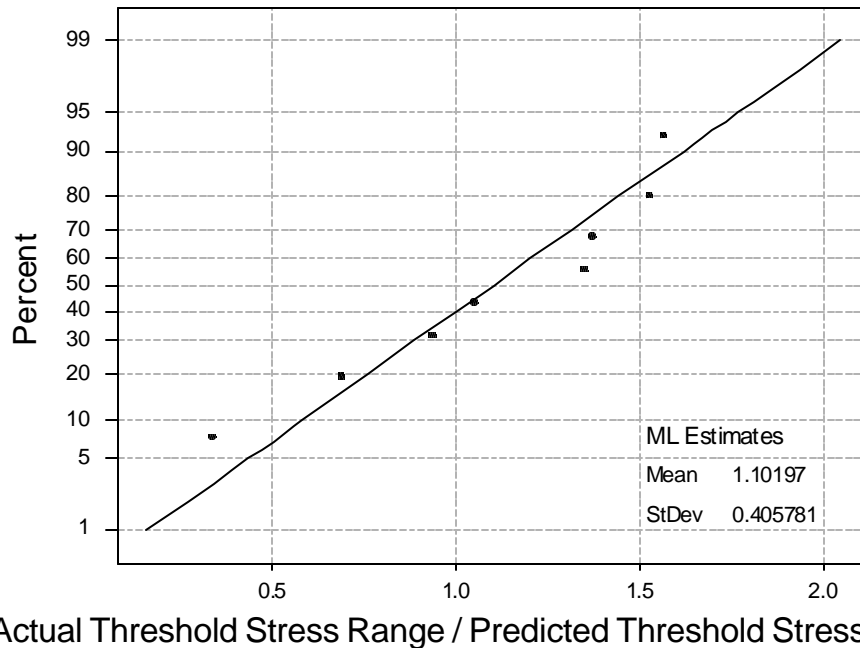


Figure 6.19 Normal cumulative distribution of A/P values of the WCF estimated threshold stresses for fretting-fatigue crack initiation (0.004-inch deep cracks).

6.4.4 Summary

The composite average and standard deviations of A/P values for the two models are summarized in Table 6.1. As noted above, neither of the two models provides a capability that approximates the target.

Table 6.1
Comparison of Fretting Models

<i>Model Parameters</i>	SWT	WCF
Average	1.182	1.102
Std Dev	0.2698	0.4058

6.5 DISCUSSION, CONCLUSIONS, AND RECOMMENDATIONS

Significant progress has been made on the understanding of the stress analysis of fretting and contact as well as on predicting the onset of crack nucleation and propagation.

Both finite element and integral equation methods have been shown to correctly predict fretting contact stresses and stress gradients. The integral equations are very computationally efficient, but are currently restricted to two-dimensional elastic analysis of contact between materials with identical elastic properties. Finite element methods are far more general and can be applied to more complex contact problems, including three-dimensional loading, dissimilar materials, and plasticity, but are not very useful in an engineering environment for this problem due to the large amount of submodeling and mesh refinement (<0.001 -inch) that is required. Future work should focus on developing hybrid approaches where the complex boundary conditions would come from FEA of complex attachments, but the detailed stress analysis would be performed efficiently using enhanced integral equation methods.

Two different methods were developed to predict the crack nucleation. Purdue developed a SWT-based method that accurately predicted the longer-life fretting fatigue tests. Purdue's method used the SWT parameter averaged on a line over a distance of 0.004-inch below the contact surface. As demonstrated in Paragraph 6.4.2, this model provided conservative estimates well above the target exit criteria. Furthermore, since the Purdue fretting-fatigue lives were relatively short, additional experimental evaluation of threshold conditions (fretting-fatigue lives approaching the HCF regime) is required to validate the SWT parameter approach to fretting. This SWT parameter also needs to be evaluated for conventional notched HCF conditions to show generality. The Weibull modified equivalent stress method described in Paragraph 3.4.3.1 was applied to the GEAE fretting tests (see Paragraph 6.3.2.1). It accurately predicted the two conditions modeled and has the feature of predicting the strong influence of local fretting displacement. However, more extensive analytical evaluation of the Weibull modified equivalent stress model is required and should include comparisons to both fretting and fretting fatigue tests in order to establish its ability for satisfying the fretting exit criteria.

Both conventional and small crack fracture mechanics were applied to fretting and fretting fatigue tests. Conventional fracture mechanics methods accurately predicted

the post-fret HCF results and illustrated the importance of including the beneficial influence of shot peening on suppressing the growth of fretting induced cracks. SwRI evaluated a WCF method based on the WCN method developed in the FOD damage state. Although the WCF model has many appealing features, it appears to provide strength estimates that are moderately conservative with unacceptable scatter (Paragraph 6.4.3). In addition, the WCF model predicts crack nucleation only as a function of bearing stress and friction, and does not predict the absence of crack nucleation observed in 0.0005-inch displacement fretting tests. This suggests that this method cannot be used as the sole method. The potential advantages of WCF relative to conventional fracture mechanics will have to be demonstrated in future work.

The experimental and analytical work performed in this investigation fully support the design method concept developed in this program (Figure 6.2) that recommends assessment of both crack nucleation and crack growth.

6.6 REFERENCES

- 6.1 J.A. Bannantine, J.J. Comer, and J.L. Handrock, Fundamentals of Metal Fatigue Analysis, Prentice Hall, Englewood Cliffs, New Jersey, 1990.
- 6.2 R.S. Bellows, K.R. Bain, and J.W. Sheldon, "Effect of step testing and notches on the endurance limit of Ti-6Al-4V", *Mechanical Behavior of Advanced Materials*, 84:27-32, 1998.
- 6.3 D.A. Hills and D. Nowell, Mechanics of Fretting Fatigue, Kluwer Academic Publishers, Dordrecht, The Netherlands, 1994.
- 6.4 J.R. Barber, Elasticity, Kluwer Academic Publishers, Dordrecht, The Netherlands, 1992.

Appendix 6A

EVALUATION OF FRETTING PARAMETERS

**Barney Lawless
Robert VanStone
Robert McClain
Michael Hartle**



General Electric Aircraft Engines

**Submitted
August 1999**

Appendix 6A

GEAE EVALUATION OF FRETTING PARAMETERS

The following parameters were evaluated in the program conducted at GEAE:

1. Fretting pad geometry
2. Contact surface condition
3. Relative displacement
4. Bearing stress
5. Number of fretting cycles

Don Hunter of Pratt & Whitney performed a survey of dovetail operating conditions to provide guidance for selection of relevant fretting parameters for laboratory experiments [1]. Included in the recommendations were bearing stresses in the range of 20 ksi to 60 ksi, and relative displacements of 0.5 to 3 mils.

FRETTING EXPERIMENTAL PROCEDURE

The fretting experiments described in this paper were performed in the fretting apparatus shown in Figure 6A.1. This apparatus has only the capability to fret a specimen, and is not capable of simultaneous fretting/fatigue of a specimen. *In this report, the term “fretting test” will refer to a test where fretting of one face of a specimen is performed, with no application of fatigue load.* In the apparatus shown in Figure 6A.1, a fatigue specimen with a rectangular cross section (Figure 6A.2) is moved vertically in contact with a horizontally fixed fretting pad. The specimen is fretted on one of the wide faces, typically at a frequency of 100 Hz. The small relative displacement used in these studies (0.5 to 3.0 mils) was monitored by a capacitance displacement gage that was mounted in the vicinity of the fretting contact. Specifically, the gage was mounted adjacent to the mid-plane of the fretting contact. The normal or bearing loads applied to the specimen through the fretting pad are controlled by application of a large spring force at the top of the load train. The accuracy of the force applied through the fretting pad has been verified with a load cell. The tangential force is continuously monitored during the test with a load cell so that the global, dynamic coefficient of friction can be determined as a function of fretting cycles.

In the initial assessment, the application of the fretting cycles was by programmed “blocks” of 500 cycles at ambient conditions, interrupted by “no fretting” periods of approximately 30 seconds. For each block of cycles, the amplitude of displacement achieved the programmed value within 10 fretting cycles, remained at the programmed value for about 480 cycles, and ramped down to zero displacement in about 10 cycles (i.e., a 10-480-10 cycle). Therefore, the displacement was at the programmed value for a minimum of 96% of the total number of fretting cycles. A continuous feed of laboratory air was directed at the fretting interface and provided cooling during the entire experiment. GEAE had previous experience with this technique on Ti-6Al-4V. Using this technique prevented any detectable temperature rise of the specimen during the experiment.

DETAILED DESCRIPTION OF FRETTING PARAMETERS

Fretting Pad Geometries

Four different fretting pad geometries were considered by GEAE in this program. The down-selected fretting pad geometry is the last one to be discussed below.

120 mil flat with a chamfered edge:

The pad geometry used at the beginning of the program can be seen in Figure 6A.3. This pad contact geometry was identical to the geometry that had been used in some recent GEAE studies on titanium alloys (including Ti-6Al-4V), consisting of a 120 mil flat with a chamfered edge.

40 mil flat with a chamfered edge:

Some of the partners had access to fretting equipment with a limited bearing load capacity, so that only a very low bearing stress could be applied to a specimen using a fretting pad with a 120 mil flat. These partners had experience using a fretting pad with a 40 mil flat. Therefore, GEAE manufactured a limited number of fretting pads with a 40 mil flat and a chamfered edge (Figure 6A.4) to provide some commonality with the experience of the partners.

120 mil flat with a 120 mil radius:

To address concerns with analytical treatment of the stress concentration at the edge of contact for a pad with a chamfered edge (an infinite stress concentration for a true break-edge), some pads were manufactured with a 120 mil flat and a 120 mil transition

(edge of contact) radius, as seen in Figure 6A.5. It should also be noted that the 120-mil radius is on the same order as the radii in engine dovetail attachments.

40 mil flat with a 120 mil radius:

To simultaneously satisfy concerns with: a) some commonality with the partners' fretting pad geometry, and b) analytical treatment of the edge of contact stress concentration, a fretting pad with 40 mil flat and a 120 mil transition radius was down-selected following the initial assessment. This geometry can be seen in Figure 6A.6.

Contact Surface Condition

The contact surface of all fretting pads was in the low stress ground (LSG) condition. For the fatigue specimens, two surface conditions were evaluated: a) chem mill, and b) chem mill + shot peened.

The "chem mill" condition is defined as: machine to a low stress ground condition + polish + vacuum stress relief for 1300F/one hour + chem mill.

Relative Displacement

In the initial assessment of fretting scars, three values of relative displacement were evaluated: 0.8 mils, 1.5 mils, and 3.0 mils. These values cover the range of displacements recommended by Hunter [1] from his survey of operating conditions. The results from the initial assessment described below suggested that a displacement of 3.0 mils is in the transition region between a "fretting" and a "galling" condition.

Bearing Stress

Bearing stress is defined here as the nominal (P/A) stress of the contact "footprint", with no consideration of edge of contact stress concentrations. In the initial assessment, bearing stresses of 17 ksi, 35 ksi, and 55 ksi were investigated. Although 17 ksi is a little below the range suggested by Hunter [1], it was used in the initial assessment as GEAE had experience using this level of bearing stress in prior investigations of the fretting behavior of titanium alloys, including Ti-6Al-4V.

Number of Fretting Cycles

In the initial assessment, 900,000 fretting cycles was used for most of the fretting experiments. This value was selected because GEAE had prior experience using

900,000 cycles in prior investigations of the fretting behavior of titanium alloys, including Ti-6Al-4V. The 900,000 cycles could be applied in about 14 hours using the block cycling method described in the “Fretting Experimental Procedure” section.

For a bearing stress of 55 ksi, two fretting tests were performed using 250,000 total cycles (one at 0.8 mils and one at 3.0 mils displacement), and one test was performed using 3.5E06 total fretting cycles at 3.0 mils displacement. This was to assess the effect of the number of fretting cycles on the condition of the wear scars.

Initial Assessment of Fretting Scars

One objective of the initial assessment was to identify the wear patterns observed in fretted test specimens and compare them with those seen in hardware. The test matrix for the initial assessment of wear scars can be seen below. Replicate fretting tests were performed for some of the fretting conditions. A complete description of all of the fretting tests in the initial assessment can be seen in Table 6A.1.

Table 6A.1.

Pad Displacement Amplitude	0.8 mil			1.5 mil			3.0 mil		
Bearing Stress	17 ksi	35 ksi	55 ksi	17 ksi	35 ksi	55 ksi	17 ksi	35 ksi	55 ksi
120 mil chamfer pad	F	F	F,P,S	F,P,S	F	F	F	F	F,P
40 mil chamfer pad				F,P,S			F,S		
120 mil radius pad		F	F,S	F,S	F				F

F = fretting completed

P = cracking observed in fretting pad

S = cracking observed in pre-fretted specimen after heat tint and 8 - 80 ksi HCF test

Shading indicates observation of cracking in pad (P) and/or specimen (S)

Every box with an “F” indicates a set of fretting parameters where at least one fretting test has been performed. A “P” indicates that cracking was observed in the fretting pad during post-test metallography and fractography. All of the fretting pads did

not receive post-test examination. Of the fretting pads that were examined, the only pad having no discernible cracking was a pad having a 120 mil flat and a 120 mil radius; the fretting had been performed at 17 ksi, 1.5 mils displacement. Cracks in the fretting pads were typically oriented at 45 degrees to the surface, and were aligned with the near surface plastic deformation (see Figure 6A.7). An "S" in the matrix indicates that a pre-fretted specimen was subsequently HCF tested at room temperature, $R = 0.1$. A total of 9 specimens were HCF tested. The cracks generated in the fatigue specimens were typically normal to the surface, and tended to propagate normal to the surface (Figure 6A.8). Wear scars for most of the specimens and the fretting pads can be seen in Figures 6A.9-6A.35. Figure 6A.36 contains a comparison of fretting scars generated at the largest (3.0 mils) and smallest (0.8 mils) values of relative displacement. The large displacement of 3.0 mils (36a) produced a scar with characteristics of galling, which is not representative of the appearance of relevant engine hardware.

The HCF tests were performed at a frequency of 1000 Hz in the GEAE high frequency fatigue system. The stress cycle of 8 to 80 ksi would result in a HCF life of approximately 10^7 cycles in an undamaged, round bar specimen. These nine specimens were heat tinted prior to the fatigue loading so that any cracks formed during the fretting experiments could be clearly identified. The bars were heat tinted at either 600F/3 hours or 650F/5 hours. Post test examination showed that both heat tints were adequate in marking shallow cracks that had been *generated from the fretting only* in all nine specimens. Figure 6A.37 shows both a pad cross section micrograph and specimen fractography revealing the small shallow cracks that formed during the fretting. All of the fretting generated cracks formed at or very close to the edge of contact location. Figure 38 shows the fracture surface of another specimen, with a pre-existing crack at the origin. Figures 6A.37 and 6A.38 show that the fretting crack typically has a "battered", featureless appearance. Fatigue crack growth from the HCF cycling results in an immediate transition to the expected transgranular fracture mode for Ti6-4.

The nine HCF test results are summarized in Table 6A.2.

Table 6A.2.

Fretting Test No.	Fatigue Specimen No.	No. of Fretting Parameters	Fretting Cycles	Fretting Pad Geometry	Fatigue Life
FW98-36	-10	17 ksi, 3.0 mils	900K	40 mil flat with chamfer	81,595
FW98-64	79-2	17 ksi, 3.0 mils	900K	40 mil flat with chamfer	97,201
FW98-24	85-3	17 ksi, 1.5 mils	900K	120 mil flat with chamfer	47,141
FW98-135	75-13	17 ksi, 1.5 mils	900K	120 mil flat, 120 mil radius	37,183
FW98-25	79-4	17 ksi, 1.5 mils	900K	40 mil flat with chamfer	35,544
FW98-68	76-9	17 ksi, 1.5 mils	900K	40 mil flat with chamfer	31,022
FW98-31	94-1	55 ksi, 0.8 mils	900K	120 mil flat with chamfer	109,571
FW98-132	94-12	55 ksi, 0.8 mils	900K	120 mil flat, 120 mil radius	130,698
FW98-51	75-8	55 ksi, 0.8 mils	250K	120 mil flat with chamfer	179,730

The specimens fretted for 900K cycles are plotted in the bar chart in Figure 6A.39. Although not appearing in the bar chart, the fatigue life of the specimen that had been fretted 250K cycles at 55 ksi, 0.8 mils displacement was 179,730 cycles, similar to the other specimens that had been fretted at 55 ksi, 0.8 mils displacement. The HCF lives for all nine tests were significantly lower than the unfretted 10^7 cycle HCF life, which is not surprising considering the presence of the small surface cracks. In Figure 6A.39, the first two bars represent specimens which had fretting displacements of 3.0 mils and bearing stress of 17 ksi. The next four bars show specimens which received a displacement of 1.5 mils with 17 ksi bearing stress. These four specimens all had HCF lives of approximately 40,000 cycles, even though the fretting pads were significantly different both in width and edge of contact geometry (chamfer vs. radius). Decreasing the fretting displacement to 0.8 mils (right two bars) resulted in improved HCF lives even though the bearing stress was much higher (55 ksi).

In these nine specimens that were HCF tested, the depth of fretting cracks ranged from about 0.5 mils to 3.5 mils in maximum depth. Figures 6A.40 to 6A.48 contain additional photographs and micrographs showing crack nucleation locations for these specimens.

Conclusions From Initial Assessment

1. Fretting cracks were observed in all nine specimens that had been HCF tested following fretting.
2. Fretting cracks were generated independent of fretting pad geometry and number of fretting cycles applied.
3. The wear scars of specimens that had been “fretted” at 3.0 mils relative displacement showed patterns more similar to galling than fretting.
4. For some of the specimens fretted at 0.8 mils displacement, the fretting caused removal of only the high spots (grinding or shot peen ridges) of the finished surface.

DOWNSELECT FRETTING PARAMETERS FROM INITIAL ASSESSMENT

Results from the initial assessment were reviewed with the PRDA team. From that review, a fretting matrix was down-selected and can be seen in Table 6A.3. This matrix was integrated with the concurrent activities of the other team members.

Table 6A.3.
Planned Fretting Test Matrix.

Bearing Stress	Displacement (mils)		
(ksi)	0.5	1.0	1.4
35	X,Y	X	X,Y
50	X	X,Z	X
65	X,Y	X	X,Y

X = 4 fretting tests (2 peened, 2 unpeened) with 400K fret cycles followed by R=0.5 HCF testing.

Y = 2 fretting tests (1 peened, 1 unpeened) with 40K fret cycles followed by R=0.5 HCF testing.

Z = 4 fretting tests (2 peened, 2 unpeened) with number of fret cycles similar to the Pratt & Whitney simultaneous fret/fatigue tests, followed by R=0.5 HCF testing.

The shotpeen parameters were: .006-.008A intensity, ASR-110 shot, and 100% coverage. The shotpeen vendor was Metal Improvement Company, Phoenix, Arizona. This vendor was a common supplier to all of the partners in the PRDA contract, and used the identical shotpeen parameters for all PRDA work.

Fretting Pad Geometry

As mentioned in the earlier discussion on fretting parameters, a fretting pad having a 40-mil flat and a 120-mil radius was down-selected for this part of the program.

FRETTING EXPERIMENTAL PROCEDURE

The fretting apparatus used for the initial assessment (Figure 6A.1) was also used here. As mentioned above, the fretting pad with a 40 mil flat was used exclusively for this matrix. All experiments up to and including #FW99-28 were performed using the identical procedure used for the initial assessment. All of these experiments were at 0.5 mils or 1.0 mils displacement. It was anticipated that the experiments at 1.4 mils displacement would be the most challenging; it was anticipated that these experiments would be susceptible to experimental shutdowns (“kickouts”) due to the combination of relatively large displacement and low bearing loads. This behavior was confirmed on “dummy” specimens. An experimental “fix” required that the amplitude of fretting displacement be ramped up over a 3 second time frame at the beginning of each block of cycles. For the “block cycling” procedure, this was unacceptable since the “displacement ramp up” time would consume about 60% of the total number of fretting cycles (500) in each block. Therefore, a continuous fretting cycling procedure was proposed. A dummy fatigue specimen and fretting pad were thermocoupled. Impinged air-cooling at the fretting interface was applied in the same manner as for the block cycling procedure. The temperature rise during a continuous cycling fretting experiment was monitored and found to be less than 10°F. This was considered to be acceptable; therefore, a continuous cycling procedure was used for all of the fretting tests following experiment #FW99-28. The initial displacement ramp up time of 3 seconds or less to the programmed value is a small fraction of the total fretting cycles in the experiments.

Fretting Test Results

All of the planned “X” and “Y” fretting tests were completed (total of 44 tests). These results are summarized in Table II. The “Z” fretting tests were not done since the Pratt & Whitney simultaneous fret/fatigue test results were not available to establish the number of fretting cycles to use for the “Z” tests.

Results of R=0.5 HCF Tests

Most of the 44 specimens were heat tinted and then HCF tested at R=0.5 as shown in Table 6A.4.

Table 6A.4.

Displacement (mils)	No. of Specimens Fretted	No. of Specimens HCF Tested
0.5	16	9
1.0	12	12
1.4	16	13

A stress range of 48 ksi was used for all experiments, which is the 1E07 smooth bar life for this material. For these HCF experiments, a “runout” life of 2E07 was used before step loading to a stress range of 50.5 ksi. All of these tests were performed at a frequency of 1000 Hz in the GEAE high frequency fatigue system. All specimens were heat tinted prior to the fatigue loading so that any cracks formed during the fretting experiments could be clearly identified. Iterating on the experience from the initial assessment, all fatigue bars were heat tinted at 650F/3 hours. Post-test examination showed that the heat tint was adequate in marking shallow cracks that had been generated from the fretting process. Figures 49 to 82 contain additional photographs and micrographs showing crack nucleation locations for the specimens that were HCF tested. The bar chart in Figure 83 shows the results of the HCF tests.

Specimens Fretted at 1.4 Mils Displacement

All specimens failed at lives less than 200,000 cycles, much less than the 1E07 life that would be expected for a smooth bar at this test condition. All specimens had shallow cracks from the fretting process that ranged from about 0.5 to 4 mils in depth. The most common depth of fretting cracks was from about 2 to 3 mils in depth. The HCF results did not appear to segregate by bearing pressure or number of fretting cycles. As a group, the shot peened bars had slightly longer lives than the bars that were not shot peened.

Specimens Fretted at 1.0 Mils Displacement

There appears to be some segregation in fatigue results by surface condition (shot peened vs. not shot peened). All of the specimens with no shot peening failed at less than 150,000 cycles, much less than the 1E07 life that would be expected for a smooth bar at this test condition. For these specimens, the depth of fretting ranged from about 0.5 to 2 mils. The typical depth was about 1 to 2 mils. The fatigue lives did not appear to segregate with bearing pressure.

Four of the six shot peened bars failed at lives greater than 1E07 cycles. In these four specimens, crack propagation occurred from cracks that were initiated remote from the fretting scar. These fatigue lives were in agreement with the smooth bar baseline HCF behavior. The fatigue lives of the shot peened bars did not segregate with bearing pressure.

These results suggest that small cracks initiated in all of the shot peened specimens. For the four specimens with lives greater than 1E07 cycles, the cracks did not propagate due to the beneficial influence of the shot peened surface.

Specimens Fretted at 0.5 Mils Displacement

For this displacement, the fatigue life of all specimens exceeded 9E06 cycles or ran out. All fatigue initiations were remote from the wear scar. The fatigue behavior was not sensitive to bearing pressure, number of fretting cycles, or surface condition (peened vs not peened). The gage sections were cut from three of the specimens (#70-1,#75-9,#75-10). Each gage section was loaded in 3 point bending so that: a) the wear scar was loaded in tension, and b) loading was beyond the proportional limit (into the plastic region) so that permanent deformation was generated in each gage section. The wear scars were then examined using light microscopy; no fretting cracks were observed. Then, metallographic mounts were prepared for the specimens; the plane of polish was from the edge of the specimen so that the fretting cracking profile in the crack depth direction could be viewed. Two-step polishes were performed. For the first step polish, 70 mils of material was removed during polishing so that the plane of view was well within the fretting contact area. No evidence of fretting cracking was observed in any of the mounts at this plane of polish. For the second step polish, an additional

30 mils of material was removed; again, no evidence of fretting cracking was observed in the mounts.

CONCLUSIONS

1. Edge of contact cracking was observed for specimens fretted at 1.0 mils and 1.4 mils displacement; edge of contact cracking was not observed for specimens fretted at 0.5 mils displacement.
2. Fretting displacement and surface condition had the greatest impact on the subsequent fatigue behavior; bearing stress and number of fretting cycles had little or no influence on the subsequent fatigue behavior.
3. The results suggest that for most of the shot peened bars with 1.0 mil relative displacement, small cracks generated from the fretting did not propagate due to the beneficial influence of the shot peened surface.

LIFE ANALYSIS

Edge of Contact Stress Analysis

The finite element analysis of the edge of contact stresses in the fretting specimens was performed using ANSYS 2D plane strain STIF42 4 node quad elements with point to surface CONTAC48 contact elements. The analysis strategy employed a submodeling methodology developed at Carnegie Melon University by Dr. Glenn Sinclair, et al. to ensure accurate calculation of edge of contact stresses. This method consists of a systematic refinement of the FEM mesh, using three consecutive 2X refinements to assess convergence and selection of submodel boundaries. The submodel boundaries must be sufficiently removed from any unconverged results in order to minimize the propagation of errors from the submodel interface.

Appropriate submodel boundaries are ensured by the use of a displacement convergence criteria, which consists of a comparison of the difference between displacement component values calculated at common nodal locations among the three progressively refined models. The difference between displacements calculated in the coarser model should be larger than that calculated in the finer models, as described by the equation

$$|U_c - U_m| > |U_m - U_f| \quad (6A.1)$$

where subscripts c, m, and f refer to the coarse, medium, and fine discretized FEM models. Displacement boundary conditions applied to the submodel boundaries are obtained by utilizing a cubic spline fit through displacements along common nodal locations from the parent model with the finest discretization. The model mesh size continues to be refined until the change in peak stresses from one mesh size to the next is reduced to a pre-defined level of convergence, which was chosen to be 5% in this case.

This methodology was used to analyze two fret specimen conditions: 55 ksi normal stress with 1.5 mils of tangential sliding, and 35 ksi normal stress with 0.5 mils sliding. The specific fretting test configuration analyzed consisted of a fret shoe with a 0.040-inch flat with 0.120-inch radius to an 11° chamfer. A global mesh beginning with 4.0 mil element sizes was the starting discretion level for both conditions. Submodeling and 2X refinement was performed until stress convergence within 5% was obtained, which occurred at element sizes of 0.0000625-inch or (1/16) mil.

Table 6A.5 lists peak stress results for the progression of mesh sizes for the 55 ksi, 1.5-mil condition. Figure 6A.84 graphically illustrates how each mesh refinement produces a better definition of the sharp tangential stress peak that occurs at the edge of contact.

Crack Nucleation Analysis

The equivalent stress methods described in the HCF-LCF damage state portion of this report were used to predict crack nucleation in the fretting tests. The stress state at the edge of contact is highly multiaxial and has very steep gradients both along the contact plane and perpendicular to it. Examples of this are shown in Figure 6A.85a for the 55 ksi, 1.5 mil displacement fretting experiment, and in Figure 6A.86a for the 35 ksi, 0.5 mil displacement fretting experiment. As the fretting pad moves back and forth (in the x direction), a given position of the fretting specimen moves relative to the fretting pad. As the pad moves to the right, the axial (σ_{xx}) tensile peak is just behind the left side pad and a highly compressive normal stress (σ_{xx}) exists under the right side of the pad as shown in the figures. When the direction of the pad is reversed, the stresses are reversed and the tensile peak occurs on the right side of the pad. Therefore, it is necessary to determine the fatigue cycle associated with the fretting. This was accomplished by comparing the stresses at each position along the fretting specimen

surface with each other point. This evaluation was performed with a version of the code NASALIFE using the methods described in the HCF-LCF damage state (equivalent stress method with Walker mean stress model and modified Manson-McKnight multiaxial parameter). The pair selected as the most damaging pair is shown by the closed triangles in the figures. Figures 6A.85b and 6A.86b shows the variation in the axial and normal stresses (σ_{xx} and σ_{yy} , respectively) associated with this multiaxial fatigue cycle. One of the most interesting discoveries for the analysis in Figure 6A.85 is that it would require the pad to slide only 0.125 mils to capture the most damaging points in the cycle. This minimizes the possibility of the fretting displacement affecting the stress pairs to be used in a damage assessment. It also suggests that this approach is very applicable to the partial slip situation experienced in engine hardware and also the Purdue fretting fatigue experiments.

The magnitude of the fretting displacement will significantly change the highly stressed surface area in the fretting experiments. This was considered using a Weibull adjusted equivalent stress method. The details of this method can be found in the HCF/LCF appendix. Figure 6A.87 shows the values of the Weibull adjusted equivalent stress method for several values of Weibull modulus. The lines in the chart represent the average, the +3s, and the -3s equivalent stress for 400,000 cycles from smooth bar data (400,000 cycles was the number of fretting cycles used for the majority of the fretting experiments). The value of equivalent stress without Weibull corrections is above the average life value for both fretting conditions. When the stressed area concept is taken into account, the values of the Weibull adjusted equivalent stress for the 0.5 mil displacement test is close to the fatigue minimum. For the 1.4-mil displacement condition, the equivalent stress value without Weibull adjustment is near the +3s smooth bar value. For two of the three Weibull moduli, the adjusted equivalent stress is a little greater than the smooth bar average value. Therefore, it is not surprising that cracks initiated for this fretting condition. This method correlates reasonably well for the two conditions modeled. This method has the characteristic of considering the local stresses through the equivalent stress methods. Also, it should be noted that this method explicitly considers the magnitude of fretting displacement. The magnitude of fretting displacement has been shown to be a key variable here, and by others [Ruiz].

Crack Propagation Analysis

GEAE has modeled the growth of fretting cracks using conventional LEFM analysis. This analysis has used the crack dimensions measured from the heat tints observed during post-test fractography. The fracture mechanics analysis used the crack growth curve and mean stress Walker exponent previously reported in the HCF/LCF damage state section. These crack dimensions are shown in Figure 6A.88 along with fracture mechanics predictions of the crack sizes which would result in lives of 48,000 and 130,000 cycles. As shown in Figure 6A.83, these lives are typical of the unpeened lives of tests with 1.4 mils and 1.0 mils displacement, respectively. Also shown in Figure 6A.88 are lines representing the threshold condition for peened and unpeened surfaces. The peening predictions were made with a Ti 6-4 shot peen fracture mechanics model created at GEAE prior to this contract and made available for interpretation of this data.

The crack sizes observed for the shorter life conditions (1.0-mil unpeened, 1.4-mil both peened and unpeened) agree fairly well with the fracture mechanics predictions. One of the most interesting points is that the 1.0-mil unpeened condition fell on the prediction curve, which is based on the PRDA V Ti6-4 threshold value. The trend line for the threshold including the effect of shot peening is above the observed crack size. This suggests that fretting can nucleate cracks that will not grow if the applied stress intensity is less than the fracture mechanics threshold. This type of fracture mechanics evaluation must take credit for the beneficial effect of shot peening.

This fracture mechanics evaluation has: a) shown the capability of accurately treating the behavior of physically short cracks, b) properly includes the effect of surface treatment, and c) is supportive of the design methodology in the proposed fretting design system.

REFERENCES

1. Hunter, D.T., "Fretting Testing at P&W", PRDA Fretting Review Meeting, December 1997.

Table 6A.5
Fretting Test Data for Initial Assessment

	Friction	Target	Actual	Fatigue Bar Wear			Shoe Wear			Fatigue Bar	Shoe	Total	Deepest	Average	Total
	Mean	Displacement	Relative	Avg.	Deepest	Highest	Avg.	Deepest	Highest	Weight	Weight	Weight	Pit	Humidity	Sliding
	μ	(mils)	Capacitance (mils)	(mils)	Pit (mils)	Peak (mils)	(mils)	Pit (mils)	Peak (mils)	(gm)	(gm)	(gm)	(mils)	%	(ft)
			1.50												
			*****Setup Tests*****												
			1.40									0.0000	0.0		61.7
	1.07	1.5	1.48	0.1	-0.2	0.4	0.1	-0.2	0.5	0.0006	0.0003	0.0009	-0.4	8.0	221.4
	0.42	1.5	1.45	0.1	-0.3	0.6	-0.06	-0.1	0.2	-0.0002	-0.0021	-0.0023	-0.4		4.5
	0.26	3.0	3.00	0.4	0.0	0.8	0.1	-0.3	0.6	-0.0006	-0.0003	-0.0009	-0.3	40.0	451.0
	0.17	0.8	0.80	0.3	-0.1	0.3	0.1	-0.1	0.1	-0.0004	-0.0003	-0.0007	0.2	23.0	125.0
	0.38	1.5	1.50	0.1	-0.1	0.5	0.2	0.0	0.3	0.0007	0.0001	0.0008	0.5	10.0	225.0
	0.49	2.0	2.00	0.3	0.2	0.6	0.3	-0.5	0.5	0.0002	0.0004	0.0006	-0.3	40.0	297.3
	0.44	2.0	2.00	0.3	0.0	0.7	0.5	-0.1	0.9	0.0000	0.0001	0.0001	0.6	35.0	299.5
	0.11	0.8	0.79	-0.1	-0.3	0.0	0.0	-0.1	0.0	0.0003	0.0001	0.0004	-0.1	48.0	118.2
	0.19	1.5	1.60	0.0	-0.1	0.1	0.0	-0.1	0.0	0.0002	0.0002	0.0004	0.0	30.0	240.7
	0.19	1.5	1.50	0.0	0.0	0.0	0.0	0.0	0.0	0.0001	-0.0001	0.0000	0.0	22.0	61.8
	0.23	2.0	1.96	0.1	-0.1	0.1	0.1	0.0	0.2	0.0000	0.0004	0.0004	0.1	49.0	294.2
	0.37	3.0	2.96	0.1	-0.1	0.4	0.4	0.3	0.7	0.0004	0.0003	0.0007	0.7	48.0	444.2
	0.41	3.0	2.97	0.2	0.1	0.4	0.2	0.1	0.4	0.0003	0.0003	0.0006	0.5	45.0	445.0
	0.08	0.8	0.73	0.1	0.0	0.2	0.0	0.0	0.2	0.0001	0.0000	0.0001	0.0	22.0	30.1
	0.14	0.8	0.90	0.2	0.2	0.4	0.3	0.2	0.3	-0.0008	-0.0006	-0.0014	0.4	25.0	131.4
	0.13	0.8	0.80	0.1	0.0	0.3	-0.1	-0.1	-0.1	0.0001	0.0002	0.0003	-0.1	42.0	126.8
	0.33	3.0	3.00	0.0	-0.1	0.1	0.1	-0.1	0.1	0.0000	0.0000	0.0000	-0.2	45.0	446.0
	0.25	3.0	3.00	0.2	-0.1	1.0	0.0	-0.2	0.4	0.0000	0.0002	0.0002	-0.3	25.0	450.2
	0.25	3.0	3.00	0.3	-0.1	1.5	0.1	-0.2	0.2	-0.0027	-0.0003	-0.0030	-0.3	25.0	448.4
	0.25	3.0	3.20	-0.1	-0.4	0.5	0.0	-0.3	0.3	0.0003	-0.0002	0.0001	-0.7	30.0	473.8
	0.28	3.0	2.90	0.1	-0.1	0.2	0.2	-0.3	0.0	-0.0069	0.0001	-0.0068	-0.4	42.0	427.7
	0.32	3.0	3.00	0.0	-0.1	0.1	0.0	-0.1	0.0	-0.0030	-0.0003	-0.0033	-0.2	30.0	1829.4
	0.28	3.0	2.90	0.2	0.1	0.3	-0.1	-0.2	-0.1	0.0001	0.0001	0.0002	-0.1	22.0	119.7
	0.45	1.5	1.40	0.8	0.5	1.2	0.2	-0.1	0.4	0.0003	-0.0002	0.0001	0.4	15.0	204.0
	0.38	1.5	1.41	0.0	-0.3	0.5	0.4	0.2	0.4	0.0001	0.0002	0.0003	-0.1	40.0	212.0
	0.46	3.0	3.10	-1.8	-1.8	-1.6	-0.8	-1.0	-0.6	-0.0015	-0.0014	-0.0029	-2.8	42.0	466.1
	0.40	3.0	3.13	-1.1	-1.4	-0.7	-2.3	-2.9	-1.3	-0.0015	-0.0021	-0.0036	-4.3	45.0	469.6
	0.11	0.8	0.86	0.0	0.0	0.0	0.0	-0.1	0.1	0.0005	0.0000	0.0005	-0.1	95.0	128.4
	0.15	0.8	0.78	-0.1	-0.3	0.0	-0.2	-0.2	-0.1	0.0000	0.0001	0.0001	-0.5	18.0	116.4
	0.16	0.8	0.79	0.0	-0.1	0.0	-0.1	-0.2	-0.1	0.0007	0.0003	0.001	-0.3	22.0	117.8
	0.57	3.0	2.93	-0.1	-0.1	0.0	0.1	0.0	0.2	0.0002	0.0001	0.0003	-0.1	32.0	439.7
	0.68	1.5	1.46	-0.1	-0.1	0.0	0.1	0.0	0.4	-0.0006	-0.0004	-0.0010	-0.1	22.0	219.6
	0.18	0.8	0.80	-0.2	-0.2	0.0	0.0	-0.1	0.0	0.0003	0.0000	0.0003	-0.3	28.0	121.0
	0.39	1.5	1.58	0.0	0.1	0.0	0.0	0.0	0.0	0.0004	0.0004	0.0008	0.1	40.0	247.8

6A-15

Table 6A.5 (Cont'd.)
Fretting Test Data for Initial Assessment.

Bearing stress (ksi)	T/N	FW#	Test type	#fret cycles	Displacement (mils)	Shot peened?	Fatigue specimen	Fretting shoe	Load (lbs)	Friction mean μ	Fatigue life
35	37	99-15	X	400K	0.5	N	75-9	160-92	199.7	0.24	2.00E+07
35	44	99-22	X	400K	0.5	N	76-13	190-54	173.8	0.28	
35	78	99-57	X	400K	0.5	Y	70-1	190-46	173.8	0.34	2.00E+07
35	79	99-58	X	400K	0.5	Y	76-12	160-105	173.8	0.36	
35	42	99-20	Y	40 K	0.5	N	79-12	160-96	173.8	0.26	
35	77	99-56	Y	40 K	0.5	Y	70-12	160-97	173.8	0.34	
50	41	99-19	X	400K	0.5	N	85-14	160-94	248.3	0.2	
50	43	99-21	X	400K	0.5	N	85-15	190-56	248.3	0.22	2.00E+07
50	81	99-60	X	400K	0.5	Y	70-2	190-53	248.3	0.27	<2.0E07
50	82	99-61	X	400K	0.5	Y	79-1	160-101	248.3	0.27	
Vary	N/A	99-14	SETUP	N/A	Vary	N	79-3	191-8	All	SETUP	
65	38	99-16	X	400K	0.5	N	75-10	160-90	323	0.18	11793202
65	40	99-18	X	400K	0.5	N	79-13	190-52	323	0.17	
65	74	99-53	X	400K	0.5	Y	70-4	190-43	323	0.21	15112986
65	75	99-54	X	400K	0.5	Y	79-5	160-98	323	0.21	9613823
65	39	99-17	Y	40 K	0.5	N	94-11	190-50	323	0.18	16591746
65	76	99-55	Y	40 K	0.5	Y	48-8	190-61	323	0.19	19776669

Table 6A.6.

Fretting data and subsequent fatigue data for down-selected fretting parameters.

Bearing stress (ksi)										Friction	
	T/N	FW#	Test type	# fret cycles	Displacement (mils)	Shot peened?	Fatigue specimen	Fretting shoe	Load (lbs)	mean μ	Fatigue life
35	47	99-25	X	400K	1.0	N	75-14	160-72	173.8	0.67	129364
35	48	99-26	X	400K	1.0	N	79-15	190-49	173.8	0.67	137382
35	68	99-47	X	400K	1.0	Y	70-7	190-45	173.8	0.69	529242
35	69	99-48	X	400K	1.0	Y	99-2	162-87	173.8	0.65	11892109
50	46	99-24	X	400K	1.0	N	75-15	162-71	248.3	0.55	135570
50	49	99-27	X	400K	1.0	N	94-8	190-51	248.3	0.49	146065
50	70	99-49	X	400K	1.0	Y	70-10	190-55	248.3	0.51	13170474
50	71	99-50	X	400K	1.0	Y	48-11	190-57	248.3	0.53	14153450
65	45	99-23	X	400K	1.0	N	79-14	162-80	323	0.38	122612
65	50	99-28	X	400K	1.0	N	75-7	162-86	323	0.39	119066
65	72	99-51	X	400K	1.0	Y	70-11	190-60	323	0.39	11550000
65	73	99-52	X	400K	1.0	Y	48-9	190-58	323	0.4	741272

Table 6A.6 (Cont'd.)

Fretting data and subsequent fatigue data for down-selected fretting parameters.

Bearing stress (ksi)	T/N	FW#	Test type	# fret cycles	Displacement (mils)	Shot peened?	Fatigue specimen	Fretting shoe	Load (lbs)	Friction mean μ	Fatigue life
35	54	99-33	X	5,850k	1.4	N	48-13	160-103	173.8	N/A	55302
35	57	99-36	X	400K	1.4	N	70-3	162-68	173.8	0.89	45617
35	55	99-34	X	400K	1.4	Y	75-2	162-66	173.8	0.86	80320
35	56	99-35	X	400K	1.4	Y	70-13	162-69	173.8	0.87	
35	80	99-59	Y	48K	1.4	N	85-13	190-63	173.8	N/A	
35	53	99-31/32	Y	41K	1.4	N	76-4	160-95	173.8	0.83	35000
35	52	99-30	Y	40 K	1.4	Y	99-3	162-79	173.8	N/A	75751
50	62	99-41	X	400K	1.4	N	48-14	190-59	248.3	0.69	49840
50	63	99-42	X	400K	1.4	N	70-5	190-41	248.3	0.7	44588
50	64	99-43	X	400K	1.4	Y	76-3	162-75	248.3	0.67	173135
50	65	99-44	X	400K	1.4	Y	85-12	162-88	248.3	0.66	
vary	999	99-99	X	400Ksetup test	1.5	N	70-6	160-102 / 190-44	323		
65	58	99-37	X	400K	1.4	N	48-15	162-67	323	0.59	45830
65	67	99-46	X	400K	1.4	N	79-11	160-104	323	0.58	57029
65	61	99-40	X	400K	1.4	Y	76-5	162-76	323	0.6	114302
65	60	99-39	X	400K	1.4	Y	94-13	162-70	323	0.57	
65	59	99-38	Y	40 K	1.4	N	70-8	162-73	323	0.55	56731
65	66	99-45	Y	40 K	1.4	Y	48-12	162-77	323	0.56	133222

Table 6A.7.

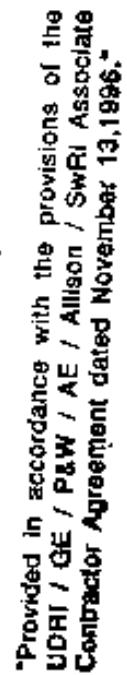
Peak Stress Values and Locations for each Mesh Size at 55 ksi
Normal (Y) Stress with 1.5 mils of Tangential (X) Sliding

	Elem Size	SX				SY			
		MAX	LOC	MIN	LOC	MAX	LOC	MIN	LOC
GlobalB	0.004	35095.4	-0.028	-74378.4	0.024	285.9	-0.032	-68120.4	0.020
% DIFF		28.19%		31.07%				24.18%	
GlobalC	0.002	48871.8	-0.024	-107896.5	0.024	1296.2	-0.024	-89840.2	0.022
% DIFF		19.34%		18.15%				6.17%	
GlobalM	0.001	60591.8	-0.023	-131821.2	0.023	1102.2	-0.023	-95747.8	0.022
% DIFF		15.79%		9.75%				5.58%	
GlobalF	0.0005	71949.1	-0.022	-146069.3	0.0235	300.9	-0.023	-101403.0	0.0225
% DIFF		0.19%		0.47%				0.57%	
SubC	0.0005	72089.3	-0.0225	-146763.3	0.0235	446.9	-0.0225	-101986.3	0.0225
% DIFF		13.26%		2.62%				1.73%	
SubM	0.00025	83113.8	-0.022	-150718.5	0.02375	324.2	-0.02225	-103784.3	0.02225
% DIFF		9.32%		0.77%				0.94%	
SubF	0.000125	91656.5	-0.022	-151880.6	0.02375	255.6	-0.02225	-104766.8	0.022375
% DIFF		4.76%		1.11%				1.90%	
SubSubC	6.25E-05	96236.0	-0.02194	-153590.0	0.02375	627.5	-0.022	-106800.0	0.022375

	Elem Size	SZ				SXY			
		MAX	LOC	MIN	LOC	MAX	LOC	MIN	LOC
GlobalB	0.004	10998.7	-0.028	-42952.3	0.020	22730.7	0.024	-1521.1	-0.024
% DIFF		30.66%		28.21%		27.38%			
GlobalC	0.002	15861.1	-0.024	-59833.6	0.022	31303.0	0.024	-1401.2	-0.022
% DIFF		18.68%		16.59%		10.36%			
GlobalM	0.001	19505.2	-0.023	-71731.7	0.023	34919.8	0.024	-510.9	-0.022
% DIFF		13.25%		4.65%		3.08%			
GlobalF	0.0005	22483.9	-0.0225	-75227.5	0.023	36029.3	0.0225	-10.8	0.0475
% DIFF		1.96%		0.52%		0.65%			
SubC	0.0005	22933.1	-0.0225	-75617.2	0.023	36266.5	0.023	392.7	-0.022
% DIFF		10.19%		1.73%		6.64%			
SubM	0.00025	25536.4	-0.02225	-76948.8	0.02325	38845.0	0.02275	282.5	-0.028
% DIFF		11.17%		0.70%		4.31%			
SubF	0.000125	28747.8	-0.022	-77492.9	0.023125	40592.8	0.0225	146.6	-0.028
% DIFF		3.62%		1.27%		3.43%			
SubSubC	6.25E-05	29827.0	-0.022	-78489.0	0.023125	42033.0	0.022438	70.2	-0.02787



Figure 6A.1. Fretting apparatus.



6A-21

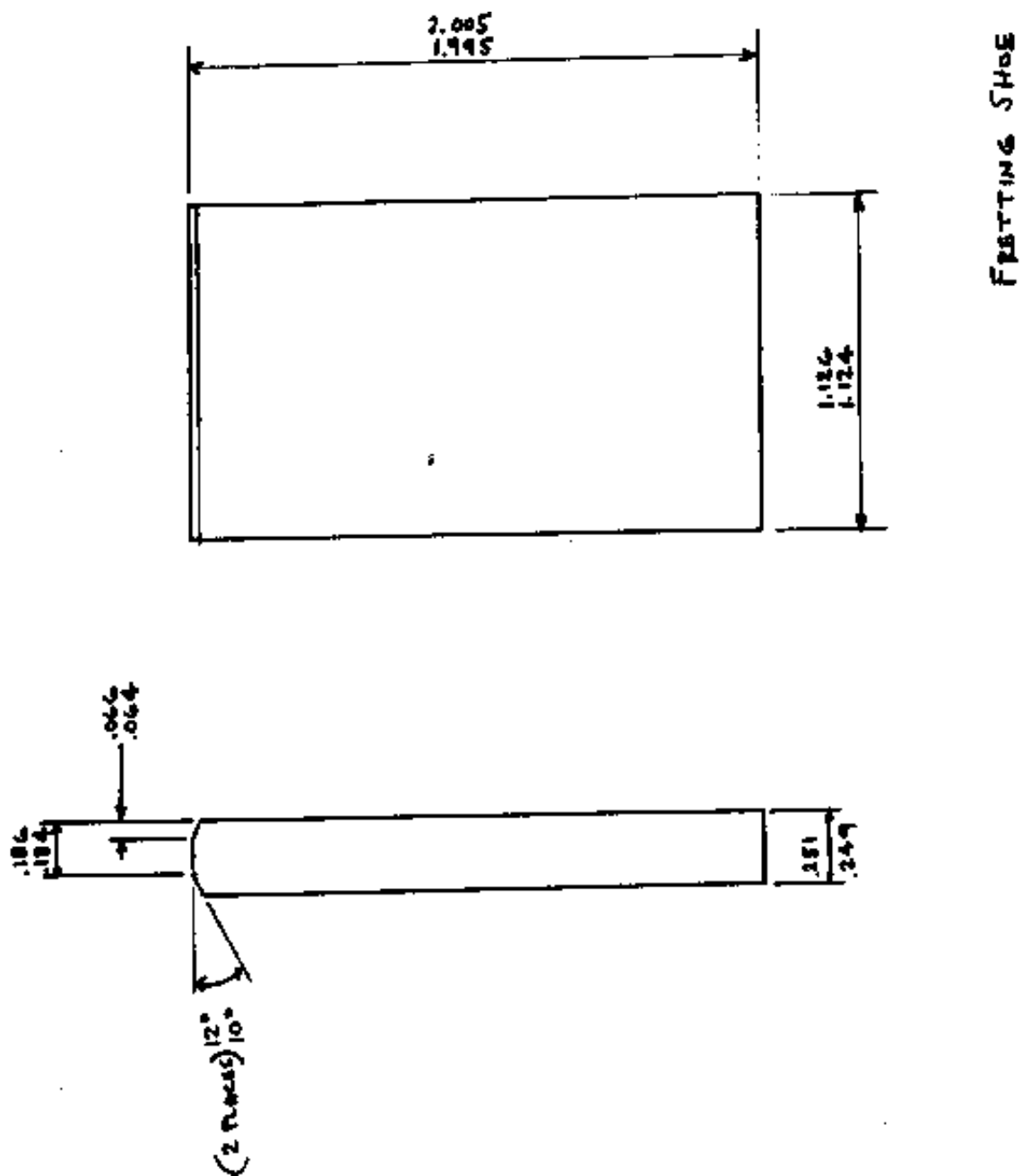
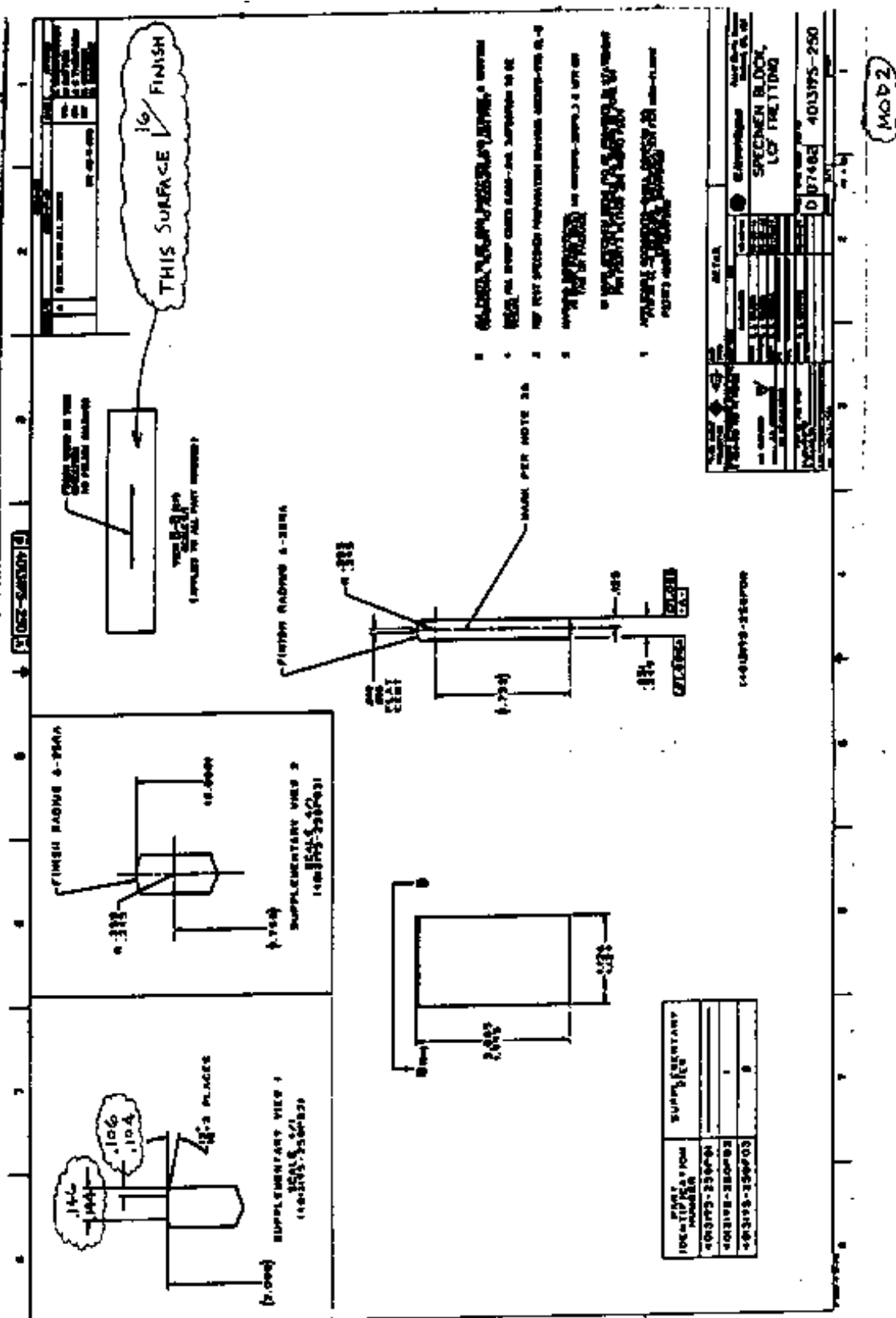
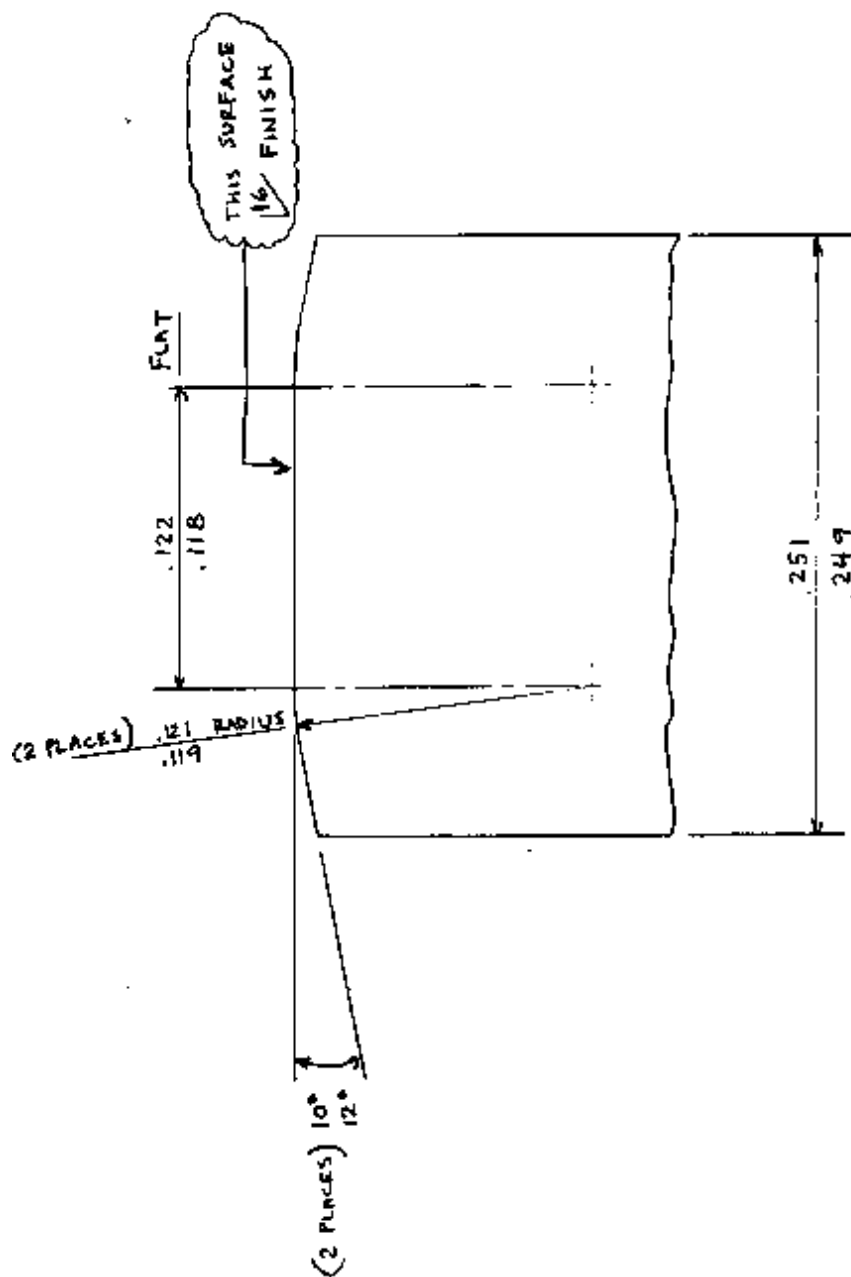


Figure 6A.3. Fretting pad – 120 mil flat with chamfer (Dimensions in inches).

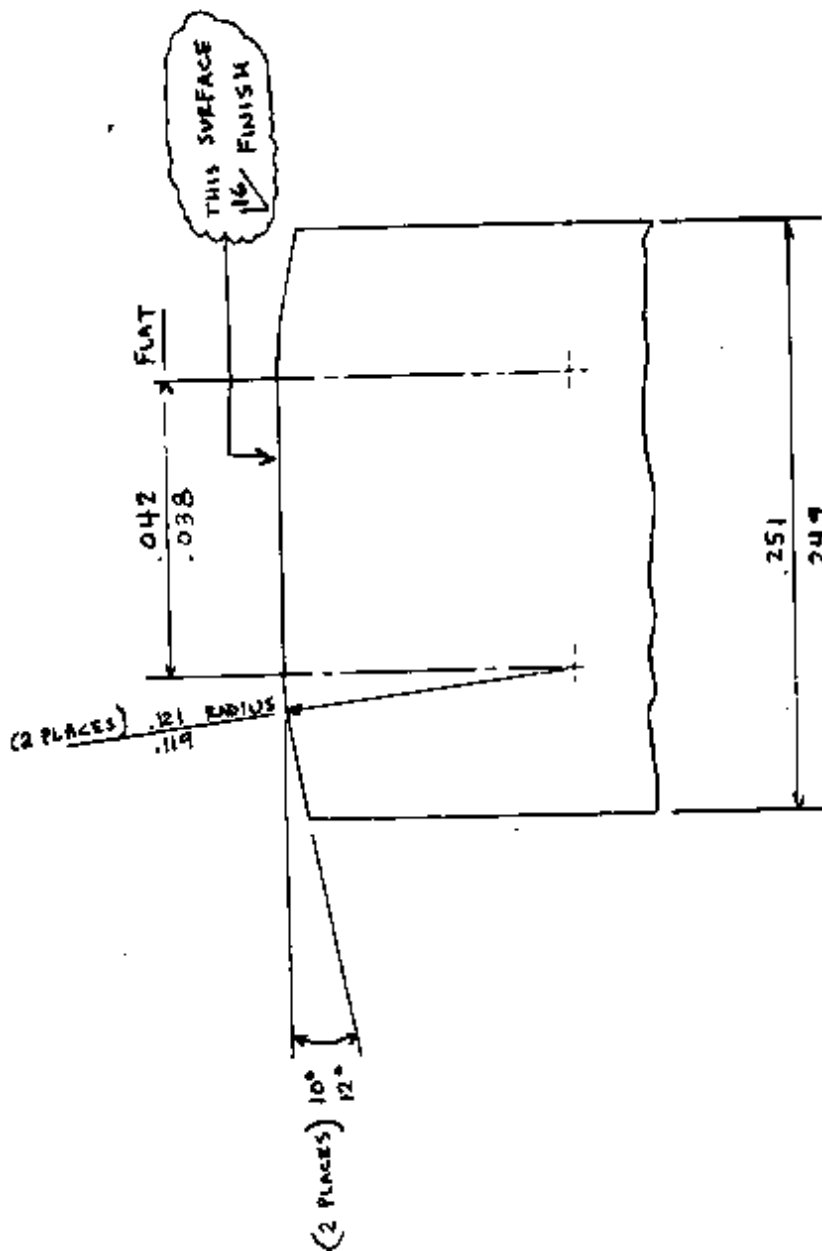




ALL OTHER REQUIREMENTS &
DIMENSIONS PER 4013195-250

4013195-250 MOD 3

Figure 6A.5. Fretting pad – 120-mil flat with a 120-mil radius (Dimensions in inches).



ALL OTHER REQUIREMENTS &
DIMENSIONS PER 4013195-250

4013195-250 MOD 4

Figure 6A.6. Fretting pad – 40-mil flat with 120-mil radius (Dimensions in inches).

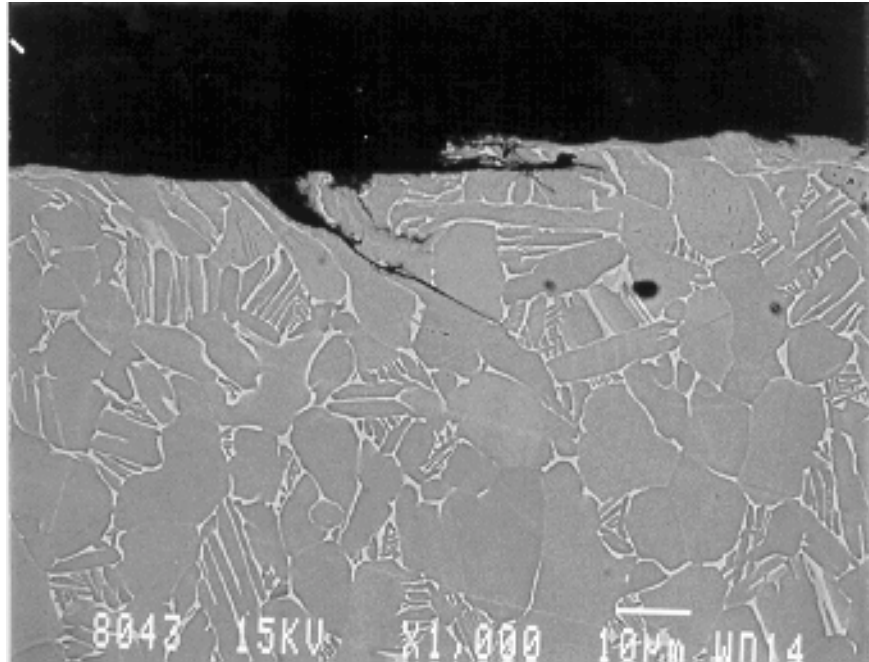


Figure 6A.7. Cracking in fretting pad #191-11.

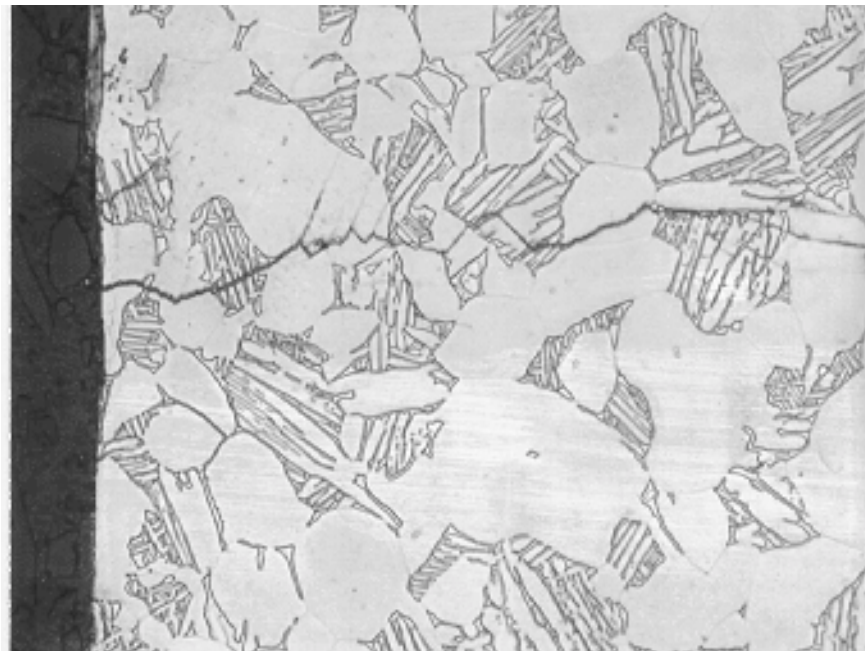


Figure 6A.8. Cracking in specimen #85-3.

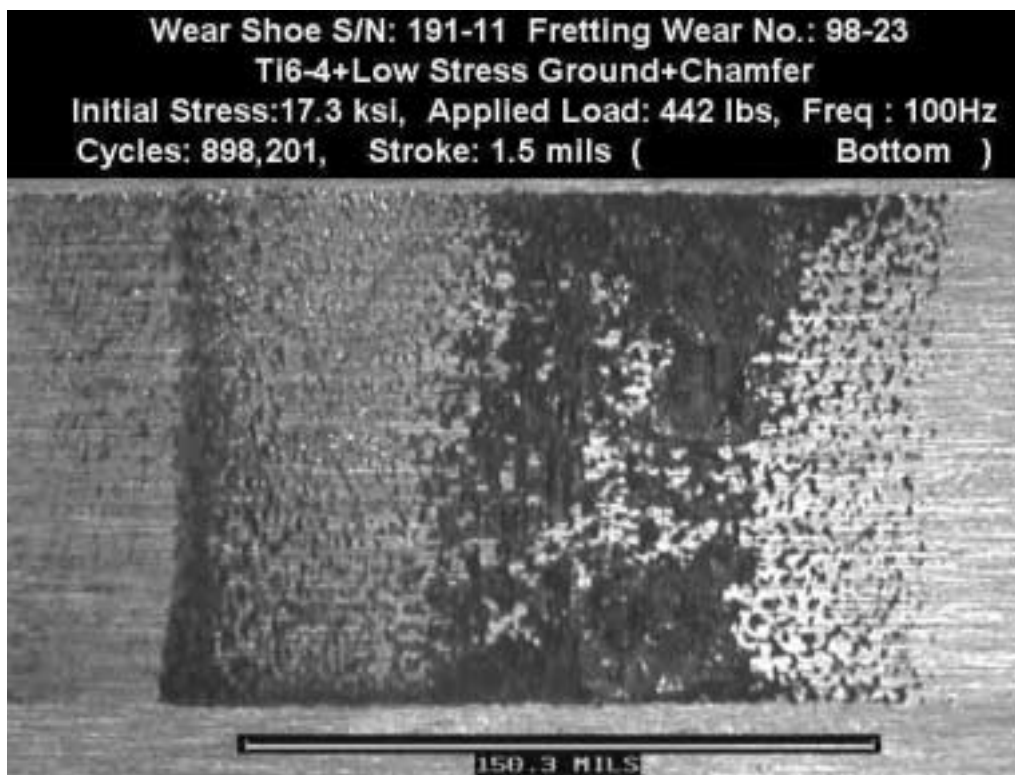


Figure 6A.9. Fretting test FW98-23. 17 ksi, 1.5 mils, 900K cycles.

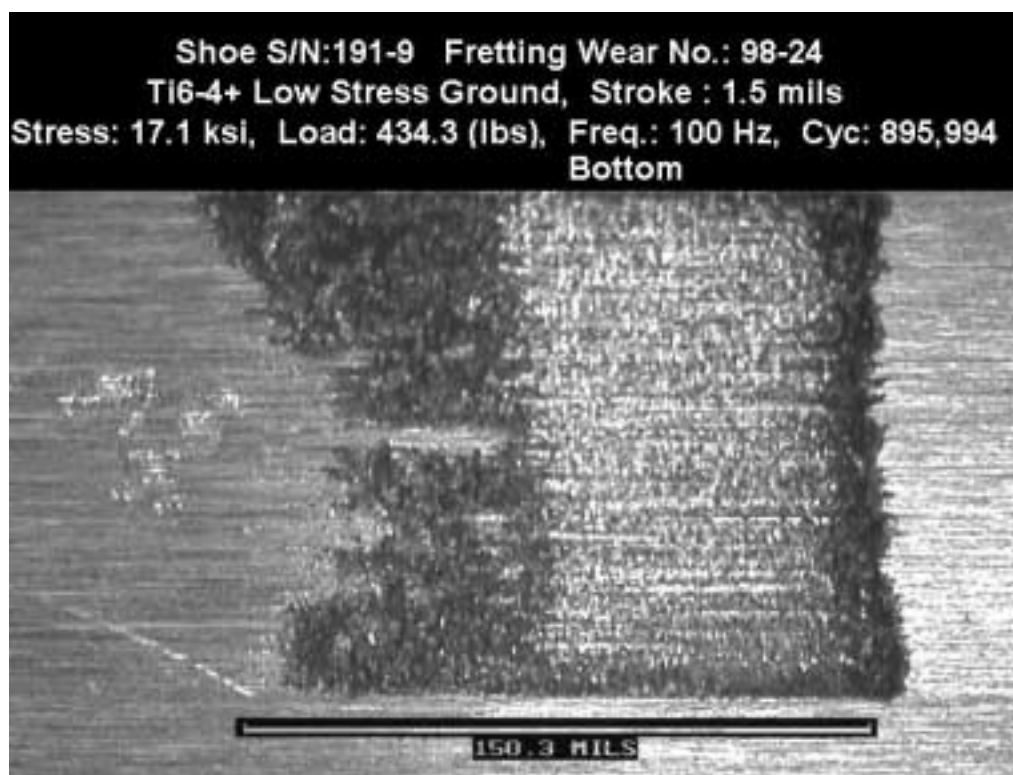
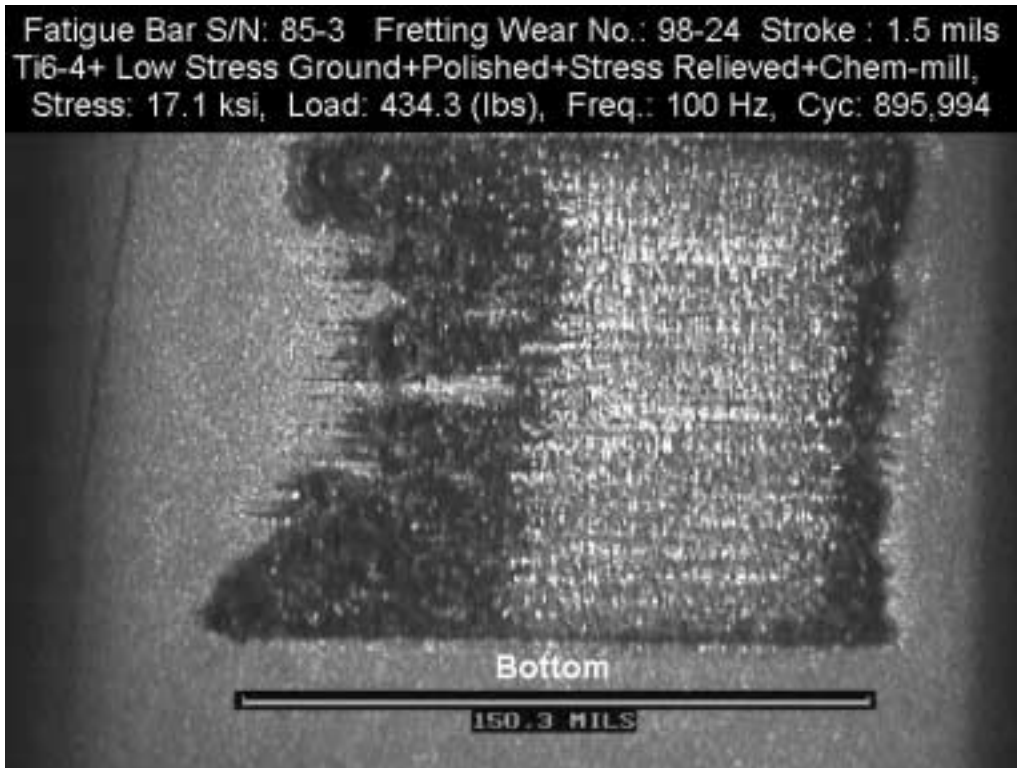


Figure 6A.10. Fretting test FW98-24. 17 ksi, 1.5 mils, 900K cycles.

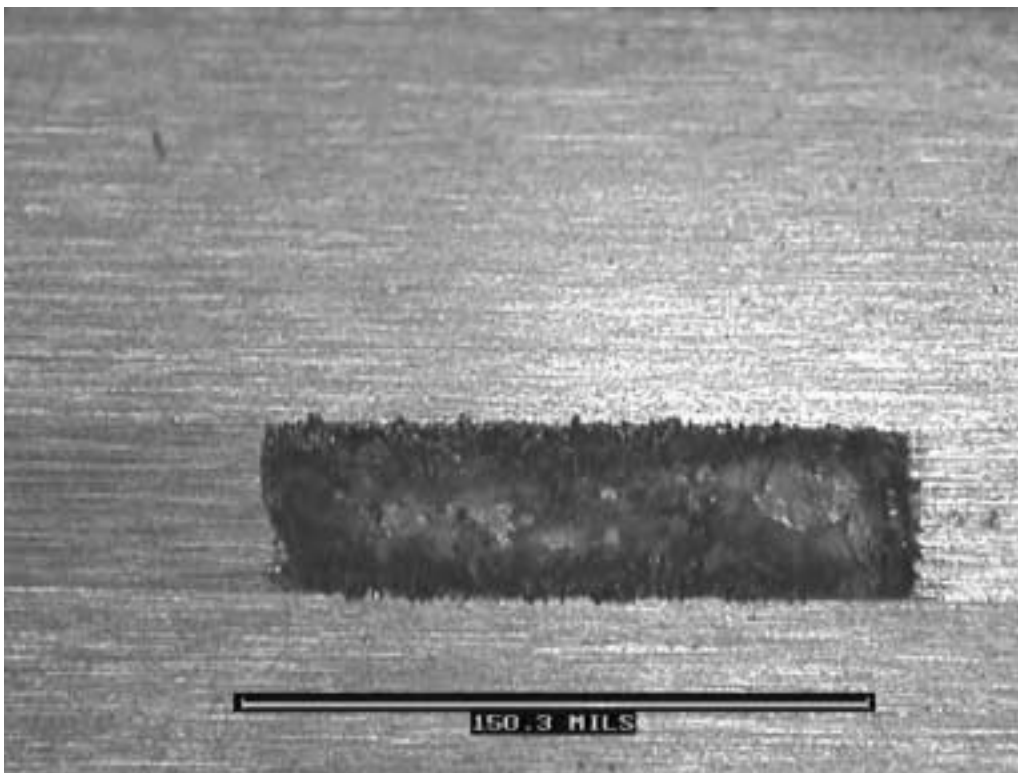
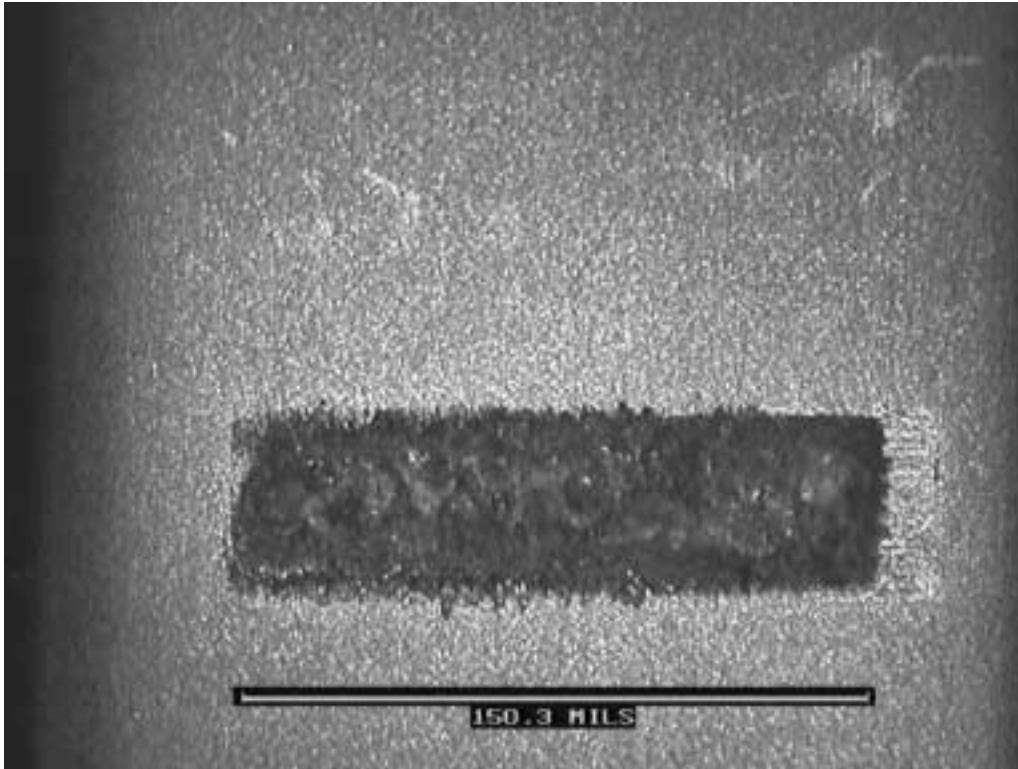


Figure 6A.11. Fretting test FW98-25. 17 ksi, 1.5 mils, 900K cycles.

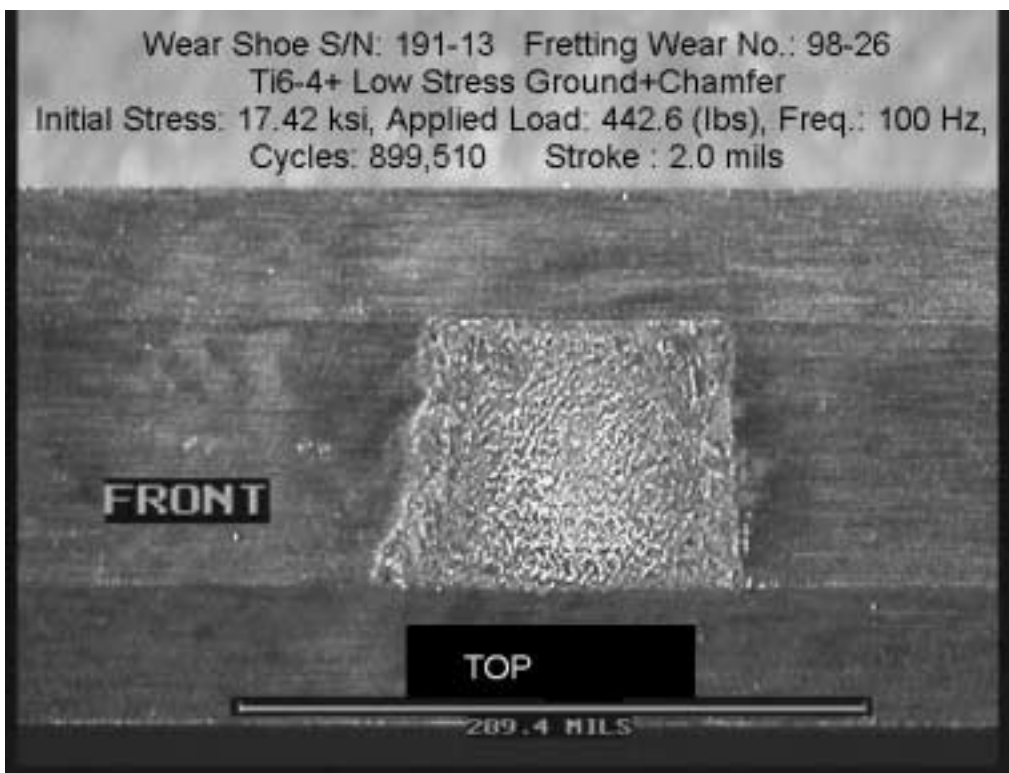
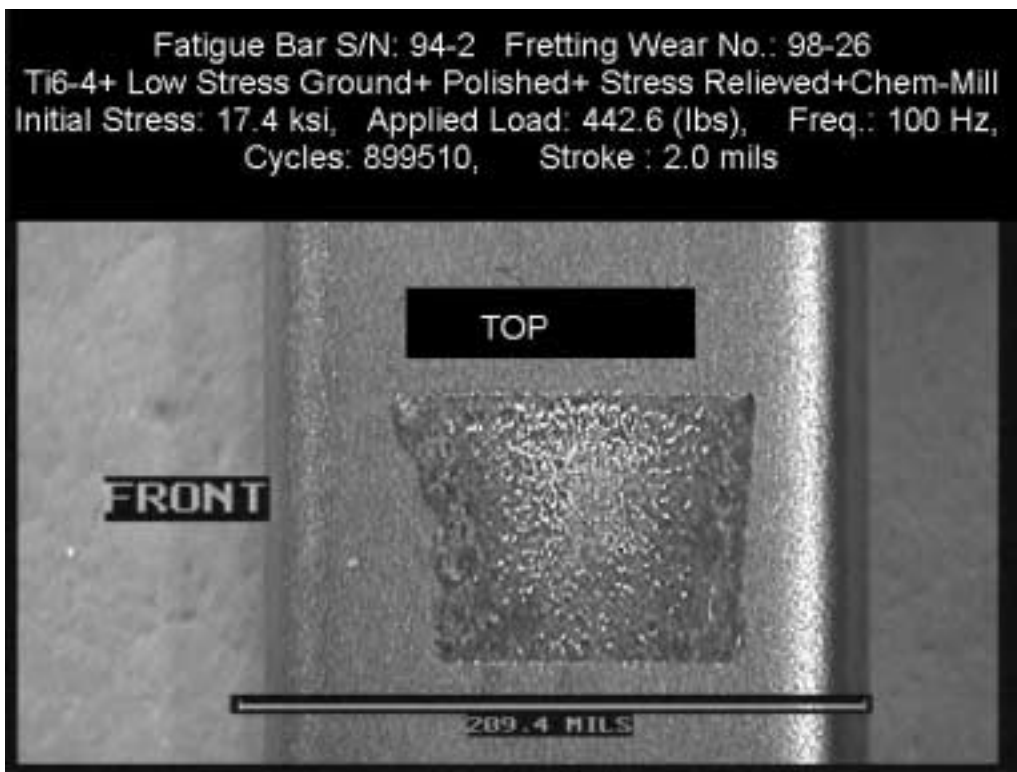


Figure 6A.12. Fretting test FW98-26. 17 ksi, 2.0 mils, 900K cycles.

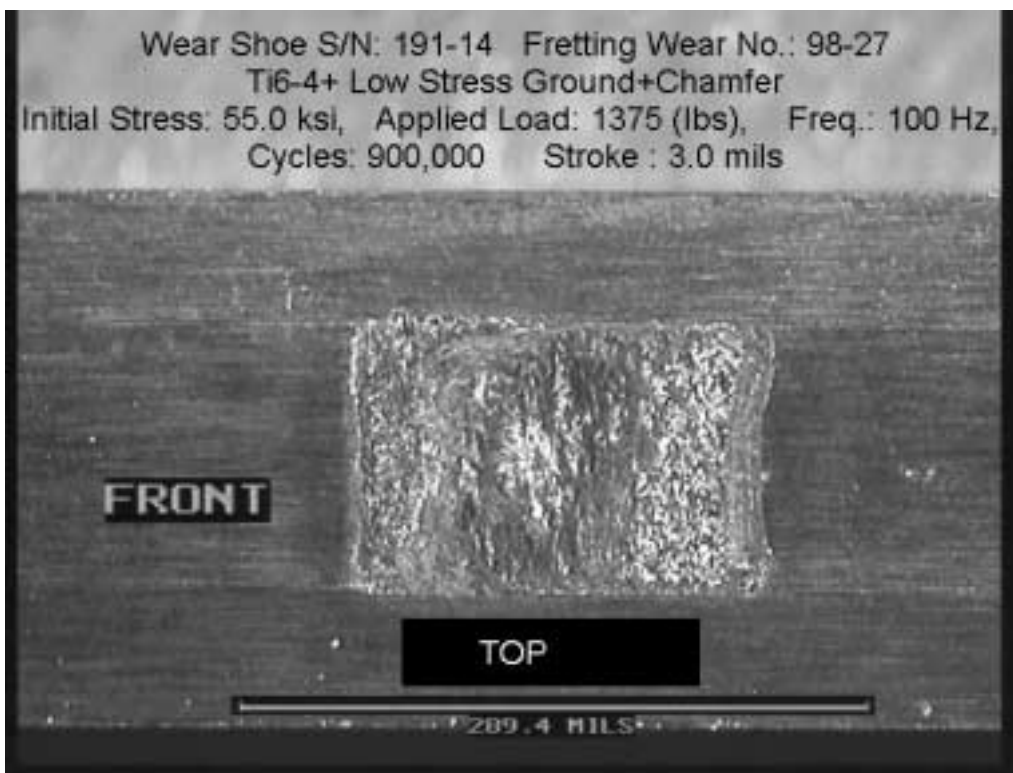
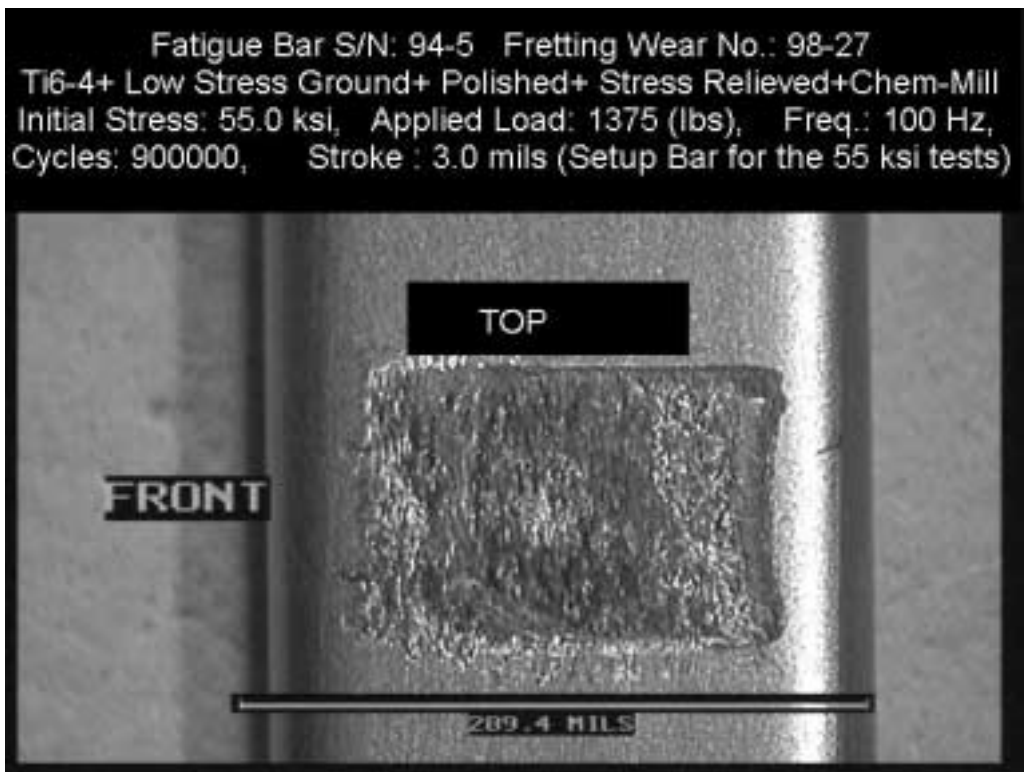


Figure 6A.13. Fretting test FW98-27. 55 ksi, 3.0 mils, 900K cycles.

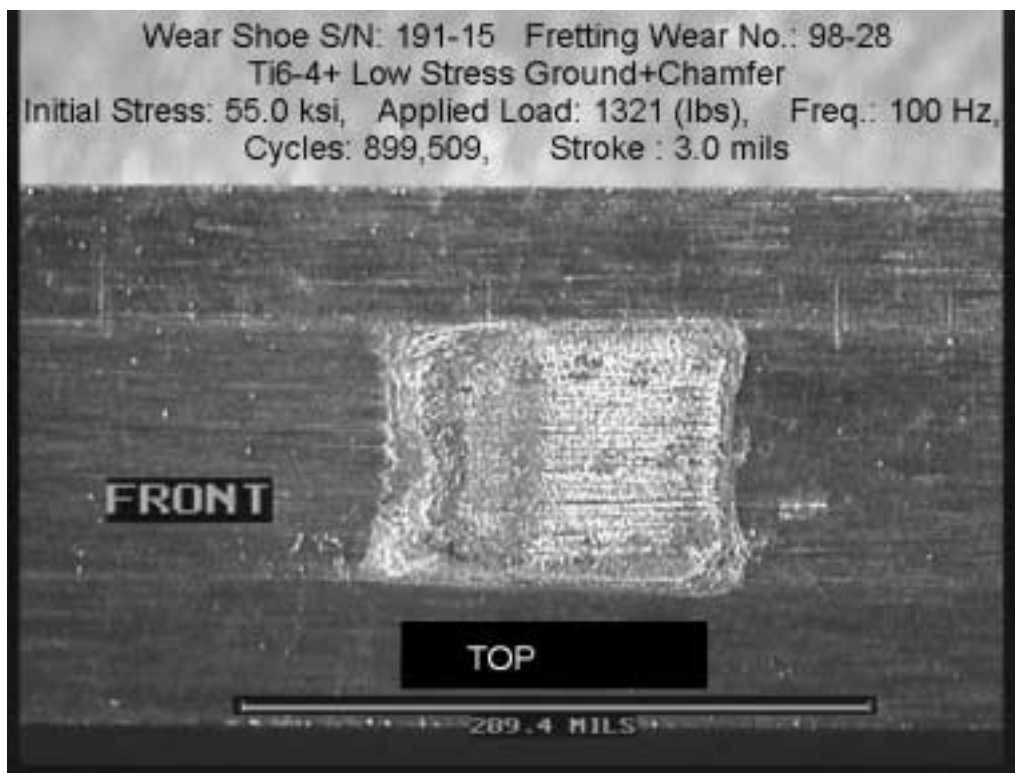


Figure 6A.14. Fretting test FW98-28. 55 ksi, 3.0 mils, 900K cycles.

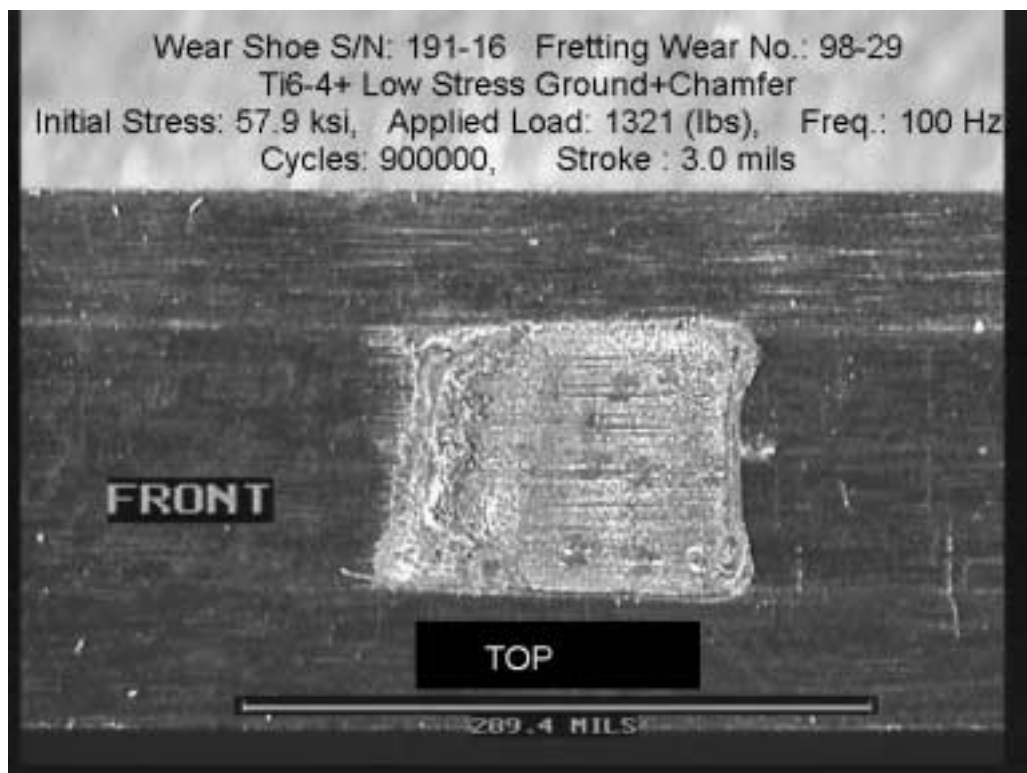


Figure 6A.15. Fretting test FW98-29. 55 ksi, 3.0 mils, 900K cycles.

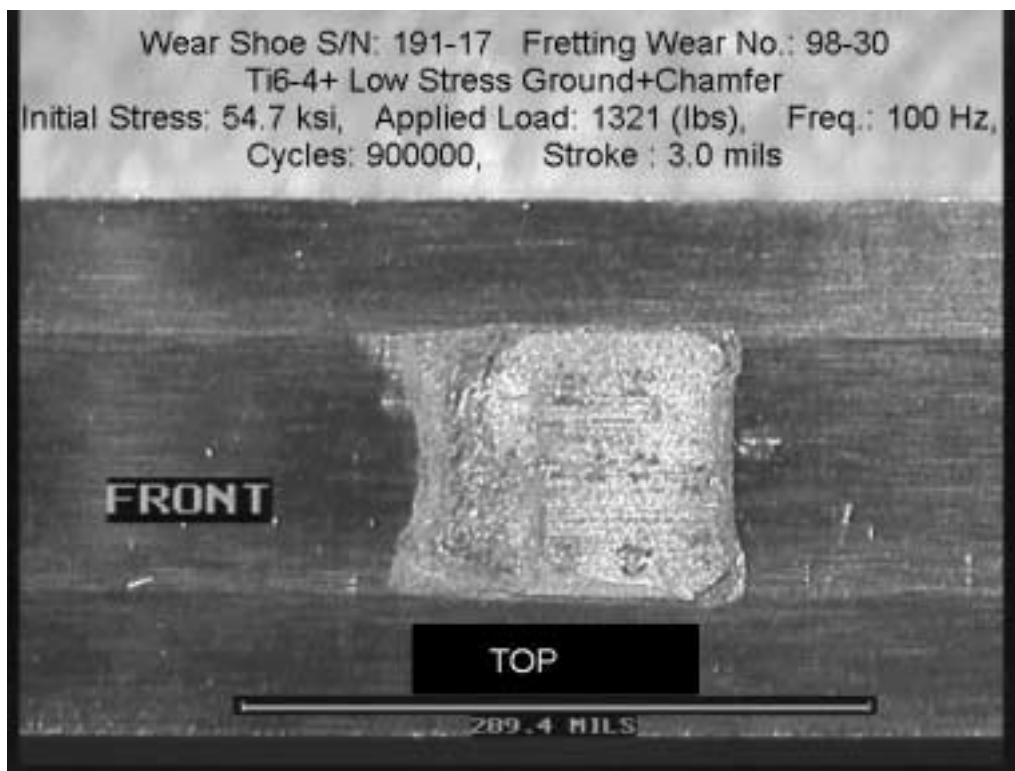
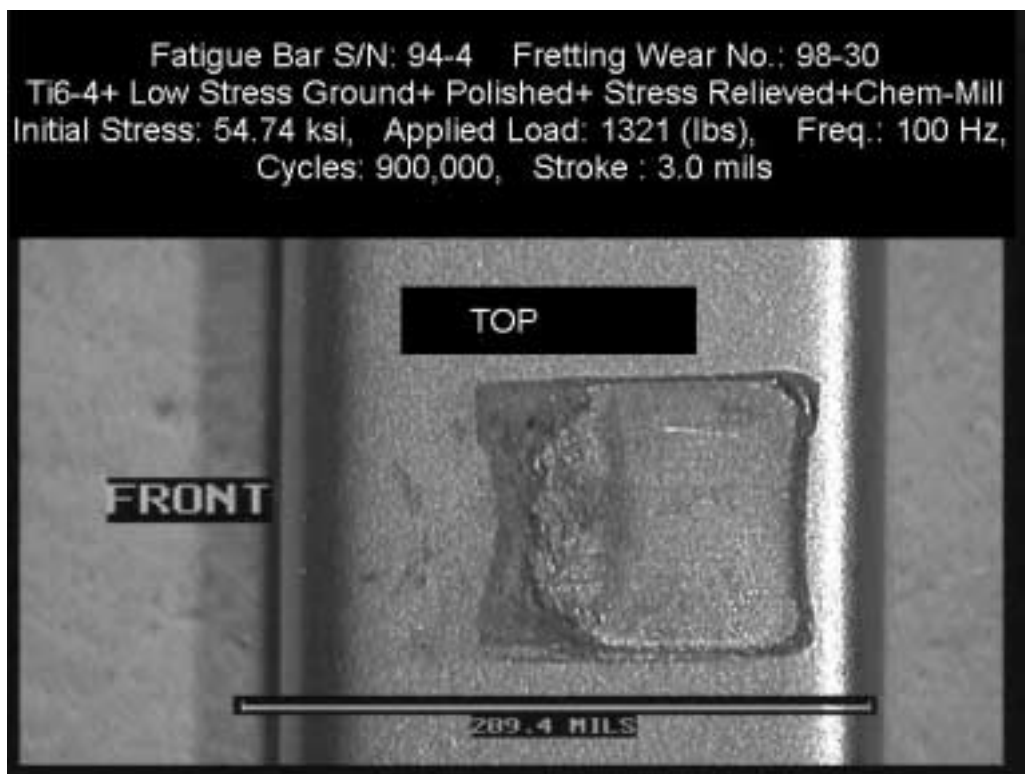


Figure 6A.16. Fretting test FW98-30. 55 ksi, 3.0 mils, 900K cycles.

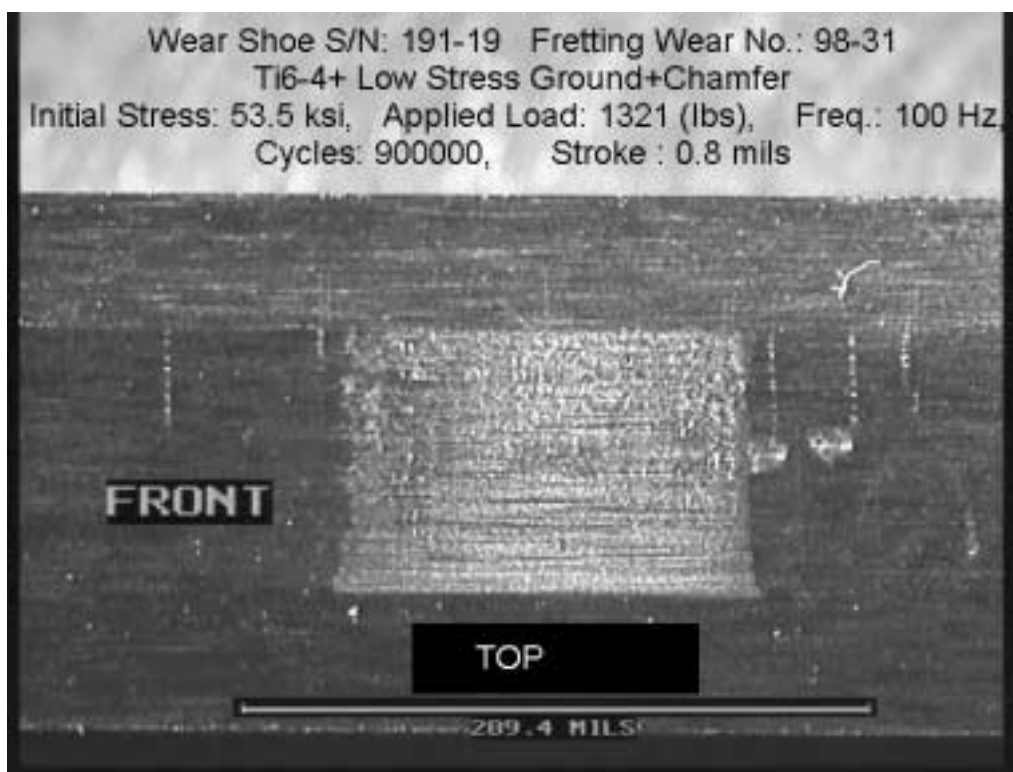


Figure 6A.17. Fretting test FW98-31. 55 ksi, 0.8 mils, 900K cycles.



Figure 6A.18. Fretting test FW98-32. 55 ksi, 3.0 mils, 900K cycles.

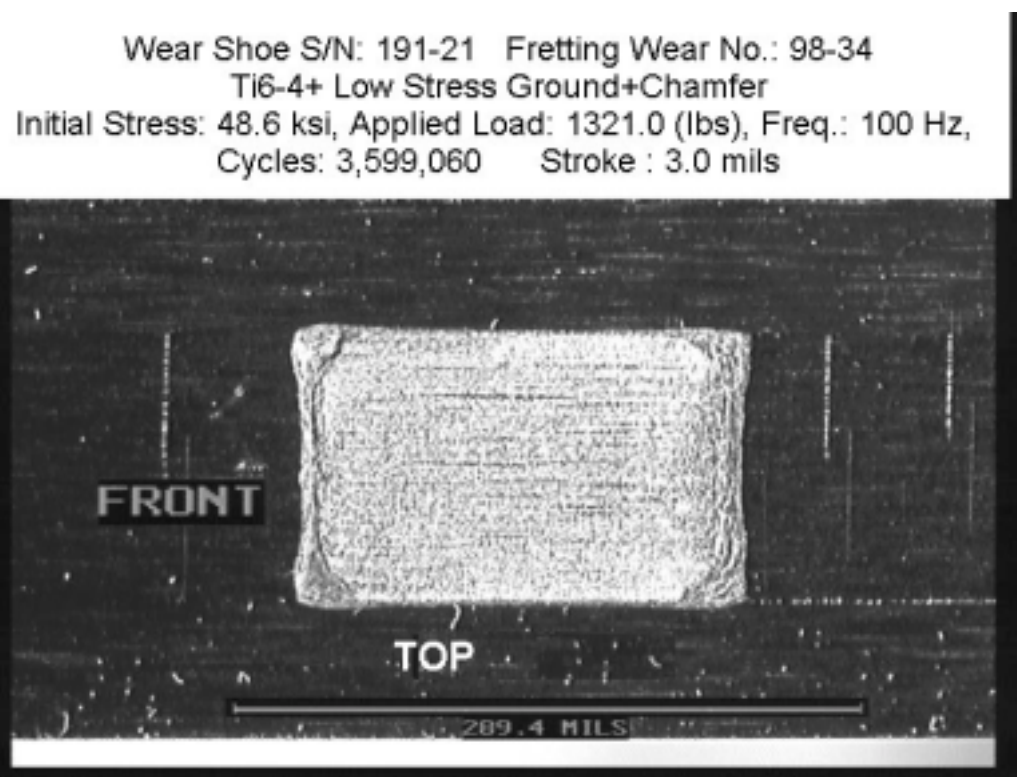
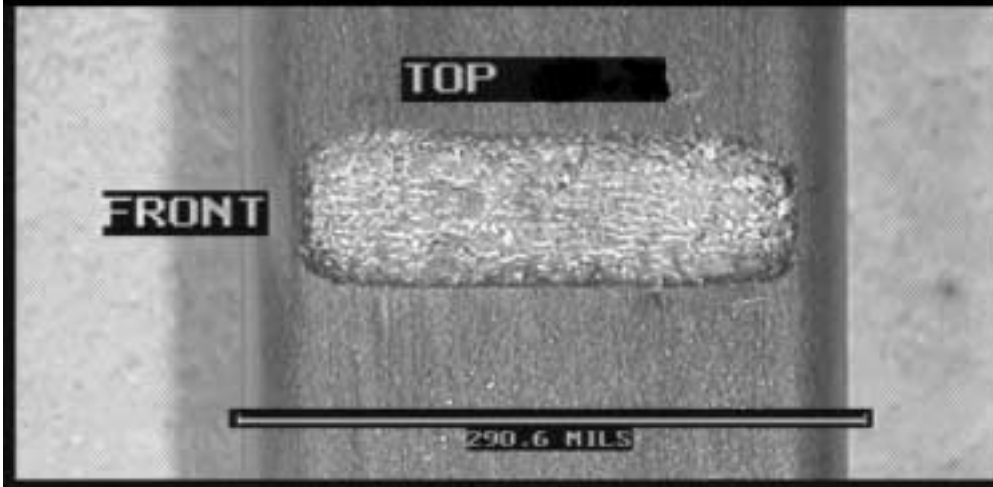


Figure 6A.19. Fretting test FW98-34. 55 ksi, 3.0 mils, 3.5E06 cycles.

Fatigue Bar S/N: 76-10 Fretting Wear No.: 98-36
Ti 6-4+ Low Stress Ground+ Polished+ Stress Relieved+ Chem Mill
Initial Stress: 14.6 ksi, Applied Load: 133.4 (lbs.), Freq.: 100 Hz.
Cycles: 900,000, Stroke: 3.0 mils



Shoe S/N: 191-15 Fretting Wear No.: 98-36
Ti 6-4+ Low Stress Ground+ Chamfer (.040")
Initial Stress: 14.6 ksi, Applied Load: 133.4 (lbs.), Freq.: 100 Hz.
Cycles: 900,000, Stroke: 3.0 mils

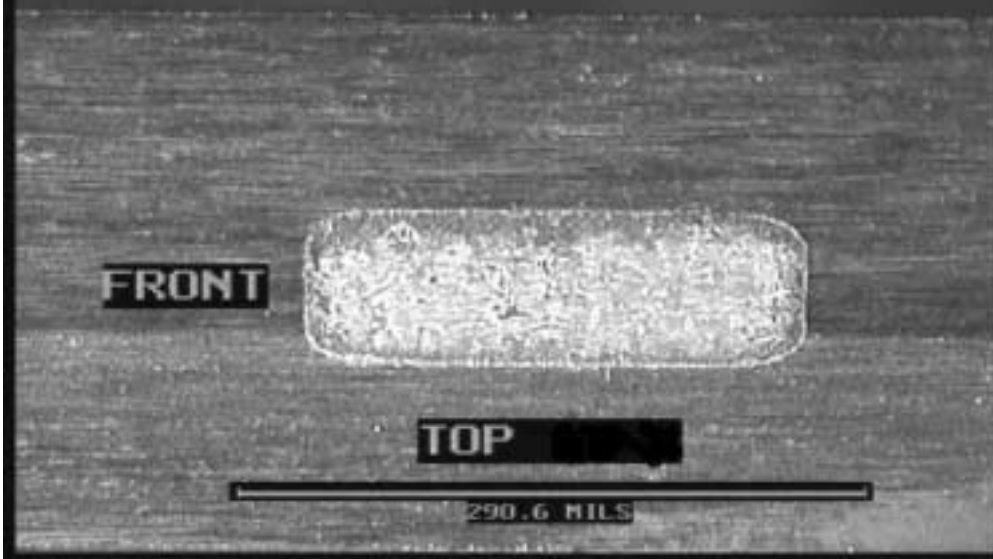


Figure 6A.20. Fretting test FW98-36. 17 ksi, 3.0 mils, 900K cycles.

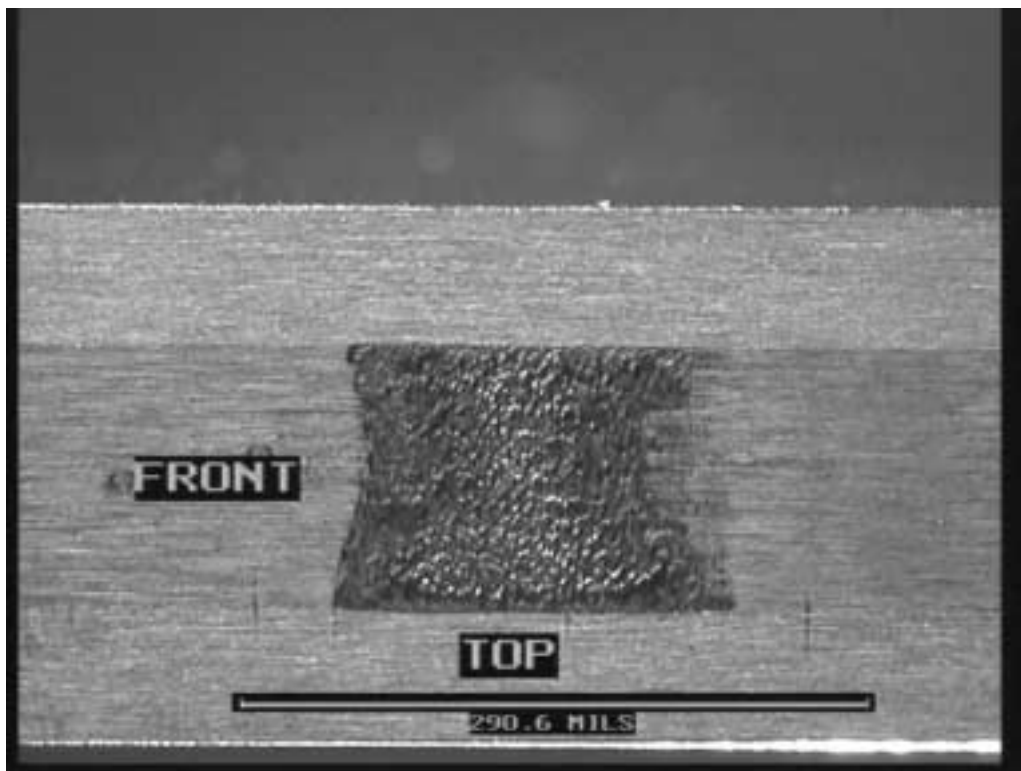
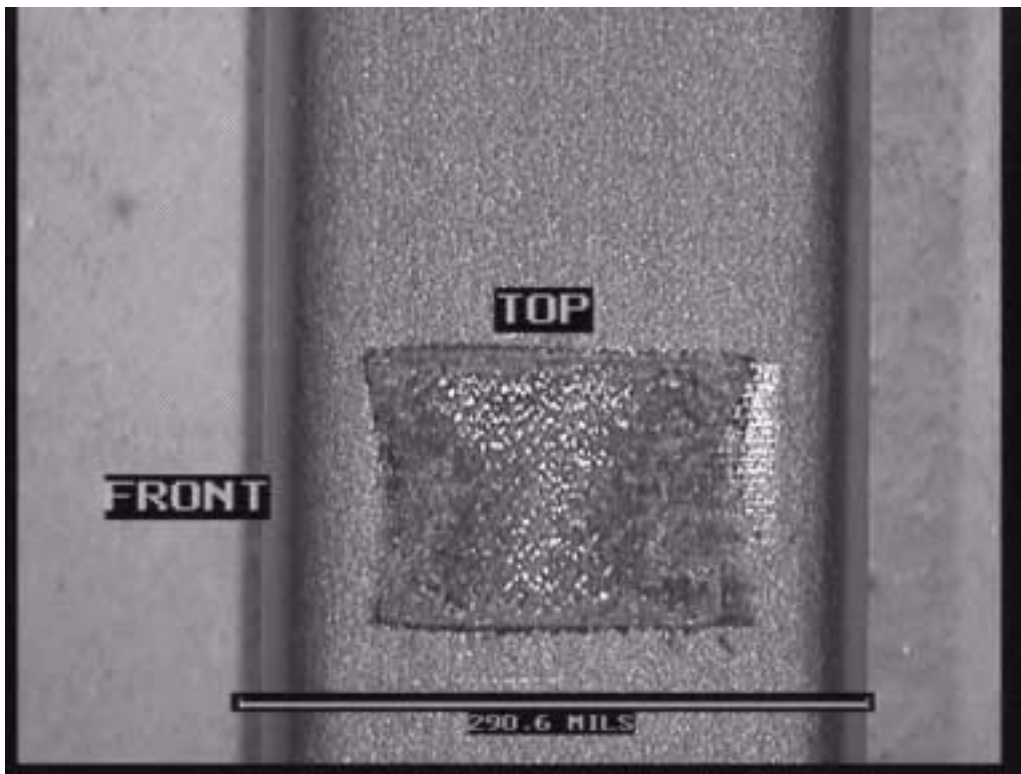


Figure 6A.21. Fretting test FW98-39. 17 ksi, 2.0 mils, 900K cycles.

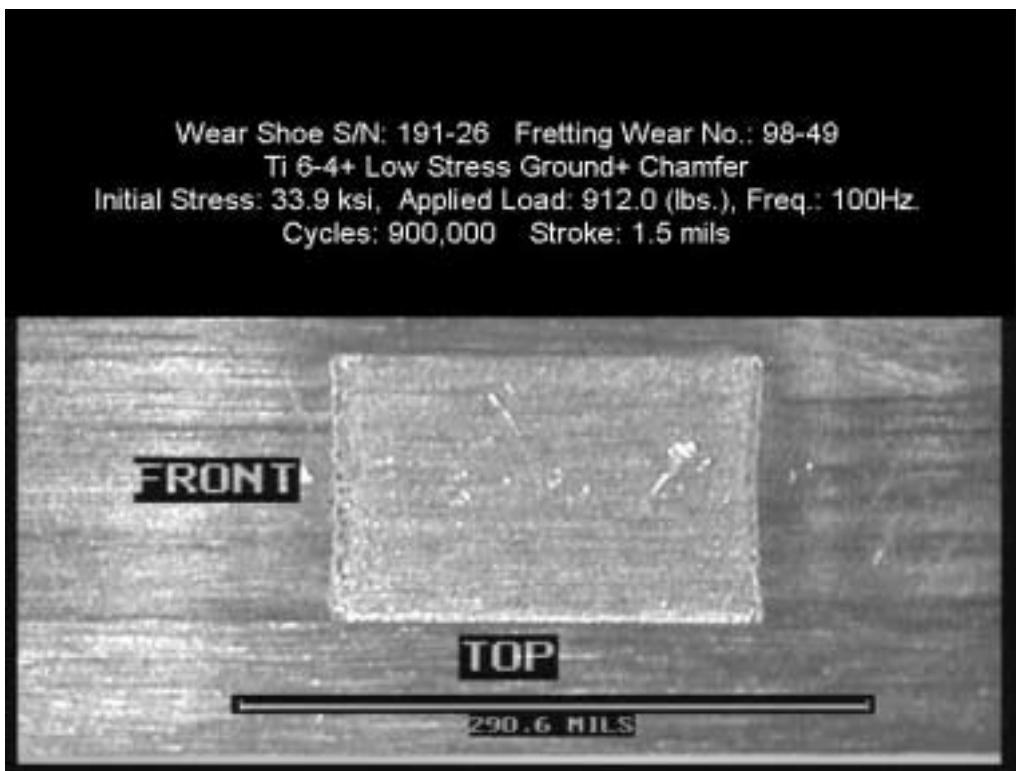
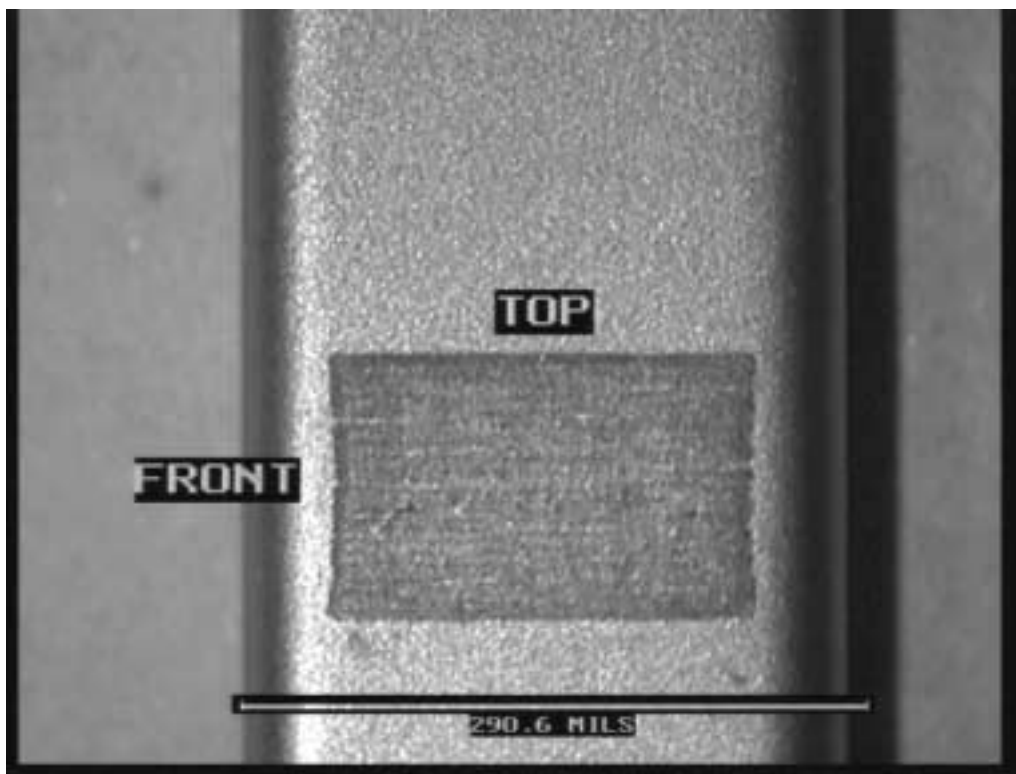


Figure 6A.22. Fretting test FW98-49. 35 ksi, 1.5 mils, 900K cycles.

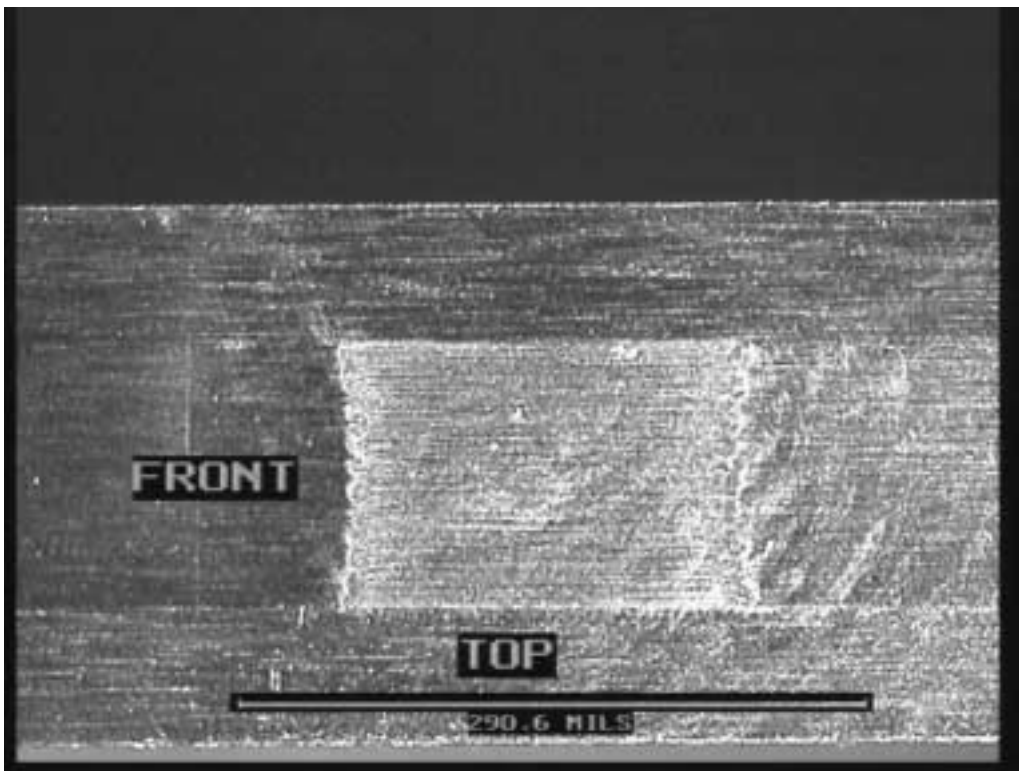
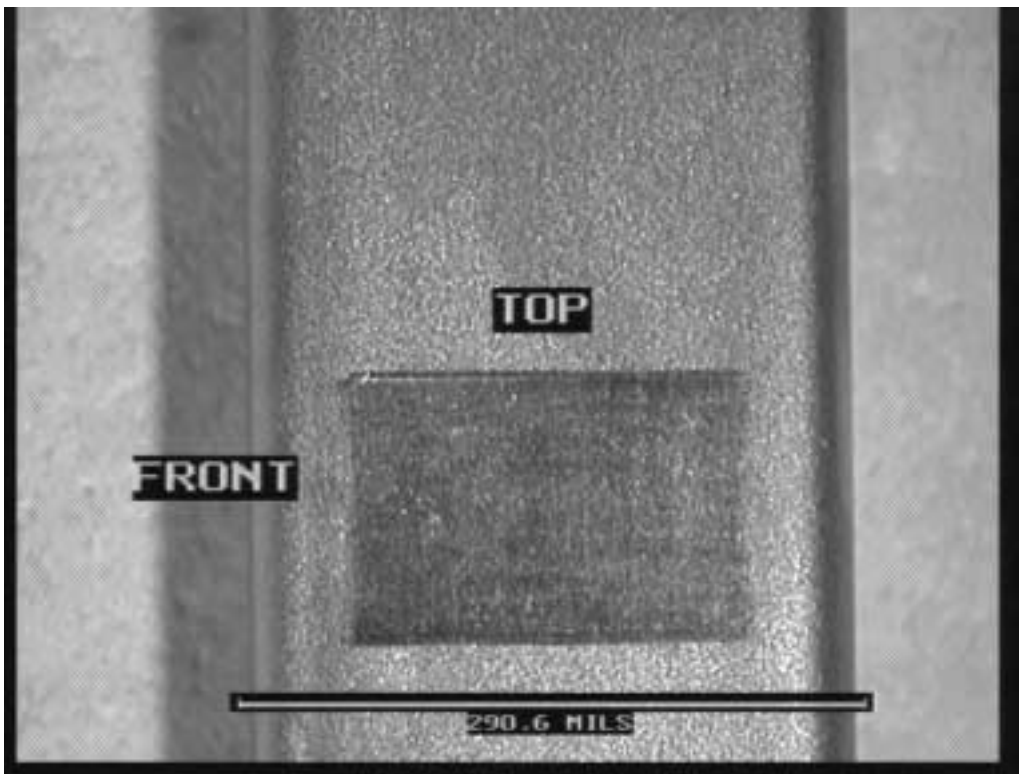


Figure 6A.23. Fretting test FW98-50. 35 ksi, 1.5 mils, 250K cycles.

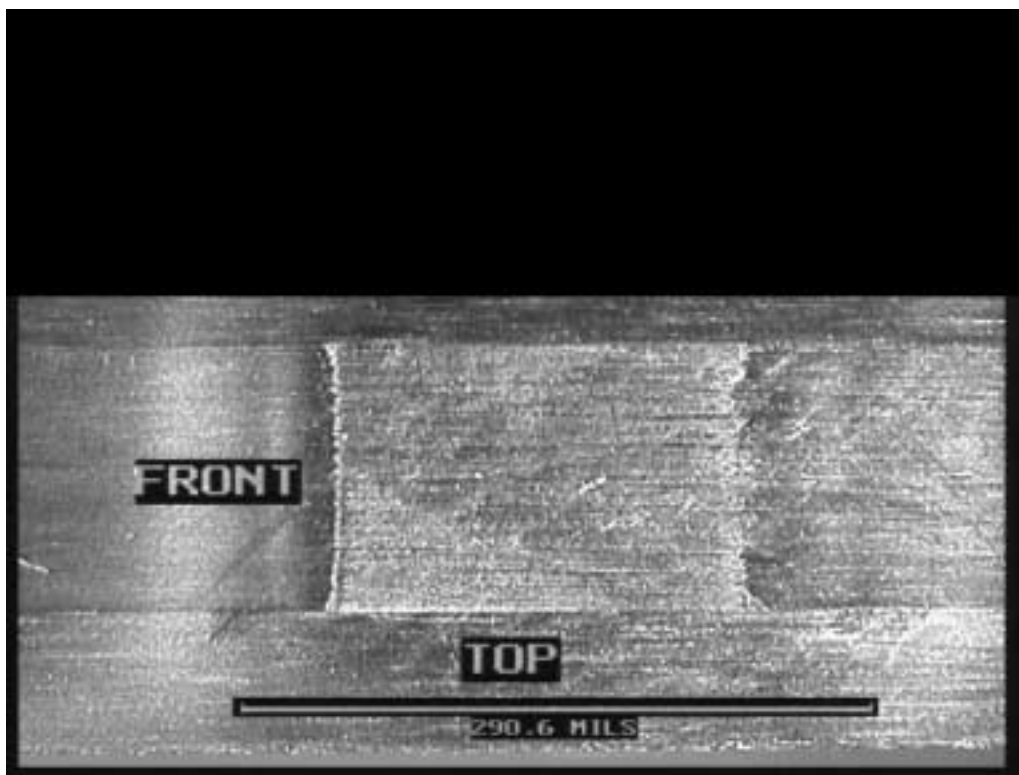
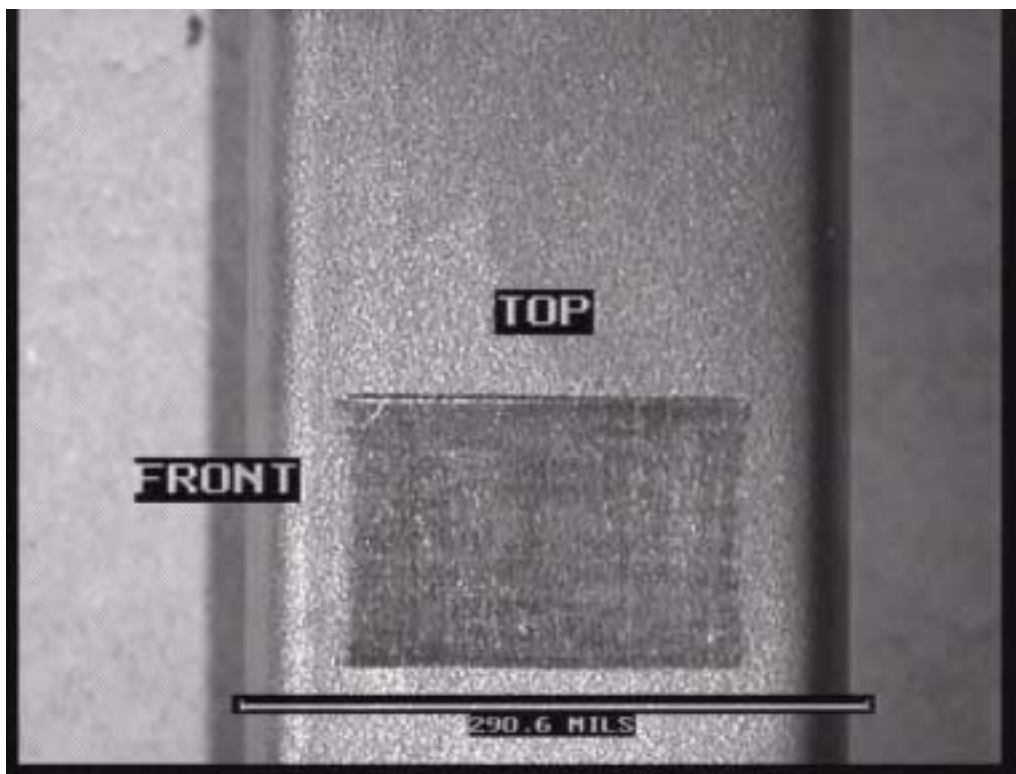


Figure 6A.24. Fretting test FW98-51. 55 ksi, 0.8 mils, 250K cycles.

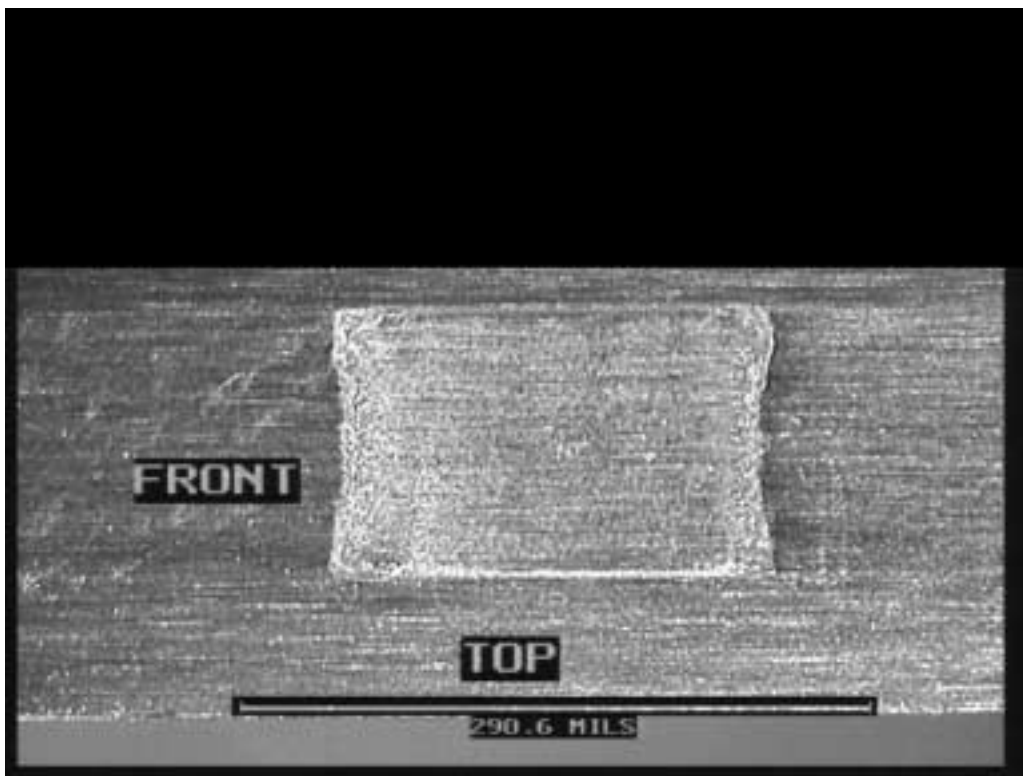
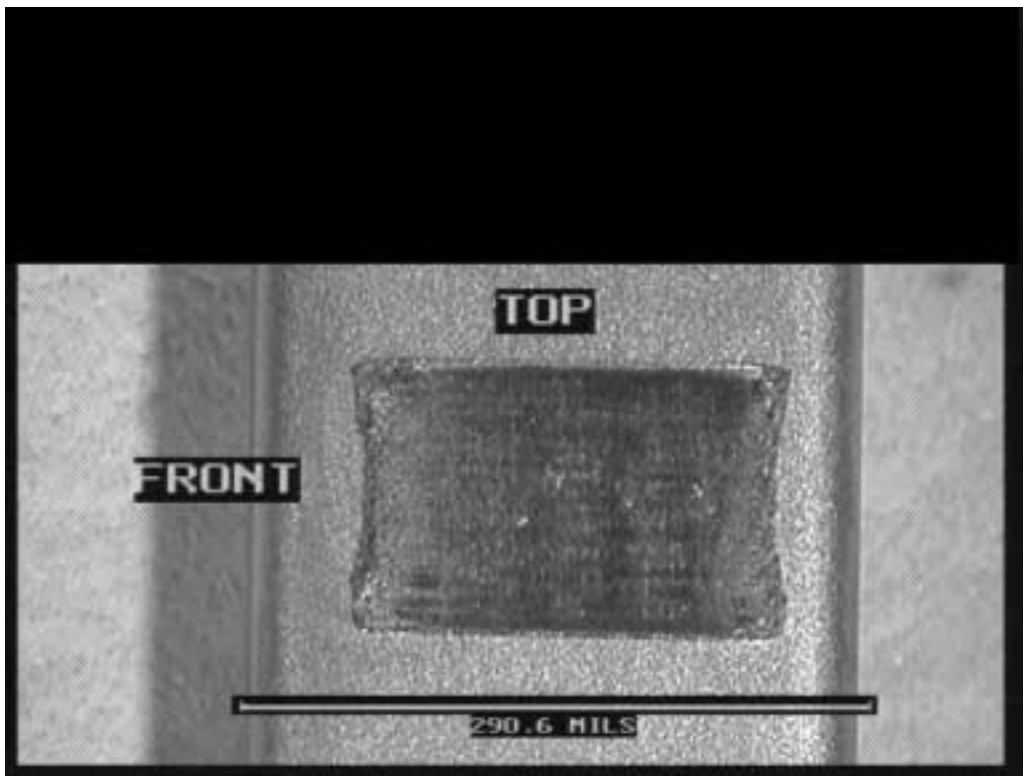


Figure 6A.25. Fretting test FW98-52. 55 ksi, 3.0 mils, 250K cycles.

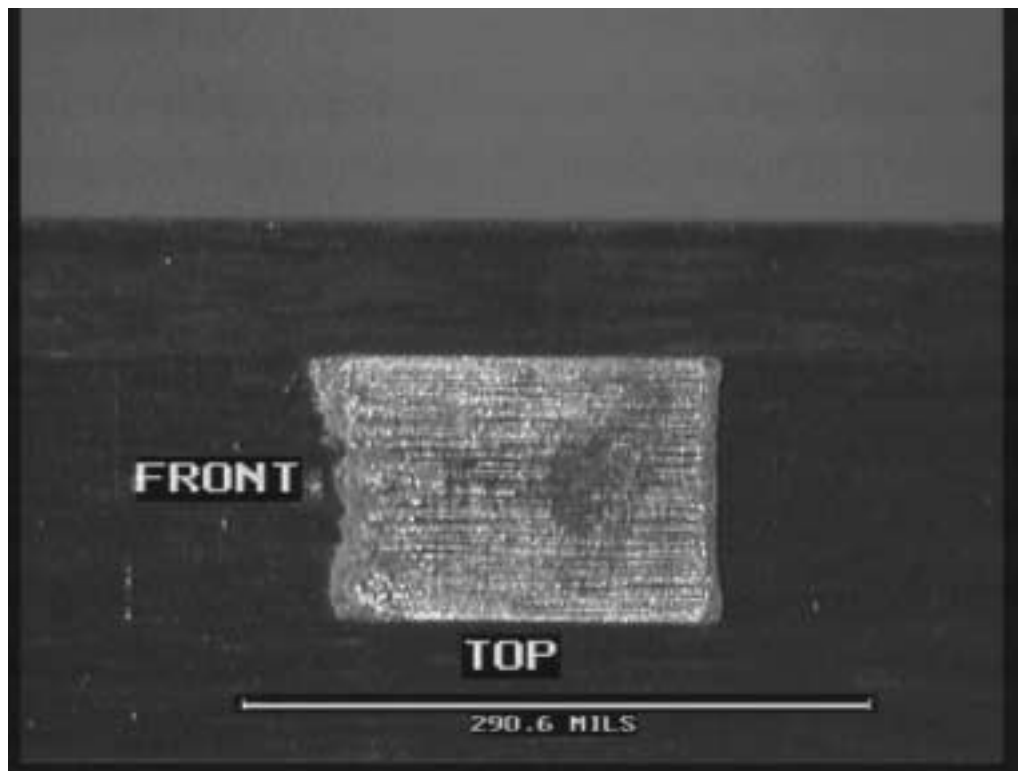
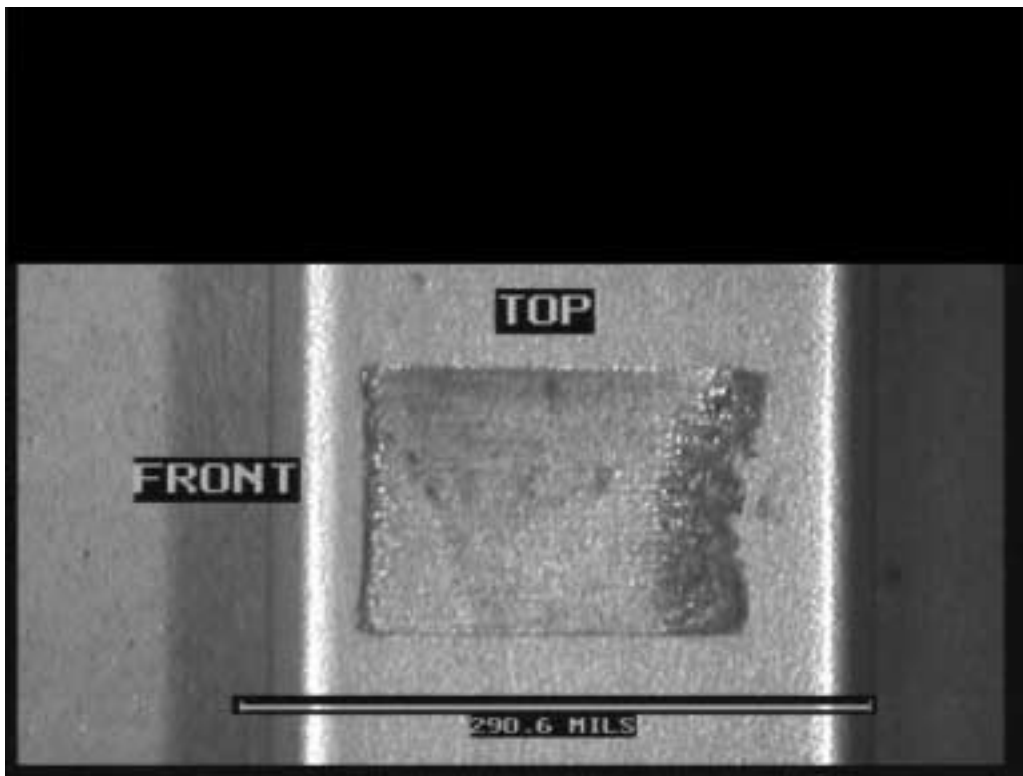


Figure 6A.26. Fretting test FW98-53. 35 ksi, 2.0 mils, 900K cycles.

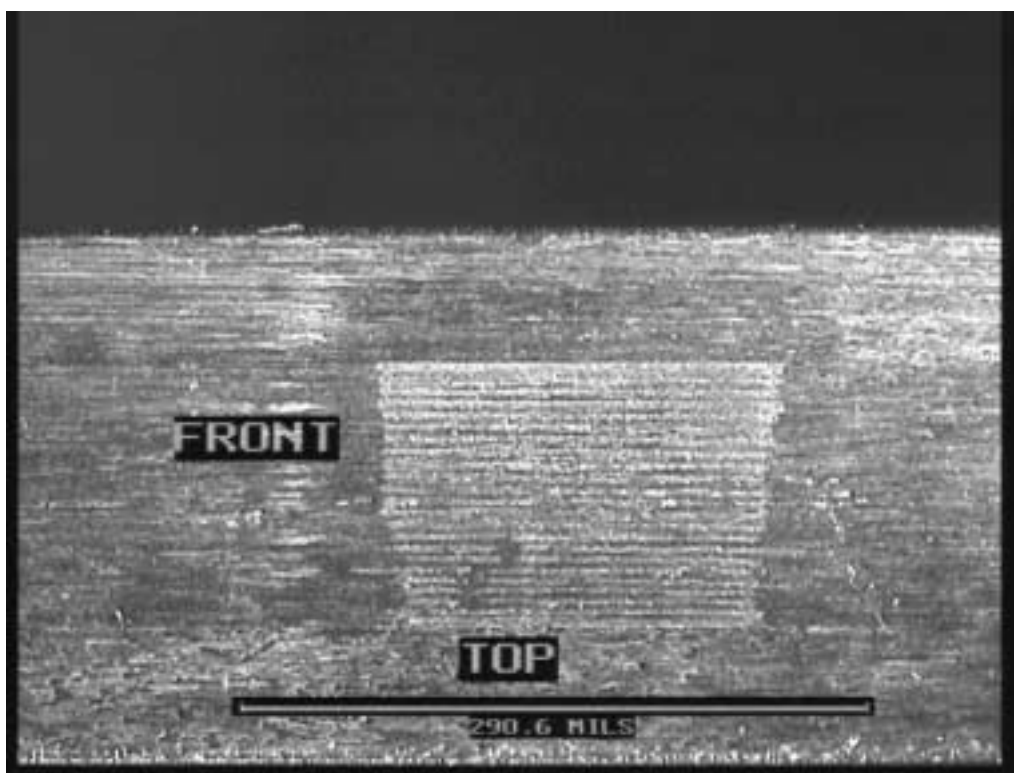
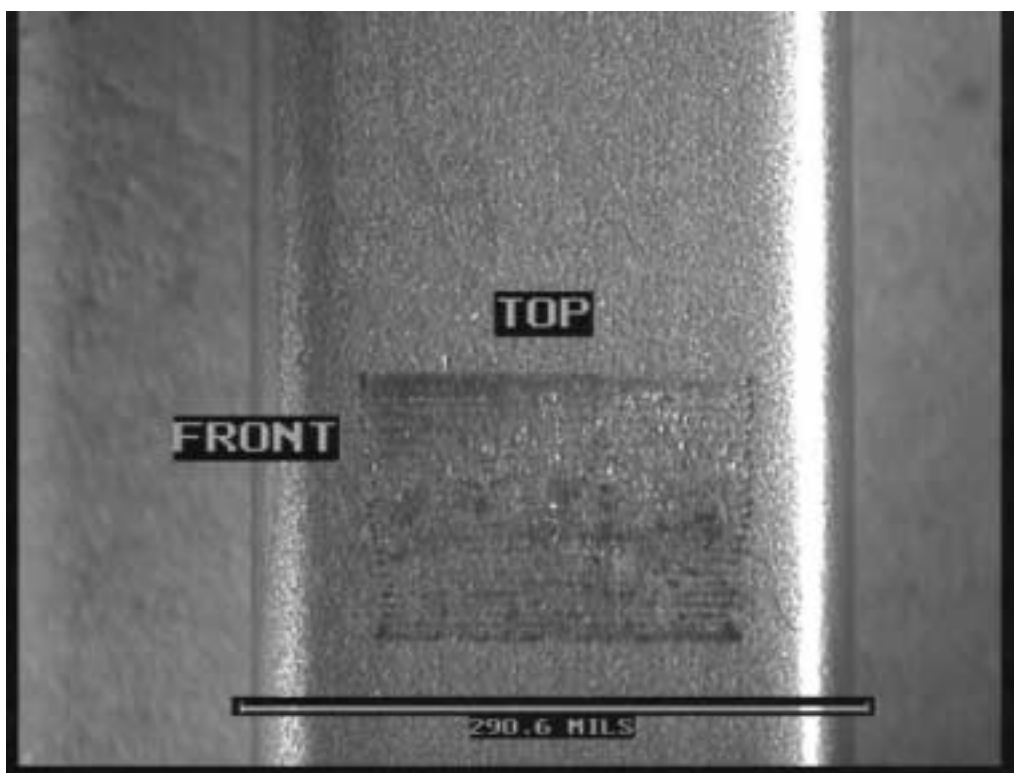


Figure 6A.27. Fretting test FW98-61. 35 ksi, 0.8 mils, 900K cycles.

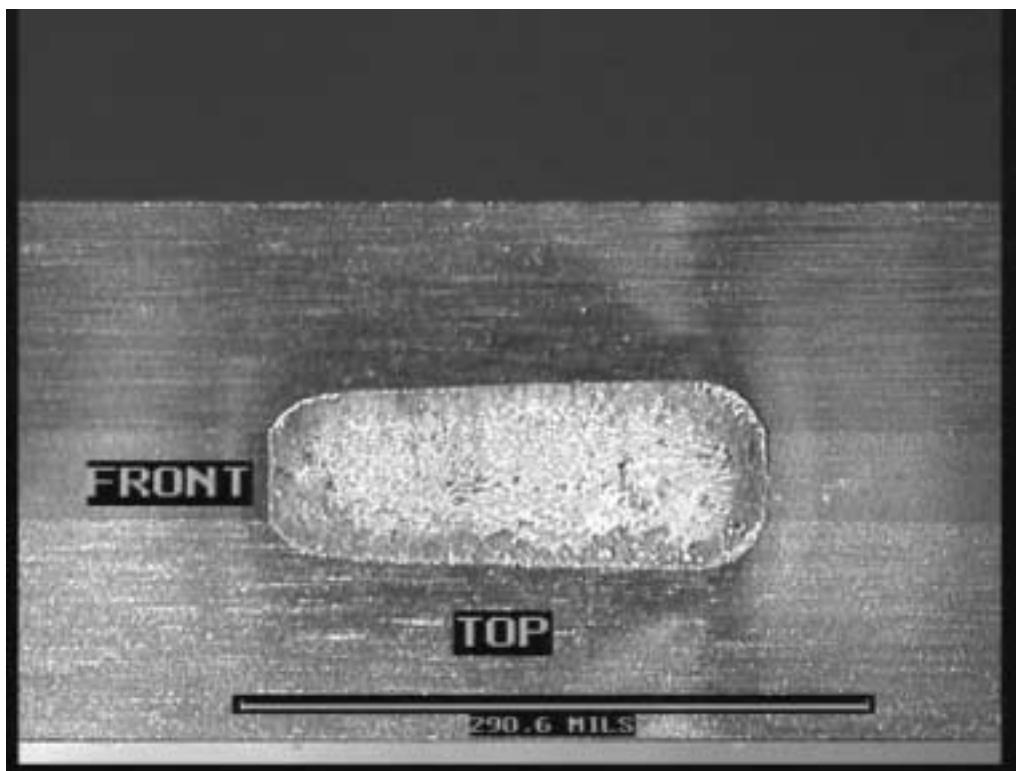
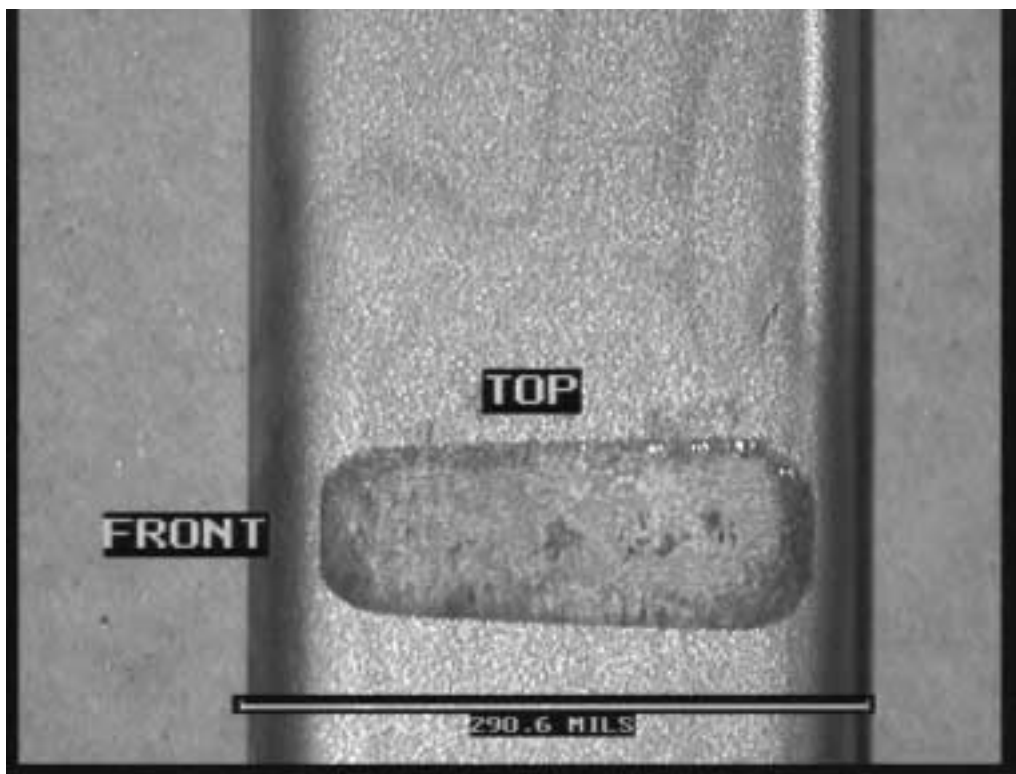


Figure 6A.28. Fretting test FW98-64. 17 ksi, 3.0 mils, 900K cycles.

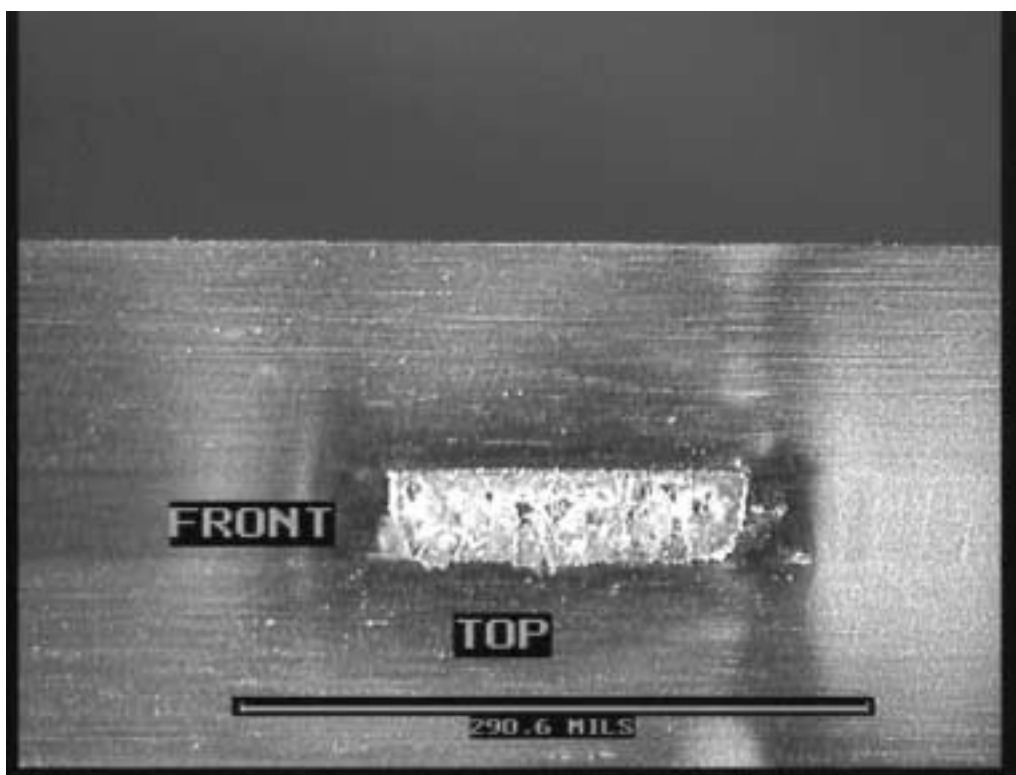
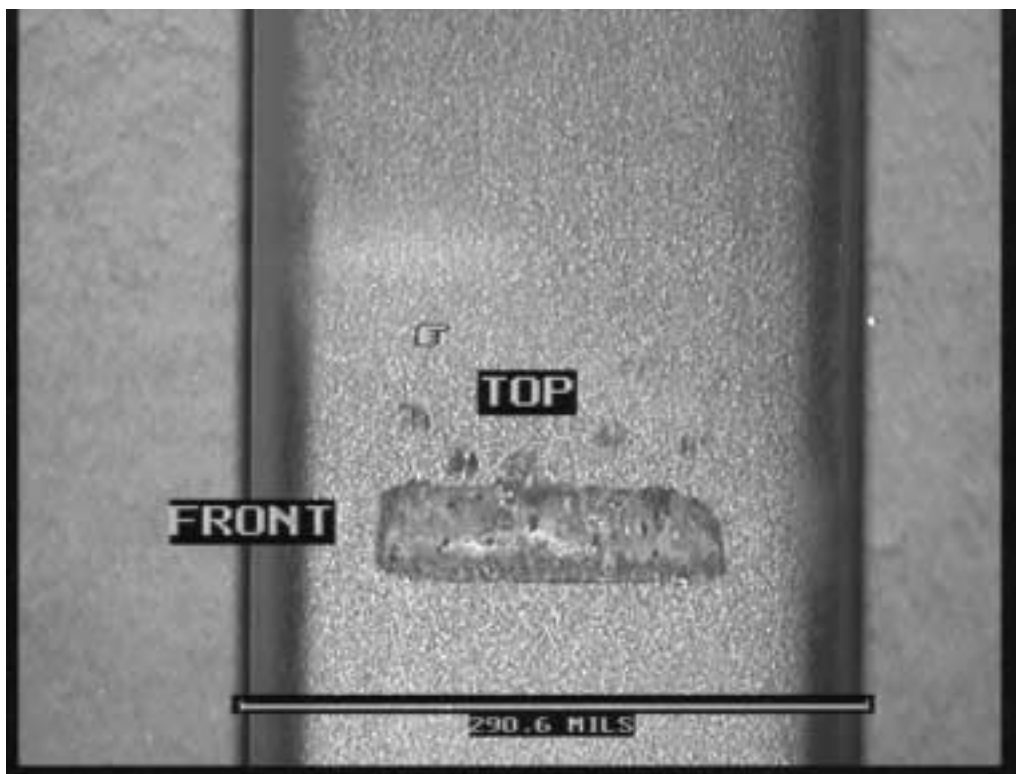


Figure 6A.29. Fretting test FW98-68. 17 ksi, 1.5 mils, 900K cycles.

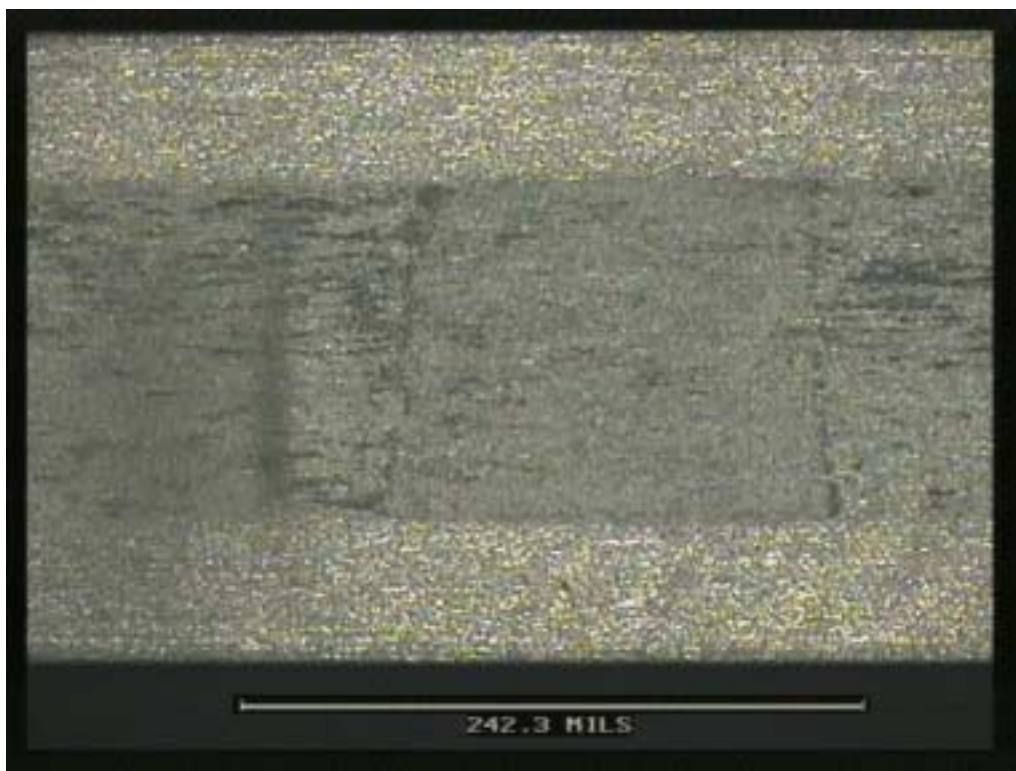
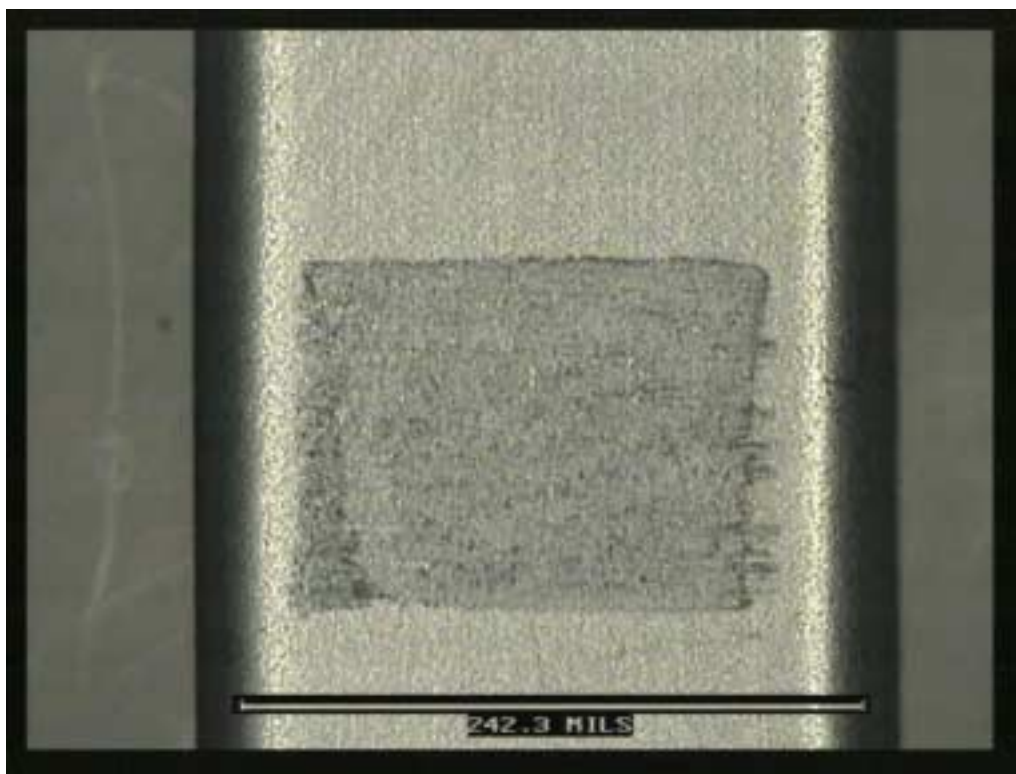


Figure 6A.30. Fretting test FW98-132. 55 ksi, 0.8 mils, 900K cycles.

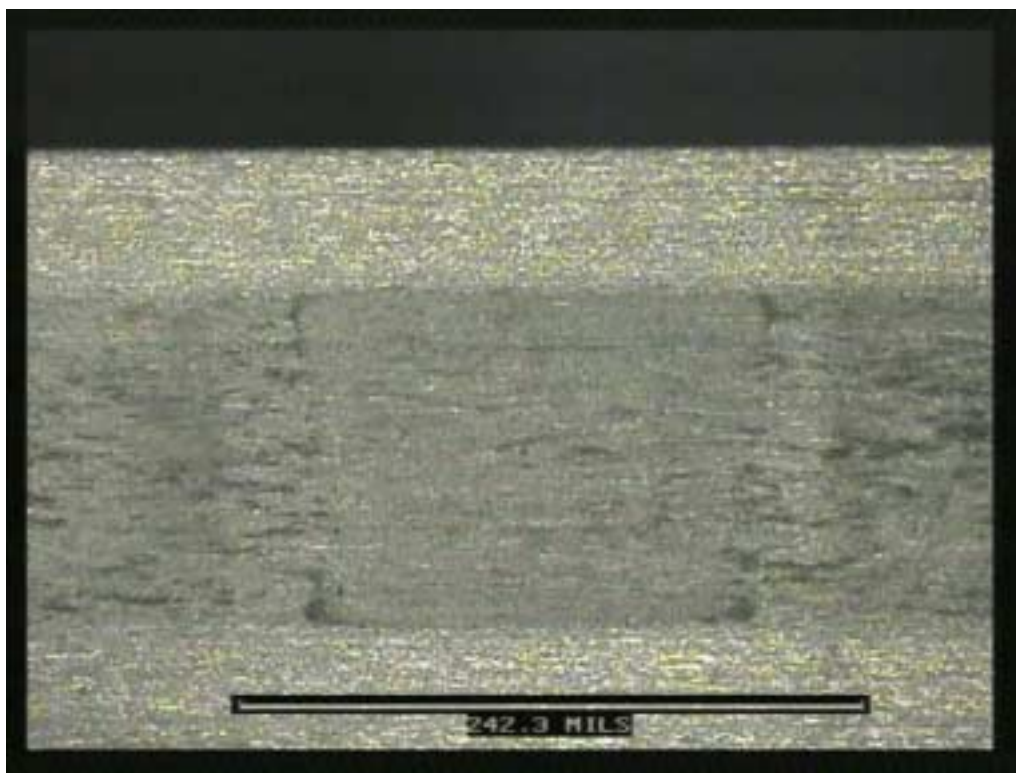
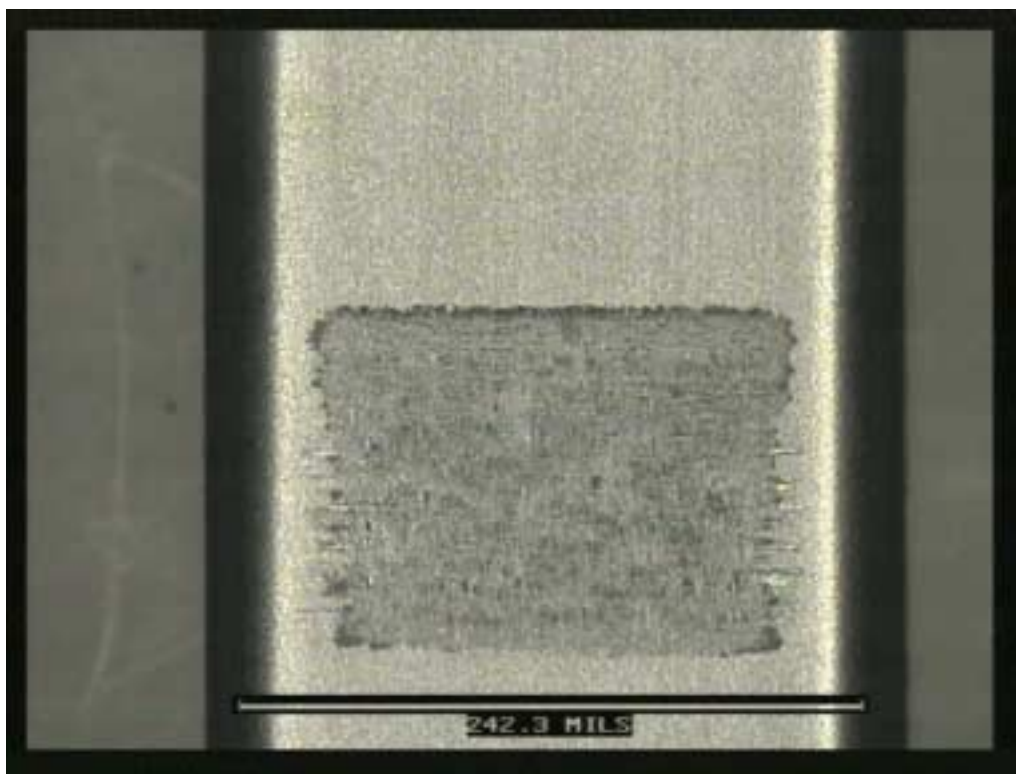


Figure 6A.31. Fretting test FW98-133. 55 ksi, 0.8 mils, 900K cycles.

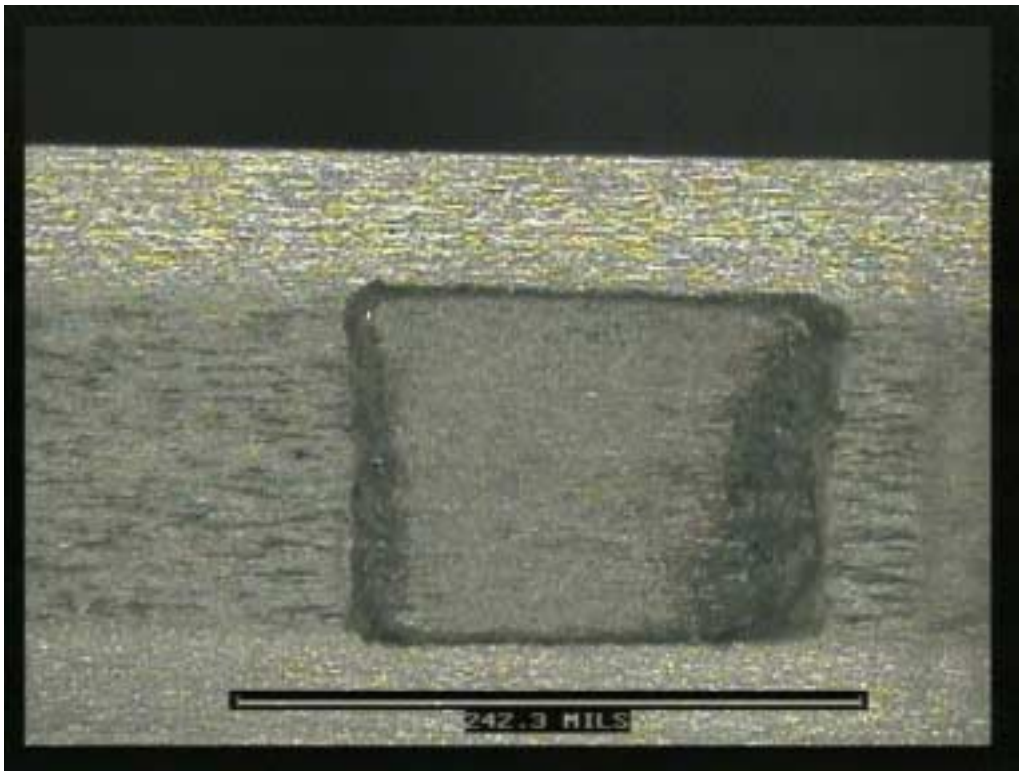
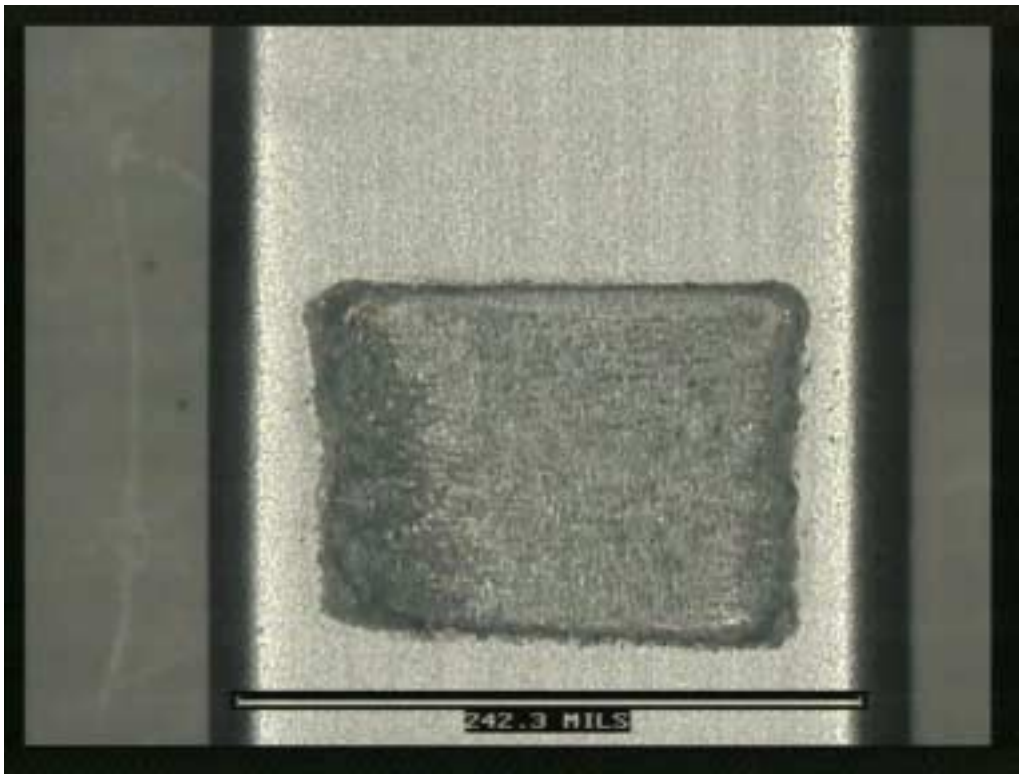


Figure 6A.32. Fretting test FW98-134. 55 ksi, 3.0 mils, 900K cycles.

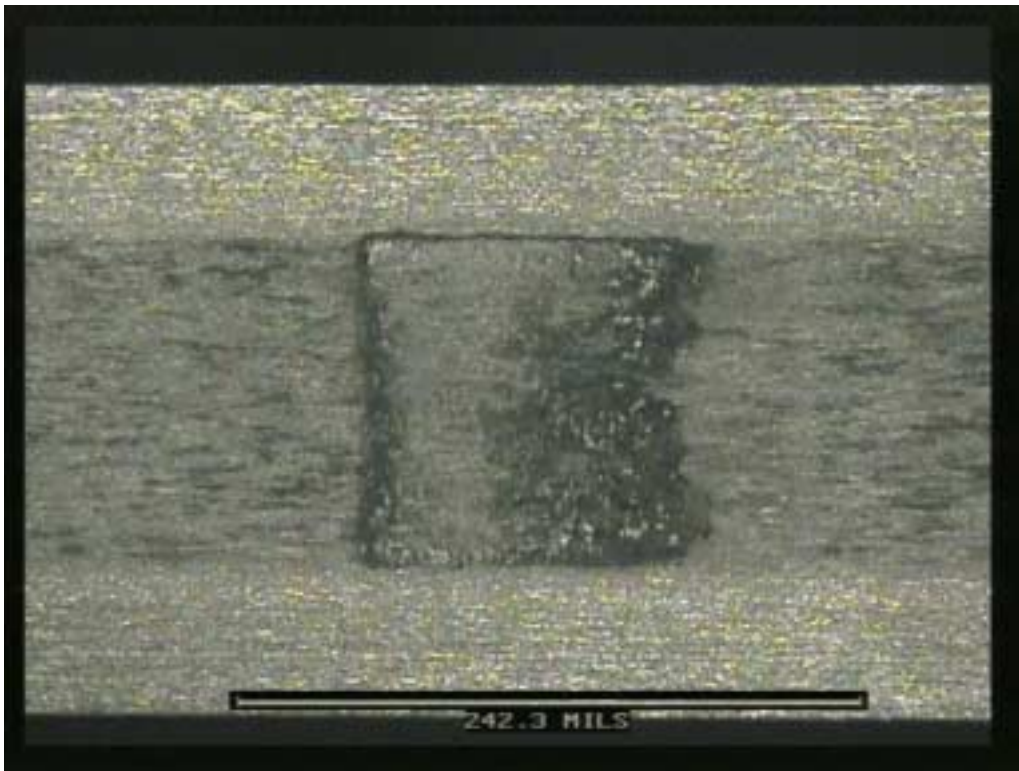
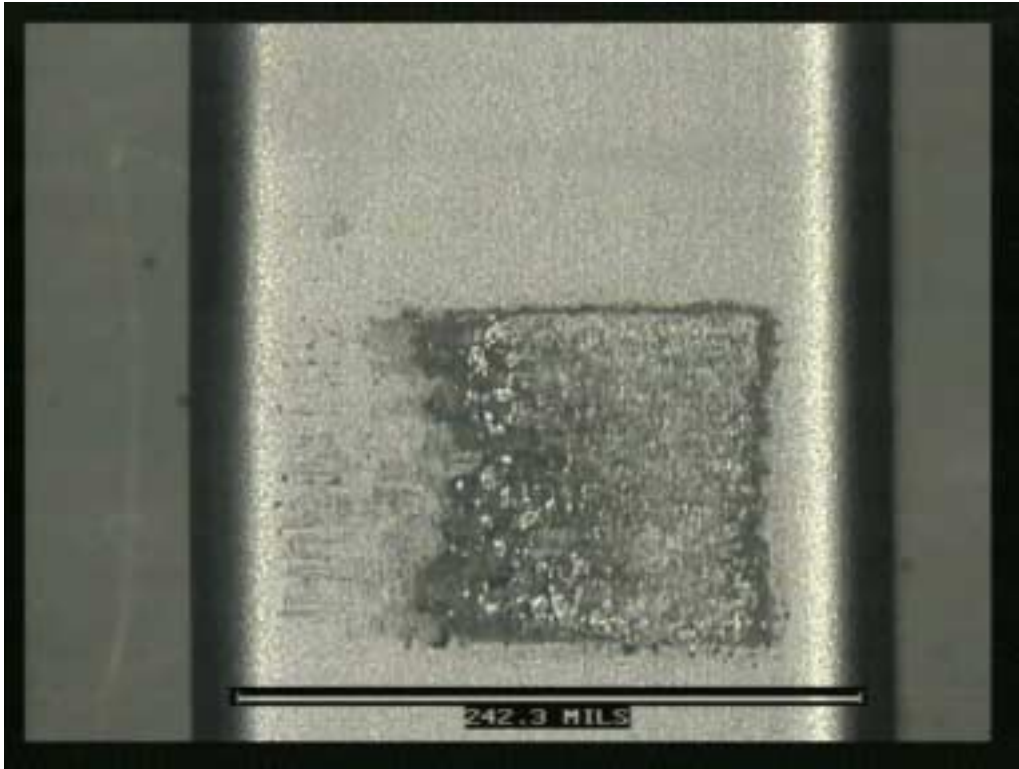


Figure 6A.33. Fretting test FW98-135. 17 ksi, 1.5 mils, 900K cycles.

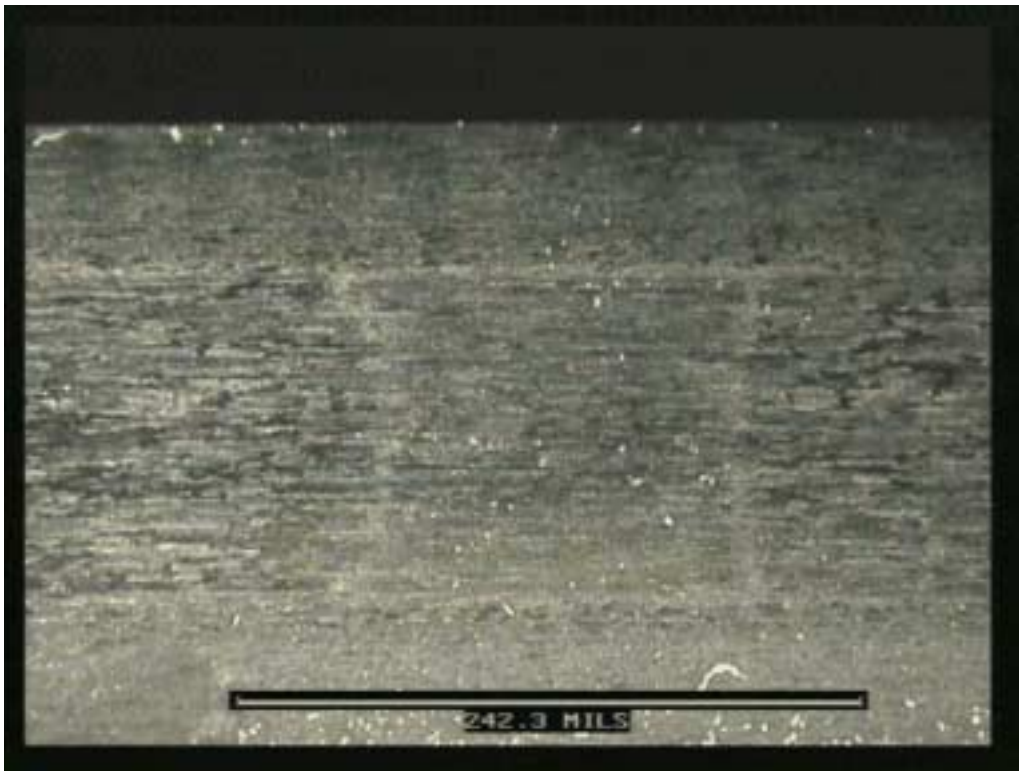
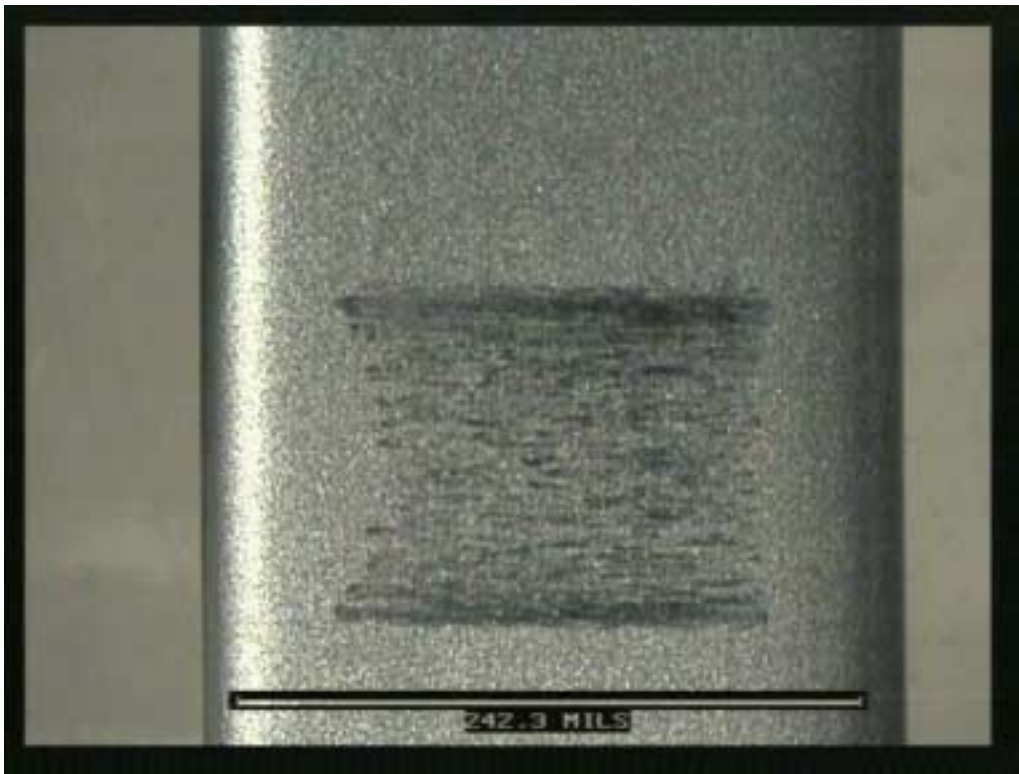


Figure 6A.34. Fretting test FW98-136. 35 ksi, 0.8 mils, 900K cycles.

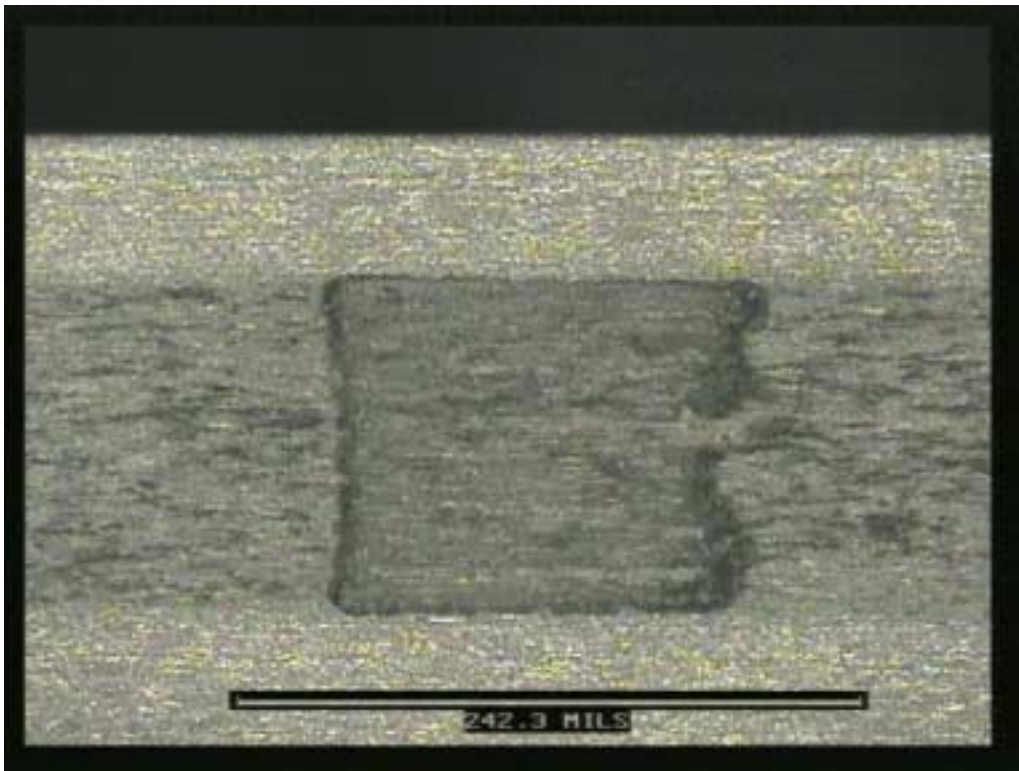
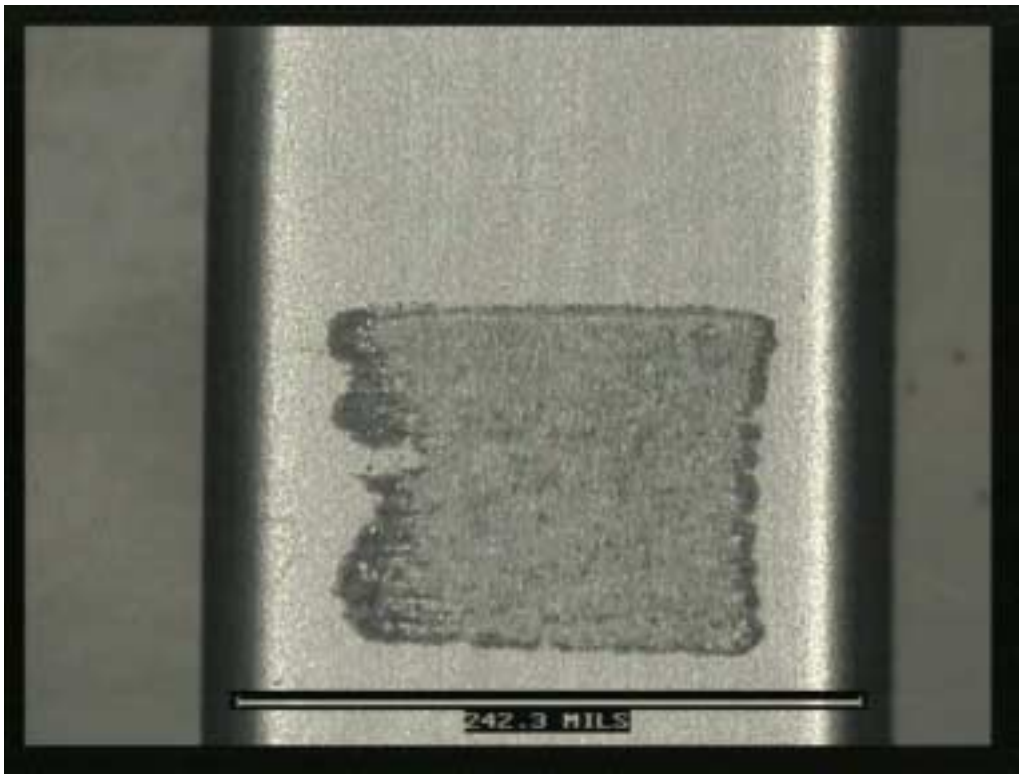


Figure 6A.35. Fretting test FW98-137. 35 ksi, 1.5 mils, 900K cycles.



Figure 6A.36. Wear scars observed in fretting tests with relative displacements of (a) 3.0 and (b) 0.8 mils.

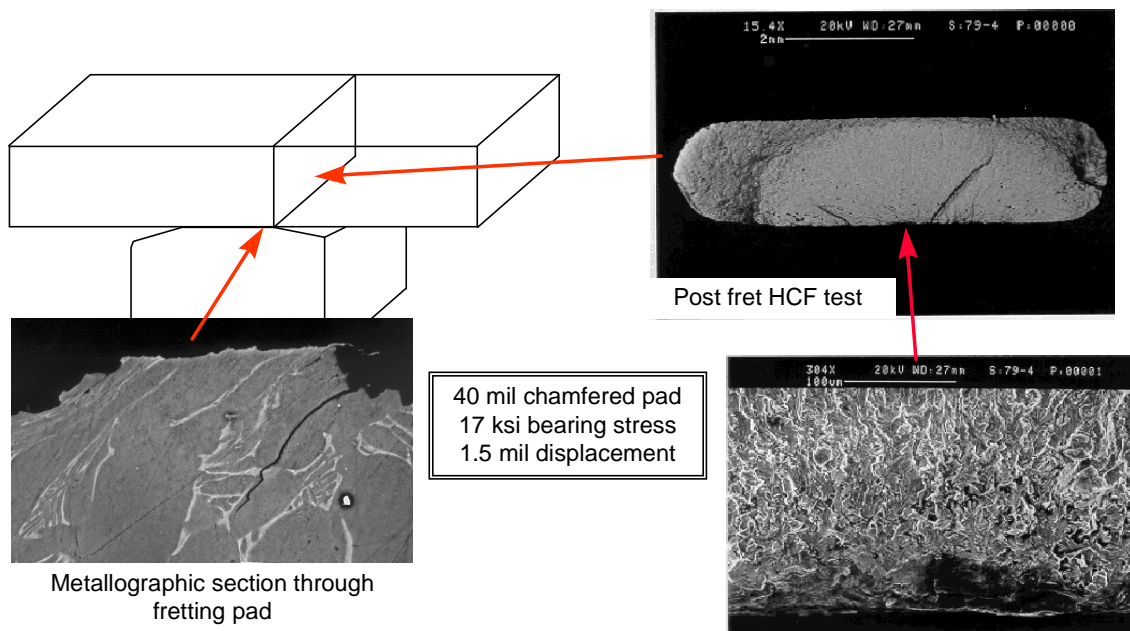
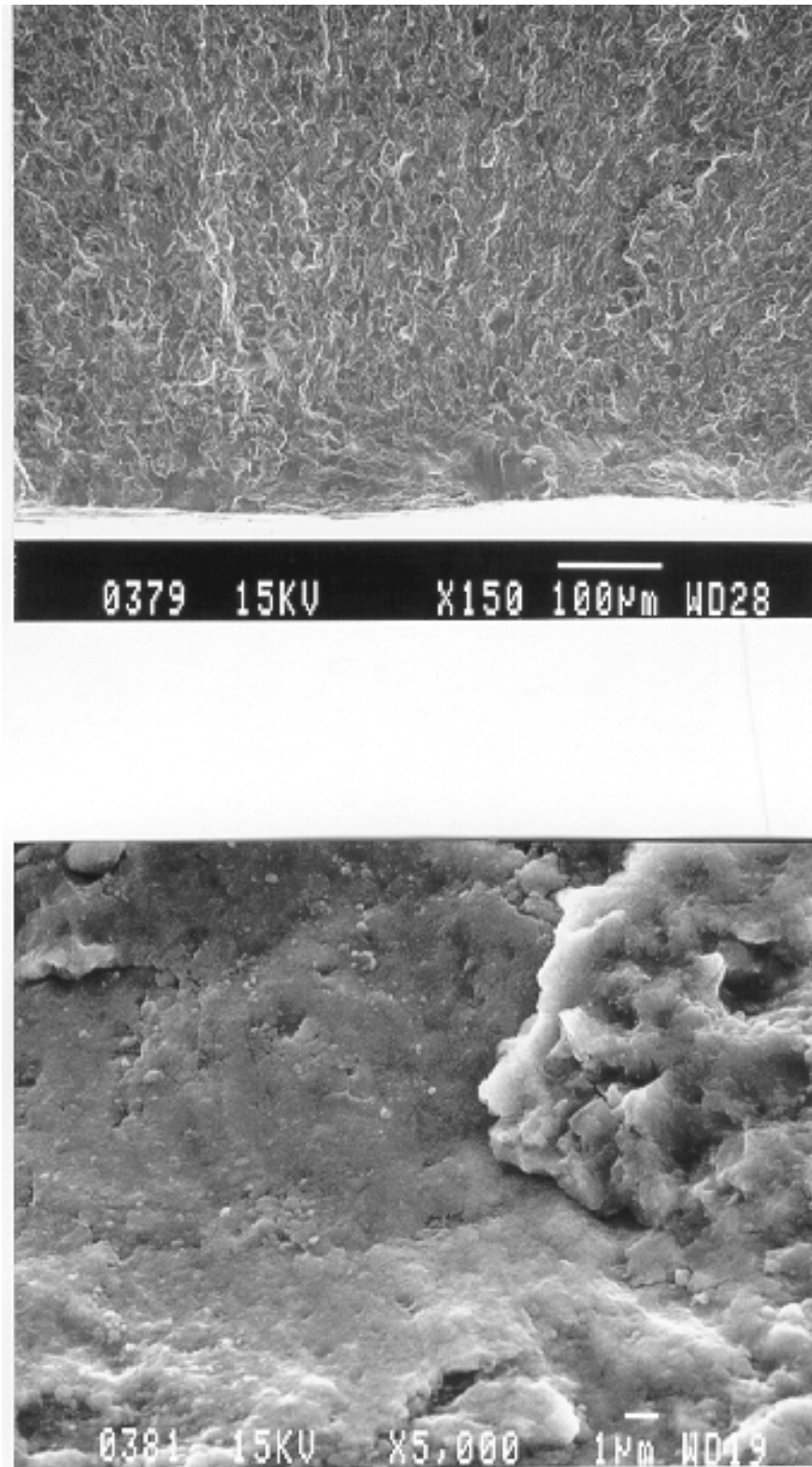


Figure 6A.37. Metallographic sections of fretting pads and fractography of the post fret HCF tests showing cracking from fretting alone.



Enlarged view of the fretting crack from above

Figure 6A.38. Specimen #79-4 – fatigue origin at pre-existing fretting crack.

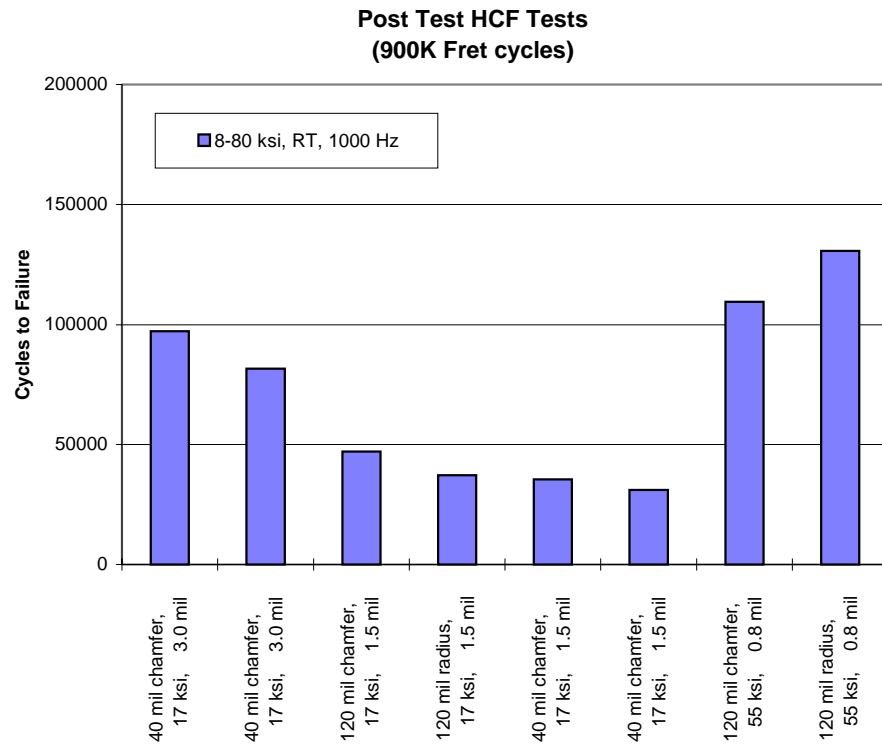


Figure 6A.39. Results of HCF test of fretted specimens.

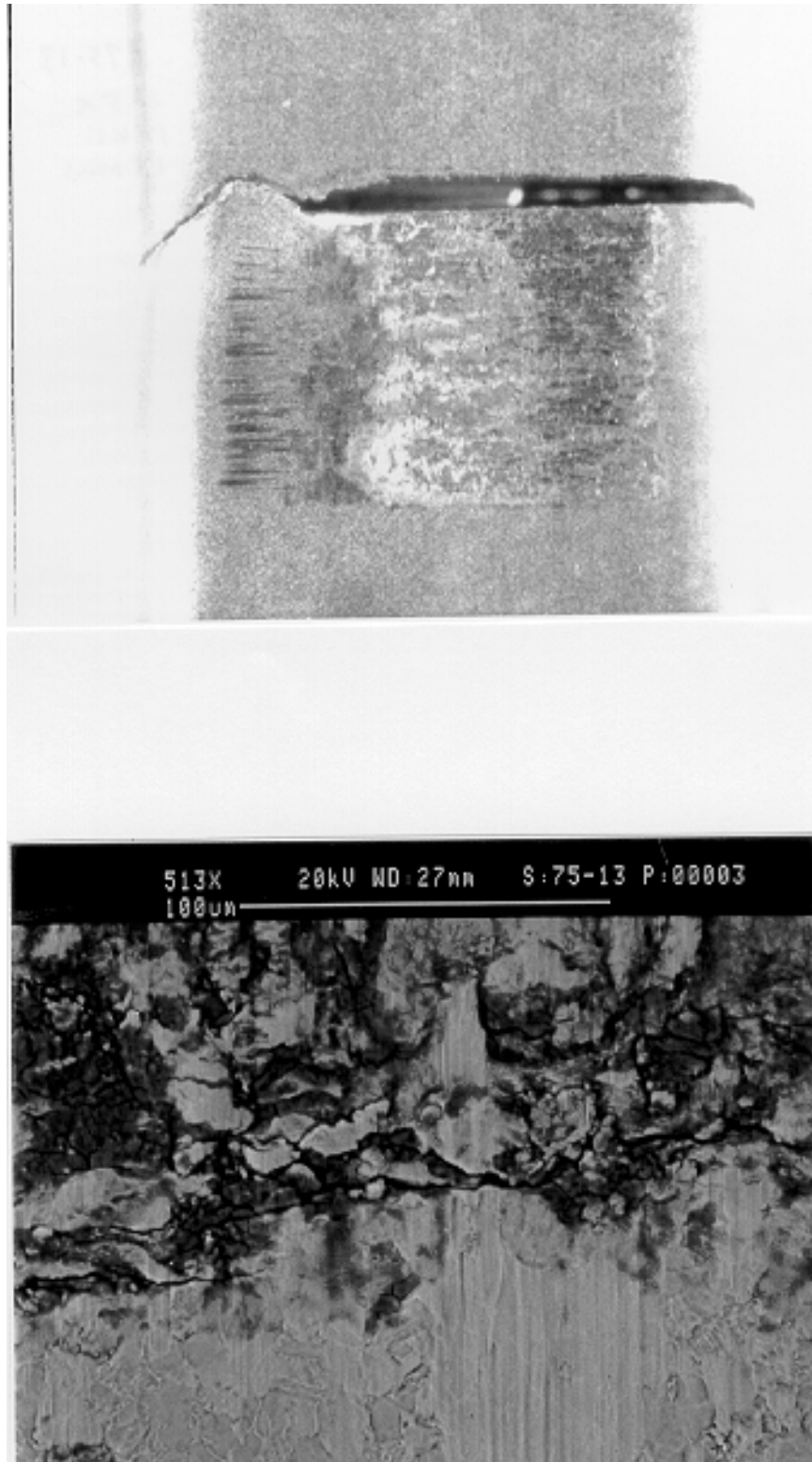


Figure 6A.40. Specimen 75-13.

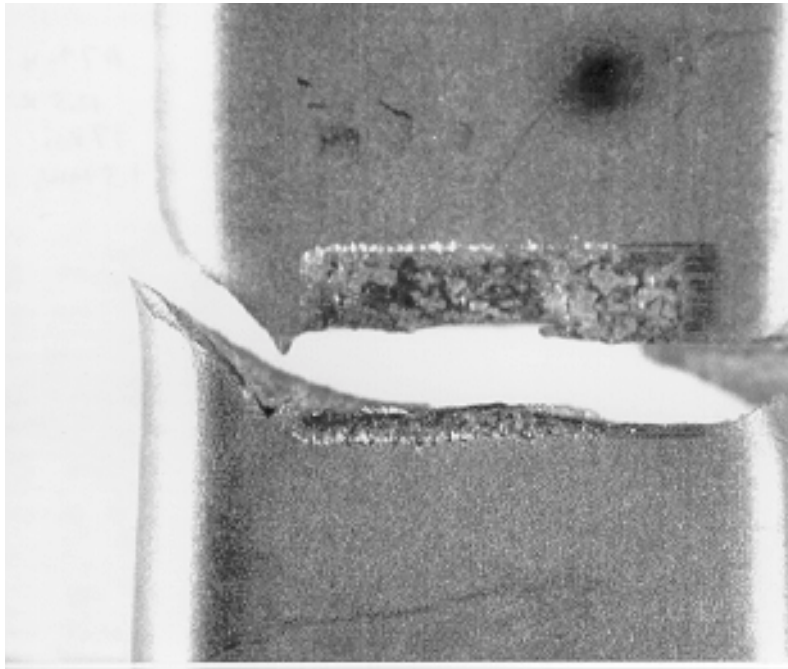


Figure 6A.41. Specimen 79-4.

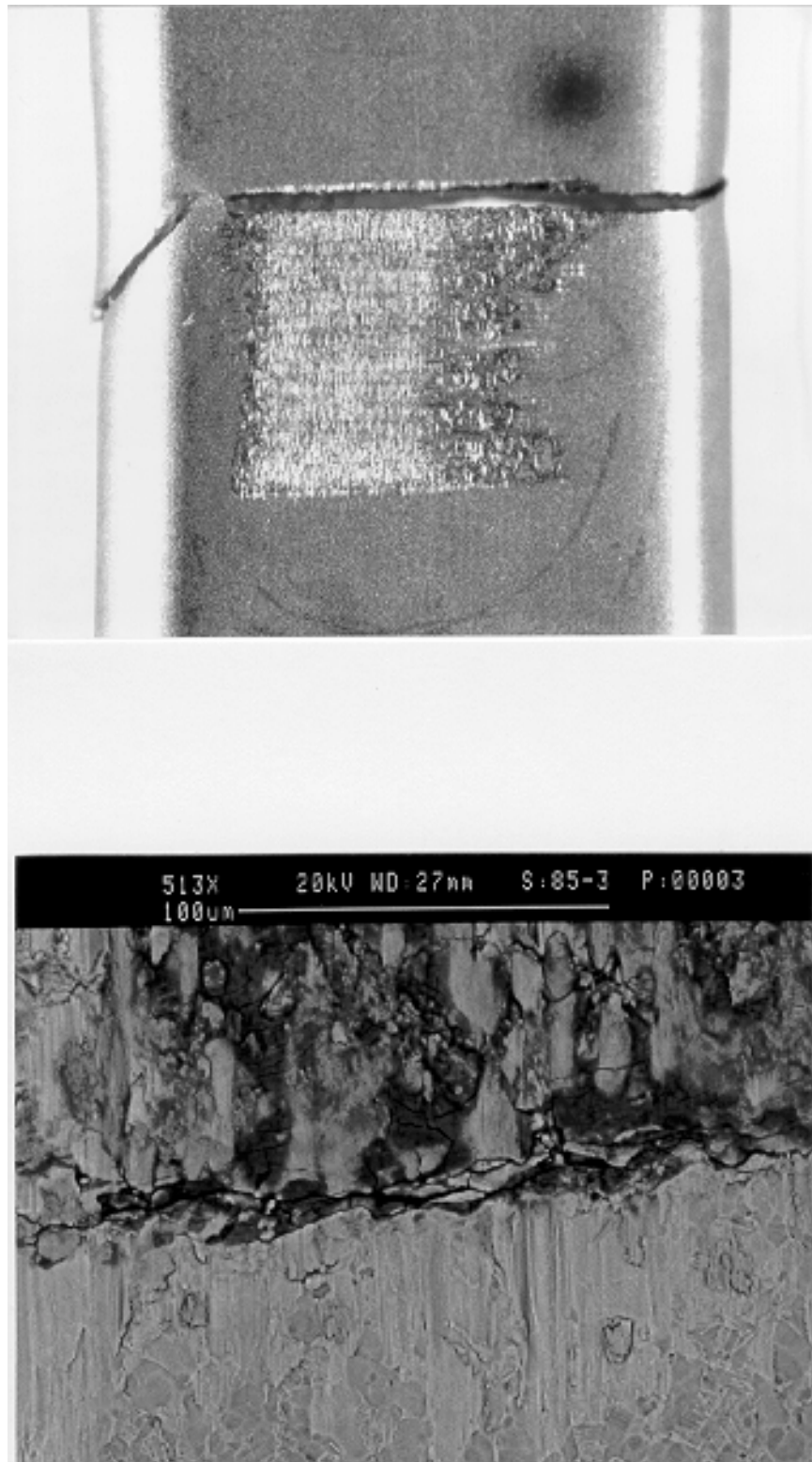


Figure 6A.42. Specimen 85-3.

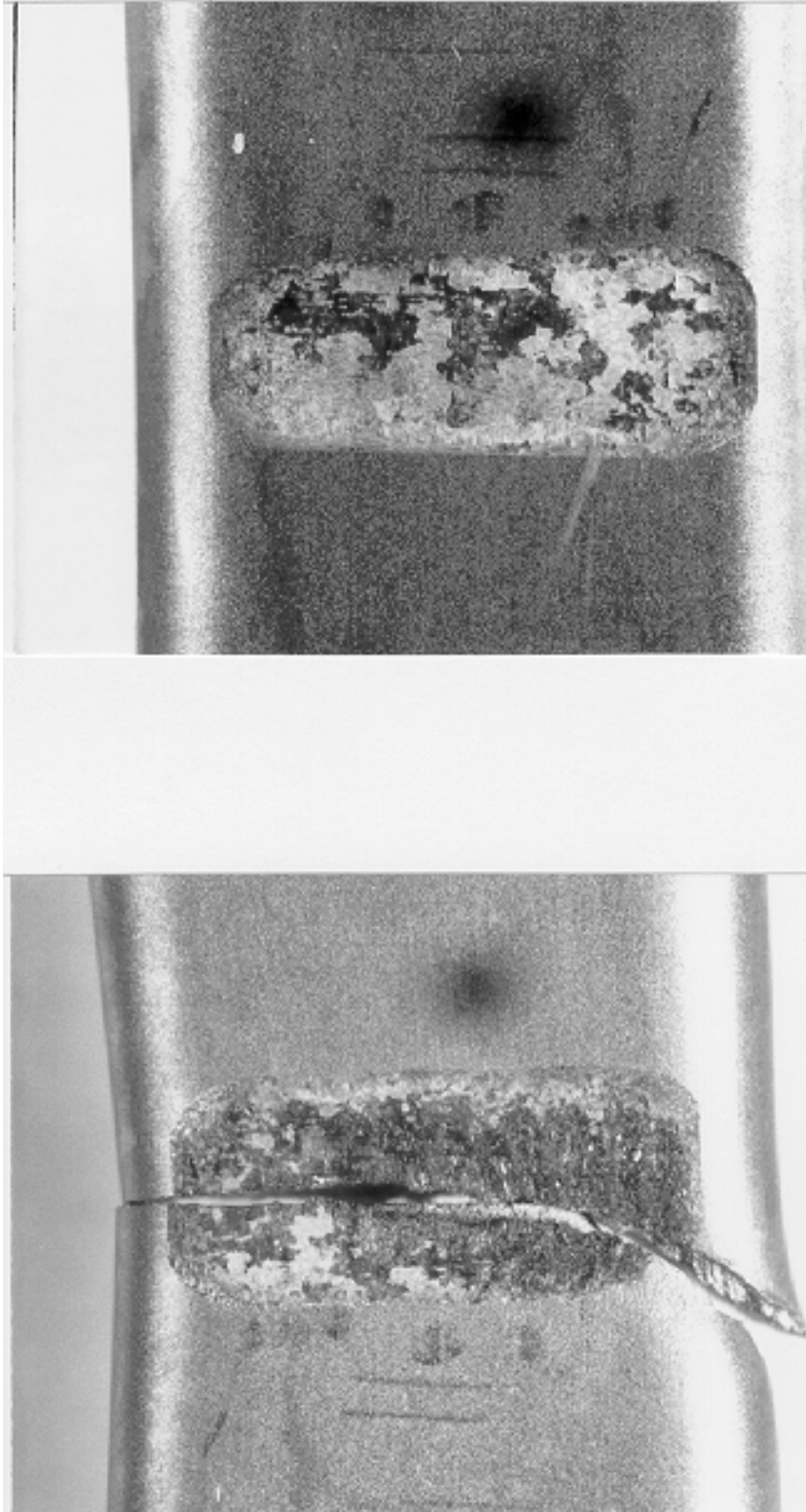


Figure 6A.43. Specimen 79-2.

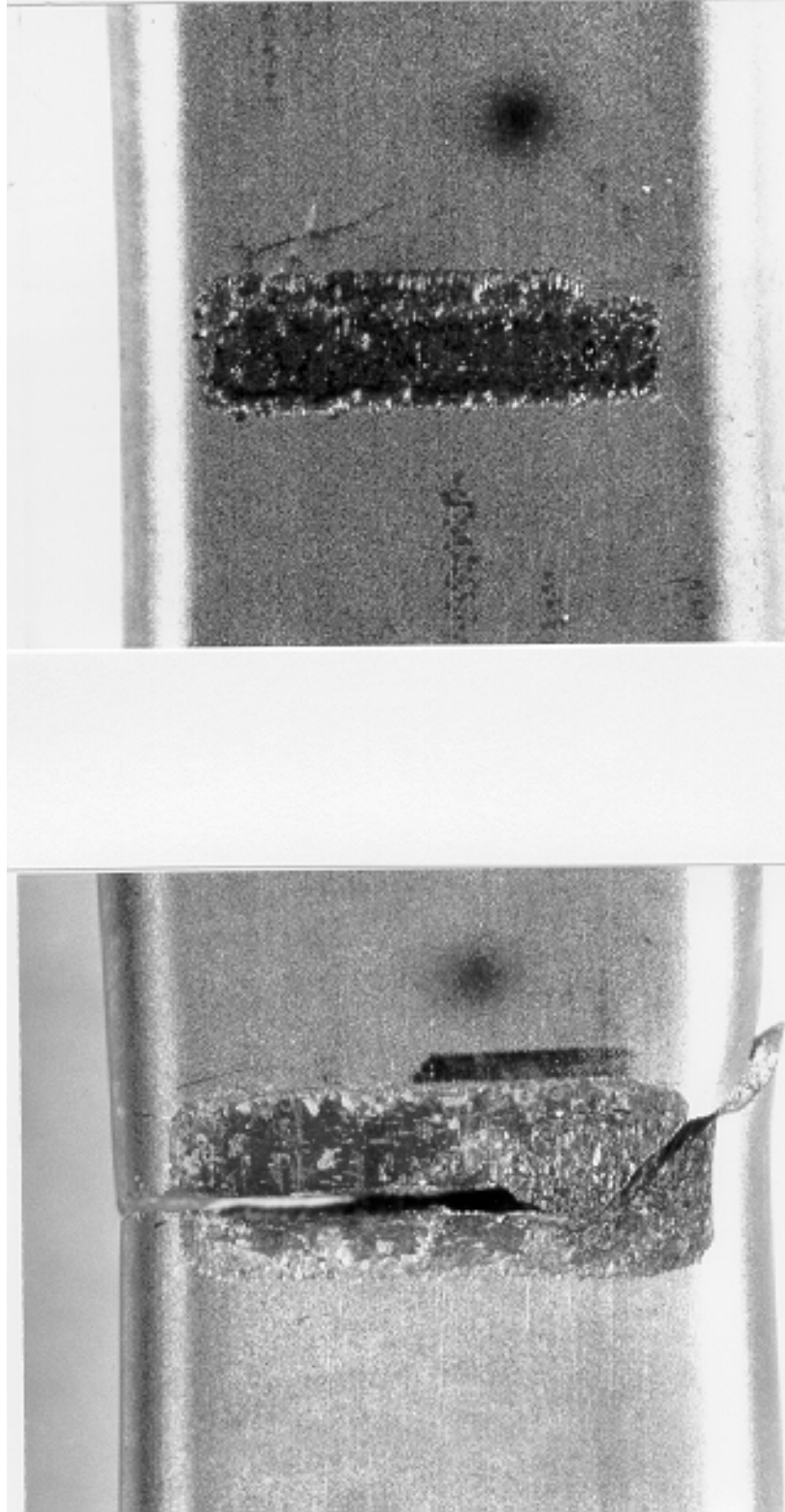


Figure 6A.44. Specimen 76-10.

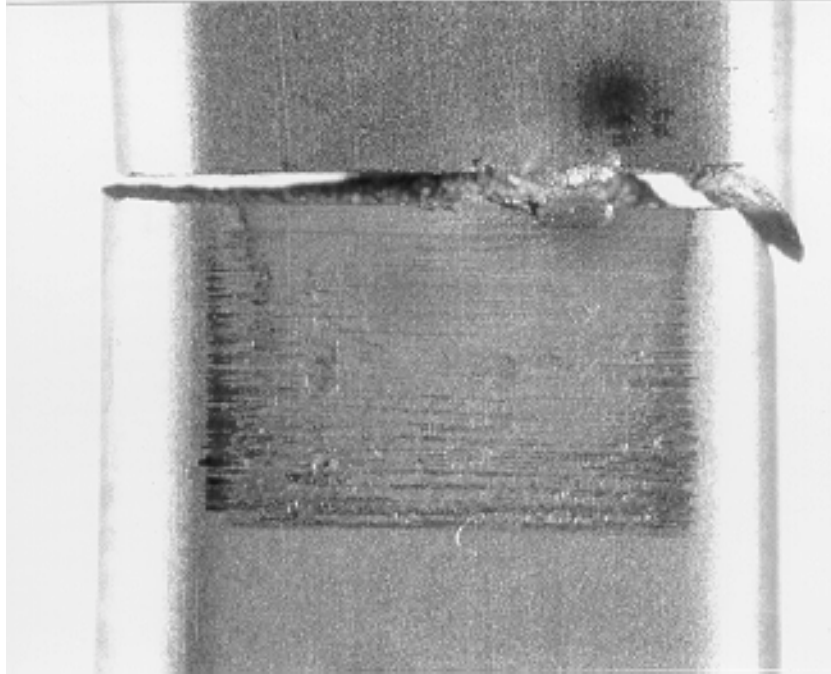


Figure 6A.45. Specimen 94-1.

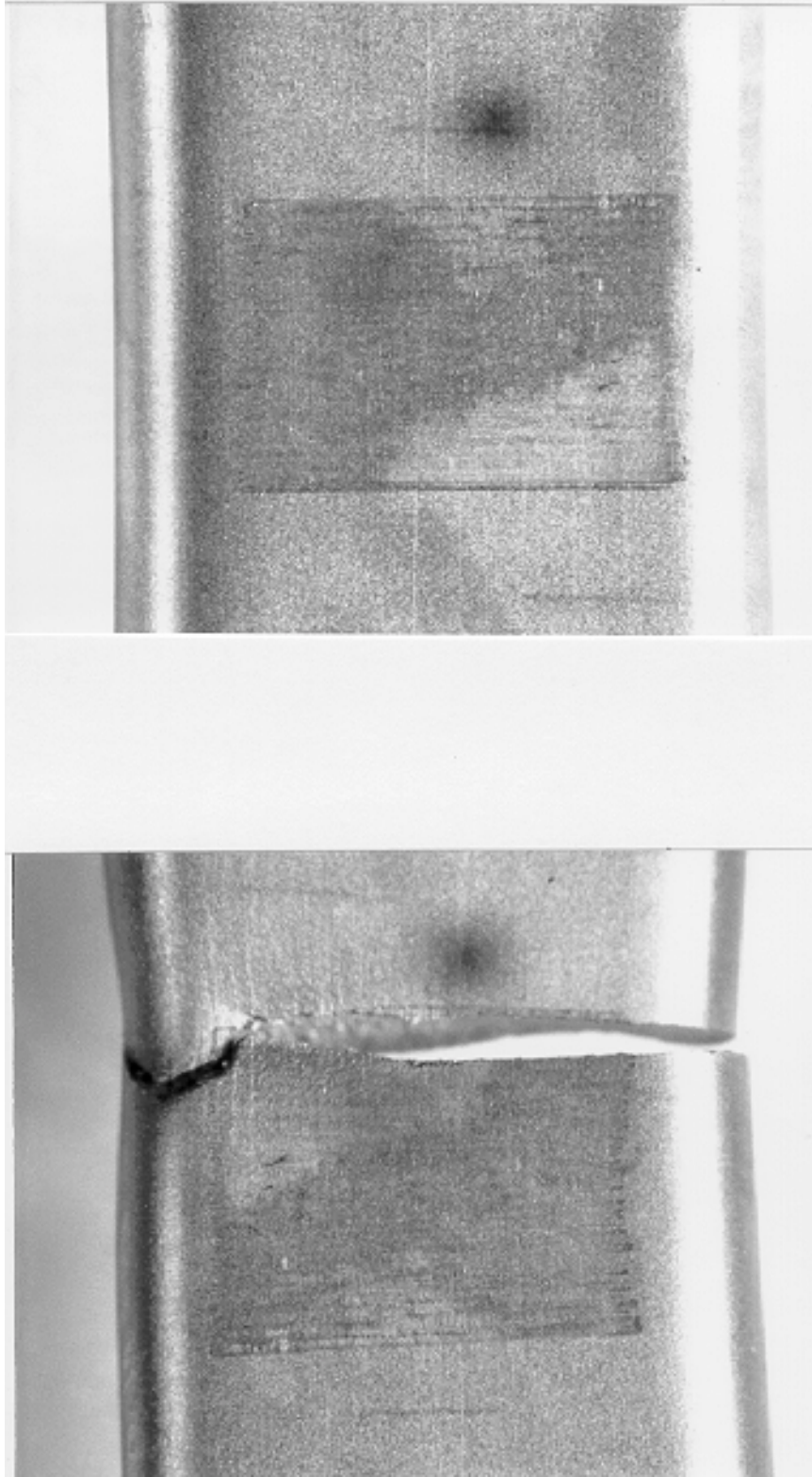


Figure 6A.46. Specimen 75-8.

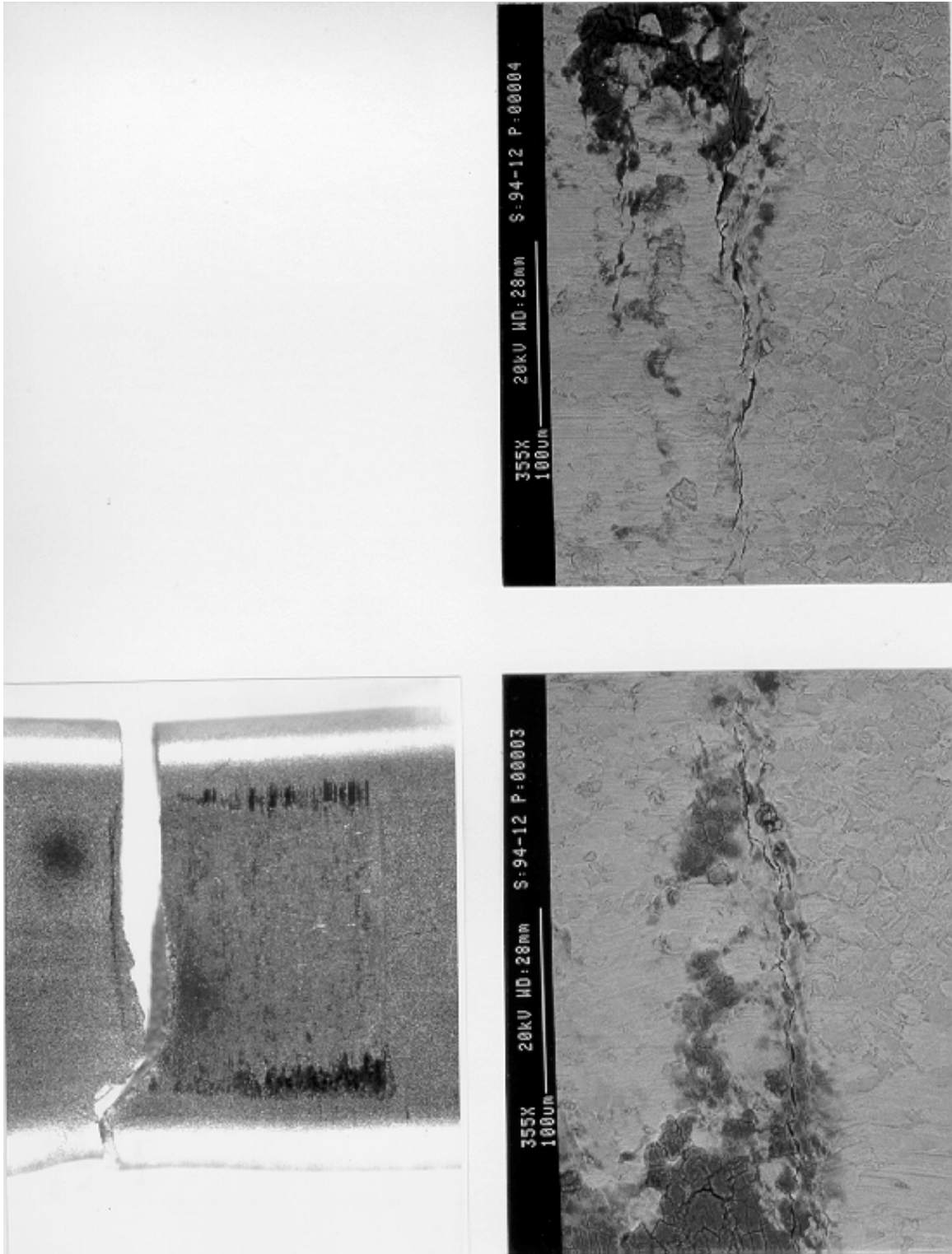


Figure 6A.47. Specimen 94-12.

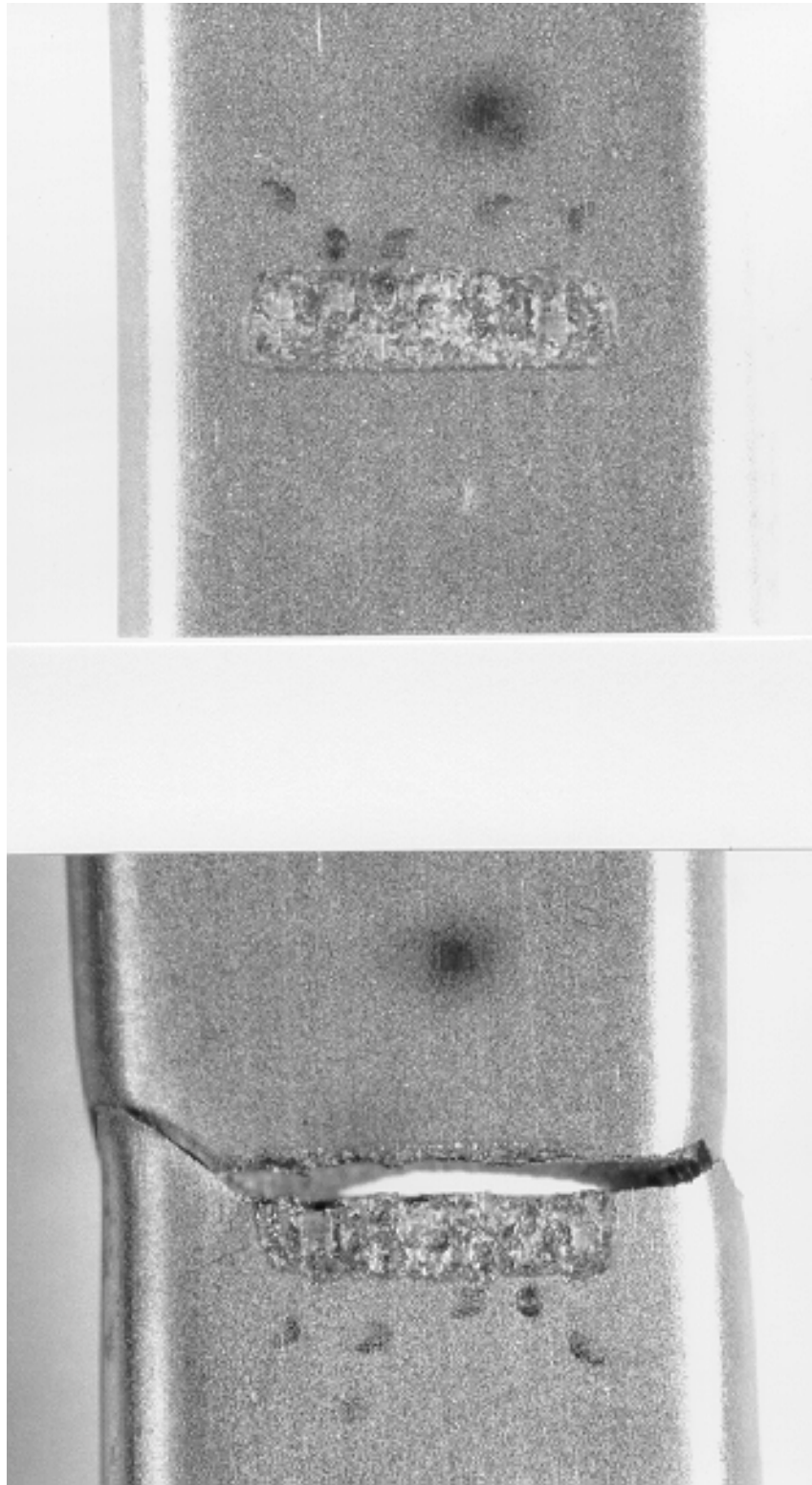


Figure 6A.48. Specimen 76-9.



Figure 6A.49. Specimen 75-9.

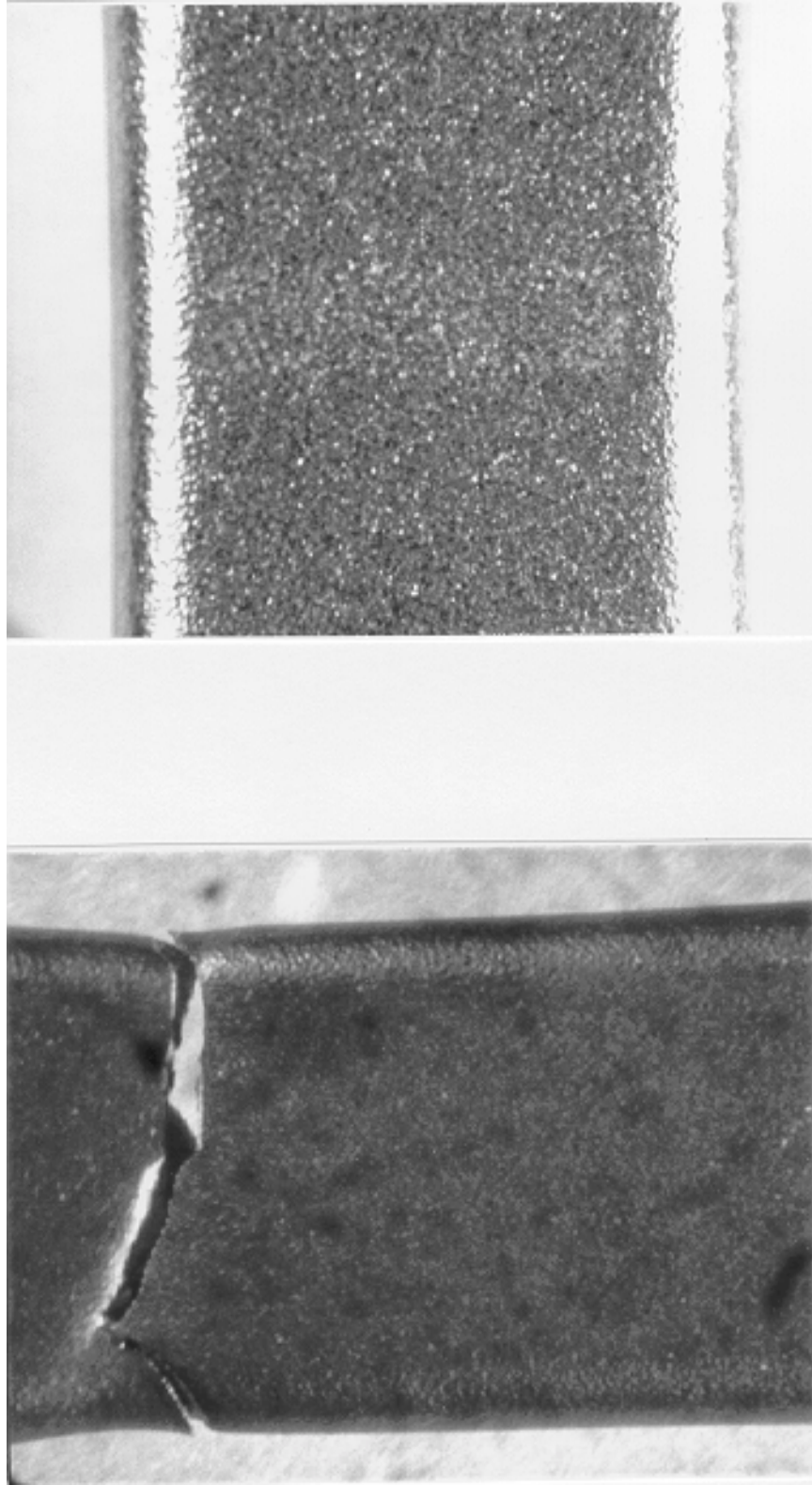


Figure 6A.50. Specimen 70-1.

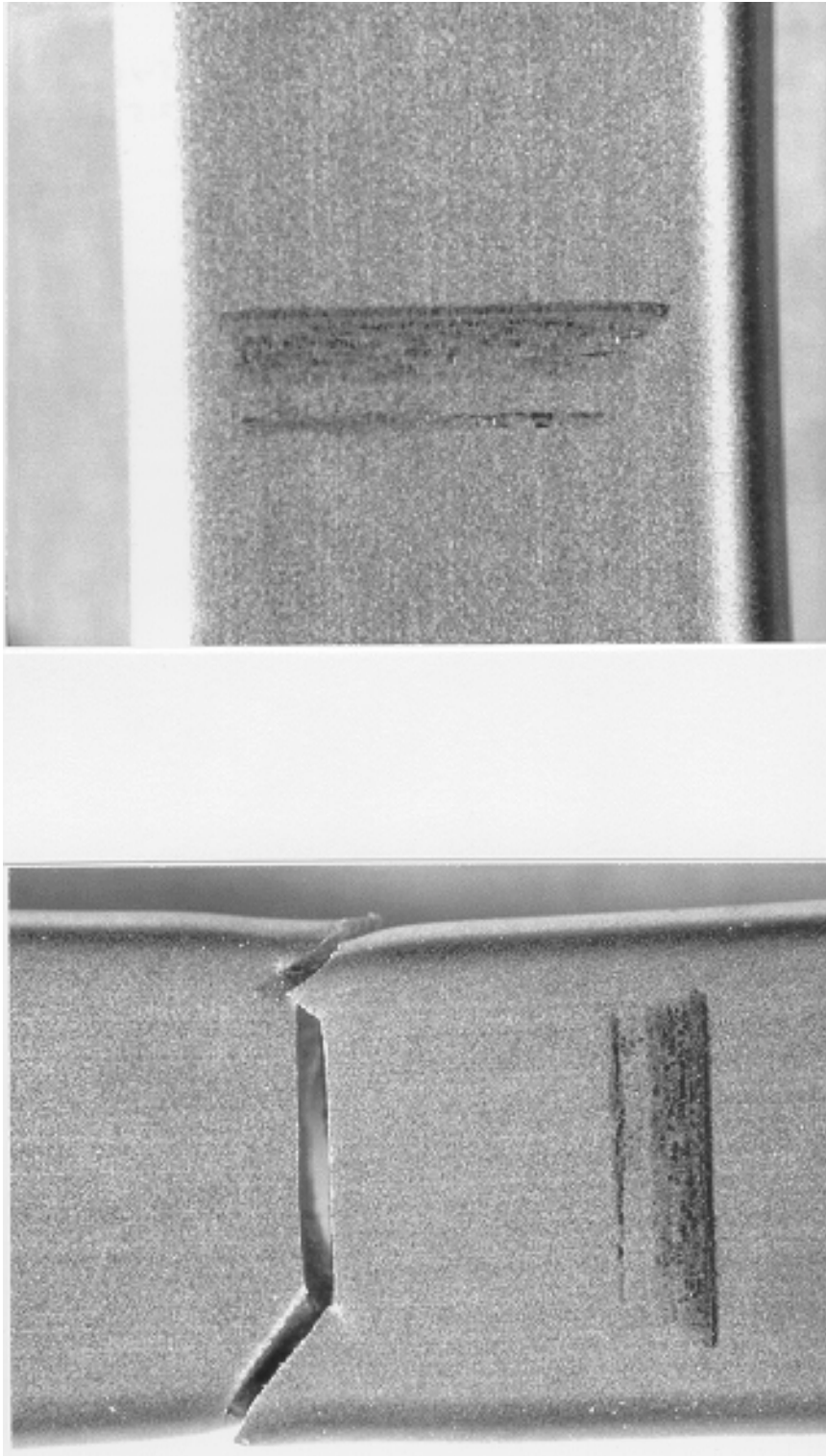


Figure 6A.51. Specimen 85-15.

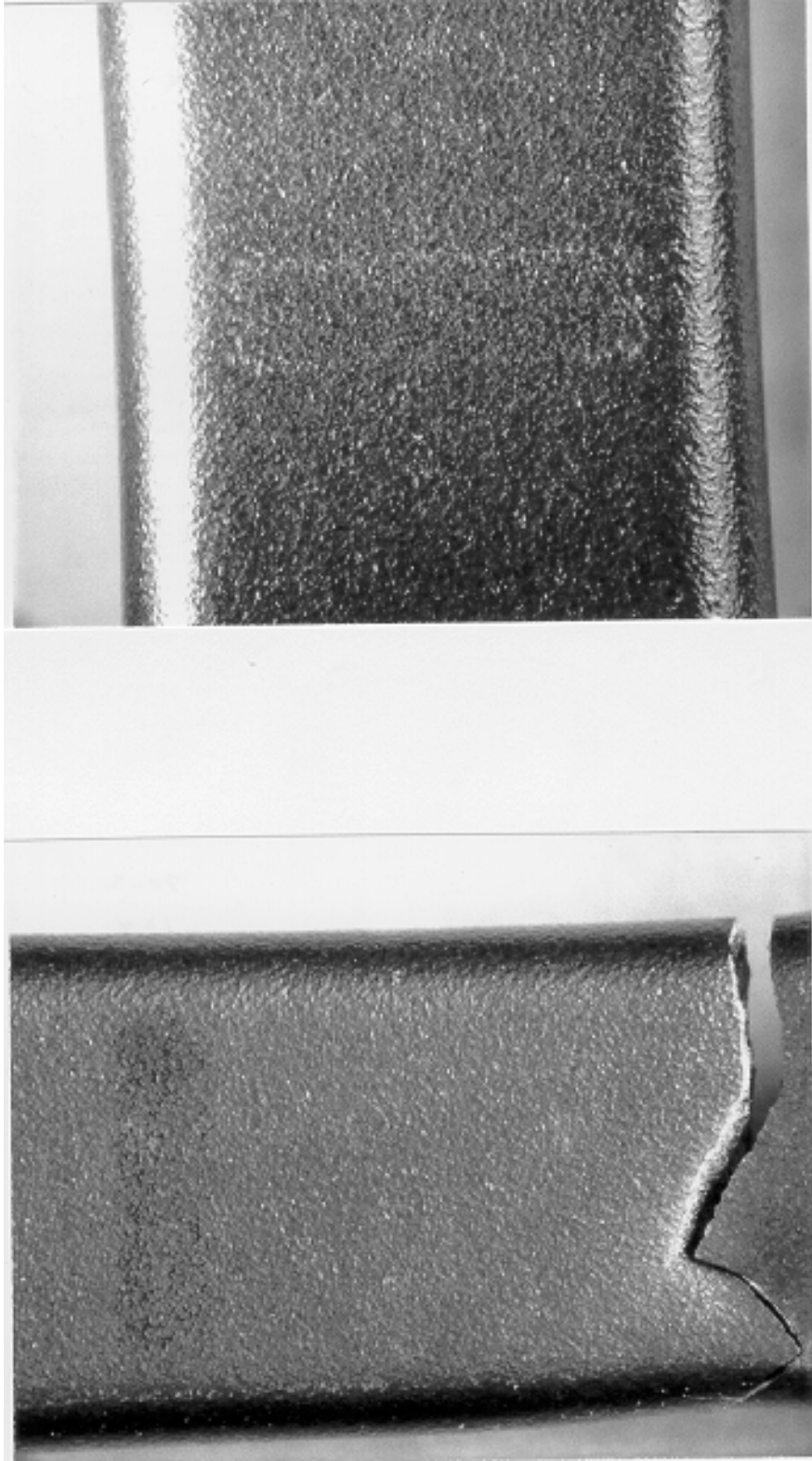


Figure 6A.52. Specimen 70-2.

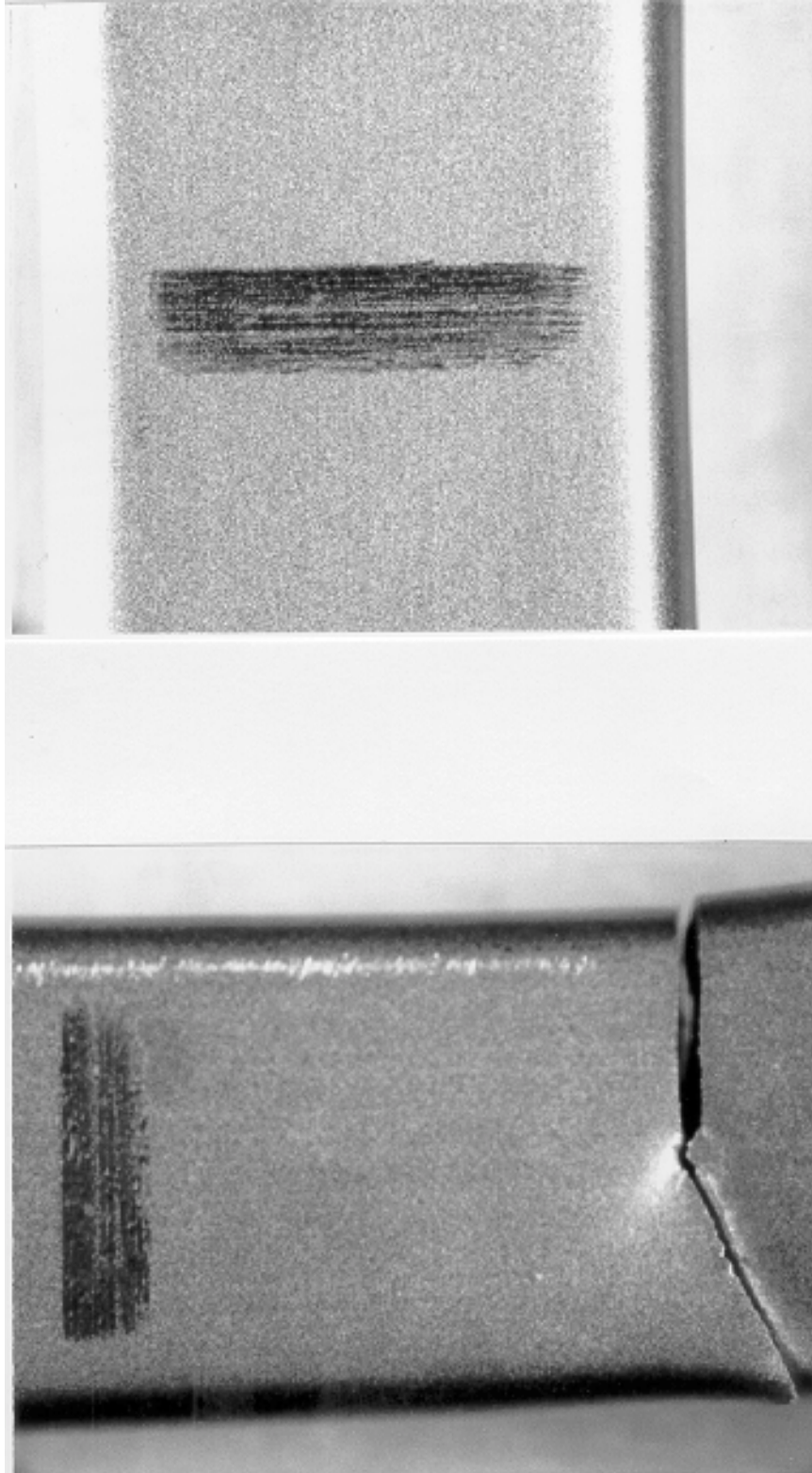


Figure 6A.53. Specimen 75-10.

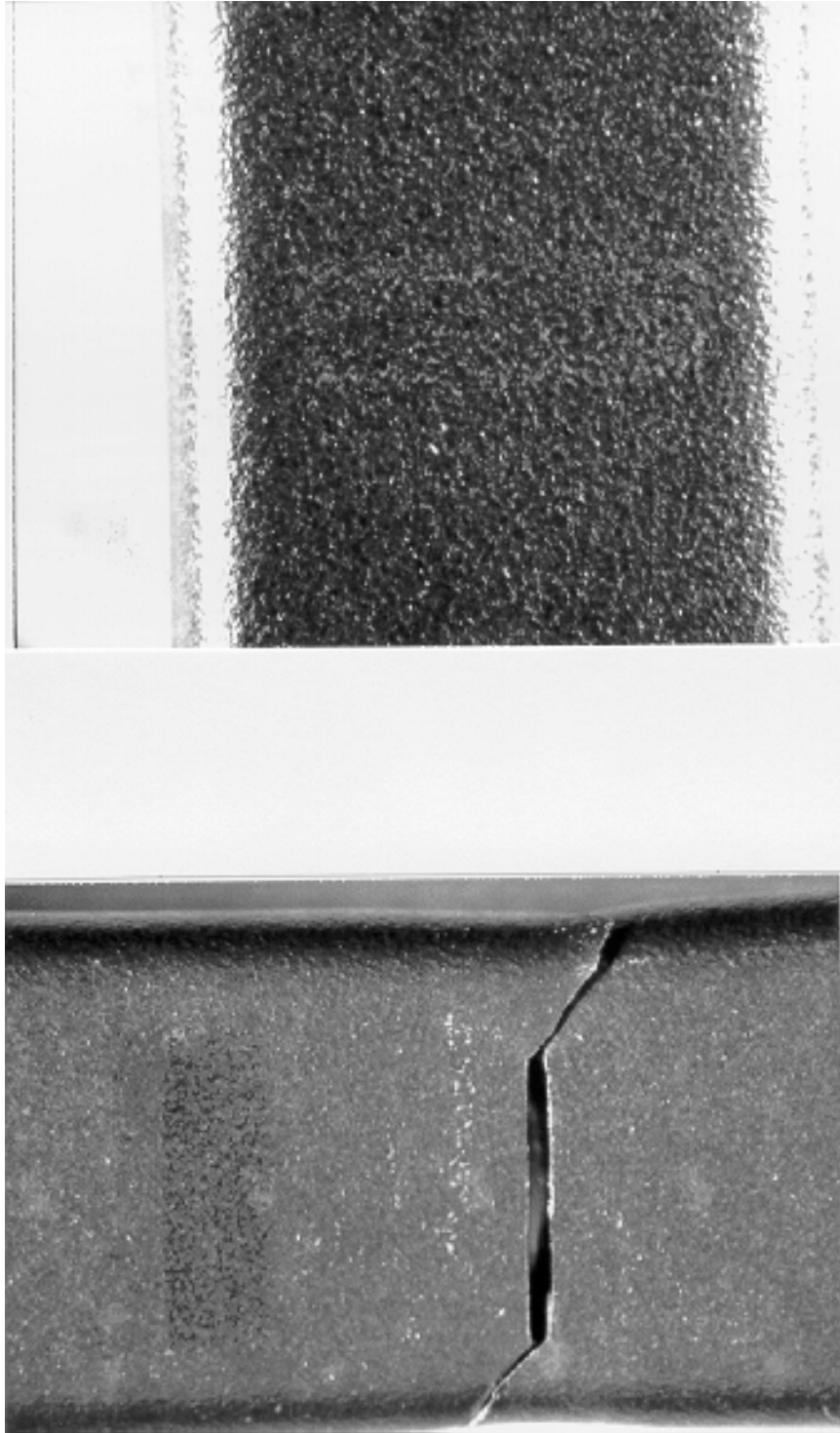


Figure 6A.54. Specimen 70-4.

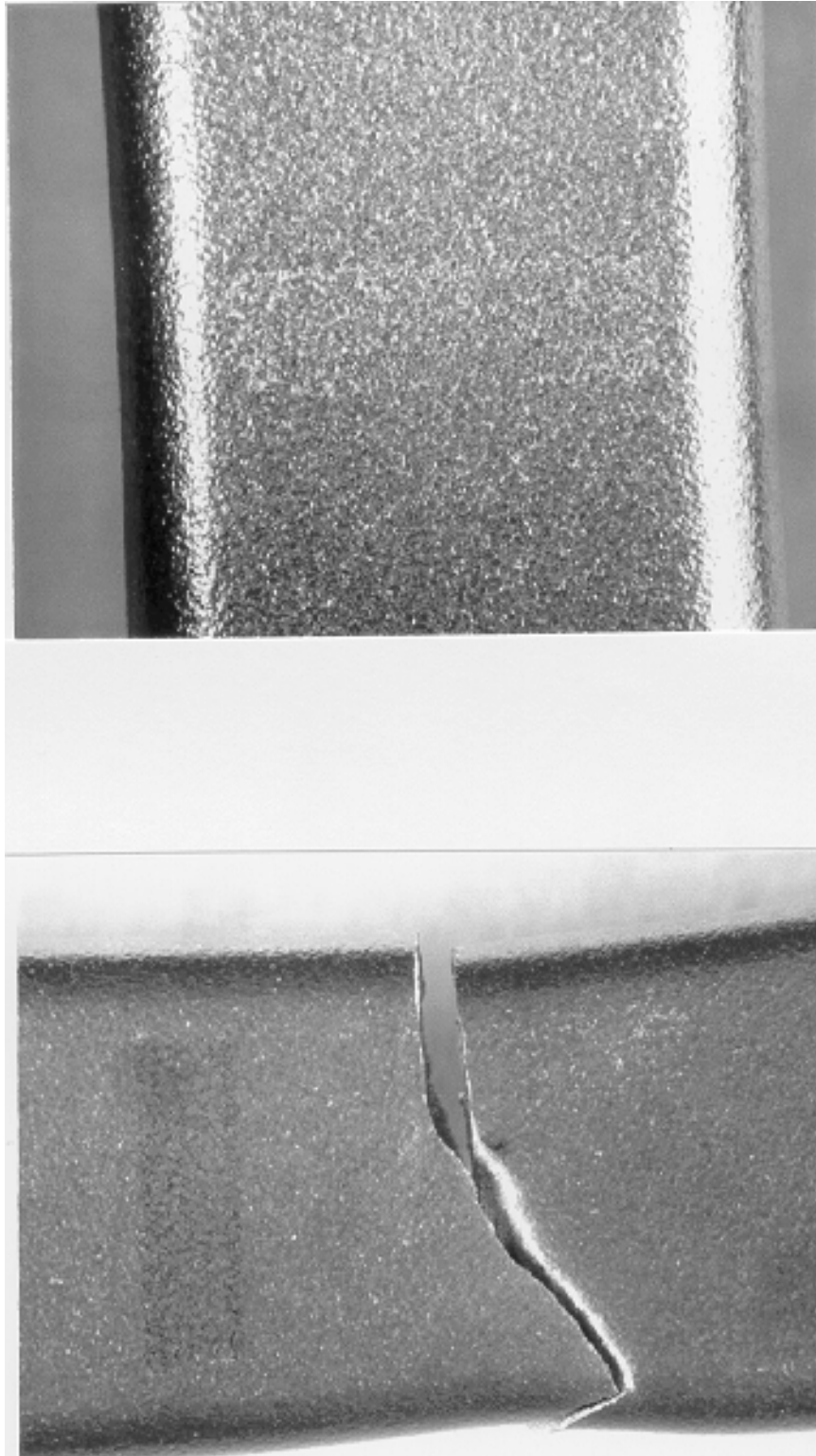


Figure 6A.55. Specimen 79-5.

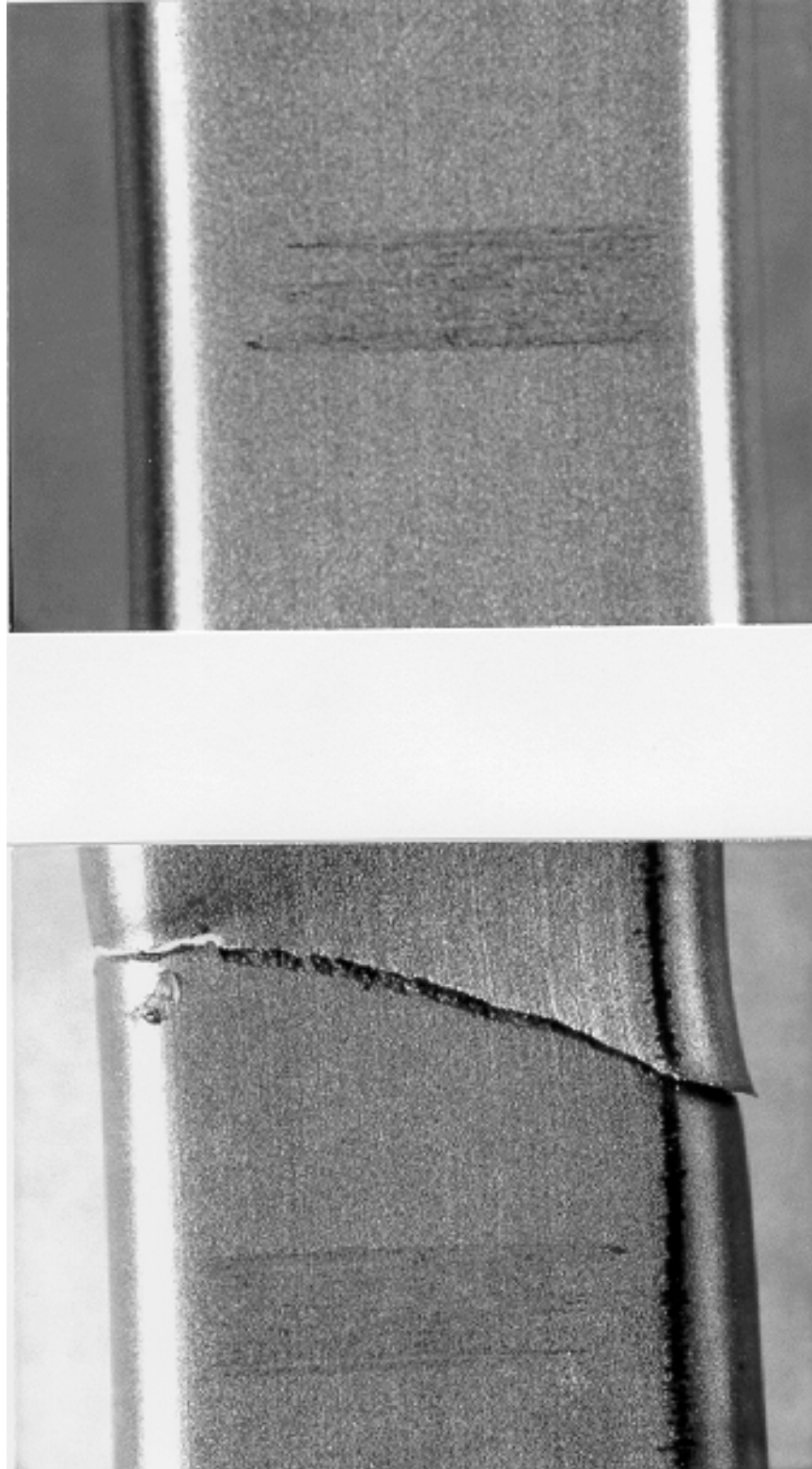


Figure 6A.56. Specimen 94-11.

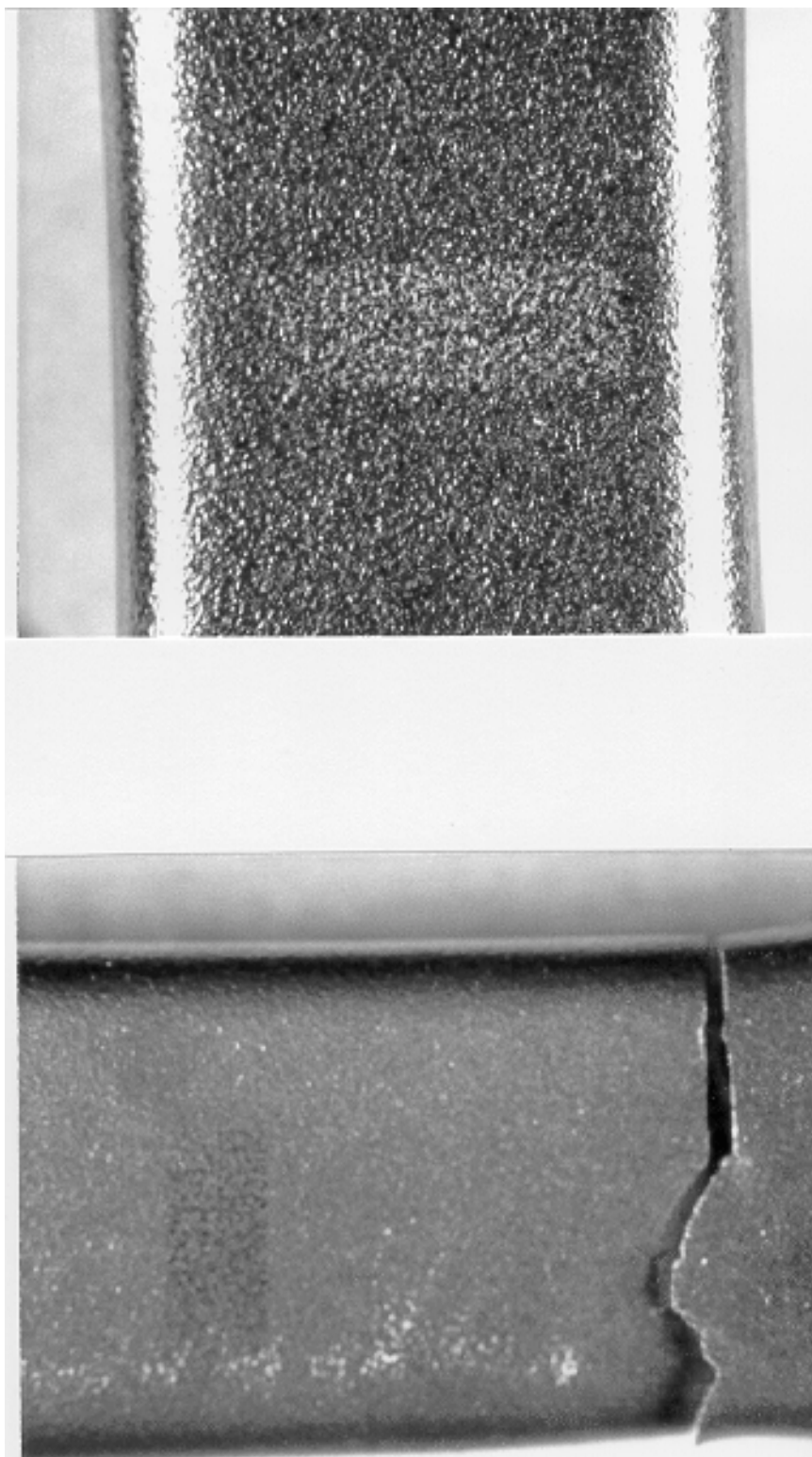


Figure 6A.57. Specimen 48-8.

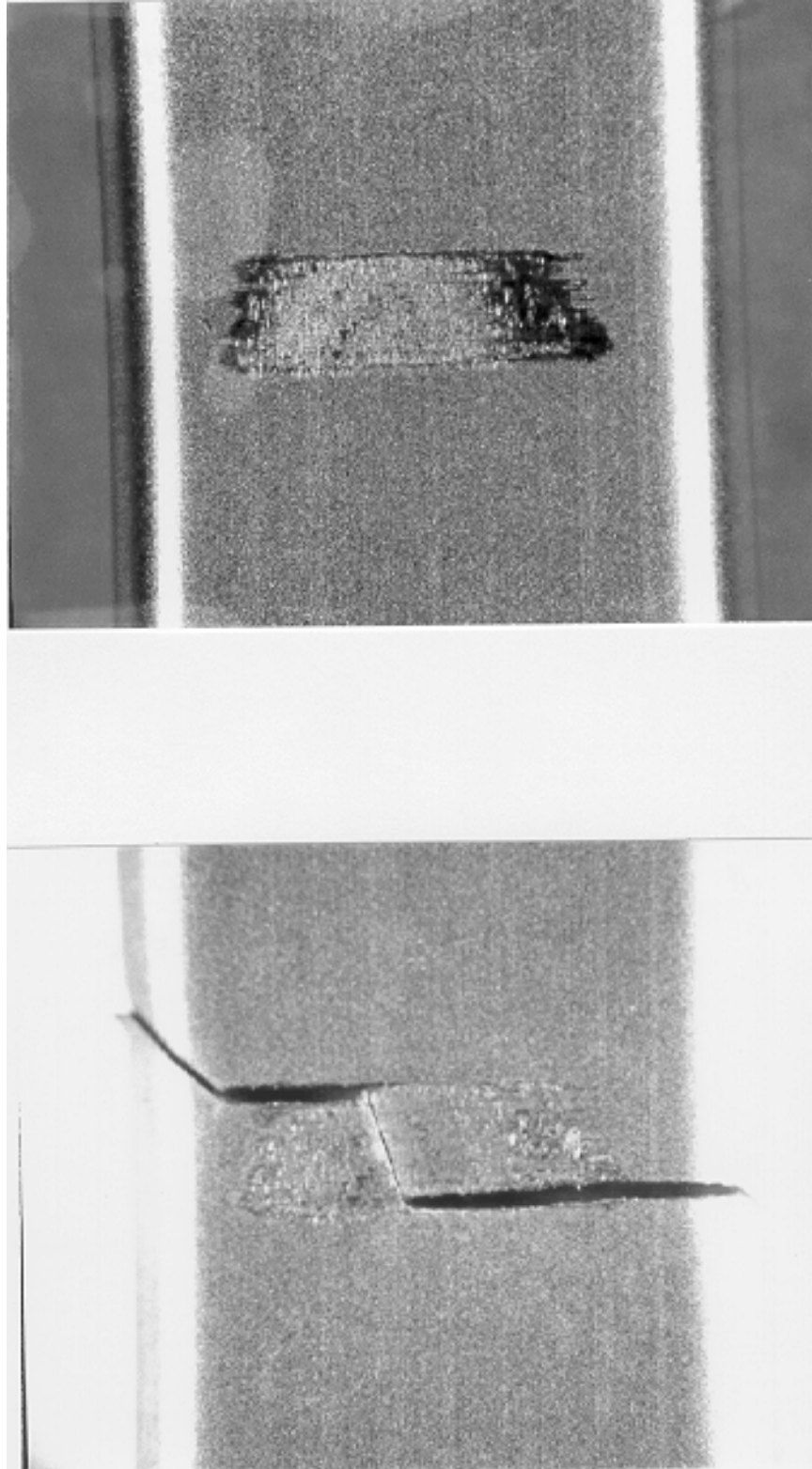


Figure 6A.58. Specimen 75-14.

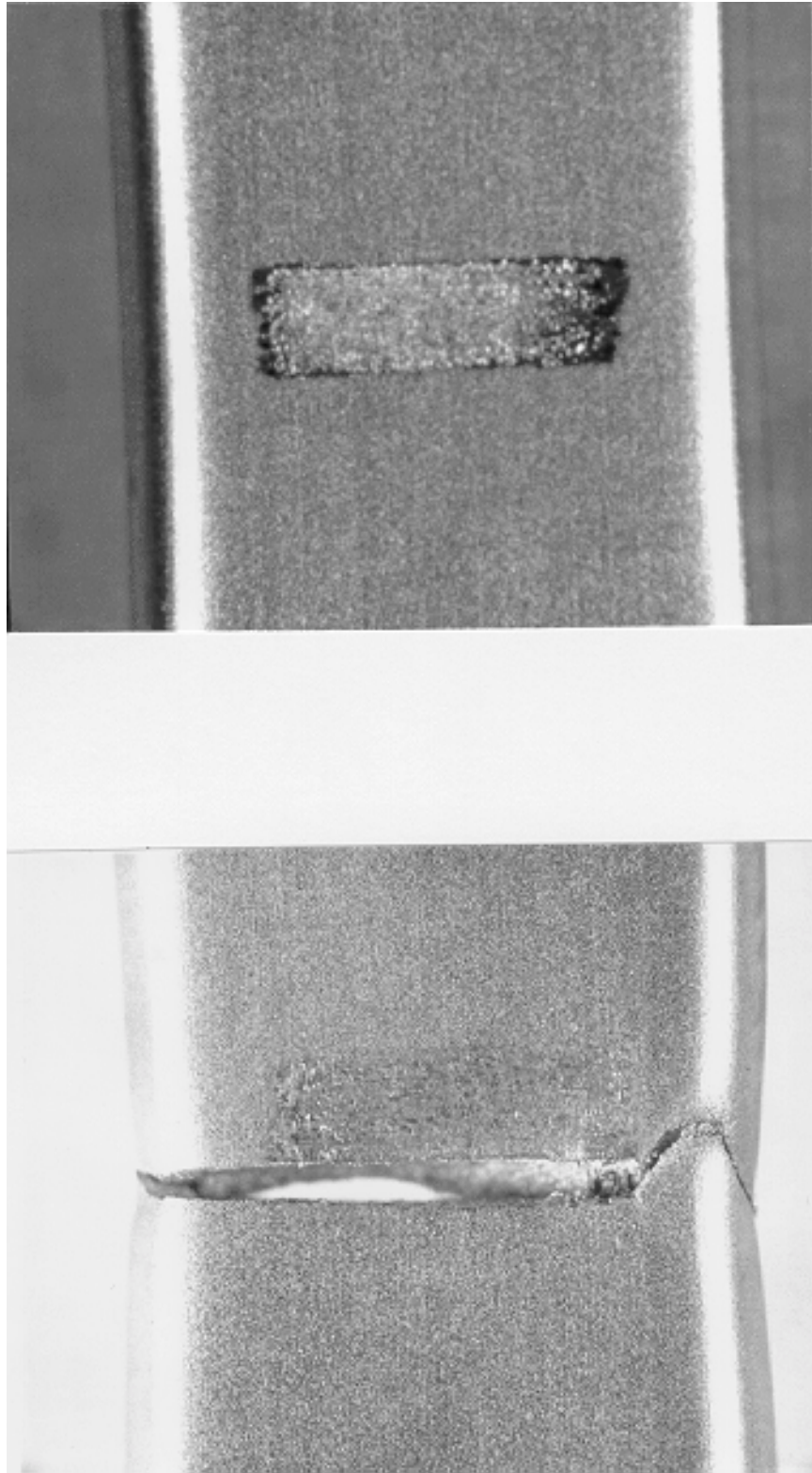


Figure 6A.59. Specimen 79-15.

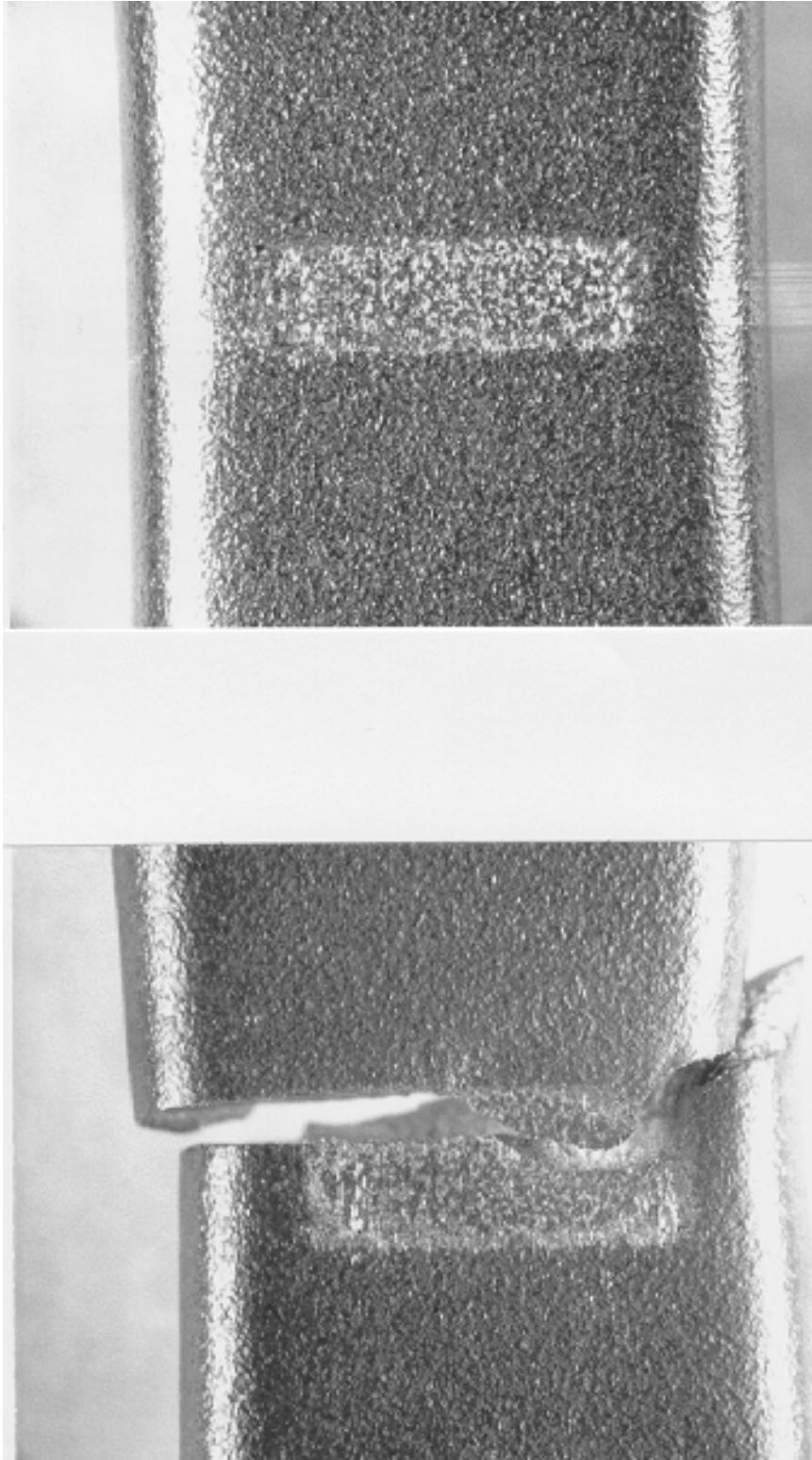


Figure 6A.60. Specimen 70-7.

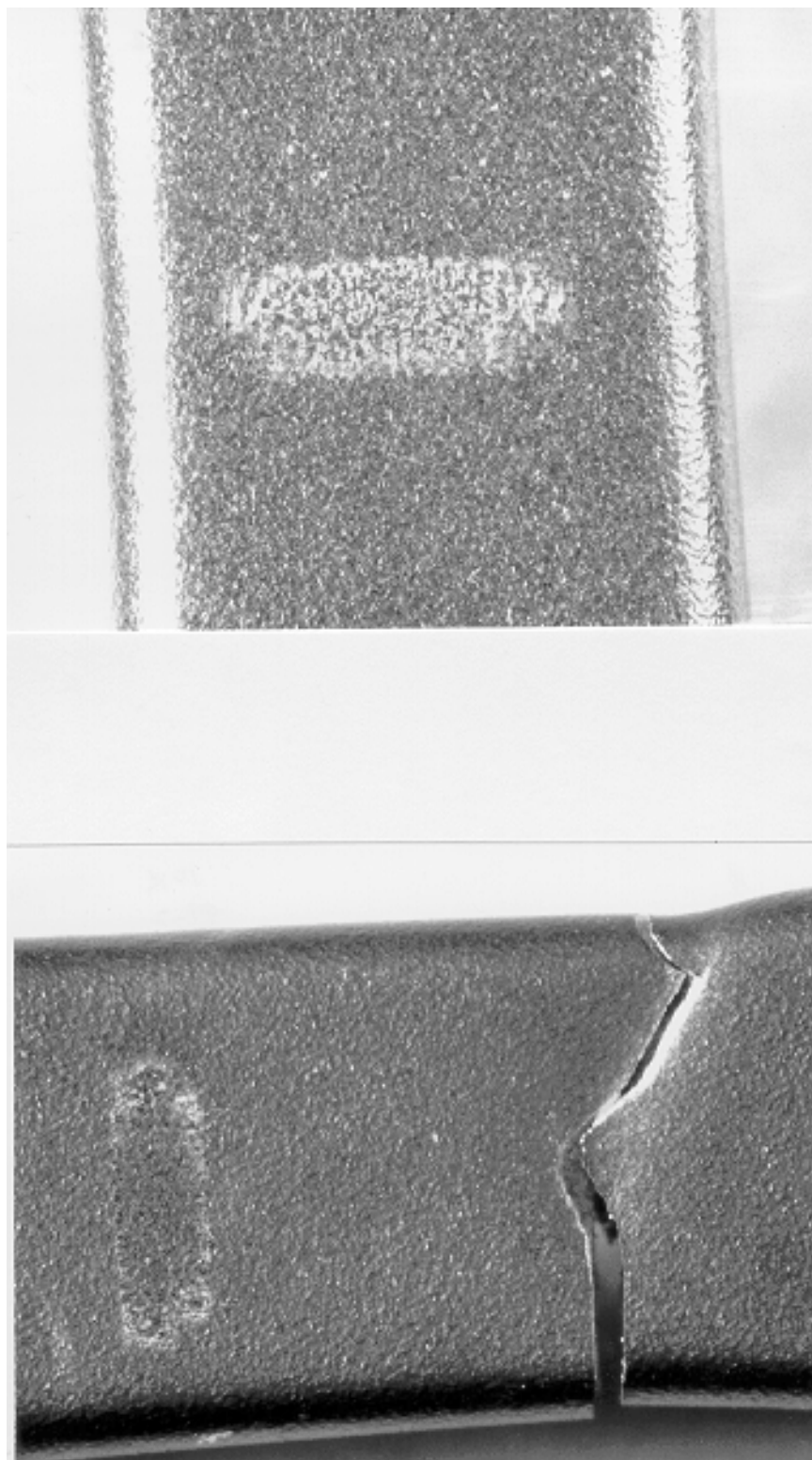


Figure 6A.61. Specimen 99-2.

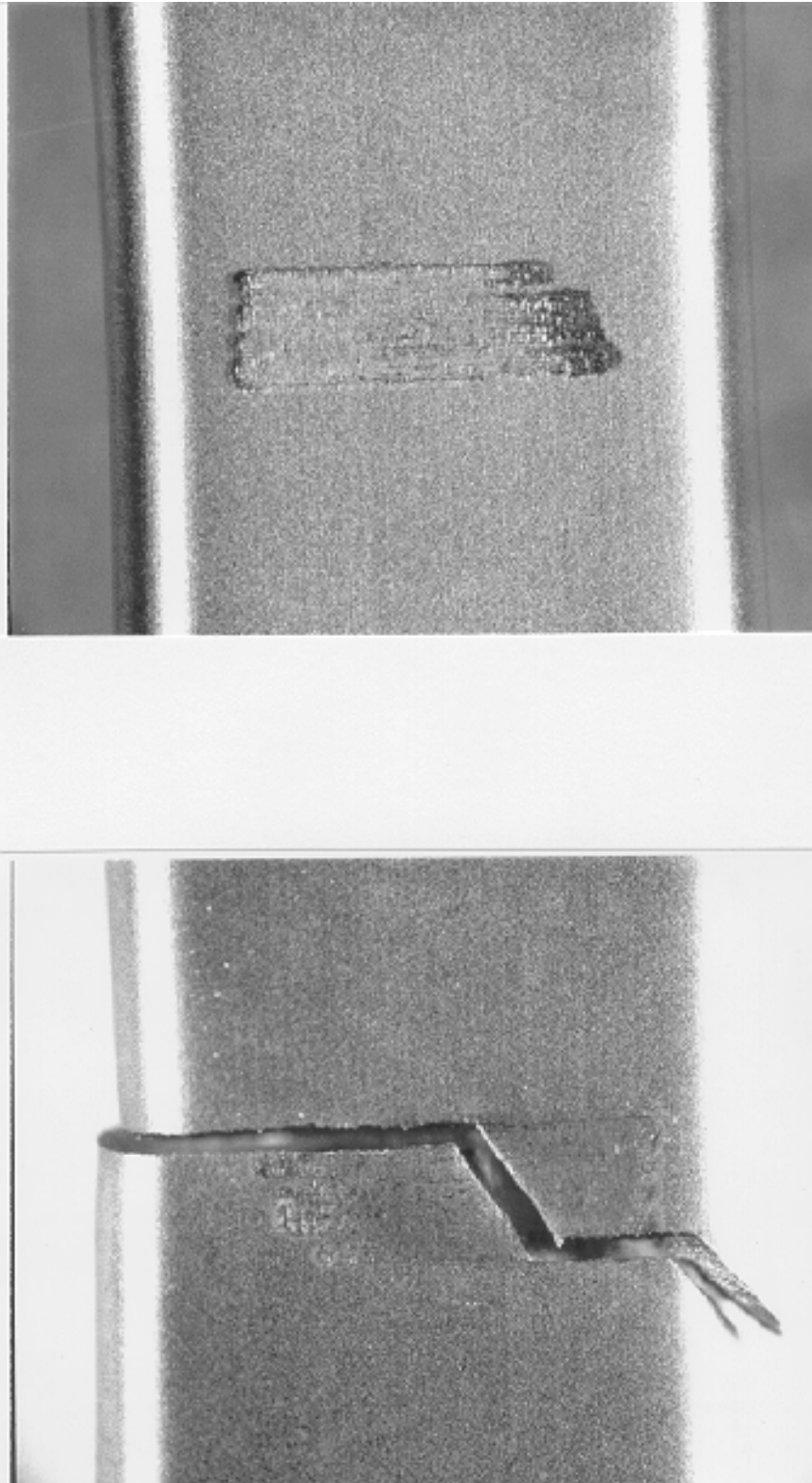


Figure 6A.62. Specimen 75-15.



Figure 6A.63. Specimen 94-8.

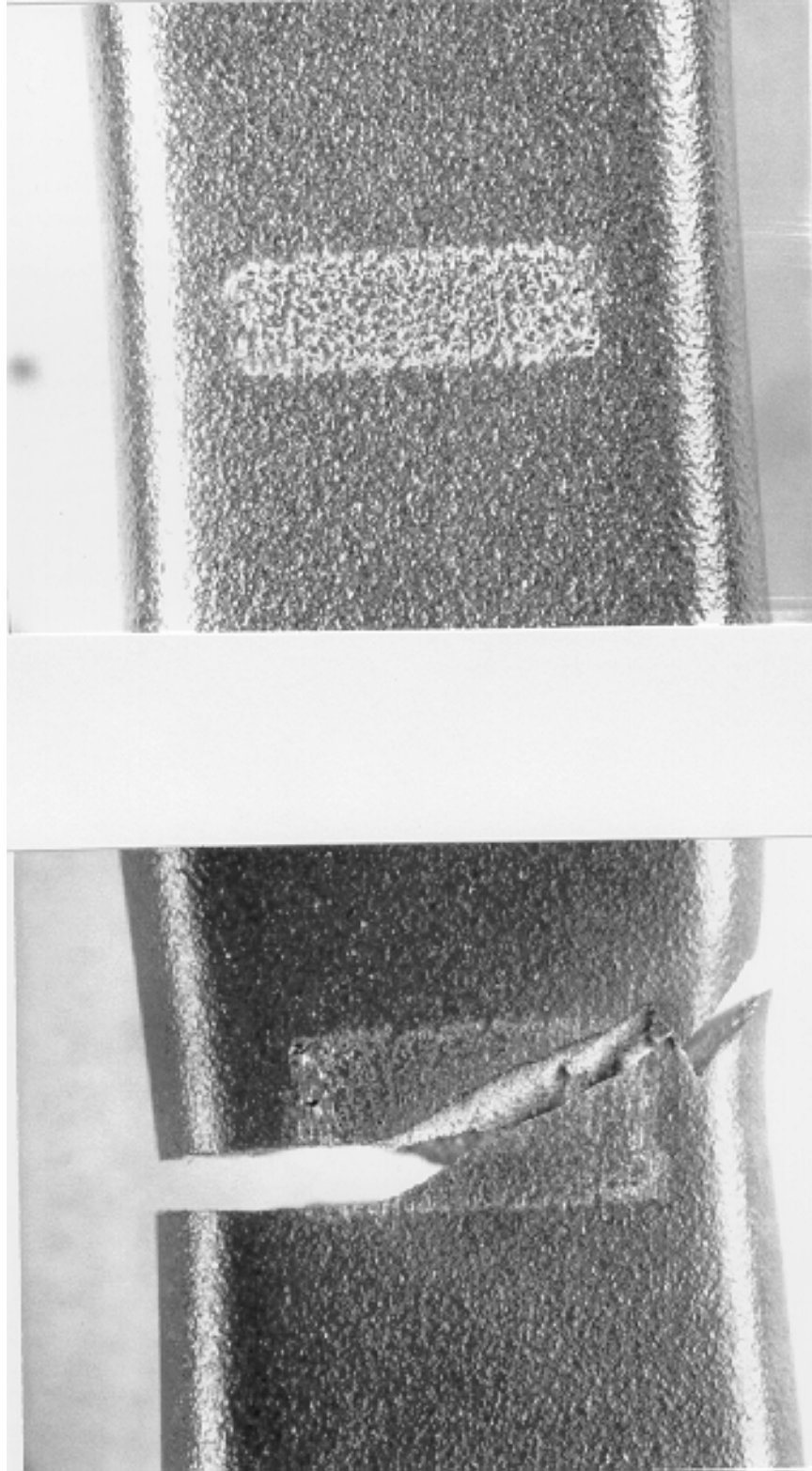


Figure 6A.64. Specimen 70-10.

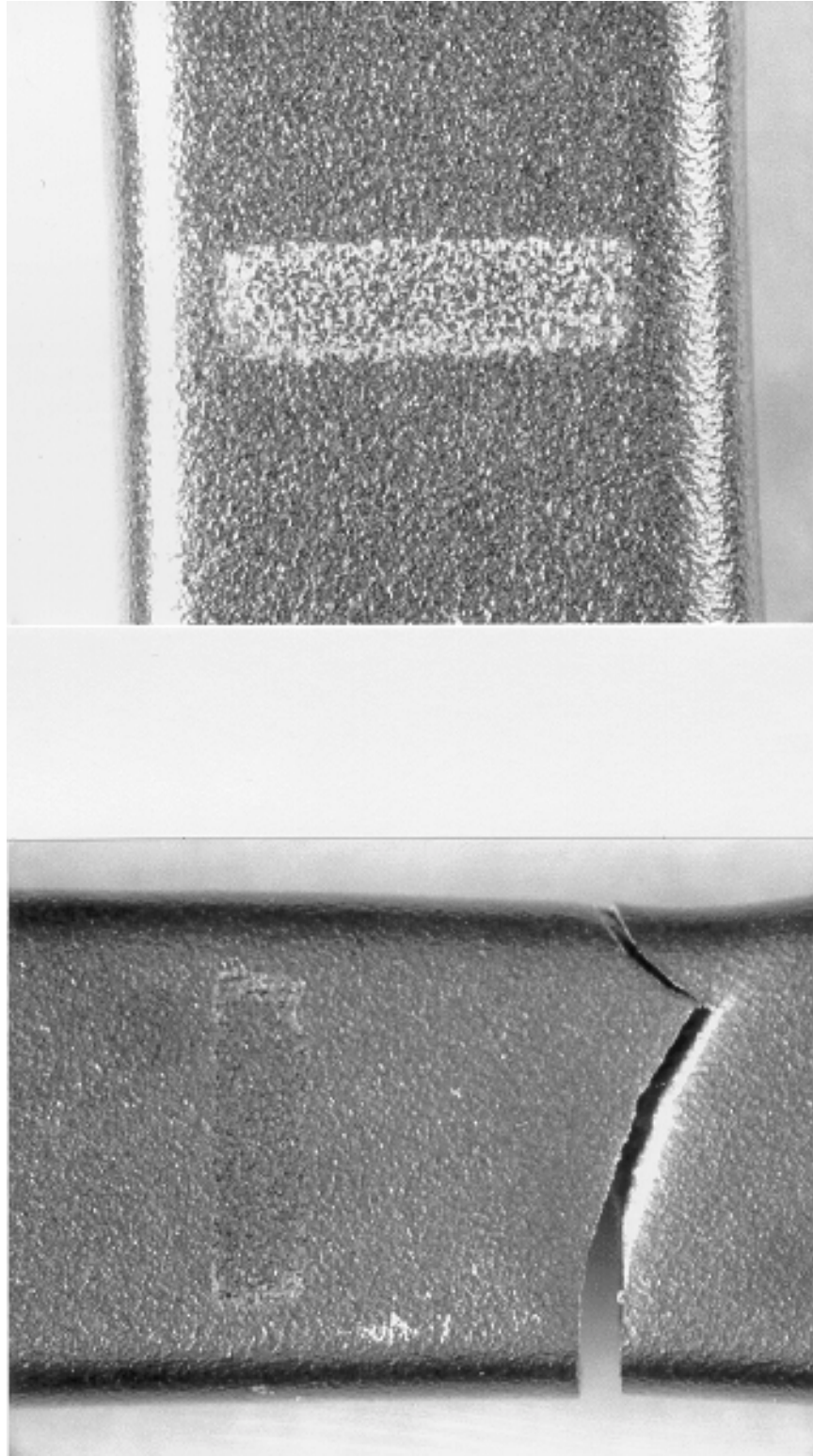


Figure 6A.65. Specimen 48-11.

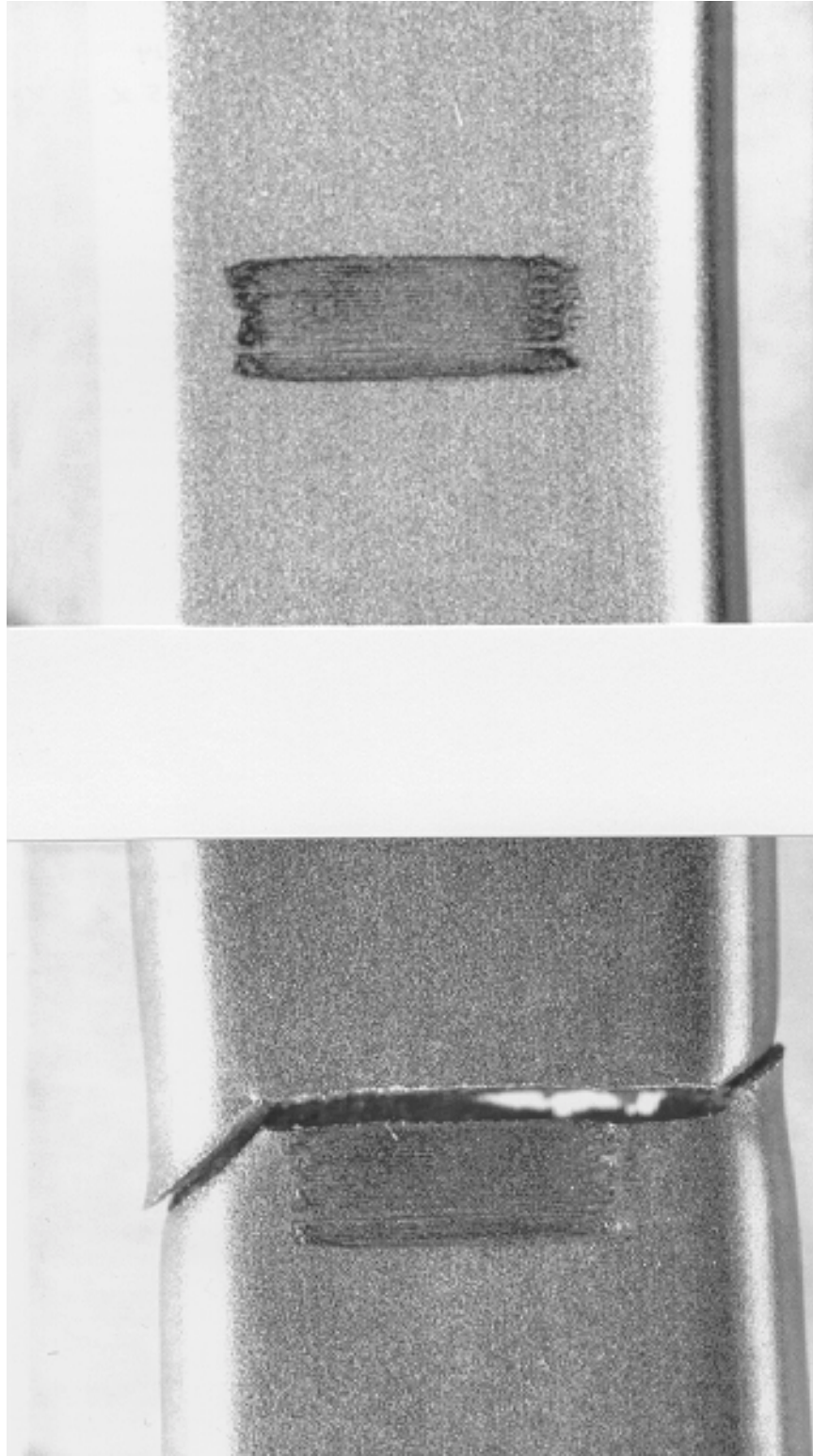


Figure 6A.66. Specimen 79-14.

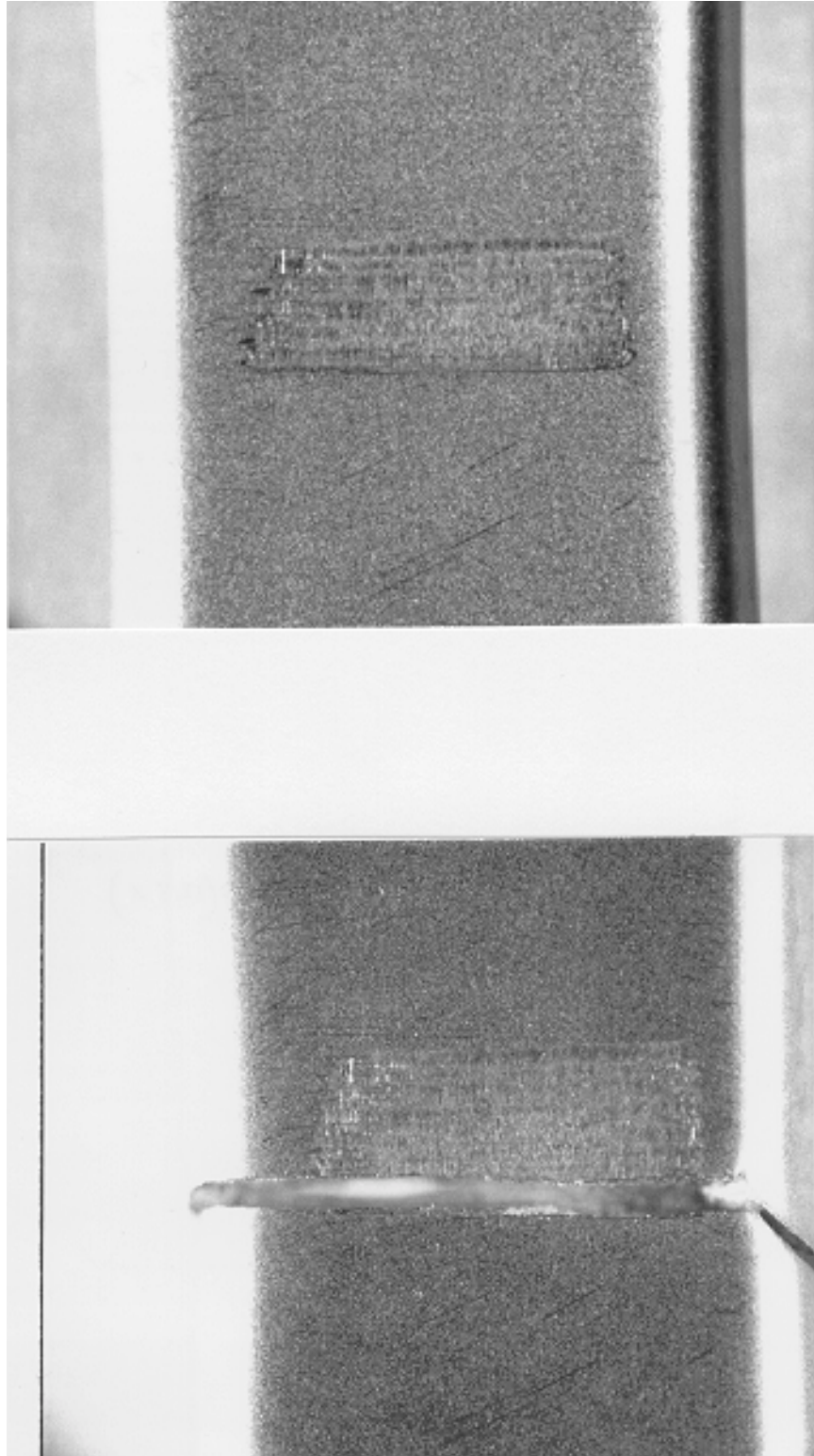


Figure 6A.67. Specimen 75-7.

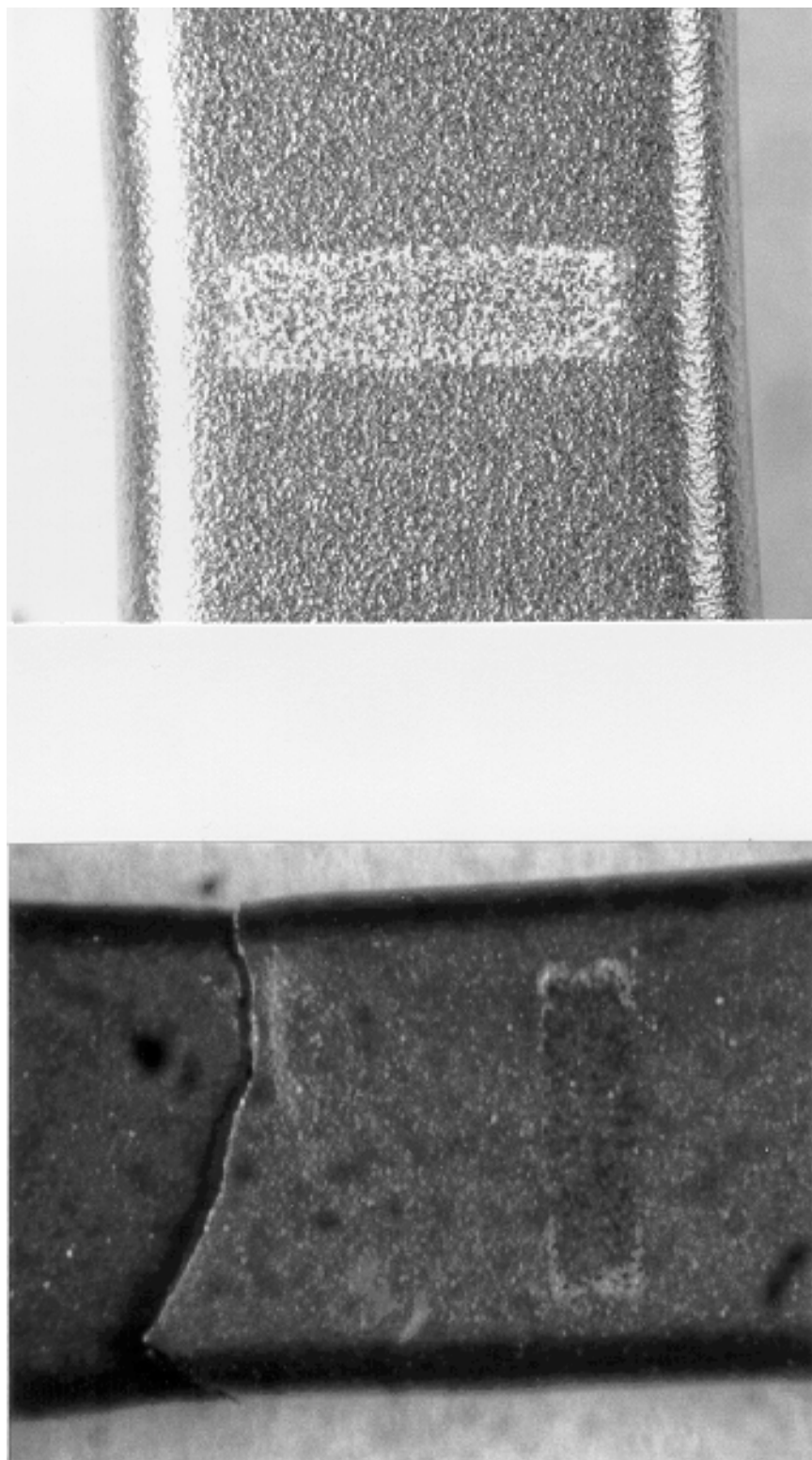


Figure 6A.68. Specimen 70-11.

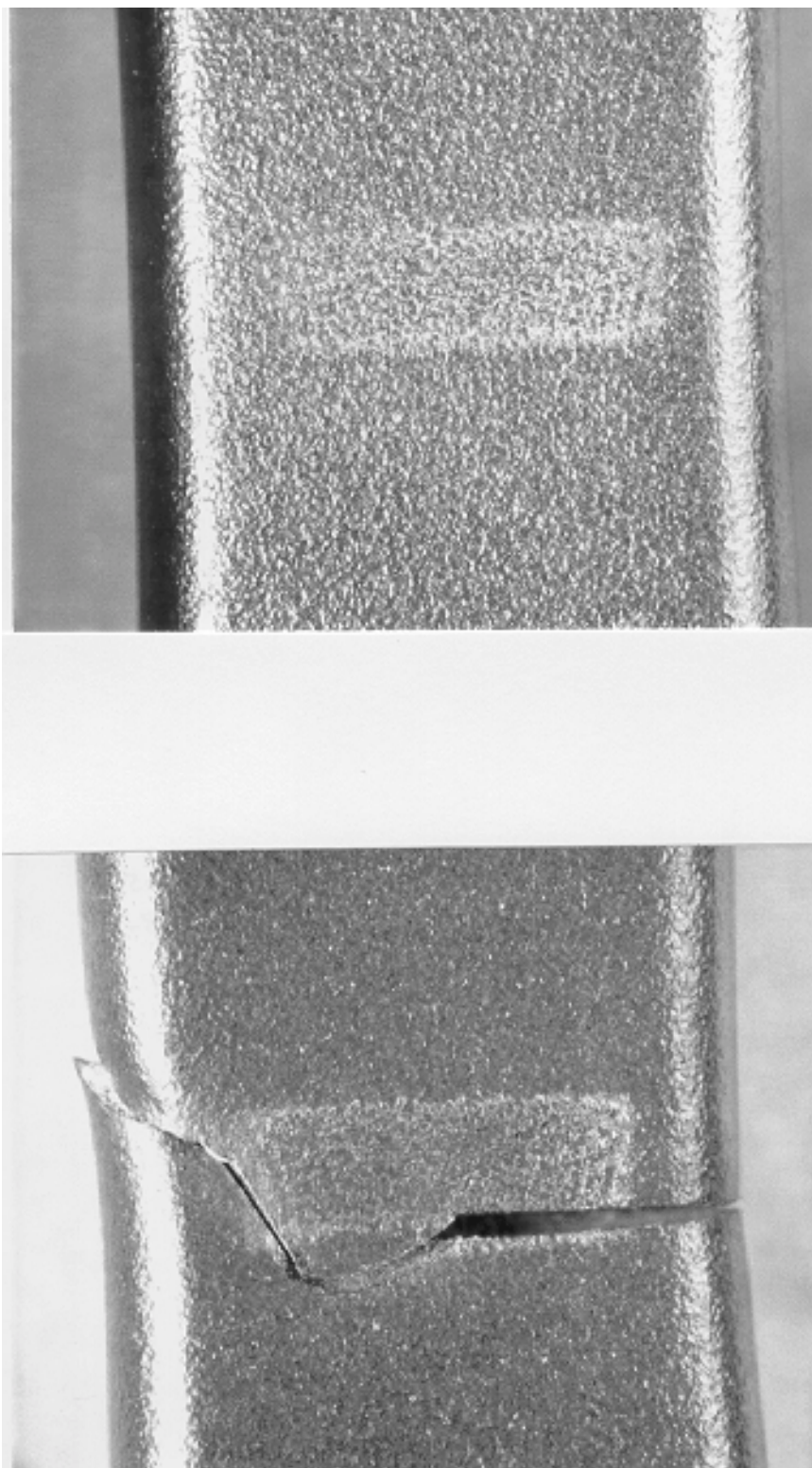


Figure 6A.69. Specimen 48-9.

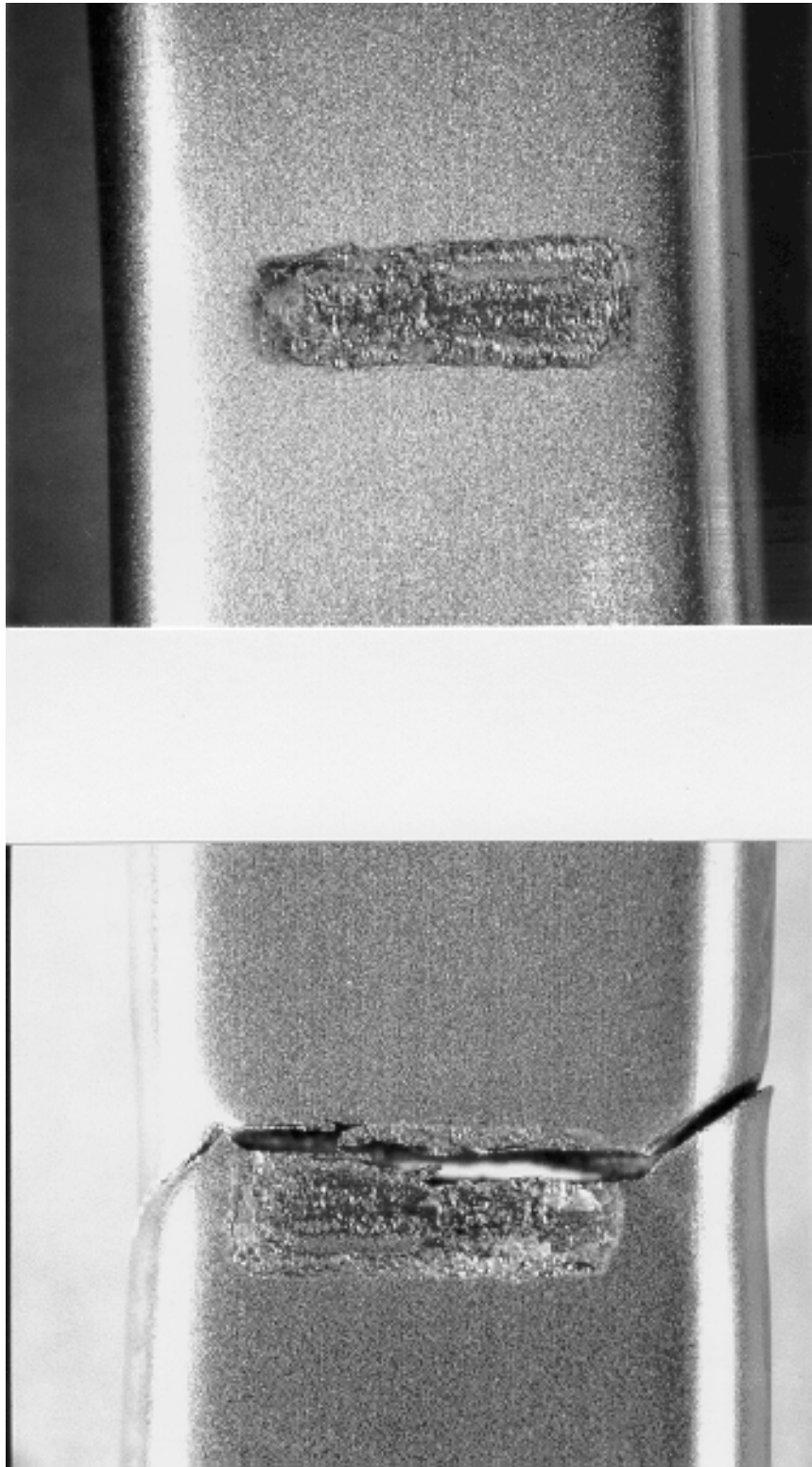


Figure 6A.70. Specimen 48-13.

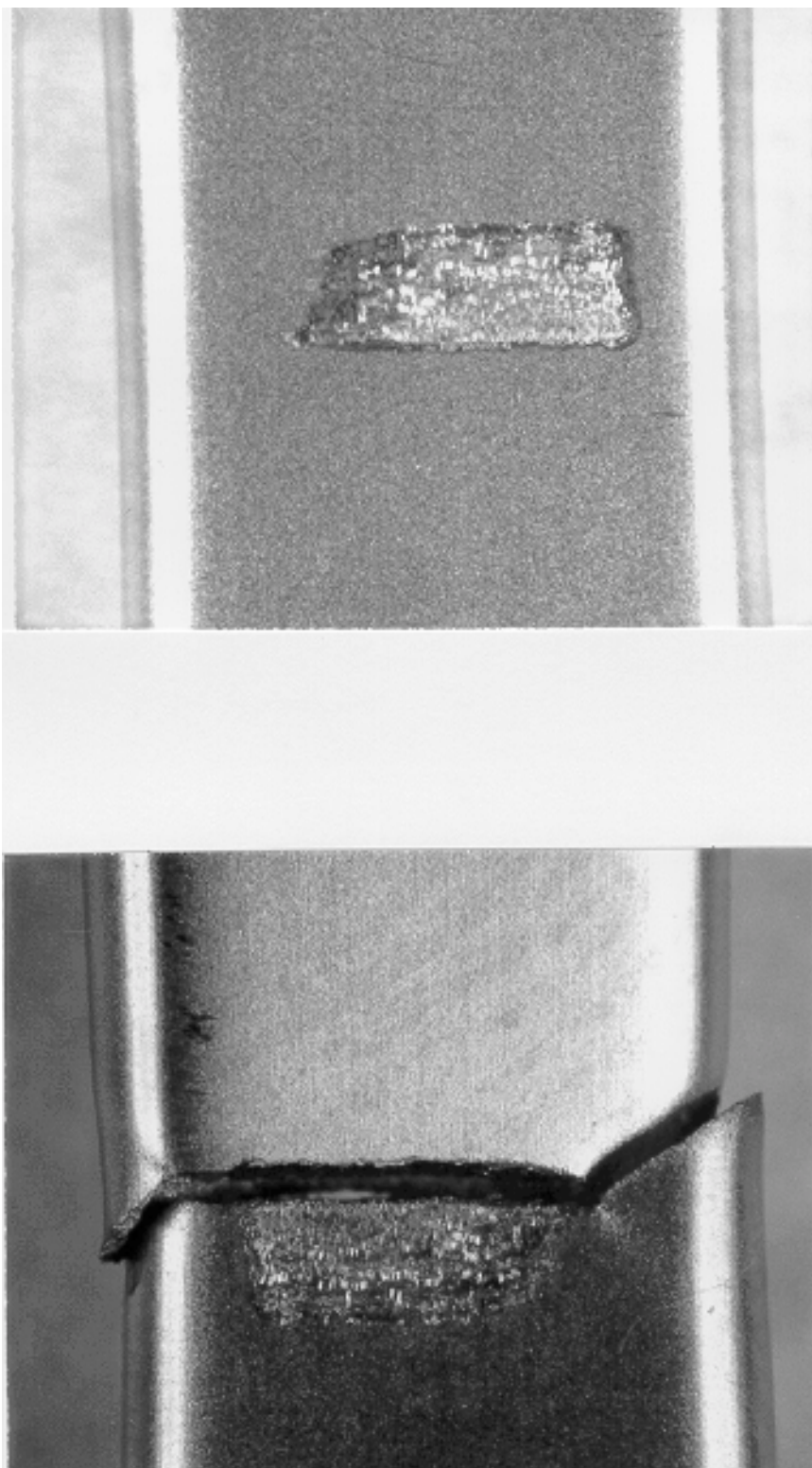


Figure 6A.71. Specimen 70-3.

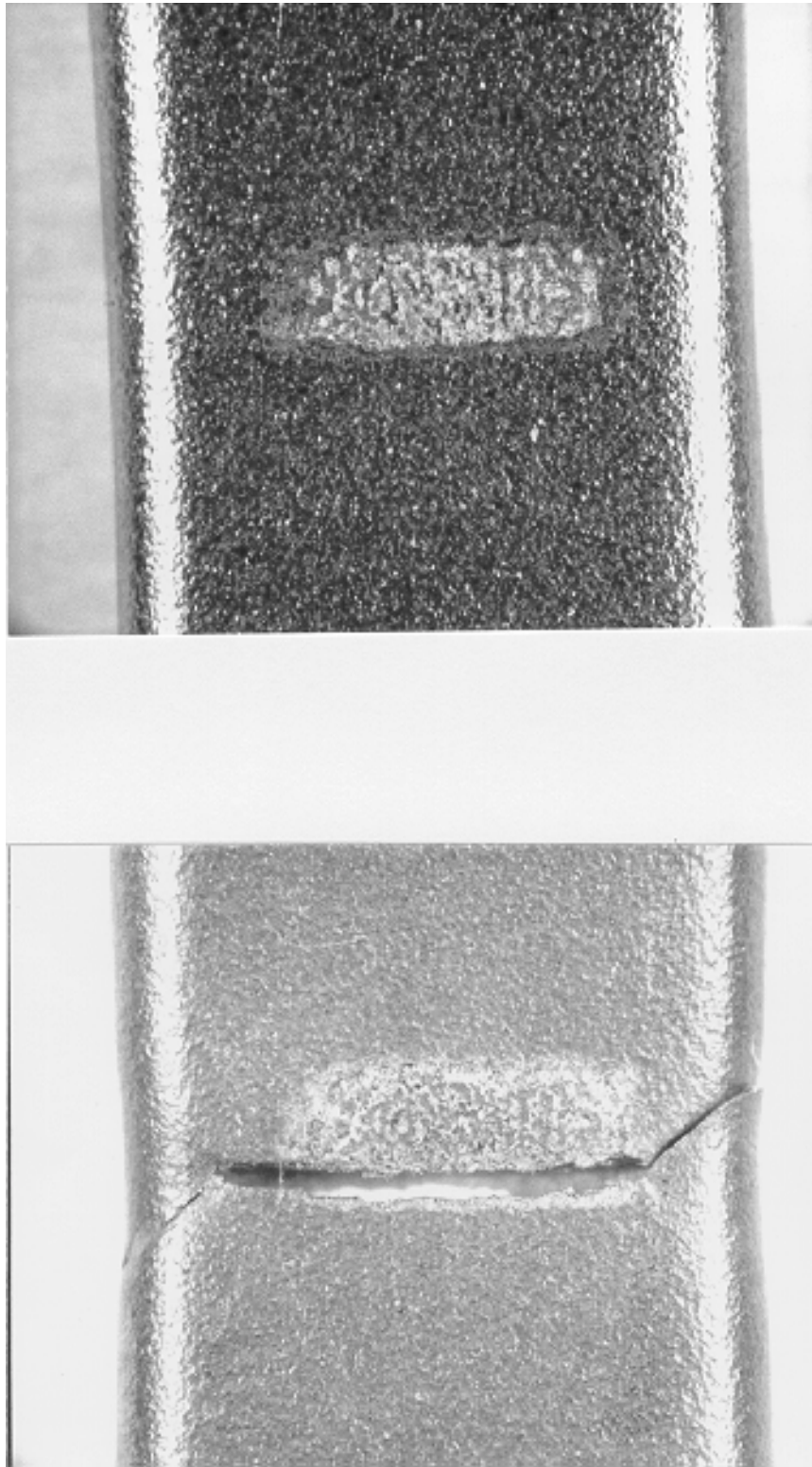


Figure 6A.72. Specimen 75-2.

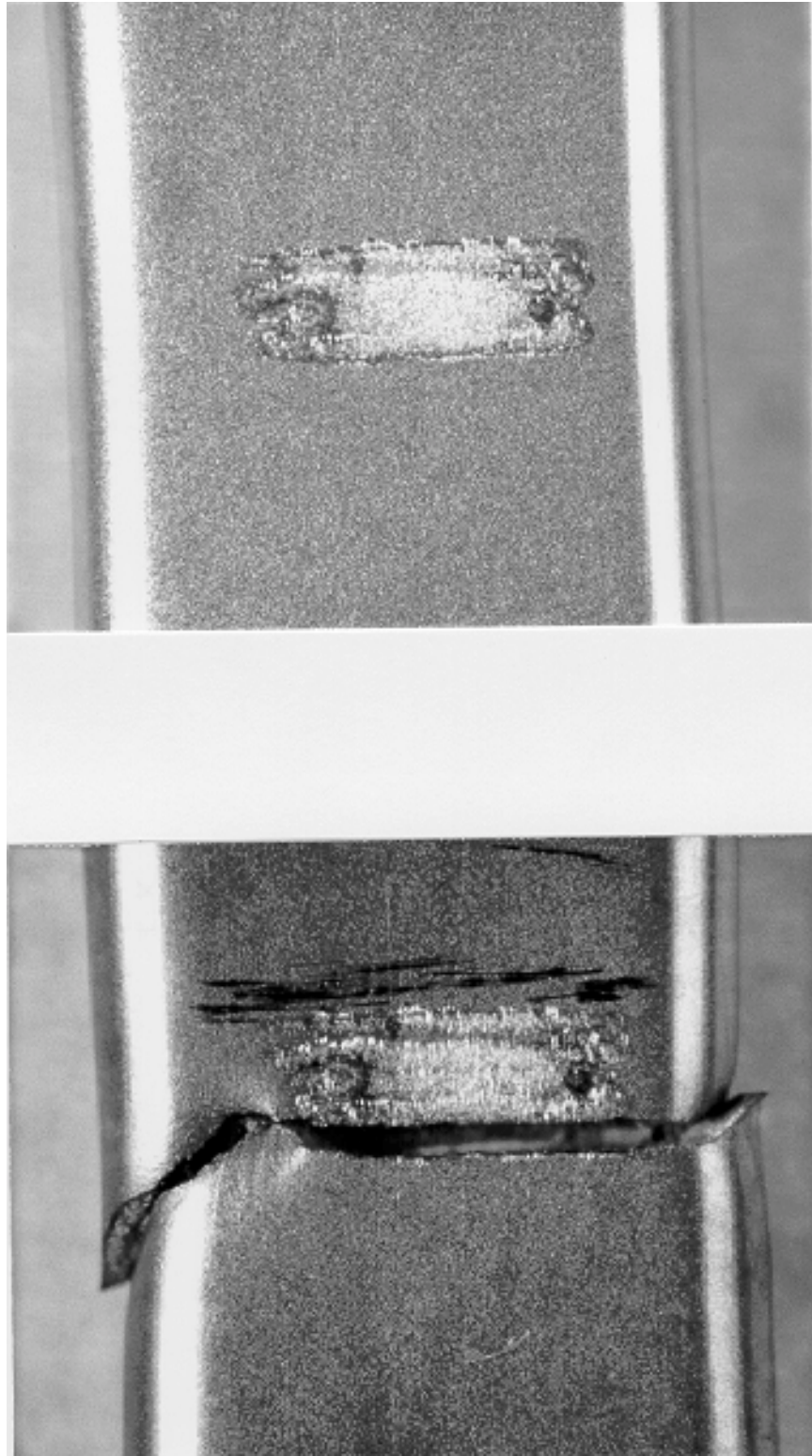


Figure 6A.73. Specimen 76-4.

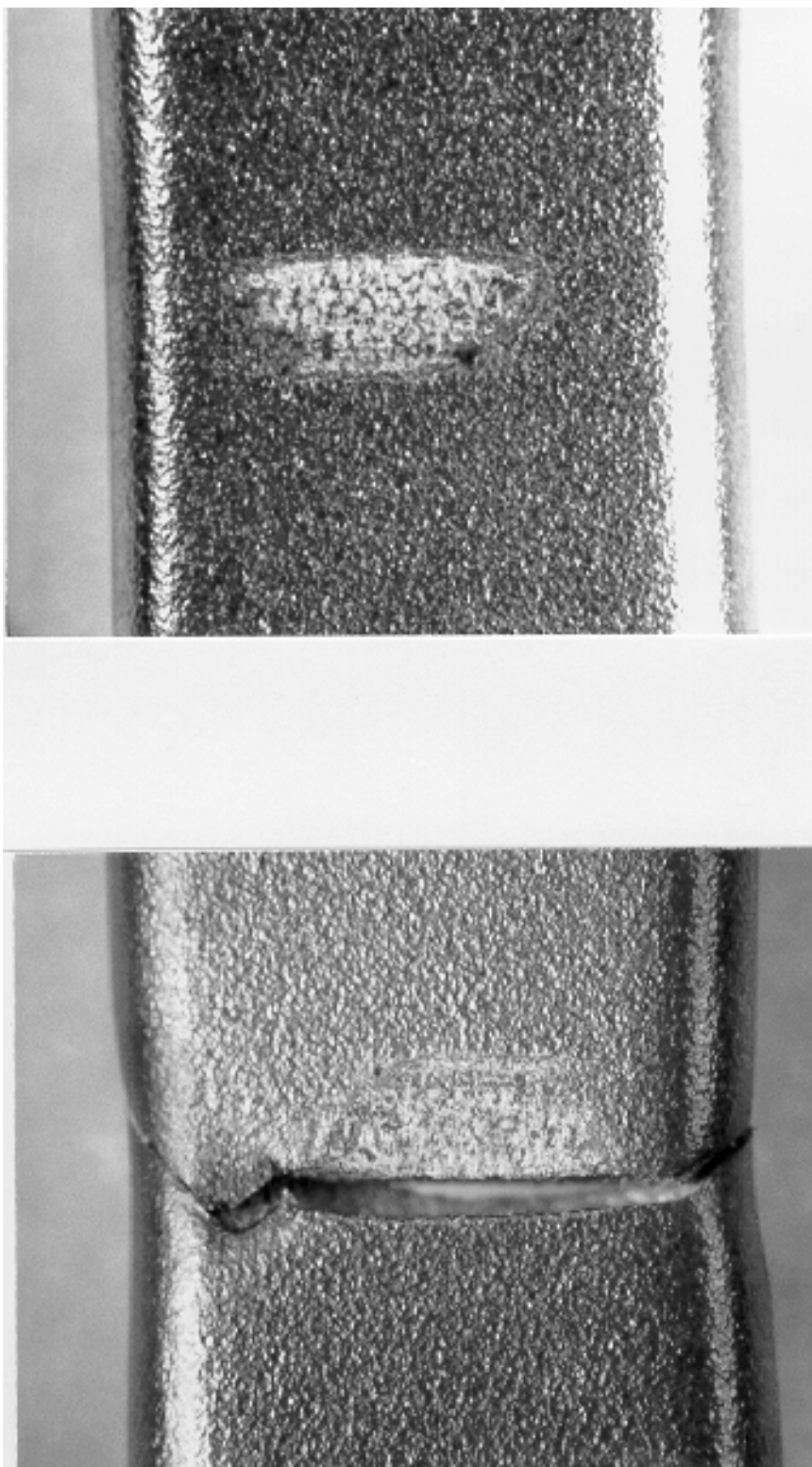


Figure 6A.74. Specimen 99-3.

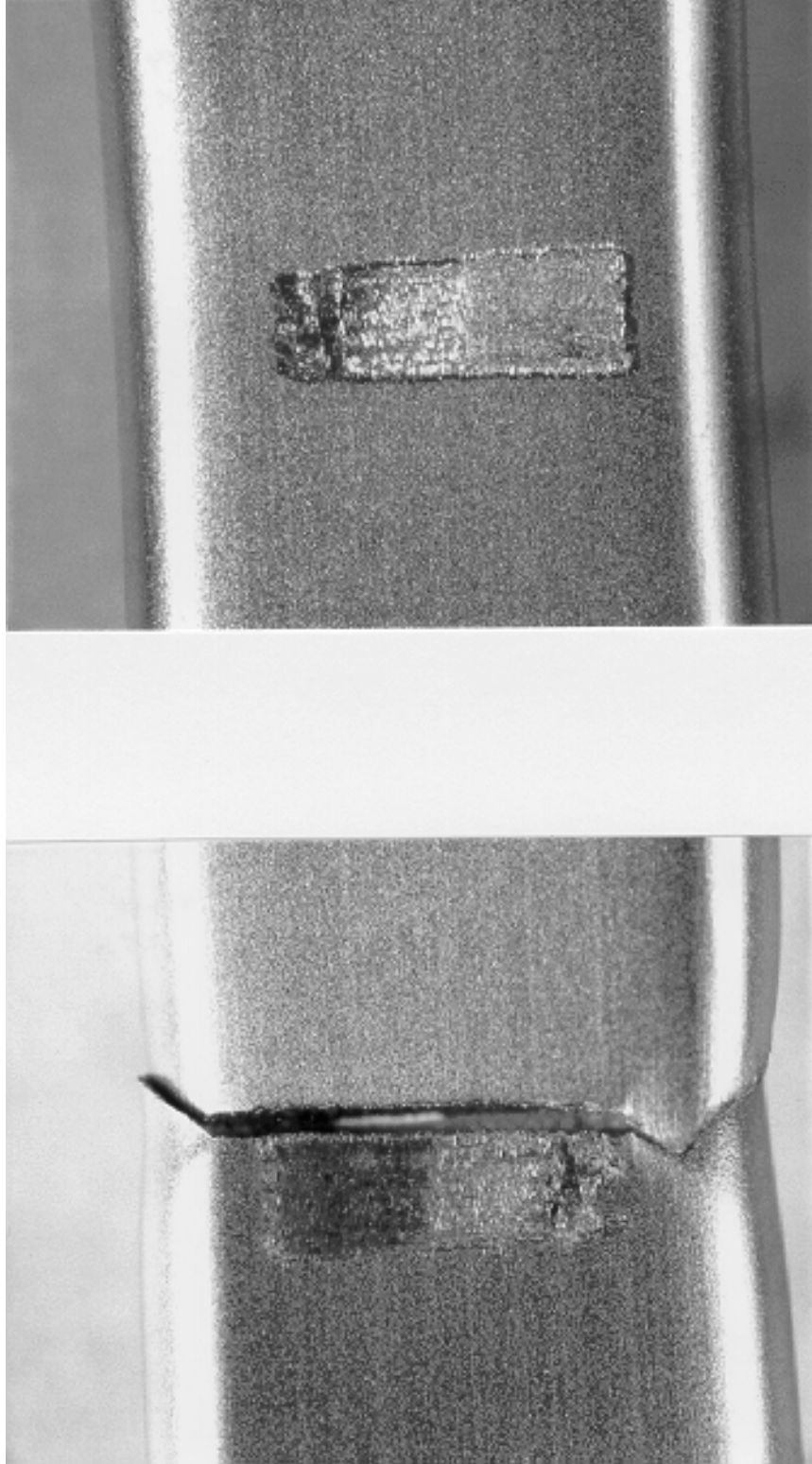


Figure 6A.75. Specimen 48-14.

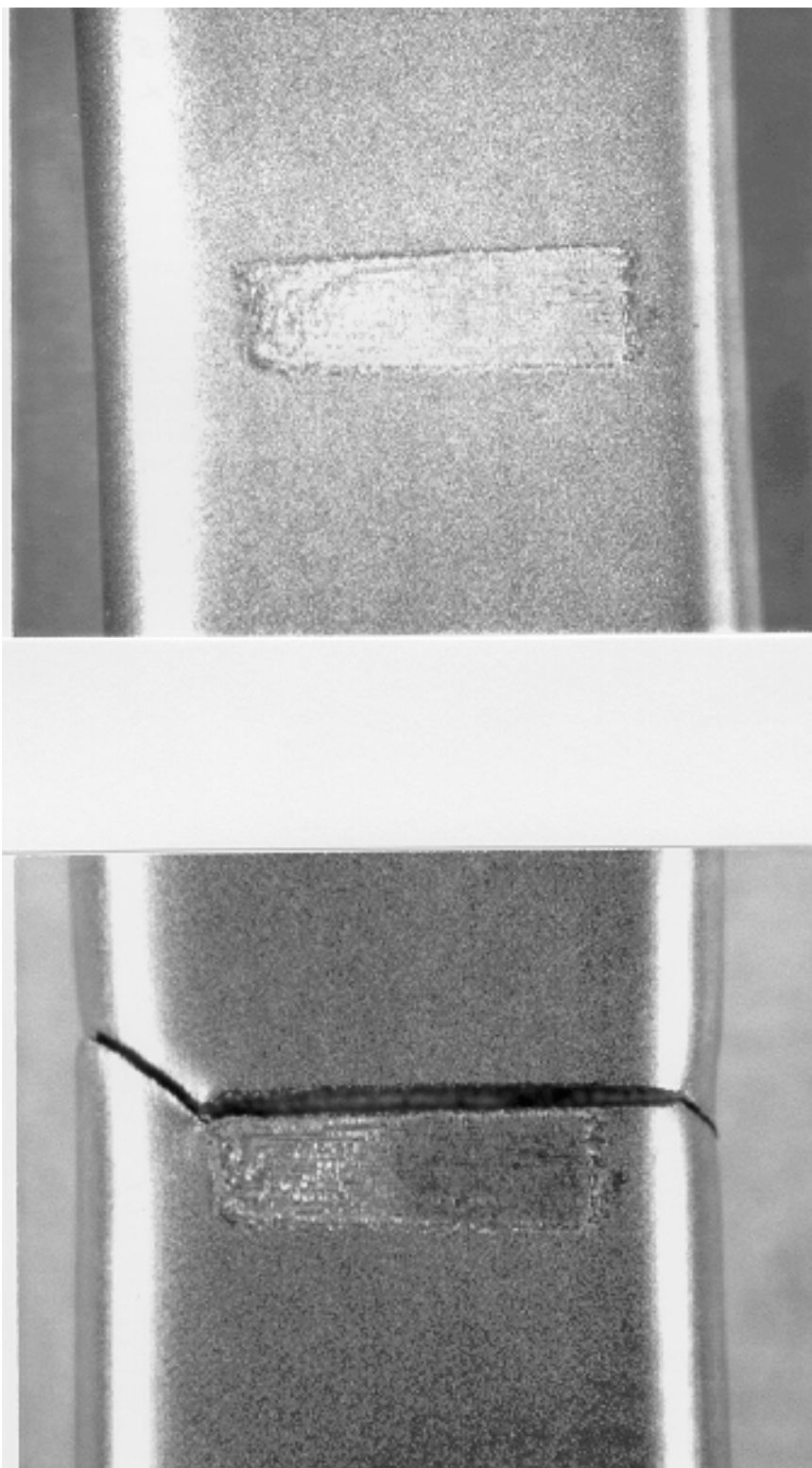


Figure 6A.76. Specimen 70-5.

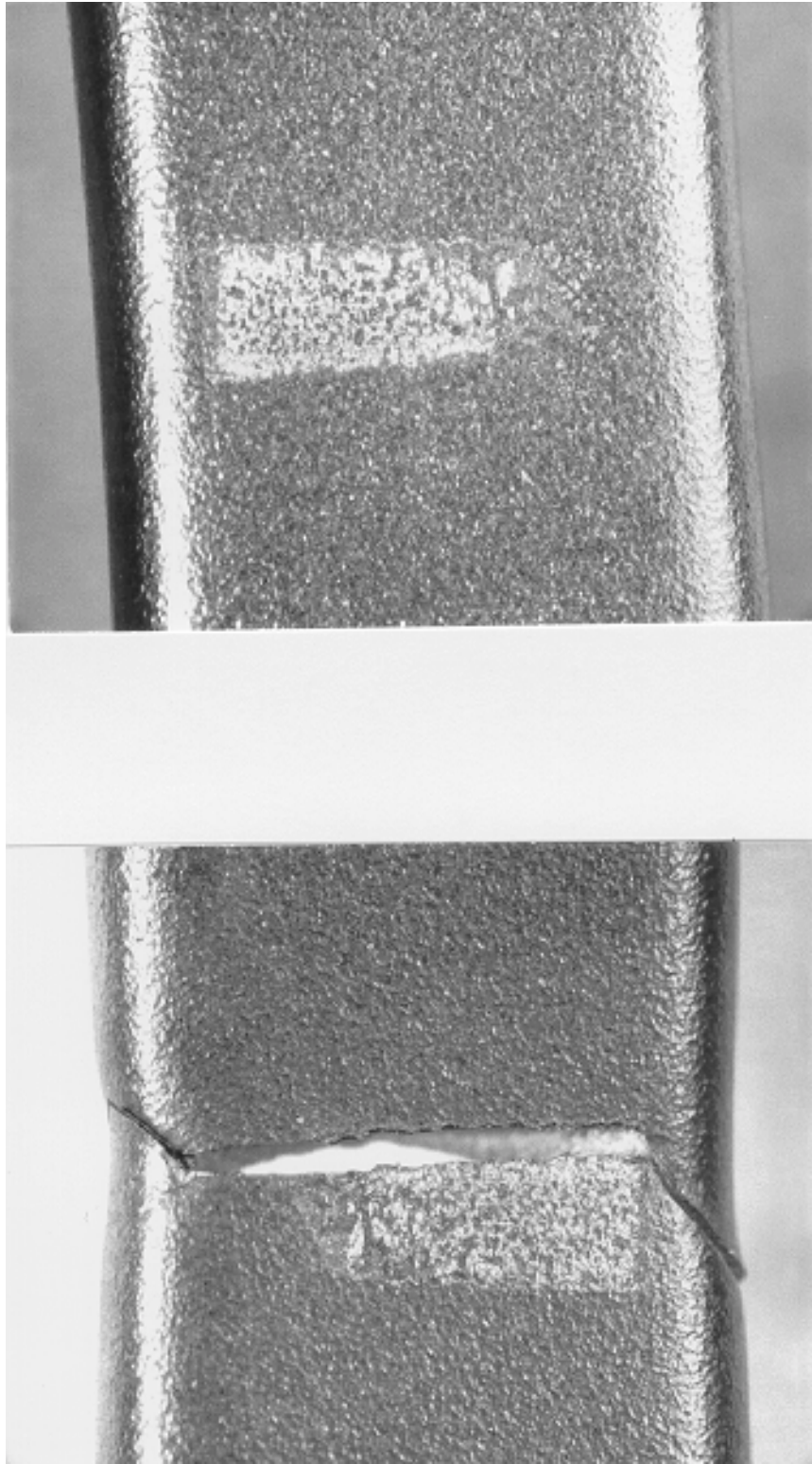


Figure 6A.77. Specimen 76-3.

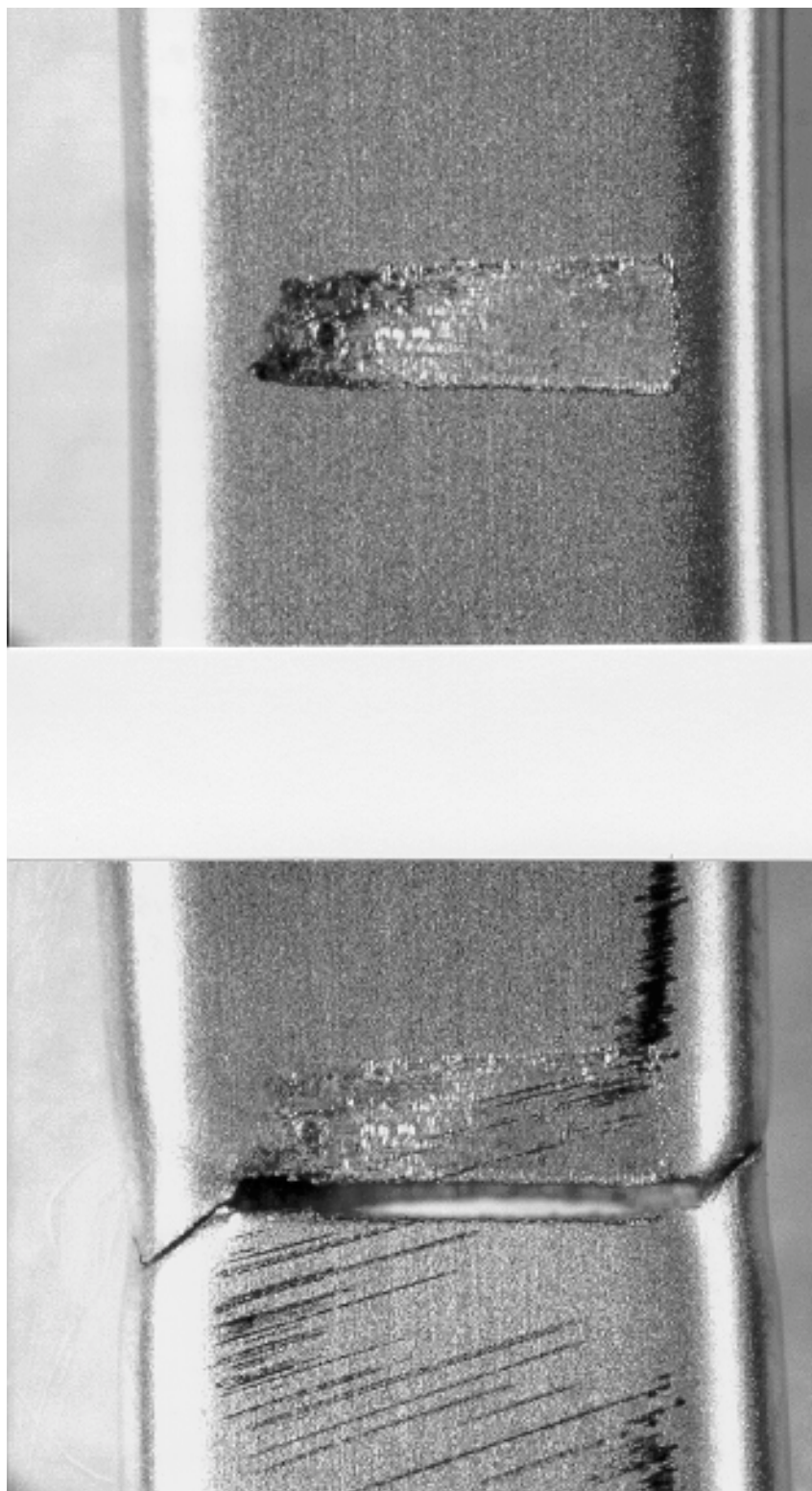


Figure 6A.78. Specimen 48-15.

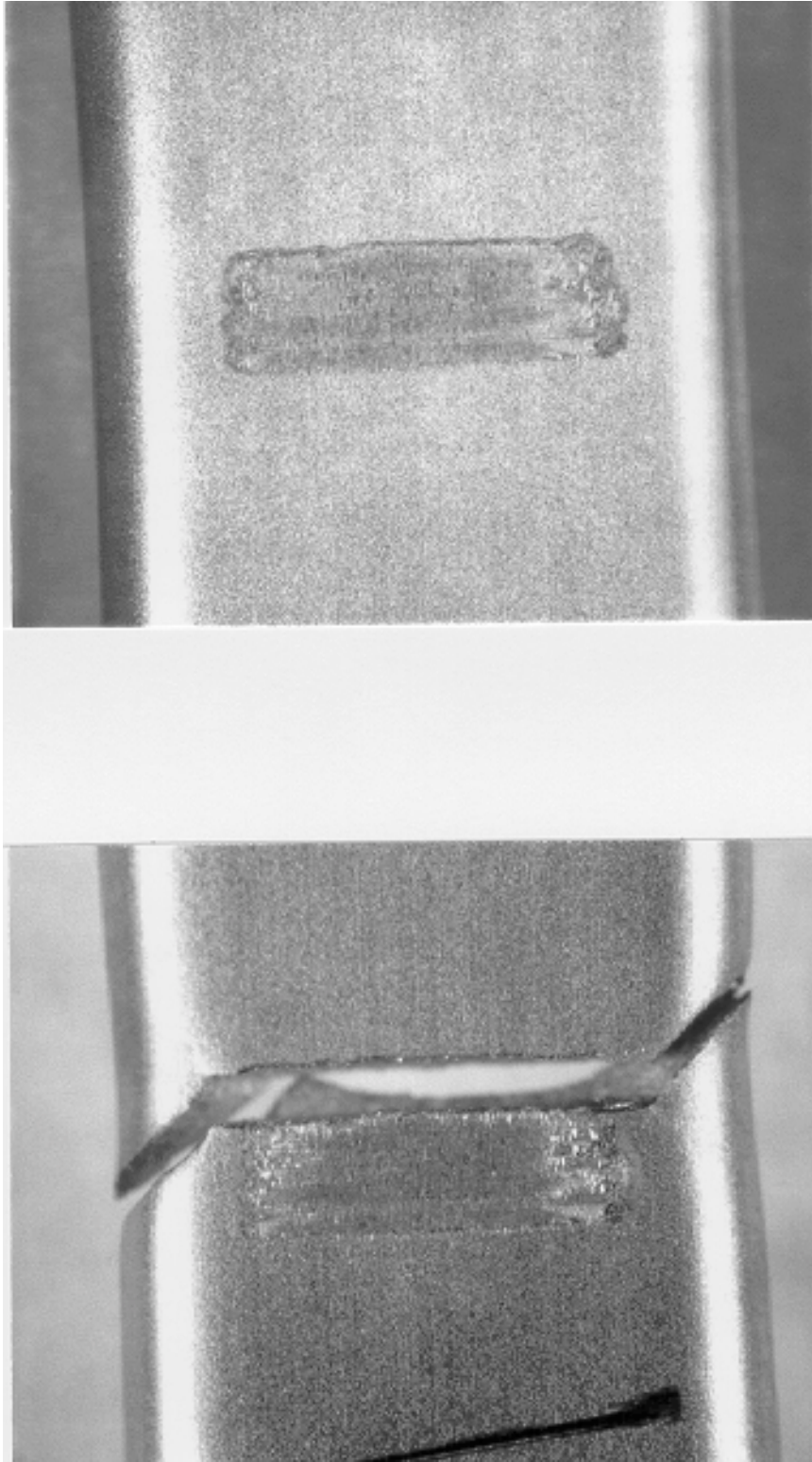


Figure 6A.79. Specimen 79-11.

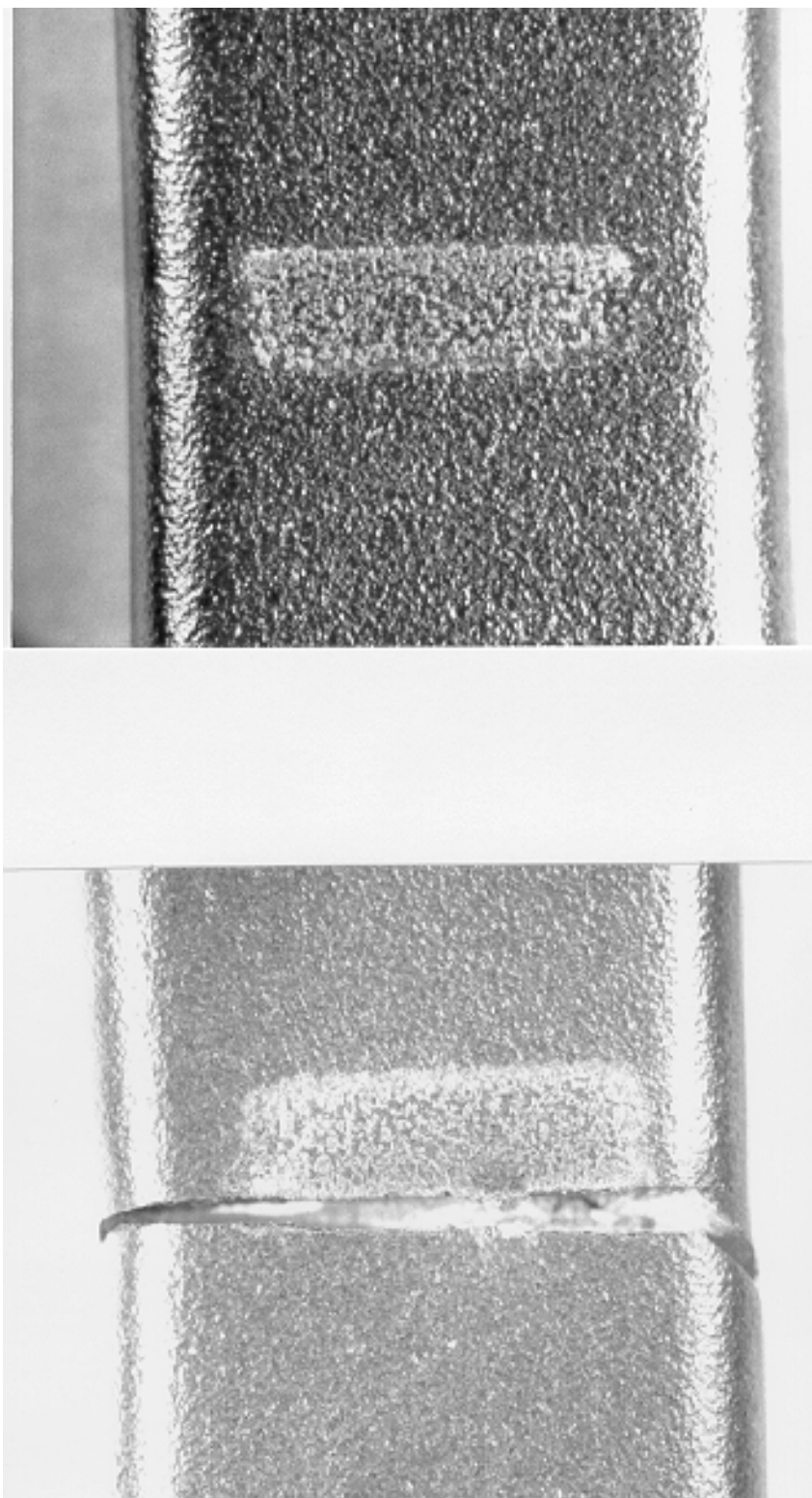


Figure 6A.80. Specimen 76-5.

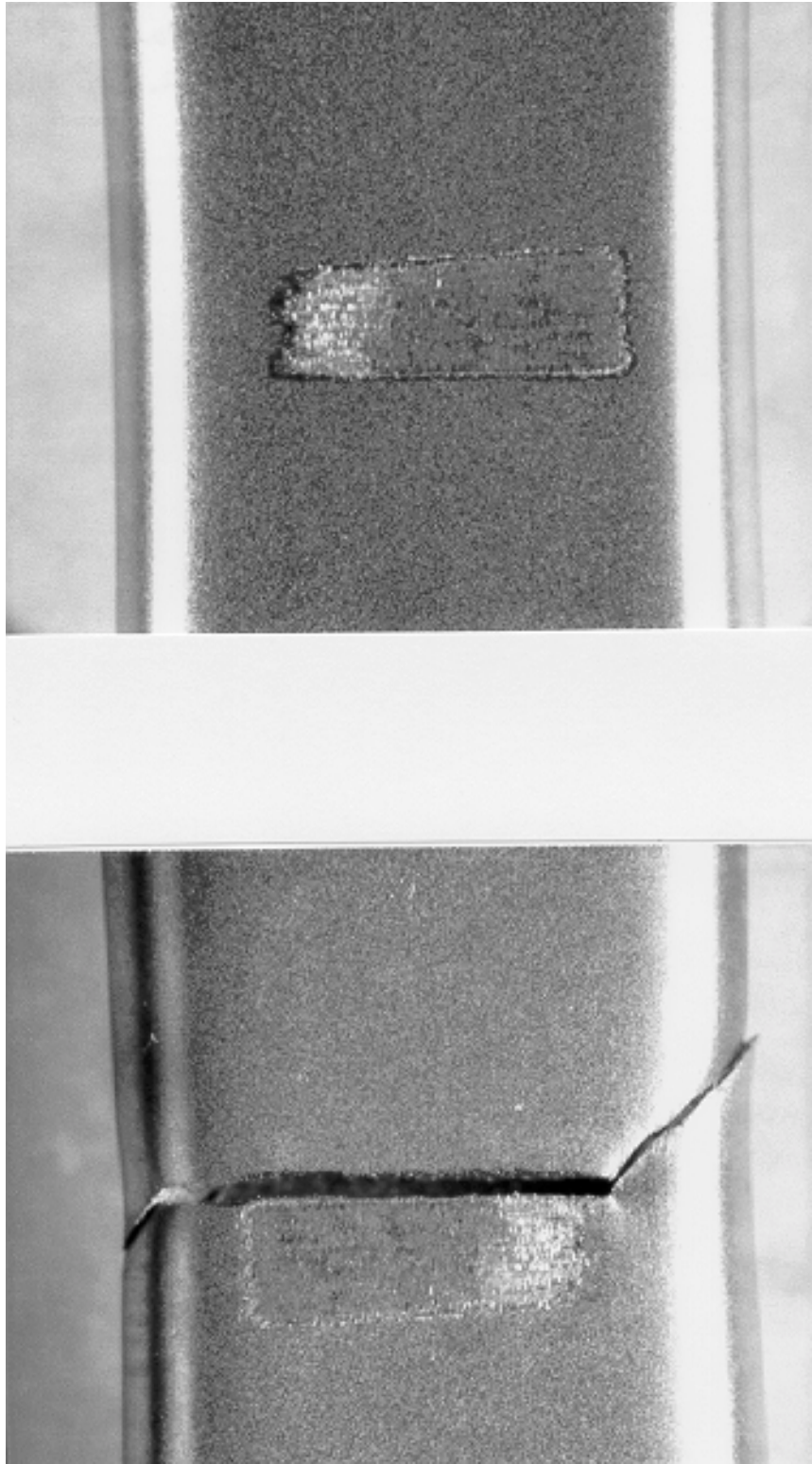


Figure 6A.81. Specimen 70-8.

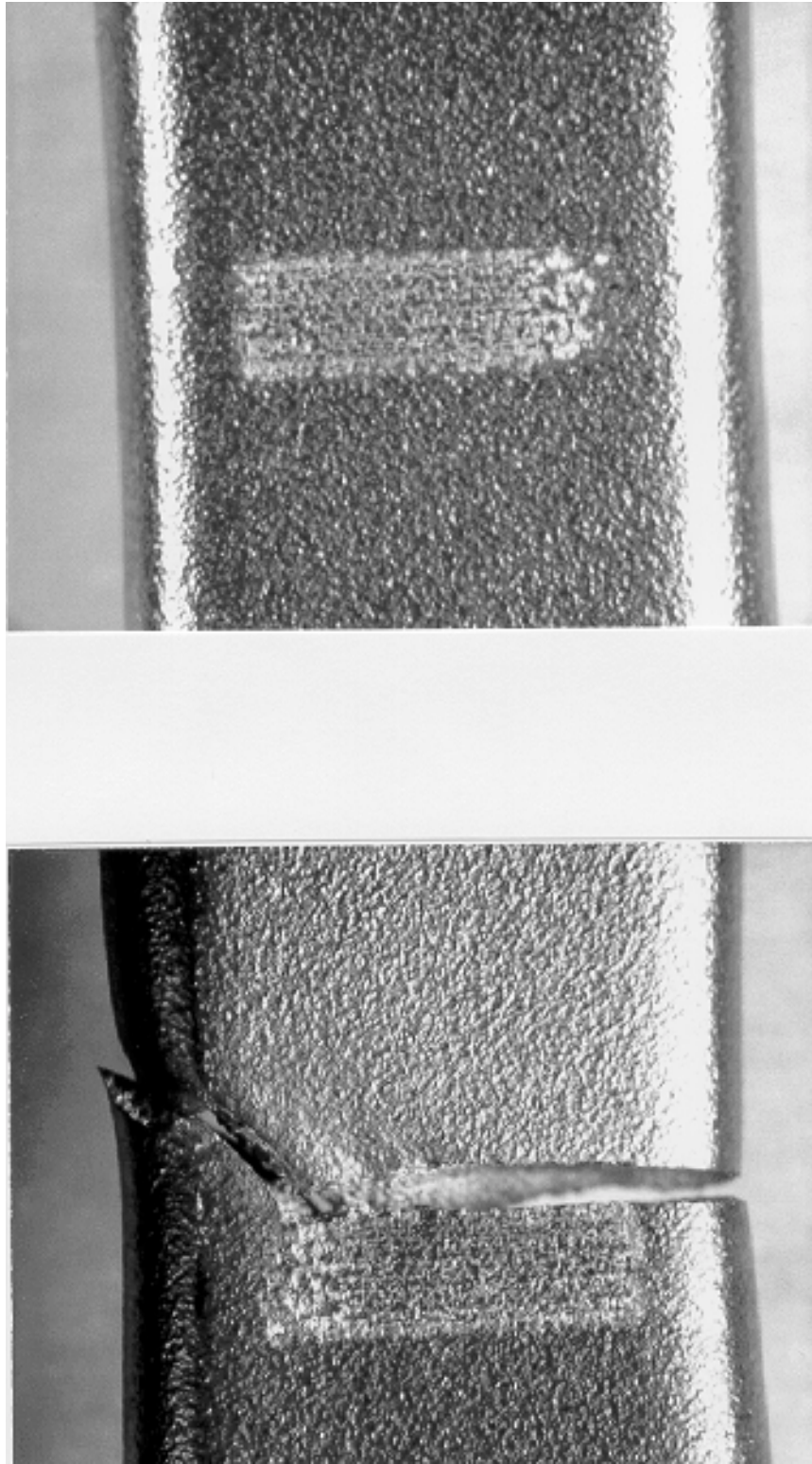


Figure 6A.82. Specimen 48-12.

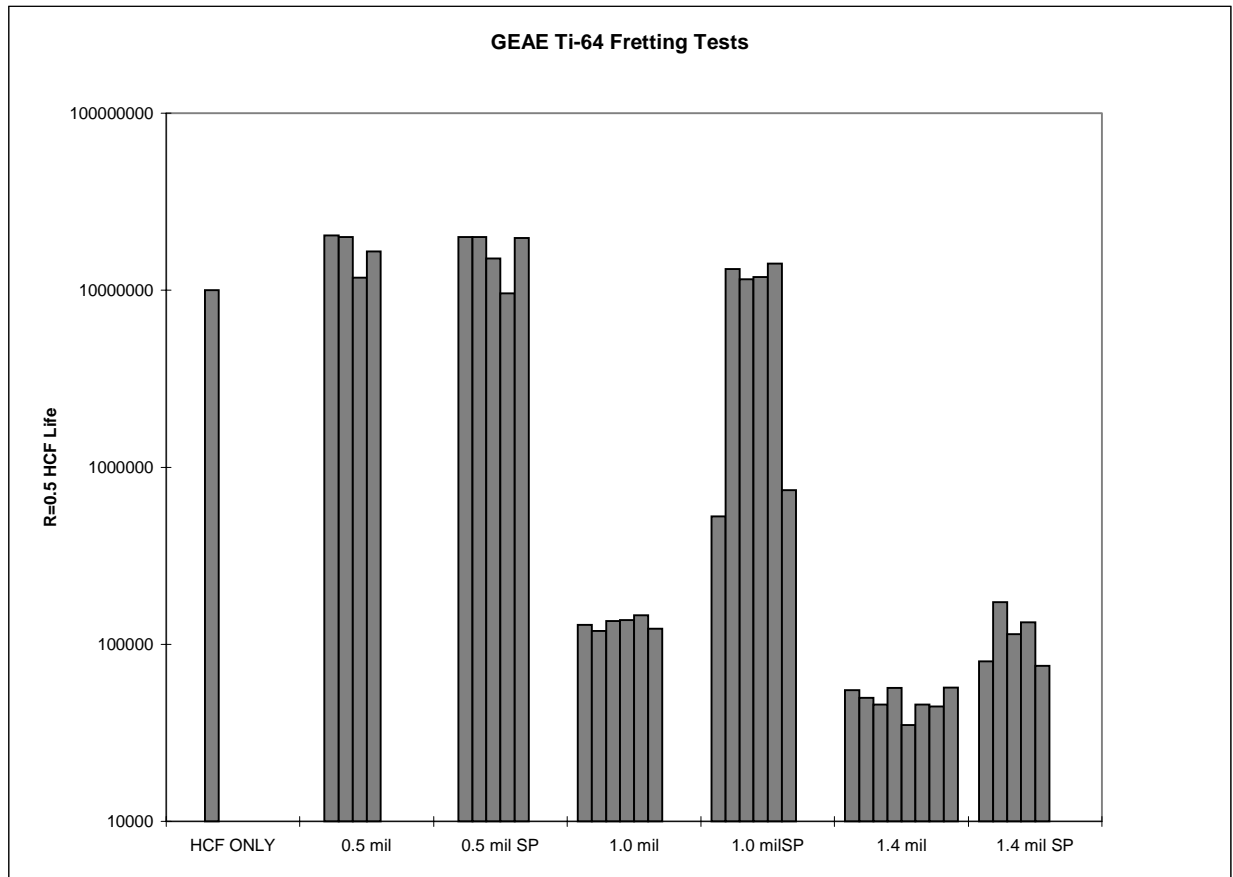


Figure 6A.83. Results of HCF tests of fretted specimens.

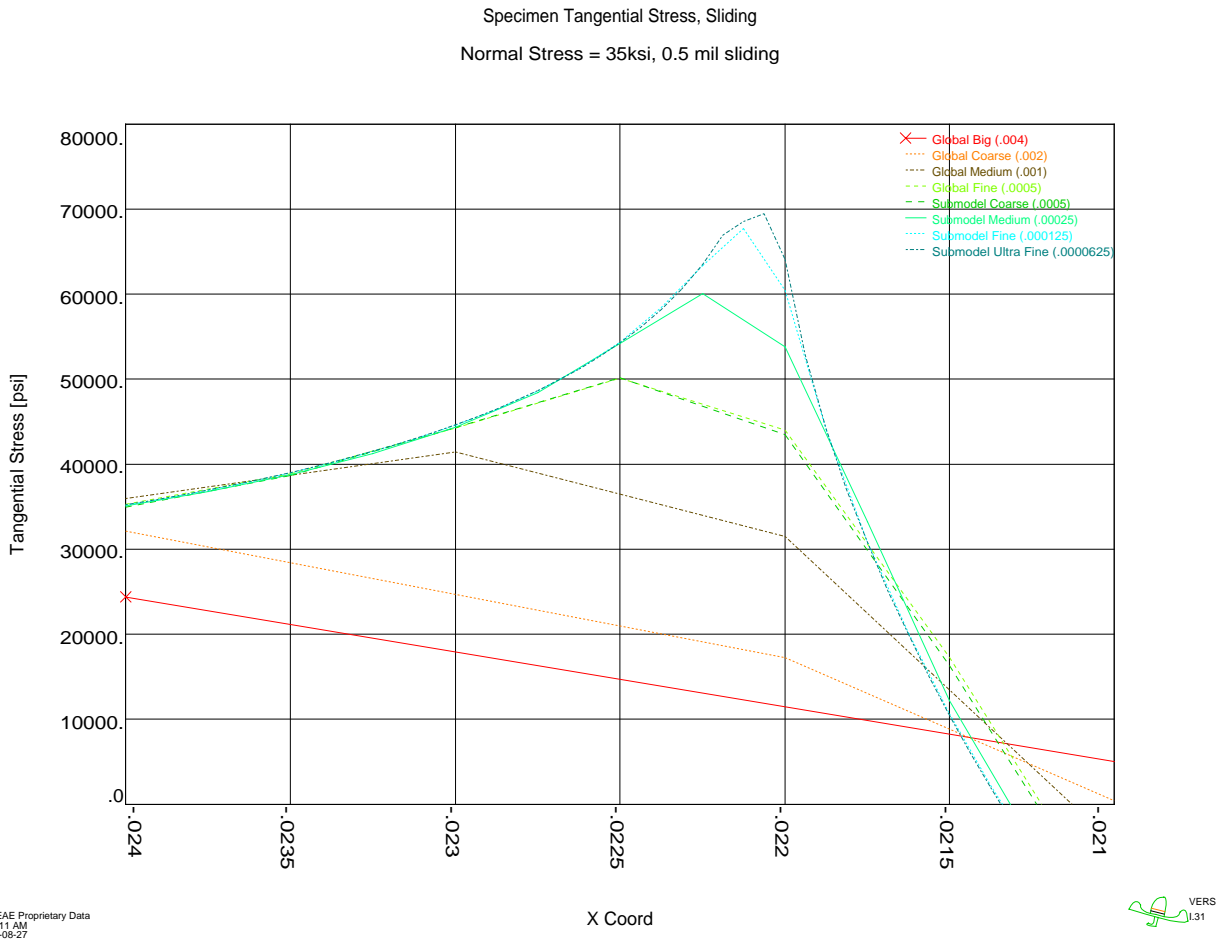
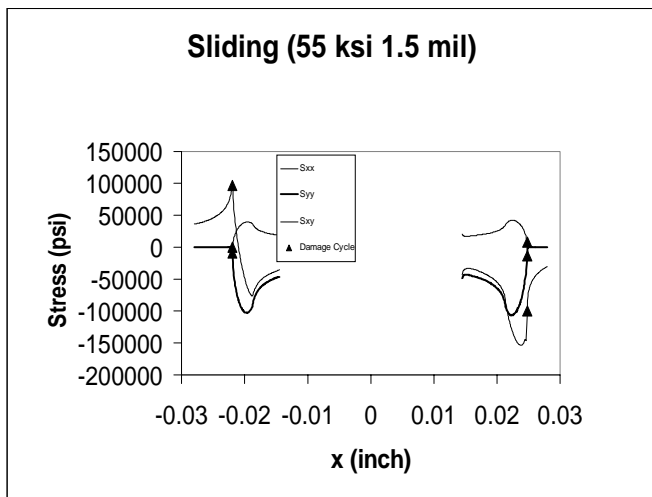
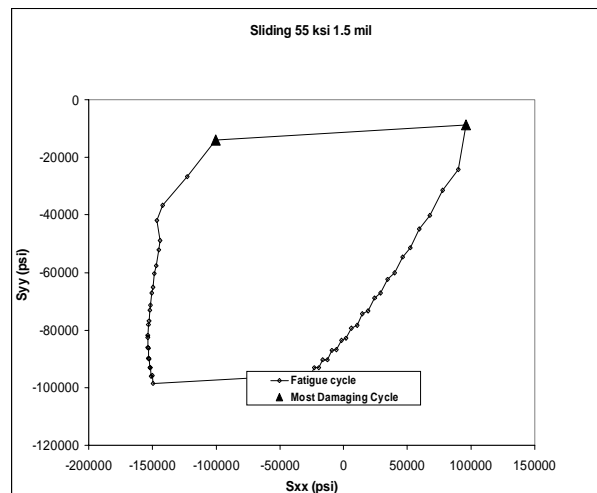


Figure 6A.84. Change in Peak Tangential Stress with Mesh Size.

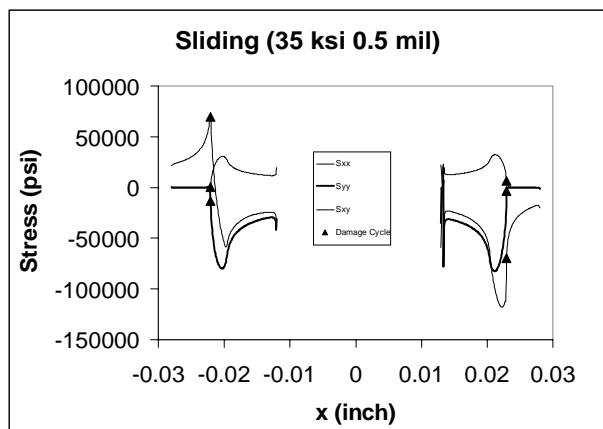


(a)

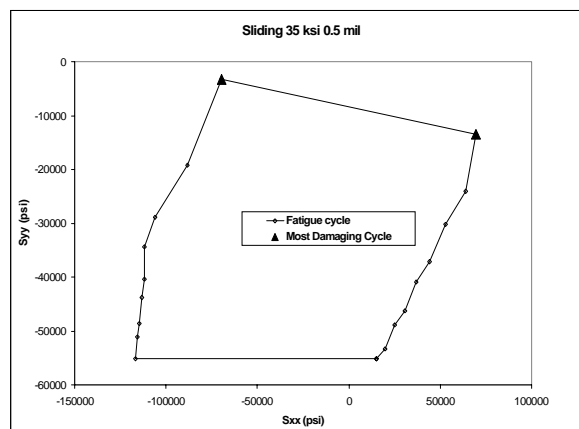


(b)

Figure 6A.85. FEM analysis of 55 ksi, 1.5 mils displacement fretting experiment showing (a) spatial distribution of stress components, and (b) corresponding fatigue cycle.



(a)



(b)

Figure 6A.86. FEM analysis of 35 ksi, 0.5 mils displacement fretting experiment showing (a) spatial distribution of stress components, and (b) corresponding fatigue cycle.

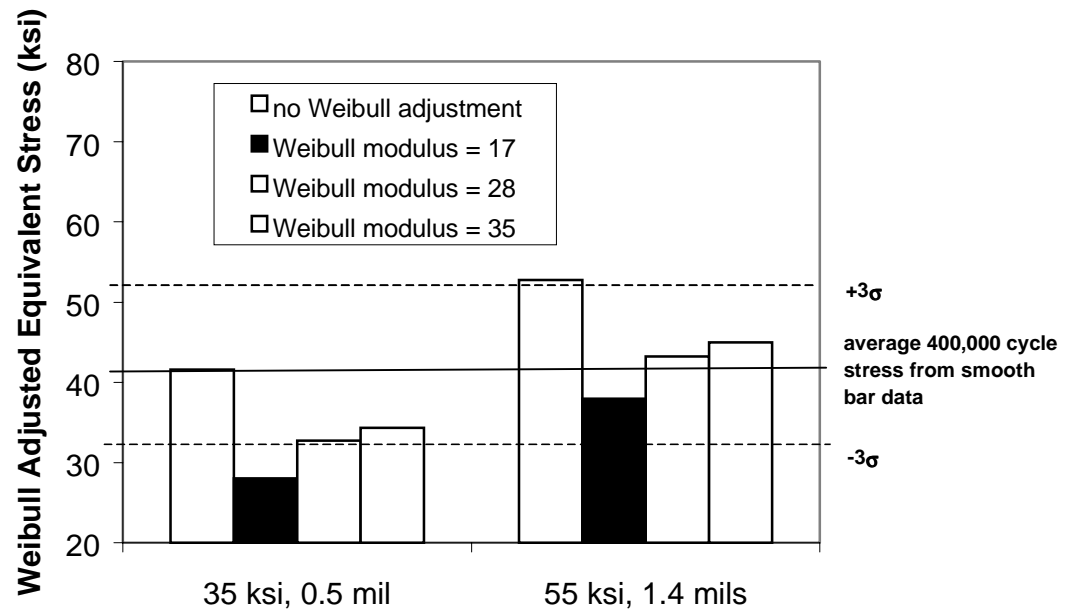


Figure 6A.87. Weibull adjusted equivalent stress predictions for two fretting test conditions.

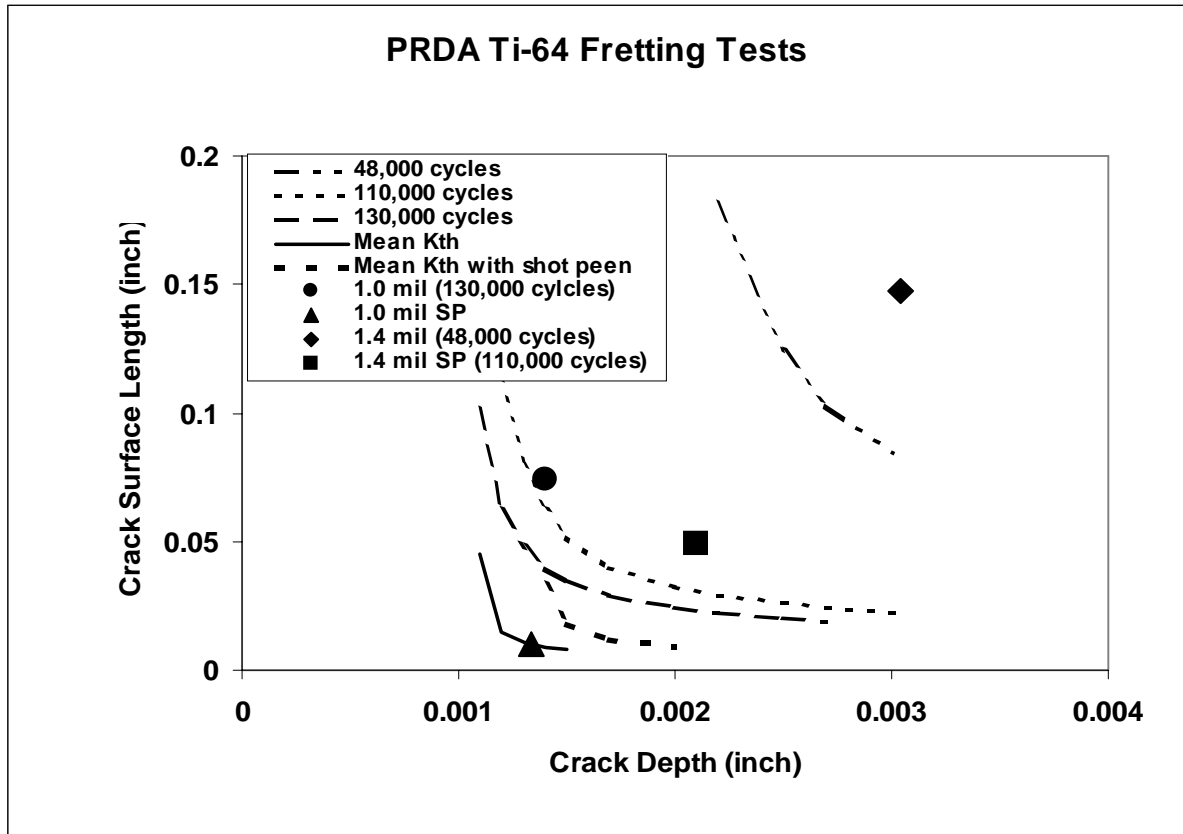


Figure 6A.88. Comparisons of crack sizes observed in fretting specimens with fracture mechanics predictions.

Appendix 6B

FRETTING FATIGUE OF Ti-6Al-4V

**T.N. Farris
H. Murthy
G. Harish
P.A. McVeigh
C. Tieche**



**Purdue University
School of Aeronautics & Astronautics**

**Submitted
August 1999**

Appendix 6B

Fretting Fatigue of Ti-6Al-4V

Executive Summary

The efforts made by Purdue University in understanding the fretting phenomenon in blade/disk contacts and in predicting the fretting lives of the components made of titanium alloy, Ti-6Al-4V, are summarized in this report. A new experimental setup was designed to conduct the fretting experiments in the laboratory. A well characterized set of experiments were conducted to probe the tribological and fatigue aspects of fretting in blade/disk contacts. Some of the tests were interrupted to study the contact surface. The evolution of coefficient of friction on the contact region was studied using a specially designed load history. The temperature fields near the contact region were studied using an infrared camera in support of the friction experiment. A computationally efficient approach based on the solution of singular integral equations has been developed to resolve the stresses at the contact edges accurately. A crack nucleation model based on the obtained stress field has been combined with fatigue crack growth calculations to predict the laboratory fretting lives. The problem of fretting was analyzed using finite element modeling. Finite element modeling served as a tool to validate the singular integral equations approach as well as to study the effect of a crack on the contact area. Due to the resolution limitations and iterative nature of finite elements in the study of cracks, an alternative numerical method was developed to study stress intensity factors. This method was used to adopt an alternative life prediction method using the equivalent initial flaw size approach.

Experimental Setup

A 22kip servo-hydraulic fatigue testing machine was used for all the experiments. A chassis was attached to the machine to hold the pads in contact with the specimens (Figure 6B.1). The chassis allows the application of the crushing load by the pad on the specimen and also acts as a spring to generate the tangential force. The specimen was gripped and loaded by the action of hydraulic actuators. The chassis applied the crushing loads using the static hydraulic actuator; the spring action of the chassis produced the required tangential force. The fretting phenomenon arising due to the combination of

the bulk loading on the specimen and normal and tangential loading applied by the pad was studied.

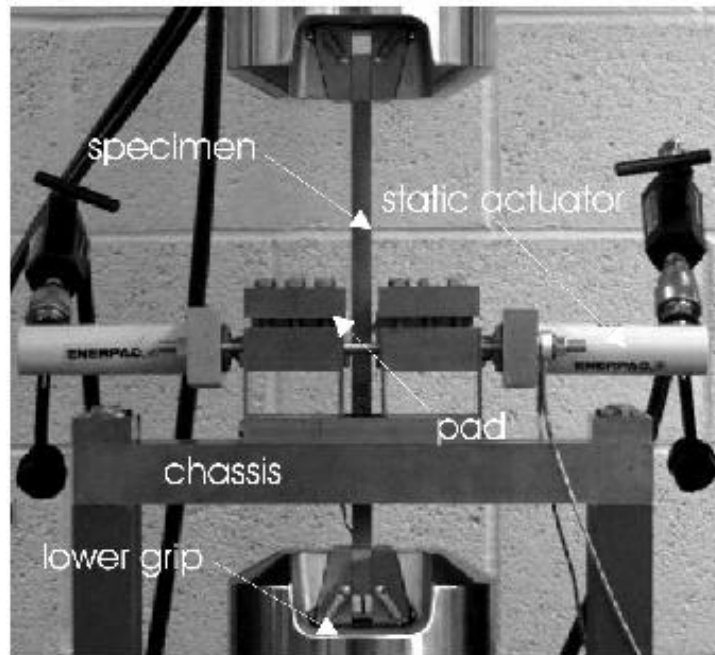


Figure 6B.1. Experimental setup.

Fretting Chassis

The fretting chassis is a superstructure built on the fatigue machine that allows the generation of tangential loads that are in phase with the bulk load, while applying a nominally constant normal load. Figure 6B.2 shows the components of the fretting chassis schematically. The **stiff beam** provides the bulk of the stiffness of the chassis. The pads rest on the top platform that also provided the means of application of the normal load. The normal load is applied via a pair of hydraulic actuators that transmit the load onto the top platform. Note that the two pressure rods ensure that the pressure is applied symmetrically to the pads. The thin steel diaphragms offer little resistance to the pressure loading, but offer a large resistance that carries the portion of the tangential load transmitted to the chassis. This ensures that almost all of the pressure is transmitted to the specimen through the pads, while maintaining the required stiffness to produce a large tangential force. A finite element analysis of the rig has shown that greater than 98% of the pressure is transmitted to the specimen. The pad-tops fix the

pads to the chassis. The tangential force produced was about 50% of the bulk load applied, subject to a maximum of the force required to produce gross sliding. This load is monitored throughout the fatigue experiments, by recording the difference of the upper and lower load cell readings.

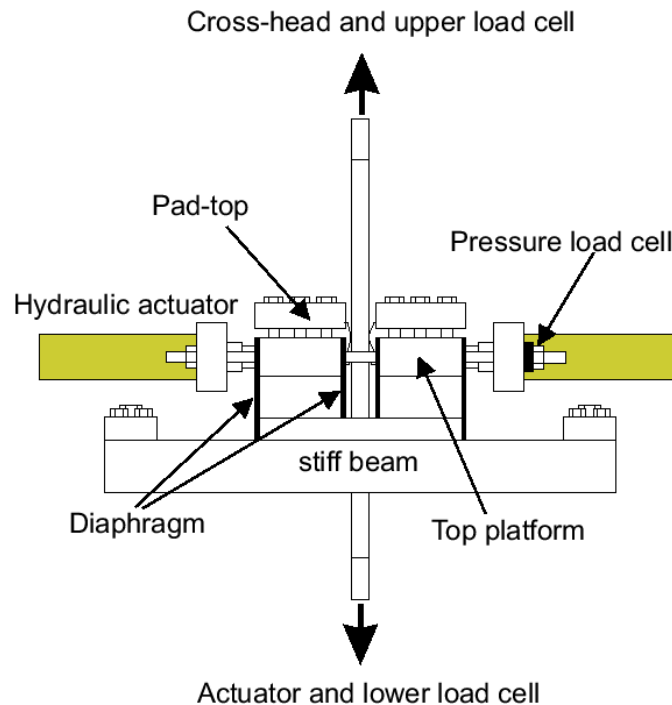


Figure 6B.2. Components of fretting chassis.

Schematic of Loads

Figure 6B.3 shows a schematic of the various loads that will be referred to in this document. P is the crush load (normal load), Q is the tangential load, F is the force applied at the bottom of the specimen (measured by the actuator load cell). The reaction force as measured by the crosshead load cell (top grip) is referred to as R . Note that the difference between F and R gives the tangential force, $2Q$. The bulk stress, σ_b , is simply F divided by the cross-sectional area of the specimen.

A number of sensors were used to keep track of the various parameters in the experiment. The experiments were conducted in load control with the controlling parameter being the load seen by the crosshead load cell (R). The load cell below the actuator measured the bulk load F . The tangential force, $2Q$, was given by the

difference of the two load cells. Note that each experiment had two pads and the experiment was assumed to have a plane of symmetry. Two load washers connected to the pressure rods measure the normal force. The cross-head load, position and cycle number were tracked via the digital interface of the fatigue testing machine, while the rest of the sensors were monitored via a National Instruments SCXI module and data acquisition card. LabVIEW was used for control and data acquisition. The computer control allowed for the machine to run unattended.

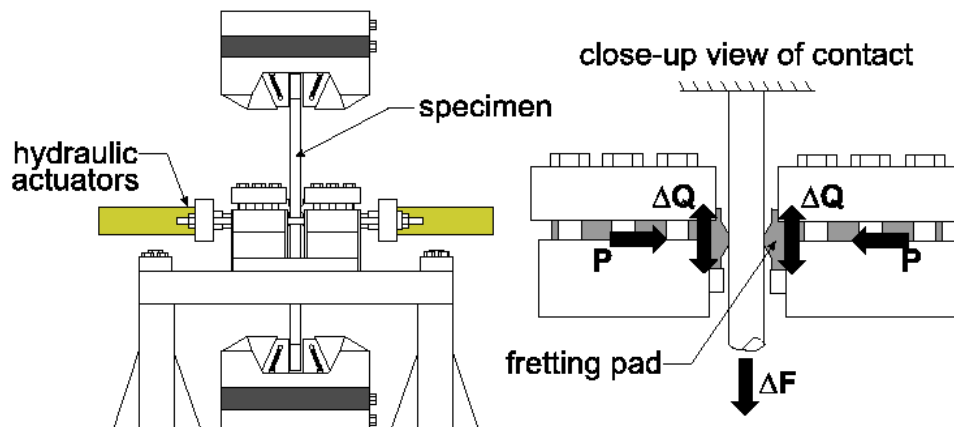


Figure 6B.3. Schematic of the fretting rig with a definition of forces applied to the rig.

Fretting Specimens and Pads

All specimens and pads were machined according to prescribed geometric specifications (Figure 6B.4). The specimen is a 16 inch long dog-bone with a cross section of 0.6 inch x 0.375 inch. The pads were 0.8 inch high, 0.375 inch deep and had a prescribed profile of a 0.120 inch flat region bounded by 0.120 inch radii on either side. The pads used for the friction tests were cylindrical pads with a radius of 5 or 7 inch. The specimens and pads were used as machined without any polishing. On the specimen, the contact is on the side with width 0.375 inch.

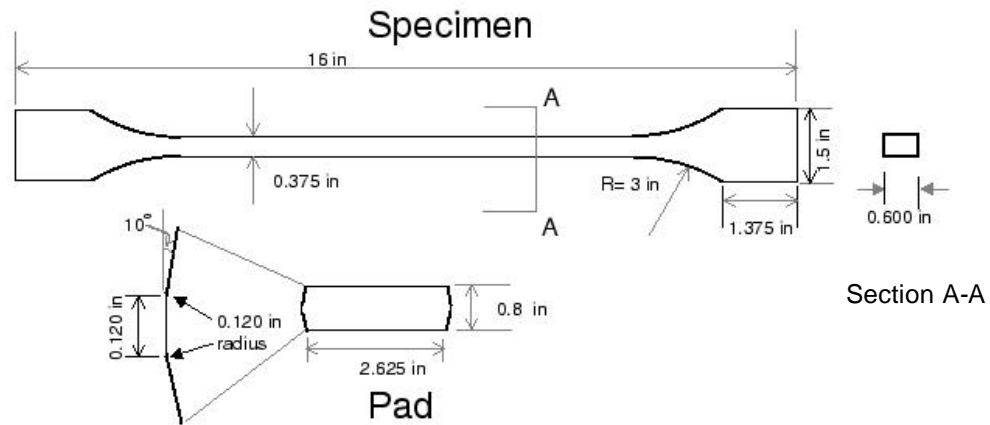


Figure 6B.4. Schematic of the specimen and pad dimensions.

Metrology

While the prescribed profile for the fretting pads was as is shown in Figure 6B.4, the machined profiles were not in exact conformance with the prescribed profiles. Since the singular integral equations (discussed later) are able to handle any arbitrary smooth profile, the machined profiles were recorded for each pad. A Talysurf profilometer was used to record a representative trace on each face of each pad used in the experiments. After centering and rotating, this trace was treated as the input to the stress analysis program discussed elsewhere in this Appendix.

Figure 6B.5 shows a typical trace of a pad before the experiment. Also plotted is the prescribed profile. The differences in the profiles do produce a large change in the pressure profile as described in the section on the stress analysis.

Traces of each pad were also taken after the experiments. This allowed a quantitative evaluation of the contact surface degradation due to fretting. Figure 6B.6 shows a typical trace of a pad before and after the experiment. The effect of this change in pad profile, due to wear, on the pressure is discussed in the section on the stress analysis.

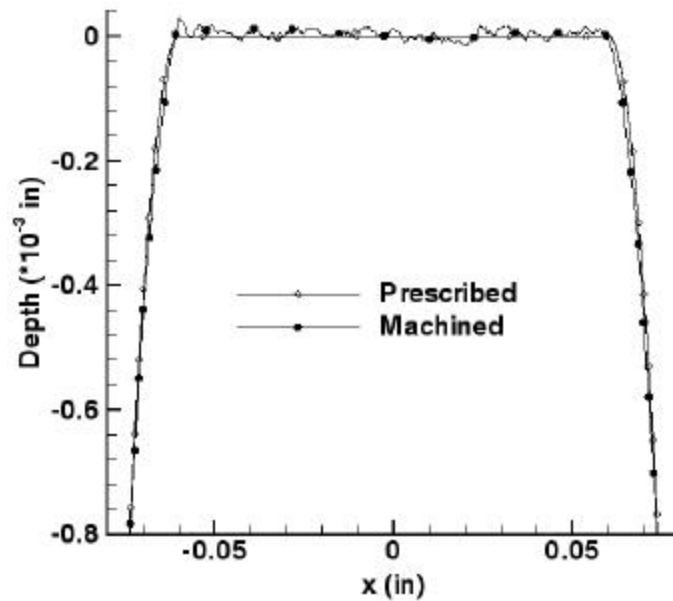


Figure 6B.5. Typical trace of pad profile as machined. The prescribed profile is also plotted for comparison.

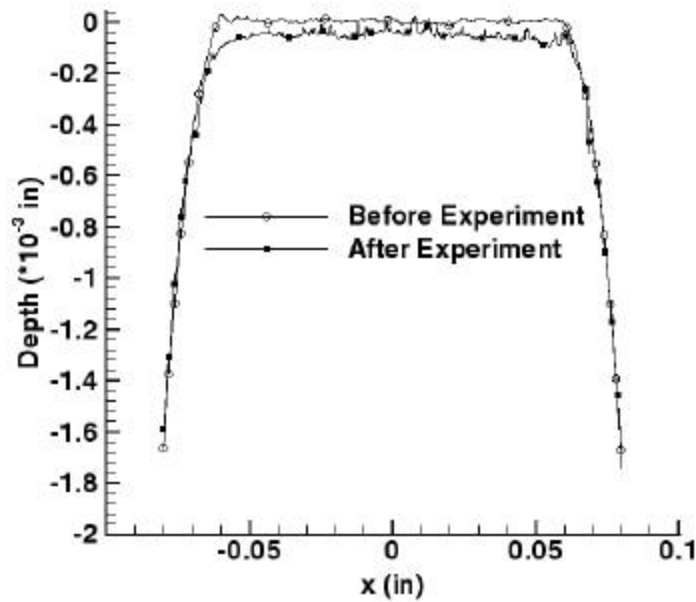


Figure 6B.6. Comparison of pads before and after the experiment.

Alignment of the Specimen

To ensure compliance with ASTM standards on specimen alignment for fatigue, an alignment specimen with eight strain gages was used. The strain gages were connected

to four Wheatstone half-bridge circuits. By loading the specimen to a prescribed bulk load and adjusting the alignment fixture, the bending strain was minimized. This resulted in the minimization of the undesirable effects of the bending strains on the results. The bending strains, if significant, could alter the fretting behavior to a great extent.

In addition, it was important to ensure that the pads were in proper contact with the specimen. Before applying the normal load, the pads were lightly pressed against the specimen, with a pressure sensitive film between the specimen and the pad. The color change on the film indicated the extent of contact. Adjustments were made to the fretting chassis and/or the machine to achieve full contact between the pads and the specimen. Once satisfactory contact was achieved, the full normal load was applied. The adequacy of this approach was borne out by observing the final wear scars that encompassed the contact zones.

Fretting Experiments

Fretting experiments were designed to determine the crack nucleation lives of specimens under various loading conditions. The tests were conducted at room temperature.

Experimental Procedure

The loads at which the fretting experiments were conducted are presented in Table 6B.1. The normal load was applied first and allowed to settle. Then the bulk load mean load was set. Finally, the cyclic load was applied at the given frequency. Note that since the load cell at the top is the controlling load cell, the cyclic load amplitude and mean at the top was set so as to provide the right steady state amplitude and mean bulk load. The frequency was determined by two conflicting issues. A high frequency would minimize the time required to perform each experiment. However, this would result in the possibility of unacceptably large temperature rises induced by the sliding velocity.

Note that the controlling load is the load at the top. Hence, initially as the coefficient of friction was low, the tangential force was limited by the frictional force required to cause sliding of the pads against the specimen. As the coefficient of friction rose and reached a steady state, the tangential force stabilized resulting in the bulk load also stabilizing. Note that the quoted values of the loads refer to the stabilized values

unless stated otherwise. As the forces stabilized, most of the experiments reached a state of partial slip, wherein the tangential force is not enough to cause gross sliding. This phenomenon of transition from sliding to partial slip is referred to as mixed-mode fretting. All the loads were monitored and stored for every cycle for the first few hundred cycles. Subsequently, data was stored at regular intervals (usually 100 cycles).

Experimental Lives and Surface Observations

The fretting fatigue experiments were either run to failure, resulting in the specimens breaking in two, or till runout. No failures were observed in the pads. Figure 6B.7 shows the typical wear scar on a pad. The fretting scar on the pad was mirrored on the specimen. In all the tests, failure was observed at the trailing edge of contact, defined as the bottom edge (nearest to the actuator). A deposit of black powder was observed all around the edges of contact. The damage due to wear was not severe in the stick region. However, in the slip region, there was a significant damage due to wear. The slip region was very small and restricted to the curved portion of the pad as expected from the analysis using singular integral equations. The damage due to wear was more severe in the pads used in high load, low-cycle experiments (e.g. PR09) as compared to the pads used in low load, high-cycle experiments (e.g. PR10). The fracture surface of the specimen used in PR12 was observed and is shown in Figure 6B.8. As can be seen from 6B.8, the fretting debris extend through the contact width, indicating that the cracks, though they might start at discrete locations, will coalesce to form a through crack extending along the width of the specimen. Further evidence of this can be seen in the four-point bend tests conducted on the specimens used in interrupted tests, details of which has been documented elsewhere (by Golden and Grandt in Appendix 6C). In most experiments, evidence of crack formation was seen on both contacts. There was no preferential side for crack formation, which leads to confidence in the alignment mechanism. Also, the wear scar was nearly uniform in all the contacts, justifying the alignment approach using pressure sensitive film mentioned earlier.

Twenty-seven fretting experiments were conducted. Of them, seventeen experiments were conducted either till the specimen failed or till runout. Six weld failures occurred during the course of the test program, some of which were treated as inter-

rupted fretting tests and used for surface observation of the contact surface. Four of the tests were stopped after predetermined number of cycles (interrupted tests) and were used for surface observation of the contact surface. The specimens, from the interrupted tests, were then used for four-point bend tests. Table 6B.1 presents the fretting data of the seventeen fretting experiments along with the important loads. The actual contact length, $2a$, exceeds the nominal flat region by about 10%. Q_{max} and Q_{min} refer to the tangential loads at maximum bulk tension and minimum bulk load respectively.

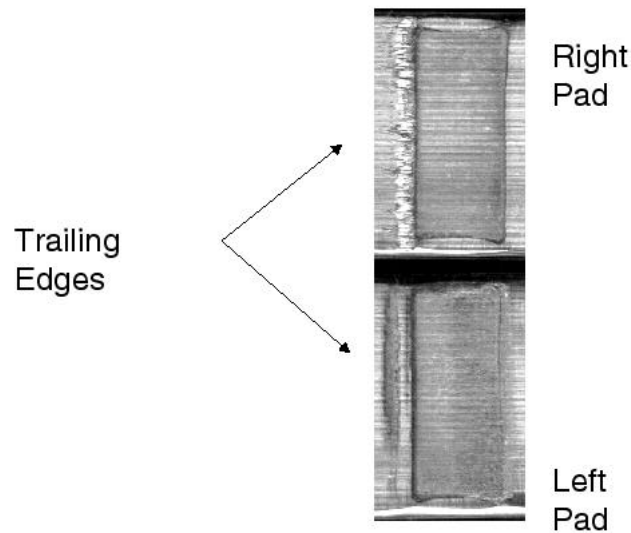


Figure 6B.7. Contact surface of the pads used in Experiment no. PR09.

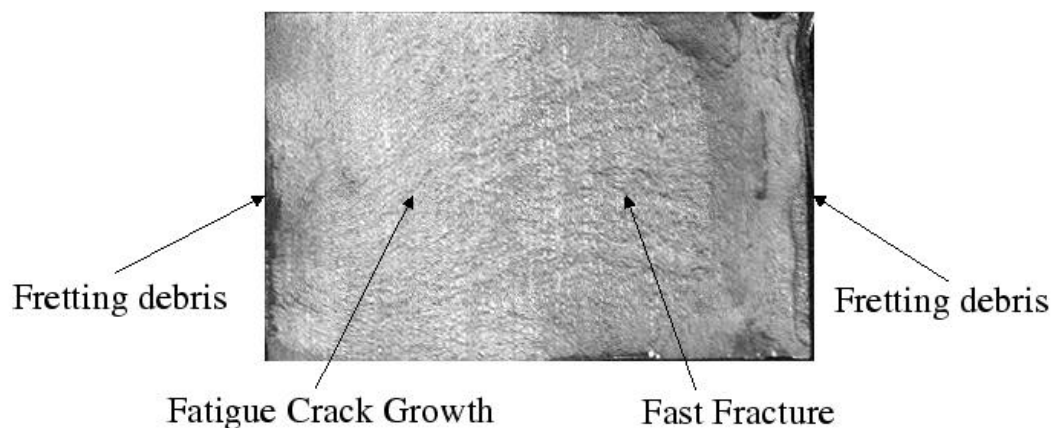


Figure 6B.8. Fracture surface. (Experiment no. PR12).

Table 6B.1.
Experimental Conditions for Fretting Experiments

Expt No.	P lb/in	Q _{max} lb/in	Q _{min} lb/in	Ave. pressure (ksi)	s _{max} ksi	Δs ksi	A in	Life Cycles	R-Ratio	Frequency Hz
PR02	9176	3916	-3337	69.41	39.7	42.4	0.0661	54 744	-0.068	5
PR03	9080	3129	-2580	69.26	32.0	33.8	0.0655	160 628	-0.055	5
PR04	9104	3220	-2636	67.38	35.2	36.1	0.0676	144 242	-0.024	5
PR05	9451	3868	-3204	69.46	42.7	43.2	0.0680	39 947	-0.011	5
PR06	9525	3739	-3283	72.93	40.5	41.7	0.0653	69 279	-0.029	5
PR07	9099	3479	-3260	68.91	38.1	39.9	0.0660	93 930	-0.047	5
PR09	9995	4607	-3775	75.89	48.4	48.8	0.0659	26 391	-0.007	5
PR10	9432	3309	-1893	71.56	29.8	30.4	0.0659	386 049	-0.020	5
PR11	6669	2337	-1425	51.48	41.9	21.2	0.0648	337 578	0.493	5
PR12	6709	2389	-2029	52.40	49.8	25.1	0.0640	161 986	0.496	5
PR13	6792	1978	-1122	52.89	34.8	17.6	0.0642	1 728 051	0.494	10
PR14	6768	1978	-1524	52.79	39.0	19.7	0.0641	1 000 038	0.495	10
PR16	6677	3080	-1461	51.93	50.1	25.3	0.0643	168 637	0.495	10
PR17	6717	2304	-1472	52.12	41.9	21.2	0.0644	1 000 863	0.495	10
PR20	6755	2436	-1079	50.65	39.0	19.8	0.0667	1 502 266	0.492	10
PR22	6763	2293	-1464	52.58	42.1	21.3	0.0643	1 285 642	0.495	10
PR23	6787	2719	-1369	52.93	46.0	23.1	0.0641	245 311	0.497	10

Nucleation and Propagation Lives

Since all the experiments were run to failure, the measured life is the sum of the nucleation and propagation lives. Crack nucleation is usually defined as the life to nucleate a crack of a fixed length. The propagation life is then the life to propagate this crack to failure under the action of the applied loads. In the current set of experiments, once the nucleated crack is greater than a few thousandths of an inch, it may be assumed that the crack is acted upon only by the bulk loads. The crack nucleation length was assumed to be 0.004 inch. The nucleation life was then estimated as the

total life less the life to propagate a crack of 0.004 inch on either side to failure. A Paris law model was used to estimate the propagation life, calculated as

$$N_p = \int_{a_{ci}}^{a_{cf}} \frac{da_c}{C(\Delta K)^m} \quad (6B.1)$$

$$\Delta K = f(g)\Delta s \sqrt{\pi a_c} \quad (6B.2)$$

$$f(g) = 1.12 + 0.203 \left(\frac{2a_c}{w} \right) - 1.197 \left(\frac{2a_c}{w} \right)^2 + 1.930 \left(\frac{2a_c}{w} \right)^3 \quad (6B.3)$$

where ΔK is the stress intensity factor change, Δs is the bulk stress range and the geometry factor, $f(g)$, is obtained from (Bannantine, Comer and Handrock 1990). a_c is the crack length, a_{ci} and a_{cf} are the initial and final crack lengths and w is the width of the specimen. The Paris law coefficient C is 5.09×10^{-9} , and the Paris exponent, m , is 2.62. Note that failure was assumed when the maximum value of the stress intensity factor reached K_{Ic} (85 ksi $\sqrt{\text{inch}}$), or when the crack propagated across the whole specimen.

Once the propagation life was obtained, the nucleation lives were calculated by subtracting the propagation life from the total life. Table 6B.2 provides the calculated propagation life and nucleation life for all the experiments.

Interrupted Tests

Some of the experiments were stopped after a predetermined number of cycles in order to study the contact surface. The conditions under which these interrupted tests were conducted are listed in the Table 6B.3. All the interrupted tests were conducted at a frequency of 10 Hz.

The contact surface comparison of the pads used in interrupted tests (Figure 6B.9) with other pads from tests to failure (Figure 6B.7) clearly showed that the contact area does expand once a crack is formed, providing experimental evidence of the phenomenon portrayed subsequently in Figure 6B.24. When a crack forms, the local compliance is reduced, leading to an increased contact area. Figure 6B.9 shows the contact surface of one of the pads used in the interrupted tests. The comparison of the contact surfaces shows that the wear damage is more in pads subjected to high load, low-cycle experiments as compared to low load, high-cycle experiments.

Table 6B.2.

Calculated nucleation and propagation lives for the experiments. Nucleation life is defined as the number of cycles to nucleate a crack of 0.004 inch.

Expt. No.	Total Life Cycles	Nucleation Life Cycles	Propagation Life Cycles
PR02	54744	28294	26450
PR03	160628	114088	46540
PR04	144242	107992	36250
PR05	39947	18097	21850
PR06	69279	44179	25100
PR07	93930	64470	29460
PR09	26391	10681	15710
PR10	386049	329969	56080
PR11	337578	200718	136860
PR12	161986	74256	87730
PR13	1728051	1505191	222860
PR14	1000038	834168	165870
PR16	168637	82717	85920
PR17	1000863	864003	136860
PR20	1502266	1338576	163690
PR22	1285642	1150462	135180

Table 6B.3.

Conditions at which the interrupted fretting tests were conducted.

Expt No.	P lb/in	Q_{max} lb/in	Q_{min} lb/in	s_{max} ksi	Δs ksi	Life Cycles
PR18	6752	2672	-1531	46.5	23.4	31875
PR19	6661	2757	-1424	46	23.2	86501
PR24	6543	2333	-1767	45.9	23.1	90000
PR25	6981	2915	-1556	50.1	25.1	60000
PR26	6858	2535	-1831	49.6	24.9	60000
PR27	6608	2391	-1276	41.8	21	1000000

Evolution of Coefficient of Friction

Direct Load Measurement

The friction experiments had the aim of characterizing the evolution of the coefficient of friction, μ , with number of cycles in a partial slip experiment. While the experimental procedure was the same as for the fretting experiments, there were two differences. Cylindrical pads were used, resulting in Hertzian pressure in the contact zone. As the coefficient of friction increased, the tangential force stabilized at a value less than that required for gross sliding. Thus, the coefficient of friction cannot be evaluated as the magnitude of tangential force divided by the normal force. Hence, an alternative approach was taken.

After running the test for a specified number of fretting cycles, the test was stopped. The average coefficient of friction was now determined in the following way. Without disturbing the pad/specimen contact, an increasing amplitude waveform was applied to the specimen. This causes the tangential force to increase during each “friction cycle”. Figure 6B.10 shows this approach schematically. Ultimately, the tangential force reaches the value required for gross sliding, and the experiment is stopped. The number of friction cycles required is usually about 50. The maximum value of the tangential force before sliding commences divided by the normal force gives the average coefficient of friction.

Two different pad radii were used (5 inch and 7 inch). The evolution of the coefficient of friction was characterized over a range of configurations of the normal force, the bulk-stress R-ratio as well as the ratio of the tangential to normal force, Q/P. Table 6B.4 shows the nominal conditions under which each of the friction tests were conducted. The average coefficient of friction is also reported in this table. Note that the values of the normal force correspond to the values that produced a nominal pressure of 55 ksi and 75 ksi in the fretting experiments. In any analysis of the fretting problem, the crucial parameter is the coefficient of friction in the slip zones, where the frictional force is enough to cause sliding. The friction experiments provide the average coefficient of friction. To obtain the slip zone friction coefficient, an approach available in literature was followed (Hills & Nowell 1994). For the cylindrical contact the equation

relating the average coefficient of friction, μ the slip zone coefficient of friction, μ_s , and the initial coefficient of friction, μ_0 is given by the following equation

$$\mu_s = \mu_0 + \frac{2}{P} \int_0^{\mu_s} \left(\frac{Q}{\mu_s P} \sqrt{1 - \frac{Q}{\mu_s P}} + \sin^{-1} \sqrt{1 - \frac{Q}{\mu_s P}} \right) d\mu_s \quad (6B.4)$$

Equation (6B.4) is obtained by assuming that the friction coefficient in the stick zone is unchanged. Using Equation (6B.4), a value of 0.5 was obtained for the steady state slip zone coefficient of friction. This value is appropriate when partial slip is prevalent and Q/P is less than 0.5. Note that when the experiment is in gross sliding regime, the coefficient of friction may be different and may be much higher. For the purpose of analysis, a value of 0.5 for the coefficient of friction was used unless the Q/P value was found to be higher, in which case the coefficient of friction was set to the value of Q/P. Table 6B.5 shows the evaluated slip zone friction coefficients. Figure 6B.11 shows the same data in a graphical form along with a logarithmic fit that describes the evolution of the coefficient of friction between 1000 and 20000 cycles.

The friction coefficient does not reach a steady state value until about 10000 cycles. This is in stark comparison to experiments done with aluminum where the steady state is reached in a few hundred cycles. This slow evolution is probably due to the resistance of Ti-6Al-4V to fretting wear. In the absence of gross sliding, the degradation of the surface is very slow, causing the slow evolution of the coefficient of friction. There is no marked dependence of the steady state slip-zone coefficient of friction on the loading conditions.

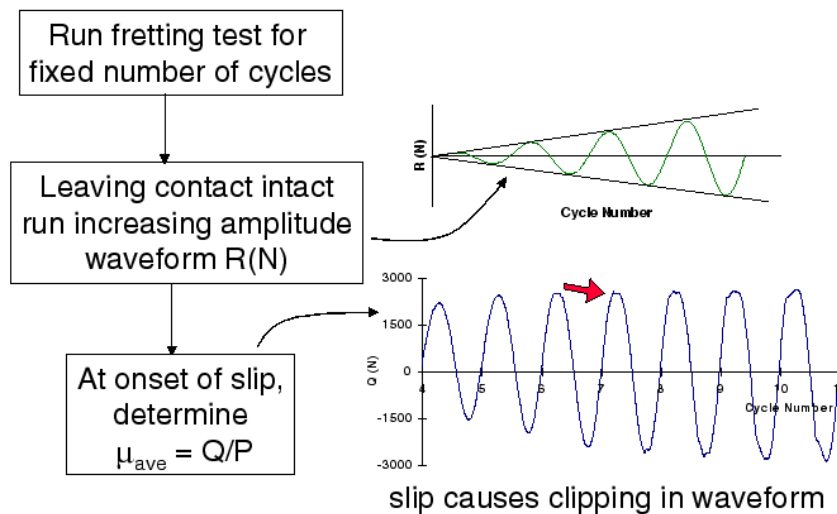


Figure 6B.10. Estimation of the coefficient of friction.

Table 6B.4.

Conditions at which the friction tests were run. Note that cylindrical pads were used. Experiments PF01 through PF05 used 7 inch radius on the pads, while the remaining tests used 5 inch.

Expt No.	P lb/in	Q/P _{max} lb/in	Q/P _{min} lb/in	s _{max} ksi	R-Ratio	Life Cycles	Ave. μ
PF01	6563	0.36	-0.202	41.1	0.49	5004	0.4
PF02	6498	0.402	-0.165	42	0.5	10000	0.425
PF03	6957	0.412	-0.135	42.8	0.5	20000	0.44
PF05	6530	0.362	-0.194	41.1	0.49	2503	0.375
PF08	9927	0.443	-0.27	23.4	-0.75	20008	0.495
PF09	9530	0.449	-0.256	40.8	0.02	20000	0.475
PF10	6851	0.39	-0.177	42.1	0.51	20016	0.45
PF11	6979	0.336	-0.192	41.1	0.49	12530	0.401
PF12	9542	0.414	-0.237	40.7	0.06	15025	0.428

Table 6B.5.

Slip zone coefficients for friction tests.

Expt. No.	Slip zone
PF01	0.418
PF02	0.432
PF03	0.449
PF05	0.378
PF08	0.52
PF09	0.483
PF10	0.486
PF11	0.448
PF12	0.431

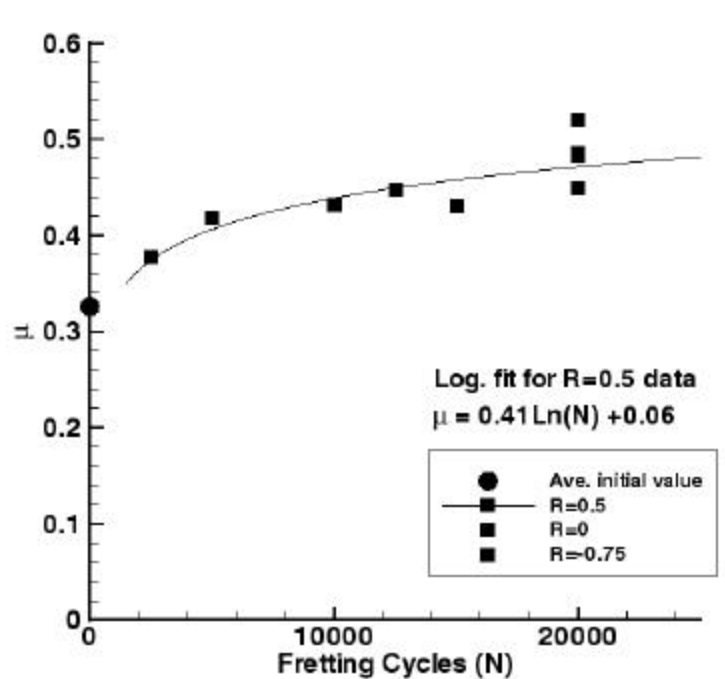


Figure 6B.11. Evolution of slip zone coefficient of friction.

Thermal Imaging

Infrared thermal imaging is a technique that can be used to measure the temperature field on the surface of a body through the measurement of the radiation emitted. This technique is particularly useful in detecting temperature changes of the order of a few degrees. In particular the temperature rise during gross sliding can be measured accurately. This technique offers an in-situ real-time full-field method for measurement of the near-surface temperature evolution. Intensity measurements are taken with an infrared camera (with a 128 x 128 pixel window and a resolution of 0.003 inch) at 100 frames/second. Figure 6B.12 shows the imaging region that encompasses the contact and the surrounding region.

A calibration curve is generated for the conversion of these intensity values into temperatures. A median filtering operation was performed on the images prior to conversion to temperature. A plate with an attached thermocouple is used for calibration. The intensity values from the camera are calibrated against the thermocouple readings, resulting in a calibration curve. The specimen and pad are painted with a commercial flat black paint to increase the emissivity and hence the infrared radiation. The accuracy

of the technique was verified by using a uniaxial cyclic test. The coupled heat conduction equation is given by

$$k\nabla^2 T = \rho C_v \dot{T} + 3KaT\dot{\epsilon}_{kk} \quad (6B.5)$$

where k is the conductivity, C_v is the specific heat at constant volume, K is the bulk modulus, α is the coefficient of thermal expansion, ρ is the density, T is the temperature and ϵ_{kk} is the first invariant of strain. If the experiment is adiabatic, the temperature change is directly related to the change in strain invariant as

$$\Delta T = -3KaT\Delta\epsilon_{kk} \quad (6B.6)$$

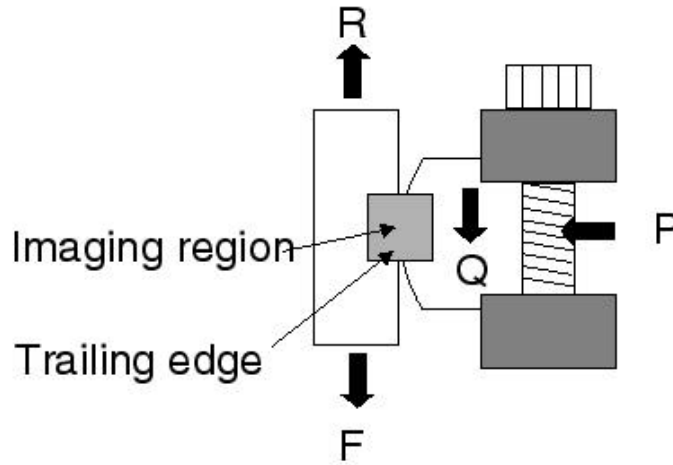


Figure 6B.12. Schematic of contact between specimen and pad showing temperature imaging region. Note that the direction shown for Q is the tangential force direction in the pad.

Of course, when applied to the friction experiments, the adiabatic nature is compromised by frictional heating and by the conduction effects caused by the temperature gradients. However, in the partial slip regime, the frictional and conduction effects are minimal at higher frequencies ($> 5\text{Hz}$) allowing for the use of the adiabatic approximation. However, using finite element techniques, the conduction effects can be accounted for, providing an extremely powerful technique to directly measure the stress state near the contact. Thus, infrared imaging may be used in conjunction with the friction tests to evaluate the correct boundary conditions such as the coefficient of friction at the contact and the effects of the possible presence of a moment. Further details of this technique are available elsewhere (Szolwinski, Harish, Farris & Sakagami 1999). Figure 6B.13

shows the temperature evolution through the duration of the test. It is seen that in this particular experiment the gross temperature rise was limited to a few cycles, as the partial slip regime set in quite quickly. This figure reveals that the temperature rises may be expected to be small when the gross sliding persists only for a few cycles. However, based on the rate of temperature rise, very high temperature rises may result if the sliding persists over a large number of cycles. This is an important consideration as laboratory experiments may be conducted at much higher frequencies as compared to the actual hardware applications and may give fictitious effects due to temperature change. The infrared camera may be used to ensure that the contact temperature is within acceptable limits by adjusting the experimental conditions.

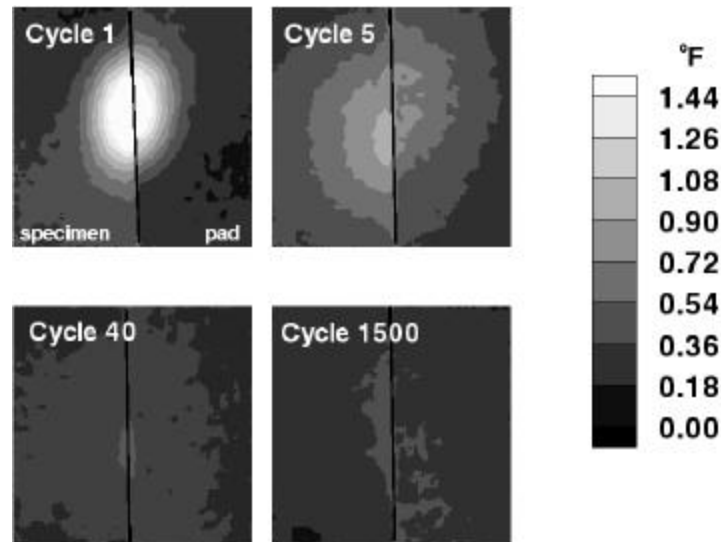


Figure 6B.13. Temperature as a function of cycle. These images show that the gross sliding was restricted to first few cycles. The image size is 0.375 inch by 0.375 inch. (Experiment PF10).

In the partial slip regime, the effects of different loading conditions can be identified by the plots showing amplitude of temperature change during a cycle. The temperature amplitudes shown in Figure 6B.14 correspond directly to the first invariant of strain as frictional heating is negligible in the partial slip regime. Figure 6B.14 also details the various aspects of the contact that may be gleaned from infrared imaging. These include the load transmission into the pad, the effect of the bulk stress on the stresses in the pad and the differences between the top and bottom of the contact due to load transfer.

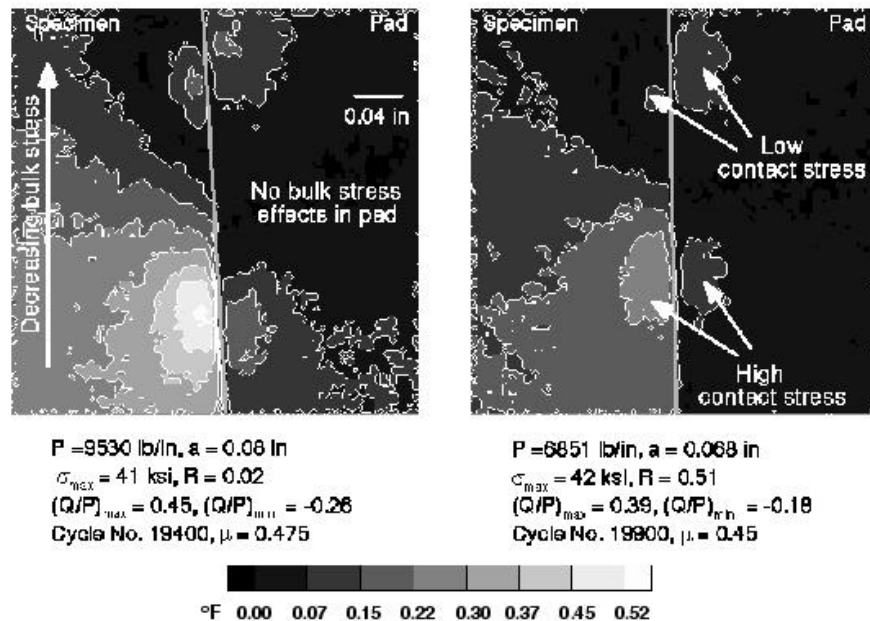


Figure 6B.14. Amplitudes of temperature over one partial slip cycle in two friction tests.

In addition, the temperature effects of friction can be characterized. Figure 6B.15 shows the change in temperature from nominal initial temperature at maximum bulk tension and maximum bulk compression towards the beginning and at the end of the experiment. Note that the contact stress effects as well as the effect of bulk stress effects on the specimen is captured. By this time, the effects of frictional heating were negligible and the temperature change due to the contact stresses dominate the temperature field. At cycle number 600, the frictional heating had caused a small rise in the bulk temperature which dissipated away by cycle 20000. This is the reason for the images at cycle 20000 having a lower bulk temperature than the ones at cycle 1500. If the amplitudes of temperature change over each cycle were plotted, they would be nearly the same. Thus, by cycle 600 the coefficient of friction in the slip zone was pretty close to the final value. This is not surprising as the Q/P value was about 0.39 for this particular experiment and the final slip zone friction coefficient was about 20% higher.

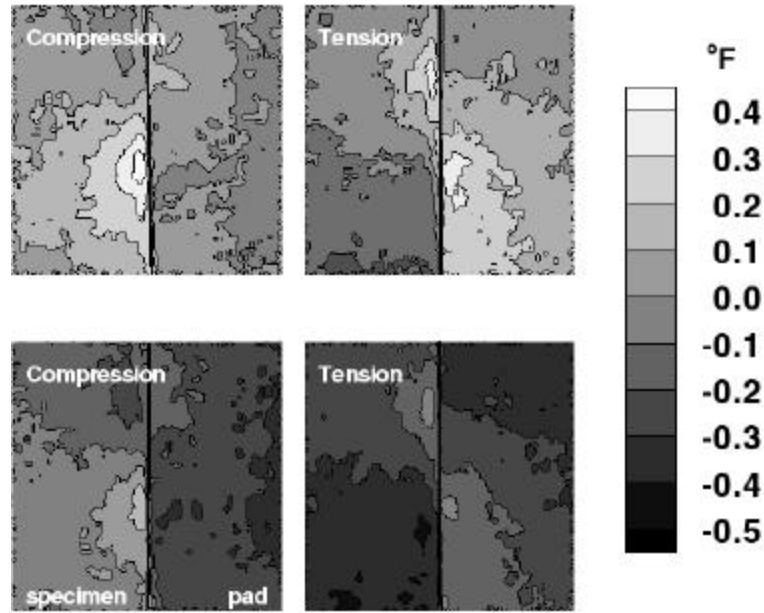


Figure 6B.15. Snapshots of temperature during one partial slip cycle of a friction test. Top row images were taken at 600 cycles, while bottom row images were taken at 20000 cycles. The image size is 0.375 inch by 0.375 inch. (Experiment PF10).

The images show a lower temperature change at the top of the specimen as compared to bottom. This is due to the load transfer into the fretting chassis (Figure 6B.3). The pad does not show any bulk stress effects. From Table 6B.4, experiment PF10 was done at a stress ratio of 0.5 and did not have Q/P_{max} equal in magnitude to Q/P_{min} , i.e., the loads were not symmetric about the mean. This causes the temperature changes from nominal to be different in tension and compression. This effect is manifested in the temperature contours, particularly at cycle 20000, where the minimum temperature during tension is higher in magnitude than the maximum temperature in compression. Thus, critical information about the loading is embedded in the thermal images.

Thermal imaging provides valuable information about the evolution of frictional conditions at the fretting contact interface. The transition of the contact from gross sliding to a partial slip regime can also be established. Also, the nature of the contact distribution, including effects of moment, can be studied in-situ.

Singular Integral Equations

Nomenclature and Problem Description

The various notations used in this section are presented below.

Parameter	Description	Units
P	Normal load per unit depth	lb/in
Q_{\max}	Maximum tangential load per unit depth	lb/in
Q_{\min}	Minimum tangential load per unit depth	lb/in
a	Half-contact area	in
e	Eccentricity in contact	in
A	Material constant	lb/in ²
E	Young's Modulus	lb/in ²
OXY	Global coordinate system	
oxy	Local coordinate system	
$H(X)$	Contact pad profile (global coordinates)	in
$h(x)$	Contact pad profile (local coordinates)	in
C_0	Rigid body translation of pad	in
C_1	Rigid body rotation of pad	

The profile $H(x)$, of a pad in contact with a semi-infinite half-space, is given. A force, P , and moment, M , are applied on the half-space (an equal and opposite force-moment pair acts on the pad). The pressure distribution for this loading is to be calculated. In addition, the shear traction on the half-space and pad are to be calculated for a tangential load of Q , applied on the pad. Figure 6B.16 shows the schematic representation of this problem. Note that the shear traction distribution is history dependent.

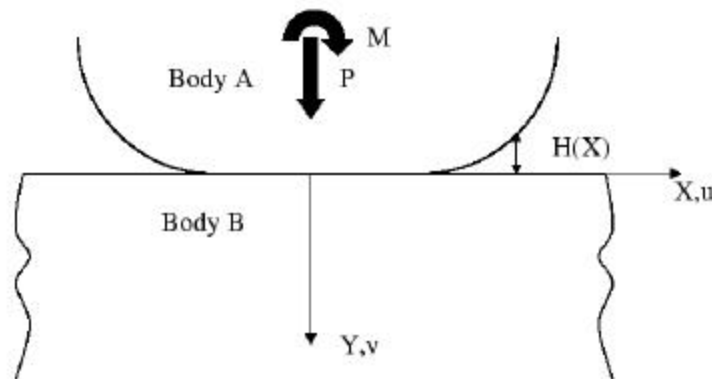


Figure 6B.16. Schematic of the problem.

Formulation of Pressure Solution

The singular integral equation that governs the plane strain elastic contact of surfaces can be derived from classical theory of elasticity results relating the slope of the contacting surfaces to the resulting interfacial tractions. This equation uses a local coordinate system centered at the contact region. For this given coordinate system, it can be shown that the difference in normal displacements of each surface within the contact region, $v_A - v_B$, is equal to the initial gap between the surface, $h(x)$, plus terms associated with a rigid body displacement and clockwise rotation, $-C_0$ and $-C_1 x$, respectively.

$$(\bar{v}_A - \bar{v}_B) = h(x) - C_0 - C_1(x) \quad (6B.7)$$

The elastic displacements of each surface are related to the normal traction, $p(x)$, across the region of contact $|x| \leq a$ by the following singular integral equation, which adopts the convention $p(x) > 0$ in the region of contact. Noting that $h(x)$ is the profile in the local coordinate system, the equation may be written as

$$\frac{dh(x)}{dx} - C_1 = \frac{d}{dx} (\bar{v}_B - \bar{v}_A) = A \int_{-a}^{+a} \frac{p(s)}{(x-s)^2} ds \quad (6B.8)$$

$$A = \frac{4(1-\nu^2)}{pE} \quad (6B.9)$$

The form of this expression assumes both plane strain conditions and half-spaces with identical elastic properties. If the origins of the local coordinate system oxy , and OXY are apart by an eccentricity, e , then Equation (6B.8) may be written in the global coordinate system as

$$\frac{dH(X)}{dX} - C_1 = A \int_{-a+e}^{+a+e} \frac{\bar{p}(t)}{(X-t)^2} dt \quad (6B.10)$$

$$X = x + e \quad (6B.11a)$$

$$H(X) = h(x) \quad (6B.11b)$$

$$\bar{p}(X) = p(x) = p(X - e) \quad (6B.11c)$$

The above equation relates the pressure, profile and contact area in the local and global coordinate systems. Further discussion will be restricted to the equations in the local coordinate systems, with the eccentricity, e , being specified.

Equilibrium Conditions

The force and moment equilibrium conditions are

$$P = \int_{-a}^{+a} p(x) dx \quad (6B.12a)$$

$$M = \int_{-a}^{+a} p(x) x dx \quad (6B.12b)$$

In addition, the pressure must vanish at $x = \pm a$. Instead of specifying M , the rotation C_1 may also be specified, in which case, Equation (6B.12b) will be replaced by a different condition, which will be derived later.

Solution Procedure

The solution for the pressure induced by a force on a general smooth interfacial profile is now reduced to the solution of Equation (6B.8). Since, for most surface profiles, inverting these equations to obtain closed-form solutions for $p(x)$ is not feasible, a method of solution based on a trigonometric variable transformation is used (Barber 1992). This transformation leads to a computationally efficient, robust tool for analyzing arbitrarily smooth contact surfaces.

The local coordinate system is used in the solution process. After introducing the transformations $x = a \cos \mathbf{f}$ and $s = a \cos \mathbf{q}$ and using the chain rule of differentiation

$$\frac{dh}{d\mathbf{f}} = \frac{dh}{dx} \frac{dx}{d\mathbf{f}} = a \frac{dh}{dx} \sin \mathbf{f} \quad (6B.13)$$

Equation (6B.8) may be re-written as

$$\frac{1}{a \sin \mathbf{f}} \frac{dh}{d\mathbf{f}} + C_1 = -A \int_0^{\mathbf{f}} \frac{p(\mathbf{q}) \sin \mathbf{q}}{(\cos \mathbf{f} - \cos \mathbf{q})} d\mathbf{q} \quad (6B.14)$$

where $p(\mathbf{q})$, a and the eccentricity e are unknown (Note that $X = x+e$). Then, if the traction distribution $p(\theta)$ is expressed as a cosine series of the form,

$$p(\mathbf{q}) = \sum_{n=0}^{\infty} \frac{p_n \cos n\mathbf{q}}{\sin \mathbf{q}} \quad (6B.15)$$

the singular integral on the right-hand side of Equation (6B.14) may be expressed as an infinite series

$$\frac{dh}{d\mathbf{f}} + C_1 a \sin \mathbf{f} = -a \sin \mathbf{f} \mathbf{P} \sum_{n=1}^{\infty} \frac{p_n \sin n\mathbf{f}}{\sin \mathbf{f}} \quad (6B.16)$$

The following result has been used in obtaining Equation (5.4.4)

$$\int_0^{\mathbf{P}} \frac{\cos n\mathbf{q}}{(\cos \mathbf{f} - \cos \mathbf{q})} d\mathbf{q} = -\frac{\mathbf{P} \sin n\mathbf{f}}{\sin \mathbf{f}} \quad (6B.17)$$

Finally, by expressing the composite slope of the surface, $dh/d\mathbf{f}$, as a Fourier sine series, a simple relationship may be established between the Fourier coefficients representing the slope of the geometry and the associated pressure distribution.

$$\frac{dh}{d\mathbf{f}} = \sum_{n=1}^{\infty} h_n \sin n\mathbf{f} \quad (6B.18)$$

$$p_n = \frac{h_n}{\mathbf{P} A a}, \quad n > 1 \quad (6B.19a)$$

$$p_1 = \frac{h_1 + C_1 a}{\mathbf{P} A a}, \quad n = 1 \quad (6B.19b)$$

The relationship between h_n and p_n can be written as:

$$p_n = \frac{h_n}{\mathbf{P} A a}, \quad n > 1 \quad (6B.19a)$$

$$p_1 = \frac{h_1 + C_1 a}{\mathbf{P} A a}, \quad n = 1 \quad (6B.19b)$$

The consideration of the boundary conditions in Equation (6B.12) yields expressions for p_0 and p_1 . If the moment, M is expressed as Pd , where d is the offset from the global origin at O , then

$$P = \int_{-a}^{+a} p(x) dx \quad \Rightarrow \quad p_0 = \frac{P}{\mathbf{P} a} \quad (6B.20a)$$

$$P(d - e) = \int_{-a}^{+a} p(x) x dx \quad \Rightarrow \quad p_1 = \frac{2P(d - e)}{\mathbf{P} a^2} \quad (6B.20b)$$

Note that if C_1 were specified instead of moment, M , Equation (6B.19b) would replace Equation (6B.12b) as the condition from which p_1 should be evaluated. The

condition that the pressure must vanish at $x = \pm a$ reveals the following relations between the p_0 and p_n

$$p_0 = -\sum_{k=1}^{\infty} p_{2k} \quad (6B.21a)$$

$$p_1 = -\sum_{k=1}^{\infty} p_{2k+1} \quad (6B.21b)$$

Solution Procedure

The solution procedure consists of finding a and e to satisfy the integral equation (Equation (6B.8)) as well as the boundary conditions. The resulting pressure distribution $p(x)$ is the traction solution that is required. Usually, this is achieved by iterating for a and e . Figure 6B.17 shows this procedure schematically.

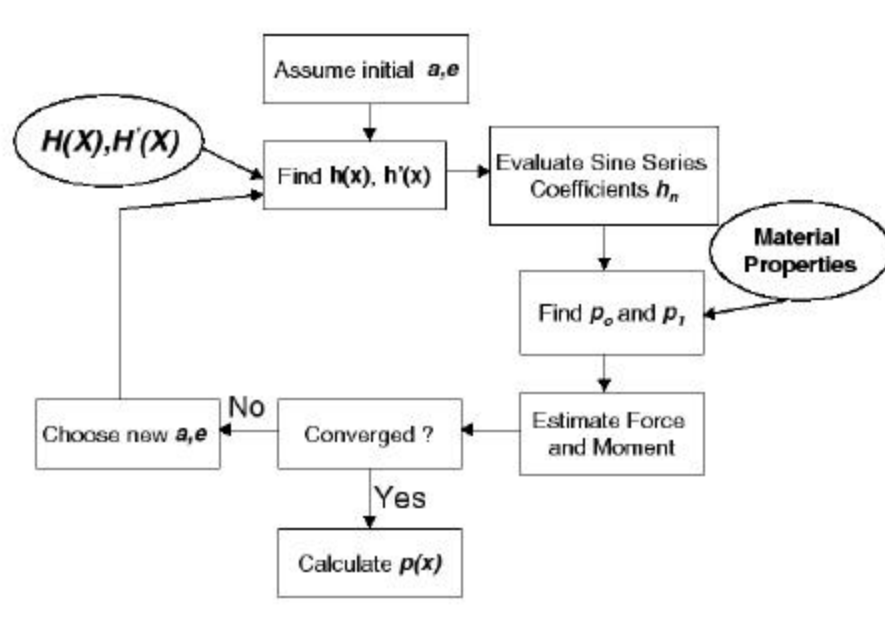


Figure 6B.17. Flow diagram for evaluation of pressure.

Validation of Analytical Formulation

To validate this formulation, the solution approach was used to determine pressure distributions associated a flat pad with rounded edges, using closed form expressions for h_n for the geometry presented in Figure 6B.18. Figure 6B.19 presents a set of non-dimensionalized normal tractions, $ap(x) / P$, obtained with a small number of terms

($N = 1000$) in the series representation. As shown on the plot, these results are also consistent with those of Ciavarella, Hills & Monno (1998), who have derived recently a closed-form expression for the pressure distribution arising in this specific contact configuration of a flat pad with rounded edges.

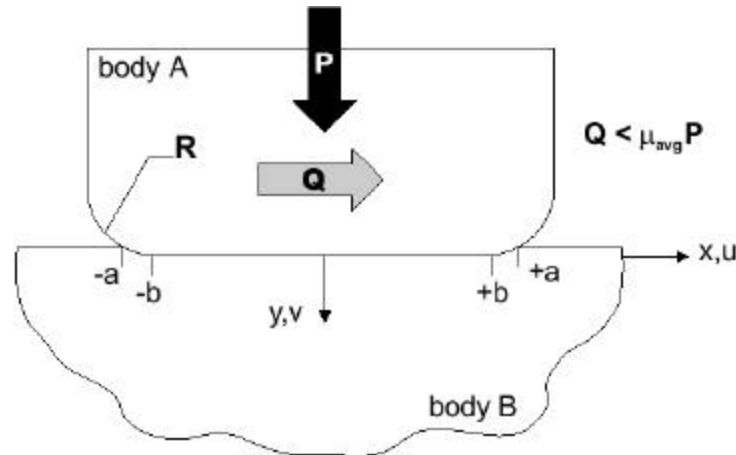


Figure 6B.18. A schematic of the contact configuration used to validate the quasi-analytical solution approach. Note that for such two-dimensional contacts, P and Q are line loads (loads per unit depth).

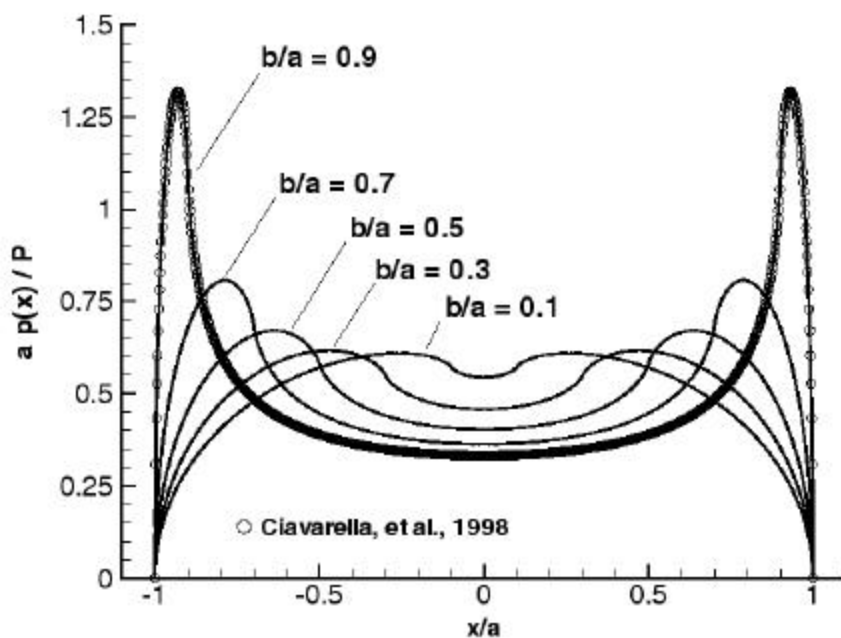


Figure 6B.19. Plot of non-dimensionalized normal pressure, $ap(x)/P$, for a range of values of b/a .

Shear Traction

The equation that relates shear traction to the tangential displacements is similar to Equation (6B.8) and may be written as

$$\frac{d}{dx}(\bar{u}_B - \bar{u}_A) = -A \int_{-a}^{+a} \frac{q(s)}{(x-s)} ds \quad (6B.22)$$

We now introduce the function $g(x)$ and the constant C_2 such that

$$\frac{dg(x)}{dx} - C_2 = \frac{d}{dx}(\bar{u}_B - \bar{u}_A) \quad (6B.23)$$

Equation (6B.22) may now be written as

$$\frac{dg(x)}{dx} - C_2 = A \int_{-a}^{+a} \frac{q(s)}{(x-s)} ds \quad (6B.24)$$

Partial Slip

If the shear traction, $q(x)$ is equal to the coefficient of friction times the pressure at every point ($\mathbf{m}p(x)$), then there is sliding throughout the contact. Using Equation (6B.8), the slope of the tangential displacement may now be written as

$$\frac{dg(x)}{dx} - C_2 = \mathbf{m}A \int_{-a}^{+a} \frac{p(s)}{(x-s)} ds = \mathbf{m} \left(\frac{dh(x)}{dx} - C_1 \right) \quad (6B.25)$$

This implies that $dg/dx = \mathbf{m} dh/dx$ and $C_2 = \mathbf{m}C_1$. Thus the solution of shear traction when there is sliding is quite simple.

When the applied tangential force is not enough to cause global sliding, the contact is divided into zones of relative slip ($(\bar{u}_B - \bar{u}_A) \neq 0, q(x) = \mathbf{m}p(x)$) and stick ($(\bar{u}_B - \bar{u}_A) = 0, q(x) < \mathbf{m}p(x)$). This is referred to as partial slip. We will consider cyclic loading of the tangential force, Q , to a maximum value (Q_{max}), unloading to a minimum value (Q_{min}) and reloading back to Q_{max} again. If the coefficient of friction, \mathbf{m} is assumed to be constant, then the equivalent pressure distribution of the shear traction is defined as

$$p_{eq}(x) = \frac{q(x)}{\mathbf{m}} \quad (6B.26)$$

We now introduce the function $G(X)$ to describe the tangential displacement in global coordinates. The relations connecting $G(X)$ and $g(x)$ are

$$X = x - e \quad (6B.27a)$$

$$G(X) = g(x) = g(X + e) \quad (6B.28b)$$

Also, the notations, $F_{[a,e]}$, $M_{[a,e]}$ and $p_{[a,e]}(X)$ are introduced. $F_{[a,e]}$ and $M_{[a,e]}$ are the force and moment applied at the global origin that would produce a contact area of a , with eccentricity e and pressure distribution described by $p_{[a,e]}(X)$. Thus, $p_{[a,e]}(X)$ is the solution to Equation (6B.10).

Tangential Force $Q = Q_{max}$

When the applied tangential force is less than that required for sliding, there is a region of stick within the contact. Assume that there is one region of slip on either side and that the slip zones exist from $-a+e \leq X \leq -c_1+e_1$ and $c_1+e_1 \leq X \leq a+e$. Also, the shear traction may be assumed to consist of two components as follows

$$q(X) = \mu p_{[a,e]}(X) - q'(X) \quad (6B.28)$$

Using the equivalent pressure concept

$$p_{eq}(X) = p_{[a,e]}(X) - p^1(X) \quad (6B.29)$$

In terms of force

$$F_{eq} = F_{[a,e]} - F^1 \quad (6B.30)$$

To evaluate the unknown function $p^1(X)$, we use the kinematic condition that relative displacement must be zero in the stick region. The displacement caused by the sliding traction $\mu p_{[a,e]}(X)$ is

$$\mu \left(\frac{dH}{dX} - C_1 \right) \quad -a+e < X < a+e \quad (6B.31)$$

Now, if the stick region extends from $-a+e \leq X \leq -c_1+e_1$ and $c_1+e_1 \leq X \leq a+e$, the slope of the displacement produced by corrective traction must be

$$\mu \left(\frac{dH}{dX} - C_1 \right) \quad -c_1+e_1 < X < c_1+e_1 \quad (6B.32)$$

Thus, the slope of the displacement produced by the equivalent pressure traction must be

$$\frac{dG}{dX} = \left(\frac{dH}{dX} - C_1 \right) \quad -c_1+e_1 < X < c_1+e_1 \quad (6B.33)$$

Substituting this into Equation (6B.10), we can see that the pressure traction is equal to $p_{[c_1,e_1]}(X)$. Equation (6B.28) will then give the required shear traction. Note that in this case, the moment is not explicitly known, but the rotation term C_1 is known from the

pressure solution. Thus, Equation (6B.19b) replaces Equation (6B.12b) as a boundary condition. The other boundary conditions are same as for the pressure solution. Finally $q(X)$ is obtained as

$$q(X) = m(p_{[a,e]}(X) - p_{[c_1,e_1]}(X)) \quad (6B.34)$$

Tangential Force Reduction

When the tangential force is now reduced from the maximum value of Q_{max} , we can use the same approach. Say the tangential force is reduced to a value of Q . This will result in a region of reversed slip, where the shear traction is opposite to the original direction. Thus, there is a region in which there is reversed slip (opposite to the direction of original slip obtained at Q_{max}) and a region where there is stick. It is extremely important to note that the relative slip is now measured from the displacement state at Q_{max} . Thus, in the stick region, the relative displacement will remain the value attained at Q_{max} , which is the reference point.

If the region of reversed slip extends as $-a+e \leq X \leq -c_2+e_2$ and $c_2+e_2 \leq X \leq a+e$, then there is no relative slip from $-c_2+e_2$ to c_2+e_2 . In the reversed slip region $q(X) = -mp_{[a,e]}(X)$. To obtain this traction from the traction at Q_{max} , we subtract $2mp_{[a,e]}$ from Equation (6B.34). The intermediate value of $q(X)$ is obtained as

$$q(X) = m(p_{[a,e]}(X) - p_{[c_1,e_1]}(X)) \quad (6B.35)$$

Now the relative slip produced by the subtraction of $2mp_{[a,e]}$ is

$$-2m\left(\frac{dH}{dX} - C_1\right) \quad -a+e < X < a+e \quad (6B.36)$$

where the -ve sign indicates the reversed direction. Once again, to produce the condition of no relative slip, the corrective shear traction $q^2(X)$ must produce the slope of tangential displacement of

$$2m\left(\frac{dH}{dX} - C_1\right) \quad -c_2+e_2 < X < c_2+e_2 \quad (6B.37)$$

The equivalent pressure distribution for this will have the slope of tangential displacement as

$$\frac{dG}{dX} = \left(\frac{dH}{dX} - C_1\right) \quad -c_2+e_2 < X < c_2+e_2 \quad (6B.38)$$

with the solution $p_{[c2,e2]}(X)$. Thus, the shear traction becomes

$$q(X) = \mu \{ -p_{[a,e]}(X) - p_{[c1,e1]}(X) + 2p_{[c2,e2]}(X) \} \quad (6B.39)$$

If $Q = Q_{min}$, then the contact parameters will correspond to those at minimum tangential force.

Tangential Force Reloading

Now, when the tangential force is increased from the value of Q_{max} , a similar approach to that detailed in the above section may be used, with the directions reversed. Thus, the tangential traction would be of the form

$$q(x) = \mu \{ -p_{[a,e]}(X) - p_{[c1,31]}(X) + 2p_{[c2,e2]}(x) - 2p_{[c3,e3]}(X) \} \quad (6B.40)$$

If the tangential force is increased back to Q_{max} , Equation (6B.34) is realized and a full load cycle is completed. If the tangential load is cycled, the traction would also follow the cycle detailed above. If the tangential load does not cycle between Q_{max} and Q_{min} , then the approach detailed above must be continued for each loading and unloading path.

Thus, the entire problem of finding the contact tractions may be reduced to finding the pressure distributions corresponding to a known force and a moment or rotation condition. This simplifies the numerical implementation greatly as only one integral equation needs to be solved. It must be noted that there exists a one-to-one relationship between the contact parameters and the corresponding force-moment pair.

Subsurface Stress Calculation

Fourier Transform Technique

Given the pressure and shear traction at the surface, the subsurface tractions can be evaluated using a Fourier transform technique. The method relies on the representation of the traction as a sum of periodic tractions. Using the local coordinate system about which the pressure is centered, the augmented pressure distribution may be expressed as

$$P_f(\mathbf{a}) = \int_0^{\infty} p_f(s) e^{-i\mathbf{a}s} ds \quad (6B.41)$$

The sign is negative because $p(x)$ has been defined as positive when there is a non-zero pressure. Positive pressure corresponds to negative traction. A similar condi-

tion for tangential traction may be written down (without the negative sign). The Fourier transform of $p_f(x)$ may be written down as

$$P_f(\mathbf{a}) = \int_0^{\infty} p_f(s) e^{-i\mathbf{a}s} ds \quad (6B.42)$$

with the inverse transform given by

$$p_f(x) = \int_0^{\infty} P_f(\mathbf{a}) e^{i\mathbf{a}x} d\mathbf{a} \quad (6B.43)$$

If the depth, y , is taken as positive into the body, then the subsurface stresses for a traction (normal or shear) of the form $P_f e^{i\mathbf{a}x}$ may be obtained from elasticity. The boundary conditions are imposed at the surface and at infinity (stresses must be finite at infinity). Table 6B.6 gives the subsurface stresses as function of P_f and y . From Equation (6B.43) and Table 6B.6, the subsurface stresses may be written down. For example,

$$\mathbf{s}_{xx}(x, y) = \int_0^{\infty} \overline{\mathbf{s}}_{xx}(\mathbf{a}, y) e^{i\mathbf{a}x} d\mathbf{a} \quad (6B.44)$$

gives \mathbf{s}_{xx} for a pressure loading $p_f(x)$. Similar equations may be constructed for the remaining stresses for normal and shear traction.

Table 6B.6.

Subsurface stresses for a normal traction, $P_f e^{i\mathbf{a}x}$, and a tangential traction, $Q_f e^{i\mathbf{a}x}$. Note that $p(x) = -\mathbf{s}_{yy}(x, 0)$.

Stress	Normal Traction	Tangential Traction
σ_{xx}	$\overline{\mathbf{s}}_{xx}(\mathbf{a}) e^{i\mathbf{a}x}$	$\overline{\mathbf{s}}_{xx}(\mathbf{a}) e^{i\mathbf{a}x}$
σ_{yy}	$\overline{\mathbf{s}}_{yy}(\mathbf{a}) e^{i\mathbf{a}x}$	$\overline{\mathbf{s}}_{yy}(\mathbf{a}) e^{i\mathbf{a}x}$
τ_{xy}	$\overline{\mathbf{t}}_{xy}(\mathbf{a}) e^{i\mathbf{a}x}$	$\overline{\mathbf{t}}_{xy}(\mathbf{a}) e^{i\mathbf{a}x}$

$$\begin{aligned} \overline{\mathbf{s}}_{xx} &= P_f [1 - \mathbf{a}y] e^{-\mathbf{a}y} \\ \overline{\mathbf{s}}_{yy} &= P_f [1 + \mathbf{a}y] e^{-\mathbf{a}y} \\ \overline{\mathbf{t}}_{xy} &= iP_f [1 - \mathbf{a}y] e^{-\mathbf{a}y} \end{aligned}$$

$$\begin{aligned} \overline{\mathbf{s}}_{xx} &= iQ_f [-2 + \mathbf{a}y] e^{-\mathbf{a}y} \\ \overline{\mathbf{s}}_{yy} &= iQ_f [-\mathbf{a}y] e^{-\mathbf{a}y} \\ \overline{\mathbf{t}}_{xy} &= Q_f [1 - \mathbf{a}y] e^{-\mathbf{a}y} \end{aligned}$$

Discrete Implementation

Since a finite interval is needed for a discrete implementation of the Fourier Transform, we modify the augmented traction to a periodic function.

$$p_f(x) = \begin{cases} p(x) & |x| \leq a, \\ 0 & w \geq |x| > a. \end{cases} \quad (6B.45)$$

$$p_f(x + 2kw) = p(x) \quad k = 1, 2, 3, \dots$$

By St. Venant's principle, if w is large enough, then the subsurface stresses in the contact area will be nearly the same for the traction distributions given by Equation (6B.41) and Equation (6B.45). Using the Discrete Fourier Transform, the augmented traction (with N discrete points) may be written as

$$p_f(x_n) = \frac{1}{2w} \sum_{k=0}^{N-1} P_k e^{\frac{i k \pi x_n}{2w}} \quad (6B.46)$$

The subsurface stresses for each component may be obtained from Table 6B.6 by setting

$$P_f \text{ (or } Q_f) = \frac{P_k}{2w} \quad a = \frac{2pk}{2w}$$

The addition of the stresses for each of the components (similar to the integration in Equation (6B.44)) gives the required subsurface stresses.

Figure 6B.20 shows how this method is implemented. The use of the FFT enables this operation to be done in an extremely efficient manner. Note that the coefficients that determine the stresses are dependent on the depth, y . Hence, they must be determined for each depth where the solution is desired.

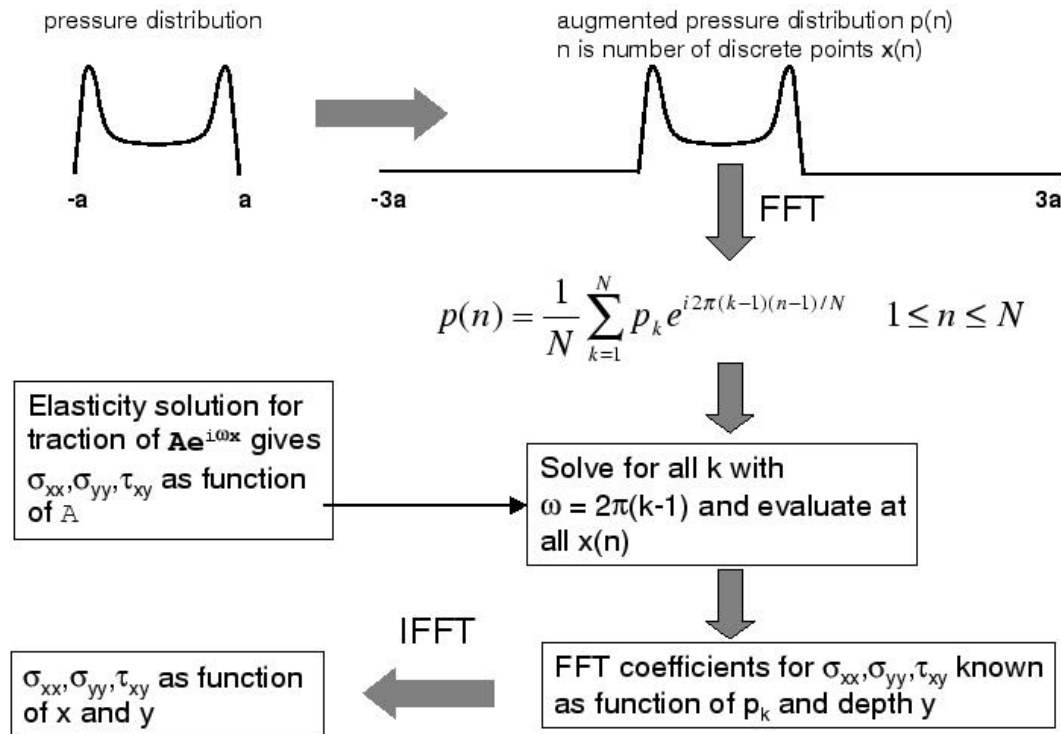


Figure 6B.20. Evaluation of subsurface stresses.

Finite Element Analysis

In order to lend some confidence to the integral equation results, a complementary finite element analysis was also undertaken. All models were built using ABAQUS/STANDARD, which provides special interface elements for use in contact regions where small relative motions exist. The model dimensions and material properties were chosen to match those present in the experiment. The details of the Finite Element (FE) analysis can be found elsewhere in the literature (McVeigh 1999). Figure 6B.21 shows a comparison of surface tractions found from the FE model and from the integral equations. The agreement between the two results is very good.

While the $p(x)$ and $q(x)$ results are interesting, it is actually s_x that is necessary for life predictions. Figure 6B.22 shows these results for both FE loading schemes and for the integral equations. Note that the peak value for the FE experimental loading system can be estimated quite nicely by adding the value of s_0 applied to the specimen to the peak value for the FE Mindlin loading system. This result is of great significance as far as using the integral equations to predict crack nucleation is concerned. This is

not only true at the surface, but also below the surface of the specimen at the trailing edge of contact. This is evident in Figure 6B.23.

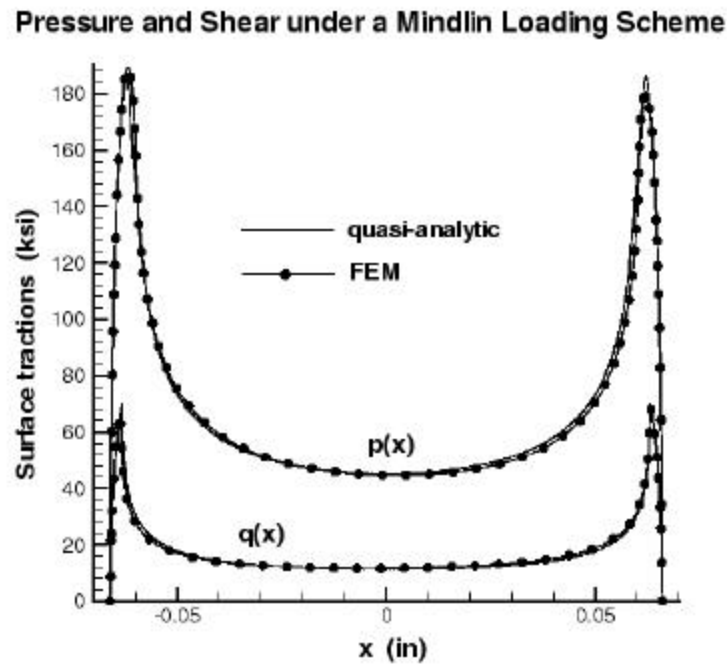


Figure 6B.21. Comparison of surface traction results from the FE model and the integral equation method.

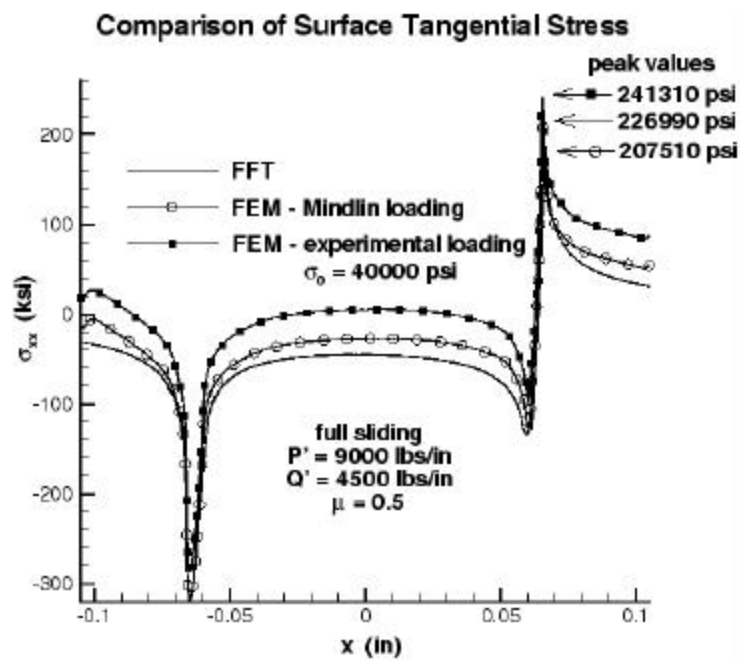


Figure 6B.22. Various results of σ_0 found with different methods.

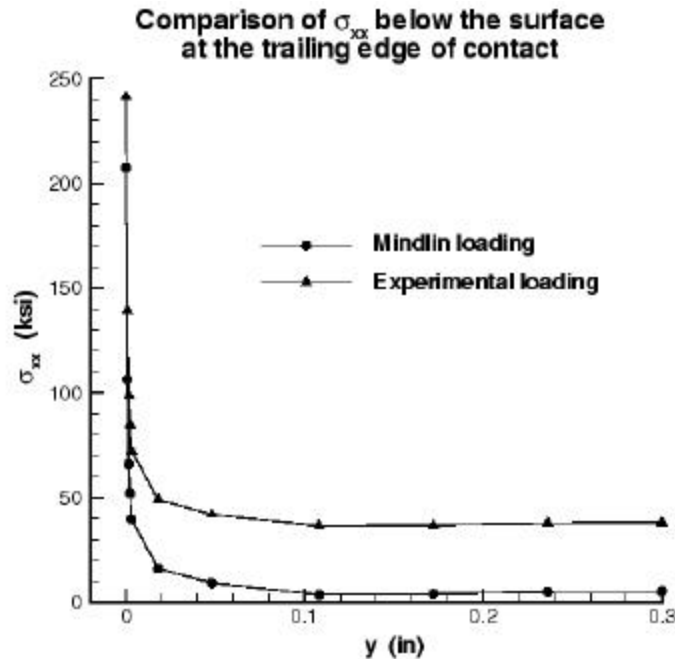


Figure 6B.23. Plot of σ_x below the surface of the specimen, at the trailing edge of contact.

Effect of Crack on Contact Stress

Although the remainder of this section will deal with a cylindrical pad as opposed to a round-edged flat pad, the general principles that will be discussed still apply for both cases. Figure 6B.24 shows how the contact changes once a crack is nucleated. The contact expands and a severe peak is present at the discontinuity. This spreading of the contact zone has caused some experimentalists to conclude that nucleation occurs within the contact instead of at the trailing edge.

A crack was built into the FE mesh at the trailing edge of contact. A crack was also simulated with the integral equation method by introducing a line of dislocations at the trailing edge of contact. This has allowed the stress intensity factors (SIFs) to be approximated. A plot of these SIFs can be seen in Figure 6B.25. Note that the FE and integral equation methods agree quite well again. Also, a plot of pure bulk load, without any contact, was included for comparison. Note how the contact results in a severe increase in the SIFs close to the surface, but that the influence of the contact dies out fairly quickly.

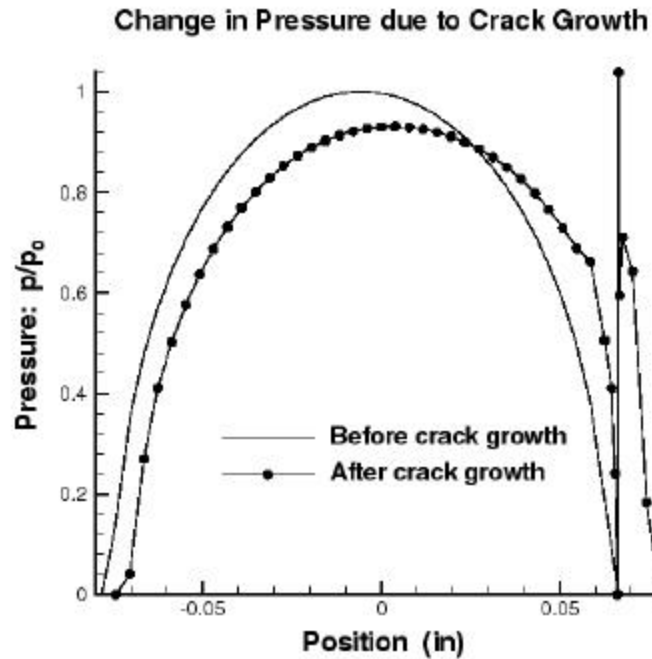


Figure 6B.24. Comparison of pressure profiles for a cracked vs. uncracked specimen.

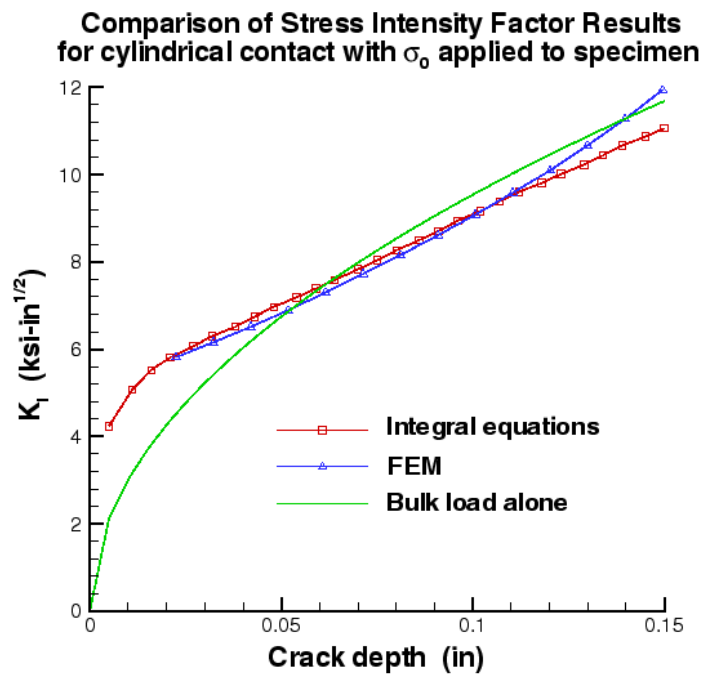


Figure 6B.25. Comparison of SIF results for cylindrical pad on flat contact.

Extension of Integral Equation Approach to Machined Pad Surfaces

The comparisons of the singular integral equation with the FEM and other results engender confidence in the quasi-analytical method. While closed form solutions exist for regular shapes, they break down for arbitrary profiles of the surfaces. The real strength of this formulation, though, lies in its ability to simulate partial slip contacts of surfaces with arbitrary smooth profiles. To illustrate this point, the variations in pressure profiles because of the deviations in the pad profile due to the machining tolerances and due to the wear during the experiments were considered. As reflected in Figure 6B.5, the manufacturing processes led to slight deviations in the machined profile, which was determined with a contacting surface profilometer. Unlike the specific aforementioned closed-form solutions, the present formulation facilitates the determination of the interfacial conditions associated with *actual* pad profiles to be determined from straightforward metrology of the as-machined pad surfaces.

The normal traction induced upon application of a normal line load $P = 9000$ lb/in to the machined pad in Figure 6B.5 in contact with a flat, elastic specimen surface is shown in Figure 6B.26. A surface profile was determined by fitting 1000 discrete data points collected from a Talysurf contacting stylus profilometer and subsequently smoothed with a thirteen-order polynomial fit to ensure continuous contact along $|x| \leq a$. The smoothing prevents the high frequency noise from causing spurious effects. The derivative of the profile is taken from the smoothed profile and interpolation is used when values are required at intermediate values. A total of 16384 sine series terms ($N = 16384$) were used to determine the resulting pressure distribution on a Pentium personal computer. The program takes only a few seconds to run. The pressure distribution resulting from the prescribed surface profile is presented for sake of comparison. As is immediately evident in Figure 6B.26, the local variations in the actual surface geometry from the prescribed profile results in a substantially different pressure distribution. However, when calculating crack-nucleation parameters like maximum stress or strain amplitude, the difference is not as marked. This is because the peak stress parallel to the surface depends on the entire pressure profile and not just on the peak value of the pressure.

It must be noted here that for the experimental loads, no moment was assumed to be present. However, since all the profiles are not symmetric about the center, and

the analysis was run with zero moment, the solution predicted that the pads would rotate so as to provide zero moment.

The shear tractions are similarly determined. Once the surface tractions are known, the subsurface stresses are calculated as detailed earlier. This method was used for all the pads involved in the experiments. Thus, the combination of the metrology and the force measurements during the experiments enable a more accurate characterization of the experimental data for analysis purposes.

Furthermore, the small-amplitude relative motion in the slip zones leads to wear-induced modification of the initial profile, which can be accounted for with the current technique. Figure 6B.6 shows the comparison of the pad profiles before and after an experiment. The profiles were smoothed and analyzed as described earlier. Figure 6B.27 shows the variation in pressure distribution due to the deviations in the pad profiles caused by wear that occurs during the experiment.

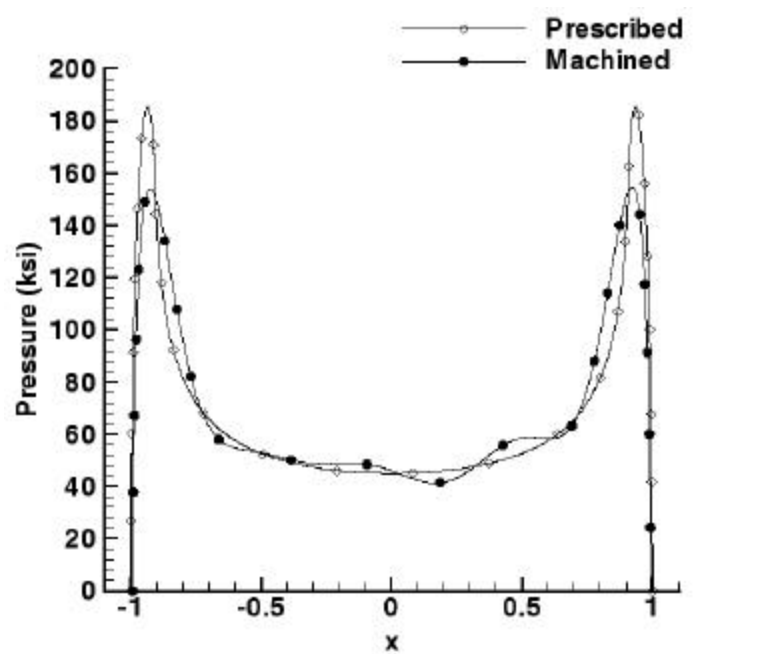


Figure 6B.26. A comparison between the pressure distributions associated with the prescribed and actual fretting pad profiles, as determined by the quasi-analytical solution method.

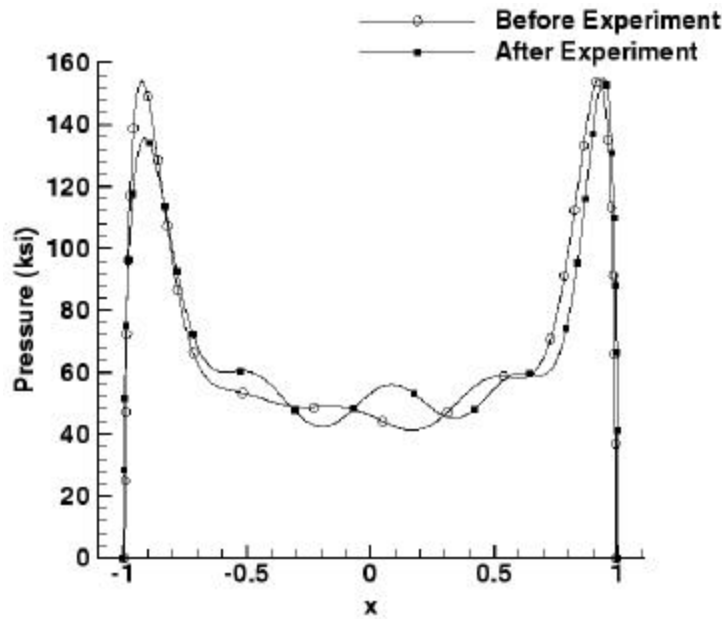


Figure 6B.27. A comparison between the pressure distributions associated with the pad profiles before and after experiment, as determined by the quasi-analytical solution method.

Life Prediction

Choice of Critical Multiaxial Fatigue Parameter

The complexity of fretting adds another level to the already intricate phenomenon of fatigue crack nucleation. While many theories for fretting crack nucleation have been proposed, most of them fall short of quantitative prediction of the cycles to crack nucleation. A detailed analysis of these methods may be found in the literature (Szolwinski & Farris 1996). From the stress analysis, it was clear that the stress state underneath the contact is a highly complex and multiaxial one. For the purposes of fatigue, a multiaxial state of stress is defined by the three principal stresses being non-proportional or by the directions of the principal stresses changing during the loading cycle (Bannantine et al. 1990).

Encouraged by the recent success in using a multiaxial fatigue model for aluminum dogbone specimens (Szolwinski & Farris 1998) as well as in lap joints (Szolwinski et al. 1999), the same approach was taken for life prediction in the Ti-6Al-4V experiments. The critical parameter is the multiaxial parameter, Γ , defined as

$$\Gamma = s_{\max} \frac{\Delta \mathbf{e}}{2} \quad (6B.47)$$

where s_{max} is the normal stress, and $De/2$ is the normal strain amplitude. This critical parameter was evaluated as follows. A program was developed that took the results from the stress analysis and evaluated Γ at every point for all angles (numerically, an increment of 1° was taken for the angle). The crack was then assumed to nucleate at the point where Γ was maximum and the angle was given by the orientation of the plane where Γ was maximum. The critical plane, on which the crack was defined, was perpendicular to this angle.

Normally, this value is assumed to nucleate a crack of a fixed length, usually 0.5 to 1 mm. However, in the present case the stress gradients are so severe that the value of Γ decays rapidly into the bulk of the body. So, the crack nucleation length was taken as 0.004 inch (*100 μm*) and the value of Γ was calculated as the average value over a length of 0.004 inch into the surface from the location of the maximum value of Γ . Note that the choice of *0.004 inch* is arbitrary. Choosing a smaller length would decrease the nucleation life and increase the growth life in both the fretting fatigue and smooth bar fatigue experiments. Note that the maximum value occurred at the trailing edge of the contact and the predicted crack orientation was perpendicular to the applied bulk loading direction.

While the stress analysis provides the effects of the contact tractions, the effect of the bulk stress is not characterized. Prior applications have demonstrated that a good approximation is just to add on the bulk stress. This works particularly well at the trailing edge (McVeigh & Farris 1997). The results from the finite element analysis (Figure 6B.23) show that indeed, the effect of the bulk loading is to add on the magnitude of the bulk stress value at the trailing edge. In the present experiments, the bulk stress values were added on to the contact stresses before estimating Γ . The peak stress in Table 6B.7 includes the bulk stress. This enables all the loading parameters to be accounted for in the analysis.

Baseline Data

Once the critical parameter has been identified, a relationship between this parameter and the nucleation life has to be established. Here lies the lucidity of the multiaxial fatigue approach. The relationship between Γ and the crack nucleation life is given by the uniaxial strain-life curve as determined by standard uniaxial fatigue tests.

For the purpose of this analysis the uniaxial fatigue data was obtained from Bellows , Bain & Sheldon (1998). The relationship between Γ and life may be expressed using a equation that is simply the Smith-Watson-Topper equation for uniaxial fatigue. Thus the constants would be determined from the uniaxial fatigue data. The equation may be expressed as

$$\Gamma = s_{\max} \frac{\Delta e}{2} = \frac{s_f'^2}{2} (2N_i)^{2b} + s_f' e_f' (2N_i)^{b+c} \quad (6B.48)$$

where the fatigue constants s_f' , e_f' , b , and c are evaluated from uniaxial data. N_i is the number of cycles to nucleate a crack of length 0.004 inch. Essentially, the first term is a curve fit of the elastic strain amplitude and the second term corresponds to the plastic strain amplitude. Note that since the plastic strain amplitude was available only for one condition, it was not realistic to estimate c and e_f' from the data. Hence only the elastic part was evaluated. Once again, since only total life is available, a fracture mechanics approach, similar to the way propagation life was estimated for the fretting experiments, was used to estimate the propagation life. The nucleated crack was assumed to be a semi-circular crack of radius 0.004 inch (the fatigue specimens were 0.25 inch diameter). The geometry factor, $f(g)$, for a round specimen of radius r , with a semi-circular crack of radius b , is

$$f(g) = 0.416 \left(\frac{b}{r} \right)^2 - 0.012 \left(\frac{b}{r} \right) + 0.66 \quad (6B.49)$$

Since only the elastic strains were used, the strain-life equation was effectively reduced to

$$\Gamma = \frac{s_f'^2}{2} (2N_i)^{2b} = 1209 (2N_i)^{-0.1165} \quad (6B.50)$$

Prediction of Fretting Crack Nucleation

Table 6B.7 provides the details of the parameters obtained from the stress analysis that are relevant to the crack nucleation. Note that all the critical Γ values were obtained at the trailing edge of contact with the crack angle being perpendicular to the bulk stress. The peak stress is the maximum tensile stress obtained at the edge of contact perpendicular to the normal force. It consists of the peak contact stress plus the bulk stress value. While calculating the values of Γ , the stresses were capped at 110 ksi as a first

approximation to account for plasticity. The Γ value is the mean of value over a distance of 0.004 inch into the bulk. The mean was calculated by obtaining the values of Γ at 20 points over the distance of 0.004 inch, along the direction in which the crack grows, and averaging them. The 20 points were equidistant in vertical direction i.e, perpendicular to the contact interface. Figure 6B.51 shows this data graphically. Note that the 3 σ bounds have also been plotted for clarity.

The relation between Γ and life was obtained using the data from Bellows et al. (1998) for the R-ratio of -1 since locally, at the contact, R-ratio is close to -1 among all the data documented, but it is not exactly -1. The relations were calculated assuming that the plastic strain is negligible. But, as we can see from the values of peak stresses (Table 6B.7), the stresses near the contact region are very high and hence the plastic strains are not negligible, especially in the first few experiments which deviate to a great extent from the curve obtained using the data from Bellows et al. (1998). Thus, the curve fit may not be appropriate in the cases where the contact stress is much higher than the yield strength. Even though the stress decays rapidly into the bulk of the specimen, it is still above yield for a considerable portion of the 0.004 in length. Though an attempt was made to account for plasticity by capping the stresses at 110 ksi, the approach does not seem to be sufficient to capture the effects of plasticity, due to high plastic strains involved. Note that if the plastic strains are available, they may be used in conjunction with the full form of Equation (6B.48) with the appropriate constants. Future work should address this issue. The current method may be thought of as a useful design tool to assist in the a priori estimation of life debit due to fretting damage.

Table 6B.7.

Calculated values of multiaxial parameter Γ , peak stress and the predicted nucleation lives. Estimated lives are nucleation lives obtained by subtracting a propagation life from the observed failure life.

Expt. No.	Expt. Γ (psi)	Peak stress (ksi)	Experimental Total Life (cycles)	Est. Nucleation Life Total life - propagation (cycles)	Nucleation Life Predicted (cycles)	Pred. Γ (psi)
PR02	514	219.7	54744	28294	775	338
PR03	335	196.7	160628	114088	30121	287
PR04	352	221	144242	107992	19900	289
PR05	501	229.2	39947	18097	964	356
PR06	491	211.6	69279	44179	1142	321
PR07	448	209.1	93930	64470	2500	307
PR09	669	252.5	26391	10681	80	378
PR10	310	196.2	386049	329969	59640	254
PR11	238	167.4	337578	200718	579690	269
PR12	296	172.9	161986	74256	87990	302
PR13	159	146.1	1728051	1505191 (no failure)	18264070	<213
PR14	192	155	1000038	834168 (no failure)	3673617	<228
PR16	361	195.9	168637	82717	16166	298
PR17	237	167.9	1000863	864003 (no failure)	587163	<227
PR20	215	186.5	1502266	1338576 (no failure)	1366461	<216
PR22	228	174.9	1285642	1150462	813071	219
PR23	296	191.2	245311	136131	87357	281

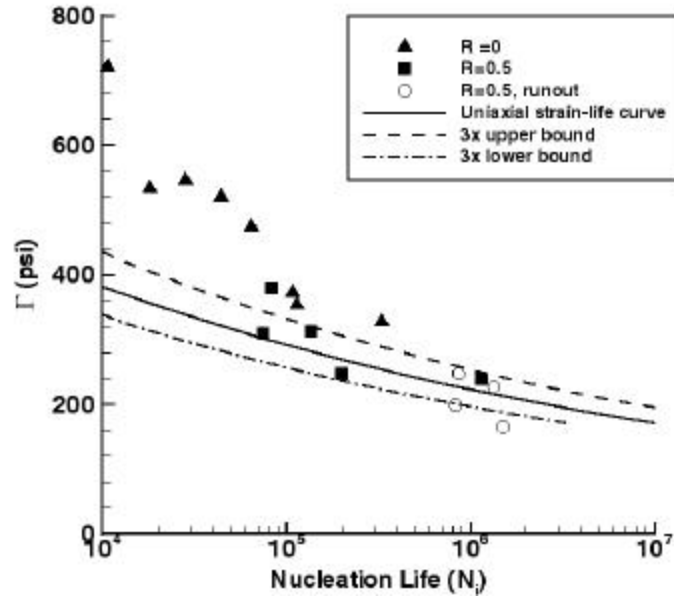


Figure 6B.28. Comparison of experimental nucleation lives (estimated) with predicted values using G as the critical parameter. Uniaxial curve is defined by Equation (6B.50).

Evaluation of Stress Intensity Factors

Due to the resolution limitations and iterative nature of finite elements in the study of cracks, an alternative numerical method is desired for the study of SIFs. Such a method was developed and is based on work done by Hills & Nowell (1994). First, the subsurface stresses under a contact loading scenario are obtained. Then, a distribution of dislocations is introduced along the line of the crack, allowing the crack faces to be traction free. (Note that for the formulation which follows, the coordinate axes are assumed to be oriented as shown in Figure 6B.8).

The governing equation for this case is:

$$N(y) = s_T(y) + \frac{E}{8p(1-\nu^2)} \int_0^b B_x(c) K(y, c) dc \quad (6B.51)$$

where $N(y) = 0$ for the traction free constraint. Note that $s_T(y)$ are the stresses present along the line of the crack before growth begins. b is again the length of the crack. B_x is the density of the distribution of dislocations:

$$B_x(c) = \frac{db_x}{dy}(c) \quad (6B.52)$$

$K(y,c)$ is a generalized Cauchy kernel:

$$K(y,c) = 2 \left[\frac{1}{y-c} - \frac{1}{y+c} - \frac{2c}{(y+c)^2} + \frac{4c^2}{(y+c)^3} \right] \quad (6B.53)$$

The resulting integral equation can be solved by introducing a change of variables, and the stress intensity factors are then easily obtained. Details of this approach may be found in the literature (McVeigh 1999).

Validation of this formulation was done by comparing with the classical problem of a crack in a half-space. The resulting excellent agreement bolsters confidence in the method. Though attention is mostly confined to K_I results in the following discussion, this integral equation method can also be extended in order to predict mode II SIFs. For the same crack geometry, one simply switches to the density of dislocation distribution described by:

$$B_y(c) = \frac{db_y}{dx}(c) \quad (6B.54)$$

Note that τ_T , the shear traction, will appear in place of s_T . Once again, validation was performed and the results were in excellent agreement.

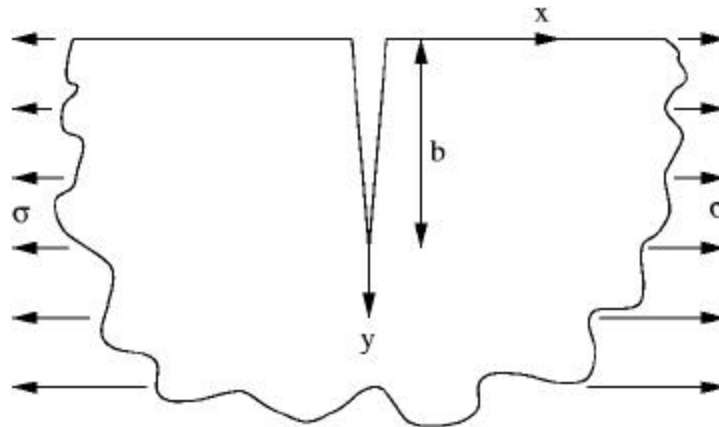


Figure 6B.29. Schematic of loading configuration and crack location. The origin is at the trailing edge of contact.

Fretting SIF Results

Experimental fretting loads were now applied in the integral equations models in order to estimate the SIFs of cracks growing in this situation. A “bulk load alone” curve, without fretting loads, is included in Figure 6B.30 for the sake of comparison. Notice that the main effect of fretting on the SIF occurs very close to the surface for short cracks. If a threshold SIF exists in the region between the “bulk load alone” curve and the fretting fatigue curve, it becomes evident why fretting is so detrimental.

Figure 6B.31 shows the effect of the machining variances from the prescribed pad profile. While the differences are negligible for large crack lengths, they are quite significant near the surface, particularly for K_{II} . Thus, accurate characterization of the pad profile is crucial to the proper understanding of the failure mechanism. Figure 6B.32 shows some results DK_I for a number of experimental conditions. The kinks in some of the curves are due to the crack closure effects that come into picture at some crack depth for some cases. An important observation is that the stress intensity factors are dependent on all the loading conditions and so all relevant loads must be quoted when describing loading configurations.

While both Q' and s_0 are cycled in-phase, P' remains constant, resulting in non-proportional loading effects. K_I is largely produced by s_0 , while K_{II} is thought to be influenced mainly by P' . This would imply that the change in K_{II} should be small since P' is not cycled. However, analysis results show a significant difference between the maximum absolute value minimum. Thus, the true crack growth behavior is governed by mixed-mode non-proportional loading.

This approach was used to adopt an alternative life prediction method based on the Equivalent Initial Flaw Size (EIFS) concept. Experimental lives were used to calculate EIFS for each of the experiments, using the above approach. An average value of the EIFS was then taken and used to predict the lives. The average value of the EIFS was 0.0001104 inch. The comparison of lives predicted from this approach with the experimental lives is presented in Figure 6B.33. This provides an alternative approach to predict lives. Future work should include the use of a 3D EIFS calculation.

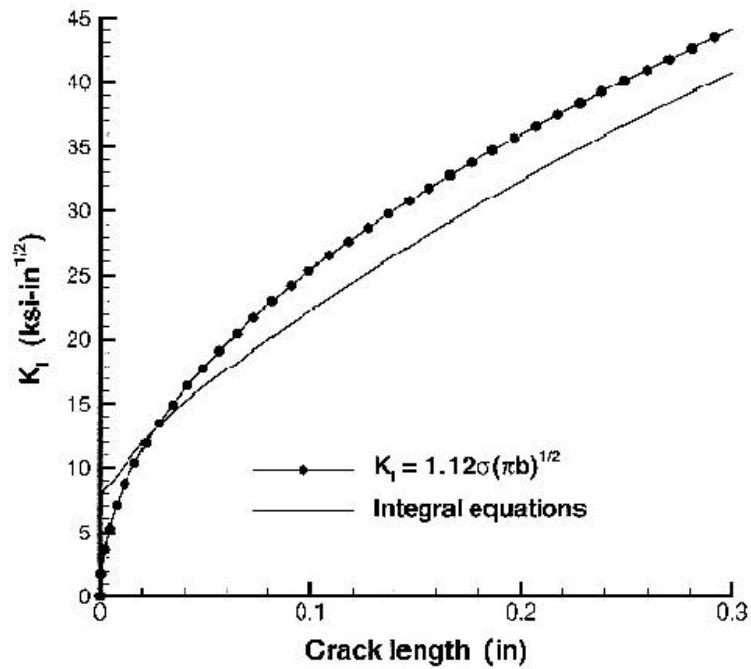


Figure 6B.30. Comparison of stress intensity factors under fretting loads with those for a crack in a half-space. Configuration is from experiment number PR06.

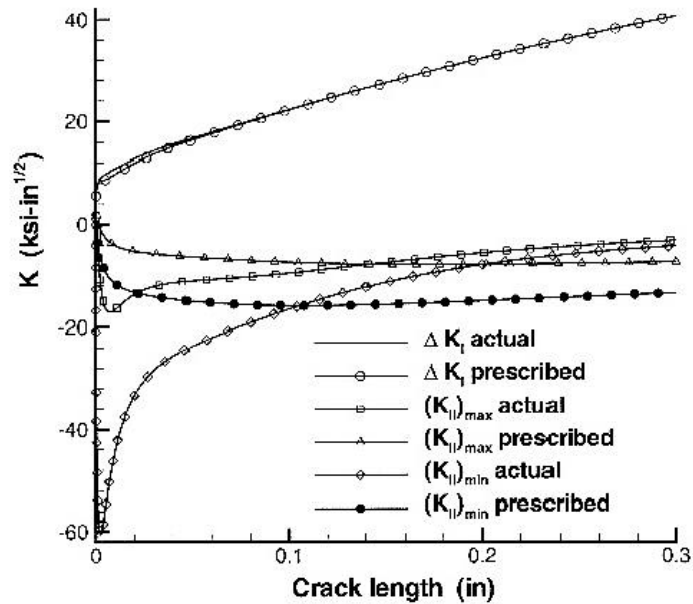


Figure 6B.31. K_I values for actual pad profile as compared to prescribed profile. Configuration is from experiment number PR06.

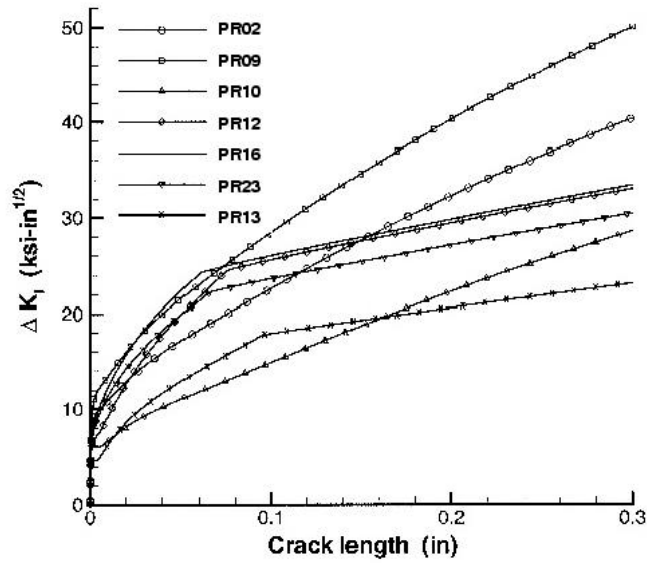


Figure 6B.32. K_I values for various experiments. Loading configurations may be found in Table 6B.1.

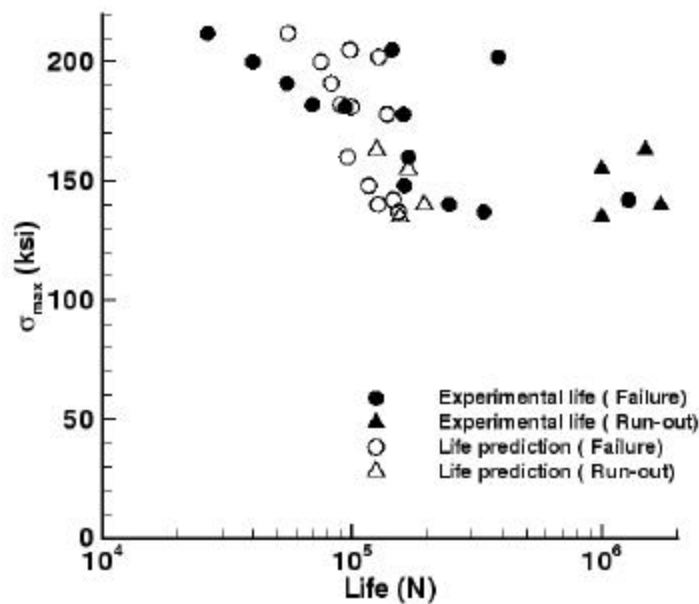


Figure 6B.33. Comparison of lives obtained from EIFS with experimental lives.

Closure

Stress analysis has been combined with fatigue crack nucleation and growth concepts to develop a model that predicts fretting fatigue lives of contacts relevant to blade/disk connections. The predictions are compared to measurements made under

controlled laboratory conditions with some success. While the comparison reveals that the model is capable of success, it also points to further research issues. These include the inelastic nature of the near surface stress field as well as the appropriateness of the crack nucleation model.

References

1. Bannantine, J. A., Comer, J. J. & Handrock, J. L. (1990), *Fundamentals of Metal Fatigue Analysis*, Prentice Hall, Englewood Cliffs, New Jersey.
2. Barber, J. R. (1992), *Elasticity*, Kluwer Academic Publishers, Dordrecht, Netherlands.
3. Bellows, R. S., Bain, K. R. & Sheldon, J. W. (1998), 'Effect of step testing and notches on the endurance limit of Ti-6Al-4V', *Mechanical Behavior of Advanced Materials* 84, 27-31.
4. Ciavarella, M., Hills, D. A. & Monno, G. (1998), 'The influence of rounded edges on indentation by a flat punch', *Proceedings of the Institution of Mechanical Engineers, Part C, Journal of Mechanical Engineering Science* 212(4), 319-328.
5. Hills, D. A. & Nowell, D. (1994), *Mechanics of Fretting Fatigue*, Kluwer Academic Publishers, Dordrecht, Netherlands.
6. McVeigh, P. A. (1999), *Analysis of Fretting Fatigue in Aircraft Structures : Stresses, Stress Intensity Factors and Life Predictions*, PhD. thesis, School of Aeronautics and Astronautics, Purdue University, West Lafayette, IN.
7. McVeigh, P. A. & Farris, T. N. (1997), 'Finite element analysis of', *Journal of Tribology* 119, 797-801.
8. Szolwinski, M. P., Harish, G., Farris, T. N. & Sakagami, T. (1999), 'In-situ measurement of near-surface fretting contact temperatures in an aluminum alloy', *Journal of Tribology*, pp. 11-19.
9. Szolwinski, M. P. & Farris, T. N. (1996), 'Mechanics of fretting fatigue crack nucleation', *Wear* 198, 93-107.
10. Szolwinski, M. P. & Farris, T. N. (1998), 'Observation, analysis and prediction of fretting fatigue in 2024-T351 aluminum alloy', *Wear* 221, 24-36.

Appendix 6C

CHARACTERIZATION OF FRETTING FATIGUE INITIATED CRACKS

**P.J. Golden
A.F. Grandt**



**Purdue University
School of Aeronautics & Astronautics**

**Submitted
August 1999**

Appendix 6C

INTRODUCTION

The objective of this work was to characterize the fatigue cracks in Ti-6Al-4V specimens initiated by fretting fatigue on the Purdue fretting rig. The specimens have a gauge length of approximately 8 inches and a height and width of 0.60 by 0.375 inches with the contact occurring on the 0.375 inch wide sides. The specimens were subjected to contact pressure combined with a remote cyclic load. The contact pressure applied by the pads was nominally the same for each test.

To accomplish the objective several fretting tests were stopped prior to failure for examination. Previous fretting fatigue tests were conducted to failure and these failure lives were used as the basis for choosing an appropriate number of fretting fatigue cycles that would not result in failure. Next, these pre-fretted specimens were subjected to additional cyclic loading without contact pressure, and any existing cracks were allowed to grow. Photographs of the crack nucleation site were taken periodically with a digital camera as the specimen was loaded. This procedure allowed for two observations to be made. First, the growth of the fretting fatigue induced cracks on the surface could be recorded. Second, the pictures were used to trace the fatigue cracks that caused failure, which were easy to see, back to the initial fretting fatigue cracks, which were very difficult to distinguish from the wear scars. Heat tinting and fractography were also used in an attempt to further characterize the fretting cracks.

PROCEDURE

Seven interrupted fretting fatigue specimens have been tested until failure with a four-point bend fixture. Four-point bend was chosen because earlier specimens failed at the welded grip end in tension tests. In fact two fretting fatigue specimens that had a weld failure were used as interrupted tests in the four point bend fixture. The test setup includes an MTS 22 kip servo-hydraulic test machine, four point bend apparatus, a Bausch and Lomb Stereo-zoom 7 microscope, and a Polaroid Digital Microscope Camera. Figure 6C.1 contains a schematic drawing of the loading fixture. A mirror was placed at 45° under the lower contact area that was loaded in tension. It was then possible to use the camera and microscope to photograph the crack nucleation site with

the specimen under load so that the cracks were open. Since the specimen is wide relative to the desired field of view, the microscope was used to image a fraction of the specimen width, and was then traversed across the specimen to obtain a set of photos at each desired cycle. These photos were then merged into a single image of the full specimen width at each cycle count. Paint Shop Pro was used to sharpen and adjust brightness and contrast of each image to allow easier viewing of the desired features. As many photos as would fit were placed on the computer screen at one time to allow changes from picture to picture to be observed. Examples of these pictures are shown in Figure 6C.2. Typically there are 500 to 5000 cycles between pictures.

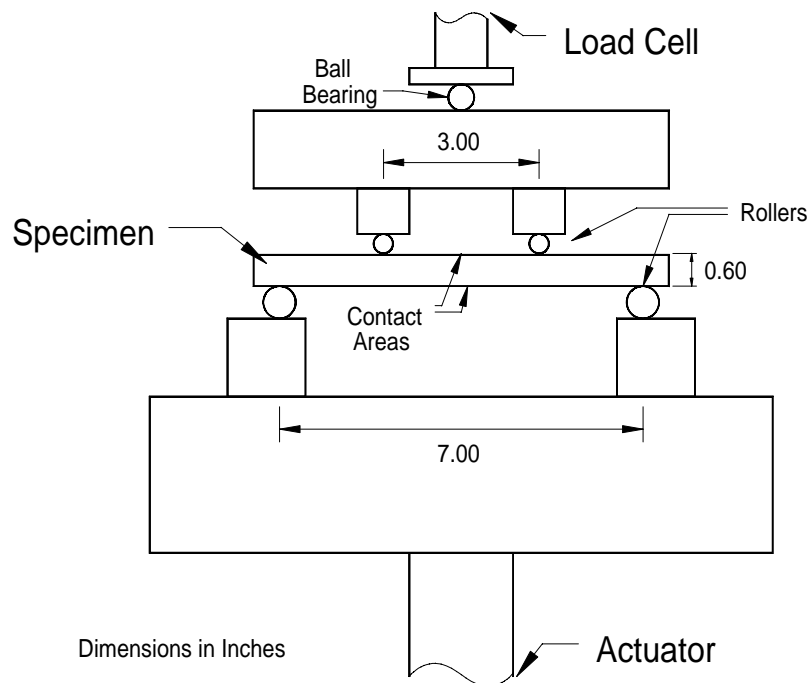


Figure 6C.1. Schematic drawing of the four-point bend setup used to apply cyclic bending to the fretting fatigue specimens.

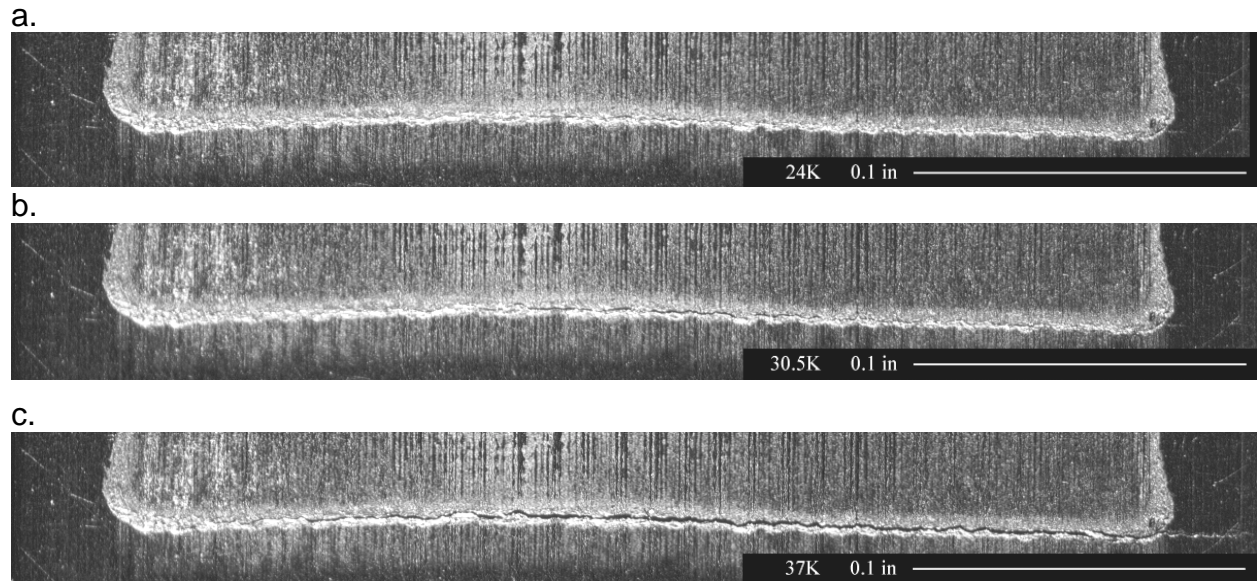


Figure 6C.2. Photographs of a representative specimen at a) 24,000 cycles, b) 30,500 cycles, and c) 37,000 cycles.

Two of the specimens were heated at 343°C for 3 hours in air prior to the four-point bend loading. This resulted in a faint yellowish tint intended to mark the ‘initial’ fretting induced cracks. The purpose was to confirm measurements of the surface length of these ‘initial’ cracks as well as allow measurement of their aspect ratio or depth. Observations of the fracture surfaces were made with a Bausch and Lomb Stereo-zoom 7 microscope.

RESULTS

The results presented include a description of the crack growth of the fretting fatigue cracks subjected to cyclic bending. This includes the size of the fretting fatigue initiated cracks after a number of pre-fret cycles. Fractographs are examined to see if they are consistent with the previously measured fretting fatigue crack distributions. Finally, heat tinting is evaluated for the purpose of marking the fretting fatigue cracks. Table 6C.1 gives a summary of the testing conducted.

Table 6C.1
Summary of the Four-Point Bend Tests

Name	Pre-Fretting σ_{\max} (ksi)	Pre-Fretting Cycles	4-Pt-Bend σ_{\max} (ksi)	4-Pt-Bend Cycles	Comments
PR14	39	1,000,000	80	17,859	No Data
PR17	42	1,000,000	80	135,399	19 sets of photos
PR18*	46	31,875	90	19,809	No Data
PR19*	46	86,501	80	79,159	12 sets of photos
PR24	46	90,000	80	41,577	39 sets of photos
PR25	50	60,000	80	93,844	20 sets of photos
PR26	50	60,000	80	226,342	26 sets of photos; Heat tinted
PR27	42	1,000,000	80	125,856	28 sets of photos; Heat tinted

*These specimens failed at the welded grip in the fretting rig.

Crack Tip Growth

Initial surface crack length and positions were recorded from the photographs taken during the fatigue tests. Specimens PR14 and PR18 provided no useful initial crack or crack growth data. Table 6C.2 lists the surface length and position of the initial fretting induced cracks in each specimen. The position of the crack is measured from the left edge of the specimen to left crack tip as seen in the photographs. There is a high degree of confidence in the existence of the cracks listed and the accuracy of their measurements. It is likely, however, that more cracks existed that were too small to be observed with the techniques used here.

Crack tip positions were recorded for each cycle count and used to create a plot of crack tip position versus cycles. This analysis has been completed for PR17, PR19, PR24, PR25, PR26, and PR27. Figures 6C.3 through 6C.8 are plots of the crack tip positions for the six specimens respectively. The dark lines at a cycle count of zero represent what is thought to be the 'initial' fretting fatigue crack. The data points represent the crack tip position at a given cycle count. Crack growth is represented by motion of the left or right crack tip. Coalescence of neighboring cracks is indicated by the solid line connecting the two respective crack tips. In Specimen PR17 four fretting

fatigue cracks have been found with confidence. When subjected to cyclic bending, Figure 6C.3 shows that these cracks began to grow and link up after about 80,000 cycles until a large corner crack was formed. PR19 appeared to have at least five initial fretting fatigue cracks, however, crack growth and coalescence were not captured in the photographs. PR24 appeared to have many initial cracks that grew and linked up primarily from the large surface crack near the center. (As summarized in Table 6C.2, this specimen contained 15 cracks with surface lengths ranging between 0.001 and 0.042 inch.) PR25 also appears to have 15 initial cracks, ranging in length from 0.007 to 0.018 inch. These grew and linked up into a larger corner crack that eventually caused failure. Although PR26 also has many apparent initial cracks, some did not grow by cyclic bending. Note in Figure 6C.9 for example, that the larger corner crack did not link-up with the other initial fretting cracks (marked by arrows). The dark lines at zero cycles indicate the cracks are bypassed and did not grow. Finally, PR27 had many initial cracks that appeared to simultaneously grow and coalesce into a through-the-thickness crack.

Table 6C.2
Initial Fretting Fatigue Induced Surface Crack Size and Position as Determined
from Surface Photographs*

	PR17		PR19		PR24		PR25		PR26		PR27	
#	a (in)	x (in)	a (in)	x (in)	a (in)	x (in)	a (in)	x (in)	a (in)	x (in)	a (in)	x (in)
1	0.005	0.186	0.057	0.017	0.006	0.030	0.004	0.017	0.083	0.020	0.008	0.016
2	0.013	0.228	0.014	0.096	0.013	0.044	0.014	0.021	0.009	0.105	0.006	0.041
3	0.006	0.268	0.023	0.154	0.004	0.059	0.018	0.042	0.024	0.125	0.004	0.050
4	0.015	0.297	0.021	0.214	0.012	0.076	0.010	0.063	0.013	0.176	0.015	0.087
5			0.010	0.314	0.012	0.098	0.007	0.078	0.011	0.196	0.053	0.111
6					0.015	0.120	0.015	0.088	0.015	0.214	0.009	0.169
7					0.006	0.156	0.013	0.106	0.006	0.238	0.029	0.179
8					0.042	0.167	0.017	0.128	0.012	0.302	0.027	0.227
9					0.010	0.212	0.004	0.150	0.027	0.328	0.006	0.255
10					0.006	0.224	0.014	0.161			0.014	0.276
11					0.001	0.255	0.017	0.193			0.008	0.295
12					0.005	0.285	0.008	0.224			0.008	0.305
13					0.009	0.300	0.017	0.248			0.006	0.333
14					0.005	0.319	0.007	0.289			0.005	0.343
15					0.009	0.341	0.009	0.343				

*Crack size "a" is the total crack length measured on the specimen surface, and crack position "x" is the distance the left hand crack tip is from the left side of the specimen.

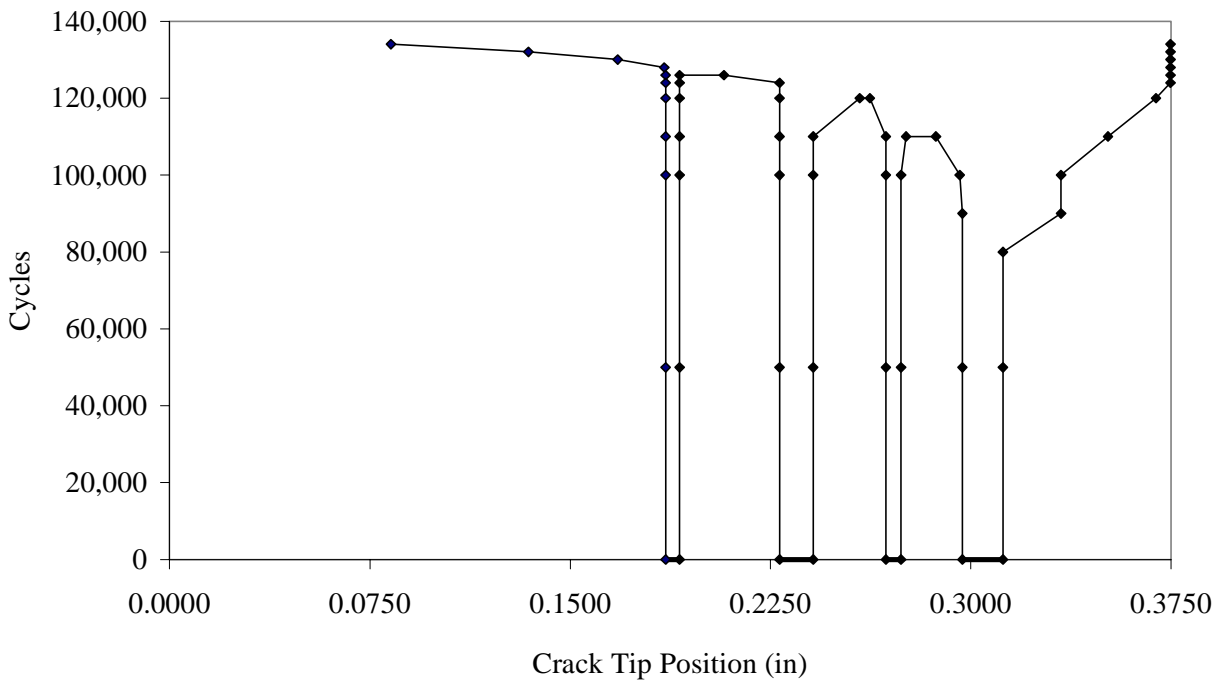


Figure 6C.3. Growth of fretting fatigue initiated cracks on Specimen PR17.

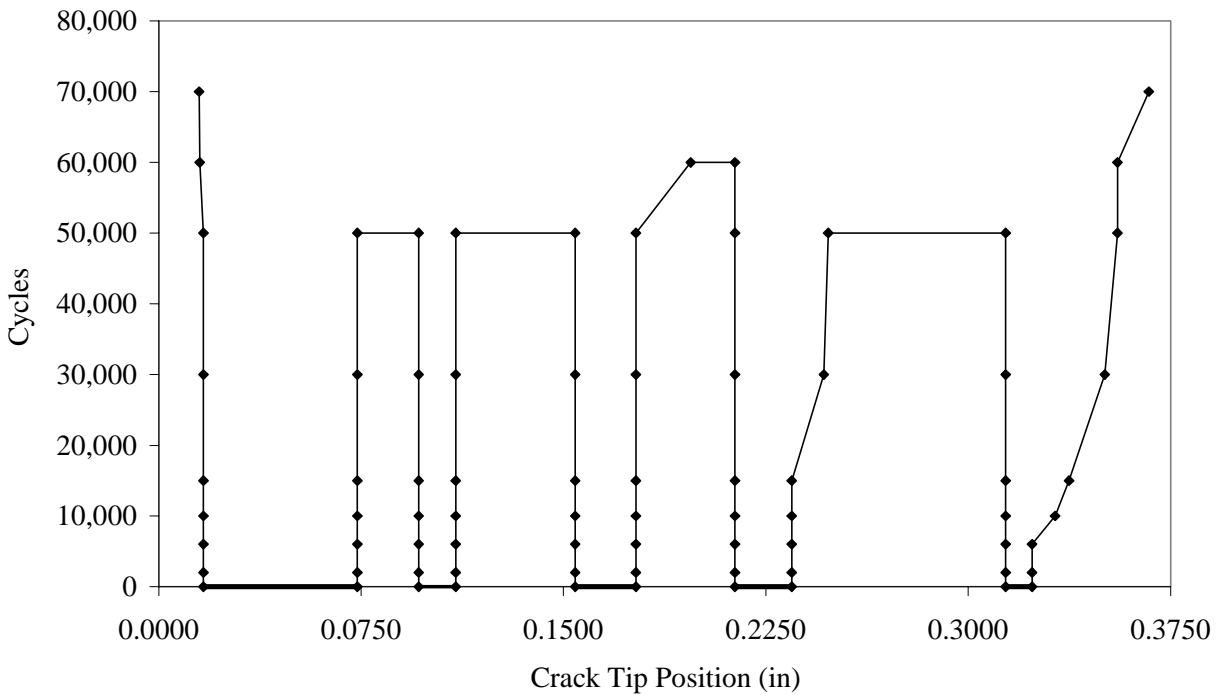


Figure 6C.4. Growth of fretting fatigue initiated cracks on Specimen PR19.

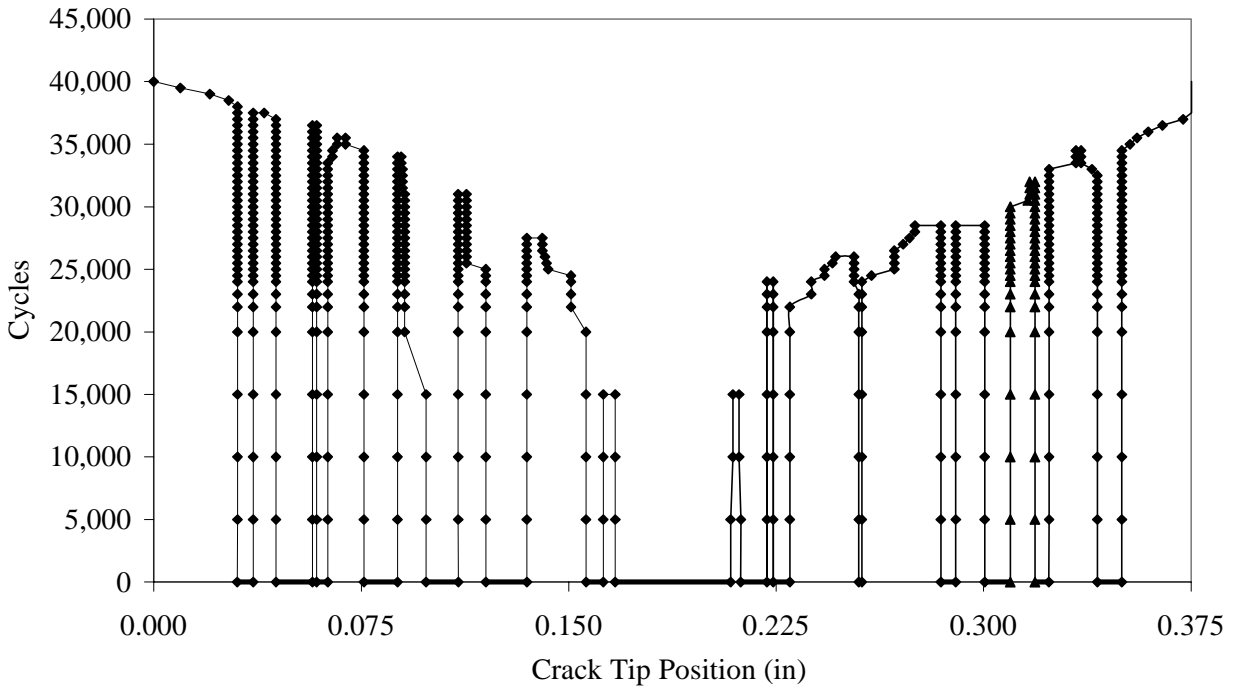


Figure 6C.5. Growth of fretting fatigue initiated cracks on Specimen PR24.

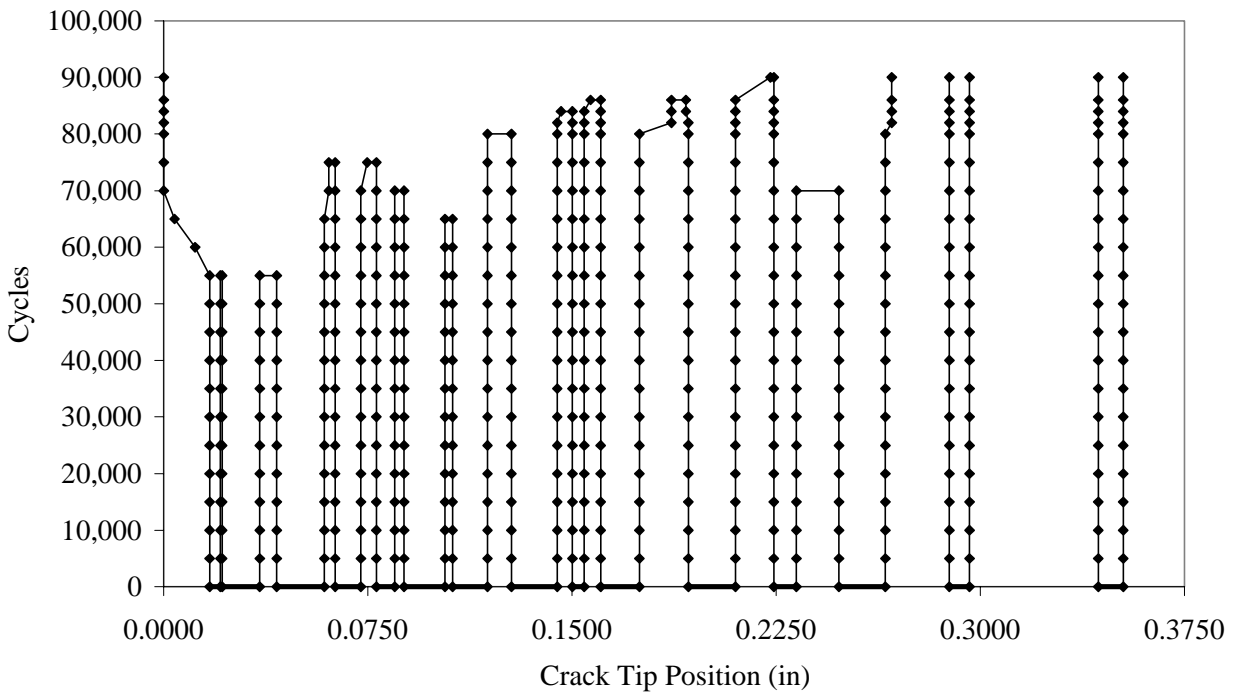


Figure 6C.6. Growth of fretting fatigue initiated cracks on Specimen PR25.

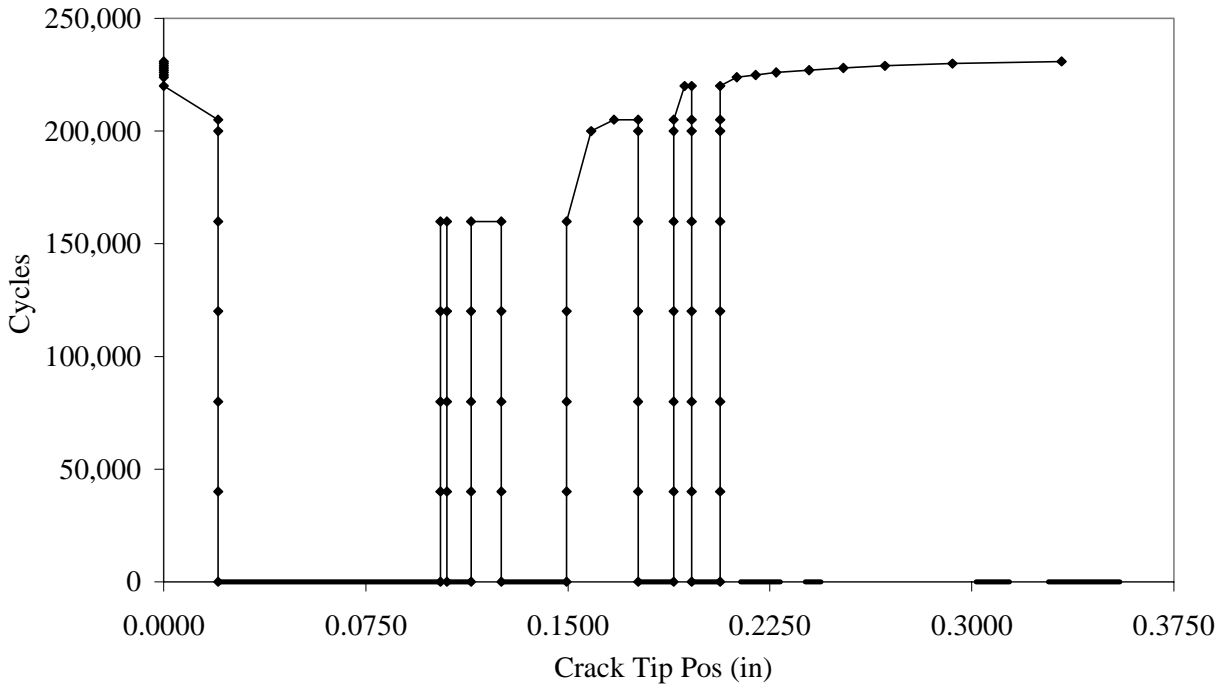
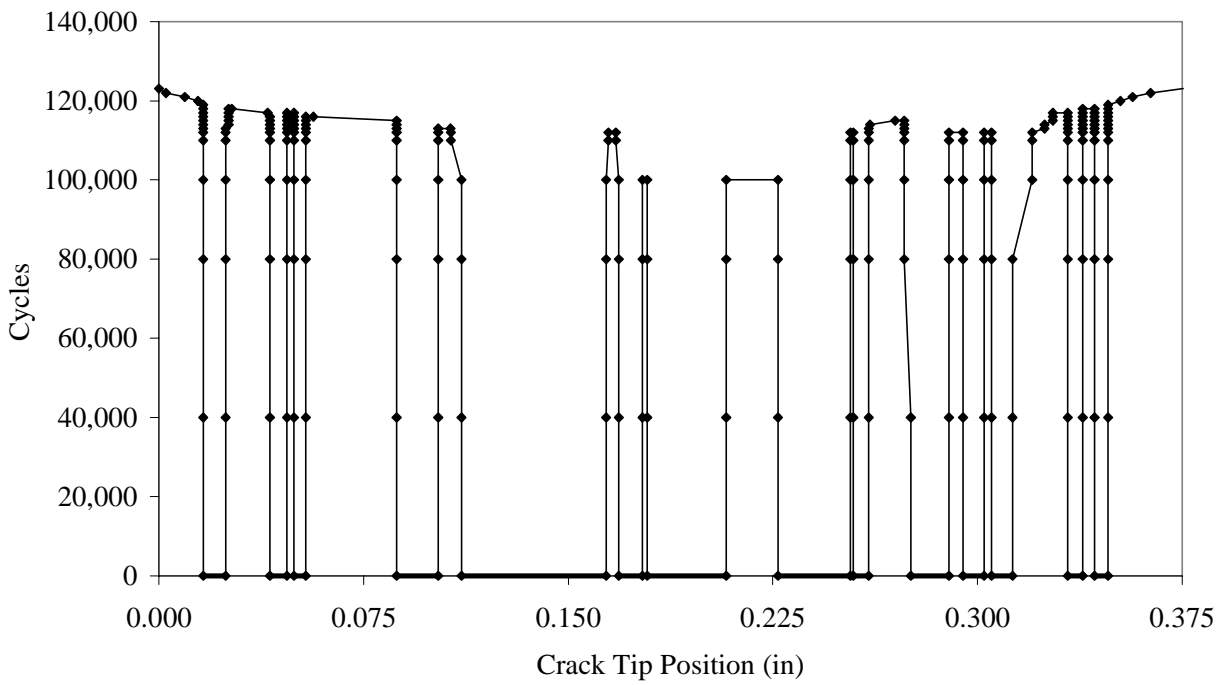


Figure 6C.7. Growth of fretting fatigue initiated cracks on Specimen PR26.



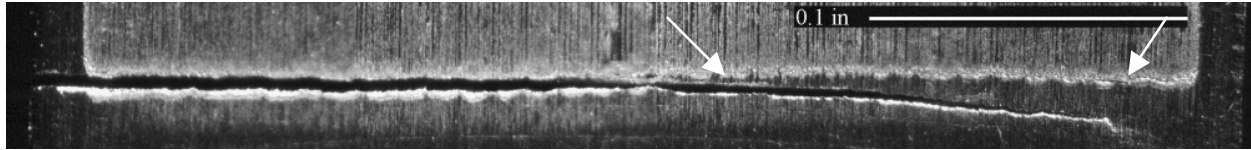


Figure 6C.9. Photo of PR26 showing large corner crack growing away from fretting nucleation site.

Fractography

The fracture surfaces of the specimens with crack growth data have been examined and photographed. Figures 6C.10 through 6C.15 show fractographs of specimens PR14, PR17, PR18, PR19, PR24, and PR25 respectively. The bending stresses were normal to the surface shown and the bottom edge experienced the maximum tensile bending stress. All crack growth was mode I. The size of the initial fretting cracks that ultimately caused failure cannot be clearly resolved from the fractographs, although the crack location is consistent with the observations recorded in Figures 6C.8. The initial crack plane appears to be perpendicular to the length direction of the specimen (same as the subsequent crack growth). This was determined by examining the fracture surfaces from many directions including on edge.

The crack growth of PR17 seems to initiate from a crack on the left side (marked by arrow) as seen in Figure 6C.10, and is consistent with Figure 6C.3 (orientation is reversed). Although not as clear, the fractograph of PR19 in Figure 6C.11 is also consistent with Figure 6C.4 (orientation is consistent) since both indicate crack growth from different locations across the width. Similarly, the fractograph of PR24 in Figure 6C.12 seems to show initial cracks across the width as indicated in Figure 6C.5 (orientation is consistent). Additionally, the crack growth appears to start in the center and move to the edges as was observed. The fractograph of PR25 shows growth of an initial crack on the far right side (marked by arrow) with only small features across the rest of the width. This is fairly consistent with the dense cracking on the left side of Figure 6C.6 (orientation reversed). The PR26 fractograph shows signs of crack growth from several initial cracks across the width of the specimen. This indicates that perhaps a second row of initial cracks existed on the right side of the specimen where the crack grew away from the expected path (see Figure 6C.9), although no direct observations of such cracks were made. Finally, the PR27 fractograph indicates crack

growth started primarily on the right side (marked by arrow), which is fairly consistent with the crack tip position plot of Figure 6C.8.

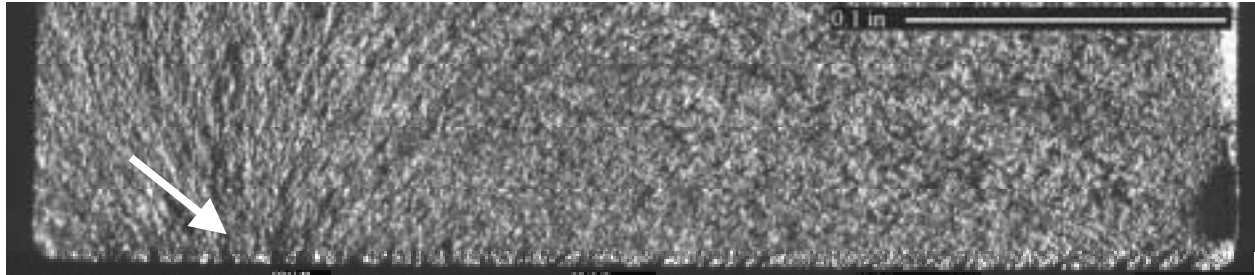


Figure 6C.10. Fractograph of PR17.

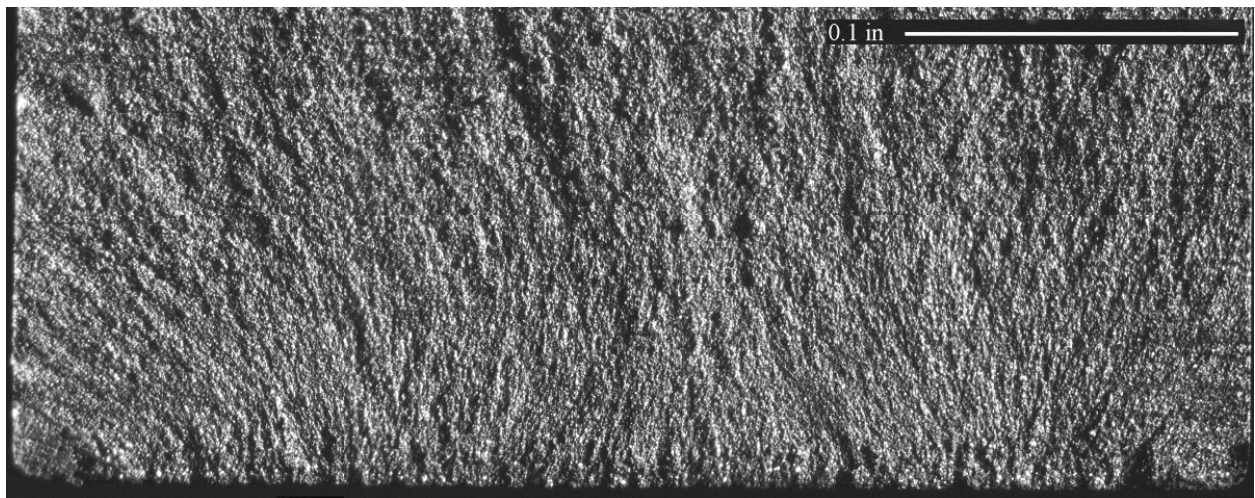


Figure 6C.11. Fractograph of PR19.

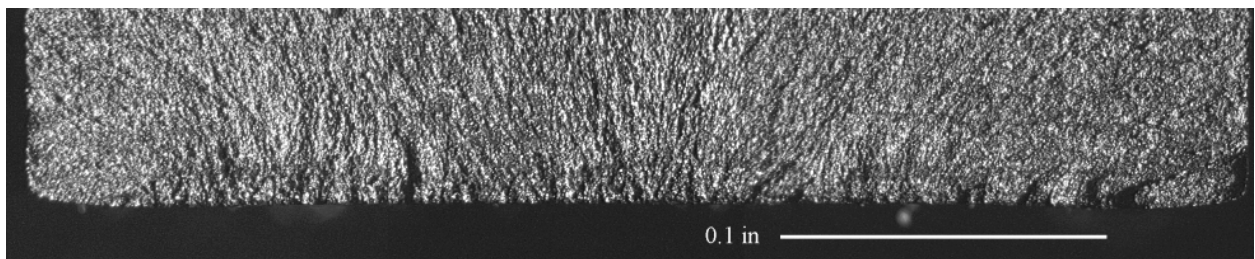


Figure 6C.12. Fractograph of PR24.

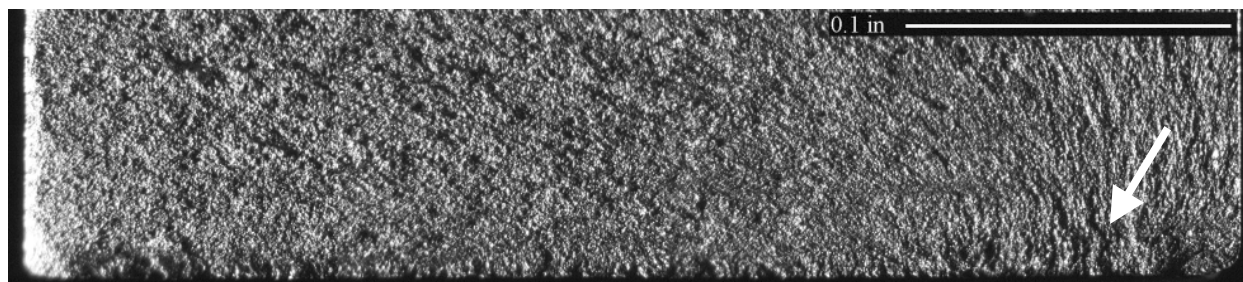


Figure 6C.13. Fractograph of PR25.

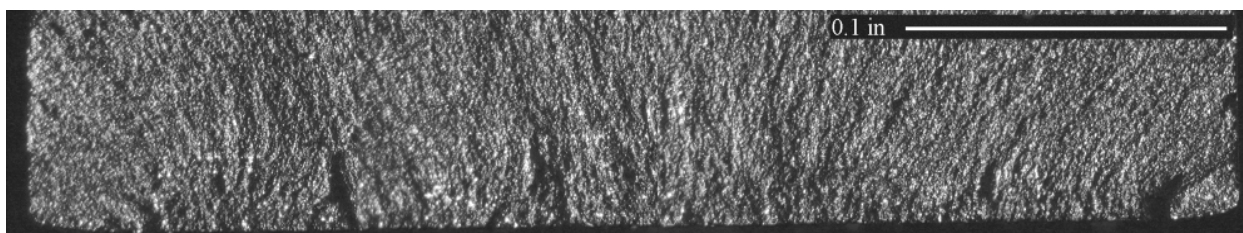


Figure 6C.14. Fractograph of PR26.

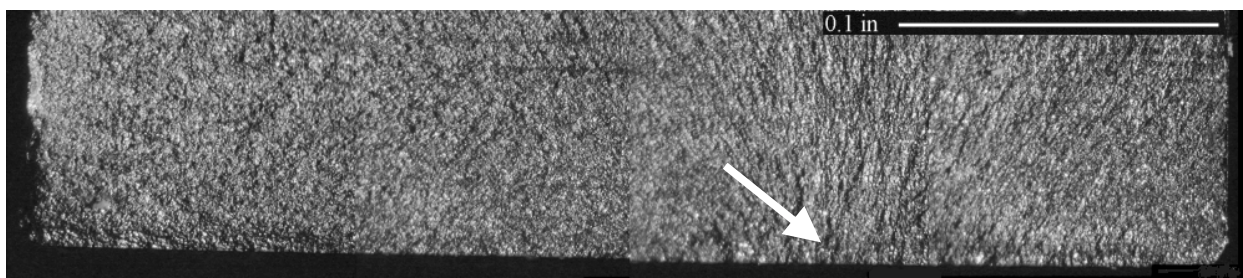


Figure 6C.15. Fractograph of PR27.

Heat Tinting

Specimens PR26 and PR27 were heated to 343°C (650°F) for 3 hours in an attempt to highlight the initial fretting fatigue cracks on the fracture surface. Examination of the fracture surface shows that the heat tinting was either not successful at marking the fretting fatigue cracks or it was too faint to be distinguished from the surrounding surfaces. Initially a yellowish tint was thought to exist about 0.001 to 0.002 inches deep across much of the width of the fracture surface of PR26. This would indicate that the initial fretting fatigue cracking was very shallow and spanned most of the width. It was then noticed, however, that much of the fracture surface of PR26 was not formed from the expected fretting initiated cracks. As noted earlier, during cyclic bending a large corner crack formed but did not follow the expected crack growth path (see Figure A.3.7).

This showed that the yellow tint seen on the fracture surface was not necessarily due to the heat tinting. For future work a darker heat tinting may be better.

SUMMARY AND CONCLUSIONS

Several conclusions can be made from this investigation of the fretting fatigue initiated cracks in Ti-6-4 specimens.

1. The interrupted fretting fatigue tests resulted in specimens with multiple small, shallow surface cracks located at the 'trailing edge' of the contact area, which was the location of the maximum tensile stress.
2. With contact loading removed and remote stresses increased these cracks coalesced and grew to failure. This growth was recorded and plotted for six of the specimens.
3. Heat tinting was used on two specimens in an attempt to mark the fretting fatigue initiated cracks before additional loading was applied. The results were inconclusive but they possibly showed that the depth of these shallow surface cracks was about 0.002 inches.
4. The distributions of the fretting fatigue initiated crack sizes and positions were recorded for six specimens tested under three different conditions. The results were qualitatively verified with fractography of the failed specimens.
5. The angle of the fretting fatigue initiated cracks appeared to be perpendicular to the length of the specimen. This was the same as the subsequent mode I crack growth due to bending without contact stress.

Appendix 6D

SIMULTANEOUS FRETTING AND FATIGUE OF Ti-6Al-4V ON Ti-6Al-4V

Donald L. Anton



United Technologies Research Center

**Submitted
June 1999**

Appendix 6D

ABSTRACT

A new state-of-the-art fretting fatigue testing facility, incorporating independent control of bulk specimen stress, fretting contact stress and slip distance has been developed at UTRC. This equipment has been used to study the effects of fretting contact stress and slip distance on fatigue resistance of forged Ti-6Al-4V in the α/β condition. A fretting/fatigue knock down factor (KDF) of 67% was measured. Serial section analysis was performed on representative fretting scars cycled to failure and at intervals prior to failure. Optical and electron microscopy were utilized to characterize the fretting scar surface with regard to surface and penetrating cracks, debris type, structure, location and chemistry and metal damage adjacent to the fretting contact surface. Cracks did not develop until after 10% of fretting life had been expended when the fretting scar had shown full damage characterized by metal transfer and third body debris across the entire fretting scar area. Dynamic coefficient of friction and energy of fretting measurements were made during the course of testing. The coefficient of friction increased from 0.25 to 0.65 within the first 1000 cycles after which saturation occurred. The energy of fretting similarly decreased rapidly from a high to a low saturation level, driven primarily by the increasing coefficient of friction. A two dimensional elastic-plastic finite element model of the specimen and the fretting contact material used in the test program has been developed. The analysis using this model has determined stress-strain behavior in the contact region along with a numerical assessment of slip amplitude. Three models predicting fretting fatigue crack nucleation have been studied all of which lead to reasonable predictions of fretting crack nucleation life.

INTRODUCTION

Titanium alloys and especially Ti-6Al-4V are used extensively in aerospace structural applications where maximum temperature requirements are below 400°C, including rotorcraft dynamic component applications. The majority of these applications require mechanical joining to other structural members, also typically Ti-6-4. Where these joints interfaces are subjected to vibratory loading, they are potentially susceptible to fretting fatigue mechanisms. Many studies have shown previously that titanium alloys are

particularly susceptible to fretting fatigue. Design factors need to be taken into account when such jointed structures are used. The typical high-cycle fatigue strength reduction for fretting fatigue is 50% [6D.1]. That is, the stresses must be reduced by 50% in the region susceptible to fretting fatigue, as compared to open section areas, in order to insure that the component will not fail prematurely due to fretting fatigue. This is usually accomplished through enlarging part dimensions and thus reducing somewhat the high strength to density benefits titanium alloys possess. This reduction in fatigue allowable strength is typically known as the fretting fatigue Knock Down Factor, KDF.

The mechanisms of fretting fatigue surface degradation under spherical contact in titanium alloys as deduced from friction log plots are (i) surface oxide elimination, (ii) metal to metal contact, (iii) debris generation and (iv) stable debris layer [6D.2]. Microscopic investigations of the fretted surfaces revealed the debris to consist largely of titanium oxide (rutile TiO_2) with fragments of unoxidized metal [6D.3]. The accumulation of wear debris partially separates the metal surfaces causing wear to intensify in the remaining areas of metal contact, leading to the formation of pits. Failure is associated with the formation of ridges on the specimen surface which developed into piles of platelets as the fretting action continued. These ridges also tended to trap the wear debris [6D.4]. Crack nucleation occurred at the boundary of the fretting wear damage area. This is the site of the fretting stick on each cycle, and thus the region of maximum surface shear.

A fretting fatigue map under spherical contact conditions has been defined for Ti-Al-4V having regions of (i) no degradation, (ii) cracking and (iii) particle detachment [6D.4], roughly correlating to the stick/slip and gross slip defined by Vingsbo and Söderberg [6D.5]. In the region of zero to 50 μm slip, slip amplitude was found to have a much greater influence on fretting mechanism than contact stress.

In order to achieve higher reliable and lighter weight aircraft, design methodologies must be developed to better predict fretting wear and its associated debt on fatigue properties. This debt can be defined as the summation of contact stresses and surface degradation such that:

$$D_{Sff} = D_{Sc} + D_{Sc} K_F \quad (6D.1)$$

where s_c is the maximum damaging complex triaxial stress resulting from contact, K_f is the stress concentration factor resultant from the surface damage due to fretting and s_{ff} is the total fretting fatigue stress which acts to nucleate a crack. The goal of this study is to elucidate factors affecting both s_c and K_f in the fretting fatigue of Ti-6Al-4V.

Utilizing a new fretting fatigue testing apparatus [6D.6] which incorporates independent control of applied stress and slip amplitude, this study is intended to produce a baseline of simultaneous fretting and fatigue (fretting/fatigue) data for a representative gas turbine engine contact stress state. The materials couple of interest is Ti-6Al-4V in the **ab** heat treated condition in contact with itself with no surface conditioning. In addition to testing specimens to failure, a number of interrupted tests were performed to monitor surface degradation during fretting/fatigue. Comparisons are made to another testing technique, fretting followed by fatigue (fretting+fatigue), utilized by General Electric Aircraft Engines Co., GEAE. This experimental work was backed up by a modeling effort utilizing FEM to determine near surface stress state resulting from contact and sliding. The modeled data is combined with known fretting fatigue and contact models to predict fretting fatigue cycle lives. By obtaining empirical derivation of fretting fatigue lives, and modeled predictions, it is attempted to define a methodology by which designers can better accommodate the knock down factor associated with fretting fatigue.

EXPERIMENTAL PROCEDURES

Test Equipment

The equipment used in this study, and its functionality have been described elsewhere [6D.6], and will only be reviewed here for clarity. Simultaneous fretting/fatigue was carried out on a specially designed co-axial servo hydraulic testing machine modified to independently control axial stress and slip amplitude. By use of a capacitance displacement gage, the fretting pin carrier which applies hydraulically loaded pins against the fatigue specimen, is moved via computer control to the prescribed distance. Control is maintained up to a cyclic frequency of 10 to 60 Hz depending on specimen compliance and coefficient of friction.

Material

Ti-6Al-4V¹ forgings were received from UDRI and used as base material for all of the testing reported on here. The alloy was double VAR melted into 2.5 inch diameter bar stock produced in accordance with AMS 4928 in mill annealed condition, 1300°F/2Hr/AC. The bars were preheat at 1720°F ($\pm 20^\circ\text{F}$) for minimum of 30 minutes and solution heat treatment at 1710°F ($\pm 25^\circ\text{F}$) for 75 min/fan air cool. The mill anneal was performed at 1300°F ($\pm 25^\circ\text{F}$) in vacuum for 2 hours followed by an argon fan cool. This resultant alloy was in the α/β mill anneal state with approximately 66% alpha phase and 34% transformed β in cells approximately 0.00008 inch (2 μm) in size having a yield stress of 134.9 ksi (930 MPa), an ultimate stress of 141.8 ksi (978 MPa) and an elastic modulus of 17.1 Msi (118 GPa).

Test Procedures

Simultaneous Fretting/Fatigue

The fretting fatigue specimen had a gage section 1 inch (25.4mm) in length with a rectangular cross section of 0.360 x 0.280 inch (9.14 x 7.12mm). Gripping was achieved through precision threads at both ends and alignment maintained with precision ground annulus rings and ends (see Figure 6D.1). The fretting contact geometry was a 0.040 inch (1.016mm) flat contact extending the short width of the specimen of the fretting specimen (see Figure 6D.2).

Fretting fatigue tests were conducted at various stress amplitudes, Ds_a , ranging from 14 – 36ksi (100-250MPa) maintaining a constant R ratio of 0.5, a contact stress, S_f , of 29ksi (200MPa) and a command slip amplitude of 0.001 inch (25 μm). Testing was conducted under ambient laboratory conditions at a test frequency of 20Hz. During the course of testing both the coefficient of friction and energy of fretting were recorded continuously. Tests were conducted to specimen failure and the cycles to failure recorded. After test termination profilometry was performed on both the pins and fretting scars. Optical and SEM documentation made of fretting scars and fracture surfaces and a serial section analysis performed

¹ All compositions given in atomic per cent

Interrupted Fretting Fatigue

Once an S-N curve was determined, one stress amplitude was chosen for interrupted testing, 21.75ksi (150MPa) which led to failures in 300,000 cycles. Tests were conducted at 10, 1, 0.1, 0.01 and 0.001% of this cycle life (30,000, 3,000, 300, 30 and 3 cycles). To reduce the number of fatigue specimens required for this testing, specimens tested to 3,000 and 30 cycles were tested on the same specimen with the larger cycle count performed first and the fretting pad and contact location changed. This test sequence was repeated for 300 and 3 cycle testing. After testing, profilometry was performed on both the pins and specimens, and a serial section analysis performed on the fretting fatigue specimens scar with both optical and SEM microscopy performed to evaluate surface damage.

Fretting+Fatigue

Due to the nature of the control algorithm used in this test system, true fretting with no fatigue could not be performed within the time and budget constraints of this program. In order for the fretting action to be performed, a nominal fatigue load needs to be applied to the specimen. To perform this nominal fatigue both ends of the fatigue specimen need to be gripped. This results in both a non-reacted and reacted fatigue load resultant from the fretting loads applied.

Fretting+Fatigue testing was completed by inserting the specimen into both the upper and lower grips of the machine. Fretting was performed using a nominal cyclic command fatigue stress, Ds_a , of 150 psi (1 KPa) at $R=0.25$. A command slip amplitude, δ , of 0.001 inch (25 μ m) was applied at a contact stress, $\sigma_f = 29$ ksi (200MPa). The number of applied fretting cycles was varied to duplicate the number of fretting/fatigue cycles obtained experimentally for a given applied fatigue load, Ds_a (see Figure 6D 3). In this way, a plot of Ds_a vs N_f is representative of the number of fretting cycles to failure. Cycles to failure were recorded.

FEM Modeling

A two dimensional finite element model was constructed of the fretting fatigue contact utilizing a variable mesh size with minimum mesh occurring below the contact and having a size of 0.0005 inch (12.5 μ m). The contact model was run under ANSYS using elastic plastic conditions for both pin and substrate with the assumption of plane stress conditions. The fretting action was broken into 20 individual time steps representative of the simultaneous fatigue stress and fretting sliding on the specimen. The calculation stress was made at each time step and saved in a matrix for later analysis. The contact algorithm required a coefficient of friction, COF, which was obtained experimentally and input. It will be shown later that the COF rises from an initial condition and saturates after ~1000 cycles, the saturated COF was used for modeling, ~0.65 in this case.

RESULTS

Fretting/Fatigue Knock Down

The tabular results of the fretting fatigue tests conducted here are given in Table 6D.1 and graphically represented in Figure 6D.3. The open section data given in this figure is from other testing conducted under the High Cycle Fatigue Contract [6D.7].

A term commonly used in industrial design when referring to the fretting fatigue debt is the Knock Down Factor, KDF. This term is defined as:

$$KDF^{N_f} = 1 - \left(\frac{\Delta \mathbf{s}_{ff}^{N_f}}{\Delta \mathbf{s}_{of}^{N_f}} \right) \quad (6D.2)$$

where $\Delta \mathbf{s}_{ff}$ is the stress amplitude resulting in fretting fatigue run out (typically to cycle counts greater than 10^7 but could be calculated at any intermediate N_f as reflected by the super-script) and $\Delta \mathbf{s}_{of}$ is the stress amplitude in open section fatigue or plain fatigue resulting in run out (again calculated at any intermediate cycle count to failure). A KDF of 0.5, or alternately 50%, is typically used in design when fretting is possible or anticipated. This 50% KDF for the R=0.1 open section fatigue is also plotted in Figure 6D.3 for reference. The fretting data created here is in significant deviation from this 50% KDF rule, especially at lower stress amplitudes approaching the run out stress. The stress amplitudes chosen for test were made assuming the 50% KDF would be

applicable. Since very large KDF's were observed, fretting lives did not exceed 10^6 significantly.

Fractography & Materials Damage

The fretting scars were optically examined to determine the nature of fretting wear and the origin of fretting fatigue fracture. A typical fretting fatigue scar is given in Figure 6D.4 with the two fractured specimens halves pictured together. All of the specimens failed in close proximity to the tensile-trailing edge of the contact, but specifically not at the edge of contact. The tensile-trailing edge of contact is defined as the edge of contact which is at the trailing edge of the pin while the fatigue specimen is in tension. This is a semi-intuitive result since the greatest surface tension can be expected during bulk tension in the region behind the sliding contact. The average percent distance of the fracture surface from the fretting scar tensile-trailing edge was 18%. Thus the fretting fatigue failures all occurred under the fretting contact but in proximity to the tensile trailing edge.

The actual fretting scars of failed specimens did not yield significant insight into the damage mechanism as seen in Figure 6D.5. The scars were covered with the prominent third body debris which was identified as a mixture of TiO_2 and metallic Ti-6-4 alloy flecks and particles interspersed.

Fractographic analysis was quite illuminating concerning the development of embryonic fretting fatigue cracks. The SEM images depicted in Figure 6D.6 show the entire width of one fretting fatigue specimen. One observes that the contact occurred at the bottom of these photomicrographs and propagated towards the top of the page. Clear indications of multiple crack nucleation are clearly observed. These embryonic cracks nucleated at or near the contact surface and propagated in a thumbnail shape into the specimen. This is highlighted by the higher magnification photomicrographs in the figure. Since a number of nucleation sites are identified, all occurring at approximately the same longitudinal location with respect to the tensile-trailing edge of contact as cited in the previous section, the cracks eventually meet and link together. The nucleation sites are evenly distributed along the fretting contact, and thus linkage across the entire specimen width occurs rapidly. The depth of the individual nucleated cracks is approximately 0.008 inch (200 μm) when linkage across the specimen width occurs.

Serial section analysis resulted in a very good view of material damage state and crack nucleation site identification. Figure 6D.7 shows typical propagating and embryonic cracks in the region of the tensile trailing edge. The cracks have the typical slant growth mode commonly associated with fretting fatigue nucleated cracks. Note that one of these cracks had propagated significantly longer than the others and is approximately 900 μm in length while the smaller cracks are approximately 100-150 μm in length. This longer crack may have linked with near-by cracks and begun to propagate at an accelerated rate. The appearance of longer cracks adjacent to the fracture surface was common, indicating that not all linked cracks joined into the crack which eventually led to catastrophic failure.

The damage occurring in the near surface region has been classified into two categories by Vincent et. al. [6D.8] as the mechanically disturbed layer and the metallurgically disturbed layers. Here the mechanically disturbed layer consists of the roughened material and the third body debris layer. Figure 6D.8 shows this layer to be locally $\sim 10\mu\text{m}$ thick. Under lying this region is the metallurgically disturbed region in which the surface tractions have caused multiple plastic strain reversals. In this photograph, the metallurgically disturbed layer is witnessed by the disturbed β plates remnant from the α/β structure of this titanium heat treatment. The metallurgically disturbed layer here is $\sim 30\mu\text{m}$ thick. It should be noted that this layer was not always in evidence along the fretting scar. There were also areas where both the mechanically and metallurgically disturbed layers were thicker. This is caused by typically by pitting and flaking in the fretting contact region. The 10 and 30 μm layer thicknesses reported here are typical of the fretting damage which was observed in this study, and under the reported contact conditions.

Coefficient of friction measurements were taken during the course of fretting and typical results given in Figure 6D.9. The starting COF is the typical 0.25 figure cited in the literature [6D.9]. The COF is seen to increase rapidly through the first 10 cycles to a value of 0.45. Subsequent cycling through 1000 cycles shows a steady rise in COF to 0.65 after which saturation occurs and the COF stabilizes. A number of data points are seen to drop far below the general trend in data. The regular occurrence of these lower measured values would indicate that they are real measurements and not artifacts. They can be attributed to loss of third body debris and a short term change in the

surface contact until new third body debris can be built up. The loss of third body debris will allow for a less actual contact area and thus a reduced frictional load.

Along with coefficient of friction measurements, the energy of fretting was measured and recorded continuously during the fretting test. A typical plot is given in Figure 10a where the energy of fretting, E_f , is plotted vs. the cycle number. The E_f is seen to initially have a very high value of 6.63×10^{-5} Btu (0.07 joules) per cycle which drops dramatically over the first 10 cycles to a minimum value of 1.41×10^{-5} Btu (0.015 joules) per cycle. E_f recovers to a saturation level of approximately 2.84×10^{-5} Btu (0.03 joules). Per cycle after 1000 cycles and maintains this value until test termination. This large change in the energy absorbed during fretting is due to the substantial change in the fretting loop shapes as shown in Figures 6D.10b&c which plots the difference in upper and lower load cell measurements, DP , vs. the measured slip displacement, d . During the first cycle, the pin sliding is long while the coefficient of friction, m is low (where the simple formula used for COF is $m = \{DP \times S_f\} / A_o$, where A_o is the area of fretting contact) as indicated in Figure 6D.9. This leads to a large inscribed area within the DP vs. d trace and a large E_f . As m (and thus DP) increases, the inscribed loop area must decrease for the same sliding length, the E_f decreases. The closing of the DP vs. d loop is direct measured evidence of the transformation from full slip to stick slip with increasing m .

The development of damage to the titanium alloy during the course of fretting was investigated by interrupting fretting tests prior to failure and serial section examination of the fretting layer. The results listed in order of fretting cycles are given below.

0 cycles

The original surface of the chemically milled fretting fatigue specimens is characterized under SEM analysis in Figure 6D.11a by a mottled appearance with residual machining and polishing marks.

3 cycles

After 3 cycles, surface examination showed minimal damage to the chemically milled surface due to contact as shown in Figure 6D.11b. Surface aspirates on the fatigue specimen have been diminished resulting in a polished appearance but

evidence of sliding or material transfer is not generally present. Adhesive contact evidently occurred at only a few distinct points, widely spread across the surface.

30 cycles

Fatigue specimen surface sites of adhesive contact have become more numerous but still isolated at point contacts after 30 fretting fatigue cycles as shown in Figure 6D.11b. Serial sectioning showed the beginning of third body generation, which occurred, also in isolated pockets. The pockets of third body debris could not be associated with individual contact sites in the serial section analysis.

300 cycles

Surface roughening is becoming more pronounced as shown in Figure 6D.11c after 300 fretting cycles. This roughening is associated with the 600 μ m scratches on the fretting pins. The geometric configuration of these scratches is clearly evident in this figure. Serial section analysis showed widely spaced signs of pitting and flaking.

3,000 cycles

The wear patch is fully developed after 3,000 fretting fatigue cycles with a typical region given in Figure 6D.11d with full sliding and metal transfer covering the entire contact region. The third body debris is thick and ubiquitous in serial section viewing. Pitting and flaking are regularly observed and shown in Figure 6D.12.

30,000 cycles

Characterization of the surface viewed wear scar is unchanged from the previous specimen. Cracking is now evident across the entire half of the wear scar towards the tensile trailing edge of the pin. Some typical cracks are given in Figure 6D.13a&b which characterizes the third body debris in this vicinity as well. The cracks observed occurred along the entire width of fretting fatigue specimen and were measured to be between 20 and 100 μ m in length. Cracking often occurred in small clusters with cracks likely emanating from a common pit. The cracks were always significantly wider at the surface with debris tightly packed into their opening. The occurrence of these cracks at the tensile trailing edge of the contact and their being filled with third body debris is in agreement with previous results [6D.10].

Profilometer traces were taken of both the fretting scars and fretting pin surfaces for the interrupted tests. The results are given tabularly in Table II and graphically in Figure 6D.14 a&b. Measurements of R_a , R_q , R_z , P_t and R_k were recorded. R_a is the arithmetic mean deviation, R_q the root mean square deviation, R_z the mean roughness depth, P_t the profile depth, and R_k the core roughness depth. For further definition of these terms and their derivations, see Mahr Profilometer Users Guide [6D.11]. All of these roughness values behaved similarly and thus only R_a and R_q were plotted for clarity. R_a values are seen to decrease slightly from the as received chem milled surface values after 3 cycles and then increase rapidly after 300 cycles. This is in complete correlation with the visual and SEM observations noted above. A typical profilometer trace is given for the 190,000 cycle specimen AFTI39-7 in Figure 6D.14c. The pin roughness here is seen to be ± 0.005 inch ($\pm 12\mu\text{m}$).

A model of fretting fatigue damage development can now be hypothesized taking into account the interrupted testing, serial section, COF and E_f data. The first ~10 cycles incorporate seating of the pin against the fretting fatigue specimen surface and polishing this surface during gross sliding. The greatly increased contact area occurring in the first 10 cycles leads to a rapid rise in m . During cycles 10~300 the pin begins to break down the surface oxide on the specimen and points of metal to metal contact develop. At the discontinuous points of metal to metal contact, debris is being formed in the form of TiO_2 . Continued growth of metal to metal contact increased the m . After cycling for 3,000 cycles, the total contact surface has been roughened, pitting has developed and the third body debris bed has been generated, which now fills the gaps between the roughened mating surfaces. Cracks do not nucleate until ~30,000 cycles. At this point the cracks are 20-100 μm in length, quite numerous in the vicinity of the tensile-trailing edge of the pin and distributed along the entire width of the contact. Crack propagation continues driven by first the surface tractions resulting from the fretting action and finally from the far field fatigue stresses.

Fretting + Fatigue

The results of the fretting+fatigue tests are given in Figure 6D.15 and in Table 6D.3. Due to the machine control peculiarities, fretting without fatigue actually resulted in a significant reacted fatigue load resulting in an effective $Ds_a^R = 13.8\text{ksi}$ (95MPa). When the applied Ds_a was high, the reacted fatigue load was relatively insignificant and the results of fretting+fatigue matched those observed for fretting/fatigue very closely. At lower Ds_a 's however, the reacted load became dominant and failure from this load significantly lowered the cycle lives, and failure occurred during fretting before fatigue cycling could be applied.

To normalize the effect of pre-fretting reacted load on fatigue failure, also plotted in Figure 6D.15 are the total fretting and fatigue cycles to failure using the reacted stress amplitude in the cases where failure occurred during fretting alone. One sees that these results track the fretting/fatigue data especially at lower stress amplitudes. At higher stress amplitudes, the fretting cycles applied with the lower reacted stress amplitude inflated the number of cycles to failure.

The results of this experimental study indicate that fretting + fatigue is a reasonable approximation to fretting/fatigue testing. One must take into consideration both applied and reacted stresses in calculating cyclic lives to failure, but this can be accomplished readily. If at all possible, fretting+fatigue testing should be conducted with one specimen end free, but reacted loading on the fixed the specimen end still needs to be considered.

Modeling

The finite element analysis was conducted using the ANSYS program, Version 5.3. The analysis was two dimensional, using four-noded linear quadrilateral elements. For most of the analyses, plane stress was employed. Comparisons with three dimensional analyses validated the plane stress assumption. Material properties included plasticity.

Large deflection contact, with friction, was included by adding contact elements between the pin face and the specimen surface.

The system models were built parametrically, so that the mesh densities could easily be updated. The model used for the analyses herein consisted of 10,699 quadrilaterals, and 2830 contact elements. For this model, the specimen nodes under the pin

were distanced by 0.0006 inch. Figure 6D.16a shows the overall mesh. Figure 6D.16b shows the mesh local to the contact surfaces.

Model Analysis Procedure

The analysis procedure consisted of a series of load steps to, sequentially:

1. Seat the pin,
2. Establish the specimen mean stress, and the pin fretting stress, and
3. Cycle the pin motion and the specimen stress (in phase with each other).

The ANSYS analysis procedure uses Time as an analysis step counter. The time sequence employed herein was as follows:

Time	Loading
0.5	Seat the pin
1.0	Apply Fret Stress, Specimen Mean Stress
1.1 to 2	Pin Right (on Figs) Motion, Max Specimen Stress, in .1 increments
2.1 to 3	Cycle back to neutral position
3.1 to 4	Pin Left Motion, Min. Specimen Stress
4.1 to 5	Back to neutral position
5.1 to 6	Pin Right Motion, Max Specimen Stress

For all loads past the time of 1.0, increments of .1 were used, to ensure that the linear load applications closely matched the sinusoidal test sequence. For each load increment, equilibrium iterations were performed, to capture all appropriate nonlinear effects.

Solution Data Extraction/Processing

To ensure steady state solutions for the path-dependent solution, only those time values greater than 2.0 were considered. For cycle extremes, times 4.0 and 6.0 were studied.

For damage calculations, a group of specimen elements local to the contact region was selected. For those elements, the appropriate stress components, such as the X, Y, and XY shear stresses, were stored as ANSYS Etable items, and then saved to a text file. Damage parameters, such as the SWT parameter, were calculated using an external "C" language program, that read in the element data, and then calculated the element damage parameter data.

For damage contour plots, the "C" program output the element damage data in ANSYS DESOL command format to text files, using available element data items, such as SRAT. These files, imported into ANSYS, were then color contour plotted, for data summary and visualization.

Modeling Analysis

In order for the design community to be able to more accurately design contact problems, a tool needs to be developed which will lend itself to rapid application. The most expeditious means of accomplishing this goal is to use the output of the FEM analysis described above to calculate the most damaging stress state at the contact site and relate this damaging contact stress state to uniaxial data previously generated. The precise nature of the *most damaging stress state* is the subject of some debate in the fretting fatigue community. This effort will show the application of three models, (i) a principal stress model developed at UTRC, (ii) a critical plane maximum stress model pioneered by Socie [6D.12] and Farris [6D.13] and (iii) a triaxial stress materials damage model developed by Dan Van [6D.14] and Fouvry et. al. [6D.15].

Principal Stress Model

For this model, it is assumed that the principal stress, independent of its vector direction, acting at any point beneath the contact is driving materials damage, and that this damage can be related to the HCF-LCF damage obtained from uniaxial fatigue testing. To accomplish calculation, the difference between the minimum and maximum principal stresses, $DS_p = s_{p-max} - s_{p-min}$, is calculated for each element during the entire fretting cycle. Using these two stresses, an R-ratio, s_{p-min}/s_{p-max} is calculated for that element. Contour plots of DS_p and R were constructed and are given in Figure 6D.17a&b respectively. The maximum principal stress difference, DS_p , was found to be 97 ksi (669MPa). This element was located at the tensile trailing edge of the fretting contact. This element underwent the lowest R-ratio as seen in Figure 6D.17b with a value of 0.149. Comparison with data previously noted in Figure 6D.3 leads to an approximate solution to cycle life to element failure which can be used as a surrogate for crack nucleation. Here, high cycle fatigue data is cited for tests conducted at R = 0.1, a very close approximation to the R-ratio of 0.149 identified in this model. For a critical DS_p of 97 ksi (669MPa) at an R-ratio of 0.1 a fatigue cycle life to nucleation of 1.1

$\times 10^5$ cycles is predicted. The graphical derivation of this prediction is given in Figure 6D.17c.

A computer modeling code, NASGROW [6D.16], was employed to predict the fatigue crack growth life expectancy to propagate a 0.008 inch (200 μ m) embryonic fretting fatigue crack fully linked across the specimen width to failure. This life was calculated to be 53,000 cycles. This is a significant fraction of the fatigue cycle life which averaged 1.1×10^5 cycles, or ~48%. Crack growth cycle life was subtracted from total cycle life to gain insight as to the time under fretting fatigue required to nucleate a 0.008 inch (200 μ m) crack. Nucleation life was determined to be 5.7×10^4 cycles. This result is in reasonable agreement with the predicted 8.0×10^4 cycles required for crack nucleation under the principal stress model obtained above.

The striking result from this analysis is that the fretting/fatigue life can be predicted only with knowledge of the contact stress state. No further information is required on metal surface degradation by oxidation, corrosion, erosion etc. With reference to Equation (6D.1), we can now see that $Kf \approx 0$ and Equation (6D.2) reduces to:

$$\Delta\sigma_{ff} = \Delta\sigma_c(\gamma, \sigma_f, \Delta\sigma_a, \mu[\delta, \sigma_f]) \quad (6D.3)$$

where γ is the geometric effect on stress. This is a revealing finding which vastly simplifies the design methodology to a stress calculation. The stress calculation still requires knowledge of the coefficient of friction, μ which is a function of the surface materials damage state produced by δ and σ_f and possibly other factors such as frequency, temperature, humidity, etc.

Critical Plane Model

The critical plane model requires the calculation of the maximum uniaxial stress, $s_{max}(\mathbf{q})$, strain amplitude, $D\epsilon(\mathbf{q})$, multiple during the fretting cycle across a plane of specified orientation. To accomplish this calculation, maximum uniaxial stresses and strains were calculated normal to a plane whose orientation was rotated in 1° increments through 180° for each element. The maximum stress-strain range multiple, $D\epsilon(\mathbf{q}) \cdot s_{max}(\mathbf{q}) = G_{max} = \mathbf{G}_{max}$, defined as the SWT damage parameter [6D.17], was calculated for each rotational increment. This damage parameter can then be used in the Smith-Watson-Topper, SWT, formulation for predicting fatigue failures independent of mean stress as

was first applied to fretting fatigue by Szolwinski and Farris et. al. [6D.13]. The SWT formula, which simply multiplies the Coffin-Manson, C-M, formulation times the maximum fatigue stress to account for mean stress effects in cycle life is given below as:

$$\Gamma_{\max} = s_{\max}(\mathbf{q}) \left(\frac{\Delta \mathbf{e}(\mathbf{q})}{2} \right) = \frac{(s'_f)^2}{E} (2N_f)^{2b} + s'_f e'_f (2N_f)^{b+c} \quad (6D.4)$$

where \mathbf{G}_{\max} is the SWT damage parameter consisting of the strain range, maximum stress multiple, $\mathbf{De}(\mathbf{q})$ and $s_{\max}(\mathbf{q})$ have been defined above, while b , c , s'_f and e'_f are the Coffin-Manson defined uniaxial fatigue parameters. Iso- \mathbf{G}_{\max} contours for the fretting fatigue cycle modeled in the previous section are given in Figure 6D.18a. Once again, one observes that the maximum damage, \mathbf{G}_{\max} , occurs at the tensile trailing edge of the fretting fatigue contact, having a value of 288 psi (41,8 Pa). This maximum damage parameter can then be used with the C-M fatigue parameters to predict the cycle to failure of the most critically stresses element under the fretting contact. This is most easily accomplished graphically, thus saving solution of the quadratic C-M equation. The low and high cycle fatigue data in the literature indicates that the C-M parameters are: $b = -0.126$ ksi, $c = -0.860$, $s'_f = 320$ ksi and $e'_f = 2.802$ from [6D.18]. Solution for cyclic failure lives are given in Fig. 6D.18b as 1.3×10^5 cycles.

This cycle life to crack nucleation, when added to the crack growth life of 5.3×10^4 cycles yields a total fatigue life of 1.8×10^5 cycles, again in good agreement with the average 1.1×10^5 cycles obtained experimentally.

Triaxial Materials Model

The triaxial damage model is based on work pioneered by Dang Van [6D.14, 6D.19, 6D.20]. This model is predicated on the assumption that both hydrostatic tension and shear stresses are required to nucleate a crack and propagate it respectively. Thus a critical materials damage parameter is assumed which has the form:

$$d = \max_{\vec{n}, t} \left\{ \frac{\|\mathbf{t}(\vec{n}, t)\|}{\mathbf{t}_d - \mathbf{a} \cdot \hat{\rho}(t)} \right\} \quad (6D.5a)$$

and

$$\mathbf{a} = \frac{\mathbf{t}_d - s_d/2}{s_d/3} \quad (6D.5b)$$

where d = multi-axial damage factor, $t(n,t)$ = shear stress, $p(t)$ = hydrostatic tensile stress, t_d = run-out fatigue shear stress and s_d = run out fatigue tensile stress. When d exceeds this critical value, cracking and failure is predicted. If this critical value of damage can be avoided, failure is not predicted.

To calculate critical damage values spatially under the fretting fatigue contact, both the shear and hydrostatic tension components of each cell were calculated over the entire twenty steps of the fretting cycle. Also required for this calculation are pure shear fatigue test data. A literature survey yielded no shear fatigue data for Ti-6-4 or any other titanium alloy. For ferrous alloys a reasonable approximation of shear stress fatigue is $t_d \sim 2/3 s_d$. It is assumed that titanium alloys behave similarly and thus $\alpha = 1/2$. Iso- d contours of the maximum value of d for each cell is given in Fig. 6D.19a. One observes that the maximum value of d , occurs ~ 0.0005 inch ($12\mu\text{m}$) below the surface under the tensile trailing edge of the fretting pin. The value of $d = 1.27$ greater than 1 thus predicting failure. The highest damaged element node was surveyed during the entire fretting cycle, and these results are given in Figure 6D.19b where shear stress is plotted as a function of hydrostatic stress. The damage parameter, d , is seen to extend past the damage limit at its furthest excursion during the full tensile load and maximum slip displacement. Since this model is based on fatigue run-out stress typically assumed to be 10^7 cycles, and the calculated damage parameter of 1.27 found, we can infer approximately a 20% reduction in local triaxial stress to yield fretting fatigue run out. A more accurate prediction of fretting failure would require the determination of shear fatigue failure at a number of shear stress amplitudes. Refinement of the triaxial model would be required to be used a cycle life predictive tool.

CONCLUSIONS

- Fretting/fatigue was found to be more damaging than the typically defined 50% KDF under the contact condition studied. The fretting/fatigue KDF was determined to be approximately 67% at a cycle life of 10^6 .
- Fretting/Fatigue failure locations were located under the fretting contact area but within 20% of the contact width of the tensile trailing edge of the contact pin. This is significant since the tensile trailing edge of contact is where both the

fatigue loading and fretting surface shears will add to the highest surface tensile stresses. It is also significant that failure did not occur at the edge of contact. This was hypothesized to be due to a change in geometry of the fretting pins which profilometry showed was severely modified from the initial flat condition.

- Coefficient of friction, μ measurements conducted during the fretting tests showed an initial rapid increase in μ from 0.25 to 0.65 during the first 1000 cycles. The COF then saturates at this level and remains constant for the remainder of testing. The rapid increase in μ was attributed to surface oxide break-down, surface roughening and third body debris generation.
- Concurrent to the rapid COF rise was a measured similar decrease in the energy of fretting absorbed per cycle, E_f . The E_f dropped from 6.6×10^{-5} Btu/cycle to 2.8×10^{-5} Btu/cycle (0.07 joules/cycle to 0.03 joules/cycle). This was shown to be due to a change in the slip amplitude driven by the raising COF. Slip decreased significantly during cycling with a rapid decrease in the absorbed energy of fretting.
- The near surface metal was seen to display two distinct layers. At the surface the mechanically deformed layer, composed of the third body debris bed and surface scratches and pits was between 0.0005 to 0.001 inch (10 and 25 μm) in depth. This was followed by the metallurgically disturbed layer, ~ 0.001 inch ($\sim 30 \mu\text{m}$) in depth, which consisting of a highly plastically deformed metal which displayed distorted β plates.
- Interrupted fretting fatigue testing elucidated the mechanism of fretting fatigue damage. Initial surface polishing was followed by localized point regions of metal contact transfer. Finally, the point contact regions grew until general contact occurred with third body debris generation and pitting. Cracks did not form during testing until 30,000 fretting fatigue cycles or 10% of cycle life was consumed. Micro-crack nucleation occurred in the vicinity of the tensile trailing edge of contact. Many fretting fatigue cracks nucleated at point origins in small clusters, typically at a pit, and propagated in a thumb-nail shape until they joined adjacent cracks and linked across the specimen surface to form an edge crack 0.008 inch (200 μm) in depth. At this point, the far field fatigue stress amplitude propagated the cracks to failure in the typical Mode I manner.

- Fretting + Fatigue testing was found to be a close approximation to Fretting/Fatigue testing under the testing conditions investigated here. The test equipment utilized here was not optimized for fretting + fatigue testing, however.
- A 2-D ANSYS FEM model utilizing contact elements and elastic-plastic conditions under plane strain conditions was used to determine the surface and subsurface stress state of the fretting fatigue specimen under the contact conditions studied here. The element size was variable, with the smallest elements being 0.0005 inch (12 μ m). A convergence study indicated that the model was not fully converged, but further refinement would bring resolution of the surface in conflict with experimental results, which indicate surface roughening on the order of 0.0003-0.0008 inch (10-15 μ m). These triaxial stresses were used successfully in three materials modeling studies.
- A computer crack growth simulation program, NASGROW, calculated that 53,000 cycles of fatigue life was attributed to crack growth alone, fully 48% of total fatigue life.
- Three damage models were investigated, (i) Principal Stress Model, (ii) Critical Plane Model and (iii) Triaxial Materials Damage Model. All three of these models accurately predicted fretting fatigue failure.
- Fretting fatigue damage was found to be primarily developed through complex triaxial contact stresses which could be adequately modeled. Additional fatigue life degradation due to surface oxidation or wear was found to be negligible and within the scatter of ordinary fatigue data.

ACKNOWLEDGEMENTS

The material contained in this report is based upon work supported by the US Air Force Research Laboratory under contract no. F33615-96-C-5269. The assistance of Dr. K. Brown in development of the finite element modeling portion of this study is gratefully acknowledged. The fretting fatigue tests were conducted by Mr. H. Roman and the metallographic examinations conducted by Mr. R. Brown for which I am indebted.

REFERENCES

- 6D.1. Cowles, B.A., *Int. J. of Fracture*, vol. 80, pp147-163 (1996).
- 6D.2. Chamount, C., Y. Honnorat, Y. Berthier, M. Godet and L. Vincent, in the proceedings of the *Sixth World Conf. On Titanium*, pp. 1883-7 (1988).
- 6D.3. Anton, D.L., R. Guillemette, J. Reynolds and M. Lutian, in Surface Performance of Titanium, J. Gregory et. al. eds., TMS, Warrendale, PA, USA, pp187-99 (1997).
- 6D.4. Blanchard, P., C. Colombie, V. Pellerin, S. Fayeulle and L. Vincent, *Met. Trans. A*, 22A, pp. 1534-44 (1991).
- 6D.5. Vingsbo, O. and Södergerg, *Wear*, 126, pp. 131-47 (1988).
- 6D.6. Favrow, L.H., D. Werner, D.D. Pearson, K.W. Brown, M.J. Lutian, B.S. Annigeri and D.L. Anton, in Fretting Fatigue: Current Technology and Practices, ASTM STP 1367, D.W. Hoepfner, V. Chandrasekaran and C. B. Elliott, Eds., American Society for Testing and Materials, West Conshohocken, PA (1999) in press.
- 6D.7. Air Force Contract Number F33615-96-C-5269.
- 6D.8. Vincent, L. in Fretting Fatigue, R. Waterhouse and T. Lindley et. al. eds., Mechanical Engineering Publications Ltd., London, U.K., pp. 323-37 (1994).
- 6D.9. Nutt, S.R., in *Wear of Materials*, 1983, ASME, NY, NY, USA, pp. 426-33 91983).
- 6D.10. Antoniou, R.A. and T.C. Radtke, *mater. Sci. and Eng. A*, A237, pp.229-40 (1997).
- 6D.11. Perthometer Surface Texture Parameters, Mahr GmbH, Göttingen, Germany, (1995).
- 6D.12. Socie, D., in *Advances in Multi-Axial Fatigue*, ASTM-STP 1191, ASTM, Philadelphia, PA, USA, pp.7-36, (1993).
- 6D.13. Szolwinski, M.P. and T.N. Farris, *Wear*, 221, pp. 24-36 (1998).
- 6D.14. Dang Van, K., B. Griveau and O. Message, in *Biaxial and Multiaxial Fatigue*, M. Brown and K. Miller eds., Mechanical Engineering Publishers, London, U.K., pp. 479-96 (1989).
- 6D.15. Fouvry, S., Kapsa, and L. Vincent, in *Fretting Fatigue: Current Technology and Practices*, ASTM STP 1367, D.W. Hoepfner, V. Chandrasekaran and C.B. Elliott,

Eds., American Society for Testing and Materials, West Conshohocken, PA (1999) in press.

- 6D.16. Fatigue Crack Growth Computer Program "NASGROW" Version 3.00, JSC-22267B, NASA, Engineering Directorate, Johnson Space Ctr., Houston, TX (1996).
- 6D.17. Smith, K.N., P. Watson and T.H. Topper, Journal of Materials, 5(4) pp.767-78 (1970).
- 6D.18. Boller, C. and T. Seeger, Materials Data for Cyclic Loading part D: Aluminum and Titanium Alloys, Elsevier, Amsterdam, Netherlands, pp. 130-141 (1987).
- 6D.19. Dang Van, K., A. LeDouaron and H.P. Lieurade, in Advances in Fracture Research, Pergamon Press, Oxford, U.K., pp.1879-85 (1984).
- 6D.20. Petiot, C., L. Vincent, K. Van Dang, N. Maouche, J. Foulquier and B. Journet, Wear, 181-183, pp. 101-111 (1995).

Table 6D.1
Fretting Fatigue Data

Spec. ID	Applied Stress Amplitude, $\Delta\sigma_a$		Fretting Stress σ_f		Slip Amplitude δ		Cycles to Failure N_f
	(MPa)	(ksi)	(MPa)	(ksi)	(μm)	(inches)	
AFTI39-4	228	33	200	29	25	0.001	115,899
AFTI39-1	228	33	200	29	25	0.001	49,479
AFTI39-6	228	33	200	29	25	0.001	109,067
AFTI39-5	193	28	200	29	25	0.001	194,082
AFTI39-2	193	28	200	29	25	0.001	58,361
AFTI39-10	172	25	200	29	25	0.001	135,319
AFTI39-3	172	25	200	29	25	0.001	165,101
AFTI39-7	150	22	200	29	25	0.001	191,759
AFTI39-9	150	22	200	29	25	0.001	210,694
AFTI39-11	103	15	200	29	25	0.001	1,015,642
AFTI39-12	103	15	200	29	25	0.001	1,446,572
AFTI39-13	124	18	200	29	25	0.001	427,774
AFTI39-14	124	18	200	29	25	0.001	202,957

Table 6D.2
Profilometry Results on Interrupted Tests

Cycles	Scar					Pin				
	R _a	R _q	R _z	P _t	R _k	R _a	R _q	R _z	P _t	R _k
1	0.17	0.21	1.03	1.45	0.52	0.11	0.13	0.67	32.45	0.37
3	0.08	0.10	0.60	1.37	0.26	0.07	0.09	0.45	46.96	
30	0.11	0.14	0.71	4.23	0.30	0.12	0.17	0.84	47.75	0.30
300	0.12	0.15	0.70	2.91	0.46	0.10	0.15	0.66	53.17	0.23
3,000	0.82	1.02	4.31	16.63	2.75	0.72	0.92	4.08	37.51	2.39
210,000	0.77	1.08	4.51	119.06	2.15	0.88	1.18	4.52	88.53	2.58

Table 6D.3
Fretting + Fatigue Test Results

Specimen ID	Vibratory Stress $\Delta\sigma_{aT}$		Fretting Stress σ_f		Slip Amplitude δ		Fretting with no Fatigue	Fretting + Fatigue HCF Cycles to Failure	Fretting + Fatigue Total Cycles to Failure
	(MPa)	(ksi)	(MPa)	(ksi)	(μm)	(inches)	(cycles)	(cycles)	(cycles)
AFTI39-15	228	33	200	29	25	0.001	50,420	236,098	286,518
AFTI39-16	193	28	200	29	25	0.001	100,069	136,852	236,921
AFTI39-17	172	25	200	29	25	0.001	200,013	277,006	477,019
AFTI39-18	150	22	200	29	25	0.001	300,014	111,695	411,709
AFTI39-19	125	18	200	29	25	0.001	563,069	10,000	573,069
AFTI39-20	125	18	200	29	25	0.001	422,065	10,000	432,065

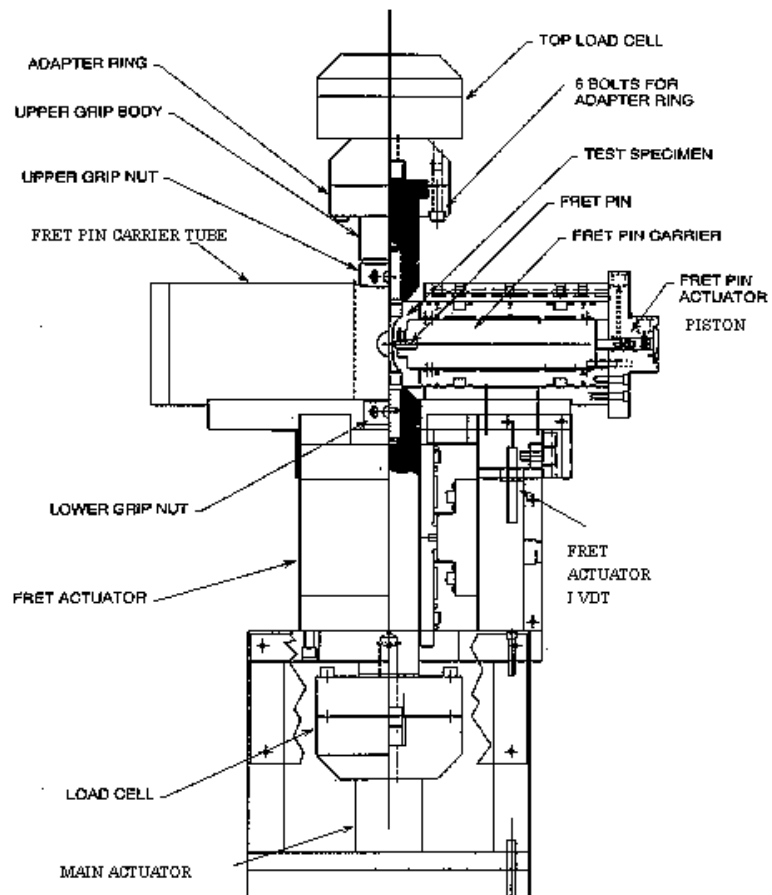


Figure 6D.1. Schematic diagram of fretting fatigue rig used for simultaneous fretting and fatigue.

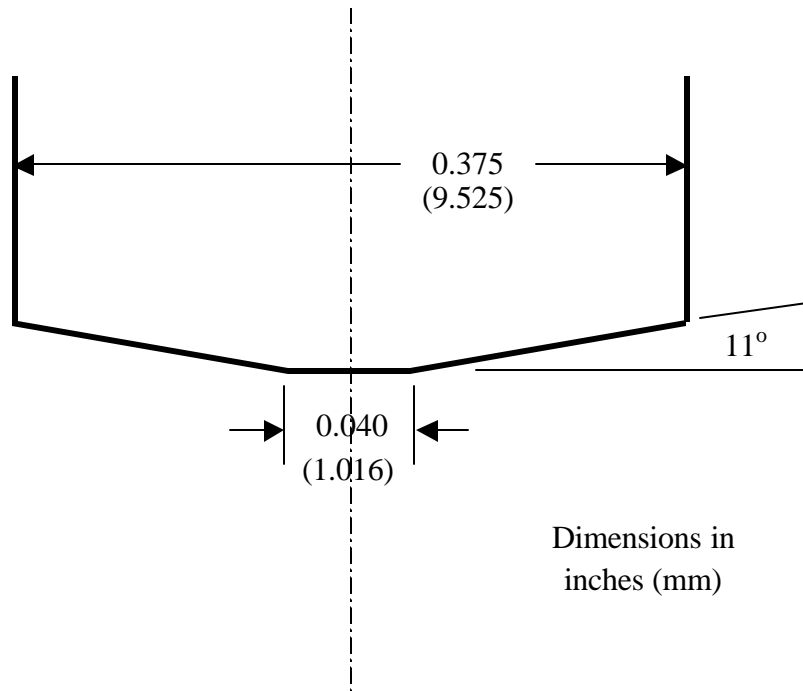


Figure 6D.2. Geometry of fretting contact.

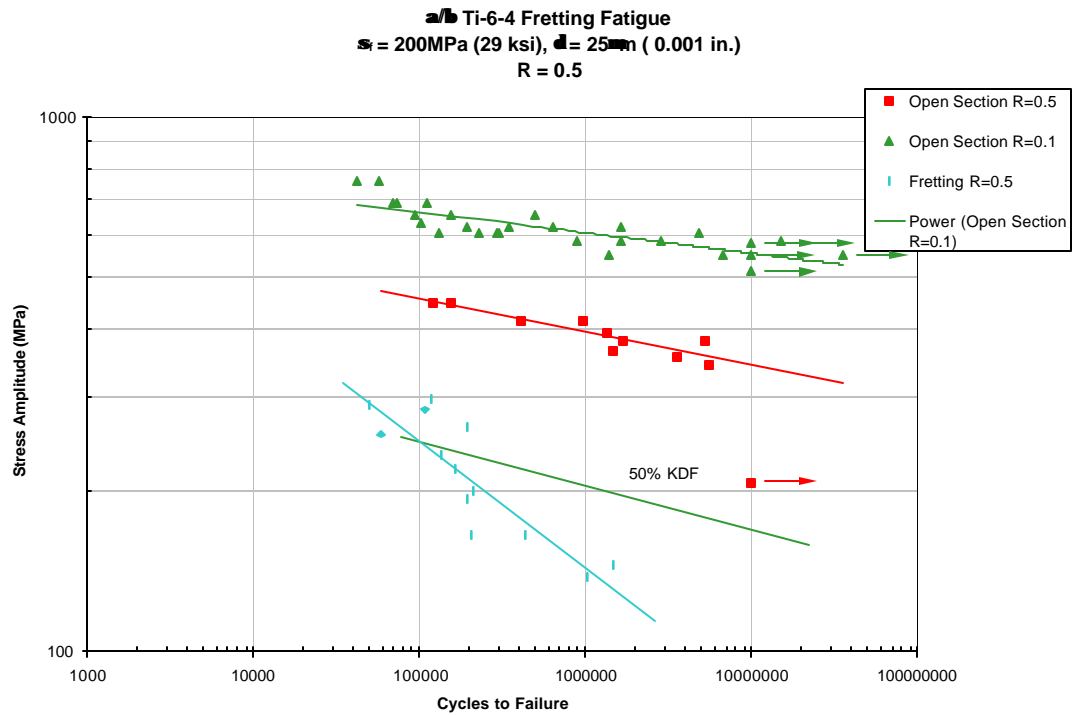


Figure 6D.3. Fretting fatigue results showing 67% KDF from open section testing at 10^6 cycles to failure.

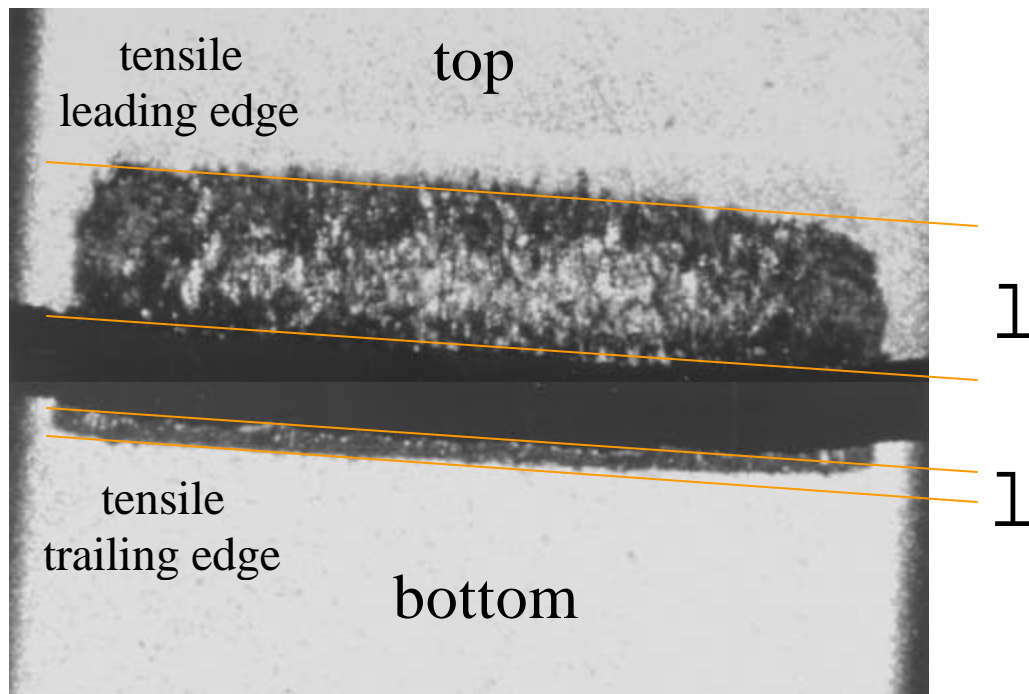


Figure 6D.4. Optical photograph of the fretting/fatigue scar showing fracture to be in close proximity to the tensile trailing edge of contact but not at the edge of contact.

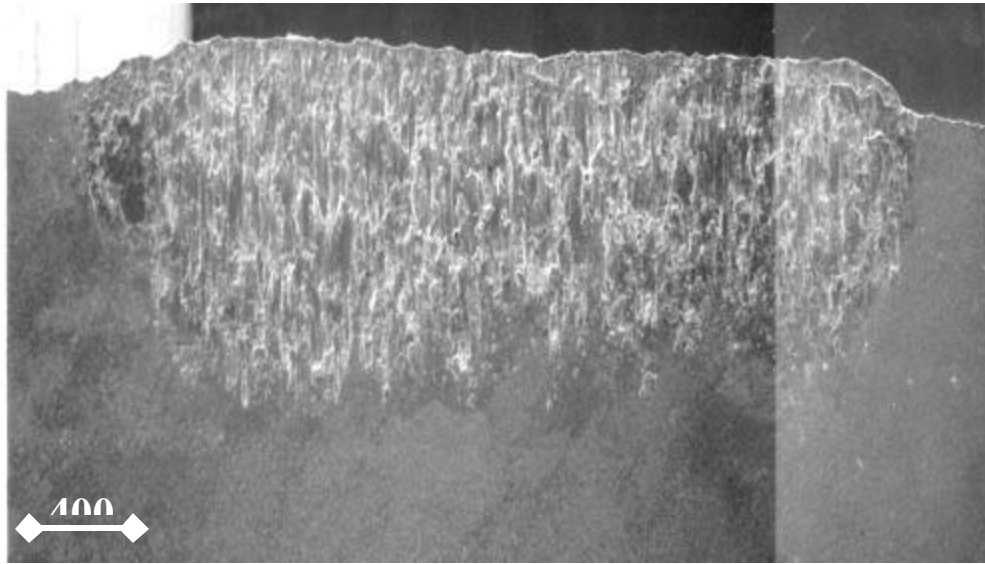


Figure 6D.5. Fretting/fatigue scar viewed by the SEM showing the contact region to be dominated by metal transfer and third body debris.

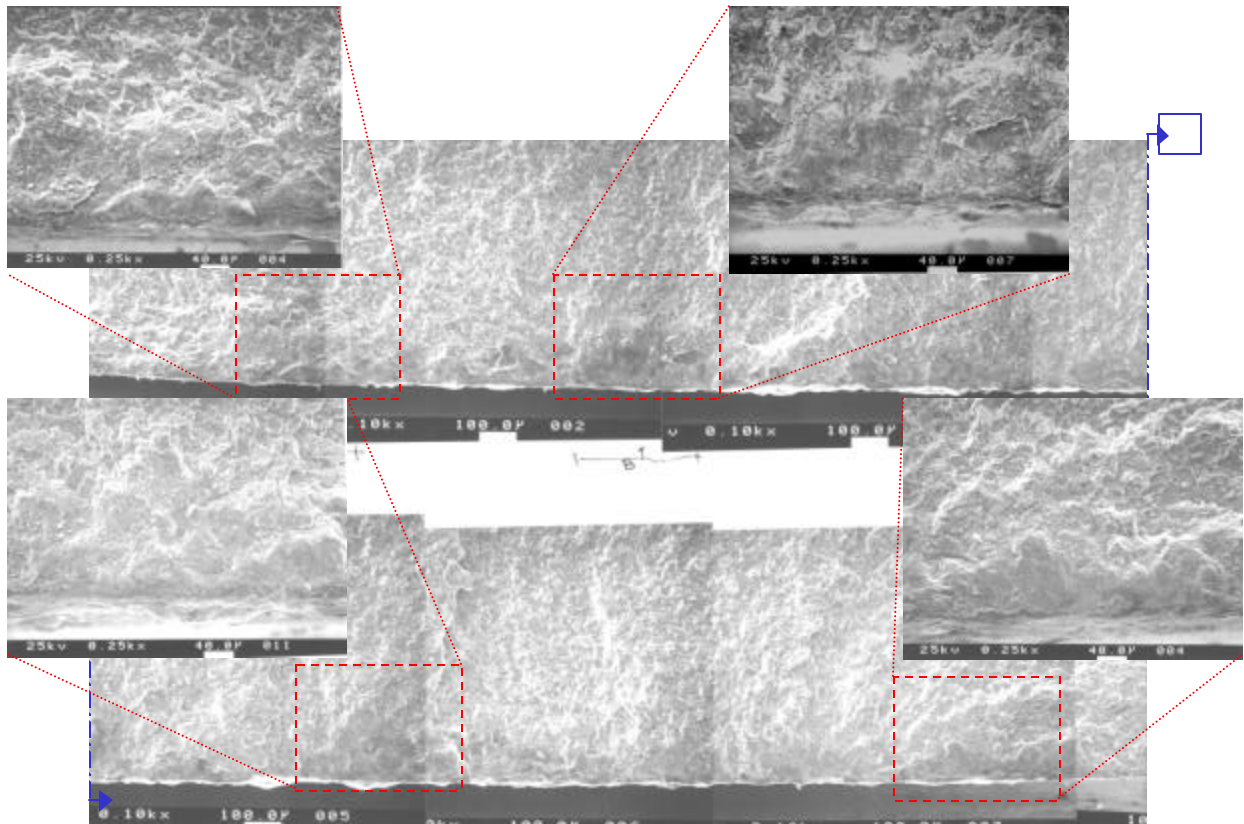


Figure 6D.6. Fretting/Fatigue fracture surface showing multiple nucleation sites which originally grew in thumb-nail shape and eventually linked together to form an edge crack ~0.008" (200 μ m) deep.

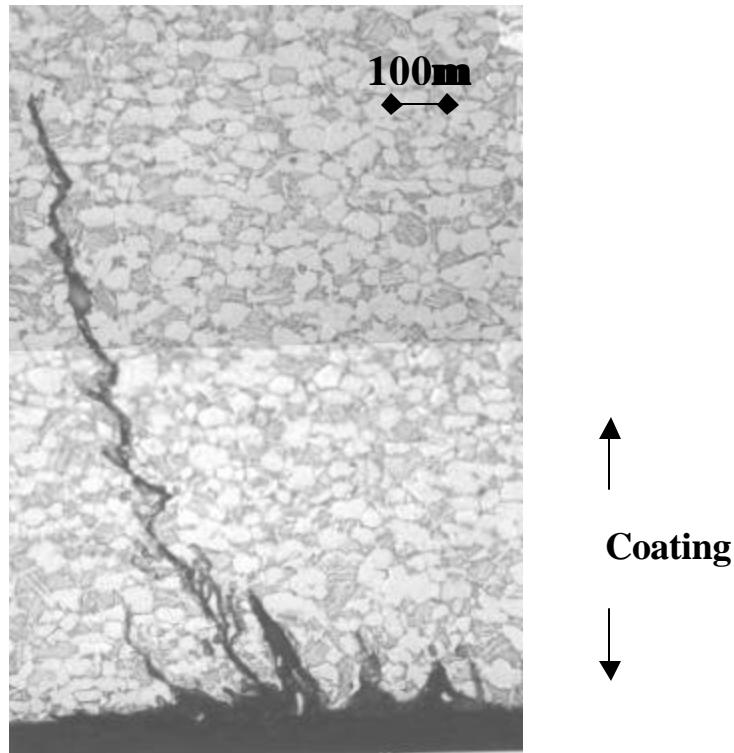


Figure 6D.7. Fretting fatigue cracks propagating at an angle to the fretting surface clustered in an originating pore.

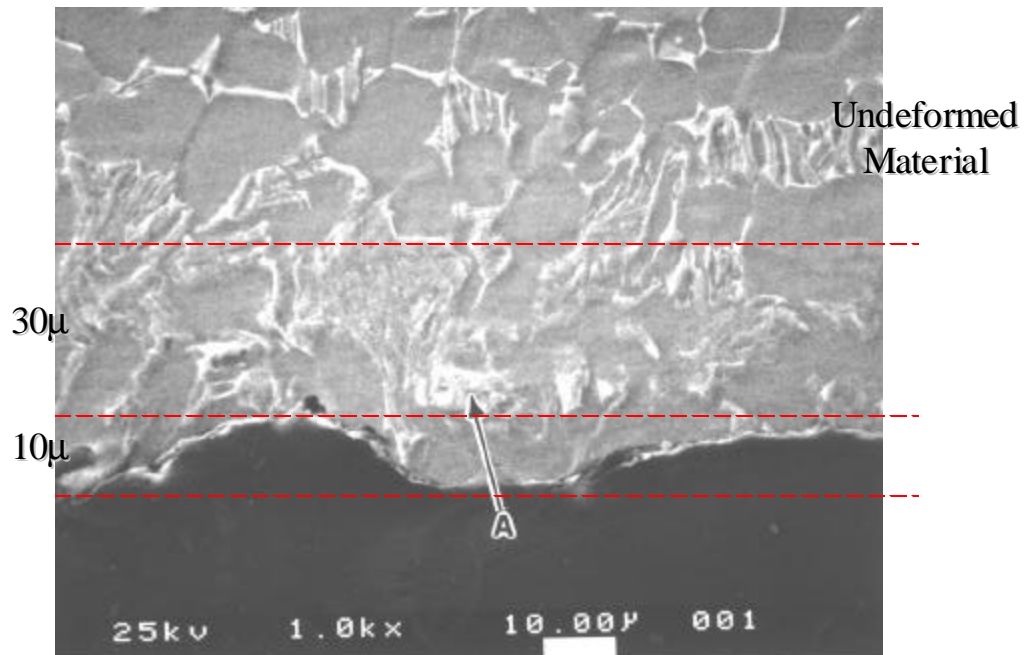


Figure 6D.8. Two distinct layers under the fretting contact include the mechanically disturbed layer consisting of pits and scratches and the metallurgically disturbed layer consisting of a high plastically deformed layer denoted by disturbed β plates.

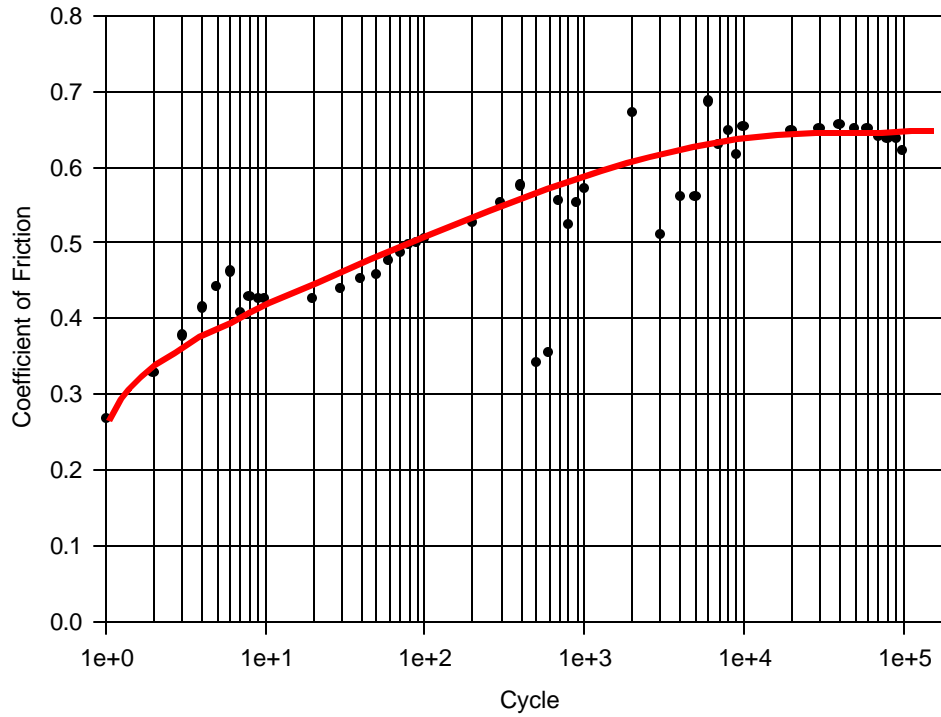
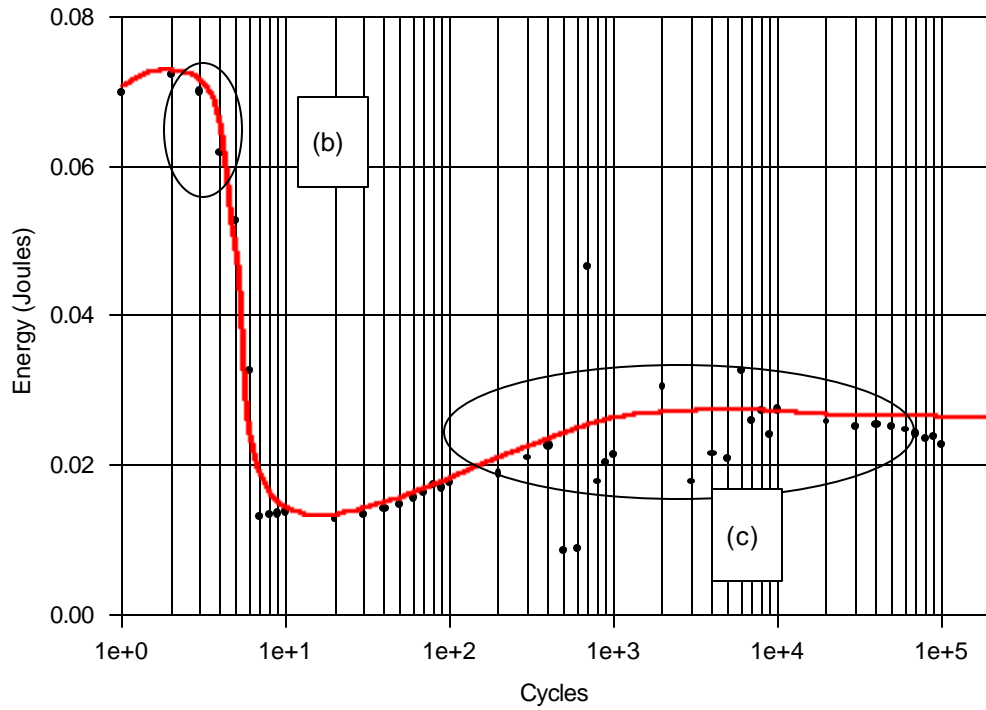
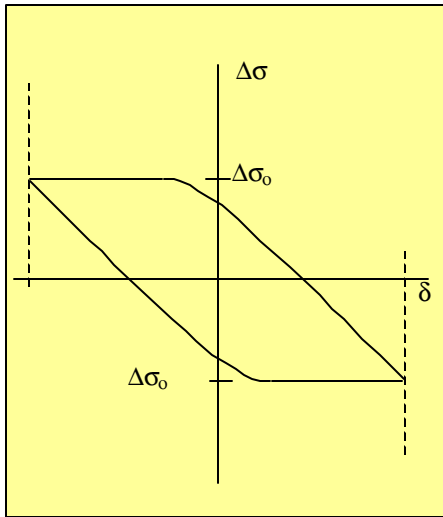


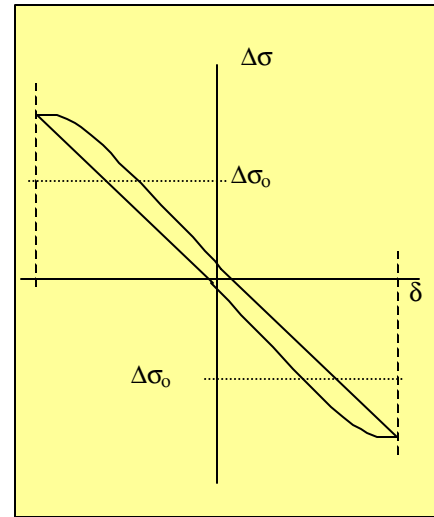
Figure 6D.9. Coefficient of friction plot as a function of fretting fatigue cycles showing initial rapid rise to a saturation level after 1000 cycles.



(a)



(b)



(c)

Figure 6D.10. (a) Energy of friction vs. fretting/fatigue cycles showing rapid decrease during first 10 cycles followed by saturation, (b) schematic slip displacement vs. fretting load plot for first fretting/fatigue cycle and (c) schematic slip displacement vs. fretting load plot for saturated fretting/fatigue cycle.

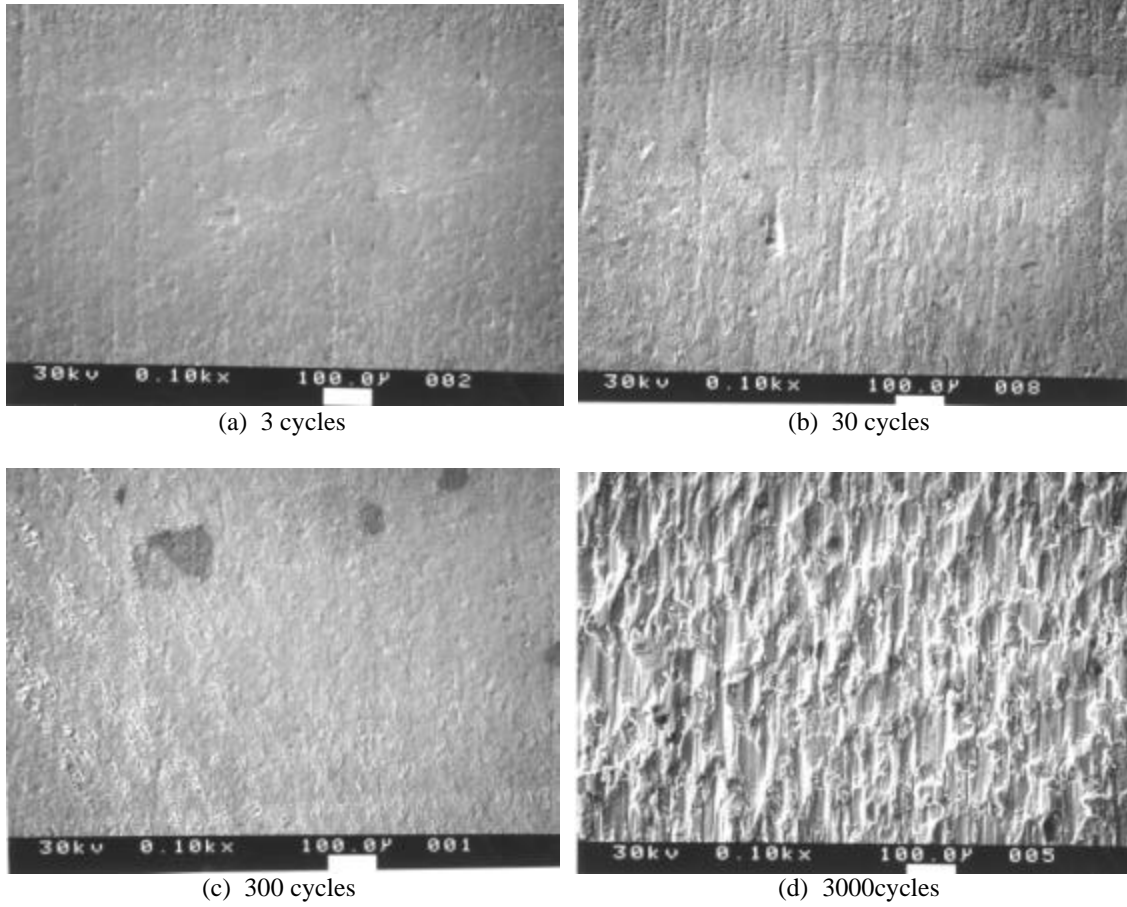


Figure 6D.11. Development of fretting fatigue scar during cycling taken from interrupted tests.

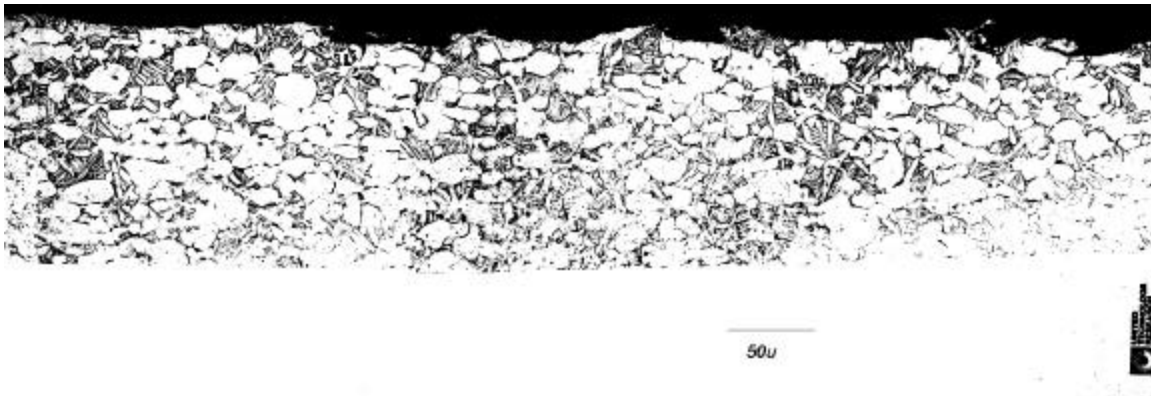
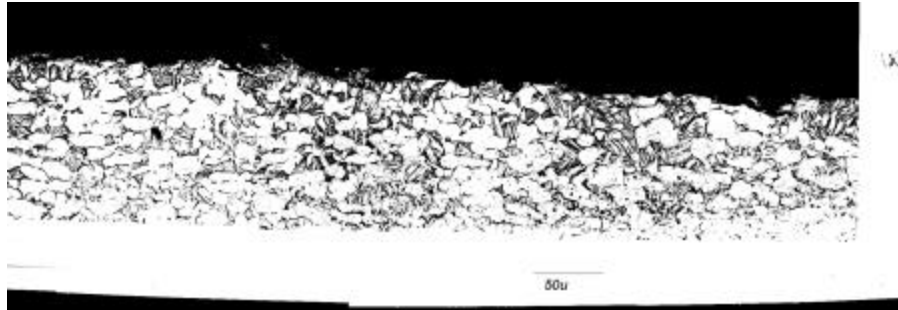
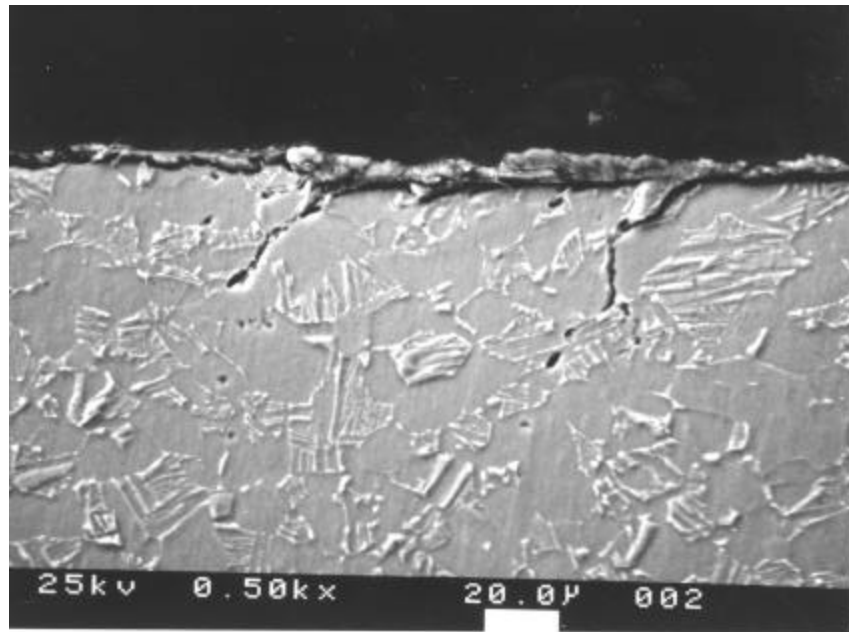
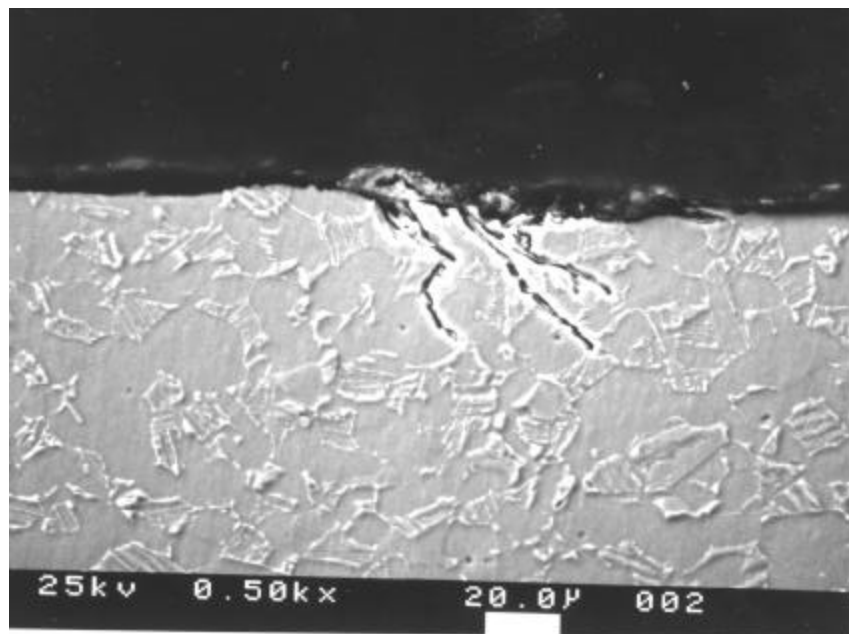


Figure 6D.12. Pitting and flaking first identified in 3,000 cycle interrupted tests.

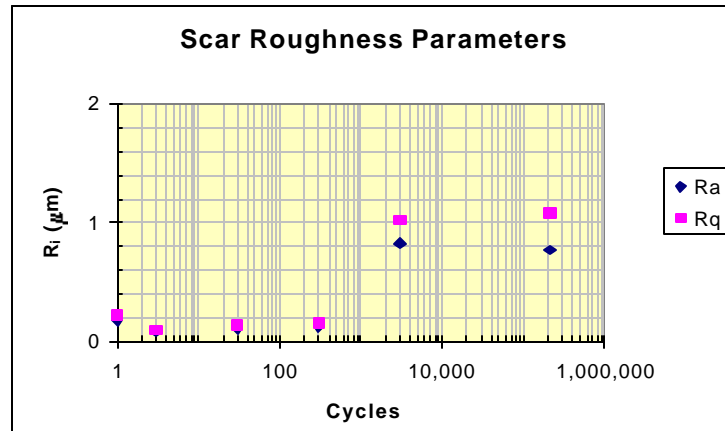


(a)

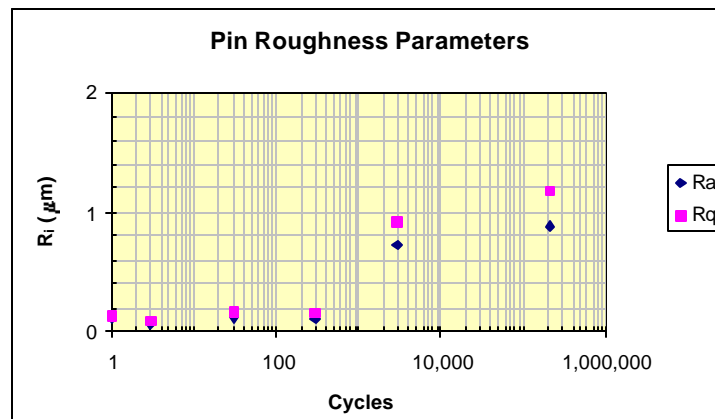


(b)

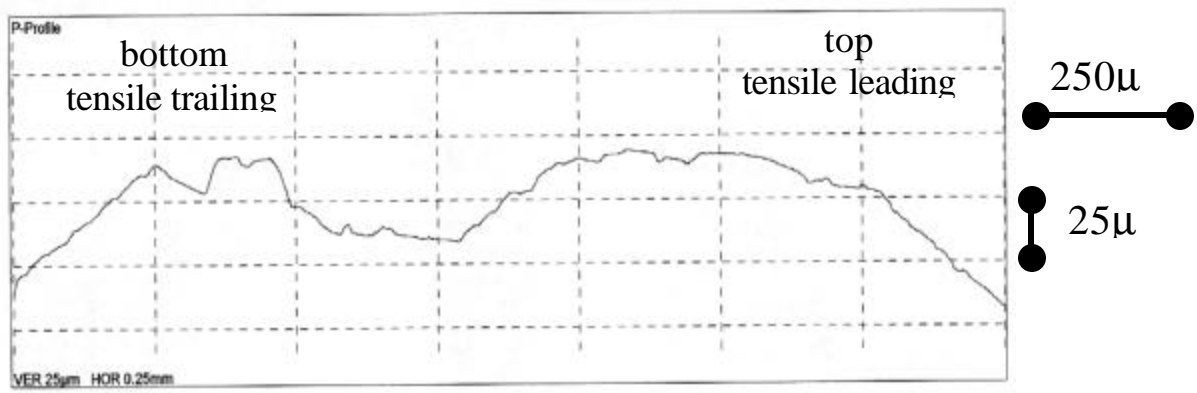
Figure 6D.13. Cracks found after 30,000 cycles; interrupted prior to specimen failure.



(a)



(b)



(c)

Figure 6D.14. Results of profilometry analysis on interrupted specimen (a) scars, (b) pins and (c) pin profilometry trace after cycling 190,000 cycles to failure.

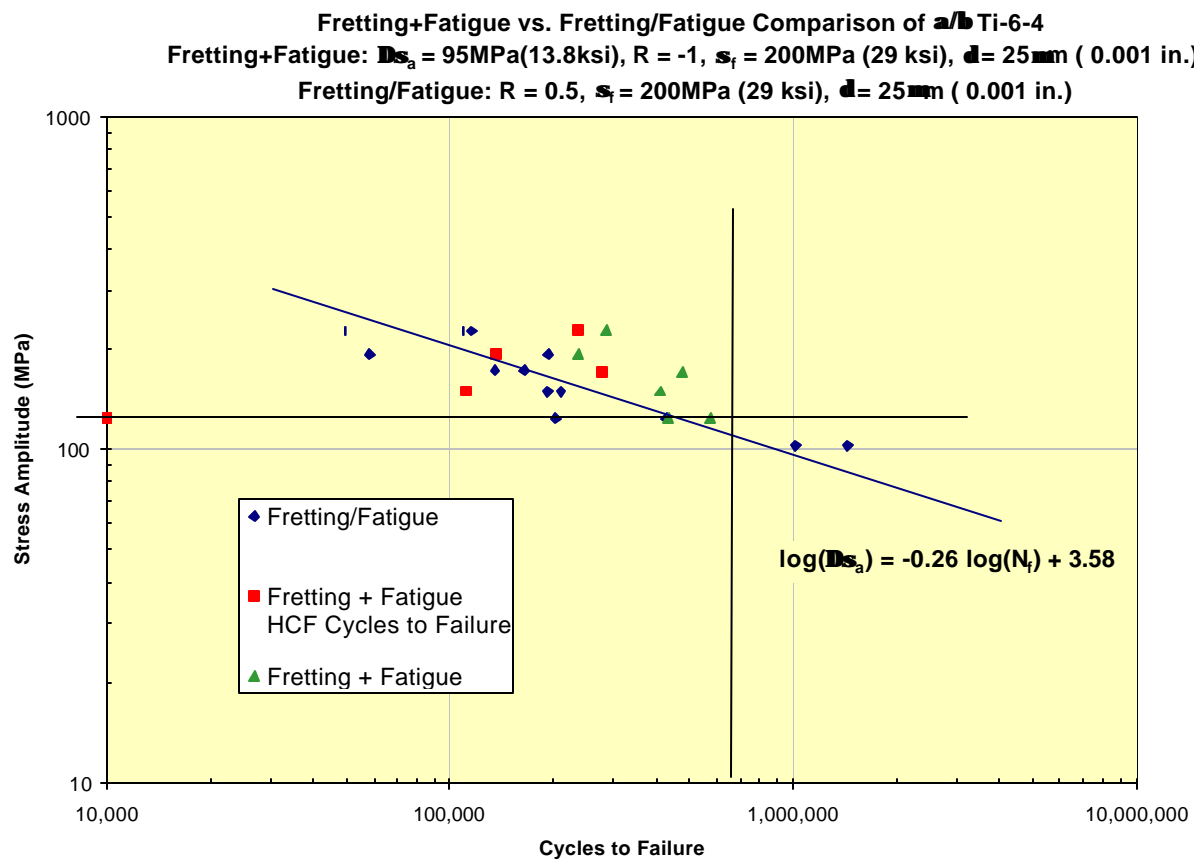
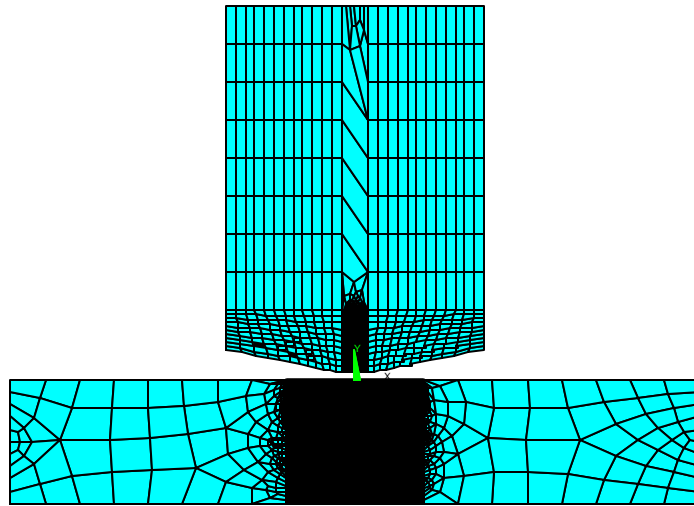
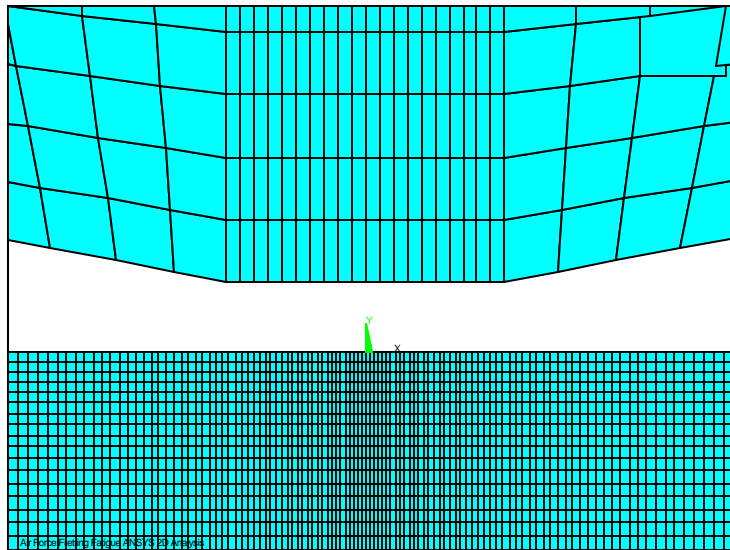


Figure 6D.15. Results of Fretting + Fatigue Testing showing comparable cyclic lives at high stress values and premature failures at lower stress.

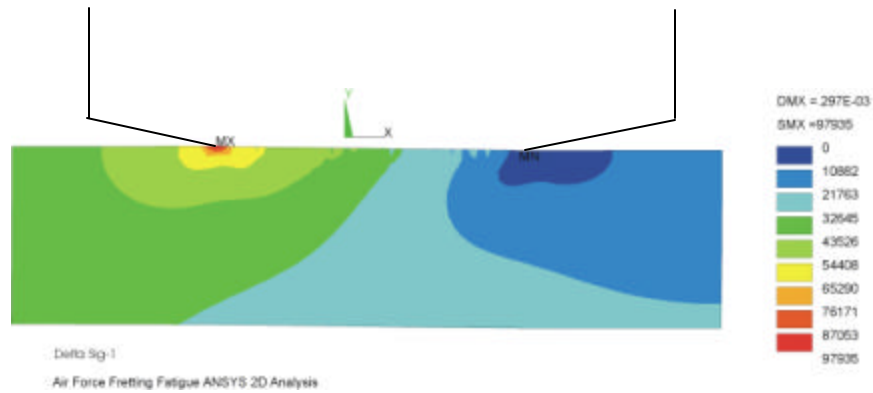


(a)

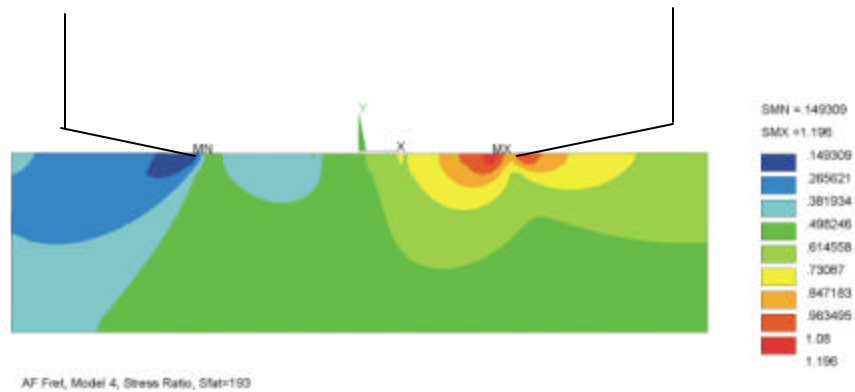


(b)

Figure 6D.16. Finite Element model used showing detail of element size under contact region (a) full model and (b) details under contact.



(a) $\Delta\sigma_p$



(b) R-Ratio

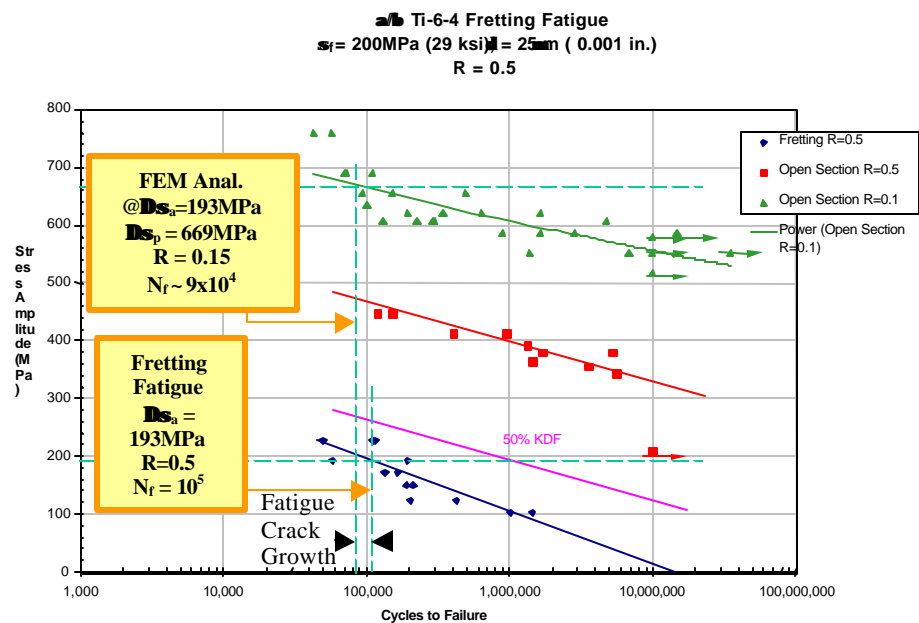


Figure 6D.17. Principal Stress Model results showing (a) iso- $\Delta\sigma_p$ plot in the region of fretting fatigue contact, (b) iso-R-ratio plot in region of fretting fatigue contact and (c) graphical comparison of model results with empirical results showing very good correlation in cycle life.

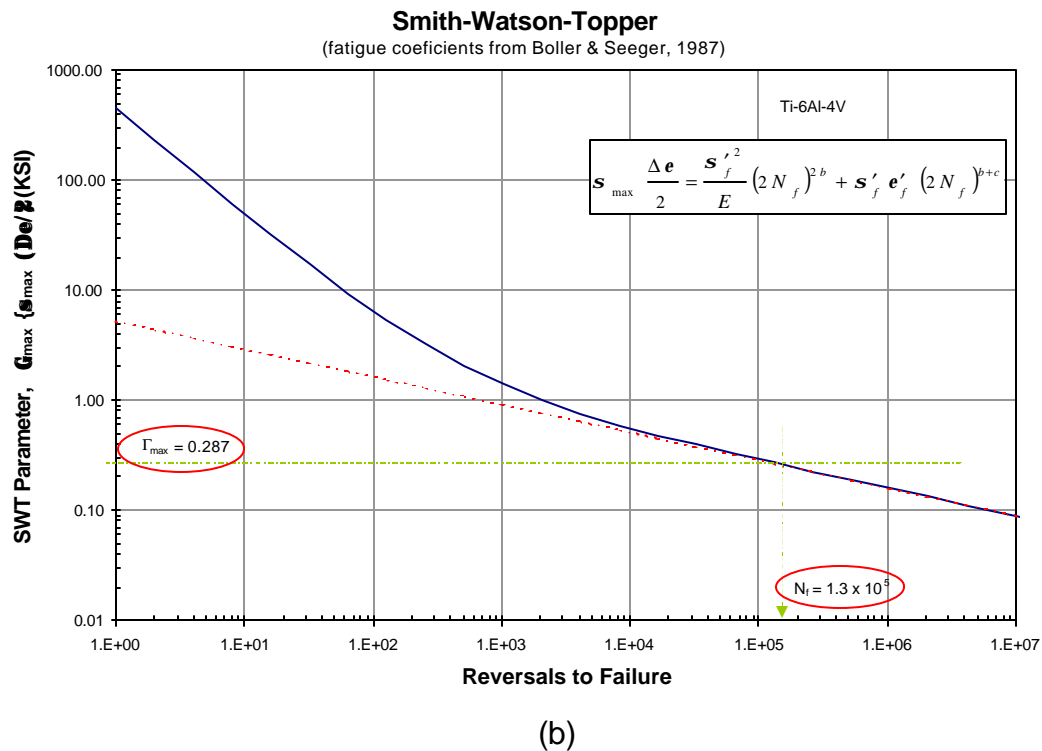
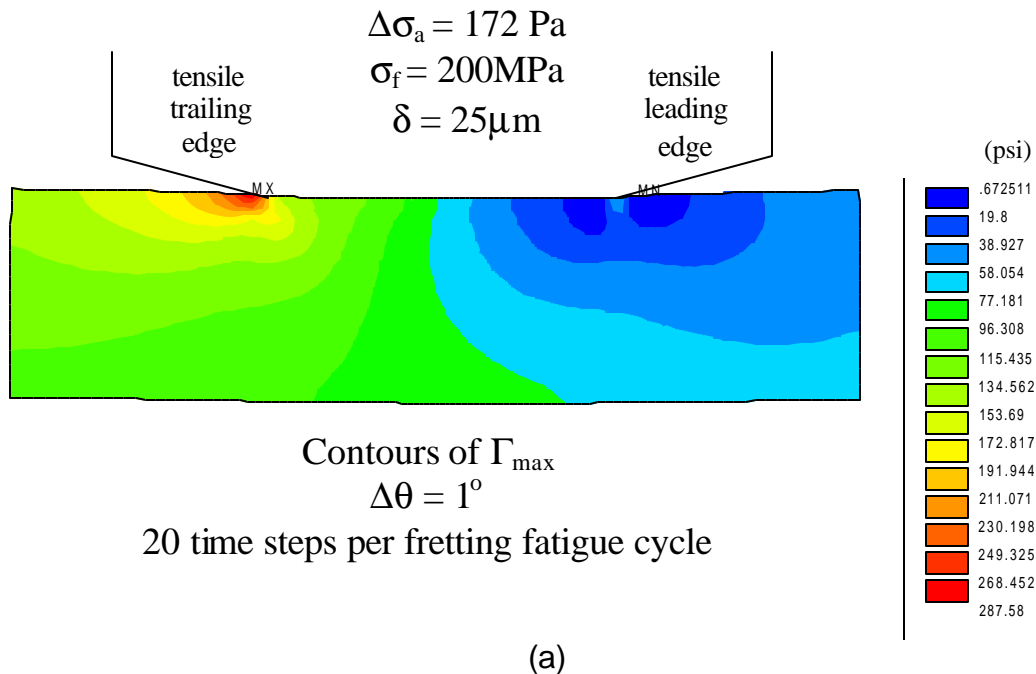


Figure 6D.18. Critical plane maximum stress model showing (a) iso- Γ_{\max} contours for full fretting/fatigue cycle and (b) Γ_{\max} vs. cycles to failure graphically depicting predicted cycle life.

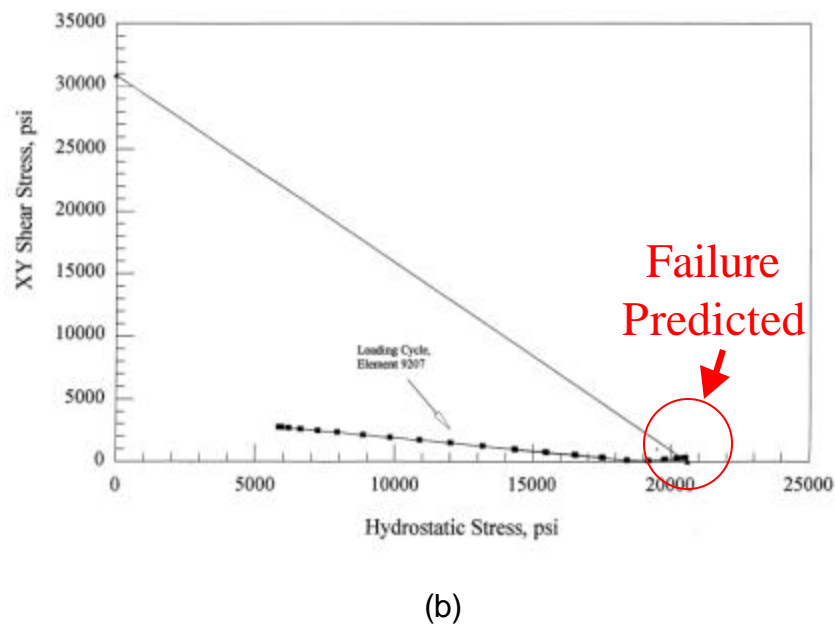
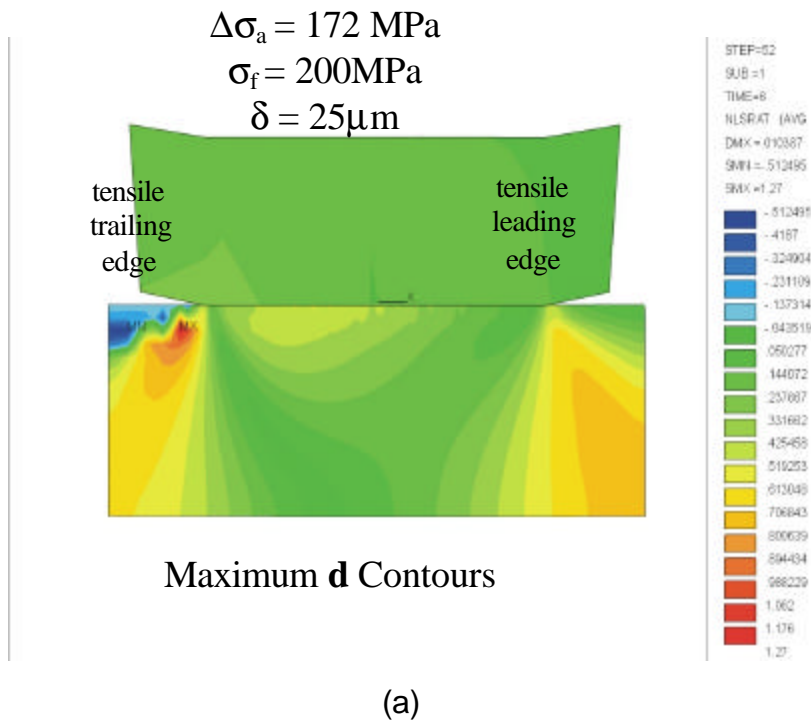


Figure 6D.19. Triaxial materials damage model showing (a) iso-**d** contours for full fretting/fatigue cycle indicatsing predicted fretting fatigue failure at sub-surface site and (b) shear stress vs. hydrostatic stress plot for element having highest **d** state showing excursion above materials damage line predicting failure.

Appendix 6E

DEVELOPMENT AND APPLICATION OF WORST CASE FRET (WCF) MODEL TO ATTACHMENT FATIGUE

**Kwai Chan
Y. D. Lee
Stephen J. Hudak, Jr.
And
David L. Davidson**



Southwest Research Institute

**Submitted
31 August 1999**

Appendix 6E

High-Cycle Fretting Fatigue

The objectives of this task are (1) to improve current understanding of the damage processes associated with high-cycle fretting fatigue in aircraft turbine engine components and to identify the most significant variables influencing the fretting fatigue damage process, (2) to develop a fracture mechanics based approach for treating high-cycle fretting fatigue, and (3) to obtain critical experimental data of fretting fatigue needed to validate engineering models.

An integrated analytical modeling/experimental approach has been used to achieve the above objectives. An improved understanding of high cycle fretting fatigue has been developed by performing metallographic and fractographic examinations of fretted Ti engine components and through discussions with engine manufacturers to identify relevant fretting mechanisms and parameters. This information, which has been reported earlier [6E.1], has been used to guide both the modeling and experimental efforts in this work.

An analytical model for treating fretting fatigue was developed first and relevant variables on high-cycle fretting fatigue failure were elucidated by parametric studies. The key fretting fatigue parameters were identified and used to design critical experiments for model verification. The experimental approach employed a kilohertz HCF fretting fatigue rig to generate critical data to verify fretting fatigue mechanisms, including crack nucleation, nonpropagation, and propagation to failure. Based on these results, a fracture mechanics-based life prediction methodology was developed for treating high-cycle fretting fatigue and verified against experimental data. This section summarizes the effort to develop this methodology for Ti compressor blades and disks.

WORST CASE FRET (WCF) CONCEPT

The approach taken to develop this life-prediction methodology, referred to as the worst case fret (WCF) methodology, is an extension of the worst case notch (WCN) concept used in foreign object damage modeling described in Appendix 5E. In notch fatigue, the limiting threshold stress for the occurrence of nonpropagation of microcracks remains a constant and does not increase with increasing stress concentration at the

notch root when a certain notch condition, i.e., the worst case notch, is exceeded. Nonpropagation of microcracks is expected to occur during fretting fatigue because of the similarity of the fretting and notch stress fields. The WCF concept envisions several damage characteristics in fretting fatigue, which are as follows:

- (1) a large stress concentration and a step stress gradient within the contact stress field;
- (2) microcracks that are initiated within the contact stresses might not propagate because of the step stress gradient.;
- (3) the life-limiting process in high-cycle fretting fatigue is the growth of microcracks;
- (4) the propagation of microcracks ceases to occur when the stress intensity range is below a crack-size-dependent threshold (see Appendix 4B).

The goal of the WCF methodology is to predict the threshold stress below which fretting fatigue cracks will not propagate after nucleation. The method requires an analysis of the contact stress field of a fretting pad acting on a flat surface. The local stress distribution within the contact zone is utilized to obtain the stress intensity factor ranges of the fretting fatigue cracks, which are subsequently used in a life prediction formulation that treats the propagation and non-propagation of mixed mode small cracks. The limiting threshold stress range for crack nonpropagation is predicted as a function of pertinent fretting fatigue conditions and material parameters. In addition to the analytical modeling effort, an experimental program was also conducted to verify the WCF concept and model predictions for Ti-6-4 at ambient temperature.

WCF MODEL DEVELOPMENT

The WCF model has been developed by considering a flat pad with round edges of radius, r , fretting on a half plane, as shown in Figure 6E.1. The flat pad is subjected to a normal load, P , and a shear force, Q , per unit thickness. In addition, a uniform stress, S , is applied in the half plane. The width of the flat region of the pad is $2b$, while the contact region is $2d$. During fretting fatigue, the shear force oscillates between a minimum, Q_{min} , and a maximum, Q_{max} , under a constant P while the bulk stress oscillates between the minimum, S_{min} , and the maximum, S_{max} . Under the combined action of the cyclic shear force, (ΔQ) , and the cyclic bulk stress, (ΔS) , a fretting fatigue

crack is envisioned to initiate at the trailing edge of the contact zone and the crack is inclined at an angle, q , from the normal to the fretting surfaces. The worst-case fret model described herein is intended to treat the nonpropagation of small cracks under the influence of the fretting stress field in the presence of a remotely applied bulk stress.

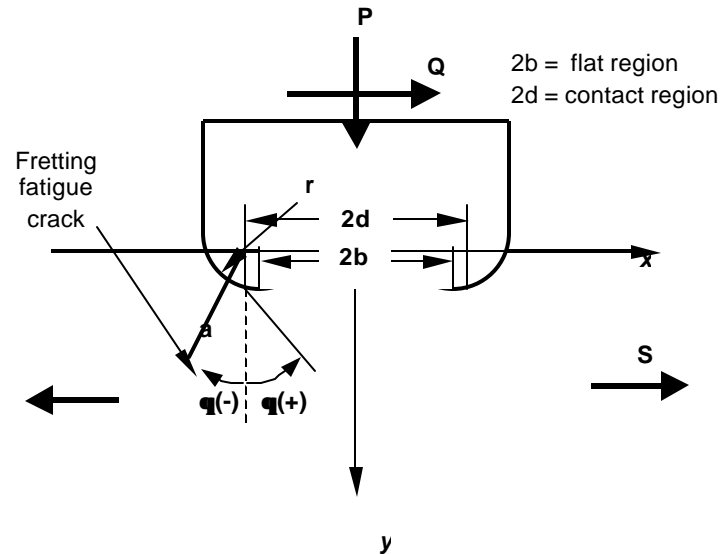


Figure 6E.1. Schematics of a flat pad with rounded edges acting on a half plane. The flat pad is subjected to a bearing load, P , and a shear force, Q , while a bulk stress, S , is applied in the half plane. A crack of length, a , and angle, q , is envisioned to initiate at the edge of the contact zone.

As summarized in Figure 6E.2, the essential features of the fracture-mechanics - based WCF model include: (1) the contact stress field, (2) K solutions for fretting-fatigue cracks, (3) a crack size-dependent threshold criterion for the growth of mixed mode cracks, and (4) a numerical procedure for computing the threshold stress for crack nonpropagation. Development of each of these components of the WCF life-prediction methodology is described in details in the next four subsections.

Worst-Case Fret Methodology

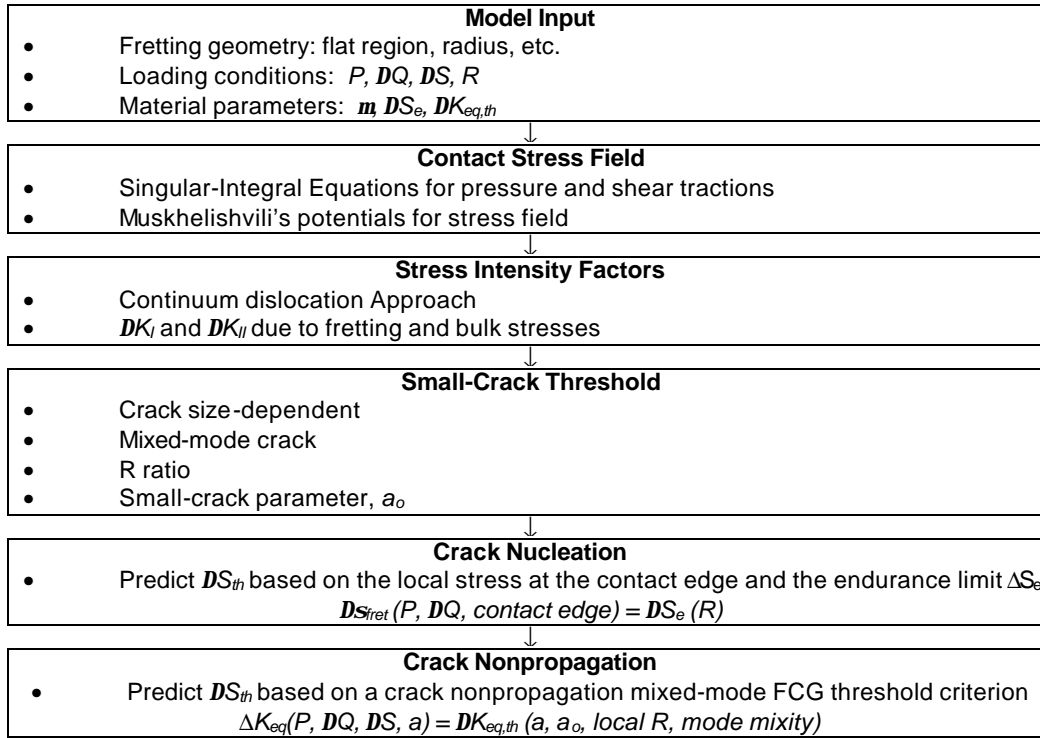


Figure 6E.2. Overview of the Worst-Case Fret (WCF) methodology for treating fretting fatigue crack nucleation, nonpropagation, and propagation to failure

Analysis of Contact Stress Field

The contact stress field for a flat pad with rounded edges acting on a half plane has been obtained using the singular-integral-equations formulation by Ciavarella, et al. [4.2]. The distributions of normal traction, $p(x)$, and shear traction, $q(x)$, on the fretting surfaces are first computed. Series expansion is then performed for $p(x)$ and $q(x)$ in terms of Chebyshev's polynomials, which are then utilized to obtain the Muskhelishvili's potential. Subsequently, the interior stress field is evaluated from the Muskhelishvili's potential using standard equations.

Normal and Tangential Tractions

The distribution of normal traction, $p(x)$, and tangential traction, $q(x)$, at a distance, x , on the contact surface of a flat pad with round edges on a half plane has been obtained by Ciavarella, et al., [4.2] using a singular-integral-equation method.

According to their analysis, the normal traction $p(x)$ can be determined from a closed form equation given by [4.2]

$$\frac{dp(f)}{P} = -\frac{2/p}{p - 2f_0 - \sin 2f_0} \left\{ (p - 2f_0) \cos f + \ln \left[\frac{\sin(f + f_0)}{\sin(f - f_0)} \right]^{\sin f} \left| \tan \frac{f + f_0}{2} \tan \frac{f - f_0}{2} \right|^{\sin f_0} \right\} \quad (6E.1)$$

where b and d are, respectively, the half-width of the flat region of the fretting pad and the half of the contact length, Figure 6E.1. The angular parameters f and f_0 are related to the distance, x , and the half-width, b , and the half contact length, d , through the transformations

$$x = b \frac{\sin f}{\sin f_0}, \quad -d \leq x \leq d \quad (6E.2)$$

and

$$d = b/\sin f_0 \quad (6E.3)$$

which are used to simplify the expression given in Eq. (6E.1). In such a mapping, f varies from $-p/2$ to $p/2$. The half contact length, d , is determined from the overall force equilibrium using the expression for the normal traction [4.2],

$$\frac{2Pr}{b^2 E^*} = \frac{p - 2f_0}{4 \sin^2 f_0} - \frac{\cot f_0}{2} \quad (6E.4)$$

where r is the radius of the round edges, P is the normal load per unit thickness, and E^* is the equivalent stiffness contributed by the pad and the semi-infinite medium. The expression for E^* is given by [4.2]

$$\frac{1}{E^*} = \frac{1 - \nu_1^2}{E_1} + \frac{1 - \nu_2^2}{E_2} \quad (6E.5)$$

where E_i and ν_i are Young's modulus and Poisson's ratio of body i , respectively. For a known value of b , the angle f_0 is obtained by solving Eq. (6E.4) numerically. The result is then used to compute the half contact length based on $\sin f_0 = b/d$. Once d is determined, the normal traction, $p(x)$, is evaluated as a function of x using Eqs. (6E.1), (6E.2) and (6E.3).

The determination of the shear traction distribution, $q(x)$, requires consideration of the stick zone and the frictional force. Such a consideration leads to a governing equation expressed in terms of a corrective tangential force, Q^* , and a corrective shear

traction, $q^*(x)$. The distribution of the corrective tangential traction $q^*(x)$ has a similar form to Eq. (6E.1). In terms of the contact length ($2d$) and the stick-zone width ($2c$), $q^*(x)$ is given by

$$\frac{mq^*(y)}{Q^*} = -\frac{2/p}{p - 2y_0 - \sin 2y_0} \left\{ (p - 2y_0) \cos y + \ln \left[\frac{\sin(y + y_0)}{\sin(y - y_0)} \right]^{\sin y} \left| \tan \frac{y + y_0}{2} \tan \frac{y - y_0}{2} \right|^{\sin y_0} \right\} \quad (6E.6)$$

with

$$Q^* = Q + mP \quad (6E.7)$$

and

$$q^*(x) = q(x) + mp(x) \quad (6E.8)$$

where c is the half-width of the stick zone, and m is the coefficient of friction. The angular parameters y and y_0 are related to x , b , and c through the transformations given by

$$x = b \frac{\sin y}{\sin y_0}, \quad -c \leq x \leq c \quad (6E.9)$$

and

$$c = b/\sin y_0 \quad (6E.10)$$

which are used to simplify Eq. (6E.6). The remotely applied tangential force Q is expressed in terms of Q^* and mP through Eq. (6E.7). The ratio of Q and mP is used to determine the half length of the stick zone c , leading to

$$\frac{|Q|}{mP} = 1 - \left(\frac{c}{d} \right)^2 \left[\frac{p - 2y_0 - \sin 2y_0}{p - 2f_0 - \sin 2f_0} \right] \quad (6E.11)$$

which is solved numerically for y_0 based on known values of b , f_0 , and the relations of $d = b/\sin f_0$ and $c = b/\sin y_0$. Once c and y_0 are determined, $q^*(x)$ is computed based on Eq. (6E.6) and then $q(x)$ is calculated via Eq. (6E.8).

Once the numerical results are determined, series expansion is performed to express $p(x)$ and $q(x)$ in terms of Chebyshev's polynomials of the second kind, $U_n(x)$, in order to evaluate Muskhelishvili's potentials for the interior stress field. This leads to

$$p(x) = -\sqrt{1-x^2} \sum_{n=0}^{\infty} b_n U_{2n}(x) \quad (6E.12)$$

$$q(x) = -\sqrt{1-x^2} \sum_{n=0}^{\infty} d_n U_{2n}(x) \quad (6E.13)$$

where b_n and d_n are Chebyshev's coefficients. Using the orthogonality condition of

$$\frac{1}{\rho} \int_{-1}^1 U_j(x) U_k(x) \sqrt{1-x^2} dx = \begin{cases} 0 & , j \neq k \\ \frac{1}{2} & , j = k \end{cases} \quad (6E.14)$$

the coefficients b_n and d_n are obtained as

$$b_n = -\frac{2}{\rho} \int_{-1}^1 \rho(x) U_{2n}(x) dx \quad (6E.15)$$

$$d_n = -\frac{2}{\rho} \int_{-1}^1 q(x) U_{2n}(x) dx \quad (6E.16)$$

both of which are evaluated using the Gauss-Chebyshev numerical integration scheme and the trigonometric expression for Chebyshev's polynomials of the second kind of order n , $U_n(x) = \sin[(n+1)\cos^{-1} x] / \sin(\cos^{-1} x)$ [6E.3].

Muskhelishvili's Potentials

Muskhelishvili's potential in terms of normal traction is given by [4.4]

$$\Phi(z) = \frac{1}{2\pi i} \int_{-1}^1 \frac{\rho(t)}{t-z} dz \quad (6E.17)$$

where $z = x+iy$ is a complex variable used to signify the location of interest (x,y) . Using the series expansion form of $\rho(t)$ in terms of the Chebyshev's polynomials, the corresponding Muskhelishvili's potential becomes [4.4]

$$\Phi(z) = -\frac{i}{2} \sum_{n=0}^{\infty} b_n R_{2n+1}(z) \quad (6E.18)$$

where

$$R_n(z) = \left(z - \sqrt{z^2 - 1} \right)^n \quad (6E.19)$$

Similarly, the Muskhelishvili's potential, $\Psi(z)$, for the tangential traction $q(x) = \rho(x) - q^*(x)$ is given by [4.4]

$$\Psi(z) = \frac{1}{2\pi i} \int_{-1}^1 \frac{q(t)}{t-z} dz \quad (6E.20)$$

which can be determined using the coefficients derived from the series expansion of Chebyshev's polynomials for $q(x)$, leading to

$$\Psi(z) = -\frac{i}{2} \sum_{n=0}^{\infty} d_n R_{2n+1}(z) \quad (6E.21)$$

with $R_{2n+1}(z)$ given by Eq. (6E.19) after substituting $n+1$ for n . When evaluating the potentials, the number of terms required for the expansion is determined by a least-square analysis that minimizes the error of the expansion against the actual traction distribution.

Interior Stress Field

The stress components for the symmetric Muskhelishvili's potential are given by [4.4]

$$\begin{aligned} s_x &= 2 \operatorname{Re}[\Phi(z)] - 2y \operatorname{Im}[\Phi'(z)] \\ s_y &= 2 \operatorname{Re}[\Phi(z)] + 2y \operatorname{Im}[\Phi'(z)] \\ t_{xy} &= -2y \operatorname{Re}[\Phi'(z)] \end{aligned} \quad (6E.22)$$

and the stress components for the skew-symmetric potential are [4.4]

$$\begin{aligned} s_x &= y \operatorname{Re}[Z'(z)] + 2 \operatorname{Im}[Z(z)] \\ s_y &= -y \operatorname{Re}[Z'(z)] \\ t_{xy} &= \operatorname{Re}[Z(z)] - y \operatorname{Im}[Z'(z)] \end{aligned} \quad (6E.23)$$

where Re and Im indicate the real and imaginary parts of a complex function, respectively; $Z'(z)$ is the first derivative of the complex function $Z(z)$, and $Z(z) = y'(z)$. The fretting stress field is the sum of the symmetric components, which are due to $p(x)$, and the skew-symmetric components, which are due to $q(x)$.

Benchmark of Contact Stress Model

The contact stress field algorithm developed at SwRI was benchmarked against results from Purdue University and those by Ciavarella, et al. [4.2]. Figure 6E.3 shows a comparison of SwRI's and Purdue's calculations of the pressure distribution under a flat pad subjected to a bearing pressure of 35 ksi. Purdue's result, which was supplied by Professor Thomas Farris, was obtained using an integral-equation method that was verified previously by FEM results [4.5]. The calculations by SwRI and Purdue, which

are essentially identical, show pressure peaks at the contact edges. Pressure distributions reported in the literature [4.2, 4.5] for other pad geometries were also reproduced by SwRI.

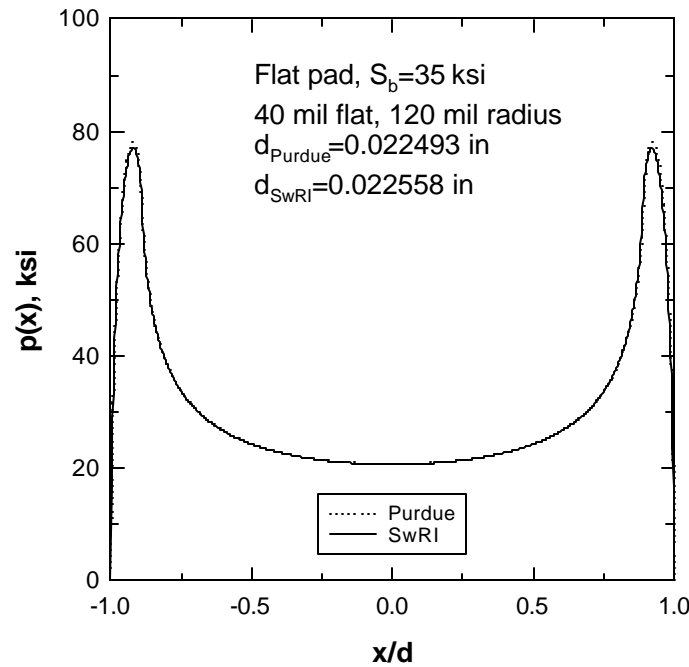


Figure 6E.3. Comparison of pressure distributions obtained by SwRI and Purdue University for fretting of a 40 mil flat pad subjected to a 35 ksi bearing pressure.

Interior stress field calculations were benchmarked by comparing stress contour plots, shown in Figure 6E.4, for a contact problem whose results are available from Ciavarella, et al. [6E.2]. Using reported fretting conditions, stress contour plots reported by Ciavarella, et al. [4.2], were reproduced by the contact stress algorithm developed at SwRI. These results are shown in Figure 6E.4 and they correspond to the results shown in Figure 4 in Ciavarella, et al. [6E.2].

$$b/d=0.8, \mu=0.3, \nu=0.3$$

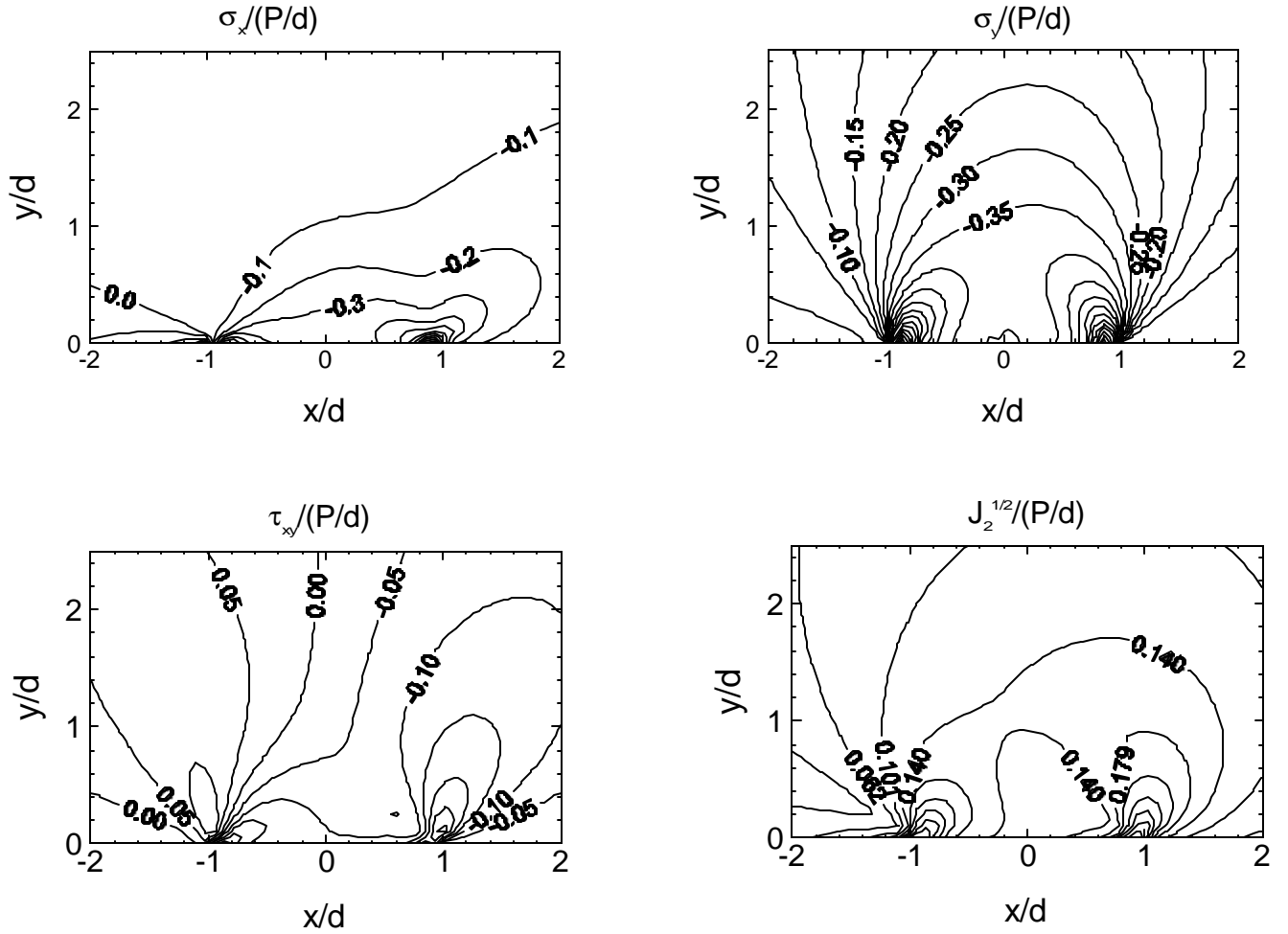


Figure 6E.4. Contour plots show the fretting stress field of a flat pad with rounded edges subjected to a compressive load, P , where P is load per unit thickness, over a contact region, d . The stresses (σ_x , σ_y , and τ_{xy}) and $J_2^{1/2}$, where J_2 is the second invariant of the deviatoric stress, are normalized by the average bearing pressure, P/d . The SwRI stress contours are in agreement with those reported by Ciavarella, et al. [4.2].

Development of Stress Intensity Factor Solutions

Figure 6E.5 shows a slant, through-thickness, surface-breaking edge crack of length a in the \hat{x} and \hat{y} coordinate system. The crack is inclined at an angle θ measured from the x -axis of the xy coordinate system, where x is taken to lie normal and y is parallel to the free surface. The slant crack is subjected to normal and shear stresses applied in the xy plane. The stress intensity factors of the slant edge crack

have been obtained using the stress field of a dislocation with edge and screw characters of the Green's function. The mixed-mode crack is modeled as a continuous distribution of continuum dislocations. Imposing the condition of a traction-free crack surface leads to a set of singular-integral-equations that are solved numerically to obtain the K solutions.

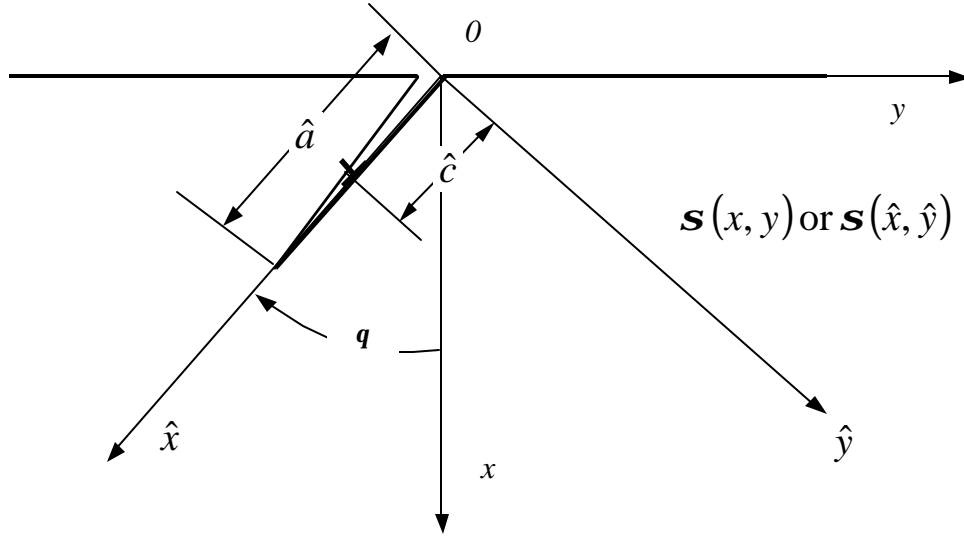


Figure 6E.5. Configuration of a slant edge crack subjected to a stress field $s(x,y)$.

Stress Field of a Continuum Dislocation

As summarized by Nowell and Hills [4.6], the stress field of a continuum dislocation with the Burgers vector located at $(\hat{c}, 0)$ in the $\hat{x} \hat{y}$ coordinate is given by

$$t_{\hat{x}\hat{y}} = \frac{m^*}{p(k+1)} [b_{\hat{x}} K_{\hat{x}}^S(\hat{x}, \hat{c}) + b_{\hat{y}} K_{\hat{y}}^S(\hat{x}, \hat{c})] \quad (6E.24)$$

$$s_{\hat{y}} = \frac{m^*}{p(k+1)} [b_{\hat{x}} K_{\hat{x}}^N(\hat{x}, \hat{c}) + b_{\hat{y}} K_{\hat{y}}^N(\hat{x}, \hat{c})] \quad (6E.25)$$

where μ^* is the shear modulus; $\kappa = 3-4\nu$ in plane strain; ν is Poisson's ratio; $b_{\hat{x}}$ and $b_{\hat{y}}$ are the components of the unit Burgers vector resolved in \hat{x} and \hat{y} directions. The functions $K_{\hat{x}}^S, K_{\hat{y}}^S, K_{\hat{x}}^N$, and $K_{\hat{y}}^N$ are given by [6E.7]

$$\begin{aligned}
K_x^S &= \frac{\sin 2q}{2} [(G_{xxx} \cos q - G_{yxx} \sin q) - (G_{xyy} \cos q - G_{yyy} \sin q)] + \cos 2q (G_{xxy} \cos q - G_{yxy} \sin q) \\
K_y^S &= \frac{\sin 2q}{2} [(G_{xxx} \sin q + G_{yxx} \cos q) - (G_{xyy} \sin q + G_{yyy} \cos q)] + \cos 2q (G_{xxy} \sin q + G_{yxy} \cos q) \\
K_x^N &= \frac{1}{2} [(G_{xxx} \cos q - G_{yxx} \sin q) + (G_{xyy} \cos q - G_{yyy} \sin q)] - \\
&\quad \frac{\cos 2q}{2} [(G_{xxx} \cos q - G_{yxx} \sin q) - (G_{xyy} \cos q - G_{yyy} \sin q)] + \sin 2q (G_{xxy} \cos q - G_{yxy} \sin q) \quad (6E.26) \\
K_y^N &= \frac{1}{2} [(G_{xxx} \sin q + G_{yxx} \cos q) + (G_{xyy} \sin q + G_{yyy} \cos q)] - \\
&\quad \frac{\cos 2q}{2} [(G_{xxx} \sin q + G_{yxx} \cos q) - (G_{xyy} \sin q + G_{yyy} \cos q)] + \sin 2q (G_{xxy} \sin q + G_{yxy} \cos q)
\end{aligned}$$

where G_{ijk} , the Green's functions of an unit dislocation [6E.7], are given by Dundars and Sendeckyj [6E.7].

Singular-Integral-Equations Representation of a Mixed-Mode Crack

For a slant, traction-free, crack originated from (0,0) of an angle q , the total normal and tangential tractions can be expressed in terms of a continuous distribution of continuum dislocations with Burgers vectors of densities $B_{\hat{x}}(\hat{c})$ and $B_{\hat{y}}(\hat{c})$ varying along the crack surface. Imposing the condition of a traction-free crack surface results in a set of dual singular integral equations with Cauchy kernels with unknown functions $B_{\hat{x}}(\hat{c})$ and $B_{\hat{y}}(\hat{c})$, which are given by [6E.6]

$$s_S(\hat{x}) + \frac{m^*}{p(k+1)} \int_0^{\hat{a}} [B_{\hat{x}}(\hat{c}) K_{\hat{x}}^S(\hat{x}, \hat{c}) + B_{\hat{y}}(\hat{c}) K_{\hat{y}}^S(\hat{x}, \hat{c})] d\hat{c} = 0 \quad (6E.27)$$

$$s_N(\hat{x}) + \frac{m^*}{p(k+1)} \int_0^{\hat{a}} [B_{\hat{x}}(\hat{c}) K_{\hat{x}}^N(\hat{x}, \hat{c}) + B_{\hat{y}}(\hat{c}) K_{\hat{y}}^N(\hat{x}, \hat{c})] d\hat{c} = 0$$

where \hat{a} is the crack length, and s_S and s_N are the tangential and normal traction of the uncracked body.

A standard procedure established by Erdogan, et al., [6E.8] has been used for solving the dual singular integral equations numerically. A normalization procedure with variables given by

$$u = \frac{2\hat{c}}{\hat{a}} - 1, v = \frac{2\hat{x}}{\hat{a}} - 1, -1 \leq u \leq 1 \text{ and } -1 \leq v \leq 1 \quad (6E.28)$$

is first applied to Eq. (6E.27). The singularity is then extracted by writing the solutions for $B_{\hat{x}}(u)$ and $B_{\hat{y}}(u)$ in terms of bounded functions $f_{\hat{x}}(u)$ and $f_{\hat{y}}(u)$ and a fundamental function, leading to

$$B_{\hat{x}}(u) = f_{\hat{x}}(u)(1-u)^{-1/2}(1+u)^{1/2}, B_{\hat{y}}(u) = f_{\hat{y}}(u)(1-u)^{-1/2}(1+u)^{1/2} \quad (6E.29)$$

which are substituted into Eq. (6E.27). Applying the Gauss-Jacobi quadrature to the dual integral equations, the discretization process leads one to a system of equations that can be easily solved numerically. These equations are given by

$$-s_S(v_k) = \frac{m}{p(k+1)} \cdot \frac{2p}{2n+1} \cdot \frac{\hat{a}}{2} \sum_{i=1}^n (1+u_i) [f_{\hat{x}}(u_i) K_{\hat{x}}^S(v_k, u_i) + f_{\hat{y}}(u_i) K_{\hat{y}}^S(v_k, u_i)] \quad (6E.30)$$

$$-s_N(v_k) = \frac{m}{p(k+1)} \cdot \frac{2p}{2n+1} \cdot \frac{\hat{a}}{2} \sum_{i=1}^n (1+u_i) [f_{\hat{x}}(u_i) K_{\hat{x}}^N(v_k, u_i) + f_{\hat{y}}(u_i) K_{\hat{y}}^N(v_k, u_i)]$$

where

$$u_i = \cos\left(\frac{2i-1}{2n+1}p\right), i = 1, \dots, n$$

$$v_k = \cos\left(\frac{2k}{2n+1}p\right), k = 1, \dots, n \quad (6E.31)$$

which give $2n$ simultaneous equations in the $2n$ unknowns, $f_{\hat{x}}(u_i)$ and $f_{\hat{y}}(u_i)$.

Stress Intensity Factors

The stress intensity factors, K_I and K_{II} , are related to the bounded functions, $f_{\hat{x}}(u)$ and $f_{\hat{y}}(u)$, according to [4.9]

$$K_I = 2\sqrt{2p\hat{a}} \frac{m^*}{k+1} f_{\hat{x}}(1), K_{II} = 2\sqrt{2p\hat{a}} \frac{m^*}{k+1} f_{\hat{y}}(1) \quad (6E.32)$$

where $f_{\hat{x}}(1)$ and $f_{\hat{y}}(1)$ are $f_{\hat{x}}(u)$ and $f_{\hat{y}}(u)$ evaluated at the crack tip ($u=1$), respectively. Since the function values of $f_{\hat{x}}(u)$ and $f_{\hat{y}}(u)$ are evaluated only at the integration points, an extrapolation procedure is required to evaluate the function values at the crack. An extrapolation procedure has been developed by Krenk [4.9], yielding

$$f_{\hat{x}}(1) = \frac{2}{2n+1} \sum_{i=1}^n \cot\left(\frac{2i-1}{2n+1} \cdot \frac{p}{2}\right) \cdot \sin\left[\frac{n}{2n+1}(2i-1)p\right] f_{\hat{x}}(u_i)$$

$$f_{\hat{y}}(1) = \frac{2}{2n+1} \sum_{i=1}^n \cot\left(\frac{2i-1}{2n+1} \cdot \frac{p}{2}\right) \cdot \sin\left[\frac{n}{2n+1}(2i-1)p\right] f_{\hat{y}}(u_i) \quad (6E.33)$$

which are used in conjunction with Eq. (6E.32) to compute K_I and K_{II} . Converged solutions are obtained for almost all cases examined in this study. However, care must be taken when the traction distributions are not continuously well-behaved such as an impulse function. This situation occurs when the fretting fatigue crack is very long. Under this circumstance, poor convergence or non-convergence of K solutions may occur and a different solution is required. Eq. (6E.33) is more than adequate for the range of crack lengths considered in this study.

Benchmarking the K-Solution Algorithm

The K-solution for a fretting crack emanated from the contact edge of a 40 mil flat pad with 120 mil radius edges was analyzed for a bearing pressure of 35 ksi and a shear traction of $0.8 \mu P$ or $-\mu P$. The K_I and K_{II} for a perpendicular crack ($\theta = 0^\circ$) were calculated and the results are shown as solid lines in Figure 6E.6. K-solutions for the same fretting crack geometry were independently obtained by Professor Farris' group at Purdue University. The Purdue results are shown as dotted lines in Figure 6E.6, which shows that almost identical results are obtained by Purdue and SwRI.

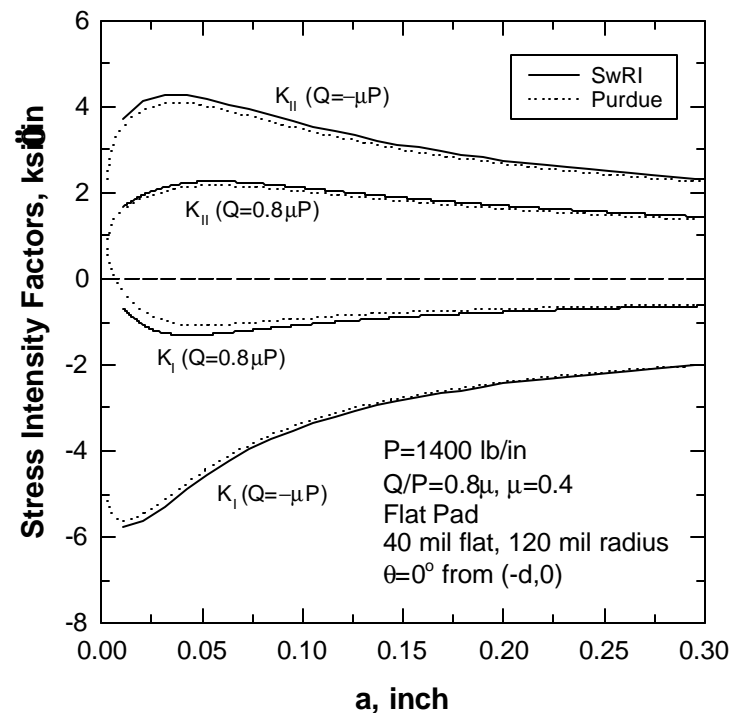


Figure 6E.6. Comparison of stress intensity factors obtained at SwRI and Purdue University for a perpendicular fretting crack ($\theta = 0^\circ$) subjected to a bearing pressure of 35 ksi and a Q/P ratio of either 0.8μ or $-\mu$

The K-solution algorithm described in Section 4.2.2.3 was utilized to compute stress intensity factor (SIF) solutions for fretting under a flat pad for various bearing pressures and crack angles. Several pad geometries were investigated, including: (1) a 40 mil flat pad with 120 mil radius edges, (2) a 120 mil flat pad with 120 mil radius edges, (3) a cylindrical pad with 120 mil radius, and (4) a cylindrical pad with 1 inch radius. The SIF results were normalized to develop analytical expressions and boundary correction factors. Analysis of the SIF results indicates that for fretting with a bulk tension, S , the stress intensity factors of a crack of length, a , and angle, θ , that is subjected to a bearing load, P , and a shear force, Q , per unit thickness can be described by

$$K_I = f_1(\mathbf{q}, a/d)P\sqrt{\frac{p}{a}} + f_2(\mathbf{q}, a/d)Q\sqrt{\frac{p}{a}} + F_1(\mathbf{q})S\sqrt{pa} \quad (6E.34)$$

and

$$K_{II} = f_3(\mathbf{q}, a/d)P\sqrt{\frac{p}{a}} + f_4(\mathbf{q}, a/d)Q\sqrt{\frac{p}{a}} + F_2(\mathbf{q})S\sqrt{pa} \quad (6E.35)$$

where $f_i(\mathbf{q}, a/d)$ are the boundary correction factors for the angled crack subjected to the P and Q forces and $F_i(\mathbf{q}, a)$ are boundary correction factors for the angled crack subjected to the bulk stress S .

The boundary correction factors are function of the crack angle, θ , and the ratio of crack length, a , to the half contact length, d . Figure 6E.7 presents the results for the boundary correction factors, f_i , for the 40 mil flat and with 120 mil radius edges subjected to a bearing pressure of 35 ksi. The crack angles are 0° , -25° , -45° , and 45° . The results clearly indicate that f_1 , f_2 , f_3 , and f_4 depend on the crack angle, \mathbf{q} . For a given \mathbf{q} , f_i varies with a/d but becomes a constant when $a/d > 10$, which is the results given for an edge crack subjected to point loads P and Q [4.10]. Thus, the fretting loads P and Q behave like point loads and the SIFs decrease with increasing crack lengths when the crack length is larger than five times the contact length.

The boundary correction factors f_i are independent of bearing pressure, S_b , with $S_b = Pb$, when the results are normalized by the a/d ratio. Figure 6E.8 shows a comparison of the f_i results for bearing pressures of 35 ksi and 65 ksi. Identical results were obtained for both cases. The half contact length, however, increases with increasing bearing pressure, as shown in Figure 6E.9. The results in Figure 6E.8 and 6E.9

allow the SIFs for a fretting crack of a given crack angle to be calculated for various bearing pressures by using the appropriate a/d and d values.

The boundary correction factors F_i for an angled edge crack subjected to a remote tension, S , in a semi-infinite plate are presented in Figure 6E.10. In this case, F_i depends only on the crack angle but not the crack length because the crack lies in a semi-infinite plate. The solutions for F_1 and F_2 become those of an edge crack in a semi-infinite plate when $\theta = 0$.

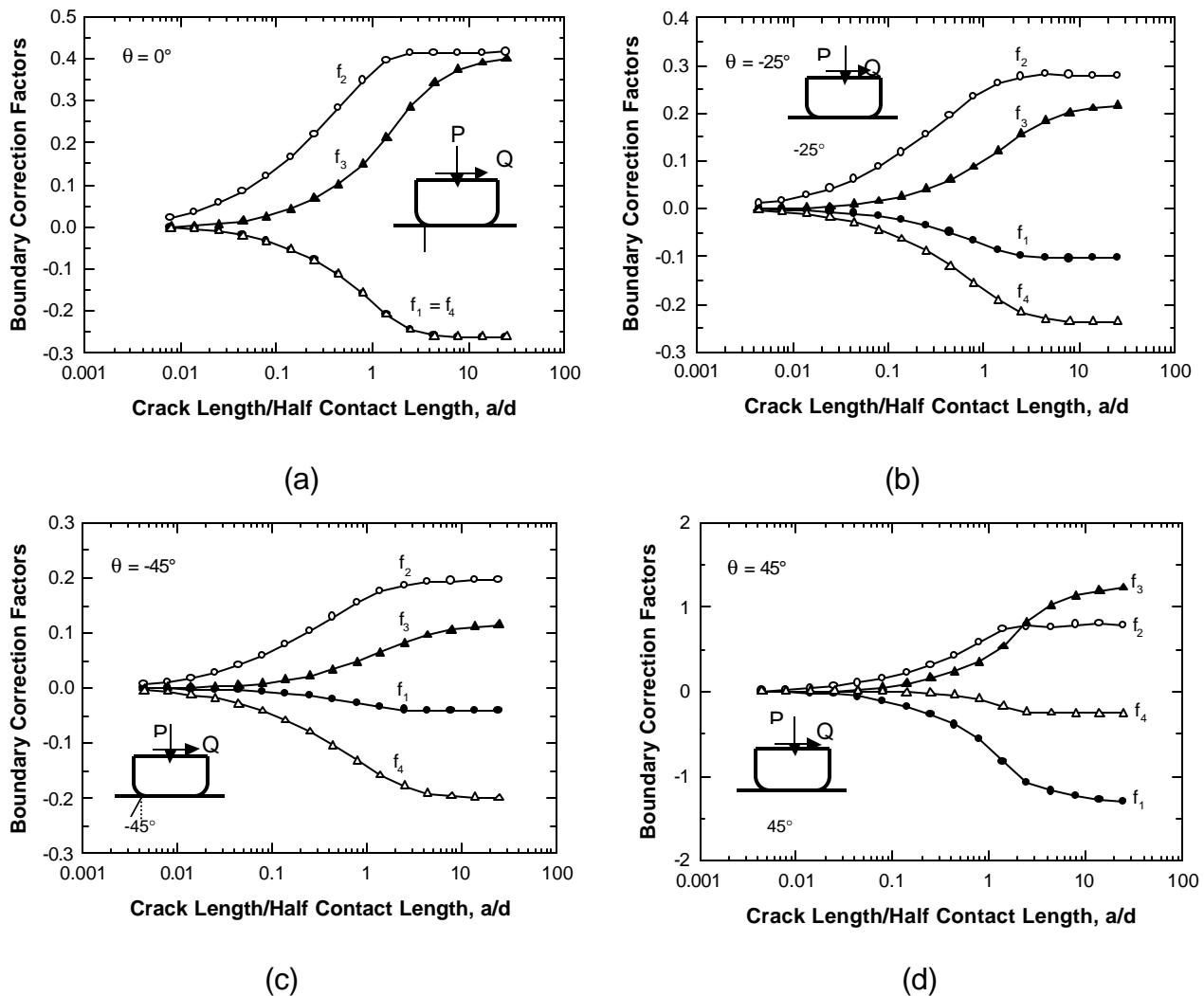


Figure 6E.7. Boundary correction factors ($= SIF / P \sqrt{\pi a}$ with $Q = mP$ and $m = 0.5$) as a function of crack length, a , normalized by the half length, d , of the contact zone for various crack orientation subjected to a 35 ksi bearing pressure: (a) $q = 0^\circ$ (perpendicular crack), (b) $q = -25^\circ$, (c) $q = -45^\circ$, and (d) $q = 45^\circ$.

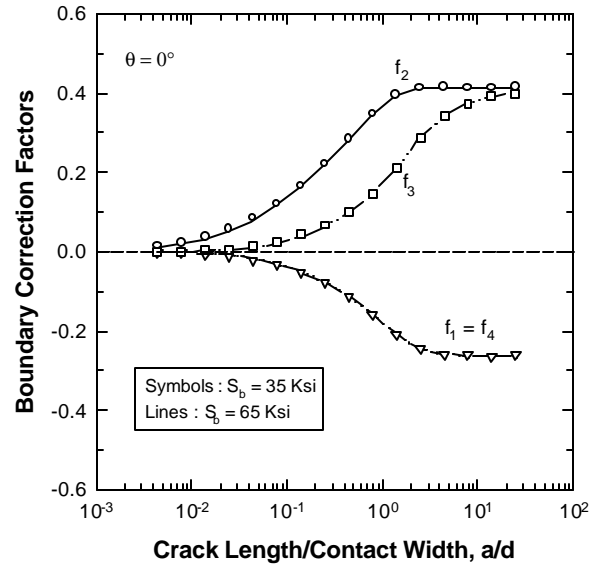


Figure 6E.8. Boundary correction factors ($= SIF / P \ddot{O}p/a$ with $Q = mP$ and $m = 0.5$) as a function of crack length, a , normalized by the half length, d , of the contact zone of a perpendicular crack ($q = 0^\circ$) subjected to a bearing pressure of 35 or 65 ksi. The boundary correction factors are independent of bearing pressure in this normalized plot.

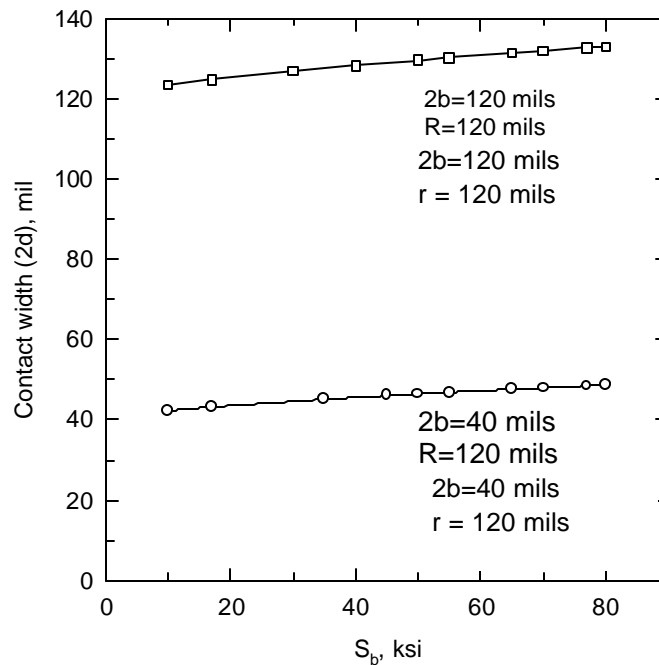


Figure 6E.9. Calculated width ($2d$) of the contact zone as a function of bearing pressure for 40 mil pad and 120 mil pad.

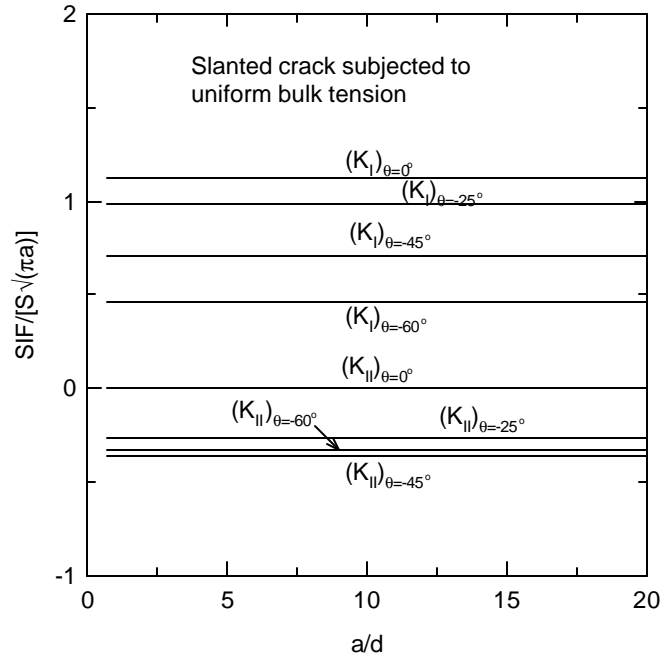


Figure 6E.10. Boundary correction factors ($= SIF / S \sqrt{\pi a}$) for an angled crack in a semi-infinite plate subjected to a bulk stress, S , and crack length, a .

Mixed-Mode Threshold Stress Intensity for Small Cracks

Fatigue cracks that propagate within the fretting stress field are subjected to normal and shear stresses. As a result, fretting fatigue cracks are mixed-mode cracks whose arrest is affected by mode mixity. Mixed-mode fatigue crack growth threshold were determined by Campbell, et al. [6E.11], for large cracks in Ti-6Al-4V at ambient temperature as parts of the MURI HCF program. Their results indicate that the mixed-mode threshold, measured in terms of DG_{th} or an equivalent $DK_{eq,th}$ defined in terms of DG_{th} , is increased when DK_{II} is increased. In general, DG_{th} or $DK_{eq,th}$ should be a function of the stress ratio, R , and mode mixity. The results obtained by Campbell, et al. [6E.11], have been analyzed and fitted to an empirical relation of the form given by

$$\Delta K_{eq,th} = \Delta K_{I,th} [c_1 + (1 - c_1) \exp(-c_2 b)]$$

with

$$c_1 = \frac{\Delta K_{II,th}}{\Delta K_{I,th}} \quad (6E.36)$$

and

$$b = \tan^{-1} \left| \frac{\Delta K_{II}}{\Delta K_I} \right|$$

where $DK_{eq,th}$ is equivalent DK threshold and b is the phase angle (in degrees) for the mixed-mode crack; $DK_{I,th}$ is the threshold of the Mode I large crack; c_1 is the ratio of the Mode I threshold to the Mode II threshold, $DK_{II,th}$; and c_2 is an empirical constant. Since $DK_{I,th}$ is a function of the stress ratio, $DK_{eq,th}$ depends on both the stress ratio, R , and the phase angle, b . The $DK_{eq,th}$ for Ti-6Al-4V at ambient temperature is given by

$$\Delta K_{eq,th}(ksi\sqrt{in}) = (3.973 - 2.206R)[1.50 - 0.5 \exp(-0.0418b)] \quad (6E.37)$$

since $c_1 = 1.5$, $c_2 = 0.0418 \text{ degree}^{-1}$, and $DK_{I,th} = 3.973 - 2.206R \text{ ksi}\sqrt{in}$, based on fitting of Eq. (6E.36) to experimental data. Figure 6E.11 shows a comparison of Eq. (6E.37) against experimental data from Campbell, et al. [6E.11].

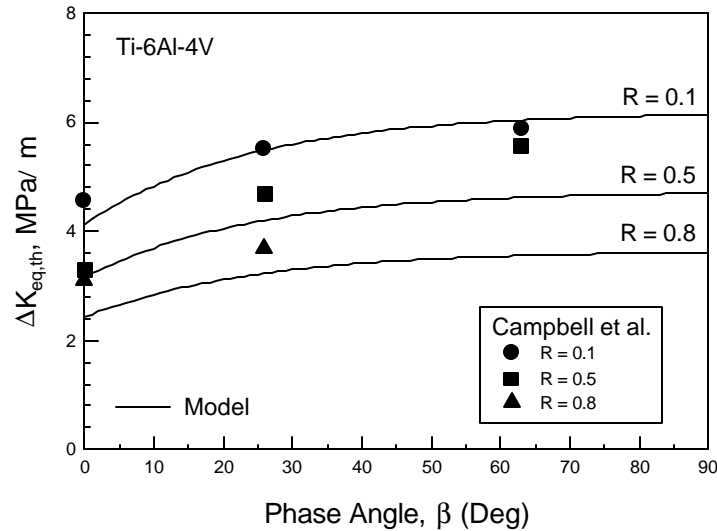


Figure 6E.11. Experimental data of equivalent stress intensity threshold, $DK_{eq,th}$, for mixed-mode large crack from Campbell, et al. [4.11] fitted to an empirical model that is a function of the stress ratio, R , and the phase angle, b , of mode mixity.

For mixed-mode small cracks, the growth threshold is taken to exhibit a crack-size dependence, following the development in Section 2, given by

$$\Delta K_{eq,th}^{SC}(a) = \Delta K_{eq,th} \sqrt{\frac{a}{a + a_0}} \quad (6E.38)$$

where the equivalent threshold, $\Delta K_{eq,th}$, for the mixed-mode large crack, Eq. 6E.37, is taken to be independent of crack length and the small-crack parameter, a_0 , which is defined as

$$a_0 = \frac{1}{p} \sqrt{\frac{\Delta K_{I,th}}{F_1 \Delta S_e}} \quad (6E.39)$$

and relates the large crack Mode I threshold to the endurance limit, ΔS_e . Combining Eqs. (6E.36) and (6E.38) leads to

$$\Delta K_{eq,th}^{SC} = \Delta K_{I,th} [c_1 + (1 - c_1) \exp(-c_2 b)] \sqrt{\frac{a}{a + a_0}} \quad (6E.40)$$

or more precisely,

$$\Delta K_{eq,th}^{SC} (ksi\sqrt{in}) = (3.973 - 2.206R) [1.50 - 0.5 \exp(-0.0418b)] \sqrt{\frac{a}{a + a_0}} \quad (6E.41)$$

as the FCG threshold expression for a mixed-mode small crack in Ti-6-4 at ambient temperature.

Computation of Threshold Stress for Nonpropagating Fretting Fatigue Cracks

The nonpropagation of a mixed-mode fretting fatigue crack is predicted on the basis that the driving force for the crack growth is equal to the fatigue crack growth threshold. The driving force of the mixed-mode crack is taken to be the equivalent stress intensity range, ΔK_{eq} , which is a function of the cyclic normal load (ΔP), cyclic shear force (ΔQ), cyclic bulk stress (ΔS), and crack length (a). The corresponding FCG threshold for the mixed-mode crack is $\Delta K_{eq,th}$, which is a function of, a , the small-crack parameter (a_0), the stress ratio (R), and the phase angle, b . The governing equation for determining the threshold stress for crack nonpropagation is given by

$$\Delta K_{eq}(\Delta P, \Delta Q, \Delta S, a) = \Delta K_{eq,th}^{SC}(a, a_0, R, b) \quad (6E.42)$$

which is solved numerically to obtain the threshold stress range, ΔS_{th} . The numerical procedure for computing the threshold stress, ΔS_{th} , includes the following steps:

- Step (1) Using the procedure described in the earlier section, evaluate the stress intensity factors due to fretting only, i.e., $K_{I,max}^{fret}$, $K_{I,min}^{fret}$, $K_{II,max}^{fret}$, and $K_{II,min}^{fret}$. The subscripts *max* and *min* indicate maximum and minimum stress intensity factors, and the superscript *fret* signifies fretting. The normal force, P , is

kept constant while the tangential force, Q , oscillates between Q_{max} and Q_{min} that,

- Step (2) Determine the normalized stress intensity factors, F_i , due to the remote bulk tension, S . The remote bulk tension cycles between S_{max} and S_{min} .

Start the iteration for solution of DS_{th} with an initial guess for the maximum bulk tension, $S_{max}^{(i)}$.

- Step (3) Evaluate the minimum bulk tension based on a prescribed, constant global stress ratio, R_G , which is defined as $R_G = S_{min}^{(i)} / S_{max}^{(i)}$.

- Step (4) Using the normalized quantities defined in Step (2), compute the corresponding stress intensity factors with any given crack length due to the remote bulk tension, i.e., $K_{I,max}^{bulk}$, $K_{I,min}^{bulk}$, $K_{II,max}^{bulk}$, and $K_{II,min}^{bulk}$.

- Step (5) Evaluate the stress intensity factors for fretting fatigue by combining the components resulting from fretting and bulk tension.

$$\begin{aligned} K_{I,max} &= K_{I,max}^{bulk} + K_{I,max}^{fret}, \quad K_{I,min} = K_{I,min}^{bulk} + K_{I,min}^{fret} \\ K_{II,max} &= K_{II,max}^{bulk} + K_{II,max}^{fret}, \quad K_{II,min} = K_{II,min}^{bulk} + K_{II,min}^{fret} \end{aligned} \quad (6E.43)$$

- Step (6) Evaluate the equivalent stress intensity range on the basis of individual K components of the mixed mode fretting crack according to

$$\Delta K_{eq}(a) = \sqrt{[\Delta K_I(a)]^2 + [\Delta K_{II}(a)]^2} \quad (6E.44)$$

where $\Delta K_I = K_{I,max} - K_{I,min}$ and $\Delta K_{II} = K_{II,max} - K_{II,min}$. DK_I is taken to be zero if both $K_{I,max}$ and $K_{I,min}$ have negative values (compressive).

- Step (7) Compute the local stress ratio, $R_L = K_{I,min} / K_{I,max}$, and the phase angle of mode mixity (in degrees), $b = \tan^{-1} |\Delta K_{II} / \Delta K_I|$.

- Step (8) Using the local R_L and β quantities, evaluate the corresponding endurance limit, ΔS_e , and the large crack threshold of the mixed mode crack, $\Delta K_{eq,th}$, according to

$$\Delta S_e (ksi) = \begin{cases} (78.33 - 53.62R_L - 12.08R_L^2) & R_L > -2 \\ 137.27 & , R_L \leq -2 \end{cases} \quad (6E.45)$$

and

$$\Delta K_{eq,th}(ksi\sqrt{in}) = (3.973 - 2.206R_L) \cdot (1.5 - 0.5e^{-0.0418b}) \quad (6E.46)$$

the endurance limit was set to a constant value of 137.27 ksi where the local stress ratio goes beyond the validity limit of available experimental data.

- Step (9) Compute the small crack parameter, a_0 , based on the Mode I large-crack threshold as given by

$$a_0 = \frac{1}{P} \left(\frac{\Delta K_{I,th}}{\sqrt{F_I^2 + F_{II}^2} \Delta S_e} \right)^2 \quad (6E.47)$$

where the normalized stress intensity factors, F_i , are given in Step (2) and F_I and F_{II} are used to account for mixed mode loading.

- Step (10) Compute the size-dependent crack growth threshold

$$\Delta K_{eq,th}^{SC}(a) = \Delta K_{eq,th} \sqrt{\frac{a}{a + a_0}} \quad (6E.48)$$

and compare it with the equivalent stress intensity range obtained from Step (6), i.e., $\Delta K_{eq}(a) = \Delta K_{eq,th}^{SC}(a)$. If both are equal (to within $\pm 1 \times 10^{-4}$), the iteration is terminated and the threshold bulk tension range is $\Delta S_{th} = (1 - R_G) S_{max}^{(i)}$. If they are not equal, the value of $S_{max}^{(i)}$ is either decreased or increased and the iteration procedure is repeated starting from Step (3).

Parametric Studies Using WCF Model

The fretting fatigue crack model is capable of predicting the crack nonpropagation conditions for fretting and fretting fatigue. Some of the predictive capabilities of the model are: (1) threshold stress for the nonpropagation of fretting fatigue cracks; (2) the dependence of the threshold stress on loading parameters such as bearing pressure, shear force, and stress ratio; (3) the dependence of the threshold stress on fretting geometry, coefficient of friction, and crack orientation; (4) the length and orientation of arrested fretting fatigue cracks at stresses below the threshold stress. These model capabilities are illustrated by parametric calculations presented below.

Effect of FCG Threshold Criterion on Threshold Stress (DS_{th})

Prediction of the threshold stress for crack nonpropagation requires a crack growth threshold criterion. The question of whether a large-crack or a small-crack threshold should be used for treating the nonpropagation of fretting fatigue cracks has been addressed by comparing the calculated crack growth driving forces against both the large-crack and small crack thresholds for the same fretting conditions. Figure 6E.12 shows a comparison of the large-crack threshold and the equivalent stress intensity range, which is the root of the sum of the squares of the individual K components, of the mixed mode fretting crack. The comparison is based on a crack angle, q , of 0° because it gives the lowest DS_{th} . The large crack threshold exceeds the equivalent stress intensity range, DK_{eq} , for all crack lengths. Thus, the mixed-mode fretting crack is expected not to propagate if it behaves like a large crack after crack nucleation. In contrast, the fretting crack propagates and then arrests if it is treated as a small crack with a size-dependent crack growth threshold.

Figure 6E.12 shows that for a bearing pressure of 35 ksi, the equivalent stress intensity range, DK_{eq} , of the fretting crack exceeds the small-crack threshold when the crack length is less than 0.8 mil. Thus, the fretting crack is expected to propagate when the crack length is less than 0.8 mil but to arrest when the crack length reaches 0.8 mil. For a bearing stress of 65 ksi, the arrest crack length is increased to about 4 mil, Figure 6E.12. Thus, these results suggest that fretting cracks can propagate even when their crack growth threshold is significantly less than the large-crack threshold, implying the growth of fretting cracks is controlled by the small crack behavior.

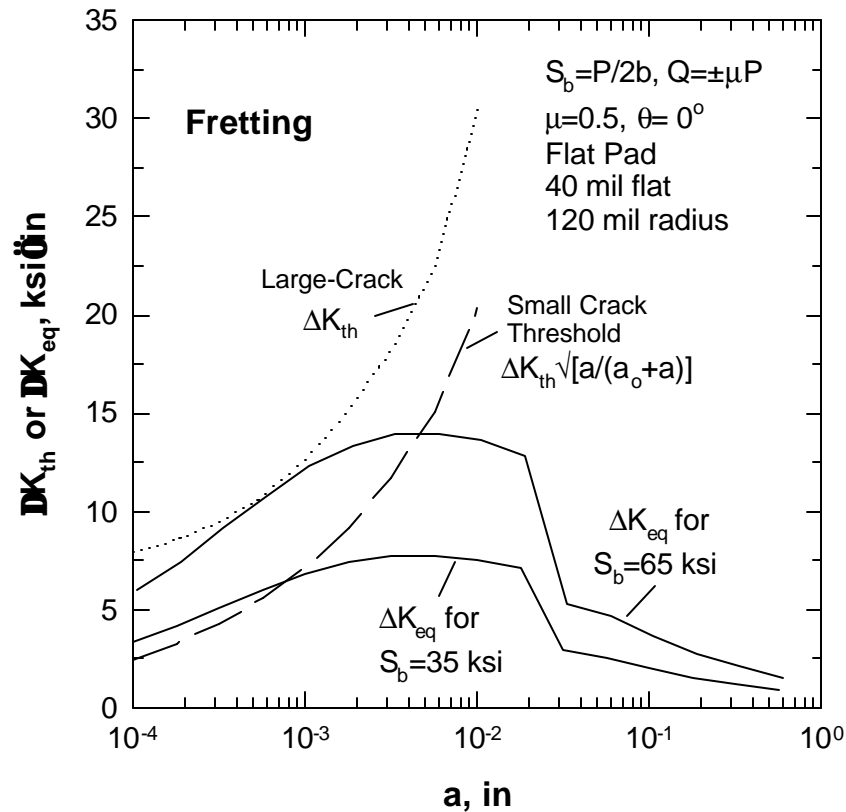


Figure 6E.12. Comparison of calculated crack driving force, DK_{eq} , against large-crack and small-crack thresholds as a function of crack length. The large-crack threshold is larger than effective stress intensity range, DK_{eq} , and predicts crack nonpropagation for all crack sizes. In contrast, the small-crack threshold is smaller than DK_{eq} and predicts crack propagation and arrest when the crack length is small. The crack arrest length increases with increasing bearing pressure.

Effect of Bearing Stress on DS_{th} and Crack Arrest Length

The limiting stress conditions for the nonpropagation of fretting fatigue cracks were calculated for flat pads with a 40 mil flat and 120 mil radius rounded edges. The threshold stress was calculated at the applied stress range required to make the local equivalent stress intensity range equal the small-crack threshold. The calculated threshold stress, DS_{th} , is plotted as a function of crack length, a , for various bearing stresses in Figure 6E.13. For large bearing stresses, the threshold stress generally increases with crack length, reaches a maximum, and then decreases with increasing crack lengths. There is a maximum threshold stress range above which crack arrest does not occur at any crack length. The maximum stress range corresponds to the threshold stress and the corresponding crack length is the arrest length, L_{ff} , of the

fretting fatigue crack. In contrast, the crack length, L_f , at a zero value of DS_{th} represents the arrest length of the fretting crack for the same bearing stress. For example, the arrest length for a fretting crack subjected to a bearing stress of 35 ksi is 0.84 mil. The arrest length of a fretting fatigue crack subjected to a bearing stress of 35 ksi and an applied stress range of 6 ksi is about 3 mil. In contrast, the large-crack threshold predicts a higher threshold stress whose value decreases with increasing crack length without a local peak. Thus, a fretting fatigue crack is predicted not to arrest once propagation has occurred if it behaves like a large crack and the stress is sufficiently high to start the propagation process.

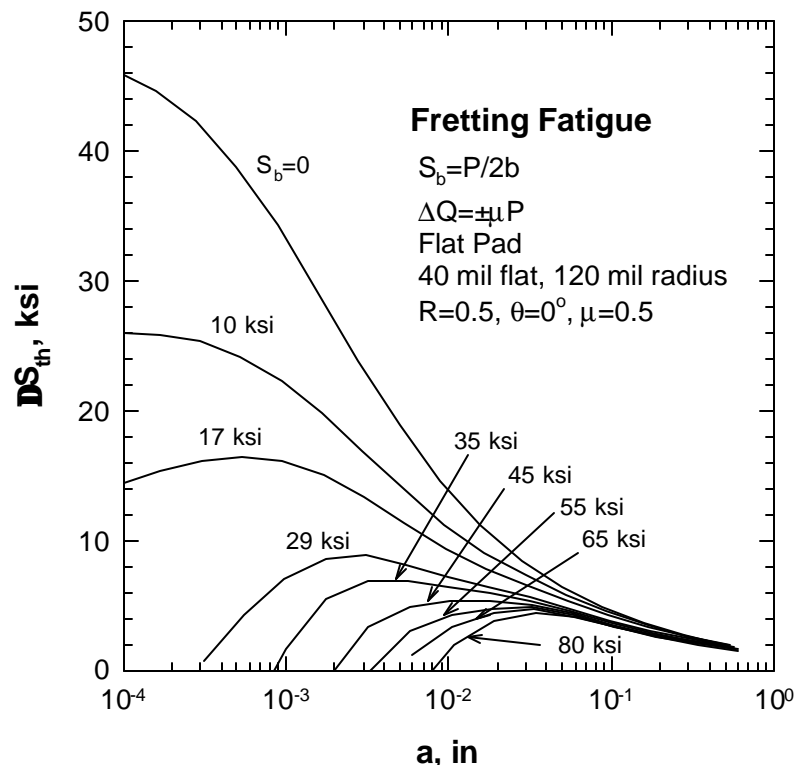


Figure 6E.13. Calculated threshold stress, DS_{th} , for crack nonpropagation as a function of crack length for a 40 mil flat pad subjected to various bearing pressures and shear forces.

The value of the threshold stress decreases with increasing bearing pressures for fretting fatigue, Figure 6E.14, and the value of the crack arrest length increases with increasing bearing pressures for both fretting and fretting fatigue, Figure 6E.15. In Figure 6E.14, the threshold stress decreases rapidly with increasing bearing pressures because the contribution of the fretting stresses to the crack driving force increase with

bearing pressure. Therefore, fretting fatigue cracks propagate further before arresting at higher bearing pressures, Figure 6E.15.

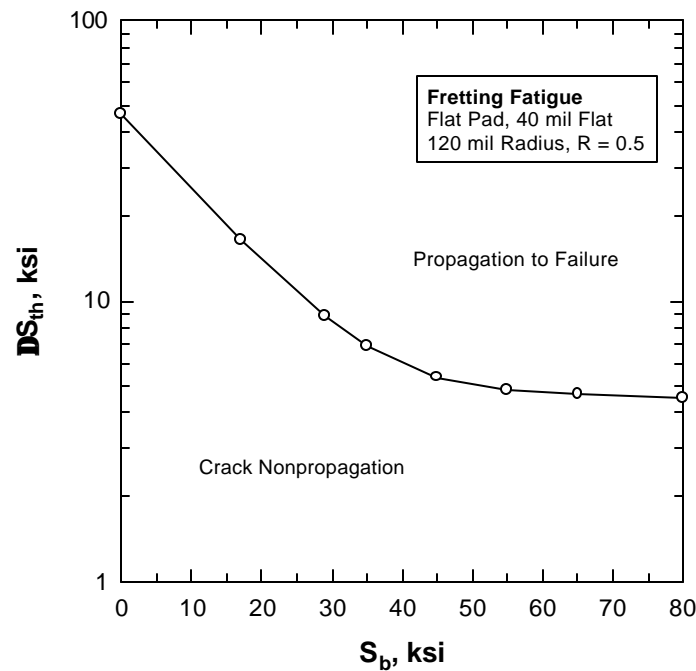


Figure 6E.14. Calculated threshold stress, DS_{th} , for crack nonpropagation as a function of bearing pressure.

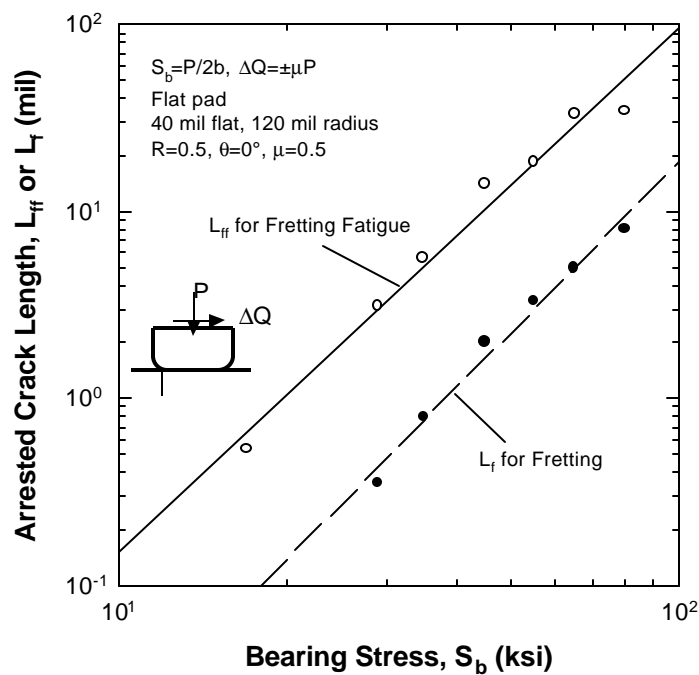


Figure 6E.15. Computed values of the arrested crack length for fretting, L_f , and fretting fatigue, L_{ff} , as a function of bearing pressure for a perpendicular crack ($q = 0^\circ$).

Effect of Crack Orientation and Mode-Mixity on ΔS_{th}

The WCF model is capable of computing the stress intensity factors of a fretting fatigue crack with an arbitrarily crack angle, θ . K calculations for various crack angles indicates that fretting or fretting fatigue cracks are generally mixed-Mode I and II when they lie within the contact stress field, even for cracks propagating normal to the fretting surfaces ($\theta = 0^\circ$) because of the normal and shear tractions in the contact surfaces. The K -field of a fretting crack without a cyclic bulk tension is shown in Figure 6E.16 for a 40 mil flat pad subjected to a bearing pressure of 35 ksi. The fretting crack, with a crack angle $\theta = 0^\circ$, is located at the trailing edge of the contact zone. For the crack length investigated, both K_I and K_{II} exist. As an illustration, Figure 6E.17 shows the ratio of $\sqrt{K_{II}}/\sqrt{K_I}$ for a perpendicular fretting fatigue crack ($\theta = 0^\circ$) at $R = 0.5$. This ratio is between 0.24 to 0.4, indicating the presence of a moderate Mode II component. The result clearly indicates that the crack angle is not a good indicator of the mode mixity of a fretting or fretting fatigue crack. In general, a fretting crack or a fretting fatigue crack must be treated as a mixed-mode crack.

The threshold stress was computed as a function of crack lengths for fretting fatigue cracks with crack angles of 0° , -25° , -45° , and 45° , subjected to a bearing pressure of 35 ksi. Presented in Figure 6E.18, the results indicate that the lowest limiting threshold stress occurs at a crack angle, θ , of 0° . Thus, for this pad and associated contact stress field, the preferred fretting fatigue crack growth direction is normal to the fretting surfaces and it proceeds under mixed-Mode I and II. Figure 6E.18 also shows that the curves for all cracks intersect $\Delta S_{th} = 0$ at about 0.3-0.8 mils. Thus, nucleation of fretting cracks with crack angles of 0° , -25° , -45° , and 45° are all feasible under fretting, but they are expected to arrest at about 0.3-0.8 mils below the fretting surfaces at 35 ksi bearing pressure. In the presence of a cyclic bulk tension, the straight crack ($\theta = 0^\circ$) is expected to dominate because of a lower threshold stress and maintain its crack propagation path if the applied stress range exceeds the corresponding threshold stress. All angled cracks exhibit higher threshold stresses than the perpendicular crack ($\theta = 0^\circ$) at identical bearing pressures. Consequently, the angled cracks are expected to arrest if they maintain their current crack orientation or they must deflect to propagate in the $\theta = 0^\circ$ crack path because of a lower threshold stress in the 0° direction. The transition length of a fretting fatigue crack of an angle, θ , is predicted to lie between L_f

(q) and $L_{f(q=0^\circ)}$, since both are dependent on the bearing pressure. For 35 ksi bearing pressure, path transition is predicted to occur at a crack length (or depth) of about 1 mil. This value has been obtained by finding the crack length at which $DS_{th}(q)$ equals the peak value of DS_{th} for $q = 0$. In general, $L_{f(q)} \neq L_{f(q=0)}$, the transition length is expected to be on the order of $L_{f(q=0)}$, which are shown in Figure 6E.15.

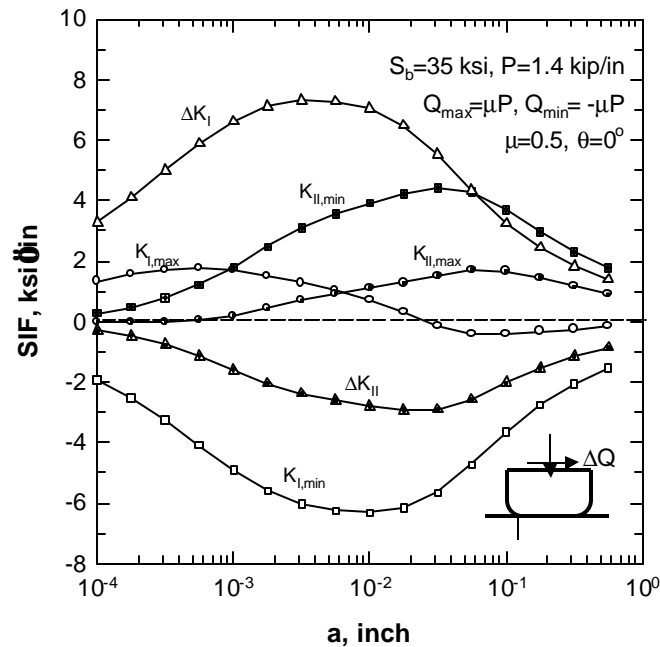


Figure 6E.16. Stress intensity factors for a fretting fatigue crack subjected to a bearing pressure, S_b , of 35 ksi and a cyclic shear force $\Delta Q = \pm \mu P$. ΔK_I is calculated as $K_{I,max} - K_{I,min}$ without correcting for negative values of $K_{I,max}$ and $K_{I,min}$ at $a > 0.025$ inch.

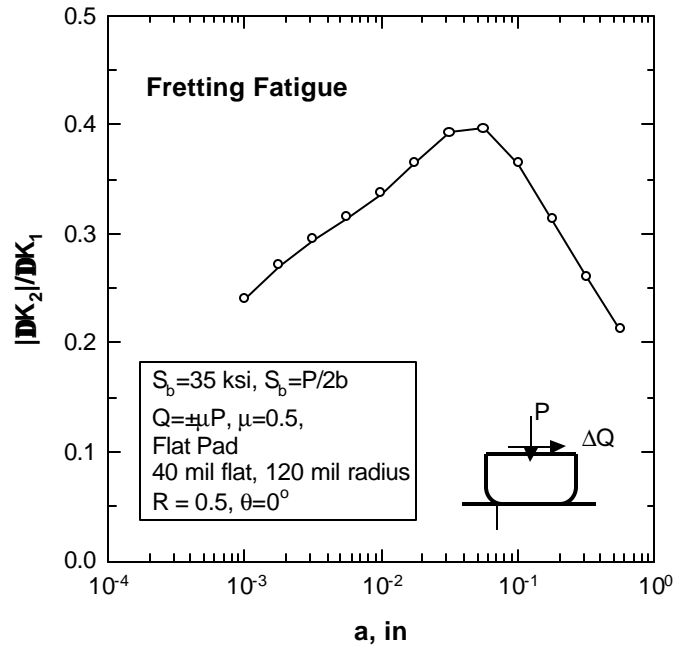


Figure 6E.17. Calculated ratio of Mode II to Mode I stress intensity factors for a perpendicular crack ($q = 0^\circ$) subjected to fretting fatigue.

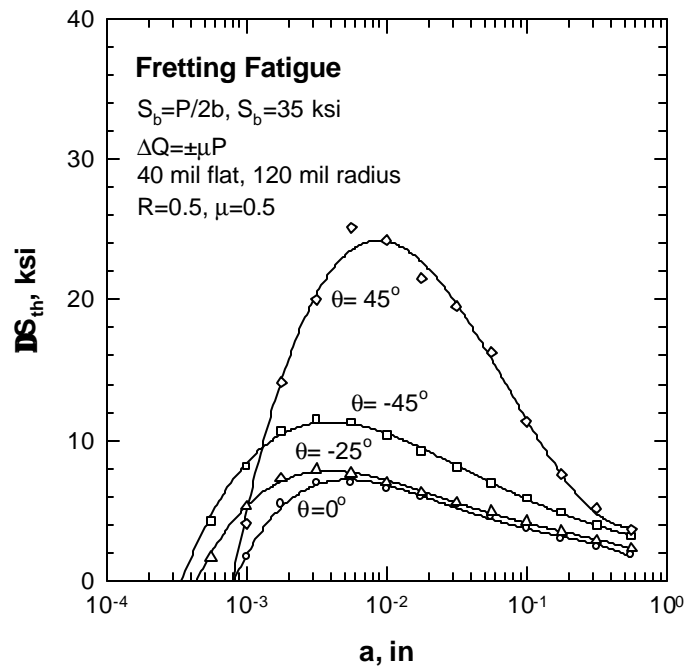


Figure 6E.18. Threshold stress, DS_{th} , for crack nonpropagation as a function of crack length, a , for various crack orientations.

Effect of Mean Stress and R -Ratio on DS_{th}

A systematic evaluation of the influence of mean stress on the threshold stress was conducted by varying the stress ratio, R , of the cyclic bulk stress, while maintaining a constant bearing load and shear force at the onset of gross slip ($DQ = \pm .5P$). The R -value was varied from -1 to 0.98 . Results of the threshold stress, which is plotted as a function of crack length in Figure 6E.19 for various R ratios, indicates that the threshold stress is reduced significantly when the stress ratio, R , is increased from -1 to 0.98 , but the crack arrest lengths, L_f and L_{ff} , for fretting and fretting fatigue cracks, respectively, do not vary with the R . Figure 6E.20 presents the threshold stress range as a function of R ; the decrease in the threshold stress with increasing R ratio is the result of decreasing FCG threshold with increasing R . At a high R , or mean stress, the DK_{eq} due to the fretting stress field, is a significant fraction of the FCG threshold. As a result, the fretting-induced DK_{eq} is sufficient and very low cyclic bulk stresses are needed, to propagate the fretting fatigue crack to failure; hence, the low threshold stress at high R and mean stress.

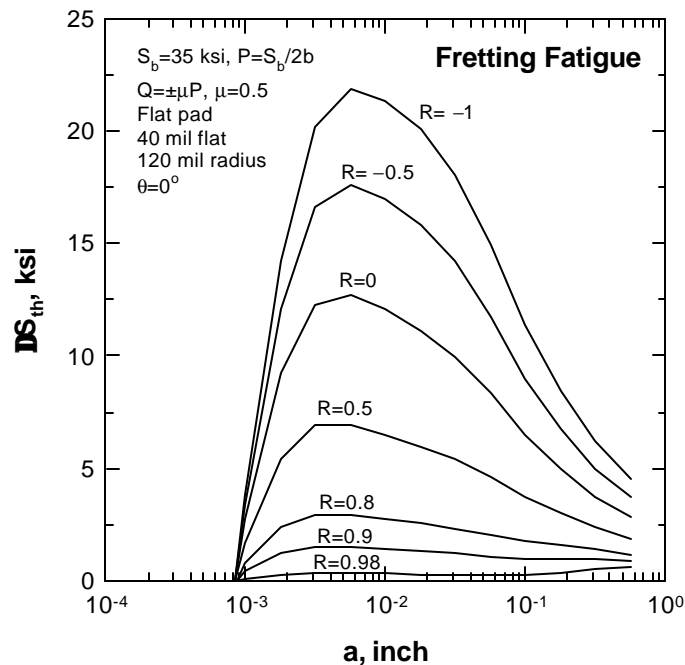


Figure 6E.19. Calculated threshold stress, DS_{th} , as a function of crack length, a , for various R ratios for fretting fatigue of a flat pad subjected to 35 ksi bearing pressure and a cyclic shear force of $DQ = \pm mP$.

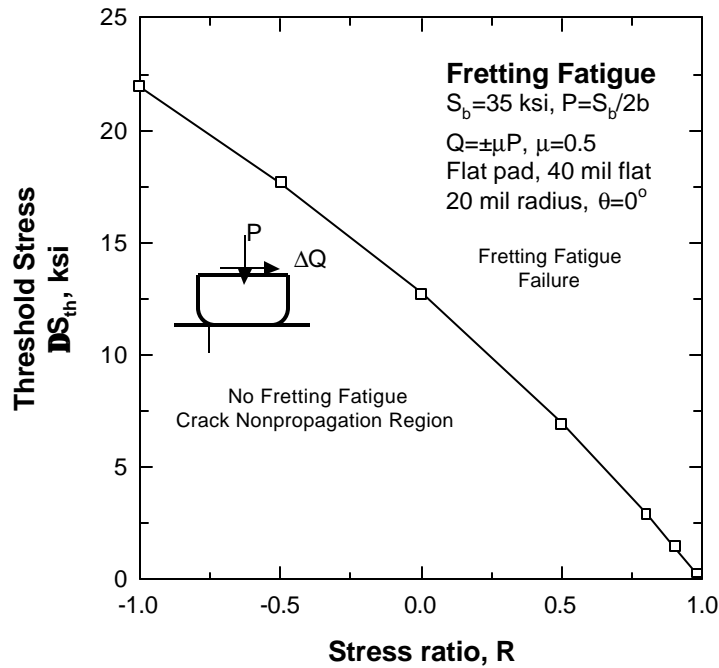


Figure 6E.20. Threshold stress, DS_{th} , decreases with increasing values of the stress ratio, R .

A comparison of the influence of R on fatigue, fretting + fatigue, and fretting fatigue is shown in Figure 6E.21. The curve labeled fatigue is an regression fit of the smooth-bar fatigue data generated for various R ratios. The curve labeled fretting fatigue is the threshold stress shown in Figure 6E.20 for fretting in the presence of a cyclic bulk stress. The curve labeled fretting + fatigue is the threshold stress calculated for fretting without a cyclic bulk stress until crack arrest, which is then followed by fatigue under a cyclic bulk stress without fretting. Using the length of the arrested crack from the fretting analysis, the threshold stress is calculated based on the small-crack threshold according to the expression given by

$$\Delta S_{th} = \frac{\Delta K_{I,th}}{F_1 \sqrt{p} (a_0 + L_f)} \quad (6E.49)$$

where $F_1 = 1.1215$, a_0 is the small crack parameter, and L_f is the crack arrest length of the fretting crack with $q = 0^\circ$. The threshold stress for fretting + fatigue is lower than that for fatigue because of the existence of fretting-induced cracks in the fretted materials. The threshold stress is further reduced for fretting fatigue because both the contact stresses and the bulk stress contribute to the driving force of the fretting fatigue crack.

Figure 6E.21 indicates that the threshold stress is lowest and the propensity for HCF failure is greatest when fretting fatigue occurs at a high R ratio.

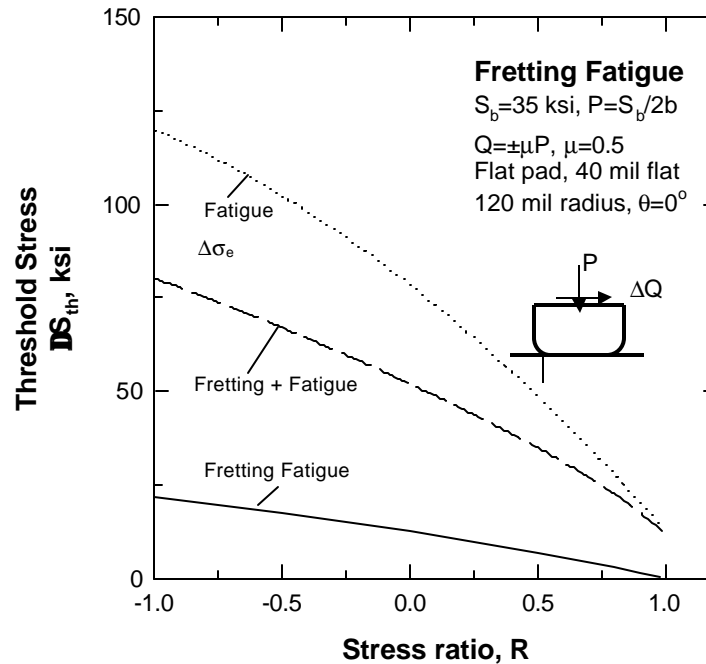


Figure 6E.21. Comparison of threshold stress for fatigue (DS_e), fretting + fatigue, and fretting fatigue as a function of the stress ratio, R .

Effect of Pad Geometry on DS_{th}

Four different fretting pads were analyzed to evaluate the effect of pad geometry on the threshold stress, including (1) a 40 mil flat pad with 120 mil radius, (2) a 120 mil flat pad with 120 mil radius, (3) a cylindrical pad with 120 mil radius, and (4) a cylindrical pad with 1 inch radius. The cylindrical pad geometry was obtained by shrinking the flat region of the pad to 10^{-4} mils. The threshold stress was calculated for a bearing pressure, S_b , of 35 ksi, $R = 0.5$, and a coefficient of friction of 0.5. For flat pads, the bearing pressure was calculated as $S_b = P/2d \approx P/2b$ since $d \gg b$, while $S_b = P/2d$ for the cylindrical pads.

Figure 6E.22 presents results of the threshold stress as a function of bearing pressure for the four pad geometries. For all cases, the threshold stress decreases with increasing bearing pressures. At a given bearing pressure, the 120 mil radius cylindrical pad gives the highest threshold stress, followed by the 1 in radius cylindrical pad, the 40 mil flat pad, and lastly, the 120 mil flat pad. The contact stresses are higher in the

flat pad than in the cylindrical pads. For the flat pads, the contact stress increases with the flat region, b because of increasing bearing loads and aspect ratios, b/r , of the pad geometry. Consequently, the 120 mil flat pad gives the lower threshold stress at a given bearing pressure. For a cylindrical pad, the contact stress increases with decreasing radii. The threshold stresses, however, are lower for the 1 inch cylindrical pad because a higher bearing load, P , is required to maintain the specified 35 ksi bearing pressure due to a larger contact width, $2d$. These results clearly indicate that the contact geometry affects the threshold stress for the nonpropagation of fretting fatigue cracks.

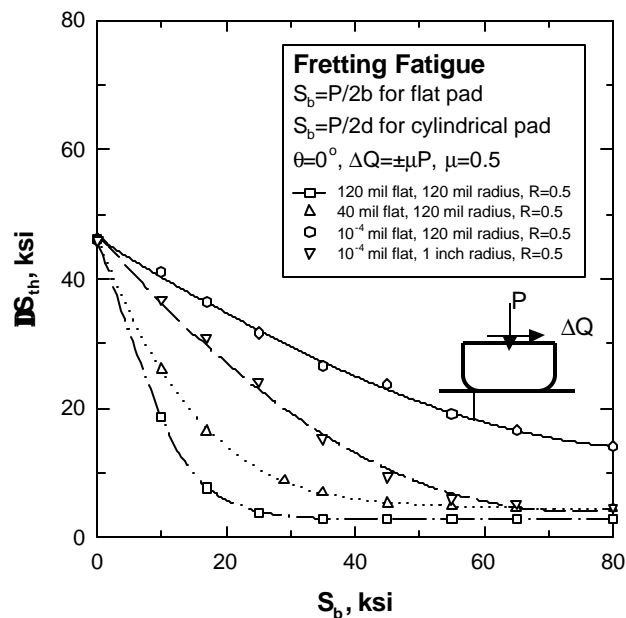


Figure 6E.22. Dependence of the threshold stress, DS_{th} , for crack nonpropagation on pad geometry.

Effect of Coefficient of Friction on DS_{th}

The influence of the coefficient of friction on the limiting threshold stress was predicted for fretting fatigue of a 40 mil flat pad with 120 mil radius on a flat specimen subjected to a cyclic bulk tension at $R = 0.5$. The bearing pressure was 35 ksi and the cyclic shear traction, ΔQ , was taken to be $\pm mP$. The coefficient of friction was varied from 0 to 0.5. Figure 6E.23 shows the calculated threshold stress as a function of crack length. The peak value in the DS_{th} versus crack length curve for a particular m value corresponding to the threshold stress range below which crack nonpropagation occurs.

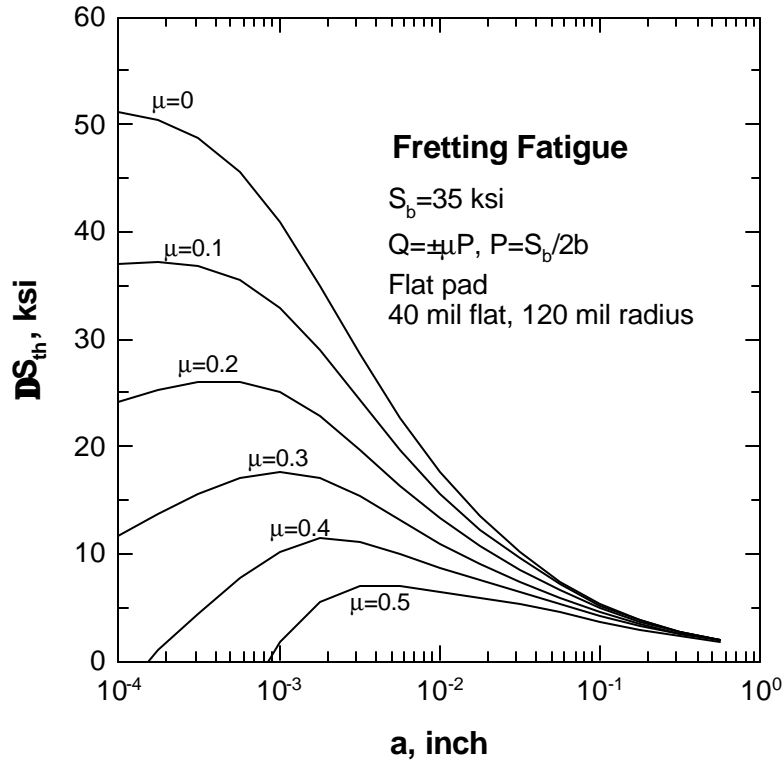


Figure 6E.23. Dependence of the DS_{th} vs. a curve on the coefficient of friction, μ

A plot of the threshold stress range as a function of the coefficient of friction is presented in Figure 6E.24, which shows that the threshold stress decreases with increasing values of the coefficient of friction. Thus, a reduction in the coefficient of friction (e.g., a coating, or elevated-temperature-oxide, with a low μ value) has a significant effect in increasing the threshold stress and, thereby, reducing fretting fatigue.

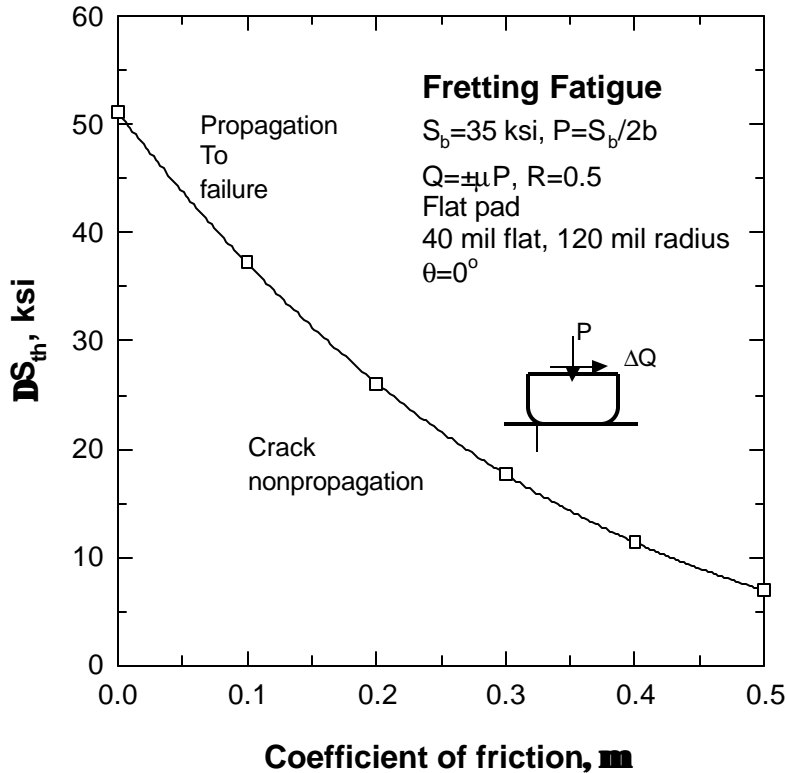


Figure 6E.24. The threshold stress, DS_{th} , for crack nonpropagation decreases with increasing values of the coefficient of friction, μ

Effect of Ratio of Shear to Bearing Stress on DS_{th}

The contact stress field and the SIF's of a fretting or fretting fatigue crack depends on both the shear force per unit thickness, Q , and the bearing load per unit thickness, P , acting on the contact region. Figure 6E.25 illustrates the dependence of the shear force, Q , on the slip distance, du_x , and the bearing pressure, $S_b = P/2b$, where $2b$ is the flat region of flat pad. At a given bearing pressure, the shear force, Q , increases linearly with the slip distance, du_x , in the partial slip region until Q attains its maximum value, $Q_{max} = \mu P$, at the onset of gross slip. Increasing the bearing pressure increases both the value of Q_{max} and the critical slip distance for gross slip. Since the SIF's of a fretting crack depends on both P and Q , the threshold stress, which is computed based on the SIF's and the FCG threshold, is expected to depend on both P and Q .

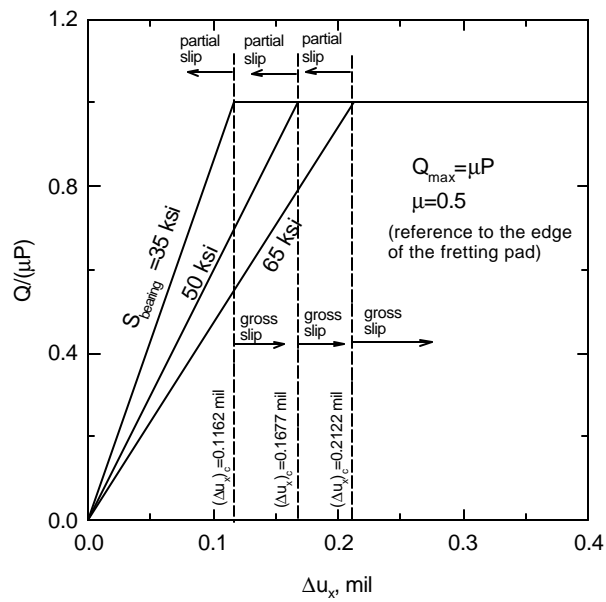


Figure 6E.25. Dependence of the shear force normalized by μP on the slip distance, Δu_x , in the x direction (along the fretting surface).

The effect of the DQ/P ratio of the threshold stress is illustrated in Figure 6E.26, which shows the results for $DQ/P = 0.56$ and 1.0 for the 120 mil flat pad with 120 mil radius. Partial slip prevails for $DQ/P = 0.56$, while $DQ/P = 1.0$ corresponds to the onset of gross slip. Because of a higher DQ value, the calculated threshold stress is lower for $DQ/P = 1.0$ when compared to that for $DQ/P = 0.56$.

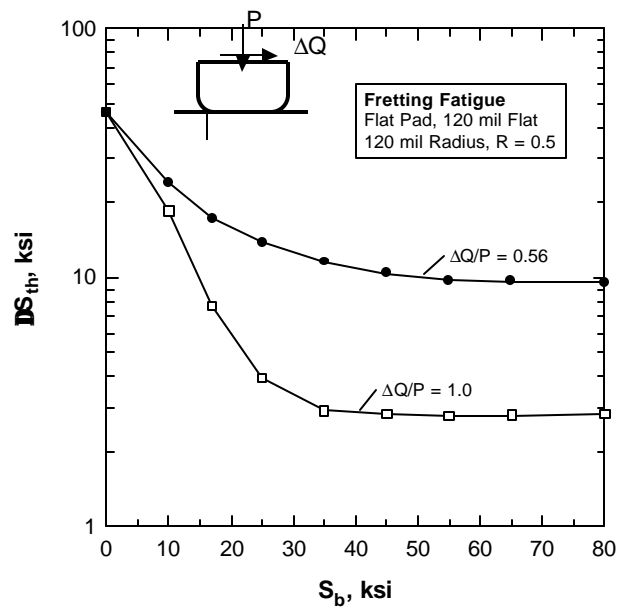


Figure 6E.26. The effect of the DQ/P ratio on the threshold stress, DS_{th} , for crack nonpropagation.

The threshold stress range depends on the shear stress range, $\Delta\tau$, on the fretting surfaces, where $\Delta\tau = \Delta Q/2b$. Figure 6E.27 shows the calculation of the threshold stress range ΔS_{th} as a function of $\Delta\tau$ for fretting fatigue under a 40 mil flat pad with 120 mil radius edge at $R = 0.5$. At $\Delta\tau = 0$, the threshold stress range corresponds to the fatigue limit for $R = 0.5$. The threshold stress is seen to decrease substantially with increasing $\Delta\tau$ values. Fretting fatigue cracks are predicted not to propagate at stresses below the threshold stress boundary, but propagate when they are above the boundary. Thus, the shear stress range on the fretting surfaces is an important factor influencing the threshold stress range for crack nonpropagation.

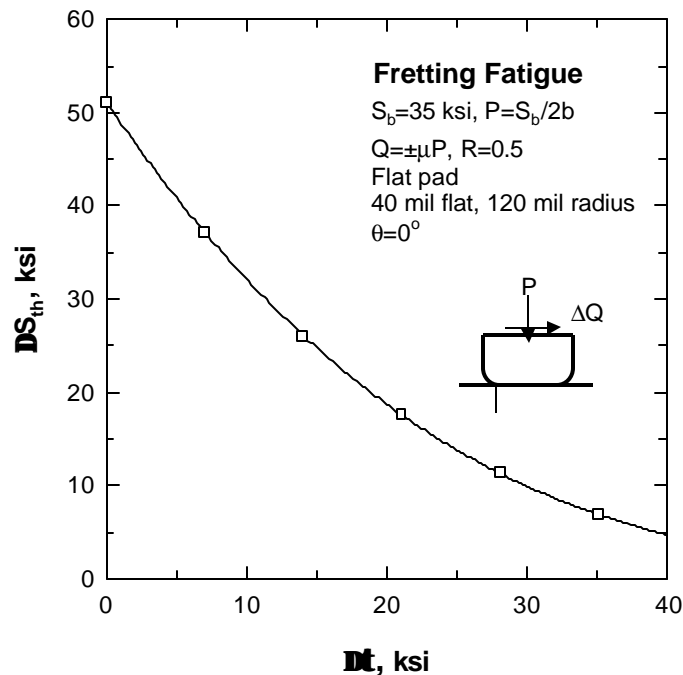


Figure 6E.27. Dependence of ΔS_{th} on the shear stress, $\Delta\tau$, on the fretting surfaces.

HIGH-FREQUENCY FRETTING FATIGUE EXPERIMENTS

Kilohertz Fretting Fatigue Machine

A high-frequency cyclic loading system has been developed as a modular attachment for supplemental operation as part of conventional laboratory materials testing machines. This system consists of an elongated axial loading column with specimen-holding grips at its midpoint. The loading column allows the specimen to be placed in

static tension at loads up to approximately 6,000 lbf. The specimen grips are made large enough to contain piezoelectric dynamic transducer elements capable of generating an oscillatory force of up to $\pm 1,200$ lbf applied to the test specimen. The loading column assembly permits the dynamic load to be applied to the test specimen while it is simultaneously subjected to static tensile loading. The specimen grip assemblies containing stacked piezoceramic discs that apply load to the specimen. The latter form concentrated masses that are designed to mechanically resonate at a high frequency depending on the stiffness of the test specimen. The typical mechanical resonance frequency of this system using test specimens having gauge sections of 0.125 inch x 0.500 inch cross-section and 0.75 inch length is in the range of 2,000-2,500 Hz. When excited by an appropriate power amplifier, an adjustable sinusoidal dynamic loading force of up to 2,400 lbf peak-to-peak can be applied continuously to the test specimen.

The symmetrical spring-mass mechanical resonator and loading column design ensures that the vibrational nodal (stationary) point is located at the center of the specimen. As a result, high-cycle fatigue stresses are accurately applied to the central gauge section of the specimen. Further, when operating at a typical resonance frequency of 2,200 Hz, cyclic loading tests can be performed at a rate of approximately 8 million cycles per hour. High-cycle fatigue tests have been performed on titanium alloy specimens using this resonant loading system. Figure 6E.28 shows a close-up view of the kilohertz fatigue test rig with a test specimen and fretting fatigue attachment.

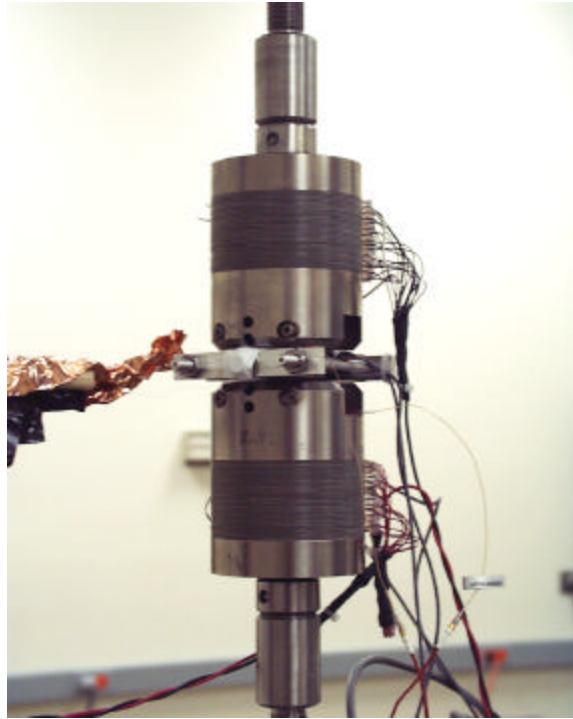


Figure 6E.28. A close-up view of SwRI's kilohertz fretting fatigue test rig that operates in the 2100-2500 Hz frequency range.

A fretting fatigue testing attachment was recently designed for use with the high-frequency loading system. This attachment is designed to be clamped directly onto the titanium test specimen, as shown in Figure 6E.28, and is capable of applying a normal force of up to 350 lbf on a small fretting test pad in contact with the wide surface of the rectangular test specimen. The clamping fixture, shown in Figure 6E.29, consists of a rectangular reaction load frame with two symmetric tungsten blocks. The fretting pad is attached to the left tungsten block, which is connected to a bolt that applies a pressure to the fretting pad. The bolt is instrumented to a load cell to measure the bearing pressure on the fretting pad continuously. The test specimen is placed between the fretting pad and a square Ti block attached to the right tungsten block, which is instrumented with an accelerometer to measure the acceleration and the shear force.

A sheet of Teflon is placed between the specimen and the square Ti block in order to prevent fretting at this location. A square block is used because it provides a stiffer system and eliminates unwanted vibrations during excitation. The fretting rig is attached to the specimen by tightening the nuts to the bolts on the frame.

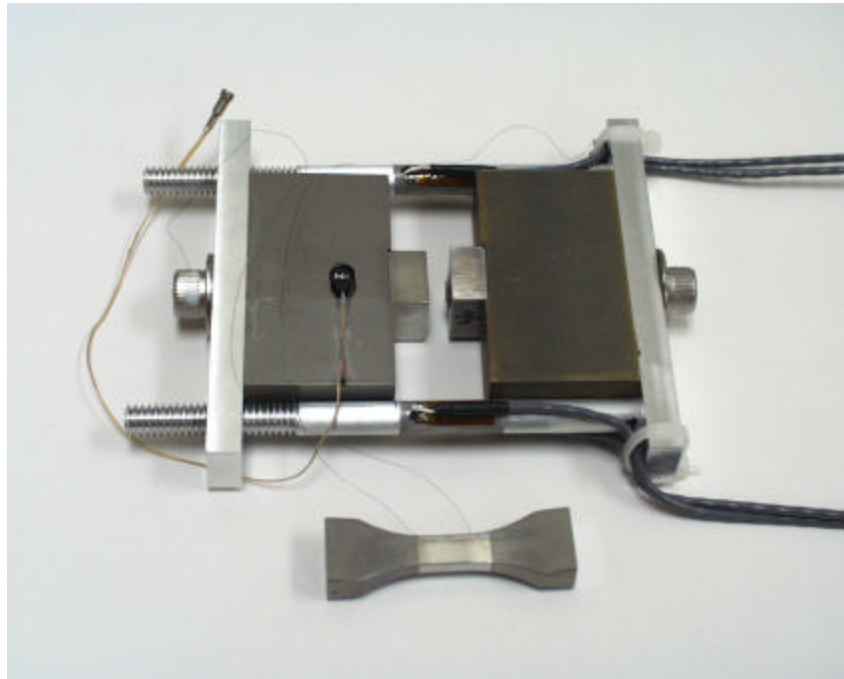


Figure 6E.29. Assembled fretting fatigue rig and a Ti-6-4 test specimen.

The fretting fatigue fixture is designed to be as compact and symmetrical as practical so as to act as an inertial mass which, in response to axial displacements of the test specimen, will impart a shear reaction force at the point of normal force contact under the fretting pad. In order to create sufficiently high shearing forces for fretting tests, the spring-mass resonance system is operated in a non-symmetrical mode of vibration by applying unbalanced driving voltages to the piezoelectric transducers. This asymmetrical excitation causes the test specimen to undergo oscillatory translational motion along the loading axis. Accelerometers mounted on the fretting pad inertial mass and on the specimen grip masses are used to measure the resulting fretting shear stress applied to the specimen surface. Mechanical resonance of the elongated loading column is also important in this fretting mode of operation in order to amplify the mechanical forces present and to allow fretting fatigue tests to be performed at appropriate frequencies. The cyclic loading rate for these fretting fatigue tests is 8 million cycles per hour, corresponding to the same mechanical resonance as used in the fatigue tests. This fretting fatigue test configuration is capable of providing quantitative measurements and monitored control of specimens testing under a range of high frequency testing

conditions. The load capacity of the test rig includes superimposed mean tensile loads up to 6,000 lbf and dynamic tensile loads up to approximately ± 600 lbf at cyclic rates in the range of 2,000-2,500 Hz, and fretting pad shear forces up to approximately ± 120 lbf under a static normal force at the fretting pad clamping fixture of up to 350 lbf.

Electrical excitation of the piezoceramic vibration transducers and associated mechanical resonance operation provide an accurate and responsive means of controlling the high-frequency cyclic loads applied to both fatigue specimens and fretting fatigue specimens. The force amplifying effects of mechanical resonance make possible the relatively high dynamic forces in a physically compact system operating in a frequency range typical of many HCF problems.

Experimental Procedures

Fretting fatigue tests were conducted on the kilohertz rig for Ti-6-4 using 40 mil flat pads with 120 mil radius edges. Both step-stress and interrupted tests were performed for several stress ranges at a stress ratio, R , of 0.5 and bearing pressures of 35 ksi and 55 ksi. The test conditions, shown in Table 6E.1, were guided by an analytical prediction of the threshold stress boundary based on the worst case fret model. All the tests were performed at about 2100 Hz under load-controlled conditions. The pressure on the fretting pad, the shear stress on the fretting surfaces, and the static and dynamic stresses on the fretting specimen were measured during the tests. For the step-stress tests, the stress ranges were increased by about 2 ksi after 10^7 fatigue cycle at each stress level until failure. The stress-stepping procedure involved first unloading the dynamic stress while maintaining the static mean stress, the mean stress was then increased to the desired level for the next stress step. Subsequently, the dynamic stress was imposed and raised to the desired level. The unloading and reloading sequence offered an advantage in that it created crack arrest marks on the fracture surfaces that allowed the crack lengths and depths corresponding to individual stress steps to be identified. For interrupted tests, the specimen was fretting fatigued for 10^7 cycles at a prescribed stress range; the test was then terminated and the specimen was examined for possible cracks nucleated by fretting fatigue. SEM metallography and fractography were performed to determine the existence of nonpropagating and propagating microcracks, as well as their respective surface crack length and crack depth.

Table 6E.1

Summary of fretting fatigue test results for 40 mil flat pads, including bearing pressure (S_b), mean stress (S_m), stress range (ΔS), stress ratio (R), fretting shear stress range ($\Delta \tau$), fatigue cycles (N), frequency (f), surface crack length ($2a_s$), and crack depth (a).

Specimen	Step	S_b , ksi	S_{max} , ksi	ΔS , ksi	R	$\Delta \tau$, ksi	N , cycle	f , Hz	Crack Length $2a_s$, mil (start-end)	Crack Depth a , mil (start-end)	Pad Type	Remarks
631	1	35	60.6	43.6	0.47	28.1	31,000	2100	0 – 69.4	0 – 28.0	40 mil flat pad	Increased ΔS to 55.2 ksi
	2	35	60.6	55.2	0.37	47.7	108,000	2100	69.6E.failure	28-failure		Failure
632	1	35	36.0	24.0	0.5	7.0	10^7	2100	—	—	40 mil flat pad	Step up ΔS to 26 ksi
	2	35	39.0	26.0	0.5	7.4	10^7	2100	7	2		Step up ΔS to 25 ksi
	3	35	42.0	28.0	0.5	11.3	10^7	2100	7-15	2-44		Step up ΔS to 30 ksi
	4	35	45.0	30	0.5	14.5	10^7	2100	25-123	9-44		Step up ΔS to 32 psi
	5	35	48.0	32	0.5	19.5	10^7	2100	123-145	46E.76		Step up ΔS to 33.6 ksi
	6	35	50.4	33.6	0.5	22.3	1.4×10^6	2100	145-failure	76-failure		Failure
635	1	35	45.0	30	0.5	16.3	10^7	2100	0.2-.6*	—	40 mil flat pad	Interrupted test
636	1	35	42.0	28	0.5	11.3	10^7	2100	0.2-1.3*	—	40 mil flat pad	Interrupted test
633	1	35	45	30	0.5	9.5	10^7	2130	—	—	40 mil flat pad	Step up ΔS to 32 ksi
	2	35	48	32	0.5	11.1	10^7	2100	—	—		Step up ΔS to 34 ksi
	3	35	51	34	0.5	16.0	10^7	2100	—	—		Step up ΔS to 36 ksi
	4	35	54	36	0.5	17.1	10^7	2100	—	—		Step up ΔS to 38 ksi
	5	35	57	38	0.5	22.4	7.4×10^6	2100	—	—		Grip failure
634	1	55	36	24	0.5	11.3	10^7	2100	—	—	40 mil flat pad	Step up ΔS to 26 ksi
	2	55	39	26	0.5	14.5	10^7	2100	—	—		Step up ΔS to 28 ksi
	3	55	42	28	0.5	16.3	10^7	2100	—	—		Step up ΔS to 30 ksi
	4	55	45	30	0.5	17.3	10^7	2100	—	—		Step up ΔS to 32 ksi
	5	55	48	32	0.5	18.8	10^7	2100	—	—		Step up ΔS to 35 ksi
	6	55	52.5	35	0.5	21.8	4.4×10^6	2100	—	—		Grip failure
587	1	35.8	45.8	30.7	0.5	0	2×10^7	1300	—	—	1" radius cylindrical pad	No cracks
	2	40	59.1	22.4	0.5	0	10^7	1300	—	—		
596	1	35.8	59.1	22.4	0.5	0	6.4×10^6	1300	—	—	125 mil radius cylindrical pad	No cracks

* range

Several fretting fatigue tests were also performed for Ti-6-4 using cylindrical pads either 1 inch or 1/8 inch radius. These tests were conducted using another kilohertz fretting fatigue rig, that operates inside a scanning electron microscopy (SEM). This fretting fatigue rig operated at about 1300 Hz and provided symmetric dynamic loads to the test specimen. The fretting attachment was placed at the center of the specimen and testing was conducted in air under a bearing pressure of about 35 ksi or 40 ksi. Because of the symmetric dynamic loads, no shear force was induced on the fretting pad in this test fixture arrangement. Testing was interrupted periodically; the fretting pad was removed and the fretting surface was characterized by SEM at various fretting fatigue cycles. The fretting pad was then placed on the specimen and the fretting fatigue test continued. Great effort was made to place the fretting pad to its previous location, but it was not always successful. Fretting fatigue cycles up to 10 - 30 million cycles were performed for these interrupted tests.

Experimental Results

Flat Pads

Fretting fatigue tests generated using 40 mil flat pads are summarized in Table 6E.1, which include the bearing pressure (S_b), mean stress (S_m), stress range (DS), stress ratio (R), fretting shear stress range (Dt), number of fatigue cycle (N), frequency (f), surface crack length ($2a_s$), and crack depth (a). The values of the fretting shear stress range were calculated by dividing the shear force, measured using an accelerometer, by the area of the flat pad. Specimens 631, 632, 633, and 634 were step-stress tests, while Specimens 635 and 636 were interrupted tests. In the step tests, the stress range was increased by an increment, usually 2 ksi, after 10^7 cycles at a given stress range. Specimens 631 and 632 were successful tests as fretting fatigue crack initiated and propagated to failure under the fretting pad. Specimens 633 and 634 showed fretting failure at the grips. Both Specimens 635 and 636 were successful tests that were stopped after 10^7 cycles for the purpose of interrogating the possible existence of nonpropagating cracks. After fretting fatigue, SEM fractography and metallography were performed on the fracture and fretting surfaces, respectively, to determine the crack size and the extent of crack growth at individual stress levels in both the step-stress and interrupted tests.

Figure 6E.30 shows the benign-looking fretting scar observed at low magnification for the flat pad after 10^7 fretting fatigue cycles at 35 ksi pressure and 30 ksi stress range at $R = 0.5$ (Specimen 635). At high magnification, the fretting surfaces exhibited large amounts of oxides and smeared metal layers, Figure 6E.31, as well as microcracks, Figure 6E.32. The microcracks were determined to be nonpropagating because they exhibited little or no Mode I crack opening when they were loaded to the maximum fatigue stress. The microcracks observed on the fretting surfaces were about 0.2-1.3 mils in length for the interrupted tests (Specimens 635 and 636). Despite failure at the grips, both specimens 633 and 634 showed fretting fatigue cracks under the fretting pad. The fretting fatigue cracks were located close to the edge of contacts, as shown in Figure 6E.33.

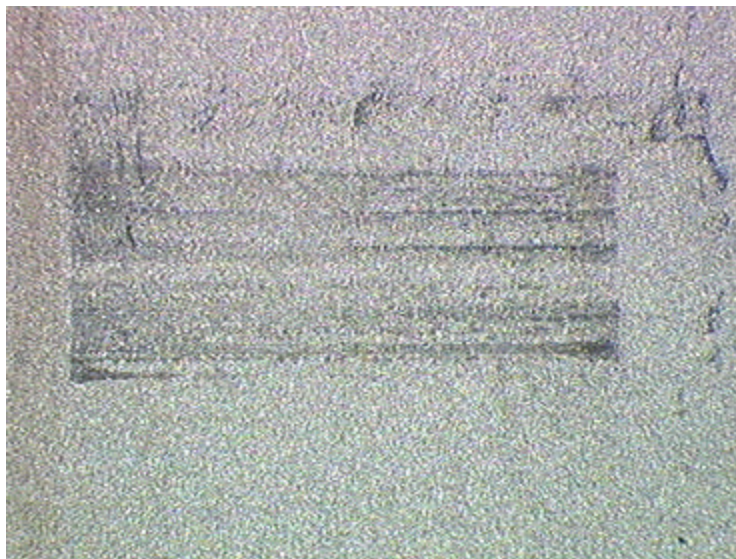


Figure 6E.30. A SEM micrograph of the benign-looking fretting scar formed by a flat pad after 10^7 cycles at 35 ksi bearing pressure and a stress range of 30 ksi at $R = 0.5$ (Specimen 365).

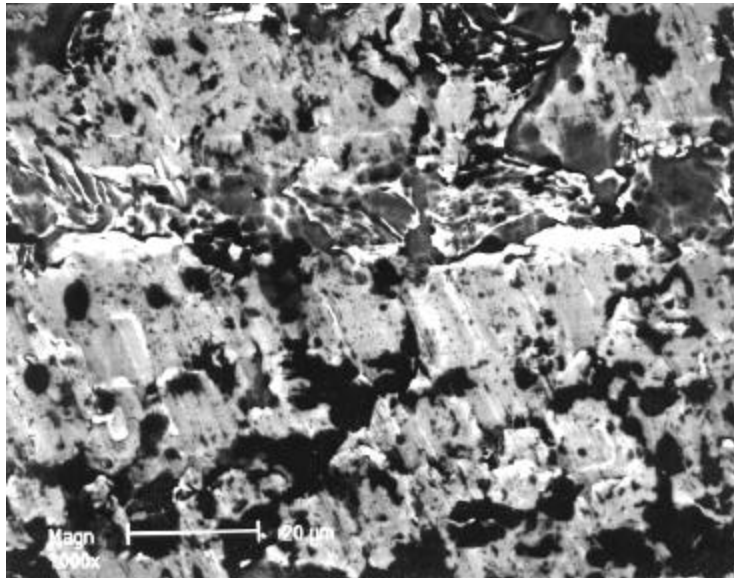


Figure 6E.31. Oxides (black) and smeared metal layers on a fretting fatigue surface under the 40 mil flat pad after 10^7 fretting fatigue cycles (Specimen 365).

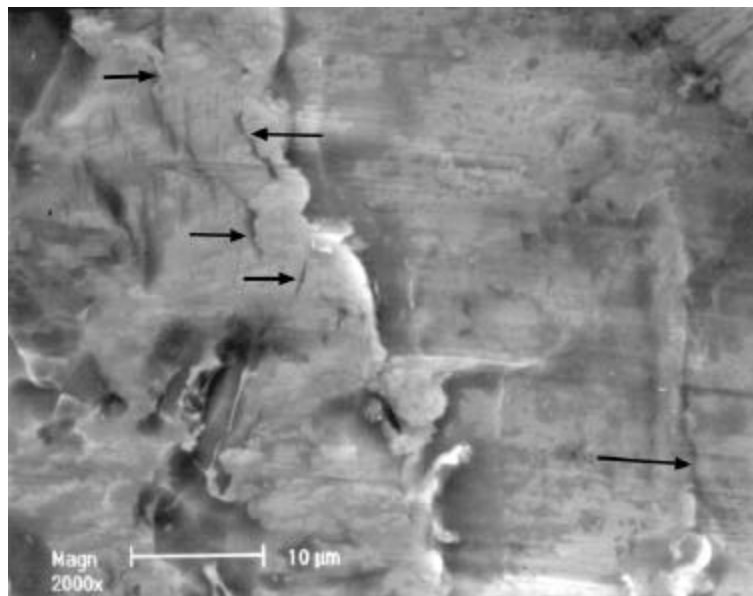


Figure 6E.32. Nonpropagating microcracks observed at high magnification on the fretting fatigue surface after 10^7 cycles (Specimen 365). Test conditions are the same as those indicated in Figure 6E.30.

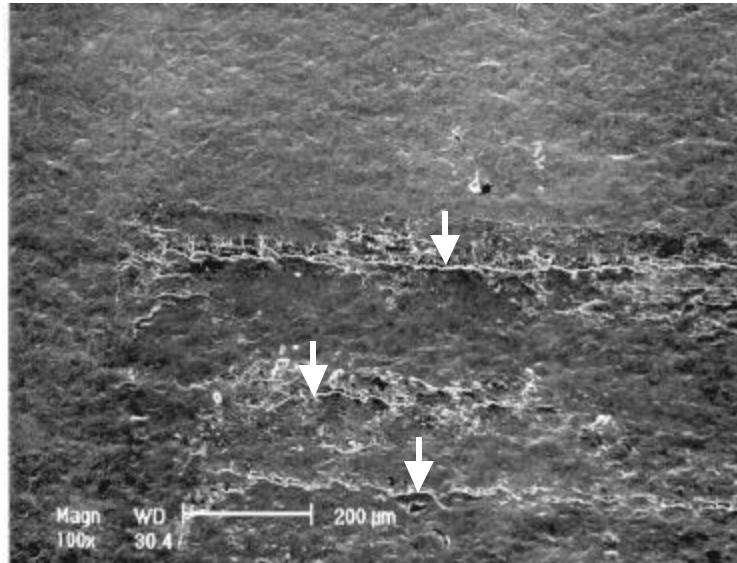


Figure 6E.33. Propagating fretting fatigue cracks formed near the contact edges and at the center of the fretted region (Specimen 633). Three-point bending was used to open up the cracks to ensure that they were indeed cracks.

Fractography performed on the step-stress specimens indicated multiple crack nucleation sites under the fretting pad, as shown in Figure 6E.34 for Specimen 632. The cracks were nominally perpendicular to the fretting surfaces, i.e., the crack angle, q , was $\approx 0^\circ$. The fracture surfaces also showed crack blunting marks, Figure 6E.35, associated with individual load increases in the step-stress tests. Based on these blunting marks, the surface crack length ($2a_s$) on the fretting surface and the crack depth (a) of the fretting fatigue cracks were measured and correlated with the start and the end of individual load ranges in the step-stress tests. These crack length measurements were obtained for Specimens 631 and 632 and are presented in Table 6E.1. Once the crack lengths were known, they were correlated with the fatigue stress history to determine whether or not crack propagation occurred at a particular stress range.

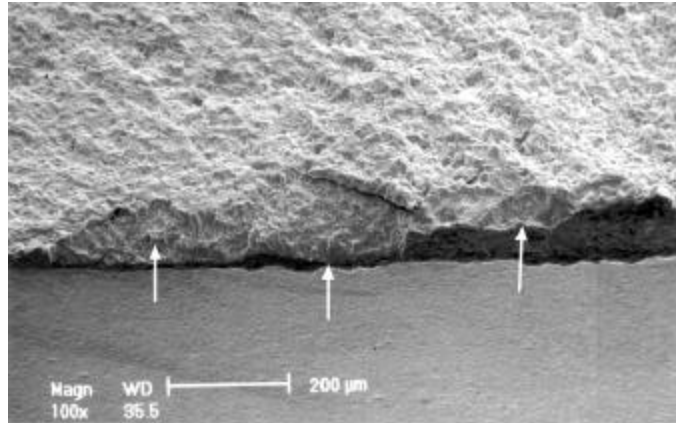


Figure 6E.34. Typical multiple crack nucleation sites observed on the fretting-fatigue surfaces (Specimen 362) generated at 2100 Hz.

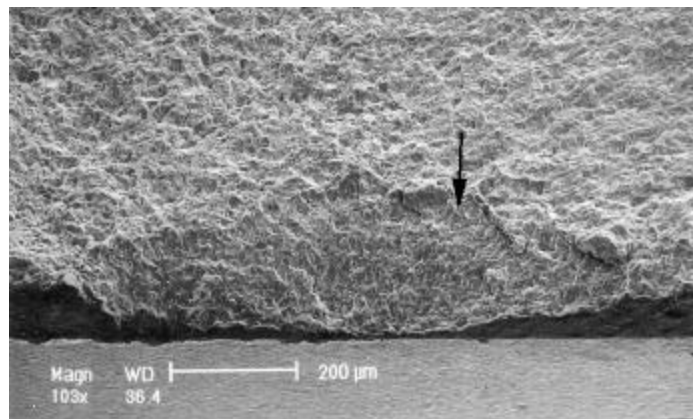


Figure 6E.35. Typical crack blunting mark associated with a stress increase from 26 ksi to 28 ksi (Specimen 362) in the step-stress tests.

Cylindrical Pads

Specimens tested with a cylindrical pad under symmetric dynamic loads exhibited considerable surface damage during fretting fatigue. The surface topography varied with fatigue cycles and fretting products, which appeared to be oxides, were created and removed continuously by fretting. This is illustrated in Figure 6E.36 (a), (b), (c), and (d), which shows the same fretting surface after 8.5, 12.5, 16.5, and 20 million cycles, respectively, for fretting fatigue under a bearing pressure of 35 ksi and a stress range of 31 ksi. Despite considerable fretting damage, the specimen did not fail after 20 million cycles. Subsequent metallographic analysis of the fretting surface revealed no detectable cracks, indicating fretting fatigue cracks were not initiated. Similar results were obtained for another fretting condition, as summarized in Table 6E.I.

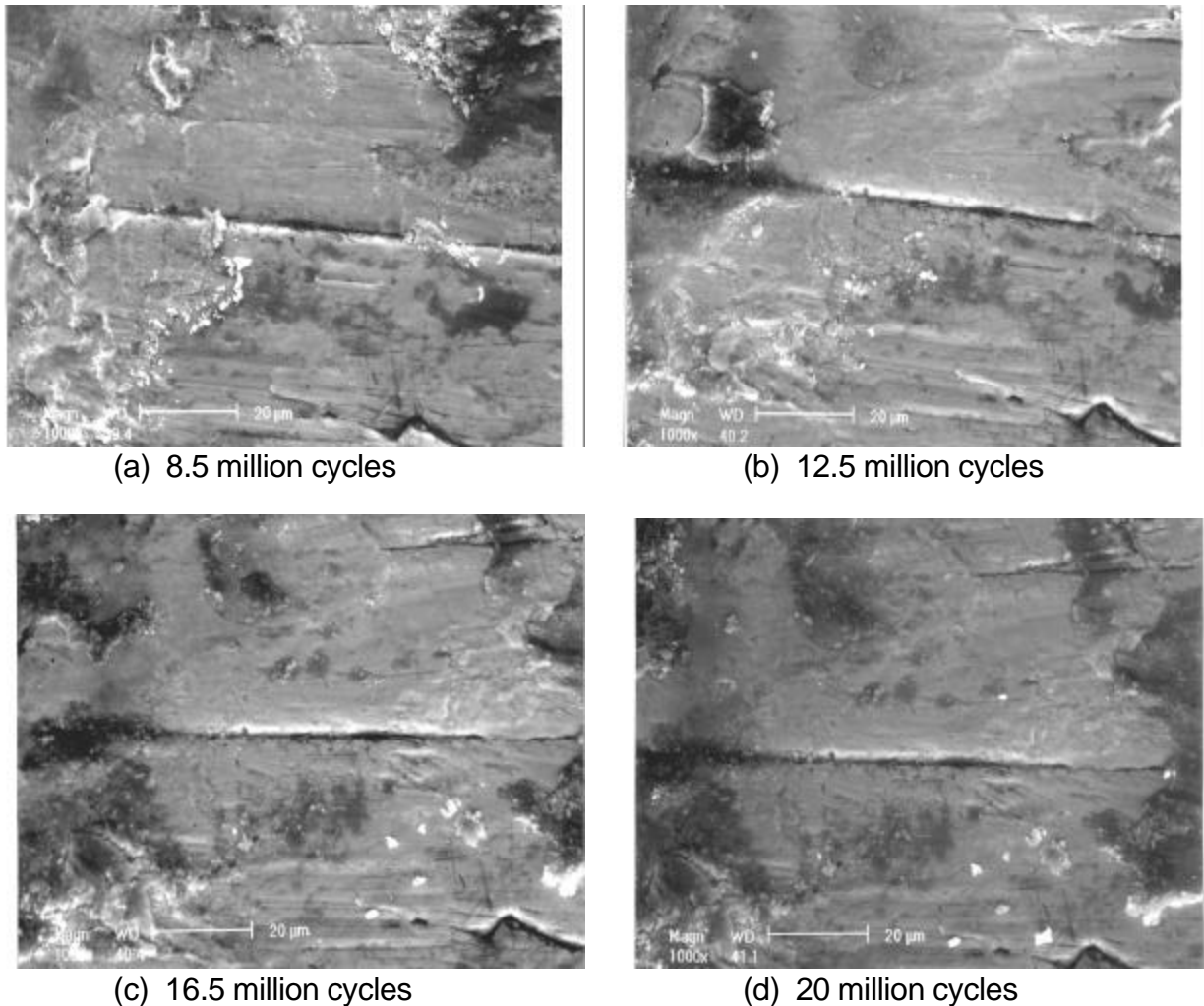


Figure 6E.36. In-situ observation of fretting surface topography with fatigue cycles showing that fretting products were created and removed continuously by fretting under a cylindrical pad subjected to 35 ksi bearing pressure and 31 ksi cyclic bulk tension.

Comparison of Model Predictions and Experimental Results

Effect of Bearing Stress on DS_{th}

A significant predictive capability of the WCF model is the treatment of both crack nucleation and propagation of small cracks. Figure 6E.37 shows the predicted threshold stresses for fretting crack nucleation, nonpropagation, and propagation to failure as a function of bearing pressure for Ti-6-4 subjected to gross slip conditions ($DQ^3 \pm mP$ with $m = 0.5$, where m is the coefficient of friction and P is the bearing load). The crack nucleation boundary was computed by setting the local fretting stress at the edge of

contact equal to the endurance limit at 10^7 cycles for $R = -1$, which is the stress ratio at the edge of contact. As seen in Figure 6E.37, the crack nucleation stress decreases rapidly with increasing bearing pressures. At or above 16 ksi bearing pressure, the local fretting stress is sufficiently large to initiate fatigue cracks without the aid of a cyclic bulk stress. Under this circumstance, the limiting HCF stress is controlled by the non-propagation of small cracks. The calculated crack nonpropagation boundary is in good agreement with experimental data generated at UTRC and SwRI. The UTRC data were generated at 20 Hz with fatigue lives in the range of 50 - 1000 k cycles. The HCF failure stress was obtained by extrapolating the experimental results to 10 cycles, Figure 6E.38. The SwRI data, which were generated at 2100 Hz under partial slip conditions, have been adjusted for gross slip based on the UTRC data, which were generated under gross slip condition. This was done so the data could be plotted on the same figure.

The GEAE data, which were obtained under fretting without a cyclic bulk stress, are shown at $DS = 1$ ksi because of the logarithmic axis. The local fretting stress at the contact edge is predicted to be less than the yield stress, 135 ksi, for bearing pressures less than 55 ksi. Thus, local yielding under the fretting pad is expected only when the bearing pressure exceeds 55 ksi.

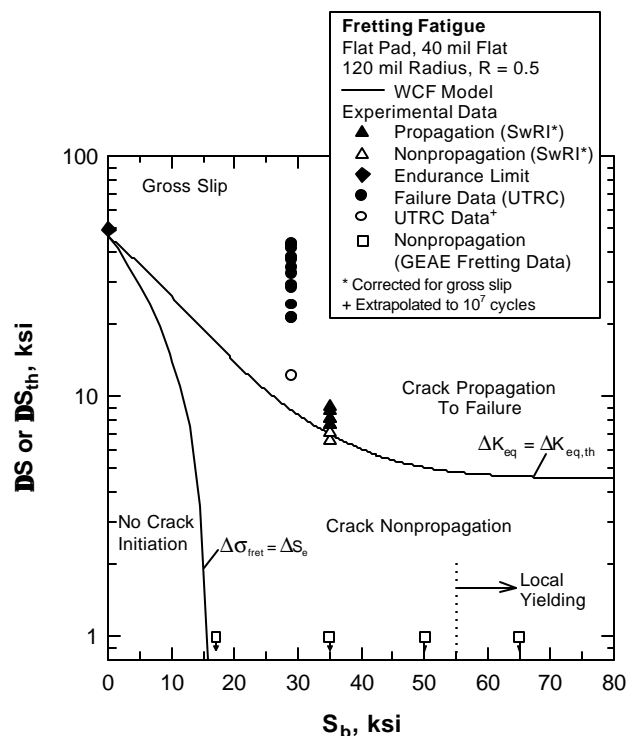


Figure 6E.37. Predicted threshold stresses for crack nucleation, nonpropagation and propagation to failure compared to fretting data (UTRC and SwRI) and fretting data (GEAE).

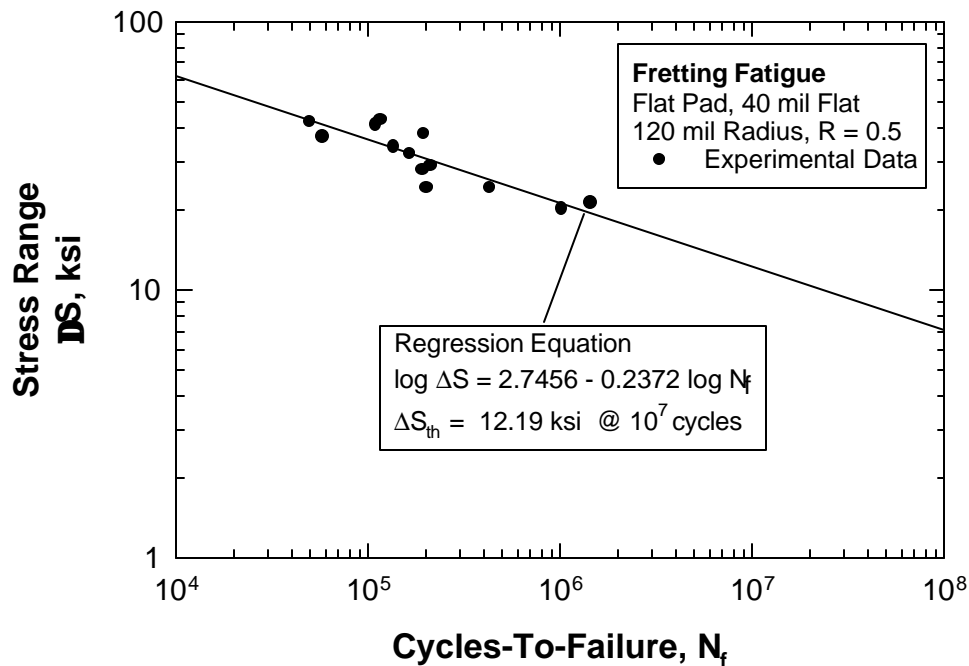


Figure 6E.38. Experimental data of failure stress for the $10^4 - 10^6$ lives from UTRC are extrapolated to 10^7 cycles to obtain the failure stress for comparison with the WCF model.

Figure 6E.39 shows the comparisons of the model against fretting fatigue data under partial slip conditions of $DQ/P = 0.56 - 0.73$. These data were generated at Purdue University for $R = 0$ and 0.5 at 10 Hz , with fatigue lives in the range of $50 - 1000 \text{ k cycles}$. For these cases, the calculated threshold stresses are compared against the failure stress values obtained by extrapolating the experimental results to 10^7 cycles, Figure 6E.39. Figures 6E.37 and 6E.39 indicate that the actual failure stresses and the extrapolated stresses all lie above the predicted threshold stress boundary for crack nonpropagation. Since all the experimental data were generated in the $10^4 - 10^6$ cycle range, the discrepancy might be indicative of difficulties in extrapolating a small range of LCF life data to the HCF regime due to variability in the slope of the S-N curve.

A comparison of the model calculation against experimental data for fretting fatigue tests with cylindrical pads and $DQ = 0$ is presented in Figure 6E.40. The threshold stress for this fretting fatigue condition is an horizontal line independent of bearing pressure because both DP and DQ are zero so that the only contributor to FCG

is the cyclic bulk stress. All three experimental data points lie below the predicted threshold stress, i.e., the dotted horizontal line and all exhibited no fatigue failure, despite the presence of considerable damage and debris on the fretting surfaces, Figure 6E.36. Since $DQ = 0$ for these test, the absence of fatigue failure in these specimens can be attributed to a cyclic bulk stress that is well below the endurance limit. For comparison, the predicted threshold stresses for gross slip with $DQ = \pm mP$ are also shown in Figure 6E.40 as the solid curve for the 1 inch radius pad and as the dashed line for the 120 mil. Both are lower than the dotted line for $DQ = 0$. The comparison indicates, in an indirect way, the importance of the DQ term during fretting fatigue under a constant bearing pressure. The result also explains the lack of fatigue crack nucleation in these specimens despite the presence of extensive fretting damage on the surface, Figure 6E.36.

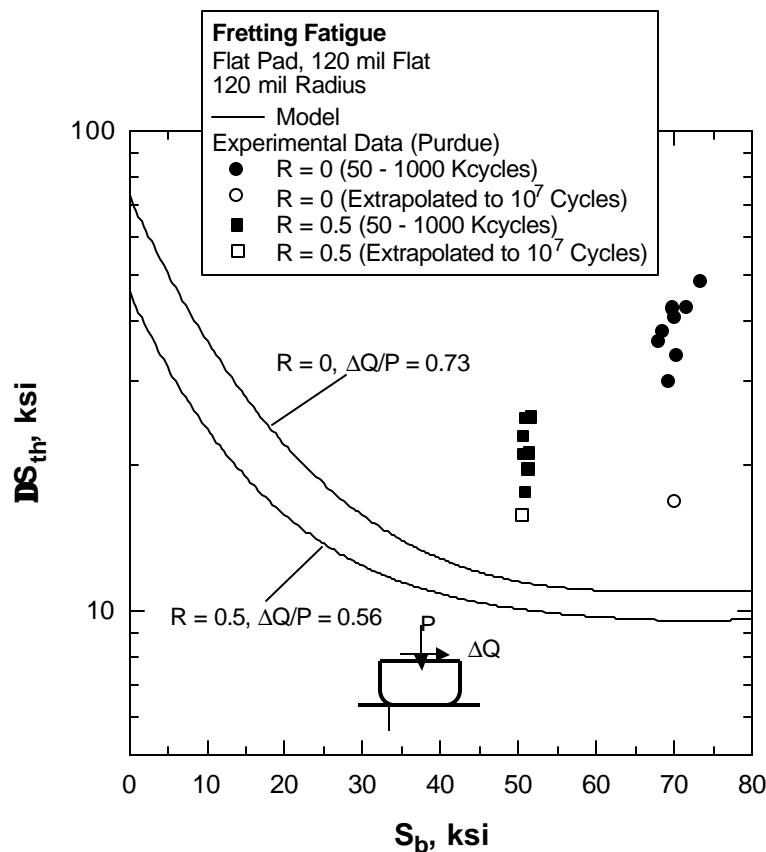


Figure 6E.39. Comparison of the WCF model against experimental data from Purdue for DQ/P ratios of 0.56 and 0.73.

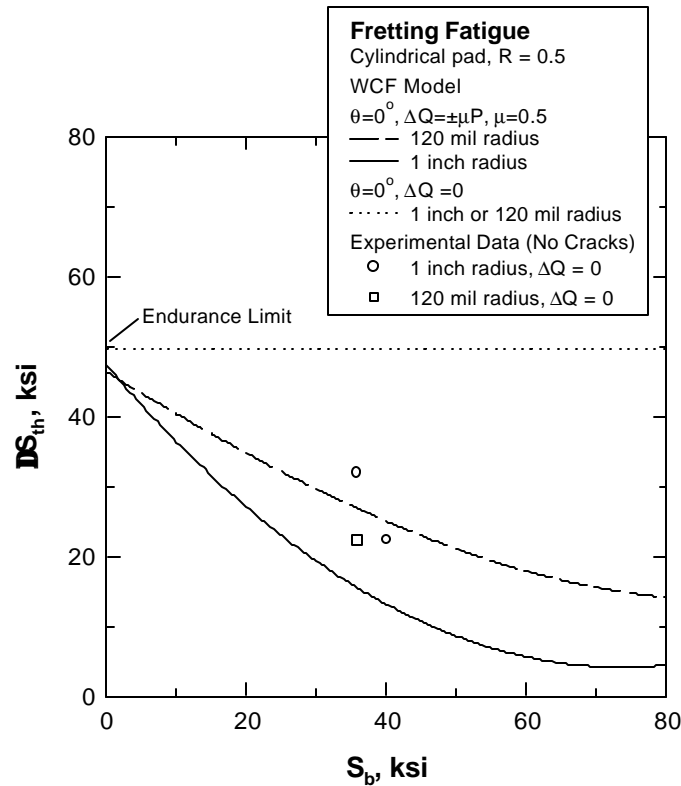


Figure 6E.40. Comparison of calculated threshold stress, DS_{th} , against SwRI experimental data for cylindrical pads subjected to a bearing pressure with and without a cyclic shear force DQ .

Exit Criteria Data

Table 6E.2 summarizes the data and the stress ranges estimates used to make the Actual / Predicted calculations that were used in Chapter 6 (Paragraph 6.4.3). This table was added by UDRI after SwRI provided the data in an EXCEL spreadsheet format. UDRI also dropped the points associated with specimens 633, 634 and 635 as a result of its evaluation of the test procedures or failure location for these specimens.

Table 6E.2
Actual to Predicted Axial Stress Ranges Based on WCF Model

Specimen No.	Test Type	Test Organization	Loading Axis (ksi)	Bearing Pressure (ksi)	Frequency Hz	R	Crack Shape/Size % %	Number of Cycles	Experimental (Actual) Axial Threshold Stress Range (ksi)	Predicted Axial Threshold Stress Range (ksi)	A/P Ratio
632	Fretting Fatigue	SwRI	Step Test*	35	2100	0.5	!	10 ⁷	28	30	0.93
636++	Fretting Fatigue	SwRI	Step Test*	35	2100	0.5	!	10 ⁷	28	30	0.93
633++	Fretting Fatigue	SwRI	30	35	2100	0.5	!	10 ⁷	30	25.4	1.18
635++	Fretting Fatigue	SwRI	30	35	2100	0.5	!	10 ⁷	30	23.1	1.30
	Fretting Fatigue	UTRC	Multiple Tests	29	20	0.5	!	10 ⁷	12.2*	8.9	1.35
	Fretting Fatigue	UTRC	Multiple Tests	29	20	0.6	!	10 ⁷	2.4**	7.14	0.34
	Fretting Fatigue	UTRC	Multiple Tests	29	20	0.83	!	10 ⁷	2.2**	3.2	0.69
	Fretting Fatigue	Purdue Univ.	Multiple Tests	50	10	0.5	!	10 ⁷	15.8*	10.1	1.56
	Fretting Fatigue	Purdue Univ.	Multiple Tests	70	10	0.5	!	10 ⁷	16.8*	11.0	1.53
	Fretting	GE	0	17	160	!	!	10 ⁷	72	68.7	1.05
	Fretting	GE	0	35	160	!	!	10 ⁷	48	35.6	1.35
	Pure Fatigue	Allied-Signal	Step Tests	0	60	0.5	!	10 ⁷	49.5	51.1	0.97

++ Later judged to be invalid tests by UDRI

* Threshold stresses obtained by extrapolating 10⁴-10⁶ cycle failure stresses to 10⁷ cycles.

** Failure stresses

% Step test starting at a stress range of 26 ksi with a 2 ksi stress increment after 10⁷ cycles at a load step.

%% Through thickness (2D) cracks were assumed in the worst-case fret model, but no assumption was made on the crack size

Effect of Shear Stress on DS_{th}

Figure 6E.41 shows a plot of the stress range as a function of the shear stress range on the fretting surface. The result for Specimen 632 indicates that nonpropagating microcracks were present at low stress levels (DS # 26 ksi), while propagating microcracks were observed at higher stress levels (DS # 28 ksi). Both the interrupted tests showed nonpropagating microcracks. The experimental data appear to show there is a stress level that separates crack nonpropagation and propagation. That stress boundary occurs over a small range of DS and Dt stresses, probably due to experimental variability. The boundary between nonpropagation and propagation cracks was predicted by the worst case fret model. As shown in Figure 6E.41, the threshold decreases with increasing Dt_{th} on the fretting surfaces. The predicted transition boundary is in good agreement with the experimental data for the loading path investigated. Also included in Figure 6E.41 are the fatigue limits for 10^7 cycles and the extrapolated fretting fatigue stress data from UTRC, which were obtained under gross slip conditions. In the case of the UTRC data, the fretting fatigue stress was obtained by extrapolating the experimental data to 10^7 cycles, Figure 6E.38. The experimental data are in agreement with the predicted crack-nonpropagation boundary.

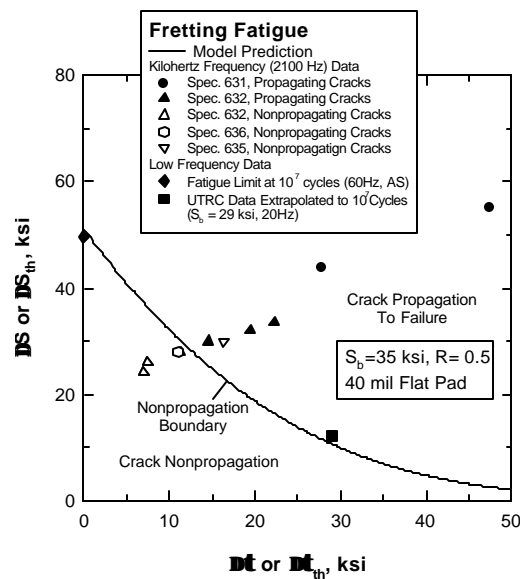


Figure 6E.41. Experimental data of threshold stress, DS_{th} , versus shear stress, Dt_{th} , on the fretting surfaces and comparison against the WCF model predictions.

Effect of Mean Stress and R-Ratio on DS_{th}

Model prediction of the mean stress effects on fretting fatigue was evaluated against the fretting fatigue data generated at UTRC. These data were generated for 40 mil flat pad with 120 mil radius edge using a bearing pressure of 29 ksi under gross slip conditions. The R ratios were 0.5, 0.6, and 0.83. The experimental conditions were used in the model calculations. For simulating gross slip, the condition of $\Delta Q = 2mP$ with $m = 0.5$ was used. The threshold stress range was calculated as a function of R and the result is presented in Figure 6E.42, which shows that DS_{th} decreases with increasing R values. The calculated crack-nonpropagation boundary for fretting fatigue is in reasonable agreement with the UTRC data of failure stress. Both the calculated and experimental fretting fatigue stresses are considerably lower than the smooth-bar endurance limit data from Allied Signal.

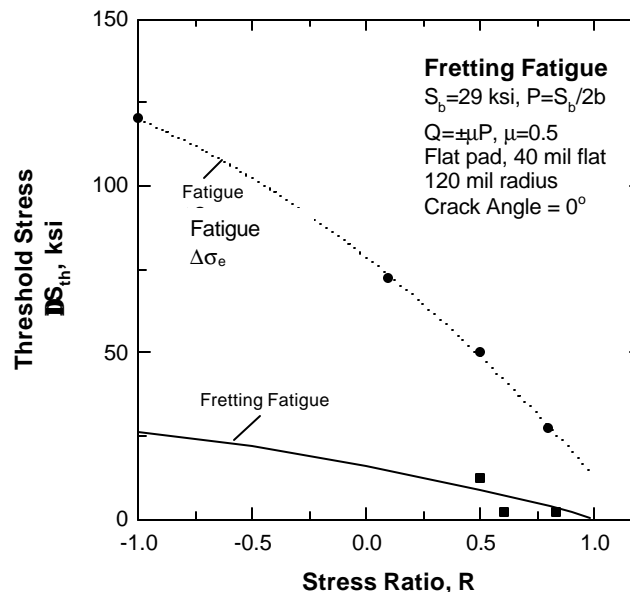


Figure 6E.42. Comparison of predicted threshold stress for fretting fatigue (at a bearing pressure, S_b , of 29 ksi) under gross slip conditions against the endurance limit for fatigue from Allied Signal and fretting fatigue data from UTRC as a function of R ratio.

Effect of Fatigue, Fretting, and Fretting Fatigue on DS_{th}

The threshold stresses for fatigue, fretting + fatigue, and fretting fatigue are compared as a function of the bearing pressure in Figure 6E.43 (a) and (b) for $R = 0.5$

and 0.1, respectively. The smooth specimen 10^7 fatigue limit is shown as a horizontal dotted line. Both the fretting + fatigue and fretting fatigue curves were computed for the gross slip condition since the experimental data were obtained under those conditions. The fretting + fatigue boundary was computed by applying the fretting condition to obtain the crack arrest length, L_f , for fretting under various bearing pressures. Subsequently, L_f was used in the small-crack threshold formulation, Eq. (6E.49), to compute the threshold stress for crack nonpropagation under fatigue in the absence of the fretting stress field. For the fretting fatigue boundary, both the fretting and fatigue stress fields were used simultaneously in the calculation. Figure 6E.43 indicates that the threshold stress for fretting + fatigue is consistently higher than that for fretting fatigue at the same bearing pressure and gross slip conditions. This is because the fretting stress field is not present during the fatigue portion of the test. At low bearing pressure, the threshold stress for fretting + fatigue is essentially the same as the endurance limit. This is because the lengths of the fretting cracks induced at low bearing pressures are smaller than the small crack parameter a_0 so that the existing fretting cracks have no effect on the subsequent fatigue behavior. The behavior is analogous to the observation that crack size exerts no effect on the threshold stress for crack size less than a_0 in the Kitagawa diagram [6E.13].

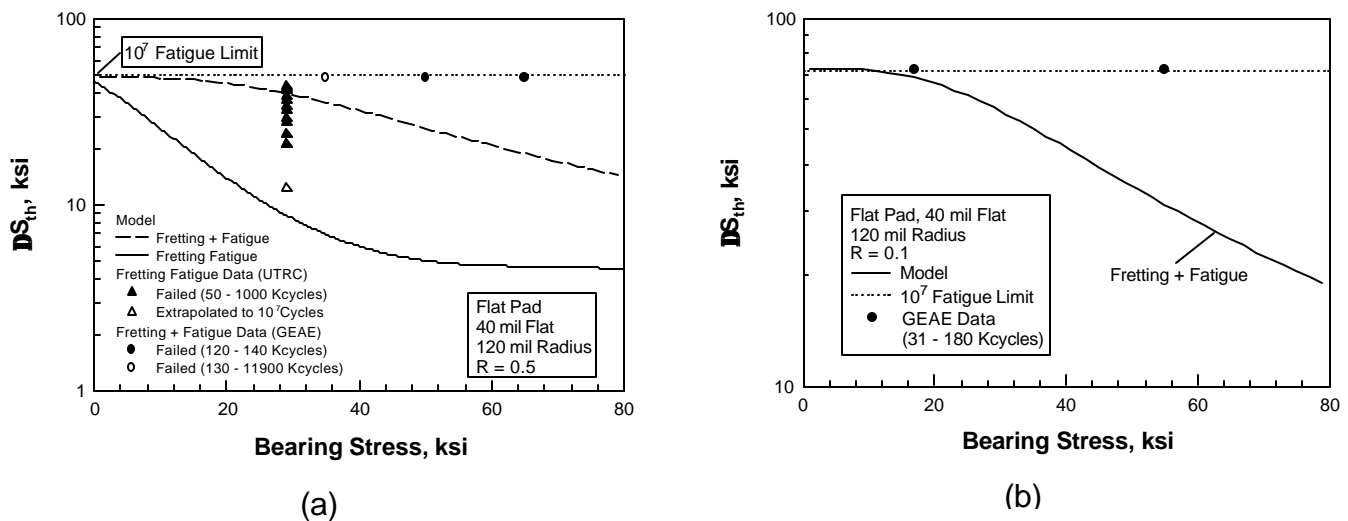


Figure 6E.43. Comparison of calculated and measured values of threshold stresses for fatigue (endurance limit), fretting & fatigue, and fretting fatigue: (a) $R = 0.5$, and (b) $R = 0.1$.

The calculated fretting fatigue boundary is in agreement with the fretting fatigue data from UTRC when the failure stress is extrapolated to 10^7 cycles, Figure 6E.43(a). All the fretting fatigue data lie above the fretting fatigue boundary, but are on or below the fretting + fatigue boundary. The fretting + fatigue data from GEAE are for fatigue under a stress range of 48 ksi only. They showed fatigue lives in the range of 120 – 140 k cycles at bearing pressures of 55 and 65 ksi; both are substantially above the predicted fretting + fatigue boundary. For 35 ksi bearing pressure, the fatigue life ranged from 120 – 12000 k cycles and the failure stress just lie above the predicted fretting + fatigue boundary for 10^7 fatigue cycles. In Figure 6E.43(b), the data showed fatigue life in the range of 31 – 180 k cycles. Since fretting + fatigue tests at lower stress levels were not conducted, it was not possible to extrapolate the experimental data to 10^7 fatigue cycles. Nonetheless, the fatigue life after fretting increases with decreasing bearing pressures used in fretting and approaches that of the endurance limit; this behavior is in agreement with the fretting + fatigue calculation.

Effect of Crack Orientation and Mode-Mixity on DS_{th}

The fretting fatigue cracks in the failed specimens propagated normal to the fretting surface and showed a nominal crack angle of 0° when viewed from the sides of the fractured specimens. An attempt was made to identify the crack angle close to the fretting surface, but the effort, which was not detailed or systematic, revealed no evidence that the crack angle was anything other than 0° . Fractography revealed the presence of rubbing and small, spherical debris on the fracture surfaces near the fretted region. The results are shown in Figure 6E.44 and they are indicative of the presence of a Mode II component during fretting fatigue.

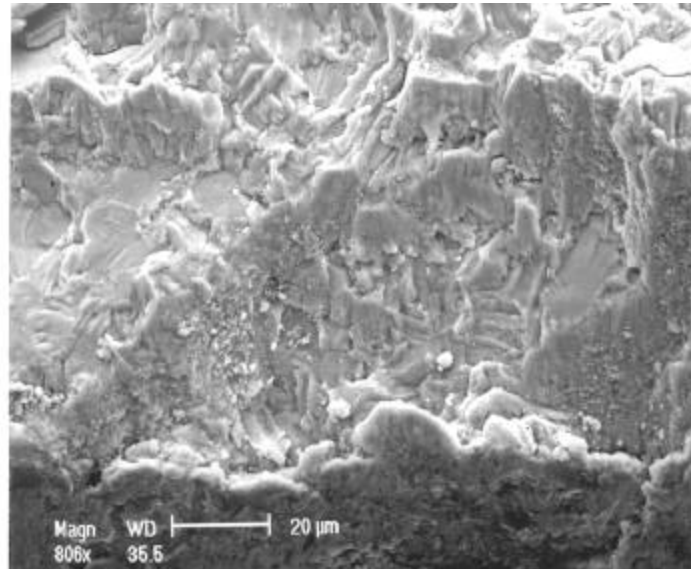


Figure 6E.44. Small, spherical oxide debris observed on the fracture surfaces of a Ti-6-4 fretting fatigue specimen. The oxide balls are indicative of rubbing of the fracture surfaces during mixed-mode crack propagation.

Measured vs Predicted Fretting Crack Arrest Lengths

Experimental values of the crack depth of fretting cracks observed in fretting tests performed at GEAE are compared against the model calculation in Figure 6E.45, which shows the arrested crack depth as a function of bearing pressure. For the conditions examined, the critical slip for the onset of gross slip was about 0.12-0.21 mil. Since the GEAE fretting tests were performed under slip distances of 0.5, 1, and 1.4 mils, gross slip was assumed in the model calculation. The model under-predicted the arrested crack lengths for 35 ksi pressure, but agreed with the experimental data for 50 and 65 ksi bearing pressures. The model predicted increasing arrested crack depths with increasing bearing pressure, while the experimental data did not show such dependence. Currently, there is no obvious explanation for the observed discrepancy. One possibility is that the experimental test conditions were not duplicated exactly in the model calculations.

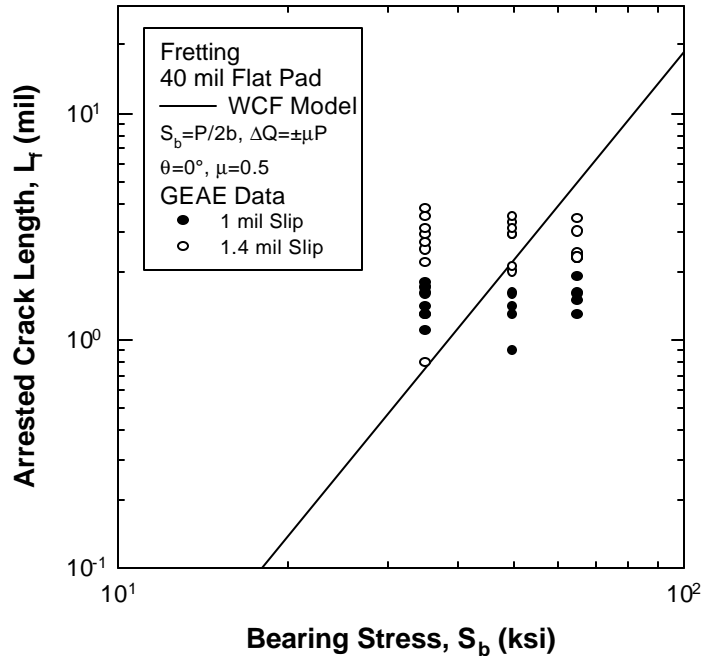


Figure 6E.45. Measured arrested crack lengths compared against WCF prediction for fretting in the absence of a cyclic bulk stress.

The findings of arrested cracks during fretting and fretting fatigue provided strong experimental support for the small-crack threshold formulation used in the WCF model. As presented earlier in Figure 6E.12, the large-crack threshold formulation predicted the absence of any fatigue crack growth for fretting cracks initiated under a bearing pressure of 35 ksi or 65 ksi. The observation of 1-4 mils cracks at these bearing pressures suggests that the fretting-initiated cracks propagated as small cracks and arrested when the FGG threshold exceeded the local crack driving force as the crack extended.

Similarly, the observation of crack arrests in the fretting fatigue experiments, Figure 6E.41, provides solid evidence for the small-crack behavior. The large-crack threshold predicts a decreasing threshold stress with increasing crack length and is capable of predicting crack arrest after an increment of crack extension.

Exit Criterion for WCF Model

Figure 6E.46 shows a comparison of the actual and predicted threshold stresses for all the predictions made by the WCF model. The comparison shows that the actual threshold stress is predicted to within a factor of two, with the exception of one data point that corresponds to fretting fatigue at a high R ratio. It should also be noted that the WCF threshold stress results are independent predictions since no experimental data, other than material properties, have been used to obtain the model predictions.

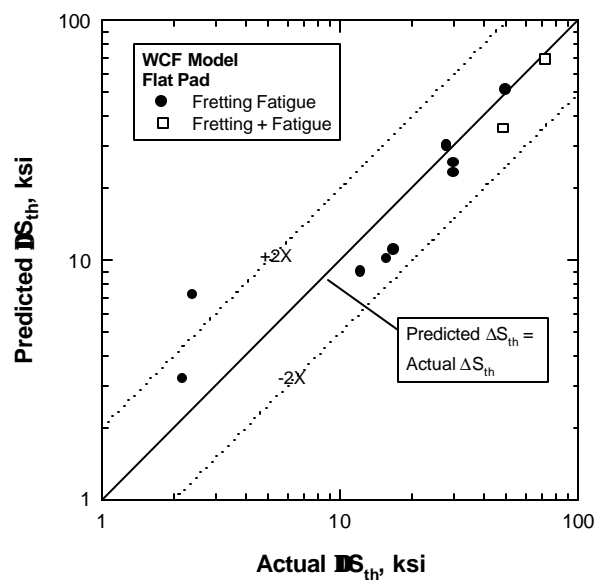


Figure 6E.46. Comparison of predicted threshold stresses from the WCF model against experimental values.

The cumulative distribution function, CDF, of the ratio of actual to predicted values for the WCF model is presented in Figure 6E.47, which includes results in terms of the threshold stress, ΔS_{th} , cyclic shear stress threshold, $\Delta \tau_{th}$, of fretting cracks, and the baseline mixed-mode threshold data, $\Delta K_{eq,th}$, in a Weibull distribution plot. The $\Delta \tau_{th}$ at a particular ΔS_{th} at the crack nonpropagation boundary is predicted most accurately by the WCF model. The WCF model also predicts the threshold stresses for fretting fatigue and fretting + fatigue quite well. The largest discrepancy is observed at fretting fatigue at high R ratios ($R = 0.6 - 0.83$), which correspond to the two points with the lowest A/P values. For all three types of prediction, the mean ratios are ≈ 1.10 , and the coefficients of variations (CoV) of the predicted quantities, ΔS_{th} and $\Delta \tau_{th}$, are less than 2.5 times of the CoV for the baseline data. These results are summarized in the insert shown in Figure 6E.47. Thus, the exit criteria set by the HCF team are met by the WCF methodology.

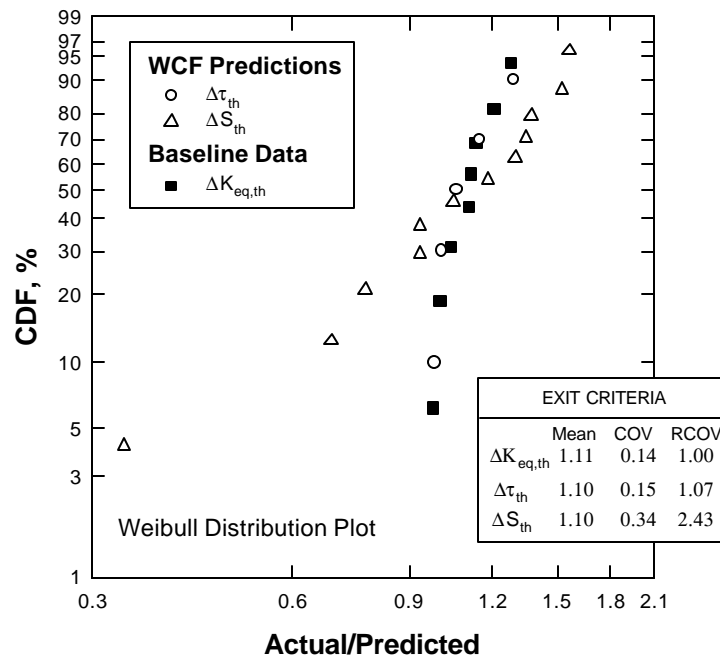


Figure 6E.47. A Weibull distribution plot of CDF vs A/P ratio for the WCF methodology. The insert shows evaluation of the model performance against the exit criteria. The goals of a mean ratio of less than 1 ± 0.15 and a relative coefficient of variation, RCoV, of 2.5 or less are met by the WCF model. The RCoV is defined as the CoV of the predicted quantity ($\Delta \tau_{th}$ or ΔS_{th}) normalized by the CoV of the baseline data, $\Delta K_{eq,th}$.

DISCUSSION

Transition of Laboratory Tests to Engine Components

The methodology developed in this program is applicable to predicting threshold stresses for engine conditions. The conditions used in the laboratory tests to verify the methodology, however, are substantially different from those encountered in the field. Thus, it is important to note the difference in the driving force for the growth of fretting fatigue cracks under laboratory and engine conditions. The K solution obtained in this program indicates that the stress intensity factors of a fretting fatigue crack are of the following form

$$\Delta K_I = f_1 \Delta P \sqrt{\frac{p}{a}} + f_2 \Delta Q \sqrt{\frac{p}{a}} + F_1 \Delta S \sqrt{pa} \quad (6E.50)$$

and

$$\Delta K_{II} = f_3 \Delta P \sqrt{\frac{p}{a}} + f_4 \Delta Q \sqrt{\frac{p}{a}} + F_2 \Delta S \sqrt{pa} \quad (6E.51)$$

where \mathbf{DP} is the cyclic normal load and ΔQ is the cyclic shear force per unit thickness on the fretting surfaces; \mathbf{DS} is the cyclic bulk stress; a is crack depth; f_i , and F_i are boundary correction factors. For laboratory fretting or fretting fatigue tests, the bearing pressure is generally constant so that $\mathbf{DP} = 0$, while $\mathbf{DP} \neq 0$ in the field. Because of this, the threshold stresses computed based on laboratory conditions cannot be applied directly to the field. Instead, the methodology developed in this program, which include the contact stress field, K solutions, the small-crack threshold formulation, and the computation procedure should be applied to calculate the appropriate \mathbf{DK} values and then the threshold stresses corresponding to values of \mathbf{DP} , \mathbf{DQ} , and \mathbf{DS} that are typical of engine operations.

Vibratory loads in engine operation typically involve \mathbf{DP} and \mathbf{DQ} superimposed on a relative constant bulk stress, S . A previous analysis [4.14] indicated that fretting under \mathbf{DP} and S can be simulated in laboratory specimens using a constant bearing load, P , and a cyclic bulk stress range, \mathbf{DS} , by matching the local stresses and slip displacements at the edge of contact. In contrast, such a matching of local stresses and slip displacements cannot be obtained for \mathbf{DQ} loading. Thus, tangential (shear) force loading must be present in fretting fatigue of laboratory specimens. Then, engine

loading scenarios can be simulated in laboratory fretting fatigue specimens using a combination of constant bearing pressure, cyclic shear traction, and cyclic bulk stress. The inertia-induced DQ and DS at a constant P in the high-cycle fretting fatigue rig at SwRI provide the capability of simulating fretting fatigue loading scenarios that are similar to those in engine components.

Local Plasticity and Crack Nucleation

The WCF model has been developed on the basis of the nonpropagation of small fatigue cracks in an elastic stress field. The assumption that an elastic analysis applies to this problem has been examined by computing the elastic stresses (s_x , s_y , and t_{xy}) at the trailing edge ($x = -d$, $y = 0$) of the contact zone. At this location, the only non-zero stress is s_x , which is tensile. Figure 6E.48 shows the local fret stress, s_x , at the trailing edge as a function of the bearing pressure. As seen in Figure 6E.48, s_x increases with increasing bearing pressure. Two important findings are obtained from Figure 4 48, which are (1) the endurance limit for $R = -1$ is exceeded by the local stress, s_x , when the bearing pressure is above 16 ksi, and (2) the yield stress of Ti-6-4, which is 135 ksi, is not exceeded until the bearing pressure exceeds 55 ksi. The endurance limit of $R = -1$ was used in this comparison because an R ratio of -1 occurs at the trailing edge during fretting.

The implications of the results shown in Figure 6E.48 are: (1) fretting is controlled by crack nucleation only at bearing pressures below 16 ksi, e.g., see Figure 6E.37, and (2) the K -based analysis used in the WCF methodology is applicable at least up to a bearing pressure of 55 ksi because the material is elastic. For bearing pressures above 55 ksi, the WCF methodology might also be applicable because plastic flow under the fretting pad is likely to be localized and contained.

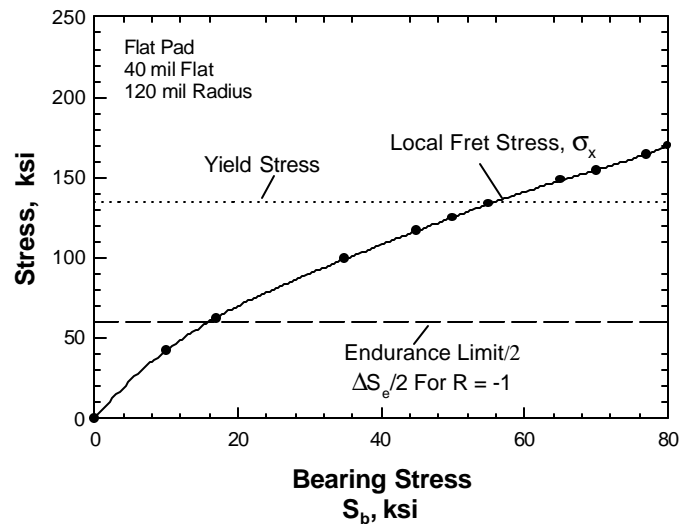


Figure 6E.48. Fretting stress, s_x , at the trailing edge of contact for various bearing pressures compared to the endurance limit for $R = -1$ and the yield stress, 135 ksi, for Ti-6Al-4V. The stress state at the trailing edge corresponds to $R = -1$.

Threshold Stress for Nonpropagating Fretting Fatigue Cracks

The results of this investigation demonstrated that the threshold stress for crack nonpropagation is dominated by the small-crack behavior. In particular, accurate prediction of the threshold stress for nonpropagation requires the use of a crack size-dependent FCG threshold that is characteristic of small fatigue cracks. The use of the large-crack threshold grossly overpredicts the limiting threshold stress when the crack size is small, e.g., less than about 2-mil. Interrupted and step-stress fatigue tests indicated that FCG represents a significant portion (more than 50%) of the total fatigue life. The experimental evidence indicates that high-cycle fretting fatigue failure is not controlled by crack nucleation, but involves, if not being controlled, the propagation/nonpropagation of small cracks. Thus, the small-crack fracture mechanics methodology developed in this program is a relevant and important technology for treating and designing against high-cycle fretting fatigue.

The threshold stress for fretting fatigue is significantly lower than those of fretting + fatigue or the fatigue limit. The threshold stress is especially low for fretting under gross slip at high R ratios. A high mean stress is detrimental for fretting fatigue resistance because it reduces the FCG threshold to a value smaller than the crack driving force of a fretting crack such that further crack propagation requires little or no contribution from

the bulk stress. Because of the low threshold stress, fretting at a high mean stress, or R ratio, would likely lead to HCF failure and should be eliminated by design.

Fretting + fatigue tends to overpredict the threshold stress for crack nonpropagation. Its possible use as a predictor for the onset of fretting fatigue does not appear to be supported by the experimental or analytical results. The largest difference between fatigue, fretting + fatigue, and fretting fatigue occurs at low bearing pressures. Under this circumstance, fretting + fatigue can yield a threshold stress that is almost identical to the fatigue limit. This occurs when the crack length induced by fretting at a low bearing pressure is substantially less than the small crack parameter a_o . As in smooth specimens, the threshold stress for small cracks less than a_o is independent of crack length and has a value virtually equal to the fatigue limit. For small crack sizes, fretting fatigue cracks exhibit substantially lower threshold stresses because both the contact and the far-field stresses contribute to the growth of the fretting fatigue cracks.

SUMMARY AND CONCLUSIONS

A fracture mechanics-based methodology for treating high-cycle fretting fatigue has been developed on the basis of the worst-case fret concept. The essential feature of this methodology are (1) an integral-equation method for computing the contact stress field, (2) a continuum dislocation method for calculating the stress intensity factors of an arbitrary oriented crack, (3) an equivalent stress intensity range for representing the crack driving force and a crack-size dependent fatigue crack growth threshold for governing the nonpropagation of mixed mode small fatigue cracks, and (4) a numerical procedure for computing the threshold stress for crack nonpropagation on the basis that the equivalent stress intensity range equals the FCG threshold for the local conditions.

A significant predictive capability of the worst case fret model is the prediction of the threshold stress for fretting crack nucleation, nonpropagation, and propagation to failure as a function of bearing pressure. Other capabilities of the model include predictions of the effects of stress ratio, coefficient of friction, pad geometry, and loading mode on the threshold stress, as well as predictions of crack orientation and crack arrest lengths.

For laboratory fretting or fretting fatigue tests, the bearing pressure is generally constant so that $DP = 0$, while $DP \neq 0$ in the field. Because of this, the threshold stresses computed based on laboratory conditions cannot be applied directly to the field. Instead, the methodology developed in this program, which include the contact stress field, K solutions, the small-crack threshold formulation, and the computation procedure should be applied to calculate the appropriate DK values and then the threshold stresses corresponding to values of DP , DQ , and DS that are typical of engine operations.

The proposed methodology has been evaluated by comparing independent model predictions against a wide range of laboratory data generated by the fretting team for Ti-6-4. Many essential features of the WCF methodology have been verified by experimental results both in the low-cycle and high-cycle life regimes. Important conclusions that have been obtained for the laboratory conditions examined in this study are as follows:

1. Fretting fatigue cracks in Ti-6-4 initiate relatively early in life and high-cycle fretting fatigue life (or endurance limit) is controlled by the nonpropagation of mixed-mode small cracks at bearing pressures greater than 16 ksi. Crack nucleation dominates the fretting fatigue life when the bearing pressure is less than 16 ksi. The threshold stress for crack nonpropagation can be substantially higher than that for crack nucleation.
2. A small-crack threshold is essential for predicting the threshold stress for nonpropagation of fretting fatigue cracks in Ti-6-4. The large-crack threshold overpredicts the threshold stress and is incapable of predicting crack arrest after an increment of crack extension. Experimental observation of crack arrest suggests that fretting fatigue cracks propagated as small cracks.
3. Crack arrest lengths measured in fretting tests indicate that the fretting cracks propagated as small cracks after nucleation. The large-crack threshold predicted either no crack growth or much smaller crack arrest lengths under identical conditions.
4. The threshold stress for nonpropagation of fretting cracks depends on the shear traction on the fretting surfaces. The value of the threshold stress decreases with increasing shear traction.

5. The threshold stress for fretting fatigue decreases with increasing bearing pressure; however, a minimum threshold stress is reached at high bearing pressure.
6. Fretting fatigue cracks are inherently mixed-mode cracks even when they propagate normal to the fretting surface. For conditions examined here, the crack orientation with the lowest threshold stress is a crack angle of 0° , which corresponds to crack propagation perpendicular to the fretting surfaces.
7. The driving forces for fretting fatigue cracks originate from the cyclic bearing load, cyclic shear force, and the cyclic bulk tension. The cyclic bearing load term is not represented in laboratory fretting fatigue experiments performed under a constant bearing pressure, but its effect can be simulated through the use of a proper cyclic bulk stress.
8. Threshold stresses for fatigue, fretting + fatigue, and fretting fatigue are all reduced by increasing R. Fretting fatigue exhibits the lowest threshold stress because both the fretting and bulk stresses contribute to the propagation of the fatigue cracks.
9. Stress intensity factors due to the fretting stresses can be described in a form that is similar to those of normal and shear point loads.
10. The WCF methodology developed herein meets the exit criteria set by the HCF team.

REFERENCES

- 6E.1 Hudak, S.J., JR, McClung, R.C., Chan, K.S., Chell, G.G., and Davidson, D.L., "High Cycle Fatigue of Turbine Engine Materials, PRDAV Improved High-Cycle Fatigue Life Prediction Annual Report, University of Dayton, Dayton, OH, 1997.
- 6E.2 Ciavarella, M., Hills, D.A. and Monno, G., "The Influence of Rounded Edges on Indentation by a Flat Punch," Proc. Instn. Mech. Engrs., Vol. 212, Part C, 1998, pp. 319-328.
- 6E.3 Gradshteyn, I.S. and Ryzhik, I.M., Table of Integrals Series and Products (Translated by Alan Jeffrey), 1965 (Academic Press).
- 6E.4 Muskhelishvili, N.I., Some Basic Problems of the Mathematical Theory of Elasticity, 1953 (Noordhoff, Groningen).

- 6E.5 Szolwinski, M.P., Harish, G., and Farris, T.N., "The Development and Validation of Design-Oriented Metrics for Fretting Fatigue in Titanium Engine Components," *Mech. Behavior of Advanced Materials*, ASME, MD-Vol. 89, 1998, pp. 11-18.
- 6E.6 Nowell, D. and Hills, D.A., "Open Cracks at or Near Free Edges," *Journal of Strain Analysis*, Vol. 22, No. 3, 1987, pp. 177-185.
- 6E.7 Dundurs, J. and Sendeckyj, G.P., "Behavior of an Edge Dislocation Near a Bimetallic Interface," *J. App. Phys.*, Vol. 36, 1965, pp. 3353-3354.
- 6E.8 Erdogan, F. and Gupta, G.D. and Cook, T.S., "Numerical Solution of Singular Integral Equations," in *Methods of Analysis and Solutions of Crack Problems* (Edited by G.C. Sih), 1973, pp. 368-425 (Noordhoff, Leyden).
- 6E.9 Krenk, S., On the Use of the Interpolation Polynomial for Solutions of Singular Integral Equations, *Q. Appl. Maths*, Vol. 32, 1975, pp. 479-484.
- 6E.10 Murakami, Y., ed., *Stress Intensity Factors Handbook*, Vol. 1, 1981 (Pergamon Press), p. 107.
- 6E.11 Campbell, J.P. Thompson, A.W., and Ritchie, R.O., "Mixed-Mode Crack-Growth Thresholds in Ti-6Al-4V under Turbine-Engine High-Cycle Fatigue Loading Conditions," *The 4th National Turbine Engine High Cycle Fatigue (HCF) Conference*, Monterey, CA, February 1999.
- 6E.12 Hudak, S.J., Jr., Chell, G.G., Rennick, T.S., McClung, R.C., and Davidson, D.L., "A Damage Tolerance Approach to FOD Based on the Worst Case Notch Concept, *Proceedings of the 4th National Turbine Engine High Cycle Fatigue Conference*, Monterey, CA, February 1999.
- 6E.13 Kitagawa, H., and Takahashi, S., "Applicability of Fracture Mechanics to Very Small Cracks or the Cracks in the Early Stage," *Proceedings of the 2nd International Conference on Mechanical Behavior of Materials*, Boston, MA, 1967, pp. 627-631.
- 6E.14 Hudak, S.J., Jr., "High Cycle Fatigue of Turbine Engine Materials," *Monthly Status Reports for April and May, 1998*, SwRI Project No. 18-8653, Southwest Research Institute.